THE JOURNAL
OF
CHEMICAL PHYSICS

VOLUME 35, NUMBER 3 SEPTEMBER, 1961

Wave Functions and Intensity Calculations for a Rotating Anharmonic Oscillator

THOMAS C. JAMES *

Department of Chemistry, Northwestern University, Evanston, Illinois

(Received November 21, 1960)

Wave functions which are good through second-order perturbation theory are given for a harmonic oscillator perturbed by a potential of the form $V=\hbar w(ax+bx^2+cx^3)$. These results are then applied to the case of a rotating anharmonic oscillator. Expressions are also given for overlap integrals $\langle \bar{n} \mid m \rangle$ between different unperturbed harmonic oscillator wave functions. A brief comparison of this treatment with similar treatments is given and a discussion of rotation-vibration interaction in non $^1\Sigma$ states is included. The application to intensity calculations in electronic and infrared spectra is discussed. An approximate expression for the dipole moment matrix element $\langle 1J' \mid u \mid 0J \rangle$ is given.

INTRODUCTION

DURING the past few years there has been a considerable interest in calculations of rotational line intensities which take into account the interaction between vibration and rotation.[1,2] Although the majority of these calculations have been concerned with line intensities in infrared vibration-rotation spectra, there have been a few calculations of this nature applied to electronic transitions.[3–5] The difference in the shapes and positions of the potential energy curves involved in an electronic transition increases the complexity of these calculations considerably. Since the results of a calculation are sensitive to the differences in the two potential energy curves involved, it will frequently be desirable to have more exact expressions in electronic transitions than would be required for vibration-rotation spectra. In this paper expressions are given, which are correct through second-order perturbation theory, for the calculation of rotational line intensities in a rotating anharmonic oscillator.

Since a number of investigations have shown that it is necessary to take into account the variation of the electronic transition moment with internuclear distance in order to calculate reliable intensities,[6,7] one has to calculate the variation with rotational quantum numbers of matrix elements of the form

$$\int \Phi_{v'J'}(r-r_e/r_e)^n \psi_{v''J''} dr$$

as well as the variation with rotational quantum numbers of overlap integrals or Franck-Condon factors. These overlap integrals and matrix elements can be reduced to a sum of terms involving the product of J dependent coefficients and overlap integrals between two different harmonic oscillator wave functions. While the actual calculation of the J dependence of the electronic transition moment matrix elements still remains a lengthy process, the expressions given in this paper reduce the amount of labor to the point where they are feasible. Expressions are only given for the three lowest vibrational levels of the electronic states involved. For these lower levels a second order perturbation calculation which takes into account the cubic term in the vibrational anharmonicity should provide fairly reliable results.

THEORY

Apart from populations of states involved and frequency dependent factors, line intensities in electronic

* Present address: Physics Section, Convair, San Diego, California.

[1] R. Herman and R. F. Wallis, J. Chem. Phys. **23,** 637 (1955).
[2] R. Herman, R. Rothery, and R. Rubin, J. Mol. Spectroscopy **2,** 369 (1958).
[3] R. C. M. Learner and A. G. Gaydon, Nature **183,** 242 (1959).
[4] T. C. James, J. Chem. Phys. **32,** 1770 (1960).
[5] P. A. Fraser, Scientific Rept. No. 6, Molecular Excitation Group, Department of Physics, University of Western Ontario (1958).
[6] P. A. Fraser, Can. J. Phys. **32,** 515 (1954).
[7] R. W. Nicholls, Proc. Phys. Soc. (London) **A69,** 741 (1956).

Copyright © 1961 by the American Institute of Physics

TABLE I.[a]

$A_0^0=0$
$A_1^0=-(1/\sqrt{2})(a+\frac{3}{2}c)$
$A_2^0=-(\sqrt{2}/4)(b)$
$A_3^0=-(\sqrt{3}/6)(c)$
$A_0^1=(1/\sqrt{2})(a+\frac{3}{2}c)$
$A_1^1=0$
$A_2^1=-(a+3c)$
$A_3^1=-[(6)^{\frac{1}{2}}/4](b)$
$A_4^1=-(\sqrt{3}/3)(c)$
$A_0^2=(\sqrt{2}/4)(b)$
$A_1^2=a+3c$
$A_2^2=0$
$A_3^2=-(3/2)^{\frac{1}{2}}[a+(9/2)c]$
$A_4^2=-(\sqrt{3}/2)(b)$
$A_5^2=-\frac{1}{3}(15/2)^{\frac{1}{2}}(c)$
$B_0^0=-\frac{1}{4}[a^2+3ac+(29/12)c^2+\frac{1}{4}b^2]$
$B_1^0=(b/\sqrt{2})[\frac{3}{2}a+(7/2)c]$
$B_2^0=(1/2\sqrt{2})[a^2+5ac+(27/4)c^2+b^2]$
$B_3^0=(\sqrt{3}/3)[\frac{3}{4}ab+(19/8)bc]$
$B_4^0=\frac{1}{4}(\frac{3}{2})^{\frac{1}{2}}[(4/3)ac+(7/2)c^2+(b^2/2)]$
$B_5^0=(15^{\frac{1}{2}}/12)(bc)$
$B_6^0=(5^{\frac{1}{2}}/12)(c^2)$
$B_0^1=-(b/\sqrt{2})[2a+(21/4)c]$
$B_1^1=-\frac{1}{4}[3a^2+15ac+(251/12)c^2+\frac{3}{4}b^2]$
$B_2^1=(5/4)(ab)+(53/8)(bc)$
$B_3^1=[(6)^{\frac{1}{2}}/2][\frac{1}{2}a^2+(23/6)ac+(67/8)c^2+\frac{1}{2}b^2]$
$B_4^1=(b\sqrt{3}/3)[\frac{3}{2}a+7c]$
$B_5^1=\frac{1}{4}[(15/2)^{\frac{1}{2}})^{\frac{1}{2}}][(4/3)ac+(11/2)c^2+1/2b^2]$
$B_6^1=(5/4)(10)^{\frac{1}{2}}(bc)$
$B_7^1=[(35)^{\frac{1}{2}}/4](c^2)$
$B_0^2=(\sqrt{2}/2)[\frac{1}{2}a^2+\frac{3}{2}ac-(9/8)c^2-\frac{1}{2}b^2]$
$B_1^2=(-b/4)[9a+(87/2)c]$
$B_2^2=-\frac{1}{4}[5a^2+39ac+(965/12)c^2+(7/4)b^2]$
$B_3^2=(\frac{3}{2})^{\frac{1}{2}}b[a+(107/12)c]$
$B_4^2=(\sqrt{3}/2)[a^2+(31/3)ac+(121/4)c^2+b^2]$
$B_5^2=\frac{3}{2}(15/2)^{\frac{1}{2}}b[\frac{3}{2}a+(37/4)c]$
$B_6^2=\frac{3}{4}(5/2)^{\frac{1}{2}}[(4/3)ac+(15/2)c^2+\frac{1}{2}b^2]$
$B_7^2=\frac{1}{4}(35)^{\frac{1}{2}}(bc)$
$B_8^2=(1/6)(35)^{\frac{1}{2}}(c^2)$

[a] This table gives the values of the quantities A_n^v and B_n^v of Eq. (4) in terms of the quantities a, b, and c defined in Eq. (5) of the text. Expressions for the A_n^v and B_n^v's are given only for the first three vibrational levels.

transitions are proportional to the quantity

$$\left[\int\Phi_{v'J'}R(r)\psi_{v''J''}dr\right]^2 S_{J'J''}. \qquad (1)$$

In the above expression $S_{J'J''}$ is the rotational line strength.[8] The values for this quantity depend on the type of electronic transition, but are independent of any vibration-rotation interaction. Vibration-rotation interaction affects intensities because it causes the vibrational wave functions to depend on the rotational quantum numbers of the particular levels involved. The functions $\Phi_{v'J'}$ and $\psi_{v''J''}$ are vibrational wave functions corresponding to the v' and v'' levels. Different symbols have been used as a reminder that the vibrational wave functions involved correspond to different electronic states of a molecule. If one allows for the fact that, in general, the transition moment varies with internuclear distance, the transition moment matrix element becomes

$$R(r_e)\left[\int\Phi_{v'J'}\psi_{v''J''}dr+\chi\int\Phi_{v'J'}\xi\psi_{v''J''}dr\right], \qquad (2)$$

where $\chi=(\partial R/\partial r)_{r_e''}r_e''/R(r_e'')$ and $\xi=(r-r_e'')/r_e''$. From this expression it is seen that in order to calculate line intensities it is necessary to calculate both of the quantities

$$\int\Phi_{v'J'}\psi_{v''J''}dr$$

and

$$\int\Phi_{v'J'}\xi\psi_{v''J''}dr.$$

The wave functions ψ_{vJ} can be expressed as a linear combination of harmonic oscillator functions ϕ_n. The functions ψ_{vJ} are then solutions to the equation $\mathcal{H}\psi_{vJ}=E_{vJ}\psi_{vJ}$ where the Hamiltonian $\mathcal{H}$ is given by $\mathcal{H}=\mathcal{H}_0+V$. $\mathcal{H}_0$ is the Hamiltonian for a harmonic oscillator and V is a perturbation which takes into account the anharmonicity and the rotation of the molecule.

Consider a harmonic oscillator with energy $\hbar w(n+\frac{1}{2})$, which is perturbed by a term $V=\hbar w(ax+bx^2+cx^3)$, where x obeys the relation

$$x\phi_n=[(n+1)/2]^{\frac{1}{2}}\phi_{n+1}+(n/2)^{\frac{1}{2}}\phi_{n-1}. \qquad (3)$$

The solutions to this problem, correct to second order, are then given by $\psi_v=\phi_v+\sum_n c_n^v\phi_n$. The quantities $c_n^v=A_n^v+B_n^v$ are the sum of a first-order correction term A_n^v and a second-order correction term B_n^v which are given by

$$A_n^v=\frac{V_{nv}}{E_v^0-E_n^0}; \qquad A_v^v=0$$

$$B_n^v=\sum_m{}'\frac{V_{nm}V_{mv}}{(E_v^0-E_m^0)(E_v^0-E_n^0)}-\frac{V_{vv}V_{vn}}{(E_v^0-E_n^0)^2};$$

$$B_v^v=-\tfrac{1}{2}\sum_n|A_n^v|^2. \qquad (4)$$

[8] G. Herzberg, *Spectra of Diatomic Molecules* (D. Van Nostrand Company, Inc., New York, 1950), 2nd ed.

By using these expressions and the result (3), the quantities A_n^v and B_n^v can be calculated in a straightforward manner. The results for the first three vibrational levels are summarized in Table I.

The results for a rotating anharmonic oscillator can be obtained from Table I by noting that the quantities a, b, and c which appear in the expressions for A_n^v and B_n^v are given by

$$\begin{aligned} a&=-\gamma^{3/2}J(J+1)\\ b&=\tfrac{3}{2}\gamma^2 J(J+1)\\ c&=(a_1/2)\gamma^{1/2}-2\gamma^{5/2}J(J+1), \end{aligned} \tag{5}$$

where $\gamma=2B_e/w_e$. a_1 is the coefficient of $a_0\xi^3=a_0[(r-r_e)/r_e]^3$ in the expansion of the potential energy $U(r)=a_0\xi^2(1+a_1\xi+\cdots)$. The remaining terms in the above expressions come from the expansion of the rotational energy in powers of ξ, neglecting terms beyond ξ^3.

Thus the coefficients c_n^v in the expansion of the wave functions in terms of harmonic oscillator functions are J dependent and would best be written as $c_n^v(J)$. The results of Table I apply to either of the electronic states involved. The values of γ and a_1 will be different, of course, in the two different electronic states. Therefore we have

$$\begin{aligned} \psi_{v''J''}&=\phi_{v''}+\sum_n c_n^{v''}(J'')\phi_n\\ \Phi_{v'J'}&=\bar{\phi}_{v'}+\sum_n \bar{c}_n^{v'}(J')\bar{\phi}_n. \end{aligned} \tag{6}$$

The quantities c_n^v are given in Table I and depend on the rotational quantum number. For compactness of notation they will hereafter be designated as simply c_n^v and $\bar{c}_n^v$, with the understanding that they actually depend on J'' and J'.

In order to calculate the matrix element (2) each of the quantities

$$\int \Phi_{v'J'}\psi_{v''J''}d\tau \quad \text{and} \quad \int \Phi_{v'J'}\xi\psi_{v''J''}d\tau$$

can be calculated separately. The resulting expressions for overlap integrals, correct to second order, are as follows[9]:

$$\begin{aligned}
\int \Phi_{0J'}\psi_{0J''}d\tau &= \langle\bar{0}\mid 0\rangle+\sum_{k=0}^{6}c_k^0\langle\bar{0}\mid k\rangle+\sum_{k=0}^{6}\bar{c}_k^0\langle\bar{k}\mid 0\rangle+\sum_{l=1}^{3}\sum_{m=1}^{3}\bar{A}_l^0A_m^0\langle\bar{l}\mid m\rangle\\
\int \Phi_{1J'}\psi_{0J''}d\tau &= \langle\bar{1}\mid 0\rangle+\sum_{k=0}^{6}c_k^0\langle\bar{1}\mid k\rangle+\sum_{k=0}^{7}\bar{c}_k^1\langle\bar{k}\mid 0\rangle+\sum_{l=0}^{4}\sum_{m=1}^{3}\bar{A}_l^1A_m^0\langle\bar{l}\mid m\rangle\\
\int \Phi_{2J'}\psi_{0J''}d\tau &= \langle\bar{2}\mid 0\rangle+\sum_{k=0}^{6}c_k^0\langle\bar{2}\mid k\rangle+\sum_{k=0}^{8}\bar{c}_k^2\langle\bar{k}\mid 0\rangle+\sum_{l=0}^{5}\sum_{m=1}^{3}\bar{A}_l^2A_m^0\langle\bar{l}\mid m\rangle\\
\int \Phi_{1J'}\psi_{1J''}d\tau &= \langle\bar{1}\mid 1\rangle+\sum_{k=0}^{7}c_k^1\langle\bar{1}\mid k\rangle+\sum_{k=0}^{7}\bar{c}_k^1\langle\bar{k}\mid 1\rangle+\sum_{l=0}^{4}\sum_{m=0}^{4}\bar{A}_l^1A_m^1\langle\bar{l}\mid m\rangle\\
\int \Phi_{2J'}\psi_{1J''}d\tau &= \langle\bar{2}\mid 1\rangle+\sum_{k=0}^{7}c_k^1\langle\bar{2}\mid k\rangle+\sum_{k=0}^{8}\bar{c}_k^2\langle\bar{k}\mid 1\rangle+\sum_{l=0}^{5}\sum_{m=0}^{4}\bar{A}_l^2A_m^1\langle\bar{l}\mid m\rangle\\
\int \Phi_{2J'}\psi_{2J''}d\tau &= \langle\bar{2}\mid 2\rangle+\sum_{k=0}^{8}c_k^2\langle\bar{2}\mid k\rangle+\sum_{k=0}^{8}\bar{c}_k^2\langle\bar{k}\mid 2\rangle+\sum_{l=0}^{5}\sum_{m=0}^{5}\bar{A}_l^2A_m^2\langle\bar{l}\mid m\rangle.
\end{aligned} \tag{7}$$

In the above expressions, the bars refer to the upper electronic state. Expressions for the overlap integrals

$$\int \Phi_{0J'}\psi_{1J''}d\tau, \qquad \int \Phi_{0J'}\psi_{2J''}d\tau,$$

and

$$\int \Phi_{1J'}\psi_{2J''}d\tau$$

are not given since these can be obtained from

$$\int \Phi_{1J'}\psi_{0J''}d\tau, \qquad \int \Phi_{2J'}\psi_{0J''}d\tau,$$

and

$$\int \Phi_{2J'}\psi_{1J''}d\tau$$

by interchanging the barred and unbarred quantities. For example,

$$\int \Phi_{1J'}\psi_{2J''}d\tau$$

[9] By going to second order perturbation theory only a limited number of terms in the Eq. (4) occur for a perturbed harmonic oscillator.

is given by

$$\int \Phi_{Lv'} \psi_{2J''} d\tau = \langle \bar{1} \,|\, 2 \rangle + \sum_{k=0}^{8} c_k{}^2 \langle \bar{1} \,|\, k \rangle + \sum_{k=0}^{7} \bar{c}_k{}^1 \langle \bar{k} \,|\, 2 \rangle + \sum_{l=0}^{5} \sum_{m=0}^{4} \bar{A}_m{}^1 A_l{}^2 \langle \bar{m} \,|\, l \rangle. \quad (8)$$

The quantities $\langle \bar{n} \,|\, m \rangle$ refer to overlap integrals between unperturbed harmonic oscillator functions which are not orthogonal

$$\langle \bar{n} \mid m \rangle = \int \bar{\phi}_n \phi_m d\tau \neq \delta_{nm}$$

since the vibrational frequency and internuclear distance are in general different in the two electronic states involved in an electronic transition. Expressions for the matrix elements

$$\int \Phi_{v'J'} \xi \psi_{v''J''} d\tau$$

may be obtained from the above expressions for the overlap integrals by replacing the quantities $\langle \bar{n} \mid m \rangle$ by $\langle \bar{n} \mid \xi \mid m \rangle$. Thus, for example,

$$\int \Phi_{0J'} \xi \psi_{0J''} d\tau$$

is given by

$$\int \Phi_{0J'} \xi \psi_{0J''} d\tau = \langle \bar{0} \mid \xi \mid 0 \rangle + \sum_{k=0}^{6} c_k{}^0 \langle \bar{0} \mid \xi \mid k \rangle + \sum_{k=0}^{6} \bar{c}_k{}^0 \langle \bar{k} \mid \xi \mid 0 \rangle + \sum_{l=1}^{3} \sum_{m=1}^{3} \bar{A}_l{}^0 A_m{}^0 \langle \bar{l} \mid \xi \mid m \rangle. \quad (9)$$

Once having obtained all of the coefficients $c_n{}^v$ the only additional quantities which are required for the evaluation of the above integrals are overlap integrals and matrix elements between the unperturbed harmonic oscillator functions. Of these, the matrix elements $\langle \bar{n} \mid \xi \mid m \rangle$ are given by

$$\int \bar{\phi}_n \xi \phi_m d\tau = \gamma^{\frac{1}{2}} \{ [(m+1)/2]^{\frac{1}{2}} \langle \bar{n} \mid m+1 \rangle + (m/2)^{\frac{1}{2}} \langle \bar{n} \mid m-1 \rangle \}. \quad (10)$$

Thus the completion of the problem requires only the calculation of the overlap integrals of the form

$$\int \bar{\phi}_n \phi_m d\tau,$$

where $\bar{\phi}_n$ and ϕ_m refer to two different harmonic oscillators. These integrals can be evaluated by means of the generating function for Hermite polynomials and have the form

$$\langle \bar{n} \mid m \rangle = (n! m!/2^{n+m})^{\frac{1}{2}} \lambda q_m{}^n. \quad (11)$$

The quantity λ is given by

$$\lambda = e^k \left(\frac{2\beta}{1+\beta^2} \right)^{\frac{1}{2}},$$

where

$$k = \frac{-\delta^2}{2(1+\beta^2)}; \qquad \delta = \left(\frac{w_e'}{2B_e'} \right)^{\frac{1}{2}} \left(\frac{r_e'' - r_e'}{r_e'} \right); \qquad \beta = \left(\frac{w_e'}{w_e''} \right)^{\frac{1}{2}}.$$

It is only necessary to calculate the coefficients $q_0{}^0$, $q_1{}^0$, $q_2{}^0$, $q_0{}^1$, $q_0{}^2$, and another quantity defined by $g = 4\beta/(1+\beta^2)$. The rest of the coefficients $q_m{}^n$ can then be expressed in terms of these quantities. The first few coefficients are

$$q_0{}^0 = 1,$$

$$q_0{}^1 = \frac{2\delta}{1+\beta^2},$$

$$q_1{}^0 = \frac{-2\beta\delta}{1+\beta^2},$$

$$q_0{}^2 = \frac{\beta^2-1}{1+\beta^2} + \frac{2\delta^2}{(1+\beta^2)^2},$$

$$q_2{}^0 = \frac{1-\beta^2}{1+\beta^2} + \frac{2\beta^2\delta^2}{(1+\beta^2)^2}. \quad (12)$$

The quantity λ is the same for all of the matrix elements $\langle \bar{n} \mid m \rangle$ for a given electronic transition. The remaining $q_m{}^n$ may be obtained from the following relations:

$$q_3{}^0 = q_1{}^0 q_2{}^0 - \tfrac{1}{3}(q_1{}^0)^3,$$

$$q_4{}^0 = \tfrac{1}{2}[(q_2{}^0)^2 - \tfrac{1}{6}(q_1{}^0)^4],$$

$$q_5{}^0 = -q_4{}^0 q_1{}^0 + q_3{}^0 q_2{}^0 - (4/5!)(q_1{}^0)^5,$$

$$q_6{}^0 = \tfrac{1}{3} q_2{}^0 q_4{}^0 - \tfrac{1}{18}(q_1{}^0)^4 [q_2{}^0 - \tfrac{2}{5}(q_1{}^0)^2],$$

$$q_7{}^0 = q_6{}^0 q_1{}^0 + q_5{}^0 q_2{}^0 - q_4{}^0 q_3{}^0 + (8/7!)(q_1{}^0)^7,$$

$$q_8{}^0 = q_2{}^0 q_6{}^0 - \tfrac{1}{2}(q_4{}^0)^2 + (1/7!)(q_1{}^0)^8,$$

$$q_9{}^0 = -q_3{}^0 q_1{}^0 + q_7{}^0 q_2{}^0 + q_6{}^0 q_3{}^0 - q_5{}^0 q_4{}^0 + (16/9!)(q_1{}^0)^9. \quad (13)$$

The coefficients $q_0{}^k$ may be obtained from the above $q_k{}^0$ coefficients by interchanging subscripts and superscripts. Thus $q_0{}^6$ would be given by

$$q_0{}^6 = \tfrac{1}{3} q_0{}^2 q_0{}^4 - \tfrac{1}{18}(q_0{}^1)^4 [q_0{}^2 - \tfrac{2}{5}(q_0{}^1)^2]. \quad (14)$$

The coefficients $q_m{}^n$, where neither n nor m is equal to zero, may be expressed in terms of the above $q_m{}^0$ and $q_0{}^n$ as illustrated below:

$$q_1{}^1 = q_0{}^1 q_1{}^0 + g,$$

$$q_2{}^1 = q_0{}^1 q_2{}^0 + g q_1{}^0,$$

$$q_3{}^1 = q_0{}^1 q_3{}^0 + g q_2{}^0,$$

$$q_3{}^2 = q_0{}^2 q_3{}^0 + g q_0{}^1 q_2{}^0 + (g^2/2!) q_1{}^0,$$

$$q_4{}^2 = q_0{}^2 q_4{}^0 + g q_0{}^1 q_3{}^0 + (g^2/2!) q_2{}^0,$$

$$q_3{}^3 = q_3{}^0 q_0{}^3 + g q_2{}^0 q_0{}^2 + (g^2/2!) q_1{}^0 q_0{}^1 + (g^3/3!). \quad (15)$$

The above expressions for q_m^n where neither n nor m equal zero have the general form,

$$q_m^n = q_0^n q_m^0 + g q_0^{n-1} q_{m-1}^0 + \cdots (g^k/k!) q_0^{n-k} q_{m-k}^0. \quad (16)$$

It should be apparent that negative values of the subscripts and superscripts do not occur and that one may interchange all of the subscripts and superscripts occurring in a given formula. Thus q_2^3 would be given by

$$q_2^3 = q_0^3 q_2^0 + g q_0^2 q_1^0 + (g^2/2!) q_0^1.$$

Although these expressions do not result in any particular saving of time for the calculation of one particular overlap integral, they result in a considerable saving in time when one has to calculate a large number of these overlap integrals. The calculation of

$$\int \Phi_{0J'} \psi_{0J''} d\tau,$$

for example, requires the evaluation of twenty harmonic oscillator overlap integrals, a process in which the above relations are of considerable help.

Application to Non-$^1\Sigma$ States

The preceding results strictly apply to only $^1\Sigma$ states of diatomic molecules. That is, for the results obtained it was assumed that the Hamiltonian could be expressed in the form $\mathcal{H}_{\text{vib}} + BJ(J+1)$, where

$$B = \hbar^2/2\mu r^2 = B_e(1 - 2\xi + 3\xi^2 - 4\xi^3 \cdots); \qquad \xi = (r - r_e)/r_e.$$

For non-$^1\Sigma$ molecules which can be described by Hund's case (a), the rotational energy is given by

$$B[J(J+1) - \Omega^2],$$

where $|\Omega|$ is the component of the total electronic angular momentum along the molecular axis. Thus one might expect for this case that the previously derived results could be generalized by substituting $J(J+1) - \Omega^2$ for $J(J+1)$ in all of the above expressions. This is still not quite correct, however. The Hamiltonian describing the vibrational and rotational motions is given by the expression[10]

$$\mathcal{H} = \mathcal{H}_{\text{vib}} + [J(J+1) - \Omega^2 + \bar{M}_x^2 + \bar{M}_y^2 + S(S+1) - \Sigma^2]. \quad (18)$$

Here M_x and M_y refer to the x and y components of the electronic orbital angular momentum in a molecule fixed coordinate system. The other symbols have their usual significance. For most applications it is customary to absorb the terms $\bar{M}_x^2$ and $\bar{M}_y^2$ into the part $\mathcal{H}_{\text{vib}}$ of the Hamiltonian. For the purpose of calculating the variation with J of the transition moment (or dipole moment for infrared transitions) matrix element, one might equally well absorb all of the additional terms except $BJ(J+1)$ into $\mathcal{H}_{\text{vib}}$. Then for a fixed Ω component of a particular electronic state one can use the formulas given in previous sections with the restriction that J has the values $J = |\Omega|, |\Omega|+1, \cdots$. If this is done, the r_e and w_e which occur in the expression (11) and the a_1 of Eq. (5) would have to be corrected by multiplicative factors of order $(1+\gamma^2)$ where $\gamma = 2B_e/w_e$. Since the order of magnitude of γ never exceeds 10^{-2}, it is apparent that the expressions which hold for $^1\Sigma$ states will be entirely adequate for most purposes. In cases where Hund's case (b) is a better description, similar remarks will also hold. Now, however, J is restricted to the values $J = |\Lambda|, |\Lambda|+1, \cdots$. At higher values of J where the effects of rotation-vibration interaction are more likely to be most pronounced, Hund's case (b) will generally be a better approximation than Hund's case (a) for a large number of molecules. For the same reasons that it was possible to neglect all the terms except $BJ(J+1)$ in Hund's case (a), one will not introduce a significant error by using the expression appropriate to Hund's case (b) for both case (a) and case (b) calculations.

The considerations of the preceding paragraph show that to a good approximation one may use the results of the preceding sections with the requirement that J have the values $J = |\Lambda|, |\Lambda|+1, \cdots$ if the state involved is not a Σ state. This will introduce a small error into the magnitude of the quantities

$$\int \Phi_{v'J'} \psi_{v''J''} d\tau \quad \text{and} \quad \int \Phi_{v'J'} \xi \psi_{v''J''} d\tau$$

but will have very little effect on their variation with J. This means that experimentally determined values for the quantities $R(r_e)$ and χ of Eq. (2) could be in error by less than one percent as a result of this approximation. This is well below the uncertainty in present day intensity measurements.

DISCUSSION

In applying the results of the preceding section to the actual calculation of the transition moment matrix element one can proceed in one of two ways; either one can calculate the values of the various coefficients c_n^v and $\bar{c}_n^v$ at the desired values of J'' and J' or one can obtain an expression for the matrix element which has the form

$$\int \Phi_{v'J'} R(r) \psi_{v''J''} d\tau = A + BJ''(J''+1) + CJ'(J'+1) + DJ''^2(J''+1)^2 + EJ'^2(J'+1)^2 + FJ''(J''+1)(J')(J'+1).$$

This latter approach is probably the better one if the matrix element is going to be calculated at a large number of values for J' and J''. The coefficients of the various powers of J' and J'' in this expression can easily be calculated from the Eqs. (7) and the results presented in Table I. The easiest way of doing this is

[10] R. Kronig, *Band Spectra and Molecular Structure* (Cambridge University Press, New York, 1930).

probably first to collect all terms in a^2, bc, $\bar{a}b$, etc. Since these results are easily obtained and take up a large amount of space, they will not be given.

Although the preceding results have been derived for the case where the initial and final vibrational wave functions belong to different electronic states, the same results apply when the initial and final electronic state is the same. This is the case in infrared vibration-rotation spectra. In this case the transition moment matrix element becomes the dipole moment matrix element. These dipole moment matrix elements are the quantities which are necessary for a discussion of the effect of rotation-vibration interaction on intensities in infrared spectra. Several of these matrix elements for the case where the initial and final electronic levels are the same have been calculated by other investigators so that in this simple case it is possible to compare the results obtained in this paper with previously obtained results.

Herman and Wallis have derived an expression for the dipole moment matrix element for the 0–1 band of a vibration-rotation spectrum. Their result, from a first-order perturbation treatment, for terms up to order $\gamma^{5/2}$ is given by[11]

$$\langle 1J' \mid u \mid 0J\rangle = \frac{M_1 r_e \gamma^{\frac{1}{2}}}{\sqrt{2}}\left[1-2\theta\gamma m\left(1+\frac{15}{4}a_1\gamma+3\gamma - \frac{5a_1}{4\theta}+\frac{3a_1\gamma}{8\theta}(m-1)+\frac{3\gamma}{8\theta}(m-1)\right)\right],$$

$$m = J+1 \; R_{\text{branch}}; \qquad -J P_{\text{branch}};$$

$$M_1 = (\partial\mu/\partial r)_{r_e}; \qquad \theta = \mu(r_e)/M_1 r_e.$$

The results of this paper give an expression which agrees with that of Herman and Wallis to the same order in a_1 and γ, but now there are some additional terms of a higher order in a_1 and γ which can be included because the calculation extends through second order perturbation theory. If the results of this paper are put in the same form as those of Herman and Wallis the result for the 0–1 band is

$$\langle 1J' \mid u \mid 0J\rangle = \frac{M_1 r_e \gamma^{\frac{1}{2}}}{\sqrt{2}}\left[1+\frac{11}{16}a_1^2-2\theta\gamma m\left(1+\frac{15}{4}a_1\gamma+3\gamma - \frac{3}{4}\gamma^2(7m^2+m)-\frac{5a_1}{4\theta}(1-\frac{188}{15}\gamma)(m-1) + \frac{3a_1\gamma}{8\theta}(1+\frac{317}{9}\gamma)(m-1)+\frac{3\gamma}{8\theta}(m-1) + \frac{\gamma^2}{2\theta}(m^3+m^2+m)\right)\right].$$

In this expression a number of higher order terms in γ have been omitted. It is clear from the above expression that at high values of J for molecules with large values of γ that some of the extra terms which are not included in the expression given by Herman and Wallis can be as large as many of the terms which were included in their expression.

Similarly, in the general case of an electronic transition, it is possible for many of the terms in $J''^2(J''+1)^2$ and $J'^2(J'+1)^2$ to be as large as terms in $J''(J''+1)$ and $J'(J'+1)$. This fact could have been anticipated from the results presented in Eqs. (5) where a term in c^2 would be $2a_1\gamma^3 J(J+1)$ which is the same order in γ as $a^2=\gamma^3 J^2(J+1)^2$. A first order term in $b=\frac{3}{2}\gamma^2 J(J+1)$ will not be any larger than a second order term in a if $\gamma J(J+1)\sim 1$. In this case the rotational energy is of the same order of magnitude as the vibrational energy and a rapid convergence of a perturbation treatment would not be expected.

The approach used in the present paper differs somewhat from that of Herman and Wallis. Instead of adding a perturbation of the form $ax+bx^2+cx^3$, they made a transformation of variables to eliminate the first power term in x and obtained a harmonic oscillator type potential in terms of this new variable. The cubic term was then treated as a perturbation to first order. If one wants to go to second-order perturbation theory and then apply the results to the case where the vibrational wave functions correspond to different electronic states, it seems to be more convenient to proceed in the way followed in this paper. In their method one would have expressions similar to our Eqs. (7) but both the coefficients and the overlap integrals between the unperturbed harmonic oscillators would depend on rotational quantum numbers. This would make the calculations of intensities in an electronic transition extremely more complicated than they are in our case where the unperturbed overlap integrals involved are independent of J and may be evaluated once and for all.

Finally it is perhaps worthwhile to indicate the conditions under which the variation of the electronic transition moment matrix element with rotational quantum numbers might be expected to be large. The variation being considered is the variation in the "vibrational" matrix elements

$$\int \Phi_{v'J'} R(r) \psi_{v''J''} dr.$$

There will also be a regular variation from the terms $S_{J'J''}$ of Eq. (1). A similar discussion of the variation of

$$\int \Phi_{v'J'} R(r) \psi_{v''J''} dr$$

with rotational quantum numbers has been given in a previous paper dealing with the affect of these considerations on rotational "temperature" determinations.[4]

The manner in which the transition moment matrix element varies with J depends on the variation of each

[11] See reference 1, Eq. (16).

of the quantities

$$\int \Phi_{v'J'}\psi_{v''J''}d\tau \quad \text{and} \quad \int \Phi_{v'J'}\xi\psi_{v''J''}d\tau.$$

For molecules with large $\gamma=2B_e/w_e$, both of these quantities can be expected to show noticeable variations with J. The largest variations, however, will be expected to occur when both of the terms in Eq. (2) have nearly the same magnitude and opposite sign. A glance at Eqs. (11) and (12) shows that normally in the (0, 1) and (1, 0) bands the quantity

$$\int \Phi_{v'J'}\psi_{v''J''}d\tau$$

changes sign, while the quantity

$$\int \Phi_{v'J'}\xi\psi_{v''J''}d\tau$$

does not change sign. Therefore, if both of these terms have nearly the same magnitude, then one of the bands (0, 1) or (1, 0) will be much weaker than one would expect merely from a comparison of overlap integrals involved. As a qualitative guide, if

$$(r_e''-r_e'/r_e')(1/\gamma''\chi)\simeq+1$$

then the (0, 1) band would be expected to be weak and could show large changes in the transition moment matrix element with rotational quantum numbers. On the other hand if $(r_e''-r_e'/r_e')(1/\gamma''\chi)\simeq-1$ the (1, 0) band is the one which would be expected to be weak and might have a strong J dependence for the transition moment matrix element. If this ratio

$$(r_e''-r_e'/r_e')/(\gamma''\chi)$$

is much greater or smaller than 1, then the intensity will be controlled by one or the other of the terms

$$R(r_e)\int \Phi_{v'J'}\psi_{v''J''}d\tau \quad \text{or} \quad R(r_e)\chi\int \Phi_{v'J'}\xi\psi_{v''J''}d\tau.$$

In this case the variation with J would not be expected to be as great as in the above cases. It could still be significant in molecules with large γ. Finally it should be mentioned that even in molecules with smaller values of γ the variation of the transition moment matrix element with J could be large in the (0, 1) or (1, 0) band when $(r_e''-r_e'/r_e')/(\gamma''\chi)\simeq\pm1$. If it should turn out that band systems exist for which $\gamma^4\chi\simeq-1$, then the $\Delta v=0$ bands could also show quite large changes of the transition moment matrix element with rotational quantum numbers.

In some band systems it appears necessary to include another term in the expansion of the transition moment as a function of internuclear distance. The results of the present paper could easily be extended to this case since the quantities $\langle \bar{n} \mid \xi^2 \mid m \rangle$ may be easily calculated. Since the variation of internuclear distance with rotational quantum numbers is small, one could probably obtain reliable results by using a slightly different value for $R(r_e)$ and χ in each of the bands and neglecting the term in $(\partial^2 R/\partial r^2)_{r_e}$.

ACKNOWLEDGMENT

Partial support for this work was obtained from a Du Pont grant-in-aid.

Infrared Spectra of Sodium and Potassium Cyanide

GEORGE E. LEROI* AND WILLIAM KLEMPERER†

Department of Chemistry, Harvard University, Cambridge, Massachusetts

(Received March 2, 1961)

The infrared absorption spectra of sodium cyanide and potassium cyanide vapors have been measured in the region 3500 to 200 cm^{-1}. Two absorptions assigned as fundamental frequencies of the monomeric species were found in each system. The absorption frequencies and their present assignments are: NaCN $\nu_2=238$, $\nu_3=2176$ cm^{-1}; KCN $\nu_2=207$, $\nu_3=2158$ cm^{-1}. A third absorption at 2076 cm^{-1} in sodium cyanide vapor is assigned to the dimer of NaCN.

The bond-stretching force constant of the CN group in XCN molecules is sensibly independent of the electronegativity of X. The angle-bending force constant varies directly with the electronegativity of X.

COMPARATIVELY little is known of the structural parameters of polyatomic molecules containing strongly electropositive groups. Although there is a wealth of knowledge available for diatomic molecules of the alkali metals such as the halides,[1] and hydrides,[2] it is only in polyatomic molecules that the effects of strong electropositive *substitution* may be learned. The cyanides of hydrogen and the halogens have been very thoroughly investigated.[3–5] In this note we report the observed infrared spectra of gaseous sodium and potassium cyanide. There is comparatively little structural information on gaseous alkali metal cyanides. Kusch, Millman, and Rabi[6] determined the nuclear magnetic moment of nitrogen in NaCN and KCN by the molecular beam magnetic resonance method. Their spectra show a considerable width which is probably due to the quadrupole interaction of the nitrogen nucleus; however, the value of the quadrupole coupling constant at the nitrogen nucleus was not determined.

The geometric structure of the alkali metal cyanides has not been determined. Throughout this paper it is assumed that the monomeric species is linear. For this geometry there are three normal modes of vibration all having infrared-active fundamental frequencies, namely the two nondegenerate parallel stretching motions ν_1 and ν_3 and the doubly degenerate perpendicular bending motion ν_2.

EXPERIMENTAL

The infrared absorption spectra of gaseous NaCN and KCN were obtained in the region 4000 to 200 cm^{-1} using a modified Perkin-Elmer model 98 prism spectrometer and the general techniques described previously.[7] Commercial samples of the cyanides were dried in vacuum above their melting points for several hours. Carbon monoxide and carbon dioxide were observed in the spectra but no purification to eliminate these impurities was considered necessary. The infrared absorption cell was a Vycor tube equipped with cesium iodide windows. The cell was heated from 800°C to 1000°C. Three absorptions of sodium cyanide and two of potassium cyanide were observed. The frequencies of the absorption maxima are given in Table I.

The two high frequency absorptions in sodium cyanide are difficult to attribute to monomeric NaCN. Using a double-oven technique in which the pressure of the sodium cyanide is controlled by a low-temperature oven while the second oven heating the bulk of the cell is several hundred degrees hotter, the higher frequency absorption at 2176 cm^{-1} was observed strongly while the absorption at 2076 cm^{-1} became very weak. This establishes the carrier of the 2076 cm^{-1} absorption as a polymeric species. Mass spectrometric studies of saturated sodium cyanide vapor by Porter[8] show that the monomer-dimer pressure ratio is near unity at the temperatures of the present experiments. No absorption of dimeric potassium cyanide was observed. As in the alkali halides it appears that the potassium salt is less highly dimerized than the sodium salt.

A thorough search of the region 210 to 3500 cm^{-1} failed to show additional absorptions by either substance. During these searches the temperature of the sample was maintained 200° hotter than was necessary to develop the bands listed in Table I.

At a given temperature in the range 800° to 1000°C the 2158-cm^{-1} band of KCN was weaker than the 2170-cm^{-1} band of NaCN. In general a 20° to 50° temperature difference was necessary to obtain equal absorption. Assuming the equality of the absorption coefficients for the bands in both systems, the volatility of NaCN is higher than that of KCN.

Crystals of KCN grown in the course of these experi-

* Present address: Department of Chemistry, University of California, Berkeley, California.

† Alfred P. Sloan Fellow.

[1] A. Honig, M. Mandel, M. L. Stitch, and C. H. Townes, Phys. Rev. **96**, 629 (1954).

[2] G. Herzberg, *The Spectra of Diatomic Molecules* (D. Van Nostrand Company, Inc., Princeton, New Jersey, 1950), 2nd ed.

[3] G. Herzberg, *Infrared and Raman Spectra* (D. Van Nostrand, Company, Inc., Princeton, New Jersey, 1955), pp. 173–175.

[4] C. H. Townes and A. L. Schawlow, *Microwave Spectroscopy* (McGraw-Hill Book Company, Inc., New York, 1956).

[5] H. C. Allen, E. D. Tidwell, and E. K. Plyler, J. Chem. Phys. **25**, 302 (1956).

[6] P. Kusch, S. Millman, and I. I. Rabi, Phys. Rev. **55**, 1176 (1939).

[7] W. Klemperer and S. A. Rice, J. Chem. Phys. **26**, 618 (1957).

[8] R. F. Porter (private communication).

ments were examined. In addition to the bands reported previously,[9,10] two new absorptions in solid KCN were found at 620 and 245 cm^{-1}.

DISCUSSION

In this work only two absorptions carried by monomeric alkali cyanides were observed. There can be little doubt that the high frequency vibration is primarily the CN stretching vibration ν_3. The assignment of the low frequency oscillation in both molecules is less certain. This vibration is assigned as the bending motion ν_2 on the basis of the reasonability of the value of the bending constant thus obtained. Estimating the bond lengths of the gaseous alkali cyanides from crystal distances and the contraction observed in the alkali halides we obtain angle-bending constants of 1.5×10^{-12} and 1.3×10^{-12} d cm/rad in NaCN and KCN, respectively. The bending constants of ClCN and HCN are 4.0×10^{-12} and 2.5×10^{-12} d cm/rad.[3] It should be noted that there is a strong dependence of the angle-bending force constant in an XCN molecule upon the electronegativity of X.

Since both bond lengths change in each of the parallel stretching vibrations, strictly the single high frequency observed does not give a unique stretching force constant for the CN group even under the assumption of a simple valence force field. However, a good estimate of this force constant can be made from the position of ν_3 alone, in view of the expectation that ν_1 is at a much lower frequency. For NaCN and KCN $k_2=17.5\pm0.5\times10^5$ d/cm.

The bond-stretching force constant of the CN group appears to be insensitive to its molecular environment. The range of values observed in XCN molecules where X is H, Na, K, Cl, Br, and I is between 18.0 and 16.7×10^5 d/cm. The variation in force constant with distance of the attached group is extremely small in the one analyzable instance, HCN.[5,11] Here the bond-bond interaction constant is less than 1% of the CN bond-stretching constant. Furthermore, the CN radical, which may be regarded as the limiting group under adiabatic stretching of the XC bond, has a force constant of 15.9×10^5 d/cm.

TABLE I. Vibrational frequencies of gaseous NaCN and KCN (in cm^{-1}).

Molecule	ν_2	ν_3	Dimer
NaCN	239±10	2176±5	2076±5
KCN	207±20	2158±5	...

In order to account for this behavior of the CN group, it is useful to consider the molecules CO and CO^+, isoelectronic with CN^- and CN, whose bonding has been discussed in considerable detail by Moffitt.[12] The configuration of the ground electronic state of CO^+ and CN is $(K)(K)(s\sigma)^2(t\sigma)^2(w\pi)^4(u\sigma)$. There is a considerable body of experimental and theoretical evidence that the orbital $u\sigma$ is highly localized on the carbon atom and is of a nonbonding character. It is the $u\sigma$ orbital of the carbon which is used in forming the XC bond in the cyanides. The relative electronegativity of X in the molecule XCN will have slight effect upon the CN bond; the effect being an indirect one operating through the polarization of the $p\pi$ electrons. This is seen clearly in the bond properties of CO and CO^+ where there are only slight differences in the bond length and force constant. (The difference in force constant is 3%.) The effects of polarization of the $p\pi$ electrons upon the CN bond-stretching force constant are too small to deduce from the relatively crude infrared observations. A definite indication that changes in the electron distribution in the CN bond do occur, however, is given by the nitrogen quadrupole coupling constants in HCN and the halogen cyanides,[4] in which there is a 15% change between HCN and the halogen cyanides.

ACKNOWLEDGMENTS

This research has been aided by support from the National Science Foundation and the Research Corporation.

[9] A. Maki and J. C. Decius, J. Chem. Phys. **31,** 772 (1959).
[10] F. A. Miller and C. H. Wilkens, Anal. Chem. **24,** 1253 (1952).
[11] J. Pliva, Collection Czech. Chem. Commun. **23,** 777 (1958).
[12] W. Moffitt, Proc. Roy. Soc. (London) **A196,** 524 (1949); reference to a considerable body of earlier work by Mulliken is given in this paper.

Structure of the Band Spectrum of CuCl Molecule. I. Additional Knowledge in the Coarse Structure*

P. RAMAKOTESWARA RAO† AND J. K. BRODY

Argonne National Laboratory, Argonne, Illinois

(Received January 18, 1961)

A number of new bands in the A, B, C, D, and E systems of CuCl, recorded in the spectrum of the molecule excited in an electrodeless discharge tube by a microwave oscillator, are reported. Because of the employment of high dispersion and the use of a single isotopic species of CuCl ($Cu^{63}Cl^{35}$), it has been possible to investigate the phenomenon of formation of head of heads in the $\Delta v=-4$ sequence of the E system. This phenomenon has also been detected in the $\Delta v=-3$ sequence of the A system.

The weak F system has been photographed for the first time under suitable dispersion so that a satisfactory vibrational analysis of the same could be made. The R heads of this system of the $Cu^{63}Cl^{35}$ molecule are represented by the formula

$$\nu^{F}{}_{63,35}=25287.0+386.8(v'+\tfrac{1}{2})-1.64(v'+\tfrac{1}{2})^2-417.1(v''+\tfrac{1}{2})^2+1.50(v''+\tfrac{1}{2})^2.$$

It has been shown that the lower state of the F system is the same as the common lower state of all the other known band systems, which is also the ground state of the molecule. Data on the A and F systems of the $Cu^{65}Cl^{35}$ molecule also are given.

INTRODUCTION

THE perfection of the performance of the Argonne 30-ft 15 000 line/in. grating spectrograph by Tomkins and Fred,[1] the use of the Argonne photoelectric comparator[2] for extensive spectral measurements with relative ease and the availability of the IBM 650 computer[3] for the rapid reduction of the comparator readings to vacuum wave numbers offered excellent possibilities for investigations of the structure of band spectra in this laboratory.

It is well known that natural CuCl is a mixture of four isotopic species, $Cu^{63}Cl^{35}$, $Cu^{65}Cl^{35}$, $Cu^{63}Cl^{37}$, and $Cu^{65}Cl^{37}$ with approximate relative abundances of 7:3:2.25:1. Six band systems are known for CuCl. They are designated as the A system (5150–5501 A), the B system (4620–5110 A), the C system (4660–5170 A), the D system (4140–4530 A), the E system (3990–4580 A), and the F system (3780–4180 A). Ritschl[4] made detailed investigations of the B, C, D, and E systems of CuCl in absorption at high temperatures. With a 15-cm absorption cell, the D and E systems were recorded at temperatures below 840°C, whereas the B and C systems were recorded at about 1000°C. At the highest temperatures employed, i.e., 1200°C, about half a dozen bands of the A system were recorded and the F system was not recorded at all. Gaydon[5] made some observations on the relative intensities of the A, B, C, D, and E systems as they occurred in the spectra of cool flames of carbon monoxide with oxygen and with nitrous oxide in which CuCl was present as an impurity. Sinha[6] recorded some bands in the region 3500–4000 A in the spectrum of a flame containing CuCl and thought they might possibly be the higher members of the $v''=3$ progression of the E system. Bloomenthal[7] photographed the F system under low dispersion (16.8 to 24.6 A/mm) in the glow obtained when solid Cu_2Cl_2 was bombarded with a jet of active nitrogen. Terrien[8] made a partial rotational analysis of the O–O bands of the D and E systems.

Any attempt to make a rotational analysis of the CuCl band systems is beset with difficulties due to the fact that natural CuCl is a mixture of four isotopic species with not very different relative abundances. However, with the availability of some compounds containing separated copper and chlorine isotopes, it has become possible to prepare copper chloride[9] with any desired Cu and Cl isotopes. This, coupled with the fact that the electrodeless discharge tube proved to be a very intense source for CuCl bands, has enabled us to undertake extensive investigations of the coarse and fine structures of the CuCl band systems. In this paper only the additional knowledge in the coarse structure of CuCl band systems obtained in the present investigations is communicated. Results of the fine structure investigations of the B, C, D, E, and F systems of CuCl will be communicated in the following papers of this series.

Due to the very high intensity obtained in the electrodeless discharge tube, a number of new bands have been recorded in all the known CuCl band systems and it has been possible to photograph the weak A and F systems under sufficient dispersion (1.8 A/mm) for an accurate vibrational analysis. However, it may

* Based on work performed under the auspices of the U. S. Atomic Energy Commission.

† Presently an affiliate in the International Institute for Nuclear Science and Engineering of the Argonne National Laboratory. Permanent address: Analytical Division. Atomic Energy Establishment Trombay, Bombay, India.

[1] F. S. Tomkins and M. Fred, Spectrochim. Acta **6**, 139 (1954).

[2] F. S. Tomkins and M. Fred, J. Opt. Soc. Am. **41**, 641 (1951).

[3] We gratefully acknowledge the assistance of Angelo Sandrin who ran all IBM 650 computer programs for us.

[4] R. Ritschl, Z. Physik **42**, 172 (1927).

[5] A. G. Gaydon, Proc. Roy. Soc. (London) **A182**, 199 (1943).

[6] S. P. Sinha, Current Sci. **17**, 208 (1948).

[7] S. Bloomenthal, Phys. Rev. **54**, 498 (1938).

[8] J. Terrien, Ann. phys. **9**, 477 (1938).

[9] Only the band spectrum of the CuCl molecule is obtained whether cuprous chloride (CuCl) or cupric chloride ($CuCl_2$) is used in the discharge tube. A similar observation had also been made by Ritschl.

be pointed out that the finer features in the vibrational structure of the E and A systems could be studied due to the fact that a single isotopic species of CuCl ($Cu^{63}Cl^{35}$) was used in the investigations. For instance,

TABLE I. New bands in the E system of $Cu^{63}Cl^{35}$.

λ in air (A)	ν in vac. (cm^{-1})	Rel. int.	v'	v''
3936.24	25397.8	0	7	1
3941.14	25366.2	1	8	2
3946.32	25332.9	2	9	3
3951.58	25299.2	2	10	4
3991.38	25046.9	0	5	0
4005.49	24958.7	3	8	3
4010.34	24928.5	3	9	4
4015.27	24897.9	3	10	5
4020.28	24866.9	2	11	6
4076.00	24526.9	4	9	5
4080.55	24499.6	3	10	6
4085.33	24470.9	2	11	7
4143.27	24128.7	2	9	6
4147.16	24106.1	1	10	7
4347.45	22995.6	2	6	6
4350.06	22981.8	1	7	7
4419.71	22619.6	1	4	5
4501.74	22207.4	3	6	8
4503.27	22199.9	2	7	9
4504.84	22192.1	1	8	10
4506.05	22186.2	0	9	11
4579.56	21830.1	2	3	6
4580.27	21826.6	3	4	7
4581.07	21822.8	3	5	8
4581.93	21818.8	4	6	9
4582.90	21814.1	4	7	10
4583.96	21809.1	4	8	11
4585.14	21803.5	4	9	12
4586.37	21797.6	4	10	13
4587.90	21790.3	4	11	14
4589.47	21782.9	3	12	15
4591.30	21774.2	3	13	16
4593.21	21765.2	3	14	17
4595.24	21755.6	2	15	18
4597.58	21744.5	2	16	19
4664.16	21434.1	2	0	4
4663.94	21435.1	2	1	5
4663.92[a]	21435.2[a]	2	2	6
4663.94	21435.1	2	3	7
4664.00	21434.8	2	4	8
4664.16	21434.1	2	5	9
4664.41	21433.0	2	6	10
4664.74	21431.4	3	7	11
4665.19	21429.4	3	8	12
4665.76	21426.8	3	9	13
4666.46	21423.5	2	10	14
4667.31	21419.6	1	11	15
4668.34	21414.9	2	12	16
4669.56	21409.3	1	13	17

[a] Turning point of the sequence.

it would have been impossible to investigate the phenomenon of formation of head of heads in the $\Delta v = -4$ sequence of the E system in the spectrum of natural CuCl. This becomes particularly evident when it is realized that near the head of heads, the separation

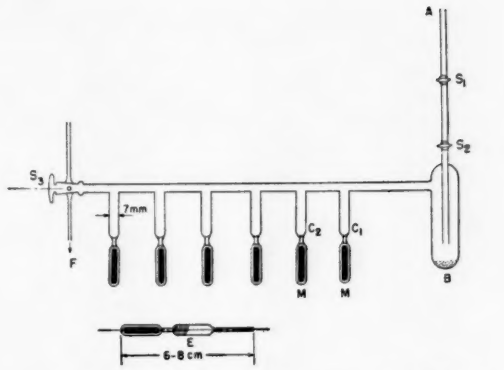

FIG. 1. Vacuum system used for preparing $Cu^{63}Cl_2^{35}$ and $Cu^{65}Cl_2^{35}$. E is the sample tube containing the deposit of a few mg of $Cu^{63}Cl_2^{35}$ or $Cu^{65}Cl_2^{35}$.

between successive bands of the sequence is about 0.1 cm^{-1} (see Table I) and that the bands due to all the other less abundant isotopic molecules would lie on the short-wavelength side of those of the most abundant $Cu^{63}Cl^{35}$ molecule. Similarly, by looking at Fig. 9 and Table II it will be clear that, even with the dispersion employed, it would have been almost impossible to sort out the bands in the $\Delta v = -1$ and $\Delta v = -2$ sequences of the A system in the spectrum of natural CuCl.

With a view to providing isotope shift data, the A and F systems of $Cu^{63}Cl^{35}$ and $Cu^{65}Cl^{35}$ were investigated. The extensions reported in the B, C, D, and E systems refer to the $Cu^{63}Cl^{35}$ molecules.

EXPERIMENTAL

$Cu^{63}Cl_2^{35}$ and $Cu^{65}Cl_2^{35}$ were prepared from $NaCl^{35}$, $Cu^{63}O$ and $Cu^{65}O$ in the simple system, made with Pyrex glass, shown in Fig. 1. Attached to each side arm C_1, C_2, etc. is a sealed Pyrex tube M containing an iron slug. About 25 mg of $NaCl^{35}$ was placed in the bulb B and about 1 mg of $Cu^{63}O$ or $Cu^{65}O$ in each of the side arms C_1, C_2, etc. With the stop cock S_2 open, the system was evacuated by a mechanical pump connected at F. The stop cocks S_3 and S_2 were then closed and reagent-grade sulphuric acid, diluted 1:1 with distilled water, was introduced at A. A portion of it was admitted between stopcocks S_1 and S_2 and then dosed into B. One by one the side arms were mildly heated with a

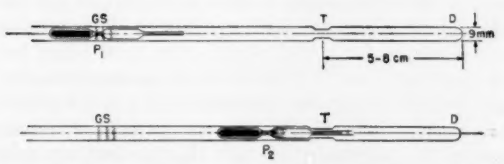

FIG. 2. The discharge tube: P_1 is the position of the sample tube, when the discharge tube is being degassed. P_2 is the position of the sample tube when the sample is distilled into the discharge tube.

TABLE II. *A* system.

	$Cu^{63}Cl^{35}$				$Cu^{65}Cl^{35}$		
	λ in air (A)	ν in vac. (cm^{-1})	ν in vac. calc. (cm^{-1})	v'	v''	λ in air (A)	ν in vac. (cm^{-1})
	5626.08	17769.4	17764.8	0	3		
	5626.16	17769.2	17766.2	1	4		
	5626.23	17769.0	17767.3	2	5		
	5626.31	17768.7	17768.3	3	6		
	5626.37	17768.5	17769.1	4	7		
A[a]	5626.43	17768.3	17769.7	5	8	5624.14	17775.6 A_1[a]
	5626.57	17767.9	17770.0	6	9		
	5626.75	17767.3	17770.2[b]	7	10		
	5626.92	17766.8	17770.1	8	11		
	5627.05	17766.4	17769.9	9	12		
	5627.28	17765.7	17769.4	10	13		
			17768.8	11	14	5625.49	17771.3
	5627.52	17764.9	17767.9	12	15	5625.81	17770.3
B[a]	5628.06	17763.2	17766.9	13	16	5626.38	17768.5 B_1[a]
	5628.64	17761.4	17765.6	14	17	5626.75	17767.3
	5629.36	17759.1	17764.1	15	18	5627.10	17766.2

[a] Measured intensity peaks. The structure was not sufficiently resolved for unambiguous v', v'' assignments (see Fig. 11 and text).
[b] Turning point of the sequence.

microburner so that the $Cu^{63}O$ or $Cu^{65}O$ reacted with HCl^{35}, resulting from the reaction between H_2SO_4 and $NaCl^{35}$, to form $Cu^{63}Cl_2^{35}$ or $Cu^{65}Cl_2^{35}$. After the reaction in each side arm was completed, which was apparent by the complete disappearance of the black CuO, the system was opened to the atmosphere. Each side arm was heated at the top, drawn into a capillary and cut apart from the system to yield the sample tube *E* shown below in Fig. 1.

The discharge tube was prepared in a manner similar to that described by Tomkins and Fred.[10] A quartz tube, 9-mm diameter, sealed at one end and having a constriction at about 6 cm from the sealed end constituted the discharge tube *DT*, Fig. 2. The discharge tube was attached to a quartz-to-Pyrex graded seal *GS* and, after the sample tube *E* had been introduced into it, sealed to a high-vacuum system. With the sample tube in position P_1, the discharge tube was degassed by heating it to about 900°C in a laboratory-built tube furnace for four to five hours. After degassing was over, the sample tube was moved by the action of a magnet on the iron slug to position P_2 so that its capillary projected into the discharge tube. The furnace was then shifted so as to heat the sample tube and distill the $CuCl_2$ into the discharge tube which was cooled with wet asbestos. The furnace was removed and the sample tube returned to position P_1. Neon was introduced into the system from the supply bulb to a pressure of 2–3 mm Hg and the microwave discharge started. After running the discharge for a few minutes, the neon filling was pumped out. This process, meant to ensure removal of any volatile impurities present in $CuCl_2$ was repeated two or three times. Finally neon was introduced into the system to a pressure of 1–3 mm Hg, the discharge tube sealed off at the constriction, and a piece of quartz rod attached to the sealed-off end.

[10] F. S. Tomkins and M. Fred, J. Opt. Soc. Am. **47**, 1087 (1957).

The discharge tube was excited by a Raytheon microtherm microwave, 2450 Mc/sec, oscillator operating between 40 and 60% of its maximum power of 125 w. The CuCl spectrum showed up strongly when the discharge tube was heated to about 400°C. A 20 cm length of quartz tube, 1 cm i.d., wound with a few turns of Nichrome wire, served as the furnace for heating the discharge tube.

The furnace supported itself on the central peg of the microwave director, which just fitted into the former. The discharge tube was slipped into the furnace and rested on the control peg of the microwave director. Neither the furnace nor the discharge tube needed any other support.

The discharge tube was started cold and the furnace then heated slowly until the CuCl spectrum appeared strongly as observed with a hand spectroscope. At low temperatures, neon spectrum was the strongest feature. As the temperature slowly rose, the discharge tube gradually changed from red to bluish white color, and when the temperature reached about 400°C, the CuCl spectrum predominated and only the strongest neon and chlorine lines were present. The life of a discharge tube varied from 10 to over 20 hr, by which time most of the CuCl was dissociated as evidenced by a red deposit of copper on the inner walls of the discharge tube. Impurity spectra such as that of CN then began to appear.

The spectra were recorded almost exclusively in the first order of the Argonne 30-ft, 15 000 line/in. grating spectrograph at a dispersion of about 1.8 A/mm. Exposure times ranged from a few seconds for the strong bands of the *D* and *E* systems to about two hours for the weak bands of the *A* and *F* systems. A few plates were taken in the third order of the spectrograph at a dispersion of 0.55 A/mm with a view to resolving the structure near the head of heads in the $\Delta v = -4$ se-

TABLE III. *F* system.

$Cu^{63}Cl^{35}$					$Cu^{65}Cl^{35}$			Isotope shift[b]	
λ in air (A)	ν in vac. (cm^{-1})	Rel. int.	v'	v''	λ in air (A)	ν in vac. (cm^{-1})	Rel. int.	$\Delta\nu$(cm^{-1}) Exptl.	$\Delta\nu$ (cm^{-1}) Theoret.
3694.34	27060.8	1	7	2					
3732.18	26786.4	2	4	0	3733.28	26778.5	0	+7.9	+8.1
3732.37[a]	26785.0[a]								
3738.30	26742.5	3	5	1	3739.40	26734.7	1	+7.8	+7.9
3744.39	26699.0	3	6	2	3745.49	26691.2	2	+7.8	+7.5
3750.60	26654.9	3	7	3					
3785.00	26412.6	3	3	0	3785.84	26406.7	3	+5.9	+6.1
3785.20[a]	26411.2[a]				3786.09[a]	26405.0[a]			
3790.82	26372.0	4	4	1	3791.63	26366.4	4	+5.6	+5.8
			5	2	3797.68	26324.4	3		
			6	3	3803.81	26281.9	2		
3839.77	26035.8	5	2	0	3840.39	26031.7	5	+4.1	+4.1
3839.97[a]	26034.5[a]				3840.65[a]	26029.9[a]			
3845.18	25999.2	4	3	1	3845.86	25994.6	5	+4.6	+3.8
3850.85	25960.9	3	4	2					
3896.70	25655.4	6	1	0	3897.01	25653.4	6	+2.0	+2.0
3897.06[a]	25653.1[a]				3897.23[a]	25652.0[a]			
3901.82	25621.8	4	2	1	3902.02	25620.5	4	+1.3	+1.8
3907.25	25586.2	3	3	2					
3912.63	25551.0	1	4	3					
3955.87	25271.7	8	0	0	3955.84	25271.9	7	−0.2	−0.1
3956.20[a]	25269.6[a]				3956.11[a]	25270.2[a]			
3965.51	25210.3	5	2	2	3965.44	25210.7	5	−0.4	−0.5
3970.37	25179.5	3	3	3	3970.24	25180.3	3	−0.8	−0.6
4021.80	24857.5	10	0	1	4021.43	24859.8	10	−2.3	−2.4
4022.16[a]	24855.3[a]				4021.78[a]	24857.6[a]			
4026.24	24830.0	7	1	2	4025.76	24833.0	7	−3.0	−2.6
4030.82	24801.8	5	2	3					
4089.42	24446.5	8	0	2	4088.67	24450.9	8	−4.4	−4.6
					4089.03[a]	24448.8[a]			
4093.51	24422.0	9	1	3	4092.73	24426.7	9	−4.7	−4.7
4097.60	24397.6	9	2	4	4096.79	24402.5	8	−4.9	−4.8
4158.74	24039.0	7	0	3	4157.65	24045.3	7	−6.3	−6.7
4162.46	24017.5	7	1	4	4161.29	24024.2	7	−6.7	−6.9
4166.14	23996.3	8	2	5					
4169.87	23974.8	7	3	6					
4173.88	23951.8	7	4	7					

[a] These measurements refer to *Q* heads.
[b] $\Delta\nu=\nu(Cu^{63}Cl^{35})-\nu(Cu^{65}Cl^{35})$.

quence of the *E* system. The plates were measured on the Argonne photoelectric comparator. The accuracy of measurement of sharp bands on the first-order plates was about ±0.02 A.

F SYSTEM

The data on the bands of the *F* system of the $Cu^{63}Cl^{35}$ and $Cu^{65}Cl^{35}$ molecule, together with the vibrational analysis, is shown in Table III. These bands exhibit two close heads, the *R* and the *Q* heads. For a few bands the *Q* heads could also be measured and these are included in Table III. Figure 3 is a reproduction of the spectrogram showing the *F* bands of $Cu^{63}Cl^{35}$ and $Cu^{65}Cl^{35}$ molecules.

The *R* heads of the *F* bands of the $Cu^{63}Cl^{35}$ and $Cu^{65}Cl^{35}$ molecule can be represented, respectively, by the formulas

$$\nu_{63,35}{}^{F}=25287.0+386.8(v'+\tfrac{1}{2})-1.64(v'+\tfrac{1}{2})^2 -417.1(v''+\tfrac{1}{2})+1.50(v''+\tfrac{1}{2})^2 \quad (1)$$

$$\nu_{65,35}{}^{F}=25287.0+384.8(v'+\tfrac{1}{2})-1.65(v'+\tfrac{1}{2})^2 -415.0(v''+\tfrac{1}{2})+1.44(v''+\tfrac{1}{2})^2. \quad (2)$$

The vibrational constants $\omega_e''=417.1$ and $\omega_e''x_e''=1.50$ of Eq. (1) agree closely with the corresponding quantities in the band formulas for the other five band systems of the $Cu^{63}Cl^{35}$ molecule. Hence it follows that for $Cu^{63}Cl^{35}$ the lower state of the *F* system is the same as the common lower state of the *A*, *B*, *C*, *D*, and *E* band systems, which is also the ground state of the

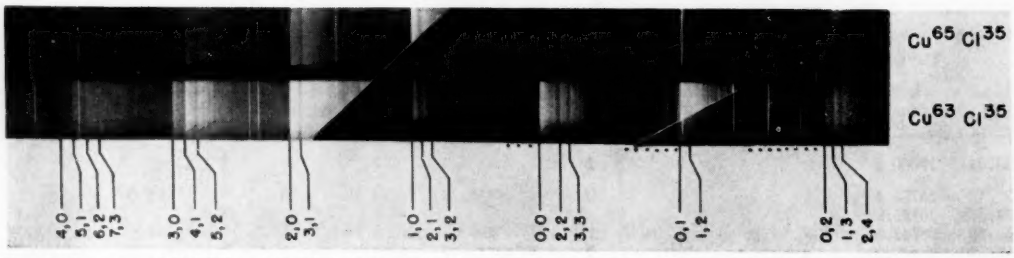

FIG. 3. F system of $Cu^{63}Cl^{35}$ and $Cu^{65}Cl^{35}$ photographed in the first order of the Argonne 30-ft spectrograph. The bands indicated by dots belong to the E system.

molecule. The same would be true for the other isotopic molecules also.

The last two columns of Table III show the observed and calculated isotope shifts.

E SYSTEM

Only the new bands recorded in the present investigation in the E system are shown in Table I along with their v', v'' assignments. These bands, as well as the new bands recorded in the other band systems, can be easily seen to represent one or both of the following two categories: First, intrinsically weak bands (due to the Franck-Condon principle) which have been recorded in the present investigation due to the high intensity obtained in the electrodeless discharge tube and secondly, bands which involve high v'' values and which were therefore not recorded by Ritschl in this absorption spectrum investigations. The formula

$$\nu_{63,35}{}^{E}=23077.4+405.3(v'+\tfrac{1}{2})-1.71(v'+\tfrac{1}{2})^2 -417.2(v''+\tfrac{1}{2})+1.57(v''+\tfrac{1}{2})^2, \quad (3)$$

the constants in which were obtained from our data by a least-squares program on the IBM 610 computer,[11]

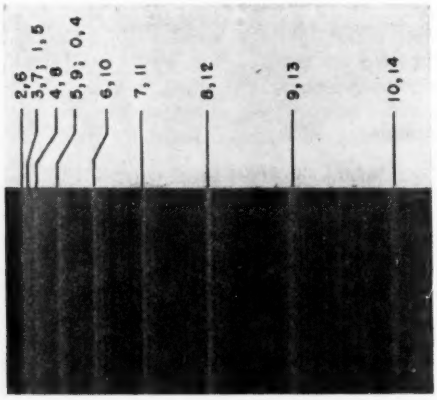

FIG. 4. $\Delta v=-4$ sequence of the E system of $Cu^{63}Cl^{35}$ photographed in the third order of the Argonne 30-ft grating spectrograph.

[11] We wish to express our thanks to Dr. George Winslow for helpful suggestions in connection with the use of the IBM 610 computer.

represents satisfactorily almost all bands of the E system except a few bands involving high v' and v'' values.

Figure 4 is a reproduction of the spectrogram showing the $\Delta v=-4$ sequence of the E system photographed in the third order of the Argonne 30-ft grating spectrograph. This sequence gives a clear demonstration of the formation of head of heads. Apart from the reasons mentioned earlier, it may be noted, that the head of heads in this sequence is clearly noticeable due to the circumstances obtained in this case (see below) whereby a molecular band can give rise to a narrow intensity maximum which has the appearance of an atomic line.

The formation of head of heads in a sequence and the usually accompanying phenomenon of tail bands are well known (see Herzberg[12a]). However, the structure of the $\Delta v=-4$ sequence of the E system of CuCl appears quite different from the structure of the well-known band sequences[13–16] showing heads of heads and/or tail bands. This difference can be clearly understood by reference to a graphical procedure for determining the turning point in a sequence, described by Herzberg.[12a]

The turning point in the course of a sequence or the head of heads occurs when, for two successive bands of the corresponding diagonal in the Deslandres table, the vertical difference, i.e., the difference between the two rows containing these bands is equal to the horizontal difference, i.e., the difference between the two columns containing these bands. Thus, when the $\Delta G'$ values and the $\Delta G''$ values are plotted against v in the same diagram and the $\Delta G'$ curve shifted by an amount $|\Delta v|$ to the left or to the right according as Δv is positive or negative, the intersection of this shifted $\Delta G'$ curve with the unshifted $\Delta G''$ curve give the v'' value at which the course of the sequence is reversed; see Fig. 7(a)–(c).

It is known[12b] that for different electronic states of a molecule, ω_e/B_e is nearly constant and α_e/B_e is approxi-

[12] (a) G. Herzberg, *Spectra of Diatomic Molecules* (D. Van Nostrand Company, Inc., Princeton, New Jersey, 1959), 2nd ed., sixth printing, Chap. IV, pp. 160, 161, 173; (b) Chap. IV, p. 174; (c) Chap. IV, pp. 174, 175.

[13] F. A. Jenkins, Phys. Rev. **31,** 539 (1928).

[14] G. Herzberg, Ann. Physik **86,** 189 (1928).

[15] J. G. Phillips, Astrophys. J. **108,** 434 (1948).

[16] G. Herzberg and R. B. Sutton, Can. J. Research **A18,** 74 (1940).

mately equal to $\omega_e x_e/\omega_e$ and hence $\omega_e x_e/\alpha_e$ is approximately constant. From these relationships it can be seen that B_v curves of two electronic states intersect at approximately the same v value and making nearly the same angle as do the corresponding ΔG curves. Thus, the bands in a sequence undergo a change in the direction of their shading at about the same point where the reversal in its course takes place.

With the above considerations in mind two typical cases represented in Fig. 5(a) and (b) and in Fig. 6(a) and (b) may be considered. In the first case the

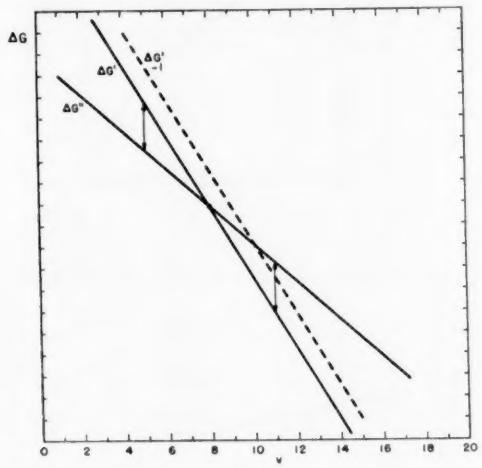

(a)

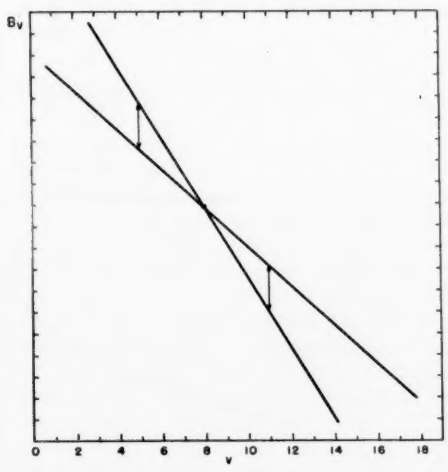

(b)

FIG. 5. (a) ΔG curves typical to case I (see text). The broken line curve is the $\Delta G'$ curve shifted by 1 unit to the right. Compare $(\Delta G' \sim \Delta G'')$ at $v=5$, 8 and 11 with the corresponding quantities in Fig. 6(a). Note that the $\Delta G'$ and $\Delta G''$ curves intersect at $v=8$ and the $\Delta G_{-1}'$ and $\Delta G''$ curves intersect at only a slightly higher v value, namely $v=10$. (b) B_v curves typical to case I (see text). Compare $(B_v' \sim B_v'')$ at $v=5$, 8 and 11 with the corresponding quantities in Fig. 6(b).

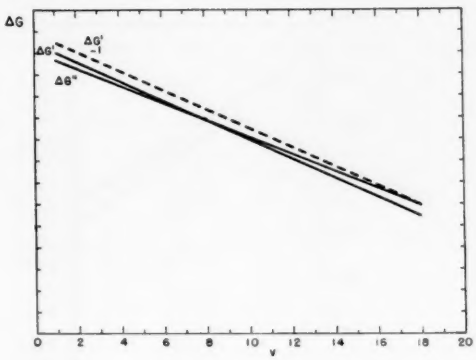

(a)

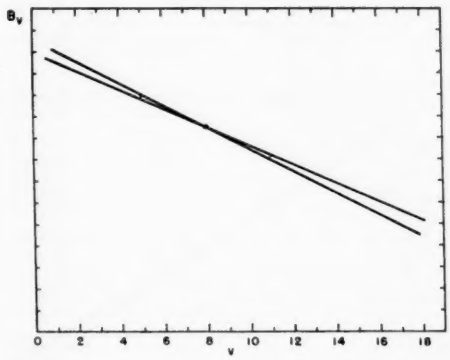

(b)

FIG. 6 (a) ΔG curves typical to case II (see text). The broken line curve is the $\Delta G'$ curve shifted to the right by 1 unit. Compare $(\Delta G' \sim \Delta G'')$ at $v=5$, 8 and 11 with the corresponding quantities in Fig. 5(a). Note that the $\Delta G'$ and $\Delta G''$ curves intersect at $v=8$ and the $\Delta G_{-1}'$ and $\Delta G''$ curves intersect only at an appreciably higher v value, namely $v=18$. (b) B_v curves typical to case II (see text). Compare $(B_v' \sim B_v'')$ at $v=5$, 8 and 11 with the corresponding quantities in Fig. 5(b).

ΔG curves, Fig. 5(a) and the B_v curves, Fig. 5(b), are comparatively steep and intersect at an appreciable angle, i.e., $\omega_e' x_e'$, $\omega_e'' x_e''$, and $\alpha_e' \alpha_e''$ are comparatively large and, in addition, $\omega_e' x_e'$ and α_e' are appreciably different from $\omega_e'' x_e''$ and α_e'', respectively. In the second case the ΔG curves, Fig. 6(a), and the B_v curves, Fig. 6(b), are comparatively flat and are nearly parallel to each other, i.e., $\omega_e' x_e'$, $\omega_e'' x_e''$, and α_e',α_e'' are comparatively small and, in addition, $\omega_e' x_e'$ and α_e' do not differ appreciably from $\omega_e'' x_e''$ and α_e'', respectively. The following remarks may be made concerning the structure of sequences showing heads of heads and tail bands of molecules representing the above two cases:

Case I

(A) The differences in wave numbers of successive bands, even near the turning point of a sequence, is comparatively large; see Fig. 5(a).

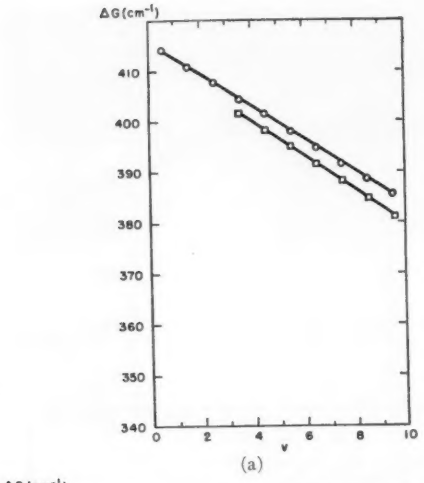

(a)

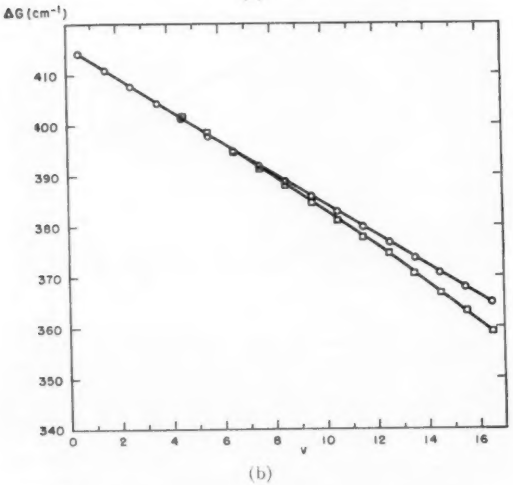

(b)

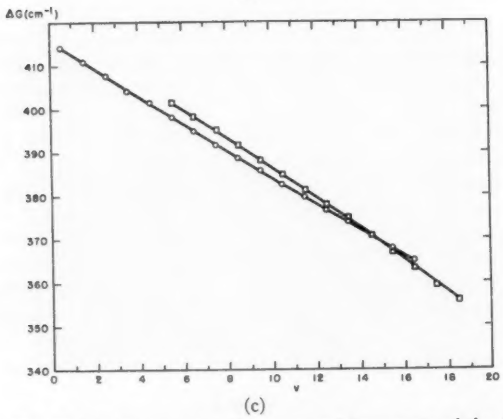

(c)

FIG. 7. (a) ΔG curves for the upper and lower state of the E system of $Cu^{63}Cl^{35}$. The $\Delta G'$ curve is shifted by 3 units to the right. (b) ΔG curves for the upper and lower state of the E system of $Cu^{63}Cl^{35}$. The $\Delta G'$ curve is shifted by 4 units to the right. (c) ΔG curves for the upper and lower state of the E system of $Cu^{63}Cl^{35}$. The $\Delta G'$ curve is shifted by 5 units to the right.

(B) If the ΔG (also B_v) curves intersect at a certain v'' value in any sequence, e.g., $\Delta v=0$ sequence, they intersect at only a slightly higher v'' value in the next, i.e., $\Delta v=-1$ sequence; see Fig. 5(a). Thus, in general,

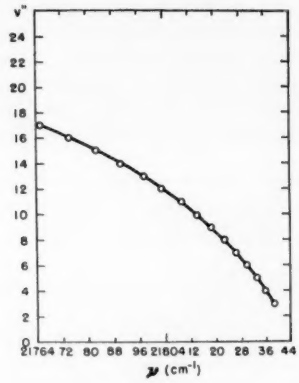

(a)

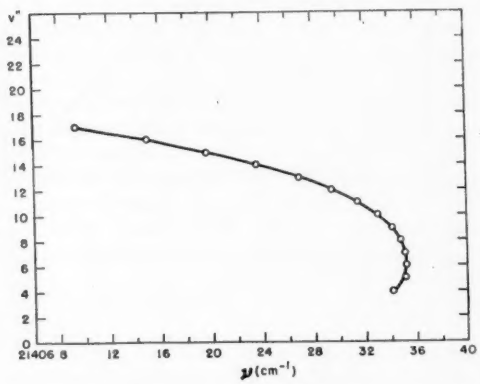

(b)

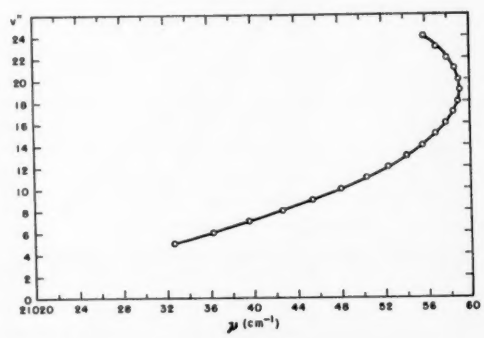

(c)

FIG. 8. (a) Graphical representation of the $\Delta v=-3$ sequence of the E system of $Cu^{63}Cl^{35}$. (ν's are experimental values.) (b) Graphical representation of the $\Delta v=-4$ sequence of the E system of $Cu^{63}Cl^{35}$. (ν's are experimental values.) (c) Graphical representation of the $\Delta v=-5$ sequence of the E system of $Cu^{63}Cl^{35}$. (ν's are calculated values, see text.)

TABLE IV. New bands in the D system of $Cu^{63}Cl^{35}$.

λ in air A	ν in vac. cm^{-1}	Rel. int.	v'	v''	λ in air A	ν in vac. cm^{-1}	Rel. int.	v'	v''
4173.88	23951.8	3	8	5	4603.57	21716.2	1	1	4
4180.27	23915.2	2	9	6	4604.62	21711.3			
4186.93	23877.1	1	10	7	4606.47	21702.5	2	2	5
4244.49	23553.3	3	8	6	4607.53	21697.5			
4250.56	23519.7	2	9	7	4609.42	21688.6	2	3	6
4256.86	23485.0	1	10	8	4610.48	21683.7			
4386.13	22792.7	4	7	7	4612.53	21674.0	3	4	7
4391.24	22766.2	4	8	8	4613.60	21669.0			
4396.54	22738.8	3	9	9	4615.73	21659.0	3	5	8
4402.11	22710.0	3	10	10	4616.84	21653.8			
4407.95	22679.9	2	11	11	4619.10	21643.2	3	6	9
4458.41	22423.2	6	6	7	4620.18	21638.1			
4462.81	22401.1	4	7	8	4622.65	21626.6	3	7	10
4467.41	22378.1	3	8	9	4623.80	21621.2			
4472.08	22354.7	2	9	10	4626.39	21609.1	3	8	11
4533.78	22050.4	6	5	7	4627.47	21604.0			
4534.64[a]	22046.3[a]				4630.37	21590.5	3	9	12
4537.64	22031.7	5	6	8	4631.39	21585.7			
4538.49	22027.6				4634.60	21570.8	2	10	13
4541.69	22012.1	5	7	9	4635.63	21566.0			
4542 59	22007.7				4639.17	21549.5	2	11	14
4545.96	21991.4	4	8	10	4640.26	21544.5			
4546.77	21987.5				4644.10	21526.7	2	12	15
4550.34	21970.2	3	9	11	4644.98	21522.6			
4551.16	21966.3				4649.48	21501.8	1	13	16
4555.09	21947.3	3	10	12	4655.36	21474.6	1	14	17
4555.89	21943.5				4656.30	21470.3			
4560.11	21923.2	2	11	13	4661.96	21444.2	0	15	18
4561.02	21918.8				4662.77	21440.5			
4565.48	21897.4	2	12	14					
4566.39	21893.0								

[a] These and the corresponding entries below (i.e., the second entries, wherever there are two entries against any v', v'') refer to Q heads.

it is possible to experimentally observe the formation of head of heads in at least a few sequences.

(C) $|B_v' \sim B_v''|$ changes by an appreciable amount within a few v units from the point of intersection of the B_v curves, Fig. 5(b), so that the first members of the sequence are clearly shaded in one direction, a few bands on either side of the turning point (remembering that the B_v curves intersect at about the same v value as do the ΔG curves) show no clearly developed heads, whereas the remaining bands are clearly shaded in a direction opposite to that of the first members of the sequence.

The CN violet bands,[13] the $(B\,^2\Sigma_u^+ - X\,^2\Sigma_g^+)N_2^+$ bands,[14] the Swan,[15] and the Deslandres—d'Azambuja[16] bands of C_2 illustrate the above case.

Case II

The E and A systems of CuCl and some band systems of indium and gallium halides[17,18] represent the second case. This case is discussed in detail below with special reference to the E system of CuCl.

(A) The successive bands near the turning point of a sequence are very close to each other; see Fig. 6(a). For instance, the two closest bands in the $\Delta v = -4$ sequence of the E system differ by just one-tenth of a wave number. A cluster of unresolved bands will be observed unless high dispersion and resolution are employed. This, in fact, is the case with the $\Delta v = -3$ sequence of the A system of CuCl (see below).

(B) If the ΔG (also B_v) curves intersect at a certain v'' in any sequence, e.g., the $\Delta v = 0$ sequence, they intersect only at a considerably higher v'' value in the next, i.e., $\Delta v = -1$ sequence; see Fig. 6(a). Thus, in general, it is possible to experimentally observe the formation of head of heads in one or at best two sequences only.

The $\Delta G''$ curve and the $\Delta G'$ curve shifted to the right by 3, 4, and 5 units, designated as the $\Delta G_{-3}'\Delta G_{-4}'$ and $\Delta G_{-5}'$ curve for the E system of $Cu^{63}Cl^{35}$, are shown in Fig. 7(a), (b), and (c), respectively. Figure 8(a), (b), and (c) are graphical representations of the $\Delta v = -3$, -4 and -5 sequences, respectively.

[17] M. Wehrli and E. Miecher, Helv. Phys. Acta **7**, 298 (1934).
[18] E. Miecher and M. Wehrli, Helv. Phys. Acta **7**, 331 (1934).

TABLE V. New bands in the *C* system of $Cu^{63}Cl^{35}$.

λ in air (A)	ν in vac. (cm^{-1})	Rel. int.	v'	v''
5168.13	19344.0	5	6	9
5170.41	19335.5	5	7	10
5172.79	19326.6	5	8	11
5175.17	19317.7	4	9	12
5177.67	19308.3	4	10	13
5180.30	19298.5	4	11	14
5183.01	19288.4	4	12	15
5185.89	19277.7	3	13	16
5188.94	19266.4	3	14	17
5192.25	19254.1	2	15	18

The $\Delta G''$ and $\Delta G_{-3}'$ curves do not intersect. We have therefore only the upper limb of the parabola with no vertex in Fig. 8(a). This situation is also true for the sequences $\Delta v=-2$, $\Delta v=-1$ and so on.

The $\Delta G''$ and $\Delta G_{-4}'$ curves intersect at $v''=6$, so that the corresponding graph of the $\Delta v=-4$ sequence, Fig. 8(b), shows the vertex and the beginning of the lower limb of the parabola also.

In our plates the bands of the $\Delta v=-5$ sequence of the *E* system were badly overlapped by the rotational structure of some bands belonging to other systems of CuCl and it was not possible to make any useful measurements on these bands. Therefore, ν values calculated from Eq. (3) were used in the graphical representation of this sequence, i.e., in Fig. 8(c). The lower limb of the parabola[19] is well developed in this figure. It is seen from Figs. 7(c) and 8(c) that the turning point of the $\Delta v=-5$ sequence occurs at relatively high v'' values. Even so, if the bands of this sequence were not overlapped by other bands, it would have perhaps been possible to notice the head of heads in this sequence also under very favorable experimental conditions.

TABLE VI. New bands in the *B* system of $Cu^{63}Cl^{35}$.

λ in air (A)	ν in vac. (cm^{-1})	Rel. int.	v'	v''
4806.56	20799.1	...	5	4
5002.00	19986.4	3	6	7
5005.83	19971.1	2	7	8
5009.35	19957.1	1	8	9
5013.34	19941.2	0	9	10
5195.75	19241.2	2	1	4
5197.65	19234.1	2	2	5
5199.41	19227.6	2	3	6
5201.30	19220.6	2	4	7
5203.27	19213.3	2	5	8
5205.38	19205.6	1	6	9
5207.62	19197.3	1	7	10

[19] Each band on this limb lies to the short-wavelength side of the previous member of the sequence.

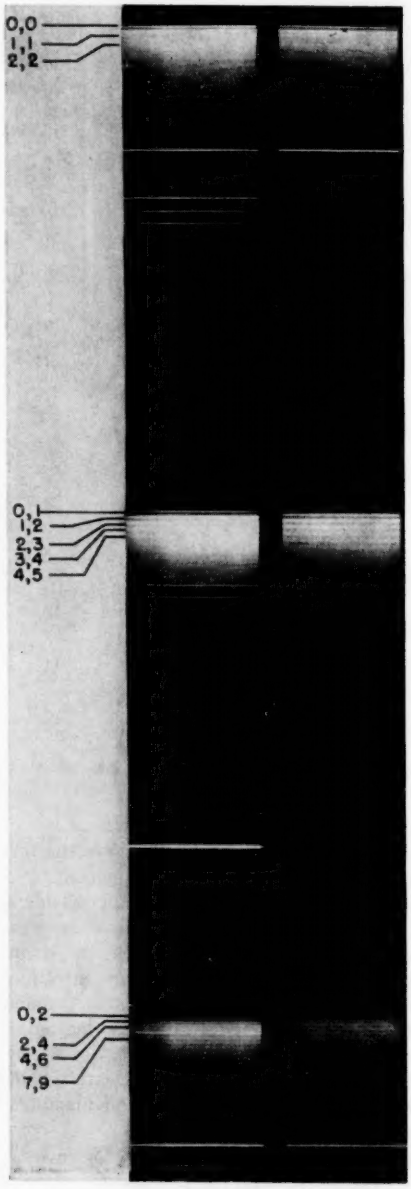

FIG. 9. *A* system of $Cu^{63}Cl^{35}$ and $Cu^{65}Cl^{35}$ photographed in the first order of the Argonne 30-ft grating spectrograph.

The $\Delta G_{-6}'$ $\Delta G_{-7}'$ etc. curves intersect the $\Delta G''$ curve at higher and higher v'' values. Thus, even if the $\Delta v=$

TABLE VII. *A* System.

$Cu^{63}Cl^{35}$					$Cu^{65}Cl^{35}$			Isotope shift[b]	
λ in air A	ν in vac. (cm^{-1})	Rel. int.	v'	v''	λ in air (A)	ν in vac. (cm^{-1})	Rel. int.	$\Delta\nu$(cm^{-1}) Exptl.	$\Delta\nu$(cm^{-1}) Theoret.
5152.36	19403.2	5	1	0	5152.86	19401.3	5	+1.9	+2.2
5155.45	19391.6	4	2	1	5156.00	19389.5	4	+2.1	+2.1
5158.50	19380.0	3	3	2					
5262.44	18997.3	10	0	0	5263.44	18997.3	10	+0.0	−0.02
5263.32[a]	18994.1[a]				5263.32[a]	18994.1[a]			
5264.76	18988.9	6	1	1	5264.69	18989.2	6	−0.3	−0.10
5265.68	18985.6				5265.73	18985.4			
5267.02	18980.8	4	2	2	5266.93	18981.1	4	−0.3	−0.10
5269.35	18972.4	2	3	3					
5379.69	18583.3	8	0	1	5379.06	18585.4	8	−2.1	−2.3
5380.76	18579.6				5380.07	18581.9			
5381.19	18578.1	7	1	2	5380.46	18580.6	7	−2.5	−2.3
5382.21	18574.6				5381.49	18577.1			
5382.69	18572.9	7	2	3	5381.97	18575.4	6	−2.5	−2.3
5383.73	18569.3				5382.97	18571.9			
5384.19	18567.7	6	3	4	5383.53	18570.0	5	−2.3	−2.3
5385.87	18561.9	4	4	5	5385.13	18564.5	4	−2.6	−2.3
			5	6	5386.84	18558.6	2		−2.4
			6	7	5388.79	18551.9	1		
5501.33	18172.4	2	0	2	5499.94	18177.0	2	−4.6	−4.4
5501.85	18170.6	3	1	3	5400.47	18175.2	3	−4.6	−4.4
5502.43	18168.7	4	2	4	5401.04	18173.3	4	−4.6	−4.4
5503.60	18164.9				5402.30	18169.5			
5503.08	18166.6	5	3	5	5401.75	18171.0	5	−4.4	−4.4
5504.30	18162.6								
5503.86	18164.0	4	4	6	5402.52	18168.5	4	−4.5	−4.4
5504.73	18161.1	3	5	7	5403.35	18165.7	3	−4.6	−4.4
			6	8	5504.33	18162.5	2		
5506.77	18154.4	2	7	9	5505.36	18159.1	2	−4.7	−4.4
5507.85	18150.9	2	8	10	5506.52	18155.2	2	−4.3	−4.4
5509.12	18146.7	1	9	11	5507.72	18151.3	1	−4.6	−4.4
			10	12	5509.05	18146.9	1		

[a] These and the corresponding entries below (i.e., the second entries, wherever there are two entries against any v', v'') refer to *Q* heads.
[b] $\Delta\nu=\nu(Cu^{63}Cl^{35})-\nu(Cu^{65}Cl^{35})$.

-6, $\Delta v=-7$, etc. sequences are observed, they would hardly extend till their turning points are reached. Their graphical representations would show only the lower limbs of the respective parabolas away from the vertices.

(C) $|B_v'\sim B_v''|$ differs only slightly from zero for a number of members of a sequence on either side of its turning point, (again remembering that the B_v curves intersect at about the same v value as do the ΔG curves); see Fig. 6(b). Consequently, a number of bands on either side of the turning point of a sequence show the structure, characteristic of bands involving nearly equal B_v' and B_v''.

When B_v' is approximately equal to B_v'', in a band having only *P* and *R* branches, the branches extend with approximately equal separations of the lines. If, in addition, a *Q* branch is also present, all the lines of the *Q* branch nearly coincide at $\nu=\nu_0$, resulting in an intense linelike *Q* branch. However, when high rotational levels are involved and, in addition, $D_v'-D_v''$ is relatively large and has the same sign as $B_v'-B_v''$, due to the influence of the rotational constants D_v' and D_v'', a band shows extra heads and in certain circumstances the band gives rise to a narrow intensity maximum and resembles a line. Herzberg[12e] has discussed such cases in detail and Wehrli and Miescher[17,18] attributed the linelike bands observed by them in the spectra of indium and gallium halides to this cause.

As may be seen in Fig. 4, the bands of the $\Delta v=-4$ sequence are narrow and linelike, and, as has been pointed out earlier, the formation of head of heads in this sequence could be followed due to this fact. Apparently the linelike structure of these bands is due to the influence of the rotational constants D_v mentioned above. However, this will be clear when the fine structure analysis of some bands of the *E* system is made and at least a few B_v', D_v' and B_v'', D_v'' values are obtained. This matter will be discussed in more detail in our later communications.

D SYSTEM

Only the new bands recorded in the present investigations in the *D* system are shown in Table IV along with their v', v'' assignments. The formula

$$\nu_{63,35}{}^{D}=22971.6+395.6(v'+\tfrac{1}{2})-1.90(v'+\tfrac{1}{2})^2 -416.9(v''+\tfrac{1}{2})+1.56(v''+\tfrac{1}{2})^2, \quad (4)$$

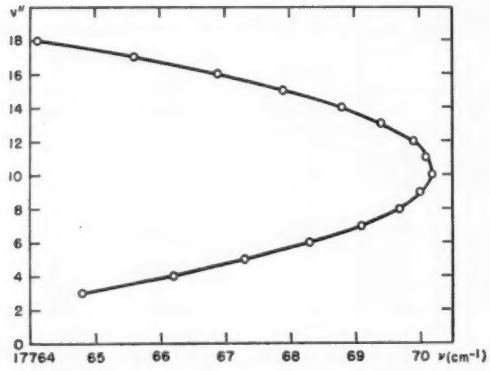

FIG. 10. Graphical representation of the $\Delta v=-3$ sequence of the A system of $Cu^{63}Cl^{35}$. (νs are calculated values, see text.)

the constants in which are obtained from our data by the least-squares procedure, represents satisfactorily the R heads of almost all the bands of the D system except a few bands involving high v' and v''. Though the Q heads could be measured for a number of bands, the accuracy of their measurements was considerably less than that of the R heads. For this reason and for a reason mentioned later the Q head data were not used for the calculation of the vibrational constants.

C AND B SYSTEMS

The minor extensions of the C and B systems recorded in the present investigations are shown in Tables V and VI, respectively. It may again be noticed that most of these new bands involve high v'' values and were therefore not recorded by Ritschl.

A SYSTEM

In the absorption spectrum of CuCl at very high temperatures (1200°C) Ritschl recorded about half a dozen bands of the A system, fitted them into a band formula, and concluded that this system has for its lower state, the ground state of the molecule. In view of the meager information existing on the A system, the complete data obtained in the present investigations on this system is given.

The data on the A system of the $Cu^{63}Cl^{35}$ and $Cu^{65}Cl^{35}$ molecule, together with the vibrational analysis, are given in Table II. The bands exhibit two heads, the R and the Q heads. For a few bands the Q heads could also be measured and these are included in Table VII. Figure 9 is a reproduction of the spectrogram showing the A system of $Cu^{63}Cl^{35}$ and $Cu^{65}Cl^{35}$ molecule.

The R heads of the bands of the A system of $Cu^{63}Cl^{35}$ and $Cu^{65}Cl^{35}$ can be represented respectively by the formulas

$$\nu_{63,35}{}^{A}=19001.4+409.2(v'+\tfrac{1}{2})-1.72(v'+\tfrac{1}{2})^2 -417.3(v''+\tfrac{1}{2})+1.62(v+\tfrac{1}{2})^2 \quad (5)$$

and

$$\nu_{65,35}{}^{A}=19001.4+407.0(v'+\tfrac{1}{2})-1.70(v'+\tfrac{1}{2})^2 -415.1(v''+\tfrac{1}{2})+1.59(v''+\tfrac{1}{2})^2. \quad (6)$$

In the third column of Table II are given the calculated values of the wave numbers of the bands of the $\Delta v=-3$ sequence of $Cu^{63}Cl^{35}$ using formula (5), and Fig. 10 is a graphical representation of the same sequence using these calculated values of ν. It is seen from this figure that the $\Delta v=-3$ sequence of the A system of $Cu^{63}Cl^{35}$ forms head of heads. The same is true for $Cu^{65}Cl^{35}$ also.

Figure 11 is an enlarged reproduction of the $\Delta v=-3$ sequences of the A systems of $Cu^{63}Cl^{35}$, and $Cu^{65}Cl^{35}$. It is seen that in each case this sequence consists of two features. These are designated A and B for $Cu^{63}Cl^{35}$ and A' and B' for $Cu^{65}Cl^{35}$. The features A and A' are the unresolved clusters of R heads, and features B and B' are the unresolved clusters of Q heads (see also below) of the bands of the $\Delta v=-3$ sequence of the two molecules. The dispersion and resolution available in the first order of the grating were not sufficient to resolve these features. The high exposure time that would have been required and the limited life of the discharge tubes made it difficult to photograph these bands in the higher orders of the grating. These features showed several poorly resolved peaks on the oscilloscope screen of the photoelectric comparator. These have been measured and are given in Table II. Similarly, a microphotometer tracing of these features showed several intensity peaks. However, in both cases the appearance of the peaks was such that it was not quite possible to distinguish the real intensity peaks from possible spurious peaks due to local nonuniformities in the grain of the photographic plate. The v', v'' values

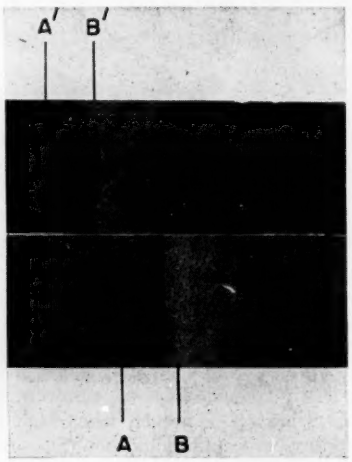

FIG. 11. An enlarged picture showing the $\Delta v=-3$ sequence of the A system of $Cu^{63}Cl^{35}$ and $Cu^{65}Cl^{35}$, photographed in the first order of the Argonne 30-ft grating spectrograph.

of columns 4 and 5 of Table II refer to the calculated ν values of column 3 and do not apply to the measured values. The measured values presented only to show that structure was observed in the vicinity of the calculated ν values, are therefore included in brackets.

It has been mentioned above that the features B and B' are the unresolved clusters of Q heads of the $\Delta v=-3$ sequence of $Cu^{63}Cl^{35}$ and $Cu^{65}Cl^{35}$, respectively. This can be seen from the following considerations:

The head of the Q branch lies very close to the origin of the band. For the bands of a v'' progression the interval between the band origin and the band head, which for the present purpose can be taken to be the same as the interval between the Q and the R heads, is given[20] by the equation

$$\nu^{or}-\nu^{H}=\nu^{Q}-\nu^{R}=\Delta\nu^{QR}=a-b(v''+\tfrac{1}{2})-c(v''+\tfrac{1}{2})^2, \quad (7)$$

where the constants a and b have different values for different v'' progressions. The constant c (involving $\alpha_e''^2$) is much smaller than the constant b (involving α_e''). Neglecting the third term, i.e., the term involving c, on the right-hand side of the equation (7), one obtains

$$\Delta\nu_{v',v''}{}^{QR}-\Delta\nu_{v',v''+1}{}^{QR}=b, \quad (8)$$

which is a constant for a given v'' progression. In other words, to a good approximation the interval between the Q and R heads in a v'' progression of band changes by a constant amount. It is seen from Table VII that $\Delta\nu_{0,0}{}^{QR}=-3.2$ cm^{-1} and $\Delta\nu_{0,1}{}^{QR}=-3.7$ cm^{-1}. Therefore $\Delta\nu_{0,2}{}^{QR}$ (see reference 21) and $\Delta\nu_{0,3}{}^{QR}$ should have values -4.2 cm^{-1} and -4.7 cm^{-1}. It may be seen from the second column of Table II that the interval between the long-wavelength edges of the features A and B is -4.6 cm^{-1} in perfect agreement with the calculated value.

[20] R. C. Johnson, *An Introduction to Molecular Spectra* (Pitman Publishing Corporation, New York, 1949). Chap. 2, p. 19.

[21] In the $\Delta v=-2$ sequence one or two Q heads could be distinguished but the others were overlapped by the R heads of later bands in the sequence.

REMARKS

As is well known, the vibrational constants obtained making use of the R or P head data are not very accurate. More accurate constants are obtained using Q head measurements for band systems which have Q branches, if a sufficient number of the Q heads can be accurately measured. In any case, the best vibrational constants are obtained by making use of band origins. From three to six bands have been selected for rotational analysis in each of B, C, D, E, and F band systems. When this is completed, there would be data on the band origins for three to six bands of each of the above band systems. With the help of these data, the band origins of the other bands of these systems can be calculated, and it would then be possible to give the best possible vibrational constants for the electronic states involved in these band systems.

From the considerable extensions of bands recorded in the D and E systems, a sufficient number of ΔG values exists to enable one to arrive at approximate values of the dissociation energies of the three electronic states involved in these band systems by the extrapolation method. However, it is again clear that more accurate ΔG values will be obtained using the band origin data rather than the band head data. For this reason the discussion of dissociation energies would be taken up in our later communications.

ACKNOWLEDGMENTS

The authors wish to express their thanks to Dr. F. S. Tomkins and Dr. Mark Fred for their encouragement. One of the authors (P.R.R.) wishes to express his thanks to Dr. R. G. Taecker, Director of the International Institute for Nuclear Science and Engineering of the Argonne National Laboratory for encouragement and Dr. R. K. Asundi, Dr. V. T. Athavale and Dr. N. A. Narasimham, of the Atomic Energy Establishment Trombay, Bombay, India, for their interest in this work. The authors are also indebted to Professor R. S. Mulliken for a preliminary reading of the manuscript.

Vapor Pressure of Antimony by the Torsion-Effusion Method*

GERD M. ROSENBLATT† AND C. ERNEST BIRCHENALL‡

The James Forrestal Research Center and Department of Chemistry, Princeton University, Princeton, New Jersey

(Received January 3, 1961)

The pressures and mean molecular weights of the vapors over solid antimony (420–550°C) and solid zinc (250–335°C) have been determined by simultaneous measurements by the torsion-momentum and Knudsen weight loss methods. The torsion measurement was calibrated with mercury at 30° using a mercury vapor pressure of 2.96×10^{-3} mm Hg determined by concurrent weight loss experiments. Zinc vapor is confirmed to be monatomic. The zinc pressure data are represented by $\log P_{\text{mm}}=(8.741\pm0.218)-(6630\pm125)/T$ giving $\Delta H_{298}°$ (vap) $=30.73\pm0.57$ and 31.18 ± 0.12 kcal/mole by the second law and third law of thermodynamics, respectively, in excellent agreement with previously reported results. The vapor over solid antimony is all Sb_4 molecules within experimental error. Least-squares analysis of the antimony data yields $\log P_{\text{mm}}=(10.571\pm0.090)-(10\,300\pm68)/T$, pressures 10%–40% lower than those previously reported. The heat of vaporization of $Sb_4(g)$ at 298.16°K is 49.83 ± 0.31 kcal/mole by the second law and 49.45 ± 0.09 by the third law of thermodynamics. This thermodynamic consistency and the agreement of the zinc results with accepted measurements indicate that the antimony pressures presented should be preferable to those previously reported.

SINCE the early vapor density measurements of Meyer and Biltz[1] it has been known that antimony vapor consists mainly of polyatomic molecules. Meyer and Biltz report the vapor over liquid antimony to be predominantly Sb_2 molecules with some Sb_4 present. Niwa and Yoshiyama[2] measured the pressure and molecular weight of the vapor over solid antimony using the torsion-effusion method and report the vapor to be 100% Sb_4 at 530°C within their limits of error. This result appears to be essentially correct despite discrepancies in the treatment of their data. In the torsion-effusion method the molecular weight of the vapor is obtained from the square of the ratio of two pressures. One pressure is obtained by measuring the momentum of the molecular beam effusing through an orifice. The other is calculated from the weight of vapor which escapes through the orifice in unit time. The weight loss measurement is dependent upon the square root of the molecular weight of the vapor while the momentum measurement is independent of the molecular weight. Niwa and Yoshiyama corrected the pressure they measured by weight loss for finite thickness of the effusion orifice, but they did not make the corresponding correction to the pressure they measured simultaneously by torsion. This difference in treatment greatly affects the calculated molecular weight. Moreover, Niwa and Yoshiyama calibrated their apparatus with potassium chloride using a different torsion fiber for the calibration than that used for the antimony measurements. The vapor over potassium chloride was assumed to be diatomic KCl, but more recently it has been shown[3] that about 11% of the vapor over solid potassium chloride at 650°C is K_2Cl_2. In view of these discrepancies Niwa and Yoshiyama's results leave some ambiguity about the pressure and composition of antimony vapor.

The pressure over solid antimony has also been measured by Nesmeyanov and Iofa[4] who assume a vapor of Sb_4 on the basis of Niwa and Yoshiyama's results. Calculations of $\Delta H_{298}°$ (vap) from their data by the second and third laws of thermodynamics differ by 2.1 kcal/mole. Stull and Sinke[5] have approximated a set of consistent thermodynamic quantities for antimony vapor by using the available spectroscopic data for Sb(g) and $Sb_2(g)$ along with enthalpies and entropies for $Sb_4(g)$ estimated from the above quoted vapor pressure measurements. Their tabulation shows Sb_4 to be the predominant vapor species up to about 1450°K with the vapor at 800°K containing about 0.9% Sb_2.

This paper presents measurements of the pressure and average molecular weight of the vapor over solid antimony from 420–550°C made by simultaneous use of the Volmer[6] torsion and Knudsen[7] effusion methods. The torsion measurement was calibrated with mercury at 30°C against the absolute pressure measured in concurrent Knudsen weight loss experiments. The vapor pressure over solid zinc was measured from 250–335°C to check on the accuracy and precision of the apparatus.

---

* This article is based upon a dissertation submitted by Gerd M. Rosenblatt in partial fulfillment of the requirements for the degree of Doctor of Philosophy at Princeton University. Work supported in part by the Office of Naval Research. Reproduction in whole or in part is permitted for any purpose of the United States Government.

† E. I. DuPont de Nemours Postgraduate Fellow 1957–1958. Present address: Department of Chemistry, University of California, Berkeley 4, California.

‡ Present address: Department of Chemical Engineering, University of Delaware, Newark, Delaware.

[1] V. Meyer and H. Biltz, Ber. deut. chem. Ges. **22,** 725 (1889).

[2] K. Niwa and M. Yoshiyama, J. Fac. Sci. Hokkaido Imp. Univ. Ser. III **3,** 75 (1940).

[3] R. C. Miller and P. Kusch, J. Chem. Phys. **25,** 860 (1956).

[4] A. N. Nesmeyanov and B. Z. Iofa, Doklady Akad. Nauk. S.S.S.R. **98,** 983 (1954).

[5] D. R. Stull and D. C. Sinke, *Thermodynamic Properties of the Elements* (American Chemical Society, Washington, D. C., 1956).

[6] M. Volmer, Z. physik. Chem., Bodenstein-Festband, 863 (1931).

[7] M. Knudsen, Ann. Phys. **29,** 179 (1909).

EXPERIMENTAL

Apparatus

The torsion-effusion apparatus[8] is illustrated in Fig. 1. The torsion fiber was a 50-cm-long tungsten wire, having a torsion constant on the order of 0.1 dyne-cm/rad, which had been annealed under tension in hydrogen at 1600°K for 3 hr. After this treatment the zero point was quite stable if the vacuum system was well outgassed and the pressure was less than 10^{-4} or 10^{-5} mm Hg. The zero point was affected by gross (10 g) changes in the weight suspended but not by the small weight changes occurring during a run. The torsion suspension could be raised, lowered, and rotated to put the mirror "on scale" and could be removed from the vacuum chamber and replaced without loss of this alignment. The ½-in. plane mirror was clamped to its mount as its position varied erratically with changes in pressure if it was cemented or waxed.

The two effusion cells were loaded through vertical tubing coming up from the center. In the Pyrex cell, this tubing was sealed off about 2 in. up while the quartz cell was closed with a 7/15 ground joint. The two, opposed, offset orifices of the Pyrex cell, about 2×10^{-3} cm² in area, were made by blowing a small dimple in the glass. The dimple was then ground down to an almost knife-edged orifice. To produce the smaller orifices, 8×10^{-4} cm², desired for the quartz cell the dimple was made by pushing a Kanthal needle into the softened quartz through a temporary large hole opposite the desired orifice position.

A 4-in. i.d. resistance furnace was wound so that, at any instant, the current in adjacent Kanthal windings flowed in opposite directions to prevent electromagnetic induction effects. The windings were spaced closer at the top and a 1-in. wall, aluminum cylinder was placed inside the furnace core to diminish and smooth the temperature gradient. The furnace was controlled to ±0.1°C for a few hours and ±1°C for longer periods.

Attempts to damp the swing of the torsion pendulum magnetically resulted in large zero point changes which persisted after the electromagnet was turned off. However, the swing could be damped sufficiently to be completely "on scale", without affecting the zero point, by alternately holding a small magnet close to one side of the brass mirror mount as this side swung away from the magnet and then withdrawing the magnet on the return swing. It was necessary to coat the interior of the vacuum chamber with *Aquadag*[9] and to ground this graphite coating, frame, furnace, and aluminum cylinder inside the furnace to eliminate erratic zero point readings. To reduce vibrations the vacuum chamber was rigidly fastened to a heavy angle iron frame mounted upon vibration damping felt and was isolated from auxiliary vacuum equipment by rubber hose or metal bellows. The furnace, which could be raised and lowered, was mounted independently and did not touch the vacuum chamber.

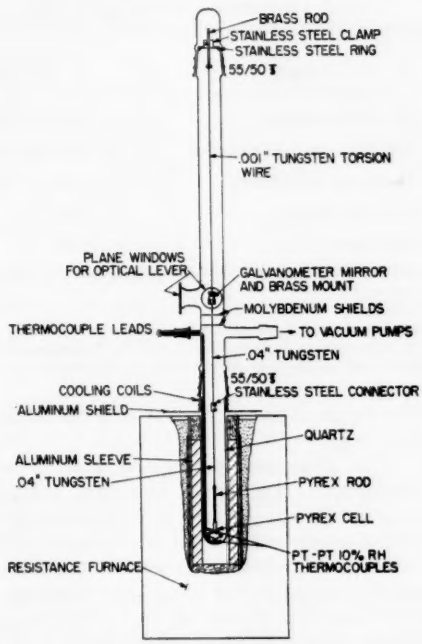

FIG. 1. Apparatus used for torsion-effusion measurements.

Measurement of Parameters

The equations used to determine the vapor pressure and molecular weight are:

$$P_T=[L_0x/s(a_1q_1f_1+a_2q_2f_2)] \quad (1)$$

$$P_W=[w/(a_1f_1'+a_2f_2')t](2\pi RT/M')^{\frac{1}{2}} \quad (2)$$

$$M=M'(P_W/P_T)^2, \quad (3)$$

where P_T and P_W are the pressures obtained from the torsion and weight loss measurements respectively, L_0 is the torque required to twist the suspension one radian, x is the deflection observed on the scale, s is the distance from the scale to the mirror, a_1 and a_2 are the areas of the orifices, q_1 and q_2 are the perpendicular distances from the torsion wire to the effusing vapor beams, f_1, f_2, f_1', and f_2' are corrections for finite orifice thickness,[10,11] w is the weight loss in time t, M' is the assumed

[8] For greater experimental details and tables of all measurements and experimental parameters, see the Doctoral Dissertation of Gerd M. Rosenblatt, Princeton University (1960) L. C. Card No. Mic 60-5045 available from University Microfilms, 313 N. First Street, Ann Arbor, Michigan.

[9] Acheson Colloids Company, Division of Acheson Industries, Inc., Port Huron, Michigan.

[10] P. Clausing, Ann. Physik (5) **12**, 961 (1932).

[11] R. D. Freeman and A. W. Searcy, J. Chem. Phys. **22**, 762 (1954).

TABLE I. Vapor pressure of mercury at 30°C.

Source	Pressure 10^{-3} mm Hg
This work, av P_W	2.96±0.05
This work, av P_T (absolute)	3.31±0.27
Ernsberger and Pitman[a]	2.96
Stull and Sinke[b]	3.01
Hultgren[c]	2.93

[a] See footnote 13.
[b] See footnote 5.
[c] R. Hultgren, *Selected Values for the Thermodynamic Properties of Metals and Alloys* (Minerals Research Laboratory, Institute of Engineering Research, University of California, Berkeley, March, 1958), Hg data sheets 1–8.

molecular weight of the vapor, and M is the calculated molecular weight.

The orifice areas were determined from calibrated photomicrographs. The orifice thickness, needed to calculate f and f'[11] was obtained from photomicrographs of additional orifices, made in the same manner as those in the effusion cell, mounted in plastic, and sectioned perpendicular to the orifice plane. The thickness was about 0.05 mm with an uncertainty of ±20% resulting in correction factors of about 0.9 uncertain to ±3%. The sum of the lever arm lengths was obtained from a photograph of the cell while water was forced through the orifices. The camera was on the axis of rotation of the cell. To measure the relative lengths of the individual lever arms, which were about 1 cm long, a reference plumb line, parallel to the torsion wire, was suspended in the plane defined by the torsion wire and cell lever arms. A traveling microscope mounted on a cathetometer stand with its line of sight perpendicular and its directions of motion parallel to this plane was used to measure the distance between orifice and plumb line. Then the microscope was raised to measure the distance between torsion wire and plumb line. The difference between these two measurements was the distance between torsion axis and orifice.

The two Pt-Pt 10% Rh thermocouples, one adjacent to the cell at the level of a cell sidearm and the other just below the center of the cell, were calibrated in the evacuated chamber over the temperature range of the measurements against a secondary standard couple. For this calibration the secondary standard thermocouple, which had been calibrated against a NBS thermocouple, was placed inside a dummy effusion cell held in the normal cell position for making a run. The calibration of the measuring thermocouples was repeated after an extensive series of runs including zinc, arsenic, and antimony and found to be unchanged in spite of the bare hot junctions. The temperature is estimated to be known to better than 1°C.

The torsion constant of the suspension L_0 was determined by measuring the period of the suspension system alone and the period with a brass disk of known moment of inertia attached. Experimentally, the torsion constant was independent of the amplitude of swing, residual pressure, furnace temperature, and mass suspended, with values reproducible to better than 0.5% and unchanging with time. The use of such a dynamically derived torsion constant in the static measurement assumes that the deflection is linear and symmetric, i.e., that $F=k\theta$ and that k is the same in both directions. The vapor pressure data show that deflections are linear from below 5×10^{-3} rad to the largest observed. The data also show that the pressures calculated from the torsion observations on an absolute basis using the dynamically obtained L_0 are consistently about 10% higher than those calculated from the measured weight losses. For this reason the torsion measurement was calibrated with mercury. Constant speed motion pictures were taken of the scale through the telescope and swinging mirror to ascertain if asymmetry of the torsion suspension was the cause of the discrepancy. These pictures indicate that asymmetry probably accounts for an error in P_T in the observed direction on the order of 2%. A twist imposed on the fiber texture of tungsten wire in the drawing process apparently is not unusual and may cause asymmetric behavior.

Procedure

To prepare for a run the clean cell was filled with sample, closed, dried, and weighed to the nearest 0.1 mg. After the cell was attached to the suspension the bottom of the vacuum chamber was replaced and the system was pumped down to about 10^{-6} mm Hg. Meanwhile the furnace was brought to the temperature of the run and raised enough to heat the cell to 200°C below the temperature of the run. Periodic zero point readings were taken to 0.1 cm on a scale about 2.2 m from the mirror. The furnace was raised the rest of the way to start the run. Scale and thermocouple readings were taken every two minutes until they were essentially constant and periodically thereafter. The resulting plot of deflection vs time was later used to correct for the time required to heat up the cell. The correction was in the range of 5–10 min, while runs lasted from 4 to over 24 hr. At the end of a run the furnace was low-

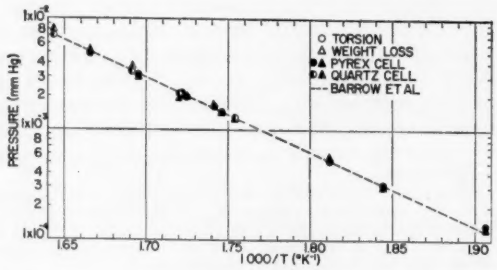

FIG. 2. Vapor pressure over solid zinc as a function of $1000/T$ °K^{-1}. The broken line represents the equation given in reference 16.

TABLE II. Antimony vapor pressure measurements.

Run	T °C	x cm	w mg	t min	P_T mm Hg	P_W mm Hg	M
1 av	479.4	71.6	25.15	415	6.29×10^{-3}	5.43×10^{-3}	363
final	479.4	11.4	...	...	1.00×10^{-3}	...	...
2 av	485.3	14.2	4.75	355	1.25×10^{-3}	1.20×10^{-3}	449
final	485.3	12.9	...	...	1.13×10^{-3}	...	...
3 av	489.7	15.2	5.2	353	1.33×10^{-3}	1.33×10^{-3}	487
final	489.7	14.4	...	...	1.26×10^{-3}	...	...
4	473.1	6.9	10.3	1490	6.06×10^{-4}	6.18×10^{-4}	506
5	420.3	0.8	1.0	1450	7.02×10^{-5}	5.94×10^{-5}	349
6	431.2	1.3	1.6	1570	1.14×10^{-4}	8.84×10^{-5}	293
7	445.8	2.0	3.2	1640	1.76×10^{-4}	1.71×10^{-4}	460
8	459.3	3.8	5.1	1430	3.34×10^{-4}	3.16×10^{-4}	436
9	496.6	17.9	5.9	356	1.57×10^{-3}	1.50×10^{-3}	445
10	508.8	28.9	9.5	354	2.54×10^{-3}	2.46×10^{-3}	457
11	482.2	9.8	4.9	520	8.61×10^{-4}	8.48×10^{-4}	472
12	438.2	1.4	1.4	1160	1.23×10^{-4}	1.05×10^{-4}	355
13	480.0	3.6	6.2	1440	7.45×10^{-4}	1.06×10^{-3}	...
14	508.6	12.1	2.9	295	2.50×10^{-3}	2.46×10^{-3}	472
15	460.0	1.7	2.0	1435	3.52×10^{-4}	3.38×10^{-4}	449
16	534.2	31.0	7.7	296	6.41×10^{-3}	6.61×10^{-3}	518
17	548.1	51.2	10.0	236	1.06×10^{-2}	1.09×10^{-2}	515

ered, the zero point was redetermined, and the cell was reweighed. A slightly different procedure was used for the mercury runs for which the furnace was replaced by a water bath.

Materials

The samples were all best available commercial purity and were not purified further. The mercury was instrumental grade, and the zinc was listed as 99.99% pure. The antimony was quoted to be 99.8% pure. Spectrographic analysis[12] of the Sb powder showed the chief metallic impurity to be 0.06% As. The Sb lumps used for some of the runs were labeled to contain 0.01% As. Trace impurities, except those forming volatile compounds when heated, should have little effect on the vapor pressure measurements.

RESULTS

Mercury

The results of three determinations of the vapor pressure of liquid mercury at 30.0°C are summarized in Table I along with the very accurate results of Ernsberger and Pitman[13] and the values recommended in two critical compilations of thermodynamic data. The uncertainties listed in Table I and in other portions of this paper are 95% confidence limits calculated from the deviations from the mean. Although they are considerably greater than average deviations or probable errors, they do not account for systematic errors and are only measures of precision, not estimated accuracy. The P_T (absolute) values were calculated by direct substitution of measured quantities into Eq. (1) without any correction for asymmetry of the torsion suspension. The weight loss values agree very well with the literature values while the torsion results are high, causing the calculated molecular weight to be about 20% below the atomic weight of mercury. To correct for this systematic error, the average of the mercury weight loss determinations P_W was divided by the average of the mercury P_T (absolute) torsion determinations to yield a correction factor of 0.893. All subsequent torsion pressure determinations were multiplied by this factor to obtain the results reported as P_T and to calculate the molecular weight.

Zinc

The vapor pressure of zinc was determined in order to evaluate the apparatus in its higher temperature form and to check the mercury calibration over a range of temperature and pressure. The measured pressures are shown in Fig. 2 in which the torsion and weight loss

[12] Courtesy of G. W. Davis and G. V. Downing, Jr., of the Merck Sharpe and Dohme Research Laboratory, Rahway, New Jersey.

[13] F. M. Ernsberger and H. W. Pitman, Rev. Sci. Instr. **26**, 584 (1955).

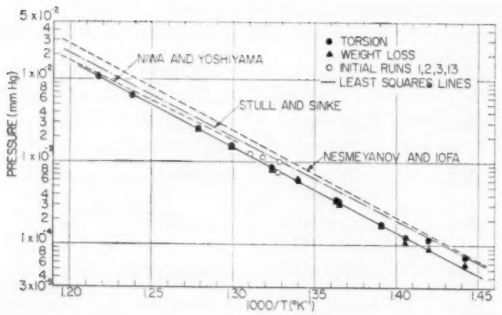

FIG. 3. Vapor pressure of Sb_4 molecules over solid antimony as a function of $1000/T$ °K^{-1}. The unfilled circles are the initial runs described in the text. The broken lines represent data presented in references 2, 4, and 5.

results are differentiated as are the runs made in the pyrex and quartz cells. Runs were carried out with zinc from two sources and with two torsion wires. A least-squares analysis of the data yields

$$\log P_{\text{mm}} = (8.741 \pm 0.218) - (6630 \pm 125)/T \quad (254\text{–}608°\text{C}). \quad (4)$$

The average of 14 measurements of the molecular weight of the zinc vapor is 65±18.

Antimony

The results of 17 determinations of the vapor pressure of antimony are presented in Table II and Fig. 3. One loading of the Pyrex cell with antimony metal powder was used for runs 1 through 12. Antimony metal lumps were used for runs 13 through 17 in a single loading of the quartz cell. The same torsion wire used for the last 10 zinc runs was used for all the antimony determinations. The weight loss pressures were calculated assuming the vapor to consist only of Sb_4 molecules.

Both average and final torsion pressures are tabulated for runs 1, 2, and 3 because the observed scale deflection decreased steadily as these runs progressed. This change in deflection was greatest during run No. 1 and had ceased entirely by the end of run No. 3 when about 4% of the original sample had been vaporized. Assuming the pressure of Sb_4 to be that calculated from subsequent runs, the additional vapor coming off during these three runs and during a preliminary heating of the sample at 200°C is estimated to have a molecular weight on the order of 100. This suggests that the extraneous high pressure is due to a light adsorbed gas, probably H_2O, N_2, or O_2. The first run with the antimony lumps, No. 13, also showed a large initial deflection. The pressure however, leveled off to the value tabulated in Table II by the end of the run. As the weight loss pressure is necessarily an average value, no meaningful molecular weight can be calculated from these two pressures. That the extraneous vapor was completely distilled off the lumps when less than 0.5% of the sample had been vaporized again indicates an adsorbed gas, as the powder has a surface area many times that of the lumps. It was also observed, in all the antimony runs, that when the furnace was first raised to start the run there was an initial high pressure deflection which subsided in the first few minutes. It is unlikely that these bursts were caused by ordinary outgassing of the cell as the runs were started after the cell had been held at about 200°C and 10^{-6} mm for more than 12 hr, and the bursts were not observed during the zinc runs. They might have been caused by some readsorption of gas by the antimony sample when the cell was removed from the vacuum chamber for weighing. The final torsion pressures from runs 1, 2, 3, and 13 are indicated by open circles in Fig. 3. Runs 1, 2, 3, approach the line in order but are clearly above it while No. 13 is on the line, another indication that all the adsorbed gas was evolved in the initial stages of this run.

TABLE III. Enthalpies and entropies of vaporization of antimony, 750°K.

Source	ΔH_{750}° kcal/mole	ΔS_{750}° cal/deg mole
This work	47.13±0.31	35.19±0.41
Nesmeyanov and Iofa[a]	48.09	37.35
Niwa and Yoshiyama[b]	44.58	32.24

[a] See footnote 4.
[b] See footnote 2.

Excluding the initial runs for the reasons described above, and also excluding the three runs at the lowest temperatures because of the very large weighing and scale reading errors at such low pressures, the average molecular weight is 474±56. This result is less than 3% below the formula weight of Sb_4, 487, which is well within the error of the molecular weight determination. Thus the vapor over solid antimony at these temperatures is completely Sb_4 molecules within the limits of error. Even if the deviation is real, the vapor contains less than 5% Sb_2 molecules. A least-squares treatment

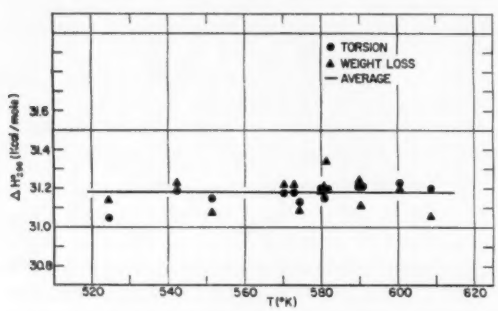

FIG. 4. The standard heats of vaporization of solid zinc calculated by the third law of thermodynamics as a function of temperature. The average value is 31.18 kcal/mole.

of the pressures in Table II, excluding the same unreliable runs, yields the solid line drawn through the experimental points in Fig. 3 for which the equation is

$$\log P_{mm} = (10.571 \pm 0.090) - (10\,300 \pm 68)/T \quad (693\text{—}821°\text{C}). \quad (5)$$

DISCUSSION

Mercury

The excellent agreement of the measured weight loss pressure with the accurate determination of Ernsberger and Pitman and with the pressures extrapolated from high temperature data indicates that there are no serious systematic errors in the measurement of the parameters used to calculate an absolute weight loss pressure. Thus the discrepancy of the absolute torsion measurement, which appears to be outside random experimental error, cannot be due to errors in the measurement of the orifice areas or thickness. The discrepancy is an order of magnitude greater than the total estimated inaccuracy of lever arm lengths, mirror to scale distance, deflection reading at all but the lowest pressures, and dynamic torsion constant. The other pressure measurements show the discrepancy to be, within experimental error, independent of the cell used, temperature, deflection, and the particular length of tungsten wire taken from the spool. Thus it is probable that the systematic error in the absolute torsion measurement is due to the use of a dynamically derived torsion constant assuming a symmetrical fiber. It is possible, but less likely, that the cell geometry and the vapor flow do not meet the assumptions contained in the kinetic theory derivation of the equations used. The weight loss pressure, and the mercury pressures in Table I reported by other authors, are 6 or 7% higher than those listed in the International Critical Tables and reproduced in the common handbooks to four significant figures.

A third law treatment of the weight loss pressure yields $\Delta H_{298}°$ (vap) = 14 660±8 cal/mole using the free energy functions tabulated by Stull and Stinke.[5] The standard entropy of Hg(c) used to calculate these free energy functions may be high by 0.02 cal/deg mole, as it is based upon low temperature heat capacity measurements of Pickard and Simon[14] who report an anomaly at 6°K not found in the later measurements of Smith and Walcott.[15] A change in the Hg(c) free energy functions of 0.02 cal/deg mole would raise the above heat of vaporization by 7 cal/mole.

TABLE IV. $\Delta H_{298}°$ for $4Sb(s) = Sb_4(g)$ in kcal/mole.

Source	Second law	Third law
This work	49.83±0.31	49.45±0.09
Nesmeyanov and Iofa[a]	50.79	48.68
Niwa and Yoshiyama[b]	47.28	49.04

[a] See footnote 4.
[b] See footnote 2.

[14] G. L. Pickard and F. E. Simon, Proc. Phys. Soc. (London) **61**, 1 (1948).

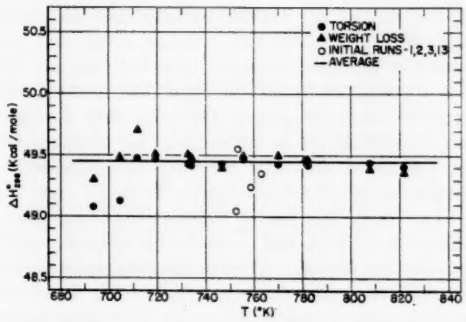

FIG. 5. The standard heats of reaction for $4Sb(s) = Sb_4(g)$ calculated by the third law of thermodynamics as a function of temperature. The open circles are the initial runs in Fig. 3 and described in the text. The average value is 49.45 kcal/mole.

Zinc

The measured zinc vapor pressures, represented by Eq. (4), yield $\Delta H_{298}°$(vap) = 30.73±0.57 kcal/mole using the second law of thermodynamics and heat contents tabulated by Stull and Sinke.[5] The heat of vaporization calculated from each pressure measurement using tabulated free energy functions[5] is plotted as a function of temperature in Fig. 4. The heats show no trend with temperature indicating that the data contain no serious temperature dependent errors. The average third law heat of vaporization at 298.16°K is 31.18±0.12 kcal/mole. Barrow and co-workers[16] have reviewed zinc vapor pressure measurements and report a best value for $\Delta H_{298}°$ = 31.18 kcal/mole. Using this value for the heat of sublimation they derive the vapor pressure curve drawn through the points in Fig. 2. The agreement in the third law heat of vaporization, the fit of the measurements to Barrow's line, the lack of a discernible temperature trend in Fig. 4, and the excellent average molecular weight indicate that the procedure used gives reliable results and that the mercury calibration factor can be applied over a range of temperature and pressure.

Antimony

The enthalpy and entropy of vaporization at 750°K obtained from Eq. (5) are compared with the second law results of other investigators in Table III. As the mean temperature of Niwa and Yoshiyama's measurements is 800°K their results have been converted to 750°K using Stull and Sinke's[5] estimated heat contents over this limited temperature range. Although the

[15] P. L. Smith and N. M. Wolcott, Phil. Mag. **1**, 854 (1956).
[16] R. F. Barrow, P. G. Dodsworth, A. R. Downie, E. A. N. S. Jeffries, A. C. P. Pugh, F. J. Smith, and J. M. Swinstead, Trans. Faraday Soc. **51**, 1354 (1955).

present second law thermodynamic data are between those of Nesmeyanov and Iofa and Niwa and Yoshiyama the absolute pressures reported here are 10%–40% lower as can be seen in Fig. 3. The lower measured pressures cause the average third law heat of vaporization, in Table IV, to be higher than that calculated from the results of the two previous investigators. The standard heats of sublimation in Table IV were calculated using the free energy functions and heat contents estimated by Stull and Sinke.[5] The third law heat of vaporization calculated from each pressure determination is plotted against temperature in Fig. 5. Although the data seem to show a very slight trend towards lower ΔH_{298}° (higher pressure) with increasing temperature, this plot and the reasonable agreement between the heats of vaporization calculated by the second and third law methods again indicate that there is no serious temperature dependent error. As the free energy functions are only estimates, the third law standard heats of vaporization are only approximate.

As mentioned in the introductory paragraphs there is some ambiguity in the way Niwa and Yoshiyama treated their data, raising the possibility that there is a systematic error in their reported pressure. The deviation between the second and third law heat of vaporization calculated from their data would support this view. The 2.1 kcal/mole difference between the two enthalpies calculated from Nesmeyanov and Iofa's results also suggests the possibility of a systematic error in their measurements. Thus, application of the only available test, thermodynamic consistency, to the conflicting results indicates that the pressures reported here are probably preferable to those in previous investigations. This conclusion and the heats of vaporization reported are, however, dependent upon the uncertain free energy function and should be re-evaluated when molecular constants for $Sb_4(g)$ are available. The conclusion is also supported by the excellent agreement of the zinc and mercury results with those previously reported in the literature.

THE JOURNAL OF CHEMICAL PHYSICS VOLUME 35, NUMBER 3 SEPTEMBER, 1961

Self-Nucleation in the Sulfuric Acid-Water System

GEORGE J. DOYLE*

Stanford Research Institute, Southern California Laboratories, South Pasadena, California

(Received February 13, 1961)

Howard Reiss' "Vector model" was adapted to calculate the self-nucleation rate for the sulfuric acid-water system and similar systems.

A numerical calculation was carried out for the typical case of 50% relative humidity at 25°C. It was concluded that rapid self-nucleation would take place at sulfuric acid partial pressures in the range 10^{-8}–10^{-10} mm Hg. The considerable uncertainty is principally due to lack of data on the partial pressure of sulfuric acid above its aqueous solutions and on the dominant sulfuric acid-bearing species in humid atmospheres.

INTEREST in the rate of nucleation of sulfuric acid-water systems has been stimulated by recent discoveries in air-pollution chemistry. It has been found that traces of sulfur dioxide are essential for the formation of aerosol during photooxidation of trace amounts of certain olefins and nitric oxides in air.[1,2] During these photooxidations, the sulfur dioxide undergoes a chemical reaction which has been hypothesized to be a cophotooxidation to sulfur trioxide and, ultimately, hydration to sulfuric acid. It is supposed that the particles of the aerosol of aqueous sulfuric acid then act as condensation centers for organic products of the photooxidation. The hypothesis suggests an immediate practical question—what is the minimum amount of sulfuric acid required to initiate nucleation in humid air.

The problem of nucleation rate in this system has its own intrinsic interest. It is an example of nucleation where the embryos and nuclei can be considered to consist of spherical droplets of a non-ideal solution with a surface tension which varies with composition. It is not proposed to treat the case where the nucleation rate is very rapid and the nuclei are near molecular dimensions.

The quasi-thermodynamic approach is the most easy to apply and can be expected to give a good order-of-magnitude estimate. In this theory, the rate of nucleation is given by an equation of the form $I=C\exp(-\Delta G^*/kT)$, where C is a frequency factor and ΔG^* is the free energy of formation of the nucleus. Some objection has been raised to this approach, and the usual model for the embryo[3–5] which will be used here. However, this approach has been verified experimentally as a good order-of-magnitude estimate, provided that it is not applied to cases in which the liquid-drop model of the embryos and the accompanying kinetic assumptions cannot be expected to be good approximations.[6,7] While the most extensive use of this method has been for single-component systems, multicomponent systems have been treated,[6,8–12] and the approach of Reiss[10] will be used here. The most facile use of this approach is based on the existence of a saddle point on the free energy surface and on the evaluation of the rate of flow of embryos through this pass in the barrier to approximate the rate of nucleation.

THE FREE-ENERGY SURFACE

The free energy of formation of an embryo is taken to be

$$\Delta G={}^2n_1({}^2\mu_1-{}^1\mu_1)+{}^2n_2({}^2\mu_2-{}^1\mu_2)+4\pi r^2\gamma, \qquad (1)$$

where n=number of moles, μ=chemical potential taken for a bulk phase of the same composition, r=embryo radius, and γ=surface tension also taken for the bulk phase. The anterior superscript denotes the phase, 1 for gas and 2 for liquid (embryo). The posterior subscript denotes the component (for example, 1 for water, 2 for sulfuric acid). It is assumed that the embryos are sufficiently large to allow rotational and vibrational contributions to be neglected completely. Contribution of the so-called surface phase to the extensive properties of the embryo droplet will also be neglected, except for the surface energy contribution $4\pi r^2\gamma$.

A necessary condition for a saddle point is that the tangent plane to the surface representing Eq. (1) be

* This investigation was supported by the Air Pollution Foundation, San Marino, California, and by a Public Health Service Research Grant from the Division of General Medical Science, U. S. Public Health Service.

[1] M. J. Prager, E. R. Stephens, and W. E. Scott, Ind. Eng. Chem. **52,** 521–4 (1960).

[2] E. A. Schuck and G. J. Doyle, "Photooxidation of hydrocarbons in mixtures containing oxides of nitrogen and sulfur dioxide," Rept. No. 29, Air Pollution Foundation, San Marino, California, 1959.

[3] Howard Reiss, Ind. Eng. Chem. **44,** 1284–1288 (1952); also see other papers in this symposium, pp. 1269–1304.

[4] F. P. Buff and J. G. Kirkwood, J. Chem. Phys. **18,** 991–2 (1950).

[5] Howard Reiss, J. Chem. Phys. **20,** 1216–27 (1952); *ibid.* **21,** 1312 (1953).

[6] M. Volmer, *Kinetik der Phasenbildung* (Steinkopf, Leipzig, 1939).

[7] Chester T. O'Konski, "Kinetics of gas phase nucleation," Final Rept. to ONR, Chemistry Branch, University of California (Project No. NR 051-302), Berkeley, California, January 1, 1958.

[8] W. Döring and K. Neumann, Z. physik. Chem. **A186,** 193–202 (1940).

[9] K. Neumann and W. Döring, Z. physik. Chem. **A186,** 203–26 (1940).

[10] Howard Reiss, J. Chem. Phys. **18,** 840–8 (1950).

[11] Howard Reiss, J. Chem. Phys. **19,** 253–4 (1951).

[12] H. Flood, Z. physik. Chem. **A170,** 286 (1934).

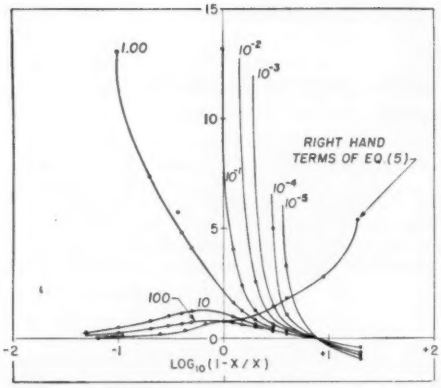

FIG. 1. Graphical solution of Eq. (5) at 25°C and 50% relative humidity.

parallel to the $({}^2n_1, {}^2n_2)$ plane—that is, that

$$\partial(\Delta G)/\partial({}^2n_1)=\partial(\Delta G/\partial({}^2n_2)=0.$$

If one makes use of the Gibbs-Duhem identity for the μ's and the relationship $4\pi r^3/3={}^2n_1\,{}^2V_1+{}^2n_2\,{}^2V_2$, then this condition becomes

$$\begin{aligned}{}^2\mu_1-{}^1\mu_1+(2\gamma^2V_1/r)+4\pi r^2(\partial\gamma/\partial({}^2n_1))=0,\\ {}^2\mu_2-{}^1\mu_2+(2\gamma^2V_2/r)+4\pi r^2(\partial\gamma/\partial({}^2n_2))=0,\end{aligned}\qquad(2)$$

where ${}^iV_j$ is the partial molar volume of component j in phase i. Equations (2) may be reduced to a form convenient for graphical solution by transforming the partials of the surface tension to the form

$$\begin{aligned}\partial\gamma/\partial({}^2n_1)&=-3x[(1-x)({}^2V_1)+x({}^2V_2)][d\gamma/dx]/4\pi r^3,\\ \partial\gamma/\partial({}^2n_2)&\\ &=3[1-x][(1-x)({}^2V_1)+x({}^2V_2)][d\gamma/dx]/4\pi r^3,\end{aligned}\qquad(3)$$

where x=mole fraction of component 2 in the embryo. Substitution of (3) into (2) yields

$$\begin{aligned}{}^2\mu_1-{}^1\mu_1+\{[2\gamma^2V_1-3xV(d\gamma/dx)]/[r]\}=0,\\ {}^2\mu_2-{}^1\mu_2+\{[2\gamma^2V_2+3(1-x)V(d\gamma/dx)/[r]\}=0,\end{aligned}\qquad(4)$$

where $V=x\,{}^2V_2+(1-x)\,{}^2V_1$ is the molar volume of the solution. The equations used for graphical solution are derived directly from (4); these are

$$\begin{aligned}A({}^2\mu_1-{}^1\mu_1)/{}^2\mu_2-{}^1\mu_2)&\\ =\frac{1-x({}^2V_2/V)+(3/2)(d\ln\gamma/d\ln A)}{x({}^2V_2/V)-(3/2)(d\ln\gamma/d\ln A)},&\qquad(5)\end{aligned}$$

$$1/r=-\frac{(x/2V\gamma)({}^2\mu_2-{}^1\mu_2)}{x({}^2V_2/V)-(3/2)(d\ln\gamma/d\ln A)},\qquad(6)$$

where $A=(1-x)/x$ is the molar ratio of component 1 to component 2. Equation (5) can be solved by plotting the left- and right-hand terms against $\log A$, with the abscissa of intersection determining the composition at the tangent point. Note that the right-hand side is essentially independent of chemical potentials in phase 1—hence, one such curve will serve for all pre-assumed activities in phase 1. The left-hand terms define a family of curves, one for each assumed pair of potentials for the gas phase.

With a solution to Eq. (4) assumed, it remains to demonstrate that such a solution is a saddle point. With questions of singularity excluded, the radius of curvature R of a normal section through the surface at the point in question at angle ϕ to the ${}^2n_1$ axis is given by

$$1/R=\rho\cos^2\phi+2\sigma\cos\phi\sin\phi+\theta\sin^2\phi,\qquad(7)$$

where $\rho=\partial^2(\Delta G)/[\partial({}^2n_1)]^2$, $\sigma=\partial^2(\Delta G)/\partial({}^2n_1)\partial({}^2n_2)$, and $\theta=\partial^2(\Delta G)/[\partial({}^2n_2)]^2$. When $\sigma^2-\rho\theta>0$, the radius of curvature undergoes a change of sign with varying ϕ[13] which, when combined with conditions (2), essentially proves the existence of a saddle point.

In connection with Eq. (7) and Reiss' theory,[10] other quantities are of interest. These are the direction of steepest ascent and descent (extrema in curvature) at the saddle point and the second derivatives of ΔG with respect to axes rotated about the saddle point so that they coincide with these perpendicular directions. The directions are obtained by setting the derivative of (7) with respect to ϕ equal to zero, which results in the equation $\tan 2\phi=2\sigma/\rho-\theta$. The derivatives in the directions of steepest ascent, $\partial^2(\Delta G)/\partial b^2$, and descent, $\partial^2(\Delta G)/\partial a^2$, can then be obtained by using the usual methods of differential calculus. The second partials ρ, σ, and θ, at the saddle point, are obtained through use of Eq. (1), taking advantage of thermodynamic identities and of the simplification offered by Eqs (2) and/or (4). The results are

$$\begin{aligned}4\pi r^3\rho/3=&-[Vx^2(d^2\mu_2/dx)]/[1-x]+[({}^2\mu_1-{}^1\mu_1)^2V_1]/3\\ &+\{Vx\}\{[2\gamma x(d\,{}^2V_2/dx)]/[1-x]\\ &+[6x({}^2V_2-{}^2V_1)-{}^2V_1][d\gamma/dx]\\ &+3xV[d^2\gamma/dx^2]\}/r,\end{aligned}\qquad(8)$$

$$\begin{aligned}4\pi r^3\sigma/3=&-Vx(d^2\mu_2/dx)+[({}^2\mu_2-{}^1\mu_2)^2V_1]/3\\ &-\{Vx\}\{2\gamma(d^2V_2/dx)\\ &+[6(1-x)({}^2V_2-{}^2V_1)-{}^2V_2][d\gamma/dx]\\ &+3(1-x)V(d^2\gamma/dx^2)\}/r,\end{aligned}\qquad(9)$$

$$\begin{aligned}4\pi r^3\theta/3=&V(1-x)(d^2\mu_2/dx)+[({}^2\mu_2-{}^2\mu_1)^2V_2]/3\\ &+\{V(1-x)\}\{2\gamma(d^2V_2/dx)\cdot\\ &+[6(1-x)({}^2V_2-{}^2V_1)-{}^2V_2][d\gamma/dx]\\ &+3(1-x)V(d^2\gamma/dx^2)\}/r,\end{aligned}\qquad(10)$$

where all quantities are evaluated at the assumed saddle point.

[13] Edouard Goursat, *A Course in Mathematical Analysis* (Ginn and Company, Boston, Massachusetts, 1904), pp. 497–503, or any other book treating differential geometry.

To locate the saddle point and calculate the various quantities of interest at that point, use was made of the extensive data on sulfuric acid in the literature. Partial-molar free energies were taken from the recent article by Giauque *et al.*[14] Partial-molar volumes were computed from the data on density and composition given in the Chemical Engineer's Handbook.[15] Surface tension data as a function of composition at 25°C was obtained by linear interpolation between the curves given in the International Critical Tables.[16] Figure 1 shows the graphical solution of Eq. (5) at 25°C and 50% relative humidity. The numbers attached to the curves representing the left-hand terms of (5) denote sulfuric acid vapor activity relative to that in equilibrium with 99.090% sulfuric acid ($A=0.05$). Table I gives the values of various quantities of interest at the composition and size satisfying Eqs. (4). Column 9 demonstrates that all of the determined points are saddle points. Column 4 indicates that the droplet model is rapidly becoming inapplicable at activities around $10^{-3}-10^{-2}$.

The values of $\Delta G^*/kT$ given in column 5, Table I, combined with the increasing inaccuracy of the calculation as activity increases, do not allow a clear-cut decision for the point of inception of rapid self-nucleation. It is apparent that an estimate will have to be made of the frequency factor C.

ESTIMATE OF THE RATE OF NUCLEATION

Reiss[10] gives an estimate of the frequency factor C based on the rate of passage of the embryos through the pass at the saddle point.

$$C=\frac{\beta b[1+\tan^2\phi]FS^*}{(\beta b/\beta a)+\tan^2\phi}\left(-\frac{P^*}{Q^*}\right), \qquad (11)$$

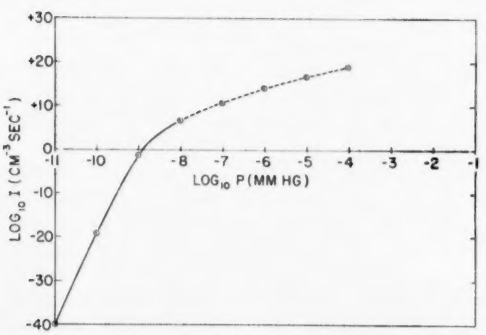

FIG. 2. Dependence of calculated nucleation rate on partial pressure of sulfuric acid vapor at 25°C and 50% relative humidity. (Dotted portion of curve indicates approximate region of invalidity of theory.)

[14] W. F. Giauque, E. W. Hornung, J. E. Kunzler, and G. R. Rubin, J. Am. Chem. Soc. **82,** 62–70 (1960).

[15] John H. Perry, editor, *Chemical Engineer's Handbook* (McGraw-Hill Publishing Company, Inc., New York, 1950), 3rd ed., pp. 184–185.

[16] *International Critical Tables* (McGraw-Hill Publishing Company, Inc., New York, 1928), Vol. IV, p. 464.

TABLE I. Quantities characterizing the saddle point at 25°C and 50% relative humidity for various assumed gas-phase sulfuric acid activities.[a]

Acid vapor activity	Composition[b] x^*	Radius r^*, A	Molecules per nucleus	$\Delta G^*/kT$	$4\pi r^{*2}\sigma^*/3\times10^{-12}$	$4\pi r^{*2}\psi^*/3\times10^{-12}$	$(4\pi r^{*2})^2x/3(\sigma^{*2}-\rho^{*2}\theta)^*\times10^{-25}$	$4\pi r^{*2}P^*/3^c\times10^{-12}$	$4\pi r^{*2}Q^*/3^d\times10^{-12}$	$\tan\phi^{*e}$
10^{-5}	0.186	13.9	298	149.5	−1.51	−5.74	+23.2	+ 6.81	− 2.84	+24.5	0.220
10^{-4}	0.220	10.4	118	82.5	−2.02	−6.43	+20.7	+ 8.32	− 3.71	+22.4	0.264
10^{-3}	0.248	7.3	40.6	41.1	−2.59	−7.11	+18.8	+ 9.92	− 4.73	+21.0	0.302
10^{-2}	0.280	5.69	18.2	24.3	−3.26	−7.61	+16.4	+11.1	− 5.86	+19.0	0.342
10^{-1}	0.320	4.83	10.6	17.5	−4.05	−7.86	+13.2	+11.5	− 7.09	+16.3	0.387
1	0.357	3.83	5.0	10.9	−5.17	−7.64	+ 9.8	+10.9	− 8.38	+13.0	0.420
10	0.415	3.29	3.1	7.83	−8.06	−5.78	+ 4.1	+6.65	−10.4	+ 6.4	0.400
100	0.500	2.75	1.6	5.30	−9.83	−6.05	+ 2.1	+ 5.72	−12.4	+ 4.6	0.419

[a] All quantities are in cgs units unless otherwise specified.
[b] The asterisk indicates that the quantity is evaluated at the saddle point.
[c] P^* is the second partial of ΔG in the direction of steepest descent, evaluated at the saddle point.
[d] Q^* is the second partial of ΔG in the direction of steepest ascent, evaluated at the saddle point.
[e] ϕ^* is the angle of the axis of steepest descent with the $^2n_1$ axis (water).

TABLE II. Estimates of the rate of nucleation of sulfuric acid at 25°C and 50% relative humidity.

Acid vapor activity	Estimated acid pressure (mm Hg)	C (cm^{-3} sec^{-1})	$\exp(-\Delta G^*/kT)$	I (cm^{-3} sec^{-1})
10^{-5}	10^{-11}	1.41×10^{15}	1.26×10^{-65}	1.78×10^{-40}
10^{-4}	10^{-10}	6.68×10^{15}	1.58×10^{-35}	1.06×10^{-20}
10^{-3}	10^{-9}	3.04×10^{16}	1.58×10^{-18}	4.80×10^{-2}
10^{-2}	10^{-8}	1.71×10^{17}	2.51×10^{-11}	4.29×10^{6}
10^{-1}	10^{-7}	1.17×10^{18}	2.51×10^{-8}	2.94×10^{10}
1	10^{-6}	7.82×10^{18}	1.86×10^{-5}	1.45×10^{14}
10	10^{-5}	9.98×10^{19}	3.98×10^{-4}	3.97×10^{16}
100	10^{-4}	8.33×10^{20}	5.01×10^{-3}	4.17×10^{18}

where S^* = surface area of embryo at saddle point, βa = rate of collision of molecules of component 1 (water) cm^{-2} sec^{-1}, βb = rate of collision of molecules of component 2 (sulfuric acid) cm^{-2} sec^{-1}, F = total molecular concentration (cm^{-3}), P^* = second partial of ΔG in direction of steepest descent at the saddle point, and Q^* = second partial of ΔG in direction of steepest ascent at the saddle point.

A knowledge of the pressure of sulfuric acid vapor in the gas phase is necessary to evaluate C. Estimates have been made of this quantity for aqueous sulfuric acid at 25°C. Abel's estimate[17,18] is apparently much too high.[19] An order-of-magnitude estimate by La Mer[19] of 10^{-6} mm above 99% sulfuric acid seems about right, based on extrapolation of data at higher temperatures by the author of this paper. Table II shows the result of assuming this value for the partial pressure, and Fig. 2 shows the data as a log–log plot.

TABLE III. Composition of sulfuric acid in equilibrium with the acid vapor-phase activities shown in Tables I and II.

Acid vapor activity	Mole fraction	Weight %
10^{-5}	0.222	60.796
10^{-4}	0.272	67.052
10^{-3}	0.332	73.102
10^{-2}	0.411	79.202
10^{-1}	0.530	85.956
1.00	0.952	99.090
10.00	...	...
100.00	...	...

[17] E. Abel, J. Phys. Chem. **50,** 260 (1946).
[18] E. Abel, J. Phys. & Colloid Chem. **52,** 908 (1948).
[19] V. K. La Mer, E. C. Y. Inn, and I. B. Wilson, J. Colloid Sci. **5,** 471 (1950).

DISCUSSION

Figure 2 indicates that self-nucleation becomes appreciable at about 10^{-9} mm sulfuric acid partial pressure. This estimate is subject to several errors:

1. The liquid droplet model is beginning to fail at this supersaturation.
2. The partial pressure of acid is uncertain to at least one order of magnitude.
3. The dominant sulfuric acid-bearing gaseous species in a humid atmosphere is probably a hydrate.

The first source of error probably introduces an error of no more than one order of magnitude, since the nucleus at 10^{-9} mm still contains a considerable number of molecules.

The third source of error will also introduce into the calculations an error of no more than one order of magnitude—that is, it would change the scale of the axes against which one plots ΔG and would alter collision frequencies somewhat.

To sum up the estimate of errors, the rate of self-nucleation is probably uncertain by three to four orders of magnitude at a nominal pressure of 10^{-9} mm or at an activity of 10^{-3} relative to 99% sulfuric acid. To be considered along with this error estimate, of course, are those errors inherent in the quasi-thermodynamic approach. Because of the rapid change of I with sulfuric acid pressure, it is probable that appreciable nucleation rates are achieved somewhere between 10^{-8} and 10^{-10} mm Hg sulfuric acid pressure at 50% relative humidity; it is also probable that acid pressures above this range cannot be sustained at 50% relative humidity. A pressure of 10^{-8} mm is a very low concentration indeed, corresponding as it does to 1.3×10^{-5} ppm by volume at 1-atm total pressure.

The photooxidation rate of sulfur dioxide in sunlight has been experimentally estimated as 2×10^{-5} min^{-1} [20]

[20] Earl R. Gerhard and H. F. Johnstone, Ind. Eng. Chem. **47,** 972 (1955).

and also as 4×10^{-3} min^{-1}.[2] At such rates, 10^{-2} ppm of sulfur dioxide are sufficient to build up a sulfuric acid concentration of at least 10^{-5} ppm in one hour. The presence of olefin and nitrogen oxide pollutants will accelerate this rate by as much as tenfold. It may be concluded that there will be no lack of a source of acidic nuclei in any neighborhood of a heavily populated area.

It is probable that the rate of nucleation shown in Fig. 2 is more accurately determined by the assigned vapor-phase activity relative to 99% sulfuric acid. An interesting aspect is brought out in Table III which shows bulk compositions in equilibrium with these gas-phase activities. These data suggest that sulfuric acid of around 75 weight percent or above should fume in air at 50% relative humidity. However, the mass loading will be so small that such fumes will be unobservable by ordinary techniques. This suggests a simple experimental test of the correctness of the estimates given in this paper.

Generalizing from this particular system leads to the suggestion that the potency of gas passed over moderately concentrated sulfuric acid, acting as a nucleating agent for aerosol formation in the La Mer-Sinclair generator,[19] has its explanation in multicomponent nucleation—that is, sulfuric acid, water, and the aerosol material being used. These components form a very fine nucleating aerosol upon which the bulk of aerosol material may condense.

THE JOURNAL OF CHEMICAL PHYSICS VOLUME 35, NUMBER 3 SEPTEMBER, 1961

Electrical Conductivity of Synthetic Crystalline Zeolites

DONALD C. FREEMAN, JR., AND DENNIS N. STAMIRES*

Research Laboratory, Linde Company, Division of Union Carbide Corporation, Tonawanda, New York

(Received February 16, 1961)

The electrical conductivity of anhydrous Linde zeolite types A, X, and Y in various cationic forms has been measured between 20 and 400°C. The conductivity is ohmic, essentially noncapacitive, and appears to be strictly ionic with unusually low activation energy. From the effect of zeolite channel size, type of cation and cation density on ΔH, ΔG, and ΔS for the conduction process, some conclusions as to the zeolite internal structure and surface energy have been obtained. The heterogeneity of the internal surface energy found by the measurement of adsorption heats is discussed in the light of these conclusions.

INTRODUCTION

CRYSTALLINE zeolites are composed of silica and alumina tetrahedra arranged in a lattice so spacious that the migration of small molecules and ions through the interior of the crystal is permitted.[1,2] The basic tetrahedra form polyhedra of several types such as cubes, hexagonal prisms, or truncated octahedra. These polyhedra may be arranged in several different ways, which give rise to various species of zeolite having specific pore or channel sizes and channel configurations. Some of the zeolite species are found in nature, others may be formed synthetically.

Since each 4-coordinated aluminum atom possesses a unit negative charge, the crystal contains a sufficient number of cations to allow electrical neutrality. Because of the porous nature of the crystal, these cations can be easily exchanged for other cationic species provided that certain size and charge requirements are satisfied.[3] These highly mobile cations result in an unusually high electrical conductivity for ionic crystals.

Rabinowitsch and Wood[4] studied the conductivity of a number of natural chabazites and concluded that the conduction mechanism is ionic. They were, however, unable to obtain ohmic behavior and were thus limited in their conclusions. Beattie[5,6] has studied the conductivity of a number of ion exchanged forms of analcite and chabazite and obtained values of the activation energy for conduction. She did not find the very important dependence of activation energy on the channel size or the degree of "openness" of the zeolite framework.

The objective of our work has been to determine the mobility, energetics, and distribution of the conducting species as a function of the type of cation and the nature of the anionic zeolite framework. We have chosen Linde synthetic-zeolite types A, X, and Y for this study because these structures represent a wide gradation in channel size and can be obtained in pure

* Present address: Frick Chemical Laboratory, Princeton University, Princeton, New Jersey.

[1] D. W. Breck, W. G. Eversole, R. M. Milton, and T. L. Thomas, J. Am. Chem. Soc. **78,** 5963 (1956).

[2] R. M. Barrer, J. Chem. Soc. **1950,** 2342.

[3] R. M. Barrer, J. Chem. Soc. **1950,** 481.

[4] H. E. Rabinowitsch and W. C. Wood, Elektrochem. **39,** 562 (1933).

[5] I. R. Beattie, Trans. Faraday Soc. **50,** 581 (1954).

[6] I. R. Beattie, Trans. Faraday Soc. **51,** 712 (1955).

TABLE I. Crystallographic description of the three zeolites studied.

Type of zeolite	Anhydrous unit-cell composition[a]	Crystal symmetry	Type of rings interconnecting the large cages in the channel system	Effective diameter of the large rings, A
NaA	$Na_{12}[(AlO_2)_{12}(SiO_2)_{12}]$	Cubic	8-membered rings (6 per cage)	4.2
NaX	$Na_{88}[(AlO_2)_{88}(SiO_2)_{104}]$	Cubic	12-membered rings (4 per cage)	8–9
NaY	$Na_{56}[(AlO_2)_{56}(SiO_2)_{136}]$	Cubic	12-membered rings (4 per cage)	8–9

[a] Usually a small, variable percentage of the sodium ions are absent and are presumed to be replaced by protons.

and homogeneous form. Furthermore, these zeolites, particularly zeolite Y, are quite stable, so that a high degree of ion exchange of cations less favorable to structural stability can be achieved. They also have sufficient thermal stability to allow dehydration of the resulting ion exchanged forms in most cases.

From each of the above zeolite types, we have prepared a series of homoionic forms by ion exchange with alkali or alkaline-earth cations. From the measured temperature dependence of conductivity of the anhydrous zeolites, we have obtained values for the activation energy and diffusion constants of the charge carriers. The variation of these parameters with the type of zeolite and the cation is interpreted in the discussion and is shown to yield information on the internal nature of the basic zeolite lattice.

EXPERIMENTAL

Single crystals of zeolites A, X, and Y large enough for conductivity measurements are not available.[7] It was thus necessary to employ polycrystalline compacts. Table I shows the chemical composition, pore size, and symmetry of Linde zeolites A, X, and Y. It is possible by isomorphous replacement of silica by alumina during the synthesis procedure to prepare species having considerable variation from the tabulated compositions. In particular, various compositions between the tabulated X and Y end members can be achieved. The zeolites used were synthesized in the sodium form from the purest available starting materials (greater than 99.9%) by methods described elsewhere.[8] Emission spectroscopic analyses showed the presence of about 0.01% iron, 0.1% calcium, and 0.01% magnesium in a typical sample.

X-ray diffraction patterns of the samples employed displayed the characteristic sharp spectrum of each structure with no foreign peaks. One of the most reliable means of demonstrating complete crystallinity is by quantitative adsorption measurements with adsorbate molecules of different molecular dimension.[9] The crystallinity of all samples was verified by this method.

Ion exchange. Several different methods of ion exchange have been described.[10,11] The most general procedure used by us was that of percolation, in which a concentrated solution of the exchanging ion was allowed to flow slowly through a bed of the zeolite. The hydrolytic acidity of the exchanging solution was always maintained at a value well below that which can cause structural degradation. The tolerance to acidity for each zeolite was determined in a separate study.

The three zeolites used can be completely exchanged by silver ion with the percolation technique. In the case of those forms where a sufficiently high degree of ion exchange was impossible, the silver form was exchanged by one of the following two methods. When the thiocyanate of the desired cation was available, the silver form was treated with it. Formation of the stable, soluble, silver thiocyanate complex constituted a driving force by which a high degree of exchange could be achieved. In some cases, particularly in order to obtain completely exchanged forms for the establishment of x-ray diffraction standards, the silver form was exchanged with the chloride of the desired cation. In this case, the highly insoluble silver chloride drove the exchange to completion.[12] The silver chloride was then removed by repeated washing with a 50% aqueous solution of ethanolamine. In many cases, a compromise was necessary between the degree of ion exchange and the thermal stability, since some forms, highly exchanged with cations unfavorable to the structural requirements of the basic zeolites, are not stable to dehydration. As will be pointed out in the discussion, although complete exchange is desirable, it is probably not necessary for the determination of the activation energy for conduction by the incompletely exchanged cation. Table II shows the method and degree of exchange for each form.

Preparation of compacts. Polycrystalline compacts were prepared from zeolite powders of roughly 5-μ average crystal diam by vacuum hot pressing. Since it was found that heat and pressure can cause crystal

[7] Some natural zeolites occur in the form of large single crystals, but these are so imperfect as to make reliable measurements impossible.

[8] E. M. Flanigen and D. W. Breck, Abstract 137, Meeting ACS, April, 1960, Cleveland, Ohio.

[9] R. M. Barrer, F. W. Bultitude, and J. W. Sutherland, Trans. Faraday Soc. **53**, 1111 (1957).

[10] R. M. Barrer and L. Hinds, J. Chem. Soc. **1953**, 1879.

[11] R. M. Barrer, J. Chem. Soc. **1950**, 2342.

[12] R. M. Barrer and T. D. Falconer, Proc. Roy. Soc. (London) **A234**, 227 (1956).

TABLE II. Description and method of preparation of ion exchanged samples.

Type of zeolite	Method of ion exchange	% ion exchange	Number of exchanged cations per unit cell	Number of sodium ions remaining in the unit cell
LiA	Percolation by LiCl	98.6	12	0
NaA	Originally synthesized	100.0	0	12
KA	Percolation of AgA with KCNS	99.8	12	0
AgA	Percolation with $AgNO_3$	99.7	12	0
LiY	Percolation with LiCl	62.0	33.0	20.3
NaY	Originally Synthesized	100.0	0.0	53.4
KY	Percolation of AgY with KCNS	97.6	52.9	1.1
RbY	Percolation with RbCl	61.4	33.2	21.0
CsY	Percolation with CsCl	77.1	42.4	12.6
TlY	Percolation with Tl_2SO_4	78.0	42.6	12.0
MgY	Percolation with $MgCl_2$	71.0	18.6	15.9
CaY	Percolation with $CaCl_2$	95.7	25.9	2.9
SrY	Percolation with $SrCl_2$	74.2	19.5	14.0
BaY	Percolation of AgY with $Ba(CNS)_2$	95.6	26.0	2.4

damage under extreme conditions, a study of zeolite stability vs pressure and temperature was carried out. It was observed that the zeolites are more susceptible to structural damage in the presence of adsorbed water. It was therefore desirable to partially dehydrate the samples before compaction.

In general, pressures between 30 000 and 50 000 psi at temperatures between 150 and 200°C, with roughly 80% dehydrated zeolite, were found to give coherent, dense, and structurally intact compacts. Electron micrographs showed that the individual zeolite crystallites tended to fracture in such a manner as to allow closest packing. Densities close to 90% of the single-crystal value could thus be obtained. Higher densities

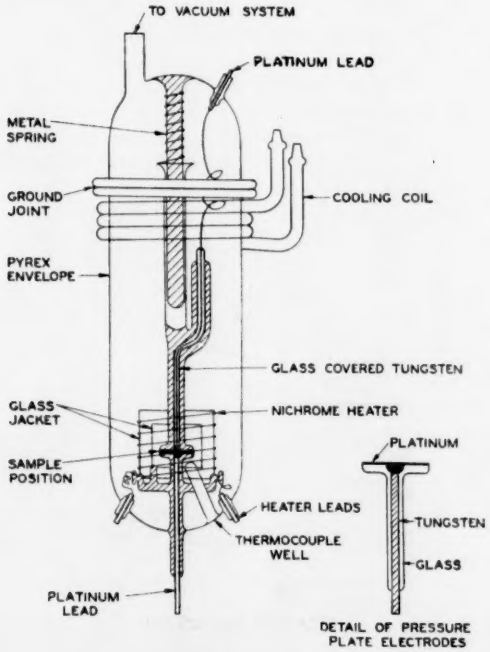

FIG. 1. Conductivity cell.

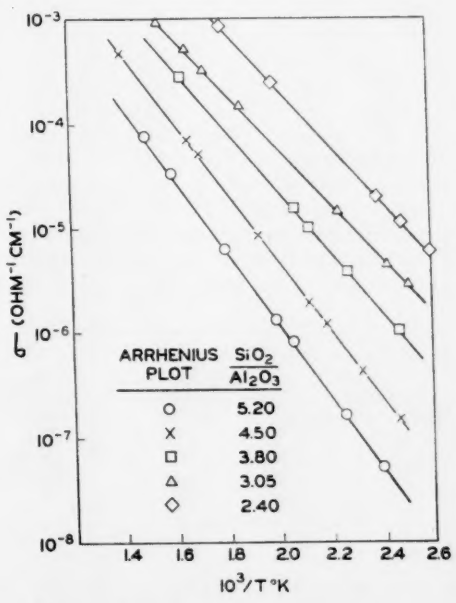

FIG. 2. Arrhenius plots for the X–Y zeolite series.

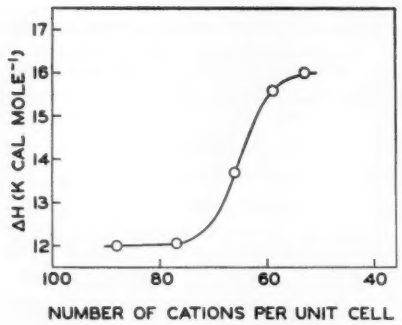

FIG. 3. Variation in activation energy with cation density in the X and Y zeolite series.

could be obtained at higher pressures with some crystal structural damage.

It was found that zeolites, presumably because of their basic nature, severely gall stainless steel. A die of stainless steel with a highly polished Carbolloy liner and a Carbolloy piston was therefore employed. Compacts of both $\frac{1}{4}$-in. and $\frac{1}{2}$-in. diameter were routinely prepared. After placing the hydrated zeolite and the electrodes in the die, the compaction cell was evacuated and heated to 150°C for roughly 1 hr. The pressure was then applied and the assembly allowed to cool. The application of pressure for longer periods of time did not result in superior compacts.

The type of electrode material and the method of attachment was found to be particularly important. Frequency-dependent and nonohmic results had been obtained with aluminum, silver, and zinc electrodes. This was attributed to an oxide layer between the zeolite and the electrode. Gold-foil electrodes, pressed on during the compaction operation, were found to be free of spurious effects. Gold electrodes attached by pressing were compared with gold electrodes attached by vacuum sputtering and were found to have identical and excellent characteristics.

Conductivity measurement. Direct-current conductivity measurements were ruled out because of polarization and electrolysis effects. Several conventional ac methods have been employed with identical results.

TABLE III. Description of the X and Y zeolite series.

SiO_2/Al_2O_3	Number of cations per unit cell	Volume of the unit cell $(a_0)^3$ A[a]	Average intercation distance, A
2.4	88	15,531	5.6
3.0	77	15,368	5.8
3.8	66	15,197	6.1
4.5	59	15,051	6.3
5.2	53	14,923	6.5

[a] D. W. Breck, E. M. Flanigen (reference 10).

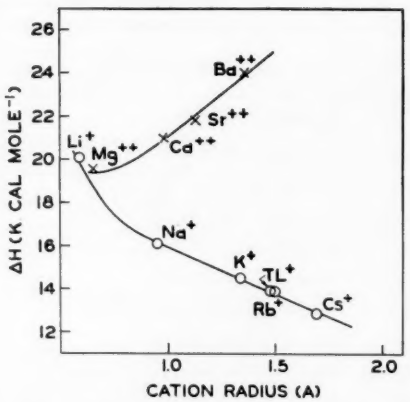

FIG. 4. Activation-energy values for monovalent- and divalent-cation exchanged Y zeolites.

The majority of the data herein reported were obtained with a General Radio type 544-B megohm bridge modified for use at 200 cps. A General Radio model 736-A wave analyzer was employed as a filter and null detector. This method was particularly useful for the high-resistance ranges. No significant dependence of the conductivity on frequency was found between 100 and 10 000 cps and an excellent null could be obtained without capacitance compensation. In order to verify that the measurements represented pure resistive impedance, a Cintel model No. 1862 wide-range capacitance bridge was employed. It was found that the capacitive impedance, while present and temperature dependent, was always less than 5% of the resistive impedance provided that precautions were taken to minimize lead capacitance.

The samples were mounted in the conductivity cell shown in Fig. 1. The use of an internal heater was

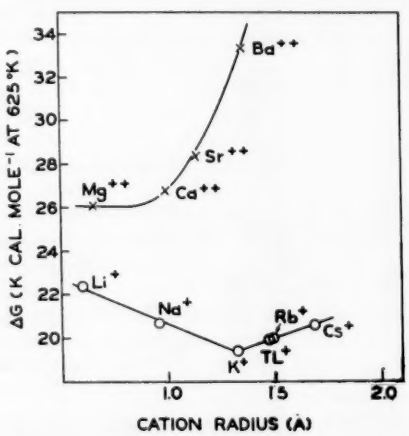

FIG. 5. Free-energy values for monovalent- and divalent-cation exchanged Y zeolites.

found to be more reliable and convenient than a previously used external heater. The conductivity cell was connected to a system capable of evacuation to 10^{-6} mm Hg. The system was suitably trapped to completely remove the effluent vapor from a sample during activation. Each sample was activated in the cell for at least 12 hr at 350–400°C under vacuum. These conditions have been found in other studies to be necessary for complete dehydration, which is essential because of the marked dependence of the conductivity on adsorbed molecules. After activation, conductivity measurements were made during both heating and cooling, care was taken to insure that thermal equilibrium was reached at each increment of temperature. A Brown Pyrovane electronic temperature controller with calibrated chromel-alumel thermo-

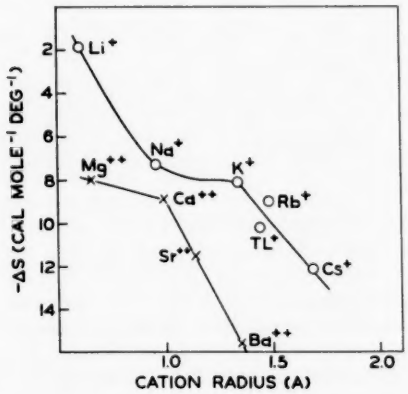

FIG. 6. Entropy values for monovalent- and divalent-cation exchanged Y zeolites.

couples was employed. The compact temperature was measured with a Leeds and Northrup potentiometer.

RESULTS AND DISCUSSION

Rabinowitsch and Wood, and Beattie and Dyer[13] have shown that electrical conduction in zeolites occurs by migration of the cations. No evidence for electronic conduction has been observed. We have demonstrated that actual cation transfer occurs in a silver X zeolite compact. After 12 hr at 110 v dc, 1 wt-% zinc ion was found adjacent to a zinc electrode, and 2 wt-% silver metal was found adjacent to the opposite electrode of gold. The original silver concentration in the zeolite was 24%. These analyses were taken from thin layers and do not represent the total mass transfer.

An ionic-conduction mechanism is consistent with the dependence of conductivity parameters on the type of cation as described hereafter. The diffusion of cations along a potential gradient through the large intracrystalline channels could be described either as

[13] I. R. Beattie and A. Dyer, Trans. Faraday Soc. **63,** 61 (1957).

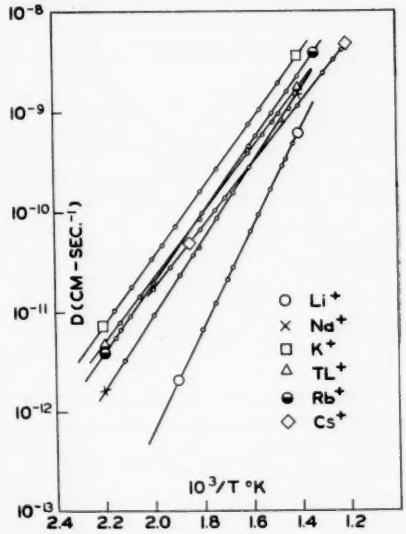

FIG. 7. Diffusion constants vs temperature for various monovalent ionic forms of Y zeolite.

"surface" diffusion or interstitial diffusion, so that a description of the mechanism in conventional terms is not explicit. The occurrence of mass transfer rules out cation vacancies, or negative holes, as the principal charge carriers. Because of the complexity of the crystalline structure, the electrostatic-field asymmetry, and our ignorance as to the precise energy of the cation

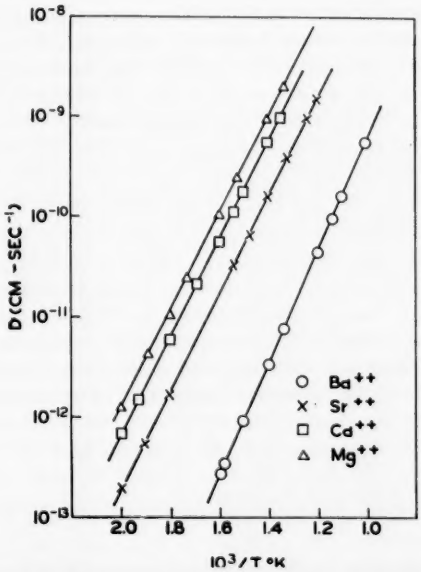

FIG. 8. Diffusion constants vs temperature for various divalent ionic forms of Y zeolite.

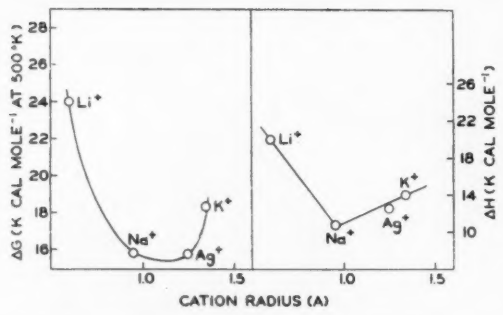

FIG. 9. Free-energy and activation-energy values for A zeolite.

positions, we have not been able to calculate the energy required for the formation of vacancies or for migration.

We assume that the conductivity values measured represent the actual bulk conductivity because (1) no dependence of conductivity on initial crystallite size has been observed, (2) the fact that, roughly, only $\frac{1}{700}$ of the cations occur on the crystallite surface is inconsistent with the specific-resistivity values obtained, and (3) the strong dependence of conductivity on zeolite-channel size suggests that the process cannot take place exclusively on the crystallite external surface.

Effect of cation density. The mole ratio of silica to alumina can vary uniformly between 2.1 and 3.0 in the X form and from 3.0–5.2 in the Y form. Consequently, a series of zeolite species having the same basic lattice structure (as proven by x-ray analysis) but with decreasing cation density can be prepared. The variation of specific conductivity with temperature for this series is shown in Fig. 2. The study of such a series is important because it has been postulated[14] that there is more than one type of cation site. Assuming that these site types are energetically discrete, we would expect, in going to lower cation densities, that the least favorable (lowest binding energy) sites will become depopulated. Simultaneous removal of cations from more than one type of site would imply that either the sites were not energetically discrete to begin with or that the site types change in relative energy in going from high- to low-cation density. The latter is unlikely because the site energy should be dictated by the structure only, which does not change except for the size difference of aluminum and silicon atoms.

In fact, the activation energy (ΔH) for conduction (Fig. 3) does change drastically with cation density at a cation density of about 65/unit cell. Thus, at least two types of cation sites are present, so that as the most mobile (weakly bound) cations are eliminated ΔH shifts to a higher value characteristic of a more strongly bound cation type.[15]

The actual number of charge-carrying cations in the two sites thus revealed can be calculated. From the absolute reaction-rate theory,[16] the following expression for the unidirectional self-diffusion constant of ions in a lattice is obtained:

$$D=\lambda^2 kT/h \exp(\Delta S/R)\exp(-\Delta H/RT),$$

where λ is the distance between cation sites. Combining this result with the Nernst-Einstein equation

$$\sigma/D=Nq^2/kT \qquad N=\text{number of carriers}$$
$$q=\text{carrier charge}$$

gives for the conductivity

$$\sigma=N\lambda^2 q^2/h \exp(\Delta S/R)\exp(-\Delta H/RT),$$

assuming that the self-diffusion coefficient is equivalent to the field-diffusion coefficient.

Provided that the energy required to promote a cation to a state in which it can migrate (defect formation) is negligible in these open structures compared to the actual energy of migration, the total conductivity will be

$$\sigma_T=n_1(q^2\lambda^2/n)\exp(-\Delta G_1/RT)$$
$$+n_2(q^2\lambda^2/h)\exp(-\Delta G_2/RT).$$

Here, λ has been obtained simply by assuming a uniform distribution of cations in the unit cell of known volume, which will give only an average value. The value of λ is also probably different for different cation-

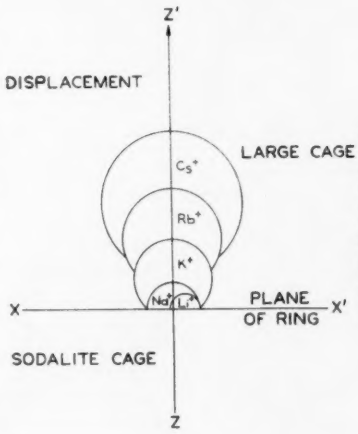

FIG. 10. The displacement of various sized cations from the plane of a six-membered oxygen ring, XX' represents the plane of the ring. Cations larger than sodium are displaced along the axis ZZ' toward the center of a large cage.

[14] D. W. Breck and E. M. Flanigen, Abstract 134 of the meeting of the American Chemical Society, September, 1958, Chicago, Illinois.

[15] The x-ray structure of the X zeolite ($SiO_2/Al_2O_3=2.4$) suggests actually three unipositive cation-site types having 16, 32, and 40 unipositive cations per unit cell in order of decreasing stability.

[16] S. Glasstone, H. Eyring, and K. J. Laidler, *The Theory of Rate Processes* (McGraw-Hill Book Company, Inc., New York, 1941), p. 516.

site types so that the values given in Table III are only approximate. Taking ΔG_1 as the free energy for conduction on the high cation-density end of the series and ΔG_2 the free energy for conduction at the low cation-density end, a value for n_1 of 40 ± 5 is obtained. We have made the risky assumption that $n_1+n_2=n_T$, where n_T is the total number of cations. If there is a third site type present (as crystallographic evidence suggests), we are forced to assume either that (1) ΔG_3 is roughly the same as ΔG_2, or (2) that n_3 is very small, for this calculation to be valid. The fact that the half-way point in the change of ΔH with cation density occurs at a cation density of about 65 (which means that half of the lowest energy sites have been lost) implies that the above assumptions as to the third site type are correct.

Effect of cation size and charge. Figures 4–6 show the variation of ΔH, ΔG, and ΔS with cation radius[17,18] in the Y zeolite. The uniform decrease in ΔH with increasing monovalent-cation radius reflects the diminishing coulombic attraction between the cation and the cation-lattice site as the cation becomes larger. The curve for ΔG indicates that all of the Li^+, Na^+, and K^+ ions participate in the conduction process but that the larger cations become subject to a steric restriction which decreases the number capable of migration. The ΔS curve suggests that a change in site configuration takes place as cation size is increased. Specifically, the general decrease of ΔS with increasing cation radius represents a reduction in the bonding energy at the equilibrium state, probably together with an increase in the restriction imposed by the activated state on cation mobility. Lithium ion seems somewhat anomalous, probably because its small size allows greater penetration into the alumina tetrahedra and because of its tendency toward covalent-bond formation.

Each divalent cation must, of course, be associated with two sites of negative charge in the lattice. Calcium ion, for example, would be expected to have twice the activation energy of sodium ion from electrostatic considerations, provided that a calcium ion site is completely equivalent to two sodium ion sites. The fact that the calcium ion must reside between two relatively widely separated negative charges reduces the bond strength considerably. The sharp increase in ΔH and ΔG with increasing cation size reflects the greater ease of bonding to two crystallographically separated sites for the larger, more polarizable cations.

The divalent-cation entropy curve indicates that even though the entropy of the equilibrium state is expected to decrease with increasing cation size, a greater decrease of the entropy of the transition state occurs. This results in a net decrease of ΔS for the larger ions. Plots of ΔG vs temperature are linear for all cation species studied, indicating that the number and type of charge carriers does not change in the temperature region studied.

The diffusion coefficients determined from the conductivity data are shown in Figs. 7 and 8. The high D values attest to the openness of the zeolite structure. No tracer determinations of D for anhydrous zeolites, or for zeolites of comparable channel size, are available for comparison.

Effect of zeolite structure. The A zeolite, cubic in symmetry, is composed of sodalite "cages" in such a manner that two channel systems are formed.[1] The smallest opening in the large channel system is an eight-membered oxygen ring, having an effective diameter of 4.2 A. The small channel system is restricted by the six-membered rings of the sodalite cages and has an effective diameter of 2 A. The X and Y zeolites, which both have structures composed of sodalite "cages," also have a small channel system restricted by six-membered rings. These structures, however, possess a large channel system, the smallest constrictions of which are 12-membered oxygen rings, with an effective diameter of 8–9 A.

Figure 9 shows the variation of ΔH and ΔG with cation radius for the A zeolite. It is immediately apparent that the larger cations are either more strongly bound or are sterically restricted. The latter explanation is correct in view of the smooth decrease in ΔH for the same cations in the Y zeolite, and the fact that the cation sites, locally, should be the same in both cases. The increase in ΔH for cations larger than sodium is therefore attributed to the greater potential-energy barrier to cation migration offered by the eight-membered rings. This steric hindrance is sufficient to overrule the coulombic tendency toward a decrease in ΔH with increasing cation size as seen in the unrestricted Y zeolite series.

The results and explanation for the A zeolite series are in accordance with the data of Beattie[5] for analcite and chabazite, both of which also have eight-membered oxygen ring constrictions in the largest channel systems.

Effect of degree of hydration. We wish to emphasize that all of the results covered thus far are for anhydrous zeolites. There is a pronounced change in the conductivity upon adsorption of water or other polar substances. The adsorption of water at room temperature results in a sharp increase in conductivity and a continuous decrease in ΔH to a value essentially the same as that for an aqueous solution of the pertinent cation when complete hydration is reached. The same results were obtained for the A, X, and Y structures except that different inflection points occurred in the plots of conductivity vs degree of hydration which could be correlated with the number and type of cation sites. A detailed study of the effect of polar and nonpolar adsorbates on zeolite conductivity will be reported in a later paper.

---

[17] R. L. Broussard and D. P. Shoemaker, J. Am. Chem. Soc. **82**, 1041 (1960).

[18] L. Pauling, *The Nature of the Chemical Bond* (Cornell University Press, Ithaca, New York, 1960), 3rd ed.

CONCLUSIONS

The measured conductivity in zeolite compacts is bulk and ohmic and appears to occur strictly by an ionic mechanism. The activation-energy values so obtained represent the coulombic and steric barriers to cation migration. The activation energies for conduction and the specific resistivities are considerably smaller than those found for other ionic crystals. This attests to the openness of the zeolite crystalline framework.

The conductivity depends on the size and charge of the cation and on the size of the zeolitic channels. The conductivity also depends upon the crystallographic location, or the energetic configuration, of the cation sites. This configuration is determined primarily by the basic zeolite framework but it also depends on the size of the cation itself.

In the X and Y zeolite structure, there are at least two types of cation sites of different potential energy. The highest energy-site type is eliminated as the cation density is decreased by increasing the silica alumina ratio. In this site type, the cations are only weakly bonded to the lattice, and the site probably consists of three or four oxygen atoms of the AlO_4^- units located in the large cavities or in the eight- or twelve-membered oxygen rings which form the "windows" between cavities. The strong bonding site type is formed by either single or double six-membered oxygen rings. Here, the oxygen atoms conform more nearly to the charge requirements of the cation than do the more nearly planar oxygen atoms in the weak bonding sites.

The greater overlap of the cation-cation site electrostatic fields in the strong bonding sites will screen the cations and thus reduce their polarizing power toward adsorbate molecules. This site type will then constitute an adsorption site which will be characterized by a low heat of adsorption. The weak bonding cation sites, in which the cations retain considerable polarizing power, will give rise to high heat of adsorption. Since the X zeolite contains both site types, the internal surface energy will be inhomogeneous so that there will be a strong variation in heat of adsorption with coverage.[19] Because the weak bonding sites are gradually eliminated in going from high to low cation density (type X to type Y), the internal surface energy should become more homogeneous and the heat of adsorption more constant with coverage. This also implies that the heats of adsorption should vary with cation size. Of the divalent cations in the X zeolite, the smallest are least able to overlap two adjacent sites and thus the adsorption heat should be higher than for the larger divalent cations. This has been observed to be the case.

The entropy and free-energy values obtained for different cationic forms of the Y zeolite suggest that as the cation size increases, the cation position is displaced. Sodium ion is small enough to reside in the plane and probably in the center of a six-membered oxygen ring. Larger cations, however, must be located out of the plane of the ring and further into the adjacent cavity. This is illustrated in Fig. 10.

The zeolite channel size has an important effect on the conductivity and activation energy. As the channel size approaches the cation dimension, the motion of the cation is impeded. In the case of the A zeolite, and other small pore zeolites, this steric factor predominates over the coulombic factor in determining values of the thermodynamic parameters for cation migration.

ACKNOWLEDGMENTS

We appreciate the advice and encouragement of Dr. D. W. Breck and Dr. E. O. Brimm. The assistance of E. J. Smolarek is gratefully acknowledged.

[19] R. M. Barrer and G. C. Bratt (to be published).

Transition Probabilities in Multilevel Systems: Calculation from Impulsive and Steady-State Experiments*

TUCKER CARRINGTON

National Bureau of Standards, Washington, D.C.

(Received February 23, 1961)

The study of collision-induced transitions of molecules in a system of many energy levels is discussed in an analysis of time-dependent and steady-state experiments. These results are used in a discussion, with numerical examples, of the difficulties in calculating the transition probabilities from observed population distributions.

An intimate conceptual and mathematical relationship is established between two types of experiments which are possible at present. One is an impulse, or time-dependent experiment such as excitation with a fast flash lamp and snapshot observation after a known delay time. The other is a steady-state experiment in which molecules are fed into the system (a gas or a surface) at a single energy level, for example, and undergo transitions among the available levels in competition with a first-order removal process such as spontaneous radiation or desorption from a surface.

The ideas summarized above are used to develop procedures for calculating transition probabilities from observed population distributions. Numerical examples and qualitative considerations indicate that when transitions involving more than single quantum jumps are involved, the experimental data must be known to much higher accuracy than that desired in the transition probabilities. The difficulties increase rapidly as the number of levels in the system increases.

TRANSITION probabilities describing inelastic molecular collisions have been the object of much theoretical interest, but very few experimental values have been obtained. Most experiments which have been done in the field of rotational and vibrational energy transfer (i.e., shock waves, sound dispersion, and impact tube experiments) yield average relaxation times which cannot be interpreted to derive transition probabilities between individual molecular energy levels except in the very simplest cases. This is partly because a single relaxation time does not give much information, and partly because a multilevel system will not in general follow the simple behavior characterized by a single relaxation time.[1] For the calculation of detailed transition probabilities, more detailed experiments are required, and it is now becoming possible to perform these experiments. Thus it is appropriate to pose carefully, and answer as clearly as possible, questions of what data should be obtained and just how precise these data need to be. The present paper is devoted to discussion of these points. The treatment and application of the results is general, but the development is guided by thoughts of vibrational and especially rotational energy transfer and problems presented by a recent experiment[2,3] whose purpose was to derive values for rotational transfer probabilities.

We now mention some factors relevant to the theoretical calculations of collisional transition probabilities, and the theoretical treatments which have used these results to derive predicted population distributions (i.e., the fraction of molecules in each available energy level) for certain types of experiments. The theoretical calculations of transition probabilities will be least reliable when interactions are strong (i.e., when use of perturbation theory is inappropriate) and when collision times are comparable to the characteristic times of the degrees of freedom being excited. This is the case for vibrational-translational energy exchange when vibrational quanta are small, as in a weakly bound molecule, or in high vibrational levels of other molecules. It is also the case in general for rotation-translation exchange. In these cases one does not expect the interactions to be confined to adjacent levels, so that transitions involving change of the relevant quantum number by several units are expected to be important. A multilevel system will then have many more transition probabilities than levels. It will be shown later that this fact is the crucial one in determining the difficulty of the problem of going from observed population distributions to the set of transition probabilities which are regarded as having "caused" the distributions.

Calculation of predicted population distributions resulting from assumed initial distributions and assumed nearest-neighbor transition probabilities have been made for vibrational[4,5] and rotational[6] systems, but no comparable experimental results are available. We are concerned here with the inversion of calculations such as these, with the properties of a transformation which will take observed population distributions $\mathbf{x}$ into experimentally defined transition probabilities $\mathbf{w}$. In general, the transformation will not be equally easy in the two directions, and it will be seen below that the precision required in the observed distribution of population is much higher than that required in the

* This research was supported by the Aeronautical Research Laboratory, Air Force Research Division.

[1] K. E. Shuler, Phys. Fluids **2**, 442 (1959).

[2] T. Carrington, J. Chem. Phys. **31**, 1418 (1959).

[3] T. Carrington, Eighth Symposium on Combustion, 1960 (to be published).

[4] E. W. Montroll and K. E. Shuler, Advances in Chem. Phys. **1**, 361 (1958).

[5] R. Herman and R. J. Rubin, J. Chem. Phys. **29**, 591 (1958).

[6] R. Herman and K. E. Shuler, J. Chem. Phys. **29**, 366 (1958).

transition probabilities. The situation is similar to the problem of trying to determine the slope and intercept of a straight line from measurements of two points which are very close together.

We present in the next section a formal description of the calculation of transition probabilities from data which might be obtained from (a) a time dependent, or impulsive, type of experiment, and (b) from a steady-state experiment. It will be seen that the two types of experiment are intimately related. In later sections, procedures for calculating the transition probabilities from experimental data are discussed and several sample calculations are given.

FORMAL DESCRIPTION OF EXPERIMENTS AND RESULTS

The mathematical results will be presented and briefly discussed in this section. We seek to present a formulation of the steady-state and time-dependent experiments which emphasizes the intimate relationship between the two and at the same time brings out the fact that certain methods of approach are more natural in one system than in the other. The first step is to define the two general types of experiment—time-dependent and steady-state—and to establish the notation.

The Time-Dependent Problem

In the time-dependent case, consider a dilute system of noninteracting molecules which interact with a heat bath, and describe a population distribution over n available molecular quantum states by a vector $\mathbf{x}$, of which the elements x_i give the fraction of molecules in state i. The normalization is $\sum_i x_i = 1$. If $\mathbf{x}$ is any vector other than the equilibrium distribution $\mathbf{x}^e$, it will vary in time according to the equation[4]

$$dx_i/dt = \sum_j (w_{ij}x_j - w_{ji}x_i) \equiv \sum_j A_{ij}x_j, \qquad (1)$$

in which w_{ij} is the probability per unit time that a molecule makes a transition from state j to state i.[7] These transition probabilities are simply parameters describing the approach of the system to equilibrium, as produced by interactions with the heat bath. If the interaction is by collision with inert molecules, the transition probabilities will depend on the nature of these molecules and on the temperature of the heat bath. In matrix notation, Eq. (1) is

$$d\mathbf{x}/dt = \mathbf{A}\mathbf{x}, \qquad (2)$$

with

$$A_{ij} = w_{ij} - \delta_{ij}\sum_k w_{ki}$$

and

$$\sum_i A_{ij} = 0.$$

[7] Quantities w_{ii} representing collisions which do not change the state of a molecule are experimentally unobservable and mathematically unknowable, since they cancel in all the equations.

In a typical experiment one produces an initial distribution $\mathbf{x}(0)$, perhaps using a shock wave or a flash lamp, and after a known time delay one measures $\mathbf{x}(t)$. The simplest initial distributions are those in which only a single level is populated, and Boltzmann distributions corresponding to a temperature other than that of the heat bath. The results of all experiments described by (2) are contained in the matrix $\mathfrak{X}(t)$ in which the jth column is the vector $\mathbf{x}(t)$ arising from the initial distribution $x_i(0) = \delta_{ij}$ corresponding to initial excitation of level j only. The result of the experiment with an arbitrary initial distribution is then

$$\mathbf{x}(t) = \mathfrak{X}(t)\mathbf{x}(0). \qquad (3)$$

$\mathfrak{X}$ has the property $\sum_i \mathfrak{X}_{ij}(t) = 1$ for all j and all t, since each column is a normalized probability distribution. Also $\mathfrak{X}(nt) = [\mathfrak{X}(t)]^n$. The transition probabilities are related by the principle of detailed balancing: $w_{ij}x_j^e = w_{ji}x_i^e$. Because of this, one can form from $\mathbf{A}$ the symmetric matrix

$$\mathbf{B} = (\mathbf{X}^e)^{-\frac{1}{2}}\mathbf{A}(\mathbf{X}^e)^{\frac{1}{2}}, \qquad (4)$$

in which the matrix $\mathbf{X}^e$ is the diagonal matrix whose elements are those of the vector $\mathbf{x}^e$. For future use we define $\mathbf{T}$ as the orthogonal matrix whose columns are the eigenvectors of $\mathbf{B}$. The largest eigenvalue of $\mathbf{A}$ and $\mathbf{B}$ is zero; all others are negative.[4]

The Steady-State Problem

The steady-state experiment corresponding to the discussion just given is formulated as follows. In the time-dependent case, $\mathbf{x}(0)$ was the initial distribution suddenly established at the beginning of the experiment, or an existing equilibrium distribution suddenly rendered unstable by a change of conditions. In the steady-state experiment we are constantly introducing molecules uniformly throughout the volume of the system, and we consider $y_i(0)$ to describe the probability that a starting molecule is in state i. Balancing this input is a steady loss of molecules from the system by a first-order process, so that the molecules have a mean lifetime τ in the system, independent of quantum state. The actual lifetime of a particular molecule in the system may be quite differeat from the average. During this lifetime the molecule is exposed to collisions with heat-bath molecules which alter the initial distribution. The experimental observations give the distribution $\mathbf{y}(\tau)$, which gives the fractional population of available energy levels in molecules at the instant of leaving the system.

This model corresponds to a fluorescence experiment[2,3] in which molecules are excited to a single sublevel of an upper electronic state and undergo collisional transitions between these sublevels during the time interval before they undergo spontaneous radiation or quenching collisions to the electronic ground state. The model also corresponds to the thermal accommoda-

tion of molecules with a specified initial energy distribution which reside on a surface for an average length of time τ before desorption. The stipulation that the average lifetime τ is independent of quantum level is an assumption used in defining the model. In a particular experimental situation this approximation may or may not be valid. It should be valid, for example, in a fluorescence experiment where the lifetime is determined only by spontaneous radiation. In more complex cases it is usually an assumption one has to make, in the absence of more information, to reduce the problem to tractable form.

In the steady state, the total rate of input and output is N/τ, where N is the steady-state number of molecules in the system. The input is divided among the available energy levels according to $\mathbf{y}(0)$, and the output according to $\mathbf{y}(\tau)$. The steady-state equations are

$$-(dy_i/dt)=(N/\tau)y_i-(N/\tau)y_i(0)+N\sum_j(w_{ji}y_i-w_{ij}y_j)=0 \quad (5)$$

or

$$\tau\sum_j(w_{ji}y_i-w_{ij}y_j)+y_i=y_i(0). \quad (6)$$

From the solutions $\mathbf{y}(\tau)$ of this system of equations arising from n different $\mathbf{y}(0)$ vectors, one can form the matrix $\mathfrak{Y}(\tau)$, which has for the τ problem the same significance that $\mathfrak{X}(t)$ has in Eq. (3).

The close relationship between the t problem and the τ problem is expressed in the fact that $\mathbf{y}(\tau)$ is simply an average of $\mathbf{x}(t)$ taken over the broad range of lifetimes which will occur in the steady-state system.[8] If the average lifetime is τ, the probability of a lifetime t is

$$P(t)=(1/\tau)\exp(-t/\tau). \quad (7)$$

The width of this distribution, and the fact that its maximum is at $t=0$ rather than at the average, $t=\tau$, mean that the averaging process is very important, and that the average lifetime τ is not a very useful quantity. This point has been discussed elsewhere,[3] and it has been shown that there is a considerable spread in the number of collisions a molecule in the steady-state system may undergo before it radiates. For example, when the average number of collisions during the radiative lifetime is 2, one-third of the excited molecules undergo no collisions at all before radiating, and only one-sixth of the molecules undergo the average number of collisions.

[8] Another interesting steady-state experiment is a flow system in which molecules are excited by radiation or chemical reaction at one point (ideally) in the flow, and observed at another point downstream. Here again, the experimental observations are to be interpreted as an average over transit times from the point of excitation to the point of observation. Here the width of the distribution of transit times may be due to the width of the regions in which the gas is excited and observed, a finite reaction velocity (when the molecules are excited by a chemical reaction), and to wall effects on the hydrodynamics of gas flow.

Comparison of the Two Problems

Having defined the two general problems of interest and stated the physical relationship that one is an average of the other, we can discuss in a unified way the formal properties of the defining equations (1) and (6) and their solutions. The results are presented here with corresponding equations side by side. Comments on their derivation and significance are collected at the end of the section. [The equation for the t problem will be given on the left-hand side in Eqs. (9)–(17), with the corresponding equation for the τ problem following on the right.] The fundamental relationship between formulations of the two problems is

$$(1/\tau)\int_0^\infty \mathbf{x}(t)\exp(-t/\tau)\,dt=\mathbf{y}(\tau), \quad (8)$$

in which $\mathbf{x}(t)$ is averaged over the distribution (7). This is simply the Laplace transformation and relates the defining equations for the two problems:

$$\frac{d\mathbf{x}(t)}{dt}=\mathbf{A}\mathbf{x}(t), \qquad \frac{\mathbf{y}(\tau)-\mathbf{y}(0)}{\tau}=\mathbf{A}\mathbf{y}(\tau) \quad (9)$$

These have the formal solutions

$$\mathbf{x}(t)=\exp(\mathbf{A}t)\,\mathbf{x}(0), \qquad \mathbf{y}(\tau)=(\mathbf{I}-\tau\mathbf{A})^{-1}\mathbf{y}(0); \quad (10)$$

$$\mathfrak{X}(t)=\exp(\mathbf{A}t), \qquad \mathfrak{Y}(\tau)=(\mathbf{I}-\tau\mathbf{A})^{-1}, \quad (11)$$

and the expansions

$$\mathfrak{X}(t)=\mathbf{I}+t\mathbf{A}+\tfrac{1}{2}t^2\mathbf{A}^2+\cdots,$$
$$\mathfrak{Y}(\tau)=\mathbf{I}+\tau\mathbf{A}+\tau^2\mathbf{A}^2+\cdots. \quad (11)$$

The solutions may also be given in a form analogous to that given by Montroll and Shuler[4]

$$\mathfrak{X}(t)=(\mathbf{X}^e)^{\frac{1}{2}}\mathbf{T}\exp(\mathbf{\Lambda}t)\,\mathbf{T}'(\mathbf{X}^e)^{-\frac{1}{2}},$$
$$\mathfrak{Y}(\tau)=(\mathbf{X}^e)^{\frac{1}{2}}\mathbf{T}(\mathbf{I}-\tau\mathbf{\Lambda})^{-1}\mathbf{T}'(\mathbf{X}^e)^{-\frac{1}{2}}, \quad (13)$$

in which, for example, $\mathbf{\Lambda}$ is a diagonal matrix in which the jth diagonal element is λ_j, and λ_j is the jth eigenvalue of $\mathbf{A}$ and $\mathbf{B}$.

It is important to be able to estimate the effect on the observed distributions of small changes in the transition probabilities. We consider a perturbed transition matrix $A=A^{(0)}+\epsilon A^{(1)}$, in which $A^{(1)}$ is a matrix in which only a few elements may be different from zero, and ϵ is a scalar which we allow to approach zero. In general, $A^{(0)}$ and $A^{(1)}$ will not commute. The perturbation expressions are

$$\frac{\partial\mathfrak{X}(t)}{\partial\epsilon}=\int_0^t\mathfrak{X}(t-s)\mathbf{A}^{(1)}\mathfrak{X}(s)\,ds; \qquad \frac{\partial\mathfrak{Y}}{d\epsilon}=\tau\mathfrak{Y}\mathbf{A}^{(1)}\mathfrak{Y}. \quad (14)$$

It is useful to give these results for the special case $A_{pq}{}^{(1)}=(\delta_{pj}-\delta_{pk})/(\delta_{kq}-\alpha_{kj}\delta_{jq})$ corresponding to a

change of w_{jk} and detailed balancing in the matrix $\mathbf{A}$.

$$\frac{\partial \mathfrak{X}_{il}}{t\partial w_{jk}} = (1/t)\int_0^t \{\mathfrak{X}_{ij}(t-s)-\mathfrak{X}_{ik}(t-s)\] \times[\mathfrak{X}_{kl}(s)-\alpha_{kj}\mathfrak{X}_{jl}(s)\]ds;$$

$$\partial \mathfrak{Y}_{il}/\tau\partial w_{jk}=[\mathfrak{Y}_{ij}(\tau)-\mathfrak{Y}_{ik}(\tau)\][\mathfrak{Y}_{kl}(\tau)-\alpha_{kj}\mathfrak{Y}_{jl}(\tau)\]. \tag{15}$$

Corresponding expressions can be written if we consider the effects of a perturbation on $\mathfrak{X}$ or $\mathfrak{Y}$. Writing

$$\mathfrak{X}(t)=\mathfrak{X}^{(0)}(t)+\epsilon\mathfrak{X}^{(1)}(t); \qquad \mathfrak{Y}(\tau)=\mathfrak{Y}^{(0)}(\tau)+\epsilon\mathfrak{Y}^{(1)}(\tau),$$

we have

$$\frac{t\partial \mathbf{A}}{d\epsilon}=\mathfrak{X}^{(1)}-\int_0^t(\mathbf{A}\mathfrak{X}^{(1)}+\mathfrak{X}^{(1)}\mathbf{A})dt+\int_0^t\int_0^t\mathbf{A}\mathfrak{X}^{(1)}\mathbf{A}(dt)^2;$$

$$\frac{\tau\partial \mathbf{A}}{d\epsilon}=(\mathbf{I}-\tau\mathbf{A})\mathfrak{Y}^{(1)}(\mathbf{I}-\tau\mathbf{A}). \tag{16}$$

For completeness, we compare the t and τ derivatives:

$$d\mathbf{x}/dt=\mathbf{A}\mathbf{x}, \qquad d\mathbf{y}/d\tau=\mathfrak{Y}\mathbf{A}\mathbf{y}. \tag{17}$$

The τ derivative in (17) is obtained by implicit differentiation of (9).

Though the derivation of these results is straightforward, some discussion is in order. In all of the pairs (8) through (16), the τ expression is the Laplace transform of the corresponding t expression. Certain results which are more easily derived for one problem may thus be transformed into the other. In (9), the time derivative in the t problem is replaced by the average of the corresponding derivative in the τ problem. The matrix exponential, Eq. (10) as a solution of (9), is discussed, for example, by Bellman.[9] $\mathfrak{X}$ is the Green's function for the differential equation (9). The expansions (12) emphasize that the two problems become identical in the limit of small t and τ. This is to be expected, since in this limit the distribution (7) becomes sharp and τ is well defined.

Equations (11) and (13) provide the means of calculating $\mathbf{A}$ from $\mathfrak{X}$ or $\mathfrak{Y}$, as discussed in the next section. The representations (13) may be taken as defining the matrix functions (11). This representation is possible because of the transformation (4) which symmetrizes $\mathbf{A}$. In this connection, the problem of calculating the effect on the experimental results of changes in the transition probabilities is treated in (14). The τ expression is derived by expanding $\mathfrak{Y}(\tau)=[\mathbf{I}-\tau(\mathbf{A}^{(0)}+\epsilon\mathbf{A}^{(1)})\]^{-1}$ in powers of ϵ and retaining the first term. The t expression can be derived from this using the inverse Laplace transform and the Faltung theorem. It is a well-known result, derived directly by Bellman,[9] for instance. Here the equation is much simpler in the τ problem, and a knowledge of the general form of the matrices $\mathfrak{X}$, $\mathfrak{Y}$ enables one to estimate the relative magnitudes of expressions of the type $\partial\mathfrak{X}_{il}/\partial w_{jk}$ in the two problems. The expression in (16) is derived by expanding $\tau\mathbf{A}=\mathbf{I}-(\mathfrak{Y}^{(0)}+\epsilon\mathfrak{Y}^{(1)})^{-1}$ in powers of ϵ. The t expression is derived from this by the inverse Laplace transform. The τ expression will be used in the next section to develop a means of deciding just what data must be measured to calculate certain transition probabilities. These perturbation expressions are of value in estimating the sensitivity of the observed distributions to small changes in the transition probabilities; that is, the physical behavior of the system. They cannot be used to estimate the accuracy of a particular procedure for calculation of transition probabilities from experimental data, except in the sense of setting an upper limit to that accuracy. The accuracy of the calculation depends critically on the choice of data to be used, and on the detailed steps in the computation itself; for example, on the order in which the solutions are obtained.

From a purely mathematical point of view, discussion of the steady-state problem amounts to applying Laplace transform techniques to the solution of the time-dependent problem, Eq. (2). The advantage of doing this is particularly clear in the perturbation expressions. The fact that the transformed problem corresponds closely to certain types of steady-state experiments which are becoming practical[2,3] gives it a clear physical significance in its own right.

The Laplace transform has been used by Berman and Schoenfeld[10] as a mathematical device for obtaining the solution to Eq. (2). They have applied this equation to tracer experiments in biological systems; particularly, open systems in which detailed balance was not important. They have discussed the problem of determining transition probabilities from a knowledge of time-dependent population distributions, using an approach somewhat different from that presented in this paper.

CALCULATIONS OF TRANSITION PROBABILITIES

We now revert to the question of how to calculate the transition probabilities w_{ij} when some or all of the elements of $\mathbf{X}$ or $\mathfrak{Y}$ are known. These matrices collect the results of all successive experiments in each of which the system is started out in one of its energy levels and allowed to relax, for a given t or τ, toward equilibrium.

The Steady-State Problem

Here, the calculation of transition probabilities is equivalent to inversion of the matrix $\mathfrak{Y}(\tau)$ in Eq. (11). Since we know from (2) that the off-diagonal elements of $(\mathbf{I}-\tau\mathbf{A})$ are the transition probabilities τw_{ij}, we can equate these transition probabilities to corresponding elements of a computed inverse of the experi-

[9] R. Bellman, *Introduction to Matrix Analysis* (McGraw-Hill Book Company, Inc., New York, 1960).

[10] M. Berman and R. Schoenfeld, J. Appl. Phys. **27**, 1361 (1956).

mentally determined $\mathfrak{Y}$. It is clear on physical grounds that if τ is large, so that the system is near equilibrium, it must be harder to get information about the mechanism of approach to equilibrium than would be the case for smaller τ. As τ becomes large, all columns of $\mathfrak{Y}$ approach the same equilibrium distribution, so that its determinant approaches zero, while the elements do not change much in magnitude. This means that the computation of the inverse becomes increasingly more difficult. This mathematical difficulty means in practical terms that the system of equations for determining w_{ij} loses its uniqueness, so that several quite different sets of w_{ij} will satisfy the equations to the same computational precision. Physically, any set of transition probabilities consistent with detailed balancing would give the equilibrium distribution. This difficulty of inversion, or of solution of certain types of linear algebraic systems, is known as ill conditioning.[11,12] It may arise from physical causes, as in the case above, or for more trivial reasons, in which case the situation may be improved by certain transformations of the equations.

There is also trouble when τ is near zero. Here the inversion is easy enough, but in both matrices $\mathfrak{Y}$ and $\mathfrak{Y}^{-1}$ the off-diagonal elements are so small that accurate transition probabilities cannot be calculated. In other words, one cannot calculate transition probabilities when there has been no time for transitions.

Concerning the condition of the equations between the two limiting values of τ, one can say in general that the larger the number of levels, n, the worse the situation will be, especially since the number of equations to be solved is of order n^2. Rounding-off errors will become increasingly important in a system of many levels, but more important is the fact that the fractional population in each level decreases with increasing n. Equation (15) then indicates that a given observable $\mathfrak{Y}_{il}$ will depend less on a given transition probability w_{jk} as n increases. An indication of the difficulty of solution or inversion of a system of linear algebraic equations is the condition number[11] $P=|\mu|_{\max}/|\mu|_{\min}$ where the μ are the eigenvalues of the matrix involved. If λ represents the eigenvalues of $\mathbf{A}$, the corresponding eigenvalues of $\mathfrak{Y}^{-1}=\mathbf{I}-\tau\mathbf{A}$ are $\mu=1-\tau\lambda$. Since the λ are all negative except for one zero, we have $P=1+\tau|\lambda|_{\max}$. The $\log_{10}P$ gives roughly the number of significant figures lost in an inversion by elimination. It is seen that P increases slowly with τ, and it will be seen in terms of an upper bound to be given for $|\lambda|_{\max}$ that it may be expected to increase with the number of levels. This will be particularly true when the nearest-neighbor transition probability is proportional to the level number.

In the τ problem, the expression

$$\mathfrak{Y}^{-1}\mathfrak{Y}=\mathbf{I} \tag{18}$$

represents n^2 equations linear in w_{ij} when the molecules have n possible energy states. Of these only n^2-n are independent, however, because of the condition of conservation of number of molecules in each experiment described by a column of $\mathfrak{Y}$. There are, however, only n^2-n values of w_{ij} to be determined, since the w_{ii} are of no interest. Each of the equations represented by (18) is identical with one of the equations of the system (6) when the initial and final $\mathbf{y}$ vectors in (6) are those which define $\mathfrak{Y}$.

The fact that the transition probabilities must be related by detailed balance,

$$w_{ij}=w_{ji}x_i^e/x_j^e\equiv w_{ji}\alpha_{ij}, \tag{19}$$

means that the matrix $\mathbf{A}$ can be transformed to symmetric form, and that any function of $\mathbf{A}$ can also be symmetrized by the same transformation. The elements of $\mathfrak{Y}$ must then be related by

$$\mathfrak{Y}_{ij}=\mathfrak{Y}_{ji}\alpha_{ij}, \tag{20}$$

and similarly for $\mathfrak{X}$. Because of (19), there are only $\frac{1}{2}n(n-1)$ independent unknown transition probabilities, and one need measure only this number of independent data in $\mathfrak{Y}$. According to (20), $\mathfrak{Y}$ and $\mathbf{A}$ are fully determined by measurement of $\mathfrak{Y}_{ij}$ *either* for $i<j$ *or* for $i>j$. The most natural experiments, however, lead to measurements of an entire column of $\mathfrak{Y}$, and it is interesting to consider cases in which some of the elements of $\mathbf{A}$ can be calculated from knowledge of only certain columns of $\mathfrak{Y}$. This is most clearly the case when $\mathbf{A}$ is of the tridiagonal or continuant form, corresponding to transitions between nearest-neighbor levels only.

To consider the dependence of specific elements of $\mathbf{A}$ on specific elements of $\mathfrak{Y}$, we start with the perturbation expression (16). The perturbation must satisfy the conditions of column normalization, $\sum_i\mathfrak{Y}_{ij}=1$, and the condition (20). If the perturbation arbitrarily increases the element $\mathfrak{Y}_{pk}$, these conditions require a corresponding increase in $\mathfrak{Y}_{kp}$ and corresponding decreases in $\mathfrak{Y}_{qk}$ and $\mathfrak{Y}_{kq}$ where q is arbitrary. The perturbation is then

$$\mathfrak{Y}_{ij}^{(1)}=(\delta_{ip}-\delta_{iq})\delta_{jk}+\delta_{ik}(\alpha_{kp}\delta_{jp}-\alpha_{kq}\delta_{jq}), \tag{21}$$

and substitution of this in (16) gives

$$\tau\frac{\partial A_{rs}}{\partial\epsilon}=(\mathfrak{Y}_{rp}^{-1}-\mathfrak{Y}_{rq}^{-1})\mathfrak{Y}_{ks}^{-1}+\mathfrak{Y}_{rk}^{-1}(\alpha_{kp}\mathfrak{Y}_{ps}^{-1}-\alpha_{kq}\mathfrak{Y}_{qs}^{-1}), \tag{22}$$

where we have put $\mathbf{I}-\tau\mathbf{A}=\mathfrak{Y}^{-1}$. Thus the off-diagonal elements of $\mathfrak{Y}^{-1}$ are the same as those of $\tau\mathbf{A}$, and $\mathfrak{Y}^{-1}$ is a continuant when $\mathbf{A}$ is a continuant. Many elements of $\mathfrak{Y}^{-1}$ are then zero, and there will be certain combinations of indexes r, s, p, q, k for which the derivative in Eq. (22) is zero. In other words, when $\mathbf{A}$ is of continuant form, there are certain elements of $\mathfrak{Y}$ which do not

[11] A. M. Turing, Quart. J. Mech. and Appl. Math. **1**, 287 (1948).
[12] J. Tod, J. Research Natl. Bur. Standards **60**, 1 (1958).

TABLE I. The transition probability matrix and the equilibrium distribution.[a]

$\tau_0 \mathbf{A}$						$\mathbf{x}^e$
−0.6419	0.4500					0.20000
0.6419	−1.3648	0.9000				0.28528
	0.9148	−1.6340	1.3500			0.28998
		0.7340	−1.9719	1.8000		0.15768
			0.6219	−2.3216	2.2500	0.05448
				0.5216	−2.2500	0.01263

[a] Note that the sum of elements in any column is zero, and that the product $\tau_0 \mathbf{A} \mathbf{x}^e$ is also zero.

influence certain elements of $\mathbf{A}$, so that these elements of $\mathbf{A}$ can be calculated without knowledge of all elements of $\mathfrak{P}$. As a specific example, consider a matrix $\mathfrak{P}$ with six rows and columns. If the last three columns are known, then by (20), the last three rows are also known, and only elements in a 3×3 square in the upper left corner are unknown. In Eq. (22) we then ask for those values of r and s for which $\tau\partial A_{rs}/\partial\epsilon=0$ when p, q, and k are all ≤ 3. When $\mathfrak{P}^{-1}$ is a continuant, this will be the case when $s>4$ or when $r>4$. Thus measurements of the last three columns of $\mathfrak{P}$ enable us to calculate the last two columns and the last two rows of $\mathbf{A}$. It is clear that severe ill-conditioning will arise if one tries to carry through a calculation of the above type when $\mathbf{A}$ is in fact not a continuant. In the general case, one must know the entire matrix $\mathfrak{P}$ before any element of $\mathbf{A}$ can be calculated.

If measurements of some elements of $\mathfrak{P}$ are to be repeated, to get higher precision, Eq. (22) can be used to estimate which elements are most crucial for the determination of specific elements of $\mathbf{A}$.

Since the continuant form of $\mathbf{A}$ is often assumed for mathematical convenience, and has much physical justification in some systems of vibrational levels, it is desirable to have a test which may be applied to the data in $\mathfrak{P}$ to determine whether or not it corresponds to a transition matrix of this form. We make use of the fact that in a matrix which is the inverse of a continuant, all 2×2 subdeterminants which do not contain elements on both sides of the main diagonal are zero. That is, we have

$$\begin{vmatrix} \mathfrak{P}_{ij} & \mathfrak{P}_{i,j+n} \\ \mathfrak{P}_{i+m,j} & \mathfrak{P}_{i+m,j+n} \end{vmatrix} = 0 \qquad \begin{matrix} i+m\leq j, \text{ or} \\ i\geq j+n. \end{matrix} \tag{23}$$

This can be demonstrated by making use of the fact that any minor determinant in the reciprocal matrix is proportional to the complement determinant of the corresponding minor in the original matrix.[18] It is easily verified that all determinants formed from the continuant $\mathbf{I}-\tau\mathbf{A}$ by striking out a pair of adjacent rows and a pair of adjacent columns will be zero when this process removes more than two diagonal elements from the original matrix. In an n-dimensional matrix which is the inverse of a continuant, there are $(n-1)(n-2)$ independent relationships of this kind. The fact that the elements of each column add to unity provides another n relationships among the elements of $\mathfrak{P}$, leaving $n^2-(n-1)(n-2)-n=2(n-1)$ independent elements. This is just the number of independent elements in $\mathbf{A}$, since the total number $3n-2$ is reduced by n because of the column normalization in $\mathbf{A}$.

[18] G. Kowalewski, *Einfuhrung in die Determinantentheorie* (Walter de Gruyter Company, Berlin, 1942), p. 72.

The Time-Dependent Problem

Here the general task of calculating the w's from knowledge of the full matrix $\mathfrak{X}$ at one instant of time may be presented as follows. Symmetrize $\mathfrak{X}$ by the transformation $\mathfrak{Z}=(\mathbf{X}^e)^{-\frac{1}{2}}\mathfrak{X}(\mathbf{X}^e)^{\frac{1}{2}}$ and find the eigenvectors and eigenvalues of $\mathfrak{Z}$. The eigenvectors are those of $\mathbf{B}$, and the eigenvalues are simply exponentials of the eigenvalues of $\mathbf{B}$. Thus $\mathbf{B}$ can be found as $\mathbf{B}=\mathbf{T}\Lambda\mathbf{T}'$, where Λ is the diagonal matrix whose elements are the eigenvalues of $\mathbf{B}$. $\mathbf{B}$ can then be converted to $\mathbf{A}$ by the inverse of the transformation used to symmetrize $\mathfrak{X}$. All the transition probabilities are explicitly contained in $\mathbf{A}$. The matrix algebra involved here is not difficult with an electronic computer, and the inverse of this calculation is useful in deriving $\mathfrak{X}(t)$ from an assumed set of transition probabilities $\mathbf{A}$.

In general, however, one will not have available all the data required to form the matrix $\mathfrak{X}$. To most natural thing to do is to use a single initial distribution and observe the system at several different times. The simplest procedure is to measure both $\mathbf{x}$ and $d\mathbf{x}/dt$ at as many different time values as may be necessary to get enough independent data to determine all the unknown transition probabilities in the matrix $\mathbf{A}$. If, for example, the number of transition probabilities to be determined is twice the number of levels in the system, corresponding to jumps of one and two quantum steps, one needs $\mathbf{x}$ and $d\mathbf{x}/dt$ at two times, corresponding to distributions which are as different as possible from one another and also from the initial and equilibrium distributions.

Equation (2) is then considered as a set of linear equations for the determination of the independent elements of **A**. A numerical calculation illustrating this procedure is presented in the next section.

Some qualitative indications can be given as to the best choice of times at which to make the measurements. The relaxation times of the system are the reciprocal eigenvalues of **A** [see Eq. (13)]. The time dependence of an element of $\mathfrak{X}$ is a series of exponentials $\exp(\lambda_i t)$ summed over all eigenvalues λ_i. The times at which observations are made should be chosen such that as many as possible of these terms make a significant contribution to the sum. The eigenvalue of largest absolute magnitude, corresponding to the shortest relaxation time, has as upper bound[14] the sum of the absolute magnitudes of the elements in that column of **A** in which this sum is the largest, $|\lambda| \leq \max_j \sum_i (A_{ij})$. From the form of **A**, Eq. (2), this is $|\lambda| \leq 2 \max |A_{jj}|$. In some cases, when **A** is a continuant, the smallest nonzero eigenvalue will be approximately equal to the smallest transition probability. We ignore difficulties which arise if any eigenvalues are equal or nearly equal.

NUMERICAL CALCULATIONS

To illustrate the procedure and the difficulties which arise in trying to calculate collisional transition probabilities from observed population distributions, we assume in this section a set of transition probabilities for a six-level system, calculate predicted distributions which would be observed in typical time-dependent and steady-state experiments, and then use these synthetic "data" to try to calculate the transition probabilities initially assumed. Five decimal places have been carried in most of the calculations presented, and these results should be good to four places. If we regard elements of the calculated matrix $\mathfrak{Y}$, as representing experimental data, we must consider how random experimental error is to be represented. This may be thought of as fluctuations of two different types. One type is a background noise in the measuring instrument, essentially independent of the amplitude of the signal being measured. Examples are amplifier noise, dark current noise in a photomultiplier, or the effect of building vibrations on a galvanometer. This constant background noise corresponds to keeping a certain number of decimal places in the calculated synthetic data. A second possible type of fluctuation is proportional to the signal amplitude. An example would be mechanical instability of an arc or electric discharge in which one is trying to measure spectral line intensities. Such a fluctuation, which has the same relative effect on weak and strong signals, is represented by keeping a constant number of significant figures in the data, rather than a constant number of decimal places. The calculations have been carried out with a constant number of decimal places both because the constant background noise situation is a very general one, and for computational convenience.

TABLE II. The matrix $\mathfrak{Y}(\tau_0) = (\mathbf{I} - \tau_0 \mathbf{A})^{-1}$.

	0[a]	1	2	3	4	5
0	0.66782	0.15032	0.06008	0.03127	0.01901	0.01316
1	0.21442	0.54846	0.21920	0.11407	0.06936	0.04802
2	0.08710	0.22280	0.53307	0.27744	0.16868	0.11678
3	0.20465	0.06305	0.15086	0.46405	0.28214	0.19533
4	0.00518	0.01324	0.03169	0.09748	0.39705	0.27488
5	0.00083	0.00213	0.00509	0.01564	0.06372	0.35181

[a] The column indexes indicate the level which is initially populated. The row indexes distinguish the levels in each calculated distribution after the average lifetime τ_0.

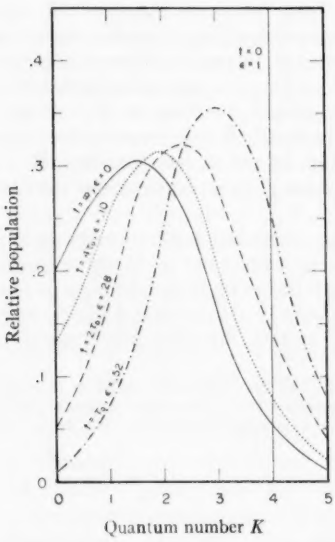

FIG. 1. Calculated distributions at several times after initial excitation in level 4. The quantity ϵ is defined as

$$\epsilon = [E(t) - E(\infty)] / [E(0) - E(\infty)]$$

where

$$E(t) = \Sigma_i E_i x_i(t)$$

and E_i is the energy of the ith level.

Transition Probability Model

The transition probabilities are taken as

$$w_{j-1,j} = j w_{0,1}, \qquad w_{i,j} = 0 \quad \text{for} \quad |i-j| > 1, \quad (24)$$

in accordance with certain theoretical results for interaction of rotation with translation[15,16] and of vibration with translation.[17] To restrict the numerical labor, a system of only 6 levels has been assumed. For the sake of a specific model, the first 6 rotational energy

[14] R. Zurmühl, *Matrizen* (Springer-Verlag, Berlin, 1958), 2 Aufl., p. 205.

[15] R. Brout, J. Chem. Phys. **22**, 1189 (1954).

[16] K. Takayanagi, Prog. Theoret. Phys. (Kyoto) **8**, 497 (1952); K. Takayanagi and J. Kishimato, *ibid.* **9**, 378 (1953).

[17] K. F. Herzfeld, in *Thermodynamics and Physics of Matter*, edited by F. D. Rossini (Princeton University Press, Princeton, New Jersey, 1955), Sec. H.

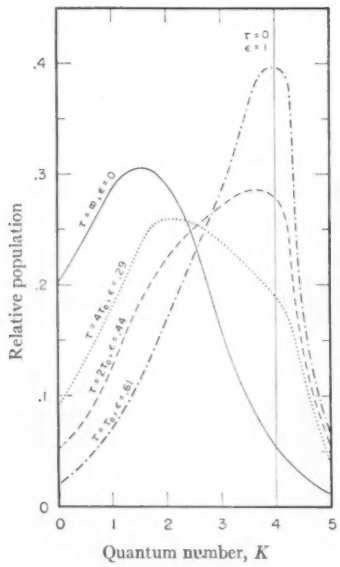

FIG. 2. Calculated steady state distributions for several average lifetimes when initial excitation is in level 4. Smooth curves connecting points calculated for each quantum level are somewhat arbitrary, and are drawn mostly as an aid to visualization.

levels of OH are used,[18] and the heat-bath temperature is taken to be 144°K (where $kT=100$ cm^{-1}) so that the equilibrium population in higher levels is negligible. As for the question of absolute magnitude of the transition probabilities, one is interested only in the product $\tau_0 w_{0,1}$, where τ_0 is the average lifetime in the steady-state experiment or a typical observation delay time in the impulse experiment. The numerical values are given in Table I.

Predicted Results of Experiments

For the t problem, we have calculated, using Eq. (13), predicted distributions for initial excitation at the fourth level, and observations at later times τ_0, $2\tau_0$, and $4\tau_0$. The results are given in Fig. 1. It is clear from this figure that there are not many distributions which are substantially different both from each other and from the initial and final distributions.

The matrix $\mathfrak{P}(\tau)$ has been calculated, using Eq. (11). The result is given in Table II. Here, each column gives the steady-state distribution when the excited molecules are formed exclusively in the level corresponding to the position of that column in the matrix. The maximum in each column lies on the diagonal, that is, at the initially excited level, so the process of rotational relaxation has not progressed very far. The diagonal elements decrease from left to right because the transition probability for leaving the initial level is increasing as the initial excitation goes into higher levels. Figure 2 shows column 4 of this matrix, and the corresponding distributions for average lifetimes $\tau=\tau_0$, $2\tau_0$, and $4\tau_0$.

[18] G. H. Dieke and H. M. Crosswhite, "The ultraviolet bands of OH", Bumblebee Rept. No. 86, The Johns Hopkins University, 1948.

Transition Probabilities Calculated from Predicted Results in the t Problem

First one uses Eq. (19) to eliminate half of the unknown transition probabilities in $\mathbf{A}$ [see Eq. (2)]. We arbitrarily decide to eliminate those w_{ij} in which $i>j$. The $\mathbf{A}$ matrix then becomes

$$A_{ij}=w_{ij} \qquad j>i$$

$$A_{ij}=w_{ji}\alpha_{ij} \qquad j<i$$

$$-A_{ii}=\sum_{j<i}w_{ji}+\sum_{j>i}w_{ij}\alpha_{ji}. \tag{25}$$

In the t problem we regard $\mathbf{x}$ and $d\mathbf{x}/dt$ as measured quantities in Eq. (2) and calculate the elements of $\mathbf{A}$ as given in (25). In the system of equations $\mathbf{Ax}=d\mathbf{x}/dt$ we have as coefficient of the unknown w_{pq} in the ith equation the expression

$$(x_q-\alpha_{qp}x_p)(\delta_{ip}-\delta_{iq}). \tag{26}$$

In a system of n levels, there will be $\frac{1}{2}(n^2-n)$ w's to be determined, and these can be distinguished by a single index j and collected in the vector $\mathbf{w}$. The expression (26) is then the typical element R_{ij} of the matrix $\mathbf{R}$ defined by

$$\mathbf{Rw}=d\mathbf{x}/dt. \tag{27}$$

The term $(x_q-\alpha_{qp}x_p)$ in (26) is the difference between the observed population in level q and the population which would exist in that level if it were in equilibrium with the observed population in level p. This means that if the distribution is too close to equilibrium the corresponding rows of $\mathbf{R}$ will be near zero.

The system of linear algebraic equations (2) contains only $n-1$ independent equations because of the condition of conservation of total number of molecules. In order to determine $\frac{1}{2}n(n-1)$ transition probabilities we need $n/2$ independent distributions $\mathbf{x}$ and corresponding $d\mathbf{x}/dt$. The matrix $\mathbf{R}$ then contains $n-1$ rows for each distribution. In the six-level problem, $\mathbf{R}$ is a 15×15 matrix involving three experimental distributions.

Before presenting numerical results for the general problem, we solve the simpler one in which we assume only the single-jump transition probabilities to be nonzero. Thus we eliminate 10 unknowns and 10 equations. The resulting 5×5 system, involving only one experi-

TABLE III. Derivative of the fractional population in level i with respect to the transition probability relating levels 3 and 4 when the initial excitation is in level 4. See Eq. (15). Data from Tables I and II.

i	0	1	2	3	4	5
$\partial\mathfrak{P}_{i4}/\tau\partial w_{34}$	0.004	0.01	0.03	0.05	−0.09	−0.01
$w_{34}\partial\mathfrak{P}_{i4}/\mathfrak{P}_{i4}\partial w_{34}$	0.36	0.26	0.32	0.32	−0.41	−0.30

mental distribution, is easily solved and gives transition probabilities which agree with those initially assumed, to an accuracy equal to that of the data in the observed distribution itself. We next solve the larger system in which we assume both single and double jump transitions are allowed, but no others. This is a 9×9 system, but is still easily tractable with a desk calculator because many of the elements of $\mathbf{R}$ are zero. In this case, the mean deviation of the calculated values from those initially assumed is 20 times greater than for the 5×5 system, so that the experimental data have to have an accuracy roughly ten times the accuracy required of the transition probabilities. If one solves the 12×12 system including three-jump transitions, the accuracy of the solution is essentially the same as in the two-jump case. The full 15×15 system in (27) has been inverted on an IBM 704 computer and the solution obtained. The elements of the inverse are mostly of order 10^4, which means roughly that four places of accuracy are lost in obtaining the solution. Thus, for the problem of determining the full set of transition probabilities in the six-level problem, the requirements of accuracy of the experimental data are severe. It should be emphasized that the condition of the equations depends strongly on the choice of distributions and on details of the computational procedure. The example treated here is an experimentally reasonable one, however.

Perturbation of Observed Distributions in the τ Problem due to Changes in the Transition Probabilities

Equation (15) may be used to estimate these effects in the case at hand. From the $\mathbf{A}$ matrix of transition probabilities, Table I, we form the matrix $\mathbf{I}-\tau\mathbf{A}$ and take the inverse. This matrix $\mathfrak{Y}$, given in Table II, has the significance that each column gives the distribution that will be observed when the initial excitation populates only one of the available levels. Using in Eq. (15) the elements of $\mathfrak{Y}$ thus calculated, we can calculate, as typical examples useful in developing intuition, certain derivatives of the form $\partial\mathfrak{Y}_{il}/\tau\partial w_{jk}$. These are given in Table III. The values indicate that the matrix $\mathfrak{Y}$ serves to specify the transition probabilities with good accuracy when the calculation is made by inversion of $\mathfrak{Y}$. One can make useful estimates of derivatives of this type even when all the elements of $\mathfrak{Y}$ are not known, since the clear physical significance of that matrix, and a little intuition, enable one to estimate the shape of the distributions which make up its columns.

It is difficult to say precisely how corresponding derivatives in the t problem and in the τ problem will compare, but in general they will not be very different. They are of course identical in the limits $t=0$, $\tau=0$ and $t=\infty$, $\tau=\infty$.

Transition Probabilities Calculated from Predicted Results in the τ Problems

If one has all the data represented in the full matrix $\mathfrak{Y}$, $\mathbf{A}$ is found simply by inversion, using (11). For the six-level model this involves little loss of accuracy. If, however, one has only three columns of $\mathfrak{Y}$, one must use the relationships (19) and solve the system

$$\tau\mathbf{R}\mathbf{w}=\mathbf{y}-\mathbf{y}(0) \tag{28}$$

corresponding to (27) and involving the same matrix $\mathbf{R}$. Instead of inverting a 6×6 matrix, we now have to solve a 15×15 system, a considerably harder task. The relationships (23) mean that certain subdeterminants in $\mathbf{R}$ are also zero, so that it is not possible to determine all the transition probabilities $\mathbf{w}$ from $n/2$ distributions. The choice of the distributions used in forming $\mathbf{R}$ determines which w's can be calculated, as indicated in the discussion of Eq. (22). If one assumes in advance that $\mathbf{A}$ is a continuant, perhaps as a result of applying the test indicated in (23), the $(n-1)$ independent transition probabilities can be calculated from a single column of $\mathfrak{Y}$. In the six-level problem there is no loss of accuracy.

DISCUSSION

The first part of the paper establishes a compact notation for describing impulse and steady-state systems and experimental observations on these systems. The intimate conceptual and formal relationship between these systems is displayed. This speaks for itself without need of further comment. A qualitative discussion is in order on the results of the model calculations.

The difficulty in calculating an accurate set of transition probabilities from observed population distributions $\mathfrak{X}$ or $\mathfrak{Y}$ is an expression of the fact that the observed distribution may be insensitive to rather large changes in the transition probabilities. This becomes more and more true, the larger the number of levels in the system. Sample calculations have been made comparing the transition probability mode. (24) with the model independent of rational level

$$\begin{aligned} w_{ij}&=w, \qquad |\,i-j\,|=1;\\ w_{ij}&=0, \qquad |\,i-j\,|>1 \end{aligned} \tag{29}$$

for a 17-level system. When the absolute values of the transition probabilities are scaled to give a population of 22% in the initial eleventh level, the predicted distributions differ by no more than 2% over most of the curve, and never by more than 5%. There are several alternate routes, several different sets of transition probabilities, by which one can arrive at almost the same distribution.

There are also qualitative indications of trouble when one looks at the problem from the point of view of the actual computation. The matrix $\mathbf{R}$ in (27) contains elements of the form $(x_q-\alpha_{qp}x_p)$ which

approach zero at equilibrium, and most of them also approach zero as the number of levels increases, since the fractional population in any one level decreases in this limit. Most of them also approach zero at $t=0$. The more transition probabilities are required, the more different distributions must be included in **R**. If any two of these distributions are not sufficiently different, corresponding rows in **R** will be nearly equal. This leads to a system in which the solution cannot be obtained with good accuracy.

In systems of many levels, it may be useful to combine some of the levels into groups, and calculate average transition probabilities between groups. It may be that the difficulties of interpretation connected with the significance of the averages will be less than the difficulties caused by insufficient quantity or accuracy of the data in the system with the full number of levels.

In summary, it is a reasonable thing to calculate single-jump transition probabilities for a system of a few levels, perhaps five or six, but the requirements of accuracy of the data increase greatly when more transition probabilities are included. In a system of many more levels it is probably impractical to calculate even single-jump transition probabilities.

Note added in proof. Recently model calculations with a somewhat similar motivation to those presented here have been reported by D. J. Wilson, B. Noble and B. Lee, J. Chem. Phys. **34,** 1392 (1961).

Atomic Wave Functions for the Ground States of Na^+, Ne, and F^-

WILM E. DONATH
International Business Machines Corporation Watson Laboratory, New York, New York

(Received January 16, 1961)

Calculations of wave functions for the ^1S ground states of Na^+, Ne, and F^- which essentially correlate the outer shell are presented here. The "root" function in each case is an analytic Hartree-Fock function. The improved 13-configuration function yields an improvement in energy of about 50% of the estimated correlation energy.

I. INTRODUCTION

THE problem we are faced with is the calculation of atomic wave functions better than the Hartree-Fock functions. A very promising start has been made by Boys[1] and co-workers in that direction. Particularly valuable in that work is the general scheme of computing the angular part of the interaction integrals between different vector-coupled detors.[2] Extensive use was made of Bernal and Boys[1a] coefficients. A few were calculated for this computation, using his methods. Boys'[1] actual calculations for wave functions suffer in so far as they are not clear-cut improvements on the Hartree-Fock functions in every respect. It seems to this writer that the H—F functions yield a very good approximation for the radial distribution of electrons, while Boys' functions—which do not start from Hartree functions—do not necessarily yield a good radial density. The reason for this seems to be the limited number of basis functions Boys used which, in turn, apparently was demanded by the limited capacity of the computer.

The calculations described here start out by using Hartree-Fock functions fitted with analytic exponential functions. I then introduce ten correlation terms, which are doubly excited states, and two singly excited states, which modify the ground-state orbitals $2s$ and $2p$.

II. ANALYTIC FITS TO THE HARTREE-FOCK FUNCTIONS

For Na^+ the functions of Fock and Petrashin[3] were fitted by Löwdin,[4] and those were used for the Na^+ "root" function. For Ne and F^- the Hartree-Fock functions were calculated by Worsley,[5] and Froese,[6] respectively. These functions were fitted by calculating the decay rate of the tail, fitting it with an exponential function, and subtracting its contribution. Another function was used to fit the new tail and step by step the numerical function was used up.

To increase the accuracy of the fit a least-squares fit was made at the end. The resulting functions are given in Table I in terms of N_K, Z_K, and A_K. The equation for the orbitals is written as

$$P(r)=\sum_K A_K \exp(-Z_K r) r^{N_K+1} \times[(2Z_K)^{(2N_K+3)}/(2N_K+2)!]^{\frac{1}{2}}. \quad (1)$$

The factor within brackets normalizes the exponential term, which in turn keeps the values for A_K in reasonable bounds.

As the next step, all the orbitals were normalized and the $2s$ orbital was made orthogonal to the $1s$ orbital by varying the one coefficient which has $1s$ character.

III. CHOICE OF CONFIGURATIONS

I limited myself to such configurations which correlated the $2p$ electrons with one another and with the $2s$ electrons in simple fashion radially and angularly. This is reasonable for chemical effects which depend only on the outermost subshell. This leads to the following states:

$$\begin{aligned}
&\Psi_1 \text{ (Root term)} && 1s^2S^1 2s^2S^1 2p^6S^1S^1 \\
&\Psi_2 && 1s^2S^1 2s^2S^1 2p^4S^1 3p'^2S^1S^1 \\
&\Psi_3 && 1s^2S^1 2s^2S^1 2p^4P^3 3p^2P^3S^1 \\
&\Psi_4 && 1s^2S^1 2s^2S^1 2p^4D^1 3p^2D^1S^1 \\
&\Psi_5 && 1s^2S^1 2s^2S^1 2p^4S^1 3d^2S^1S^1 \\
&\Psi_6 && 1s^2S^1 2s^2S^1 2p^4P^3 3d^2P^3S^1 \\
&\Psi_7 && 1s^2S^1 2s^2S^1 2p^4D^1 3d^2D^1S^1 \\
&\Psi_8 && 1s^2S^1 2s^2S^1 2p^4S^1 3s^2S^1S^1 \\
&\Psi_9 && 1s^2S^1 2s^2S^1 2p^2P^2 3p''S^1S^1 \\
&\Psi_{10} && 1s^2S^1 2s3s'S^1 2p^5P^2 3p'S^1S^1 \\
&\Psi_{11} && 1s^2S^1 2s3s''S^1 2p^6S^1 \\
&\Psi_{12} && 1s^2S^1 2s3p'P^1 2p^5P^2 3dP^1S^1 \\
&\Psi_{13} && 1s^2S^1 2s^2S^1 2p^4D^2 3s^1 3dD^1S^1
\end{aligned} \quad (2)$$

[1] (a) S. F. Boys, Proc. Roy. Soc. (London) **A200,** 542 (1950); (b) **A201,** 125 (1950); (c) **A206,** 197 (1951); (d) **A207,** 181 (1951); (e) **A207,** 197 (1951); (f) Phil. Trans. Roy. Soc. (London) **A245,** 95 (1952); (g) M. J. M. Bernal and S. F. Boys, *ibid.* **A245,** 116 (1952); (h) **A245,** 139 (1952); (i) S. F. Boys, Proc. Roy. Soc. (London) **A217,** 136 (1953); (j) **A217,** 235 (1953); (k) S. F. Boys and V. E. Price, Phil. Trans. Roy. Soc. (London) **A246,** 451 (1959); (l) S. F. Boys and R. C. Sahni, *ibid.* **A246,** 463 (1959).

[2] Detor is defined by S. F. Boys[1c] to be an antisymmetrized product of orthonormal orbitals, i.e., a single determinant.

[3] V. Fock and M. J. Petrashin, Physik. Z. Sowjetunion **6,** 368 (1939).

[4] P. O. Löwdin, Phys. Rev. **90,** 120 (1953).

[5] B. H. Worsley, Can. J. Phys. **36,** 289 (1958).

[6] C. Froese, Proc. Cambridge Phil. Soc. **53,** 206 (1957).

TABLE I. Fitted and orthonormalized Hartree-Fock functions.

		$K=1$	2		
Ne					
$1s$	N_K	0	0		
	Z_K	8.953	13.47		
(Fitted)	A_K	0.85402	0.15381		
(Orthonormal)	A_K	0.8540681	0.153816		
		Max error 0.007 Av error 0.003			
$2s$	N_K	0	1	1	
	Z_K	7.70	2.537	4.796	
(Fitted)	A_K	0.33091	−0.79324	−0.33983	
(Orthonormal)	A_K	0.331624	−0.806055	−0.328945	
		Max error 0.011 Av error 0.006			
$2p$	N_K	1	1	1	
	Z_K	1.793	3.739	8.0	
(Fitted)	A_K	0.54320	0.50993	0.04481	
(Orthonormal)	A_K	0.542964	0.509712	0.044792	
		Max error 0.007 Av error 0.005			
F^-					
$1s$	N_K	0	0		
	Z_K	7.70	10.96		
(Fitted)	A_K	0.71699	0.29290		
(Orthonormal)	A_K	0.716707	0.292782		
		Max error 0.011 Av error 0.005			
$2s$	N_K	0	1	1	1
	Z_K	7.0	1.787	2.915	3.68
(Fitted)	A_K	0.30431	−0.42845	−0.39600	−0.30166
(Orthonormal)	A_K	0.305437	−0.428378	−0.395929	−0.301606
		Max error 0.006 Av error 0.002			
$2p$	N_K	1	1	1	1
	Z_K	1.0288	2.2476	2.915	5.75
(Fitted)	A_K	...	...	...	...
(Orthonormal)	A_K	0.342484	0.458627	0.222514	0.119467
(Improved)	A_K	0.365415	0.440053	0.222480	0.119448
		Max error 0.006 Av error 0.002			

It should be noted that the $3s'$ and $3s''$ as well as the $3p'$ and $3p''$ orbitals are not identical, but have an overlap of less than 1.0. However, they are orthonomal to the $2s$ and $2p$ orbitals, respectively. For these calculations the $3s''$ and $3p''$ orbitals were chosen such that they could be readily mixed with the $2s$ and $2p$ orbitals. However, this was not necessary except for F^-. Apparently the fitted H—F function was not as good as it could be and an improvement of 0.005 a.u. was obtained by the mixing. However, once the $3p''$ was mixed into the $2p$, $3p''=3p'$ was used for F^-. No such mixing was necessary for Ne and Na^+.

IV. CALCULATIONS

The Hamiltonian integrals are given as

$$H_{LK}=\sum_{l,k}\alpha_{lk}[\langle lTk\rangle+\langle lVk\rangle]+\sum_{k,l,m,n,p}\beta_{p,k,l,m,n}([kl\mid mn]^p) \quad (3)$$

Here L, K refer to configurations; k, l, m, and n refer

TABLE II.

		N_K	Z_K	A_K
F^-	$1s$	0	7.70	0.716707
		0	10.96	0.292781
	$2s$	0	7.0	0.305437
		1	1.987	−0.428378
		1	2.915	−0.395929
		1	3.68	−0.301606
	$3s'$	0	7.0	0.585676
		1	2.98	−2.951510
		2	2.98	2.794365
	$3s''$	0	7.0	−0.347368
		1	1.987	−2.053772
		1	2.915	2.069523
	$2p$	1	1.0288	0.365415
		1	2.3476	0.440053
		1	2.915	0.222480
		1	5.75	0.119448
	$3p'$	1	2.78	−2.073197
		2	2.62	2.076903
	$3p''$	1	2.78	−2.073197
		2	2.62	2.076903
	$3d$	2	1.64	1.0
Ne	$1s$	0	8.953	0.854068
		0	13.47	0.153816
	$2s$	0	7.70	0.331624
		1	4.796	−0.328945
		1	2.537	−0.806055
	$3s'$	0	7.0	0.573930
		1	3.3	−0.293379
		2	3.3	0.281102
	$3s''$	0	7.70	−0.724892
		1	2.537	−1.543638
		1	4.796	−2.075329
	$2p$	1	1.793	0.542964
		1	3.739	0.509712
		1	8.0	0.044792
	$3p'$	1	3.08	−2.192280
		2	3.00	2.275587
	$3p''$	1	1.793	−1.340210
		1	3.739	1.326238
	$3d$	2	3.70	1.0
Na^+	$1s$	0	8.10943	0.277723
		0	11.577	0.731616
	$2s$	0	9.1285	−0.306074
		1	2.365	0.364383
		1	3.931	0.732925
	$3s'$	0	9.0	0.502840
		1	3.5	−2.764293
		2	3.5	2.752281
	$3s''$	0	9.1285	−0.387648
		1	2.365	−2.010524
		1	3.9031	2.058446
	$2p$	1	2.3718	0.538375
		1	3.8934	0.383378
		1	6.5076	0.150480
	$3p'$	2	3.36	−2.307752
		1	3.44	−2.155801
	$3p''$	1	3.3718	−1.904918
		1	3.8934	1.857330
	$3d$	2	4.2	1.0

TABLE III. Coefficients of the wave functions and energies.

	F^-	Ne	Na^+
Ψ_1 (1)	0.9861617	0.9881283	0.9871280
Ψ_2 $(2p^2/3p'^2S')$	0.04519	0.04104	0.03913
Ψ_3 $(2p^2/3p'^2P^2)$	0.06690	0.06039	0.05314
Ψ_4 $(2p^2/3p'^2D^2)$	−0.08017	−0.07146	−0.06029
Ψ_5 $(2p^2/3d^2S')$	−0.04482	−0.04408	−0.04057
Ψ_6 $(2p^2/3d^2P^2)$	−0.06087	−0.05669	−0.05512
Ψ_7 $(2p^2/3d^2D^1)$	0.04792	0.04807	0.04323
Ψ_8 $(2p^2/3s'^2)$	−0.01766	−0.01758	−0.01836
Ψ_9 $(2p/3p'')$	0.01108	−0.00154	−0.00809
Ψ_{10} $(2s2p/3s'3p')$	0.05315	0.05095	0.04941
Ψ_{11} $(2s/3s'')$	−0.02116	−0.01587	0.06180
Ψ_{12} $(2s2p/3p'3d)$	0.04296	0.02722	0.01637
Ψ_{13} $(2p^2/3s'3d)$	0.03123	0.04239	0.06435
a. Hartree-Fock Energy	−99.4508	−128.5406	−161.6671
b. Calculated (this paper)	−99.6341	−128.7414	−161.8923
c. Bernal & Boys[1]	−99.5279	−128.6920	−161.8784
d. Correlation Energy (this paper)	0.1833	0.2008	0.2252
e. Correlation Energy (Bernal & Boys[1])	0.0771	0.1514	0.2113
f. Correlation Energy (Estimated[7])	0.393		

to one-electron orbitals

$$\langle lTk\rangle = -\tfrac{1}{2}\int l^*(1)\Delta_1 k(1)\,dT_1$$

$$\langle lVk\rangle = -Z\int l^*(1)[1/r_1]k(1)\,dT_1$$

$$[kl\,|\,mn]^p = \int_0^\infty k^*(1)l(1)r_1^{1-p}dr_1\int_0^{r_1} m^*(2)n(2)r_2^{2+p}dr_2 + \int_0^\infty m^*(1)n(1)r_1^{1-p}dr_1\int_0^{r_1} k^*(2)l(2)r_2^{2+p}dr_2. \quad (4)$$

The α and β coefficients can be evaluated by means of the Boys' scheme.[1e–g] Many of those necessary for this calculation are given in reference 1g.

The evaluation of the integrals in Eq. (4) is relatively straightforward and can be done analytically. The IBM 650 computer was programmed to evaluate these.

Once the Hamiltonian matrix H_{LK} was calculated, the next step was to solve the equations

$$\sum_{K,L} H_{LK}C_K C_L = E, \quad (5)$$

for the lowest state.[7]

Table II gives the values for all the orbitals used in the calculations. The energies were minimized with respect to the exponents (Z_K) of the $3p'$ and $3d$ orbitals, and it was also determined that the energy was not

[7] Mr. Ken King of the Watson Laboratory was good enough to make available a routine which diagonalized matrices up to 20×20 and solved for eigenvalues and eigenvectors.

sensitive to the $3s'$ exponents. The $3p$ and $3d$ exponents are roughly accurate to about 0.05.

V. RESULTS AND DISCUSSION

In Table III the coefficients of the wave functions, the H—F energies, the energies of the 12-term function, and correlation energies are shown. The energies can be compared to Bernal and Boys' results[1g,h] and a value for the correlation of F^- calculation from the H—F relativistic, and experimental energies by Froman.[8] It can be seen that the correlation energy of our wave functions varies only slowly with nuclear charge. It is possible that this variation will be less with higher order terms so that little significance can be attached to the variation observed. However, the approximate constancy is gratifying. The energies calculated in this paper represent a great improvement on Bernal and Boys[1h] for F^- and Ne and are approximately equal for Na^+. It seems that the Bernal and Boys' function is quite good for Na^+, but leaves much to be desired for F^- and Ne. This is quite reasonable, since Bernal and Boys were indeed primarily interested in improving on the Fock and Petrashin[3] value for Na^+, which is -161.8, and most likely inaccurate.

This is also the first time that a Hartree-Fock function was used as basis function. The advantages of such a method can be seen clearly, at least for $'S$ states.

It should be mentioned here that the most difficult part of the calculation is the calculation of the interaction coefficients from the Boys' scheme. Work is in progress to mechanize that part of the calculations.

[8] A. Froman, Phys. Rev. **112**, 870 (1959).

ACKNOWLEDGMENTS

My sincere thanks go to IBM at whose Watson Laboratory I performed this research, to Professor H. L. Thomas for his guidance and help, to Mr. King for advice and help in programming the calculations, and to Dr. R. C. Sahni for several discussions.

THE JOURNAL OF CHEMICAL PHYSICS VOLUME 35, NUMBER 3 SEPTEMBER, 1961

Law of Corresponding States for Fused Salts*

H. REISS AND S. W. MAYER

Research Department, Atomics International, A Division of North American Aviation, Inc., Canoga Park, California

AND

J. L. KATZ†

Institute for the Study of Metals, University of Chicago, Chicago 37, Illinois

(Received February 20, 1961)

Reduced equations of state are developed for strictly ionic salts through an analysis of the configuration integral. In this way, appropriate laws of corresponding states are developed for vapor pressures, surface tensions, and melting points. Agreement between theory and experiment is satisfactory for a large class of salts.

I. INTRODUCTION

THE quantitative theoretical basis for the law of corresponding states as applied to simple substances has been demonstrated by Pitzer[1] through dimensional analysis of the configuration integral. This analysis is necessarily limited to those systems whose potential energies are for a form suitable for such dimensional considerations. For example, the pair potential between molecules ought to possess no more than a single distance parameter.

The question arises as to whether or not a law of corresponding states can be developed for more complicated substances by sacrificing some degree of exactness in treating the configuration integral. For example, one might modify the pair potential in some reasonable manner and be in a position to proceed with a dimensional analysis not possible with the original pair potential. We have attempted an extension of Pitzer's ideas by sacrificing exactness in this way, and have been able to arrive at a reasonably successful treatment of fused salts. The present article is an exposition of this work.

II. THEORY

For purposes of illustration, attention will be confined at first to symmetric salts, the ions of which are monatomic. We shall always require the ions to be monatomic, but the restriction to symmetric salts will be lifted later.

* This work was performed under the auspices of the Research Division of the U. S. Atomic Energy Commission.

† American Chemical Society Petroleum Research Fund Predoctoral Fellow.

[1] K. S. Pitzer, J. Chem. Phys. **7**, 583 (1939).

The configuration integral is

$$Z=\int\cdots\int_V \exp(-W/kT)\,(dv_a)^N(dv_c)^N, \quad (2.1)$$

where W is the potential energy of all the ions in the salt, N anions and N cations, k is the Boltzmann constant, and T the temperature. The integrations are carried over the volume V of the salt and $(dv_a)^N$ is the symbol for the volume elements of the anions while $(dv_c)^N$ similarly applies to the cations.

As usual, W will be considered pairwise additive, so that

$$W=\sum_{1\le i<j\le 2N}\sum u_{ij}(r_{ij}), \quad (2.2)$$

where u_{ij} is the pair potential between the ith and jth ions, dependent only upon r_{ij}, the distance between the ith and jth ions.

We now introduce certain reasonable approximations into the representations of the various u_{ij} which will make possible a corresponding states treatment. The ultimate validity of these approximations will depend upon how well they are supported by experiment, but certain of their general features are to be anticipated on the basis of very simple considerations. These considerations are based upon our knowledge of those configurations of the salt which on the average ought to be more probable than others. For example, configurations in which similarly charged ions approach each other closely are bound not to carry as much weight in the integral of Eq. (2.1) as those in which oppositely charged ions are close.

TABLE I. Melting point and interatomic distance for symmetric compounds.

Salt	Melting[3] point T_m (°K)	Interatomic[4] distance in solid cm×10⁸	$\lambda T_m/z^2=\tau_m$ cm deg×10⁵
MgO	3073	2.10	1.61
CaO	2873	2.40	1.73
SrO	2733	2.54	1.74
BaO	2198	2.75	1.51
NaF	1265	2.31	2.92
NaCl	1074	2.81	3.02
NaBr	1023	2.98	3.04
NaI	933	3.23	3.01
KF	1129	2.67	3.02
KCl	1045	3.14	3.28
KBr	1013	3.29	3.34
KI	958	3.53	3.39
RbF	1048	2.82	2.96
RbCl	988	3.29	3.26
RbBr	953	3.43	3.27
RbI	913	3.66	3.34
CsF	955	3.01	2.88
CsCl	918	3.47	3.18
CsBr	909	3.62	3.29
CsI	894	3.83	3.42
LiF	1121	2.01	2.25
LiCl	887	2.57	2.27
LiBr	823	2.75	2.27
LiI	718	3.02	2.21

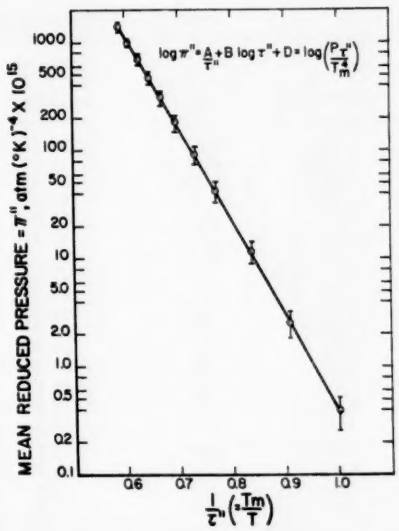

FIG. 1. Mean reduced vapor pressure curve for the halides of sodium, potassium, rubidium, and cesium. Average deviation from the mean is shown by the vertical lines. The curve is fitted, with an average deviation of less than 2%, by the equation $\log_{10}\pi''=-(9.20/\tau'')-0.894\,\log_{10}\tau''-6.21$ atm $(\text{deg})^{-4}$.

At large separations u_{ij} for oppositely charged ions ought to be represented fairly well by a Coulomb potential,

$$u_{ij}=-(z\epsilon)^2/\kappa r_{ij}; \quad (2.3)$$

where ϵ is the electronic charge, z the valence of the salt, and κ a dielectric constant. κ is not to be taken as the macroscopic dielectric constant, but merely some factor capable of accounting for microscopic effects due to the polarizabilities of the ions. We include it in Eq. (2.3), but we hope in most cases that it will be close to unity, or at least reasonably constant from salt to salt. Later we will be concerned with two kinds of reduced equations of state, which for lack of a better terminology shall be called a "molecular theory" reduced equation of state and a "thermodynamic" equation of state, respectively. The latter will be much less informative than the former, but even if κ varies from salt to salt, it will still remain a valid reduced equation of state. The same will not be true for the "molecular theory" equation.

When the oppositely charged ions are brought close to one another we assume them to behave as though they had rigid cores, the sum of whose radii is λ. Thus we write

$$u_{ij}=\infty, \qquad r_{ij}\leqslant\lambda. \quad (2.4)$$

The value of this approximation will also depend upon how accurately it is able to account for the macroscopic behavior of the salt. The pair potential for interaction between unlike ions can therefore be summarized as

TABLE II. Corresponding state vapor pressures for molten alkali halides.

Salt	T_m (°K)	Pressure[6] at 1.30 T_m (mm Hg)	$\pi_{1.30}''$ [mm (deg)$^{-4}\times10^{12}$]	Pressure[6] at 1.55 T_m (mm Hg)	$\pi_{1.55}''$ [mm (deg)$^{-4}\times10^{12}$]
NaF	1265	84.4	33.0	908	354
NaCl	1074	36.9	27.8	430	323
NaBr	1023	34.9	31.9	387	353
NaI	933	17.8	23.5	257	339
KF	1129	71.9	44.2	650	400
KCl	1045	42.4	35.5	467	392
KBr	1013	38.1	36.2	397	377
KI	958	27.8	33.1	300	357
RbF	1048	45.1	37.4	512	425
RbCl	988	26.6	27.9	308	323
RbBr	953	18.9	22.9	239	289
RbI	913	14.3	20.6	193	277
CsF	955	49.6	59.6	508	611
CsCl	918	21.1	29.7	242	340
CsBr	909	16.4	24.0	210	307
CsI	894	17.1	26.8	203	317
LiF	1121	7.1	4.5	143	91
LiCl	887	4.6	7.4	72	116
LiBr	823	2.4	5.3	44	97
LiI	718	0.2	0.8	10	37

follows:

$$u_{ij}=\infty, \qquad r_{ij}\leqslant\lambda$$
$$=-(z\epsilon)^2/\kappa r_{ij}, \qquad r_{ij}>\lambda. \tag{2.5}$$

For the pair potential between similarly charged ions, the Coulomb potential (with change of sign) is once more suitable when r_{ij} is large. When the ions are close to one another, however, the situation with respect to approximation is not as simple as in the case of oppositely charged ions. In the first place, the results will be less sensitive to the details of the approximation than for the oppositely charged case because the configuration itself is one of lower probability. In fact, the configuration in which the rigid cores of the similarly charged ions are in contact can probably be discounted completely. Since the Coulomb potential goes to infinity as $r_{ij}\to0$ we might just as well omit the infinity due to the hard core. Thus for the u_{ij} between ions of like sign we may write, in approximation,

$$u_{ij}=(z\epsilon)^2/\kappa r_{ij}, \qquad r_{ij}\geqslant0. \tag{2.6}$$

With the potentials assumed in Eqs. (2.5) and (2.6) there is only one distance parameter λ, and Pitzer's technique can be employed. Introducing the transformation

$$r_{ij}=\xi_{ij}\lambda \tag{2.7}$$

renders it possible to write Eqs. (2.5) and (2.6) in the respective forms

$$u_{ij}(\xi_{ij})=\infty, \qquad \xi_{ij}\leqslant1$$
$$=-(z\epsilon)^2/\lambda\kappa\xi_{ij}, \qquad \xi_{ij}>1, \tag{2.8}$$

and

$$u_{ij}(\xi_{ij})=(z\epsilon)^2/\lambda\kappa\xi_{ij}, \qquad \xi_{ij}\geqslant0. \tag{2.9}$$

From this it is apparent that Eq. (2.1) can be given the form

$$Z=\lambda^{6N}I[(\lambda\kappa T/z^2),(V/\lambda^3),(A/\lambda^2),N], \tag{2.10}$$

where I is the integral of Eq. (2.1) in which all distances are measured in units of λ in conformance with Eq. (2.7). The symbol A stands for the interfacial area between any two phases which happen to be in coexistence. Both V/λ^3 and A/λ^2 appear as arguments n I because they define the limits of integration in terms of the reduced distance. Ordinarily, the influence of A (for bulk systems) will be negligibly small, but we retain it in Eq. (2.10) in order to be able to consider corresponding states for surface tension.

TABLE III. Constancy of vapor pressure ratios at constant reduced temperature ratios.

Salt	$\log\frac{p_m}{p_{1.30}}$	$\log\frac{p_{1.20}}{p_{1.30}}$	$\log\frac{p_{1.37}}{p_{1.30}}$	$\log\frac{p_{1.55}}{p_{1.30}}$	$\log\frac{p_{1.65}}{p_{1.30}}$
NaF	−2.018	−0.550	0.332	1.032	1.346
NaCl	−2.080	−0.567	0.343	1.067	1.392
NaBr	−2.027	−0.553	0.335	1.044	1.364
NaI	−2.255	−0.615	0.372	1.159	1.514
KF	−1.878	−0.511	0.308	0.956	1.247
KCl	−2.023	−0.553	0.335	1.043	1.362
KBr	−1.977	−0.540	0.327	1.017	1.329
KI	−2.020	−0.550	0.332	1.032	1.347
RbF	−2.063	−0.562	0.339	1.055	1.378
RbCl	−2.064	−0.564	0.341	1.063	1.390
RbBr	−2.133	−0.584	0.353	1.100	1.439
RbI	−2.197	−0.600	0.362	1.127	1.463
CsF	−1.979	−0.538	0.326	1.011	1.319
CsCl	−2.066	−0.563	0.340	1.057	1.380
CsBr	−2.158	−0.589	0.355	1.106	1.435
CsI	−2.097	−0.572	0.345	1.074	1.402
LiF	−2.539	−0.692	0.419	1.304	1.704
LiCl	−2.341	−0.638	0.385	1.197	1.563
LiBr	−2.450	−0.669	0.406	1.264	1.652
LiI	−3.170	−0.809	0.528	1.651	2.160

TABLE IV. Corresponding state vapor pressures for divalent halides.

Halide	T_m (°K)	p at[6] $T/T_m=1.30$ (mm Hg)	$\pi_{1.30}''$ [mm (deg)$^{-4}\times10^{12}$]	p at[6] $T/T_m=1.55$ (mm Hg$\times10^{-2}$)	$\pi_{1.55}''$ [mm (deg)$^{-4}\times10^{10}$]
MgF_2	1536[2]	21.6	3.9	3.47	0.63
CaF_2[a]	1691	19.8	2.4	3.54	0.43
SrF_2[a]	1673	19.7	2.5	3.28	0.42
BaF_2[a]	1563	24.9	4.2	4.22	0.71
BeF_2	1070	121	92	13	10
$BeCl_2$	683	2080	9540	176	807
$BeBr_2$	761	8360	24970	407	1210
BeI_2	753	9810	30550	366	1140
$MgCl_2$	987	28	30	2.7	2.8
$MgBr_2$	983	78	83	7.7	8.3
MgI_2	923	891	1230	45	62
ZnF_2	1145	59	34	7.3	4.3
$ZnCl_2$	591	7.4	61	1.8	15
$ZnBr_2$	667	124	626	18	93
CdF_2	1383	136	37	16	4.4
$CdCl_2$	841	156	311	15	29
$CdBr_2$	840	509	1020	37	75
CdI_2	663	45	229	5.3	27
$HgBr_2$	511	2540	37300	121	1770
HgI_2	523	1830	24400	86	1150
PbF_2	1097	219	150	20	13
$PbCl_2$	771	46	131	5.9	17
$PbBr_2$	761	60	179	6.6	20
PbI_2	685	25	115	3.3	15

[a] Vapor pressure data have not been found for the chlorides, bromides, or iodides of calcium, strontium, and barium.

Now the pressure p of the system is determined by the well-known statistical mechanical relation.[2]

$$p=kT(\partial \ln Z/\partial V)_{T,N}, \tag{2.11}$$

ignoring the dependence upon A. Substitution of Eq. (2.10) in (2.11) gives

$$p=\frac{kT}{\lambda^3}\left\{\frac{\partial}{\partial(V/\lambda^3)}\left[\ln Z\left(\frac{\lambda\kappa T}{z^2},\frac{V}{\lambda^3},N\right)\right]\right\}_{(\lambda\kappa T/z^2),N}$$
$$=(z^2/\kappa\lambda^4)\,p[(\lambda\kappa T/z^2),(V/\lambda^3),N]. \tag{2.12}$$

By defining

$$\pi=\kappa\lambda^4 p/z^2,$$
$$\tau=\lambda\kappa T/z^2,$$
$$\vartheta=V/\lambda^3, \tag{2.13}$$

as reduced pressure, temperature, and volume, Eq. (2.12) is transformed into the reduced equation of state (taking N to correspond to a mole)

$$\pi=\pi(\tau,\vartheta). \tag{2.14}$$

This relation is universal for all symmetrical salts which possess pair potentials of the forms Eqs. (2.5) and (2.6).

Equation (2.14) is a "molecular theory" reduced equation of state, since the reduced variables Eq. (2.13) depend in a special way upon the molecular parameters λ and z^2/κ.

[2] T. L. Hill, *Statistical Mechanics* (McGraw-Hill Book Company, Inc., New York, 1956), p. 70.

A "thermodynamic" reduced equation of state can be derived by noting that the reduced variables π_m, τ_m, and ϑ_m corresponding to p_m, T_m, and V_m, the pressure, temperature, and volume at the melting point, are universal constants. (In fact, any triple point can be employed in place of the melting point.) Then

$$p/p_m=\pi/\pi_m=\pi',$$
$$T/T_m=\tau/\tau_m=\tau',$$
$$V/V_m=\vartheta/\vartheta_m=\vartheta' \tag{2.15}$$

represent a set of new "thermodynamic" reduced variables such that

$$\pi'=\pi'(\tau',\vartheta') \tag{2.16}$$

is a universal relation.

However, Eq. (2.16) is satisfied by a more general set of pair potentials than Eqs. (2.5) and (2.6). Consequently, it is less informative than Eq. (2.14) when compared with experiment.

If the molecular parameter λ is not known reliably, Eq. (2.14) can still be utilized through application of the following device. According to Eq. (2.13)

$$\lambda=z^2\tau_m/\kappa T_m. \tag{2.17}$$

Since τ_m is a universal constant,

$$\pi''=\pi/\tau_m{}^4=(z^6/\kappa^3)\,(p/T_m{}^4),$$
$$\tau''=\tau/\tau_m=T/T_m,$$
$$\vartheta''=\vartheta\tau_m{}^3=(\kappa T_m/z^2)^3 V, \tag{2.18}$$

TABLE V. Surface tension and interatomic distance for alkali halides.

Halide	σ_m (dyne cm^{-1})	Interatomic distance[4] in solid, (cm$\times 10^8$)	Σ_m (dyne cm$^2\times 10^{23}$)
NaF	202[8]	2.31	249
NaCl	116[7]	2.81	257
NaBr	99[7]	2.98	262
NaI	88[7]	3.23	297
KF	142[8]	2.67	270
KCl	99[7]	3.14	306
KBr	89[7]	3.29	312
KI	79[7]	3.53	348
RbF	131[8]	2.82	294
RbCl	99[8]	3.29	352
RbBr	91[8]	3.43	367
RbI	83[8]	3.66	407
CsF	107[8]	3.01	292
CsCl	90[8]	3.47	376
CsBr	85[8]	3.62	403
CsI	75[8]	3.83	421
LiF	251[8]	2.01	204
LiCl	138[8]	2.57	234

are reduced variables satisfying the universal equation

$$\pi''=\pi''(\tau'',\vartheta''). \tag{2.19}$$

This is still a "molecular theory" equation requiring the entry of T_m into the reduced variables in a special way.

The restriction to symmetrical salts can be lifted, but we shall treat the classes of uni-divalent salts, uni-trivalent salts, etc., separately. This procedure is to be distinguished from the above, in which uni-univalent, di-divalent, etc., are treated simultaneously through the use of the symbol z. If λ once again refers to the cation-anion distance, the preceding argument goes through unchanged except for the absence of z in relation to the temperature (the valence is invariant in any one class). Then the proper reduced variables are Eq. (2.13), (2.15) or (2.18) with z set equal to unity.

A corresponding states treatment can also be advanced for the surface tension σ of the molten salt. The statistical relation[2] for the surface tension is

$$\sigma=-kT(\partial \ln Z/\partial A)_{T,V,N}. \tag{2.20}$$

Applying the same procedure employed in connection with the pressure as it was derived from Eqs. (2.10), (2.11), and (2.12), we arrive at the reduced equation

$$\Sigma=\kappa\lambda^3\sigma/z^2=\Sigma(\tau,\vartheta), \tag{2.21}$$

where Σ is the reduced surface tension, and τ and ϑ have their original meanings. In the case of unsymmetrical salts z is set equal to unity. Furthermore, just as in the case of pressure, reduced variables Σ' and Σ'' can be introduced:

$$\Sigma'=\Sigma/\Sigma_m \tag{2.22}$$

$$\Sigma''=(z/\kappa)^2(\sigma/T_m^3). \tag{2.23}$$

III. COMPARISON WITH EXPERIMENT

The comparison of the foregoing results with experiment is conveniently begun with reference to the symmetric salts. The easiest relation to check is Eq. (2.17) in which τ_m should be a universal constant. In accordance with the program outlined above, we shall assume that κ equals unity (or is at least constant). Part of the effects due to polarization will have been included in the measured value of λ, so that the required value of κ ought not to be so variable. Any failure of this assumption will of course show up as a variation in the computed value of τ_m.

The values of the melting temperature T_m are easy to come by,[3] but experimental data for λ are difficult to obtain. In fact, it is really not possible to acquire values of λ when this parameter is truly the distance of closest approach between two ions. Instead we shall use for λ the sum of the ionic radii as measured in the crystal,[4] in the hope that these will be proportional to the distances of closest approach. Table I is a compilation of $\tau_m=\lambda T_m/z^2$ for a series of symmetrical salts including both uni-valent and di-divalent examples. The first column in the table lists the salt, the second and third, the measured values of T_m and λ, while the fourth column lists the computed value of τ_m.

It is to be noted that the values of τ_m are really very constant for the uni-univalent salts, being on the average in the neighborhood of 3×10^{-5} deg cm. This must be considered striking agreement with theory, expecially in view of the uncertainties surrounding the values of λ. The principal failures are the salts of lithium, which show values of τ_m in the neighborhood of 2.2×10^{-5} deg cm. This class, however, exhibits a high degree of internal consistency. The di-divalent salts do not conform, but like the case of lithium show internal consistency. The internal consistency of the di-divalent salts may indicate that the disparity with the uni-univalent salts is due to an increased κ associated with the greater polarizability of the doubly charged oxygen ion. If κ had been included in Table I it would have multiplied λ, thus tending to raise the value of τ_m.

On the basis of the foregoing, we may write as a formula for the melting point of most uni-univalent salts:

$$T_m=[(3\times10^{-5}/\lambda]\text{deg K}. \tag{3.1}$$

Next, we shall investigate the "molecular theory" reduced equation of state (2.14). The only part of the equation of state for which accurate data are available is the two-phase region in which liquid and vapor coexist. In this case, the system possesses but one degree of freedom and Eq. (2.19) can be simplified to

$$\pi''=\pi''(\tau''). \tag{3.2}$$

[3] O. Kubaschewski and E. L. Evans, *Metallurgical Thermochemistry* (Pergamon Press, New York, 1958).

[4] L. Pauling, *The Nature of the Chemical Bond* (Cornell University Press, Ithaca, New York, 1960), 3rd ed., p. 526.

TABLE VI. Corresponding state surface tensions for alkali halides.

Salt	T_m (°K)	σ at T_m (dyne cm^{-1})	Σ_m'' [a] ($\times 10^9$)	σ at 1.10 T_m (dyne cm^{-1})	$\Sigma_{1.10}''$ [a] ($\times 10^9$)
NaF	1265	202	100	189	93
NaCl	1074	116	94	106	86
NaBr	1023	99	93	93	87
NaI	933	88	108	80	98
KF	1129	142	99	135	93
KCl	1045	99	87	91	80
KBr	1013	89	86	82	78
KI	958	79	90	71	81
RbF	1048	131	114	118	102
RbCl	988	99	103	91	94
RbBr	953	91	105	84	97
RbI	913	83	109	75	99
CsF	955	107	123	100	114
CsCl	918	90	116	85	109
CsBr	909	85	113	77	102
CsI	894	75	105	69	96
LiF	1121	251	178	241	171
LiCl[b]	887	138	198	131	188

[a] The average deviations from the mean are less than 9%, and would be less than 7.5% if Dworkin and Bredig's [Dworkin and M. A. Bredig, J. Phys. Chem. **64**, 259 (1960)] melting points were used.

[b] No surface tension data for LiBr and LiI are available.

Data for the vapor pressure p in this region are readily available[5] for a variety of uni-univalent salts.

It should be noted that a larger variation is to be expected for supposedly corresponding pressures than for corresponding temperatures. This is because our approximations, Eqs. (2.5) and (2.6), are on the energy, and pressure is related exponentially to the energy. The fairest test of the theory should really compare *logarithms* of corresponding pressures. Even so, we shall see that the corresponding pressures themselves are remarkably constant.

Table II lists values of $\pi'' = p/T_m^4$ at different values of $\tau'' = T/T_m$ for a variety of uni-univalent salts. The first column lists the salt; the second, the melting temperature; the third and fifth, the vapor pressure at τ'' equal to 1.30 and 1.55 respectively[5]; and the fourth and sixth, the computed values of π'' at the two respective values of τ''. At both values of τ'' the constancy of π'' is very good, except for the salts of lithium, which are once again out of line.

Excepting the salts of lithium, the mean deviation for π'' at $(\tau'' = 1.30)$ is 21% and at $(\tau'' = 1.55)$ is 14%. This is excellent, considering the exponential dependence of pressure upon energy. In terms of heats of vaporization, these deviations are of the order of 1–2%. The slightly better agreement at the higher value of τ'' is partly related to the fact that the experimental data are more reliable in this range.

The mean π'''s for all salts except those of lithium have been evaluated at a number of values of τ''. In this way the curve representing the mean reduced equation of state shown in Fig. 1 has been constructed. From it one may read the vapor pressure (at any temperature) of a uni-univalent salt if the melting temperature is known. It remains to test the "thermodynamic" reduced equation of state, Eq. (2.16). Since values of p are relatively inaccurate because the percent error in vapor pressure equations[6] is large at the melting point, the test can be performed by testing the constancy of the ratio p_2/p_1, where p_2 is the actual pressure at a reduced temperature τ_2', and p_1 the pressure at τ_1'. This ratio should be constant because the relationship

$$\pi_2'/\pi_1' = p_2/p_1 \tag{3.3}$$

is constant if Eq. (2.16) holds.

Table III lists $[\log(p_2/p_1)]$ for $\tau_1' = 1.30$ and $\tau_2' =$ 1.00, 1.20, 1.37, 1.55, and 1.65 for alkali halides. Once again agreement is as good as can be expected for a crude model, except for the case of lithium.

Next we pass to consideration of some unsymmetrical salts. The data here are more sparse. Furthermore, most of the salts for which data exist are rather covalent, and deviations from the law of corresponding states must be expected. The easiest thing to test is Eq. (3.2). Now, however, π'' is to be evaluated without z (or with z set to unity). Table IV is a compilation of values of $\pi'' = p/T_m^4$ for values of $\tau'' = 1.30$, 1.55. Column 1 lists the compound, column 2 the melting temperatures,[3] columns 3 and 5, the pressures[6] at $\tau'' = 1.30$ and 1.55, respectively, and columns 4 and 6 show values of π'' at the two reduced temperatures.

The first four substances are normally regarded as ionic. Unfortunately, these are the only ionic substances

[5] Notice that even the reduction of temperature to τ'' without reducing p to π'' effects an increased constancy in p (see columns 3 and 5, Table II). Further improvement in constancy is obtained by reduction to π''.

[6] Reference 3, Table D, p. 326–335.

for which data could be found. The remaining substances are covalent in varying degrees. It is seen that for the ionic substances π'' is relatively constant in accordance with the expectations of theory, while for the remaining substances an enormous amount of variation takes place.

We have yet to consider surface tension. According to Eq. (2.21),

$$\lambda^3\sigma_m/z^2=\Sigma_m, \tag{3.4}$$

where σ_m, the surface tension at the melting point, should be a universal constant for symmetrical salts. Since λ appears raised to the third power in Eq. (3.4), any errors in λ will be magnified. Thus it is probably more desirable to test surface tension through use of Eq. (2.23) rather than Eq. (3.4). We shall, however, do both.

Table V lists values of Σ_m for a number of uni-univalent salts. λ is chosen from the same source used in connection with Table I. The data for σ are from a variety of sources.[7,8] We note that Σ_m is reasonably constant but that some fairly pronounced variation occurs. This is probably partly due to errors in connection with λ^3. Lithium is once again out of line with the other salts. From this table it is possible to write an estimate for the surface tension at melting point of any conforming uni-univalent salt. This is

$$\sigma_m=[(3.3\times10^{-21})/\lambda^3]\ \text{dyne cm}^{-1}. \tag{3.5}$$

The validity of Eq. (2.23) as a reduced surface tension Σ'' remains to be tested. In Table VI this is done for values of $\tau''=T/T_m$ of 1.0 and 1.1, respectively. The values of Σ'' are listed in columns 4 and 6. Lithium is again out of line, but the values of Σ'' for the other salts are very constant, more so than in Table V. This confirms the idea that the variability in Table V is largely due to errors in λ^3. From Table VI another estimate of σ_m for symmetrical salts can be made. This is

$$\sigma_m=[(1.03\times10^{-7}T_m^3)/z^2]\ \text{dynes/cm}. \tag{3.6}$$

IV. CONCLUSIONS

From the foregoing it may be concluded that the derived laws of corresponding states are applicable to a large class of salts. As such they may serve as guide posts for the classification of data. Those salts which do not conform are either known or suspected to depart from the simple Coulomb picture described by Eqs. (2.5) and (2.6).

[7] J. O. Bockris, *Modern Aspects of Electrochemistry* (Academic Press, Inc., New York, 1959), Vol. 2, p. 198.
[8] F. M. Jaeger, Z. anorg. Chem. **101**, 1 (1917).

Least-Squares Local-Energy Method for Molecular Energy Calculations Using Gauss Quadrature Points

A. A. FROST, R. E. KELLOGG, B. M. GIMARC, AND J. D. SCARGLE

Department of Chemistry, Northwestern University, Evanston, Illinois

(Received January 17, 1961)

The least-squares local-energy method previously described and tested in calculations on H_2^+ has been further tested on H_2^+, He, and H_2. The theory of Gauss quadrature is used to provide a better basis of points over which to average the local-energy. The electronic energy is easily calculated to six significant figures for H_2^+ and to three or four significant figures for He and H_2.

INTRODUCTION

THE familiar variation method for the approximate solution of the Schrödinger equation runs into difficulty when applied to many-electron molecules if interelectronic distances are used explicitly in the wave function. Already for three-electron systems the integrals become next to impossible.

An alternative method has been proposed and an initial test on the hydrogen molecule-ion has been reported.[1,2] This method is based on the idea that the best wave function in a given set will be that one which minimizes the variance of the local-energy for a suitable set of points in space. Because the local-energy at a point, defined as $\epsilon = H\varphi/\varphi$ where H is the Hamiltonian operator and φ is an approximate wave function, involves only differentiation of the wave function, there is no restriction on the complexity of the function.

The present paper reports the results of test calculations using an improved choice of points, namely, the same choice as in the corresponding Gauss quadrature. Test calculations have been made on the hydrogen molecule-ion, the helium atom and the hydrogen molecule.

GENERAL FORMULATION

As in reference 2 the calculation is set up in terms of minimizing the variance V of the local energy ϵ_P at a number of points P with respect to a variation of several linear parameters c_i.

$$V = \langle \epsilon^2 \rangle - \langle \epsilon \rangle^2, \tag{1}$$

where

$$\langle \epsilon \rangle = \sum_P g_P \epsilon_P / \sum_P g_P, \tag{2}$$

and

$$\langle \epsilon^2 \rangle = \sum_P g_P \epsilon_P^2 / \sum_P g_P, \tag{3}$$

with g_P being a set of weighting factors.

For a linear variation function where

$$\varphi = \sum_i c_i \varphi_i, \tag{4}$$

it is convenient to take the weighting factor proportional to the square of the wave function (only real functions being considered here) as in the Ritz variation method.

$$g_P = w_P \varphi(P)^2,$$

where w_P is related to the volume element associated with the given point and will include the Gauss weights.

The minimization of V has been shown[2] to require the solution of a set of simultaneous Eqs. (6)

$$\sum_i c_i [G_{ik} - 2\langle \epsilon \rangle H_{ik} + (\langle \epsilon \rangle^2 - V) S_{ik}] = 0, \tag{6}$$

where the matrix components are defined as follows in equations (7)

$$\begin{aligned} S_{ij} &= \sum_P w_P \varphi_i(P) \varphi_j(P) \\ H_{ij} &= \tfrac{1}{2} \sum_P w_P [\varphi_i(p) H \varphi_j(p) + \varphi_j(p) H \varphi_i(p)] \\ G_{ij} &= \sum_P w_P H\varphi_i(p) H\varphi_j(p). \end{aligned} \tag{7}$$

CHOICE OF POINTS

In the test of the least square local-energy method previously reported[2] the points were chosen at constant intervals in each of the coordinates. In order to improve the efficiency of the method it would appear that a more careful choice of points could be made. If the matrix components, defined as summations in Eqs. (7), were changed to the corresponding integrals the mean energy and mean square energy of Eqs. (2) and (3) would be precisely the quantum mechanical expectation values. It would therefore probably be most desirable to choose points and weights in such a way that the sums of Eqs. (7) become as accurately as possible the corresponding integrals. One way to do this is to choose the points and weights according to the method of Gauss quadratures.[3]

Two forms of Gauss quadrature have been found useful in this work: The Gauss-Legendre,

$$\int_{-1}^{+1} f(x)dx = \sum_{i=1}^{n} H_i f(x_i), \tag{8}$$

[1] A. A. Frost, J. Chem. Phys. **10**, 240 (1942).

[2] A. A. Frost, R. E. Kellogg and E. C. Curtis, Revs. Modern Phys. **32**, 313 (1960).

[3] Z. Kopal, *Numerical Analysis* (Chapman and Hall, Ltd., London, 1955); see Chap. VII and tables in the Appendix.

TABLE I. Calculated results for the hydrogen molecule ion.

	This paper, Gauss points		Previous calculation[2] 40 points, uniform
	32 points	12 points	
Mean energy, Hartrees[a]	−1.102629	−1.102630	−1.10276
Variance, (Hartrees)^2	1.06×10^{-6}	4.8×10^{-6}	5.8×10^{-6}
Coefficients			
C_1	1.00000	1.00000	1.00000
C_2	0.40045	0.40384	0.4119
C_3	0.04905	0.04964	0.03372
C_4	0.26430	0.26131	0.25874
C_5	0.11164	0.10679	0.09411
C_6	0.01551	0.01372	0.03499
C_7	−0.02266	−0.02190	−0.0216
C_8	−0.01042	−0.00915	−0.00482
C_9	−0.00194	−0.00128	−0.00907

[a] Compare with the correct energy, −1.10263 Hartrees, reference 4.

and the Gauss-Laguerre,

$$\int_0^\infty e^{-x}f(x)dx=\sum_{j=1}^{n}H_jf(x_j), \tag{9}$$

where the coordinates x_i or x_j are chosen as the roots of nth degree Legendre or Laguerre polynomials, respectively, and H_i and H_j can correspondingly be chosen to make the integrals and sums equal for any $f(x)$ which is a polynomial of a degree no more than $2n-1$.

The Gauss-Legendre form (8) is used in this work for any coordinate that does not appear in an exponential in the wave function, e.g., the elliptical coordinate $\nu=(r_a-r_b)/R$ of an electron in a diatomic molecule, and the interelectronic distance coordinate as in He and H_2. The Gauss-Laguerre form (9) is used for coordinates such as $\mu=(r_a+r_b)/R$ in diatomic molecules, and electron-nuclear distance coordinates. With wave functions expressed generally as exponentials multiplied by power series the matrix elements (7) likewise appear in this form. However the G_{ij} will sometimes contain negative powers in which case the integral formulas (8) and (9) are not exact. It may even be the case that the corresponding integrals are divergent. The finite sums however are not divergent, the singular point never being included among the Gauss points. In applying (8) or (9) a transformation of the coordinate will usually be required in order to obtain the proper limits of integration or in (9) to remove a constant from the exponential.

THE HYDROGEN MOLECULE ION

As in our previous work,[1,2] we use the elliptical coordinates μ and ν and a function which is a linear combination of nine terms of the form

$$\mu^j\nu^k\exp(-z\mu)$$

with $j=0, 1, 2$ and $k=0, 2, 4$. Z is set at 1.485 and the internuclear distance is 2.00 Bohrs, the known equilibrium value for the ground state.

Preparatory to the choice of points the coordinate μ must be transformed to one which ranges from zero to infinity rather than from one to infinity. The coordinate ν is already satisfactory for the Gauss quadrature formula (8) since it ranges from -1 to $+1$.

At first eight values each of μ and ν were chosen, making a total of sixty-four points. These occur in pairs corresponding to the symmetry of the wave function (g state) with respect to reflection of the ν coordinate. Therefore the calculation of the local energy and the summations of equations (7) needed to be carried out over only thirty-two points, say those with positive ν. This number, which is of the order of four times the number of parameters c_i, was thought to be necessary for a statistically satisfactory least squares solution.

A second set of only twelve points was chosen by the following consideration. If the wave function is of highest degree s and t in μ and ν respectively, the matrix elements are of the form of an exponential times a power series of highest degree $2s+2$ and $2t+2$ the extra two coming from the volume element factor $(\mu^2-\nu^2)$ which enters w_P. In order for the Gauss quadrature formulas to be exact the number of points in a coordinate n must be such that

$$2n-1\geq 2s+2,$$

or

$$2n-1\geq 2t+2.$$

Therefore

$$n\geq s+2,$$

or

$$n\geq t+2.$$

For our wave function $s=2$ and $t=4$ and so we need 4 and 6 points, respectively. Again because of symmetry the 6 points for the ν coordinate can be cut to 3, making a total of $4\times3=12$ points. This reasoning would be exact if it were not for the negative powers that enter through the differentiations in the Hamiltonian.

Table I shows the results for H_2^+. The energy for even the twelve-point calculation is in six-place agreement with the accurately calculated result.[4] The use of Gauss points is therefore far superior to the uniform distribution previously used.

[4] D. R. Bates, K. Ledsham, and A. L. Stewart, Phil. Trans. Roy. Soc. (London) **A246**, 215 (1953).

THE HELIUM ATOM

A better test of the least squares local-energy method is on two-electron systems such as He and H_2.

Although Pekeris,[5] following James and Coolidge,[6] has shown the great advantage of perimetric coordinates for the helium atom we use the interparticle coordinates for this test because the calculations can be generalized in such coordinates to apply to more complex systems.[7] The interparticle coordinates are taken as r_1 and r_2, the distances between the nucleus and electrons 1 and 2, respectively, and r_3, the interelectronic distance.

$$0 \leq r_1, r_2 \leq \infty$$

$$|r_1 - r_2| \leq r_3 \leq r_1 + r_2$$

The wave function is of the same form as in the classical calculations of Hylleraas,[8] i.e., an exponential multiplied by a power series in the three coordinates. The individual terms, when used as a linear combination (4), are of the form

$$\varphi_i = \exp[-z(r_1+r_2)]r_1^{n_1}r_2^{n_2}r_3^{n_3}. \qquad (10)$$

All possible terms are considered with n_1 and n_2 equal to 0, 1, and 2, and n_3 equal to 0 and 1. This provides 18 terms, which after symmetrization of the spatial function in the two electrons results in an unnormalized linear combination with 12 independent parameters.

To set up the points according to Gauss quadrature the coordinates are first transformed by setting

$$x_1 = 2zr_1; \qquad x_2 = 2zr_2; \quad x_3 = 2zr_3.$$

For x_1 and x_2 the range is zero to infinity and the Gauss-Leguerre formula (9) applies, the factors $2z$ being necessary to give the simple exponential without constants in the formulas for the matrix elements (7). x_3, which ranges from $|x_1 - x_2|$ to $x_1 + x_2$, is further transformed to y_3 such that

$$x_3 = x_1 y_3 + x_2,$$

and

$$-1 \leq y_3 \leq +1,$$

for the case $x_2 \geq x_1$. Therefore values of x_1 and x_2 are chosen according to tabulated values for Gauss-Laguerre quadrature and values of y_3 are chosen from tables for Gauss-Legendre quadratures.

Similarly the weighting coefficients from the tables must be modified for corresponding values of x_3. If H_{j3} is the tabulated weighting coefficient for a value of y_3 then because of the transformation to x_3 the corresponding weighting factor for x_3 is $x_1 H_{j3}$.

Since the wave function is symmetrical with respect to interchange of x_1 and x_2 it is sufficient to restrict the numerical calculation to points for which $x_2 \geq x_1$. A factor P is included in the weighting factor w_P of (7) such that $P=2$ if $x_2 > x_1$ and $P=1$ if $x_2 = x_1$. The over-all weighting factor w_P is then

$$w_P = P x_1^2 x_2 x_3 H_{j1} H_{j2} H_{j3},$$

where the combination $x_1 x_2 x_3$ is proportional to the volume element.

Reasoning similar to that employed for H_2^+ can be used to determine a suitable minimum number of points. For our twelve-term function there are needed five values, each, of x_1 and x_2 and two values of x_3. The total of fifty points is reduced to thirty by symmetry considerations. In addition to this "thirty-point" calculation, twelve-point, fifty-six point, and sixty-point calculations were also carried out corresponding to the number of values of x_1, x_2, and x_3 equal to(3. 3, 2), (7, 7, 2), and (5, 5, 4), respectively.

TABLE II. Calculated results for helium.

Number of points	Distribution of points	Z	Mean energy[a] (Hartrees)	Variance (Hartrees)^2
12	(3, 3, 2)	1.816	−2.89579	2.8×10^{-6}
30	(5, 5, 2)	1.816	−2.89425	1.35×10^{-2}
30	(5, 5, 2)	1.94	−2.89459	1.46×10^{-2}
56	(7, 7, 2)	1.816	−2.89769	8.83×10^{-3}
60	(5, 5, 4)	1.816	−2.89705	1.79×10^{-2}

[a] Compare with the correct energy, −2.90372 Hartrees, reference 5.

Table II shows the resulting mean energy and variance calculated for He with the usual assumption of infinite nuclear mass. Comparing the wave function parameters for the different calculations shows that the twelve-point calculation is certainly inadequate for the twelve-term function althouth the energy is good. The two thirty-point calculations with differing exponential parameters show the insensitivity of the energy to this parameter for a function of twelve terms.

By comparison with H_2^+ where the minimum number of points, as based on the degrees of the variables in the function, gave a result for the energy good to six significant figures the result for helium, good to only three figures, is rather crude. One can argue that for helium the wave function should have many more terms for a corresponding accuracy but it is also true that the Gauss quadrature scheme is not expected to be as good when applied to helium in the way we have used it. In terms of integrations some of the matrix components have integrands which are absolute values of polynomials and which are therefore not necessarily polynomials over the whole range of coordinates x_1 and x_2.

THE HYDROGEN MOLECULE

As a further test of the present method the electronic energy of H_2 was calculated for the equilibrium inter-

[5] C. L. Pekeris, Phys. Rev. **112,** 1649 (1958); **115,** 1216 (1959).
[6] H. M. James and A. S. Coolidge, Phys. Rev. **51,** 857 (1937).
[7] A. A. Frost, J. Chem. Phys. (to be published).
[8] E. A. Hylleraas, Z. Physik **54,** 347 (1929).

TABLE III. Calculated results for the hydrogen molecule.

Number of terms in wave function	Mean electronic energy[a] (Hartrees)	Variance (Hartrees^2)
For 144 point calculation		
1	−1.1326	0.2104
2	−1.1495	0.1991
3	−1.1533	0.1785
4	−1.1516	0.1776
5	−1.1613	0.1702
6	−1.1817	0.0327
7	−1.1828	0.0318
14	−1.1777	0.0042
For 288 point calculation		
14	−1.1728	0.0056

[a] Compare with accurate mean energy, −1.1744 Hartrees, reference 9. To get dissociation energy subtract from 1.0000.

nuclear distance, 1.40 Bohrs. The electronic spatial configuration was described by the five interparticle coordinates, r_1 to r_5. r_1 and r_2 are the distances from nucleus a to electrons 1 and 2, respectively, r_3 and r_4 from nucleus b, and r_5 the interelectronic distance. The wave function was a linear combination with terms of the form

$$\exp[-z(r_1+r_2+r_3+r_4)]r_1^{n_1}r_2^{n_2}r_3^{n_3}r_4^{n_4}r_5^{n_5}.$$

Terms were taken for which n_1 through n_4 totalled from zero up to three and for which n_5 was zero or one. Because of the symmetry of the ground-state wave function with respect to interchange of electrons and with respect to interchange of nuclei, and omitting for convenience all cubic cross terms, the following fourteen symmetrized terms were included.

$$\varphi_1 = \exp\cdot 1$$

$$\varphi_2 = \exp\cdot(r_1+r_2+r_3+r_4)$$

$$\varphi_3 = \exp\cdot(r_1r_2+r_3r_4)$$

$$\varphi_4 = \exp\cdot(r_1r_3+r_2r_4)$$

$$\varphi_5 = \exp\cdot(r_2r_3+r_1r_4)$$

$$\varphi_6 = \exp\cdot(r_1^2+r_2^2+r_3^2+r_4^2)$$

$$\varphi_7 = \exp\cdot(r_1^3+r_2^3+r_3^3+r_4^3)$$

and a second set of seven terms the same as the first set but multiplied by r_5.

Before choosing Gauss points it is convenient to transform to elliptical coordinates for each electron:

$$\mu_1=(r_1+r_3)/R \qquad \mu_2=(r_2+r_4)/R$$

$$\nu_1=(r_1-r_3)/R \qquad \nu_2=(r_2-r_4)/R,$$

and then convert μ_1 and μ_2 to x_1 and x_2 by

$$x_1=2zR(\mu_1-1) \qquad x_2=2zR(\mu_2-1),$$

so that not only will x_1 and x_2 range from zero to infinity but the matrix components will have $\exp(-x_1-x_2)$ as a factor and so be appropriate for Gauss-Laguerre quadrature.

The fifth coordinate r_5 is replaced as an independent variable by

$$x_3=\phi/\pi,$$

where ϕ is the angle about the internuclear axis between the two electrons. x_3 together with ν_1 and ν_2 range from -1 to $+1$ and are therefore appropriate for Gauss-Legendre quadrature.

The volume element in these five dimensions is proportional to

$$(\mu_1^2-\nu_1^2)(\mu_2^2-\nu_2^2)=\frac{16}{R^4}r_1r_2r_3r_4,$$

and so the w_P of Eq. (5) may be taken as

$$w_P=r_1r_2r_3r_4H_1H_2H_3H_4H_5$$

with the H_i's found in tables[3] for the particular kind of Gauss quadrature and the chosen number of values of each coordinate.

Four values of each coordinate were considered. This means a total of 4^5 or 1024 points in the five-dimensional configuration space. Since the summations over ν_1 and x_3 contain duplicate terms because of symmetry the number of points is reduced to 4^32^2 or 256 points. However, when the points are put in terms of r_1, r_2, r_3, r_4 and r_5 it can be seen that there is additional symmetry in the points corresponding to the operation of (a) interchanging the electrons and (b) simultaneously interchanging the electrons and interchanging the nuclei. By combining the symmetrically related points the number of points is reduced to 144. A second calculation using 288 points was also performed where the number of values of x_3 was doubled.

The summations were carried out to produce the matrix elements (7). Equations (6) were then solved to minimize the variance and get the mean energy. The results are shown in Table III. One value of z was used such that zR equalled 0.75 as found by James and Coolidge.[9]

It is noted that as terms are added to the wave function the variance decreases as it should, a large decrease showing up when the last seven terms are added which bring in electron correlation directly through the interelectronic distance r_5. The mean energy at first trends downwards becoming even more negative than the true value but with all fourteen terms returns upwards to give the best value, one which is in error by about 0.007 Hartrees in the 144 point calculation and 0.0016 Hartree for the 288 point calculation. The result of the 288 point calculation is comparable in accuracy with von Mohrenstein's[10] 48 point calculation by a

[9] H. M. James and A. S. Coolidge, J. Chem. Phys. **1**, 825 (1933).
[10] A. von Mohrenstein, Z. Physik **134**, 488 (1953).

similar method. The wave functions, however, are not strictly comparable.

DISCUSSION

It is desirable to have a method of calculation of molecular energies that will provide binding energies to within 1 kcal per mole, or about 0.001 Hartree per molecule. In this work it is shown that the least-squares local-energy method will accomplish this result, at least for small molecules. The limitation in accuracy depends upon the number of terms in the wave function and the number of points used, which in turn depend upon the speed of the computer available. All calculations were performed at the Northwestern Computing Center with an IBM 650 with FORTRANSIT programming in floating-point arithmetic but without automatic floating-point hardware. To reproduce the results quoted for the hydrogen molecule the calculation would require about eight hours. With a higher speed machine the same calculation could be completed in minutes and so it is clear that a somewhat more accurate calculation could be obtained if desired.

The use of the theory of Gauss quadrature to choose points for the local-energy averaging makes this method approach the more usual methods where integrals are actually evaluated. In particular, if enough points are used so that the matrix components S_{ij} and H_{ij} approach integrals, they could be put into the usual determinantal or secular equation instead of into the equations for minimizing the variance. This idea has been tested with some success in simple cases. With a larger number of points it may possibly turn out that such a scheme would be preferable to the least square method presented here.

ACKNOWLEDGMENTS

This research has been supported by a National Science Foundation grant to Northwestern University and by a National Science Foundation Fellowship to one of us, (R.E.K.). The senior author wishes to thank the several persons who have impressed him with the methods of Gauss quadrature.

THE JOURNAL OF CHEMICAL PHYSICS VOLUME 35, NUMBER 3 SEPTEMBER, 1961

Momentum-Correlation Function in a Rayleigh Gas

ROBERT M. MAZO

Gates and Crellin Laboratories of Chemistry, California Institute of Technology, Pasadena, California*

(Received February 3, 1961)

The time-correlation function in an equilibrium ensemble of the momentum of a heavy particle imbedded in a gas of noninteracting light particles is calculated. The technique used is a density expansion of the correlation function. No statistical hypothesis beyond that of canonical ensemble at the initial time is used.

THE time-correlation functions of dynamical variables of a thermodynamic system at equilibrium are of interest because of their close connection with the transport coefficients of the system. Since the correlation functions are equilibrium properties of the system, there is no ambiguity in the prescription for their computation; however, since they depend on the detailed dynamics of the system they have hardly ever been computed from the first principles. It has almost always been necessary to introduce some sort of "stosszahlansatz" or other stochastic hypothesis into the calculation.

In this paper we compute the momentum correlation function for a particularly simple system directly from the basic principles of equilibrium statistical mechanics, without the aid of auxilliary hypotheses. To be sure, it will be necessary to make some approximations in the course of the calculation. However, these will be well defined kinematical approximations, used to simplify the description of the many body dynamical problems which are encountered.

The model we wish to consider is that of a Rayleigh gas, i.e., one particle of mass M (particle number zero) in a gas of N particles of mass m, where $M \gg m$. We shall assume that the light particles do not interact among themselves, but only collide with the heavy particle. Furthermore we shall assume that the momentum change of the heavy particle on collision is that appropriate to hard spheres; i.e.,

$$\Delta \mathbf{p}_0 = 2(\mathbf{p}\cdot\mathbf{n})\mathbf{n}, \tag{1}$$

where $\mathbf{p}$ is the relative momentum of the collision partners, and $\mathbf{n}$ is the outward normal to the surface of the heavy particle at the point of contact.

* Contribution No. 2675.

The momentum correlation function is defined by ($\beta=1/kT$)

$$\mathbf{R}(t)=\langle \mathbf{p}_0(0)\,\mathbf{p}_0(t)\rangle$$

$$=\frac{\int \exp[-\beta H(0)]\,\mathbf{p}_0(0)\,\mathbf{p}_0(t)\,d^{N+1}\mathbf{p}\,d^{N+1}\mathbf{R}}{\int \exp[-\beta H(0)]\,d^{N+1}\mathbf{p}\,d^{N+1}\mathbf{R}}, \quad (2)$$

i.e., for fixed $\mathbf{p}_0(0)$, $\mathbf{p}_1(0)$, $\cdots\mathbf{p}_N(0)$, $\mathbf{R}_0(0)\cdots\mathbf{R}_N(0)$ we must compute $\mathbf{p}_0(t)$ from the equations of motion of the system, and then average over all initial conditions with the canonical weighting function appropriate to equilibrium. The correlation function must clearly have the following two properties

$$\mathbf{R}(0)=MkT\mathbf{1} \quad (3)$$

$$\mathbf{R}(\infty)=0 \quad (4)$$

Eq. (3) follows by the equipartition theorem and Eq. (4) must at least hold for an infinite system where Poincaré cycles play no role.

An expression for $\mathbf{R}(t)$ can easily be derived from the phenomenological theory of Brownian motion based on the Langevin equation.[1]

$$R(t)=MkT\mathbf{1}\exp(-\zeta t), \quad (5)$$

where ζ is the frictional coefficient, whose value is not determined by the phenomenological theory. The value of ζ for the present model was first computed by Lorentz,[2] and the problem has been studied extensively by M. S. Green[3] on the basis of a stosszahlansatz. Green gives further historical references. ζ is given by

$$\zeta=\tfrac{8}{3}(N/\Omega)[(2\pi mkT)^{\frac{1}{2}}/M]\sigma^2, \quad (6)$$

where N/Ω is the number density of the light particles (Ω is the volume of the system) and σ is the radius of the heavy particle. It is readily seen that ζ^{-1} is much greater than the mean time between collisions, τ, which is obtainable from elementary kinetic theory; in fact

$$\zeta\tau=\tfrac{4}{3}(m/M) \qquad [(m/M)\ll 1].$$

One way to calculate ζ is the following. For a gas of heavy particles dilutely dispersed in a gas of light particles which are always constrained to be at equilibrium, the Boltzmann equation can be reduced to a Fokker-Planck differential equation with friction constant

$$\zeta=(16\pi^2/3)(m^5/MkT)[1/(2\pi mkT)^{\frac{1}{2}}]\int_0^\infty g^5$$

$$\times\exp(-mg^2/2kT)\,dg\int I(g,\theta)\,\sin^2(\theta/2)\,\sin\theta\,d\theta, \quad (7)$$

where g is the relative velocity and $I(g,\theta)$ is the differential scattering cross section.[4] For hard spheres Eq. (7) reduces to Eq. (6). The method used in this paper relies on the fact that $\mathbf{R}(t)$ refers to a correlation in an equilibrium ensemble, and hence can be expanded in a power series in the density, analogous to the virial expansion of the equation of state. The power series can be explicitly summed to yield Eq. (5) with ζ given by Eq. (6).

A theory of density expansions of ensemble averages of dynamical variables which is applicable when these variables are explicitly time dependent has been given previously[5]; we merely state the results here. $\mathbf{R}(t)$ is given by

$$\mathbf{R}(t)=D_0+(N/\Omega)[D_1-\beta_1 D_0]$$

$$+(N/\Omega)^2[D_2-2\beta_1 D_1-(\beta_2-\tfrac{1}{2}\beta_1^2)D_0]+\cdots \quad (8)$$

$$D_n=u_{1,n}/\Omega. \quad (9)$$

The β_n are the familiar irreducible cluster integrals of gas theory and the $u_{1,n}$ are determined recursively from

$$w_{1,n}=\sum_{l=0}^{n}u_{1,l}w_{0,n-l}, \quad (10)$$

where

$$w_{0,n}=[n!(2\pi MkT)^{\frac{1}{2}}(2\pi mkT)^{[3(n-1)/2]}]^{-1}\int \exp(-\beta H_n)$$

$$\times d^n\mathbf{p}\,d^n\mathbf{R}, \quad (11)$$

$$w_{1,n}=[n!(2\pi MkT)^{\frac{1}{2}}(2\pi mkT)^{3n/2}]^{-1}\int \exp(-\beta H_{n+1})$$

$$\times\mathbf{p}_0(0)\,\mathbf{p}_0(t)\,d^{n+1}\mathbf{p}\,d^{n+1}\mathbf{R}. \quad (12)$$

The procedure is completely analogous to the determination of U functions in terms of W functions in the usual theory of the virial expansion.

D_0 is quite simple to evaluate; it is just

$$D_0=MkT\mathbf{1} \quad (13)$$

D_1 is a bit more difficult, but can be computed exactly.

---

[1] S. Chandrasekhar, Revs. Modern Phys. **15**, 1 (1943).
[2] H. A. Lorentz, *Les Theories Statistique en Thermodynamique* (B. G. Teubner, Leipzig, Germany, 1912).
[3] M. S. Green, J. Chem. Phys. **19**, 1036 (1951).

[4] We have not been able to find the above-mentioned derivation in the literature. However, the result is apparently known to a good many people [cf., G. E. Uhlenbeck and C. S. Wang Chang, *Proceedings of the International Symposium on Transport Processes in Statistical Mechanics, Brussels*, 1956, edited by I. Prigogine (Interscience Publishers, Inc., New York, 1958), p. 164] so that we do not give our derivation here. A derivation of the Fokker-Planck equation from the Boltzmann equation for the case of fixed scattering centers has been given by J. Keilson and J. E. Storer, Quart. J. Appl. Math. **10**, 243 (1952).
[5] R. M. Mazo and A. C. Zemach, Phys. Rev. **109**, 1564 (1958).

When written out, the expression for D_1 is

$$D_1=(1/\Omega)[1/(2\pi MkT)^{\frac{3}{2}}][1/(2\pi mkT)^{\frac{3}{2}}]$$
$$\times\int\{\exp[-\beta(p_0^2/2M)+p_1^2/2m+V)]\mathbf{p}_0(0)\,\mathbf{p}_0(t)$$
$$-\exp[-\beta(p_0^2/2M+p_1^2/2m)]\mathbf{p}_0(0)\,\mathbf{p}_0(0)\}$$
$$\times d\mathbf{p}_0 d\mathbf{p}_1 d\mathbf{R}_0 d\mathbf{R}_1. \quad (14)$$

Now $\mathbf{p}_0(t)$ can be written

$$\mathbf{p}_0(t)=\mathbf{p}_0(0)+2\epsilon(t)\,\mathbf{p}\cdot\mathbf{nn}, \quad (15)$$

where $\mathbf{p}$ is the relative momentum of the two particles before collision, $\mathbf{n}$ is the outward normal to the heavy particle at the point of collision, and $\epsilon(t)$ is zero if the initial phase of the pair is such that no collision occurs in time t. ϵ is unity if a collision does occur in the time t. Furthermore $\mathbf{p}\cdot\mathbf{n}<0$. Thus

$$D_1=(1/\Omega)[1/(2\pi MkT)^{\frac{3}{2}}][1/(2\pi mkT)^{\frac{3}{2}}]$$
$$\times\Big\{2\int\exp[-\beta(p_0^2/2M+p_1^2/2m+V)]$$
$$\times\epsilon\mathbf{p}_0\mathbf{p}\cdot\mathbf{nn}d\mathbf{p}_0 d\mathbf{p}_1 d\mathbf{R}_0 d\mathbf{R}_1$$
$$+\int\exp[-\beta(p_0^2/2M+p_1^2/2m)]$$
$$\times\mathbf{p}_0\mathbf{p}_0 d\mathbf{p}_0 d\mathbf{p}_1\int[\exp(-\beta V)-1]d\mathbf{R}_0 d\mathbf{R}_1\Big\}. \quad (16)$$

The second integral in Eq. (16) is clearly $\beta_1 D_0$, which cancels the $-\beta_1 D_0$ in the coefficient of N/Ω in Eq. (8). In the first integral, we may write

$$\mathbf{p}_0=[M/(M+m)]\mathbf{P}-\mathbf{p} \quad (17)$$

where $\mathbf{P}$ is the momentum of the center of mass of the pair. Writing $M_0=M+m$, $\mu=mM/(M+m)$ we have

$$D_1-\beta_1 D_0=(-2/\Omega)[1/(2\pi M_0 kT)^{\frac{3}{2}}][1/(2\pi\mu kT)^{\frac{3}{2}}]$$
$$\times\int\exp[-\beta(P^2/2M_0+p^2/2\mu+V)]$$
$$\times\epsilon(\mathbf{p}\cdot\mathbf{n})\,\mathbf{pn}d\mathbf{P}d\mathbf{p}d\mathbf{R}_0 d\mathbf{R}_1. \quad (18)$$

We have left out of Eq. (18) the term involving $\mathbf{P}$, since this integrates to zero because of the independence of center of mass and relative momenta.

ϵ is nonzero only if the initial relative position of the pair lies somewhere in a tube

$$d\mathbf{R}=(-\mathbf{p}\cdot\mathbf{n}/\mu)\sigma^2 t d\Omega, \quad (19)$$

where $\sigma^2 d\Omega$ is the element of surface area of the sphere at the point of collision. Thus

$$D_1-\beta_1 D_0=[1/(2\pi M_0 kT)^{\frac{3}{2}}][1/(2\pi\mu kT)^{\frac{3}{2}}]$$
$$\times(2\sigma^2 t/\mu)\int_{\mathbf{p}\cdot\mathbf{n}<0}\exp[-\beta(P^2/2M_0+P^2/2\mu)]$$
$$(\mathbf{p}\cdot\mathbf{n})^2\mathbf{pn}d\mathbf{P}d\mathbf{p}d\Omega. \quad (20)$$

The integral over center of mass momentum just cancels the $(2\pi M_0 kT)^{-\frac{3}{2}}$ factor. In the integral over relative momentum, only the component of $\mathbf{p}$ along $\mathbf{n}$ contributes; i.e. we may replace $\mathbf{p}$ by $\mathbf{p}\cdot\mathbf{nn}$. The resulting integral is again easily evaluated, and one finally finds

$$D_1-\beta_1 D_0=-\frac{8}{3}\frac{(2\pi\mu kT)^{\frac{1}{2}}}{M_0}\sigma^2 tMkT\mathbf{1}. \quad (21)$$

If we replace μ by m and M_0 by M, which is correct to order m/M, then Eq. (21) looks like the second term in the expansion of Eq. (5) with ζ given by Eq. (6). Nevertheless, we must investigate the higher order terms. This is a task of some difficulty, entailing the solution of many body dynamical problems; however the simplifying features of our model make possible approximate calculations to relative order $(m/M)^{\frac{1}{2}}$.

The momentum of the heavy particle after collision with j light particles is

$$\mathbf{p}_0^{(j)}=\mathbf{p}_0(0)$$
$$+2\mu\sum_{\alpha=0}^{j-1}\left(-\frac{2\mu}{M}\right)^{\alpha}\sum_{k=1}^{j-\alpha}\sum_{l=k+1}^{j-\alpha+1}\cdots(\alpha\text{ sums})\cdots\sum_{q=p+1}^{j}$$
$$\times(\mathbf{p}_k/m-\mathbf{p}_0/M)\cdot\mathbf{n}_k\mathbf{n}_k\cdot\mathbf{n}_l\mathbf{n}_l\cdots(\alpha+1)\text{ dyads}\cdots$$
$$\cdot\mathbf{n}_p\mathbf{n}_p\cdot\mathbf{n}_q\mathbf{n}_q. \quad (22)$$

This result obviously holds for $j=1$ and the general result follows by induction on j. It is perhaps best to look at a special case; for $j=2$

$$\mathbf{p}_0^{(2)}=\mathbf{p}_0(0)+2\mu(\mathbf{p}_1/m-\mathbf{p}_0/M)\cdot\mathbf{n}_1\mathbf{n}_1$$
$$+2\mu(\mathbf{p}_2/m-\mathbf{p}_0/M)\cdot\mathbf{n}_2\mathbf{n}_2$$
$$-(4\mu^2/M)(\mathbf{p}_1/m-\mathbf{p}_0/M)\cdot\mathbf{n}_1\mathbf{n}_1\cdot\mathbf{n}_2\mathbf{n}_2. \quad (23)$$

The last term is the "excess" momentum change over the momentum change for independent collisions with particles 1 and 2 if particle 0 were to have the same momentum, $\mathbf{p}_0$, at the beginning of each of these collisions. The "excess" momentum change is of order m/M relative to the leading terms.

We now consider the coefficient of $(N/\Omega)^2$ in Eq. (8). The phase space of three particles can be divided into three regions from which two, one, or no collisions take place in time t. A detailed calculation shows that the latter two regions give rise to contributions to D_2 which *exactly* cancel the terms $2\beta_1 D_1+(\beta_2-\frac{1}{2}\beta_1^2)D_0$ in the coefficient of $(N/\Omega)^2$. The calculation is straightforward, but too lengthy to reproduce here. Similar cancellation will occur in the higher order terms; the coefficient of $(N/\Omega)^n$ will only involve regions of phase space giving rise to n collisions, the effects of regions corresponding to $m<n$ collisions being accounted for in lower order terms. By the assumption that the light particles do not collide among themselves, no more than n collisions can occur.

When written out in full, the remaining part of D_2 is given by

$$D_2=(1/2\Omega)[1/(2\pi MkT)^{\frac{3}{2}}][1/(2\pi mkT)^{3}]\int \exp(-\beta H_3)$$

$$\times[\mathbf{p}_0^{(2)}-\mathbf{p}_0^{(1)}(1)-\mathbf{p}_0^{(1)}(2)+\mathbf{p}_0]d^3\mathbf{p}d^3\mathbf{R}. \quad (24)$$

The integral is to be taken only over that portion of phase space giving rise to three collisions. Hence the three-body Hamiltonian. H_3 refers only to kinetic energy. $\mathbf{p}_0^{(2)}$ is given by Eq. (23) and $\mathbf{p}_0^{(1)}(1)$ and $\mathbf{p}_0^{(1)}(2)$, which refer to collisions with particles 1 and 2, respectively, are given by Eq. (15). Actually, there are regions of phase space in which the temporal order of collisions is (1, 2) and other regions in which the order is (2, 1). We need only consider one of these regions and multiply the final result by 2. (In the nth order term their are $n!$ possible collision sequences, of which we need only consider one and multiply by $n!$.) Eq. (23) expresses $\mathbf{p}_0^{(2)}$ for the sequence (1, 2). Inspection of Eq. (24) shows that the first two terms of Eq. (23) cancel against similar contributions from other terms in the integrand of Eq. (24). At first sight it appears as though the third term also cancels against the third term of the integrand. It is important to realize that this is not the case, for the allowable regions of configuration space are different in the two terms. The effective configuration space volume is proportional to the relative velocity before collision, and this velocity differs according to whether particle zero has collided with 1 before 2 or has not done so.

Let us first consider the contribution to $\mathbf{p}_0^{(2)}$ given by the last term of Eq. (23). The configuration space volume element is given by

$$d^3\mathbf{R}=d\mathbf{R}_0\,|\,(\mathbf{p}_1/m-\mathbf{p}_0/M)\cdot\mathbf{n}_1\,|$$

$$\times|\,[\mathbf{p}_2/m-\mathbf{p}_0/M-(2\mu/M)(\mathbf{p}_1/m-\mathbf{p}_0/M)]\cdot(\mathbf{n}_1\mathbf{n}_1)\cdot\mathbf{n}_2\,|$$

$$\times\sigma^4 d\Omega_1 d\Omega_2\int_0^t dt_1\int_{t_1}^t dt_2. \quad (25)$$

Up to this point the development has been exact; we now find it necessary to make approximations in order to evaluate the integrams which arise. The approximations are all based on the fact that the mean value of p_0/M, $\langle p_0/M\rangle$, is less than $\langle p_j/m\rangle$ by a factor of $(m/M)^{\frac{1}{2}}$. The Boltzmann factor insures that contributions to the integrals from regions of momentum space in which p_0/M is much greater than its mean are negligible. Therefore, in Eq. (25) we replace the second absolute value by $|\,\mathbf{p}_2/m\cdot\mathbf{n}_2\,|$ and require $\mathbf{p}_2\cdot\mathbf{n}_2<0$. It is neither necessary nor desirable to make a similar approximation in the first absolute value. The physical meaning of this approximation is clearly that the mass of particle zero is so large that its mean velocity is very small, and furthermore, the velocity does not change very much on collision.

The value of the time integral in Eq. (25) is $t^2/2$. In the nth order term, an n-fold time intergal of similar structure appears. Its value is $t^n/n!$. Thus the contribution to D_2 of the term we are now considering is

$$-\frac{4\mu^2}{M}\frac{\sigma^4 t^2}{2}\int \exp[-\beta(p_0^2/2M+p_1^2/2m+p_2^2/2m)]$$

$$\times(\mathbf{p}_1/m-\mathbf{p}_0/M)\cdot\mathbf{n}_1\mathbf{n}_1\cdot\mathbf{n}_2\mathbf{n}_2\mathbf{p}_0$$

$$\times|(\mathbf{p}_1/m-\mathbf{p}_0/M)\cdot n_1\,||\,\mathbf{p}_2\cdot\mathbf{n}_2/m\,|\,d\Omega_1 d\Omega_2 d\mathbf{p}_0 d\mathbf{p}_1 d\mathbf{p}_2. \quad (26)$$

We have multiplied by 2 already to account for the fact that we have considered only one of the two possible collision sequences. This integral can be evaluated by the same method used for the evaluation of Eq. (18). The result is

$$MkT\mathbf{1}\zeta^2 t^2/4, \quad (27)$$

where we have incorporated the $(N/\Omega)^2$ factor and ζ is defined by Eq. (6). But this is only part of D_2.

The term $2\mu[(\mathbf{p}_2/m)-(\mathbf{p}_0/M)]\cdot\mathbf{n}_2\mathbf{n}_2$ in $\mathbf{p}_0^{(2)}$ also contributes to D_2. The configuration space volume element for particle 2 is proportional to $\sigma^2 v d\Omega dt$ where v is the appropriate relative velocity

$$v=|\,[\mathbf{p}_2/m-\mathbf{p}_0/M-(2\mu/M)(\mathbf{p}_1/m-\mathbf{p}_0/M)\cdot\mathbf{n}_1\mathbf{n}_1]\cdot\mathbf{n}_2|. \quad (28)$$

$\mathbf{p}_0^{(1)}(2)$ has the same contribution, but here the relevant relative velocity is

$$v=|\,(\mathbf{p}_2/m-\mathbf{p}_0/M)\cdot\mathbf{n}_2\,|, \quad (29)$$

since by definition of $\mathbf{p}_0^{(1)}(2)$, particle 1 imparts no momentum to particle zero. We say it is "uncoupled." Since $\mathbf{p}_0^{(2)}$ and $\mathbf{p}_0^{(1)}(2)$ enter in Eq. (24) with opposite signs, only the difference of Eq. (28) and (29) should occur in the configuration space volume element for particle 2. This difference is

$$v_{\text{eff}}=(2\mu/M)(\mathbf{p}_1/m-\mathbf{p}_0/M)\cdot\mathbf{n}_1\mathbf{n}_1\cdot\mathbf{n}_2. \quad (30)$$

When Eq. (30) is used in constructing the volume element, one finds exactly the same expression as Eq. (26) for this contribution to D_2. Thus the second term in the expansion of $\mathbf{R}(t)$ is twice Eq. (27) or

$$\mathbf{R}(t)=MkT\mathbf{1}(1-\zeta t+\zeta^2 t^2/2+\cdots). \quad (31)$$

The higher order terms in the expansion have not been analyzed in anything like the same detail as have the first three. The following remarks can be made, however. There will be a contribution to D_n containing $\mathbf{p}_0^{(n)}$. In $\mathbf{p}_0^{(n)}$ the term of highest order in m/M [see Eq. (22)] gives, upon integration, a contribution to $\mathbf{R}(t)$ of

$$MkT\mathbf{1}(-1)^n\zeta^n t^n/n!2^{n-1}. \quad (32)$$

Furthermore, it appears from the structure of the coefficients, that only regions of phase space giving rise to n collisions contribute to the coefficient of $(N/\Omega)^n$.

Now there are $2^{n-1}-1$ ways in which particles 1, 2, $\cdots n-1$ can be "uncoupled" from particle zero, for we may "uncouple" one particle in $n-1$ ways, 2 particles in $(n-1)(n-2)/2$ ways, etc. By close analogy to the foregoing argument for $n=2$, each of these "uncouplings" produces a contribution to the $(N/\Omega)^n$ term which is the same as (32). This has not been proved in detail because of the increasing aglebraic complexity as n increases. We may argue, however, that, although $n=1$ is atypical, being concerned with a 2-body problem, the three-body problem for the case $n=2$ is entirely typical of the higher terms in the expansion.

$\mathbf{R}(t)$ is therefore given by

$$\mathbf{R}(t)=MkT\mathbf{1}\sum_{n=0}^{\infty}\left[-\frac{8}{3}\frac{N}{\Omega}\sigma^2 t\frac{(2\pi mkT)^{\frac{1}{2}}}{M}\right]^n\Big/ n!$$

$$=MkT\mathbf{1}\exp(-\zeta t). \tag{33}$$

It is noteworthy that our derivation shows unambiguously that $\mathbf{R}(t)$ has a cusp at the origin of time. For it follows, regardless of the dynamical approximations we have made, that the time dependence of the nth order term is t^n. Hence the $n=1$ term, which we have calculated exactly, determines $d\mathbf{R}/dt$ at $t=0$, and this derivative does not vanish. The cusp is a result of the impulsive nature of hard sphere collisions, and presumably would be rounded off for a smoother interaction potential.

Thus, we have shown by a direct dynamical calculation, that $\mathbf{R}(t)$ is given by Eq. (5) with ζ given by Eq. (6). As we have stated previously, the final result is not new. The main purpose of this paper is the presentation of the novel method of derivation. The only other case which we know of in which correlation functions have been computed from strictly dynamical arguments is the case of harmonic oscillators.[6] Our results depend on the assumption that $m/M\ll 1$, so that the formula for ζ is only correct to lowest order in that parameter. Corrections to ζ of higher order in m/M are probably related to momentum dependent corrections to the friction constant.

We should state explicitly that the limit $N\to\infty$, $\Omega\to\infty$, $N/\Omega=$constant is implied in this work. This limit enters in two ways. First of all we have assumed that a given light particle can collide with the heavy particle at most once. This would not be the case if the possibility of wall reflection were allowed. Secondly, our exponential form for $\mathbf{R}(t)$ was arrived at as the sum of an infinite series.

The friction constant ζ can also be expressed in terms of the time autocorrelation function of the force acting on the heavy particle.[7] A density expansion of this function can also be carried out with the same result for ζ. The calculations, however, parallel so closely a similar calculation in Green's paper[3] (not based on a density expansion) that they will not be reported here.

---

[6] R. J. Rubin, J. Math. Phys. **1**, 309 (1960); *Proceedings of the International Symposium on Transport Processes in Statistical Mechanics Held in Brussels*, 1956, edited by I. Prigogine (Interscience Publishers, Inc., New York, 1958), p. 155.

[7] J. G. Kirkwood, J. Chem. Phys. **14**, 180 (1946).

Elastic and Inelastic Scattering of Low-Velocity H^+ and H_2^+ in Hydrogen*

W. H. CRAMER

College of Engineering, University of Florida, Gainesville, Florida

(Received February 10, 1961)

Cross sections have been measured in the energy range 4 to 400 ev for elastic scattering and charge exchange of H^+ and H_2^+ ions in hydrogen. The results are compared with similar measurements for deuterium ions in deuterium. Charge exchange was observed over the entire energy range for H_2^+, but was detected only above 50 ev for H^+. Constants for empirical potential functions have been evaluated and are tabulated.

INTRODUCTION

RECENTLY reported values[1] of elastic cross sections in the energy range 4 to 400 ev for deuterium ions in deuterium gas were in fair agreement with results of earlier measurements by other investigators[2,3] involving hydrogen ions in hydrogen gas. The inelastic cross sections, however, were different. Charge exchange was detected for D^+ in D_2; none had been observed for H^+ in H_2. Furthermore, D_2^+ in D_2 showed considerably greater charge exchange cross sections than had been exhibited by H_2^+ in H_2 at corresponding energies, and the discrepancy increased with decreasing energy.

TABLE I. Elastic and inelastic collision cross sections for H^+ in H_2.

W(ev)	α_T(cm^{-1})	α_S(cm^{-1})	α_I(cm^{-1})
4	120	120	0
5	92.5	92.5	0
6.5	84.6	84.6	0
10	73.8	63.8	0
16	58.9	58.9	0
20	47.1	47.1	0
25	39.2	39.2	0
32	29.8	29.8	0
40	25.6	25.6	0
50	20.5	19.7	0.8
65	13.5	11.9	1.6
80	11.6	10.2	1.4
100	9.29	7.76	1.53
150	4.56	2.80	1.76
200	3.91	1.92	1.99
250	3.65	1.36	2.29
300	3.80	1.11	2.69
400	5.02	0.86	4.16

The work reported here involves new and extended measurements of elastic and inelastic collision cross sections for hydrogen ions in hydrogen, using the same apparatus and experimental techniques as were employed for the investigation[1] of the interactions of deuterium ions with deuterium. Determinations made at various ion energies of the loss of intensity of a beam of ions traversing a collision chamber filled with scattering gas at low pressure yield values of α_T, the total collision cross section. Appropriate voltages applied between a helical grid and a cylinder,[4] both coaxial with the ion beam, produce a separation of the current due to slow ions formed in the process of charge exchange from the current of elastically scattered ions. This separation of currents of slow and fast ions makes possible evaluation of α_S, the elastic cross section and α_I, the inelastic (charge exchange) cross section.

TABLE II. Elastic and inelastic collision cross sections for H_2^+ in H_2.

W(ev)	α_T(cm^{-1})	α_S(cm^{-1})	α_I(cm^{-1})
4	107	69	38
5	87.9	55.3	32.6
6.5	84.1	49.9	34.2
8	82.4	46.7	35.7
10	81.6	45.0	36.6
12.5	76.1	39.9	36.2
16	77.8	38.8	39.0
25	66.1	29.6	36.5
32	56.5	23.6	32.9
40	53.6	22.6	31.0
50	48.0	18.2	29.8
65	43.1	15.2	27.9
80	39.0	12.6	26.4
100	35.7	10.5	25.2
150	30.0	8.5	21.5
200	26.3	7.4	18.9
250	22.8	6.0	16.8
300	21.0	5.0	16.0
400	18.2	4.1	14.1

The hydrogen, obtained from a commercial cylinder, was stated to be 99.9% pure. It was introduced into the apparatus through a trap containing activated charcoal held at liquid air temperature.

RESULTS

The results of the present experiments are presented in Tables I and II and in Figs. 1 through 4. No ordinary ionization, with production of free electrons, was observed with either H^+ or H_2^+. Central one-term potential functions, with parameters obtained from the $\log\alpha_S$ vs $\log W$ plots as described previously,[4] are collected in Table III. It is assumed that the inter-

* Supported by a grant from the National Science Foundation.

[1] W. H. Cramer and A. B. Marcus, J. Chem. Phys. **32**, 186 (1960).

[2] J. H. Simons, C. M. Fontana, E. E. Muschlitz, and S. R. Jackson, J. Chem. Phys. **11**, 307 (1943).

[3] J. H. Simons, C. M. Fontana, H. T. Francis, and L. G. Unger, J. Chem. Phys. **11**, 312 (1943).

[4] W. H. Cramer and J. H. Simons, J. Chem. Phys. **26**, 1272 (1957).

TABLE III. Summary of potential functions.[a]

	H^+ in H_2	
$V=-22.2r^{-4.04}$	4–20 ev	3.0–2.0 A
$V=-6.67r^{-1.78}$	20–100 ev	2.0–0.8 A
	D^+ in D_2[b]	
$V=-22.4r^{-4.03}$	3–20 ev	3.2–2.0 A
$V=-6.56r^{-1.69}$	20–100 ev	2.0–0.8 A
	H_2^+ in H_2	
$V=66.5r^{-6.44}$	4–25 ev	2.6–2.0 A
$V=10.9r^{-2.91}$	25–400 ev	2.0–0.7 A
	D_2^+ in D_2[b]	
$V=211r^{-7.02}$	4–25 ev	2.7–2.0 A
$V=14.3r^{-3.00}$	25–400 ev	2.0–0.8 A

[a] r in angstrom units, V in electron volts.
[b] Reference 1.

action of a proton and a hydrogen molecule is attractive over the entire range of distances involved, while that of a molecular ion and a molecule is repulsive.[1]

DISCUSSION

There is little difference between the elastic scattering of H^+ in H_2 and D^+ in D_2 between 4 and 400 ev ion energy, and there is agreement to better than 5% in elastic cross sections up to about 50 ev energy between the present values and those determined by Simons and co-workers.[2] Charge exchange cross sections for H^+ in H_2 are considerably greater than those for D^+ in D_2 at corresponding energies, and charge transfer occurs in measurable amounts at a lower energy in the former case. This discrepancy persists if cross sections are compared at energies such that the incident ions have the same velocity. Such factors as the small difference in the ionization potentials of the two isotopic atoms, as well as the differences in zero-point energies and vibrational levels of the molecules, appear to have a greater effect on inelastic than on elastic cross sections for the systems of atomic ion and molecule.

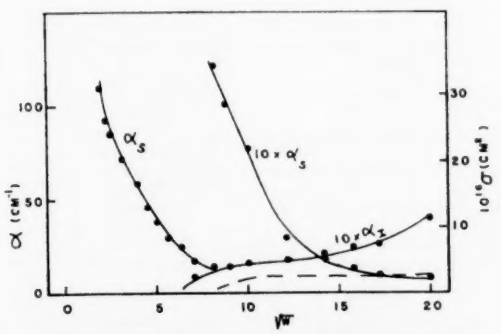

FIG. 1. Scattering cross sections for H^+ in H_2. The dashed line corresponds to $10\times\alpha_I$ for D^+ in D_2, reference 1.

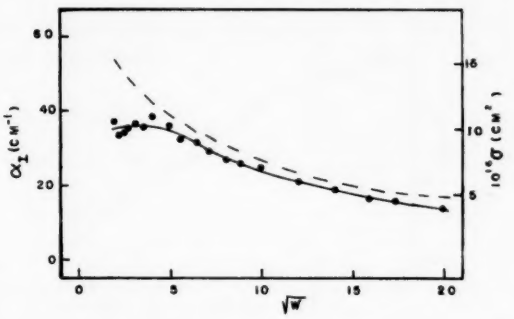

FIG. 2. Charge exchange cross sections. Solid line: H_2^+ in H_2; dashed line D_2^+ in D_2, reference 1.

Both elastic and charge exchange cross sections for H_2^+ in H_2 are somewhat smaller than are those for D_2^+ in D_2 at the same energies, as shown in Figs. 2 and 4. The difference in the case of elastic cross sections does not change markedly with ion energy; the difference increases with decreasing energy for the charge exchange cross sections. There is again no evidence for the ion-molecule reaction

$$H_2^+ + H_2 \rightarrow H_3^+ + H$$

although this possibility cannot absolutely be ruled out, as was the case for D_2^+ in D_2[1].

There is very little information available about vibrationally excited states of molecular ions. However, it is reasonable to assume that electron bombardment of molecules may produce ions in such states. It is also likely that the probabilities of formation, energies, and lifetimes of various levels are different for hydrogen and deuterium. The ion source conditions were about the same for the production of both D_2^+ and H_2^+ for these collision experiments; however, it is not possible to directly detect excited states of ions with the apparatus used in this work.

The observed cross section is an average over separate cross sections for ions in each possible state in which they may exist in the ion beam in the collision region. In general, cross sections would be expected to

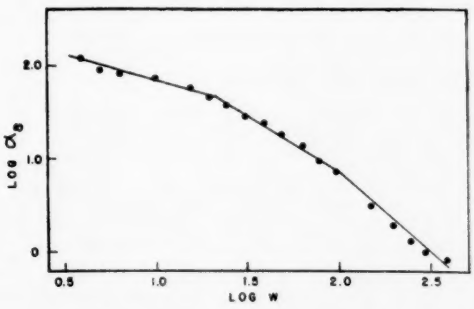

FIG. 3. Logσ_s vs log$W$ for H^+ in H_2.

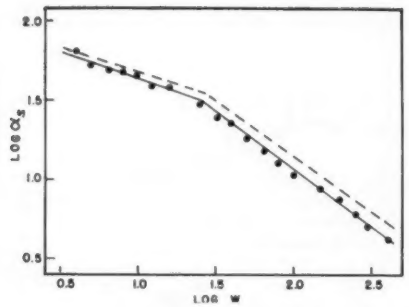

FIG. 4. Logα_S vs log$W$. Solid line: H_2^+ in H_2; dashed line D_2^+ in D_2, reference 1.

be larger for vibrationally excited ions than for ones in the ground state. The fact that cross sections were larger for the D_2^+–D_2 system than for the H_2^+–H_2 system could be explained, at least in part, if it could be shown that excited D_2^+ ions reached the collision chamber in considerably greater concentrations than did excited H_2^+ ions. Lifetimes of the excited states would have to be at least of the order of microseconds.

Values of the elastic cross sections for H_2^+ in H_2 as measured by the present method were somewhat smaller than corresponding values as measured by Simons and co-workers[3]; the converse is true of the charge exchange cross sections. There is good agreement between total cross sections, i.e., the sum of the elastic and inelastic cross sections. These observations indicate that the efficiency of the grid system for the collection of slow ions is greater than the efficiency of a cylinder with an electrically separate lid, as used in the earlier work.

Electron Coupling of Proton Spins in Heterocyclic Molecules. *N*-benzylthieno[3,2-*b*]pyrrole*

H. S. GUTOWSKY AND A. L. PORTE†

Noyes Chemical Laboratory, University of Illinois, Urbana, Illinois

(Received January 23, 1961)

The high-resolution proton magnetic resonance spectrum of the four protons attached to the heterocyclic rings of *N*-benzylthieno[3,2-*b*]pyrrole (I) has been examined in detail at 16.2 Mc/sec. The spectrum is of the type ABCD perturbed by two nuclei X_2 which couple with A, and it involves three long-range proton-proton couplings, 0.5, 1.3, and 0.3 cps over five, six, and six bonds, respectively, which can be accounted for only by pi-electron interactions. The analysis of the spectrum indicates that all of the coupling constants have the same sign, which is presumed to be positive on theoretical grounds. This analysis illustrates the great value of obtaining unambiguous magnitudes of the coupling constants and chemical shifts from high-frequency spectra in order to determine the relative signs of the coupling constants from low-frequency spectra. The coupling constants found in each of the rings in I are compared with those of the monocyclic compounds, thiophene and pyrrole. Although angular effects may govern the coupling via sigma electrons in HCCH groups, the pi-electron contribution appears to be sensitive to electronegativity differences. In addition, heteroatoms and ionic structures are important in determining the long-range coupling via the pi electrons.

INTRODUCTION

IN many organic molecules, coupling of the proton spins via the sigma-electronic framework provides the dominant contribution ($J_{HH'}{}^{\sigma}$) to the observed value of the coupling constant ($J_{HH'}$). This coupling through the sigma electrons has been shown, both by experiment[1–5] and by theory,[6] to be rapidly attenuated by a factor of about five for each carbon-carbon bond which separates the protons. Coupling of protons via pi-electronic frameworks, on the other hand, usually makes only a small contribution ($J_{HH'}{}^{\pi}$) to the observed coupling constant. This is particularly true in the case of the aromatic hydrocarbons, for which theoretical studies, both from the molecular oribtal[7] and valence bond[8] points of view by McConnell, have shown that $J_{HH'}{}^{\pi}$ should be small, $\approx\pm 0.1$ cps, at least for even-alternant cyclic hydrocarbons.

Recently, however, long-range couplings have been reported[9–17] between protons, separated by three and four carbon atoms in acyclic molecules, and the sign of the observed long-range coupling constant (J_{13}) in derivatives of propene[1,10,18] and in methyl acetylene[19] has been determined to be negative relative to other constants assumed to be positive on theoretical grounds. In such molecules the protons H and H' are too far apart for the sigma-electronic framework to contribute appreciably to the observed $J_{HH'}$. Therefore, the coupling must involve the pi electrons. Furthermore, these long-range coupling constants are surprisingly larger than the $J_{HH'}{}^{\pi}$ values found in the aromatic hydrocarbons. These results have led Karplus to consider coupling via pi-electron interactions[20] in unsaturated systems. His valence bond approach shows that in some instances $J_{HH'}{}^{\pi}$ can be quite large, as much as $+7.8$ cycles in the case of butatriene, and it has accounted for

* This investigation was supported in part by the Office of Naval Research. Also, grateful acknowledgment is made to the donors of the Petroleum Research Fund, administered by the American Chemical Society, for partial support of this work.

† Now at the Department of Chemistry, The University, Glasgow W.2, Scotland.

[1] C. N. Banwell, A. D. Cohen, N. Sheppard, and J. J. Turner, Proc. Chem. Soc. **1959,** 266.

[2] H. S. Gutowsky, C. H. Holm, A. Saika, and G. A. Williams, J. Am. Chem. Soc. **79,** 4596 (1957).

[3] R. E. Richards and T. Schaefer, Trans. Faraday Soc. **54,** 1447 (1958).

[4] R. E. Richards and T. Schaefer, Mol. Phys. **1,** 331 (1958).

[5] J. B. Leone and R. E. Richards, Trans. Faraday Soc. **55,** 707 (1959).

[6] H. M. McConnell, J. Chem. Phys. **24,** 460 (1956).

[7] H. M. McConnell, J. Mol. Spectroscopy **1,** 11 (1957).

[8] H. M. McConnell, J. Chem. Phys. **30,** 126 (1959).

[9] S. Alexander, J. Chem. Phys. **28,** 358 (1958).

[10] R. W. Fessenden and J. S. Waugh, J. Chem. Phys. **30,** 944 (1959).

[11] E. B. Whipple, J. H. Goldstein, and L. Mandell, J. Chem. Phys. **30,** 1109 (1959).

[12] E. B. Whipple, J. H. Goldstein, and W. E. Stewart, J. Am. Chem. Soc. **81,** 4761 (1959).

[13] N. Muller and D. E. Pritchard, J. Chem. Phys. **31,** 768 (1959).

[14] E. B. Whipple, J. H. Goldstein, L. Mandell, G. S. Reddy, and G. R. McClure, J. Am. Chem. Soc. **81,** 1321 (1959).

[15] A. D. Cohen and N. Sheppard, Proc. Roy. Soc. (London) **A252,** 488 (1959).

[16] F. S. Mortimer, J. Mol. Spectroscopy **3,** 335 (1959).

[17] R. R. Fraser, Can. J. Chem. **38,** 549 (1960).

[18] S. Alexander, J. Chem. Phys. **32,** 1700 (1960).

[19] P. T. Narasimhan and M. T. Rogers, J. Chem. Phys. **33,** 727 (1960).

[20] M. Karplus, J. Am. Chem. Soc. **82,** 4431 (1960); J. Chem. Phys. **33,** 1842 (1960).

the magnitude and signs of the observed coupling constants in several acyclic hydrocarbons.

Another class of compounds in which long-range pi-electron contributions to proton-proton coupling appear to be important are the heterocyclic, aromatic compounds. For example, a coupling constant J_{48} of 0.8 cps has been reported for some quinoline derivatives,[21] in which the protons are separated by five bonds. Also, long range coupling constants of the order of 1 cps have been reported for protons separated by four or five bonds in a number of thiophene derivatives.[22–24] In

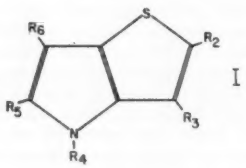

I

addition, we have reported coupling constants, $J_{25}\approx 1.2$ cps and $J_{36}\approx 0.5$ cps, for protons separated by six and five bonds, respectively, in derivatives of thieno-[3,2-*b*]pyrrole (I).[25] These results, particularly the surprisingly large value for the coupling via six bonds, demonstrate the need for the theoretical analysis of the proton-proton coupling in heterocyclic, unsaturated molecules. The signs of the coupling constants are important in their interpretation, so we have extended our studies of I to obtain this information and now report the results and discuss their significance.

RESULTS AND DISCUSSION

Analysis of the Spectrum

Earlier[25] we analyzed in detail that part of the proton high-resolution magnetic resonance spectrum at 60 Mc/sec of *N*-benzylthieno[3,2-*b*]pyrrole ($R_2=R_3=R_5=R_6=H$; $R_4=CH_2C_6H_5$) which arises from the four protons attached to the heterocyclic rings. This spectrum obeys fairly well the first-order splitting rules and, by using approximate chemical shifts and coupling constants measured directly on the observed spectrum, followed by calculations of spectra with some trial and error variation of these parameters,[26] we obtained the following numerical values for the chemical shifts (ν_H) and coupling constants ($J_{HH'}$), all in cps: $\nu_2=0$, $\nu_3=16.3$, $\nu_5=8.9$, and $\nu_6=33.8$; $J_{23}=4.9$, $J_{25}=1.3$, $J_{26}\cong 0$, $J_{35}\cong 0$, $J_{36}=0.5$, and $J_{56}=2.9$. The coupling constants are absolute values only. These assignments and numerical values are unambiguous because of the close approach to the first-order rules and the relative simplicity of the spectra.[25] Moreover, the spectrum at 40 as well as that at 60 Mc/sec is insensitive to the relative signs of the coupling constants; the spectra calculated for the different possible sign combinations of the coupling constants are indistinguishable with present day instrumentation at both 40 and 60 Mc/sec.

However, calculation showed that the relative signs of the coupling constants produce differences in the spectrum which are observable at radiofrequencies of about Mc/sec. These calculations were made with an electronic digital computer (Illiac) using exact expressions for the four-proton system on the heterocyclic rings.[26] It proved possible to obtain experimental spectra[27]

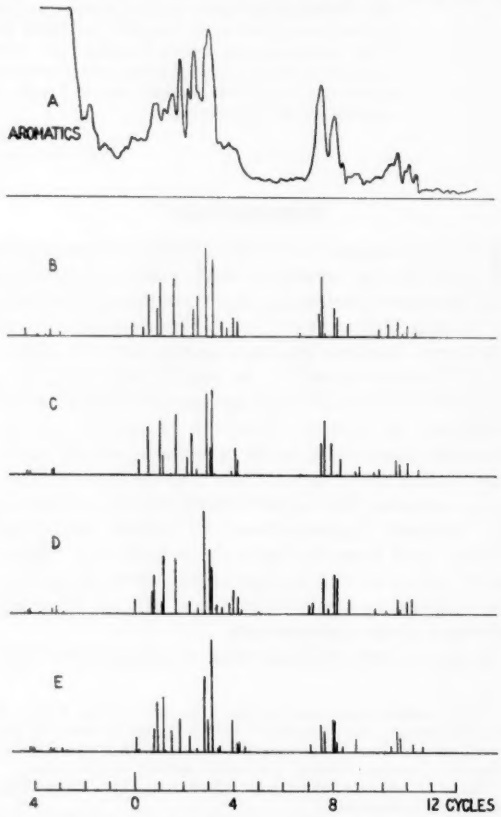

FIG. 1(a). The high resolution magnetic resonance spectrum of the heterocyclic ring protons in *N*-benzylthieno[3,2-*b*]pyrrole at a resonance frequency of 16.2 Mc/sec. The spectrum at the top, A, is that observed at room temperature in a saturated solution in deuterochloroform; the line spectra B—E were computed using the parameters and relative signs listed in Table I. The abscissa corresponds to the magnetic field increasing from left to right; the zero of the scale is ν_2.

[21] F. A. L. Anet, J. Chem. Phys. **32,** 1274 (1960).
[22] S. Gronowitz and R. A. Hoffman, Arkiv Kemi **13,** 279 (1958); Acta Chem. Scand. **13,** 1687 (1959).
[23] P. L. Corio and I. Weinberg, J. Chem. Phys. **31,** 569 (1959).
[24] R. Abraham and H. Bernstein, Can. J. Chem. **37,** 2095 (1959).
[25] R. J. Tuite, H. R. Snyder, A. L. Porte, and H. S. Gutowsky, J. Phys. Chem. **65,** 187 (1961).
[26] We are indebted to Geneva G. Belford for the program and to the staff of the Digital Computer Laboratory for their assistance with the calculations.
[27] The spectra were determined with a Varian Associates V-4300-B high resolution NMR spectrometer on a saturated solution of I in deuterochloroform. We wish to thank Dr. J. N. Shoolery of Varian Associates for his assistance in obtaining the spectra.

at 16.2 Mc/sec which are suitable for the sign determinations. A typical spectrum of I observed at 16.2 Mc/sec is shown in Fig. 1(a), spectrum A. Line spectra were calculated for 16.2 Mc/sec for all eight permutations of signs of the four coupling constants, using the numerical values obtained from the 60 Mc/sec spectrum. The chemical shifts were, of course, scaled down by the factor 16.2/60.

The results are plotted in Figs. 1(a), (b), spectra B–I. The chemical shifts are referred to an arbitrary zero, the resonance position of proton-2; a larger positive value of ν corresponds to an upfield shift. The sets of parameters used in calculating the line spectra are summarized in Table I. When the observed and calculated spectra are compared, particularly in the vicinity of 4—11 cps, it is apparent that spectrum B agrees most closely with experiment. This spectrum was calculated assuming that the signs of all the coupling constants connecting the spins of the protons attached to the heterocyclic rings in *N*-benzylthieno[3,2-*b*]pyrrole are the same. The spectrum is, of course, insensitive to inversion of the signs of all of the coupling constants,

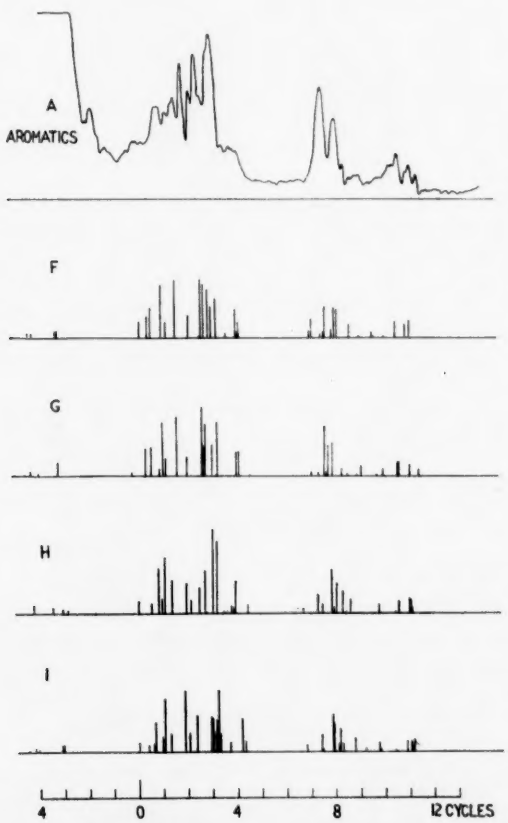

FIG. 1(b). The high resolution spectrum of the heterocyclic ring protons in *N*-benzylthieno[3,2-*b*]pyrrole at 16.2 Mc/sec.

TABLE I. The relative signs and numerical values of the coupling constants used in calculating the line spectra given in Figs. 1(a), (b), spectra B–I.[a]

Spectrum	J_{23}	J_{24}	J_{36}	J_{56}
B	+4.9	+1.3	+0.5	+2.9
C	+4.9	−1.3	+0.5	+2.9
D	+4.9	+1.3	−0.5	+2.9
E	+4.9	+1.3	+0.5	−2.9
F	+4.9	−1.3	−0.5	+2.9
G	+4.9	−1.3	+0.5	−2.9
H	+4.9	+1.3	−0.5	−2.9
I	+4.9	−1.3	−0.5	−2.9

[a] In all cases it was assumed that $J_{26}=J_{35}=0$; the values used for the chemical shifts are $\nu_2=0$, $\nu_3=4.4$, $\nu_5=2.5$, and $\nu_6=9.1$. All numerical values are in cps.

so we have not determined whether all signs are positive or negative. However, theoretical arguments substantiate the assignment of a positive sign to J_{23} and thus to all of the coupling constants.

A careful comparison of the calculated spectrum, B, shown in Fig. 1(a), with the observed one shows that although there is good over-all agreement between the two, and an excellent agreement in the range 1.8–12 cps, that part of the spectrum which falls within the range 0–1.8 cps does not fit the observed spectrum as well as the rest does. At first this suggested to us that our parameters were not quite correct. The peaks lying within the range 0–1.8 cps arise essentially from the 2-H and we calculated additional spectra with small alterations in the chemical shifts and coupling constants given for spectrum B in Table I to try to obtain a better fit for this lower region of the observed spectrum. All such changes caused a marked worsening of the over-all agreement between the observed and calculated spectra and it soon became apparent that the only way to account for the discrepancy in the 0-1.8 cps region was to have the 2-H couple with at least one additional nucleus absorbing at a higher applied magnetic field. It was further noted that the sign of this additional coupling constant must be positive. The additional coupling does not appear to involve any of the other protons attached to the heterocyclic rings. Therefore, we concluded that the spin of the 2-H proton couples with those of the CH_2 protons of the benzyl group. Trial and error variation of this coupling constant $J_{2a}\equiv J_{HH'}$(2-H, N-CH_2) led to good agreement between the calculated and observed spectra for a value of +0.3 cps. The final results are summarized in Fig. 2.

Factors Governing the Proton-Proton Coupling

The origin of the couplings in I can best be approached by first considering the more basic problem of the coupling of protons within the mononuclear heterocyclic molecules. The coupling constant $J_{23}=$

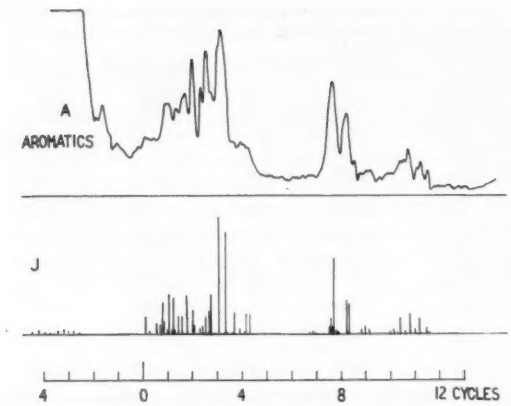

FIG. 2. The high resolution spectrum of the heterocyclic ring protons in *N*-benzylthieno[3,2-*b*]pyrrole at 16.2 Mc/sec. The line spectrum J was calculated using the same parameters as those used for B in Fig. 1 and Table I, except for the inclusion of coupling between the 2–H and the N–CH_2 protons, $J_{2\alpha}=0.3$ cps, and the use of a nonrounded-off value, 9.13 cps, for the chemical shift ν_6.

(+)4.9 cps found in the thiophene ring of I is comparable with the values found for $J_{\alpha\beta}$ in several mononuclear thiophenes.[22] The proton spectrum of thiophene itself (II) has been analyzed in some detail[24] and the numer-

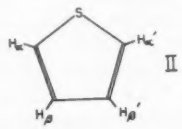

II

ical values obtained for the coupling constants are listed in Table II. In this, two features are particularly striking. The first is that the values $J_{\alpha\beta}=5.0$ cps and $J_{\alpha\beta'}=1.1$ cps are systematically less than their *ortho* and *meta* counterparts $J_o\approx 7$ to 10 cps and $J_m\approx 2$ to 3 cps in benzenes.[2] The second is that $J_{\beta\beta'}$, 3.3 cps, is significantly less than the other "*ortho*" coupling constant $J_{\alpha\beta}$, 5.0 cps, in thiophene, whereas in substituted benzenes the various J_o values within a given molecule are very similar.

In discussing these differences, it is convenient to consider separately the sigma- and pi-electron contributions to the coupling constants. The differences in the sigma contribution can be explained mainly in terms of the larger HCC bond angles, ≈125°, in the five-membered ring[28,29] compared to the 120° angles in benzene. Valence bond methods have been developed[30] and applied to the calculation of the sigma-electron contribution to the proton-proton coupling in the H—C—C—H fragment.[31] With the same approximations and assumptions, extension of the latter calculations to a planar, *cis* H—C—C—H group with HCC bond angles of 125° gives a contribution[32] $J_{HH'}{}^{\sigma}$ of approximately +4 cps, which is appreciably less than the corresponding value of 6.1 cps appropriate for benzene.[31]

The pi-electron contribution has been calculated for benzene by McConnell[8] who found values of about +0.5, −0.2, and +0.2 cps, respectively, for the *ortho*, *meta*, and *para* interactions. Thiophene differs, however, in the weights and types of canonical structures which contribute to the complete π-electronic wave function.[28,29] These include structures such as III to V as well as the conventional form, II. Fortunately, for our purposes, the latter is the most important form and to a good first approximation we can estimate the pi-electron contributions to the coupling by considering only it.

In form II, the C_β—$C_{\beta'}$ bond is single and there would be no pi-electron contribution to the proton-proton coupling $J_{\beta\beta'}$. Therefore, $J_{\beta\beta'}$ would be determined by the sigma-electron contribution $J_{HH'}{}^{\sigma}$ which we have already pointed out should be about +4 cps because of the 125° HCC bond angles in the H—C—C—H fragment. This predicted value of +4 cps compares favorably with the observed value of 3.3 cps.

On the other hand, the pi-electron contribution to $J_{\alpha\beta}$ should be significant.[20] If we treat the C_α—C_β bond as double, $J_{\alpha\beta}{}^{\pi}$ may be approximated by neglecting angular distortion and conjugation effects in the ring and assuming that the sigma-pi exchange interaction volved in the contribution is that of a ·C—H radical fragment. With the further assumption of a hyperfine splitting constant of −65 Mc/sec for the latter, we obtain[20] $J_{\alpha\beta}{}^{\pi}$ to be +1.4 cps. The sigma-electron contribution to $J_{\alpha\beta}$ should be virtually the same as for $J_{\beta\beta'}$, +4 cps, so the net value predicted for $J_{\alpha\beta}$ is +5.4 cps which compares favorably with the observed absolute value of 5.0 cps.

In the case of $J_{\alpha\beta'}$, the separation of the two protons by a second C—C bond reduces the sigma-electron

TABLE II. Summary of proton-proton coupling constants observed in some heterocyclic five-membered ring compounds.[a]

Compound	$J_{\alpha\beta}$	$J_{\beta\beta'}$	$J_{\alpha\beta'}$	$J_{\alpha\alpha'}$
thiophene[b]	5.0 cps	3.3 cps	1.1 cps	2.7 cps
pyrrole[c]	≈2.1	2.8[d]	≈2.1	...
furan[c]	≈1.3	3.4 to 3.8[d]	≈1.3	...

[a] The coupling constants are defined by molecular structure II.
[b] Taken from reference 24; see reference 22 for results on substituted thiophenes.
[c] R. J. Abraham and H. J. Bernstein, Can. J. Chem. **37**, 1056 (1959).
[d] These values are for derivatives.

[28] V. Schomaker and L. Pauling, J. Am. Chem. Soc. **61**, 1769 (1939).
[29] B. Bak, D. Christensen, J. Rastrup-Andersen and E. Tannenbaum, J. Chem. Phys. **25**, 892 (1956).
[30] M. Karplus, D. H. Anderson, T. C. Farrar and H. S. Gutowsky, J. Chem. Phys. **27**, 597 (1957); M. Karplus and D. H. Anderson, J. Chem. Phys. **30**, 6 (1959).
[31] M. Karplus, J. Chem. Phys. **30**, 11 (1959).
[32] H. S. Gutowsky, unpublished results.

contribution from +4 cps to something the order of +1 cps. One would expect the pi-electron contribution to be similar to that for a planar H—C═C—C—H group, which is very nearly zero.[20] The net predicted value for $J_{\alpha\beta'}$ is, therefore, about +1 cps, which is to be compared with an observed value of 1.1 cps. The sign of the latter does not seem to have been determined experimentally[24] but, if our model is not in serious error, it should be positive with respect to both $J_{\alpha\beta}$ and $J_{\beta\beta'}$.

At present, we will not attempt a quantitative explanation for $J_{\alpha\alpha'}$, the 2.7 cps coupling between the two α protons.[33] However, it seems unlikely that coupling *via* the three carbon-carbon bonds and the two sigma carbon-sulfur bonds in form II would give a net value as large as that observed. This leads to the suggestion that the nominally unshared electron pairs on the sulfur atom make an appreciable contribution to $J_{\alpha\alpha'}$ by pi-electron interactions in the non-ionic structure III and in ionic structures such as IV and V. Of course,

III IV V

inclusion of these structures in the ground-state wave function would modify somewhat the values used for the pi-electron contribution to the other coupling constants, in the previous discussion.

In the pyrrole ring of I, the observed value of (+)2.9 cps for J_{56} compares favorably with the result, ≈2.1 cps, listed in Table II for $J_{\alpha\beta}$ in pyrrole itself, although it does imply that fusion of the thiophene ring may have altered the HCC bond angles in the pyrrole ring. However, both this value and the ≈1.3 cps value observed for $J_{\alpha\beta}$ in furan are significantly smaller than the 5 cps found for $J_{\alpha\beta}$ in thiophene. On the other hand, the experimental results summarized in Table II for $J_{\beta\beta'}$ and also for $J_{\alpha\beta'}$ are very similar in all three compounds. The HCC angles differ by no more than a degree or two in the three compounds[28,29] so, at least to a first approximation, one might expect the sigma- and pi-electron contributions and the net values of $J_{\alpha\beta}$, as well as the values of $J_{\beta\beta'}$ and $J_{\alpha\beta'}$, to be the same in all three compounds. We suggest that the observed differences in $J_{\alpha\beta}$ are consequences of the differences in electronegativity of the heteroatom. The electronegativity of S is the same as *C*, 2.5, while N and O are more electronegative, 3 and 3.5, respectively.

The possible importance of electronegativity differences is suggested by the proton-proton coupling in pyridine,[34] for which $J_{\beta\gamma}$ is 7.5 cps, which is in the range of *ortho* H—H coupling in benzene,[2] while $J_{\alpha\beta}$ is significantly less, 5.5 cps. Similar, much smaller effects have been observed in substituted ethanes for which the H—C—C—H coupling constant is given by[35] $8.4-0.4E$, where E is the electronegativity of the substituent. In the ethanes, the coupling is via the sigma electrons, so the larger effects observed in the heterocyclic compounds may result from the pi-electron contributions being more sensitive to electronegativity differences than the sigma. However, differences in bond angles and bond orders may also affect the coupling constants observed in pyridine.

This brings us to the question of the three long-range cross-ring coupling constants found in *N*-benzylthieno[3,2-*b*]pyrrole. It follows from the foregoing discussion that the proton-proton coupling involves the pi electrons J^{π} and that the presence of the heteroatom is an important factor in the relatively large magnitudes observed. In general J^{π} depends first upon the $\sigma-\pi$ exchange interaction at the carbon atoms in the C—H bonds.[8] But this is relatively insensitive to the molecular structure, including substituents. Secondly, J^{π} is proportional to the pi-electron density π_C at the carbons to which the protons are bonded, and π_C is strongly dependent upon the location and neighbors of the carbon atoms in the molecule. Finally, J^{π} and its sign depend upon the manner in which the pi-electrons contributing to π_C are delocalized. These factors require further investigation in order to obtain a full, quantitative understanding of the coupling constants observed in I, or in any heterocyclic molecule for that matter. Valence-bond methods are suitable for this purpose; unfortunately the necessity of including ionic structures makes the calculations more complicated than those for J^{π} in even-alternate, cyclic aromatic hydrocarbons.[8] Procedures have been outlined for including polar structures in the valence-bond approach,[36] and it appears possible to adapt them for calculating J^{π} in heterocyclic systems.[33]

At present, it is of interest to note that there are only two ionic structures, VI and VII, which have a charge

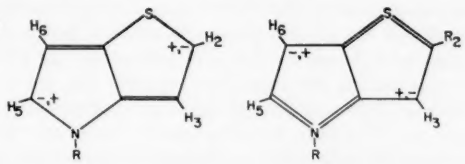

VI VII

on one of the C—H carbons in each of the two rings in the *N*-benzylthieno[3,2-*b*]pyrrole. Structure VI de-

[33] Further work on this question is in progress in this laboratory.

[34] J. A. Pople, W. G. Schneider, and H. J. Bernstein, *High-Resolution Nuclear Magnetic Resonance* (McGraw-Hill Book Company, Inc., New York, 1959), p. 266.

[35] R. E. Glick and A. A. Bothner-By, J. Chem. Phys. **25,** 362 (1956).

[36] M. Simonetta and V. Schomaker, J. Chem. Phys. **19,** 649 (1951); M. Simonetta, J. chim. phys. **49,** 68 (1952). For a review of this procedure and its application to spin density calculations in free radicals, see J. C. Schug, Ph.D. thesis, University of Illinois (1960).

scribes the preferential conjugation of the pi electrons on carbons 2 and 5, while in structure VII the conjugation is between carbons 3 and 6. In other words, interring delocalization of π-electrons occurs preferentially between orbitals centered on C_2 and C_5 and between C_3 and C_6. This delocalization leads to correlation of electron spins in the orbitals and thereby to proton-proton coupling, which is consistent with the observation that $J_{25}>J_{26}\approx 0$ and that $J_{36}>J_{35}\approx 0$. Structure VII is less stable than VI because it involves the nitrogen d orbitals, so it is reasonable to find that $J_{25}>J_{36}$. Prediction of the signs of J_{25} and J_{36} is complicated by the existence in each case of three sets of bonds through which coupling might occur. However, only one of the three sets of bonds ($C_2C_3CCC_6C_5$) is involved in the conjugation which converts structure I into VI, and coupling *via* it (J_{25}) would be positive, as observed. Similar arguments apply to VII and J_{36}. The case of $J_{2\alpha}$(2-H, NCH_2) does not lend itself to such a simple qualitative interpretation.

ACKNOWLEDGMENTS

We are indebted to Professor H. R. Snyder and Dr. R. J. Tuite for awakening our interest in the proton spectrum of I, and to Dr. Gerd Michel for preparing the sample used in these experiments.

THE JOURNAL OF CHEMICAL PHYSICS VOLUME 35, NUMBER 3 SEPTEMBER, 1961

Photoionization of Ce^{3+} in Glass

JACKSON S. STROUD

Corning Glass Works, Corning, New York

(Received January 19, 1961)

The photoionization of Ce^{3+} is investigated by determining the optical absorption changes and the electron spin resonance changes that occur when cerium-containing silicate glasses are illuminated with ultraviolet light. The results are: (1) The room temperature quantum yield of photoelectrons from Ce^{3+} is 0.1. (2) The optical absorption and the electron spin resonance bands caused by trapped photoelectrons are found. (3) A Ce^{3+} ion from which a fourth electron has been removed by photoionization is different from a Ce^{4+} ion.

CERIUM-containing silicate glasses were exposed to near-ultraviolet light. The resulting changes in their optical absorption spectra and in their electron spin resonance spectra were determined. This was done to show experimentally that Ce^{3+} in a silicate glass can be photoionized, to find the optical absorption and the electron spin resonance of trapped electrons in glass, and to learn more about how cerium sensitizes photosensitive glasses to ultraviolet light. These photosensitive glasses are silicate glasses in which a permanent photographic image consisting of submicroscopic metal crystals can be developed by exposing the glass to ultraviolet light and then giving it an appropriate heat treatment.[1,2] Cerium in these glasses sensitizes them to ultraviolet light with wavelengths in the cerium absorption band.[2] This sensitization by cerium has been interpreted by Stookey[1] as the photoionization of Ce^{3+} to Ce^{4+}. It was this interpretation which suggested the work presented here.

After discussing experimental procedure, this paper describes the absorption spectra of Ce^{3+} and of Ce^{4+} in glass. These spectra are used in the following section to assign qualitative models to the absorption bands caused by irradiating the glass with ultraviolet light. This section in which models are assigned consists of a series of interrelated experiments which show that Ce^{3+} is photoionized and which identify the optical absorption and the electron spin resonance of the photoelectrons after they are trapped. Each of these experiments is discussed and conclusions drawn before proceeding to the next experiment. The next two sections reconsider some of these experiments quantitatively in order to compute absorption cross sections and the quantum yield of photoelectrons from Ce^{3+}. The final sections discuss the state of a Ce^{3+} ion from which a fourth electron has been removed by photoionization and summarize the results.

EXPERIMENTAL PROCEDURE

Glasses having the approximate weight percent composition 75% SiO_2, 25% Na_2O, and 0.060% cerium oxide were melted under different reducing and oxidizing conditions. Reduction was done by adding mannitol and oxidation by adding $NaNO_3$. The other raw materials were the purest commercially available quartz sand, $NaHCO_3$, and $(NH_4)_2Ce(NO_3)_6$. For some

[1] S. D. Stookey, Ind. Eng. Chem. **41**, 856 (1949).
[2] S. D. Stookey and F. W. Schuler, in *Travaux du IV^e Congrès International du Verre*. (Imprimerie Chaix, Paris, 1957), pp. 390–395.

glasses the sand was replaced by SiO_2 made by high-temperature hydrolysis of $SiCl_4$. The absorption spectra of glasses made from SiO_2 showed that they had lower impurity concentrations than did the glasses made from sand. These "purer" glasses were not always used, because the cerium could not be completely reduced in them.

To minimize contamination by impurities, the glasses were melted in transparent 96% silica (Vycor brand) crucibles covered with platinum lids. The molten glass was hand-stirred with a 96% silica rod.

The absorption spectra before and after irradiation with ultraviolet light were determined with a Cary model 14 spectrophotometer. Since the glasses contained many small bubbles, it was necessary to correct the resulting curves for scattering. This was done by measuring the absorbance in the visible where light loss from the sample beam was due solely to reflection and scattering. This absorbance was independent of wavelength and of slitwidth in the visible. Subtracting it from the total measured absorbance in the ultraviolet gave the absorption spectra of the glasses.

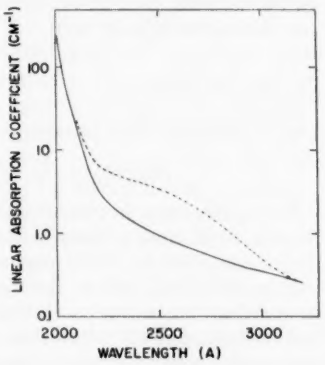

FIG. 1. Absorption spectra of glasses with the weight percent composition 75% SiO_2, 25% Na_2O. —— glass made from SiO_2. --- glass made from commercial sand.

The measured density of these glasses was 2.42 g/cm³.

Electron spin resonance measurements were made using a Varian V-4500 EPR spectrometer and standard techniques.

EXPERIMENTAL RESULTS

Absorption Spectra of Cerium Before Irradiation With Ultraviolet Light

Figure 1 shows the absorption spectra of cerium-free glasses melted from both SiO_2 and commercial sand. The absorption of the glass made from SiO_2 compares favorably with that reported by Kats and Stevels.[3] The glass made from sand has some additional absorption caused by impurities in the sand. These impurities had no effect on the experimental results reported below. This was determined by doing the experiments with glasses made both from SiO_2 and from sand.

[3] A. Kats and J. M. Stevels, Philips Research Repts. **11**, 115 (1956).

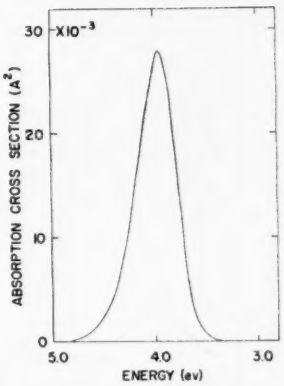

FIG. 2. Absorption spectrum of Ce^{3+} in silicate glass.

Figure 2 shows the absorption of Ce^{3+}. This was obtained by subtracting the absorption of a cerium-free glass from that of a cerium-containing glass in which all the cerium was reduced. This Ce^{3+} absorption is an asymmetrical band with a single maximum at 3.95 ev (3140 A) and an integrated absorption cross section of 0.0138 A² ev. The estimated accuracy of this result is ±3%. Substituting this integrated cross section into Smakula's equation in a form given by Lax[4] and using the free electron mass, refractive index equal to 1.50, and unit effective field factor ($E_e = E$ in Lax's notation) gives an oscillator strength of 0.0190.

The cerium could not be completely oxidized. Consequently, the Ce^{4+} absorption must be obtained from the total absorption of partially oxidized cerium by subtracting the Ce^{3+} absorption. This is done in Fig. 3, which shows the total absorption of 5.33×10^{18} cerium ions/cm³, some of which are present as Ce^{4+}. Also shown is the absorption of 5.33×10^{18} Ce^{3+}/cm³ and the difference between these two absorption curves. This difference consists of a decrease in the

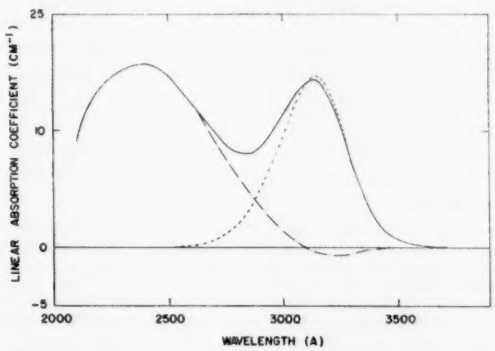

FIG. 3. Absorption spectrum of Ce^{4+} in silicate glass with 5.33×10^{18} cerium ions/cm³. —— absorption of cerium when part is present as Ce^{4+}. --- absorption of 5.33×10^{18} Ce^{3+}/cm³. -·-·- difference between the other two curves.

[4] M. Lax, *Photoconductivity Conference*, edited by R. G. Breckenridge *et al.* (John Wiley & Sons, Inc., New York, 1956), p. 127.

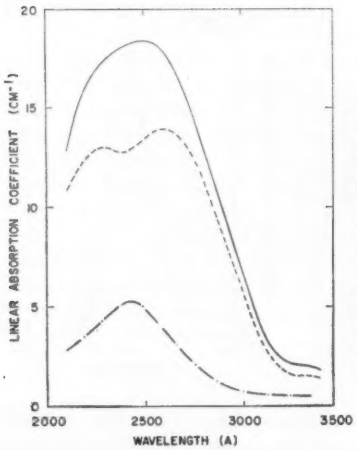

FIG. 4. Change in absorption spectra caused by irradiating cerium-containing glasses with near ultraviolet light. —— initially contained 5.33×10^{18} Ce^{3+}/cm^3 and less than 10^{16} Ce^{4+}/cm^3. --- initially contained 4.6×10^{18} Ce^{3+}/cm^3 and 7×10^{17} Ce^{4+}/cm^3. -·-·- difference between the other two curves.

Ce^{3+} absorption and an increased absorption due to Ce^{4+}. The decrease in Ce^{3+} absorption causes the negative part of the difference curve. The Ce^{4+} absorption causes the band peaked at 2400 A.

The Ce^{4+} concentration in the oxidized glass is equal to the decrease in the Ce^{3+} concentration. The latter can be determined from the decrease in the Ce^{3+} absorption. However, the observed Ce^{3+} absorption decrease is less than the actual decrease because of overlap of the Ce^{3+} and Ce^{4+} bands. The importance of this overlap can be estimated from the absorption spectra in Fig. 3 and from the fact that the Ce^{3+} and Ce^{4+} spectra have an isosbestic point[5] near 3100 A. A plausible estimate is that $\sigma(Ce^{4+})\approx\frac{1}{2}\sigma(Ce^{3+})$ at 3250 A where the observed absorption decrease is 0.7 cm^{-1}. (The σ's are the absorption cross sections of the ions.) Using this estimate and $\sigma(Ce^{3+})$ from Fig. 2, one finds that the oxidized glass has 7×10^{17} Ce^{4+}/cm^3. Dividing the Ce^{4+} absorption coefficient by this concentration gives $\sigma(Ce^{4+})=0.2$ A^2 at 2400 A, the Ce^{4+} absorption maximum. The accuracy is about $\pm50\%$ and is limited by overlap of the spectra and the lack of a measure of the Ce^{3+} concentration independent of the optical absorption.

The Ce^{3+} and the Ce^{4+} spectra agree with the results of Wargin and Karapetjan.[6] These authors have shown that the absorption cross sections of Ce^{3+} and of Ce^{4+} are independent of concentration for the concentrations used here. Hence, the absorption cross sections can be used to determine the concentrations of these ions in other samples of the same host glass.

The absorption spectra of Ce^{3+} and Ce^{4+} are qualitatively the same in silicate glasses with different compositions.[6] This fact makes it valid to compare the cerium absorption spectra in this glass with the cerium absorption in photosensitive glass.[1,2] The comparison shows that the cerium absorption which sensitizes photosensitive glass to ultraviolet light[2] is the Ce^{3+} band.

Absorption Changes Caused by Irradiation with Ultraviolet Light

Cerium-free glasses made from commercial sand and from SiO_2 were given the same exposures to ultraviolet light as were the cerium-containing glasses. These exposures are described below. The absorption spectra of the cerium-free glasses were not changed by any of these exposures. This negative result shows that all absorption changes which occurred during ultraviolet irradiation of cerium-containing glasses were due to photon absorption by the cerium.

Photo-Ionization of Ce^{3+}

Two glasses were irradiated with ultraviolet light for 26 min, 20 in. from a Hanovia type-7420 mercury arc. A Corning filter No. 9700 removed light with wavelengths less than 2600 A. Both glasses had the same total cerium concentration (5.33×10^{18} cm^{-3}). The one had no detectable Ce^{4+} (less than 10^{16} cm^{-3}) while the other had 7×10^{17} Ce^{4+}/cm^3. The change in their absorption spectra caused by irradiation is shown in Fig. 4.

In the glass with no Ce^{4+}, the change is a broad band with a single maximum at 2500 A and what appears to be an unresolved band on its long-wavelength tail (near 3300 A). The absorption change in the glass with 7×10^{17} Ce^{4+}/cm^3 is a broad band with two maxima, one at 2275 A and the other at 2600 A. Again there appears to be an unresolved band on the long-wavelength tail of this absorption. The difference between the absorption changes in these two glasses is also shown. It is a band with a single maximum at 2425 A.

TABLE I. Characteristics of the absorption bands of Ce^{4+} and Ce^{3++}.

Absorption center	Ce^{4+}	Ce^{3++}
Position of the maximum (A)	2400	2500
Half-width (ev)	0.65	0.72
Absorption cross section at the maximum (A^2)	0.2	0.3

[5] If an ion in some host material can exist in two different states both of which have optical absorption bands, then the total absorption coefficient is $\alpha=n_3\sigma_3+n_4\sigma_4$. n_3 and n_4 are the concentrations of the ion in the two states. The σ's are the absorption cross sections. The total concentration of ions is $n=n_3+n_4$. Substituting this equation into the expression for α gives $\alpha=n\sigma_3+n_4(\sigma_4-\sigma_3)$. If the absorption bands of the two states overlap, there will, in some cases, be a wavelength such that $\sigma_4=\sigma_3$; $\alpha=n\sigma_3$. At this wavelength α depends only on n. It is independent of the relative populations of the two states. The absorption curves obtained by holding n constant and by varying n_3/n_4 all pass through one point at this wavelength. This point is the isosbestic point.

[6] W. W. Wargin and G. O. Karapetjan, Glastech. Ber. **32**, 443 (1959).

The absorption change in the glass with no Ce^{4+} is the result of the following three processes:

1. Formation of Ce^{3+} + centers. These centers, discussed below, are Ce^{3+} ions which have lost a fourth electron by photoionization. One would expect these centers to be similar, but not necessarily identical, to Ce^{4+} ions. The broad band with the maximum at 2500 A is attributed to Ce^{3+} + centers on the basis of its similarity to the Ce^{4+} absorption. This similarity is illustrated by Table I, which shows that the absorption spectra of Ce^{3+} + and of Ce^{4+} have nearly the same wavelength of maximum absorption, half-width,[7] and maximum absorption cross section (estimated below for Ce^{3+} +).

2. Decrease in the Ce^{3+} absorption. This causes a "dip" in the absorption change near 3150 A. This "dip" is partly responsible for the shape of the long-wavelength tail of the Ce^{3+} + band.

3. Trapping of photoelectrons. Trapped electrons contribute little to the absorption changes in Fig. 4. Their spectra are discussed below.

These three mechanisms are the only ones which contribute to the absorption changes. In particular, there is no absorption caused by holes trapped at sites characteristic of the cerium-free glass. Centers due to such trapped holes could be formed in only two ways, neither of which actually produces them. First, they could be formed by the trapping of holes thermally released from Ce^{3+} + centers. This does not occur because the Ce^{3+} + center is thermally stable up to 400°C. Thermal bleaching experiments have shown this. Second, they could be formed by photon absorption by the host glass or by the impurities in it. This mechanism does not produce them either. This is shown by the fact that the absorption spectra of cerium-free glasses are unchanged by exposure to near-ultraviolet light.

The experiments described so far show experimentally that Ce^{3+} is photoionized by near-ultraviolet light. The cerium absorption spectra show that Ce^{3+} absorbs this light. Ce^{3+} must be present in order for exposure to this light to alter the absorption spectra of the glass. No Ce^{4+} need be present. Finally, the absorption changes which occur when Ce^{3+} absorbs this light show that the Ce^{3+} is changed into a state similar to that of Ce^{4+}. In other words, it is photoionized.

Figure 4 shows that the absorption change in the glass with 7×10^{17} Ce^{4+}/cm^3 differs from the absorption change just discussed. In this glass the change caused by ultraviolet illumination is altered by the presence of Ce^{4+}. This effect increases with increasing Ce^{4+} concentration. At sufficiently high concentrations ($>10^{18}$ Ce^{4+}/cm^3) the absorption change has a single maximum reduced in height and shifted to 2700 A.

[7] The half-width used here is the energy difference between the absorption maximum and the long wavelength point where the absorption is half the maximum.

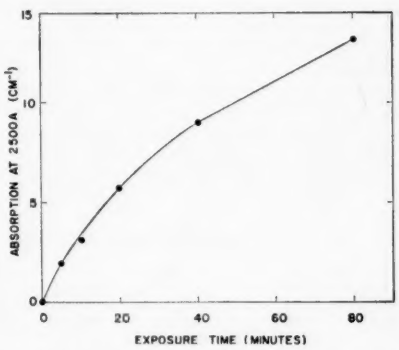

FIG. 5. Growth curve of the Ce^{3+} + absorption. Absorption increase at 2500 A vs exposure time to 3130-A light.

The difference between the absorption changes of the two glasses, one with 7×10^{17} Ce^{4+}/cm^3 and one with no Ce^{4+}, is similar to the Ce^{4+} absorption. This can be seen by comparing the "difference" absorption band, shown in Fig. 4, with the Ce^{4+} band in Fig. 3. The "difference" band has an absorption maximum at 2425 A and a half-width of 0.54 ev. The corresponding parameters for the Ce^{4+} band are 2400 A and 0.65 ev. This similarity suggests that irradiation with the ultraviolet light decreases the Ce^{4+} absorption. The absorption change in the glass which initially had 7×10^{17} Ce^{4+}/cm^3 is due to a decrease in the Ce^{4+} absorption superimposed on the previously discussed absorption changes.

The cause of this Ce^{4+} absorption decrease has not been determined. It could be due to the trapping of photoelectrons by Ce^{4+} ions or to photon absorption in the long-wavelength tail of the Ce^{4+} band. In either case the state of the Ce^{4+} ions is altered in such a way that their absorption band at 2400 A disappears.

Absorption of Trapped Electrons

A glass with 5.2×10^{18} Ce^{3+}/cm^3 and 10^{17} Ce^{4+}/cm^3 was illuminated at 25°C with 3130-A light having a flux of 3.6×10^{14} photons cm^{-2} sec^{-1}. The light was obtained by using suitable filters to isolate the mercury-arc lines near 3130 A. The flux was determined with a thermopile.

The growth curve of the absorption increase at 2500 A, the peak of the Ce^{3+} + band, is shown in Fig. 5. This is essentially a plot of the Ce^{3+} + concentration as a function of exposure time. The spectrum of the absorption change caused by an 80-min exposure is shown in Fig. 6. This absorption change has a broad band below 3000 A, a minimum at 3250 A, and a low maximum near 3400 A. From this low maximum the absorption trails off into the visible. It is detectable out to 5000 A.

These absorption changes are typical of the absorption changes shown in Fig. 4. The broad band below 3000 A is the Ce^{3+} + band. It has the appearance of

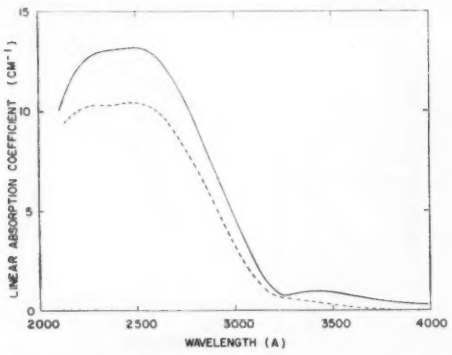

FIG. 6. Change in absorption spectra caused by irradiation of a glass with 5.2×10^{18} Ce^{3+}/cm^3 and 10^{17} Ce^{4+}/cm^3. —— after 80-min exposure to 3130 A light. --- after additional exposure of 19 hr to $\lambda\gtrsim3500$ A.

two unresolved bands, because exposure to ultraviolet light has decreased the absorption of the 10^{17} Ce^{4+}/cm^3. The minimum at 3250 A is due partly to a decrease in the Ce^{3+} concentration. The weak band trailing off into the visible is a feature not previously discussed. It is designated the f_1 band.

The f_1 band is assigned to trapped photoelectrons on the basis of the following optical bleaching experiment. After photoionization of the Ce^{3+} by the 80-min exposure to 3130-A light, the glass was illuminated for 19 hr with mercury-arc emission having $\lambda\gtrsim3500$ A. The total absorption change after this second exposure is shown in Fig. 6. The large absorption band below 3000 A, the $Ce^{3+}+$ band, has been reduced by about 20%, while the absorption between 3400 and 5000 A, the f_1 band, has been reduced by 50–100%. This is what one expects if the f_1 band is due to trapped photoelectrons. If $\frac{1}{5}$ of the photoelectrons produced by photoionization of Ce^{3+} are trapped to form the f_1 band, then complete optical bleaching of this band causes a 100% decrease in the f_1 band and also a 20% decrease in the $Ce^{3+}+$ band if all of the electrons recombine with $Ce^{3+}+$ centers.

There is a second absorption band due to trapped electrons different from those causing the f_1 band. This second band, labeled the f_2 band, lies below 2500 A. In Fig. 4 it causes the small unresolved band on the short-wavelength shoulder of the $Ce^{3+}+$ band. Assignment of the f_2 band to trapped electrons is based on the absorption changes caused by bleaching the f_1 band. This bleaching produces electrons which can be retrapped to increase the f_2 band or which can recombine with $Ce^{3+}+$ centers. Increasing the f_2 band increases the absorption change below 2500 A. Recombination of electrons with $Ce^{3+}+$ centers decreases the $Ce^{3+}+$ absorption. This decrease is greater than the f_2 band increase. The net result is that the total absorption change decreases, but the fractional decrease below 2500 A is less than at $\geq$ 2500 A. This effect can be seen in Fig. 6. The result shown there is typical. It is the basis for assigning the otherwise unresolved f_2 band to trapped electrons.

Electron Spin Resonance

R. F. Tucker of this laboratory measured the electron spin resonance of these glasses before and after photoionization of the Ce^{3+} and after optical bleaching of the f_1 band. No resonance was found before irradiation with ultraviolet light. Figure 7 shows a typical resonance absorption curve, obtained by numerical integration of a resonance derivative curve, after photoionization of Ce^{3+}. This curve has a broad background resonance with a maximum at a spectroscopic splitting factor of $g=2.05$. Superimposed on this is a relatively sharp (about 70 gauss wide) double-peaked band with maxima at $g=1.96$ and $g=1.95$.

Optical bleaching of the f_1 band leaves the background resonance unchanged, but diminishes the height and changes the shape of the double-peaked line. This is also shown in Fig. 7. The resonance after optical bleaching is given by the broken line where it differs from the other resonance curve. The double-peaked line now has a single maximum at $g=1.94$.

The broad background resonance and the double-peaked resonance near $g=1.95$ are attributed to trapped electrons because these are the only paramagnetic centers produced by photoionization of Ce^{3+}. (The $Ce^{3+}+$ center should not be paramagnetic since it is essentially a Ce^{4+} ion which has a closed-shell configuration.) Previously only a resonance near $g=1.96$ has been attributed to trapped electrons.[8]

The double-peaked resonance near $g=1.95$ is the sum of the resonances from electrons in two different kinds of traps. This is shown by its change in shape during bleaching of the f_1 band. Subtraction of the two curves in Fig. 7 shows that both resonances decreased during bleaching of the f_1 band. On this basis, both of these resonances are attributed to the trapped electrons which cause the f_1 band.

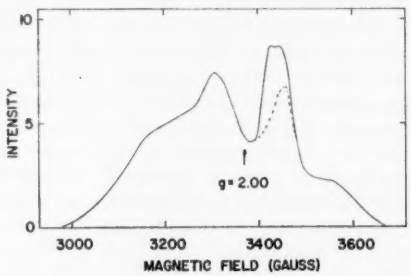

FIG. 7. Electron spin resonance absorption spectra caused by irradiation with ultraviolet light. —— after exposure to mercury-arc emission with $\lambda\geq3000$ A. --- after an additional exposure to mercury arc emission with $\lambda\gtrsim3500$ A.

[8] J. S. van Wieringen and A. Kats, Philips Research Repts. **12**, 432 (1957).

The broad background resonance has not been correlated with any optical absorption. Neither has the f_2 band been correlated with any electron spin resonance.

Absorption Cross Section of $Ce^{3+}+$

From Fig. 6 one can determine the concentration of $Ce^{3+}+$ present after the 80-min illumination with 3130-A light and the subsequent optical bleaching of the f_1 band. One assumes that the f_1 band is completely gone and that the remaining absorption change near 3150 A is due solely to $Ce^{3+}+$ and to a decrease in the Ce^{3+} concentration. The $Ce^{3+}+$ concentration is equal to the decrease in the Ce^{3+} concentration. This decrease can be estimated from the decrease in Ce^{3+} absorption. The estimate is complicated because the absorption bands overlap in such a way that there is no isosbestic point between the Ce^{3+} and $Ce^{3+}+$ spectra. The absorption cross section of $Ce^{3+}+$ is greater than the absorption cross section of Ce^{3+} at all wavelengths. Because of this, the decrease in the Ce^{3+} absorption does not cause a net negative absorption change near 3150 A. It causes only a "dip" in the long-wavelength tail of the $Ce^{3+}+$ band. The Ce^{3+} absorption decrease must be estimated by adding enough Ce^{3+} absorption to fill this "dip". Dividing this estimated Ce^{3+} absorption decrease by $\sigma(Ce^{3+})$ shows that there were about 4×10^{17} $Ce^{3+}+/cm^3$ after optical bleaching of the f_1 band. The accuracy of this estimate is about $\pm50\%$. It is limited by overlap of the absorption bands and by the lack of a measure of the Ce^{3+} concentration independent of the absorption spectra.

The absorption cross section of $Ce^{3+}+$ can be computed from this estimate of the $Ce^{3+}+$ concentration. Assume that after optical bleaching of the f_1 band the shape of the absorption change near 2500 A is due solely to $Ce^{3+}+$. Dividing the $Ce^{3+}+$ absorption coefficient by 4×10^{17} cm^{-3} gives $\sigma(Ce^{3+}+)=0.3$ A^2 at 2500 A, the $Ce^{3+}+$ band peak. This is about the same as the maximum absorption cross section of Ce^{4+} (0.2 A^2 at 2400 A).

The absorption cross section of the trapped electrons which cause the f_1 band can now be estimated. Figure 6 shows that optical bleaching of the f_1 band decreased the $Ce^{3+}+$ concentration by 10^{17} $Ce^{3+}+/cm^3$. Hence, 10^{17} electrons/cm^3, supplied by optical bleaching of the f_1 band, recombined with $Ce^{3+}+$ centers. Before optical bleaching, these 10^{17} electrons contributed to the f_1 band absorption. Their contribution was approximately the decrease in the f_1 band caused by optical bleaching. At 3500 A this decrease was 0.6 cm^{-1} for the curves shown in Fig. 6. Dividing 0.6 cm^{-1} by 10^{17} cm^{-3} gives 0.06 A^2 for the absorption cross section of the f_1 band at 3500 A.

Quantum Yield of Photoelectrons

The quantum yield of photoelectrons can be computed from the $Ce^{3+}+$ growth curve in Fig. 5. This curve is the $Ce^{3+}+$ absorption at 2500 A plotted against the exposure time. From its initial slope, the photon flux, the sample thickness (1 mm), the Ce^{3+} absorption, and $\sigma(Ce^{3+}+)$, one gets a yield of 0.1 photoelectrons per photon absorbed.

TABLE II. Summary of the optical absorption and electron spin resonance of trapped electrons.

Designation	Optical absorption	Electron spin resonance
f_1 band	Nominal maximum near 3500 A with an absorption cross section of 0.06 A^2. Extends to 5000 A.	Consists of two types of centers with resonances near $g=1.95$.
f_2 band	Absorption at 2500 A.	?
None	?	Complex background with maximum at $g=2.05$.

THE $Ce^{3+}+$ CENTER

A Ce^{3+} ion from which a fourth electron has been removed by photo-ionization is designated by $Ce^{3+}+$ to show that it is similar but not identical to a Ce^{4+} ion. The similarity is shown by the similarity of the peak positions, half-widths, and maximum absorption cross sections of their absorption spectra. These are summarized in Table I. Evidence that $Ce^{3+}+$ is not identical to Ce^{4+} is found in the differences between their absorption spectra. The significant differences are:

1. The absorption maximum of Ce^{4+} is at 2400 A while that of $Ce^{3+}+$ is at 2500 A or at a slightly longer wavelength if the f_2 band is subtracted from its short-wavelength side.

2. There is an isosbestic point between the Ce^{4+} and the Ce^{3+} absorption spectra but not between the $Ce^{3+}+$ and the Ce^{3+} spectra. At wavelengths greater than 3100 A, the $\sigma(Ce^{3+}+)>\sigma(Ce^{3+})>\sigma(Ce^{4+})$.

3. The presence of Ce^{4+} markedly alters the shape of the absorption change caused by illuminating the glass with ultraviolet light. This alteration is caused by a decrease of the Ce^{4+} absorption, as previously discussed. If the Ce^{4+} and the $Ce^{3+}+$ absorption bands were identical, a decrease in the Ce^{4+} absorption would not alter the shape of the change so radically.

The differences between the $Ce^{3+}+$ and the Ce^{4+} absorption spectra reflect the differences between the environments of the $Ce^{3+}+$ center and the Ce^{4+} ion. A discussion of this point by Tashiro *et al.*[9] is amplified here, since the present work is an experimental verification of this idea. The environments of the $Ce^{3+}+$ center and the Ce^{4+} ion are different, because the nearest neighbors of the Ce^{3+} ion and of the Ce^{4+} ion have different configurations. Removal of a fourth electron from a Ce^{3+} ion by photoionization alters its bonding to the surrounding ions. The latter then shift

[9] M. Tashiro, N. Soga, and S. Sakka, J. Ceram. Assoc. Japan **68**, 169 (1960).

to new equilibrium positions. However, the extent of the shift is limited by the rigidity of the glass. The neighboring ions cannot shift to the positions they would occupy about a Ce^{4+} ion. The result is the $Ce^{3+}+$ center which has a somewhat different environment than does a Ce^{4+} ion. It is essentially a Ce^{4+} ion in a site normally occupied by a Ce^{3+} ion.

The different environments of the $Ce^{3+}+$ center and the Ce^{4+} ion cause their energy levels and their absorption spectra to be different. The differences in absorption are experimentally confirmed by this paper. The fact that their spectra do not differ very much shows that their environments are not very different. The configurations of their neighboring ions are similar even though they are not identical.

SUMMARY

The Ce^{3+} absorption spectrum in 75% SiO_2, 25% Na_2O glass has a single maximum at 3140 A. Its oscillator strength is 0.0190. The Ce^{4+} absorption spectrum has an absorption cross section of 0.2 A^2 at 2400 A, the only maximum.

Ce^{3+} can be photoionized with a quantum yield of 0.1 at room temperature.

Stookey's explanation of the role of cerium as an optical sensitizer[1] in photosensitive glasses is substantiated by the fact that Ce^{3+} can be photoionized and by the fact that the effective cerium absorption band in photosensitive glasses[2] is the Ce^{3+} band.

Photoelectrons are trapped by various kinds of traps. The optical absorption and the electron spin resonance of these trapped electrons are summarized in Table II.

A Ce^{3+} ion from which a fourth electron has been removed by photoionization is different from a Ce^{4+} ion. For this reason it is designated by the symbol $Ce^{3+}+$. It has a maximum absorption cross section of 0.3 A^2 at 2500 A.

ACKNOWLEDGMENTS

The author thanks Dr. R. F. Tucker for making the magnetic resonance measurements and Dr. D. L. Weinberg and Dr. R. D. Maurer for their constructive criticism of the manuscript.

THE JOURNAL OF CHEMICAL PHYSICS VOLUME 35, NUMBER 3 SEPTEMBER, 1961

General Theory of Monolayer Physical Adsorption on Solids*

WILLIAM A. STEELE AND MARVIN ROSS†

Department of Chemistry, The Pennsylvania State University, University Park, Pennsylvania

(Received February 27, 1961)

By suitable modifications of the general equations given previously [W. A. Steele and M. Ross, J. Chem. Phys. **33,** 464 (1960)], a theoretical monolayer adsorption isotherm is given which is written as a power series. The terms in the series involve integrals over the interaction energies of the adsorbed atoms with each other and with the solid. This treatment is based on a virial expansion of the density of the film in powers of the activity of the film, but differs from previous two-dimensional virial expansions in that it explicitly includes the effect of periodic variation of the solid-gas atom potential energy as the atom moves over the surface of the solid. It is shown that this general equation reduces to a sitewise model for large parallel variations in the solid-gas atom energy, and to a perfectly mobile film for small variations. However, when the potential energy for a gas atom over a simple solid is calculated as a function of the relative sizes of the gas and solid atoms, it appears that many adsorption systems may obey neither of the two limiting models. Some possible methods of dealing with adsorption systems which are neither completely localized or completely mobile are outlined and it is shown that some information about the nature of the solid-gas atom potential function may be obtained from an analysis of the experimental data for suitable systems.

1. INTRODUCTION

PREVIOUS theoretical treatments of the problem of physically adsorbed monolayers on solid surfaces may be divided into two general categories: Treatments based on sitewise or localized models (with or without lateral interaction),[1] and treatments based on a completely mobile or two-dimensional fluid model.[2] Although most experimental data can be shown to be reasonably consistent with one or more of the isotherm equations resulting from these models, it is often impossible to decide which of the models most nearly corresponds to a given physical system. This difficulty is due to the lack of quantitative criteria (other than the quality of the agreement between the theoretical

* This work supported in part by National Science Foundation.

† Present address: Department of Chemistry, University of California, Berkeley, California.

[1] For a review of these theories, see T. L. Hill, in *Advances in Catalysis* (Academic Press, Inc., New York, 1952), Vol. IV.

[2] For an analysis of the properties of mobile monolayers, see J. H. deBoer, *The Dynamical Character of Adsorption* (The Clarendon Press, Oxford, England, 1953).

and experimental isotherms) which might make it possible to reject an unrealistic model.

The present paper describes an attempt to derive a general theory of monolayer adsorption in which it is assumed only that the adsorbed atoms move in a potential field in the vicinity of the surface of the solid adsorbent, and that this potential field is not perturbed by the presence of adsorbed atoms. In a previous paper (hereafter referred to as I),[3] the authors gave a formal treatment of the properties of classical fluids in external fields which provides the basis for the present theoretical treatment of monolayer adsorption. In general, the potential energy of an atom near the surface of a solid depends on all three position coordinates of the interacting atom. One may expect that the potential function will show a simple minimum as the perpendicular distance to the surface is varied, but that the position and magnitude of the minimum (as well as the entire potential function) will show a periodic variation as the adsorbed atom is moved parallel to the surface. In terms of the treatment in I, monolayer adsorption will occur at temperatures and pressures such that there is a negligible probability of finding an adsorbed atom anywhere other than at (or very near to) the distances from the surface which correspond to the positions of the minima of the potential energy with respect to variations in the coordinate perpendicular to the surface. The classical computation of the thermodynamic properties of an adsorbed monolayer then consists in an evaluation of the phase integral for a collection of particles restricted to move on the surface which is the locus of these potential minima. Qualitatively, it seems likely that localized adsorption will occur if the amplitude of the periodic variations in potential energy with motion parallel to the surface is large compared to kT, and mobile adsorption if it is small. However, the extent of the correspondence between these descriptions, and the previous mathematical models for localized and mobile adsorption remains to be established.

In the following section, the partition function of a monolayer film will be expanded as a power series in the activity of the adsorbed layer. The leading terms in this series will then be explicitly written down for systems which are quantized with respect to motion perpendicular to the surface, but classical with respect to motion parallel to the surface. Since the terms in this series are dependent upon the nature of the periodic variations of the energy of an adsorbed atom, it is clear that a reasonably detailed knowledge of the form of these variations is needed to complete the computation. In order to obtain this information, the interaction energy between an atom and a simple cubic lattice has been computed as a function of the distance from the surface, and as a function of position with respect to the unit cell of the solid lattice. (Computations of this type have been previously reported for a limited choice of position coordinates[4]; however, more detailed results are required if one wishes to avoid undesirable approximations in the calculation of the thermodynamic properties of these systems.)

It is then shown that the general equation given here reduces to sitewise and mobile adsorption under certain reasonably well-specified conditions. Furthermore, the general equations are given in a form which make it possible to obtain considerable information about the nature of the surface potential from experimental data.

2. THEORY

For simplicity, it will be assumed that a gas made up of spherically symmetric molecules is placed in contact with a crystalline solid having a planar surface which is uniform in the sense that there are no imperfections present which would destroy the natural periodicity of the surface properties. In I, the number of adsorbed atoms N_a was given in terms of the probability density $\rho^{(1)}$ of adsorbed atom 1

$$N_a=\int_V(\rho^{(1)}(\mathbf{r}_1)-\rho_0)d\mathbf{r}_1, \tag{2.1}$$

where V is the volume available to the gas phase in contact with the solid, ρ_0 is the number density in the gas far from the surface, and $\mathbf{r}_1$ is the position vector for atom 1. Furthermore, the number density $\rho^{(1)}$ was written as a function of the activity z of the adsorbed phase and the interaction energy of an adsorbed atom with the solid. When this result is substituted into Eq. (2.1), and the distribution functions written in terms of the potential energy, Eq. (2.1) can be integrated to give the equation

$$N_a=z\int_V\exp[-u_s(\mathbf{r}_1)/kT]d\mathbf{r}_1-\int_V\rho_0 d\mathbf{r}_1+z^2\iint_V f_{12}\exp\{-[u_s(\mathbf{r}_1)+u_s(\mathbf{r}_2)]/kT\}d\mathbf{r}_1d\mathbf{r}_2$$

$$+z^3\iiint_V\exp\{-[u_s(\mathbf{r}_1)+u_s(\mathbf{r}_2)+u_s(\mathbf{r}_3)]/kT\}\{f_{12}f_{23}+\tfrac{1}{2}f_{12}f_{13}\exp[-u(r_{23})/kT]\}d\mathbf{r}_1d\mathbf{r}_2d\mathbf{r}_3+\cdots, \tag{2.2}$$

where

$$f_{ij}=\exp[-u(r_{ij})/kT]-1 \tag{2.3}$$

[3] W. A. Steele and M. Ross, J. Chem. Phys. **33,** 464 (1960); see also T. L. Hill and S. Greenschag, J. Chem. Phys. **34,** 1538 (1961); T. L. Hill and N. Saito, *ibid.* **34,** 1543 (1961).

[4] W. J. C. Orr, Trans. Faraday Soc. **35,** 1247 (1939); W. A. Steele and G. D. Halsey, Jr., J. Phys. Chem. **59,** 57 (1955).

and $u(r_{ij})$ is the interaction energy of adsorbed atoms i and j separated by a distance r_{ij}. Let the solid surface be made up of N_s identical elements of area A_s. A coordinate system is introduced with z axis perpendicular to the surface and origin in the plane passing through the outermost layer of surface atoms. The τ is defined to be a two-dimensional vector lying in the plane of the surface. After rearrangement, Eq. (2.2) can be written as

$$N_a=\frac{N_s(p/p_0)}{1+\beta(p/p_0)}(1+(p/p_0)^2\delta+\cdots), \tag{2.4}$$

where

$$1/p_0=1/kT\int_{A_s}\int_z(\exp[-u_s(\tau, z)/kT]-1)d\tau dz \tag{2.5}$$

$$\beta=\frac{-\int_A\int_{A_s}\int_{z'}\int_z f_{12}\exp\{-[u_s(\tau_1, z_1)+u_s(\tau_2, z_2)]/kT\}d\tau_1dz_1d\tau_2dz_2}{\left\{\int_{A_s}\int_z(\exp[-u_s(\tau, z)/kT]-1)d\tau dz\right\}^2} \tag{2.6}$$

$$\delta=p_0^2\int_A\int_A\int_{A_s}\int_{z'}\int_z\int_z\exp\{-[u_s(\tau_1, z_1)+u_s(\tau_2, z_2)+u_s(\tau_3, z_3)]/kT\}$$
$$\times\{f_{12}f_{23}+\tfrac{1}{2}f_{12}f_{13}\exp[-u(r_{23})/kT]\}d\tau_1dz_1d\tau_2dz_2d\tau_3dz_3-\beta^2/p_0. \tag{2.7}$$

Due to their complexity, δ and higher terms will not be treated quantitatively in this paper.

Formally, Eqs. (2.5)–(2.7) are applicable to multilayer adsorption as well as monolayer. Classically, they are restricted to monolayer adsorption by making the assumption that the integrands in these equations have sharp maxima at $z=z_m$. However, such systems will almost certainly be quantized in the z direction and in fact, it appears that motion in this direction is quantized in most physical adsorption systems of interest. The integrations of the classical configurational integrals with respect to z must therefore be replaced with the correct quantum sums. If it is assumed that the z dependence of u_s near z_m does not depend upon τ, then u_s can be written as

$$u_s(\tau, z)=\epsilon_z(z-z_m)+\epsilon_\tau(\tau, z_m)+\epsilon_m(0, z_m), \tag{2.8}$$

where $\epsilon_m(0, z_m)$ is the minimum of the potential energy at $\tau=0$, $\epsilon_z(z-z_m)$ is the variation in potential energy with z at constant τ, and $\epsilon_\tau(\tau, z_m)$ is the change in the magnitude of the minimum as τ varies. Monolayer adsorption occurs when $-\epsilon_m(0, z_m)/kT\gg1$, and at activities such that p/p_0 is not large. In this situation, the 1 appearing in the equations for $1/p_0$, etc., can be dropped. When the allowed values of $\epsilon_z(z-z_m)$ are denoted as $\epsilon_z(n)$, where n is the quantum number associated with the energy levels for motion in the z direction, one can write

$$1/p_0=h/(2\pi m)^{\frac{1}{2}}(kT)^{\frac{1}{2}}\exp[-\epsilon_m(0, z_m)/kT]\sum_n\exp[-\epsilon_z(n)/kT]\int_{A_s}\exp[-\epsilon_\tau(\tau, z_m)/kT]d\tau, \tag{2.9}$$

where m is the mass of the adsorbed particle;

$$\beta=\frac{-\int_A\int_{A_s}f_{12}\exp\{-[\epsilon_\tau(\tau_1, z_m)+\epsilon_\tau(\tau_2, z_m)]/kT\}d\tau_1d\tau_2}{\left\{\int_{A_s}\exp[-\epsilon_\tau(\tau, z_m)/kT]d\tau\right\}^2}. \tag{2.10}$$

It is interesting to note that the value of β is now entirely determined by the form of the variations of the potential energy due to the lateral motion of atoms 1 and 2 over the surface, while $1/p_0$ depends upon the complete potential energy function for a single adsorbed atom.

It should be noted that Eq. (2.2) and (2.4) can be obtained from the virial expansion for the density of a gas in the vicinity of a surface. The chief differences between this work and previous treatments[5] of

[5] T. L. Hill, *Statistical Mechanics* (McGraw-Hill Book Company, Inc., New York, 1956), Appendix 10.

the problem are: The three-dimensional character of u_s is explicitly included in the equations given here; and the rearrangement of Eq. (2.2) to give (2.4) results in an expression in which the coefficients of δ, γ, etc. are written as the differences of similar integrals. It is expected that these coefficients will be small in many cases, particularly in those systems where the periodic variation in u_s is large compared to the lateral interaction energy $u(r_{ij})$. If the periodic variation in u_s is small compared to kT, it is clear that this treatment is essentially equivalent to the conventional virial expansion for the density of a two-dimensional gas.[6]

In I, a simple argument was presented to show that Eq. (2.4) could be reduced to the Langmuir equation. In Sec. 4, $1/p_0$ and β are computed for a wide range of potential functions, and it is shown that these coefficients include perfectly mobile systems as special cases, as well as covering the range of intermediate systems.

3. COMPUTATION OF THE POTENTIAL ENERGY

It is clear that any attempt to express adsorption properties in terms of Eq. (2.4) requires a reasonably detailed knowledge of the general form of the potential energy of an adsorbed atom with a solid lattice. Here, this interaction energy is computed by summing the pair interactions between an adsorbed atom and the atoms in the solid. The sum is taken over the entire solid, and the pair interaction is assumed to have the form of the Lennard-Jones potential function. While this computation is rigorously applicable only to a rare gas adsorbed on a rare-gas crystal, nevertheless it should reproduce the general form of the interaction in considerably more complex systems. This is due to the fact that all of the contributions to the interaction potential in a complex system (for instance, dipolar and quadrupolar interactions, or angle-dependent dispersion interactions) have two features in common; they vary rapidly with distance, and their magnitude is determined primarily by the internuclear distances between the atoms of the solid and the atoms of the adsorbed molecule.

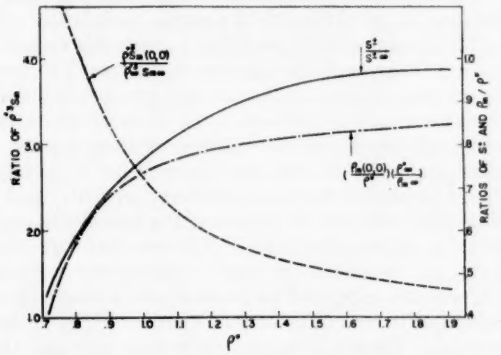

FIG. 1. The changes due to surface structure in some of the parameters of the potential function are plotted as a function of ρ^*. The maximum net attractive energy over a structureless surface is proportional to ρ^{*3} as well as to S_m, and thus the ratio shown is a direct measure of the increase in this energy at the center of a site due to structure (the scale factor for the $\rho^{*3}S_m$ ratio is given along the left-hand ordinate). If this ratio is denoted by R, then $\epsilon_m(0,0) = 2.21\,\epsilon^*\rho^{*3}R$ at any finite ρ^*. Similarly, the ratio of the shape parameter $s_{\pm}$ [defined by Eq. (3.7)] is plotted relative to the scale on the right-hand side of the figure. The third curve shows the relative values of the ratios of the distances corresponding to the maximum attractive energy above the site center to ρ^*, plotted as a function of ρ^* using the scale on the right-hand side of the figure. Note that calculations of the maximum attractive adsorption energy using the equation for the interaction of an atom with a structureless surface are greatly in error for systems in which the adsorbed atoms are roughly the same size as the solid atoms, and are still off by 80% when the gas atoms are twice as large as the solid atoms ($\rho^* \simeq 1.34$).

[6] T. L. Hill, J. Phys. Chem. **63**, 456 (1959).

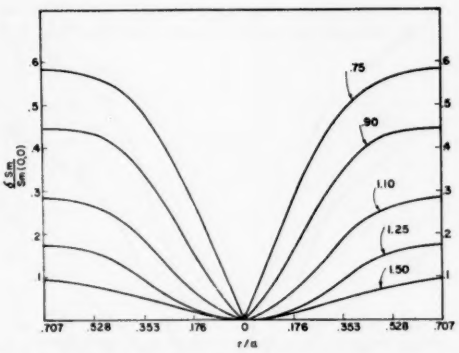

FIG. 2. The fractional change in the minimum of S is plotted as a function of the distance from the cell center. The changes shown in this figure were calculated for displacements along a perpendicular bisector of the cell edge, assuming a simple cubic lattice. The numbers next to the curves denote the values of ρ^* used in the calculation of S in Eq. (3.3). The ρ^* is proportional to the relative sizes of the gas and solid atoms, and, if it is assumed that Eq. (3.11) holds, some representative points are: ρ^* of 0.89 corresponds to gas atoms and solid atoms of equal size; ρ^* of 1.34 corresponds to a gas atom which is twice as large as a solid atom.

The Lennard-Jones pair interaction energy ϵ_{gs} between a gas atom and a solid atom separated by a distance r_{gs} is written in the form

$$\epsilon_{gs} = 4\epsilon^*[-(\sigma/r_{gs})^6 + (\sigma/r_{gs})^{12}]. \tag{3.1}$$

If the distance variables are reduced by a, the lattice parameter of the solid, then

$$u_s(\rho, x/a, y/a) = 4\epsilon^*(\rho^*)^6 S(\rho, x/a, y/a, \rho^*) \tag{3.2}$$

$$\rho = z/a, \qquad \rho^* = \sigma/a$$

$$S(\rho, x/a, y/a, \rho^*) = -S_6(\rho, x/a, y/a) + \rho^{*6} S_{12}(\rho, x/a, y/a) \tag{3.3}$$

$$S_6(\rho, x/a, y/a) = \sum (a/r_{gs})^6 \tag{3.4}$$

$$S_{12}(\rho, x/a, y/a) = \sum (a/r_{gs})^{12}, \tag{3.5}$$

where the sums in Eqs. (3.4) and (3.5) extend over the entire solid phase with fixed values of x/a, y/a. The S_6 and S_{12} have been evaluated for a number of sets

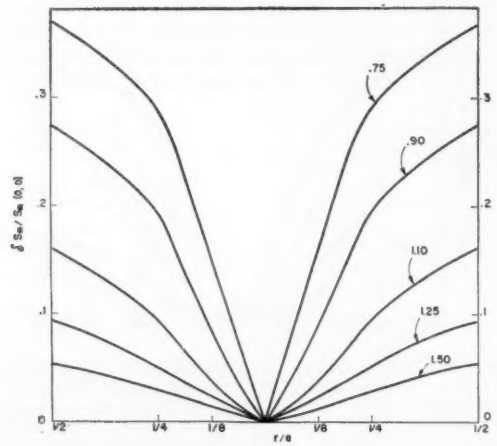

FIG. 3. The fractional change in the minimum of S as the distance from the center of the cell is varied along the diagonal bisector of the cell is plotted for several values of ρ^*.

of ρ, x/a, y/a by direct summation on an IBM 650 computer. The lattice chosen was simple cubic, made up of only one kind of atoms. (This particular lattice was chosen for its utility in giving functions for more complex cubic lattices.) The results of these computations are given in Appendix 1.

As pointed out previously, monolayer adsorption properties depend primarily upon the magnitude and variation of the minimum of the potential energy. Thus, we desire information concerning $S_m(x/a, y/a, \rho^*)$, the minimum of S with respect to ρ. Therefore, S was calculated as a function of ρ at a number of values of ρ^* for each position considered in Appendix 1.

It is convenient to present many of the results of this calculation in terms of the ratios of the parameters of the potential-energy curve at finite ρ^* to the parameters obtained with $\rho^*=\infty$. The potential-energy curve for $\rho^*=\infty$ corresponds to the well-known case of an atom interacting with a structureless planar surface. When the equation for the energy of interaction of an atom with this surface is written in the notation of the present work, one obtains

$$\epsilon=4\epsilon^*\rho_\infty^{*3}\pi\left[-\tfrac{1}{6}(\rho_\infty^*/\rho)^3+\tfrac{1}{45}(\rho_\infty^*/\rho)^9\right]$$
$$=4\epsilon^*\rho_\infty^{*3}(\rho_\infty^{*3}S_\infty). \tag{3.6}$$

The minimum value of $\rho_\infty^{*3}S_\infty$ is denoted by $\rho_\infty^{*3}S_{m\infty}$ and is equal to 0.552. The value of ρ corresponding to this minimum is denoted by $\rho_{m\infty}$ and is equal to $0.858\rho_\infty^*$. In Fig. 1, the ratio of $\rho^{*3}S_m(0, 0)$ at finite ρ^* to its value at $\rho^*=\infty$ is plotted, and it is seen that the net attractive energy of an atom over the center of an adsorption site is strongly enhanced by the presence of surface structure. The ratio of the quantity ρ_m/ρ^* at finite ρ^* to its value at $\rho^*=\infty$ is also plotted, and, as expected, shows that the adsorbed atoms penetrate more deeply into the plane of the surface as the structure of the surface becomes more coarse grained. The properties of an adsorbed atom are also dependent upon the shape of the potential curve near its minimum, and thus the numerous calculated potential curves were analyzed to ascertain if any simple empirical parameter could be obtained which would give a simple characterization of the widths and anharmonicities of the curves near their minima. It was found that these quantities depended primarily upon ρ^*, and almost not at all upon x/a, y/a. [This observation provides the basis for the assumption leading to Eq. (2.8).] Furthermore, the value of S at $\rho=\rho_m+0.1\rho^*$ was found to be equal to its value at $\rho=\rho_m-0.06\rho^*$, to within the accuracy of the calculation. In view of these facts, it was concluded that the shape of the potential curves for a given ρ^* could be reasonably well characterized by specifying a single parameter $s_\pm$, which is defined as

$$s_\pm(x/a, y/a)$$
$$=\tfrac{1}{2}[S(\rho_m+0.1\rho^*)+S(\rho_m-0.06\rho^*)-2S_m]/S_m(0, 0). \tag{3.7}$$

The final $s_\pm$ is the value of the individual $s_\pm(x/a, y/a)$ averaged over all positions at fixed ρ^*. It is easily shown that $s_{\pm\infty}$, the limiting value of $s_\pm$ at $\rho^*=\infty$, is equal to 0.102. The ratio of $s_\pm$ at finite ρ^* to $s_{\pm\infty}$ is also plotted in Fig. 1.

Figure 3 shows the fractional variation of S_m along a diagonal of the (100) face of a simple cubic lattice unit cell for a number of ρ^*, and Fig. 2 shows this variation along the perpendicular bisector of the face. The most interesting feature of Figs. 2 and 3 is the V-shaped variation near the center of the cell where the attractive energy is largest. In the absence of these results, a parabolic variation near the minimum has often been used to represent the potential energy on a site,[7] and a sinusoidal variation to represent the potential-energy function of the entire surface.[8] It is now clear that these potential functions are only qualitatively correct. (S_m was also computed for an atom over a close-packed cubic lattice by means of the equations given in Appendix 1. These calculations show that, although the absolute magnitude of S_m is larger for a given atom over a given close-packed lattice than for the simple cubic lattice, the form of the variation remains the same.)

By using the data plotted in Fig. 1 in combination with the curves shown in Figs. 2 and 3, one can estimate the values of $s_\pm$ and S_m for a wide range of ρ^* at any of the positions considered in Appendix 1. In Fig. 4, the variation of ρ_m with x/a, y/a is shown for a number of values of ρ^*. These data, combined with the curve shown in Fig. 1 allow one to estimate the value of ρ_m at any of the positions considered for a number of values of ρ^*.

[7] T. L. Hill, J. Chem. Phys. **17**, 762 (1949); W. A. Steele, J. Phys. Chem. **61**, 1551 (1957).
[8] T. L. Hill, J. Chem. Phys. **14**, 441 (1946).

The results reported here can be most conveniently used in the equations of Sec. 2 if the variation in the minimum of the potential energy over the area of the cell can be expressed as some simple function of the position coordinate. Furthermore, if a simple representation of this variation could be found, the parameters of the representation would be a measure of the degree of localization of an adsorbed monolayer at a given temperature. From Figs. 2 and 3, it is clear that a linear dependence of the potential minimum upon distance is both simple and accurate near the center of the cell. Two representations were considered,

$$\epsilon_r = 2Er/a \tag{3.8}$$

$$\epsilon_r = 2E'(x+y)/a, \tag{3.9}$$

where r is the radial distance from the center of the cell. It was found that the angular dependence of ϵ_r was not zero as implied by Eq. (3.8), but was about half that calculated from Eq. (3.9). Thus, Eqs. (3.8) and (3.9) are equally accurate, but neither of them represents ϵ_r at all angles to better than 10%. Equation (3.8) was taken to be the simplest adequate representation of ϵ_r for the purposes of this work. The E can also be written as $\epsilon_m(0, 0)$ times the slope of the curve of $\delta S_m/S_m(0, 0)$ versus reduced distance. This slope is plotted in Fig. 5 as a function of ρ^*.

Note that the form of the potential energy is in the present treatment, determined solely by the value of ρ^*, and that the magnitude of the energy depends upon ρ^* and ϵ^*. Recently, a number of papers have appeared in which approximate *a priori* estimates of σ and ϵ^* were given for specific adsorption systems.[9] ϵ^* has been calculated from various theoretical formulas for the dispersion energy and σ from the equation

$$\sigma = \tfrac{1}{2}(\sigma_{gg} + a/1.122), \tag{3.10}$$

where σ_{gg} is the parameter appearing in the Lennard-Jones expression for the interaction of a pair of gas atoms. Equation (3.10) can be used to give ρ^* in terms of the relative sizes of a gas atom and a solid atom

$$\rho^* = 0.4454(1+\sigma_{gg}/\sigma_{ss}). \tag{3.11}$$

By using these approximate expressions, the parameters required to compute the adsorption properties of a simple gas on a crystallographically perfect solid surface can be estimated from the atomic properties of the solid and gas.

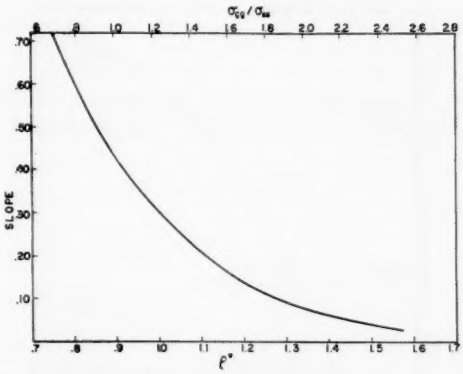

FIG. 5. The slope of the linear portions of the graphs in Figs. 2 and 3 is shown here as a function of ρ^*, and of σ_{gg}/σ_{ss} [calculated from Eq. (3.11)]. The points used in the computation were obtained by averaging the two slopes corresponding to the different directions of motions shown in Figs. 2 and 3. Thus, the curve shown involves the assumption that the angular variation of S_m can be neglected near the cell center. Since the midpoint of the cell edge corresponds to r/a of $\frac{1}{2}$, twice the slope gives the linearly extrapolated value of the fractional change in energy as the atom moves from the cell center to the cell edge. Thus, it can be seen that the energy of adsorption is 16% larger at the cell center than it is at the edge for a gas atom double the size of a solid atom.

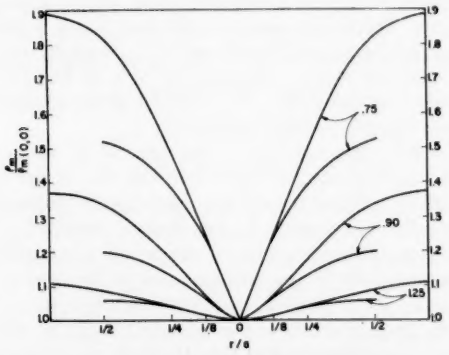

FIG. 4. The change in the most probable reduced distance ρ_m as the gas atom moves away from the cell center is plotted as a function of the distance from the cell center for various values of ρ^*. Two curves are shown for each ρ^*; the upper member of each pair shows the variation with distance along the diagonal bisector of the cell, and the lower curve shows the variation due to displacements along the perpendicular bisector of the cell edge.

[9] J. G. Aston, R. J. Tykodi, and W. A. Steele, J. Phys. Chem. **59,** 1053 (1955); R. A. Pierotti and G. D. Halsey, Jr., *ibid.* **63,** 680 (1959); E. L. Pace, *Proceedings of the Fourth Conference on Carbon* (Pergamon Press, New York, 1960), p. 35; J. R. Sams, Jr., G. Constabaris, and G. D. Halsey, Jr., J. Phys. Chem. **64,** 1689 (1960).

4. EVALUATION OF PARAMETERS

The $1/p_0$ can now be computed from Eq. (2.9). When the origin of τ is taken to be at the center of the cell, one can write

$$\epsilon_m(0, z_m) = 4\rho^{*6}\epsilon^* S_m(0, 0, \rho^*) \tag{4.1}$$

$$\epsilon_r(\tau, z) = 2E(r/a). \tag{4.2}$$

Furthermore, if one writes the z variation in ϵ_z as

$$\epsilon_z(z-z_m) = K_z/2(\Delta z)^2 + b(\Delta z)^3,$$

then it follows from the definition of $s_\pm$ and the observation that $S(\rho_m+0.1\rho^*) = S(\rho_m-0.06\rho^*)$ that

$$K_z = 422.2 s_\pm \epsilon_m(0, 0)/\sigma^2$$

$$b = -1111 s_\pm \epsilon_m(0, 0)/\sigma^3. \tag{4.3}$$

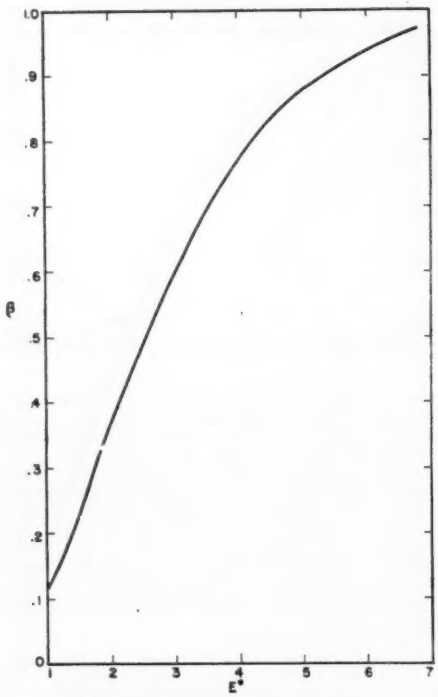

FIG. 6. Here, a plot of β calculated by numerical integration of Eq. (4.9) is shown as a function of the parameter E^*, which has been defined to be equal to $2E\sigma_{gg}/akT$. Remembering that E is equal to the difference in adsorption energy between an atom over the cell center and over the midpoint of a cell edge, calculated by linear extrapolation, it is clear that E^* large corresponds to a large variation in the potential energy with motion parallel to the surface. Thus, in this calculation, E^* large corresponds to sitewise adsorption with no intersite lateral interaction. The fact that the actual values of β are less than the Langmuir value of one is due to the contribution of those configurations in which two atoms are present in the same cell without lateral repulsive interactions. Since E^* is proportional to the ratio of adsorbed atom size to cell size, it is clear that a small E^* will correspond to an enhanced probability of finding two noninteracting atoms in the same cell.

These values of K_z and b can now be substituted into the well-known expression for the energy levels of a perturbed harmonic oscillator[10] to give

$$\epsilon_z(n)/k=(n+\tfrac{1}{2})(143.1\cdot10^{-8}/\sigma)[s_{\pm}\epsilon_m(0,0)/Mk]^{\frac{1}{2}} -[\tfrac{15}{4}(n+\tfrac{1}{2})^2+\tfrac{7}{16}](336\cdot10^{-16}/\sigma^2M), \quad (4.4)$$

where M is the gram molecular weight of the adsorbed substance.

As can be seen from Figs. 2 and 3, Eq. (4.2) is a rather poor representation of ϵ_r for ρ^* small. However, when this expression is substituted into Eq. (2.9), it emerges that the error in p_0 due to this approximation will be small when $E/kT\gg1$, and when $E/kT\ll1$. The integration in Eq. (2.9) was carried out using Eq. (4.2) and two simple boundary conditions:

Circular cell of diameter a:

$$1/p_0=(2\pi kT/m)^{\frac{1}{2}}(a^2h/4E^2) \times\{1-\exp[-E/kT](1+E/kT)\} \times\exp[-\epsilon_m(0,z_m)/kT]\sum_n\exp[-\epsilon_z(n)/kT]; \quad (4.5)$$

Square cell of edge a: The integral of (2.9) cannot be given in closed form in this case. However, one can obtain series expansions for $1/p_0$ if $E/kT\gg1$ by integrating over the circle of diameter a, and by evaluating the integral over the remainder of the area of the cell by writing a Taylor series expansion of $\exp(-E/kT)$ around the point $r=a$ and integrating term by term. Furthermore, $1/p_0$ can be obtained for $E/kT\ll1$ by expanding the exponential and integrating term by term. The results of these calculations are most conveniently given in terms of the ratio of $1/p_0$ for a square of side a to $1/p_0$ for a circular cell of diameter a, all other parameters identical;

$$\frac{(1/p_0)\ (\text{square})}{(1/p_0)\ (\text{circle})} =1+\exp[-E/kT][0.2146-0.0270(E/kT)\cdots] \qquad E/kT\gg1. \quad (4.6)$$

$$=4/\pi\{1-0.4319(E/kT)\cdots\} \qquad E/kT\ll1. \quad (4.7)$$

The evaluation of β is considerably more tedious than that of $1/p_0$, and requires more drastic approximations. This is due partly to the fact that β depends on $\epsilon_{gg}{}^*$ and σ_{gg} as well as ϵ^* and ρ^*, and partly to the fact that the range of integration of τ_2 in Eq. (2.10) extends over many cells. Nevertheless, β was evaluated for two relatively simple models.

The first case considered was that of an adsorbed atom which is small compared to the size of the cell, and which is characterized by a hard-sphere interaction with other gas atoms. It was further assumed that E/kT was sufficiently large to ensure that the adsorbed atoms remained in the neighborhood of the centers of the cells. This implies that the contributions to β due to the interaction of two adsorbed atoms in different cells is negligible, and that the limit of integration of r_1 can be taken to be ∞. Since $f_{12}=-1$ for $r_{12}\leq\sigma_{gg}$ and is equal to zero at all other r_{12}, Eq. (2.10) can be written as

$$\beta=\frac{\displaystyle\int_0^{\infty}\int_{0_{(r_{12}<\sigma_{gg})}}^{a/2}\exp[-2E(r_1+r_2)/akT]d\tau_1d\tau_2}{[(akT/2E)^2 2\pi\{1-\exp[-E/kT](1+E/kT)\}]^2} \quad (4.8)$$

[10] L. I. Schiff, *Quantum Mechanics* (McGraw-Hill Book Company, Inc., New York, 1955), p. 306.

for a circular cell of diameter a. The E^* and R^* are defined as

$$E^*=2E\sigma_{gg}/akT, \qquad R^*=r/\sigma_{gg}.$$

Let ϕ be defined as the angle between $\mathbf{r}_1$ and $\mathbf{r}_2$. Then the limits of integration of R_2^* and ϕ are obtained from the requirement that $f_{12}=-1$ only within a circle of radius $=1$, centered at R_1^*. Equation (4.9) now gives β as

$$\beta=E^{*4}/\pi\Bigg[\int_0^1 \exp[-E^*R_1^*]R_1^*dR_1^*\int_0^\pi d\phi\int_0^{R_1^*\cos\phi+(1-R_1^{*2}\sin^2\phi)^{\frac{1}{2}}} \exp[-E^*R_2^*]R_2^*dR_2^*$$

$$+\int_1^\infty \exp[-E^*R_1^*]R_1^*dR_1^*\int_0^{\sin^{-1}(R_1^*)^{-1}} d\phi\int_{R_1^*\cos\phi-(1-R_1^{*2}\sin^2\phi)^{\frac{1}{2}}}^{R_1^*\cos\phi+(1-R_1^{*2}\sin^2\phi)^{\frac{1}{2}}} \exp[-E^*R_2^*]R_2^*dR_2^*.\Bigg] \quad (4.9)$$

The expression for β now depends solely upon the value of E^*. Equation (4.9) was integrated, with the integrations with respect to R_1^* and ϕ being carried out numerically, and the results are shown in Fig. 6.

The second approximate computation of β is a partial evaluation which is designed to be of use in systems where the adsorbate-adsorbate interactions are relatively large. If f_{12} is a reasonably well-known function, β may be conveniently computed by numerical integration, using tabulated functions which depend upon the cell geometry. A new reduced distance variable is defined as $r^\ddagger=2r/a$. The β may be written as

$$\beta=-2\int_0^\infty f_{12}(r_{12}^\ddagger)I(r_{12}^\ddagger, E/kT)r_{12}^\ddagger dr_{12}^\ddagger, \quad (4.10)$$

where

$$I(r_{12}^\ddagger, E/kT)=\frac{\int_0^\pi\int_0^1 \exp[-\epsilon(r_1^\ddagger)/kT]r_1^\ddagger dr_1^\ddagger \exp[-\epsilon(r_\theta^\ddagger)/kT]d\theta}{\pi(kT/E)^4\{1-\exp[-E/kT](E/kT+1)\}^2}, \quad (4.11)$$

where θ is the angle between $\mathbf{r}_1$ and $\mathbf{r}_{12}$,

$$r_\theta^\ddagger=(|r_{12}^{\ddagger 2}+r_1^{\ddagger 2}-2r_1^\ddagger r_{12}^\ddagger\cos\theta|)^{\frac{1}{2}}. \quad (4.12)$$

It is now necessary to write down an expression for $\epsilon(r_\theta^\ddagger)$. In order to eliminate the angular dependence of the integrands in the equation for $I(r_{12}^\ddagger, E/kT)$, the following approximate form was used for $\epsilon(r_\theta^\ddagger)$,

$$\begin{aligned}\epsilon(r_\theta^\ddagger)&=Er_\theta^\ddagger & 0<r_\theta^\ddagger<1\\ &=E(2-r_\theta^\ddagger) & 1<r_\theta^\ddagger<2\\ &=E(r_\theta^\ddagger-2) & 2<r_\theta^\ddagger<3.\end{aligned} \quad (4.13)$$

Since f_{12} is finite for all r_{12}, Eq. (4.11) should be integrated for all values of $0<r_{12}^\ddagger<\infty$. For convenience, it is assumed that f_{12} is negligible for r_{12} greater than three times the cell radius. [In general, if the adsorbed atoms are sufficiently large to have an appreciable interaction at r_{12} greater than three cell radii, ρ^* will be large enough to result in relatively small values of E/kT. In such systems, $I(r_{12}^\ddagger, E/kT)$ will be nearly one at all $r_{12}^\ddagger$.] Equation (4.11) was integrated numerically for a number of values of E/kT and $r_{12}^\ddagger$ using Eq. (4.13) for $\epsilon(r_\theta^\ddagger)$. The results are tabulated in Appendix 2.

This calculation should give reasonably accurate results in those systems where either $-u(r_{ij})/kT$ or E/kT is small. However, if the value of a is such that $-u(r_{ij}=a)/kT$ is quite large, the neglect of the angular dependence of the surface energy at this distance will result in a value of β which will show a larger attractive contribution than is actually the case. This is due to the fact that $\epsilon(r_\theta^\ddagger)$ at $r_\theta=a$ is actually repulsive for much of the range of θ in contrast to the prediction of Eq. (4.13). It is interesting to note that the inclusion of the variation of the surface-energy parallel to the surface will nearly always be expected to result in an apparent decrease in the contribution of the attractive gas-gas interaction which would be calculated on the basis of a structureless surface. This is due to the fact that the variations in the surface potential are, in effect, repulsive everywhere except when an atom is at the center of a site. Thus, the attractive gas-gas pair interaction must be combined with a repulsive surface interaction at all points other than those configurations in which both atoms of the pair are at or near the centers of sites. Since the site centers take up only a small fraction of the area of integration, it is clear that it is highly likely that the presence of such surface variations in potential energy will result in a reduction of the attractive contribution to β.

One further mathematical approximation which has been made in the calculation of $1/p_0$ and β should be mentioned. This is the assumption that the domain of integration of r is a planar surface. Since the atoms are restricted to be at or near the minima of the z-dependent part of the potential, and these minima do not occur at a single value of z (see Fig. 4), this assumption is incorrect. While this is not a serious approximation in

the calculation of $1/p_0$, and can be taken into account by proper definitions of the distance scales, the calculations of β involve the approximation that r_1, r_2, and r_{12} form a triangle in the plane of the surface. If E is small, the accompanying changes in ρ_m are also small, and the domain of r is nearly planar. If E/kT is large, the chief contributions to the integrand are due to configurations in which one or both of the atoms is near the center of a site. The calculation of r_{12} will be accurate in these cases, assuming that the distance scales are properly defined; however, if both atoms are displaced from the cell centers, r_{12} will be shorter (for a given r_1 and r_2) than would be calculated in the absence of the approximation of a planar surface. However, in view of the rather drastic assumptions made here concerning the functional dependence of the parallel variations of the potential energy, it is doubtful that the additional labor required to eliminate this approximation would be worthwhile.

5. DISCUSSION

Hill[8] has discussed the transition from localized to mobile adsorption, and has shown that an appreciable amount of quantum-mechanical barrier penetration can occur at $E/kT\simeq 0.15$, using parameters which were presumed to be characteristic of the argon-potassium chloride adsorption system. Although the results of the present classical computation cannot be strictly compared with Hill's result, it is clear that the properties of such a system could not be expected to correspond to a perfectly mobile film even at temperatures considerably higher than the temperature of the maximum in the heat capacity found by Hill. It should be pointed out that the position and magnitude of this maximum are strongly dependent upon the form of the potential energy barrier, as well as its height. It is highly likely that the use of a barrier of the form shown in Figs. 2 and 3, rather than the sinusoidal barrier used by Hill, will lead to a heat-capacity curve in which the maximum is less pronounced as well as being shifted to a higher temperature.

The most general equation of state for a perfectly mobile film is that of the two-dimensional virial expansion. Equation (2.2) reduces to this equation as $E/kT\to 0$, and

$$\lim_{E/kT\to 0} 1/p_0=[A_s h/(2\pi mkT)^{\frac{1}{2}}kT]\times\exp[-\epsilon_m(0,z_m)/kT]\sum_n \exp[-\epsilon_z(n)/kT] \quad (5.1)$$

$$\lim_{E/kT\to 0} (\beta)=-2\pi/A_s\int_0^\infty f_{12}r_{12}dr_{12}. \quad (5.2)$$

Equation (5.2) implies that

$$\lim_{E/kT\to 0} I(r_{12}^{\ddagger}, E/kT)=1. \quad (5.3)$$

When $\exp(-E/kT)$ is expanded in Eq. (4.5), $1/p_0$ may be written

$$1/p_0=A_s h(2\pi m)^{-\frac{1}{2}}(kT)^{-\frac{1}{2}}\times\exp[-\epsilon_m(0,z_m)/kT]\sum\exp[-\epsilon_z(n)/kT]\times\{1-(\tfrac{2}{3})(E/kT)+\cdots\}. \quad (5.4)$$

When $E/kT=0.5$, it can be seen that $1/p_0$ is about 25% less than its limiting value. A 25% error in $1/p_0$ will generally be undetectable because of the large exponential factor in Eq. (5.4), and thus it appears that the comparison of β with its high temperature limit is a more sensitive method of determining the magnitude of E/kT than a consideration of $1/p_0$. At $E/kT=1$, it is seen that I deviates appreciably from its high temperature limit. Therefore, it does not seem that the detailed analysis of adsorption systems by means of the two-dimensional virial equation, or any of the less exact two-dimensional equations of state will give correct results unless $E/kT\simeq 0.5$ or less.

In I, it was shown that Eq. (2.2) reduces to the Langmuir equation if the adsorbed atoms in different cells do not interact, and if the cells were such as to require an infinite repulsive energy between any two atoms in the same cell. In the present notation, Eq. (2.4) reduces to the Langmuir equation when $\beta=1$, and δ and higher terms are zero. Thus, the present calculation of β for hard-sphere atoms with E/kT large is a generalized version of the Langmuir model, and it can be seen from Fig. 6 that β is very nearly equal to one for $E/kT>5$. The effect of the introduction of attractive interactions between atoms in neighboring cells will tend to reduce the value of β at constant E/kT, and to result in a greater degree of mobility within the cell. The magnitude of this effect can be estimated for a particular combination of adsorbent and absorbate by use of the results of Appendix 2. In sitewise models which include lateral interactions, the assumption is made that these lateral interactions are not sufficiently strong to influence the probability distribution function of an isolated atom within its cell, but merely influence the spatial distribution of occupied and unoccupied cells. However, in the absence of detailed calculations of the effect of lateral interactions on the cell probability distribution functions, the results of the present work may be taken to indicate that it is unlikely that sitewise models will be realistic representations of systems in which $E/kT<5$.

APPENDIX 1

Here, the results of machine calculations of the sums of inverse 6th and 12th powers of the reduced interatomic distances are tabulated as a function of the reduced distance ρ of the gas atom from the surface of a planar, semi-infinite, simple cubic solid which has its (100) face exposed. The sums are given by the expres-

TABLE I. Sums of the inverse sixth and twelfth powers of the gas atom-solid atom distances for a simple cubic solid.

ρ	$S_6(0,0)$	$S_{12}(0,0)$	$S_6(0,1/8)$	$S_{12}(0,1/8)$	$S_6(0,\frac{1}{4})$	$S_{12}(0,\frac{1}{4})$	$S_6(0,\frac{1}{2})$	$S_{12}(0,\frac{1}{2})$
0.00	3.4177(+1)	2.5639(+2)	4.3388(+1)	5.9231(+2)	7.1641(+1)	2.1550(+3)	1.3213(+2)	8.1936(+3)
0.05	3.3458	2.4873	4.2414	5.7037	6.9794	2.0544	1.2807	7.7186
0.10	3.1884	2.2752	4.0135	5.1031	6.5114	1.7844	1.1736	6.4755
0.15	2.9600	1.9673	3.6817	4.2597	5.8342	1.4211	1.0217	4.8857
0.20	2.6814	1.6143	3.2833	3.3388	5.0441	1.0478	8.5101(+1)	3.3633
0.25	2.3759	1.2636	2.8566	2.4770	4.2326	7.2377(+2)	6.8410	2.1483
0.30	2.0650	9.4896(+1)	2.4344	1.7547	3.4687	4.7417	5.3543	1.2954
0.35	1.7659	6.8794	2.0406	1.1975	2.7932	2.9826	4.1144	7.4928(+2)
0.40	1.4903	4.8437	1.6891	7.9403(+1)	2.2226	1.8216	3.1266	4.2159
0.45	1.2449	3.3315	1.3855	5.1543	1.7559	1.0908	2.3641	2.3343
0.50	1.0322	2.2504	1.1298	3.2974	1.3829	6.4576(+1)	1.7871	1.2837
0.55	8.5151(0)	1.5000	9.1835(0)	2.0906	1.0892	3.8045	1.3557	7.0616(+1)
0.60	7.0048	9.9076(0)	7.4573	1.3197	8.6008(0)	2.2424	1.0349	3.9064
0.65	5.7567	6.5075	6.0604	8.3244(0)	6.8208	1.3277	7.9643(0)	2.1816
0.70	4.7336	4.2632	4.9363	5.2622	5.4397	7.9208(0)	6.1869	1.2334
0.75	3.8994	2.7926	4.0342	3.3409	4.3666	4.7717	4.8547	7.0726(0)
0.80	3.2216	1.8327	3.3109	2.1339	3.5300	2.9072	3.8491	4.1188
0.85	2.6713	1.2070	2.7304	1.3729	2.8748	1.7932	3.0837	2.4378
0.90	2.2245	7.9882(−1)	2.2636	8.9049(−1)	2.3588	1.1204	2.4957	1.4669
0.95	1.8613	5.3176	1.8870	5.8268	1.9499	7.0931(−1)	2.0398	8.9758(−1)
1.00	1.5651	3.5634	1.5821	3.8478	1.6237	4.5505	1.6828	5.5837
1.05	1.3230	2.4052	1.3342	2.5651	1.3617	2.9579	1.4007	3.5305
1.10	1.1242	1.6360	1.1316	1.7264	1.1498	1.9477	1.1757	2.2681
1.15	9.6036(−1)	1.1217	9.6527(−1)	1.1732	9.7741(−1)	1.2988	9.9454(−1)	1.4797
1.20	8.2466	7.7546(−2)	8.2800	8.0497(−2)	8.2943	8.7678(−2)	8.4747	9.7975(−2)
1.25	7.1177	5.4056	7.1410	5.5758	7.1945	5.9894	7.2709	6.5805
1.30	6.1753	3.7998	6.1904	3.8987	6.2262	4.1386	6.2774	4.4805
1.40	4.7152	1.9252	4.7218	1.9592	4.7379	2.0416	4.7600	2.1585
1.50	3.6643	1.0080	3.6674	1.0200	3.6740	1.0490	3.6855	1.0900
1.60	2.8954	5.4480(−3)	2.8963	5.4912(−3)	2.9000	4.5955(−3)	2.9047	5.7434(−3)
1.70	2.3215	3.0350	2.3222	3.0509	2.3235	3.0893	2.3260	3.1437
1.80	1.8860	1.7399	1.8867	1.7458	1.8875	1.7603	1.8880	1.7806
1.90	1.5509	1.0246	1.5515	1.0269	1.5519	1.0324	1.5518	1.0402
2.00	1.2899	6.1871(−4)	1.2897	6.1960(−4)	1.2902	6.2174(−4)	1.2892	6.2477(−4)
2.10	1.0831	3.8245	1.0825	3.8280	1.0823	3.8364	1.0824	3.8484
2.20	9.1641(−2)	2.4159	9.1692(−2)	2.4173	9.1680(−2)	2.4207	9.1736(−2)	2.4254
2.30	7.8294	1.5570	7.8294	1.5576	7.8280	1.5590	7.8346	1.5609
2.40	6.7392	1.0224	6.7361	1.0226	6.7346	1.0232	6.7316	1.0240
2.50	5.8286	0.6830	5.8285	0.6831	5.8221	0.6833	5.8335	0.6837

ρ	$S_6(1/8,1/8)$	$S_{12}(1/8,1/8)$	$S_6(\frac{1}{4},\frac{1}{4})$	$S_{12}(\frac{1}{4},\frac{1}{4})$	$S_6(3/8,3/8)$	$S_{12}(3/8,3/8)$	$S_6(\frac{1}{2},\frac{1}{2})$	$S_{12}(\frac{1}{2},\frac{1}{2})$
0.00	6.2662(+1)	2.1143(+3)	5.2350(+2)	2.6218(+5)				
0.05	6.1023	2.0071	4.9357	2.3281				
0.10	5.6917	1.7222	4.1701	1.6523				
0.15	5.1017	1.3465	3.2152	9.7134(+4)				
0.20	4.4175	9.7073(+2)	2.3175	4.9580				
0.25	3.7185	6.5462	1.6001	2.3033				
0.30	3.0628	4.1910	1.0807	1.0140	5.6608(+2)	3.1471(+5)		
0.35	2.4835	2.5837	7.2569(+1)	4.3624(+3)	2.7975	7.5706(+4)		
0.40	1.9932	1.5531	4.9004	1.8750	1.4710	2.0439		
0.45	1.5902	9.1995(+1)	3.3528	8.1696(+2)	8.1999(+1)	6.1329(+3)		
0.50	1.2656	5.4149	2.3346	3.6427	4.8236	2.0223	6.6908(+1)	4.0971(+3)
0.55	1.0075	3.1874	1.6581	1.6715	2.9805	7.2497(+2)	3.8726	1.3060
0.60	8.0386(0)	1.8852	1.2018	7.9166(+1)	1.9257	2.7984	2.3749	4.6006(+2)
0.65	6.4380	1.1239	8.8877(0)	3.8755	1.2954	1.1535	1.5316	1.7632
0.70	5.1810	6.7697(0)	6.6990	1.9613	9.0356(0)	5.0423(+1)	1.0322	7.2634(+1)
0.75	4.1928	4.1250	5.1397	1.0255	6.5088	2.3237	7.2309(0)	3.1861
0.80	3.4136	2.5447	4.0084	5.5330(0)	4.8244	1.1233	5.2399	1.4772
0.85	2.7971	1.5900	3.1731	3.0765	3.6666	5.6720(0)	3.9109	7.1952(0)
0.90	2.3070	1.0063	2.5461	1.7598	2.8486	2.9807	2.9947	3.6642
0.95	1.9153	6.4503(−1)	2.0683	1.0338	2.2559	1.6249	2.3446	1.9430
1.00	1.6007	4.1869	1.6991	6.2261(−1)	1.8165	9.1626(−1)	1.8710	1.0691
1.05	1.3463	2.7513	1.4100	3.8373	1.4842	5.3302	1.5181	6.0852(−1)
1.10	1.1396	1.8297	1.1810	2.4164	1.2282	3.1912	1.2495	3.5736
1.15	9.7053(−1)	1.2310	9.9755(−1)	1.5521	1.0279	1.9619	1.0414	2.1599
1.20	8.3148	8.3759(−2)	8.4914	1.0156	8.6878(−1)	1.2359	8.7740(−1)	1.3405
1.25	7.1960	5.7269	7.2798	6.7591(−2)	7.4076	7.9625(−2)	7.4625	8.5247(−2)

TABLE I (*continued*)

ρ	$S_6(1/8, 1/8)$	$S_{12}(1/8, 1/8)$	$S_6(\frac{1}{4}, \frac{1}{4})$	$S_{12}(\frac{1}{4}, \frac{1}{4})$	$S_6(3/8, 3/8)$	$S_{12}(3/8, 3/8)$	$S_6(\frac{1}{2}, \frac{1}{2})$	$S_{12}(\frac{1}{2}, \frac{1}{2})$
1.30	6.2058	4.0054	6.2823	4.5705	6.3662	5.2369	6.4016	5.5439
1.40	4.7284	1.9953	4.7625	2.1819	4.7985	2.3940	4.8138	2.4896
1.50	3.6710	1.0325	3.6862	1.0963	3.7017	1.1668	3.7084	1.1980
1.60	2.8977	5.5359(−3)	2.9054	5.7608(−3)	2.9124	6.0037(−3)	2.9153	6.1097(−3)
1.70	2.3227	3.0672	2.3257	3.1486	2.3290	3.2350	2.3310	3.2723
1.80	1.8872	1.7519	1.8886	1.7821	1.8895	1.8137	1.8903	1.8272
1.90	1.5520	1.0292	1.5523	1.0406	1.5526	1.0524	1.5533	1.0575
2.00	1.2900	6.2050(−4)	1.2900	6.2490(−4)	1.2896	6.2942(−4)	1.2890	6.3134(−4)
2.10	1.0821	3.8315	1.0823	3.8488	1.0823	3.8664	1.0821	3.8738
2.20	9.1685(−2)	2.4187	9.1662(−2)	2.4256	9.1699(−2)	2.4326	9.1678(−2)	2.4355
2.30	7.8287	1.5582	7.8253	1.5610	7.8340	1.5638	7.8287	1.5650
2.40	6.7322	1.0228	6.7351	1.0240	6.7369	1.0251	6.7381	1.0256
2.50	5.8318	0.6832	5.8321	0.6837	5.8322	0.6841	5.8332	0.6843

ρ	$S_6(1/8, 3/8)$	$S_{12}(1/8, 3/8)$	$S_6(\frac{1}{4}, \frac{1}{2})$	$S_{12}(\frac{1}{4}, \frac{1}{2})$
0.00	2.8176(+2)	6.8945(+4)		
0.05	2.6899	6.2694		
0.10	2.3561	4.7557		
0.15	1.9162	3.0820		
0.20	1.4713	1.7633	9.3654(+2)	8.6232(+5)
0.25	1.0855	9.2227(+3)	5.1922	2.6216
0.30	7.8194(+1)	4.5532	2.8844	7.9517(+4)
0.35	5.5721	2.1786	1.6369	2.4955
0.40	3.9663	1.0309	9.5856(+1)	8.2495(+3)
0.45	2.8395	4.8954(+2)	5.8174	2.8931
0.50	2.0534	2.3562	3.6632	1.0777
0.55	1.5040	1.1566	2.3918	4.2569(+2)
0.60	1.1173	5.8156(+1)	1.6163	1.7774
0.65	8.4218(+0)	2.9997	1.1278	7.8172(+1)
0.70	6.4413	1.5886	8.1034(0)	3.6082
0.75	4.9966	8.6369(0)	5.9786	1.7417
0.80	3.9286	4.8177	4.5167	8.7638(0)
0.85	3.1283	2.7546	3.4851	4.5823
0.90	2.5209	1.6126	2.7398	2.4828
0.95	2.0541	9.6545(−1)	2.1898	1.3902
1.00	1.6910	5.9041	1.7758	8.0258(−1)
1.05	1.4054	3.6837	1.4589	4.7657
1.10	1.1784	2.3421	1.2124	2.9046
1.15	9.9606(−1)	1.5159	1.0179	1.8134
1.20	8.4833	9.9764(−2)	8.6236(−1)	1.1576
1.25	7.2753	6.6697	7.3668	7.5424(−2)
1.30	6.2798	4.5255	6.3393	5.0081
1.40	4.7615	2.1702	4.7869	2.3233
1.50	3.6859	1.0932	3.6974	1.1439
1.60	2.9046	5.7520(−3)	2.9099	5.9263(−3)
1.70	2.3255	3.1461	2.3277	3.2079
1.80	1.8883	1.7814	1.8888	1.8039
1.90	1.5520	1.0404	1.5520	1.0488
2.00	1.2899	6.2483(−4)	1.2891	6.2805(−4)
2.10	1.0830	3.8486	1.0829	3.8611
2.20	9.1718(−2)	2.4255	9.1679(−2)	2.4306
2.30	7.8299	1.5609	7.8305	1.5629
2.40	6.7349	1.0240	6.7344	1.0248
2.50	5.8327	0.6837	5.8377	0.6840

ρ	$S_6(0, 0)$	$S_{12}(0, 0)$
2.5	5.8553(−2)	6.8310(−5)
2.6	5.1032	4.6373
2.7	4.4734	3.1953
2.8	3.9422	2.2324
2.9	3.4916	1.5799
3.0	3.1059	1.1317
3.1	2.7743	8.1974(−6)
3.2	2.4885	6.0011
3.3	2.2384	4.4369
3.4	2.0224	3.3112
3.5	1.8337	2.4928
3.6	1.6652	1.8923
3.7	1.5168	1.4477
3.8	1.3872	1.1157
3.9	1.2712	0.8660
4.0	1.1669	0.6766

TABLE II. Computed values of $I(r_{12}^{\ddagger}, E/kT)$.

$r_{12}^{\ddagger}$ \ E	0.5	1.0	2.0	3.0	4.0	5.0	6.0	8.0
0.1	1.014	1.061	1.275	1.687	2.326	3.201	4.293	6.998
0.2	1.013	1.054	1.241	1.590	2.105	2.758	3.502	5.045
0.3	1.011	1.044	1.193	1.457	1.817	2.228	2.633	3.242
0.4	1.009	1.033	1.137	1.309	1.520	1.725	1.879	1.949
0.5	1.008	1.023	1.080	1.163	1.247	1.298	1.294	1.120
0.6	1.008	1.015	1.028	1.034	1.016	0.963	0.872	0.623
0.7	1.009	1.011	0.990	0.932	0.839	0.719	0.587	0.341
0.8	1.013	1.014	0.970	0.867	0.722	0.562	0.413	0.192
0.9	1.021	1.025	0.976	0.851	0.677	0.493	0.332	0.126
1.0	1.032	1.048	1.015	0.896	0.716	0.520	0.346	0.125
1.1	1.048	1.082	1.092	1.010	0.851	0.656	0.466	0.194
1.2	1.064	1.120	1.188	1.173	1.068	0.896	0.698	0.353
1.3	1.080	1.160	1.300	1.377	1.358	1.244	1.061	0.646
1.4	1.098	1.204	1.424	1.614	1.721	1.715	1.600	1.172
1.5	1.113	1.244	1.548	1.872	2.152	2.327	2.365	2.076
1.6	1.127	1.280	1.668	2.142	2.640	3.082	3.399	3.553
1.7	1.136	1.306	1.765	2.383	3.126	3.918	4.668	5.759
1.8	1.141	1.323	1.835	2.581	3.573	4.773	6.108	8.820
1.9	1.144	1.331	1.874	2.705	3.884	5.435	7.344	12.037
2.0	1.144	1.334	1.895	2.765	4.021	5.712	7.858	13.506

sions

$$S_{2j}=\sum_l\sum_m\sum_n\{[l+(x/a)^2]+[m+(y/a)]^2+(n+\rho)^2\}^{-j}$$
$$=\sum_l\sum_m\sum_n U^{-j}, \qquad \text{(A.1)}$$

where the triple sums is taken over all integral values of l, m from $-\infty$ to $+\infty$, and n from 0 to $+\infty$. The sums were actually taken over all points having $U<50$, and approximated by integrals over the remainder of the range of the variables. In previous calculations of this type,[4] the sums were calculated at relatively small number of values of ρ, and interpolation formulas were fitted to these points. Here, the values of ρ are spaced sufficiently close to allow the direct calculation of energy versus distance curves without interpolation. However, if interpolation is required, this can be done by means of difference tables constructed from the tabular values. For this reason, the results are given to five significant figures. The actual accuracy of the sums varies somewhat, and is lower at large ρ. It is estimated to be about 0.5% at $\rho=2.5$.

The center of a lattice cell has been taken to be the origin of the position coordinate system, and the x and y axes were set perpendicular to the lattice cell edges. Thus, the pairs of numbers above the columns of figures denote the values of x/a, y/a used in Eq. (A.1).

It can be shown that the interpolation formulas given previously[4] are quite good over most of their range of validity, but that they are noticeably in error for $\rho<1$ at position (0, 0). This is due to the occurrence of a point of inflection in the sums versus distance curve which is not reproduced in the interpolation equations. This error is largest in $S_6(0, 0)$ at $\rho=0.70$, and amounts to 2% at this point. Although this may not appear to be very significant, it should be remembered that ϵ is proportional to the difference of two fairly large numbers, and this difference may be noticeably affected by an error of this magnitude in one of the terms. The sums are tabulated only for $\rho<2.5$, since it is apparent that all positions are essentially equivalent at this distance. However, the calculated values of S_6 and S_{12} are still appreciably different from their values over a structureless surface at this point. These limiting values are given by

$$S_6=\pi/6\rho^3=3.351(-2) \qquad \text{at } \rho=2.5$$
$$S_{12}=\pi/45\rho^9=1.806(-5) \qquad \text{at } \rho=2.5. \qquad \text{(A.2)}$$

Therefore, the sums for the (0, 0) position were extended out to $\rho=4$. The accuracy of these values was improved by summing over all $U<100$, and these data are shown in a special table. It can be seen that the sums are still appreciably different from their limiting values at $\rho=4$[0.818(−2) and 2.663(−7) for S_6 and S_{12}, respectively]. Thus, it is doubtful that the comparison of experimental adsorption energies with the integrated values of S_6 and S_{12} can result in realistic values for ϵ^* except when the comparison is made at extremely large distances from the surface.

The tabulated values (see Table I) of S_6 and S_{12} can be used to calculate potential energies in cubic systems more complex than simple cubic. For instance, the energy of an atom over the (100) plane of a face-centered cubic lattice made up of one kind of atom depends upon the lattice sum S_{fcc} which is given by

$$S_{fcc}[\rho, (x/a), (y/a)]=S[\rho, (x/a), (y/a)]$$
$$+S[\rho, (x/a)+0.5, (y/a)+0.5]$$
$$+S[\rho+0.5, (x/a), (y/a)+0.5]$$
$$+S[\rho+0.5, (x/a)+0.5, (y/a)], \qquad \text{(A.3)}$$

where a is the unit cell edge length of the face-centered cubic crystal, and the nonsubscripted S's denote lattice sums for a simple cubic lattice of lattice parameter a. Similarly, the lattice sum for a body-centered cubic lattice made up of one kind of atom is

$$S_{bcc}=S[\rho, (x/a), (y/a)] + S[\rho+0.5, (x/a)+0.5, (y/a)+0.5]. \quad \text{(A.4)}$$

It is obvious that lattice sums for cubic lattices containing more than one kind of atom can also be given in terms of combinations of the sums for the simple cubic lattice.

APPENDIX 2

The results of the numerical integration of Eq. (4.11) are presented here. Equations (4.12) and (4.13) were used to calculate $\epsilon(r_\theta^{\ddagger})$. The double integral was evaluated on an IBM 650 computer using a ten-point Gaussian quadrature for the θ and for the $r_1^{\ddagger}$ integrations. The tabular values are estimated to be correct to better than 0.5% (see Table II).

THE JOURNAL OF CHEMICAL PHYSICS VOLUME 35, NUMBER 3 SEPTEMBER, 1961

Monolayer Adsorption of Helium on Argon*

MARVIN ROSS† AND WILLIAM A. STEELE

Department of Chemistry, The Pennsylvania State University, University Park, Pennsylvania

(Received February 27, 1961)

Experimental isotherms and heats of adsorption of helium on an argon surface are reported for temperatures from 10° to 20°K. The potential energy of interaction of a helium atom with an argon surface is calculated by summing the He–Ar pair interaction over the solid lattice. The experimental data are analyzed in terms of a quantum mechanical modification of the theoretical treatment presented previously [W. A. Steele and M. Ross, J. Chem. Phys. **33,** 464 (1960) (I); **35,** 850 (1961) (II)]. It is shown that the adsorption properties calculated from the *a priori* potential function are in quantitative agreement with the experiments, in the region where a quantitative comparison can be made, and that the remainder of the data is in agreement with semiquantitative theoretical estimates. A detailed description of the probable adsorption process for the He–Ar system is deduced from the comparison between experiment and theory. It is concluded that the first half of the helium atoms comprising a monolayer on this surface are highly localized at equivalent positions over the argon lattice unit cells, and are nearly all in their quantum mechanical ground state at temperatures up to 20°K. The second half of the atoms in the monolayer is adsorbed over a different position relative to the solid lattice, and is more weakly bound than the first. Although the quantitative comparison between the theory and the experiment is somewhat limited because the quantum version of the theory is not as complete as the classical, it is concluded that the agreement between experiment and theory indicates that this approach to the problem of physical adsorption may prove useful in the analysis of data taken on other suitable systems.

1. INTRODUCTION

RECENTLY, the authors[1] presented a general treatment of monolayer physical adsorption on solids in which the properties of the adsorbed film were given explicitly as functions of the intermolecular potential energy of the adsorbed atoms with the solid and with each other. In this paper, measurements of the thermodynamic properties of helium adsorbed on an argon surface at temperatures from 10° to 20°K are reported. These data are then considered in the light of the general theory developed in papers I and II. The analysis of these experiments is particularly interesting in view of the fact that it is possible to make a quantitative comparison of the observed data with an *a priori* computation of the adsorption properties. This follows from the fact that it was shown in II that the microscopic properties of the helium-argon system should be completely determined by: the helium-helium pair interaction, the helium-argon pair interaction function, and the size and crystal type of the unit cell of solid argon. Since all these quantities are known to a good degree of accuracy, it is clear that the comparison of these experiments with theory should provide a critical test of the theory.

The adsorbent used in these experiments consisted of a sample of a relatively high-area titanium dioxide powder (B.E.T. nitrogen area 65 m^2/g) which was coated with an amount of argon slightly in excess of one B.E.T. monolayer. The assumption that this mixed adsorbent is equivalent to a high-area crystal of pure argon implies that the effect of replacing argon atoms by TiO_2 molecules in the interior of the solid has a negligible effect on the surface properties of the material. In actual fact, it has been previously shown that the surface properties of the outermost layer of a TiO_2 sample are essentially the same as those of the argon-

* This work supported in part by the Office of Ordnance Research and in part by the National Science Foundation.

† Present address: Department of Chemistry, University of California, Berkeley, California.

[1] W. A. Steele and M. Ross, J. Chem. Phys. **33,** 464 (1960) (I); **35,** 850 (1961) (II).

covered sample[2] and thus the error introduced by approximating a pure argon crystal by the mixed adsorbent should be negligibly small. A somewhat more difficult problem is encountered in estimating the area of the coated sample, since it was also shown in the previous work that preadsorption can have a large effect upon the area available for further adsorption.[3] In order to have some independent measure of surface area, an argon isotherm was determined at 90°K up to relatively high coverages (in excess of three B.E.T. monolayers). The high coverage portion of this isotherm was then analyzed in terms of a generalized form of the Frenkel-Halsey-Hill isotherm equation[4] in order to determine the amount of argon adsorbed per layer in the second and higher layers. This analysis gave a layer capacity of 0.014 mole of argon in the second and third layers, compared to a B.E.T. first-layer capacity of 0.015 mole. This figure corresponds to an area of 1200 m^2 available for helium adsorption. [Although it is not important for the purposes of the present work, it is of interest to note that these data indicate that, for the particular sample of TiO_2 used here, no appreciable loss of available area occurs as more argon is adsorbed. It is estimated that the observed increase in layer capacity in the first layer is about equal to the expected increase due to the compression of the first layer calculated from Eq. (5.10) of I.]

The treatment of monolayer adsorption in II was designed to be applicable to films made up of atoms which have a quantized degree of freedom perpendicular to the surface, and two classical degrees of freedom parallel to the surface. However, when the potential energy was computed for a helium atom in the neighborhood of an argon surface, it turned out that the variations of the energy as the helium atom moves parallel to the surface were so large that it was necessary to treat all three degrees of freedoms as quantized. Therefore, the Schrödinger equation was solved for a single adsorbed helium atom, and the wave functions and energy levels obtained for the first few states of this system. These results show that helium atoms adsorbed on an argon surface are nearly all in their ground states at temperatures up to 20°K. Thus, the formalism of II must be modified to treat such a system. This modification is easily done for single helium atoms interacting with a surface, and it is found that the theoretically calculated results can be quantitatively correlated with the experimental isotherms and isosteric heats of adsorption. However, the quantum-mechanical calculation of the term involving the interaction of pairs of helium atoms with the surface is more difficult and has not been carried out as yet. Nevertheless, the experimental values of this parameter were found to be in reasonable qualitative agreement with the estimated theoretical values.

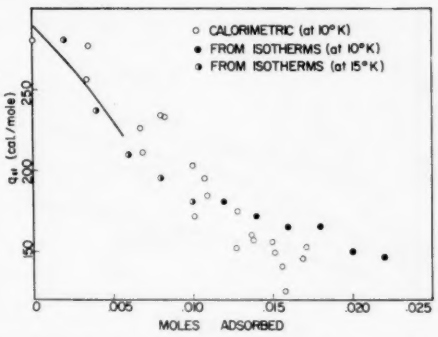

FIG. 1. The isosteric heat of desorption q_{st} is given as a function of the total moles of helium adsorbed. The curve shown is the theoretical curve calculated from Eq. (5.6).

2. EXPERIMENTAL

The experimental measurements reported here consist in a complete study of a system which has previously been considered in a preliminary way by Steele and Aston.[2] In this work heats of adsorption were extended to coverages twice as large as considered previously, and isotherms were measured over a wider temperature range. In the region where the data of the two investigations could be compared, the results were in good agreement. Measurements were also carried out on this system at 4°K; the results of these experiments and their interpretation will be reported in a subsequent paper.[4]

The calorimeter used was similar to the one described by Steele and Aston. It was filled with 19.56 g of TiO_2 having a total area of 1290 m^2 calculated from a N_2 B.E.T. isotherm and 1270 m^2 calculated from an argon B.E.T. isotherm; 0.016 mole of argon were preadsorbed in each experiment using the method described by Steele and Aston. This amount of gas is about 10% larger than the measured monolayer capacity at 89°K.

The thermometer used in this study was an ordinary ½-w, 56-ohm Allen-Bradley carbon resistor. In agreement with earlier workers,[5] it was found that the resistance of this thermometer was reproducible to ±0.2% in both absolute temperature and temperature derivative upon repeated warming and cooling from room temperature. This degree of reproducibility required at least one calibration point in each run. However, this disadvantage was minor in view of the large sensitivity of this thermometer compared to the constantan previously used. At equal power dissipation, the carbon thermometer was found to be about ten times more sensitive at hydrogen temperatures, and about 100 times more sensitive at 4°K. Since temperature differences of

[2] W. A. Steele and J. G. Aston, J. Am. Chem. Soc. **79**, 2393 (1957).
[3] W. A. Steele, J. Phys Chem. **61**, 1551 (1957).
[4] M. Ross and W. A. Steele, J. Chem. Phys. **35**, 871 (1961).
[5] J. R. Clements, in *Temperature, Its Measurement and Co ntr in Science and Industry* (Reinhold Publishing Corporation, New York, 1955), Vol. II, p. 380.

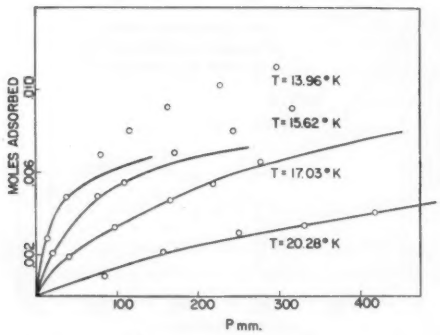

FIG. 2. The total moles of helium adsorbed plotted as a function of the pressure at various temperatures. The open circles show the experimental data; the curves are computed from Eq. (2.1), with δ and higher terms set equal to zero. The values of N_s/p_0 and β/N_s which were used are listed in Table I.

10^{-4} deg were easily detectable at 10°K using the carbon thermometer, a temperature rise of 0.1° to 0.2° was sufficient to allow accurate measurements of heat capacity and heats of adsorption.

Calorimetric heats were measured at 10°K, and isotherms were determined at temperatures of 9.673°, 9.770°, 9.941°, 13.96°, 15.62°, 17.03°, and 20.28°. The first three isotherms were used primarily to obtain heats of adsorption at high coverages (up to 0.0225 mole of helium adsorbed). By regulating the temperature of the surroundings, the temperature drift rate of the calorimeter during a measurement was held to 10^{-3} deg/min or less. Under these conditions, the change of isotherm pressure during the time of measurement was immeasureably small. A 100-ohm length of constantan wire was lacquered to the calorimeter for use as a heater and a secondary thermometer. Since the temperature-resistance curve of constantan is linear in the range 10° to 20°, as well as being quite reproducible, this wire provided an extremely convenient standard for the repeated calibrations of the carbon thermometer.

Calorimetric heats of adsorption were measured at 10°K up to coverages of 0.0174 mole of helium. These data, together with some heats which were calculated from the isotherms, are shown in Fig. 1. Figure 2 shows a portion of the isotherm data. The 10° isotherms show no new qualitative features, and have been omitted from the figure because the experimental points at this temperature were all measured at coverages outside the range of validity of the theoretical treatment of this work. The accuracy of the heats of adsorption is estimated to be about $\pm 5\%$. Heat capacities of the calorimeter and contents were also obtained in the course of the measurements. Although the heat capacity of the film could be calculated from these data, the results were rather inaccurate due to the large correction terms which appear in the calculation and are probably only good to $\pm 25\%$. To this accuracy, the partial molar heat capacity of helium adsorbed at 10° is constant and equal to 4 cal/mole deg over the coverage range 0.01 to 0.02 mole.

In II, it was shown that the general treatment of monolayer adsorption in terms of the interaction energies leads to an isotherm of the form

$$N_a/N_s=\frac{p/p_0}{1+\beta p/p_0}(1+\delta(p/p_0)^2+\cdots), \quad (2.1)$$

where N_a is the number of moles adsorbed, N_s is the number of moles of "sites," $1/p_0$ is a parameter which depends upon the interaction of a single adsorbed atom with the solid, and β, δ, etc., are parameters depending upon the interaction of pairs, triplets, etc., of adsorbed atoms with the solid. If one plots N_a/p vs N_a, the slope of the line at small N_a will be equal to $-\beta/p_0$, and the intercept at $N_a=0$ will be N_s/p_0. In the absence of additional information about N_s, it is clearly impossible to determine either $1/p_0$ or β. N_s/p_0 and β/N_s were calculated from the isotherm points shown in Fig. 2. The results are presented in Table I. The curves shown in Fig. 2 are the theoretical isotherms calculated from Eq. (2.1) if the higher terms in δ, $\cdots$ are neglected. The deviation between theory and experiment at high coverages is clearly due to the omission of these higher terms. Since the observed points at a given coverage correspond to lower pressures than the theory in the region of the disagreement, it is apparent that the higher terms which have been omitted reflect primarily the added attractive interactions between groups of three or more helium atoms on the surface.

3. CALCULATION OF THE INTERACTION ENERGY

The energy of interaction of a single helium atom with the adsorbent is now calculated as a function of the position of the helium atom with respect to the solid lattice. It is assumed that the adsorbent is a pure argon crystal, which is known to occur in a face-centered cubic structure having a unit cell whose edge length is 5.42 A at 20°K. Figure 3 is a schematic representation of the (100) surface of such a crystal. It is further assumed that the total interaction of a helium atom with this solid can be obtained by summing the pair interactions of the helium atom with the argon

TABLE I. Experimental isotherm parameters.

T (deg K)	N_s/p_0 (mole/atm)	β/N_s (mole^{-1})	$1/p_0$[a] (atm^{-1})	β[a]
20.28	0.0108	66.0	7.71	0.92
17.03	0.0374	84.8	26.7	1.19
16.47	0.0602	99.7	43.0	1.40
15.62	0.0925	108	66.1	1.51
14.84	0.165	133	117.8	1.86
13.96	0.257	136	183.6	1.90

[a] Assumed value of $N_s=0.014$ mole.

atoms over the entire solid, and that the helium-argon pair interaction is given by a Lennard-Jones potential function. The constants of this potential function were calculated from the known He-He and Ar-Ar potential functions using the generally accepted combining rules.[6,7] Thus, the He-Ar interaction potential was taken to be

$$\epsilon_{\mathrm{He-A}}=4\epsilon^*(-(\sigma/r)^6+(\sigma/r)^{12})$$
$$\epsilon^*=35.4 \text{ deg K}=71 \text{ cal/mole}$$
$$\sigma=3.00 \text{ A}. \tag{3.1}$$

In II, several lattice sums were tabulated for the energy of a single atom interacting with a simple cubic solid, and it was pointed out that more complex lattice interactions could be calculated from the sums for the simple cubic lattice. A sufficient number of positions over the unit cell were considered to make it possible to obtain energy versus perpendicular distance curves for an atom over six different positions with respect to a face centered cubic lattice unit cell. These positions are denoted in Fig. 3 by the numbers, and the lattice sums S_{fcc} for these positions are seen to be given by

$$S_{\mathrm{fcc}}(\rho, 0)=2S(\rho, 0, \tfrac{1}{2})+S(\rho+0.5, 0, 0)+S(\rho+0.5, \tfrac{1}{2}, \tfrac{1}{2}),$$
$$S_{\mathrm{fcc}}(\rho, 1)=S(\rho, 0, \tfrac{1}{4})+S(\rho, \tfrac{1}{2}, \tfrac{1}{4})+S(\rho, 0.5, 0, \tfrac{1}{4})+S(\rho+0.5, \tfrac{1}{2}, \tfrac{1}{4}),$$
$$S_{\mathrm{fcc}}(\rho, 2)=S(\rho, 0, 0)+S(\rho, \tfrac{1}{2}, \tfrac{1}{2})+2S(\rho+0.5, 0, \tfrac{1}{2}),$$
$$S_{\mathrm{fcc}}(\rho, 3)=S(\rho, \tfrac{1}{8}, \tfrac{1}{8})+S(\rho, \tfrac{3}{8}, \tfrac{3}{8})+2S(\rho+0.5, \tfrac{3}{8}, \tfrac{1}{8}),$$
$$S_{\mathrm{fcc}}(\rho, 4)=2S(\rho, \tfrac{1}{4}, \tfrac{1}{4})+2S(\rho+0.5, \tfrac{1}{4}, \tfrac{1}{4}),$$
$$S_{\mathrm{fcc}}(\rho, 5)=2S(\rho, \tfrac{3}{8}, \tfrac{1}{8})+S(\rho+0.5, \tfrac{1}{8}, \tfrac{1}{8})+S(\rho+0.5, \tfrac{3}{8}, \tfrac{3}{8}), \tag{3.2}$$

where the right-hand sides of these equations are written in the notation of II. The S_{fcc} are easily computed from the data of Appendix I of II, and thus the energy of a helium atom above one of the six positions is given by:

$$\epsilon=4\epsilon^*\rho^{*6}S \tag{3.3}$$
$$\rho^*=\sigma/a=0.554 \tag{3.4}$$
$$\epsilon=4.10S(\text{deg K})=8.15S(\text{cal/mole}) \tag{3.3}$$
$$S=-S_6+0.0289S_{12}, \tag{3.5}$$

where S_6 and S_{12} are the reduced sums of the inverse 6th and 12th powers of the distance, respectively. S_m the minimum value of S, and the corresponding minimum energies ϵ_m were calculated from Eqs. (3.3)–(3.5), and are tabulated in Table II. From the large value of S_m for an atom over position 0, one may deduce that this point will be the center of an adsorption site. The square in Fig. 3 shows the boundaries of the repeating unit of the surface if position 0 is taken to be the center point. The edge of this cell is 3.83 A long, and its area is 14.7 A^2. If the total area of the adsorbent is taken to be 1200 m^2, it follows that the total number of sites present is equal to 0.0140 mole. This estimate of N_s will later be shown to be in excellent agreement with other estimates.

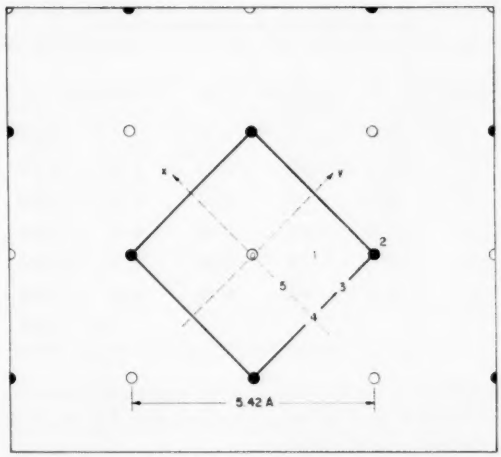

FIG. 3. A top view of the (100) plane of the face-centered cubic argon lattice. The filled points are in the plane of the surface of the crystal; the open points are 2.71 A below the plane of the surface. The numbers denote the positions of an adsorbed atom above the lattice which are considered in the text, and the square enclosed by solid lines shows the "adsorption site" or repeating unit which was derived from the computed potential energy of a helium atom over this lattice. The dotted lines show the orientation of the coordinate system which is used in Sec. 4. The length of the side of the lattice cell (denoted by a in this paper) was taken to be 5.42 A.

We now wish to compute the thermodynamic properties of an assembly of helium atoms adsorbed on these sites. First, the energy levels for motion perpendicular to the surface will be computed. This is done by estimating the changes in S as ρ changes from ρ_m to $\rho_m+0.1\rho^*$ and to $\rho_m-0.06\rho^*$. Since the two changes in S were about equal at these points at all positions, the parameter $s_\pm$ was defined as

$$s_\pm=\tfrac{1}{2}[S(\rho_m+0.1\rho^*)+S(\rho_m-0.06\rho^*)-2S_m]/S_m(0). \tag{3.6}$$

Since this definition of $s_\pm$ is essentially the same as that used in II, the energy levels in the z direction could simply be computed by substituting into Eq. (4.4) of II; $s_\pm$ is tabulated in Table II for the six positions considered. It can be seen that $s_\pm$ is nearly constant, and thus the average value of $s_\pm$ was used for all positions. Values of $s_\pm=0.094$, $M=4.003$, and $\epsilon_m(0)/k=187$ deg were substituted into Eq. (4.4) of II, and the energy levels were computed to be 66 cal/mole above

[6] J. O. Hirschfelder, C. F. Curtiss, and R. B. Bird, *Molecular Theory of Gases and Liquids* (John Wiley & Sons, Inc., New York, 1954).

[7] K. P. Srivastava, Physica **25**, 571 (1959); C. M. Knobler, J. J. M. Beenakker, and H. F. P. Knapp, Physica **25**, 909 (1959).

TABLE II. Positions and depths of computed potential minima for a helium atom over an argon lattice.

Position	$-S_m$	ϵ_m (cal/mole)	ρ_m	$\delta S_m/S_m(0)$	$s_\pm$
0	45.4	−372	0.39		0.053
1	24.3	−198	0.54	0.53	0.055
2	19.6	−160	0.61	0.57	0.064
3	21.9	−179	0.58	0.52	0.066
4	28.0	−228	0.50	0.38	0.066
5	32.3	−263	0.46	0.29	0.053
					Av $s_\pm$ 0.060

the minimum for a helium atom in its ground state with respect to motion in the z direction, and 172 cal/mole in the first excited state.

We now consider the potential energy variation with motion within the site when the adsorbed atom is in its ground state for motion perpendicular to the site. The fractional change in S_m as the atom is moved from position 0 to any other position is denoted as $\delta S_m/S_m(0)$ and is tabulated in Table II. This quantity is also plotted in Fig. 4 as a function of $(x+y)$, where the x, y coordinate axes are denoted by the dotted lines in Fig. 3. The change in potential energy near the center of the cell is shown as a linear function of the distance. Although this linear variation cannot be proved to be correct in the face-centered cubic system because of the lack of data in the region close to the minimum, it is fairly obvious that it gives a better representation than any other simple function. Furthermore, the linear variation was previously shown to reproduce the calculated changes in energy over a simple cubic cell, particularly when the adsorbed atom was small compared to the adsorbent atoms. These previous calculations for the simple cubic lattice also indicated that the variation in the slope of the linear portion of the curve with angle was intermediate between that predicted on the basis of proportionality to the quantity $(x+y)$, and that of no angular variation. In the He-Ar system, it is clear that the variation in potential near the center of the cell is best represented by an equation of the form

$$\Delta\epsilon_r=(x+y)K_x. \tag{3.7}$$

In view of the small mass of the helium atom, and the rapid variation in ϵ_r, it seems likely that the motion of the helium atom will be quantized in all three directions. In the next section, the Schrödinger equation is solved for this system and it is shown that the helium atom is in fact completely quantized.

4. SOLUTION OF THE SCHRÖDINGER EQUATION

When the three-dimensional Schrödinger equation is written in Cartesian coordinates for a single helium atom on an adsorption site, it is immediately obvious that the previous observation that $s_\pm$ does not depend upon position results in a partial differential equation in which the z variation is separable. Furthermore, if the potential energy variation for motion over the surface is approximated by Eq. (3.7), the remaining partial differential equation is separable into two equivalent ordinary differential equations in the x and y variables. The resultant differential equation to be solved can be written as

$$(-\hbar^2/2M)(\partial^2\psi/\partial x^2)+(K_x|x|-\epsilon_x)\psi=0, \tag{4.1}$$

where ψ is the wave function for motion in the x direction and ϵ_x is the total energy associated with this motion. The origin of the coordinate system is shifted by the substitution

$$u=x-\epsilon_x/K_x. \tag{4.2}$$

Equation (4.1) now becomes

$$[\partial^2\psi/\partial u^2]-(2MK_x/\hbar^2)u\psi=0, \tag{4.3}$$

where u is defined over the region $+\infty>u>-\epsilon_x/K_x$. The general solution of Eq. (4.3) is known to be a linear combination of Bessel functions. In the notation of

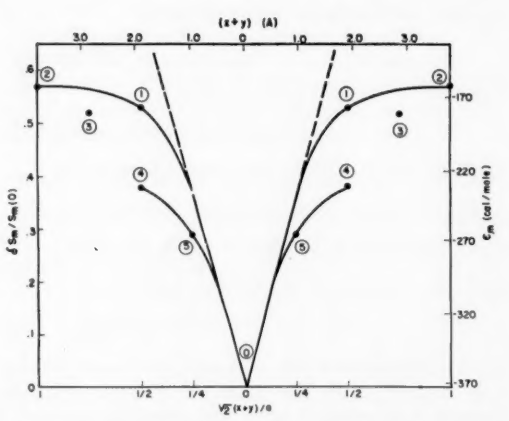

FIG. 4. The variation of the calculated minima (with respect to changes in z) of the potential energy of a helium atom over an argon lattice as the helium atom moves from one position over the surface to another. The numbers denote the positions (see Fig. 3) for which the potential curves were computed—the solid curves show the presumed variation of potential energy at an arbitrary position along the perpendicular bisector of the adsorption site (lower curve) and along the diagonal bisector of the site (upper curve). The data were plotted as a function of the reduced $(x+y)$ in order to illustrate the assumed dependence of the potential function [Eq. (3.7)]. Since either x or y is zero along the perpendicular bisector, the potential energy associated with motion in this direction is given directly as a function of the reduced distance from the cell center (the scale at the lower edge of the figure), and as a function of the distance, using $a=5.42$ A (the scale shown at the upper edge of the plot). Furthermore, since $x=y$ along the diagonal bisector, the distance scales for variations in this direction show the potential changes as a function of $2x=2y$. The fractional variation in the potential energy is given along the left hand ordinate, and the net potential energy of a helium atom on an argon surface is given along the right-hand ordinate, assuming that the minimum of the potential energy at position 0 is −372 cal/mole.

Watson's treatise,[8]

$$\psi = u^{\frac{1}{2}}\mathfrak{C}_{\frac{1}{3}}\{(2i/3)(2MK_x/\hbar^2)^{\frac{1}{2}}u^{\frac{3}{2}}\} \tag{4.4}$$

$$\mathfrak{C}_{\frac{1}{3}} = c_1 J_{\frac{1}{3}}(w^{\frac{1}{2}}) + c_2 J_{-\frac{1}{3}}(w^{\frac{1}{2}}) \quad \text{for} \quad u<0 \tag{4.5}$$

$$\mathfrak{C}_{\frac{1}{3}} = c_3 I_{\frac{1}{3}}(w^{\frac{1}{2}}) + c_4 I_{-\frac{1}{3}}(w^{\frac{1}{2}}) \quad \text{for} \quad u>0, \tag{4.6}$$

where $w=u/\alpha$,

$$\alpha = (9\hbar^2/8MK_x)^{\frac{1}{3}}.$$

If ψ is to approach zero at large u, it follows that

$$\lim_{w\to\infty}\psi = cw^n \exp(-w^{\frac{1}{2}}), \tag{4.7}$$

where n is arbitrary. This requirement, together with the requirement that ψ and $\partial\psi/\partial u$ be continuous at $u=0$, serves to determine n, c_2, c_3, c_4:

$$c_1 = c\alpha^{\frac{1}{2}} \qquad c_3 = ci^{-\frac{1}{3}}\alpha^{\frac{1}{2}} \qquad n=-\tfrac{1}{4}$$

$$c_2 = c\alpha^{\frac{1}{2}} \qquad c_4 = -ci^{\frac{1}{3}}\alpha^{\frac{1}{2}}. \tag{4.8}$$

The eigenvalues of the energy are determined by the conditions that ψ and $\partial\psi/\partial u$ join smoothly at the point $x=0$, $u=-\epsilon_x/K_x$. This restraint implies that either ψ or $\partial\psi/\partial w$ must be zero at $w=-\epsilon_x/K_x\alpha$. Thus the eigenvalues of ϵ_x can be calculated from the zeros of

$$\psi = c[J_{\frac{1}{3}}(w^{\frac{1}{2}}) + J_{-\frac{1}{3}}(w^{\frac{1}{2}})]w^{\frac{1}{4}}\alpha^{\frac{1}{2}} \tag{4.9}$$

and

$$\partial\psi/\partial w = c[J_{2/3}(w^{\frac{1}{2}}) - J_{-2/3}(w^{\frac{1}{2}})]w^{1/9}\alpha^{\frac{1}{2}}(\tfrac{3}{2}). \tag{4.10}$$

If the zeros of both functions are listed together, and the mth zero of the combined list is denoted by ξ_m, the eigenvalues of the energy are given as

$$\epsilon_x(m) = \xi_m K_x\alpha. \tag{4.11}$$

The values of ϵ_m were obtained in part from a tabulation in Watson, p. 751, and in part from the equation which is given in Watson, p. 506 for the zeros of a generalized Bessel function. The ψ^2 and $x^2\psi^2$ were calculated from the tabulated values of the Bessel functions of order $\pm\frac{1}{3}$, and the normalization constants and root mean-square displacements were computed numerically for the first three levels. These data are listed in Table III.

The energy levels for a helium atom moving over the argon surface were computed from Eq. (4.11) using $K_x=9.25.10^{-7}$ erg/cm, $\alpha=0.595$ A (calculated from the data shown in Fig. 4). These results are tabulated in column 5 of Table III. Note that the zero-point energy for the motion of a helium atom in the x or y direction is nearly as large as that in the z direction, on an argon surface, and that the energy of the first excited state of this system is considerably larger than kT for the experimental range of temperatures.

The values for the energy levels given in Table III must be considered as the first approximation to the actual energy levels. These results may be improved by taking account of the deviations of the actual potential from the linear dependence given in Eq. (3.7). Also, it must be realized that the true wave function for a single helium atom on an argon surface must reflect the fact that the helium atom has an equal probability of being in any one of the N_s sites. The changes in the energy levels due to these effects can be calculated by standard first-order perturbation theory, and it can be easily shown that, for the He-Ar system, the ground state ϵ_x and ϵ_y are lowered by 0.5 cal/mole because of deviations from the linear potential function within the site, and are essentially unaffected by interactions with neighboring sites. Although no calculations were carried out for the excited states of the He-Ar system, it is clear that the perturbations of these states will become rapidly larger as the quantum number increases.

TABLE III. Eigenvalues and associated quantities obtained from the solution of Eq. (4.1).

m	ξ_m	$c_m\alpha$	$(\langle x^2\rangle_{\text{Av}}/\alpha^2)^{\frac{1}{2}}$	$(\langle x^2\rangle_{\text{Av}})^{\frac{1}{2}}$ (A)	$\epsilon_x(m)$ (cal/mole)	η_m/ϵ_m
0	0.778	0.571	0.661	0.39	60	1.094
1	1.785	0.439	1.299	0.77	138	0.992
2	2.480	0.407	1.799	1.07	191	1.003
3	3.120					0.998
4	3.689					1.001
5	4.213					0.999

In other adsorption systems, the adsorbed atoms may not be as highly localized as in the He-Ar system, or the deviation of the actual potential function from Eq. (3.7) may be quite large. In such cases, the simple first order perturbation theory used here will not be adequate. However, since this problem is formally equivalent to the two-dimensional version of the band approximation to the properties of solids,[9] the techniques developed to treat this problem can be used. Alternately, the W.K.B. method may be used to calculate the approximate levels of an adsorbed atom.[10] The method gives reasonably accurate results when applied to systems in which the potential variations are relatively small, and thus should be quite useful in physical adsorption problems. In fact, it was found that the W.K.B. energy levels for a helium atom on an argon surface are quite near the "exact" levels [calculated from Eq. (4.11)] in all states higher than the ground state. The result of the W.K.B. calculation can be written

$$\epsilon_x(m) = \eta_m K_x\alpha$$

$$\eta_m = [\pi/2(m+\tfrac{1}{2})]^{\frac{1}{2}}. \tag{4.12}$$

The ratio of η_m to ξ_m is given in column 7 of Table III.

[8] G. N. Watson, *Theory of Bessel Functions* (Cambridge University Press, New York, 1945).

[9] F. Seitz, *The Modern Theory of Solids* (McGraw-Hill Book Company, Inc., New York, 1940), Chap. VIII.

[10] P. M. Morse and H. Feschbach, *Methods of Theoretical Physics* (McGraw-Hill Book Company, Inc., New York, 1953), Vol. II, p. 1092 ff.

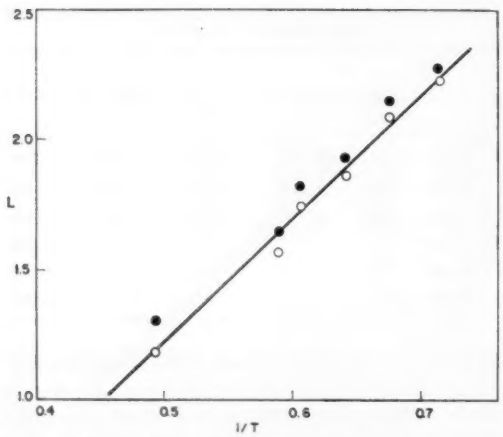

FIG. 5. The values of $L=\log(T^{5/2}N_s/p_0)$ plotted as a function of $1/T$ are shown as the filled points in this figure. The open points show the values of L which were calculated including the contribution of the first excited states of the helium atom to the Slater sum. Thus, the open points are given by $\log(T^{5/2}N_s/p_0)-\log\sigma$, where σ was calculated from Eq. (5.4) using the theoretical values of the energy levels. The solid curve is a straight line through the open points with slope=48 deg and intercept=-1.17.

Using $\epsilon_m(0)=-372$ cal/mole, $\epsilon_z(0)=66$ cal/mole and $\epsilon_x(0)=59.5$ cal/mole, the total ground-state vibrational energy of an isolated helium atom adsorbed on an argon surface may now be calculated to be $+185$ cal/mole, and the theoretically calculated net energy of the atom is -187 cal/mole.

5. COMPARISON WITH EXPERIMENT

In II, the parameter $1/p_0$ was shown to be given by the equation

$$1/p_0=1/kT\int_{V_s}\exp(-u_s/kT)\,dV \qquad (5.1)$$

for a completely classical system. This relationship is easily altered to describe a completely quantized system such as the present one. The appropriate quantum-mechanical equation for $1/p_0$ is

$$1/p_0=(1/kT)(h^2/2\pi mkT)^{\frac{1}{2}}\exp[-\epsilon_m(0)/kT]\times\sum_j\exp[-\epsilon(j)/kT], \qquad (5.2)$$

where $\epsilon_m(0)$ is the minimum of the potential energy at the center of an adsorption site, and the sum over the quantum number j is taken over all the three-dimensional quantum states available to the adsorbed atom. As a first approximation, it is assumed that only the zero-point terms in the sum are appreciably larger than zero, and thus one can write a simple equation for the experimental quantity N_s/p_0:

$$L=\log[T^{5/2}(N_s/p_0)]=\log(4.85N_s)-(1/T)(u_0/2.30R), \qquad (5.3)$$

where u_0 is the net energy of a single adsorbed atom in its quantum-mechanical ground state. When L is plotted vs $1/T$, the slope of the line gives u_0, and the intercept gives N_s. This plot is shown in Fig. 5. The filled points in this figure represent $\log T^{5/2}(N_s/p_0)$, and it is seen that these points show a slight deviation upward from linearity at high temperatures. This effect is due to the contribution of higher terms in the Slater sum in Eq. (5.2), and can be approximately corrected by subtracting $\ln\sigma$ from each of the filled points, where

$$\sigma=1+\exp\{-[\epsilon_z(1)-\epsilon_z(0)]/kT\}+2\exp\{-[\epsilon_x(1)-\epsilon_x(0)]/kT\}, \qquad (5.4)$$

where the numbers here denote quantum numbers for motion in the z and x directions. σ was calculated using the theoretical values of the energy levels, and the open circles in Fig. 5 show $L=\log[T^{5/2}(N_s/p_0)]-\log\sigma$. These points define a better straight line than the uncorrected points, and the slope and intercept of the line give $u_0=-220$ cal/mole, and $N_s=0.014$ mole, respectively.

Another estimate of the energy of a single adsorbed helium atom can be obtained from the isosteric heats of adsorption. If there are no imperfections in the surface, then it is immediately obvious that $\lim q_{st}$ as N_a approaches zero will be equal to the molar enthalpy change when a single helium atom is transferred from the adsorbed state to the gas. The molar enthalpy of an adsorbed atom can be taken to be equal to the molar energy $\bar{E}_a$ and thus

$$\bar{E}_a=\bar{H}_g-\lim_{N_a\to 0}q_{st}. \qquad (5.5)$$

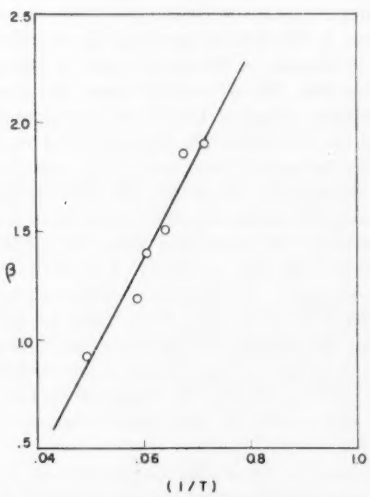

FIG. 6. The open circles show the experimental values of β plotted as a function of $1/T$; β has been computed from β/N_s given in Table I using $N_s=0.014$ mole. The data fall reasonably well on a straight line, over the temperature range of these experiments. The line shown has a slope of 47 deg.

If the gas phase is ideal, $\tilde{H}_g = 70$ cal/mole at 14°K (only the kinetic energy plus $P\tilde{V}$ are included in $\tilde{H}_g$). The experimental value of $\lim q_{st}$ is estimated to be 290 ± 20 cal/mole, and thus $\tilde{E}_a = -220 \pm 20$ cal/mole. Since the probability of finding an adsorbed atom in an excited state is very small at 14°K, $\tilde{E}_a$ should be directly equal to u_0. Thus, the two experimental estimates of u_0 are in good agreement with each other, and are also in good agreement with the theoretically computed value of -187 cal/mole (it should be remembered that there were no adjustable parameters in the theoretical calculation, and that the uncertainty in the parameters of the interaction energy which were computed from the combining rules is estimated to be $\pm 10\%$).

Note that the experimental value is comparable with the theoretical energy only if the surface is completely uniform; any irregularities, edge effects, or lattice deformations would generally lead to a larger experimental adsorption energy at zero coverage. The extent of the agreement is strong support for the previous qualitative conclusion that preadsorbed argon fills in, and thus eliminates, surface imperfections.[3]

In many previous studies of adsorption phenomena it has been assumed that surface heterogeneity is present when the experimental q_{st} decrease with increasing coverage. The observed decrease in q_{st} in this work would thus seem to be in contradiction to the assertion that the surface is uniform. This contradiction can be easily resolved by computing the theoretical q_{st} curve for a system which obeys Eq. (2.1). When the terms in $\delta, \cdots$ are omitted, the result of the differentiation of the isotherm equation can be written

$$q_{st}/R = -[\partial \ln p/\partial(1/T)]_{N_a}$$
$$= -[\partial \ln p_0/\partial(1/T)]_{N_a}$$
$$-[N_a/(N_{ss}-N_a\beta)][\partial\beta/\partial(1/T)]_{N_a}, \quad (5.6)$$

β is plotted as a function of $1/T$ in Fig. 6. Since $[\partial\beta/\partial(1/T)]_{N_a}$ is positive, Eq. (5.6) indicates that q_{st} should show an approximately linear decrease with coverage at low coverage due to the change in the two-body interaction parameter with temperature. The curve in Fig. 1 shows q_{st} calculated from Eq. (5.6) using $[\partial\beta/\partial(1/T)]_{N_a} = 47°$ and $\beta = 1.9$. Thus, there is good agreement between the measured heats and the heats calculated on the assumption of a uniform surface. Note that the curve falls below the experimental curve in the high coverage region. This observation confirms the earlier statement that the higher terms in the isotherm equation are primarily attractive in this system.

Since isolated adsorbed helium atoms have been shown to be completely quantized under the experimental conditions, it is unlikely that the esentially classical computations of β presented in II will be applicable here. However, these computations show that the classical values of β are less than one except when the reduced temperature (kT/ϵ_{gg}) is large and the size of the adsorbed atom is larger than the site dimension (i.e., $\sigma_{gg}/a > 1$). The second of these requirements is obviously not satisfied in the He-Ar system. Furthermore, it is unlikely (although not impossible) that the observed rapid increase in β with decreasing temperature would be reproduced by any realistic classical model.

TABLE IV. Positions and depths of potential minima for a helium atom over a partially covered argon surface.

Position	ϵ_m (cal/mole)	ρ_m	$\epsilon_s(0)$ (cal/mole)	$\epsilon_m - \epsilon_s(0)$ (cal/mole)
0	−76	0.85	20	−56
2	−234	0.60	74	−190
4	−148	0.70	64	−84

Nevertheless, some rough classical calculations of β were carried out using the data tabulated in Appendix 2 of II, assuming that $\sigma_{\text{He-He}}/a$ and $E/\epsilon_{\text{He-He}}$ could be taken as adjustable parameters; β was estimated to be 1.2 with $\sigma_{\text{He-He}}/a = 1.3$, $E/\epsilon_{\text{He-He}} = 10$. However, the calculated temperature dependence of β using these parameters was much smaller than the experimental value. The fact that the apparent size of the helium atom is much larger than the actual size ($\sigma_{\text{He-He}}/a \simeq 0.6$), and that the apparent energy is somewhat smaller than the actual ($E/\epsilon_{\text{He-He}} \simeq 13$) points rather strongly to the presence of quantum effects, since an increase in apparent size and a decrease in apparent interaction energy has been quite generally observed when a classical theory has been applied to a quantum phenomenon (for instance, the application of the classical theorem of corresponding states to the experimental data of state for He gives apparent σ and ϵ which are $\frac{4}{3}$ and $\frac{1}{2}$ the actual values, respectively).[11] Also, the root mean-square displacement of an adsorbed helium atom from the center of a site has been shown to be $\simeq 0.4$ A (see Table III); if this value is arbitrarily added to $\sigma_{\text{He-He}}$, one obtains an effective $\sigma_{\text{He-He}}/a$ of $\simeq 0.8$; furthermore, if the zero-point energy for one degree of freedom parallel to the surface is subtracted from E, the effective $E/\epsilon_{\text{He-He}} \simeq 8$. Thus, it may be concluded that the observed β are at least qualitatively consistent with the estimated values of the quantized He-Ar system. (It should be possible to derive the formal equations for an exact calculation of β in a quantized system by means of suitable modifications of the well-known expressions for the quantum second virial coefficient.[6] This derivation is now being undertaken.)

It can be shown that the isotherms of Fig. 2 are reasonably consistent with the simple Langmuir adsorption isotherm equation, and indeed, data taken on similar systems have often been analyzed in terms of this model. Since the Langmuir model is formally equivalent to setting $\beta = 1$, $\delta, \cdots = 0$ at all tempera-

[11] F. London, *Superfluids* (John Wiley & Sons, Inc., New York, 1954), Vol. II.

tures, it is clear that the observed variation in β will be taken up in the Langmuir $1/p_0$ and N_s. Although such an error in $1/p_0$ will generally not be detectable, an apparent temperature variation of N_s can often result from the use of the Langmuir approximation for the interaction of pairs of molecules on the surface.

Although the estimated value of 0.014 mole for the total number of sites available for helium adsorption was shown to be completely consistent with the data, it is obvious that an amount of helium considerably in excess of 0.014 mole is adsorbed at 10°K at moderate pressures (for instance, 0.023 mole at 500 mm Hg). It is highly unlikely that appreciable multilayer formation can occur under these conditions, and in fact, it turns out that this additional amount of gas on the surface can be attributed to the adsorption of more than one helium atom per site. At coverages slightly in excess of 0.014 mole, the total energy of interaction of a helium atom with the partially covered surface can be approximately calculated by computing the sum of the interaction of the helium atom with the argon lattice plus its interaction with the helium atoms already present. If it is assumed that the centers of the sites are all occupied by helium atoms, then the total potential energy at positions 0, 2, or 4 is given by the equations:

$$\epsilon(\rho,0)=8.15S(\rho,0)+0.88(\rho-0.35)^{-6}\times[-1+0.01085(\rho-0.35)^{-6}]\ \text{cal/mole}$$

$$\epsilon(\rho,2)=8.15S(\rho,2)+3.52[(\rho-0.35)^2+0.25]^{-3}\times\{-1+0.01085[(\rho-0.35)^2+0.25]^{-3}\}$$

$$\epsilon(\rho,4)=8.15S(\rho,4)+1.76[(\rho-0.35)^2+.125]^{-3}\times\{-1+0.01075[(\rho-0.35)^2+0.125]^{-3}\},\quad(5.7)$$

where the last terms of the right-hand sides of the equations give the He-He interaction for an atom with its nearest He atom neighbors only, assuming that the zero-point motion of these neighbors is negligibly small. Using the $S(\rho)$ which were calculated earlier from Eq. (3.2), one may obtain approximate values for ϵ_m, ρ_m, and $\epsilon_z(0)$. The results of this calculation are shown in Table IV. It is clear that the adsorption of helium atoms over the corners of adsorption sites is an energetically favorable situation when the centers are filled. The energy associated with the degrees of freedom parallel to the surface can also be crudely estimated from the energies tabulated in column 5 of Table IV. The value of K_z obtained in this manner is about 4.10^{-7} erg/cm, and the total zero-point energy for motion in the x and y directions is thus $\sim$80 cal/mole. The final result for the total energy of an atom adsorbed over the corner of a site with all the site centers filled is $-190+80=110\pm20$ cal/mole. The experimental q_{st} shown in Fig. 1 reach a roughly constant value of 150 ± 10 cal/mole at $N_a=0.014$ moles; when $\tilde{H}_g$ is subtracted ($\tilde{H}_g=50$ cal/mole at 10°K), the resultant estimate of the experimental energy of an adsorbed atom is -100 ± 10 cal/mole in this range of coverage, in good agreement with the theoretical estimate.

Therefore, it may now be concluded that at temperatures up to 20°K, the monolayer adsorption of helium on a uniform argon surface proceeds in the following manner: The first atoms on the surface adsorb over the position 0 which is shown in Fig. 3 with a total energy of -200 cal/mole (relative to the ideal gas at 0°K); the absorption proceeds at these points with a steadily increasing repulsive contribution to the total energy due to the pair interactions with atoms in neighboring sites; when all these positions contain adsorbed atoms (there are $1.1.10^{-9}$ mole of these sites per square centimeter of surface), any additional atoms are adsorbed over position 2 with an energy of -100 cal/mole, exclusive of the interactions between neighboring atoms over 2 positions (this interaction is calculated to be small, and attractive—of the order of -6 cal/mole per neighbor, neglecting zero-point motion). This process amounts to a net adsorption of two helium atoms per site, and indicates that the total number of moles held in a complete monolayer is equal to 0.028 in the present system. The energy of interaction of additional adsorbate atoms with the solid plus this monolayer is found to be considerably smaller than -100 cal/mole, and thus it may be tentatively concluded that multilayer adsorption will occur at coverages greater than 0.028. It will be shown in a subsequent paper that multilayer properties of this system measured at 4°K are consistent with this conclusion.

The previous experiments by Steele and Aston[2] on the adsorption of helium on surfaces prepared by preadsorbing varying amounts of argon on a high-area TiO_2 surface were interpreted in terms of the Langmuir model modified to be applicable to surfaces of varying amounts of heterogeneity. It is now apparent that this model gives a reasonably correct description of the first half of the atoms in the monolayer, but that it would predict that no further adsorption would occur after the centers of all the adsorption sites contain helium atoms (preliminary fits of the data reported in this work confirm this statement). Thus, the relative adsorption capacities of the TiO_2-Ar mixed surfaces which were computed on the basis of the Langmuir model are reasonably realistic, even though the actual capacities are about twice as large as listed.

The helium-argon system is one of the very few adsorption systems in which a reasonably realistic *a priori* computation of the adsorbate-absorbent potential energy function can be carried out. However, the excellent agreement between the experimental values of the parameters and the values computed from the theoretical potential function indicates that the present theoretical approach may be used to derive a considerable amount of information about the adsorbate atom-solid potential function from experimental meas-

urements on suitable systems with unknown (or only approximately known) potential functions. The chief advantage to be found in the present treatment is that the parameters in Eq. (2.1) are dependent solely upon the nature of the potential function, and do not involve detailed assumptions about the nature of the adsorption process. In this sense, this approach is similar to the treatment by Halsey, *et al.*[12] of the interaction of gases with solids at high temperatures and low densities. However, it is well known that equation of state data measured under these conditions are relatively insensitive to the details of the potential function (the fit of experimental second virial coefficients to theory is notoriously insensitive to the functional dependence of the potential energy curve). However, at the lower temperatures where monolayer adsorption is easily measureable (roughly speaking, at or below the critical temperature of the adsorbate), the data are considerably more sensitive to the details of the potential energy near its minima. Thus, the properties of adsorbed monolayers have been shown to be strongly affected by the variations in the minimum of the potential energy as the adsorbed atoms move across the surface, in contrast to the situation at higher temperatures, where the effect of these variations upon the macroscopic properties of the system is not completely known, and is generally assumed to be negligible.[13]

[12] T. L. Hill, *Statistical Mechanics* (McGraw-Hill Book Company, Inc., New York, 1956), Appendix 10.

[13] M. P. Freeman, J. Phys. Chem. **62**, 729 (1958).

THE JOURNAL OF CHEMICAL PHYSICS VOLUME 35, NUMBER 3 SEPTEMBER, 1961

Multilayer Adsorption of Helium on Argon*

MARVIN ROSS† AND WILLIAM A. STEELE

Department of Chemistry, The Pennsylvania State University, University Park, Pennsylvania

(Received February 27, 1961)

Multilayer isotherms and heats are reported for helium adsorbed on an argon surface at 4.2°K. The data show that, on the uniform surface used in this work, the layer capacities and energies of the first two or three layers of adsorbed helium can be estimated directly from the heats without recourse to the isotherm data. The adsorption energies are shown to be in good agreement with theoretical estimates. Two alternate approaches to the theoretical calculation of layer capacity are presented: one of the methods involves a computation of the perturbation of the density of the bulk liquid due to the presence of the surface; the other calculation is based on a computation of the density dependence of the lateral interaction energy in a layer plus the surface interaction energy of the layer. The density of a completed layer can be estimated by equating the total energies per atom in successive layers. It is shown that the results of these calculations are in good agreement with each other, and with the experiments. The high coverage isotherm data are analyzed in terms of a modified form of the Frenkel-Halsey-Hill isotherm equation, and it is shown that the parameters required to fit the experiments to this equation are consistent with other estimates. Finally, the data are fitted to the B.E.T. equation, and to several of the modified B.E.T. isotherms which have been suggested as more realistic representations of helium adsorption data. It is concluded that no B.E.T.-type model is completely successful, but that the isotherm equation proposed by Steele gives the most accurate results.

1. INTRODUCTION

ISOTHERMS and heats of adsorption are reported in this paper for helium adsorbed on an argon surface at 4.2°K. The measurements were made at coverages from 0 to ~6 layers. These experiments are analyzed in some detail in the multilayer region. The calculations are of special interest in the light of the rather detailed knowledge about the properties of the adsorbent which have been discussed in a previous paper.[1] In particular, the potential energy of a helium atom interacting with the (100) face of a face-centered cubic argon crystal was computed theoretically in III as a function of the distance of the atom from the surface and its position relative to a unit cell in the surface. It was shown that the experimental monolayer isotherms and heats at 10° to 20°K were consistent with those computed from this potential energy function on the assumption that the surface is made up of 0.0140 moles of identical sites of area 14.7 A². Thus, both the area of the adsorbent and the potential field in the vicinity of the surface can be treated as known quantities.

In principle, all the properties of helium adsorbed at 4°K are completely determined by these quantities, plus the known helium-helium interaction potential curve. In actual fact, it proved to be possible to use this information to make theoretical estimates of the layer volume of the first layer, and of several additional layers, as well as estimates of the isosteric heats of

* This work supported in part by the National Science Foundation and in part by the Office of Ordnance Research.

† Present address: Department of Chemistry, University of California, Berkeley, California.

[1] M. Ross and W. A. Steele, J. Chem. Phys. **35**, 862 (1961). (Hereinafter referred to as III.)

adsorption over a wide range of coverages. The calculated values of these parameters are in good agreement with experiment and indicate that helium adsorbed on an argon surface is appreciably compressed compared to its liquid density at coverages up to five layers, and that the heats of adsorption are also appreciably larger than the heat of liquefaction over this range of coverage.

These extensive experiments are also of interest because of the apparent anomalous properties predicted for this system by the B.E.T. isotherm. It is well known that when the B.E.T. theory is applied to helium multilayer isotherms, it is generally found that monolayer volumes are obtained which are about four times the volume predicted from a knowledge of the surface area and the assumption that the adsorbed helium is liquid packed. These large monolayer volumes have been interpreted as indicating that the adsorbed helium in the first layer is greatly compressed. However, Singh and Band[2] have shown that the large densities predicted by the B.E.T. analysis result in quantum-mechanical zero-point energies and interatomic repulsive energies which are far in excess of the attractive adsorption energies, thereby making such a film thermodynamically unstable. A number of authors[3–5] have suggested that the energy of adsorption of helium in the second layer may be considerably larger than the energy of liquefaction and therefore the apparent anomalous behavior may be due to an uncritical application of the B.E.T. theory. In particular, Aston and Mastrangelo,[3] and Steele[4] have shown that modifications of the original B.E.T. theory which take into account the large second-layer energy of adsorption will predict more realistic monolayer volumes. In view of these criticisms of the B.E.T. model, it seemed desirable to analyze the experimental data for a system in which an independent estimate of the monolayer volume can be made. The variation in the heats of adsorption with coverage can be used to obtain such an estimate in the present system. As pointed out in III, the surface of this adsorbent is essentially uniform (in the sense that it is almost entirely composed of identical adsorption "sites"). Since it is generally accepted that isosteric heats of adsorption which are measured on a uniform surface will show a sharp decrease at the completion of the first layer, the monolayer capacity can be estimated from this point. In actual fact, the isosteric heats for this system showed a detectable decrease at the completion of the second layer as well as at the end of the first. Therefore, the moles of gas held in the first and in the second layer were estimated from these measurements. This information, taken together with the isotherm data, allows one to make a critical evaluation of the applicability of the B.E.T. theory to helium adsorption as well as permitting the subsequent testing of any new isotherm equations. It will be shown that no B.E.T.-type model is completely satisfactory when applied to helium adsorption, but that the modified B.E.T. isotherm proposed by Steele gives more realistic results than any other treatment.

[2] R. P. Singh and W. Band, J. Phys. Chem. **59,** 663 (1955).
[3] J. G. Aston and S. V. R. Mastrangelo, J. Chem. Phys. **19,** 1067 (1955); **24,** 124 (1956).
[4] W. A. Steele, J. Chem. Phys. **25,** 819 (1956).
[5] L. Meyer, Phys. Rev. **103,** 1593 (1956).

2. EXPERIMENTAL

It has been found previously that equilibrium times are quite long for measurements of the adsorption of helium at 4°K or less at coverages less than a monolayer.[6] In this work, it proved to be impractical to determine low coverage heats of adsorption at 4°K. However, these heats were easily measurable at 10°K, and have been reported in III. Therefore, partial molar heat capacities of the adsorbed helium were determined over the range 4°-10°K, and the changes in the 10° heats of adsorption upon cooling to 4° were calculated from these data. (This change turned out to be smaller than the experimental error.)

The apparatus used in this work has been described in III. The temperature of the calorimeter which contained the adsorbent was measured with a carbon resistance thermometer that was calibrated against the vapor pressure of helium during each experiment. For measurements at temperatures ranging from 4.2° to 10°, a resistance versus temperature curve was constructed by fitting the measured data in the liquid helium and solid hydrogen regions to the Clement[7] equation. Since accuracy in the measurements of absolute temperature was not critical compared to the need for precise measurements of temperature differences, the Clement equation proved to give an adequate temperature calibration in this region.

In the liquid-helium region, it was not convenient to break the thermal isolation of the calorimeter by the addition of exchange gas since this technique required long pumping times to regain the high vacuum necessary for thermal isolation. Therefore, two cooling tubes were soldered to the calorimeter. These tubes passed through the liquid helium bath before entering the vacuum space surrounding the calorimeter. Gaseous or liquified helium could be circulated through these tubes and thus the calorimeter could be cooled to bath temperature by heat exchange with this helium. Thermal isolation was then regained by pumping the helium out of the tubes.

The usual equations for the computation of the calorimetric heat of adsorption from the raw experimental data require a knowledge of the change in the amount of gas on the surface during a measurement. If the amount of gas on the surface is large, and the change small, any errors in pressure measurements will appear as large errors in the heat of adsorption. This problem turned out to be rather important in the present work,

[6] S. V. R. Mastrangelo, Ph.D. thesis, The Pennsylvania State University, 1951.
[7] J. R. Clement, in *Temperature, Its Control in Science and Industry* (Reinhold Publishing Corporation, Inc., New York, 1955), Vol. II, p. 380.

since a typical measurement involved the addition of 0.00015 mole of gas to the system at total coverages of 0.025 mole or greater. In order to realize the full precision of the thermometric measurements, it was necessary to devise a procedure for smoothing the pressure measurements. This was done in the following way: a plot of the number of moles on the surface N_a versus the total number of moles in the system N_t was constructed. From this plot, the number of moles adsorbed at a constant temperature T_1, $dn(T_1)$, could be calculated from the known total moles added dN

$$dn(T_1)=dN\cdot(\partial N_a/\partial N_t)_T. \tag{2.1}$$

When dN moles are added to a system at initial conditions p_1, T_1, N_{t1}, the pressure and temperature of the system rise, giving a final state p_2, T_2, N_{t2}, and the net change in the coverage can be written as

$$dN_a=N_a(N_{t2}, T_2)-N_a(N_{t2}, T_1)+N_a(N_{t2}, T_1)-N_a(N_{t1}, T_1) \tag{2.2}$$

$$=dn(T_1)+dn(N_{t2}), \tag{2.3}$$

where $dn(T_1)$ is equal to the change in coverage at constant temperature T_1 due to the change in N_t, and $dn(N_{t2})$ is equal to the change in coverage due to a change in temperature at a constant total number of moles in the system. The isosteric heat q_{st} is calculated from the equation

$$q_{st}dN_a=C\cdot(T_2-T_1)+V\cdot(p_2-p_1)$$

$$=q_{st}\cdot[dn(T_1)+dn(N_{t2})], \tag{2.4}$$

where C denotes the heat capacity of the entire system (calorimeter plus adsorbent plus N_{t2} moles of gas). Let us now suppose that a heat capacity measurement is carried out, with starting conditions of N_{t2}, T_1, p_3 and final conditions N_{t2}, T_2, p_2. In this measurement, an amount of heat Q is added to the system. Then

$$Q=-q_{st}dn(N_{t2})+C\cdot(T_2-T_1)+V\cdot(p_2-p_3), \tag{2.5}$$

where the first term on the right-hand side of the equation gives the amount of heat adsorbed in the desorption of $dn(N_{t2})$ moles of gas during the measurement. When 2.5 is substituted into 2.4, the final result is

$$q_{st}dn(T_1)=Q-V\cdot(p_3-p_1). \tag{2.6}$$

The pressures appearing in the last term on the right-hand side of Eq. (2.6) are calculated from the isotherm at T_1, and $dn(T_1)$ is obtained from Eq. (2.1). Thus, the isosteric heat is given quite simply, if the quantity Q can be determined. Although it is a simple matter to bring the calorimeter to the initial conditions N_{t2}, T_1, p_3, it is not generally possible to regulate Q to give the exact temperature rise desired. However, by taking several heat-capacity measurements under conditions which are approximately the desired ones, it is easy to obtain the necessary quantities from the data.

Heats of adsorption were also calculated from two pairs of isotherms determined during different experiments. The temperatures of these isotherms were 4.197° and 4.330°, and 4.223° and 4.425°. It was found that the simple Clausius-Clapeyron equation did not give good results when applied to this data, due to the fact that B the second virial coefficient of gaseous helium, and V_a the molar volume of the adsorbed phase (assumed to be equal to the liquid molar volume), were not negligible. However, they were sufficiently small to allow one to calculate q_{st} from the equation

$$q_{st}=R[\partial \ln p/\partial(1/T)]_{N_a}[1+p/RT(B-V_a)]. \tag{2.7}$$

The necessary values of B and V_a were obtained from Keesom.[8]

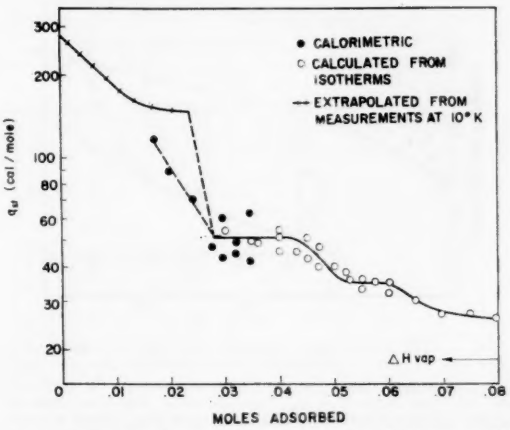

FIG. 1. The experimental heat of desorption of helium at 4°K plotted as a function of the total moles adsorbed. The heats are given on a logarithmic scale in order to show the high coverage heats in greater detail than would be possible in the conventional linear plot. The crossed solid line represents the average of the heats measured at 10° and extrapolated to 4°K with the aid of the experimental heat capacities over the range 4°–10°. The 4° data are not completely in agreement with the 10° results in the coverage region 0.020–0.025 mole, and the two dashed lines show the estimated upper and lower limits of the heats in this range.

The experimental q_{st} data are shown in Fig. 1. The solid line is the best curve through the points measured at 10°, and extrapolated to 4° by means of the partial molar heat-capacity measurements. (It may be noted that P, T, N_a data were obtained at temperatures from 4° to 10° in the course of the heat-capacity measurements. Isotherms were constructed from these data at even temperatures throughout the range.[9] Although these isotherms cannot be discussed in detail due to the lack of any theoretical treatment valid in the region of the critical temperature, it is worth noting that the data indicate that multilayer formation occurs in this system at temperatures above the critical temperature of the adsorbate.) The q_{st} shown in Fig. 1 are plotted on a logarithmic scale so as to emphasize the high coverage heats. The chief points of interest in the figure are the values of q_{st} over the regions where it is

[8] W. H. Keesom, *Helium* (Elsevier Publishing Company, Inc., New York, 1942).

[9] M. Ross, Ph.D. thesis, The Pennsylvania State University, 1960.

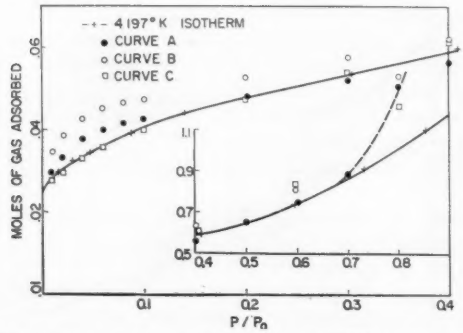

FIG. 2. The experimental isotherm at 4.197°K is shown as a solid line, with the experimental points given by the plus signs. The main figure shows the low-pressure region of the isotherm, and the inset shows the high-pressure data. The total moles of helium adsorbed are plotted as a function of p/p_0, where p_0 is the vapor pressure of bulk liquid helium at 4.197°. The points shown were calculated from the theoretical isotherm equation (A.12) using the following values of the parameters: A: $\epsilon_2-\epsilon_{liq}=-33$ cal/mole, $N_a=0.022$ mole, $K_2=1$, B: $\epsilon_2-\epsilon_{liq}=-33$ cal/mole, $N_a=0.027$ mole, $K_2=0.8$, C: $\epsilon_2-\epsilon_{liq}=-20$ cal/mole, $N_a=0.025$ mole, $K_2=1$. The parameters used in C were obtained by fitting the experiments to the equation proposed by Steele,[4] and are thus adjusted to give the best fit between his model and experiment. The parameters in A and B were estimated from the ϵ_2 and layer capacities obtained from the heats of adsorption ($K_2=0.8$, $N_a=0.025$ corresponds to a layer capacity of 0.022 mole in the second layer). It is seen that the experimental ϵ_2 appear to be too large to fit the theory in the low coverage region, and that all the models predict too much adsorption as $p/p_0\to 1$. Although the inclusion of more K_n should improve the agreement as $p/p_0\to 1$, the inclusion of more c_n will worsen the agreement. Furthermore, in the region where the theory should be most accurate (i.e., at or slightly greater than the monolayer coverage), these higher terms have a very small effect on the isotherm.

approximately constant, and the coverages at which q_{st} changes from one constant value to another. In the region from $N_a\simeq 0.020$ mole to ~ 0.025 mole, there is noticeable disagreement between the data taken at 4° and at 10°. However, the equilibrium times for the 4° measurements were quite long in this coverage range (upwards of 45 min), and it is believed that the differences which are observed are most probably due to a lack of complete equilibration at 4°K. In any case, both sets of data indicate that a sharp break occurs in the curve at $N_a=0.028$ mole. This coverage is thus assumed to correspond to the completion of the first layer. It may also be concluded that q_{st} is approximately constant and equal to 52 cal/mole during much of the adsorption of the second layer. A second rather smeared-out break in the curve occurs at about 0.050 mole, with another roughly constant region with $q_{st}=34$ cal/mole starting at $N_a=0.052$ mole. If this point is assumed to correspond to the beginning of adsorption in the third layer, then the amount of gas held in the second layer is equal to 0.024 mole.

In III, it was stated that the area available for helium adsorption on this sample amounts to 1200 m². It is possible to calculate the amount of helium held in a liquid-packed layer, and the interlayer distance from the known area of the sample, and the molar volume of liquid helium at 4.2°. The usual method of calculating these quantities involves the assumption of face-centered cubic packing in the liquid, which of course implies 12 nearest neighbors per atom. X-ray data on ordinary liquids generally support this hypothesis, giving 11 as the number of nearest neighbors, and distances of closest approach consistent with a close-packed lattice. However, this is not the case in the helium system—the data of Keesom and Taconis[10] have been interpreted as indicating six nearest neighbors at an average distance of 3.33 A (at 4.2°), rather than the distance of 4.21 A to be expected for a face-centered cubic lattice. Using this data, and the lattice structure proposed by Keesom and Taconis, one obtains an area of 14.5 A² per atom, a liquid-packed layer capacity of 0.0137 mole, and a layer separation of 3.61 A (this is to be compared with the values of 17.8 A², 0.0112 mole and 2.98 A calculated for a face-centered cubic lattice). Unfortunately, the more recent neutron-scattering experiments of Hurst and Henshaw[11] are not completely consistent with this interpretation of the structure of liquid helium. However, their data can be reasonably well approximated by assuming that the liquid has a simple cubic lattice structure with lattice spacing of 3.70 A. This alternate liquid structure leads to an interlayer separation of 3.70 A and a liquid-packed layer capacity of 0.0145 mole. Thus, although the assumed lattice structures differ, the estimates of layer capacity and interlayer distance obtained from the different experiments are nearly the same. The values used for these parameters in this work were the average of the estimates: 0.0141 mole for the layer capacity, and 3.65 A for the layer separation.

One of the more remarkable features of these experiments is that the amounts of helium held in both the first and second layers is considerably larger than that predicted on the basis of a total area of 1200 m² and liquidlike packing. In the following sections, the observed compressions and heats of adsorption will be shown to be in good agreement with theoretical estimates.

Keesom and Schweers[12] have measured heats of adsorption of helium on an oxygen-covered glass surface, and have reported second and third layer heats of 62 and 42 cal/mole, respectively. Since the interaction energy of a pair of oxygen molecules is nearly the same as that of a pair of argon atoms (the parameters of the Lennard-Jones function are $\epsilon/k=118°$ and 120°, and $\sigma=3.46$ A and 3.40 A for O_2 and Ar, respectively), one would expect that both of these prepared surfaces would be nearly equivalent with respect to their properties as adsorbents of helium. The agreement of the heats of adsorption obtained in the two studies confirms this surmise.

An isotherm at 4.197°K was constructed from the experimental points, and is shown in Fig. 2. The isotherm data were fitted to the B.E.T. theory, and an

[10] W. H. Keesom and K. W. Taconis, Physica **4**, 28, 256 (1937).
[11] D. G. Hurst and D. G. Henshaw, Phys. Rev. **100**, 994 (1955).
[12] W. H. Keesom and J. Schweers, Physica **8**, 1032 (1941).

TABLE I. Estimates of layer capacity and surface interaction energy.

Layer n	Experimental $\epsilon-\epsilon_{liq}$ (u_s)	$-n^3u_s$	Layer capacities (moles) Experimental	Perturbation Eq. (3.2)	Perturbation Eq. (3.3)	Modified F.H.H.-Eq. (3.5)	Lateral Interaction Fig. 5
1			0.028			0.027	0.030
2	−34	270	0.024	0.0378[c]	0.0224	0.022	0.021
	−48[a]	380[a]					
3	−16	430		0.0253[c]	0.0202	0.020	0.019
4	− 7	450		0.0190	0.0182	0.018	0.017
5	− 3.5[b]	450[b]		0.0168	0.0165	0.017	
6	− 2.1[b]	450[b]		0.0156	0.0155	0.015	
7	− 1.3[b]	450[b]		0.0150	0.0150		
	∞ 0		0.0141	0.0141	0.0141		

[a] Attractive energy only, estimated from Eq. (4.1).
[b] Calculated assuming that $-n^3u_s=450$.
[c] First-order perturbation theory inadequate.

apparent monolayer volume of 0.039 mole was obtained. Furthermore, the apparent $\epsilon-\epsilon_{liq}$ calculated from the B.E.T. c was −60 cal/mole. Neither of these results are in agreement with the independent estimates of these parameters. The treatment of these data by means of the modified theories will be discussed in Sec. 6.

3. ADSORPTION AT HIGH COVERAGES

It has been shown in I[13] that

$$RT\ln(p/p_0)=u_s(L_s)(1+u_s(L_s)\rho_0K_0/2+\cdots) \qquad (3.1)$$

$$\rho=\rho_0(1+u_s(L_s)\rho_0K_0+\cdots), \qquad (3.2)$$

where p is the pressure of the adsorbed film with thickness L_s, p_0 is the vapor pressure of bulk liquid helium at the temperature of the experiment, ρ_0 is the density of bulk liquid helium (in mole/cc), and K_0 is the isothermal compressibility of the bulk liquid; $u_s(L_s)$ is the perturbation energy due to the interaction of an atom at a distance L_s from the surface with the surface. If the perturbation of the system is not too large, $u_s(L_s)$ may be obtained by subtracting the heat of vaporization of the liquid from the experimental heat of adsorption values. For liquid helium at 4.2°, $\rho_0K_0=0.050$ (cal/mole)$^{-1}$, and $\Delta H_{vap}=18$ cal/mole.[8] Table I shows the values of u_s for an atom in a given layer. The numbers given for the first four layers were obtained from the experimental results; the u_s values listed for the more distant layers were calculated by assuming that u_s is proportional to L_s^{-3} in this region. (This approximation has been shown to be generally valid for van der Waals' surface-adsorbent interactions at large distances from the surface.[14] The results shown in column 3 of Table I indicate that it is reasonably accurate in the present work for layers higher than the second.) If it is assumed that the amount of helium held in a layer is proportional to the density, one can compute the expected layer capacities from Eq. (3.2) and the calculated liquid-packed layer capacity given in the previous section. These data are given in column 5 of Table I, and it is seen that the compression of these layers is quite large near the surface. In fact, the perturbation of the density in the first three layers is too large to be treated quantitatively by the first-order terms in Eq. (3.2). Formal expressions for high-order terms in this equation can be derived by extending the derivation given in I. These terms are of two types: one group of terms related to the work of compression of the liquid in the potential field, neglecting the fact that the potential field in the neighborhood of a given atom varies with position; and a second group of terms which arise from this variation of potential with position (in this case, the important variation is due to changes in the distance from the surface). The latter terms cannot be evaluated without a specific knowledge of the unperturbed radial distribution function of the atoms in the liquid. However, because of the relatively large K_0 for liquid helium at 4°, and its rapid variation with ρ_0, one might guess that the second-order "homogeneous compression" terms would make up a large fraction of the total second-order term in this system. When this term is included in the equation for the density, it appears as the second term in a Taylor series expansion of the density in terms of the compressibility, and Eq. (3.2) becomes

$$\rho=\rho_0\{1+\rho_0K_0u_s(L_s)[1+0.5u_s(L_s)(\partial K_0/\partial V)_T]+\cdots\}. \qquad (3.3)$$

Column 6 of Table I shows the values of the layer capacities calculated from 3.3 using $(\partial K_0/\partial V)_T$ equal to 0.024 (cal/mole)$^{-1}$, and it is seen that the second-order formula gives results which are quite close to the experimental, except in the first layer. These figures are probably accurate to about 10% in all layers

[13] W. A. Steele and M. Ross, J. Chem. Phys. **33,** 464 (1960); **34,** 1067 (1961). (Paper I.)
[14] T. L. Hill, in *Advances in Catalysis* (Academic Press, Inc., New York, 1952), Vol. IV.

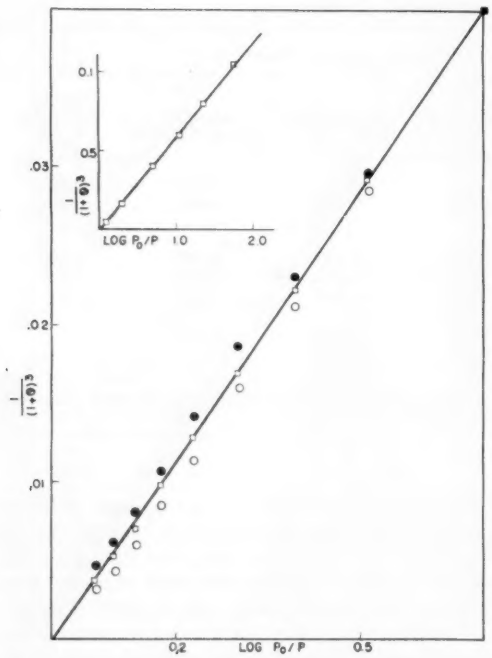

FIG. 3. The fit of the experimental isotherm points to the modified Frenkel-Halsey-Hill equation [Eq. (3.5)] is shown here. The main figure shows the high coverage points ($\theta>2$), and the insert shows the entire coverage for $\theta>1$. The points were calculated using different sets of layer capacities. The quantities used (in moles) are listed consecutively, starting with the first layer ●: 0.027, 0.022, 0.022, 0.020, 0.020, □: 0.027, 0.022, 0.020, 0.018, 0.017, 0.015, ○: 0.027, 0.022, 0.018, 0.016, 0.015, 0.015. The fit is slightly better using the □ layer capacities than the ● or ○, and this set of parameters was taken to be the best approximation to the actual values.

above the second, and accurate to perhaps 20% even in the second layer.

Equation (3.1) is a generalized version of an earlier equation known as the Frenkel-Halsey-Hill[14] equation. Equation (3.1) can be converted into this isotherm by assuming that the second-order term is negligible, that u_s is proportional to L_z^{-3}, and that θ the number of layers adsorbed, is proportional to L_z. The resultant equation can be written

$$\ln(p/p_0)=A/\theta^3, \tag{3.4}$$

where A is a constant related to u_s/RT. As pointed out above, the assumption that u_s is proportional to L_z^{-3} is generally quite accurate, and is apparently correct in this system if θ is greater than two. However, the second assumption is much more approximate, and is also somewhat arbitrary.

If one wishes to fit the helium isotherm data to Eq. (3.4) (or any other similar equation involving the parameter θ), it is immediately apparent that the large changes in layer capacities in the first few layers require that θ be considered to be a function of many adjustable parameters (specifically, a function of the number of moles held in each completed layer). In view of this, one might expect that the data could be made to fit Eq. (3.4), even if θ were not exactly proportional to L_z. However, the net result of a number of attempts to do this led to the conclusion that it was impossible to fit the data to Eq. (3.4) with any reasonable set of layer capacities. In particular, the plots of $\ln(p/p_0)$ versus θ^{-3} were not completely linear at $\theta>3$, and the best straight lines drawn through the points did not pass through the origin. It seemed most likely that the weak point in the derivation involved the assumption that $\theta\sim L_z$. Indeed, if the adsorption process is visualized as occurring layer by layer, L_z will be constant throughout the completion of each layer, and one may equally well set $\theta+x\sim L_z$ where $1>x>0$. Therefore, an attempt was made to fit the data to the equation

$$\ln(p/p_0)=B/(1+\theta)^3, \tag{3.5}$$

where B is a constant similar to the A in Eq. (3.4). The use of $1+\theta$ for θ in the isotherm equation results in a predicted p/p_0 which is closer to one, and which varies somewhat more slowly with coverage. Note that if the last term on the right-hand side of Eq. (3.1) is appreciable, it will affect p/p_0 in the same way, and thus the use of Eq. (3.5) in preference to (3.4) may be considered as a rough method of including the higher order correction term which appears in the general expression.

When the data were fitted to Eq. (3.5), it turned out that good fits and reasonable values for the parameters were obtained. In Fig. 3, the points show the values of $\ln(p/p_0)$ calculated from the experimental data at various values of $(1+\theta)^{-3}$, using three different sets of assumed layer capacities. All three sets give reasonably linear plots, but the straight line through the squared points also passes accurately through the origin. Since the points near the origin represent the high coverage region where a perturbation theory should be most accurate, this requirement that the line pass through the origin is felt to be quite important. The large figure shows the data for $\theta\geq 2$; at $\theta<2$, one would not expect that this treatment would give an accurate description of the system. Nevertheless, the plot shown in the inset of Fig. 3 indicates that there is good agreement between experiment and theory for all $\theta>1$. The layer capacities used to calculate the squared points are shown in column 7 of Table I. Since there are six adjustable parameters involved in this calculation, it is clear that the values given cannot be regarded as unique. However, it was found that the fit was quite sensitive to the choice for first and second layer capacities. If the sum of these two parameters was changed by 5%, the fit at high coverages was destroyed; if the first layer capacity was changed by 5%, the fit over the region $\theta=1$ to 2 was lost. Furthermore, at high coverages, it was necessary to pick layer capacities of 0.017 ± 0.002 mole to obtain a fit. These restrictions, together with the intuitive requirement that the density of the film be a monatonically varying function of the

distance from the surface lead to the conclusion that the layer capacities given in column 7 of Table I are probably quite close to the actual values. The slope of the line in Fig. 3 is equal to 0.079. Since it has been assumed that $\theta+1=L_z/D$, where D is the distance between successive adsorbed layers, it follows that

$$-u_z(L_z/D)^3=RT/\text{slope}=10.4\ \text{(cal/mole)};\quad (3.6)$$

u_z as a function of L_z can be obtained from the theoretical helium-argon surface interaction potential curve which is discussed in the next section.

4. ADSORPTION ENERGY

In III, it was shown that the results of the measurements made on the helium-argon adsorption system at 10°–20°K were in quantitative agreement with the properties calculated from the theoretical interaction curve obtained by summing the helium-argon pair interaction energies over the entire face-centered cubic argon crystal. This interaction energy was given by the expression

$$\epsilon(\rho, n)$$
$$=-8.15[S_6(\rho, n)-0.0289S_{12}(\rho, n)]\text{(cal/mole)},\quad (4.1)$$
$$\rho=z/a$$

where z is the perpendicular distance from the surface, a is the length of an edge of an argon unit cell (5.42A), n denotes the position of the helium atom relative to the unit cell, and S_6 and S_{12} are the appropriate reduced sums of the inverse 6th and 12th powers of the helium-argon atom separation distances. ϵ was computed as a function of ρ (up to $\rho=2$) for an atom over the midpoint of an edge of a lattice cell (position 0, in the notation of III), directly over an atom at the corner of a lattice cell (position 2), and over a point on the diagonal bisector of the cell which is midway between the corner and a center of the cell (position 4). These three points serve to characterize the main features of the variation of the potential as an atom moves over the surface of the adsorbent. It was shown that, for the adsorbent used in this work, 0.014 mole of helium would adsorb over position 0 with an energy of -180 cal/mole, and that 0.014 mole of helium would subsequently adsorb over position 2 with an energy of about -100 cal/mole. It was concluded that adsorption into the second layer would commence at coverages greater than 0.028 mole, in good agreement with the present measurements.

In this work, these calculations were extended to give two quantities of interest: the perturbation energy u_z due to the helium-solid interactions at large ρ; and the minimum energy and most probable distance from the surface for an atom adsorbed in the second layer. The calculation of u_z is carried out by remembering that $u_z=\epsilon-\epsilon_{He}$ at large ρ, where ϵ_{He} is the energy of interaction of a helium atom with a semi-infinite slab of liquid helium at a distance ρ from the atom. The ϵ_{He} is easily computed by integrating the helium-helium pair interaction energy over the slab of liquid (note that in the case of an atom interacting with a liquid, the approximation introduced in the integration process is much less serious than in the atom-solid case. This is due to the fact that the number density in a liquid does not depend upon position, thus making the integration exactly correct if the atom-liquid separation is sufficiently large to allow one to set the pair correlation function between the adsorbed atom and any atom in the liquid equal to one.) This energy is given by the expression:

$$\epsilon_{He}=-(2\pi N_0/3)\epsilon_{He-He}^{*}(\sigma_{He-He}^{6}/a^3)\rho^{-3},\quad (4.2)$$

where ϵ_{He-He}^{*} and σ_{He-He} are the constants in the Lennard-Jones expression for the He—He pair interaction, and N_0 is the number of atoms per cubic centimeter in liquid helium. When the values of these parameters are substituted into Eq. (4.2), ϵ_{He} is calculated to be equal to $-0.63/\rho^3$ (cal/mole). At $\rho>1$, the values of $\epsilon(\rho)$ calculated from Eq. (4.1) are the same at a given ρ, regardless of the position of the atom over the surface. The dotted line in Fig. 4 shows the calculated values of ϵ as a function of distance for $\rho>1$. This curve can be represented by $-26/\rho^3$ (cal/mole) to within 10% over the range $\rho=1$ to 2. Thus, $-u_z=$

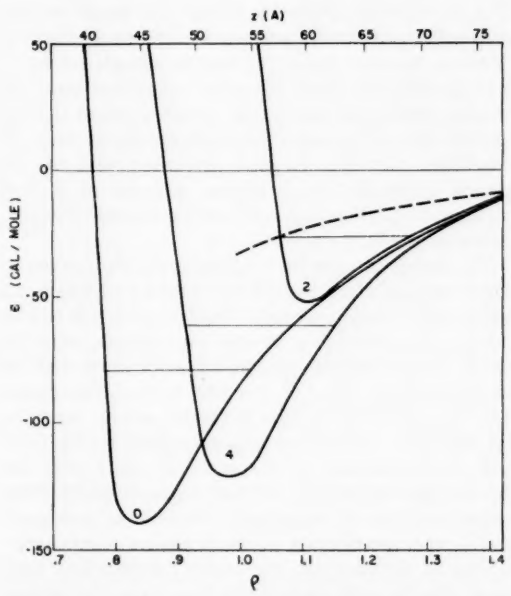

FIG. 4. The solid curves show the calculated energy of interaction of a helium atom with a helium-covered argon surface plotted as a function of the reduced distance from the surface (lower scale) and as a function of the unreduced distance from the surface (upper scale). The dotted line shows the energy of interaction of the helium atom with the argon surface, not including any helium-helium interactions. The horizontal lines show the estimated vibrational ground states for a helium atom over positions 0, 2, and 4. (See Sec. 4 for the meanings of the position numbers and the details of the assumptions made in the calculation of the energy curves). *Note*: the values of z shown should range from 4.0 to 7.5 A.

$25.4/\rho^3 = 4.1 \cdot 10^3/L_z^3$ (L_z in A). If the result of this theoretical calculation is accepted as correct, then the distance between layers D can be calculated to be 3.41 A, using Eq. (3.6). Since this value represents the average interlayer spacing in a region where the adsorbed helium is somewhat compressed, it may be concluded that it is in good agreement with the expected value for the interlayer distance of 3.65 A obtained from the x-ray and neutron-scattering experiments on the bulk liquid.

The energy of an isolated helium atom adsorbed on an argon surface which is 1200 m² in area and which has 0.028 mole of helium already adsorbed on it, will now be calculated. (According to the experiments, such an atom will go into the second adsorbed layer with an energy equal to $-q_{st}+\bar{H}_g = -53+21 = -32$ cal/mole.) The theoretical calculation is carried out by summing the adsorbent-adsorbed atom energy given by Eq. (4.1) and the interaction of the adsorbed atom with the helium atoms already on the surface. Since these atoms are believed to be highly localized at positions 0 and 2, the contribution of these helium-helium interactions to the total can be roughly calculated by summing the He—He pair interaction over the nearest four or five helium atom neighbors, assuming that these neighbors are exactly fixed at the points of maximum potential energy (i.e., at the centers of their sites). The potential energy curves calculated in this way are shown in Fig. 4 for an atom adsorbed over positions 0, 2, and 4. The horizontal lines represent the net energy when the vibrational zero-point energy perpendicular to the surface is subtracted from the total. In order to complete the calculation of the total energy of an adsorbed atom in the second layer, one must estimate the amount of energy associated with the motion of this atom parallel to the surface. The fact that the calculated energies given in Fig. 4 show an appreciable variation as the atom moves from point to point leads one to expect that there may be a considerable amount of zero-point energy associated with these degrees of freedom. However, it must be remembered that the zero-point motion of the underlying helium atoms has been entirely neglected in this calculation. Since the effect of including this motion will appear primarily as a smearing out of the individual curves, it was assumed that a reasonable estimate of the total energy could be obtained by taking a weighted average of the three energies shown in Fig. 4 (the weighting is necessary to take account of the relative numbers of each type of position to be found in this surface), and by further assuming that the energy of motion parallel to the "averaged" surface was equal to the classical kinetic energy of RT. The final value of the energy calculated in this way is -44 cal/mole. In view of the approximations involved, this result agrees reasonably well with the experimental value of -32 cal/mole. (the estimated experimental error is ± 5 cal/mole in this region). Furthermore, this calculation is certainly adequate to show that the experiments bear out the previous assertions that the amount of helium held in the first layer on this surface is 0.028 mole.

5. LATERAL INTERACTION ENERGY

In many theoretical calculations of physical adsorption properties, the surface of the adsorbent is taken to be a planar slab which is perfectly smooth and has a surface-gas interaction potential which depends only upon the perpendicular distance between the adsorbed atom and the surface. Multilayer adsorption is also treated in terms of a similar potential existing between the adsorbed atom and the system (solid plus previously adsorbed gas). In these treatments, the thermodynamic criterion for the layer density at a given gas pressure is obtained by expressing the chemical potential of the atoms in each layer as a function of the density in the layer, and equating this to the chemical potential of the gas. However, when the nth layer reaches a density which is of the order of the liquid density, the total energy of the layer begins to rise rapidly because of repulsive interactions in the layer. At this point, the layer may be said to be complete. Thus, one may obtain a reasonable estimate of the density of the nth completed layer by assuming that adsorption into the $(n+1)$th layer commences when the total energies per atom are equal in the two layers. The total energy of the nth layer is calculated by summing the surface interaction and the lateral interaction; the total energy of the $(n+1)$th layer at zero density is just equal to the surface interaction energy of an atom in the layer.

In the present system, the result of such a calculation of the density of the first layer of adsorbed helium could not be expected to be equal to the observed value because the assumption of a perfectly planar surface has been shown to be sharply at variance with the actual rapidly varying potential function. However, this computation is useful in that one can obtain an upper bound to the theoretical layer density in this way. Furthermore, the variations in potential energy in the second and higher layers are considerably less than those in the first, and thus one may expect that layer densities calculated in this way will be reasonably accurate for these layers.

As is well known, the behavior of condensed helium is dominated by the effect of zero-point energy. F. London[15] has carried out an approximate calculation of the thermodynamic properties of liquid helium. He computed the van der Waals energy of the liquid by summing the pair interactions over all the atoms in the liquid, assuming that these atoms were arranged on a regular lattice. When this quantity was added to the theoretically estimated zero-point energy of a gas of hard spheres having the density of the liquid, energies and molar volumes were obtained which were in good agreement with the experimental values of these quantities. Although the lattice structure proposed by

[15] F. London, *Superfluids* (John Wiley & Sons, Inc., New York, 1954), Vol. II.

Keesom and Taconis turned out to be the most stable lattice at low densities, it was also shown that a close packed lattice was the most stable at high densities. It is not difficult to adapt this computation to treat an adsorbed layer of helium. Since the high-density region is of primary interest here, the van der Waals energy was calculated by summing the helium-helium pair interactions over a two-dimensional hexagonal close-packed lattice as a function of the density of the atoms in the layer. The result of this calculation is shown by curve I in Fig. 5. The zero-point energy of this system can be estimated by assuming that each atom is confined to a two-dimensional square box. The solutions of the Schrödinger equation show that these energy levels are just two-thirds as large as those of the corresponding three-dimensional case. However, at the high densities of interest in this work, the levels are quite sensitive to the rather arbitrarily chosen atomic sizes and box dimensions. Therefore, it is advantageous to calculate the two-dimensional zero-point energy by taking two-thirds of the experimental zero-point energies of solid helium. Dugdale and Simon[16] have measured the C_p of solid helium over a wide range of densities, and have calculated the zero-point energies from the experimental Debye θ values. In Fig. 5, curve II gives the molar zero-point energy of a two-dimensional helium film plotted as a function of the area per atom. Curve III is the sum of I and II, and is thus the molal lateral energy of a dense helium layer. Note that the upper abcissa scale shows the number of moles adsorbed on the surface used in this work which correspond to a given layer density. It was shown in III that the maximum surface interaction energy of an isolated helium atom on an argon surface amounts to -290 cal/mole. It was also shown in the present work that the perpendicular interaction energy of an atom in the second layer amounts to approximately -60 cal/mole (this figure was obtained by averaging over the two most energetic sites—in this way, the variation in energy due to site 2 is included in the lateral contribution to the energy). The surface energies in the third and higher layers can be taken to be equal to u_s. In this way, an upper limit to the density of the first layer is obtained by reading off the density at which the lateral interaction energy given by curve III is equal to 230 cal/mole. The layer capacity corresponding to this point is estimated to be 0.030 mole. The layer capacities of the first four layers calculated from curve III are shown in column 8 of Table I. These values are seen to be in good agreement with experiment and with the various other theoretical estimates of layer capacity.

Figure 5 shows that the molal lateral interaction energy of a layer of helium rises very rapidly to large repulsive energies at an area per atom of 7 A². Since the minimum of the van der Waals energy occurs at 7.0 A² (see curve I), the rise in the total energy at these densities is due to the combined increases in the repulsive van der Waals energy and in the zero-point energy. It is therefore highly unlikely that adsorbed helium can be compressed to an area per atom much smaller than 7 A². This point corresponds to a density which is 2.2 times the liquid-packed density, or an average interatomic distance of 2.84 A in the layer.

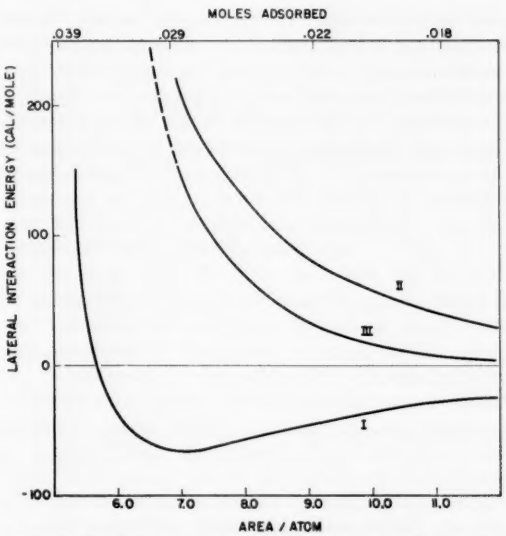

FIG. 5. Curve I shows the energy of interaction of a helium atom with its nearest neighbors in a two-dimensional hexagonal close-packed array, plotted as a function of the area per atom (lower scale), and as a function of the number of moles of gas held in a layer of area = 1200 m² (upper scale). Curve II shows the zero-point energy of an atom in such a layer, estimated from the experimental values of the zero-point energy of solid helium. Curve III is the sum of I and II and is thus the net lateral interaction energy of a helium atom in an adsorbed layer in which the surface interaction energy is constant at all points within the layer.

6. COMPARISON OF EXPERIMENT WITH SITEWISE MODELS

In view of the good agreement between the various estimates of layer capacity, and between the theoretical and experimental energies of adsorption, it is now apparent that the comparison of these data with the values of the parameters obtained from the sitewise isotherm models which have been suggested for helium adsorption would provide a critical test of these theories. The B.E.T. values of 0.039 mole for the first layer capacity and -71 cal/mole for the energy of an atom in the first layer are quite obviously poor approximations to the actual values. It has been pointed out that this failure is primarily due to the B.E.T. assumption that the energy of an atom in the second layer is equal to the energy of liquefaction. Aston and Mastrangelo[3] proposed to modify the B.E.T. equation by assuming that the energy of an atom was the same in the first two layers. In this case, the data give $\epsilon_1 = \epsilon_2 = -71$ cal/mole and the layer capacities of the first two layers become 0.0194 mole each. Thus, this model is also a

[16] J. S. Dugdale and F. E. Simon, Proc. Roy. Soc. (London) **A215**, 291 (1953).

poor approximation to the correct values. Steele[4] modified the B.E.T. isotherm to allow for an energy in the second layer different from the energy in the first, and different from the energy of liquefaction. The fit of the isotherms to this model is shown by the squares in Fig. 2, and the parameters obtained are 0.025 mole for the layer capacity (in all layers), $-\epsilon_1 \gg RT$, and $\epsilon_2 = -31$ cal/mole. It is seen that these results are reasonably close to the experimental values, even though they are not quite correct. Some of the more obvious limitations of this model are that all layer capacities are assumed to be the same, and that the energy of an atom in the third layer is assumed to be equal to the energy of an atom in the liquid. Furthermore, the correspondence between the basic assumptions of any B.E.T.-type model and physical reality is questionable, particularly in the second and higher layers. A derivation of a generalized form of the B.E.T. theory is presented in the Appendix to this paper. It is shown that a variable monolayer volume can be introduced as well as a third-layer energy which is different from the energy of liquefaction. However, the final isotherm equation involves too many adjustable parameters to be of any great use in the interpretation of experimental data. Furthermore, when these refinements are included, and the experimentally determined values for the adjustable parameters are used in the isotherm equation, the result (shown by the open circles in Fig. 2) is not noticably improved over the curve calculated from the simple model using experimental values for the adjustable parameters (the filled circles in Fig. 2). Thus, it appears that any further refinements of the theory should be along the lines of replacing the B.E.T.-type model by a more realistic physical description of the state of an adsorbed atom, rather than attempting to include details of changes of layer capacity and adsorption energy in successively higher layers.

7. CONCLUSIONS

The fact that the various estimates of the layer densities of adsorbed helium are in good agreement with each other indicates that the methods of calculation are reasonably realistic. The sharp rise in repulsive energy shown by curve III in Fig. 5 corresponds to a density which is approximately double the liquid-packed density. It seems unlikely that any adsorbent can be found having surface forces sufficiently strong to compress the first layer much more than this. Furthermore, the presence of "sites" (defined as an appreciable variation in the potential energy as the atom moves parallel to the surface) will tend to reduce this compression unless the atoms making up the surface are more closely packed than the helium at this point. This requires that the repeating unit in the surface be 2.8 A on a side or less. This condition is not fulfilled in most common adsorbents, including metal oxide powders and graphitelike materials. Furthermore, since the calculation in Sec. 5 assumes that the layer capacities are determined by the energies rather than the free energies, it is, strictly speaking, valid only at 0°K. It is to be expected that the calculated layer densities at 4.2°K will actually prove to be smaller than at 0°K.

The rather large compressions found in the second and higher layers of adsorbed helium are somewhat unexpected, particularly in view of the small surface interaction energy in those layers. The reason for this phenomenon lies primarily in the extremely large compressibility of liquid helium. If the properties of helium are compared with nitrogen or argon, it is readily seen that, although the surface energies are roughly ten times larger in the latter cases, the bulk compressibilities of the liquids at their normal boiling points are about 100 times smaller than helium. In actual fact, the estimated compressions of adsorbed nitrogen or argon amount to about 10% in the first layer, and are negligible thereafter.

The detailed analysis of the data shows conclusively that the B.E.T. theory does not give meaningful results when applied to multilayer helium adsorption. Although Steele's modification of the theory is still somewhat oversimplified, the monolayer capacity obtained from this equation is accurate to within 10%, which is the same degree of accuracy which is ordinarily claimed for the B.E.T. theory. It is worth noting that the measured heats of adsorption of the second layer of nitrogen on TiO_2[17] give an adsorption energy only 15% greater than the energy of the liquid, whereas the second-layer energies observed in this work are 250% greater than the energy of liquefaction. Consequently, it is not surprising that the analysis of nitrogen isotherms by means of the B.E.T. theory has proved to give consistently good estimates of surface area. In fact, the only adsorbate other than helium which shows such large second layer energies is hydrogen. Recently, Pace and Siebert[18] have shown that the heat of adsorption of the second layer of hydrogen on graphite at 20°K is roughly twice the heat of liquefaction. Furthermore, the apparent B.E.T. first-layer density in this system is double the density obtained from the point of dropoff of the heats. The reason for this apparent anomaly is clearly due to the inapplicability of the B.E.T. theory to these experiments.

In this paper and in III, extensive measurements of the thermodynamic properties of helium adsorbed on argon were compared with theoretical calculations. These calculations were based on equations derived in I which related these thermodynamic properties to the potential energy of interaction of atoms in the vicinity of the surface. Since this potential function could be constructed from the known helium-argon pair interaction energy, the comparison of experiment and theory involved no adjustable parameters, and assumed no particular model for the adsorption process.

[17] G. L. Kington and J. G. Aston, J. Am. Chem. Soc. **73**, 1929 (1951).
[18] E. L. Pace and A. R. Siebert, J. Phys. Chem. **63**, 1398 (1959).

Adequate agreement between experiment and theory was obtained over the entire range of comparison. In view of the success of these computations, it is hoped that it will be possible to determine the nature of the potential functions of other "well-behaved" adsorbents (i.e., those having uniform surfaces) by analysis of the data now in the literature.

APPENDIX

Here, a derivation is given of a generalized B.E.T.-type model for multilayer adsorption in which the surface energy is assumed to be finite in an arbitrary number of layers, and in which the layer capacities are assumed to be different from the liquid-packed layer capacity in an arbitrary number of layers. This derivation is carried out by evaluating the grand partition function for the system, and, except for minor changes in notation, closely follows the treatment of the ordinary B.E.T. equation given in Hill.[19] If z_n is the site partition function of an atom in the nth layer, then we define

$$x=z_\infty \exp(\mu/kT), \qquad c_n=z_n/z_\infty, \tag{A.1}$$

where z_∞ is the site partition function at infinite distance from the surface, and is assumed to be equal to the partition function of an atom in the liquid. Let there be j layers having $c=c_1, c_2, \cdots c_j$. Let the layer capacities be $N_s, N_sK_2, N_sK_2K_3, \cdots, N_sK_2K_3\cdots K_i$ for the first i layers, and $N_sK_2K_3\cdots K_i$ for higher layers. In this way, K_n is defined as the fractional decrease in the number of sites as one goes from the $(n-1)$th layer to the nth. The grand partition function Ξ is written

$$\Xi=\sum_{N_1=0}^{N_s}\frac{N_s!(c_1x)^{N_1}}{(N_s-N_1)!N_1!}\sum_{N_2=0}^{N_1K_2}\frac{(N_1K_2)!(c_2x)^{N_2}}{(N_1K_2-N_2)!N_2!}$$

$$\cdots\sum_{N_i=0}^{N_{i-1}K_i}\frac{(N_{i-1}K_i)!(c_ix)^{N_i}}{(N_{i-1}K_i-N_i)!N_i!}\sum_{N_{i+1}=0}^{N_i}\frac{N_i!(c_{i+1}x)^{N_{i+1}}}{(N_i-N_{i+1})!N_{i+1}!}$$

$$\cdots\sum_{N_j=0}^{N_{j-1}}\frac{N_{j-1}!(c_jx)^{N_j}}{(N_{j-1}-N_j)!N_j!}\sum_{N^*=0}^{\infty}\frac{(N_j+N^*-1)!}{N^*!(N_j-1)!}, \tag{A.2}$$

in which it has been assumed (for convenience) that $j>i$. The limits on the sums in layers less than the ith were obtained under the assumption that the number of sites available in the nth layer per atom in the $(n-1)$th layer is equal to K_n independent of the number of atoms in the $(n-1)$th layer. The sums can be evaluated consecutively using the relations

$$\sum_{a=0}^{\infty}\frac{(a+b-1)!}{a!(b-1)!}u^a=\frac{1}{(1-u)^b},$$

$$\sum_{a=0}^{c}\frac{c!u^a}{a!(c-a)!}=(1+u)^c, \qquad u<1.$$

Starting from the far left-hand side of Eq. (A.2), the first sum is seen to be equal to $(1-x)^{-N_i}$, and the second sum becomes

$$\sum_{N_j=0}^{N_{j-1}}\frac{N_{j-1}!}{(N_{j-1}-N_j)!N_j!}\left(\frac{xc_j}{1-x}\right)^{N_j}=\left(1+\frac{xc_j}{1-x}\right)^{N_{j-1}}. \tag{A.3}$$

Proceeding sum by sum in this way, one may write the sum for the ith layer

$$\sum_{N_i=0}^{N_{i-1}K_i}\frac{(N_{i-1}K_i)!}{(N_{i-1}K_i-N_i)!N_i!}(f-1)^{N_i}=f^{K_iN_{i-1}} \tag{A.4}$$

$$f=1+\sum_{n=1}^{j-i}[x^n\prod_{m=i}^{n+i-1}c_m]+\prod_{m=i}^{j}c_mx^{j-i+1}/(1-x). \tag{A.5}$$

Similarly, the $(i-1)$th sum can be shown to be equal to

$$\{(1+c_{i-1}xf^{K_i})^{K_{i-1}}\}^{N_{i-2}}. \tag{A.6}$$

By continuing in this way, the final expression for the grand partition function is obtained,

$$\Xi^{1/N_s}=1+c_1x\{1+c_2x[\cdots c_{i-2}x(1+c_{i-1}xf^{K_i})^{K_{i-1}}\cdots]^{K_3}\}^{K_2}. \tag{A.7}$$

The desired isotherm equation is calculated from the relation

$$\frac{N_a}{N_s}=\frac{kT}{N_s}\frac{\partial\ln\Xi}{\partial\mu}=\frac{x}{\Xi^{1/N_s}}\frac{\partial(\Xi^{1/N_s})}{\partial x}. \tag{A.8}$$

It is clear that the result of this operation will be an extremely lengthy equation in the general case. We therefore consider a particular case in which $i=2$, $j=2$,

$$\Xi^{1/N_s}=1+c_1x[1+c_2x/(1-x)]^{K_2} \tag{A.9}$$

$$\frac{N_a}{N_s}=\frac{c_1x[1+c_2x/(1-x)]^{K_2}[1+c_2K_2x/(1-x)(1-x+c_2x)]}{1+c_1x[1+c_2x/(1-x)]^{K_2}}. \tag{A.10}$$

[It can be argued that the inclusion of more terms in (A.9) will not produce a more accurate representation of any physically realistic system, since it is generally conceded that the statistical B.E.T.-type models, which are essentially lattice models in which it is assumed that no interaction exists in the two dimensions parallel to the surface, are poor approximations to experiment at coverages higher than the first layer or two.]

It is easy to show that Eq. (A.10) includes several previous isotherm equations as special cases. For instance, Band[20] has derived an equation in which $c_2=1$, $K_2\neq1$. In this case (A.10) reduces to

$$\frac{N_a}{N_s}=\frac{c_1x(1-x+K_2x)}{(1-x)(c_1x+(1-x)^{K_2})}, \tag{A.11}$$

which is equivalent to his result. It has been pointed out that $c_1\gg1$ in the case of helium multilayer adsorp-

[19] T. L. Hill, *Statistical Mechanics* (McGraw-Hill Book Company, Inc., New York, 1956), Appendix 5.

[20] W. Band, Phys. Rev. **76**, 841 (1949).

tion. In this case, Eq. (A.10) becomes

$$\frac{N_a}{N_s}=1+\frac{c_2K_2x}{(1-x)(1-x+c_2x)}. \qquad (A.12)$$

The multilayer isotherm equation proposed by Steele[4] is equivalent to (A.12) with K_2 set equal to one.

In Fig. 2, Eq. (A.12) is compared with the experimental isotherms using several pairs of c_2 and K_2 (and assuming that $c_1 \gg 1$). The c values are related to the adsorption energies by invoking the well-known approximation that the site partition function z_n is equal to $z_\infty \exp[-(\epsilon_n-\epsilon_{liq})/kT]$.

THE JOURNAL OF CHEMICAL PHYSICS VOLUME 35, NUMBER 3 SEPTEMBER, 1961

Electrical Conductivity and Thermodynamic Equilibrium in Nickel Oxide

S. P. MITOFF

General Electric Research Laboratory, Schenectady, New York

(Received January 3, 1961)

The electrical conductivity of nickel oxide has been studied at temperatures between 600° and 1350°C and partial pressures of oxygen between 1 atm and 10^{-4} atm. The slope of log conductivity vs reciprocal temperature plots increases when the temperature is high enough for the sample to come into thermodynamic equilibrium with the atmosphere, and the temperature at which the change in slope occurs is observed to depend on the rate of heating or cooling of the crystal. The heat of formation of nickel vacancies may be determined from the magnitude of the change in slope by a simple calculation. Nickel oxide is a p-type semiconductor [M. Verwey, M. Haaijman, H. Romeijn, and M. van Oosterhout, Philips Research Repts. **5,** 173 (1950)] in which the conductivity is proportional to the concentration of Ni^{3+} ions in the lattice. When thermodynamic equilibrium is established with the atmosphere the conductivity is proportional to the $\frac{1}{6}$th power of the oxygen partial pressure.

The analysis of the conduction mechanism and the conduction data may be self-consistently correlated with nickel diffusion, nickel vacancy diffusion, and weight changes resulting from equilibration with different oxygen partial pressures. The following constants may be determined from these correlations: heat of formation of nickel vacancies, activation energy for nickel vacancy migration, activation energy for electron hole migration, and concentrations of nickel vacancies and Ni^{3+} ions as a function of temperature and oxygen pressure. Combined results give the following for the concentration of nickel vacancies: $0.11(P_{O_2})^{1/6}\exp(-17\,800/RT)$ vacancies per ion pair.

INTRODUCTION

ABRUPT changes in slope are often observed in semi-log plots of conductivity vs reciprocal absolute temperature. In semiconductors and insulators this is usually interpreted as an indication that the conduction mechanism at temperatures above the break is different from that at temperatures below the break. For instance, it may result from a change from intrinsic semiconductivity above the break to impurity semiconductivity below it, or a change from impurity semiconductivity from carriers from deep energy level traps to impurity semiconductivity from carriers from shallow traps. It is the purpose of this paper to present evidence to show that, in nickel, oxide changes in slope result from a transition from a temperature region where thermodynamic equilibrium with the surrounding atmosphere exists to a temperature region where composition is constant. The phenomena to be described in this paper have also recently been reported to occur in titanium dioxide.[1] In some aspects it is similar to the intrinsic and extrinsic regions of conductivity observed in electrolytic conductors such as alkali halides.

[1] J. Rudolph, Z. Naturforsch. **14a,** 727 (1959).

Conductivity at Constant Composition

Verwey's[2] papers have led to a qualitative understanding of the conduction mechanism in NiO. Briefly, this is that the conductivity results from the excess positive charges resulting from Ni^{3+} ions on normally Ni^{2+} lattice sites. When given a sufficient amount of energy these positive holes may be transferred from the Ni^{3+} ions to the Ni^{2+} ions. The charge spends a finite length of time at each site as in a diffusion process, and under an electrical potential gradient a charge may be transferred by this process. In such a model the conductivity should be proportional to the concentration of three plus ions, which Verwey has verified by doping with lithium in order to increase the Ni^{3+} concentration.

Heikes and Johnston[3] have described electrical conductivity in transition metal oxides such as NiO by an equation which is identical in form to that for the motion of ion vacancies in an electrolytic conductor. Thus the hole conduction may be described by a

[2] M. Verwey, M. Haaijman, H. Romeijn, and M. van Oosterhout, Philips Research Repts **5,** 173 (1950).

[3] R. R. Heikes and W. D. Johnston, J. Chem. Phys. **26,** 582 (1957).

diffusion equation:

$$\sigma=\left(\frac{\nu a^2 e^2 N}{6kT}\right)[\mathrm{Ni}^{3+}]\exp\left(\frac{-\Delta H\oplus^*}{RT}+\frac{\Delta S\oplus^*}{R}\right), \quad (1)$$

where ν is jump frequency of the hole, a is the lattice spacing, e is the electronic charge, N is the number of ion pairs per cc, $[\mathrm{Ni}^{3+}]$ the fraction of the Ni ions which are in the three plus state, $\Delta S\oplus^*$ is the activation entropy for the jump, and $\Delta H\oplus^*$ is the activation enthalpy for the jump.

The term $[\mathrm{Ni}^{3+}]$ is an approximation of the probability of a forward jump for an excess of positive charge. These charges cannot jump into a site already occupied by an excess positive charge. In the case considered, i.e., pure NiO, this charge will also not jump into a spot occupied by a nickel vacancy. Therefore, more accurately the probability is

$$[\mathrm{Ni}^{3+}](1-\tfrac{3}{2}[\mathrm{Ni}^{3+}]).$$

In Eq. (1) the jump frequency and entropy terms are not known; so for the purposes of this discussion, it will be reduced to

$$\sigma=C[\mathrm{Ni}^{3+}]\exp(-\Delta H\oplus^*/RT). \quad (2)$$

The slope on a plot of $\log\sigma$ vs $1/T$ will then be determined by the activation enthalpy to transfer the positive charge from nickel ion to nickel ion, and the conductivity will be proportional to the concentration of Ni^{3+} ions.

Conductivity at Thermodynamic Equilibrium

Equation (2) will describe the temperature dependence of the conductivity only so long as the concentration of Ni^{3+} ions is constant. Now let us examine how the temperature dependence will change when temperature and time are sufficient for thermodynamic equilibrium to be established with the surrounding atmosphere. Birchenall,[4] Kröger and Vink,[5] and Rudolph[2] have shown that in electronic conductors in which the sources of charge carriers are created by thermodynamic equilibration with the surroundings, the temperature dependence of conductivity is, in part, determined by the energy required for the equilibration. When this occurs in nickel oxide, the concentration of Ni^{3+} ions will change according to the reversible equation

$$\tfrac{1}{2}\mathrm{O}_2(g)+2\mathrm{Ni}^{2+}=\mathrm{O}^{2-}+2\mathrm{Ni}^{3+}+\mathrm{Ni}\square, \quad (3)$$

where $\mathrm{Ni}\square$ indicates vacant nickel lattice sites. Approximating activities by concentrations and partial pressures, the equilibrium constant for the reaction is

$$K=[\mathrm{Ni}^{3+}]^2[\mathrm{Ni}\square]/P_{\mathrm{O}_2}^{\frac{1}{2}}, \quad (4)$$

where brackets indicate concentrations. Because very large deviations from stoichiometric NiO are not present, the activities of Ni^{2+} and O^{2-} are taken as being unity and do not appear in Eq. (4). The expression for the equilibrium constant may be solved for the concentration of Ni^{3+} by noting that there are two Ni^{3+} ions for each vacancy, so that

$$[\mathrm{Ni}^{3+}]=2[\mathrm{Ni}\square]. \quad (5)$$

On substituting,

$$K=[\mathrm{Ni}^{3+}]^3/2P_{\mathrm{O}_2}^{\frac{1}{2}}. \quad (6)$$

$$[\mathrm{Ni}^{3+}]=(2K)^{1/3}P_{\mathrm{O}_2}^{1/6}=2^{1/3}P_{\mathrm{O}_2}^{1/6}\exp\left(\frac{-\Delta H_f^\circ}{3RT}\frac{+\Delta S_f^\circ}{3R}\right), \quad (7)$$

where ΔH_f° and ΔS_f° are the enthalpy and entropy of formation for the reaction of Eq. (3). Equation (7) predicts that the concentration of Ni^{3+} ions should be proportional to the one-sixth power of the oxygen pressure. The conductivity at thermodynamic equilibrium at different temperatures may be expressed by an equation obtained by substituting the Ni^{3+} concentration in Eq. (2). Then

$$\sigma=C'P_{\mathrm{O}_2}^{1/6}\exp\left(\frac{-\Delta H_f^\circ}{3RT}\frac{-\Delta H\oplus^*}{RT}\right). \quad (8)$$

Therefore at temperatures high enough for thermodynamic equilibrium to be established during the time of measurement the slope on a plot of $\log\sigma$ vs $1/T$ will be determined by the sum of the activation energy for conduction and the energy to create defects. Also, at constant temperature, a plot of $\log\sigma$ vs $\log P_{\mathrm{O}_2}$ should be a straight line with a slope of 1/6.

Correlations with Other Experiments

As discussed above, the temperature dependence of the electrical conductivity may be used to determine the enthalpy of formation of defects in nickel oxide, and the concentration of vacancies at various temperatures can then be estimated from this value. If the observed temperature dependence of conductivity represents what we propose it does, then we should get the same numbers for the heat of formation of vacancies and concentration of vacancies determined by methods other than electrical conductivity. The following is a summary of how these quantities may be determined from conductivity measurements, diffusion rate determinations and weight loss observations. In each case we will derive an equation for the nickel vacancy concentration.

(*a*) *Electrical conductivity.* The vacancy concentration and the Ni^{3+} concentration are simply related [Eq. (5)] so that Eq. (7) solved for the nickel vacancies instead of Ni^{3+} becomes

$$[\mathrm{Ni}\square]=\left(\frac{K}{4}\right)^{1/3}P_{\mathrm{O}_2}^{1/6}=0.63P_{\mathrm{O}_2}^{1/6}\exp\left(\frac{-\Delta H_f^\circ}{3RT}\frac{+\Delta S_f^\circ}{3R}\right). \quad (9)$$

The slope of a curve of $\log\sigma$ vs reciprocal temperature in the temperature range below which thermodynamic equilibrium is established during the time of measurement yields the activation energy for charge migration,

[4] C. E. Birchenall, Met. Revs **3**, 235 (1958).
[5] F. A. Kröger and H. J. Vink, J. Phys. Chem. Solids **5**, 208 (1958).

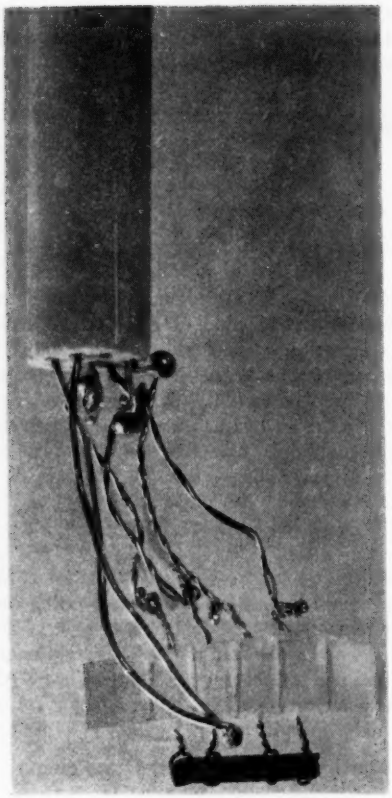

FIG. 1. Photograph of crystal wired for electrical measurements.

$\Delta H\oplus^*$. The slope in the temperature range in which thermodynamic equilibrium is quickly attained yields the sum of $\Delta H\oplus^*$ and the energy of defect formation, $\Delta H_f°/3$, so that the latter may be determined by subtraction. The only unknown is the entropy term. This may be approximated by assuming that the largest entropy change in the reaction for the formation of a vacancy is the destruction of one half a molecule of oxygen gas. Buessem and Butler[6] have found order of magnitude agreement of this type of calculation and weight change experiments on TiO_2. Thermodynamic tables give an average of about 60 entropy units per mole for oxygen, which corresponds to a change of minus thirty units for Eq. (1). Inserting this value into Eq. (9) results in

$$[\mathrm{Ni}\square]=4.0\times10^{-3}P_{O_2}{}^{1/6}\exp(-\Delta H_f°/3RT). \quad (10)$$

(*b*) *Diffusion.* If the diffusion rate constants for both nickel ions and nickel vacancies are measured independently as functions of temperature, the heat of vacancy formation and the concentration of vacancies at different temperatures can be determined by use of the relationship[7]:

$$D_{\mathrm{Ni}^{2+}}[\mathrm{Ni}^{2+}]=D_{\mathrm{Ni}\square}[\mathrm{Ni}\square], \quad (11)$$

where D indicates the diffusion constants of the respective species. In order to determine the expression for the vacancy concentration as a function of temperature, Eq. (11) may be rearranged and given in terms of Do's and exponential temperature dependencies,

$$[\mathrm{Ni}\square]=[\mathrm{Ni}^{2+}]\frac{Do_{\mathrm{Ni}^{2+}}\exp(-\Delta H_f°/3RT-\Delta H\square^*/RT)}{Do_{\mathrm{Ni}\square}\exp(-\Delta H\square^*/RT)},$$

where $\Delta H\square^*$ is the activation energy for vacancy migration. As is well known, the temperature dependence of intrinsic self-diffusion is determined by the sum of the heat of formation of vacancies plus the activation enthalpy for motion while the former term does not appear in the temperature dependence of vacancy diffusion. On simplifying and noting that the Ni^{2+} concentration is almost unity,

$$[\mathrm{Ni}\square]=\frac{Do_{\mathrm{Ni}^{2+}}}{Do_{\mathrm{Ni}\square}}\exp(-\Delta H_f°/3kT). \quad (12)$$

(c) *Weight Changes.* At thermodynamic equilibrium, the excess oxygen content and thus the weight will be determined by the equilibrium constant for the defect reaction. The absolute value of the vacancy concentration may be calculated from weighings after heating at two different oxygen partial pressures for times necessary to attain thermodynamic equilibrium using the following simultaneous equations:

$$[\mathrm{Ni}\square]=CP_{O_2}{}^{1/6}, \quad (13)$$

$$W=W_0\left(1+\frac{\text{atomic wt of } O^{2-}}{\text{molecular wt of NiO}}[\mathrm{Ni}\square]\right), \quad (14)$$

where W = actual weight; W_0 = weight of stoichiometric NiO, and

$\dfrac{\text{atomic wt of } O^{2-}}{\text{molecular wt of NiO}}[\mathrm{Ni}\square]$ = Excess oxygen weight expressed in terms of nickel vacancy concentration. Recall that $[\mathrm{Ni}\square]$ = excess $[O^2]$.

The temperature dependence of weight change at fixed oxygen partial pressures can be used to determine the heat of formation of the vacancies as can be seen from an expression for the vacancy concentration in terms of temperature such as Eq. (9).

EXPERIMENTAL

Conductivity

Resistance measurements were made on a single crystal of NiO which was grown from reagent grade

[6] W. R. Buessem and S. R. Butler in *Kinetics of High Temperature Processes*, edited by W. D. Kingery (John Wiley & Sons, Inc., New York, 1959), p. 13.

[7] N. F. Mott and R. W. Gurney, *Electronic Processes in Ionic Crystals* (Oxford University Press, New York, 1948), 2nd ed., p. 34.

NiO by the Vernouille technique. A spectrographic analysis was made of the NiO and showed typical reagent grade purity. The lithium content was below the limit of detection of the analysis. The crystal was cleaved and then ground to a size of approximately 1 mm×1 mm×1 cm. Four 5-mil platinum wires were wrapped around the bar at even spacings to serve as electrodes, as shown on Fig. 1. Resistance measurements were made with the sample suspended by the electrodes in a vertical tube furnace. The surrounding oxygen partial pressure was controlled by flowing metered mixtures of gases past the sample. The gases were oxygen plus argon, air plus argon, and CO_2. The ratios of the former two mixtures were controlled to obtain various partial pressures of oxygen. The partial pressure of oxygen in CO_2 is determined by the dissociation constant of CO_2 into CO and O_2. In all cases the gases were forced to flow past the sample at a total pressure slightly greater than one atmosphere. The flow rates were about one liter per minute.

The four electrodes allowed measurement of the resistance of the sample using the four-probe method in order to eliminate the effect of contact resistance. The applied potential to the outer electrodes varied between 0.1 and 0.001 v. No dependency of the resistance on the potential was observed. The potential drop between the two inner electrodes was determined by a null current potentiometer.

Weight Change

In order to directly determine the vacancy concencentration as a function of temperature and partial pressure of oxygen, the reversible change in weight at thermodynamic equilibrium on changing the surrounding partial pressure of oxygen was measured. Four single crystals totaling about one gram in weight were weighed after quenching from alternate heatings in oxygen and carbon dioxide at given temperatures. The time of the heat treatments was varied to determine whether equilibrium was complete and also to determine the relative importance of evaporation. Maintaining a given atmosphere and temperature for long periods of time relative to those necessary for thermodynamic equilibrium results in the evaporation of the sample being the most important weight change. Therefore, by varying times, temperatures, and atmospheres, one can assess the relative importance of evaporation weight loss to that of equilibrium weight loss or gain. The weighings were made with a Sartorius microbalance.

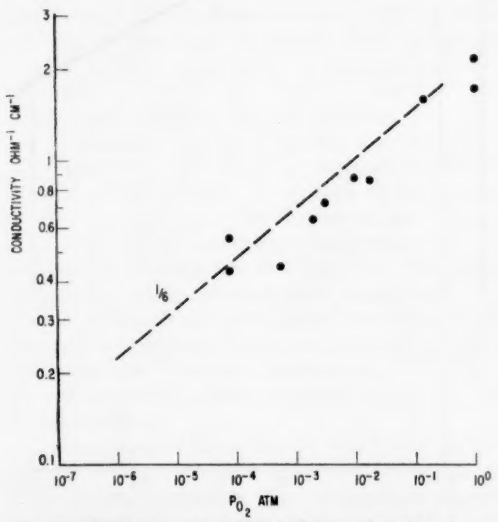

FIG. 2. Electrical conductivity of NiO as a function of oxygen partial pressure at 1300°C.

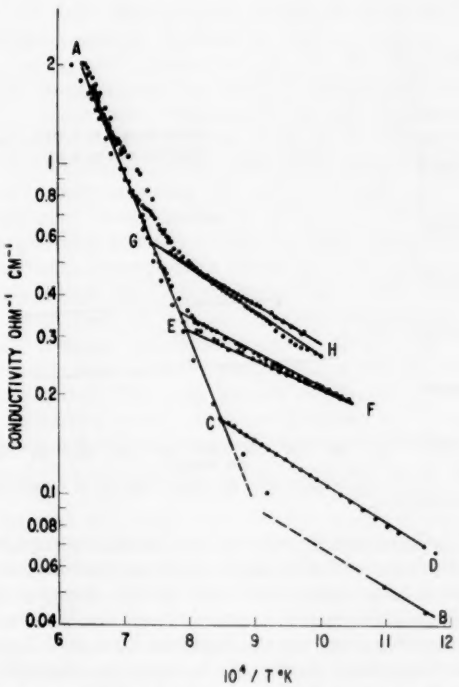

FIG. 3. Electrical conductivity of NiO in oxygen as a function of reciprocal temperature.

RESULTS

Conductivity

Two series of conductivity experiments were made. One series was at constant temperature, employing partial pressure of oxygen as a variable. The purpose of this series was to substantiate the model assumed for NiO as expressed by Eqs. (1) through (4). Figure 2 shows the results. It is a plot of log conductivity at 1300°C vs log oxygen partial pressure. The model predicts a slope of $\frac{1}{6}$. The slope observed is in this range. The conductivity was also measured in different atmospheres at 600°C and found to be independent of the surrounding oxygen partial pressures at this temperature.

A second series of experiments was performed in

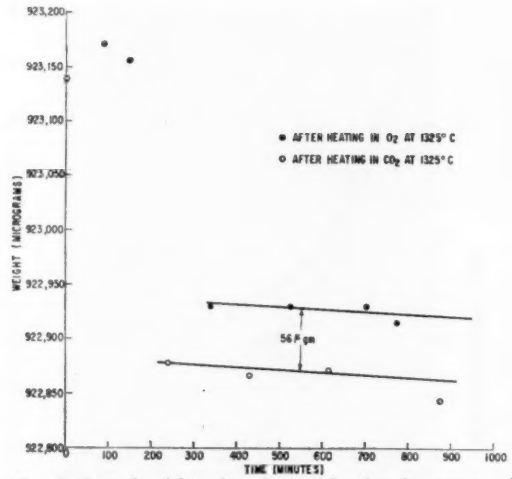

FIG. 4. Crystal weights after alternate heatings in oxygen and carbon dioxide.

which the oxygen pressure was not varied, but time and temperature were. On taking resistance measurements at high temperatures and while slowly changing the temperature to permit thermodynamic equilibrium to be obtained, we expect the slope of a log σ vs $1/T$ plot to be determined by Eq. (8) because the composition depends on the temperature. At lower temperatures and with faster heating and cooling rates we expect that Ni^{3+} concentration to be constant at the different temperatures and the smaller slope to be determined by activation enthalpy term alone [Eq. (2)].

The results of the conductivity vs temperature measurements are given in Fig. 3. All these measurements were made at one atmosphere of oxygen. The portion of the curve from A to B shows the conductivity since the sample was allowed to cool from 1300–550C° over a period of two weeks. At temperatures below point C (900°C) thermodynamic equilibrium was no longer maintained at the selected cooling rate, as indicated by the deviation from the higher temperature slope. Curve C–D was obtained by maintaining the temperature of point C for 20 hr and then taking readings as the sample was cooled to the temperature of point D, this process taking about 4 hr. Between points E and F there were two curves, one in which measurements were taken after establishing equilibrium at E, while cooling to F and one while heating from F to E. The curves between points G and H were taken under identical conditions except that equilibrium was first established at the temperature of point G (1050°C). The last mentioned runs (E–F, F–E, G–H, and H–G) were all made rapidly, taking about 2 hr for each run. At temperatures higher than that of point G equilibrium was established so rapidly that no large difference in slope was noticed between the cooling or heating of A and G in 2 hr or in two days. Points taken at various rates in the higher temperature range of rapid equilibrium rates are included in Fig. 2.

The average activation energy for conduction ($\Delta H\oplus^*$) as determined from the lower temperature slopes is 5500±1000 cal/mole. The equilibrium slope at higher temperatures yields an energy of 23 300 cal/mole. The slope is determined by $(\Delta H_f^\circ/3)+\Delta H\oplus^*$ so that $23\,300-5500=17\,800=\Delta H_f^\circ/3$. Therefore, ΔH_f° as written for one mole of the reaction in Eq. (3) is is 53 400 cal.

Weight Change

Results of the weight change experiments are given in Figs. 4 and 5. Figure 4 shows the sample weight after repeated heat treatments in CO_2 and O_2 at 1325°C. Very large weight changes such as the loss after the second oxygen heating were taken to mean that some of the sample had chipped off in handling. The negative slope of the line drawn through the points is a result of evaporation of NiO.

The vacancy concentration determined gravimetrically is given at several different temperatures on Fig. 5. The heat of formation of vacancies as determined from this Arhennius plot is 24 kcal/mole. The limits of accuracy shown were obtained by assuming a maximum error of ±12 μg in the weight difference as determined from Fig. 4.

DISCUSSION

The results of the experiments in which oxygen partial pressure was changed while maintaining constant temperature demonstrate two points. The first is that

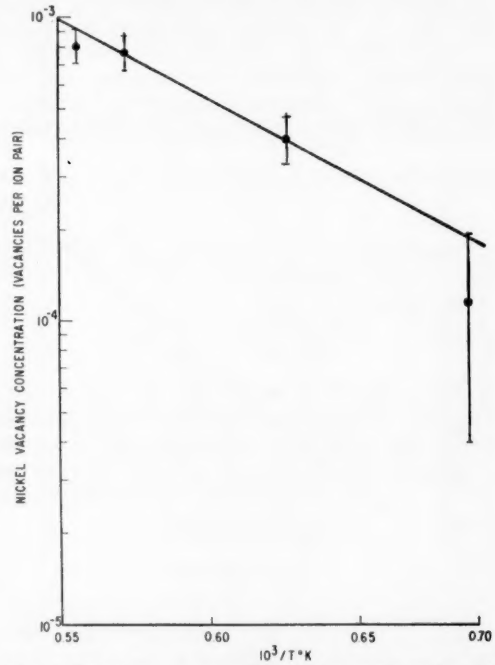

FIG. 5. Nickel vacancy concentration (vacancies per ion pair) in oxygen as a function of reciprocal temperature.

thermodynamic equilibrium with the atmosphere is readily established at a temperature as high as 1300°C while it is not established in reasonable periods of time at a temperature as low as 600°C. The second is that the results are consistent with the assumptions that the conductivity is proportional to the Ni^{3+} concentration and that the equation for the production of defects is that given, Eq. (3).

The conductivity experiments performed at constant oxygen pressure support the initial supposition—that is, that the slope on an Arrhenius plot will show a change in slope at a temperature corresponding to the lowest temperature at which thermodynamic equilibrium is established. The more rapidly the sample is cooled during measurement the higher this temperature will be because the defect concentration will have been frozen in at a higher temperature. The reversibility on heating and cooling between points E and F, G and H and the fact that the slopes are the same are definitive results in relation to the model presented.

F. J. Morin[8] has studied the electrical conductivity and Seebeck effect of single crystals of NiO and of lithium doped and undoped polycrystalline compacts. His measurements extend across the high temperature range examined here. Morin observed the same high temperature slope of 1 ev and attributed it to intrinsic conductivity. Morin's conclusion of intrinsic conductivity would be logical in the absence of data which prove the occurrence of thermodynamic equilibrium during measurement.

Our observations were that above 1050°C we could not change temperature and make measurements rapidly enough to maintain constant composition; therefore, consideration of thermodynamic equilibrium must be included in the slope in this temperature region. That the conductivity is proportional to the $\frac{1}{6}$th power of the oxygen pressure is consistent only with extrinsic conductivity. We therefore conclude that in neither investigation does the 1 ev slope at high temperature indicate intrinsic conductivity. Consequently, there is no reason to believe that the same slope at lower temperatures represents intrinsic behavior.

It is necessary to emphasize that this has been an investigation of conductivity at temperatures of 600°C and above. Furthermore, it has been an investigation in which the results are characteristic of pure NiO and not complicated by extraneous phenomena which may accompany the behavior of doped NiO. The oxygen pressure dependence of conductivity supports this conclusion. In this temperature region the behavior with time and temperature has been shown to fit a model in which the most important consideration is whether or not the crystal is in thermodynamic equilibrium with the surroundings.

At temperatures below that for which we have given data, it is apparent that other conductivity mechanisms become important. This conclusion is supported by the fact that at these lower temperatures the activation energies reported in the literature are not always the 5000 cal observed here but range from 2000 to 25 000 and higher depending on the sample preparation. Morin[9] called attention to several possible conduction mechanisms in pure (or in doped) NiO as well as the diffusional process with which we have so far been entirely concerned. The variety of possible mechanisms may be responsible for the range of activation energies observed but could not explain an increase in activation energy with decreasing temperature in a single sample. There is an interesting possible analogy in conductivity in NiO to Lidiard's[10] explanation for ionic transport phenomenon about which we may speculate and indicate as an interesting field for future investigation. This may be used to explain a change in activation energy with temperature at constant composition still relying on the electron hole diffusion mechanism as the only major contribution to conductivity. Lidiard explains that if mobile defects are associated with less mobile defects such as impurity atoms, the activation energy for their motion will be the *sum* of the energy for them to break free from the defect and the energy to move them from normal lattice site to lattice site. The analogous possibility in nickel oxide is that the activation energy for conduction by the process at constant composition referred to in Eq. (2) may include the energy to dissociate an excess positive charge (hole) from the less mobile nickel vacancies. The vacancy is neutral and exists on a normally positively charged site. Therefore, it effectively has a negative charge which will attract holes. It is reasonable to say that the activation energy for conduction will depend on the relative concentrations of hole-vacancy associations. If the association energies of these complexes are appropriate, one should observe decreasing activation energies with increasing temperature as the complexes are thermally dissociated.

The existence of such complexes and others involving impurity atoms as well as clusters of these defects is more than likely, and they could be responsible for the wide variability and changes in the temperature dependence of conductivity.

Other Data

We have at least three independent ways of determining the defect concentration and the heat of formation of the defects. The results of two of these methods have been given. A third method was recently made possible by Slack[11] who measured the diffusion rate of nickel vacancies in single crystals of NiO. His method is to heat oxygen-rich nickel oxide (black) at low oxygen partial pressures and observe the color change accompanying the advancing oxygen-poor region (green). The rate of advance of the interface is determined by the

[8] F. J. Morin, Phys. Rev. **93**, 1199 (1954).

[9] F. J. Morin in *Semiconductors*, edited by N. B. Hannay (Reinhold Publishing Corporation, New York, 1959), p. 600.

[10] A. B. Lidiard, *Handbuch der Physik*, edited by S. Flügge (Springer-Verlag, Berlin, Germany, 1957), Vol. 20, p. 246.

[11] G. A. Slack (private communication).

TABLE I. Comparison of heats of formation and concentrations of nickel vacancies.

Method	$\Delta H_f/3$ kcal/mole	$[Ni\square]_o$	Ni vacancies per ion pair 1500°C 1 atm O_2
Conductivity	17.8±3	3.1×10^{-3}	(2×10^{-5})
Diffusion	(11.4)	7.8×10^{-3}	3×10^{-4}
Gravimetric	24±8	0.77	8.6×10^{-4}

nickel vacancy diffusion rate. His preliminary results are

$$D=40\exp(-50\,600/RT)\ \text{cm}^2/\text{sec} \qquad (15)$$

for the vacancy diffusion rate. The vacancy concentration may be determined using literature values of self-diffusion of nickel in NiO and Eq. (11). Unfortunately, there is considerable variation in reported self-diffusion values, with values of D_o ranging from 2.8×10^6 to 4×10^{-4} with energies ranging from 119 500 to 42 000 cal/mole.[12–15] If one plots the various reported rates, three of the investigations are fairly close to each other. The diffusion equation which we use is one of these due to Lindner[12]:

$$D_{Ni}=0.24\exp(-62\,000/RT). \qquad (16)$$

Therefore, the concentration of vacancies may be expressed by

$$[Ni\square]=\frac{D_{Ni^{2+}}}{D_{Ni\square}}=\frac{0.24}{40}\exp\left(\frac{-62\,000}{RT}\frac{+50\,600}{RT}\right)$$
$$=6\times10^{-2}\exp(-11\,400/RT) \qquad (17)$$

in air at which oxygen pressure the diffusion experiment was performed. Since the diffusion rate is proportional to the $\frac{1}{6}$ power of the oxygen pressure the vacancy concentration will be

$$[Ni\square]=\left(\frac{1\ \text{atm}}{0.2\ \text{atm}}\right)^{1/6}6\times10^{-2}\exp(-11\,400/RT)$$
$$=7.8\times10^{-2}P_{O_2}{}^{1/6}\exp(-11\,400/RT). \qquad (18)$$

The results of all three methods are compared in Table I, in which $[Ni\square]_0$ and $\Delta H_f^\circ/3$ are given for the equation

$$[Ni\square]=[Ni\square]_0\exp(-\Delta H_f^\circ/3RT). \qquad (19)$$

The vacancy concentrations computed for 1500°C at one atmosphere of oxygen are also compared.

Of the three methods of obtaining the heat of formation, the conductivity is certainly the most accurate. The gravimetric method is much more tedious so that fewer points were available to determine the slope. The variability in the diffusion energies has already been mentioned. As to the absolute values of vacancy concentrations, the gravimetric method is the only direct determination and should be most accurate, to within a factor of two. The absolute value of vacancy concentration calculated from diffusion data should be more reliable than the heat of formation. All these experimental determinations appear to be within the accuracy of the experiments. The statistical thermodynamic approximation which was used to determine the vacancy concentration from the heat of formation yields a number which is too low to be within the accuracy of the experimental determinations. The discrepancy is in the direction which indicates that the entropy decrease assumed for Eq. (3) was too large. This probably means that the entropy of crystals of NiO is significantly increased by the presence of nickel vacancies. The best equation for the equilibrium vacancy concentration may be obtained using the intermediate temperature determinations of the gravimetric method and the temperature dependence of the conductivity results. This yields

$$[Ni\square]=0.11P_{O_2}{}^{1/6}\exp(-17\,800/RT), \qquad (20)$$

where P_{O_2} is in atmospheres and the vacancy concentration is expressed as vacancies per ion pair.

The correlations strengthen the conduction model which was proposed. For instance, the diffusion experiments show that in fact and in degree thermodynamic equilibrium is established at the temperatures which the conduction experiments indicated this to be so. The gravimetric experiments show that at thermodynamic equilibrium the oxygen and hence Ni^{3+} content in the crystals increase with increasing temperature. Therefore, since the charge carriers are increasing both in mobility *and* concentration we must observe energies for both processes on an Arrhenius plot of conductivity. This agrees with the conductivity results.

CONCLUSIONS

1. The conductivity of undoped nickel oxide is proportional to the concentration of Ni^{3+} ions. When thermodynamic equilibrium is established this concentration varies with the surrounding atmosphere and temperature. It increases both with increasing oxygen partial pressure and increasing temperature. At temperatures too low to establish equilibrium the Ni^{3+} concentration is fixed by the thermal history of the sample.

2. At low temperatures the slope on a plot of log conductivity as a function of reciprocal temperature is determined by the activation energy for carrier mobility.

3. At higher temperatures, given sufficient time for

[12] R. Lindner, "Some problems of solid state chemistry (with special regard to diffusion and reaction in oxide systems)," Proceedings of the Tenth Solvay Conference, Brussels (1956), p. 459.
[13] R. Lindner and Å. Åkerström, Z. Physik. Chem. **6**, 162 (1956).
[14] R. Lindner and Å. Åkerström, Discussions Faraday Soc. **23**, 133 (1957).
[15] M. T. Shim and W. J. Moore, J. Chem. Phys. **26**, 802 (1957).

thermodynamic equilibrium, the slope is determined by the activation energy plus the thermodynamic enthalpy for creation of nickel vacancies and Ni^{3+} ions.

4. Gravimetric determinations of the vacancy concentration and literature diffusion experiments confirm the conductivity model.

5. An equation was derived from the results for the concentration of nickel vacancies. From this equation, it can be calculated that pure nickel oxide may be made to contain between 0.1% to 0.001% vacancies depending on the equilibrium temperature and surrounding oxygen partial pressure.

ACKNOWLEDGMENTS

We wish to express our thanks to Millard R. Many who grew the single crystals, Harley Middleton who did the micro-weighings, and our colleagues, especially C. E. Birchenall, R. O. Carlson, R. E. Carter, W. B. Hillig, and Glen Slack for interesting and helpful discussions.

THE JOURNAL OF CHEMICAL PHYSICS VOLUME 35, NUMBER 3 SEPTEMBER, 196

General Theory of Polymer Solutions

MARSHALL FIXMAN

Mellon Institute, Pittsburgh, Pennsylvania

(Received February 2, 1961)

A general theory of the thermodynamic properties of polymer solutions is given. The theory is intended to be valid for every concentration range. The formalism begins with the assumption of some functional relation between the local free energy density, for an assigned polymer configuration, and the local concentration of segments belonging to various polymer chains. That is, the thermodynamic properties of the segments are presumed known, and the problem is taken to be the determination of changes in the thermodynamic properties which are induced by a joining of the segments into a polymer chain. The local segment concentration is assumed to be close enough to the bulk or average concentration that a Taylor series expansion of the local free energy can be made and cut off at the term containing the square of the fluctuation in local concentration. The resulting free energy of the whole solution can then be cast into a form which includes as one part the free energy of a random distribution of segments, and as a second part the free energy of an imperfect gas with a pairwise additive intermolecular potential, albeit a concentration-dependent potential. At low concentrations the results are identical to previous treatments based on imperfect gas theory. At high concentrations a previously introduced calculation of the radial distribution function is employed to show that the thermodynamic properties are accurately described as those of a random distribution of segments. The Flory-Huggins formula is an example of a free-energy function which can be assumed to hold locally at any concentration, but is then found to hold macroscopically only at high concentrations.

I. INTRODUCTION

THE transition between the theories of the thermodynamic properties of dilute and concentrated polymer solutions has been most difficult to attain. The early lattice models of Flory[1] and Huggins[2] gave a valuable approximate treatment of the free energy of mixing in very concentrated polymer solutions.[3] The solvent chemical potential, for example, is predicted to depend only on the volume fraction and not on the molecular weight of the polymer; this prediction is in agreement with experiment on concentrated solutions, even though there are measurable deviations from the predicted shape of the curve. The effect of molecular weight having been so neatly removed, it is reasonable to believe that the thermodynamic inadequacies of the theory at high concentrations are not peculiar to polymer systems, but are rather inadequacies common to the theory of liquids and liquid mixtures.

Thermodynamic properties in the low-concentration range, as they are affected by polymer dimensions, molecular weight, and excluded volume, are again fairly well understood. The Flory-Huggins theory breaks down qualitatively at low concentrations; for example, a second virial coefficient independent of polymer dimensions and molecular weight is predicted. However, methods analogous to those used in imperfect gas theory have proved quite successful for the theory of very dilute solutions, in the hands of Zimm,[4] Flory[5,6] and Krigbaum,[6] and others.[7–10] The qualitative reasons for the failure of the Flory-Huggins theory outside the concentrated solution range are known. The main cause of failure in the assumption of a random distribution of the polymer molecules throughout the solution. This as-

[1] P. J. Flory, J. Chem. Phys. **10,** 51 (1942).
[2] M. L. Huggins, Ann. N. Y. Acad. Sci. **43,** 1 (1942); J. Am. Chem. Soc. **64,** 1712 (1942).
[3] P. J. Flory, *Principles of Polymer Chemistry* (Cornell University Press, Ithaca, New York, 1953).
[4] B. H. Zimm, J. Chem. Phys. **14,** 164 (1946).
[5] P. J. Flory, J. Chem. Phys. **17,** 1347 (1949).
[6] P. J. Flory and W. R. Krigbaum, J. Chem. Phys. **18,** 1086 (1950).
[7] A. C. Albrecht, J. Chem. Phys. **27,** 1002 (1957).
[8] E. F. Casassa and H. Markovitz, J. Chem. Phys. **29,** 493 (1958).
[9] W. H. Stockmayer and E. F. Casassa, J. Chem. Phys. **20,** 1560 (1952).
[10] P. J. Flory, J. Chem. Phys. **13,** 453 (1945).

sumption, reasonable enough at high concentrations must break down at low concentrations, where many parts of the solution are not permeated by polymer coils, and there are clear energy gains or losses where two polymer molecules are caused to overlap or separate. The methods of imperfect gas theory, including in particular the use of a pairwise additive intermolecular potential (of average force) independent of concentration, can handle such effects very well.

The use of such a potential was carried to its logical limit when approximate solutions for the radial distribution function $g(R)$ between polymer molecules were obtained at all concentrations.[11] Osmotic pressure experiments which seemed anomalous on the basis of the first few virial coefficients were given a natural explanation involving mainly the behavior of $g(R)$ at high concentrations. It was found that $g(R)$ should approach unity for all R as the polymer concentration is increased. The physical meaning of this result is that the polymer molecules become distributed at random, and thus one of the postulates of the Flory-Huggins theory regains validity at high concentration. Nevertheless, this theory based on $g(R)$ became grossly inadequate at polymer volume fractions $v_2 \gtrsim 0.1$. The explanation given for this failure was that the intermolecular potential could not be assumed strictly independent of concentration. In the context of the Flory-Krigbaum picture, this means that the free energy of mixing segments in a small volume element should not be assumed proportional to the square of the segment concentration.

In this connection it may be observed that: (1) Orofino and Flory[12] accounted for cubic terms in the segment concentration, but they were interested only in the intermolecular potential of two polymer molecules, for the computation of the second virial coefficient, and naturally a dependence of the pair potential on concentration was irrelevant; (2) the concentration dependence of the pair potential which arises from the concentration dependence of polymer dimensions was examined by the author.[13,14] An apparent quantitative improvement of the osmotic pressure theory resulted, but there was still the failure at $v_2 \gtrsim 0.1$. This failure resulted because the local free energy of mixing segments with solvent was still assumed proportional to the square of the local segment concentration.

A suggestion has been advanced for connecting dilute and concentrated solution theory.[14] Because the imperfect gas or liquid theory seems to work fairly well even up to concentrations where extensive overlapping of polymer domains occurs, as long as $v_2 \lesssim 0.1$, it was suggested that the local free energy of mixing in a volume element might be expanded in a Taylor series around the mean, or bulk fraction, instead of around zero concentration as was done in the Flory-Krigbaum theory of the second virial coefficient. This suggestion has since been explored, and the results are reported here.

In Sec. II the theory is given for an unspecified relation connecting the local free energy of mixing with the local volume fraction of polymer segments, and for an arbitrary distribution of segments belonging to a single polymer molecule. In Sec. III approximations to the latter and to the radial distribution function are introduced.

II. THEORY

The theory must begin with a given potential of average force acting on N_2 polymer molecules in an assigned configuration in a volume V. The average is with respect to the positions of the solvent molecules, and therefore the potential of average force will be a (Helmholtz) free energy of mixing polymer and solvent for the assigned configuration relative to the free energy of mixing polymer and solvent in an infinitely dilute solution of the former; from both of these free energies the entropy arising in the random distribution of polymer centers of mass must be excluded, because of the assigned positions of the polymer molecules.

Suppose the volume fraction of polymer segments at a point $\mathbf{R}$ is $f(R)$, and the corresponding free energy of mixing per unit volume is ϵ_R. Then, by assumption,

$$\epsilon_R = \epsilon[f(R)]. \tag{1}$$

Let

$$\delta = f(R) - v_2, \tag{2}$$

where v_2 is the macroscopically observed volume fraction of polymer segments. A Taylor series expansion gives

$$\epsilon_R = \epsilon(v_2) + \epsilon^{(1)}(v_2)\delta + \tfrac{1}{2}\epsilon^{(2)}(v_2)\delta^2 + \cdots, \tag{3}$$

where

$$\epsilon^{(n)}(v_2) = d^n\epsilon(v_2)/dv_2^n.$$

The potential of average force for the whole system of polymer molecules with positions $\{\mathbf{R}_i\}$ is then

$$a\{\mathbf{R}_i\} = \int \epsilon_R d\mathbf{R} \tag{4}$$

$$= A_0 + \tfrac{1}{2}\epsilon^{(2)} \int \delta^2 d\mathbf{R}, \tag{5}$$

where $A_0 = V\epsilon(v_2)$, and the linear term in δ has dropped out because $\int \delta d\mathbf{R} = 0$ from the definition of v_2.

The validity of chopping off the Taylor series, Eq. (3), at the δ^2 term requires some further comment, as does also the whole concept of an expansion around v_2. At low concentrations customarily treated with a second virial coefficient, the coefficients $\epsilon^{(n)}/n!\,(n \geq 2)$ are all of about the same magnitude according to the Flory-Huggins theory, though the $n=2$ term will usually be

[11] M. Fixman, J. Chem. Phys. **33**, 370 (1960).
[12] T. A. Orofino and P. J. Flory, J. Chem. Phys. **26**, 1067 (1957).
[13] M. Fixman, Ann. N. Y. Acad. Sci. **89**, 657 (1961).
[14] M. Fixman, J. Polymer Sci. **41**, 91 (1960).

the smallest, particularly for a poor solvent. However, the Flory-Huggins theory probably exaggerates $\epsilon^{(3)}$. For some order-of-magnitude numerical considerations, suppose that the polymer molecules, regarded as uniform clouds of segments, fill up the solution at $v_2 \cong 0.02$. Then inside a single polymer, $f \cong 0.02$. This means that the overlapping of even three or four polymer molecules in the dilute solution range should not strain the expansion. Moreover, because the $\epsilon^{(n)}$ are not changing rapidly with v_2, the expansion around v_2 should be at least as good as an expansion around $v_2=0$, since $|\delta| < f$ unless the volume element under observation is grossly deficient in segments; but then $|\delta| \cong v_2 \ll 1$. At high concentrations, on the other hand, the $\epsilon^{(n)} (n \geq 2)$ are getting very large as n and v_2 increase. It might be thought that the extensive overlapping of polymer domains would make fluctuations relatively small. This is true, but since δ is the actual and not the relative fluctuation, the argument has no weight. At high concentrations the large magnitude of $\epsilon^{(2)}$ must be relied on to make all but the smallest values of δ grossly improbable. The previously found approach of $g(R)$ to unity adds to the credibility of this argument. In any case, the expansion can be no worse than the Flory-Huggins theory, which takes simply $\delta=0$.

As $a\{\mathbf{R}_i\}$ is defined it includes not only intermolecular energy but also the intramolecular or self-energy of the interaction of the segments of a single polymer coil with each other. There is no reason to exclude this self-energy, since if it actually depends on polymer concentration, it will enter into the chemical potential of the solvent. For the sake of some elucidation, however, a self-energy will be defined and evaluated separately as the difference between the energy of the fluid when all molecules are distributed at random and when all molecules but one are distributed at random, and it will be shown that such a self-energy appears in $a\{\mathbf{R}_i\}$. If all of the N_2 polymer molecules are distributed at random, the local polymer volume fraction is everywhere V_2N_2/V, where V_2 is the partial molecular volume of the polymer solute. If (N_2-1) molecules are distributed at random, the local volume fraction at $\mathbf{R}$ is

$$V_2\nu_i(R)+V_2(N_2-1)/V,$$

where $n\nu_i(R)$ is the number of segments per unit volume at $\mathbf{R}$ belonging to molecule i. Hence the change in density on reserving molecule i from the random distribution is

$$\delta_i = V_2\nu_i(R) - V_2/V. \tag{6}$$

The resulting change in energy is defined as the self energy a_i of molecule i and is, according to Eq. (3),

$$a_i = \epsilon^{(1)}\int \delta_i d\mathbf{R} + \tfrac{1}{2}\epsilon^{(2)}\int \delta_i^2 d\mathbf{R}. \tag{7}$$

Now $\int \nu_i(R) d\mathbf{R} = 1$, and therefore $\int \delta_i d\mathbf{R} = 0$. Also,

$$\int \delta_i^2 d\mathbf{R} = V_2^2\left[\int \nu_i^2 d\mathbf{R} - 2V^{-1}\int \nu_i d\mathbf{R} + V^{-1}\right] = V_2^2\int \nu_i^2 d\mathbf{R}, \tag{8}$$

since $V \to \infty$. Therefore,

$$a_i = \tfrac{1}{2}\epsilon^{(2)}V_2^2\int \nu_i^2 d\mathbf{R}, \tag{9}$$

and the total intramolecular or self-energy is

$$A_s = \sum_i a_i. \tag{10}$$

A further development of $a\{\mathbf{R}_i\}$ may now be undertaken, and it will be seen that $a\{\mathbf{R}_i\}$ includes A_s as a clearly distinguishable part. In Eq. (5),

$$\int \delta^2(\mathbf{R}) d\mathbf{R} = \int [f(\mathbf{R}) - v_2]^2 d\mathbf{R}$$

$$= \int f^2(\mathbf{R}) d\mathbf{R} - V v_2^2 \tag{11}$$

and

$$f(\mathbf{R}) = V_2 \sum_i \nu_i(\mathbf{R}), \tag{12}$$

so

$$\int \delta^2(\mathbf{R}) d\mathbf{R} = V_2^2 \sum_i \int \nu_i^2(\mathbf{R}) d\mathbf{R}$$

$$+ V_2^2 \sum_{i \neq j} \int \nu_i(\mathbf{R})\nu_j(\mathbf{R}) d\mathbf{R} - V v_2^2. \tag{13}$$

Equations (5), (9), and (10) now give

$$a\{\mathbf{R}_i\} = A_0 + A_s + \tfrac{1}{2}V_2^2\epsilon^{(2)}\sum_{i \neq j}\int \nu_i(R)\nu_j(\mathbf{R}) d\mathbf{R}$$

$$- \tfrac{1}{2}\epsilon^{(2)} V v_2^2. \tag{14}$$

The configurational free energy is then

$$A = -kT \ln Q,$$

where

$$Q = \int \cdots \int \exp[-a\{\mathbf{R}_i\}/kT] d\{\mathbf{R}_i\}.$$

The three terms in (14) which do not depend on $\{\mathbf{R}_i\}$ are conveniently separated:

$$A = A_0 + A_s - \tfrac{1}{2}\epsilon^{(2)} V v_2^2 - kT \ln Q_2, \tag{15}$$

where

$$Q_2 = \int \cdots \int \exp[-U\{\mathbf{R}_i\}/kT] d\{\mathbf{R}_i\} \tag{16}$$

$$U\{\mathbf{R}_i\} = \tfrac{1}{2}\sum_{i \neq j} E_{ij} \tag{17}$$

$$E_{ij} = V_2^2\epsilon^{(2)}\int \nu_i(\mathbf{R})\nu_j(\mathbf{R}) d\mathbf{R}. \tag{18}$$

The problem of the configurational free energy is now reduced to a problem in imperfect gas theory, with a pairwise additive potential, albeit a potential which is concentration dependent. The quantity of interest is not A itself but the solvent activity or osmotic pressure. (It is for this reason that it is unnecessary to subtract from $a\{\mathbf{R}_i\}$, the potential at infinite dilution. The latter is not dependent on N_1.) Denoting the partial molecular free energy of solvent by $\bar{A}_1$, we have from Eq. (15),

$$\bar{A}_1=\bar{A}_{01}+\bar{A}_{s1}+\tfrac{1}{2}\epsilon^{(2)}V_1v_2^2+\tfrac{1}{2}\epsilon^{(3)}V_1v_2^3 - kT(\partial \ln Q_2/\partial N_1)_{T,P,N_2}. \quad (19)$$

The derivative of Q_2 is conveniently obtained by the method of Green.[15] Q_2 depends on N_1 explicitly through the dependence of E_{ij} on v_2 via $\epsilon^{(2)}(v_2)$. But there is also an implicit dependence because the range of integration in (3.6) is over V, which is a function of N_1 at constant P. This latter dependence is made explicit by the introduction of reduced variables. Let

$$V=l^3; \qquad \mathbf{R}_i=l\mathbf{x}_i,$$

where the components of $\mathbf{x}_i$ range from 0 to 1.

$$Q_2=V^{N_2}\int_0^1\cdots\int \exp[-(\tfrac{1}{2}kT)\sum_{i\neq j}E_{ij}(v_2, V^{\frac{1}{3}}x_{ij})]d\{\mathbf{r}_i\}. \quad (20)$$

The dependence of E_{ij} on v_2 and, from the integral in Eq. (18), on R_{ij} has been made explicit in the notation

$$E_{ij}=E_{ij}(v_2, R_{ij})=E_{ij}(v_2, lx_{ij}).$$

The appropriate application of

$$(\partial/\partial N_1)=V_1(\partial/\partial V)=-(V_1v_2/V)(\partial/\partial v_2)$$

as needed to Eq. (20) gives

$$V_1^{-1}kT(\partial \ln Q_2/\partial N_1)=kT\rho_2 - \tfrac{1}{2}Q_2^{-1}N_2(N_2-1)\int\cdots\int[\partial E(v_2, V^{\frac{1}{3}}x)/\partial V] \times \exp[-U/kT]d\{\mathbf{R}_i\}, \quad (21)$$

where $\rho_2=N_2/V$. Now

$$V[\partial E(v_2, V^{\frac{1}{3}}x)/\partial V]=-v_2(\partial E/\partial v_2)+\tfrac{1}{3}R(\partial E/\partial R) \quad (22)$$

and

$$Q_2^{-1}\int \exp[-U/kT]d\{\mathbf{R}_i\}/d\mathbf{R}=V^{-1}g(R), \quad (23)$$

where $g(R)$ is the radial distribution function. Therefore

$$V_1^{-1}kT(\partial \ln Q_2/\partial N_1)=kT\rho_2 - \tfrac{1}{2}\rho_2^2\int[\tfrac{1}{3}R(\partial E/\partial R)-v_2(\partial E/\partial v_2)]g(R)d\mathbf{R}. \quad (24)$$

In order to have separately displayed the effects of a nonrandom distribution, put $g(R)=1-G(R)$ in Eq. (24). Now from Eq. (18) we evaluate the derivatives in Eq. (24).

$$E(R)=\epsilon^{(2)}V_2^2e(R), \quad (25)$$

where

$$e(R)=\int\nu(\mathbf{r})\nu(\mathbf{R}+\mathbf{r})d\mathbf{r}, \quad (26)$$

and

$$\partial E/\partial v_2=\epsilon^{(3)}V_2^2e(R) \quad (27)$$

$$\tfrac{1}{3}\int R(\partial E/\partial R)d\mathbf{R}=-\int Ed\mathbf{R}. \quad (28)$$

Substitution of these quantities into Eq. (24) gives

$$V_1^{-1}kT(\partial \ln Q_2/\partial N_1)=kT\rho_2+\tfrac{1}{2}v_2^2\int[\epsilon^{(2)}+v_2\epsilon^{(3)}]e(R)d\mathbf{R} - v_2^2V_1^{-1}\Gamma, \quad (29)$$

where

$$\Gamma=-\tfrac{1}{2}V_1\int[\tfrac{1}{3}R\epsilon^{(2)}e'(R)-v_2\epsilon^{(3)}e(R)]G(R)d\mathbf{R}. \quad (30)$$

Now

$$\int e(R)d\mathbf{R}=\int\nu(\mathbf{r})\int\nu(\mathbf{R}+\mathbf{r})d\mathbf{R}d\mathbf{r} =1.$$

Therefore,

$$V_1^{-1}kT(\partial \ln Q_2/\partial N_1)=kT\rho_2+\tfrac{1}{2}v_2^2(\epsilon^{(2)}+v_2\epsilon^{(3)})-v_2^2V_1^{-1}\Gamma,$$

and substitution of this result into Eq. (19) gives

$$\bar{A}_1=\bar{A}_{01}+\bar{A}_{s1}-V_1kT\rho_2+v_2^2\Gamma. \quad (31)$$

We will begin the discussion of our results by first supposing that the self-energy, or more precisely the dependence of A_s on concentration, is negligible, as is assumed in the conventional theory of the osmotic pressure. Then the behavior of this theory at low concentrations is most simply deduced from Eq. (19). Through the second virial coefficient in the osmotic pressure virial series ($\pi=-\bar{A}_1/V_1$), the present theory is exactly equivalent to the convential theory. To see this, drop the term in $\epsilon^{(3)}v_2^3$ from Eq. (19), and evaluate $\epsilon^{(2)}$ in (19) and (18) at $v_2=0$. If $\bar{A}_{01}$ is expanded in a Taylor series in v_2,

$$\begin{aligned}\bar{A}_{01}&=\partial[V\epsilon(v_2)]/\partial N_1\\ &=V_1[\epsilon(v_2)-v_2\epsilon^{(1)}(v_2)]\\ &=V_1[\epsilon(0)-\tfrac{1}{2}\epsilon^{(2)}(0)v_2^2+\cdots].\end{aligned} \quad (32)$$

Now the definition of $\epsilon(v_2)$ as a free energy of mixing polymer and solvent insures that $\epsilon(0)=0$. Consequently Eqs. (19) and (32) will give just

$$\bar{A}_1=-kT(\partial \ln Q_2/\partial N_1),$$

[15] M. Born and H. S. Green, *A General Kinetic Theory of Liquids* (Cambridge University Press, New York, 1949), p. 23.

again, with the neglect of A_s and of terms of order v_2^3 or greater. Hence, the imperfect gas theory of the second virial coefficient is reproduced.

It may be noted that the possible presence of $\bar{A}_{s1}$ in the second virial coefficient should not be surprising. $\bar{A}_{s1}$ is proportional to $\epsilon^{(3)}$ [Eq. (36)], and Orofino and Flory[12] have shown that such a term can enter into the second virial coefficient. It is usually not stated explicitly that A_s is neglected (a language suitable to different approximations is used), but rather that the segment-segment interaction energy is pairwise additive and independent of concentration. But this is equivalent to the assumption that $\epsilon^{(n)}=0$ for $n\geq 3$, and so to a neglect of $\bar{A}_{s1}$ (among other neglected things).

At high concentrations, where it is believed that $G(R)=0$, Eq. (31) shows the approach of the present theory to the segment theory on which it is based. The Γ term drops out from Eq. (31), the $V_1kT\rho_2$ term gives the partial free energy of a gas of noninteracting polymer molecules and this is just what is needed to supplement A_{01}, because the entropy of mixing polymer molecules was excluded from A_0.

Subject to a more detailed examination of the concentration dependence of A_s and also of the precise rate at which $G(R)\to 0$ as the concentration is increased, both being given in the next section, it may be said that the present theory gives an explicit connection between the former statistical mechanical theories of dilute and concentrated polymer solutions.

In the next section the general equations derived here will be examined under choices of approximate functions for $\nu(R)$ and $g(R)$. It will be seen that the comments above must, in practice, be modified in certain interesting details, and that in fact there emerges a most remarkable cancellation of intra- and intermolecular contributions to the solvent chemical potential, or segment concentration, at large v_2.

III. APPROXIMATIONS

Before the Flory-Huggins equation is employed for $\epsilon(v_2)$, some other approximations will be introduced while $\epsilon(v_2)$ is kept general. First suppose that fluctuations of the internal coordinates of a polymer molecule may be neglected. Then to a good approximation, as noted by Flory and Krigbaum,[6]

$$\nu(r)=(3/2\pi R_a^2)^{\frac{3}{2}}\exp(-3r^2/2R_a^2), \tag{33}$$

where R_a is some parameter measuring the size of the molecule; R_a will not be further specified here except to note that the same R_a is used for the internal and intramolecular energies (see comments below). Equation (26) gives

$$e(R)=(3/4\pi R_a^2)^{\frac{3}{2}}\exp(-3R^2/4R_a^2)$$
$$=(B/\pi)^{\frac{3}{2}}\exp(-BR^2), \tag{34}$$

where

$$B=3/4R_a^2$$

is a parameter previously used in the theory of $g(R)$.[11] Equations (30) and (34) give

$$\Gamma=\tfrac{1}{2}V_1\epsilon^{(2)}(B/\pi)^{\frac{3}{2}}\int\{\tfrac{2}{3}BR^2+v_2(\epsilon^{(3)}/\epsilon^{(2)})\}G(R)$$
$$\times\exp(-BR^2)d\mathbf{R}. \tag{35}$$

Equations (9), (10), and (33) give

$$\bar{A}_{s1}=-\tfrac{1}{2}V_1V_2v_2^2\epsilon^{(3)}\int[\nu(\mathbf{r})]^2d\mathbf{r}$$

$$\bar{A}_{s1}=-\tfrac{1}{2}V_1V_2v_2^2\epsilon^{(3)}(B/\pi)^{\frac{3}{2}}. \tag{36}$$

Finally, the intermolecular potential is, from Eqs. (34) and (18),

$$E(R)=kTX\exp(-BR^2), \tag{37}$$

where

$$kTX=\epsilon^{(2)}V_2^2(B/\pi)^{\frac{3}{2}}. \tag{38}$$

Now an approximate $g(R)$ has been determined for an intermolecular potential of the form (37) previously.[11] A variational method gave the values of a and δ in

$$G(R)=1-g(R)=a\exp(-\delta BR^2). \tag{39}$$

As it turned out, for a sufficiently large X only δ is a good variational parameter whereas a must be set identically equal to unity. Since $\epsilon^{(2)}$, and therefore X, does get very large as the concentration is increased [infinitely large according to the Flory-Huggins expression for $\epsilon(v_2)$, from the $\ln v_1$ term], the equation satisfied by δ at high concentrations where δ and X are large, is[16]

$$\delta^{\frac{3}{2}}=\rho_2(\pi/B)^{\frac{3}{2}}. \tag{40}$$

Substitution of Eq. (39) into (35) gives

$$\Gamma=\tfrac{1}{2}V_1\epsilon^{(2)}a(1+\delta)^{-\frac{3}{2}}[(1+\delta)^{-1}+v_2\epsilon^{(3)}/\epsilon^{(2)}]. \tag{41}$$

If it is now supposed that the concentration is high, and δ is again taken to be very large, Eq. (41) becomes

$$\Gamma=\tfrac{1}{2}V_1v_2\epsilon^{(3)}\delta^{-\frac{3}{2}}, \tag{42}$$

or, with substitution of Eq. (40),

$$\Gamma=\tfrac{1}{2}V_1V_2\epsilon^{(3)}(B/\pi)^{\frac{3}{2}}, \tag{43}$$

or

$$v_2^2\Gamma=-\bar{A}_{s1}, \qquad (!) \tag{44}$$

the last conclusion following from Eq. (36). The derivation of this remarkable cancellation of the effects of inter- and intramolecular energy, does contain a flaw, it must be admitted. The flaw is that Eq. (43) gives only the dominant part of Γ, and the remainder, though it becomes relatively smaller and smaller as the concentration is increased, does not actually vanish for two reasons: (a) $\epsilon^{(3)}\to\infty$ as $v_2\to 1$; (b) δ^{-1} does not go all the way to zero as the concentration is increased, because ρ_2 attains a maximum of V_2^{-1}. However, it seems quite

[16] Reference 11, Eq. (73).

likely that the nonvanishing remainder must be ascribed to the use of an approximate $g(R)$, or $\nu(R)$. The cancellation of $\bar{A}_{s1}$ by the dominant part of Γ seems more than accidental. In practice we have found for a Flory-Huggins $\epsilon(v_2)$ and typical choices of B that the deviation of $v_2^2\Gamma$ from $-\bar{A}_{s1}$ becomes negligible as v_2 is increased beyond about 0.05−0.3, and does not become significant again until $v_2 \gtrsim 0.98$. In the intermediate range, Eqs. (44) and (31) give

$$\bar{A}_1 = \bar{A}_{01} - V_1 kT\rho_2, \tag{45}$$

or precisely what would obtain for a random distribution of segments.

Suppose now that a Flory-Huggins $\epsilon(v_2)$ is introduced.

$$\epsilon(v_2) = kTV_1^{-1}[v_1 \ln v_1 + \chi_0 v_1 v_2]. \tag{46}$$

Then the results are conveniently summarized by

$$\bar{A}_1 = kT[\ln v_1 + v_2(1 - V_1/V_2) + \chi(v_2)v_2^2], \tag{47}$$

where $\chi(v_2)$ is a constant equal to χ_0 according to the Flory-Huggins theory but is here a function of v_2 which approaches χ_0 at high concentrations.

We have examined the behavior of $\chi(v_2)$ sufficiently to elucidate its general behavior. In good solvents $\chi(v_2)$ decreases to χ_0 as v_2 increases, and in poor solvents $\chi(v_2)$ decreases to χ_0 as v_2 increases. The main feature predicted, a rise of χ in poor solvents and a fall in good solvents, is observed,[17] but the detailed predictions are probably not confirmed. However, we have made no lengthy comparison with experiment in view of certain practical and theoretical obstacles. The main practical obstacle is the probable failure of the Flory-Huggins theory for segments (as opposed to polymer molecules). Thus Krigbaum and Geymer[18] found for the polystyrene–cyclohexane system that $\chi(v_2)$ increased steadily with v_2, and, most significantly, that the curve was independent of molecular weight. The strong implication is that the dependence of $\chi(v_2)$ on v_2 arises not in the effects considered here, but in a failure of the Flory-Huggins theory even where the segments are uniformly distributed.

The main theoretical obstacle is the handling of polymer dimensions. The observations made here on the cancellation of intermolecular and intramolecular contributions to $\chi(v_2)-\chi_0$ at large v_2, have been based on use of the same Gaussian distribution of segments for the intramolecular and intermolecular energy. However, the perturbation theory of excluded volume effects and the osmotic second virial coefficient are consistent only with different distributions.[11] Also, the polymer dimensions must change with concentration,[13,14] and so also the Gaussian segment distribution.

Another problem is that if X, in Eq. (37), becomes as large as Eq. (46) makes it at fairly small v_2, the approximate $g(R)$ of Eq. (39) almost surely needs improvement.

Although these theoretical obstacles might be negotiable, the probable failure of the Flory-Huggins theory for randomly distributed segments is not really part of the theory of polymers, *per se*, and is not susceptible to any of the methods recently developed.

One final conclusion may be drawn. The thermodynamic properties of the polymer solution at high concentrations have been found to be the properties of a random distribution of segments. The interpretation of such a random distribution is that the nonrandom distribution of segments belonging to a single polymer molecule is precisely compensated by a deficiency, in the given region, of segments belonging to other molecules. That is, the deficiency approaches a constant value, independent of concentration, as the concentration is increased.

[17] Reference 3, p. 515.
[18] W. R. Krigbaum and D. O. Geymer, J. Am. Chem. Soc. **81**, 1859 (1959).

Scattering of High-Velocity Neutral Particles. XII. He—CH_4; He—CF_4. CH_4—CH_4 and CF_4—CF_4 Interactions*

I. AMDUR AND M. S. LONGMIRE

Department of Chemistry, Massachusetts Institute of Technology, Cambridge, Massachusetts

AND

E. A. MASON

Institute for Molecular Physics, University of Maryland, College Park, Maryland

(Received March 6, 1961)

Collision cross sections have been measured for helium atoms with energies between 500 and 2100 ev, scattered in room-temperature CH_4 and CF_4. The results have been analyzed to obtain the average potential between a helium atom and a CH_4 molecule,

$$\langle V(r)\rangle_{Av}=602/r^{9.43}\text{ev},$$

for r between 1.92 and 2.37 A, and the average potential between a helium atom and a CF_4 molecule,

$$\langle V(r)\rangle_{Av}=6.18\times10^6/r^{17.51}\text{ev},$$

for r between 2.43 and 2.74 A. This He–CH_4 potential is consistent with one valid at larger separation distances which has been obtained by combining potentials derived from high-temperature viscosity and second virial coefficients of helium, and from high-temperature viscosity coefficients of methane.

A procedure which assumes the centers of force to reside in the peripheral H or F atoms has been used to analyze these average atom-molecule interactions in terms of the effective He–H and He–F interatomic potentials. These interatomic potentials have been combined with the potential previously determined for He–He to obtain effective H–H and F–F potentials for atoms in different CH_4 and CF_4 molecules. These effective interatomic potentials were then summed and averaged over all molecular orientations to yield the average potential between two CH_4 molecules,

$$\langle V(r)\rangle_{Av}=5.64\times10^6/r^{15.47}\text{ev},$$

for r between 2.47 and 3.06 A, and the average potential between two CF_4 molecules,

$$\langle V(r)\rangle_{Av}=1.17\times10^{22}/r^{39.27}\text{ev},$$

for r between 3.43 and 3.77 A. This CH_4-CH_4 potential is consistent with one valid at larger separation distances which has been derived from measurements on gaseous viscosity at high temperatures.

THE present paper reports a continuation of attempts to obtain information on the short-range forces between polyatomic molecules by the indirect procedure of studying the scattering of beams of fast neutral *atoms* by such molecules. It has been demonstrated by direct measurements that forces between pairs of unlike *atoms* can be calculated with good accuracy from the forces between the corresponding pairs of like atoms by a simple geometric mean combination rule for the potential.[1,2] Short-ranges forces between molecules are more complicated, however, in that the important forces probably act between the constituent atoms of the molecules rather than between the geometric centers of the molecules themselves, so that the simple combination rule for pairs of atoms cannot be used directly. Thus in order to obtain N_2-N_2 potentials indirectly from the results of the scattering of beams of He and Ar atoms by N_2 molecules, it was found better to assume that the forces acted between the beam atoms and the N atoms of the molecule, rather than to assume that the N_2 molecules were point centers of force.[3] In the present investigation, beams of high-velocity He atoms were scattered by the quasi-spherical polyatomic molecules CH_4 and CF_4, and the results were interpreted on the assumption that the forces act between the He atoms of the beam and the peripheral H or F atoms of the scattering molecules; the effect of the central C atoms was neglected.

The experimental procedures and the calculations involved in measurements of this type have been described in detail previously.[4] Table I lists the experimental cross sections $\bar{S}_w$ and $\bar{S}_n$, which were measured as a function of beam energy with a wide and a narrow detector having geometric apertures of 13.4 and 0.96 min, respectively. The tabulated smoothed cross sections S_w and S_n, were calculated from the following equations, obtained by least squares:

He-CH_4 system:

$$\log S_w=-0.23847\log E+1.85423, \quad (1)$$

$$\log S_n=-0.19102\log E+1.76058; \quad (2)$$

He-CF_4 system:

$$\log S_w=-0.13409\log E+1.71522 \quad (3)$$

$$\log S_n=-0.09944\log E+1.63958, \quad (4)$$

where S_w and S_n are in A^2 and E is in ev.

If the average intermolecular potential for the He-CH_4 and He-CF_4 systems is of the form $\langle V(r)\rangle_{Av}=K/r^s$, where r is the distance between the He atom and

* This research was supported in part by the U. S. Office of Naval Research.

[1] I. Amdur, E. A. Mason, and A. L. Harkness, J. Chem. Phys. **22**, 1071 (1954).

[2] I. Amdur and E. A. Mason, J. Chem. Phys. **25**, 632 (1956).

[3] I. Amdur, E. A. Mason, and J. E. Jordan, J. Chem. Phys. **27**, 527 (1957).

[4] I. Amdur and A. L. Harkness, J. Chem. Phys. **22**, 664 (1954).

TABLE I. Summary of collision cross-section results.

	Wide detector			Narrow detector		
E ev	$\bar{S}_w$ A²	S_w A²	Percent deviation	$\bar{S}_n$ A²	S_n A²	Percent deviation
			A. He—CH_4 system			
500	16.45	16.24	+1.3	17.81	17.58	+1.3
600	15.74	15.55	+1.2	17.00	16.98	+0.1
700	15.03	14.99	+0.3	16.52	16.49	+0.2
800	14.45	14.52	−0.5	15.83	16.07	−1.5
900	14.14	14.12	+0.1	15.54	15.71	−1.1
1000	13.64	13.77	−0.9	15.34	15.40	−0.4
1100	13.30	13.46	−1.2	15.05	15.12	−0.5
1200	12.97	13.18	−1.6	15.08	14.87	+1.4
1300	12.78	12.93	−1.2	14.62	14.65	−0.2
1400	12.59	12.70	−0.9	14.46	14.44	+0.1
1500	12.42	12.50	−0.6	14.30	14.25	+0.4
1600	12.22	12.31	−0.7	14.10	14.08	+0.1
1700	12.14	12.13	+0.1	13.82	13.92	−0.7
1800	12.12	11.97	+1.2	13.74	13.76	−0.1
1900	11.78	11.81	−0.2	13.63	13.62	+0.1
2000	11.82	11.67	+1.3	13.55	13.49	+0.4
2100	11.80	11.53	+2.3	13.42	13.36	+0.4
			B. He—CF_4 system			
500	22.59	22.56	+0.1	23.84	23.51	+1.4
600	22.15	22.01	+0.6	23.29	23.08	+0.9
700	21.43	21.56	−0.6	22.67	22.73	−0.3
800	21.17	21.18	−0.0	22.32	22.43	−0.5
900	20.72	20.85	−0.6	21.89	22.17	−1.3
1000	20.38	20.56	−0.9	21.66	21.94	−1.3
1100	20.22	20.30	−0.4	21.35	21.73	−1.8
1200	19.90	20.06	−0.8	21.29	21.55	−1.2
1300	19.96	19.85	+0.6	21.39	21.38	+0.0
1400	19.87	19.65	+1.1	21.51	21.22	+1.4
1500	19.87	19.47	+2.0	21.06	21.08	−0.1
1600	19.49	19.30	+1.0	21.29	20.94	+1.7
1700	19.08	19.14	−0.3	21.12	20.81	+1.5
1800	19.10	19.00	+0.5	20.99	20.70	+1.4
1900	19.00	18.86	+0.7	20.56	20.58	−0.1
2000	18.74	18.73	+0.0	20.58	20.48	+0.5
2100	18.05	18.61	−3.0	19.94	20.38	−2.2

the geometric center of the molecule, the parameters K and s can be obtained from the constants of Eqs. (1) to (4) according to the previously outlined procedure.[4] The results are shown in Table II.

For the He-CH_4 system, the ratio of the values of $\langle V(r)\rangle_{Av}$ derived from the wide-detector measurements to those derived from the narrow-detector measurements varies from 1.10 to 1.34 in the range of distances common to both, 2.06 to 2.27 A. Over the maximum range of 1.92 to 2.37 A, the ratio varies from 0.94 to 1.46. The intermediate potential function,

$$\langle V(r)\rangle_{Av}=602/r^{9.43}\text{ ev}, \qquad 1.92\text{ A}\leq r\leq 2.37\text{ A}, \quad (5)$$

is accordingly taken as representing the results derived from both detectors for the He-CH_4 system. In terms of cross sections, Eq. (5) leads to calculated values of S_w which average 0.8% lower than the corresponding values in Table I, and to calculated values of S_n which average 1.1% higher than the tabulated values.

Mason[5] has obtained a potential for He-CH_4 by combining the potential for He-He based on high-temperature viscosity and second virial coefficients[6] with that for CH_4-CH_4 based mostly on high-temperature viscosity coefficients.[7] This He-CH_4 potential, valid for separation distances greater than 2.74 A, may be written

$$\langle V(r)\rangle_{Av}=1.461\times10^{3}\exp(-3.64r)-13.6/r^{6}\text{ ev}. \quad (6)$$

As shown in Fig. 1 the potentials calculated from Eqs. (5) and (6) are quite consistent and unambiguously define the interpolated region represented by the dashed portion of the curve.

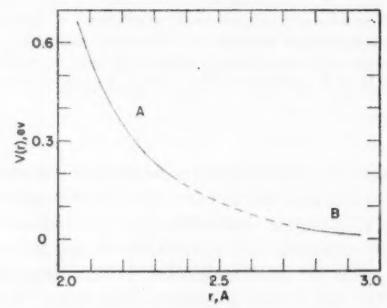

FIG. 1. Average potential energy between He and CH_4: (A) results from scattering of He in CH_4; (B) results from viscosity and second virial coefficients of He and viscosity of CH_4.

For the He-CF_4 system, the ratio of the $\langle V(r)\rangle_{Av}$ values from the wide detector to those from the narrow detector varies from 1.08 to 1.40 over the common range of 2.55 to 2.68 A, and from 0.84 to 1.57 over the entire range of 2.43 to 2.74 A. For this system the intermediate potential function representing both wide- and narrow-detector results,

$$\langle V(r)\rangle_{Av}=6.18\times10^{6}/r^{17.51}\text{ ev}, \quad 2.43\text{ A}\leq r\leq 2.74\text{ A}, \quad (7)$$

leads to calculated values of S_w which average 0.9% lower than the corresponding values of Table I, and to calculated values of S_n which average 0.6% higher than the tabulated values.

We now wish to combine the present results for He-CH_4 and He-CF_4 with the previous results[4] for He-He to

TABLE II. Average intermolecular potential parameters.

System	Detector	K, ev-A^s	s	Range, A
He—CH_4	wide	297	8.39	1.92–2.27
He—CH_4	narrow	1.22×10^{3}	10.47	2.06–2.37
He—CF_4	wide	5.67×10^{5}	14.92	2.43–2.68
He—CF_4	narrow	6.73×10^{7}	20.11	2.55–2.74

[5] E. A. Mason, J. Chem. Phys. **23**, 49 (1955).
[6] E. A. Mason and W. E. Rice, J. Chem. Phys. **22**, 522 (1954).
[7] E. A. Mason and W. E. Rice, J. Chem. Phys. **22**, 843 (1954).

obtain an estimate of the CH_4-CH_4 and CF_4-CF_4 interactions. To do this we must first decompose the present average results into effective He-H and He-F interatomic potentials, which can then be combined with the He-He potential, through the previously derived combination rules,[1,2] to obtain effective H-H and F-F interatomic potentials. These can then be recombined to obtain average CH_4-CH_4 and CF_4-CF_4 potentials. This treatment assumes that the peripheral atoms of the polyatomic molecules are the effective centers of force, and to carry the treatment through requires a further assumption about the averaging process involved in average potential functions like Eqs. (5) and (7). We make the assumption, previously used for the N_2 results,[3] that such average potentials can be obtained from the actual orientation-dependent potential by a direct average of the potential over all possible orientations. This is probably not strictly correct, and a better assumption perhaps would be that the experiments effectively average cross sections rather than potentials over all orientations.[8,9] Sinanoglu[9] has carried out some approximate calculations to compare the two methods of averaging and concludes that the potential averaging procedure leads to effective interatomic potentials which are somewhat too low (corresponding to an error of perhaps several percent in the cross sections) compared to those obtained by averaging the cross sections. Since the difference is probably of the same order of magnitude as the experimental uncertainty, we have used the easier potential averaging procedure.

The details of the averaging procedure for CH_4 and CF_4 are the same as for N_2,[3] except that there are now four peripheral atoms per molecule instead of two. The effective interatomic potential is assumed to be of the form $V(R)=K'/R^{s'}$, where R is the interatomic distance. The average molecule-beam atom potential is then obtained by adding together the four interatomic potentials and averaging over all orientations, considered equally probable, to yield

$$\langle V(r)\rangle_{Av}=4(K'/r^{s'})\lambda(\alpha,s'), \tag{8}$$

where

$$\lambda(\alpha,s')=\frac{(1+\alpha)^{s'-2}-(1-\alpha)^{s'-2}}{2\alpha(s'-2)(1-\alpha^2)^{s'-2}}, \tag{9}$$

in which r is the distance between the beam atom and the center of the molecule, and $\alpha=a/r$, where a is the C—H or C—F bond length. (In general, a is the distance between the center of mass and a bonded atom.) This expression is to be compared with the simpler expression for the average potential given in Eqs. (5) and (7), which were used to fit the experimental results. The parameters K' and s' can be chosen by a least-squares successive approximation procedure so that Eq. (8) gives a good numerical representation of Eq. (5) or Eq. (7) over its range of validity, and the following effective interatomic potentials are thereby obtained,

$$\text{He-H:}\quad V(R)=2.60/R^{6.06}\ \text{ev},\quad 1.68\ \text{A}\leq R\leq 2.18\ \text{A}; \tag{10}$$

$$\text{He-F:}\quad V(R)=34.1/R^{10.07}\ \text{ev},\quad 2.16\ \text{A}\leq R\leq 2.51\ \text{A}. \tag{11}$$

The value of a was taken as 1.0936 A for CH_4[10] and 1.317 A for CF_4.[11] The interaction distances in Eqs. (10) and (11), interatomic distances corresponding to the respective center-of-mass distances, have been estimated as suggested by Vanderslice, Mason, and Lippincott.[12] Values of $\langle V(r)\rangle_{Av}$ obtained from Eq. (10) will reproduce the results of Eq. (5) with an average absolute deviation of 1.9%, and those obtained from Eq. (11) will reproduce the results of Eq. (7) with an average absolute deviation of 1.3%.

Since Eqs. (10) and (11) now involve only central force fields, the combination rules previously tested for rare-gas systems[1,2] can be used to derive effective potentials for the H-H and F-F systems. Thus, when Eqs. (10) and (11) are combined with the corresponding potential for the He-He system,[4] namely,

$$V(R)=4.71/R^{5.94}\ \text{ev},\qquad 1.27\ \text{A}\leq R\leq 1.59\ \text{A}, \tag{12}$$

the following expressions are obtained,

$$\text{H-H:}\quad V(R)=1.44/R^{6.18}\ \text{ev},\quad 2.09\ \text{A}\leq R\leq 2.77\ \text{A}; \tag{13}$$

$$\text{F-F:}\quad V(R)=247/R^{14.20}\ \text{ev},\quad 3.05\ \text{A}\leq R\leq 3.43\ \text{A}. \tag{14}$$

These interaction potentials between two hypothetical H atoms or two hypothetical F atoms can now be used to find the average potential between two CH_4 molecules and two CF_4 molecules by adding together the appropriate interatomic potentials and averaging over all orientations as before. For an interatomic potential of the form $V(R)=K'/R^{s'}$, the average molecule-molecule potential is thus found to be

$$\langle V(r)\rangle_{Av}=16(K'/r^{s'})\psi(\alpha,s'), \tag{15}$$

where

$$\psi(\alpha,s')=\frac{(1+2\alpha)^{s'-3}+(1-2\alpha)^{s'-3}-2(1-4\alpha^2)^{s'-3}}{4\alpha^2(s'-2)(s'-3)(1-4\alpha^2)^{s'-3}}, \tag{16}$$

[8] E. A. Mason and J. T. Vanderslice, J. Chem. Phys. **27**, 917 (1957).
[9] O. Sinanoglu, J. Chem. Phys. **30**, 850 (1959).
[10] G. Herzberg, *Infrared and Raman Spectra of Polyatomic Molecules* (D. Van Nostrand Company, Inc., Princeton, New Jersey, 1945), p. 439.
[11] C. W. W. Hoffman and R. L. Livingston, J. Chem. Phys. **21**, 565 (1953).
[12] J. T. Vanderslice, E. A. Mason, and E. R. Lippincott, J. Chem. Phys. **30**, 129 (1959).

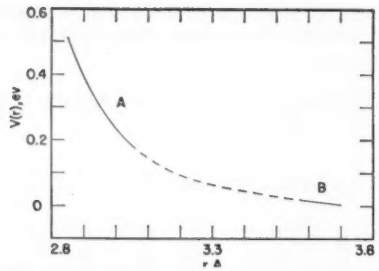

FIG. 2. Average potential energy between two CH_4 molecules: (A) results from scattering of He in CH_4 and He in He: (B) results from viscosity of CH_4.

in which r is the distance between the centers of mass of the molecules, and $\alpha=a/r$, as before.

Since it is convenient to express the final molecule-molecule potentials in a simpler algebraic form than that given by Eqs. (15) and (16), the numerical values were fitted by the usual function K/r^s by least squares. The final results are

$$CH_4\text{-}CH_4: \quad \langle V(r)\rangle_{Av}=5.64\times10^6/r^{15.47}\text{ev},$$

$$2.47\text{ A}\leq r\leq 3.06\text{ A}; \quad (17)$$

$$CF_4\text{-}CF_4: \quad \langle V(r)\rangle_{Av}=1.17\times10^{22}/r^{39.27}\text{ ev},$$

$$3.43\text{ A}\leq r\leq 3.77\text{ A}; \quad (18)$$

where the ranges of interaction distance are given in terms of the average center-of-mass distances.[12] Equation (17) reproduces the numerical results of Eqs. (13) and (15) with an average absolute deviation of 9.2%, and Eq. (18) reproduces the numerical results of Eqs. (14) and (15) with an average absolute deviation of 2.6%. The values of s in Eqs. (17) and (18) are quite high, as would be expected for such quasi-spherical molecules.[13]

It is interesting to compare the results of the present procedure with those obtained by assuming that CH_4 and CF_4 are simple point centers of force and applying the combination rules for central force systems directly. Thus, direct combination of Eqs. (5) and (12) leads to an apparent average CH_4-CH_4 potential which is lower than the potential of Eq. (17) by a factor ranging between 0.14 and 0.26, and direct combination of Eqs. (7) and (12) leads to an apparent average CF_4-CF_4 potential which is lower than that of Eq. (18) by a factor ranging between 2.4×10^{-4} and 7.1×10^{-4}. It is apparent that the two methods of deducing average molecule-molecule potentials lead to strikingly different results, particularly for CF_4. The results based on the assumption that CH_4 and CF_4 are point centers of force seem far too low to be physically reasonable.

Equation (17) for CH_4-CH_4 is consistent with a potential valid for distances greater than 3.57 A, derived in part from measurements of the viscosity of gaseous methane at high temperatures.[7] This potential is represented by the expression

$$\langle V(r)\rangle_{Av}=1.188\times10^4\exp(-3.334)-127.6/r^6\text{ ev}. \quad (19)$$

The comparison is shown in Fig. 2. Although there is a considerable gap between the ranges of validity of Eq. (17) and Eq. (19), it is clear that they are consistent. A similar comparison is not made for CF_4 because of the lack of high-temperature viscosity data. The available virial coefficients are too sensitive to the long-range attractive forces between the molecules to be used for this purpose. Further checks on the present results, for instance by scattering beams of Ar atoms in CH_4 and CF_4, would be valuable.

[13] S. D. Hamann and J. A. Lambert, Australian J. Chem. **7**, 1, 18 (1954).

Vapor Pressures of the Inert Gases

CHARLES E. HAMRIN, JR., AND GEORGE THODOS

The Technological Institute, Northwestern University, Evanston, Illinois

(Received March 4, 1961)

A single vapor-pressure relationship applicable from the triple point to the critical point has been found to exist for the inert gases argon, krypton, and xenon when the reduced vapor pressure P_R is related to T_R the reduced temperature. This vapor-pressure function resulted from the Frost-Kalkwarf Eq. (12) and can be expressed as

$$\log P_R=\alpha+(\beta/T_R)+\gamma \log T_R+0.1832\ (P_R/T_R^2),$$

where 0.1832 is a universal constant. For these inert gases $\beta=-2.2936$ and $\gamma=-2.6786$ while α can be calculated from the boundary condition, $\alpha+\beta+0.1832=0$.

The vapor-pressure data for helium and neon produced similar reduced-vapor-pressure relationships having different constants. These results are not unexpected in view of the significant quantum effects associated with helium and to a lesser degree with neon. Values calculated with this reduced-vapor-pressure equation have been found to be in excellent agreement with experimental values reported for argon, krypton, and xenon. The average deviation for these gases was 0.63%, for neon 1.51%, and for helium 0.79%.

THE use of reduced-state correlations have proved valuable for the estimation of thermodynamic,[1–3] volumetric[4–6] and transport properties.[7–10] The extension of reduced state parameters for the correlation of vapor pressures has been suggested by van der Waals[11] as early as 1899 in a form which simplifies into the expression

$$\log P_R=a[1-(1/T_R)]. \tag{1}$$

In 1906 Bingham[12] showed graphically that the vapor-pressure data for several substances based on Eq. (1) did not produce a unique reduced-vapor-pressure relationship. Following a similar approach, Weber and Meissner[13] also show that a universal reduced-vapor-pressure curve does not exist when the logarithm of reduced-vapor-pressure is plotted against the reciprocal reduced temperature. Recently Lydersen, Greenkorn, and Hougen[5] pointed the existence of a unique vapor-pressure behavior for substances having the same critical compressibility factors. Because of their molecular simplicity and consequent adaptability to kinetic theory the inert gases have been arbitrarily selected for this study.

TREATMENT OF VAPOR PRESSURE DATA

Reliable vapor-pressure data for the inert gases were selected from literature sources and were reduced using the critical constants presented in Table I. In addition, the triple points and the sources of vapor pressures are also included in this table.

A plot of the logarithm of the reduced vapor pressure, $\log P_R$ versus the reciprocal reduced temperature $1/T_R$ is presented in Fig. 1. Argon, krypton, and xenon produce a single correlation whereas the relationship for neon is somewhat shifted and shows a perceptible curvature. Both these relationships are presented from the triple point to the critical point. The vapor-pressure behavior of helium is specific in that it exhibits considerable curvature and is far removed from the other members of this family. The single vapor-pressure function for argon, krypton, and xenon can be explained by the fact that these monatomic gases possess essentially the same critical compressibility factors which are 0.291, 0.292, and 0.290, respectively. The departure from this curve by neon is not only due to its higher critical compressibility factor $z_c=0.307$, but also by its quantum deviations that cannot be completely neglected. On the other hand, since the z_c values for neon and helium are almost identical, it can be concluded that the radical vapor-pressure behavior of helium is the result of quantum effects that are of the highest order of magnitude.

In view of the results shown in Fig. 1, it is apparent that a unique vapor-pressure relationship does exist for the monatomic gases argon, krypton, and xenon. A reduced-state correlation based on the vapor pressure of neon may not prove as useful, since, aside from hydrogen and helium, no other substances have such high critical compressibility factors. For these gases quantum effects prohibit any generalized treatment; therefore the vapor-pressure behavior of neon and helium must be treated individually.

[1] W. C. Edmister, Ind. Eng. Chem. (Intern. Edition) **30,** 352 (1938).
[2] O. A. Hougen and K. M. Watson, *Chemical Process Principles* (John Wiley & Sons, Inc., New York, 1947), pp. 494–502.
[3] K. S. Pitzer and R. F. Curl, Jr., J. Am. Chem. Soc. **79,** 2369 (1957).
[4] C. E. Hamrin, Jr., and G. Thodos, A.I.Ch.E. Journal **4,** 480 (1958).
[5] A. L. Lydersen, R. A. Greenkorn, and O. A. Hougen, "Generalized thermodynamic properties of pure fluids," Rept. No. 4, Engineering Experiment Station, University of Wisconsin (1955).
[6] L. C. Nelson and E. F. Obert, Trans. Am. Soc. Mech. Engrs. **76,** 1057 (1954).
[7] W. J. Brebach and G. Thodos, Ind. Eng. Chem. (Intern. Edition) **50,** 1095 (1958).
[8] B. W. Gamson, Chem. Eng. Progr. **45,** 154 (1949).
[9] E. J. Owens and G. Thodos, A.I.Ch.E. Journal **3,** 454 (1957).
[10] O. A. Uyehara and K. M. Watson, Natl. Petrol. News, Tech. Sect. **36,** R764 (1944).
[11] J. R. Partington, *An Advanced Treatise on Physical Chemistry* (Longmans Green and Company, London, 1949), Vol. 1, p. 697.
[12] E. C. Bingham, J. Am. Chem. Soc. **28,** 717 (1906).
[13] H. C. Weber and H. P. Meissner, *Thermodynamics for Chemical Engineers* (John Wiley & Sons, Inc., New York, 1957), p. 134.

TABLE I. Critical points and triple points for the inert gases and sources of vapor-pressure data.

	Critical point			Triple point		Source vapor pressure
	z_c	T_c, °K	P_c, atm	T_t, °K	P_t, atm	
Helium	0.306[d]	5.206[a]	2.26[b]	c	c	a, d
Neon	0.307[d]	44.45[e]	26.86[f]	24.42[g]	0.426[g]	h
Argon	0.291[d]	150.72[i]	48.00[i]	83.78[j]	0.680[j]	k
Krypton	0.292[d]	209.4[e]	54.18[e]	115.97[m]	0.720[m]	l
Xenon	0.290[d]	289.75[n]	57.64[n]	161.36[o]	0.806[o]	p

[a] R. Berman and C. A. Swenson, Phys. Rev. **95**, 311 (1954).
[b] H. Kamerlingh Onnes, Communs. Phys. Lab. Univ. Leiden, No. 124b (1911).
[c] No triple point exists for helium [see W. H. Keesom, *Helium* (Elsevier Publishing Company, Inc., New York, 1942), p. 202].
[d] G. Schmidt and W. H. Keesom, Physica **4**, 971 (1937).
[e] C. A. Crommelin, Communs. Phys. Lab. Univ. Leiden, No. 162c (1923).
[f] W. H. Keesom, Physik. Ber. **4**, 613 (1923).
[g] H. Kamerlingh Onnes, Communs. Phys. Lab. Univ. Leiden, No. 147d (1915).
[h] P. G. Cath and H. Kamerlingh Onnes, Communs. Phys. Lab. Univ. Leiden, No. 152b (1921).
[i] C. A. Crommelin, Communs. Phys. Lab. Univ. Leiden, No. 115a (1910).
[j] K. Clusius and A. Frank, Z. Elektrochem. **49**, 308 (1943).
[k] A. M. Clark, F. Din, J. Robb, A. Michels, T. Wassenaar, and T. N. Zwietering, Physica **17**, 876 (1950).
[l] J. J. Meihuizen and C. A. Crommelin, Communs. Phys. Lab. Univ. Leiden, No. 245c (1937).
[m] J. J. Meihuizen and C. A. Crommelin, Physica **4**, 1 (1937).
[n] H. W. Habgood and G. W. Schneider, Can. J. Chem. **32**, 98 (1954).
[o] K. Clusius, Z. physik. Chem. **B50**. 403 (1941).
[p] A. Michels and T. Wassenaar, Physica **16**, 253 (1950).

APPLICATION OF THE FROST-KALKWARF EQUATION

A vapor-pressure equation capable of defining precisely the vapor-pressure function from the triple point to the critical point has been derived by Frost and Kalwarf.[14] Their equation has been applied extensively to define the vapor pressure of hydrocarbons[15,16] and properly accounts for the curvature prevailing in the low-pressure region and subsequent reversal near the critical point. Since this equation accounts for the actual vapor-pressure behavior, it has been applied to the inert gases in reduced form. The original vapor-pressure equation presented by Frost and Kalkwarf is

$$\log P = A + (B/T) + C \log T + D(P/T^2), \qquad (2)$$

where A, B, C, and D are constants specific to each substance. In the original development,[14] it has been shown that,

$$D = a/2.303R^2. \qquad (3)$$

Introducing the substitutions $P = P_c P_R$ and $T = T_c T_R$ and recognizing that the pressure van der Waals' constant a can be expressed as

$$a = 27R^2T_c^2/64P_c, \qquad (4)$$

it is possible to show that Eq. (2) becomes

$$\log P_R = \alpha + (\beta/T_R) + \gamma \log T_R + 0.1832(P_R/T_R^2). \qquad (5)$$

Equation (5) requires the three constants α, β, and γ for complete definition. It is interesting to note that the constant D of Eq. (2) has resolved into a universal constant equal to 0.1832. In addition, Eq. (5) possesses the unique boundary condition at the critical point

$$\alpha + \beta + 0.1832 = 0. \qquad (6)$$

It has been shown that the constants B and C of Eq. (2) can be determined graphically from vapor-pressure data provided that the constant D is known.[16] This was possible through the selection of an arbitrary reference vapor-pressure point and the calculation of temperature

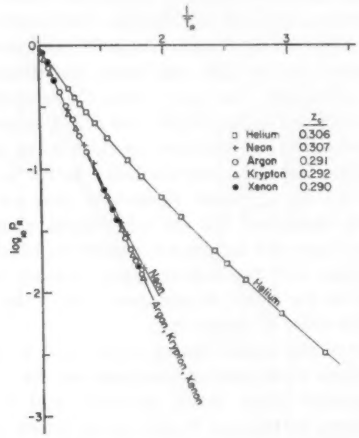

FIG. 1. Reduced vapor-pressure relationships for inert gases.

[14] A. A. Frost and D. R. Kalkwarf, J. Chem. Phys. **21**, 264 (1953).
[15] R. E. Perry and G. Thodos, Ind. Eng. Chem. **44**, 1649 (1952).
[16] N. E. Sondak and G. Thodos, A.I.Ch.E. Journal **2**, 347 (1956).

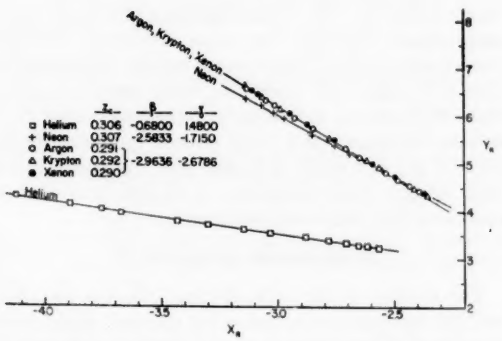

FIG. 2. Relationships of reduced vapor-pressure, temperature moduli Y_R and X_R for the inert gases.

and vapor-pressure moduli which, when plotted on rectilinear coordinates, produced straight lines of slope B and intercept C. Following an analogous procedure and utilizing the critical temperature and pressure as an arbitrary reference point, the two-constant equation results

$$\frac{\log P_R - 0.1832[(1/T_R)-1]}{\log T_R} = \beta\frac{(1/T_R)-1}{\log T_R} + \gamma, \quad (7)$$

where the reduced temperature and reduced vapor-pressure moduli are introduced for convenience as

$$X_R = \frac{(1/T_R)-1}{\log T_R} \quad (8)$$

and

$$Y_R = \frac{\log P_R - 0.1832[(P_R/T_R^2)-1]}{\log T_R}. \quad (9)$$

Using these reduced temperature and pressure moduli, Eq. (7) can be expressed simply as,

$$Y_R = \beta X_R + \gamma, \quad (10)$$

with slope β and intercept γ. The critical point has been selected as a reference for the development of the linear relationship defined in Eq. (7). The selection of a reference point should not necessarily be restricted to the critical point. Any other reliable vapor-pressure point could be used as a reference, however such a selection would complicate the numerical computational procedure for the calculation of the constants β and γ. Regardless of the reference point chosen, the resulting values of β and γ should be the same for a substance. If the critical point is believed to be reliable, it is recommended that Eq. (7) be used to establish constants β and γ.

TABLE II

	z_c	β	γ
Helium	0.306	−0.6800	1.4800
Neon	0.307	−2.5833	−1.7150
Argon	0.291		
Krypton	0.292	−2.9636	−2.6786
Xenon	0.290		

TABLE III

	A*
Helium	2.74
Hydrogen	1.80
Neon	0.58
Nitrogen	0.235
Oxygen	0.212
Argon	0.182
Krypton	0.096
Chlorine	0.067
Xenon	0.062

Reduced-temperature and reduced-vapor-pressure moduli X_R and Y_R have been calculated for the inert gases helium, neon, argon, krypton, and xenon from vapor-pressure data reported in the literature. In this connection, the critical points presented in Table I have been used as references for the treatment of the vapor-pressure data. The results of this analysis are presented in Fig. 2. The reduced-temperature and reduced-vapor-pressure moduli for argon, krypton, and xenon produced a single straight line while the linear relationship of neon was found to be of slightly different slope and that of helium was considerably removed from the others. The straight line relationships of Fig. 2 validate the Frost-Kalkwarf equation as capable of adequately representing the vapor-pressure function from the triple point to the critical point. The straight lines of Fig. 2 enable the calculation of the

TABLE IV

	No. of Points	% Deviation[a]	Source
Helium	16	0.79	b, c
Neon	12	1.51	d
Argon	18	1.02	e
Krypton	14	0.41	f
Xenon	19	0.42	g

[a] Percent deviation $= [(|P_{expt}-P_{calc}|)/P_{expt}] \times 100$.
[b] R. Berman and C. A. Swenson, Phys. Rev. **95**, 311 (1954).
[c] G. Schmidt and W. H. Keesom, Physica **4**, 971 (1937).
[d] P. G. Cath and H. Kamerlingh Onnes, Communs. Phys. Lab. Univ. Leiden, No. **152b** (1921).
[e] A. M. Clark, F. Din, J. Robb, A. Michels, T. Wassenoar, and T. N. Zwietering, Physica **17**, 876 (1950).
[f] J. J. Meihuizen, C. A. Crammelin, Communs. Phys. Lab. Univ. Leiden, No. 245c, (1937).
[g] A. Michels and T. Wassenaar, Physica **16**, 253 (1950).

vapor-pressure constants β and γ as the slopes and intercepts, respectively. These constants are listed in Table II.

Despite the fact that helium and neon have practically the same z_c values, their pronounced differences in vapor-pressure behavior can be explained in terms of their significant quantum deviations which are essentially absent for argon, krypton, and xenon. To account for these deviations de Boer and Bird[17] introduce the quantum-mechanical parameter,

$$\Lambda^* = h/\sigma(m\epsilon)^{\frac{1}{2}}, \tag{11}$$

where h=Planck constant, 6.624×10^{-27} erg sec; m=mass of molecule, g; ϵ=maximum energy of attraction for Lennard-Jones potential, ergs; σ=collision diameter for Lennard-Jones potential, cm. Values of Λ^* have been calculated not only for the inert gases, but also for a few other substances for which the Lennard-Jones force constants are available.[18] (See Table III.)

It can be seen that helium possesses the highest quantum-mechanical parameter, followed by hydrogen whose value of 1.80 is also significant. The quantum-mechanical parameter for neon $\Lambda^*=0.58$, although considerably removed for those of helium and hydrogen, cannot be neglected. Therefore, these three substances must be examined individually. Substances other than helium, hydrogen, and neon possess quantum deviations of a lesser order of magnitude; consequently for their proper characterization, it is not necessary to introduce this additional parameter.

COMPARISON OF RESULTS

The validity of the reduced-vapor-pressure equation and the constants α, β, and γ for the inert gases have been checked by comparing vapor-pressure values with corresponding experimental data. In these comparisons the entire vapor-pressure range from the triple point to the critical point was considered. The resulting percent deviations are presented with the number of points examined and the source of these data in Table IV. These results point to an excellent agreement between calculated and experimental values; consequently it is reasonable to expect that the reduced-vapor-pressure equation used in this study could be applied to other substances for which meager experimental information is available.

[17] J. de Boer, and R. B. Bird, Phys. Rev. **83,** 1259 (1951).
[18] J. O. Hirschfelder, C. F. Curtiss, and R. B. Bird, *Molecular Theory of Gases* (John Wiley & Sons, Inc., New York, 1957), pp. 1110–12.

Effect of Pressure on the Spectra of Transition Metal Ions in MgO and Al_2O_3†

S. MINOMURA AND H. G. DRICKAMER

Department of Chemistry and Chemical Engineering, University of Illinois, Urbana, Illinois

(Received February 15, 1961)

The effect of pressure to 150 kbar has been measured on the spectra of several transition metal ions in MgO and Al_2O_3. In general, there is an increase in crystal field strength with increasing pressure. The interelectronic repulsion parameter decreased slightly with increasing pressure indicating a small increase in covalency. For Al_2O_3, Dq shifts as $(V_0/V)^{5/3}$ indicating that the R^{-5} law holds, and the local compressibility is the same as the bulk compressibility. In MgO the shift is always more rapid than R^{-5}, indicating local relaxation near the foreign ion. Above about 50 kbar there is a marked increase of trigonal distortion in Al_2O_3.

INTRODUCTION

THE effect of pressure on the spectra of transition metal ions (Ti^{3+}, Cr^{3+}, Co^{2+}, and Ni^{2+}) in MgO and (Ti^{3+}, V^{3+}, Ni^{2+}, and Ni^{3+}) Al_2O_3 crystals has been studied up to 150 kbar. MgO is a crystal with face centered cubic structure. Al_2O_3 is a uniaxial crystal of trigonal system with two molecules per unit cell. The crystals are colored by doping with small quantities (below 1%) of the transition metal ions. The transition metal ions doped in MgO and Al_2O_3 crystals are assumed to substitute for Mg^{2+} and Al^{3+} and to be coordinated to six O^{2-} which are at the corners of an octahedron and a deformed octahedron, respectively. The local crystal field of transition metal ions is purely cubic in MgO, but cubic+trigonal in Al_2O_3. In a trigonal field T representations of the group of a octahedron split into A and E components of C_{3v}, which could be polarized parallel and perpendicular to the C_3 axis.

The spectra of Cr^{3+}, Co^{2+}, and Ni^{2+} in MgO have been studied by Low.[1] Some investigators have studied the spectra of V^{3+},[2] Cr^{3+},[3] or Ni^{3+} [4] in Al_2O_3. The crystal field spectra of transition metal ions owe the origin to the $d \rightarrow d$ transitions. In a cubic system the five d orbitals split into triply degenerate t orbitals and doubly degenerate e orbitals which are lower and higher than the original d levels by $-4Dq$ and $+6Dq$, where Dq is the empirical parameter of the crystal field strength. Some of the solutions of the secular equations for the transition metal ions in an octahedral field have been derived in terms of the Racah parameters B and C, and Dq by Tanabe and Sugano.[5] In a cubic field the value of Dq should vary as R^{-5} for the approximation of a point charge ligand,[4,6] and as R^{-6} for point dipoles,[4,7] where R is the distance from the center of the transition metal ions to the ligands. The rate of change in Dq with pressure might predict the local compressibility in the neighborhood of the octahedrally coordinated ligands.

In the present study on the crystal field spectra of the transition metal ions the following subjects have been discussed: (a) the change in frequencies with pressure; (b) the change in Dq with pressure; (c) the change in B with pressure; and (d) the local compressibility in the neighborhood of the ligands.

EXPERIMENT

MgO doped with Ti^{3+}, Cr^{3+}, Co^{2+}, and Ni^{2+}, and Al_2O_3 doped with Ti^{3+}, V^{3+}, Ni^{2+}, and Ni^{3+} were studied. MgO doped with Ti^{3+} and Cr^{3+} were obtained

TABLE I. Observed spectra of Ti^{3+}, Cr^{3+}, Co^{2+}, and Ni^{2+} in MgO.

No.	Crystals	Frequencies at 1 atm	Assignments	References
1	MgO:Ti^{3+}	11 360 cm^{-1}	$^2T_2 \rightarrow {}^2E$	10
2	MgO:Cr^{3+}	16 200	$^4A_2(F) \rightarrow {}^4T_2(F)$	4
			$^2E\ (G)$	1
3	MgO:Cr^{3+}	22 700	$^4T_1(F)$	4
			$^4T_2(F)$	1
4	MgO:Co^{2+}	8220	$^4T_1(F) \rightarrow {}^4T_2(F)$	1
5	MgO:Co^{2+}	18 770	$^4A_2(F)$	
6	MgO:Ni^{2+}	8845	$^3A_2(F) \rightarrow {}^3T_2(F)$	1
7	MgO:Ni^{2+}	13 700	$^1E\ (D)$	
8	MgO:Ni^{2+}	14 700	$^3T_1(F)$	
9	MgO:Ni^{2+}	21 715	$^1T_2(D)$	
10	MgO:Ni^{2+}	24 500	$^3T_1(P)$	
11	MgO:Ni^{2+}	25 950	$^1A_1(G)$	
12	MgO:Ni^{2+}	28 300	$^1T_1(G)$	

† This work was supported in part by the U. S. Atomic Energy Commission.

[1] W. Low, Phys. Rev. **105,** 801 (1957); **109,** 256 and 247 (1958).

[2] M. H. L. Pryce and W. A. Runciman, Discussions Faraday Soc. **26,** 34 (1958).

[3] B. N. Grechushnikov and P. P. Foefilov, Zhur. Eksptl. i Teoret. Fiz. **29,** 384 (1955).

[4] D. S. McClure, *Solid State Physics* (Academic Press, Inc., New York, 1959), Vol. 9, p. 399.

[5] Y. Tanabe and S. Sugano, J. Phys. Soc. Japan **9,** 753 and 766 (1954).

[6] C. K. Jørgensen, *Quelques Problemes de Chemie Minerale* (R. Scops, Brussels, 1956), p. 355.

[7] J. H. Van Vleck, J. Chem. Phys. **7,** 72 (1939).

TABLE II. Observed spectra of Ti^{3+}, V^{3+}, Ni^{2+}, and Ni^{2+} in Al_2O_3.

No.	Crystals	Light vector to C axis	Frequencies at 1 atm	Assignments	References
1	$Al_2O_3:Ti^{3+}$		17 870 cm^{-1} 17 720	$^2T_2 \rightarrow$ $^2E_{A_1}$, $^2E_{B_1}$	10
2	$Al_2O_3:V^{3+}$		17 490 17 310	$^3T_1(F) \rightarrow {}^3T_2(F)$ $^3A_1$, ^3E	2, 4
3	$Al_2O_3:V^{3+}$		25 970 25 820	$^3T_1(P)$ $^3A_2$, ^3E	
4	$Al_2O_3:Ni^{2+}$		10 050 9800	$^3A_2(F) \rightarrow {}^3T_2(F)$ $^3A_1$, ^3E	10
5	$Al_2O_3:Ni^{2+}$		15 840 15 840	$^1E(D)$	
6	$Al_2O_3:Ni^{2+}$		16 590 16 500	$^3T_1(F)$ $^3A_2$, ^3E	
7	$Al_2O_3:Ni^{2+}$		9000 8860	$^4T_1(F) \rightarrow {}^4T_2(F)$ $^4A_1$, ^4E	

from W. M. Walsh of Bell Laboratories and from J. Scott of the Norton Company, and Al_2O_3 doped with Ti^{3+} and V^{3+} from Shinkosya Company of Japan. MgO doped with Co^{2+} and Ni^{2+}, and Al_2O_3 doped with Ni^{2+} and Ni^{3+} were prepared by heating the pure crystals with powdered CoO and NiO at about 1600°C for several hours in an argon atmosphere. The authors are inclined to interpret one of the double peaks in the infrared region as the transition in $Al_2O_3:Ni^{3+}$, which was produced by an oxidation of Ni^{2+}. The MgO crystals were cleaved and the Al_2O_3 were cut parallel to the C_3 axis. The specimens were polished down to a final size of about 0.120×0.060×0.030 or 0.090×0.030 in., and used for the high-pressure cells with $\frac{1}{8}$-in. piston up to 50 kbar and with $\frac{1}{2}$-in. piston up to 150 kbar, respectively. The path length was 0.030 in.

A Perkin-Elmer infrared spectrophotometer equipped LiF prism and Beckman DUR equipped with RCA

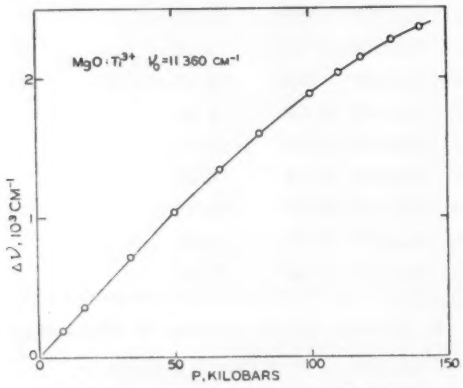

FIG. 1. Frequency shift vs pressure, MgO:Ti^{3+}.

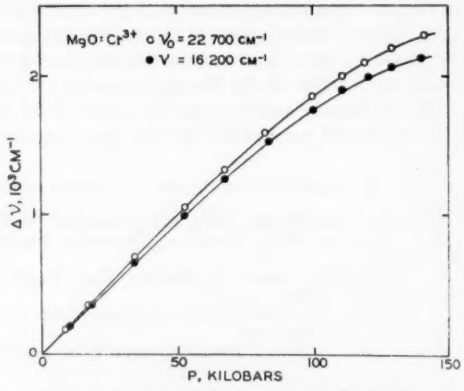

FIG. 2. Frequency shift vs pressure, MgO:Cr^{3+}.

7102, 1P21 and 1P28 photomultipliers were used for the spectral measurement. The polarized spectra were obtained for the Al_2O_3 crystals with a polarizer. Although the strained NaCl partially depolarized the light, the peak of correct polarization was sufficiently prominent. The high-pressure optical system and the techniques have been described previously.[8,9]

RESULTS

The observed frequencies at one atmosphere and the interpretations of the spectra of Ti^{3+}, Cr^{3+}, Co^{2+}, and Ni^{2+} in MgO are summarized in Table I and those of Ti^{3+}, V^{3+}, Ni^{2+}, and Ni^{3+} in Al_2O_3 in Table II. The change in frequency with pressure is shown in each crystal in Figs. 1–7. All observed transitions shift to the higher frequencies with increasing pressure. The frequency shift with pressure for the double peaks at 13 700–14 700 cm^{-1} of $MgO:Ni^{2+}$ and 15 840–16 590 cm^{-1} of $Al_2O_3:Ni^{2+}$ were not obtained because of the poor resolution of the spectra. For $Al_2O_3:Ti^{3+}$ the spectrum polarized parallel to the C_3 axis indicates a greater change in frequency with pressure above 50 kbar than the spectrum polarized perpendicular. The separation between the peaks increases with increasing pressure, as shown in Fig. 8.

DISCUSSION

A. Change in Frequency with Pressure

For $MgO:Cr^{3+}$ and $^4A_2(F)\rightarrow{}^4T_2(F)$ transition, which is equal to 10 Dq, is assigned to the 16 200 cm^{-1} band by McClure,[4] but to the 22 700 cm^{-1} band by Low.[1] The authors are inclined to interpret the 16 200 cm^{-1} band as the transition to the $^4T_2(F)$ state; this is less than the 10 Dq of 17 600 cm^{-1} for $[Cr(H_2O)_6]^{3+}$ complex.[4] The double peak at 13 700–14 700 cm^{-1} in $MgO:Ni^{2+}$ is interpreted as the $^3A_2(F)$ $^1E(D)$ and $^3A_2(F)\rightarrow{}^3T_1(F)$ transitions, respectively, by Low, but as the spin-orbit splitting of the $^3T_1(F)$ state by McClure. It is difficult to interpret from the frequency shift with pressure because of the poor resolution of the spectra. On the other hand, the lower frequency band of the double peak at 15 840–16 590 cm^{-1} of $Al_2O_3:Ni^{2+}$ shows a very small frequency shift with pressure and may be interpreted as the transition to the $^1E(D)$ state. The double peak at 9000–10 050 cm^{-1} of the Al_2O_3 crystal heated with powdered NiO may be interpreted as the $^3A_2(F)\rightarrow{}^3T_2(F)$ transition of Ni^{2+} and the $^4T_1(F)\rightarrow{}^4T_2(f)$ transition of Ni^{3+}.

The polarized spectra of $Al_2O_3:Ti^{3+}$ are split into the transitions from the $^2T_2$ ground state to the A_1 and B_1 components of the ^2E state.[10] The splitting of the ^2E state by the trigonal field is proportional to the fre-

[8] R. A. Fitch, T. E. Slykhouse, and H. G. Drickamer, J. Opt. Soc. Am. **47**, 1015 (1957).
[9] H. G. Drickamer, Rev. Sci. Instr. **32**, 212 (1961).
[10] W. Low, *Solid State Physics* (Academic Press, Inc., New York, 1960), Suppl. 2.

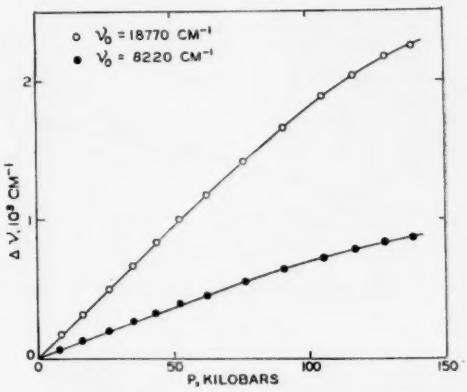

FIG. 3. Frequency shift vs pressure, $MgO:Co^{2+}$.

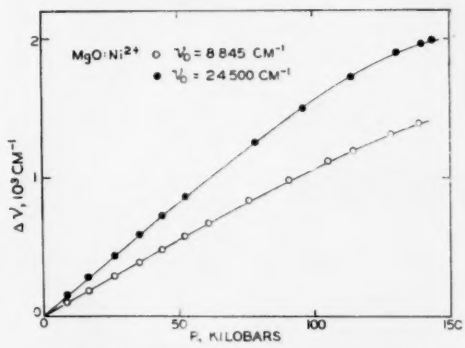

FIG. 4. Frequency shift vs pressure, $MgO:Ni^{2+}$.

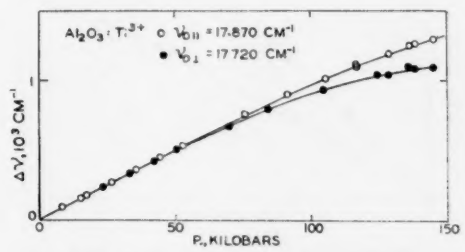

FIG. 5. Frequency shift vs pressure, $Al_2O_3:Ti^{3+}$.

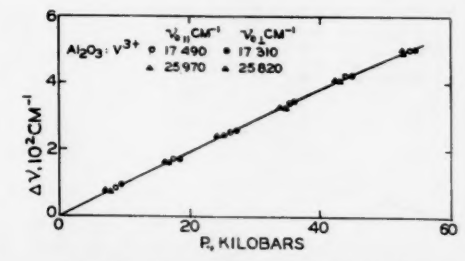

FIG. 6. Frequency shift vs pressure, $Al_2O_3:V^{3+}$.

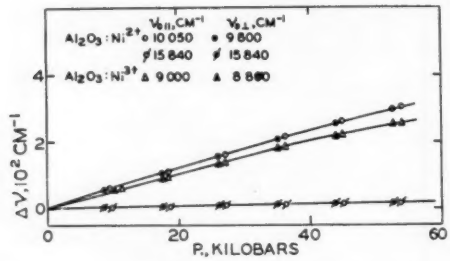

FIG. 7. Frequency shift vs pressure, Al_2O_3:Ni^{2+} and Al_2O_3:Ni^{3+}.

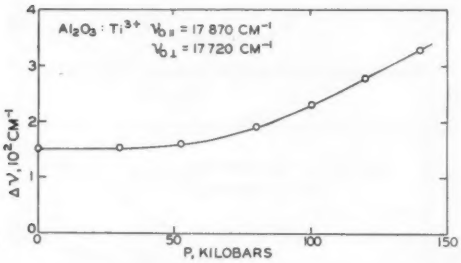

FIG. 8. Splitting of peaks polarized parallel and perpendicular to the C_3 axis, Al_2O_3:Ti^{3+}.

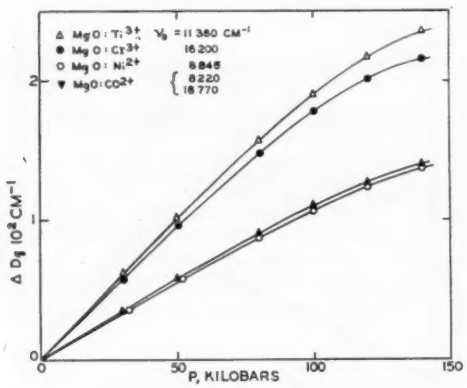

FIG. 9. Change of Dq with pressure in MgO.

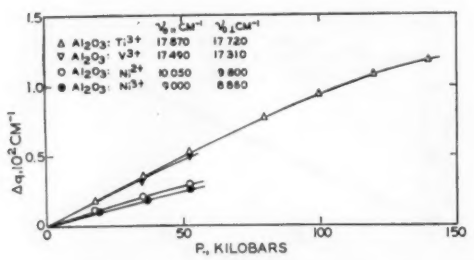

FIG. 10. Change of Dq with pressure in Al_2O_3.

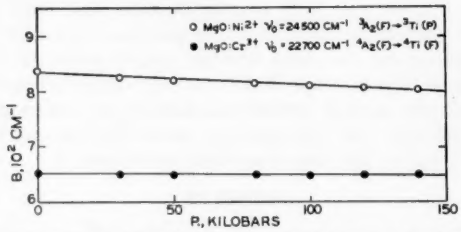

FIG. 11. Change of B with pressure in MgO:Ni^{2+} and MgO:Cr^{3+}.

quency difference between the peaks of the polarized spectra, which increased from 150 cm^{-1} at the atmospheric pressure to 330 cm^{-1} at 140 kbar.

B. Change in *Dq* with Pressure

The $^2T_2 \rightarrow {}^2E$ transition of Ti^{3+}, the $^4A_2(F) \rightarrow {}^4T_2(F)$ transition of Cr^{3+}, the $^3A_2(F) \rightarrow {}^3T_2(F)$ transition of Ni^{2+}, and the separations between the $^4T_1(F) \rightarrow {}^4T_2(F)$ and $^4T_1(F) \rightarrow {}^4A_2(F)$ transitions of Co^{2+}, and between the $^3T_1(F) \rightarrow {}^3T_2(F)$ and $^3T_1(F) \rightarrow {}^3A_2(F)$ transitions of V^{3+} are equal to the 10 Dq according to the solutions of the secular equations by Tanabe and Sugano.[5] The values of Dq for Al_2O_3:V^{3+} were obtained from the relation between energy and Dq assuming constant B, because the $^3T_1(F) \rightarrow {}^3A_2(F)$ transition could not be observed. The change in Dq with pressure for these transitions in MgO and Al_2O_3 crystals is shown in Figs. 9 and 10. Dq increases for each transition with increasing pressure.

C. Change in *B* with pressure

The change in B with pressure up to 140 kbar was calculated for the $^4A_2(F) \rightarrow {}^4T_1(F)$ transition in MgO:Cr^{3+} and the $^3A_2(F) \rightarrow {}^3T_1(P)$ transition in MgO:Ni^{2+} by the following equations,[5] where the values of 10 Dq could be given by the $^4A_2(F) \rightarrow {}^4T_2(F)$ and $^3A_2(F) \rightarrow {}^3T_1(F)$ transitions, respectively:

MgO:Cr^{3+};

$$E[{}^4A_2(F) \rightarrow {}^4T_2(F)] = 10\,Dq = \Delta \qquad (1)$$

$$E[{}^4A_2(F) \rightarrow {}^4T_1(F)] = \tfrac{3}{2}\Delta + (15/2)B - \tfrac{1}{2}[(\Delta - 9B)^2 + 144B^2]^{\frac{1}{2}} \qquad (1a)$$

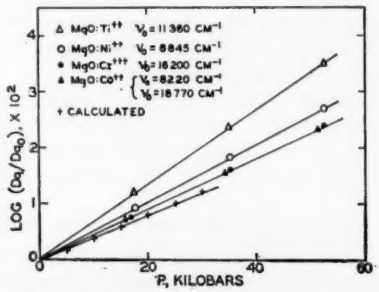
Δ MgO:Ti3+ ν0 = 11 360 CM-1
o MgO:Ni2+ ν0 = 8845 CM-1
• MgO:Cr3+ ν0=16 200 CM-1
▲ MgO:Co2+ ν0=8220 CM-1
ν0=18 770 CM-1
+ CALCULATED
LOG (Dq/Dq0), X 10²
P, KILOBARS

FIG. 12. LogDq/Dq_0 vs pressure in MgO.

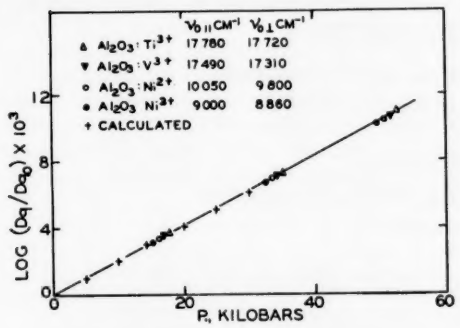

FIG. 13. LogDq/Dq_0 vs pressure in Al_2O_3.

MgO:Ni^{2+};

$$E[^3A_2(F)\rightarrow{}^3T_2(F)]=10\,Dq=\Delta \qquad (2)$$

$$E[^3A_2(F)\rightarrow{}^3T_1(P)]$$

$$=\tfrac{3}{2}\Delta+(15/2)B+\tfrac{1}{2}[(\Delta-9B)^2+144B^2]^{\frac{1}{2}}. \qquad (2a)$$

That is shown in Fig. 11. At a pressure of 140 kbar the value of B decreased by 25 cm^{-1} for the $^4A_2(F)\rightarrow{}^3T_1(F)$ transition from $B=650$ cm^{-1}, and by 40 cm^{-1} for the $^3A_2(F)\rightarrow{}^3T_1(P)$ transition from $B=840$ cm^{-1}. The decrease of B expresses the increase of the covalency between the transition metal ions and the ligands.

D. Local Compressibility

The equation relating the crystal field strength to the metal-ligands distance has been discussed in various places.[4,6]

$$10\,Dq=4q\langle r^4\rangle/3R^5, \qquad (3)$$

TABLE III. Local compressibility. Ions in MgO.

Crystals	10 Dq	$\log(Dq/Dq_0)/\log(V_0/V)^{5/3}$
MgO:Ti^{3+}	11 360 cm^{-1}	1.61
MgO:Cr^{3+}	16 200	1.12
MgO:Co^{2+}	10 550	1.10
MgO:Ni^{2+}	8845	1.24

where q is the charge of the ligand and r is the radius of $3d$ shell. The rate of change in Dq with pressure, $\log(Dq/Dq_0)$, could predict the local compressibility in the neighborhood of the octahedrally coordinated ligands by Eq. (4) derived from Eq. (3),

$$\log(Dq/Dq_0)=-(5/3)\log(V/V_0)+\text{const.} \qquad (4)$$

The change in $\log(Dq/Dq_0)$ with pressure was plotted for four MgO crystals in Fig. 12 and for four Al_2O_3 crystals in Fig. 13, comparing with $-(5/3)\log(V/V_0)$ calculated from the compressibility data up to 30 000 kg/cm^2 by Bridgman.[11] The change in $\log(Dq/Dq_0)$ with pressure coincides for the Al_2O_3 crystals with the change in $-(5/3)\log(V/V_0)$ as predicted from Eq. (3)*, but it is greater by a factor of 1.10 to 1.61 for the MgO crystals, as given in Table III. The results for Al_2O_3 are consistent with the data of Stephens and Drickamer[12] for Cr^{3+} in Al_2O_3. This indicates that the local compressibility is greater by this factor than that in the bulk crystal, i.e., there is relaxation near the foreign ion.

[11] P. W. Bridgman, Proc. Am. Acad. Arts Sci. **77**, 220 (1949).
[12] D. R. Stephens and H. G. Drickamer, J. Chem. Phys. (to be published).

Infrared and Raman Spectra, Force Constants, and the Structures of Some Polyhalide Ions: ICl_2^-, ICl_4^-, $BrCl_2^-$, and Br_3^-†

WILLIS B. PERSON, GEORGE R. ANDERSON, AND JAMES N. FORDEMWALT

Department of Chemistry, University of Iowa, Iowa City, Iowa

AND

H. STAMMREICH AND ROBERTO FORNERIS

Department of Physics, F. F. C. L., University of São Paulo, São Paulo, Brazil

(Received February 16, 1961)

The infrared and Raman spectra for the polyhalide ions (ICl_2^-, ICl_4^-, $BrCl_2^-$, and Br_3^-) are presented. From these data, the $X-Y$ stretching force constant f_r, the interaction force constants f_{rr} between bond stretching coordinates at 180° to each other, and the interaction force constant f_{rr}' for bond stretching coordinates at an angle of 90° (for ICl_4^-) have been calculated. The values of f_r for the trihalide ions are roughly one-half the values for the free halogens, and the values of the interaction force constants f_{rr} are very large (approximately 35% the value of the stretching constant f_r). These rather unusual force constants have been interpreted in terms of the description of the bonding in these ions using p orbitals, which was first suggested by Pimentel. In fact, these results offer rather strong support for the recent evidence from nuclear quadrupole coupling constant measurements of Cornwell and Yamasaki favoring this structure. Attention is drawn to the qualitative similarity between these force constants and those for the HF_2^- ion.

INTRODUCTION

THE unusual bonding in the polyhalide ions has been the subject of considerable speculation, which has recently been summarized by Cornwell and Yamasaki.[1] In that paper and in a later paper[2] these authors have shown that the nuclear quadrupole coupling constants in the polyhalide ions are not consistent with the description of the bonding which uses the d orbitals from the central iodine atom to explain the extra valence of the iodine atom. This description had been the preferred explanation for the bonding within these ions until their work. However, it now appears that the molecular orbital description using p orbitals, first suggested by Pimentel,[3] is a better representation of the bonding in these ions. Examination of his description reveals that it is equivalent to resonance between the following valence bond structures[4]

(a) $^-Cl\cdots I—Cl$

(b) $Cl—I\cdots Cl^-$.

For a symmetrical ion, these two structures should have equal energies so there should be equal contributions to the true wave function of the system from each of the wave functions corresponding to structures (a) and (b). Each ICl bond in ICl_2^- is thus only a "half-bond" perturbed by the associated ion. In this way, one easily sees that we might expect the force constant for stretching the I—Cl bond in ICl_2^- to be much lower than in the diatomic ICl molecule. On the other hand, if one were to write valence bond structures using the expanded valence shell for the central iodine atom with d orbitals, one should expect the bonds using these d orbitals to be essentially normal covalent bonds with normal force constants. Thus, it seemed worthwhile to investigate the vibrational spectra of these ions. This seemed to be an especially logical extension of the work at the University of Iowa on the infrared spectra of charge-transfer complexes of halogens with various donor molecules.[5–7]

The study of the infrared spectra of these ions was first attempted using a spectrometer with a CsBr prism. This study[8] served to establish that the upper limit for the infrared absorption frequencies for the ICl_2^- ion was less than 280 cm^{-1}. This is to be contrasted with a value of 375 cm^{-1} for the stretching frequency of the ICl molecule. However, this study was not satisfactory in that we were unable to observe the position of maximum absorption for this ion. Later this work was extended[9] to frequencies as low as 170 cm^{-1} by use of the small grating infrared spectrometer

† This is also paper IV in the series, *Infrared Spectra of Charge-Transfer Complexes* [See J. Am. Chem. Soc. **82**, 29, 1850 (1960), for papers III and V.]

[1] C. D. Cornwell and R. S. Yamasaki, J. Chem. Phys. **27**, 1060 (1957).

[2] R. S. Yamasaki and C. D. Cornwell, J. Chem. Phys. **30**, 1265 (1959).

[3] G. C. Pimentel, J. Chem. Phys. **19**, 446 (1951).

[4] It is true that the I—Cl σ bond may be best described in the LCAO method by using an orbital from the iodine atom which contains some d character. [See R. S. Mulliken, J. Am. Chem. Soc. **77**, 884 (1955).] However, what we are claiming here is that the *additional* Cl···I bond is not a normal polar covalent bond formed by using a different *spd* hybrid orbital from the iodine atom. Thus, the additional bond formed by the iodine atom in ICl_2^- does not *change* the (presumably small) amount of d character of the orbitals used by the iodine atom for ICl.

[5] W. B. Person, R. E. Humphrey, W. Deskin, and A. I. Popov, J. Am. Chem. Soc. **80**, 2049 (1958).

[6] W. B. Person, R. E. Humphrey, and A. I. Popov, J. Am. Chem. Soc. **81**, 273 (1959).

[7] W. B. Person, R. E. Erickson, and R. E. Buckles, J. Am. Chem. Soc. **82**, 29 (1960).

[8] G. R. Anderson, Ph.D. thesis, University of Iowa, Iowa City, Iowa (1961).

[9] J. N. Fordemwalt, Ph.D. thesis, University of Iowa, Iowa City, Iowa (1960).

constructed at the University of Iowa. Using this spectrometer it was possible to determine the absorption frequencies for a number of polyhalide ions.

In order to obtain any information about the force constants in these linear triatomic ions from the studies of their spectra, we would need to know both ν_1 (Raman active only) and ν_3 (infrared active only). Fortunately, the Raman spectra of halogens and polyhalide ions have been studied for a number of years at the University of São Paulo.[10,11] If the frequencies from the infrared spectra could be combined with the frequencies observed in the Raman spectra, values for the force constants could be obtained. Since neither experimental result was complete without the other, it was decided that we should combine our results into a joint publication. We therefore present the following.

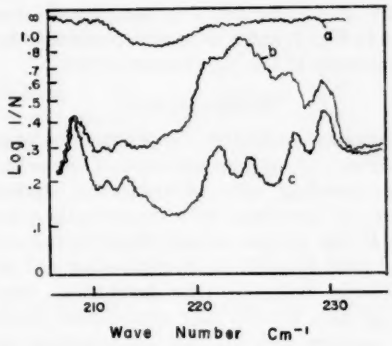

FIG. 1. Replot of the recorder tracing of the infrared spectrum of ICl_2^- ion. (a) Zero line with KBr window in the beam. (b) Spectrum of sample. (c) Spectrum of empty cell.

EXPERIMENTAL

Infrared Studies

Samples of $CsICl_2$, $RbICl_2$, trimethylammonium dichloroiodide $[(CH_3)_3NHICl_2]$, tetrabutylammonium tetrachloroiodide $[(Bu)_4NICl_4]$, and tetrabutylammonium tribromide $[(Bu)_4NBr_3]$ were obtained from Dr. A. I. Popov and Dr. R. E. Buckles; their preparation has been described elsewhere.[12] A sample of $CsBrCl_2$ was prepared by a similar method.[12]

Infrared spectra were studied in solution and with Nujol mulls of the solid samples. The mulls were made by taking two drops of Nujol and adding about an equal amount of the crystalline interhalogen compound. If the resulting mull was too thick, as indicated by the spectrum, it was thinned by adding another drop of Nujol and then rerun. The windows were polyethylene (0.5 mm thick) and no spacers were used in preparing the mulls. Most of the mulls were thin enough to be almost transparent to visible light.

It was extremely difficult to find a solvent which was transparent in this region (50 μ) and which would dissolve the polyhalide ions as well. Dichloroethylene, acetonitrile, nitromethane, dry acetone, absolute alcohol, water, chlorobenzene, and pyridine were studied in the region between 170 cm^{-1} and 280 cm^{-1} in a 1.0 mm thick liquid cell made with 0.5 mm thick polyethylene windows. These solvents were Eastman spectro grade or reagent grade and were used without further purification except for drying. Only chlorobenzene, acetonitrile, and nitrobenzene were found to be sufficiently transparent. The salts of the polyhalide ions were insoluble in the chlorobenzene, and the acetonitrile was so volatile that it could not be kept in the liquid cell long enough for a complete spectrum to be run. Therefore, all solution spectra were run using nitrobenzene as the solvent. Solutions were from 0.2 to 0.4 M in the polyhalide ion.

The grating spectrometer used in these studies has been described elsewhere.[9] This instrument is essentially similar to that described by Lord and McCubbin.[13] A Bausch & Lomb grating blazed for 45 μ was used in the single-pass mode of operation. Polyethylene windows were used in all cells. Separation of grating orders was accomplished by filters as described by Lord and McCubbin[13] using NaCl or NaF reststrahlen mirrors and a KBr chopper. In addition, we used a transmission filter of two pieces of black polyethylene 0.1 mm thick.[14]

Water vapor was removed as completely as possible by blowing out the spectrometer with compressed air which had been dried by passing it through alumina columns. Even so, the residual water-vapor background caused considerable interference with the spectrum. However, when the spectra were replotted, there was little difficulty in obtaining the absorption spectrum due to the polyhalide ion.

Because these spectra were obtained near the blaze of our grating, there was considerable difficulty in completely eliminating the higher order light. In fact, we were not successful in this until we balanced our chopper with a screen which was designed to stop about 10 to 15% of all light when the chopper was out of the beam. This compensated for the reflection from the surface of the KBr chopper and reduced the false light considerably.[15] Figure 1 shows a replotted trace of a sample spectrum obtained from the recorder. In order to have some measure of the false energy due to the higher orders, a zero line was run with a KBr window in the beam. This absorbed all the light of 45-μ wavelength and transmitted light of wavelengths

[10] H. Stammreich, Spectrochim. Acta **8**, 41 (1956).
[11] H. Stammreich and R. Forneris, Spectrochim. Acta **16**, 363 (1960).
[12] A. I. Popov and R. E. Buckles, *Inorganic Syntheses* (McGraw-Hill Book Company, Inc., New York, 1957), Vol. 5, p. 172.
[13] R. C. Lord and T. K. McCubbin, Jr., J. Opt. Soc. Am. **47**, 689 (1957).
[14] We wish to thank Dr. E. K. Plyler for providing us with our original sample of this material.
[15] We are indebted to Professor R. C. Lord and Dr. E. K. Plyler for suggesting this procedure.

less than 25 μ. The resulting spectrum is shown as curve *A* in Fig. 1, and should be a reasonable measure of the intensity of the higher order light.

Raman Studies

The samples studied in the Raman investigations consisted of: (a) aqueous solutions of the acids or of the corresponding salts of potassium, ammonium, rubidium, or strontium, with concentrations between 1 and 3 *M*; (b) samples of solid Me_4NBr_3 suspended in CCl_4, of solid Me_4NBrCl_2 in ethyl ether and of solid Me_4NICl_2 in benzene; (the polyhalides were not soluble in these liquids; they were chosen in order to have a medium with an index of refraction not too different from that for the crystalline samples); and (c) solutions of Me_4NBr_3 in ethylene dichloride (0.38 *M*) and of Bu_4NBr_3 in nitrobenzene (0.42 *M*) and in chloroform (0.45 *M*); solutions of Me_4NICl_2 in nitrobenzene (0.22 *M*) and of Me_4NBrCl_2 in nitrobenzene (0.26 *M*). The general method of preparation of the aqueous solutions was to mix the corresponding halogen or interhalogen with the respective hydro-acid or alkali halide dissolved in water. For instance, the iododichloride ion ICl_2^- was prepared by adding ICl to hydrochloric acid or to aqueous solutions of the alkali chloride. (This gave solutions free from ICl_4^- and showed only one sharp Raman shift.) The tetrachloroiodide ion (ICl_4^-) was prepared by passing a stream of chlorine into aqueous solutions containing the ICl_2^- ion. An excess of chlorine in these samples made them free from any detectable amount of ICl_2^- and the corresponding Raman spectrum showed only the shifts of the ICl_4^- ion.[11] Tetramethylammonium tribromide, iododichloride, and bromodichloride and tetrabutylammonium tribromide were prepared by adding the corresponding halogen or interhalogen to the corresponding monohalide dissolved in acetic acid and then precipitating the salt by cooling.[12] All solutions of $BrCl_2^-$, ICl_2^-, and ICl_4^- were excited by the 5876-A He radiation and sometimes also by the line at 6678 A, while the reddish solutions of the Br_3^- ion were excited only by He 6678 A. Before reaching the Raman samples the helium radiation was filtered by a saturated aqueous solution of sodium dichromate. The solid samples were excited exclusively by the He 6678-A radiation. Under normal exciting conditions the region corresponding to the exciting wavelength could appear so overexposed on the photographic plate as to mask completely the relatively weak Raman shift. This was, to a great extent, avoided by interposing between the Raman tube and the slit of the spectrograph a liquid filter consisting of a concentrated aqueous solution of erbium perchlorate of 20 mm thickness to absorb the He 6678-A exciting radiation.

Other details of the experimental technique used in the Raman work have been described earlier.[10] The spectrograph used interchangeable 600 and 1200 grooves/mm Bausch & Lomb plane reflection gratings; cameras of different apertures could also be used and the apertures ranged from *f*:1.5 to *f*:4.5. The reciprocal dispersion varied between 95 and 25 A/mm, depending on the grating and the camera used. The spectra were recorded photographically on Kodak spectroscopic plates 103 aC and 103 aF, respectively, when excitation by He 5876 or by He 6678 A was used. Exposure times for the solid samples or for the aqueous solutions ranged from 30 sec to 30 min, while for the less concentrated samples in organic solvents the times were between 15 min to 10 hr. Spectra of the ICl_4^- ion in aqueous solutions gave, as expected for a planar square molecule, three Raman shifts that were already reported in a previous publication.[11] Since the spectra did not seem to present any doubts as to the interpretation, this ion was not studied in the solid. All the other ions were studied in the solid and the spectra showed only one very narrow and well-defined Raman shift whose frequency could be determined within ± 1 cm^{-1}. A Raman shift of nearly the same frequency as the one observed in the solid was also observed in all the spectra of the corresponding solutions. However, some of the solutions showed an additional shift that in some cases could be assigned to the antisymmetrical vibrational mode supposing that it became active due to slight deformation of the ion or to the formation of weak complexes in solution. This explanation does not hold for the additional shift observed in the spectra of the Br_3^- ion in water and of ICl_2^- in nitrobenzene.

RESULTS

The infrared and Raman results are summarized in Table I.

From data of the type shown in Fig. 1 replotted infrared spectra were obtained for the polyhalide ions. Since these spectra looked so bad in the original form (Fig. 1) some replotted spectra for $CsICl_2$, $RbICl_2$, Bu_4NICl_4, and Bu_4NBr_3 are shown in Figs. 2, 3, 4, and 5, respectively, in order to prove that they are normal when replotted. Investigation of the infrared spectrum of tetrabutylammonium bromide showed that there is no absorption in this region due to that cation.

The spectra of the Br_3^- ion appear to be normal for all samples except for the solutions in water, where the band at 258 cm^{-1} is not understood. As mentioned above, the band at 195 cm^{-1} in the Raman spectrum of Br_3^- solutions is probably due to ν_3, which becomes active for an unsymmetrical ion in solution. For the ICl_2^- ion, the only unexplained features of the spectrum are the bands at 282 cm^{-1} in the infrared spectrum of solid $RbICl_2$ and the band at 299 cm^{-1} in the Raman spectrum of Me_4NICl_2 in nitrobenzene solution. Since the band at 282 cm^{-1} did not appear in the infrared spectrum of solutions of $RbICl_2$, this band is presumably due to something characteristic of the crystal sample and not characteristic of the ICl_2^- ion. The band at 299 cm^{-1} in the spectrum of Me_4NICl_2

TABLE I. Raman and infrared spectra of some polyhalide ions.

Sample	Br_3^-			ICl_2^-			$BrCl_2^-$			ICl_4^-		
	Molecule	R[a]	ir[b]	Molecule	R[a]	ir[b]	Molecule	R[a]	ir[b]	Molecule	R[a]	ir[b]
Solid	Me_4NBr_3	162		Me_4NICl_2	254.5		Me_4NBrCl_2	272		Bu_4NICl_4		218(imp.), 258
	Bu_4NBr_3		193	$CsICl_2$		218	$CsBrCl_2$		305			
				Me_3NHICl_2		218						
				$RbICl_2$		218, 282						
Solution in $C_6H_4NO_2$	Bu_4NBr_3	162	189	Me_4NICl_2	262(10), 299(2b)		Me_4NBrCl_2	273		Bu_4NICl_4		224(imp.), 266
				$CsICl_2$		224						
				$RbICl_2$		224						
				Me_3NHICl_2		224						
$(CH_2Cl)_2$	Me_4NBr_3	162(10), 196(2b)										
$CHCl_3$	Bu_4NBr_3	163(10), 192(2b)										
H_2O	K, NH_4, Rb, H, $SrBr_3$	166 258		H, $KICl_2$	272		H, K, Rb $BrCl_2$	280(10), 280–340(2bb)		H, K, NH_4 ICl_4		128(1b) 261(5) 288(10) p

[a] Wave number observed in Raman spectra.
[b] Wave number observed in infrared spectra.

may be related to the 282 cm^{-1} band in $RbICl_2$, but it is also not completely understood.[16]

Two other comments should be made concerning the infrared results given in Table I. First, the ICl_4^- ion is unstable, giving ICl_2^- and Cl_2 as products. The samples studied in the infrared spectrum always showed absorption at 218 cm^{-1} which we believe was due to the ICl_2^- ion, and not to the ICl_4^- ion itself. Finally the absorption at 305 cm^{-1} in the infrared spectrum of $BrCl_2^-$ ion was extremely weak. We believe this is actually ν_3, and its apparent weakness is due to the fact that this ion is not very stable.

FORCE CONSTANTS

The x-ray studies of the ICl_2^- ion[17] indicate that this ion, at least, is linear and symmetric in the crystal. From the values for ν_1 and ν_3, it is easy to calculate the force constants for such a linear symmetric triatomic molecule.[18] The results of these calculations give f_r the principal stretching force constant, and f_{rr} the interaction force constant between the two stretching coordinates. In order to obtain consistent values, the infrared and Raman frequencies for the ion in the solid state are used for the calculations. It is assumed that all the trihalide ions are linear and symmetric. The results for ICl_2^-, Br_3^-, and $BrCl_2^-$ are given in Table II.

The ICl_4^- ion is square and planar in the crystal, with symmetry D_{4h}.[19] The ion will have nine vibrational degrees of freedom divided as follows: A_{1g}, B_{1g}, B_{2g}, A_{2u}, $2E_u$, and B_{1u}. The first three are active in Raman, and the A_{2u} and E_u modes are active in the infrared (ir); the B_{1u} mode is inactive in both. As expected, three Raman shifts were observed and could be assigned in a straightforward manner to the three modes which are symmetric relative to the inversion center of the molecule. The species A_{1g} and B_{2g} correspond to I–Cl stretching motions with frequencies 288 and 261 cm^{-1}, respectively. The lower frequency 128 cm^{-1} must be assigned to the in-plane bending mode B_{1g}. Of the three ir active fundamentals, the A_{2u} mode and one of the E_u modes are associated with out-of-plane and in-plane bending vibrations, respectively. Due to their low frequencies these fundamentals could not be observed in the infrared spectra. The third ir active mode is a stretching vibration belonging to the class E_u and was found to have the frequency 266 cm^{-1}.

A normal coordinate analysis on a general square planar molecule XY_4 with D_{4h} symmetry has been carried out by Maccoll[20] and by Pistorius.[21] We have used the equations of Pistorius together with the

[16] This band, as well as the 258 cm^{-1} band in the water solution of Br_3^- and the broad Raman shift from 280 to 340 cm^{-1} in water solutions of $BrCl_2^-$, could very well be due to free halogen (ICl, Br_2, or BrCl) complexed with the strong donors available in these solutions.
[17] R. C. Mooney, Z. Krist. **100,** 519 (1939).
[18] G. Herzberg, *Infrared and Raman Spectra of Polyatomic Molecules* (D. Van Nostrand Company, Inc., Princeton, New Jersey, 1945), p. 187.
[19] R. Mooney, Z. Krist. **98,** 377 (1938).
[20] A. Maccoll, Proc. Roy. Soc. N.S.W. **77,** 130 (1944).
[21] C. Pistorius, Mol. Phys. **1,** 295 (1958).

TABLE II. Bond stretching constants f_r, interaction constants between bonds 180° apart f_{rr}, and interaction constants for bonds 90° apart f_{rr}', for some linear triatomic ions and molecules.

Ion	f_r(md/A)	f_{rr}(md/A)	f_{rr}'(md/A)	$f_r(xyx)/f_r(xy)$	f_{rr}/f_r
[a] ICl_2^-	1.00	0.36	...	0.46	0.36
[a] ICl_4^-	1.25	0.33	0.08	0.53	0.26
[b] ICl	2.38	...	...	...	...
[a] $BrCl_2^-$	1.29	0.26	...	0.47	0.20
[b] BrCl	2.83			...	
[a] Br_3^-	0.91	0.32	...	0.38	0.36
[b] Br_2	2.45			...	
[c] HF_2^-	2.31	1.72	...	0.23	0.72
[b] HF	10			...	
[d] CO_2	15.5	1.3		0.82	0.08
[b] CO	19.0			...	

[a] This research. Force constants are calculated using the infrared and Raman frequencies for the solids from Table I. Units an millidynes/Angstrom.
[b] Calculated from the frequencies given by G. Herzberg, *Molecular Spectra and Molecular Structure. I. Spectra of Diatomic Molecules* (D. Van Nostrand Company, Princeton, New Jersey, 1950), 2nd ed.
[c] Calculated from data by Jones and Penneman, reference 24.
[d] From Herzberg, reference 18.

infrared and Raman data presented here in order to calculate the force constants given in Table II. We have assumed the interaction constants between the bending coordinates and the stretching coordinate to be zero. The value of ν_7, the E_u bending vibration, is calculated to be 107 cm^{-1}, using the force constant from the B_{1g} bending vibration at 128 cm^{-1}.

DISCUSSION

The first striking feature of the values of the force constants listed in Table II is the very low value of f_r from the polyhalide ion when compared to the value of this force constant for the corresponding halogen. [See the column giving $f(xyx)/f(xy)$.] For comparison we include the ratio for the normal molecule, CO_2. Almost as surprising, however, is the large value of the interaction force constant f_{rr} for bonds at an angle of 180° to each other. For comparison, the force constants from CO_2 are also listed. For normal molecules such as CO_2 the order of magnitude of the interaction constant is approximately 10% of the value of the stretching constant.[22] Thus, a value of the interaction

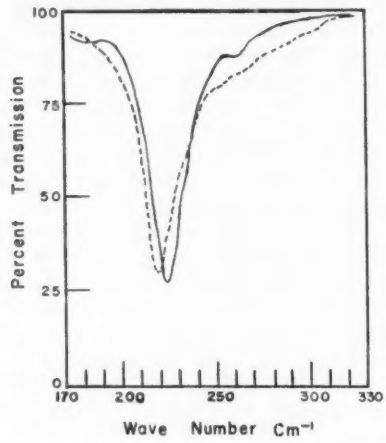

FIG. 2. Replotted spectrum of $CsICl_2$, ——— solution in nitrobenzene, - - - - solid in Nujol mull.

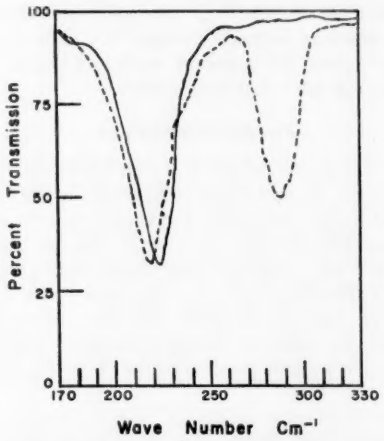

FIG. 3. Replotted spectrum of $RbICl_2$, ——— solution in nitrobenzene, - - - - solid in Nujol mull.

[22] See T. Wentink, Jr., J. Chem. Phys. **30**, 105 (1959), for some additional examples.

constant which approaches 35% of the value of the stretching constant is indeed unusual. Of all the triatomic molecules and ions we have considered, the only one with force constants more peculiar than these for the trihalide ions is the HF_2^- ion.

On further thought, it is apparent that the postulated description of the bonding in these ions by the molecular orbital description of Pimentel[3] (or by the equivalent valence bond resonance description given in the introduction) will imply just this kind of peculiarity in the force constants. Thus, a value of f_r of less than 50% of the value for a normal covalent bond is just what might be expected for a "half-bond." A very high positive value will be expected for f_{rr} because stretching one bond tends to make one of the valence structures (say *a*) more stable. In this structure the second bond has contracted while the first has stretched. Thus, stretching one bond will cause the other bond to contract, giving a large positive interaction constant. This argument is strictly parallel to the argument made by Thompson and Linnett[23] in order to explain the magnitude and sign of the interaction constant of CO_2, but the effect is more important here.

Thus, one may conclude that the magnitudes of f_r and f_{rr} and the sign of f_{rr} are consistent with the description of the bonding in the trihalide ions given in terms of *p* orbitals. It is true that this interpretation of the force constants in terms of bond order is probably over simplified, but it seems likely that the changed bond order may indeed be the most important effect in explaining these remarkable force constants. It does not seem reasonable that ordinary covalent bonding for the extra bond to the iodine atom in terms of *d* orbitals would lead to force constants of this type.

Next, let us consider the ICl_4^- ion. Cornwell and

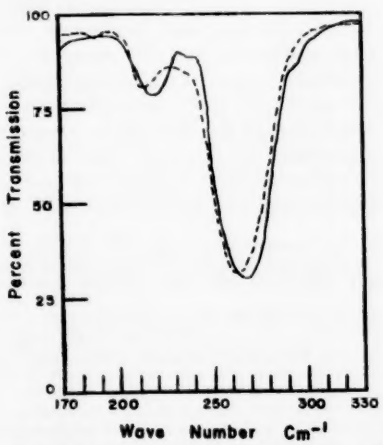

FIG. 4. Replotted spectrum of Bu_4NICl_4, ——— solution in nitrobenzene, - - - - solid in Nujol mull.

[23] H. W. Thompson and J. W. Linnett, **J. Chem. Soc. 1937,** 1384.

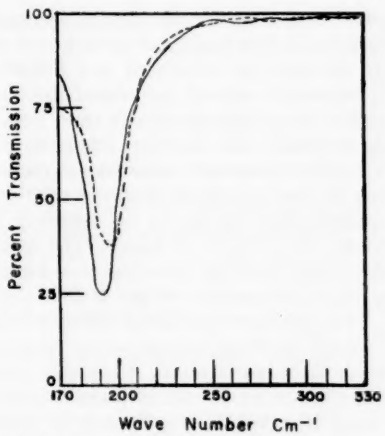

FIG. 5. Replotted spectrum of Bu_4NBr_3, ——— solution in nitrobenzene, - - - - solid in Nujol mull.

Yamasaki[1,2] have shown that the nuclear quadrupole coupling constants are consistent with a valence bond description in terms of resonance between structures of the following type

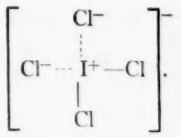

From this description, we should expect that the stretching force constant f_r would be about the same as in the ICl_2^- ion (or less than ½ the value for ICl). Furthermore, we should expect a strong interaction between stretching motions in bonds at an angle of 180° for the same reason that we did in ICl_2^-. However, we should expect the interaction force constant between bonds at 90° to each other to be quite small, because, to a first approximation, stretching a bond at an angle of 90° to another will have little effect on the electronic configuration (hence, equilibrium bond distance) for the second bond. Thus, the force constants for ICl_4^-, which seem at first to be so anomalous, also appear to be reasonable in terms of this description of the bonding.

It should be noted that when this kind of reasoning is applied to the force constants of the HF_2^- ion, the values appear to be qualitatively reasonable. The extremely peculiar values for the force constants in this ion do not seem to have been discussed previously.[24]

It will be noted that the band at 342 cm^{-1} reported by Person, Erickson, and Buckles[7,25] for very thick mulls of Bu_4NBr_3 and for concentrated solutions in benzene is properly assigned to the combination of $\nu_1+\nu_3$ (calculated value 355 cm^{-1}) rather than $\nu_2+\nu_3$

[24] L. H. Jones and R. A. Penneman, J. Chem. Phys. **22,** 781 (1954); references to the earlier literature are cited there.

as suggested earlier.[7,25] Considering the uncertainty in the frequencies in their work, it is not believed that the difference between the calculated and observed frequencies represents unusual anharmonicity, although such an effect is certainly possible in these ions.

Finally we should like to report briefly on our preliminary attempt to measure intensities of the infrared absorption in these ions in nitrobenzene solution. This was exceedingly difficult due to the tendency for our polyethylene cell window to buckle. The results we obtained indicate that the intensity of ν_3 for ICl_2^- is not very high (the number we get is 1900 $cm^{-1}cm^2/mM^{-1}$). This represents an added effective charge ϵ_a of only 1.0 D/A, when interpreted in terms of the model used for donor-acceptor complexes involving ICl.[5,7] (This model is, of course, probably very poor for this ion.) However, this result may be some indication that the decrease in intensity noted for X–H stretching vibrations in symmetrical hydrogen bonds[26] may also occur for symmetrical ICl complexes. These results are extremely tentative at the present time, and further work is needed. This is particularly true since the intensity value for the intensity of ν_3 in Bu_4NBr_3 is quite high (8200 $cm^{-1}cm^2/mM^{-1}$).

[25] W. B. Person, R. E. Erickson, and R. E. Buckles, J. Chem. Phys. **27**, 1211 (1957).

[26] See, for example, K. Nakamoto, M. Margoshes, and R. E. Rundle, J. Am. Chem. Soc. **77**, 6480 (1955).

CONCLUSION

The combination of infrared and Raman data for the trihalide ions (and ICl_4^-) has provided us with the force constants for these ions. The values of these constants provide rather strong support for the more direct evidence from the nuclear quadrupole coupling constants[1,2] supporting the description of the bonding using only p orbitals, first given by Pimentel.[3] This study illustrates once again the importance of having both Raman and infrared data, for the unusual character of the results did not become apparent until both were available. It should be possible to generalize from the results presented here and predict the spectra of other polyhalide ions.

ACKNOWLEDGMENTS

We should like to acknowledge the help of Professor A. I. Popov, now at Northern Illinois University, and Professor R. E. Buckles, at the University of Iowa, both for providing us with samples and for their stimulating discussions. It is a pleasure to acknowledge financial assistance from the Office of Ordnance Research, U. S. Army, and also from the Research Corporation for a grant which aided in the measurements with the grating infrared spectrometer. We are also grateful to the Conselho Nacional de Pesquisas, Rio de Janeiro, for support of the Raman work.

Interaction of Rare Gases with Semiconductor Surfaces

MINO GREEN† AND RUTH SEIWATZ

Zenith Radio Corporation, Chicago 39, Illinois

(Received February 9, 1961)

The interaction of krypton with clean germanium surfaces has been analyzed in terms of dispersion forces, assuming a 6:12 potential. Using the experimental value for the heat of adsorption and a computed value for the attractive term in the 6:12 potential, the repulsive term in the potential was calculated. The interaction energy at various positions on the (111) crystal plane of germanium was then computed. The method used involves recently developed techniques for the summation over a semi-infinite crystal. From this analysis an effective van der Waals radius for the surface germanium atoms can be deduced, and the value (1.8 A) seems to be, from several points of view, physically reasonable. Using an empirical combination rule, it is then possible to predict heats of adsorption for other germanium-rare gas systems, viz., (Ge–Ar) 3.3 kcal/mole; (Ge–Xe) 4.1 kcal/mole.

The contribution of the induction effect to the heat of adsorption at various positions on the (111) plane has been calculated for a specific model, and the results show that while there is a significant contribution, roughly 0.8 kcal/mole, the dominant adsorption force is the dispersion interaction. The possible contribution of surface heterogeneity to the heat of adsorption is discussed in terms of adsorption at a surface step. A description of the method of summation over the semi-infinite crystal is dealt with in an Appendix.

I. INTRODUCTION

THE London dispersion theory of van der Waals interaction[1] has been used with considerable success in accounting for the interaction of a gas molecule with a solid dielectric.[2,3] In the case of metals, physical adsorption[4] cannot, at least in principle, be described by the unmodified London theory[5] because the interaction of the adsorbate and the "free" electrons of the metal is not taken into account. Actually, Pierotti and Halsey[6] have concluded from a recent series of experiments that in practice the free electron contribution to adsorbent-adsorbate interaction can be ignored. In this paper a case of physical adsorption on a semiconductor surface is considered, the object being to investigate the consistency of the dispersion theory with the available experimental data.

Recently Rosenberg[7] has reported adsorption isotherms for krypton on clean germanium surfaces. In the same paper the author attempted an analysis of his data and concluded that, "it is clear from the results that the energy of krypton adsorption cannot be accounted for in terms of the atomic properties of germanium," and further ascribed the failure of the London theory to, "the nearly degenerate space-charge region associated with a germanium surface (which) invalidates atomic polarizability as a source of adsorptive energy." In Sec. II of this paper a theoretical analysis is made of this problem and Rosenberg's conclusions are examined in the context of this analysis.

Section III is concerned with the use of an empirical combining rule to predict heats of adsorption.

In Sec. IV an estimate is made of the contribution to adsorbent-adsorbate interaction arising from the polarization of the adsorbate by the electrostatic field due to the adsorbent, i.e., the induction effect.

A simple aspect of surface heterogeneity, adsorption near a step on a crystal surface, is considered in Sec. V.

II. INVESTIGATION OF THE CONSISTENCY OF THE DISPERSION THEORY WITH THE HEAT OF ADSORPTION OF KRYPTON ON GERMANIUM

The interaction between pairs of atoms is described in this paper by the well-known 6:12 potential. It is assumed that the forces are additive, and that the interaction energy ϕ of an adsorbate atom over a semi-infinite crystal is therefore given by

$$\phi=\sum_p aR_p^{-6}-\sum_p bR_p^{-12}, \qquad (1)$$

where a and b are constants, and R_p is the distance between the adsorbate atom and the pth atom of the crystal. The energy of adsorption (ϕ_0) at a given position on the surface is found by maximizing ϕ as a function of the height z_s of the adsorbate above the surface plane, (i.e., the plane going through the centers of the topmost atoms). The term aR_p^{-6} in Eq. (1) represents the major term in the London dispersion equation, and a can be estimated from the atomic properties of the adsorbent and adsorbate. The repulsion term bR_p^{-12} is empirical, and there is no reliable way of estimating b.

† Present Address: John Harrison Laboratory for Chemistry, University of Pennsylvania, Philadelphia, Pennsylvania.

[1] F. London, Z. physik. Chem. **11B,** 222 (1930); Trans. Faraday Soc. **33,** 8 (1939).

[2] W. J. C. Orr, Trans. Faraday Soc. **35,** 1247 (1939); Proc. Roy. Soc. (London) **173A,** 349 (1939).

[3] D. M. Young, Trans. Faraday Soc. **47,** 1228 (1951).

[4] The term physical adsorption is used in the usual sense of meaning adsorption which is not dominantly associated with electron exchange or electron transfer, and where consequently the binding energies involved are generally <10 kcal/mole.

[5] B. L. Bonch-Bruevich, Uspekhi Fiz. Nauk **40,** 369 (1950), English translation, N.R.C., T.T.–509, Ottawa, 1954.

[6] R. A. Pierotti and G. D. Halsey, J. Phys. Chem. **63,** 680 (1959).

[7] A. J. Rosenberg, J. Phys. Chem. **62,** 1112 (1958).

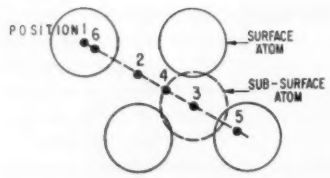

FIG. 1. The positions on the (111) germanium surface at which adsorption energy is computed.

Thus the energy of adsorption cannot be predicted *a priori* to test whether the dispersion theory can account for the heat of adsorption of krypton on germanium. Therefore, the following indirect method was adopted. A value for ϕ_0 at the most favorable site on the germanium surface was estimated from the experimental value for the heat of adsorption of krypton at zero coverage. [The surface considered was the (111) plane on the assumption that this cleavage plane was preponderant in the powder on which the measurements were made.] Then, with the use of numerical methods, a value for b was derived from Eq. (1). It was then possible to compute the energy of adsorption of krypton at other positions on the surface, and the equilibrium heights of the krypton above the surface at each of these positions. Furthermore, once b was determined, it became possible to obtain a value for the van der Waals radius of the surface germanium atoms. The reasonableness of these computed values is used as a criterion of whether or not dispersion forces can account, in large measure, for the heat of adsorption.

Six positions of interest on the germanium (111) surface were chosen for the computation of adsorption energy. These are shown in Fig. 1. For convenience, and to allow for wider application of the results (see below), Eq. (1) was converted into the dimensionless form,

$$\phi/aa_1^{-6}=\sum_p (R_p/a_1)^{-6}-f\sum_p (R_p/a_1)^{-12}. \qquad (2)$$

Here $f=b/aa_1^6$ where a_1 is the distance between two neighboring atoms on the (111) surface. At each position, several values of z_e/a_1 were assumed, and the sums over the lattice were performed. The sums of $(R_p/a_1)^{-6}$ were computed using a special series method. This computation is discussed in the Appendix, where tables of the sums are given. [The values are listed in such a way that they can be applied to the (111) plane of any face-centered cubic or diamond-type lattice.] The sums of $(R_p/a_1)^{-12}$ were performed over near-neighbors only, since repulsion between atoms with no electron overlap seems physically meaningless.

With these sums evaluated, it would be possible to maximize ϕ/aa_1^{-6} at each position as a function of z_e/a_1 if f were known. Since f was not known, various values were assumed for it, and ϕ/aa_1^{-6} maximized for each of these. (The assumed values of f were 0.2 to 0.7 in steps of 0.1.) Graphs of the resulting values of ϕ_0/aa_1^{-6} vs f are shown in Fig. 2. The height of the adsorbate at which ϕ is a maximum is denoted here by z_0. Graphs of z_0/a_1 vs f for each of the six positions are shown in Fig. 3. The graphical methods used were not precise; the maximum uncertainty in values of ϕ_0/aa_1^{-6} is about ± 0.15, while the maximum uncertainty in values of z_0/a_1 is ± 0.01. [It should be noted that the particular parameters for krypton and germanium have not yet been introduced. Therefore, the graphs in Fig. 2 and Fig. 3 can be applied to any particle adsorbed on the (111) face of an elemental crystal with a diamond type lattice.]

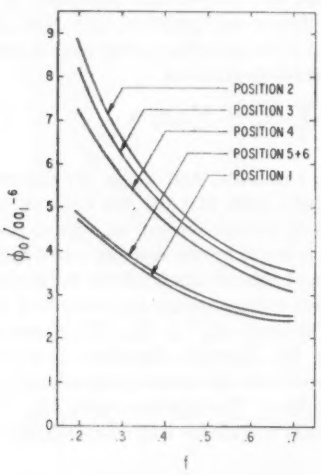

FIG. 2. ϕ_0/aa_1^{-6} vs f for each of the six positions under consideration.

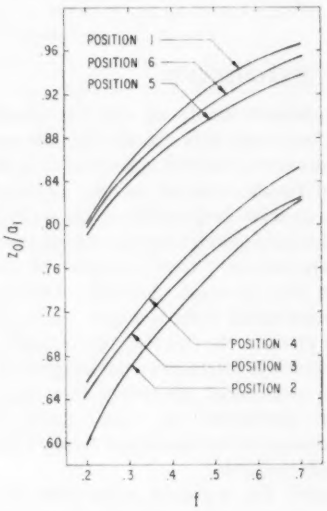

FIG. 3. z_0/a_1 vs for each of the six positions under consideration.

From Fig. 2 it is clear that position 2 is the position most favorable for adsorption. The experimental heat of adsorption of krypton on germanium at near zero coverage is about 3.8 kcal/mole.[7] As will be shown in Sec. IV, the induction interaction contributes about 0.8 kcal/mole to the heat of adsorption; therefore ϕ_0 at

position 2 is taken as 3.0 kcal/mole. For germanium, $a_1=4.00\times10^{-8}$ cm, and a for krypton-germanium is taken to be 1.56×10^{-58} erg cm^6, the mean of the values calculated from the Slater-Kirkwood and Kirkwood-Muller equations.[8] Thus ϕ_0/aa_1^{-6} is equal to 5.48. From Fig. 2 it can be seen that this is the value of ϕ_0/aa_1^{-6} at position 2 when f is equal to 0.382. This value of f corresponds to a value of b of 2.44×10^{-103} erg cm^{12}. The values of ϕ_0 and z_0 for the other positions on the surface can now be determined directly from Fig. 2 and Fig. 3, respectively. These values are listed in Table I. Note that the energy due to the induction interaction must be added to ϕ_0 at each position to derive the full energy of interaction. From the values for ϕ_0 at positions 5, 6 and 1 it is interesting to note that position 1, which has been referred to as a "site," is in fact not an equilibrium position.

From the values of a and b for the krypton-germanium interaction, it is possible to deduce a van der Waals radius for a surface germanium atom. (Since the repulsive force arises mainly between the krypton atom and the surface atoms of the crystal, the b derived above refers specifically to these atoms.) The van der Waals radius of an atom is taken to be one-half the equilibrium distance between two of these like atoms when held together by dispersion forces. An empirical combining rule that is sometimes applied to gaseous interactions states that the equilibrium distance between two unlike atoms held together by dispersion forces is the sum of the van der Waals radii of the two atoms.[9] If r_m is the equilibrium distance between two atoms, then this combining rule can be stated as follows:

$$r_m(\alpha,\beta)=\tfrac{1}{2}[r_m(\alpha)+r_m(\beta)]. \quad (3)$$

By applying Eq. (1) to a pair of atoms, it can be shown that

$$r_m=(2b/a)^{1/6}. \quad (4)$$

From the values of a and b given above, it is found that r_m for the krypton-germanium interaction is 3.83 A. By using second virial coefficient data and assuming a 6:12 potential, Whalley and Schneider[10] found that r_m for krypton is 4.13 A. Then, with the use of Eq. (4), r_m for a germanium pair is found to be 3.53 A. Thus, the van der Waals radius of the surface germanium atoms is about 1.8 A.

It is necessary to decide whether the determined van der Waals radius of about 1.8 A is physically acceptable. Only in this way is it possible to support the contention made here that the dispersion force interaction accounts for the greater part of the adsorption energy for the Kr-Ge system. According to the evidence advanced by Hagstrum,[11] there is apparently no violent rearrangement of the valency electrons of surface germanium atoms, i.e., the surface atoms are apparently bonded to the underlying plane of atoms by dominantly sp^3 orbitals. A cleaved (111) germanium surface has one broken covalent bond per surface atom, and assuming that the sp^3 hybridization is retained, there will be one electron in an sp^3 orbital projecting normal to the surface from each surface atom. The van der Waals radius v of the surface germanium atoms must correspond to the distance between the center of the atom and the outer fringe of the surface electron distribution, and not to the covalent radius, as suggested by Rosenberg,[7] since the latter terminates at a point where the electron density is still high. It would, therefore, be expected that v would be greater than 1.22 A, the covalent radius of germanium. By using a v of 2 A, Green and Maxwell[12] were able to explain, on the basis of electrostatic forces, the adsorption and nonadsorption of an extended class of molecules on germanium. A v of 1.2 A would not have been compatible with the experi-

TABLE I. Calculated values of ϕ_0 and z_0 for krypton adsorbed on the (111) surface of germanium.

Position	ϕ_0[a] (kcal/mole)	z_0 (A)
1	1.8	3.6
2	3.0	2.8
3	2.8	2.9
4	2.6	3.0
5	1.9	3.5
6	1.9	3.5

[a] Note that the energy arising from the induction effect has not been included in ϕ_0.

TABLE II. Values of ϕ_0 and z_0 for krypton adsorbed on the (111) surface of germanium according to Rosenberg (see Ref. 7).

Position[a]	ϕ_0 (kcal/mole)	z_0 (A)
1 (*C*)	3.75	3.24
2 (*B*)	15.6	1.74
3 (*A*)	6.4	2.44

[a] The letters shown in brackets are the identifying letters used in Ref. 7.

[8] These equations, together with appropriate constants for germanium and krypton, are listed in Ref. 7. However, the susceptibility of germanium was incorrectly listed there as 2.63×10^{-29} cm^3, rather than 1.34×10^{-29} cm^3. [See D. K. Stevens, J. W. Cleland, J. H. Crawford Sr., and H. C. Schweinler, Phys. Rev. **100**, 1084 (1955).] Substitution of the proper value of susceptibility into the Kirkwood-Muller equation yields a dispersion constant of 1.4×10^{-58} erg cm^6. The dispersion constant from the Slater-Kirkwood equation is 1.72×10^{-58} erg cm^6.

[9] An equivalent statement of this combining rule is that the collision diameter (the distance of zero energy) of two atoms α and β is the arithmetic mean of the collision diameter of two α atoms and the collision diameter of two β atoms. For a discussion of empirical combining rules see J. O. Hirschfelder, C. F. Curtiss and R. B. Bird, *Molecular Theory of Gases and Liquids* (John Wiley & Sons, Inc., New York, 1954), p. 168.

[10] E. Whalley and W. G. Schneider, J. Chem. Phys. **23**, 1644 (1955).

[11] H. D. Hagstrum, J. Phys. Chem. Solids **14**, 33 (1960).

[12] M. Green and K. H. Maxwell, J. Phys. Chem. Solids **11**, 195 (1959).

TABLE III. Predicted heats of adsorption at zero coverage of argon and xenon on the germanium (111) surface, compared with the value for krypton.

Adsorbate	ϕ_0 (kcal/mole) at position 2	z_0(A) at position 2	I (kcal/mole) at position 2	Estimated ΔH (kcal/mole)
Argon	2.5	2.7	0.8	3.3
Krypton	3.0	2.8	0.8	3.8
Xenon	3.5	3.1	0.6	4.1

mental data. Another source of support for $v \approx 2$ A as a reasonable figure (there can be no real proof) is the observation made by Pauling[13] that for a number of elements the van der Waals radius is about 0.8 A greater than the covalent radius. It is, therefore, concluded that the available evidence indicates that a van der Waals radius of about 1.8 A is reasonable.

Rosenberg concluded that dispersion forces could not account for the adsorption of krypton on germanium because the heat of adsorption he predicted assuming a 6:12 potential was much higher than his measured value. But the calculated value was too high only because the equilibrium heights assumed for the krypton were too low. In Table II the values of z_0 assumed in Ref. 7 are listed, together with values of ϕ_0 calculated there. These are to be contrasted with the values in Table I. The values of z_0 in Table II were derived by assuming a hard sphere model, using the van der Waals radius for krypton but the covalent radius for germanium. The covalent radius is clearly too small to be used for a packing radius; atoms which are covalently bound are always closer together than those held together by dispersion forces. An arithmetical error of about 0.5 A for z_0 at position 2 accounts for the spuriously high value of ϕ_0 listed in Table II for this position.

Rosenberg assumes that the dispersion theory is not applicable in the case of germanium because the partially degenerate nature of the clean surface causes a metal-like behavior with respect to adsorption. Handler[14] has estimated the surface space charge excess on cleaned germanium surfaces to be 10^{13} holes per cm^2 or less. Now as an extreme argument let it be assumed that the surface excess was confined in a surface layer 3 to 4 A thick; there would be at most 0.01 hole associated with each surface germanium atom. Even this concentration does not correspond to a metal-like concentration of charge carriers. Furthermore, it is not certain that the surface excess charge is as great as 10^{13} cm^{-2}; the work of Barnes and Banbury[15] suggests that cleaved surfaces have a surface excess of $<10^{11}$ free carriers cm^{-2}. Finally, there is some evidence advanced by Pierotti and Halsey[6] that the application of the dispersion theory to metals is not invalidated by the free electron "gas." It was also necessary for Rosenberg to suggest that an oxide covered germanium surface was partially degenerate while several sets of experiments[14,15] show that oxidized germanium surfaces have a near-flat band configuration.

III. PREDICTED HEATS OF ADSORPTION

On the basis of the present estimate of the van der Waals radius of the surface germanium atoms, it becomes possible to calculate the heats of adsorption of other gases on the (111) surface of germanium. This has been done in particular for argon and xenon.

To determine values of ϕ_0 from Fig. 2, it was necessary to calculate a and b for the argon-germanium and xenon-germanium interactions. The values of a were obtained by averaging the values yielded by the Slater-Kirkwood and Kirkwood-Muller equations. (The polarizability and susceptibility of argon and xenon were taken from the paper by Pierotti and Halsey[6]; the constants used for germanium were those used in Sec. I.) The average value of a for argon-germanium is 1.1×10^{-58} erg cm^6 and for xenon-germanium, 2.4×10^{-58} erg cm^6.

Values of b/a, necessary to determine f, were determined from Eq. (4), using values of r_m for the argon-germanium and the xenon-germanium interactions which were obtained from Eq. (3). In this computation, r_m values for argon and xenon were taken as 3.83 A and 4.57 A respectively, as determined by Whalley and Schneider,[10] and r_m for germanium was taken as 3.53 A, as determined in Sec. I. The resulting values of f were 0.30 for argon-germanium and 0.54 for xenon-germanium. Values of ϕ_0 and z_0 at position 2 were then obtained from the graphs in Fig. 2 and Fig. 3; these are shown in Table III. The contribution of the induction effect to the energy of adsorption in each of these cases was computed following the procedure discussed in Sec. IV. These values are also listed in Table III, together with the resulting estimates for the heats of adsorption. The estimate for argon is consistent with Sparnaaij's[16] estimate of 3 kcal/mole derived from adsorption isotherms at low coverage on cleaned germanium powder.

IV. INDUCTIVE EFFECT

The energy of adsorption I arising from the polarization of the adsorbate atom in the electrostatic field of the

[13] L. Pauling, *The Nature of the Chemical Bond* (Cornell University Press, Ithaca, New York, 1960), 3rd ed., p. 263.

[14] P. Handler, *Semiconductor Surface Physics*, edited by R. H. Kingston (University of Pennsylvania Press, Philadelphia, Pennsylvania, 1957), p. 23.

[15] G. A. Barnes and P. C. Banbury, J. Phys. Chem. Solids **8**, 111 (1959).

[16] M. J. Sparnaaij, J. Phys. Chem. Solids **14**, 111 (1960).

absorbent is given approximately by

$$I=\tfrac{1}{2}\alpha E^2, \tag{8}$$

where α is the polarizability of the adsorbate atom and E is the magnitude of the electric field at the center of the adsorbate atom.

Adsorption at positions 1, 2, 3 and 4 is considered here. It is assumed that the basic unit, as far as charge distribution is concerned, is the germanium core with a charge of $+4e$ with four compensating electrons in tetrahedral positions. The distance of each electron from the center of the germanium atom was taken to be one-half the covalent bond length in germanium. It was assumed in each case that the krypton atom was at the equilibrium height found in Sec. I. The field at this point arising from the distribution of charge on the surface was then computed. (It was assumed that a good approximation for the field could be obtained by considering the near neighbors to the adsorption position. For instance, in the case of position 1 the field was computed taking into account the Ge atom directly below the krypton atom, the six Ge atoms around this one in the surface plane, and the three nearest Ge atoms in the plane below.) Then the energy of adsorption arising from the polarization caused by this field was computed. Any change in equilibrium height arising from this added force was ignored. The results of calculations of I for various positions of the krypton atom over the (111) plane are 0.4 kcal/mole at position 1, 0.8 kcal/mole at position 2, 0.7 kcal/mole at position 3, and 0.3 kcal/mole at position 4.

V. ADSORPTION NEAR A STEP ON THE SURFACE

If an atom is physically adsorbed near a step on a solid surface, the energy of adsorption will presumably be greater than that calculated for adsorption on a perfectly flat surface. Here, an estimate is made of the additional energy of adsorption arising from the interaction of a krypton atom with the germanium atoms in a step on the (111) surface.

Figure 4 is a diagram of the step in question. It is assumed that the krypton atom is adsorbed at position 4; its height above the surface is taken to be that found in Sec. I, namely 3.0 A. The krypton atom is allowed to move slightly in the $[\bar{1}\bar{1}2]$ direction (cf. Fig. 4) until its distance from the nearest germanium atom in the step is 3.53 A, the equilibrium distance between one krypton and one germanium atom as found in Sec. I. In computing the interaction energy of the krypton atom with the atoms in the step, both the attractive and repulsive terms of Eq. (1) are used for the nearest neighbor, while attractive terms only are used for the thirty-four next nearest neighbors. The interaction energy computed in this manner is 1.3 kcal/mole. However, at position 4 the interaction energy of the krypton atom with the flat portion of the surface is about 0.9 kcal/mole less than at the most favorable position. Thus the net energy gain in this case is not too large. However, where the geometry is favorable for maximum interaction with both the flat portion of the crystal and the step, the gain in energy could be over 1 kcal/mole.

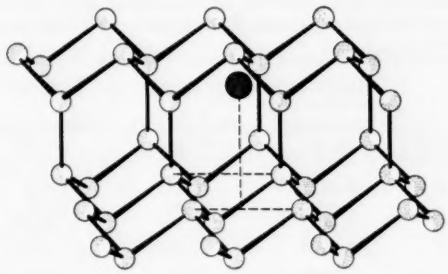

FIG. 4. Isometric projection of a step on the (111) surface of germanium. The face of the step is itself a {111} plane [namely $(11\bar{1})$] and intersects the surface along the $[\bar{1}10]$ direction. The krypton atom, shown by the heavy circle, is 3 A above position 4 on the surface (see Fig. 1).

APPENDIX

In order to compute the energy of interaction between a crystal and an atom adsorbed on its surface, it is necessary to evaluate $\sum_p R_p^{-6}$, where R_p is the distance between the adsorbate and the pth atom in the crystal, and the summation is over the entire lattice. Since convergence is slow when this sum is performed atom by atom, an alternative summation method was sought. Hove and Krumhansl[17] noted that as an adsorbate atom is moved in a plane parallel to the crystal, the function $\sum_p R_p^{-n}$ is doubly periodic, and hence the sum can be expanded in a double Fourier series, which in many cases will converge more rapidly than the atom by atom summation. Each term of this series includes an integral taken over the surface of the crystal; Hove and Krumhansl[17] show that when the lattice is cubic, these integrals are equivalent to tabulated functions. By a suitable change of variables in the integral, it can be shown that this is also the case for a general lattice; the series thus derived is expressed in terms of the lattice vectors $\mathbf{a}_1$, $\mathbf{a}_2$, and $\mathbf{a}_3$. The sums of R_p^{-6} which were needed in the preceding work were computed using this series.

Since the completion of this calculation, a derivation of this series for the summation of R_p^{-n} over a general lattice has been published by Fumi and Tosi.[18] The use of cylindrical coordinates in this derivation yields a more concise expression of the series, and the following discussion of the calculation for germanium and the rapidity of convergence of the series is given in terms of their notation.

Fumi and Tosi[18] consider a Bravais lattice of periods $\mathbf{a}_1$ and $\mathbf{a}_2$ lying in the plane $z=0$ with lattice points at the positions $\mathbf{r}_l=l_1\mathbf{a}_1+l_2\mathbf{a}_2$ (l_1, l_2 integers) and a point ($\mathbf{r}$, z) a distance z from the plane of the lattice.

[17] J. Hove and J. A. Krumhansl, Phys. Rev. **92,** 569 (1953).
[18] F. G. Fumi and M. P. Tosi, Phys. Rev. **117,** 1466 (1960).

TABLE IV. $\Sigma_p(R_p/a_1)^{-6}$ for atoms adsorbed on the (111) surface of crystals with face-centered cubic and diamond-type lattices.

Position[a]	Height of adsorbate above the surface (z_s/a_1)	$\Sigma_p(R_p/a_1)^{-6}$ face-centered cubic lattice	$\Sigma_p(R_p/a_1)^{-6}$ diamond-type lattice
1	0.4899	76.44	83.31
	0.6940	11.50	14.41
	0.8981	3.414	4.810
	1.1023	1.462	2.214
2	0.4899	17.92	24.79
	0.6940	6.873	9.780
	0.8981	2.907	4.303
	1.1023	1.396	2.148
3	0.4899	17.92	29.42
	0.6940	6.873	10.29
	0.8981	2.907	4.369
	1.1023	1.396	2.158
4	0.4899	20.64	29.34
	0.6940	7.248	10.37
	0.8981	2.957	4.382
	1.1023	1.403	2.160
5	0.4899	68.37	75.43
	0.6940	11.03	13.96
	0.8981	3.368	4.768
	1.1023	1.456	2.209
6	0.4899	68.37	75.36
	0.6940	11.03	13.95
	0.8981	3.368	4.767
	1.1023	1.456	2.209

[a] The position numbers refer to Fig. 1.

Evaluation of the sum

$$S_n(\mathbf{r},z)=\sum_l[(\mathbf{r}-\mathbf{r}_l)^2+z^2]^{-n/2}$$

yields the series

$$S_n(\mathbf{r},z)=\frac{\pi}{|\,\mathbf{a}_1\times\mathbf{a}_2\,|\,[(n/2)-1]}\left(\frac{1}{|\,z\,|^{n-2}}\right)+\frac{2\pi}{|\,\mathbf{a}_1\times\mathbf{a}_2\,|\,\Gamma(n/2)}\left(\frac{1}{2\,|\,z\,|}\right)^{(n/2)-1}\times\sum_{\mathbf{k}}{}'k^{(n/2)-1}K_{(n/2)-1}(k\,|\,z\,|)\exp(i\mathbf{k}\cdot\mathbf{r}),\quad(n>2).\quad(10)$$

Here $\mathbf{k}=k_1\mathbf{a}_1^*+k_2\mathbf{a}_2^*$ (k_1, k_2 integers and $\mathbf{a}_i\cdot\mathbf{a}_j^*=2\pi\delta_{ij}$); $k=|\,\mathbf{k}\,|$; the $\sum_{\mathbf{k}}'$ indicates summation over all possible combinations of k_1 and k_2 except $k_1=k_2=0$; and K_n is the Bessel function of the second kind for imaginary argument.[19]

The calculations here concern adsorption on the (111) face of germanium. Germanium has a diamond crystal structure, which can be considered as two interpenetrating face-centered cubic lattices. When the crystal is cut on the (111) plane, the atoms in the surface plane and in each alternate plane below that belong to one of these lattices, while the atoms in the remaining planes belong to the other. The summation of R_p^{-6} over each of these two sets of equidistant planes has been computed separately, so that the results can be applied to adsorption on the (111) face of either a face-centered cubic or diamond structure crystal.

To compute the sum of R_p^{-6} over a set of equidistant planes, the expression on the right hand side of Eq. (10) must be evaluated for each of the planes in turn. The first term in the expression summed over all the planes in the set forms a generalized Riemann zeta function, the evaluation of which is discussed by Hove and Krumhansl.[16] The second term on the right hand side of Eq. (10) is in itself an infinite series for each plane, and there are, of course, an infinite number of planes. However, the function $K_2(k|z|)$ diminishes rapidly as $k|z|$ increases, and it is for this reason that the use of of this series is preferable to atom by atom summation.

The sum of $(R_p/a_1)^{-6}$ for face-centered cubic and diamond-type lattices which were computed from Eq. (10) are listed in Table IV. In computing the sums for each set of equidistant planes, the second term on the right hand side of Eq. (10) was neglected entirely from the second plane on. The highest values of k used in computing terms for the first plane of each set ranged from $4(4\pi/\sqrt{3}a_1)$ (when the atom was furthest from the surface) to $12(4\pi/\sqrt{3}a_1)$. Neglecting the remainders of these series leads to an uncertainty of less than 0.2% in each of the sums listed in Table IV. Young[3] has computed the sums of R_p^{-6} for atoms at various heights over positions 1, 2, and 3 by summing over 300 atoms and approximating the remainder by integration; his results and the comparable ones in Table IV fall on a smooth curve when plotted on a common graph.

The method used here to arrive at an upper limit on the absolute value of the remainder of the series is as follows. Only terms for which $k|z|>4$ are neglected; in this region $K_2(k|z|)<e^{-k|z|}$. Consider a plane for which the second term on the right hand side of Eq. (10) is neglected entirely. For the planar lattice being considered here ($|\,\mathbf{a}_1\,|=|\,\mathbf{a}_2\,|\equiv a_1$ and $\mathbf{a}_1\cdot\mathbf{a}_2=\frac{1}{2}a_1^2$), and with $n=6$, this term can be written as

$$(8\sqrt{3}\pi^3/9a_1^4)\,(z)^{-2}G(z),$$

where

$$G(z)=\sum_{\mathbf{k}}{}'(k')^2K_2(Ck')\exp(i\mathbf{k}\cdot\mathbf{r}),$$

$$k'=k(\sqrt{3}a_1/4\pi),$$

and

$$C=(4\pi/\sqrt{3}a_1)\,|\,z\,|.$$

The upper limit on $|\,G(z)\,|$ can be found as follows:

$$|\sum_{\mathbf{k}}{}'(k')^2K_2(Ck')\exp(i\mathbf{k}\cdot\mathbf{r})\,|=|\sum_{\mathbf{k}}{}'(k')^2K_2(Ck')\cos(\mathbf{k}\cdot\mathbf{r})\,|<\sum_{\mathbf{k}}{}'(k')^2K_2(Ck')<\sum_{\mathbf{k}}{}'(k')^2\exp(-Ck'),\quad(Ck'>4).$$

[19] An extensive table of K_n (for integer values of n) is included in *British Association for the Advancement of Science. Mathematical Tables* (Cambridge University Press, Cambridge, 1952), Vol. X.

For the (111) plane of a face-centered cubic lattice, it can be shown that, taking all possible combinations of k_1 and k_2 except $k_1=k_2=0$, the smallest value of k' is one, and the number of combinations which yield k' such that $m\leq k'<m+1$ (where m is a positive integer) is $6(m+1)$. Since $(k')^2\exp(-Ck')$ decreases monotonically as k' increases in the range of interest, it follows that

$$\sum_{\mathbf{k}}{}'(k')^2\exp(-Ck')<\sum_{m=1}^{\infty}6(m+1)m^2\exp(-Cm).$$

The ratio of $(m+2)(m+1)^2$ to $(m+1)m^2$ monotonically decreases as m increases; for $m=1$, this ratio is six to one. Therefore this last series is less than

$$12e^{-C}\sum_{m=0}^{\infty}(6e^{-C})^m=12e^{-C}(1-6e^{-C})^{-1},$$

which in turn is less than $13.5\exp(-C)$, since the minimum value of C is 4. Thus one obtains

$$G(z)<13.5e^{-C}. \tag{11}$$

Suppose that the second term on the right in Eq. (10) is entirely neglected from the γth plane on. Then the total remainder for these planes is

$$(8\sqrt{3}\pi^3/9a_1^4)\sum_{q=\gamma}^{\infty}[z_1+(q-1)d]^{-2}G[z_1+(q-1)d],$$

where z_1 is the height of the adsorbate above the first plane and d is the distance between planes. With the use of the inequality (11) for $G(z)$, and noting that

$$[z_1+(q-1)d]^{-2}\leq[z_1+(\gamma-1)d]^{-2}$$

holds for all values of q in the summation, it can be shown that an upper limit on the absolute value of this total remainder is

$$13.5\left(\frac{8\sqrt{3}\pi^3}{9a_1^4}\right)\left(\frac{1}{z_1+(\gamma-1)d}\right)^2\exp\left\{-\frac{4\pi[z_1+(\gamma-1)d]}{\sqrt{3}a_1}\right\}\times\left[1-\exp\left(-\frac{4\pi d}{\sqrt{3}a_1}\right)\right]^{-1}. \tag{12}$$

In the first plane the terms for low values of k' are computed, while terms for higher values of k' are neglected. Through reasoning exactly analogous to that used above, it can be shown that when all terms for which $k'\geq M$ (M an integer) are neglected for a given plane, the upper limit on the absolute value of the remainder of the second term on the right hand side of Eq. (10) is

$$(8\sqrt{3}\pi^3/9a_1^4)(1/z)^2\left[6M^2(M+1)\exp\left(-\frac{4\pi M\mid z\mid}{\sqrt{3}a_1}\right)\right]\times\left[1-\frac{(M+1)(M+2)}{M^2}\exp\left(-\frac{4\pi\mid z\mid}{\sqrt{3}a_1}\right)\right]^{-1}. \tag{13}$$

On the Classical Boltzmann Equation for Gases

FRANK C. ANDREWS*

Department of Chemistry, University of California, Berkeley 4, California

(Received February 13, 1961)

With great simplicity we formulate the Boltzmann equation for dilute classical gases from the reduced Liouville equation by using the three assumptions: no three-body effects, collision time much less than the experimental time, and negligible change in local properties of the system over distances of order of the range of the intermolecular forces. The nature of these assumptions sheds some light on recent attempts to generalize the Boltzmann equation. We find that it is easy formally to relax the first assumption to permit more than two-body effects. The resulting equation is an intuitive extension of the Boltzmann equation.

FORMULATIONS of the classical Boltzmann equation from the Liouville equation are well known.[1,2] Our motivation in presenting another very similar one is twofold. The usual assumptions are required, but in our treatment once the assumptions are made, the mathematics immediately assumes the desired form. Our formulation therefore seems very "physical." The second reason is that the assumption limiting the collisions to two-body is very easily relaxed formally, yielding a generalization of the Boltzmann equation. This generalization is very intuitive, though probably difficult to solve.

We start with the complete N-particle Liouville equation for f_N and reduce it to an equation for f_1. This is done by integrating over positions and momenta of all particles except particle 1. The resulting equation has taken the name of the first Bogoliubov-Born-Green-Kirkwood-Yvon equation, and is exact for systems with only two-body forces[3]:

$$\frac{\partial f_1(1)}{\partial t}+\mathbf{v}_1\cdot\frac{\partial f_1(1)}{\partial \mathbf{x}_1}+\mathbf{X}\cdot\frac{\partial f_1(1)}{\partial \mathbf{p}_1} =-\iint d\mathbf{x}_2 d\mathbf{p}_2 \mathbf{F}_{12}\cdot\frac{\partial f_2(1,2)}{\partial \mathbf{p}_1}. \quad (1)$$

We make three assumptions in computing the collision integral of the right-hand side. The assumptions are separate mathematically, but their physical restrictions on the kind of system considered overlap considerably.

ASSUMPTION 1

No collision effect requiring a third body can play a role. This assumption would seem reasonable for sufficiently dilute gases close enough to equilibrium. It means that $f_2(1, 2)$ is a constant of the motion over the time scale used in computing the collision integral.

ASSUMPTION 2

During the time of a collision, the explicit time dependence of both f_1 and f_2 may be neglected. This is tantamount to considering collisions as instantaneous events compared to the time during which any observable property of the system undergoes an observable change. This assumption would seem reasonable for a dilute gas having macroscopic gradients, i.e., for one which is sufficiently close to equilibrium.

ASSUMPTION 3

The gradient of the inhomogeneity is so small that it may be neglected over distances of several times the range of the intermolecular forces. This assumption is good even for extreme disturbances in a dilute gas. It is not even an assumption in finding the self-diffusion coefficient; since then there is no gradient. If the system satisfies this requirement and assumption 1, then $f_2(1, 2)$ may have spatial dependence only through a function of $\mathbf{x}_{12}$, the vector $\mathbf{x}_1-\mathbf{x}_2$. Then

$$\partial f_2(1, 2)/\partial \mathbf{x}_1=-\partial f_2(1, 2)/\partial \mathbf{x}_2, \quad (2)$$

over distances of the order of the range of forces.

Assumptions 1 and 2 require $f_2(1, 2)$ to be a solution of the time-independent, two-particle Liouville equation

$$\mathbf{v}_1\cdot(\partial f_2/\partial \mathbf{x}_1)+\mathbf{v}_2\cdot(\partial f_2/\partial \mathbf{x}_2)+\mathbf{F}_{12}\cdot(\partial f_2/\partial \mathbf{p}_1) +\mathbf{F}_{21}\cdot(\partial f_2/\partial \mathbf{p}_2)=0. \quad (3)$$

For the integrand of the collision integral of Eq. (1) we substitute its value from Eq. (3). This integral becomes

$$\iint d\mathbf{x}_2 d\mathbf{p}_2[\mathbf{v}_1\cdot(\partial f_2/\partial \mathbf{x}_1)+\mathbf{v}_2\cdot(\partial f_2/\partial \mathbf{x}_2)+\mathbf{F}_{21}\cdot(\partial f_2/\partial \mathbf{p}_2)]. \quad (4)$$

The third term of this is zero because the surface integral at infinite momentum vanishes. Using Eq. (2), this collision integral becomes simply

$$\iint d\mathbf{x}_{21} d\mathbf{p}_{21}\mathbf{v}_{21}\cdot(\partial f_2/\partial \mathbf{x}_{21})=\iint d\mathbf{p}_{21} d\mathbf{S}_{21}\cdot\mathbf{v}_{21} f_2(1, 2), \quad (5)$$

* National Institutes of Health Research Fellow.

[1] J. G. Kirkwood, J. Chem. Phys. **15**, 72 (1947).

[2] H. S. Green, *The Molecular Theory of Fluids* (North-Holland Publishing Company, Amsterdam, 1952), p. 218 *et seq.*

[3] J. O. Hirschfelder, C. F. Curtiss, and R. B. Bird, *Molecular Theory of Gases and Liquids* (John Wiley & Sons, Inc., New York, 1954), p. 450 *et seq.*

where we have made $\mathbf{x}_1$ and $\mathbf{p}_1$ the origins for the integrations and have integrated the gradient by Gauss' theorem.

The surface integral is taken over a surface just outside the range of the distortion of $f_2(1, 2)$ by the intermolecular force. For incoming particles, i.e., $d\mathbf{S}_{21}\cdot\mathbf{v}_{21}<0$, assumption 1 permits our setting

$$f_2(1, 2)=f_1(1)f_1(2).$$

For incoming particles to be correlated before they feel each others' potentials, at least some third particle is required from which to bounce one of them. For outgoing particles, we may express f_2 in terms of f_1's only if we trace back along the two-body trajectory until the intermolecular force becomes zero. Then $f_2(1, 2)$ may be equated to $f_1(1)f_1(2)$, but evaluated at those positions and momenta the particles had prior to the collision. For $\mathbf{dS}_{21}\cdot\mathbf{v}_{21}>0$, we use the notation

$$f_2(1, 2)=f_1(1')f_1(2').$$

The primes mean the positions and momenta got for the particles by tracing back over the trajectory to the beginning of the interaction.

In order to obtain the usual form of the Boltzmann collision integral, one takes the surface of integration to be a cylinder about molecule 1 with axis parallel to $\mathbf{v}_{21}$. For spherical potentials then, Eq. (1) becomes

$$(\partial f_1/\partial t)+\mathbf{v}_1\cdot(\partial f_1/\partial\mathbf{x}_1)+\mathbf{X}\cdot(\partial f_1/\partial\mathbf{p}_1)$$
$$=2\pi\iint d\mathbf{p}_{21}bdbv_{21}[f_1(1')f_1(2')-f_1(1)f_1(2)], \quad (6)$$

which is the usual form of the Boltzmann equation.[3] We note that assumption 3 requires the spatial dependence of the f_1's to be so slowly varying that they may all be taken at the same place.

Recent researchers have treated the Boltzmann equation for supposedly dense hard-sphere gases.[4,5] To obtain a collision integral for hard spheres of diameter σ is simple. We just use a spherical surface of integration located infinitesimally outside molecule 1, effectively at $x_{21}=\sigma$. We get formally the collision integral

$$\sigma^2\iint_{\mathbf{k}_{21}\cdot\mathbf{v}_{21}>0} d\mathbf{p}_{21}d\mathbf{k}_{21}\cdot\mathbf{v}_{21}f_2(\mathbf{x}_1, \mathbf{p}_1', \mathbf{x}_1+\mathbf{k}_{21}\sigma, \mathbf{p}_{21}')$$
$$+\sigma^2\iint_{\mathbf{k}_{21}\cdot\mathbf{v}_{21}<0} d\mathbf{p}_{21}d\mathbf{k}_{21}\cdot\mathbf{v}_{21}f_2(\mathbf{x}_1, \mathbf{p}_1, \mathbf{x}_1+\mathbf{k}_{21}\sigma, \mathbf{p}_2), \quad (7)$$

where $\mathbf{k}_{21}$ is a unit vector. This formal result is precisely the result of Hollinger and Curtiss[5] for a "dense hard-sphere gas." It differs from that of Rice *et al.*[4] in the matter of the sign of the spatial correction within the last parenthesis.

[4] S. A. Rice, J. G. Kirkwood, J. Ross, and R. W. Zwanzig, J. Chem. Phys. **31**, 575 (1959).
[5] H. B. Hollinger and C. F. Curtiss, J. Chem. Phys. **33**, 1386 (1960).

Once again, consistent with assumption 1, we may factor the f_2's into a product of f_1's, since we are working to lowest order in concentration. Again assumption 3 requires that f_1 cannot vary appreciably over distances of the order of σ, and

$$f_1(\mathbf{x}_1+\mathbf{k}_{21}\sigma, \mathbf{p}_2)=f_1(\mathbf{x}_1, \mathbf{p}_2). \quad (8)$$

If that were not so, the breakdown of assumption 3 would make the resulting equation of a much more complicated form. We get, then,

$$\sigma^2\iint_{\mathbf{k}_{21}\cdot\mathbf{v}_{21}>1} d\mathbf{p}_{21}d\mathbf{k}_{21}\cdot\mathbf{v}_{21}[f_1(\mathbf{x}_1, \mathbf{p}_1')f_1(\mathbf{x}_1, \mathbf{p}_2')$$
$$-f_1(\mathbf{x}_1, \mathbf{p}_1)f_1(\mathbf{x}_1, \mathbf{p}_2)].$$

We note here that the investigators[4,5] using an equation with a collision integral of the form of Eq. (7), which is derived allowing only two-body collisions, plan to incorporate the effect of a "dense" system by setting

$$f_2(1, 2)=g_2(1, 2)f_1(1)f_1(2),$$

where $g_2(1, 2)$ is the appropriate correlation function for a dense system. It is the result of many-body interactions. This mixture of assumptions has been much discussed by the above researchers.

The easiest way to generalize the assumptions seems to be to weaken assumption 1 to permit more than two-body effects. Suppose we do this, allowing no collision effect requiring a $(\nu+1)$th body to play a role. This model might describe a moderately dense gas, but one would expect the situation to get complicated fast.

Instead of Eq. (3), we now have

$$\sum_{i=1}^{\nu}\mathbf{v}_i\cdot(\partial f_\nu/\partial\mathbf{x}_i)+\sum_{i\neq j=1}^{\nu}\mathbf{F}_{ij}\cdot(\partial f_\nu/\partial\mathbf{p}_i)=0.$$

We use the following identity:

$$f_2(1, 2)=N^{2-\nu}\int f_\nu\{d\mathbf{x}\}_{\nu-2}\{d\mathbf{p}\}_{\nu-2},$$

which gives for the integrand of the collision integral:

$$-\mathbf{F}_{12}\cdot\frac{\partial f_2(1, 2)}{\partial\mathbf{p}_1}$$
$$=N^{2-\nu}\Bigg[\sum_{i=1}^{\nu}\int d\mathbf{x}_3\cdots d\mathbf{x}_\nu d\mathbf{p}_3\cdots d\mathbf{p}_\nu\mathbf{v}_i\cdot(\partial/\partial\mathbf{x}_i)f_\nu(1, 2, \cdots\nu)$$
$$+\sum_{\substack{i\neq j=1\\(\neq i=1,\ j=2)}}^{\nu}\int d\mathbf{x}_3\cdots d\mathbf{x}_\nu d\mathbf{p}_3\cdots d\mathbf{p}_\nu\mathbf{F}_{ij}$$
$$\cdot(\partial/\partial\mathbf{p}_i)f_\nu(1, 2, \cdots\nu)\Bigg].$$

When this is substituted into Eq. (1), all terms in the second sum give zero for the surface integral at infinite momentum except for those whose derivatives are with

respect to $\mathbf{p}_1$. We then have

$$-N^{\nu-1}\int d\mathbf{x}_2\cdots d\mathbf{x}_\nu d\mathbf{p}_2\cdots d\mathbf{p}_\nu \mathbf{F}_{12}\cdot\frac{\partial f_\nu(1,2,\cdots\nu)}{\partial \mathbf{p}_1}$$

$$=N^{\nu-1}\sum_{i=1}^{\nu}\int d\mathbf{x}_2\cdots d\mathbf{x}_\nu d\mathbf{p}_2\cdots d\mathbf{p}_\nu \mathbf{v}_i\cdot(\partial/\partial\mathbf{x}_i)f_\nu(1,2,\cdots\nu)$$

$$+N^{\nu-1}\sum_{j=2}^{\nu}\int d\mathbf{x}_2\cdots d\mathbf{x}_\nu d\mathbf{p}_2\cdots d\mathbf{p}_\nu \mathbf{F}_{1j}$$

$$\cdot(\partial/\partial\mathbf{p}_1)f_\nu(1,2,\cdots\nu).$$

Recognizing that each of the $(\nu-2)$ terms in the last summation equals the left-hand side, we get for the collision integral of Eq. (1)

$$\frac{N^{\nu-1}}{(\nu-1)}\int d\mathbf{x}_{21}\cdots d\mathbf{x}_{\nu 1}d\mathbf{p}_{21}\cdots d\mathbf{p}_{\nu 1}\sum_{i=1}^{\nu}\mathbf{v}_i$$

$$\cdot(\partial/\partial\mathbf{x}_i)f_\nu(1,2,\cdots\nu).$$

We now use the identities

$$(\partial/\partial\mathbf{x}_1)f(\mathbf{x}_{21},\mathbf{x}_{31},\cdots\mathbf{x}_{\nu 1})=-\sum_{j=2}^{\nu}(\partial/\partial\mathbf{x}_{j1})f,$$

$$(\partial/\partial\mathbf{x}_j)f(\mathbf{x}_{21},\mathbf{x}_{31},\cdots\mathbf{x}_{\nu 1})=(\partial/\partial\mathbf{x}_{j1})f,$$

and insert the factor $N^{\nu-2}/(\nu-2)!$, which in the limit of large N is the number of ways of choosing the particular $(\nu-2)$ "dummy particles." This gives a collision integral of the form

$$\frac{1}{(\nu-1)!}\int d\mathbf{x}_{21}\cdots d\mathbf{x}_{\nu 1}d\mathbf{p}_{21}\cdots d\mathbf{p}_{\nu 1}\sum_{j=2}^{\nu}\mathbf{v}_{j1}\cdot(\partial/\partial\mathbf{x}_{j1})f_\nu$$

$$=\frac{1}{(\nu-1)!}\int d\mathbf{p}_{21}\cdots d\mathbf{p}_{\nu 1}\sum_{j=2}^{\nu}\{d\mathbf{x}_{21}\cdots d\mathbf{x}_{\nu 1}\}_{\neq j1}\mathbf{dS}_{j1}\cdot\mathbf{v}_{j1}f_\nu.$$

Again we may let the surface of integration be a cylinder about molecule 1 with axis parallel to $\mathbf{v}_{j1}$. The counterpart of Eq. (6) is then

$$\frac{\partial f_1}{\partial t}+\mathbf{v}_1\cdot\frac{\partial f_1}{\partial \mathbf{x}_1}+\mathbf{X}\cdot\frac{\partial f_1}{\partial \mathbf{p}_1}=\frac{2\pi}{(\nu-1)!}\int d\mathbf{p}_{21}\cdots d\mathbf{p}_{\nu 1}\sum_{j=2}^{\nu}$$

$$\times\{d\mathbf{x}_{21}\cdots d\mathbf{x}_{\nu 1}\}_{\neq j1}b_{j1}db_{j1}v_{j1}$$

$$\times[f_1(1')f_1(2')\cdots f_1(\nu')-f_1(1)f_1(2)\cdots f_1(\nu)]. \quad (9)$$

The operational meaning of the primed momenta of Eq. (9) may be clarified by considering a particular term of the sum, e.g., $\nu=3$, $j=2$,

$$\pi\int d\mathbf{p}_{21}d\mathbf{p}_{31}d\mathbf{x}_{31}b_{21}db_{21}v_{21}$$

$$\times[f_1(1')f_1(2')f_1(3')-f_1(1)f_1(2)f_1(3)].$$

Particle 1 is initially fixed in space. We imagine a cylinder about particle 1 with axis parallel to $\mathbf{v}_{21}$. We are integrating over b_{21}, $\mathbf{v}_{21}$, $\mathbf{x}_{31}$, and $\mathbf{p}_{31}$. So, if we are given these four quantities, we start particle 2 on the base of the cylinder at b_{21} going backwards into the cylinder with velocity $-\mathbf{v}_{21}$. We start particle 3 at $\mathbf{x}_{31}$ going backwards with momentum $-\mathbf{p}_{31}$. We trace back the exact trajectories of all three particles, all of them interacting according to how close they come to each other. Finally we shall reach a stage when the trajectories are all straight lines and the particles are not going to collide again. The momentum particle i has at this time is $(\mathbf{p}_i'-\mathbf{p}_1)$, and from this operational method the primed momenta may be found. We need not worry about positions, because Eq. (8) must hold over the entire interaction volume if Eq. (9) be valid.

We note that the base of our cylinder must be far enough from particle 1 to permit the consideration of most collisions. This cannot be so far that either assumption 2 or 3 is violated. One would expect, however, that for a considerable range of distances, not too many collisions involving particle 1 will be missed and yet assumptions 2 and 3 will remain good.

We also note that collisions which just involve particles 2 and 3, but not particle 1, *apparently* must be counted. Yet we know that particle 1, if it is not involved with other particles through its intermolecular potential, obeys Eq. (1) with the right hand side equal to zero. Thus, *we may neglect* all such collisions.

The extension of this method for $\nu>3$ is obvious.

This is, then, a way of considering formally collisions involving more than two particles. Analytic calculations of the trajectories are of course impracticable. Results identical to the above have been achieved by the Brussels group,[6-8] and the problems have been investigated further in work to be published by P. Résibois and by the author.

ACKNOWLEDGMENTS

For helpful conversations relating to this topic I am indebted to Professor I. Prigogine and Dr. P. Résibois of Brussels, to Professor I. Krieger of the Case Institute of Technology, and to Dr. B. Alder of Berkeley.

[6] I. Prigogine and R. Balescu, Physica **26**, 145 (1960).
[7] F. C. Andrews, J. Math. Phys. **2**, 91 (1960).
[8] I. Prigogine, *Non-Equilibrium Statistical Mechanics* (Interscience Publishers, Inc., New York, 1961).

Infrared Spectrum of Solid Carbon Monoxide

GEORGE E. EWING* AND GEORGE C. PIMENTEL

Department of Chemistry, University of California, Berkeley, California

(Received January 9, 1961)

The infrared spectrum of solid carbon monoxide at 20°K has been examined in the fundamental and overtone regions. Sharp features (bandwidths about one cm^{-1}) are assigned to vibrational modes of the various isotopic species: $C^{12}O^{16}$, 2138.1 cm^{-1}; $C^{12}O^{17}$, 2112.3 cm^{-1}; $C^{13}O^{16}$, 2092.2 cm^{-1}; and $C^{12}O^{18}$, 2088.4 cm^{-1}. These frequencies are examined with the aid of existing theories of frequency shifts in condensed phases. A broad absorption (bandwidth about 40 cm^{-1}) centered at 2208 cm^{-1} is assigned to combinations of the fundamental mode with lattice modes. Calculations suggest that the lattice modes involved probably include translations as well as librations.

THE vibrational spectra of many molecular crystals have been successfully interpreted in a qualitative way, in terms of the principles set down by Halford *et al.*,[1,2] Hornig,[3] and others. These successes encourage quantitative evaluation of these spectra and a few have been so treated. The spectra of the simpler molecules are the most readily understood and most likely to yield to detailed analysis. We present here infrared spectral studies of solid carbon monoxide together with some quantitative interpretation.

There are no reported infrared spectral data on either solid or liquid carbon monoxide. Recently CO was used as a solid matrix for infrared studies of other species suspended therein.[4] In the region of the carbon monoxide fundamental, five spectral features were found. This complicated spectrum encouraged our further study of pure carbon monoxide.

EXPERIMENTAL

Reagent grade carbon monoxide (Air Reduction Company) was used. Mass spectral analysis of this sample indicated the following impurities, expressed in mole percent: CO_2, 0.04; H_2, 0.03; N_2, <0.5. Chemical analysis indicated the following: N_2, <0.4; O_2, <0.1; CO_2, <0.1. Additional experiments were performed using carbon monoxide prepared by the reaction of sulfuric acid on formic acid but no spectral differences could be found.

The gas was deposited at a rate of about 1 mM/hr onto a CsBr window maintained at 20°K. The cold-cell and low-temperature techniques have been described.[5]

Infrared spectra were recorded with a Beckman IR-7 spectrophotometer with estimated frequency accuracy of ±0.3 cm^{-1}. The first overtone was recorded with a Cary model 14, with frequency accuracy estimated to be ±0.2 cm^{-1}. The spectra were calibrated against gaseous CO[6,7] by simultaneous recording with the solid in the sample beam and the gas in the reference beam. Spectral slitwidths in both fundamental and overtone regions were near 0.8 cm^{-1} as shown by the bandwidths of rotational features of gaseous CO.

RESULTS

The infrared spectrum of solid carbon monoxide was recorded many times. Figure 1 shows two of these spectra recorded, respectively, after 20 and 600 mM had been deposited. For the overtone region, 150 mM were deposited and one feature was observed with $\log I_0/I$ near 0.03. The observed frequencies are collected in Table I and compared to the frequencies of gaseous carbon monoxide.

DISCUSSION

Crystal Structure and Selection Rules

Carbon monoxide has two low-temperature solid phases with the transition at 61.55°K.[8] Since the samples studied in these experiments were maintained at 20°K it is assumed that they had the crystal symmetry of the low temperature phase. This crystal structure is reported to be cubic[9] with space group symmetry $T^4(P2_13)$ and with four molecules per unit cell located on equivalent sites of symmetry C_3.

The results of the site[1] and factor group analyses[2,3] are presented in Table II. The single vibrational mode of the molecule falls in the symmetric representation A (infrared active) in the site group symmetry. In the factor group symmetry, the four vibrational degrees of freedom fall in the A and F representations. Only the triply degenerate mode F is infrared active.

In the site group approximation all of the combina-

* Present address: Jet Propulsion Laboratories, Pasadena, California.

[1] R. S. Halford, J. Chem. Phys. **14**, 8 (1946).
[2] H. Winston and R. S. Halford, J. Chem. Phys. **17**, 607 (1949).
[3] D. F. Hornig, J. Chem. Phys. **16**, 1063 (1948).
[4] G. E. Ewing, W. E. Thompson, and G. C. Pimentel, J. Chem. Phys. **32**, 927 (1960).
[5] E. D. Becker and G. C. Pimentel, J. Chem. Phys. **25**, 224 (1956).
[6] E. K. Plyler, L. R. Blaine, and W. S. Connor, J. Opt. Soc. Am. **45**, 102 (1955).
[7] E. K. Plyler, H. C. Allen, and E. D. Tidwell, J. Research Natl. Bur. Standards **61**, 53 (1958).
[8] J. O. Clayton and W. F. Giauque, J. Am. Chem. Soc. **54**, 2610 (1932).
[9] L. Vegard, Z. Physik **61**, 185 (1930).

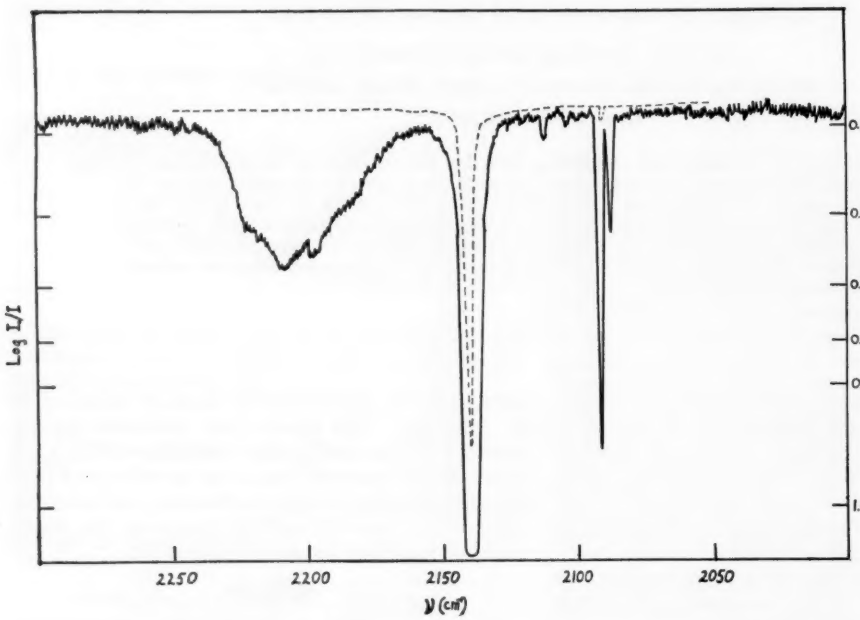

FIG. 1. The infrared spectrum of solid CO at 20°K (2000–3000 cm^{-1}). - - - - - 20 mM deposited, ——— 600 mM deposited.

tions of vibrational with translational and rotational motions are allowed by symmetry. These combinations would give rise to three modes, one nondegenerate A and two doubly degenerate E motions.

In the factor group approximation the number of combinations allowed by symmetry is 20, each triply degenerate F.

Fundamental Modes

Both the site and factor group analyses predict one absorption feature for the fundamental stretching mode of carbon monoxide. The four sharp features shown in Fig. 1 can be assigned to the various isotopic species at their natural abundance: $C^{12}O^{16}$, $C^{12}O^{17}$, $C^{13}O^{16}$, $C^{12}O^{18}$ This assignment is corroborated by the comparison of the solid-state frequencies to those found in the gas (see Table I). The small frequency differences ($\Delta\nu$) can be attributed to shifts caused by the matrix environment. A further verification is provided by the relative intensities of the features. Table III shows the natural abundance ratios[10] and the measured intensity ratios based on the assignment given above. We consider the agreement to be satisfactory in view of the large photometry errors which are likely.

TABLE I. Infrared absorption frequencies of solid carbon monoxide at 20°K.

Gas (band centers) $\nu(cm^{-1})$	Solid $\nu(cm^{-1})$	$\Delta\nu$ (cm^{-1})	Half-width $\nu_{\frac{1}{2}}(cm^{-1})$	Assignment
4260.0	4253.5	−6.5	2.0	$2\nu(C^{12}O^{16})$
...	2222 (sh)[a] 2208 2197 2182 (sh)	...	40	$\nu(C^{12}O^{16})+\nu_c$
2143.3	2138.1	−5.2	1.5	$\nu(C^{13}O^{16})$
2116.3[b]	2112.3	−4.0	1.0–2.0[c]	$\nu(C^{12}O^{17})$
2096.1	2092.2	−3.9	1.2	$\nu(C^{13}O^{16})$
2092.1	2088.4	−3.7	1.1	$\nu(C^{12}O^{18})$

[a] (sh) = shoulder.
[b] Calculated.
[c] In our spectra, the $\nu(C^{12}O^{17})$ absorption was too weak to permit an accurate bandwidth measurement.

Combinations

With this convincing assignment of the four sharp features, only the broad band centered at 2208 cm^{-1} remains to be explained. The breadth of this band (which we shall refer to hereafter as ν_c) superficially suggests the envelope of an R branch for a rotating molecule. This possible explanation can be eliminated, the most obvious basis being the complete absence of a P branch. The ν_c band can be explained in terms of the excitation of combinations of the fundamental mode with either translations or rotations. In the factor group approximation there are 20 active modes. This could account for the observed broadness of ν_c in terms of the overlap of many closely spaced features. The possible combinations are considered in turn.

Translation and Vibration

The translational motions of the unit cell can be approximated by considering the CO molecules as point

[10] D. Strominger, J. M. Hollander, and G. T. Seaborg, Revs. Modern Phys. **30**, 585 (1958).

TABLE II. Site and factor group analyses for solid CO (low temperature phase).

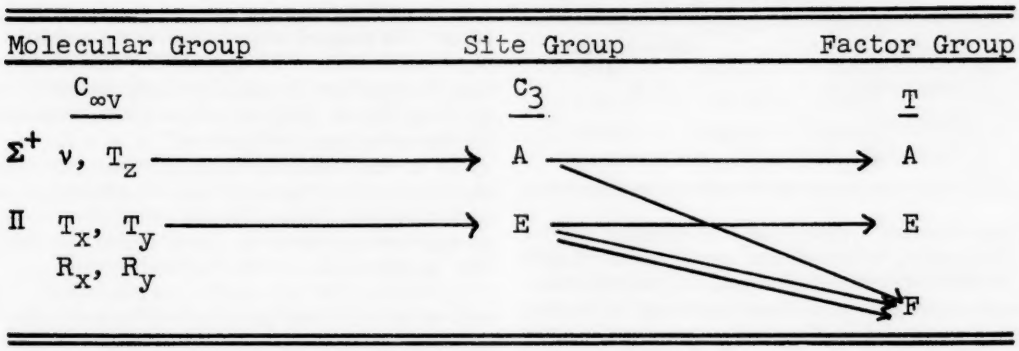

masses interacting through central forces. In the CO crystal, the centers of masses of the four molecules of the unit cell occupy T_d sites at the corners of a regular tetrahedron. Thus the problem is simply related to the vibrations of P_4.[11] However, the displacement of a molecule in a particular unit cell changes its position relative to a neighboring unit cell. In a T_d site, this implies that the restoring force is just double that of a molecule in an isolated tetrahedron. We can express the frequencies of the point mass model of solid CO in terms of the three vibrational modes of an isolated tetrahedron by substituting $2k_t$ for the force constant k of the isolated tetrahedron (where k_t is the force constant of the infinite lattice). Of course, 28 g/mole is taken as the mass. Then

$$\nu(A)=2\nu(E)=\sqrt{2}\nu(F)$$
$$\nu(E)=(1/2\pi c)(2k_t/m)^{\frac{1}{2}}.$$

Since none of the combinations are forbidden by symmetry, it is a reasonable hypothesis that the center of the broad band is fixed by the central mode $\nu(F)$. Thus, we assign $\nu(F)=\nu_c-\nu(C^{12}O^{16})=2208-2138=70$ cm^{-1}, and $k_t=0.020\cdot10^5$ d/cm. With this estimate of k_t, $\nu(A)=100$ cm^{-1} and $\nu(F)=50$ cm^{-1}. In this approximation, then, a band spread of about 50 cm^{-1} is expected. This expectation is in accord with the 40 cm^{-1} half-width of ν_c, presuming the translational combinations are diffuse.

Through a web of assumptions, the heat of vaporization of solid carbon monoxide provides an order of magnitude corroboration of the estimated value of k_t. First, the calorimetric datum must be interpreted in terms of an intermolecular potential function. We assume the familiar form

$$V=ar^{-n}+br^{-m}. \tag{1}$$

The parameters a and b are fixed to fit the experimental equilibrium intermolecular distance r_0 and the value of k_t deduced here,

$$(\partial V/\partial r)_0=0 \quad \text{at} \quad r=r_0 \tag{2}$$
$$(\partial^2 V/\partial r^2)_0=k_t. \tag{3}$$

Combining expressions (1), (2), and (3), we obtain

$$V_0=k_t r_0'2/n\cdot m, \tag{4}$$

where V_0 = the value of V at $r=r_0$. Since each molecule is bonded to four others, four bonds must be broken when a molecule is removed from the interior of the crystal. This amount of energy is just double the heat of vaporization, for each bond is shared by two molecules. Hence the potential function (1) indicates that the heat of vaporization equals $2V_0$. Inserting $k_t=0.020\cdot10^5$ and $r_0=3.80$A (the distance between occupied site positions), we calculate $2V_0=1.5$ kcal/mole for $n=6$, $m=9$ or $2V_0=1.1$ kcal/mole for $n=6$, $m=12$. These results can be compared to the heat of vaporization, 1.4 kcal/mole.[12] The fortuitous agreement is, of course, far better than could be expected in view of the uncertainties. Insofar as the heat of vaporization provides a useful criterion, *the broad band near 2208 cm^{-1}(ν_c) could be caused by combinations involving translational modes.*

Rotation and Vibration

It is necessary to consider the alternate possibility, that rotational (librational) modes are contributing to ν_c.

The problem of the coupled librational motions of the entire unit cell is complicated. A more tractable approach is the site approximation. There are two rotational degrees of freedom, and by the site symmetry, these are degenerate. Hence the site approximation provides a one-dimensional potential function $V(\theta)$ where θ is the displacement from the equilibrium orientation. By symmetry, $V(\theta=0°)=V(\theta=180°)$. The potential function suggested by Pauling[13] for librational

[11] G. Herzberg, *Infrared and Raman Spectra* (D. Van Nostrand Company, Inc., Princeton, New Jersey, 1945).

[12] Natl. Bur. Standards Circ. No. 500.

[13] L. Pauling, Phys. Rev. **36**, 430 (1930).

TABLE III. Comparison of natural abundance ratios with peak intensity ratios of the CO isotopes.

Abundance ratios[10]	Intensity ratios
$C^{12}O^{16}/C^{12}O^{16}=89$	51
$C^{12}O^{16}/C^{12}O^{18}=5.4$	4.3
$C^{12}O^{18}/C^{12}O^{17}=5.5$	4.2

motion in this type of solid is suitable: $V(\theta)=V_0(1-\cos 2\theta)$. This function has a barrier height: $V(\theta=90°)=2V_0$. We may expand the potential function in a power series of θ and retain only the leading term if we assume small angle displacements,

$$V(\theta)=V_0(1-\cos 2\theta)\cong 2V_0\theta^2.$$

This is therefore a harmonic approximation, with the rotational (librational) force constant $k_r=4V_0$. The librational frequency is related to k_r and the moment of inertia by $\nu=(1/2\pi c)(k_r/I)^{\frac{1}{2}}$. Inserting $\nu_c-\nu(C^{12}O^{16})=70$ cm^{-1} and the moment of inertia of CO, $1.45\cdot10^{-39}$ g cm^2, we find $k_r=0.025\cdot10^{-11}$ d-cm. Using this force constant the potential barrier to rotation in the solid ($2V_0$) is calculated to be 1.8 kcal/mole.[14]

It remains to seek a criterion by which the derived bending force constant (or the barrier to rotation) can be evaluated. Few librational force constants are known. Hornig and Osberg[15] have estimated the librational force constant for solid HCl to be 0.03–$0.04\cdot10^5$ d/cm (or about 0.08–$0.10\cdot10^{-11}$ d-cm). Zimmermann and Pimentel[16] have estimated the force constant for bending the hydrogen bond in ice to be about $0.09\cdot10^5$ d/cm ($0.08\cdot10^{-11}$ d-cm) and Miyazawa and Pitzer[17] find this force constant in formic and acetic acid dimers to be $0.03\cdot10^{-11}$ d-cm. These figures do no more than indicate that the value of $0.025\cdot10^{-11}$ d-cm for the librational force constant of CO in the solid is not unreasonable.

Translation-Rotation and Vibration

In the preceding sections our calculations have shown that *it is reasonable to assign the broad feature ν_c at about 2208 cm^{-1} to combinations of the vibrational mode with both translational and rotational modes.*

Combination features similar to the ones reported for solid CO have been observed in other simple molecular crystals. Vegard,[18] in studying the electronic spectrum of solid N_2, observed spectral spacings of 40 and 69 cm^{-1}. He assigned these spacings to the excitation of librational motions of the crystal. The infrared absorption of crystalline N_2 also shows this structure, and following Vegard, these features have been assigned to libration-vibration combinations.[19]

The present work suggests that consideration should be given to the assumption that this structure is due to combinations of vibration with translation (as well as, or instead of, libration). A calculation identical to that performed for carbon monoxide (using an r^{-6}, r^{-9} potential function) yields a predicted heat of sublimation of 1.0 kcal/mole. Again this is in remarkable agreement with the heat of vaporization, 1.3 kcal/mole.[12] Thus the broad absorptions of solid nitrogen could be caused, in part, by combinations involving translations.

In the infrared absorption of thick deposits of solid N_2O and CO_2 Dows[20] observed broad bands with centers located about 65 and 78 cm^{-1} higher in frequency than the fundamental bending mode. Dows assigned these bands to combinations of librational motions with the bending mode. Again these bands could be assigned as combinations involving translations, as far as heats of vaporization are concerned. In the case of CO_2, however, the crystal selection rules are such that these combinations are forbidden by symmetry. Consequently the assignment of Dows is favored. The same is probably true for N_2O in view of similarities to CO_2.

Convincing evidence that translational modes in combination with vibrational modes contribute to the spectrum of solid hydrogen has been presented by Welsh *et al.*[21] In the infrared spectrum of solid hydrogen sharp features clearly identify the rotational combinations. Additional broad absorption features (not unlike those found in CO, N_2, N_2O, and CO_2) are assigned to a combination of the (inactive) molecular vibration with translational modes of the crystal.

We conclude that combinations between vibration and translational modes contribute broad absorption features to the infrared spectra of solid H_2, CO, N_2, and possibly other molecular crystals.

Matrix Shift

There is a small decrease in the frequency of the fundamental mode ($\Delta\nu$) when gaseous CO is condensed to solid. Recent studies of such frequency shifts in terms of the solute-solvent interactions give promise of greater insight into the nature of intermolecular forces.

An early theory for explaining condensed phase frequency shifts is expressed in the Kirkwood-Bauer-

[14] One condition for accepting the harmonic approximation is that the displacement θ is small. The calculated force constant permits an estimate of the implied average square displacement in the ground state: $(\bar{\theta}^2)^{\frac{1}{2}}=0.3$ rad. Since the first anharmonic term is of order θ^4, the harmonic approximation is undoubtedly good enough for our purposes.

[15] D. F. Hornig and W. E. Osberg, J. Chem. Phys. **23**, 662 (1955).

[16] R. Zimmermann and G. C. Pimentel, Spectrochim. Acta (to be published).

[17] T. Miyazawa and K. S. Pitzer, J. Am. Chem. Soc. **81**, 74 (1959).

[18] L. Vegard, Nature **124**, 267 (1929); **125**, 14 (1930).

[19] A. L. Smith, W. E. Keller, and H. L. Johnston, Phys. Rev. **79**, 728 (1950).

[20] D. A. Dows, Spectrochim. Acta **13**, 308 (1959).

[21] A. P. Gush, W. F. J. Hare, E. J. Allin, and H. L. Welsh, Can. J. Phys. **38**, 176 (1960).

Magat relation,[22,23]

$$\frac{\nu_0-\nu}{\nu_0}=C\frac{(\epsilon-1)}{(2\epsilon+1)}, \tag{5}$$

where ν_0=gas phase frequency, ν=condensed phase frequency, ϵ=dielectric constant of the medium, and C=a property of the medium, usually determined empirically. This equation has been found to be inadequate in many cases.[24] Coulson[25] has remarked that this is not surprising since only bulk properties of the medium are treated by Eq. (5). Surely nearest-neighbor interactions can be expected to be important as well. Pullin[26] considers the influence of the medium which can be ascribed to interaction involving higher (anharmonic) terms in the expansions of the potential function for vibration and also in the electric moment. Unfortunately, the resulting relation contains several parameters difficult to evaluate and has found only limited use.

Buckingham[27] treats the problem quantum mechanically in a more general fashion for a diatomic molecule in a solvent. The interaction potential of the solvent-solute system is expanded in a power series of ξ, a quantity proportional to the internuclear displacement of the atoms of the solute molecule.

$$U=U_e+U'\xi+\tfrac{1}{2}U''\xi^2+\cdots. \tag{6}$$

The terms in (6) depending upon ξ are introduced as perturbations on the Hamiltonian which describes the anharmonic oscillator. From the perturbed energy levels the frequency shift is found to be

$$(\Delta\nu)_{m,n}=(n-m)\frac{B_e}{hc\omega_e}\left\{U''-\frac{3AU'}{\omega_e}\right\}. \tag{7}$$

In Eq. (7), the values m, n identify the initial and final vibrational states, B_e is the rotational constant, ω_e the unperturbed vibrational frequency, A the anharmonicity constant, h is Planck's constant, and c is the velocity of light. We have examined the applicability of Eq. (7) to the spectrum of solid CO.

TABLE IV. Vibrational constants of $C^{12}O^{16}$.

$C^{12}O^{16}$ (solid)	$C^{12}O^{16}$ (gas)
$\omega_e=2160.8\ cm^{-1}$	$\omega_e=2169.8\ cm^{-1}$
$\omega_e x_e=\ 11.3\ cm^{-1}$	$\omega_e x_e=\ 13.3\ cm^{-1}$
$\nu_0=2138.1\ cm^{-1}$	$\nu_0=2143.3\ cm^{-1}$

[22] W. West and R. T. Edwards, J. Chem. Phys. **5,** 14 (1937). This paper contains the equations for the dielectric shift attributed to John G. Kirkwood.
[23] H. Bauer and M. Magat, J. phys. radium **9,** 319 (1938).
[24] L. J. Bellamy, Spectrochim. Acta **14,** 193 (1959).
[25] C. A. Coulson, Proc. Roy. Soc. (London) **A255,** 69 (1960).
[26] A. D. E. Pullin, Spectrochim. Acta **13,** 125 (1958); Proc. Roy. Soc. (London) **A255,** 39 (1960).
[27] A. D. Buckingham, Proc. Roy. Soc. (London) **A248,** 169 (1958); **A255,** 32 (1960).

TABLE V. Calculated and observed frequencies for solid CO.

	Calculated	Observed	$\Delta\nu$
$C^{12}O^{16}$	(2138.1)	2138.1	(0)
$C^{12}O^{17}$	2111.2	2112.3	+1.1
$C^{13}O^{16}$	2091.1	2092.3	+1.2
$C^{12}O^{18}$	2087.1	2088.4	+1.3

Since the quantities B_e/ω_e^2 and A/ω_e are invariant with isotopic change, Buckingham's theory predicts the value of $(\Delta\nu)_{m,n}/\nu_{m,n}$ to be the same for all isotopes. For $\nu(C^{12}O^{16})$, $(\Delta\nu)_{m,n}/\nu_{m,n}$ is $2.5\cdot10^{-3}$ and for absorptions of the other isotopes, $C^{12}O^{17}$, $C^{12}O^{18}$ and $C^{13}O^{16}$, it is $1.8\pm0.1\cdot10^{-3}$. The shifts for $C^{12}O^{17}$, $C^{12}O^{18}$, and $C^{13}O^{16}$ are the same within experimental error, in agreement with the theory. The shift for $C^{12}O^{16}$ is larger than that of the other isotopes by an amount outside the experimental uncertainties.

A part of the discrepancy among the frequency shifts for the fundamentals of the various isotopes could be caused by change in the anharmonicity of CO as it is condensed. Hence we have calculated both ω_e and $\omega_e x_e$ for $C^{12}O^{16}$ in the solid. These are compared to the gas phase values in Table IV. The most striking aspect of the result is probably the smallness of the change in $\omega_e x_e$.

With these experimental values of ω_e and $\omega_e x_e$ for solid $C^{12}O^{16}$, we have calculated the expected frequencies of the isotopically substituted molecules. These are compared with the observed values in Table V. We see that the lack of correlation between $C^{12}O^{16}$ and the other three isotopic species remains. The explanation of this discrepancy and, no doubt, of the failure of the Buckingham treatment for $C^{12}O^{16}$ is undoubtedly concerned with the coupling of $C^{12}O^{16}$ with identical nearest neighbors. The isotopically substituted molecules are "isolated" in an environment of vibrationally dissimilar molecules.[28]

The proposal that $C^{12}O^{16}$ molecules are coupled in their vibrations can be tested by assigning the discrepancies in Table V entirely to coupling. This shift provides, then, a coarse estimate of the interaction force constant in solid CO. In the first order of approximation, two oscillators coupled by a force constant δk interact in phase and out of phase with effective force constant $k\pm\delta k$. The average shift of $C^{12}O^{16}$ relative to the other isotopes is 1.2 cm^{-1}. Therefore,

$$\frac{\nu+\delta\nu}{\nu}=\left(-\frac{k+\delta k}{k}\right)^{\frac{1}{2}}, \tag{8}$$

where $\nu+\delta\nu$ is the observed absorption at 2138.1 cm^{-1} and $\delta\nu$ is the anomalous shift of 1.2 cm^{-1}. With a

[28] H. J. Hrostowski and G. C. Pimentel, J. Chem. Phys. **19,** 661 (1951).

reasonable value of k, we find $\delta k = 0.021 \cdot 10^5$ d/cm. This value is in excellent (indeed, fortuitous) agreement with the intermolecular force constant calculated earlier in this paper, $k_t = 0.020 \cdot 10^5$ d/cm. The calculation adds a convincing point of self-consistency in the assignment of the translational character to the broad band ν_c together with the interpretation of the anomalous matrix shift of $C^{12}O^{16}$ as coupling between identical neighbors.

Bandwidths

The half-width of the band assigned to the $C^{12}O^{16}$ fundamental mode in the spectrum of solid CO was found to be 1.5 cm^{-1}. The half-widths of the features caused by $C^{13}O^{16}$ and $C^{12}O^{18}$ were slightly less, 1.2 cm^{-1}. The bandwidths for molecular crystals are usually attributed to anharmonic coupling between vibrational and low-frequency lattice modes.[3] This interpretation probably contains the explanation for the larger bandwidth of the $C^{12}O^{16}$ mode, since this isotopic species would couple most effectively with the lattice modes of the $C^{12}O^{16}$ crystal.

The combination features ν_c have a much larger bandwidth, ($\nu_{\frac{1}{2}} = 40$ cm^{-1}). We offer the tentative explanation that the band is composed of a large number of overlapping combination transitions (20 are expected). Each of these may be diffuse because of coupling with lower-frequency lattice modes.

CONCLUSIONS

Since the surprisingly complex infrared spectrum of solid CO can be assigned with reasonable confidence, the data presented here are of particular quantitative value. There are not many molecular crystals for which intermolecular force constants are known and even fewer for which anharmonicity constants have been estimated.

The possibility that translational modes contribute broad absorptions through combinations has received relatively less attention than the corresponding effects involving librational modes. This no doubt reflects the trend set by the early studies of hydrogen compounds for which there are low moments of inertia. When the moments of inertia are not low, the translational modes may well be comparable in frequency to the librational modes. It is well to remember that the usual relationships between intramolecular stretching and bending force constants are not necessarily to be expected because in crystals, the same intermolecular potential function which restrains translational movement is acting to restrain rotational movement (with the probable exception of hydrogen-bonded crystals). Local configurational factors will determine, then, whether the translational or the librational force constant is the larger.

The discovery of broad satellite bands in the spectra of crystalline H_2, N_2O, CO_2, N_2, and now CO suggests that such broad bands are common. No doubt they will be found in the spectra of thick samples of crystals of more complicated molecules, though they will be more difficult to identify.

ACKNOWLEDGMENTS

We would like to thank Dr. D. A. Dows for helpful discussions concerning this work. Grateful appreciation is expressed for research support by the American Petroleum Institute Research Project 54 and the U.S. Air Force through AFOSR of the Air Research and Development Command.

Infrared Spectra of Carbon Monoxide as a Solid and in Solid Matrices

ARTHUR G. MAKI

National Bureau of Standards, Washington 25, D.C.

(Received February 13, 1961)

The fundamental infrared absorption frequency of several isotopes of CO has been observed in solid carbon monoxide and in the solid matrices N_2, Ar, and CH_4. In addition, the overtone in solid carbon monoxide has been measured. It is shown that frequency shifts due to isotopic substitution in the solid state follow the formulas developed for the gas phase only when molecules of the same isotopic species are not adjacent to each other, i.e., only in dilute solutions.

INTRODUCTION

THE examination of the infrared spectrum of solid materials is becoming more and more common; still, certain aspects of the effect of the environment upon the infrared spectrum are not well understood. The solid state affords a variety of possible ways in which the spectra might be made to deviate from that expected of an isolated molecule. A number of papers[1–6] have shown various ways in which spectra might differ from the predictions for isolated molecules. There is, however, a great deal of uncertainty regarding the importance of these effects. In fact most treatments completely ignore all effects except the splitting of degenerate modes due to crystal symmetry.

As yet, few precise frequency studies of solid-state infrared spectra have been made. This is partly due to the large natural linewidths encountered in solids, and partly due to the comparative dearth of instruments of sufficient resolving power.

It is well known that the linewidths of solids are greatly reduced upon lowering the temperature. In our studies we have found that in some cases the natural linewidth at low temperatures becomes smaller than 0.9 cm^{-1}. With such sharp lines it is possible to obtain quite precise measurements of the frequencies of absorption bands.

In an effort to determine both the reliability of isotope rules for solids and the extent of change which the potential function undergoes upon going from the gas to solid phase, we have made a study of the fundamental and overtone regions of carbon monoxide in the solid state around 20°K. In this study, the overtone and fundamental of the normal $C^{12}O^{16}$ molecule have been measured, as well as the fundamental vibrational frequencies of $C^{12}O^{17}$, $C^{13}O^{16}$, and $C^{12}O^{18}$ in their normal isotopic abundances, which are, respectively 0.039%, 1.1%, and 0.204%. A study of the fundamentals in various matrices was also made.

The carbon monoxide molecule was chosen as the subject of this study for several reasons. (a) It is one of the simplest molecules. The simplicity of the vibrational spectrum removes all likelihood of interactions between different vibrational modes. (b) The gas phase spectrum is very well known. (c) The small dipole moment and other evidence indicates that CO is not very likely to interact with its neighbors in the solid, and hence is a rather unfavorable case for any interactions arising from the proximity of molecules in the solid state. (d) The similarity of CO to N_2 with respect to size and crystal structure makes CO an ideal molecule to use in a nitrogen matrix. (e) The small size of the CO molecule is also expected to allow it to fit readily into other host lattices such as argon.

EXPERIMENTAL

The spectrometer used in this work was a Perkin-Elmer 112-G grating instrument with a 1875 lines/in. grating and a NaCl fore-prism. The low-temperature cell was a Dewar of standard design with a liquid nitrogen radiation shield. The sample window was a CsBr crystal clamped to the cold block with indium metal gaskets to insure good thermal contact. The gases used in this work were obtained from The Matheson Company, Inc., and were used without further purification. Initial experiments were made using a liquid air trap in the gas manifold line, but since this had no effect upon the spectra it was not used in subsequent experiments.

Due to the uncertain geometry of the apparatus, it is not possible to give a very accurate estimate of the film thicknesses used. In some of the figures the total amount of gas deposited is given; this deposit was not evenly distributed over the entire window and probably only 60 to 30% was actually deposited in the light beam. The rate of deposition of the films was varied somewhat but was kept within the range of 50–500 micromoles of CO per hour. In the solid solution or matrix work, various solvent-to-solute ratios were used ranging from 100/1 to 600/1.

The method of calibration used in this work was very simple and yet quite accurate. Fortunately, the gas phase spectrum of carbon monoxide has been very

[1] R. S. Halford, J. Chem. Phys. **14,** 8 (1946).
[2] D. F. Hornig, J. Chem. Phys. **16,** 1063 (1948).
[3] H. Winston and R. S. Halford, J. Chem. Phys. **17,** 607 (1949).
[4] T. H. Walnut, J. Chem. Phys. **20,** 58 (1952).
[5] R. M. Hexter and D. A. Dows, J. Chem. Phys. **25,** 504 (1956).
[6] J. C. Decius, J. Chem. Phys. **23,** 1290 (1955).

TABLE I. Fundamental infrared absorption frequencies for different species of CO.

Molecule	Matrix	Calculated frequency (cm^{-1}) (using $x_e\omega_e = 12.07$ cm^{-1})	Observed frequency (cm^{-1})
$C^{12}O^{16}$	N_2	2139.58	2139.56±0.06
$C^{13}O^{16}$	N_2	2092.41	2092.34±0.10
$C^{12}O^{18}$	N_2	2088.46	2088.56±0.15
$C^{12}O^{16}$	CO	2139.38	2138.44±0.09
$C^{12}O^{17}$	CO	2112.43	2112.41±0.06
$C^{13}O^{16}$	CO	2092.22	2092.19±0.05
$C^{12}O^{18}$	CO	2088.27	2088.32±0.06

accurately measured[7] and could be used to determine wavelengths in the fundamental region. The procedure used consisted of bracketing the sample absorption with a CO gas spectrum without stopping the wavelength drive mechanism. The wavelength of the sample absorption was then found by interpolation. This process was repeated 3–10 times and the results averaged. The reproducibility of this measuring procedure was very good, giving standard deviations of the order of 0.02 to 0.08 cm^{-1}. In determining the probable errors reported, these standard deviations were combined with an estimated error due to other sources.

Although the absorption lines measured had a half-intensity width of 1.0 cm^{-1} or greater, the symmetry of many of the bands made it easy to determine the band centers to within a few hundredths of a wave number. The reproducibility of the measurements substantiates this claim.

The overtone region was calibrated in a similar way using the 6-μ atmospheric water band as measured by Plyler *et al.*[8] The grating was used in second order for this while it was used in fifth order for the sample. A simple adjustment of the fore-prism allowed rapid shifting of orders without stopping the wavelength drive mechanism.

RESULTS

CO in a Nitrogen Matrix

Carbon monoxide in a matrix of solid nitrogen at 20°K displays one sharp, strong band at 2139.56 cm^{-1} which may be attributed to the vibration fundamental of the $C^{12}O^{16}$ molecule. This band is displaced to a frequency about 4 cm^{-1} below the normal gas phase frequency. For rather large film thicknesses, a band about one hundredth as strong as the $C^{12}O^{16}$ fundamental shows up at 2092.34 cm^{-1}. This band is attributed to the $C^{13}O^{16}$ molecule. About 4 cm^{-1} below this band is another which is about a fifth as strong and must be due to $C^{12}O^{18}$. The absorption due to $C^{12}O^{17}$ would be even weaker and has not been found in a nitrogen matrix. These assignments are substantiated not only by the relative band intensities but also by agreement with the calculated frequencies (see Table I).

It is unfortunate that in this work it was not possible to observe the overtone in any of the matrices because light scattering prevented observations on sufficiently thick films. The scattering was of course not such a problem for the longer wavelength region around the fundamental.

In addition to the above listed absorption bands, a very weak absorption was found at a frequency 7.30 cm^{-1} greater than the fundamental for $C^{12}O^{16}$ (see Fig. 1). This band probably can not be attributed to any reflection phenomena as was done by Dows[9] in the case of the 670 cm^{-1} band in solid CO_2. With the very low concentration of CO in the solid nitrogen matrix, the contribution of the CO to the refractive index of the solid solution would be too small to noticeably affect the reflection properties of the matrix. This band may be due to a lattice vibration of translational or librational character. It might also arise from intermolecular coupling between CO pairs which happen to be situated on adjoining sites within the crystal. Even at the largest N_2/CO ratios used in this work, 1% of the molecules will be on adjacent sites. However, since no change in the relative intensity of this satellite band was observed upon varying the N_2/CO ratio from 600/1 to 160/1, the latter explanation seems to be incorrect.

Nitrogen has a very interesting phase change at 35°K. This phase change is believed to be accompanied by a rather large decrease in the barrier to rotation of the N_2 molecules.[10] Since CO is very similar to N_2 it was hoped that the substitution of CO in a N_2 crystal might provide a means of studying this transition. Unfortunately, with our apparatus it is not possible to hold the matrix at fixed temperatures other than 5°, 20°, and 77°K. It was, however, possible to observe the changes in the spectrum as the material slowly warmed up from a low temperature. The CO absorption remained relatively unchanged as the temperature was raised from 5°K to about 35°K. At about 35°K a

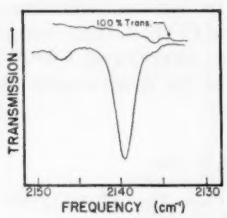

FIG. 1. CO in a nitrogen matrix at 20°K. N_2/CO=590; 110 μ moles CO.

[7] E. K. Plyler, L. R. Blaine, and W. S. Connor, J. Opt. Soc. Am. **45**, 102 (1955).
[8] E. K. Plyler, A. Danti, L. R. Blaine, and E. D. Tidwell, Natl. Bur. Standards monograph 16.
[9] D. A. Dows, Spectrochim. Acta **13**, 308 (1959).
[10] L. H. Bolz, M. E. Boyd, F. A. Mauer, and H. S. Peiser, Acta. Cryst. **12**, 247 (1959).

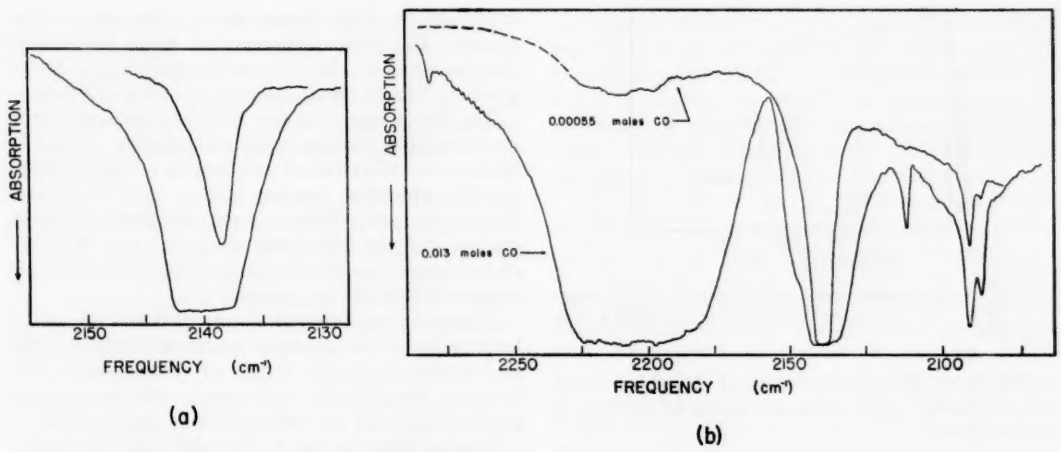

FIG. 2. Solid carbon monoxide at 20°K.

very sudden increase in bandwidth and a concomittant increase in background absorption was found. Further increases in temperature resulted in increased bandwidth and a very rapid increase in light scattering. All attempts to detect any possibility of fine structure failed. This may indicate that any fine structure is too broad or too closely spaced to be observable; or it may be a result of increased light scattering due to the phase change. Sublimation difficulties and consequent loss of thermal insulation in the apparatus prevented going to temperatures above 50°K.

Solid Carbon Monoxide

The infrared spectrum of solid CO is very similar to that of a nitrogen matrix containing CO. There is, however, no weak, sharp absorption band at a frequency slightly higher than the $C^{12}O^{16}$ fundamental. Moreover, the fundamental $C^{12}O^{16}$ absorption band is asymmetrical as may be seen in Fig. 2(a). This asymmetry, which consists of a tailing off of absorption toward higher frequencies, may be a consequence of the unisolated character of the $C^{12}O^{16}$ molecule in solid CO. All the other isotope bands are symmetrically shaped. This asymmetry of line shape could be attributed to reflection scattering. This would explain the absence of an asymmetry in the isotopic bands. Such scattering is, however, expected to cause the apparent absorption to taper off in the direction of increasing wavelength,[11] whereas the opposite behavior is observed.

Since thicker effective CO films were possible with pure CO, the $C^{12}O^{17}$ fundamental was observed; also the overtone of the $C^{12}O^{16}$ molecule was measured at 4252.7 cm^{-1}. This yields an anharmonicity constant slightly smaller than that found in the gas phase. It was not possible to observe the overtones of the other isotopic bands due to light scattering difficulties.

[11] W. C. Price and K. S. Tetlow, J. Chem. Phys. **16,** 1157 (1948).

In the very heavy films of CO, the presence of a very broad absorption around 2210 cm^{-1} and a very sharp absorption at about 2281 cm^{-1} was observed as shown in Fig. 2(b). The latter band is due to a small amount of carbon dioxide which is expected to be one of the principal impurities in the sample. The forbidden Q branch of $C^{13}O_2^{16}$ is located at about 2283 cm^{-1} in the gas phase. Pimentel and Ewing discuss the nature of the broad band in a paper appearing elsewhere in this issue.

CO in an Argon Matrix

Carbon monoxide trapped in an argon matrix at 5°K was found to have a rather asymmetric absorption band (see Fig. 3). As the temperature was increased, the absorption frequency seemed to decrease slightly and a subsidiary absorption appeared at a position 10.8 cm^{-1} from the main band in the direction of increasing frequency.

CO in a Methane Matrix

Methane has a strange phase transition at 20°K, the nature of which has been the subject of numerous papers.[12–15] This transition was originally thought to involve a sudden change in rotational freedom. However, the inability of both x ray[13] and NMR[14] to detect any changes seems to indicate that this is a transition involving the orientation of the hydrogen atoms.[15] The infrared spectrum of CO in a CH_4 matrix likewise fails to show any change in passing from 5° to 30°K, so that it seems unlikely that the transition involves any

[12] K. Clusius, Z. physik. Chem. (Leipzig) **B3,** 41 (1929).
[13] H. H. Mooy, Commun. Phys. Lab. Univ. Leiden **19,** 216a (1931).
[14] J. T. Thomas, N. L. Alpert, and H. C. Torrey, J. Chem. Phys. **18,** 1511 (1950).
[15] H. M. James and T. A. Keenan, J. Chem. Phys. **31,** 12 (1959).

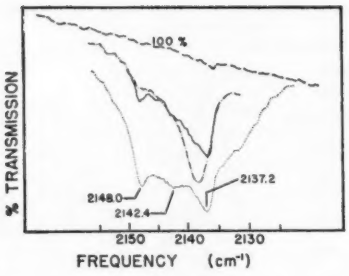

FIG. 3. CO in an argon matrix, Ar/CO=500; —— 16.5 μ moles CO at 20°K; —·— 21.6 μ moles CO at 5°K; .... 104 μ moles CO at 20°K.

sudden increased rotational freedom. A sudden broadening or change in fine structure would be expected in such an event.

Even at the lowest temperature observed, there is, however, an inexplicable complexity of the absorption spectrum. In Fig. 4 the absorption of CO in methane is shown and a definite shoulder may be seen at 5.2 and 3.7 cm^{-1} above and below the absorption maximum respectively.

DISCUSSION

Although CO is not expected to be very greatly perturbed by neighboring molecules in the solid state, it is evident that in solid carbon monoxide the fundamental of the most abundant molecule, $C^{12}O^{16}$, is displaced to a lower frequency by about 1 cm^{-1}. This displacement has been determined (see Table I) by calculating the unperturbed frequency from the other isotopically substituted molecules which are assumed to be unperturbed. These calculations have been made by using the relations

$$x_e'\omega_e'/x_e\omega_e=(\omega_e'/\omega_e)^2=\mu/\mu' \qquad (1)$$

and

$$\nu_0=\omega_e-2x_e\omega_e, \qquad (2)$$

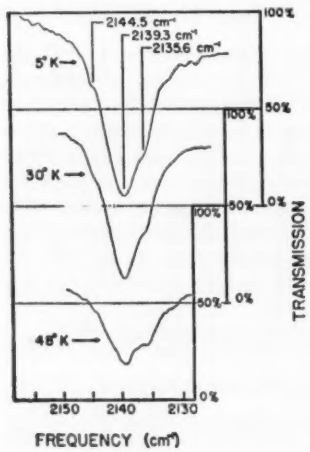

FIG. 4. CO in methane at 5°, 30°, and 48°K; CH_4/CO=217; 29.2 μ moles CO.

where μ is the reduced mass and ν_0 is the observed frequency. The prime indicates the value for another isotopic species. The column labeled "Calc. Freq." gives the best fit obtainable from the observed data.

The displacement of the $C^{12}O^{16}$ fundamental from the calculated position is evidently due to a coupling between the vibrations of neighboring molecules. Since the less abundant isotopic species have vibrational frequencies quite different from the most abundant species, they are effectively decoupled and their observed frequencies are essentially those of the molecule completely isolated in a matrix.

The agreement between all observed and calculated frequencies for the nitrogen matrix substantiates this explanation. In the N_2 matrix all isotopic species are isolated; consequently, the isotopic shift is correctly predicted for even the most abundant species $C^{12}O^{16}$.

In going from the gas to the solid state, the fundamental frequency of CO is only changed by about 0.5%, whereas the anharmonicity constant is changed by ten times this proportion (see Table II). However,

TABLE II. Infrared absorption frequencies of carbon monoxide in various matrices.

Phase	Fundamental (cm^{-1})	Overtone (cm^{-1})	$x_e\omega_e$ (cm^{-1})
Gas	2143.274	4260.06	13.24
Solid	2138.44±0.09	4252.74±0.40	12.07±0.30
N_2 matrix	2139.56±0.06	...	...
Ar matrix at 5°K	2138.67±0.30	...	...
Ar matrix at 20°K	2137.17±0.30	...	...
CH_4 matrix	2139.3±0.4	...	...

if we calculate the anharmonicity constant from the calculated unperturbed fundamental frequency, the anharmonicity constant is found to nearly coincide with that of the gas. It is unfortunate that no anharmonicity constant could be measured for an unperturbed molecule in order to determine whether the anharmonicity constant is also affected by the coupling.

The evidence presented by these measurements seems to indicate that there are at least two different mechanisms by which the frequencies of molecules in the solid state are perturbed. First there is a coupling between the vibrations of different molecules. Since the coupling is at least in part selective with respect to isotopic species, it is apparently restricted to molecules with the same vibrational frequencies. This is probably a dipole-dipole coupling similar to that treated by Decius[6] in the case of nitrate and carbonate salts. This coupling must contribute only a small part of the total energy of the solid and thus would not necessarily be expected to be related to the forces involved in any translational or librational type of lattice vibrations. If this were not so, then one would expect to find a

strong rejection of other isotopic species upon formation of the solid. Furthermore, since such a strong fractionation of isotopic species is not found in going to the solid state, it seems reasonable to conclude that the forces responsible for translational and librational crystal modes must be relatively independent of isotopic species.

The other perturbation is the well-known solvent effect. Every host crystal studied here produced nearly the same frequency displacement; consequently, one may conclude that the same factors are responsible in all cases. This means that interactions with the dipole or quadrupole moments of the host may be eliminated, because only CO is polar and argon has no quadrupole moment outside of the nucleus. As a consequence, only certain induction and dispersion terms in the potential energy of the solute molecule may be responsible for the frequency shifts. This, of course, neglects repulsion terms which would give a blue shift. Both Buckingham[16] and Pullin[17] have used these terms in deriving equations which relate the dielectric properties of a solvent to the frequency shifts of the solute. Buckingham's equation predicts an approximately linear relationship between frequency shift and $(\epsilon-1)/a^3(2\epsilon+1)$, where a is often considered to be the radius of the cavity in which the solute is located. Our data fits this relationship, but the small number of points and the inaccuracy of all constants involved are such that this agreement can be considered little more than fortuitous.

The presence of some fine structure and the broadness of the absorption band in argon and methane matrices may be due to several causes either individually or collectively. For instance, the CO molecule may have several possible orientations or different types of lattice and/or interstitial sites which would give rise to differing frequency shifts. In addition, a number of lattice vibrational or librational modes may be responsible for the fine structure. Hexter[18] has found a great deal of fine structure in the infrared absorption of GeH_4, CH_4 and NH_3 in various solid solutions which seems to be due to rotation in the solid. Rotation has similarly been shown for H_2O in solid matrices.[19]

The small size of the CO molecule makes it quite possible that the barrier to rotation in a methane or argon matrix is rather low. On the other hand, it is known that molecules in solid CO and N_2 have a rather high rotational barrier at 20°K. This may account for the marked difference in bandwidth for these two types of matrices. It must be remembered, however, that the band envelope of CO in methane is virtually unchanged in breadth and shape in going from 5° to 30°K. This would not be expected if any low-frequency modes were responsible for the bandwidth and fine structure.

CONCLUSIONS

In dealing with solids where the interatomic distances and the relative orientation of molecules are well known, it is to be hoped that frequency shifts such as are found here for the CO molecule may be quantitatively explained and predicted. Although this is not yet possible, this work does at least show that the isotopic shifts in vibrational frequency which are calculated from the gas phase or isolated molecule formulas are valid in the case of dilute solid solutions. This is important for the calculation of force constants where the number of force constants exceeds the number of vibrations as in the case of the XYZ linear molecule.

[16] A. D. Buckingham, Proc. Roy. Soc. (London) **A255,** 32 (1960); *ibid.* **A248,** 169 (1958).
[17] A. D. E. Pullin, Proc. Roy. Soc. (London) **A255,** 39 (1960).
[18] R. M. Hexter and D. E. Milligan, Fourth International Symposium on Free Radical Stabilization, Washington, D. C., September 1959.
[19] E. Catalano and D. E. Milligan, J. Chem. Phys. **30,** 45 (1959).

The OH Yield in the Co^{60} γ Radiolysis of HNO_3

H. A. MAHLMAN

Oak Ridge National Laboratory, Chemistry Division, Oak Ridge, Tennessee*

(Received January 16, 1961)

The Co^{60} γ-ray radiolysis of concentrated aqueous solutions has been investigated and interpreted as the composite of two mechanisms,

a molecular process $HNO_3 \sim\!\!\!\rightarrow HNO_3^* \rightarrow HNO_2 + \frac{1}{2}O_2$

and a radical process $HNO_3 \sim\!\!\!\rightarrow HNO_3^* \rightarrow OH + NO_2$.

Designation of these mechanisms as molecular and radical is a consequence of the products detected. The existence of these two decomposition mechanisms was gleaned from the determination of the $G(H_2)$, $G(O_2)$, G_{OH}, $G(Ce^{+3})_{No\ Tl^+}$, and $G(Ce^{+3})_{Tl^+}$ and a comparison of these yields with those determined in comparable aqueous $NaNO_3$ solutions. The G_{OH} observed in HNO_3 solutions was found to be directly proportional to the HNO_3 concentration rather than a constant as was observed in comparable $NaNO_3$ solutions. The radical process is appreciable, increasing from 0 at zero HNO_3 concentration to 1.89 at 7 M HNO_3. The data present for the first time evidence of a direct effect upon concentrated aqueous nitrate solutions that is directly proportional to nitrate concentration.

INTRODUCTION

THE radiation chemistry of dilute aqueous solutions has been interpreted upon the premise of solvent decomposition where the radiation-induced chemical changes have been ascribed to the action and interaction of the initial products H and OH. When concentrated solutions are irradiated some product yields may increase; for example, nitrite ion in concentrated nitrate solutions. These higher nitrite yields cannot be explained by currently accepted radical yields; therefore, they have been designated as direct action yields.[1] This paper presents and discusses the results of studies on irradiated concentrated HNO_3 solutions. From the data presented, the radiolytic gas yields of hydrogen and oxygen and the Ce^{+3} yields from acidic ceric solutions, a mechanism for the HNO_3 decomposition is postulated.

EXPERIMENTAL

The chemicals, reagent-grade Baker and Adamson nitric acid and sodium nitrate, G. Frederick Smith analytical reagent ceric acid sulfate, and A. D. McKay cp grade thallous sulfate, were used without purification. The Baker and Adamson cp sulfuric acid was redistilled in the presence of ceric ion using only the middle $\frac{1}{3}$ portion for the preparation of a ceric stock solution. Water from a Barnstead still was purified by distillation from an acid dichromate solution, a basic permanganate solution, and then an all silica system. Storage was in silica vessels.

Acidic ceric solutions for irradiation were prepared from the ceric stock solution to contain 0.0004 M ceric ion, 0.4 M sulfuric acid, and the desired concentration of nitric acid. Thallous ion was added to identical solutions to make the solution 10^{-3} M thallous ion.

Nitric acid solutions 0.001 to 7.0 M, containing 10^{-3} M KBr to protect the molecular hydrogen formed from OH radical attack, were also prepared. These samples were deaerated by repeated freezing, evacuating to 10^{-6} mm pressure and thawing. The residual gas volume per sample was reduced to less than 0.002 cc STP.

The acidic ceric solutions were irradiated in a 100 curie cobalt-60 γ-ray source while the deaerated nitric acid samples were irradiated in a 600 curie cobalt-60 γ-ray source. The dose rates of these sources were determined by the Fricke dosimeter assuming 15.60 ferrous ions were oxidized per 100 ev of absorbed energy.[2] The additional energy absorption due to the added nitric acid was calculated.[3] The yields, G(product), defined as the number of ions or molecules formed per 100 ev of absorbed energy, were calculated from the total absorbed energy. All analytical measurements were made directly on a Cary recording spectrophotometer. The iron was determined at 3050 A using a molar extinction coefficient of 2240 at 25°C[2] while the ceric ion concentration in the presence of nitrate ion was determined at 3200 or 3330 A using the 25°C molar extinction coefficients of 5580 at 3200 A and 5359 at 3330 A.[3]

The cells, used for the irradiation of acid-ceric solutions, had special fused quartz windows that were not colored in the ultraviolet region by γ radiation and therefore the irradiations and spectrophotometric analyses were made using the same cell. The $G(Ce^{+3})$ were calculated on the basis of total absorbed energy and in all cases are the average of four to eight individual determinations on two or more separately prepared solutions from different lots of nitric acid.

* Operated for the U. S. Atomic Energy Commission by Union Carbide Corporation.

[1] T. J. Sworski, J. Am. Chem. Soc. **77**, 4689 (1955).

[2] C. J. Hochanadel and J. A. Ghormley, J. Chem. Phys. **21**, 880 (1953).

[3] H. A. Mahlman and G. K. Schweitzer, J. Inorg. & Nuclear Chem. **5**, 213 (1958).

RESULTS

Radiolytic Hydrogen Yields

The yields of molecular hydrogen observed from the radiolysis of deaerated concentrated aqueous sodium nitrate and nitric acid solutions containing comparable nitrate concentrations are not significantly different (see Table I). Therefore, suppression of the molecular hydrogen yield by the nitrate solutes probably proceeds by the same mechanism. Since the corresponding $G(H_2)$ are essentially the same, the differences to be discussed later cannot be attributed to the suppression of the H_2 yields.

Radiolytic Oxygen Yields

The formation of molecular oxygen in the radiolysis of concentrated (1 *M* and greater) aqueous sodium nitrate solutions (see Table I) is assumed to be a direct action product. Direct action[1] is a term used to explain product yields in excess of that predicted by the established radical yields in water. In the case of $NaNO_3$ solutions, the NO_2^- and O_2 yields increase with increasing $NaNO_3$ concentration[4] qualitatively in agreement with the over-all reaction

$$NaNO_3 \rightsquigarrow NaNO_3^* \rightarrow NaNO_2 + \tfrac{1}{2}O_2. \qquad (1)$$

TABLE I. Hydrogen and oxygen yields from $NaNO_3$ and HNO_3.

	$G(H_2)$		$G(O_2)$	
Molarity	$NaNO_3$	HNO_3	$NaNO_3$	HNO_3
0.0012	0.42	0.43		
0.0032	0.39	0.41		
0.0079	0.39	0.37		
0.027	0.32	...		
0.031	...	0.34		
0.15	0.24	0.25		
0.31	0.19	0.19		
0.51	0.15	0.15		
0.7	0.12	...		
0.8	...	0.11	...	0.11
1.00	0.096	0.091	0.21	0.15
2.00	0.059	0.053	0.31	0.17
3.00	0.045	0.042	0.42	...
4.00	0.038	0.035	0.50	0.26
5.00	0.035	...	0.56	...
6.00	0.029	0.020	0.63	0.34
7.00	0.025	...	0.70	...
8.00	...	0.018	...	0.41

[4] H. A. Mahlman (unpublished results).

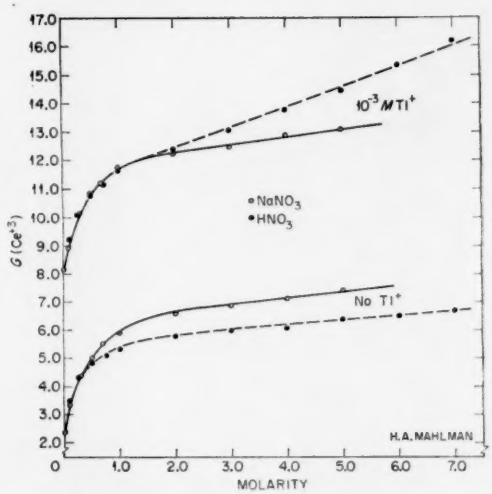

FIG. 1. Effect of $NaNO_3$ and HNO_3 on the cerous yield.

This is equivalent to that postulated by photolysis[5]

$$NaNO_3 \xrightarrow{h\nu} NaNO_2 + \tfrac{1}{2}O_2. \qquad (2)$$

The irradiation of HNO_3 solutions also produces appreciable amounts of molecular oxygen. It is assumed that decomposition of HNO_3 which leads to the formation of O_2 is a direct effect similar to that observed in $NaNO_3$ solutions viz.,

$$HNO_3 \rightsquigarrow HNO_3^* \rightarrow HNO_2 + \tfrac{1}{2}O_2. \qquad (3)$$

On this assumption the data presented in Table I indicates that the direct effect which forms molecular oxygen in HNO_3 solutions is less than that for comparable $NaNO_3$ solutions (reaction 1>reaction 3). The experiments with acid ceric solutions support this conclusion (see Fig. 1).

Ceric Reduction in Ce^{+4}—0.4 *M* H_2SO_4—$NaNO_3$ Solutions

During the cobalt-60 γ-ray irradiation of a 0.4 *M* sulfuric acid solution containing ceric ions, the reduction of the ceric ions is an indirect process illustrated by the following mechanism[6]:

$$H + Ce^{+4} \rightarrow Ce^{+3} + H^+ \qquad (4)$$

$$OH + Ce^{+3} \rightarrow Ce^{+4} + OH^- \qquad (5)$$

$$H_2O_2 + Ce^{+4} \rightarrow Ce^{+3} + H^+ + HO_2 \qquad (6)$$

$$HO_2 + Ce^{+4} \rightarrow Ce^{+3} + H^+ + O_2. \qquad (7)$$

The cerous yield is slightly greater than that predicted by reactions (4)–(7) since the $G(H_2)$ is slightly de-

[5] E. Warburg, Sitzber. preuss. Akad. Wiss., Physik.-math. Kl. 1228 (1918); Chem. Abstracts **14**, 1930 (1920).
[6] A. O. Allen, Radiation Research **1**, 87 (1954).

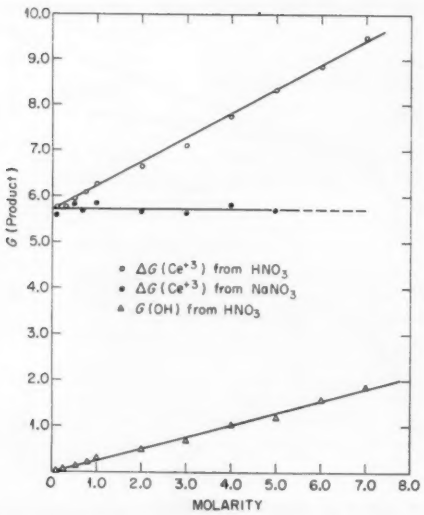

FIG. 2. $\Delta G(Ce^{+3})$ and OH yields in acidic ceric $NaNO_3$ and HNO_3 solutions as a function of nitrate concentration.

pressed by the ceric ions scavenging H atoms that normally form molecular (H_2).[7] The additional term is $2[0.45-G(H_2)_{obs}]$; therefore, the cerous yield is given by

$$G(Ce^{+3}) = G_H + 2G(H_2O_2) - G_{OH} + 2[0.45 - G(H_2)], \quad (8)$$

where G_H, G_{OH}, and $G(H_2O_2)$ represent the yields[8] in 0.4 M H_2SO_4 solutions 3.68, 2.96, and 0.81, respectively. The ceric reduction rate is enhanced in the presence of thallous ion, since the oxidizing OH radical is converted into a reductant[9] illustrated as follows:

$$OH + Tl^+ \rightarrow [Tl^{+2}] + OH^- \quad (9)$$

$$[Tl^{+2}] + Ce^{+4} \rightarrow Ce^{+3} + Tl^{+3}. \quad (10)$$

Thus the cerous yield in the presence of thallous ion becomes equal to

$$G(Ce^{+3})_{Tl^+} = G_H + 2G(H_2O_2) + G_{OH} + 2[0.45 - G(H_2)]. \quad (11)$$

Therefore, the difference in the $G(Ce^{+3})$ between the two systems, i.e., with and without thallous ion, is equal to $2G_{OH}$. The direct effects on sodium nitrate should be the same in both systems. Although an enhancement of the $G(Ce^{+3})$ occurs as the $NaNO_3$ concentration increases, this enhancement should not interfere with the OH radical yield from the radiolysis of water.

In Fig. 1 the $G(Ce^{+3})$ are presented for the systems Ce^{+4}—0.4 M H_2SO_4—$NaNO_3$ and for Ce^{+4}—0.4 M H_2SO_4—$NaNO_3$—Tl^+. The increase in the $G(Ce^{+3})_{NoTl^+}$ has been attributed to direct effects of the ionizing radiation on the dissolved solute. As previously stated a direct effect on $NaNO_3$ has been interpreted[1,4] as the formation of O_2 and NO_2^- [reaction (1)] since during the irradiation of concentrated aqueous $NaNO_3$ solutions (pH 4–5) these are the major decomposition products.[4] As readily seen, neither of these products oxidizes cerous ion in acid solution and only one of the products (NO_2^-) reduces ceric ion. Therefore, when thallous ions are added to the solution, the increase in the $G(Ce^{+3})$ is attributable to the OH radicals from the radiolysis of water. The difference $G(Ce^{+3})_{Tl^+} - G(Ce^{+3})_{NoTl^+}$ for $NaNO_3$ concentrations 0.1 to 5.0 molar was found to be constant and equal to 5.72 indicating a G_{OH} equal to 2.86.[10]

Ceric Reduction in Ce^{+4}—0.4 M H_2SO_4—HNO_3 Solutions

Figure 1 also presents the $G(Ce^{+3})$ for the systems Ce^{+4}—0.4 M H_2SO_4—HNO_3 and Ce^{+4}—0.4 M H_2SO_4—HNO_3—Tl^+. When HNO_3 is the added solute, the $G(Ce^{+3})_{NoTl^+}$ is somewhat less than that observed for comparable $NaNO_3$ concentrations. However, in the presence of Tl^+, the $G(Ce^{+3})_{Tl^+}$ in solutions containing HNO_3 is considerably larger than that observed for equal $NaNO_3$ concentrations greater than 1 molar. In these HNO_3 solutions the difference $G(Ce^{+3})_{Tl^+} - G(Ce^{+3})_{NoTl^+}$ is not constant and indicates that OH radicals are formed in addition to the OH radicals from the radiolysis of water. As shown in Fig. 2, an extrapolation of the $\Delta G(Ce^{+3})$ to zero HNO_3 concentration results in the same G_{OH} as was observed in $NaNO_3$ solutions, namely 2.86.

DISCUSSION

From the results presented in Table I and Fig. 1, one may conclude that HNO_3 decomposes by two mechanisms as given by the following equations:

$$\text{molecular} \quad HNO_3 \rightsquigarrow HNO_3^* \rightarrow HNO_2 + \tfrac{1}{2}O_2, \quad (3)$$

$$\text{radical} \quad HNO_3 \rightsquigarrow HNO_3^* \rightarrow OH + NO_2. \quad (12)$$

The term molecular is used to describe reaction (3) since the products are molecules or ions while the products of reaction (12) are radicals. The radical process is, as direct action effects are generally considered to be, directly proportional to the concentration. These conclusions will now be discussed.

The O_2 and NO_2^- yields from irradiated $NaNO_3$ solutions indicate that overall reaction (1) reflects a direct action stoichiometry. If a similar stoichiometry is assumed for HNO_3 we may then conclude that since the $G(O_2)_{HNO_3}$ is less than $G(O_2)_{NaNO_3}$ for solutions of equal nitrate concentrations the amount of NO_2^- formed in the HNO_3 solution will also be less. This will

[7] H. A. Mahlman, J. Am. Chem. Soc. **81,** 3203 (1959).
[8] H. A. Mahlman and J. W. Boyle, J. Am. Chem. Soc. **80,** 773 (1958).
[9] T. J. Sworski, Radiation Research **4,** 483 (1956).
[10] H. A. Mahlman, J. Phys. Chem. **64,** 1598 (1960).

be reflected by a decrease in the $G(Ce^{+3})$ for Ce^{+4}—0.4 M H_2SO_4—HNO_3 solutions with regard to the comparable $NaNO_3$ solutions. The data in Fig. 1 substantiate this conclusion. The radical mechanism, reaction (12), will have no effect on the $G(Ce^{+3})_{NoTl^+}$ in the Ce^{+4}—0.4 M H_2SO_4—HNO_3 solution. The OH is an oxidant and the NO_2 is a reductant and since these are equivalent no net effect is noted.

When Tl^+ is added, however, reaction (12) readily exerts itself. Figure 1 illustrates the rapid increase of the $G(Ce^{+3})_{Tl^+}$ which clearly indicates that more OH radicals are generated than the radiolysis of H_2O predicts. The OH radicals generated by the radiolysis of HNO_3 and water are readily scavenged by Tl^+ and are effectively converted into reductants. To determine the extent of reaction (12), it is necessary to correct the $\Delta G(Ce^{+3})$ caused by conversion of the OH radicals, from the radiolysis of H_2O, into reductants. The stoichiometry of reaction (12) indicates that in the presence of Tl^+, $\frac{1}{2}$ of the net increase is due to the OH. The equation for OH production from HNO_3 by reaction (12) then becomes equal to

$$\tfrac{1}{2}\{[G(Ce^{+3})_{Tl^+}-G(Ce^{+3})_{NoTl^+}]-5.72\}.$$

A plot of the G_{OH} vs HNO_3 concentration, Fig. 2, shows that this effect is directly proportional to concentration as direct effects are generally assumed to be, and that at zero HNO_3 concentration the effect is zero. These data represent the first data obtained in a nitrate system that show a direct proportionality relationship between product yield and nitrate concentration.

From data presented in Fig. 1 one may logically reason for the two methods of direct action. If only reaction (3) took place, then the $G(Ce^{+3})_{Tl^+}$—$G(Ce^{+3})_{NoTl^+}$ should be constant and the difference a measure of the G_{OH} from water radiolysis. If only reaction (12) took place then $G(Ce^{+3})_{NoTl^+}$ should be essentially constant and equal to 2.34. The OH and NO_2 would cause equivalent oxidation and reduction of Ce^{+3} and Ce^{+4} and no net change in the Ce^{+4} concentration over and above that caused by water radiolysis should occur. Furthermore, if only reaction (12) occurred, no O_2 yield would be obtained contrary to the observance of the O_2 yields reported in Table I. It should also be pointed out that the Co^{60} γ-radiolysis products of HNO_3 [reactions (3) and (12)] are the same as have been reported for the thermal decomposition of nitric acid.[11]

SUMMARY

The γ radiolysis of HNO_3 solutions indicates that the HNO_3 is decomposed by two mechanisms, a molecular process [reaction (3)] and a radical process [reaction (12)]. The products and yields observed are qualitatively consistent with the suggested mechanisms; however, equivalent reactions may be taking place. The mechanisms presented are gleaned from consideration of the $G(H_2)$, $G(O_2)$, $G(Ce^{+3})_{Tl^+}$, $G(Ce^{+3})_{NoTl^+}$, and G_{OH}.

The data presented in this paper exhibit the first evidence of a direct action effect upon concentrated aqueous nitrate solutions that is as direct action effects are generally expected, i.e., directly proportional to the nitrate concentration.

ACKNOWLEDGMENT

The author wishes to thank C. J. Hochanadel and P. S. Rudolph for their critical evaluation of this work and their constructive suggestions in the preparation of the manuscript.

[11] H. F. Cordes, N. R. Fetter and J. A. Happe, J. Am. Chem. Soc. **80**, 4802 (1958).

Studies of the Optical and Infrared Absorption Spectra of Rutile Single Crystals*

BERNARD H. SOFFER*†

Laboratory for Insulation Research, Massachusetts Institute of Technology, Cambridge, Massachusetts

(Received January 23, 1961)

The optical absorption of single crystals of synthetic rutile was investigated in the spectral range 1200 to 25 000 cm^{-1} from room temperature to 1000°C. The electronic absorption exhibits dichroic behavior. The edge moves toward lower energies as temperature is increased, with the shift depending upon the absorption coefficient; for a decadic absorption coefficient α' of 400 cm^{-1}, the shift is -7.1×10^{-4} ev/°K, while at 1 cm^{-1} it is -9.5×10^{-4} ev/°K. The broad band in the region of 6850 cm^{-1} which occurs in reduced rutile does not appear in fully oxidized rutile, even at high temperatures. At high temperatures an additional wavelength-independent absorption appears which can be correlated in good agreement with dc conductivity by applying the Drude-Zener theory of free carrier absorption. New bands in the 3300 cm^{-1} region are shown to stem from O—H valence vibrations. The main bands are unusually sharp, with peaks at 3277 and 3322 cm^{-1} and half-widths of 28 and 13 cm^{-1}. A satellite structure of combination and difference bands was also detected. Deuterium substitution produces an absorption band at 2442 cm^{-1}. The entire structure shows a marked dependence of the absorption on the polarization direction of the light. Some evidence is presented that these O—H groups cause a dielectric dispersion.

INTRODUCTION

RUTILE has been under scrutiny in the Laboratory for Insulation Research for a number of years. Studies[1–4] on the dielectric behavior of TiO_2 ceramics and single crystals as a function of frequency, field, and temperature, and an investigation of the electrical and optical properties of single crystals[5] have been published.

A discussion of the crystal structure of rutile (tetragonal: P_4mnm) and a review of its properties have been presented by Grant.[6] Cronemeyer[5] succeeded in correlating the low-temperature threshold of optical absorption at 3.03 ev with the activation energy of high-temperature conductivity and the maximum photoconductivity response. In reduced rutile, Cronemeyer correlated vacant oxygen sites with conductivity data and a broad band at about 1.85 μ using a model of heliumlike atoms modified by the dielectric environment.[7]

The present investigation is especially concerned with the effect of temperature on the electronic behavior of rutile as revealed by spectroscopy. At higher temperatures a thermal transfer of electrons from O^{2-} to Ti^{4+} may be considered to occur if a purely ionic description is chosen. Electronic conductivity may then be explained by electron exchange between Ti^{3+} and Ti^{4+}, possibly accompanied by hole transfer in the oxygen structure of the lattice. The electronic transfer would be analogous to the well-known electron exchange between ferrous and ferric ions located on octahedral lattice sites in magnetite.[8] In the case of rutile, enough of these carriers might be transferred at sufficiently high temperature to permit observation of transitions from these excited states and new absorptions. Simultaneously, the increased lattice vibrations should shift and broaden the whole system of original levels.

A temperature study of the eigenabsorption edge was made by Cronemeyer in the region 4000 to 5400 A with temperatures up to 775°K. These data indicated a general shift of the band edge at the rate of -6.3×10^{-4} ev/°K with an absorption coefficient of about 30 cm^{-1} (the only other optical temperature study of rutile is Schroder's[9] work on the decrease of the two refraction indices of natural, red rutile crystals with increasing temperatures from 25° to 680°C in a wavelength range from 0.7 to 0.5 μ).

The measurements discussed here cover a wavelength range from the electronic-absorption edge near 24 000 to 1200 cm^{-1}, the tail of the highest infrared vibration band. Special attention was paid to the broad band in reduced rutile and to a region near 3 μ because the activation energy of the dielectric dispersion suggested the possibility of finding an absorption band there.[4] The measurements range from room temperature to 1000°C.

SAMPLE PREPARATION AND MEASUREMENT TECHNIQUES

Sample Preparation

Boules of rutile[10] grown by flame fusion were oriented by backreflection Laue x-ray pictures to within 1 deg

* Supported in part by the Atomic Energy Commission.

† Present address: Quantatron Inc., 2520 Colorado Avenue, Santa Monica, California.

[1] A. von Hippel *et al.*, NDRC Report VII, August, 1944, and Report XI, October, 1945, Laboratory for Insulation Research, Massachusetts Institute of Technology.

[2] A. von Hippel, R. G. Breckenridge, F. G. Chesley, and L. Tisza, Ind. Eng. Chem. **38,** 1097 (1946).

[3] A. von Hippel, Revs. Modern Phys. **22,** 221 (1950).

[4] K. G. Srivastava, Technical Report 127, June, 1958, Laboratory for Insulation Research, Massachusetts Institute of Technology. Also see Phys. Rev. **119,** 516, 520 (1960).

[5] D. C. Cronemeyer, Phys. Rev. **87,** 876 (1952).

[6] F. A. Grant, Revs. Modern Phys. **31,** 646 (1959).

[7] See also D. C. Cronemeyer, Phys. Rev. **113,** 1222 (1959).

[8] E. J. W. Verwey, P. W. Haayman, and F. C. Romeijn, J. Chem. Phys. **15,** 181 (1947).

[9] A. Schröder, Z. Krist. **67,** 485 (1928).

[10] Boules courtesy of Dr. C. H. Moore of the National Lead Company, South Amboy, New Jersey; others were purchased from Linde Air Products Company, Indianapolis, Indiana.

and cut with a diamond saw into slabs of various sizes. The samples were polished by hand and specimens ranging in thickness from 18 mm to 30 μ were prepared. With thick specimens, the light between crossed polarizers could not be extinguished and the optical axis figure appeared biaxial. This strain was not discernible with x rays since the latter penetrate only a short distance into TiO_2.

Light scattering caused by polishing marks and crystalline imperfections can falsify the value of α in the case of rutile with its high anisotropic index of refraction (e.g., $n_\perp = 2.74$ and $n_{||} = 3.06$ at 0.48 μ; $\perp$ and $||$ refer to the orientation of the electric vector in reference to the optical axis). Hence, especially careful polishing is required.

During the course of the study it became necessary to oxidize and reduce rutile and to introduce deuterium into it by heating the crystals to high temperatures in appropriate atmospheres. For this purpose the samples were placed in alumina boats in a Vycor tube and heated to 1100°C. It is known that the reduction of rutile when not carried too far is nearly reversible[6,11] by heating it in oxygen. Since rutile will reduce in vacuum or even in air at sufficiently high temperature, the partial pressure of oxygen had to be kept high during measurements. This may also be inferred from measurements[12] of the conductivity as a function of oxygen pressure greater than 30 mm Hg at elevated temperature, where

$$\sigma \propto P(O_2)^{-1/4.3}.$$

Instrumentation

Absorption spectra were investigated primarily with a Beckman IR-3 spectrophotometer using CaF_2 prisms (spectral range 25 000 to about 1200 cm^{-1}). Line spectra of gases accurately measured on grating instruments[13] served for calibration. To detect any drift in the instrument adjustment, the spectra of water, carbon dioxide, and mercury vapors were recorded as secondary calibration. The use of a chopped light beam (10 cps) made it possible to measure the absorption of heated samples by eliminating thermal background radiation. The beam was chopped between the sample and the light source. Stray light was negligible over the entire spectral range.

Three signal detectors of various spectral ranges were used: Golay cell from 1000 to 14 000 cm^{-1} in combination with a Nernst glower; a photomultiplier from 14 000 to 25 000 cm^{-1} in conjunction with a tungsten lamp; and a PbS cell from 12 500 to 3600 cm^{-1}, which gave increased sensitivity, especially when cooled with solid CO_2.

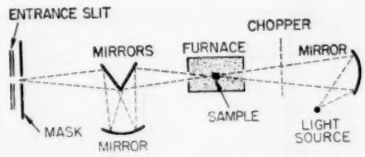

FIG. 1. External optical plan for high-temperature experimentation.

Some measurements were made with a Cary model-12 spectrophotometer, which when used as a quartz-prism double monochrometer, affords more resolution than CaF_2 in the region of 25 000 cm^{-1}.

The cell used in the high-temperature study is constructed of a small alumina tube wound with platinum heater wire inserted in a water-cooled steel tube insulated with Sil-O-Cel; the furnace ends, made of Transite, support the alumina tube and the sapphire windows. The furnace is suspended from a steel plate by two hollow bolts that carry the electrical leads for the heater.

Thin samples were placed between two precrimped platinum foils which were cut out over a portion of the specimen's faces. The foil, serving both as holder and mask, was placed over the hole of an Al_2O_3 plate and laced on with fine platinum wire. Larger samples were mounted in tubular holders made from fire brick or clamped between polished sapphire plates. A thin stainless steel tube was inserted into the cell to provide an oxygen atmosphere. Before each run, the cell was dried and outgassed at a high temperature to avoid window contamination.

An external-focusing optical system was employed in absorption and electro-optical experiments. This system (Fig. 1) permits optical masking of any portion of the sample or its surroundings and thus allows for correction of furnace-window contamination.

For polarization measurements in the visible region Polaroid disks and a Nicol prism were used. In the infrared, four sheets of AgCl at the Brewster angle provided 90% polarization.

Von Hippel and associates[1,2] made an analysis of the reflection data of Liebisch and Rubens[14] to obtain the values of n and k. Cronemeyer[5] correlated these values of n with values measured by others and extended their measurement to 4359 A by means of a small prism. Thus, one can calculate reflection loss and obtain the true absorption coefficient.[15]

RESULTS

The general features of the absorption near the electronic edge of sample 1 before any oxidation treatment are shown in the upper curve of Fig. 2. This spectrum and that of Fig. 5 correspond in general to those previously reported,[5,6] with the exception of certain spurious

[11] N. Nasu, Science Reports, Tôhoku Imp. Univ. First Ser. **25**, 510 (1936).
[12] M. D. Earle, Phys. Rev. **61**, 56 (1942).
[13] A. R. Downie, M. C. Magoon, T. Purcell, and B. Crawford, Jr., J. Opt. Soc. Am. **43**, 941 (1953).
[14] Th. Liebisch and H. Rubens, Sitzber. preuss. Akad. Wiss. Physik-math. Kl. **8**, 211 (1921).
[15] H. Y. Fan, Repts. Progr. in Phys. **19**, 107 (1956).

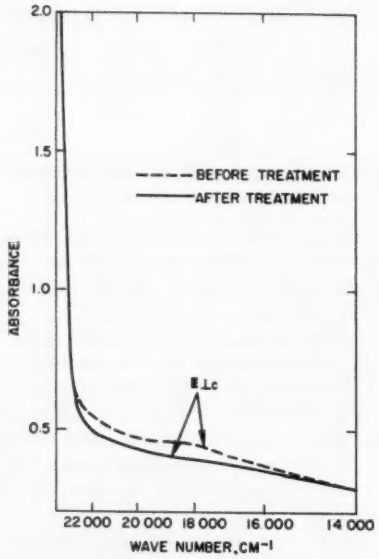

FIG. 2. Absorption of rutile sample 1 (path length 18.32 mm) at room temperature before and after oxidation treatment.

absorptions at about 0.73, 1.5, 2.3, and 3.2 μ attributed by Cronemeyer to impurities in the lattice, but which were probably caused by changes of prisms and instruments. The tail can be explained by imperfections and may result from indirect transitions.[16]

Superimposed is a small residual absorption at 17 900 cm^{-1} with a maximum decadic coefficient $\alpha' < 0.01$ cm^{-1}. Replotting the upper curve of Fig. 2 logarithmically (Fig. 3) shows an inflection point near 19 000 cm^{-1}, and the existence of a band at 17 900 cm^{-1} seems doubtful. A curve showing the theoretical reflection loss is also included in Fig. 3 for the region of

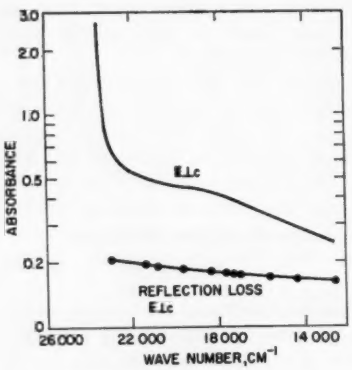

FIG. 3. Logarithmic representation of the absorbance at room temperature of sample 1 before treatment showing theoretical reflection loss.

[16] L. H. Hall, J. Bardeen, and F. J. Blatt, Phys. Rev. **95**, 559 (1954).

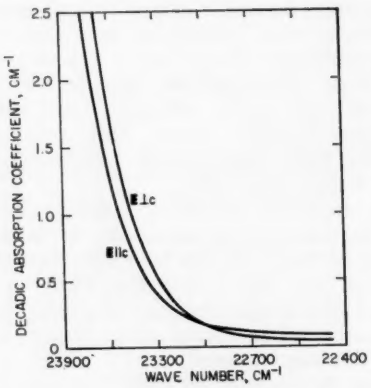

FIG. 4. Dichroism of absorption coefficient of rutile sample 2 (path length 8.52 mm) at room temperature.

small absorption; it is apparent that the absorption is higher and rises faster than explained by reflection alone.

Dichroism of the electronic absorption edge has not been previously noted in the literature; this effect is shown for sample 2 in Fig. 4. The edge for $\mathbf{E} \perp c$ occurs at an energy lower than that for $\mathbf{E} \| c$ when instrumental polarization effects are avoided. (A Nicol prism was used because it has a flat transmission characteristic in the region of interest; both sets of measurements were taken through a single pair of sample a faces to obviate effects of differing polish.)

A spectrum of sample 1 from 14 000 to 1800 cm^{-1} (Fig. 5) gives the absolute transmission, assuming that outside of the absorption band the transmission is determined entirely by reflection loss. The tail of the first infrared vibration band makes its appearance at 2700 cm^{-1}. The exciting feature is the very narrow absorption near 3300 cm^{-1} with its satellite structure, which includes the absorption at 4340 cm^{-1}. The main absorption is shown in more detail in Fig. 6 (effective slit width less than 7 cm^{-1} through this region). There is a large peak with an absorption maximum at 3277 cm^{-1}

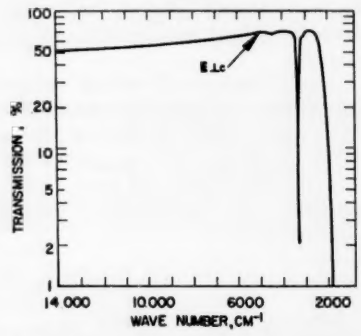

FIG. 5. Infrared spectrum of sample 1 at room temperature.

(peak absorption coefficient $\alpha' = 0.78$ cm^{-1}) and a sharp side band at 3322 cm^{-1}. A graphical separation, assuming harmonic oscillator shape, gives 28 cm^{-1} for the half-width of the former and 13 cm^{-1} for that of the latter band. The peak absorption α' at 3322 cm^{-1}, corrected[17,18] for finite slitwidth, is about 0.43 cm^{-1}.

There are two shoulders on the long wavelength tail: at 3070 and 3170 cm^{-1}. On the short-wavelength side, structure may exist, but the presence of atmospheric water bands begins to cause a residual distortion from about 3420 to 3950 cm^{-1} which obscures the detailed structure.

The 3300 cm^{-1} region was also examined at liquid-nitrogen temperature. The entire structure shifted to shorter wavelengths by 12 cm^{-1}; no new absorptions appeared, but the old ones were sharpened.

The absorption proved very sensitive to the direction of polarization. Because of the limited efficiency of the polarizer and the strains in the crystals, no absolute value of the effect can be given. However, the entire structure, including the band at 4340 cm^{-1}, behaves identically and the absorption coefficient is at least seven times greater for $\mathbf{E} \perp c$ than for $\mathbf{E} \| c$.

An attempt was made to remove the band by heating sample 1 in oxygen for 30 hr at 1000°C. No significant change resulted except for a slight drop in absorbance near the edge (cf. the lower curve of Fig. 2) and removal of the bump near 17 900 cm^{-1}. Cronemeyer,[5] in contrast, found an increased absorbance near the edge in his crystal after similar treatment. It was found in the present investigation that the bands in the 3300-cm^{-1} region could be removed by strong reduction followed by reoxidizing of the specimen, but not by oxidation alone.

Certain atomic and molecular groups create characteristic bands in particular environments.[19] The band near 3300 cm^{-1} lies in the O–H stretching region and suggests the presence of O–H groups in the crystal. To test this hypothesis, deuterium was introduced in substitution for H. Heating in gaseous deuterium caused difficulties: The specimen reduced and a very broad, dense band appeared, as expected, and completely obscured the region of interest. It was found that in order to substitute as much deuterium as possible without severe reduction, heating above 900°C for short periods (less than 1 min) was necessary. Now a new absorption band at 2442 cm^{-1} appeared in these deuterated specimens in the expected region, with bands of the same shape as the previous ones. However, the over-all opacity caused by reduction made observation of the line structure impossible.

The substitution of deuterium for hydrogen should shift the frequency of vibration in the ratio $\omega_H/\omega_D = 1.37$. This numerical value was obtained by assuming

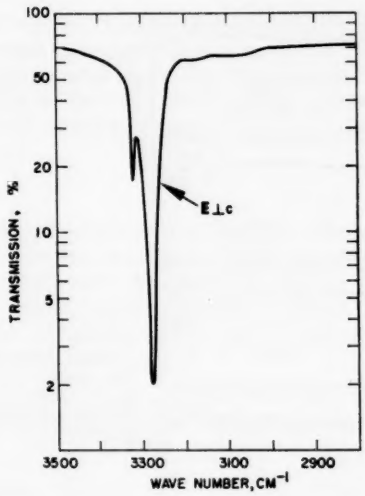

FIG. 6. Infrared spectrum of sample 1 in the 3300-cm^{-1} region.

that the vibration was normal and that the reduced mass was to be computed with the mass of oxygen. A further assumption was that the same force constant could be used for both vibrations since x-ray evidence[20] showed that for weak hydrogen bonds, e.g., those in ice, the intermolecular distance is the same for O–D and O–H. We may therefore assume that the potential energies are practically equivalent. The experimentally determined ratio is $\omega_H/\omega_D = 1.35$, which confirms the existence of hydrogen in the lattice. The hydrogen is presumably introduced by the flame in crystal growth.

There is probably an organized system of hydrogen bonded to the oxygen of the rutile lattice; weak hydrogen bonding may be indicated by the splitting into two absorption bands at 3277 and 3322 cm^{-1}. The O–H valence frequency (e.g., methyl alcohol 3682 cm^{-1} and solid LiOH 3678 cm^{-1}) has been generally observed in condensed phases shifted toward longer wavelengths.[21] The shifts found here, however, are unusually large and may be caused partly by the large dielectric constant of rutile. It may be noted that these bands are unusually sharp for O–H bands in the solid state.

Interpolating from the theory and from results obtained on other hydrogen-bonded systems,[22] we can estimate from the shift in O–H frequency that the H-bond energy is about 3 kcal/mole. There is a relationship[23] between the change of dipole moment with the normal coordinate $\partial\mu/\partial r$, the number of oscillators per cm^3 N, and the integrated absorption coefficient

[17] K. S. Gibson, Natl. Bur. Standards Circ. 484 (1949).
[18] D. A. Ramsay, J. Am. Chem. Soc. **74,** 72 (1952).
[19] L. J. Bellamy, *The Infrared Spectra of Complex Molecules* (John Wiley & Sons, Inc., New York, 1958).
[20] J. M. Robertson and A. R. Ubbelohde, Proc. Roy. Soc. (London) **A170,** 222 (1939); A. R. Ubbelohde, *ibid.* **A173,** 417 (1939).
[21] L. Kellner, Repts. Progr. in Phys. **15,** 1 (1952).
[22] E. R. Lippincott and R. Schroeder, J. Chem. Phys. **23,** 1099 (1955).
[23] R. D. Waldron, Phys. Rev. **99,** 1727 (1955).

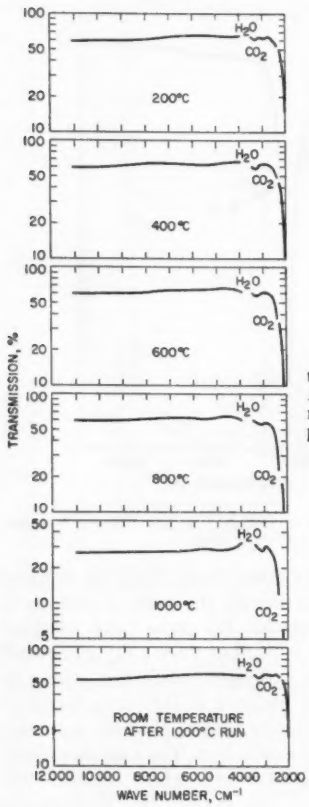

FIG. 7. Infrared absorption spectra of sample 2 $E \| c$ (path length 8.52 mm) as a function of temperature.

A (cm^{-2}):

$$N = \frac{m^*}{(\partial\mu/\partial r)^2} A\,(1.975)\times 10^{21},$$

where m^* is the reduced mass. Estimating $\partial\mu/\partial r$ from its value in hydrogen-bonded phenols,[24] we calculate that there are 1.5×10^{17} O–H groups per cm^3 in the sample shown in Fig. 5. Other samples showed the same order of magnitude.

One of the long-range investigations of the laboratory concerns dielectric relaxation spectra. Originally such spectra were analyzed according to Debye's[25] model of dipoles rotating with high frictional damping. Frequently, however, dipole orientation by rotation is inconceivable while orientation by inversion might still occur, as for example in the shifting of hydrogen bonds or of polar molecular or atomic groups.[26] In addition, a new kind of dipole connected with crystalline lattice defects has been invoked to explain dielectric spectra.[27] Optical absorptions associated with lattice defects have been observed, for instance, in neutron-irradiated silicon.[28] Dielectric-inversion spectra resulting from polar centers of some kind have been found in synthetic crystals of TiO_2 under certain conditions.[4,29] It appeared important to correlate these spectra with possible optical manifestations of such polar centers.

The activation energy of the dielectric dispersion discovered in rutile[4] might lead one to expect an optical absorption near 3000 cm^{-1}. This would correspond to the absorption of hydrogen-bonded character found here, which might allow dipole orientation by inversion.

The dielectric dispersions have the property of being strongly polarized with respect to the direction of the electric vector. The infrared absorption of the O–H group is polarized by 90 deg to the dielectric dispersion. This correlation should be studied further; since we have shown that the hydrogen can be driven out of the crystal, the relation between both effects can be investigated in detail.

The broad band appearing in even weakly reduced TiO_2 extends from the nearest vibrational band to the electronic edge. In the case presented here, the minimum transmission occurs in the region of 6850 cm^{-1} (1.46 μ); Cronemeyer[5] reported a slightly different value, 5405 cm^{-1} (1.85 μ), for his sample.

In order to determine whether high temperature alone would produce such a band (or any new absorption) in fully oxidized rutile, high-temperature spectra were measured. The shift of the electronic eigenabsorption edge for temperatures up to 1000°C for the cases $\mathbf{E}\perp c$ and $\mathbf{E}\|c$ were identical within the errors of the high-temperature experiments. The theoretical reflection loss is accounted for simply, for as Schröder[9] has shown, the indices of both the ordinary and extraordinary rays change only slightly with temperature. The rate of change of the edge position was measured in the region of high absorption where the curves become almost parallel. At an absorption coefficient α' of 400 cm^{-1}, the average shift is -7.1×10^{-4} ev/°K toward longer wavelength in a sample of 29.5 μ thickness. For a sample thickness of 11.94 mm at an absorption coefficient α' of about 1 cm^{-1}, the average rate of shifting of the edge is -9.5×10^{-4} ev/°K. These values are to be compared with Cronemeyer's result[5] of -6.3×10^{-4} ev/°K at $\alpha'=30$ cm^{-1} up to 775°K.

Macroscopically, the temperature variation of the gap should be given by an expression[15] containing the change of the energy gap with temperature at constant pressure, which has been measured here, and by terms describing the effect of lattice dilation, which are of the form $(\partial E_g/\partial p)_T$. Therefore, in order to correlate the experimental results with any theory of high-

[24] H. Tsubomura, J. Chem. Phys. **24,** 927 (1956).
[25] P. Debye, *Polar Molecules* (Chemical Catalog Company, New York, 1929), Chap. 5.
[26] A. von Hippel, Progress Report No. XXI (1957), p. 3, Laboratory of Insulation Research, Massachusetts Institute of Technology.
[27] R. G. Breckenridge, J. Chem. Phys. **18,** 913 (1950).
[28] M. Becker, H. Y. Fan, and K. Lark-Horowitz, Phys. Rev. **85,** 730 (1952).
[29] Y. L. Sandler, Progress Report No. XVII (1955), Laboratory of Insulation Research, Massachusetts Institute of Technology, p. 16.

temperature behavior, measurements of the isothermal variation of gap with pressure should be made as well.

A portion of the infrared transmission spectra of sample 2 at high temperatures is shown in Fig. 7. They reveal a marked achromatic drop in transmission at 1000°C representing an increase of absorption coefficient: $\Delta\alpha' = 0.42 \pm 0.02$ cm^{-1}. At 800°C there is already a slight increase of absorption coefficient: $\Delta\alpha' = 0.03 \pm 0.02$ cm^{-1}. Re-examination after the heating experiment at room temperature revealed a slight over-all drop in transmission from the starting value $\Delta\alpha' = 0.05 \pm 0.02$ cm^{-1}, probably resulting from a slight contamination by Pt at elevated temperatures.

It is evident that no absorption corresponding to the reduction band appeared. The observed regions marked H_2O and CO_2 were caused by vapors in the cell; at high temperatures, their absorption modifies and broadens.

The band in the 3300-cm^{-1} region was observed to broaden, diminish, and shift to longer wavelengths at high temperatures when examined with $\mathbf{E} \perp c$.

The frequency-independent high-temperature absorption (cf. Fig. 7) can be attributed to free carrier absorption according to the theories of Drude-Kronig-Zener.[30] The absorption coefficient and conductivity due to free carriers in nonmagnetic media are, respectively,

$$\alpha = (nc\epsilon_0)^{-1} \frac{\sigma_0}{1+(\omega\mu m^*/e)^2} \text{ [m}^{-1}\text{]}$$

and

$$\sigma = 2nk\omega\epsilon_0 = Ne\mu \text{ [ohm}^{-1}\text{ m}^{-1}\text{]},$$

where σ_0 is the low-frequency conductivity and the other symbols have their conventional meanings.

If $(\omega\mu m^*)/e < 1$, no significant wavelength dependence can be expected. The inequality may be written

$$10^4 (m^*/m) \frac{\mu[\text{m}^2/\text{v-sec}]}{\lambda[\text{microns}]} < 1.$$

The Hall mobility μ of electrons in slightly reduced rutile crystals and ceramics is less than 10^{-4}[m^2/volt-sec] and decreases with increasing temperature.[31] Using the relation for the variation of mobility with temperature[32] due to lattice scattering,

$$\mu \propto T^{-\frac{3}{2}}$$

(which should predominate at high temperatures), we estimate that the mobility at 1000°C should be less than 10^{-5}[m^2/v-sec]. Assuming an effective mass of order 1,[31] we see that the inequality is obeyed. For this limit the absorption coefficient is approximately constant and equals

$$\alpha'[\text{cm}^{-1}] = \frac{\sigma 10^{-2} (\log_{10} e)}{n\epsilon_0 c} = 0.63\sigma[\text{ohm}^{-1}\text{ m}^{-1}]$$

for $n_{||} = 2.6$.

Observed here is an absorption coefficient $\alpha' = 0.42$ cm^{-1} at 1000°C, which leads to a conductivity of 0.67 ohm^{-1} m^{-1}. Cronemeyer reports a value $\sigma_{0||} = 0.77$ ohm^{-1} m^{-1} at 1000°C. At 800°C the optically measured $\alpha' = 0.03 \pm 0.2$ cm^{-1} gives an order-of-magnitude agreement with Cronemeyer's value $\sigma_0 = 0.04$ ohm^{-1} m^{-1}. The correlation is surprisingly good; there was no *a priori* reason to expect that lattice and impurity scattering would produce a mobility in the infrared equal to the dc mobility.

ACKNOWLEDGMENTS

The author is greatly indebted to Professor Arthur R. von Hippel for the suggestion of the problem and constant encouragement and advice. The assistance and advice of Dr. Robert D. Waldron was generously given throughout the entire investigation. Gratitude is expressed to the entire staff of the Laboratory for Insulation Research for help on various occasions.

[30] Cf. T. S. Moss, *Optical Properties of Semi-Conductors* (Academic Press, Inc., New York, 1959), p. 29. (Note that Moss used K for α.)

[31] R. G. Breckenridge and W. R. Hosler, Phys. Rev. **91**, 793 (1953).

[32] H. Y. Fan, Phys. Rev. **82**, 900 (1951).

THE JOURNAL OF CHEMICAL PHYSICS VOLUME 35, NUMBER 3 SEPTEMBER, 1961

Molecular Weight Distribution from the Normal Coordinate Theory of Viscoelasticity

EMORY MENEFEE

Western Regional Research Laboratory, Albany, California*

AND

WARNER L. PETICOLAS

IBM Advanced Systems Development Division Laboratory, Monterey and Cottle Roads, San Jose, California

(Received February 22, 1961)

The normal coordinate theory of viscoelasticity has been shown to provide a bridge between the measurable rheological properties of linear polymers and their molecular weight distribution functions, as well as their average molecular weights. Equations have been derived relating the molecular weight distribution function of a linear polymer to a sum of functions of a measurable rheological property such as stress relaxation or dynamic viscosity. Thus, a method for the simple and rapid determination of molecular weight distribution has been developed within the limitations of the normal coordinate theory.

I. INTRODUCTION

RECENTLY, Zimm[1] has suggested that normal-coordinate viscoelastic theory might be used to obtain some knowledge of the molecular-weight distribution of linear polymers. To do this it is first necessary to invert the theoretical expressions so that molecular-weight-dependent functions are given in terms of measurable rheological quantities. In general, the latter involve two types of summation: (1) the summation over the integer normal-modes of relaxation for each molecule, and (2) the summation over the molecular-weight distribution. The first sum comes about because of an internal polydispersity in the relaxation times of an individual polymer molecule; the second summation represents an external polydispersity due to the presence of species with different molecular weights. The purpose of this paper is to show how these two summations may be inverted to provide a new method for obtaining molecular-weight distributions.

II. BACKGROUND AND BASIC RELATIONSHIPS

Rouse[2] and several others[3,4] have derived expressions for the frequency dependence of the complex viscosity of a monodisperse polymer in solution. From Rouse's result the real part of this viscosity may be written as

$$\eta_i(\omega)-\eta_s=\frac{6}{\pi^2}(\eta_{0i}-\eta_s)\sum_{p=1}^{N}\frac{1}{p^2}\frac{1}{1+\omega^2\tau_{pi}^2},$$

with

$$\tau_{pi}=\frac{6(\eta_{0i}-\eta_s)M_i}{cRT\pi^2p^2},$$

where $\eta_i(\omega)$ is the real part of the complex viscosity of a polymer of molecular weight M_i at an angular shear frequency ω. The viscosity at zero frequency is η_{0i} and η_s is the solvent viscosity. The vibration mode p is carried in integral values to N, the total number of such modes. Polymer concentration in grams per cubic centimeter is denoted by c, and other symbols have their usual significance.

Polydispersity can be accommodated by choosing a suitable fraction for mixing monodisperse components; more about the nature of this fraction will be said later. For this problem, a mixing of viscosities by weight fractions is chosen; this is valid in the polymer solutions of low concentration. Its applicability to bulk polymers will be discussed later.

For a polydisperse polymer, the pth relaxation time of the ith polymer molecule τ_{pi} is given by the equation,

$$\tau_{pi}=L^2/6kTB\lambda_{pi},$$

where L^2 is the mean-square end-to-end distance of a submolecule, B is the mobility factor, and λ_{pi} is the pth eigenvalue of the ith polymer molecule. For linear polymers,

$$\lambda_{pi}^{-1}\approx N_i^2/\pi^2p^2=K^2M_i^2/\pi^2p^2,$$

where Ni is the number of modes of the ith molecule with molecular weight M_i and k is a constant for a given type of polymer. Consequently, we have $\tau_{pi}=SM_i^2/p^2$ with S a parameter yet to be evaluated in terms of measurable properties.

At zero shear rate the rule for mixing by weight fractions is given by the relation

$$\eta_0-\eta_s=\sum_i w_i(\eta_{0i}-\eta_s)$$

$$=\sum_i w_i\sum_{p=1}^{N}(cRT/M_i)\tau_{pi}.$$

Incorporating τ_{pi} it is found that

$$S=6(\eta_0-\eta_s)/\pi^2cRT\langle M_w\rangle_{Av}.$$

* A laboratory of the Western Utilization Research and Development Division, Agricultural Research Service, U. S. Department of Agriculture.

[1] B. H. Zimm, in *Rheology*, edited by F. R. Eirich (Academic Press, Inc., New York, 1960), Vol. 3.

[2] P. E. Rouse, Jr., J. Chem. Phys. **21**, 1272 (1953).

[3] F. Bueche, J. Chem. Phys. **22**, 603 (1954).

[4] B. H. Zimm, J. Chem. Phys. **24**, 269 (1956).

Hence, on resubstitution,

$$\tau_{p\,i}=[6(\eta_0-\eta_s)/\pi^2 cRT\langle M_w\rangle_{Av}](M_i^2/p^2),$$

where η_0 is the zero-shear-rate viscosity of the whole polymer solution and $\langle M_w\rangle_{Av}$ is the weight-average molecular weight of the whole polymer. This is a remarkable result since it states that the pth relaxation time of a molecule of molecular weight M_i is related to the molecular weight by a factor dependent on the average properties of the whole polymer, namely, $(\eta_0-\eta_s)/\langle M_w\rangle_{Av}$.

The over-all expression for the polydisperse viscosity may be conveniently written, using a continuous distribution of molecular weights, as

$$\eta(\omega)-\eta_s\equiv\Phi(\omega)=\frac{cRT}{a^2}\sum_{p=1}^{N}\frac{1}{p^2}\int_0^\infty\frac{MW(M)dM}{1+(\omega^2M^4/a^4p^4)}, \quad (1)$$

where $W(M)dM$ is the weight fraction of polymer with molecular weight between M and $M+dM$. The term a^2 is $cRT\pi^2\langle M_w\rangle_{Av}/6(\eta_0-\eta_s)$.

By using the moduli and relaxation times defined by the form of Eq. (1), one may write down immediately an analogous expression for the stress relaxation following steady-state shearing. For the polydisperse polymers it is

$$\frac{\sigma(t)}{\dot\gamma_0}\equiv\Phi(t)=\frac{cRT}{a^2}\sum_{p=1}^{N}(1/p^2)\int_0^\infty MW(M)\times\exp[-a^2p^2t/M^2]dM, \quad (2)$$

where $\sigma(t)$ is the stress remaining at time t after flow at a steady strain rate $\dot\gamma_0$ has been suddenly stopped. Equation (2) differs from that derived by Bueche[3] in that he sums p over odd integers only. Experiments by Rouse and Sittel[5a] and Tobolsky and Murakami[5b] appear to indicate that all integers contribute, so the form of Eq. (2) will be retained for this discussion.

Theoretical expressions for the dependence of steady-state viscosity on shear rate have been given by Bueche[3] and Pao[6] using a normal-coordinate approach. They may be treated by the methods of this paper, but since their form is more complex the discussion will be restricted to Eqs. (1) and (2). A further note should be added concerning sources of experimental stress-relaxation data. One usually measures relaxation following either sudden straining or cessation of steady-state flow. The latter method is recommended, since it avoids some of the problems mentioned by Bueche[3] attributable to a nonzero loading time inherent in the sudden-straining method. If desired the sudden-strain result may be obtained as the negative time derivative of the steady-flow data.

[5] (a) P. E. Rouse and K. Sittel, J. Appl. Phys. **25,** 690 (1954); (b) A. V. Tobolsky and K. Murakami, J. Polymer Sci. **40,** 443 (1959).

[6] Y. H. Pao, J. Chem. Phys. **25,** 1294 (1956).

III. METHOD

A. Molecular Weight Distribution from Dynamic Viscosity

As an initial step in the inversion of Eq. (1), it may be rewritten in a condensed form,

$$\Phi(\omega)=(cRT/a^2)\sum_{p=1}^{N}(1/p^2)I(\omega^2/p^4), \quad (3)$$

where

$$I(\omega^2/p^4)=\int_0^\infty\frac{MW(M)dM}{1+(\omega^2M^4/a^4p^4)}.$$

It should be noted at this point that if the function $I(\omega^2)$ is obtained in terms of $\Phi(\omega)$, then a Stieltjes inversion can be applied to give $W(M)$.

Sums of the sort exemplified by Eq. (3) may be written generally as

$$f(x)=\sum_{p=1}^{N}p^b g(p^c x^d), \quad (4)$$

where b, c, and d are arbitrary constants. If N is reasonably large, an inversion theorem due to Moebius[7,8] may be applied, giving the result

$$g(x^d)=\sum_{n=1}^{\infty}n^b\mu(n)f(n^{c/d}x). \quad (5)$$

The function $\mu(n)$ is the Moebius μ function, and is defined as equal to $+1$ if n is $+1$ or if n is factorable into an even number of unlike primes, equal to -1 if n is factorable into an odd number of unlike primes, and equal to zero for other values of n. For example, the first few terms for $\mu(n)$ are 1, -1, -1, 0, -1, 1, -1, 0, 0, etc.

Comparison of Eq. (3) with Eq. (4) gives for the parameters of Eq. (4), $x=\omega$, $f(x)=\Phi(\omega)(a^2/cRT)$, $b=-2$, $c=-4$, $d=2$, and $g(p^cx^d)=I(\omega^2/p^4)$. From Eq. (5) one has immediately

$$I(\omega^2)=\int_0^\infty\frac{MW(M)dM}{1+(\omega^2M^4/a^4)}=\frac{a^2}{cRT}\sum_{n=1}^{\infty}\frac{\mu(n)}{n^2}\Phi\left(\frac{\omega}{n^2}\right). \quad (6)$$

The integral of Eq. (6) can be inverted by means of a theorem due to Widder.[9] If one has a Stieltjes integral of the form

$$F(y)=\int_0^\infty[G(z)/(y+z)]dz,$$

then its transform is

$$G(z=y)=\lim_{\nu\to\infty}[(-1)^\nu/2\pi](e/\nu)^{2\nu}(d^\nu/dy^\nu)\times\{y^{2\nu}[d^\nu F(y)/dy^\nu]\}. \quad (7)$$

[7] A. F. Moebius, J. angew. Math. **9,** 105 (1932).

[8] J. V. Uspensky and M. A. Heaslet, *Elementary Number Theory* (McGraw-Hill Book Company, Inc., New York, 1939).

[9] I. I. Hirschman and D. V. Widder, *The Convolution Transform* (Princeton University Press, Princeton, New Jersey, 1955).

In Eq. (6) one may let $z=a^4/M^4$ and $y=\omega^2$ and apply Eq. (7) to obtain the complete form for the weight distribution of molecular weights from dynamic viscosity,

$$W(M)=\frac{2\omega}{\pi cRT}\lim_{\nu\to\infty}(-1)^\nu\left(\frac{e}{\nu}\right)^{2\nu}\frac{d^\nu}{d(\omega^2)^\nu}\times\left[(\omega^2)^{2\nu}\frac{d^\nu}{d(\omega^2)^\nu}\sum_{n=1}^{\infty}\frac{\mu(n)}{n^2}\Phi\left(\frac{\omega}{n^2}\right)\right], \quad (8)$$

where $M=a\omega^{-\frac{1}{2}}$.

Since this expression, exact in the limit, is quite cumbersome, approximations may be most useful. The first-order approximation, obtained from Eq. (8) by letting $\nu=1$, is

$$W(M)\simeq-\frac{4\omega^3}{\pi cRT}e^2\left\{\frac{dS(\omega)}{d(\omega^2)}+\frac{\omega^2}{2}\frac{d^2S(\omega)}{d(\omega^2)^2}\right\}, \quad (9)$$

where

$$S(\omega)=\sum_{n=1}^{\infty}[\mu(n)/n^2]\Phi(\omega/n^2).$$

B. Molecular Weight Distribution from Stress Relaxation

The derivation of the distribution function for this example closely follows that given in the last section. Equation (2) may be condensed to

$$\Phi(t)=(cRT/a^2)\sum_{p=1}^{N}(1/p^2)I(p^2t),$$

where

$$I(p^2t)=\int_0^\infty MW(M)\exp\left[-\frac{a^2p^2t}{M^2}\right]dM.$$

For the parameters of Eq. (4), $x=t$, $f(x)=\Phi(t)$, $b=-2$, $c=2$, $d=1$, and $g(p^cx^d)=I(p^2t)$. Applying Eq. (5) one has immediately

$$I(t)=\int_0^\infty MW(M)\exp\left[-\frac{a^2t}{M^2}\right]dM=\frac{a^2}{cRT}\sum_{n=1}^{\infty}\frac{\mu(n)}{n^2}\Phi(n^2t). \quad (10)$$

By making the transform $x=a^2/M^2$ the integral of Eq. (10), takes the form of a Laplace transform. Hirschman and Widder[9] invert the integral as follows. If

$$F(t)=\int_0^\infty G(x)\exp(-xt)\,dx,$$

then

$$G(x=t^{-1})=\lim_{\nu\to\infty}[(-1)^\nu/\nu!](\nu t)^{\nu+1}[(d^\nu/dt^\nu)F(\nu t)].$$

Applying this inversion formula to Eq. (10) gives for the weight distribution

$$W(M)=(2/cRT)\lim_{\nu\to\infty}[(-1)^\nu/\nu!]\nu^{\nu+1}t^{\nu-1}\times\sum_{n=1}^{\infty}\frac{\mu(n)}{n^{2-2\nu}}\frac{d^\nu\Phi(\nu n^2t)}{d(\nu n^2t)^\nu}, \quad (11)$$

where $M=at^{\frac{1}{2}}$.

In the first approximation, where $\nu=1$, Eq. (11) reduces to the form

$$W(M)\simeq(-2/cRT)\sum_{n=1}^{\infty}\frac{\mu(n)}{n^2}\frac{d\Phi(n^2t)}{dt},$$

where, again, $M=at^{\frac{1}{2}}$.

IV. RELATIONSHIPS INVOLVING THE DISTRIBUTION FUNCTIONS

The following discussion will be concerned only with the molecular weight distribution functions derived from stress relaxation, since they have an inherently simple form. Let us define the integral

$$I_\alpha^M=\int_0^M M^\alpha W(M)\,dM. \quad (12)$$

Furthermore, the stress relaxation function will be represented in the conventional way as

$$\Phi(t)=\sum_i G_i\tau_i\exp(-t/\tau_i), \quad (13)$$

where the moduli G_i and relaxation times τ_i are found from experimental data. This equation is derived conventionally by the usual springs and dash-pots.

Combining Eqs. (11), (12), and (13) gives

$$I_\alpha^M=\frac{a^{\alpha+1}}{cRT}\lim_{\nu\to\infty}\frac{\nu^{\nu+1}}{\nu!}\sum_{n=1}^{\infty}\frac{\mu(n)}{n^{2-2\nu}}\sum_i G_i\tau_i\int_0^{t_m}t^{[(\alpha-1)/2]+\nu-1}\times\exp(-\nu n^2t/\tau_i)\,dt, \quad (14)$$

where $t_m=M^2/a^2$. The first case to be considered is the limiting one in which t_m is allowed to go to infinity. The integral of Eq. (14) becomes exactly integrable, giving

$$I_\alpha^\infty=\frac{a^{\alpha+1}}{cRT}\lim_{\nu\to\infty}\frac{\nu^{[(3-\alpha)/2]}}{\nu!}\Gamma\left(\frac{\alpha-1}{2}+\nu\right)\sum_{n=1}^{\infty}\frac{\mu(n)}{n^{\alpha+1}}\sum_i G_i\tau_i^{[(\alpha+1)/2]}. \quad (15)$$

The terms containing ν now become unity in the limit. Also, from Eqs. (4) and (5) it can be shown that

$$\sum_{n=1}^{\infty}\frac{\mu(n)}{n^{\alpha+1}}=\left[\sum_{m=1}^{\infty}(1/m^{\alpha+1})\right]^{-1}$$

When $\alpha>0$, the right side is also the reciprocal of the Riemann zeta-function $\zeta(\alpha+1)$. In total, one has the

interesting result, obtained without approximation, that

$$\int_0^\infty M^\alpha W(M)\,dM = \frac{a^{\alpha+1}}{cRT\sum_{m=1}^{\infty}(1/m^{\alpha+1})}\sum_i G_i\tau_i^{[(\alpha+1)/2]}. \quad (16)$$

This equation provides a bridge between the classical moduli and relaxation times, obtained from spring and dash-pot models, and the average molecular weights of a polymer. Since the G_i's and τ_i's may be experimentally determined, this equation indicates a means for determining the weight average of M^α for $\alpha>1$. The use of Eq. (13) in the derivation in no way restricts the generality of the approach, since Eqs. (11) and (12) only can be combined and integrated by parts to give an equation similar to Eq. (16), but involving $\Phi(t)$ directly.

Putting $\alpha=1$ in Eq. (16) and making use of the fact that

$$\sum_i G_i\tau_i=\eta_0-\eta_s,$$

the equation reduces to an identity, as it should. When $\alpha=3$, one obtains

$$\int_0^\infty M^3W(M)\,dM=(90a^4/\pi^4cRT)\sum_i G_i\tau_i^2.$$

Making use of the relation for elastic compliance,[10]

$$J_\infty=[1/(\eta_0-\eta_s)^2]\sum_i G_i\tau_i^2,$$

and noting that

$$\int_0^\infty M^3W(M)\,dM=\langle M_{z+1}\rangle_{Av}\langle M_z\rangle_{Av}\langle M_w\rangle_{Av},$$

the expression above reduces to the familiar form

$$J_\infty=\tfrac{2}{5}cRT(\langle M_{z+1}\rangle_{Av}\langle M_z\rangle_{Av}/\langle M_w\rangle_{Av}).$$

This derivation offers substantiation of the internal consistency of the method. Equation (16) is of course not restricted to particular values of α, even non-integral values may be used. However, a problem arises with $\alpha=0$ or -1 which will be discussed subsequently.

Turning now to the more general development in which the integral of Eq. (14) is allowed to take on finite limits in t, one finds immediate difficulty. It is no longer integrable in general except in terms of an incomplete gamma function; furthermore, ν cannot be carried conveniently to the limit. Fortunately there is probably no need to try to include all values of α, since Eq. (12) with a finite limit represents various cumulative molecular-weight distribution functions. Let us consider only the example of $\alpha=1$. This defines the cumulative Z distribution, denoted as Z_c, as

$$Z_c(M)=\frac{1}{\langle M_w\rangle_{Av}}\int_0^M MW(M)\,dM.$$

From Eq. (14) one has then,

$$Z_c(M)=\frac{a^2}{\langle M_w\rangle_{Av}cRT}\lim_{\nu\to\infty}\frac{\nu^{\nu+1}}{\nu!}\sum_{n=1}^{\infty}\frac{\mu(n)}{n^{2-2\nu}}\sum_i G_i\tau_i^{1-\nu}\int_0^{t_m} t^{\nu-1}\times\exp(-\nu n^2t/\tau_i)\,dt. \quad (17)$$

When $\nu=1$, the first approximation is

$$Z_c(M)=\frac{\pi^2}{6(\eta_0-\eta_s)}\sum_{n=1}^{\infty}\frac{\mu(n)}{n^2}\sum_i G_i\tau_i[1-\exp(-n^2t/\tau_i)],$$

or, in terms of the original function Φ,

$$Z_c(M)=1-\frac{\pi^2}{6(\eta_0-\eta_s)}\sum_{n=1}^{\infty}\frac{\mu(n)}{n^2}\Phi(n^2t), \quad (18)$$

where M, as usual, equals at^b.

In the second approximation, when $\nu=2$, Eq. (17) reduces to

$$Z_c(M)=\frac{\pi^2}{6(\eta_0-\eta_s)}\sum_{n=1}^{\infty}\frac{\mu(n)}{n^2}\sum_i G_i\tau_i\times\left[1-\left(1+\frac{2n^2t}{\tau_i}\right)\exp(-2n^2t/\tau_i)\right],$$

or, in terms of Φ,

$$Z_c(M)=1-\frac{\pi^2}{6(\eta_0-\eta_s)}\sum_{n=1}^{\infty}\frac{\mu(n)}{n^2}\left[\Phi(2n^2t)-t\frac{d\Phi(2n^2t)}{dt}\right]. \quad (19)$$

The form of Eq. (18) is particularly useful for obtaining an estimate of the cumulative Z distribution from experimental stress-relaxation measurements. Various other distribution-dependent functions can be evaluated by extension of the procedure of this section.

V. DISCUSSION OF THE METHOD: LIMITATIONS

In going from monodisperse systems to polydisperse, use is made in this paper only of averaging viscosities by weight fractions; that is,

$$\eta_0-\eta_s=\sum_i W_i(\eta_{0i}-\eta_s).$$

There is no reason why other mixing rules could not be applied. For example, in bulk polymers a more valid rule might be

$$\eta_0=(\sum_i W_i\eta_i^{1/B})^B,$$

where B is usually 3.4. This could be used as the basis for an equation similar to Eq. (1), although with more difficulty. In a companion paper[11] the authors discuss a general formulation for testing fractions for mixing

[10] F. W. Schremp, J. D. Ferry, and W. W. Evans, J. Appl. Phys. **22**, 711 (1951).

[11] W. L. Peticolas and E. Menefee, J. Chem. Phys. **35**, 951 (1961).

components with molecular-weight-dependent properties.

It is one of the weaknesses of the original theory that the viscosity of a monodisperse polymer is predicted to vary as only the first power of the molecular weight. While this is occasionally true in solutions, it is far from the case for bulk polymers. However, the original theory may be applicable to bulk polymers since the relaxation time τ_{pi} is related to the molecular weight M_i through a factor $(\eta_0/\langle M_w\rangle_N)$ where η_0 is the melt viscosity of the whole polymer. This would mean that $\tau_{pi}\propto\langle M_w\rangle_N^{2.4}M_i$.

The most serious problem which arises in inversion of normal-coordinate theory is that of terminating the modal index N. One would expect that the maximum number of allowable modes would be proportional to the molecular weight of a molecule; that is, $N_i=KM_i$. If such an assumption is used, then the summation over modes in Eqs. (1) and (2) must be done under the integral-over-molecular-weight. This makes the entire procedure extremely complicated, especially since even the Moebius inversion procedure can no longer be rigorously applied. This lack of termination of N is responsible for Eq. (15) becoming spurious when $\alpha\leq 0$. However, one may make use of this property in a very crude way to find the maximum allowable N.

If N in Eq. (4) is finite, then Eq. (5) is not strictly true; the $\mu(n)$ function must be replaced by some other function of the integers, say $R(n)$. Every subsequent equation containing an infinite sum over $\mu(n)$ would then contain the corresponding infinite sum over $R(n)$. Ultimately Eq. (15) would contain, instead of

$$\sum_{n=1}^{\infty}[\mu(n)/n^{\alpha+1}],$$

the term

$$\sum_{n=1}^{\infty}[R(n)/n^{\alpha+1}].$$

It again can be shown that

$$\sum_{n=1}^{\infty}[R(n)/n^{\alpha+1}]=[\sum_{m=1}^{N}(m^{\alpha+1})^{-1}]^{-1}.$$

Hence, Eq. (16) now becomes

$$\int_0^{\infty}M^{\alpha}W(M)\,dM = \{a^{\alpha+1}/[cRT\sum_{m=1}^{N}(m^{\alpha+1})^{-1}]\}\sum_i G_i\tau_i^{(\alpha+1)/2}. \quad (20)$$

Now, when $\alpha=-1$, one finds from Eq. (20) that

$$1/\langle M_n\rangle_N=G_0/NcRT, \quad (21)$$

where $G_0=\sum_i G_i$, the "instantaneous" modulus. Also, when, $\alpha=0$, Eq. (20) reduces to

$$1=[a/(cRT\sum_{m=1}^{N}m^{-1})]\sum_i G_i\tau_i. \quad (22)$$

Within small error (1% or less), the partial sum of the harmonic series,

$$\sum_{m=1}^{N}m^{-1},$$

may be replaced by $\ln N+\gamma+[(1-\gamma)/N]$, where γ is Euler's number, 0.5772+.

Thus these equations give two ways for estimating N; if optimistic one could say even that $\langle M_n\rangle_N$ could be determined by using the N found from Eq. (22) in Eq. (21). This rough approach implies that the magnitude of N is determined by small molecules, and that whatever its value the summations involving long molecules will be unaffected, since the predominant term is that of the first vibration mode anyway.

If N is small and one desires to evaluate Eqs. (11) or (18) for distributions, it is necessary to specify the $R(n)$ function which replaces $\mu(n)$. For a specific N, a recursion relation can be given

$$R(n)_N=-\sum_{m=1}^{n-1}R(m)_N\Delta(n/m),$$

where $\Delta(n/m)=1$ if n/m is an integer $\leq N$, and zero otherwise, and $R(1)_N\equiv 1$ for all N. For example, when $N=4$, the first few terms of the $R(n)_4$ series are 1, -1, -1, 0, 0, 2, 0, 1, 1, 0, etc. Terms in which $n\leq N$ are identical with the $\mu(n)$ series.

Ordinarily, the experimental determination of the molecular-weight distribution function of a polymer is an extremely time-consuming and difficult process involving very tedious fractionation procedures. On the other hand, measurement of stress relaxation, viscosity-frequency, or viscosity shear-rate curves is a comparatively simple process if suitable equipment is available. By means of these equations then, a much simpler and more rapid method of determining the molecular distribution functions has been developed within the limitations of the normal-coordinate theory.

THE JOURNAL OF CHEMICAL PHYSICS VOLUME 35, NUMBER 3 SEPTEMBER, 1961

Molecular-Weight Dependence of the Viscoelastic Properties of Whole Polymers

WARNER L. PETICOLAS

IBM Advanced Systems Development Division Laboratory, Monterey and Cottle Roads, San Jose, California

AND

EMORY MENEFEE

Western Regional Research Laboratory, 800 Buchanan Street, Albany 10, California

(Received February 22, 1961)

A method has been developed by which it is possible to determine the type of molecular weight averaging upon which viscoelastic properties of polymers may depend and which may be used to verify the normal-coordinate theory of viscoelasticity for various types of polymers. The method is extraordinarily simple to carry out since it involves only measurement of the property on whole polymers and mixtures of whole polymers. Neither fractionation nor molecular-weight measurements themselves are required.

Methods of determining the correct average-molecular-weight dependence of melt viscosity and steady-state elastic compliance have been worked out in detail and are illustrated with data on linear polyethylenes.

The method is also applicable to other polymer properties which are molecular-weight dependent.

I. INTRODUCTION

THE normal-coordinate treatment of the viscoelastic properties of polymers[1-3] has been shown to yield an expression for the molecular-weight distribution in terms of a sum of measurable quantities.[4] Before this method can be applied with any confidence, however, some experimental verification of the normal-coordinate theory must be obtained for the polymer system under study. A necessary, but not sufficient, experimental criterion for the normal-coordinate theory is that the elastic compliance be related to certain average molecular weights.[5,6] Unfortunately, the testing of this theory has proved very difficult in the past, partly because of the difficulty of measuring the higher average molecular weights, and partly because of the incorrect belief that the polymer samples must be monodisperse fractions or that some assumed molecular-weight distribution function must apply.[7,8]

We have developed a new method for determining the type of molecular-weight average upon which a viscoelastic property may depend by merely measuring that property on whole polymers and intimate molecular mixtures of whole polymers which provides a way of evaluating the normal-coordinate theory on a given type of polymer system in an extremely simple and straightforward manner. Once this experimental verification has been carried out, it is then possible to proceed with some confidence to use the normal-coordinate theory for the determination of molecular-weight distributions.[4]

Although we have developed this method with particular reference to rheological properties, the method is actually a completely general one. It may be used to determine the average molecular weight or any average function of the molecular weight upon which any measurable polymer property may depend.

II. CALCULATION OF THE AVERAGE MOLECULAR WEIGHT OF A MIXTURE OF WHOLE POLYMERS FROM THE AVERAGE MOLECULAR WEIGHTS OF THE COMPONENTS

Consider a number of whole polymers of different average molecular weights which will be called components and designed by the subscript j where $j=1, 2\cdots X$, X being the number of such components. A molecularly homogeneous mixture of these whole polymers is itself a whole polymer and will be designated by the subscript m. The $(n+\alpha)$th average of the molecular weights in the whole polymers may be written as

$$\langle M\rangle_{(n+\alpha),m}=\sum_i M_i^{\alpha+1}N_{im}/\sum_i M_i^{\alpha}N_{im}, \tag{1}$$

$$\langle M\rangle_{(n+\alpha),j}=\sum_i M_i^{\alpha+1}N_{ij}/\sum_i M_i^{\alpha}N_{ij}, \tag{2}$$

where the angular bracket indicates an average value, M_i is the molecular weight of a polymer containing i monomers, N_{ij} and N_{im} are the number of such molecules in the whole polymers j and m, respectively, and α is an index which determines the type of averaging to be made. Setting $\alpha=0$, 1, 2, 3, respectively, in Eqs. (1) and (2) generates the equations for the number-average, weight-average, z-average, $(z+1)$-average molecular weights. Now since $N_{im}=\sum_j N_{ij}$, Eqs. (1) and (2) may be combined to give

$$\langle M\rangle_{(n+\alpha),m}=\sum_{j=1}^{X}\langle M\rangle_{(n+\alpha),j}\sum_i M_i^{\alpha}N_{ij}/\sum_i\sum_j M_i^{\alpha}N_{ij}. \tag{3}$$

Now we can define the $(n+\alpha)$th fraction of the jth

[1] P. E. Rouse, Jr., J. Chem. Phys. **21,** 1272 (1953).
[2] F. Bueche, J. Chem. Phys. **22,** 603 (1954).
[3] B. H. Zimm, J. Chem. Phys. **24,** 269 (1956).
[4] E. Menefee and W. L. Peticolas **35,** 946 (1961).
[5] J. D. Ferry, M. L. Williams, and D. M. Stern, J. Phys. Chem. **58,** 987 (1954).
[6] F. Bueche, J. Appl. Phys. **26,** 783 (1955).
[7] J. M. Watkins, J. Appl. Phys. **27,** 419 (1956).
[8] H. Leadermann, R. G. Smith, L. C. Williams, J. Polymer Sci. **36,** 233 (1959).

component as

$$(n+\alpha)_j = \sum_i M_i^{\alpha} N_{ij} / \sum_j \sum_i M_i^{\alpha} N_{ij}, \tag{4}$$

and obtain

$$\langle M \rangle_{(n+\alpha),m} = \sum_{j=1}^{X} (n+\alpha)_j \langle M \rangle_{(n+\alpha),j}, \tag{5}$$

which relates the average molecular weight of a blend of whole polymers to the average molecular weight of the blend components. Equation (4) is a generalization of the fraction concept. Setting $\alpha=0, 1, 2, 3$ generates the number fraction, weight fraction, z fraction, and $(z+1)$ fraction, respectively.

By similar reasoning it is possible to show that the $(n+\alpha)$th average of the ath power of the molecular weights in a molecularly homogeneous mixture of whole polymers is related to the $(n+\alpha)$th average of the ath power of the molecular weights of the components by the relation

$$\langle M^a \rangle_{(n+\alpha),m} = \sum_{j=1}^{X} (n+\alpha)_j \langle M^a \rangle_{(n+\alpha),j}, \tag{6}$$

and indeed Eq. (2) may be written to include powers using our generalized fractions as

$$\langle M^a \rangle_{(n+\alpha),j} = \sum_i (n+\alpha)_{ij} M_i^{a}, \tag{7}$$

where $(n+\alpha)_{ij}$ is the $(n+\alpha)$th fraction of the ith molecular weight in the jth component, i.e.,

$$(n+\alpha)_{ij} = M_i^{\alpha} N_{ij} / \sum_i M_i^{\alpha} N_{ij}. \tag{8}$$

It is apparent that the $(n+\alpha)$th fraction of the jth component in the mixture is related to the $(n+\alpha)$th fraction of the ith molecular weight in the jth blend component by the relation

$$(n+\alpha)_i = \frac{\sum_i (n+\alpha)_{ij} [\sum_i N_{ij} M_i^{\alpha}]}{\sum_i \sum_j (n+\alpha)_{ij} [\sum_i N_{ij} M_i^{\alpha}]}. \tag{9}$$

Taking the ath root of both sides of Eq. (7) we have

$$\langle M^a \rangle_{(n+\alpha),m}^{1/a} = [\sum_j (n+\alpha)_j \langle M^a \rangle_{(n+\alpha),j}]^{1/a}. \tag{10}$$

This equation is a generalized viscosity-average molecular weight. With $\alpha=1$ and $0.5 \leq a \leq 1.0$, it is the Flory viscosity average.[9] Letting a go to zero provides the relation

$$\langle \ln M \rangle_{(n+\alpha),m} = \sum_j (n+\alpha)_j \langle \ln M \rangle_{(n+\alpha),j}. \tag{11}$$

The general theorem is stated as follows. Let $\phi(M)$ be any function of the molecular weight of a polymer. Let the $(n+\alpha)$th average of that function be defined as

$$\langle \phi(M) \rangle_{(n+\alpha),j} = [\sum_i M_i^{\alpha} N_{ij} \phi(M_i) / \sum_i M_i^{\alpha} N_{ij}]$$
$$= \sum_i (n+\alpha)_{ij} \phi(M_i). \tag{12}$$

Then, the average of $\phi(M)$ for a mixture of whole polymers is given in terms of the components by the relation

$$\langle \phi(M) \rangle_{(n+\alpha),m} = \sum_j (n+\alpha)_j \langle \phi(M) \rangle_{(n+\alpha),j}. \tag{13}$$

In order to use the above equations, it is necessary to be able to obtain experimentally the various fractions of the components. The weight fraction is simply obtained as the weight of a component divided by the sum of the weights of all the components. As we shall show below, if the average molecular weights of the components of a mixture are greatly different, many of the other fractions may be calculated from a knowledge of the weight fractions alone. This results in an enormous simplification in the experimental determination of the correct molecular-weight average upon which some measurable property of a polymer might depend. The number fraction n_j, the z fraction z_j, and the $(z+1)$ fraction $(z+1)_j$; of the jth component of a polymer blend may be written in terms of the weight fraction, $w_j = (n+1)_j$, as

$$n_j = \frac{w_j / \langle M \rangle_{n,j}}{\sum_j w_j / \langle M \rangle_{n,j}} \tag{14}$$

$$z_j = (n+2)_j = \frac{w_j \langle M \rangle_{(n+1),j}}{\sum_j w_j \langle M \rangle_{(n+1),j}} \tag{15}$$

$$(z+1)_j = (n+3)_j = \frac{w_j \langle M \rangle_{(n+1),j} \langle M \rangle_{(n+2),j}}{\sum_j w_j \langle M \rangle_{(n+1),j} \langle M \rangle_{(n+2),j}}. \tag{16}$$

III. DETERMINATION OF THE AVERAGE MOLECULAR WEIGHT UPON WHICH SOME POLYMER PROPERTY MAY DEPEND

The extraordinary simplicity of this new method may be shown as follows: Let some measurable polymer property θ be a function of some average of some function $\phi(M)$, of the molecular weight, i.e.,

$$\Theta = f[\langle \phi(M) \rangle_{(n+\alpha)}]. \tag{17}$$

Inversion of (17) yields

$$\langle \phi(M) \rangle_{(n+\alpha)} = f^{-1}(\Theta), \tag{18}$$

which when substituted into Eq. (13) gives

$$f_m^{-1}(\Theta) = \sum_j (n+\alpha)_j f_j^{-1}(\Theta). \tag{19}$$

Thus we have a simple linear dependence of a function of a measurable property of the mixture in terms of the

[9] P. Flory, *Principles of Polymer Chemistry* (Cornell University Press, Ithaca, New York, 1953).

corresponding functions of the measurable property of the components.

In this paper, we are concerned only with viscoelastic properties and with functions of the form $\phi(M)=M^a$, but the method is equally applicable to other properties of polymers which may depend on other functions of the molecular weight.

IV. CALCULATION OF THE RHEOLOGICAL PROPERTIES OF A MIXTURE FROM THE RHEOLOGICAL PROPERTIES OF THE MIXTURE COMPONENTS

At present, there are at least three proposals for the dependence of melt viscosity η on average molecular weights. The empirical equation of Fox and Flory[10] is

$$\eta = A\langle M\rangle_{(n+1)}^{3.4}, \tag{20}$$

where A is a function of the temperature. Bueche[11] has suggested that for very broad molecular-weight distribution

$$\eta = A\langle M\rangle_{(n+2)}^{3.4}, \tag{21}$$

while Fujita and Ninomiya[12] have suggested on the assumption of the linear additivity of distribution of relaxation times that

$$\eta = A\langle M^{3.4}\rangle_{(n+1)}. \tag{22}$$

Each of these equations may be tested by the use of Eq. (5) or (9).

For simplicity, let us take a blend of two components. Inversion of Eq. (20) gives $\langle M\rangle_{(n+1)}=(A^{-1}\eta)^{0.29}$, and substitution in Eq. (6) yields upon rearrangement

$$\Phi(w_2)=\frac{\eta_m^{0.29}-\eta_1^{0.29}}{\eta_2^{0.29}-\eta_1^{0.29}}=w_2. \tag{23}$$

Similarly, from Eq. (21) we have

$$\Phi(w_2)=\frac{\eta_m^{0.29}-\eta_1^{0.29}}{\eta_2^{0.29}-\eta_1^{0.29}}=\frac{w_2 r}{w_1+w_2 r}, \tag{24}$$

where

$$r=\langle M\rangle_{(n+1),1}/\langle M\rangle_{(n+1),2}$$

and from Eq. (22)

$$(\eta_m-\eta_1)/(\eta_2-\eta_1)=w_1. \tag{25}$$

If $r\gg 1$, it is a simple matter to distinguish among these three possibilities from a measurement of only the weight-fraction and the viscosities of mixtures of whole polymers and their components.

Ferry and Bueche[5,6] have independently shown that a necessary consequence of the normal-coordinate theory is the relation between the steady-state elastic compliance and certain average molecular weights, namely,

$$J=K\langle M\rangle_{(n+2)}\langle M\rangle_{(n+3)}/\langle M\rangle_{(n+1)}^2$$
$$=\langle M^3\rangle_{(n+1)}/(\langle M\rangle_{(n+1)})^2. \tag{26}$$

Combining this equation with Eq. (6) gives

$$J_m=\sum_j (z_j^2/w_j)J_j. \tag{27}$$

If $\langle\eta\rangle=A\langle M\rangle_{(n+1)}^B$ where $\langle\eta\rangle$ may be either a melt viscosity or a solution viscosity, then Eq. (28) may be written

$$\langle\eta\rangle_m^{2/B}J_m=\sum_j w_j\langle\eta\rangle_j^{2/B}J_j. \tag{28}$$

This is a particularly simple equation involving easily measurable quantities. For $B=3.45$, we have for a two component mixture

$$\chi(w_2)\equiv\frac{J_m\eta_m^{0.58}-J_1\eta_1^{0.58}}{J_2\eta_2^{0.58}-J_1\eta_1^{0.58}}=\omega_2. \tag{29}$$

Equation (29) presents a simultaneous test of Eqs. (20) and (26).

In general, properties which depend upon a product of average molecular weights, such as the elastic compliance, may be treated in the following manner. Let be some measurable property related to the product of average molecular weights by the general relation

$$\Theta=A\prod_{\alpha=r}^{R}(\langle M\rangle_{(n+\alpha)})^{B\alpha}.$$

Then the property of a mixture is related to the property of the components through the relation

$$\Theta_m^{1/B_R}\xi_m^{1/B_R}=\sum_{j=1}^{X}(n+r)_j\Theta_j^{1/B_R}\xi_j^{1/B_R}, \tag{30}$$

where

$$\xi=\prod_{\alpha=1}^{R-1}(\langle M\rangle_{(n+\alpha)})^{B_R-B\alpha}.$$

V. TREATMENT OF EXPERIMENTAL RESULTS

The details of our experimental results on a number of different types of polymers will be the subject of another paper. However, we may illustrate the use of the above equation with some data on linear polyethylenes. A series of homogeneous mixtures of two polyethylenes, a marlex 20 and a marlex 50 were made using a solution-precipitation technique. The viscosities and compliances were measured on the melt in a cone and plate rheometer designed by E. Menefee.[13] The weight-average molecular weights of the polymers were estimated from a measurement of the zero-shear-rate melt viscosity using the equations of Peticolas and Watkins.[14]

[10] For review, see T. G. Fox and S. Loshaek, J. Appl. Phys. **26**, 1080 (1955).
[11] F. Bueche, J. Polymer Sci. **43**, 527 (1960).
[12] H. Fujita and K. Ninomiya, J. Polymer Sci. **24**, 233–60 (1957).
[13] E. Menefee (unpublished work).
[14] W. L. Peticolas and J. M. Watkins, J. Am. Chem. Soc. **79**, 5083 (1957).

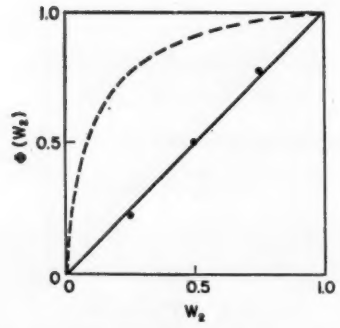

FIG. 1. A plot of Eqs. (23) (solid line) and (24) (dashed line) together with experimental points on high-density polyethylenes. $\Phi(w_2) \equiv (\eta_m^{0.29} - \eta_2^{0.29})/(\eta_2^{0.29} - \eta_1^{0.29})$, where η_2 and η_1 are the melt viscosities of two high-density polyethylenes and η_m is the melt viscosity of a mixture containing a weight fraction w_2 of the high viscosity component.

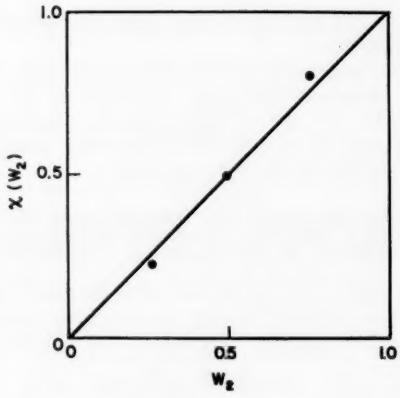

FIG. 2. A plot of Eq. (29) where

$$\chi(w_2) = (J_m\eta_m^{0.58} - J_2\eta_2^{0.58})/(J_2\eta_2^{0.58} - J_1\eta_1^{0.58}),$$

J_2 and J_1 being the steady-state elastic compliances of two high density polyethylenes and J_m is the compliance of a mixture containing a weight fraction w_2 of the high viscosity component.

These molecular weights allow an estimation of the z fractions over a wider range of concentration than would be otherwise possible. However, this is actually not necessary. Since the ratio of molecular weights is large, a plot of $\Phi(w_2)$ should approach unity with zero slope if Eq. (24) is correct and with a slope of unity if Eq. (23) holds.

Plots of Eqs. (23), (24), and (29) are shown in Figs. 1 and 2. It is apparent that these data are in agreement with the requirements of normal-coordinate theory. They also appear to obey the Fox-Flory relationship, Eq. (23).

Although the method which we have outlined here is very simple, a number of precautions should be taken in preparing mixtures for measurement: (1) The properties of all components must obey the same functional relationship to the same average molecular weight. In the case of melt viscosity, the functionality changes abruptly at some critical molecular weight[10] and, consequently, the average molecular weight of both polymers must be below or above this critical molecular weight; (2) Extreme care must be taken in preparing the mixtures to make certain that the final preparation is homogeneous and that no oxidative cross linking has occurred. Both inhomogeneous mixing and cross linking will result in anomalously high elastic compliances.

The elastic-compliance measurements on polyisobutylene by Leadermann, Smith, and Williams[8] do not follow Eq. (29). The reasons for this are not clear. Possibly polyisobutylene fails to follow the Ferry-Bueche relation. It also may be possible that their low molecular-weight component was too close to the break in the $\eta_0 - M$ curve. However, with the method of this paper, it is very simple matter to check the Ferry-Bueche relation for a large number of different types of polymers.

Theory and Measurement of Pressure-Induced Shifts of HCl Lines Due to Noble Gases*

A. BEN-REUVEN,† S. KIMEL,‡ M. A. HIRSHFELD, AND J. H. JAFFE

The Weizmann Institute of Science, Rehovoth, Israel

(Received March 1, 1961)

Pressure shifts of HCl absorption lines in both the 1–0 and 2–0 bands caused by five noble gases have been measured. An outstanding feature of these measurements is that the shifts are not the same for all lines of a band, but there is a strong dependence on the rotational quantum number J. However, there is evidence that the shifts tend to a constant limit for high J numbers. In order to interpret these results induction- and dispersion-type van der Waals forces were considered and used in conjunction with existing line-shape theories. In cases where perturbation theory can be applied, the limit shifts were accounted for fairly well, although no satisfactory explanation has emerged for the J dependence. Attention is drawn to the significance of observations of this sort as a means of obtaining information about intermolecular forces and molecular constants. Of particular interest is the possibility of obtaining such information for molecules in specific quantum states.

INTRODUCTION

THE shape of lines in molecular absorption spectra depends for the most part on the nature of the forces acting between individual molecules in the sample under examination. Conversely a study of spectral line shape yields information about intermolecular forces. Generally speaking the effect of increasing the pressure of a gas is to cause broadening and shifting of its spectral lines. In vibration-rotation bands it is desirable to study these effects at rather low pressures (preferably below atmospheric) because then the lines are sharp and the rotational fine structure is observed. At low pressures the main experimental problem is that the instrumental slitwidth is not small compared to the linewidth and errors and uncertainties occur in the process of making instrumental corrections.

It is found that the broadening is not the same for all lines of a vibration-rotation band but varies steadily from one end of a branch to the other. This interesting feature of pressure broadening was discovered by Herzberg and Spinks[1] and has stimulated a great deal of theoretical work on the subject.[2]

Pressure shifts are rather small and if it is desired to study the shifts of individual vibration-rotation lines, that is, to confine observations to the pressure range 0–1 atm, then it is necessary to measure shifts of the order of 0.01 cm^{-1}. However, in spite of the smallness of the effect, it has been found possible to measure it fairly easily by developing special techniques.[3] If both the lines themselves and the slit function of the spectrometer are symmetrical then the shifts can be measured directly with no necessity for making instrumental corrections.

A brief history of work done on line shifts together with some of our own early results have already been published.[3,4] This work has been pursued by Rank and co-workers.[5] In this paper an investigation is reported of a case that was thought to be a simple one: the spectrum of HCl perturbed by noble gases. Although several features of the observed shifts are explained, it seems that there is much more to be done before a complete interpretation can be presented.

EXPERIMENTAL

The experimental techniques were essentially the same as those already described.[3] Briefly the procedure was to compare the spectra of HCl samples in a pair of identical absorption cells. Each contained the same small quantity of HCl but in one there was added about 60 cm Hg pressure of a noble gas. It was established in preliminary experiments that the observed pressure shifts are proportional to pressure. The magnitude of the shifts actually measured was in the neighborhood of 0.02 cm^{-1}. The average deviation of the observations on an individual line was approximately 0.0015 cm^{-1}.

The shifts of the lines of the HCl 1–0 and 2–0 bands due to five noble gases are presented in Figs. 1 and 2. The addition of argon, krypton, or xenon causes a decrease of the frequencies of the HCl lines [except $R(0)$ for argon and krypton]. These "red" shifts increase with increasing J number and at least in the case of argon tend to a limit for high J numbers. At low J numbers the shifts of corresponding lines are greater in the P branch than in the R branch. The J dependence of the shifts is the most striking feature of the observations and the most difficult one to explain.

* This research was supported in part by the Geophysics Research Directorate, U. S. Air Force Cambridge Research Center, through the European Office, ARDC.

† Part of the work reported here forms the subject of a master's thesis submitted by A. Ben-Reuven to the Israel Institute of Technology, Haifa.

‡ C. P. Scott Research Associate.

[1] G. Herzberg and J. W. T. Spinks, Proc. Roy. Soc. (London) **A147,** 434 (1934).

[2] For a review see R. G. Breene, Revs. Modern Phys. **29,** 94 (1957).

[3] S. Kimel, M. A. Hirshfeld, and J. H. Jaffe, J. Chem. Phys. **31,** 81 (1959).

[4] M. A. Hirshfeld, J. H. Jaffe, and S. Kimel, J. Chem. Phys. **32,** 297 (1960).

[5] D. H. Rank, W. B. Birtley, D. P. Eastman, and T. A. Wiggins, J. Chem. Phys. **32,** 296, 298 (1960); **33,** 323, 327 (1960).

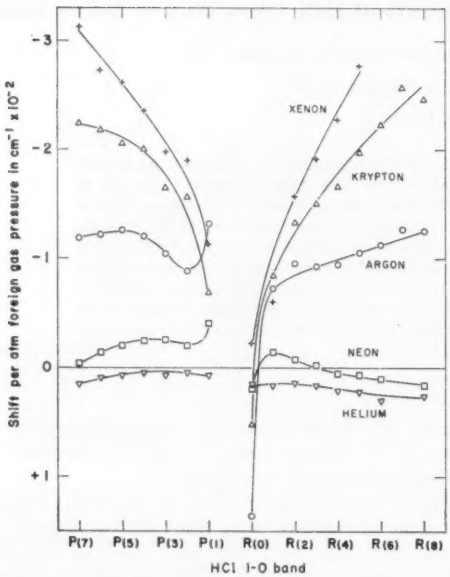

FIG. 1. Pressure-induced shifts of lines in the 1–0 band of HCl due to noble gases (at 297°K).

The shifts are larger in the 2–0 band than in the 1–0 band. The magnitude of the shifts increases with the size and polarizability of the perturbing molecules. This suggests that they may be interpreted in terms of interactions involving these polarizabilities. For helium and neon the polarizabilities are very small and other types of forces may assume importance.

INTERACTION ENERGY

A theoretical treatment of the effect of pressure on the shape of spectral lines of gaseous substances requires an intimate knowledge of intermolecular forces. These forces and their variation with the relative configuration of the colliding molecules affect the process of absorption of the light quantum either by perturbing the energy levels or by inducing transitions.

As we are concerned with low pressures we consider binary collisions only. We assume at the outset that for not too near collisions, and at moderate velocities, only long-range electrostatic forces between pairs of colliding molecules need be taken into account. The interaction energy may be regarded to a first approximation as that of a system of two electric dipoles

$$V_{\text{d.d.}}=\{\boldsymbol{\mu}_a\cdot\boldsymbol{\mu}_b-3(\boldsymbol{\mu}_a\cdot\mathbf{R})(\boldsymbol{\mu}_b\cdot\mathbf{R})R^{-2}\}R^{-3}. \quad (1)$$

Here $\boldsymbol{\mu}_a$ and $\boldsymbol{\mu}_b$ are the dipole moment operators of the two molecules a and b, and $\mathbf{R}$ is the radius vector which joins their centers of mass. In the case of collisions between a diatomic molecule and a noble gas atom, the interaction given by (1) does not cause a first-order perturbation since the dipole moment operator of the spherically symmetrical noble gas atom cannot have nonvanishing matrix elements in the electronic ground state. The dipole moment operator of a polar diatomic molecule on the other hand has nonvanishing matrix elements in the electronic ground state, in addition to elements which connect the ground state with other electronic states. Of the second-order perturbation terms those which involve only the electronic ground state of the diatomic molecule correspond to the so-called induction interaction. The terms with nondiagonal matrix elements in the electronic states of the diatomic molecule correspond to the so-called dispersion interaction. Let μ be the dipole moment function of the diatomic molecule in the electronic ground state; α_b the electronic polarizability of the noble gas atom extrapolated to zero frequency (which is approximately equal to the polarizability in the optical region); α_a the corresponding polarizability of the diatomic molecule averaged over its three principal axes; γ the anisotropy of α_a, defined by $\gamma=(\alpha_{||}-\alpha_\perp)/(2\alpha_\perp+\alpha_{||})$ where $\alpha_{||}$ and $\alpha_\perp$ are, respectively, the polarizabilities parallel and perpendicular to the internuclear axis. Then it can be shown[6] that when the rotational energies are negligible compared with the electronic energies, the second-order perturbation due to Eq. (1) can be replaced by first-order perturbations due to

$$V_{\text{induction}}=-\alpha_b\mu^2R^{-6}(\tfrac{1}{2}+\tfrac{3}{2}\cos^2\theta) \quad (2)$$

and

$$V_{\text{dispersion}}=-\tfrac{3}{4}\alpha_a\alpha_b IR^{-6}\{1+\gamma(\tfrac{3}{2}\cos^2\theta-\tfrac{1}{2})\}. \quad (3)$$

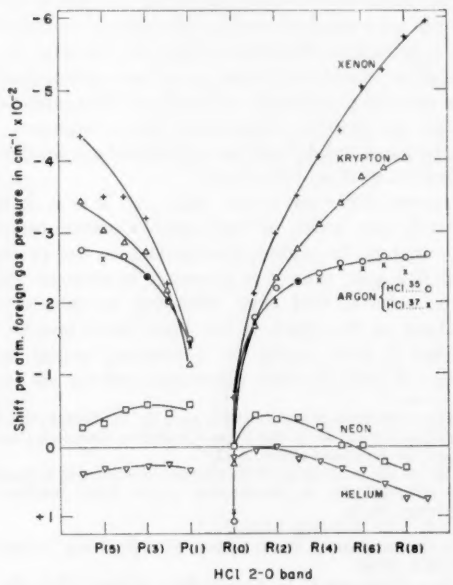

FIG. 2. Pressure-induced shifts of lines in the 2–0 band of HCl due to noble gases (at 297°K).

[6] P. W. Anderson, thesis, Harvard University, 1949.

Here θ is the angle between the internuclear axis and $\mathbf{R}$ (Fig. 3); $W=2W_aW_b/(W_a+W_b)$ where W_a and W_b are average excitation energies of the two molecules and for practical purposes may be taken to be the ionization energies. Equations (2) and (3) can be combined and expressed in terms of Legendre polynomials,

$$V=-\alpha_b R^{-6}[(\mu^2+\tfrac{3}{4}\alpha_a W)P_0(\cos\theta) + (\mu^2+\tfrac{3}{4}\gamma\alpha_a W)P_2(\cos\theta)]. \quad (4)$$

In order to calculate the first-order perturbation with (4) a knowledge is required of the dependence of μ^2 and α_a on the vibrational states. Both quantities can be expanded in terms of the displacement x from the equilibrium internuclear separation

$$\mu(x)=\mu_0+\mu_1x+\mu_2x^2+\cdots$$

$$\mu^2(x)=\mu_0^2+2\mu_1\mu_0x+(2\mu_2\mu_0+\mu_1^2)x^2+\cdots \quad (5)$$

$$\alpha_a(x)=\alpha_0+\alpha_1x+\cdots. \quad (6)$$

With the quantization axis chosen along the intermolecular axis, the angle θ is the polar angle (Fig. 3) of the diatomic molecule, treated as a linear vibrator-rotator. We proceed now to calculate the perturbations of the energy levels of the vibrator-rotator, with R taken as a classical coordinate. The Legendre polynomials may be written in terms of normalized spherical harmonics,

$$P_k(\cos\theta)=2\pi^{\frac{1}{2}}(2k+1)^{-\frac{1}{2}}Y_0^k(\theta,\phi).$$

In general matrix elements of Y_m^k can be expressed[7] in terms of vector coupling coefficients[8]

$$\langle JM \mid Y_m^k \mid J'M'\rangle=\left[\frac{(2k+1)(2J'+1)}{4\pi(2J+1)}\right]^{\frac{1}{2}} \times(kJ'mM' \mid kJ'JM)(kJ'00 \mid kJ'J0)\delta_{M,M'+m}$$

so that we have

$$\langle JM \mid P_k(\cos\theta) \mid J'M'\rangle =\left[\frac{2J'+1}{2J+1}\right]^{\frac{1}{2}}(kJ'0M \mid kJ'JM)(kJ'00 \mid kJ'J0)\delta_{M,M'}.$$

In what follows we shall require the average of the perturbations over the allowed values of the quantum number M for each value of J. It can be shown from the symmetry and orthogonality properties of the vector coupling coefficients, that

$$(2J+1)^{-1}\sum_M\langle JM \mid P_k(\cos\theta) \mid JM\rangle=\delta_{k,0}. \quad (7)$$

[7] M. E. Rose, *Multipole Fields* (John Wiley & Sons, Inc., New York, 1955).

[8] The vector coupling coefficients are written here in the notation of E. U. Condon and G. H. Shortley, *The Theory of Atomic Spectra* (Cambridge University Press, New York, 1935).

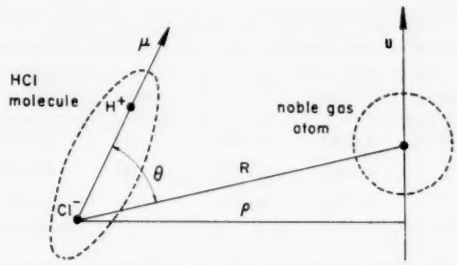

FIG. 3. Representation of collision between an HCl molecule and a noble gas atom.

Further, since μ^2 and α_a depend only on the vibrational quantum number v (neglecting vibration-rotation coupling) the first-order perturbations of the vibration-rotation levels of the diatomic molecule, averaged over the allowed values of M, are independent of J and are given by

$$\Delta E_{vJ}=-\alpha_b R^{-6}(\mu^2+\tfrac{3}{4}\alpha_a W). \quad (8)$$

These results are now applied to the case of HCl perturbed by the three heavier noble gases. For HCl, the polarizabilities[9,10] are

$$\alpha_0=2.63\ \text{A}^3, \qquad \alpha_1=1.0\ \text{A}^2, \qquad \gamma=0.094;$$

the dipole moment coefficients[11] are

$$\mu_0=1.093\ \text{debye}, \qquad \mu_1=0.933\ \text{debye A}^{-1},$$
$$\mu_2=-0.037\ \text{debye A}^{-2};$$

and the ionization potential[12] is

$$W_a=13.8\ \text{ev}.$$

For the noble gases the polarizabilities[9] and the ionization potentials[12] are

$$\alpha_{\text{Ar}}=1.63\text{A}^3, \qquad \alpha_{\text{Kr}}=2.48\ \text{A}^3, \qquad \alpha_{\text{Xe}}=4.01\ \text{A}^3;$$
$$W_{\text{Ar}}=15.68\ \text{ev}, \quad W_{\text{Kr}}=13.93\ \text{ev}, \quad W_{\text{Xe}}=12.08\ \text{ev}.$$

The expectation values of x and x^2 were calculated using anharmonic oscillator wave functions[13] for HCl. The resulting expectation values of μ^2 and α_a in the three lowest vibrational states are listed in Table I.

Using these data it follows that the dispersion interaction is an order of magnitude larger than the induction interaction; furthermore the P_2 term in (4), which gives the angular dependence, is smaller than the P_0 term; and the differences between the energies (8) in the various vibrational states are small compared

[9] *Landolt-Bornstein Tables* (Springer-Verlag, Berlin, 1950–51), Vol. I.

[10] E. J. Stansbury, M. F. Crawford, and H. L. Welsh, Can. J. Phys. **31**, 954 (1953).

[11] S. Kimel, thesis, University of Amsterdam, 1960.

[12] *Handbook of Chemistry and Physics* (Chemical Rubber Publishing Company, Cleveland, Ohio, 1957–58), 39th ed.

[13] R. C. Herman and K. E. Shuler, J. Chem. Phys. **22**, 481 (1954).

TABLE I. Matrix elements of x, x^2, μ^2, and α_a for HCl calculated with anharmonic oscillator wave functions.

v	$\langle v \mid x \mid v \rangle$ (10^{-8} cm)	$\langle v \mid x^2 \mid v \rangle$ (10^{-16} cm^2)	$\langle v \mid \mu^2 \mid v \rangle$ (debye^2)	$\langle v \mid \alpha_a \mid v \rangle - \alpha_0$ (10^{-24} cm^3)
0	0.0146	0.0061	1.229	0.0146
1	0.0424	0.0196	1.296	0.0424
2	0.0796	0.0369	1.386	0.0796

to the absolute values of the interaction energy in these states.

THE LINE SHIFT

We proceed to calculate shifts of HCl lines using theories which are applicable at high values of the rotational quantum number J. These theories give shifts which do not depend on J.

Phase Shift Method

According to the phase shift theory[14,15] the intensity distribution in a spectral line which arises from a transition from a state i to a state f is given by[16]

$$I_{if}(\omega) = \lim_{T\to\infty} (1/T)\left\{\left| \int_0^T dt e^{-i\omega t}\langle \Psi_f(t) \mid \boldsymbol{\mu} \mid \Psi_i(t)\rangle \right|^2\right\}_{Av}. \quad (9)$$

The averaging in (9) is carried out over all possible paths (treated classically) traversed by the colliding molecules. Here $\Psi_s(t)$, $s=i, f$, are the wave functions, in the Schrödinger representation, of the respective states.

In the adiabatic case, when one can neglect collision-induced transitions, the wave functions are given by[17]

$$\Psi_s = \psi_s[\mathbf{R}(t)] \exp\left\{-(i/\hbar)\int_0^t E_s[\mathbf{R}(t')]dt'\right\},$$

where the functions ψ_s and the energies E_s are the instantaneous solutions of the eigenvalue equation

$$H(\mathbf{R})\psi(\mathbf{R}) = E(\mathbf{R})\psi(\mathbf{R})$$

in the configuration $\mathbf{R}=\mathbf{R}(t)$. In this case Eq. (9) may be rewritten as

$$I_{if}(\omega) = \lim_{T\to\infty} (1/T)\left\{\left| \int_0^T \langle \psi_f(\mathbf{R}) \mid \boldsymbol{\mu} \mid \psi_i(\mathbf{R})\rangle \times \exp\left[i\int_0^t \omega_{fi}(t')dt' - i\omega t\right]dt \right|^2\right\}_{Av},$$

where $\hbar\omega_{fi}(t) = E_f(\mathbf{R}) - E_i(\mathbf{R})$. At low pressure the deformation effects of the collisions are negligible and the matrix elements of $\boldsymbol{\mu}$ may be considered constant in time (pure broadening[16]). Thus

$$I_{if}(\omega) = |\langle f \mid \boldsymbol{\mu} \mid i\rangle|^2 \cdot 2\mathrm{Re}\int_0^\infty dt e^{-i\omega t} \times \left\{\exp i\int_0^t \omega_{fi}(t')dt'\right\}_{Av}. \quad (10)$$

If one assumes, in addition, that the duration of a collision is very short compared with the mean time between successive collisions, then one obtains a Lorentz-type spectral line[15]

$$I_{if}(\omega) \propto \Gamma/[(\omega-\omega_{fi}-2\pi\Delta)^2+(\pi\Gamma)^2],$$

with a half-width

$$\Gamma = (1/\pi)\left\langle \int d\eta (1-\cos\eta)\, p(\eta)\right\rangle_{Av}, \quad (11a)$$

and a shift of the position of the line peak

$$\Delta = (1/2\pi)\left\langle \int d\eta \sin\eta p(\eta)\right\rangle_{Av}. \quad (11b)$$

Here η is the phase shift, defined by

$$\eta = (1/\hbar)\int (\Delta E_f - \Delta E_i)dt;$$

$p(\eta)d\eta$ is the average number of collisions per second which induce a phase shift between η and $\eta+d\eta$. The averaging in (11) should be carried out over a Boltzmann distribution of the relative velocities on which η and $p(\eta)$ depend. But to a good approximation one can use instead an average value of the velocity $u=(8kT/\pi m)^{\frac{1}{2}}$ where m is the reduced mass of the colliding pair. For a collision with a given u, each of the possible paths is uniquely characterized by the asymptotic collision parameter ρ. Therefore the distribution of phase shifts can be expressed as a function of ρ as follows,

$$p(\eta)d\eta = nu\cdot 2\pi\rho d\rho,$$

where n is the number of perturbers per unit volume. Equation (11b) can therefore be written in the form

$$\Delta = nu\int \rho \sin[\eta(\rho, u)]d\rho. \quad (12)$$

Equations (11) depend on the assumption of adiabatic collisions. However it has been pointed out[18] that this assumption cannot be made when there is spatial degeneracy. Rotational levels, for example, have a $(2J+1)$-fold degeneracy corresponding to the possible values of M.

Van Kranendonk suggested a way to extend the phase shift method in cases of spatial degeneracy.[16] Let ψ_{JM} be the state functions with respect to an arbitrary axis fixed in space, and let φ_{JM} be those functions with

[14] E. Lindholm, thesis, University of Uppsala, 1942.
[15] H. M. Foley, Phys. Rev. **69**, 616 (1946).
[16] J. van Kranendonk, thesis, University of Amsterdam, 1952.
[17] L. I. Schiff, *Quantum Mechanics* (McGraw-Hill Book Company, Inc., New York, 1955).
[18] L. Spitzer, Phys. Rev. **58**, 348 (1940).

respect to the intermolecular axis whose configuration in space, relative to the fixed coordinate system, is given by $\mathbf{R}=\mathbf{R}(t)$. Then the transformation between the two systems is given by

$$\varphi_{JM}=\sum_{M'}D_{M'M}^{(J)}(\mathbf{R})\psi_{JM'},$$

where the matrices $D^{(J)}(\mathbf{R})$ form the J representation of the three-dimensional rotation group. Clearly, if the molecule remains in a fixed M state in one reference system, it will not remain in a fixed M state in the other system. When no transitions are induced among the various states ψ_{JM}, that is when the interaction is weak, transitions among the states φ_{JM} will occur, in spite of the fact that the interaction energy operator (4) is diagonal in M with respect to those states. The energy eigenvalues E_{JM} which correspond to φ_{JM} should then be replaced by

$$\bar{E}_{JM}=\sum_{M'}|\,D_{MM'}^{(J)}(\mathbf{R})\,|^2E_{JM'}. \tag{13}$$

Using matrix elements of $\mathfrak{v}$ given with respect to the functions ψ_{J_iM} and ψ_{J_fN}, Eq. (10) becomes

$$I_{if}(\omega)=\sum_{MN}|\,\langle iM\,|\,\mathfrak{v}\,|\,fN\rangle\,|^2\cdot 2\Re e\int_0^\infty dt e^{-i\omega t}\times\left\{\exp\left[i\int_0^t\bar{\omega}_{NM}(t')dt'\right]\right\}_{Av},$$

where

$$\hbar\bar{\omega}_{NM}=\bar{E}_{fN}(\mathbf{R})-\bar{E}_{iM}(\mathbf{R}).$$

For high J numbers the spacings between neighboring energy sublevels E_{JM} are small compared to the over-all perturbations, and the effect of (13) is to average out the possible energy sublevels which belong to a certain J value. In this case a simple average

$$\bar{E}_J=(2J+1)^{-1}\sum_M E_{JM}$$

may be taken instead of (13). Then

$$I_{if}(\omega)=[\sum_{MN}|\,\langle iM\,|\,\mathfrak{v}\,|\,fN\rangle\,|^2]\cdot 2\Re e\int_0^\infty dt e^{-i\omega t}\times\left\{\exp\left[i\int_0^t\bar{\omega}_{fi}(t')dt'\right]\right\}_{Av}. \tag{14}$$

This equation is equivalent to Eq. (10) for the nondegenerate case. According to (7) the first-order perturbations resulting from any interaction of the type

$$V(R,\theta)=\sum_k A_k(R)P_k(\cos\theta) \tag{15}$$

do not depend on J when averaged over M. Since the interaction energy (4) is of the general type (15), Eq. (14) leads to a J-independent shift of the vibration-rotation lines.

This result is confirmed by Anderson's theory of impact broadening.[19] In this theory, which includes the effect of nonadiabatic transitions, the width and shift of a line are expressed in terms of a complex differential cross section $S(\rho)\cdot 2\pi\rho d\rho$, by the relation

$$\tfrac{1}{2}\Gamma-i\Delta=nu\int\rho S(\rho)d\rho.$$

Now, $S(\rho)$ can be expanded in powers of the operator

$$P=(1/\hbar)\int\exp(H_0t/i\hbar)\,V(t)\,\exp(-H_0t/i\hbar)dt,$$

where H_0 is the unperturbed Hamiltonian of the molecular system, so that

$$S=S_0+iS_1+S_2+iS_3+\cdots. \tag{16}$$

Then, to the first approximation, the shift is given by

$$\Delta=-nu\int\rho S_1(\rho)d\rho,$$

where

$$S_1=(2J_i+1)^{-1}\sum_M\langle J_iM\,|\,P\,|\,J_iM\rangle-(2J_f+1)^{-1}\sum_N\langle J_fN\,|\,P\,|\,J_fN\rangle.$$

The matrix elements are calculated with respect to an arbitrary fixed quantization axis. Let θ' and ϕ' be the polar angles of the axis of the diatomic molecule, with respect to the fixed coordinate system, and θ'' and ϕ'' be the corresponding polar angles of $\mathbf{R}$. Then, according to the addition theorem of Legendre polynomials[8]

$$P_k(\cos\theta)=\frac{4\pi}{2k+1}\sum_m Y_m^{\,k}(\theta',\phi')\,Y_m^{\,*k}(\theta'',\phi''), \tag{17}$$

an interaction of the type (15) can be expressed in terms of the spherical harmonics $Y_m^{\,k}(\theta',\phi')$. But the average over M of the expectation values of these spherical harmonics vanishes except for $k=m=0$. Therefore only the P_0 term in (15) contributes to S_1, yielding

$$S_1=-\eta=-(1/\hbar)\int(\Delta\bar{E}_f-\Delta\bar{E}_i)dt,$$

where $\Delta\bar{E}_i$ and $\Delta\bar{E}_f$ are the average perturbations which for the present case are given by (8). Anderson's theory therefore gives to the first order a J-independent shift equal to that given by the phase-shift method if only the first term in the Taylor expansion of $\sin\eta$ is considered.

Calculation of the Limit Shift

If the kinetic energy of the relative motion is large enough, a smooth rigid-spheres model can be applied

[19] P. W. Anderson, Phys. Rev. **76**, 647 (1949).

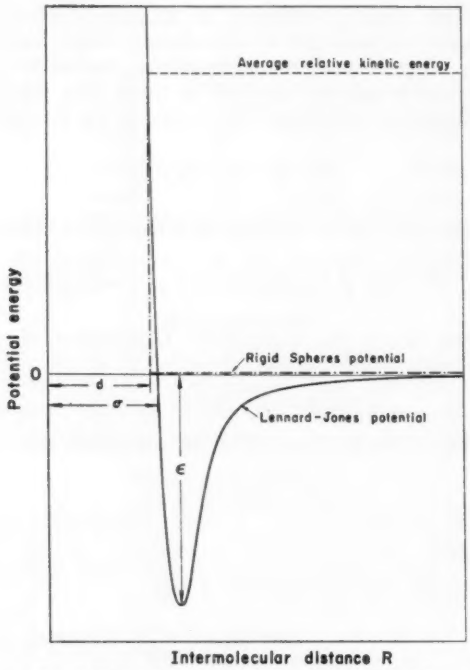

FIG. 4. Lennard-Jones and rigid-spheres potentials.

to the kinematics of the collision (Figs. 3 and 4). Let d be the rigid-spheres radius of collision. It is convenient to classify the collisions into two types[20]: those where $\rho>d$ and those where $\rho<d$. When $\rho>d$ the intermolecular distance as a function of the time t is given by

$$R=(u^2t^2+\rho^2)^{\frac{1}{2}}. \tag{18}$$

With an interaction of the type (8) the difference in the average perturbations of the final and initial levels has the form $-\beta R^{-6}$, hence

$$\eta=-\int\frac{\beta}{\hbar R^6}dt=-\frac{3\pi}{8}\cdot\frac{\beta}{\hbar u\rho^5}$$

The contribution to the shift due to collisions with $\rho>d$ (type I) is therefore

$$\Delta_I=nu\int_d^\infty\rho\sin[\eta(\rho)]d\rho=-nu\rho_0^2\int_{d/\rho_0}^\infty x\sin(x^{-5})dx,$$

where $\rho_0=(3\pi\beta/8\hbar u)^{1/5}$ is the collision parameter which corresponds to a phase shift $\eta=1$.

The collision radius may be expressed in terms of the parameters of the Lennard-Jones potential energy function[21] (Fig. 4)

$$V_{L.J.}=4\epsilon[(\sigma/R)^{12}-(\sigma/R)^6] \tag{19}$$

by equating $V_{L.J.}$ to the kinetic energy $\frac{1}{2}mu^2$, yielding

$$d=\sigma\{\tfrac{1}{2}[1+(1+mu^2/2\epsilon)^{\frac{1}{2}}]\}^{-1/6}. \tag{20}$$

For an interaction between the two different molecules a and b, σ and ϵ may be estimated as follows[21]:

$$\sigma=\tfrac{1}{2}(\sigma_a+\sigma_b);\qquad\epsilon=(\epsilon_a\cdot\epsilon_b)^{\frac{1}{2}}. \tag{21}$$

Values of d and ρ_0 obtained in this way for collisions of HCl with argon, krypton, and xenon, are listed in the second and third columns of Table II, for the 1–0 and 2–0 bands.

In collisions where $\rho<d$ (type II) the rigid-spheres model leads to

$$R=(u^2t^2+d^2+2|ut|d\cos\chi)^{\frac{1}{2}};\qquad\chi=\sin^{-1}(\rho/d). \tag{22}$$

In view of the fact that this gives η as a complicated function of χ, we consider only the two extreme possibilities: (a) $\rho=d$, and hence $R=(u^2t^2+d^2)^{\frac{1}{2}}$, and (b) $\rho=0$, and hence $R=|ut|+d$. In case (a), $\eta=-3\pi\beta/8\hbar ud^5$, and the contribution to the shift is

$$\Delta_{II(a)}=-nu\cdot\tfrac{1}{2}d^2\sin(\rho_0/d)^5, \tag{23a}$$

while in case (b), $\eta=-2\beta/5\hbar ud^5$, and

$$\Delta_{II(b)}=-nu\cdot\tfrac{1}{2}d^2\sin[(16/15\pi)(\rho_0/d)^5]. \tag{23b}$$

It may be supposed that the true result for collisions of type II lies somewhere between those given by (23a) and (23b). Values of Δ_I and of the two approximations for Δ_{II} are listed in Table II.

A Statistical Method

If the relative motion of the two molecules is considerably slower than the internal motions of the vibration and rotation, the shift problem may also be approached using a simple statistical model. The duration of a collision between an HCl molecule and one of the heavier noble gas atoms, with a collision parameter of about 3 to 4 A, is of the order of 10^{-12} sec, which is about the same as the period of the rotation of an HCl molecule in the state $J=1$. Therefore at high J numbers the conditions for a statistical treatment are realized.

The interaction energy (4) is of the general type (15) and can be expanded in terms of spherical harmonics with respect to a fixed-coordinate system, according to the addition theorem (17). The coordinates θ' and ϕ' of the linear molecule are treated quantum mechanically in a calculation of the perturbed energy levels. The coordinates of the relative configuration of the molecules R, θ'' and ϕ'', on the other hand, can be treated classically. In a simple statistical approach, all directions in space are equally probable, and the spherical harmonics $Y_m{}^k(\theta'',\phi'')$ have to be averaged over all the directions. But this average vanishes unless $k=m=0$. Therefore this approach also leads to a J-independent shift. Assuming a homogeneous distribution of perturbers in space, with a minimum distance of approach

[20] F. Schuller and B. Vodar, Compt. rend. **251**, 1877, 1998 (1960).

[21] J. O. Hirschfelder, C. F. Curtiss, and R. B. Bird, *Molecular Theory of Gases and Liquids* (John Wiley & Sons, Inc., New York, 1954).

TABLE II. Limit shifts Δ (in 10^{-2} cm^{-1} per atm at 297°K) for HCl pressurized by noble gases calculated with the phase-shift and statistical approximations, together with the experimental values.

			Phase shift approximation					Statistical approx.	Observed limit shifts
	d	ρ_0	Δ_I	Δ_{II}		$[\Delta_I+\Delta_{II}]$		Δ_s	
	(10^{-8} cm)			(a)[a]	(b)[a]	(a)	(b)		
1–0 band									
HCl—Ar	3.21	2.81	0.82	1.21	0.43	2.03	1.25	1.43	1.3
HCl—Kr	3.31	3.12	1.09	1.53	0.56	2.62	1.65	1.90	~3
HCl—Xe	3.53	3.43	1.35	1.84	0.70	3.19	2.05	2.36	>4
2–0 band									
HCl—Ar	3.21	3.34	1.86	2.28	0.98	4.14	2.84	3.35	2.8
HCl—Kr	3.31	3.69	2.31	2.22	1.25	4.53	3.56	4.43	~5
HCl—Xe	3.53	4.06	2.78	2.17	1.53	4.95	4.31	5.52	>8[b]

[a] The (a) and (b) stand for the approximations (23a) and (23b), respectively.
[b] Observations on the 2–0 band with Xe have been extended to $J=17$ by D. H. Rank (private communication).

d, the shift for a given β is

$$\Delta_s = -n\int_d^\infty (\beta/hR^6)4\pi R^2 dR = -4\pi n\beta/3hd^3. \quad (24)$$

The shifts calculated with (24) are listed in Table II.

DISCUSSION

The calculated results given in Table II are in fair agreement with the observed shifts in the wings of the bands, in such cases where these shifts approach a constant limit value[22] (with argon, and probably with krypton). The theory also accounts for the ratios between the observed shifts in the 2–0 and 1–0 bands, as can be seen from Table III. However, the treatment is inadequate both in the cases of xenon and of light perturbers (helium and neon).

During the course of the calculations it was seen that the more important contribution to the shifts comes from collisions where the minimum distance of approach is about 3 to 5 A. Using Eq. (8) a calculation for the ground state of HCl shows that the interaction energy at a separation of 4 A is about 100 cm^{-1} with argon and about 200 cm^{-1} with xenon. This energy is larger than the spacings $2BJ \approx 20J$ cm^{-1} of the rotational energy levels of HCl for low J numbers. A perturbation treatment is therefore applicable only when J is more than 10 in the case of argon and even higher in the case of krypton or xenon where the interaction energies are larger. Since first-order perturbation theory leads to a J-independent result this is in agreement with the fact that the limit shift is reached sooner with argon than with krypton or xenon. Therefore, at least for low J numbers, the interaction energy for near collisions should be treated in a different manner.

The strong J dependence of the shifts has not yet been explained satisfactorily. Neither has the fact that in both the 1–0 and 2–0 bands, the J dependence is of the same magnitude as the limit shifts. Therefore it is not likely that the J dependence is caused merely by higher order effects, such as the higher order terms appearing in Anderson's expansion (16). Other theories

TABLE III. Ratios of corresponding limit shifts in the 2–0 and 1–0 bands of HCl.

	Phase-shift approx.		Statistical approx.	Observed ratio	Line used
	(a)[a]	(b)[a]			
HCl—Ar	2.04	2.27	2.34	2.1	$R(8)$
HCl—Kr	1.73	2.16	2.33	1.6	$R(8)$
HCl—Xe	1.55	2.10	2.34	1.6	$P(6)$

[a] The (a) and (b) stand for the approximations (23a) and (23b), respectively.

[22] A distinction should be made between the limit shift introduced here and the band shift measured at high densities or in solutions.

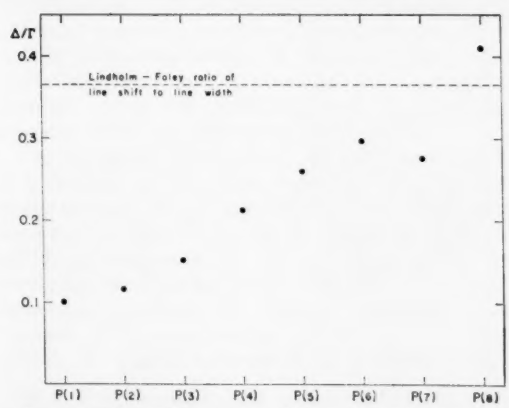

FIG. 5. Ratios of HCl–Ar line shifts to linewidths in the P branch of the 1–0 band. The shift of $P(8)$ was estimated from Fig. 1 by extrapolation.

put forward, using first-order perturbations only, are also incapable of explaining this phenomenon.[23]

It should be pointed out that theory leads to a constant limit shift only by neglecting: (a) transitions between various M states with respect to a fixed-coordinate system; (b) higher order interaction terms, which are J dependent and which, in spite of their smallness, may assume importance since the shifts arise from small differences between the otherwise J-independent perturbations (8); (c) the J dependence of the vibrational expectation values of x and x^2, due to vibration-rotation coupling.

The same arguments in the present theory which lead to a J independence of the shifts Δ at high J numbers should also lead to a J independence of the corresponding widths Γ. This means a fixed value of the ratio Δ/Γ in the wings of a band.[24] A comparison of the HCl–Ar widths recently measured in the P branch of the 1–0 band[25] with the corresponding shifts is presented in Fig. 5. The theoretical ratio seems to be reached for high J numbers, in agreement with L–F theory. It would be interesting to confirm the L–F theoretical value of Δ/Γ in other cases. It is worth noting that our shift data taken together with the L–F ratio imply larger linewidths in the wings of the 2–0 band than in the 1–0 band of HCl pressurized with noble gases.

With the limited amount of information on line shifts available it has not been possible to make a choice between the approximations presented above. Nevertheless it is clear from Table II that in nearly all cases the calculated limit shifts are too small. This may partially be attributed to inaccurately known molecular quantities.

For example we consider the use of Morse oscillator functions in the calculation of vibrational matrix elements for HCl. This would give[26] for the expectation value of x in the states $v=0$, 1 and 2 the values 0.0163, 0.0500, and 0.0854 A, respectively. Somewhat better agreement between theory and experiment could be obtained in this way. It should also be borne in mind that the first derivative α_1 of the polarizability, which plays a crucial role in the calculation of the shifts, is not known very accurately.[10] Taking an earlier estimate[27] $\alpha_1=1.23\times10^{-16}$ cm^2 instead of the value used above (1.0×10^{-16} cm^2) would also increase the results. Finally it should be remembered that the parameters σ and ϵ have not been obtained directly for the gas mixtures but have been calculated here with the relations (21). Small errors in σ will affect the calculations considerably through expression (20). Indeed recent studies[28] suggest that lower values of σ should be taken and this would lead to closer agreement between the magnitudes of the interaction energy given by (8) and the attractive part of (19). This would of course increase the calculated shifts.

A more detailed discussion must await the development of a more refined theory. It is also desirable to extend the measurements with krypton and xenon to higher J numbers. It is planned to continue the present work and it will also be extended to include studies on other absorbers.

ACKNOWLEDGMENTS

The authors wish to thank Dr. W. M. Benesch, Dr. R. Englman, and Dr. A. S. Reiner for many helpful discussions.

[23] B. Oksengorn and B. Vodar, Compt. rend. **251,** 361 (1960); F. Schuller and B. Oksengorn, *ibid.* **251,** 541 (1960).

[24] This is in agreement with Lindholm and with Foley (See works cited in references 14 and 15). However these authors (henceforth called L–F) did not distinguish between collisions of the two types (18) and (22) and therefore predicted a constant ratio $\Delta/\Gamma=0.363$, for all cases where the interaction energy is of the form βR^{-6}. In the present theory slightly different ratios are expected with different perturbers and in different bands.

[25] H. Babrov, G. Ameer, and W. Benesch, J. Chem. Phys. **33,** 145 (1960). The linewidths α given in this reference correspond to our $\Gamma/2$.

[26] B. F. Gray and H. O. Pritchard, J. Mol. Spectroscopy **2,** 137 (1958).

[27] R. P. Bell, Trans. Faraday Soc. **38,** 422 (1942).

[28] E. A. Guggenheim and M. L. McGlashan, Proc. Roy. Soc. (London) **A255,** 456 (1960); Mol. Phys. **3,** 563 (1960).

THE JOURNAL OF CHEMICAL PHYSICS VOLUME 35, NUMBER 3 SEPTEMBER, 1961

Excited States of Molecules and the Scattering of Fast Electrons

J. KARLE

U. S. Naval Research Laboratory, Washington 25, D. C.

(Received September 19, 1960)

When fast electrons are scattered by molecules which undergo excitation in the course of the scattering process, the patterns associated with discrete energy losses show the characteristic molecular-diffraction features associated with interatomic distances. A theory is developed here in agreement with experimental results thus far obtained which describes the possible forms for these diffraction features, and shows that the molecular scattering does not necessarily disappear on averaging over all states of excitation, as has been generally assumed for the "incoherent" scattering. In developing the theory, the wave function for the molecule is formed from a linear combination of atomic orbitals assumed to be S functions. By means of group theoretical methods the proper linear combinations of S functions may be composed for the possible types of excited electronic states of the molecule. The theoretical analysis also employs the Franck-Condon principle and the Born scattering theory.

From the theory developed here it is possible to predict and interpret gross features of the molecular scattering from molecules in the process of excitation. The accurate prediction of energy changes and atomic background scattering are interesting problems for future consideration. This new electron-diffraction technique should be a valuable adjunct to the field of photon spectroscopy.

1. INTRODUCTION

THE development of an experimental technique which exhibits the scattering processes of fast electrons in considerable detail has afforded an opportunity to make a new approach to the study of the excited states of molecules. The technique[1] involves the application of an electron-velocity analyzer of the Mollenstedt type[2] which resolves the ordinary scattering pattern into many patterns, each corresponding to a particular quantum loss of energy, including zero, in the scattering process. The patterns formed by the analyzer may be termed homogeneous patterns, since ideally each one is formed from electrons having the same energy. From this point of view the ordinary diffraction pattern is inhomogeneous. Each homogeneous pattern is concerned with two eigenstates of the molecule, the one occurring before and the one occurring after the scattering process. The magnitude of the electron energy loss is determined by the energy difference between the two eigenstates as determined by the Franck-Condon principle.[3] Thus the energy change is not necessarily the difference in energy at equilibrium between the two states since the equilibrium positions of the two states may not be the same. It is the purpose of this paper to develop a simple theory from which the nature of the possible homogeneous scattering patterns, arising from the excitation of molecules of any symmetry, may be predicted.

Ordinarily electron-diffraction photographs consist of the integration of all patterns formed in the scattering process and the portion derived from all possible energy losses (excluding zero) is called incoherent scattering. The basis for this terminology is the belief that the integration over all the homogeneous patterns involving energy loss for fast electrons gives a monotonically decreasing intensity function showing no distinct features related to the arrangements of interatomic distances in the molecules. It will be seen that the results of this paper indicate that the total of all scattering involving energy loss may have distinct features for many molecules. The presumed absence of these features in the incoherent scattering has given rise to a continuing impression that individual patterns related to processes involving a particular energy change would also be devoid of the usual maxima and minima characterizing the interatomic distances in the molecule. Many years ago Massey and Mohr[4] discussed this matter concluding that when it is possible to separate out the different inelastically scattered waves, each will show diffraction effects. Recent work with fast electrons[1] in our laboratory has verified this conclusion. A velocity analyzer of the Mollenstedt type has yielded the scattering patterns of several molecules for various energy changes, each showing diffraction effects. A particular advantage arises from using fast electrons in the experiments since the nature and interpretation of the scattering processes are simpler than those for slow electrons.

The development of a theory for the interpretation of scattering patterns from molecules incurring an energy loss has, up until now, been limited to homopolar diatomic molecules.[4,5] In order to extend the theory to include all molecules, we employ Born's theory of scattering, the Franck-Condon principle, and a group theoretical procedure for forming molecular wave functions from proper linear combinations of atomic orbitals. A valuable set of tables for S functions have

[1] D. A. Swick, Rev. Sci. Instr. **31,** 525 (1960).
[2] G. Mollenstedt, Optik **5,** 499 (1949).
[3] H. S. W. Massey and E. H. S. Burhop, *Electronic and Ionic Impact Phenomena* (Clarendon Press, Oxford, England, 1952), p. 221 ff.
[4] H. S. W. Massey and C. B. O. Mohr, Proc. Roy. Soc. (London) **A135,** 258 (1932).
[5] E. V. Ivash, Phys. Rev. **112,** 155 (1958).

been composed by Gunthard, Heilbronner, and Messikommer[6] which facilitate the formation of proper linear combinations of atomic orbitals. In addition, a general method for forming proper linear combinations of P functions has also been developed by Heilbronner and Gunthard.[7a–c]. In this paper we consider only spherically symmetric atomic electron distributions, i.e., S functions.

In the development of the scattering theory, it will be seen that it is important to have wave functions representing the eigenstates of a molecule. These functions have certain restrictions on their mathematical form consistent with the point group symmetry of the molecule. By means of group theory it is possible to derive the proper mathematical form for the eigenstates. As in the case for electron scattering from the normal state of a molecule without a change in energy, it is quite convenient to represent the molecular wave function as a linear combination of atomic orbitals. These atomic functions may be zeroth-order approximation, but they nevertheless reveal the major features of the homogeneous scattering patterns.

2. THEORY OF THE DISCRETE SCATTERING PATTERNS

The discrete electron scattering patterns are formed by inelastic processes leading to the various excited states of molecules. The energy changes most readily resolved involve changes in the electronic states although changes in the vibrational and rotational energy may also occur.

In developing a scattering theory, consideration must be given to the question of how the interatomic distances in a molecule are affected during the scattering process. As pointed out by Massey and Mohr[4] this question is answered by the application of the Franck-Condon principle, which implies that the interatomic distances do not change during the scattering processes involving excitation. We assume that the principle holds.

The intensity of electron scattering for a homogeneous scattering pattern is given by the collision theory of Born. We have approximately

$$I(\theta) = \frac{4\pi m^2 k'}{r^2 h^4 k} \left| \iint V \psi_p \psi_q^* \exp[i(k\mathbf{n}_0 - k'\mathbf{n}_1)\cdot\mathbf{r}] d\tau_M d\tau_e \right|^2, \tag{2.1}$$

where V is the interaction energy, ψ_p and ψ_q are the wave functions of the initial and final states of the molecule with interatomic distances those of the initial state, $k=2\pi/\lambda$ with λ the wavelength of the incident electron, $k'=2\pi/\lambda'$ with λ' the wavelength of the scattered electron, $\mathbf{n}_0$ is a unit vector in the direction of the incident beam, $\mathbf{n}$ is a unit vector in the direction of the scattered beam, $\mathbf{r}$ is a vector from some origin in the molecule to the colliding electron, r is the distance from the origin in the molecule to the point of observation of the scattering process (r is not the magnitude of $\mathbf{r}$), $d\tau_M$ is the volume element in the coordinates of the molecular electrons, and $d\tau_e$ is the volume element in the coordinates of the colliding electron.

From tables,[6] ψ_p and ψ_q can be obtained as the proper zeroth-order linear combinations of S functions for the various states of any molecule. We define these as

$$\psi_p = \sum_{t=1}^{v} \sum_{i=1}^{g(t)} h_{i,t}(p)\varphi_{p,t}(R_{i,t}), \tag{2.2}$$

where v is the number of types of atoms in the molecule, $g(t)$ is the number of equivalent atoms of each type, $h_{i,t}(p)$ is a coefficient read from the N matrix,[6] and $\varphi_{p,t}(R_{i,t})$ is an S function of the pth state expressed as a function of $R_{i,t}$, a coordinate measured from the center of the ith atom of type t. For a molecule composed entirely of atoms of the same type, (2.2) reduces to

$$\psi_p = \sum_{i=1}^{q} h_i(p)\varphi_p(R_i). \tag{2.3}$$

Similarly, we may also write

$$\psi_q = \sum_{i=1}^{q} h_i(q)\varphi_q(R_i). \tag{2.4}$$

For simplicity we restrict our attention at present to the equal atom case described by (2.3) and (2.4). We form $\psi_p\psi_q^*$ assuming that the atoms are discrete, thereby eliminating the cross terms, since the function $\varphi_p(R_i)$ would be negligible where $\varphi_q(R_j)$ has a significant value ($i\neq j$).

We obtain

$$\psi_p\psi_q^* = \sum_{i=1}^{q} h_i(p)h_i^*(q)\varphi_p(R_i)\varphi_q^*(R_i). \tag{2.5}$$

On substituting (2.5) into (2.1) it is seen that the integration over the molecular electron distribution can be expressed as the sum of integrations over the electron distributions of one atom at a time.

We must now associate an interaction energy V with each atom. For atom i we have

$$V = -\frac{Ze^2}{R_i'} + \frac{e^2}{|\mathbf{R}_i' - \mathbf{R}_i|}, \tag{2.6}$$

where Z is the atomic number of atom i, $\mathbf{R}_i$ is a vector of magnitude R_i from the center of atom i, marking the position of an atomic electron which is interacting with the colliding electron whose position from the

[6] H. Gunthard, E. Heilbronner, and B. Messikommer, Helv. Chim. Acta **35**, 2149 (1952). See the end of reference 7(a) for errata.

[7] (a) E. Heilbronner and H. Gunthard, Helv. Chim. Acta **37**, 1037 (1954); (b) **37**, 1534 (1954); (c) E. Heilbronner, *ibid.* **39**, 401 (1956).

center of atom i is indicated by the vector $\mathbf{R}_i'$ of magnitude R_i'. The first term on the right side of (2.6), which gives rise to the scattering, makes no contribution to (2.1) except when $p=q$, the condition for no change in state on scattering. As pointed out by Bethe,[8] this is due to the orthogonality of ψ_p and ψ_q, which are functions only of the positions of the molecular electrons. The scattering theory for the normal or lowest state given by $p=q=0$ is well known.

If we define $\mathbf{r}_i$ as a vector from the origin of the molecule to the center of atom i, we have

$$\mathbf{r}=\mathbf{r}_i+\mathbf{R}_i'. \tag{2.7}$$

Substitution of (2.5), (2.6), and (2.7) into (2.1) gives

$$I(\theta)=\frac{4\pi^2m^2k'}{r^2h^4k}\left|\sum_{i=1}^{g}h_i(p)h_i^*(q)\exp[i(k\mathbf{n}_0-k'\mathbf{n}_1)\cdot\mathbf{r}_i]\iint\left(-\frac{Ze^2}{R_i'}+\frac{e^2}{|\mathbf{R}_i'-\mathbf{R}_i|}\right)\right.$$
$$\left.\times\varphi_p(R_i)\varphi_q^*(R_i)\exp[i(k\mathbf{n}_0-k'\mathbf{n}_1)\cdot\mathbf{R}_i']d\tau(\mathbf{R}_i)d\tau(\mathbf{R}_i')\right|^2 \tag{2.8}$$

or

$$I(\theta)=(1/r^2)\,|\sum_{i=1}^{g}h_i(p)h_i^*(q)\exp[i(k\mathbf{n}_0-k'\mathbf{n}_1)\cdot\mathbf{r}_i]f_{pq}(\theta)\,|^2, \tag{2.9}$$

where

$$f_{pq}(\theta)=(2\pi m/h^2)(k'/k)^{\frac{1}{2}}\iint\left(-\frac{Ze^2}{R_i'}+\frac{e^2}{|\mathbf{R}_i'-\mathbf{R}_i|}\right)\varphi_p(R_i)\varphi_q^*(R_i)\exp[i(k\mathbf{n}_0-k'\mathbf{n}_1)\cdot\mathbf{R}_i']d\tau(\mathbf{R}_i)d\tau(\mathbf{R}_i'), \tag{2.10}$$

θ being the angle between the vectors $\mathbf{n}_0$ and $\mathbf{n}_1$. We have

$$(k\mathbf{n}_0-k'\mathbf{n}_1)\cdot\mathbf{R}_i'=(k^2+k'^2-2kk'\cos\theta)^{\frac{1}{2}}R_i'\cos\alpha, \tag{2.11}$$
$$=s'R_i'\cos\alpha, \tag{2.12}$$

α being the angle between $(k\mathbf{n}_0-k'\mathbf{n}_1)$ and $\mathbf{R}_i'$. We take the vector $(k\mathbf{n}_0-k'\mathbf{n}_1)$ as the polar axis and proceed to integrate (2.10). Employing spherical polar coordinates we have

$$d\tau(\mathbf{R}_i')=R_i'^2\sin\alpha d\beta d\alpha dR_i', \tag{2.13}$$

and (2.10) becomes

$$f_{pq}(\theta)=(2\pi me^2/h^2)(k'/k)^{\frac{1}{2}}\iint\left(-\frac{Z}{R_i'}+\frac{1}{|\mathbf{R}_i'-\mathbf{R}_i|}\right)\varphi_p(R_i)\varphi_q^*(R_i)\exp[is'R_i'\cos\alpha]R_i'^2\sin\alpha d\beta d\alpha dR_i'd\tau(\mathbf{R}_i). \tag{2.14}$$

The polar angle α is integrated from 0 to π, the equatorial angle β from 0 to 2π and R' from 0 to ∞. Integrating over α and β gives

$$f_{pq}(\theta)=(8\pi^2me^2/h^2)(k'/k)^{\frac{1}{2}}\iint_{R'=0}^{\infty}\left(-\frac{Z}{R_i'}+\frac{1}{|\mathbf{R}_i'-\mathbf{R}_i|}\right)\varphi_p(R_i)\varphi_q^*(R_i)(\sin s'R_i'/s'R_i')R_i'^2dR_i'd\tau(\mathbf{R}_i). \tag{2.15}$$

This integral may be expressed in the form

$$f_{pq}(\theta)=(8\pi^2me^2/h^2)(k'/k)^{\frac{1}{2}}[Z\delta_q^p-F_{pq}(\theta)/s'^2], \tag{2.16}$$

where $\delta_q^p=1$ if $p=q$ and zero otherwise, and

$$F_{pq}(\theta)=4\pi\int_0^{\infty}\varphi_p(R)\varphi_q^*(R)(\sin s'R/s'R)R^2dR. \tag{2.17}$$

We now have a convenient expression for $f_{pq}(\theta)$ and continue with the evaluation of $I(\theta)$ given by (2.9). Taking the square of the absolute value gives

$$I(\theta)=(1/r^2)\sum_{i=1}^{g}\sum_{j=1}^{g}f_{pq}(\theta)f_{pq}^*(\theta)h_i(p)h_i^*(q)h_j^*(p)h_j(q)\exp[i(k\mathbf{n}_0-k'\mathbf{n}_1)\cdot\mathbf{r}_{ij}], \tag{2.18}$$

where $\mathbf{r}_{ij}=\mathbf{r}_i-\mathbf{r}_j$.

[8] H. Bethe, Ann. Physik **5**, 325 (1930), particularly p. 339.

Expression (2.18) refers to a molecule with fixed orientation. We must average over all orientations in space. This average is

$$\langle \exp[i(k\mathbf{n}_0 - k'\mathbf{n}_1)\cdot \mathbf{r}_{ij}]\rangle = (1/4\pi)\int_0^{2\pi} d\beta_{ij}\int_0^{\pi} \exp[is'r_{ij}\cos\alpha_{ij}]\sin\alpha_{ij}d\alpha_{ij} \tag{2.19}$$

$$= \sin s'r_{ij}/s'r_{ij}. \tag{2.20}$$

We thus obtain from (2.18) the intensity function for a molecule composed of similar atoms,

$$I(\theta) = (1/r^2)\sum_{i=1}^{g}\sum_{j=1}^{g} f_{pq}(\theta) f_{pq}{}^*(\theta) h_i(p) h_i{}^*(q) h_j{}^*(p) h_j(q)\,(\sin s'r_{ij}/s'r_{ij}), \tag{2.21}$$

where $f_{pq}(\theta)$ is defined by (2.16) $h_i(p)$ is obtained from group theoretical tables and the r_{ij} are the interatomic distances for the molecule in state p. The scattering factor $f_{pq}(\theta)$ defined by (2.16) is real when $p=q$, as a consequence of employing the first Born approximation. However, this approximation gives $f_{pq}(\theta)$ generally as a complex function. We note that $f_{pq}(\theta)f_{pq}{}^*(\theta) = |f_{pq}(\theta)|^2$, so that no special effect is imposed on the diffraction patterns for molecules composed of one type of atom, even though the $f_{pq}(\theta)$ may be complex functions.

For the case of a molecule containing v kinds of dissimilar atoms we have

$$I(\theta) = (1/r^2)\sum_{t=1}^{v}\sum_{i=1}^{g(t)}\sum_{u=1}^{v}\sum_{j=1}^{g(t)} f_{t,pq}(\theta) f_{u,pq}{}^*(\theta) h_{i,t}(p) h_{i,t}{}^*(q) h_{j,u}{}^*(p) h_{j,u}(q)\frac{\sin s'r_{it,ju}}{s'r_{it,ju}}, \tag{2.22}$$

where

$$f_{t,pq}(\theta) = (8\pi me^2/h^2)\,(k'/k)^{\frac{1}{2}}\{[Z_t\delta_q{}^p - F_{t,pq}(\theta)]/s'^2\}, \tag{2.23}$$

$$F_{t,pq}(\theta) = 4\pi\int_0^{\infty} \varphi_{p,t}(R)\varphi_{q,t}{}^*(R)\,(\sin s'R/s'R)\,R^2dR, \tag{2.24}$$

$$= s'(k^2 + k'^2 - 2kk'\cos\theta)^{\frac{1}{2}}; \tag{2.25}$$

$h_{i,t}(p)$ and $h_{i,t}(q)$ are obtained from group theoretical tables, their values depending upon which of the $g(t)$ atoms, of type t in states p and q, the label i refers to, and $r_{it,ju}$ is the distance between the ith atom of type t to the jth atom of type u. When we are concerned only with the lowest or normal state of the molecule $p=q=0$, the $h_{i,t}$ are unity, $\delta_q{}^p = 1$, $k=k'$, and (2.22) is seen to reduce to the well-known expression for this case.

As already mentioned, $f_{t,pq}(\theta)$ calculated from the first Born approximation is real when $p=q$, and is generally complex otherwise. We may write

$$f_{t,pq}(\theta) = |f_{t,pq}(\theta)|\exp[i\eta_{t,pq}(\theta)], \tag{2.26}$$

where

$$\eta_{t,pq}(\theta) = \arg f_{t,pq}(\theta). \tag{2.27}$$

We thus obtain

$$f_{t,pq}(\theta)f_{u,pq}{}^*(\theta) = |f_{t,pq}(\theta)||f_{u,pq}(\theta)|\exp\{i[\eta_{t,pq}(\theta) - \eta_{u,pq}(\theta)]\}, \tag{2.28}$$

and (2.22) may be written

$$I(\theta) = (1/r^2)\sum_{t=1}^{v}\sum_{i=1}^{g(t)}\sum_{u=1}^{v}\sum_{j=1}^{g(t)} |f_{t,pq}(\theta)||f_{u,pq}(\theta)|\cos[\eta_{t,pq}(\theta) - \eta_{u,pq}(\theta)]h_{i,t}(p)h_{i,t}{}^*(q)h_{j,u}{}^*(p)h_{j,u}(q)\frac{\sin s'r_{it,ju}}{s'r_{it,ju}}. \tag{2.29}$$

It is seen that the function $\cos[\eta_{t,pq}(\theta) - \eta_{u,pq}(\theta)]$ is a function of the scattering angle θ, and when widely differing atoms are present in a molecule, the consequent differences in the phase angles will have a significant effect on the scattering pattern.

In considering some difficulties which arose in the determination of molecular structure for molecules containing atoms of widely differing atomic number, Schomaker and Glauber[9a,b] made the important discovery that the first Born approximation did not always suffice for experiments performed with 40-kv electrons. These investigations concerned the theory of scattering for molecules in their normal state for which the first Born approximation leads, with atomic potential functions, to scattering factors which are real, as indicated previously. Schomaker and Glauber pointed out that carrying out the scattering theory more accurately than the first Born approximation would lead to complex scattering amplitudes even when no excitation occurred on scattering. They found that neglecting the phase of the scattering amplitude could, at times, lead to serious errors in the determination of structure. It should be noted that the scattering factors computed from the first Born approximation are approximately equal to the absolute values of the complex scattering amplitudes for fast electrons.

[9] (a) V. Schomaker and R. Glauber, Nature **170**, 290 (1952); (b) Phys. Rev. **89**, 667 (1953).

Calculations have been made of the complex atomic scattering factors by Ibers and Hoerni[10] using more accurate solutions of the Schrödinger equation. These concerned mainly the scattering of electrons accelerated at approximately 40 kv by atoms in their normal state. The determination of scattering factors for atoms in transition between their excited states is a research problem for the future. However, the more accurate investigations for atoms in their normal state are helpful in indicating the nature and magnitude of the problem in general for molecules composed of atoms with greatly differing atomic numbers.

For a discussion of the excitation of molecular vibration and rotation by electron impact, the reader is referred to p. 276 ff. of reference 3.

3. APPLICATION OF THE THEORY

The application of the theory to predict the nature of the molecular electron scattering, associated with the excitation process, will be illustrated by means of a homonuclear diatomic molecule, and the molecules of carbon tetrachloride and benzene.

A. The Homonuclear Diatomic Molecule

The homonuclear diatomic molecule belongs to the point group C_i. There are two types of electronic states A_g and A_u. In this case (2.21) may be greatly simplified. At some fixed point of observation, (2.21) becomes

$$I(\theta)=K\,|\,f_{0q_1}(\theta)\,|^2[1+(\sin s'r/s'r)], \qquad (3.1)$$

$$I(\theta)=K\,|\,f_{0q_2}(\theta)\,|^2[1-(\sin s'r/s'r)], \qquad (3.2)$$

where K is some positive constant and the subscripts on the q's indicate that different states are involved. Formula (3.1) applies to a transition from the normal state to a state of type A_g and (3.2) applies to a transition to a state of type A_u, since $p=0$, $h(p)=1$ and $h_1(q)=h_2(q)=1$ for A_g, whereas $h_1(q)=1$ and $h_2(q)=-1$ for A_u. The values for these h's are read from Table IV of reference 6. We note that if we associate the orbital φ_1 with atom 1 and φ_2 with atom 2, the proper linear combination for A_g is $\varphi_1+\varphi_2$ and for A_u it is $\varphi_1-\varphi_2$.

As is customary, we designate that portion of the total scattering which is dependent upon interatomic distances as the molecular scattering and the remainder as atomic scattering. For the diatomic molecule, the molecular scattering is given by the second term in the parentheses of (3.1) and (3.2). The curve with the plus sign is similar to that for the normal state without transition and that with the minus sign is the rotation of the normal curve through 180° about the abscissa.[10a]

[10] J. Ibers and J. Hoerni, Acta Cryst. **7**, 405 (1954).

[10a] *Note added in proof.* The inversion of the molecular scattering pattern has recently been observed in our laboratory for an excitation of the diatomic molecule Br_2. A discussion of this result has been submitted to this *Journal* by D. Swick and J. Karle.

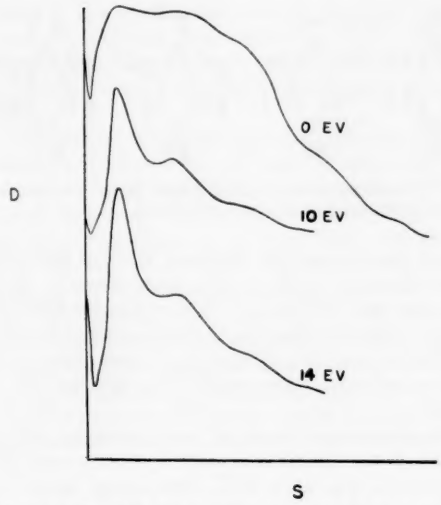

FIG. 1. Microphotometer traces of electron scattering curves with energy loss for CCl_4. Energy losses are indicated.

B. The Molecule CCl_4

The molecule CCl_4 belongs to the point group T_d. The proper linear combinations of orbitals for the Cl atoms are

$$A_1:\varphi_1+\varphi_2+\varphi_3+\varphi_4 \qquad (3.3)$$

$$F_2:\begin{cases}\varphi_1-\varphi_2+\varphi_3-\varphi_4\\ \varphi_1-\varphi_2-\varphi_3+\varphi_4\\ \varphi_1+\varphi_2-\varphi_3-\varphi_4.\end{cases}$$

We now consider the nature of the molecular scattering curves for transitions from the normal state to states of type A_1 and F_2. The coefficient of the carbon atom is $+1$, $p=0$, $h(p)=1$, and $v=2$ (one type is carbon and the other chlorine). At some point of observation for the scattering, the molecular intensity formula associated with the transition from the normal state, which is of type A_1, to one of type A_1 is [from (2.30) and (3.3)].

$$I_m(\theta)=K\Big\{4f_{C,0q_1}(\theta)f_{Cl,0q_1}(\theta)\frac{\sin s'r_{CCl}}{s'r_{CCl}}+6f_{Cl,0q_1}{}^2(\theta)\frac{\sin s'r_{ClCl}}{s'r_{ClCl}}\Big\}, \qquad (3.4)$$

where K is a positive constant. This formula evidently resembles the expression for scattering without transition. The molecular intensity formula associated with the transition from the normal state to one of type F_2 is [from (2.30) and (3.3)],

$$I_m(\theta)=K\Big\{-2f_{Cl,0q_2}{}^2(\theta)\frac{\sin s'r_{ClCl}}{s'r_{ClCl}}\Big\}, \qquad (3.5)$$

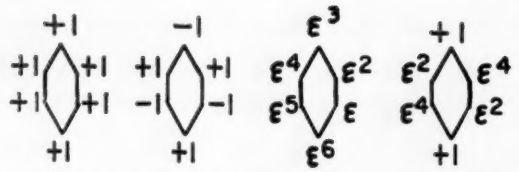

FIG. 2. Coefficients for forming proper linear combinations associated with the carbon atoms of benzene.

where K is some positive constant. Each of the triply degenerate states leads to the same formula. It is interesting that in this case the contribution from the carbon to chlorine distances is eliminated and that the contribution from the chlorine to chlorine distances is negative and three times weaker than that for the A_1 transition.

Microphotometer traces of total intensity curves obtained in our laboratory with a velocity analyzer[1] are shown in Fig. 1 for CCl_4. The energy losses are indicated on the curves. Although these results are preliminary in the sense that it is hoped to improve their accuracy with the development of new apparatus, the positions of the maxima and minima in the molecular portion indicate clearly that the two excited levels are similar to the zero or normal level and therefore are presumably of type A_1. It is of interest in this connection that a transition from an A_1 state to an A_1 state is optically forbidden.[11] Equation (2.1) may be treated in a manner similar to that given by Mott and Massey[12] for the excitation of discrete levels in atoms. The implication is that these transitions are associated with a quadrupole moment but no dipole moment.

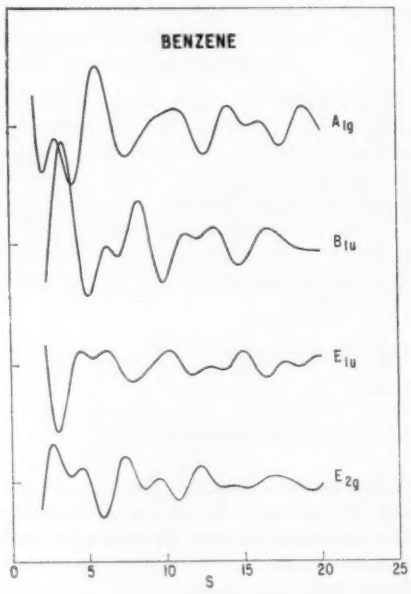

FIG. 3. Theoretical molecular scattering patterns for four types of electronic states of benzene.

[11] H. Sponer and E. Teller, Revs. Modern. Phys. **13**, 75 (1941).

C. The Benzene Molecule

The molecule benzene belongs to the point group D_{6h}. In order to obtain the general features of the scattering with excitation we can restrict our attention to the hexagon of carbon atoms. We do so for simplicity.

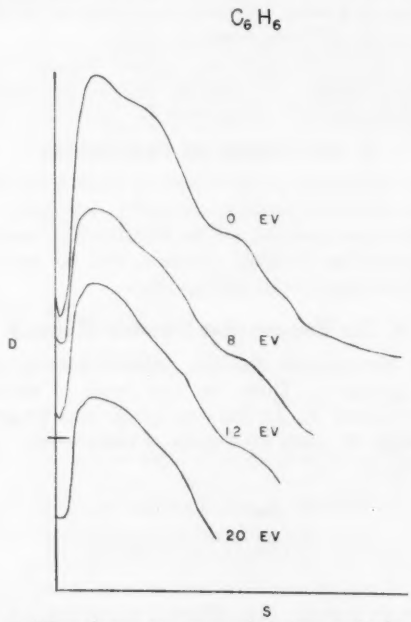

FIG. 4. Microphotometer traces of electron scattering curves with energy loss for benzene. Energy losses are indicated.

The proper linear combinations of orbitals for the carbon atoms are,

$$
\begin{aligned}
&A_{1g}: \varphi_1+\varphi_2+\varphi_3+\varphi_4+\varphi_5+\varphi_6,\\
&B_{1u}: \varphi_1-\varphi_2+\varphi_3-\varphi_4+\varphi_5-\varphi_6,\\
&E_{1u}: \begin{cases} \varphi_1+\epsilon\varphi_2+\epsilon^2\varphi_3+\epsilon^3\varphi_4+\epsilon^4\varphi_5+\epsilon^5\varphi_6 \\ \varphi_1+\epsilon^5\varphi_2+\epsilon^4\varphi_3+\epsilon^3\varphi_4+\epsilon^2\varphi_5+\epsilon\varphi_6, \end{cases} \qquad (3.6)\\
&E_{2g}: \begin{cases} \varphi_1+\epsilon^2\varphi_2+\epsilon^4\varphi_3+\varphi_4+\epsilon^2\varphi_5+\epsilon^4\varphi_6 \\ \varphi_1+\epsilon^4\varphi_2+\epsilon^2\varphi_3+\varphi_4+\epsilon^4\varphi_5+\epsilon^2\varphi_6, \end{cases}
\end{aligned}
$$

where $\epsilon=\exp[2\pi i/6]$.

The molecular scattering curves for transitions from the normal state to those of the types given in (3.6) are readily obtained from (2.21). We have again $p=0$, $h(p)=1$ and the $h(q)$ may be read from (3.6). They are illustrated in Fig. 2.

[12] N. F. Mott and H. S. W. Massey, *The Theory of Atomic Collisions* (Clarendon Press, Oxford, England, 1952), p. 241.

The molecular scattering associated with transitions to states of the following types is therefore,

$$A_{1g}: I(\theta) = K \mid f_{C,0q_1} \mid^2 \left\{ 6\frac{\sin s'r_s}{s'r_s} + 6\frac{\sin s'r_m}{s'r_m} + 3\frac{\sin s'r_l}{s'r_l} \right\} \tag{3.7}$$

$$B_{1u}: I(\theta) = K \mid f_{C,0q_2} \mid^2 \left\{ -6\frac{\sin s'r_s}{s'r_s} + 6\frac{\sin s'r_m}{s'r_m} - 3\frac{\sin s'r_l}{s'r_l} \right\} \tag{3.8}$$

$$E_{1u}: I(\theta) = K \mid f_{C,0q_3} \mid^2 \left\{ 3\frac{\sin s'r_s}{s'r_s} - 3\frac{\sin s'r_m}{s'r_m} - 3\frac{\sin s'r_l}{s'r_l} \right\} \tag{3.9}$$

$$E_{2g}: I(\theta) = K \mid f_{C,0q_4} \mid^2 \left\{ -3\frac{\sin s'r_s}{s'r_s} - 3\frac{\sin s'r_m}{s'r_m} + 3\frac{\sin s'r_l}{s'r_l} \right\}, \tag{3.10}$$

where K is a positive constant, r_s, r_m, and r_l are the small, medium and large carbon to carbon distances, respectively. We note that each of a pair of doubly degenerate states contributes the same scattering pattern.

Calculations were made of the expressions in the braces for (3.7)–(3.10), the variable scattering factor for carbon being neglected, and the result is shown in Fig. 3. It is seen that they differ considerably. Microphotometer tracings of the total scattering from an investigation of benzene employing the velocity analyzer are shown in Fig. 4. They extend to a value of $s' \sim 10$. Although there appear to be slight differences in the features of the curves at various levels, it appears that no definitive conclusions can be drawn from a comparison of these curves with Fig. 3, even if the background atomic scattering were removed. A more detailed analysis awaits improved experimental data.

THE JOURNAL OF CHEMICAL PHYSICS VOLUME 35, NUMBER 3 SEPTEMBER, 1961

Microwave Faraday Effect in Weakly Magnetic Gases*

MARTIN L. SAGE†

Mallinckrodt Chemical Laboratory, Harvard University, Cambridge 38, Massachusetts

(Received January 19, 1961)

The microwave Faraday effect is proposed as a method of measuring rotational magnetic moments in gases. The theory of the Faraday effect is developed by using the method of Karplus and Schwinger. In particular, it is applied near a microwave absorption frequency of the gas. The magnitude of the effect indicates that the Faraday effect may be a more satisfactory method of measuring small (less than 0.1 nuclear magneton) magnetic moments than the Zeeman effect. However, it requires intensity rather than frequency measurements and is therefore difficult.

INTRODUCTION

THE magnetic moments of most molecules are due to nuclear spin and to rotating charges. These moments are of the order of a nuclear magneton. These moments are satisfactorily measured by magnetic resonance and molecular beam techniques. It is of interest to see if the Faraday effect, the rotation of the plane of polarization of radiation propagating parallel to a magnetic field, would be a useful technique for measuring these moments.

A determination of the rotational magnetic moment would reveal how the charge distribution of the molecule rotates. The contribution of the nuclei and the closed shell electrons surrounding each nucleus to the magnetic moment can readily be calculated. On the other hand, the behavior of the valence electrons depends on the details of their wave function.[1] Thus, information about these wave functions can be obtained from the measurement of the rotational magnetic moments.

FARADAY EFFECT[2]

The rotation of the plane of polarization of electromagnetic radiation propagating parallel to a magnetic field arises from a difference in the indices of refraction for right and left circularly polarized light. The rotation α in a distance d is $\alpha = (\omega d/c)\frac{1}{2}(n'_l - n'_r)$, where ω is the circular frequency of the light and n'_l and n'_r the index of refraction for left and right circular polarization

* This research was supported in part by the Office of Naval Research and by a grant from the California Research Corporation.

† General Electric Foundation Fellow, 1957–59. Present address: Department of Physics, Brandeis University, Waltham, Massachusetts.

[1] C. H. Townes and A. L. Schawlow, *Microwave Spectroscopy* (McGraw-Hill Book Company, Inc., New York, 1955), p. 290.

[2] Wilhelm Schutz, "Magnetooptik I. Teil" in *Handbuch der Experimentalphysik* (Akademische Verlagsgesellschaft, Leipzig, 1936), Band 16, 1. Teil.

respectively. The Verdet constant V is the rotation per unit distance per unit magnetic field

$$V=\omega(n'_l-n'_r)/2cB, \tag{1}$$

where B is the magnetic field.

MOLECULAR POLARIZATION IN THE PRESENCE OF A MAGNETIC FIELD

Karplus and Schwinger[3] have derived the molecular polarization of a molecule in free space undergoing random strong collisions at an average time interval τ. We shall extend their derivation to the case in which there is a magnetic field B in the Z direction. We shall calculate the molecular polarization for right and left circularly polarized light propagating in the Z direction. The Hamiltonian of the molecule is given by

$$H(t)=H_0-\mu_X E\cos\omega t\pm\mu_Y E\sin\omega t. \tag{2}$$

The electric field is $\mathbf{E}(t)=\hat{x}E\cos\omega t\mp\hat{y}E\sin\omega t$. H_0 is the Hamiltonian of the isolated molecule, E the intensity of the electric field of the light, $\hat{x}$ and $\hat{y}$ unit vectors along the X and Y axes, respectively, μ_X and μ_Y the X and Y components of the electric dipole moment of the molecule, and ω the circular frequency of the radiation. The upper sign refers to right circular polarization and the lower to left. We now calculate the dipole moment $\boldsymbol{\mu}(t)$ of the molecule in a space fixed coordinate system as a function of time.

$$\boldsymbol{\mu}(t)=\chi'\mathbf{E}(t)+\chi''\mathbf{E}[t-(\pi/2\omega)], \tag{3}$$

where χ' and χ'' are the in-phase and out-of-phase components of the molecular polarizability, respectively.

Introducing the density matrix ρ we have

$$\boldsymbol{\mu}(t)=\mathrm{Tr}(\boldsymbol{\mu}\rho). \tag{4}$$

The assumption of random collisions at an average time interval τ means that the probability at a time t that the last collision occurred in the time interval $t-\theta$ and $t-\theta-d\theta$ is $\exp(-\theta/\tau)(d\theta/\tau)$. The assumption of a strong collision at $t_0=t-\theta$ means that following the collision there is, on the average, complete thermal equilibrium with the instantaneous value of the Hamiltonian at t_0, i.e.,

$$\rho_0(t_0)=\exp(-H(t_0)/kT)/\mathrm{Tr}\exp(-H(t_0)/kT). \tag{5}$$

This assumption implies that the duration of a collision is short compared to $1/\omega$. This is indeed the case for microwave frequencies but not for ultraviolet frequencies.

[3] R. Karplus and J. Schwinger, Phys. Rev. **73**, 1027 (1948).

The essence of the treatment is that, at any given time t, the molecules are divided into sets according to the time t_0 at which the members of a set suffered their last collision. The density matrix of the t_0 set $\rho(t, t_0)$ is assumed to equal $\rho_0(t_0)$ at t_0.

Between collisions the density matrix develops in time according to

$$i\hbar(\partial/\partial t)\rho(t, t_0)=[H, \rho(t, t_0)]. \tag{6}$$

We must solve Eq. (6) subject to the initial condition $\rho(t_0, t_0)=\rho_0(t_0)$ and then average over all t_0. We are interested in the average density matrix $\bar{\rho}(t)$, where

$$\bar{\rho}(t)=\int_0^\infty \rho(t, t-\theta)\exp(-\theta/\tau)(d\theta/\tau). \tag{7}$$

It is convenient to introduce

$$D(t)=\bar{\rho}(t)-\rho_0(t). \tag{8}$$

$D(t)$ measures the deviation of the density matrix from instantaneous thermal equilibrium. It develops according to

$$(\partial/\partial t)D(t)=-(i/\hbar)[H, D]-\tau^{-1}D-(\partial/\partial t)\rho_0. \tag{9}$$

We shall solve this equation in the representation in which the unperturbed Hamiltonian H_0 is diagonal with eigenvalues E_m. We shall assume a weak radiation field so that we may ignore terms involving $[(H-H_0), D]$. Equation (9) becomes

$$[(\partial/\partial t)+i\omega_{mn}+\tau^{-1}]D_{mn}=-[(\partial/\partial t)\rho_0]_{mn}, \tag{10}$$

where $\omega_{mn}=(E_m-E_n)/\hbar$.

It can be shown by an obvious adaptation of Karplus and Schwinger that

$$(\rho_0)_{mn}=P_m\delta_{mn}+\frac{P_m-P_n}{E_m-E_n}E(-\mu_X\cos\omega t\pm\mu_Y\sin\omega t)_{mn} \tag{11}$$

to the first order in E. P is the density matrix of the molecule in the presence of the static magnetic field only. Substituting into Eq. (10) and writing

$$D_{mn}(t)=D_{mn}^{(+)}\exp(-i\omega t)+D_{mn}^{(-)}\exp(i\omega t), \tag{12}$$

we find

$$D_{mn}^{(+)}=\frac{P_n-P_m}{2\hbar\omega_{mn}}E\omega\frac{(-\mu_X\pm i\mu_Y)_{mn}}{[\omega-\omega_{mn}+(i/\tau)]}$$

$$D_{mn}^{(-)}=\frac{P_n-P_m}{2\hbar\omega_{mn}}E\omega\frac{(-\mu_X\mp i\mu_Y)_{mn}}{[\omega+\omega_{mn}-(i/\tau)]}. \tag{13}$$

Thus,

$$\bar{\rho}_{mn}(t)=P_m\delta_{mn}+\frac{P_n-P_m}{2\hbar\omega_{mn}}E\left[\left(\frac{\omega}{\omega-\omega_{mn}+(i/\tau)}-1\right)(-\mu_X\pm\mu_Y)_{mn}\exp(-i\omega t)\right.$$
$$\left.+\left(\frac{\omega}{\omega+\omega_{mn}-(i/\tau)}-1\right)(-\mu_X\mp\mu_Y)_{mn}\exp(i\omega t)\right], \quad (14)$$

$$\mathfrak{y}(t)=\sum_{m,n}\mathfrak{y}_{nm}\bar{\rho}_{mn}(t). \quad (15)$$

We now diverge from the treatment of Karplus and Schwinger and consider the effects of the magnetic field on the system. Due to the symmetry in the presence of the magnetic field,

$$x_{mn}x_{nm}=y_{mn}y_{nm}$$
$$x_{mn}y_{nm}=-y_{mn}x_{nm}$$
$$x_{mn}z_{nm}=z_{mn}x_{nm}=0$$
$$y_{mn}z_{nm}=z_{mn}y_{nm}=0 \quad (16)$$

or any vector with components x, y, and z along the X, Y, and Z axes, respectively.

By using the symmetry relations, we find

$$\chi'=\sum_{m,n}|\,(\mu_X)_{mn}\,|^2\frac{P_n-P_m}{\hbar\omega_{mn}}\left[1-\frac{\omega(\omega-\omega_{mn})}{(\omega-\omega_{mn})^2+(1/\tau^2)}\right]$$
$$\pm i\sum_{m,n}(\mu_X)_{nm}(\mu_Y)_{mn}\frac{P_n-P_m}{2\hbar\omega_{mn}}\left[\frac{\omega(\omega-\omega_{mn})}{(\omega-\omega_{mn})^2+(1/\tau^2)}-\frac{\omega(\omega+\omega_{mn})}{(\omega+\omega_{mn})^2+(1/\tau^2)}\right], \quad (17)$$

where the upper sign refers to right circular polarization and the lower to left.

$$n'^2=1+4\pi N\chi', \quad (18)$$

where N is the number of molecules per unit volume. The Verdet constant is

$$V=\frac{\omega(n'_l-n'_r)}{2cB}=\frac{\omega\pi N}{\bar{n}'cB}(\chi'_l-\chi'_r) \quad (19)$$

where $\bar{n}'=(n'_l+n'_r)/2$.

$$V=-\frac{i\omega^2\pi}{cB\bar{n}'}\sum_{n,m}(\mu_X)_{nm}(\mu_Y)_{mn}\frac{P_n-P_m}{\hbar\omega_{mn}}\left[\frac{(\omega-\omega_{mn})}{(\omega-\omega_{mn})^2+(1/\tau^2)}-\frac{(\omega+\omega_{mn})}{(\omega+\omega_{mn})^2+(1/\tau^2)}\right]. \quad (20)$$

For the case of zero linewidth this reduces to the usual expression for the Verdet constant[2] and is in agreement with the experimental data for Faraday rotations due to electric dipole transitions.

VERDET CONSTANT NEAR A MICROWAVE RESONANCE FREQUENCY

We shall calculate the Verdet constant on the assumption that it is independent of the magnetic field B, i.e., we shall evaluate all terms in Eq. (20) that are linear in the magnetic field. Furthermore, we shall only consider the term which is near resonant at ν_0 since a microwave linewidth is small compared to its frequency at low pressures (0.1 mm). Under these conditions (20) reduces to

$$V(\nu)=\frac{4\pi^2N\nu^2i}{ckTB}\sum_{\text{Z.C.}}P_n(\mu_X)_{nm}(\mu_Y)_{mn}\frac{\nu-\nu_{nm}}{(\nu-\nu_{nm})^2+(\Delta\nu)^2}, \quad (21)$$

where the sum over Zeeman components (Z.C.) is the sum over all transitions for which $E_m-E_n\sim h\nu_0$. We have set $\bar{n}'=1$ and have written $(\Delta\nu)=1/2\pi\tau$. $(\Delta\nu)$ is the usual half-width at half maximum for microwave absorption lines. We have set

$$(P_n-P_m)/(E_n-E_m)=-P_n/kT$$

since $|\,E_n-E_m\,|\ll kT$ for ν_{nm} in the microwave region and $T\geqslant 200°\text{K}$.

In cases where the Faraday effect might prove useful, the linewidth is large compared to the Zeeman splittings. Here Eq. (21) becomes

$$V(\nu)=\frac{4\pi^2N\nu^2 i}{cKT}\Bigg\{\sum_{\text{Z.C.}}P_n^{(1)}(\mu_X^{(0)})_{nm}(\mu_Y^{(0)})_{mn}\frac{\nu-\nu_{nm}^{(0)}}{(\nu-\nu_{nm}^{(0)})^2+(\Delta\nu)^2}$$
$$+P_n^{(0)}\frac{(\nu-\nu_{nm}^{(0)})}{(\nu-\nu_{nm}^{(0)})^2+(\Delta\nu)^2}\sum_{\text{Z.C.}}\left[(\mu_X^{(0)})_{nm}(\mu_Y^{(1)})_{mn}+(\mu_X^{(1)})_{nm}(\mu_Y^{(0)})_{mn}\right]$$
$$+\frac{(\nu-\nu^{(0)}{}_{nm})^2-(\Delta\nu)^2}{[(\nu-\nu_{nm}^{(0)})^2+(\Delta\nu)^2]^2}P_n^{(0)}\sum_{\text{Z.C.}}\nu_{nm}{}^{(1)}(\mu_X^{(0)})_{nm}(\mu_Y^{(0)})_{mn}\Bigg\},\qquad(22)$$

where we have retained only those terms in V which are independent of the magnetic field B. We have written

$$P=P^{(0)}+BP^{(1)}+\cdots$$
$$\underline{\mu}=\underline{\mu}^{(0)}+B\underline{\mu}^{(1)}+\cdots$$
$$\nu=\nu^{(0)}+B\nu^{(1)}+\cdots.$$

For small linewidth the third term in (22) dominates. Ignoring the other terms we find that the Verdet constant near a resonant frequency has three extrema: one at the resonant frequency and the other two at a distance $\sqrt{3}\tau$ away. The extremum at the resonant frequency is eight times as large as the other extrema and is of the opposite sign.

EVALUATION OF THE VERDET CONSTANT FOR A NEAR SYMMETRIC TOP

We shall evaluate the quantity

$$\sum_{\text{Z.C.}}i[\mu_X^{(0)}]_{nm}[\mu_Y^{(0)}]_{mn}\nu_{nm}^{(1)}$$

which appears in Eq. (22) assuming that the z axis of the molecule has the unique moment of inertia. The rotational magnetic moment tensor is $\mathbf{G}$ with components g_{xz}, g_{xy}, $\cdots$ along the molecular axes. The electric dipole moment has components μ_x, μ_y, and μ_z along these axes. We shall define

$$g(J,K)=\tfrac{1}{2}(g_{xx}+g_{yy})+[g_{zz}-\tfrac{1}{2}(g_{xx}+g_{yy})]K^2/J(J+1)$$
$$+i\frac{K}{J(J+1)}\tfrac{1}{2}(g_{yx}-g_{yx}{}^*-g_{xy}+g_{xy}{}^*).\qquad(23)$$

The first-order correction to the frequency of the transition from (J,K,M) to (J',K',M') is[4]

$$\nu_{JKM,J'K'M'}{}^{(1)}=(M/h)g(J,K)-(M'/h)g(J',K').\qquad(24)$$

We evaluate

$$F_j(JK;J'K')$$
$$\equiv i\sum_{M,M'}\nu_{JKM,J'K'M'}{}^{(1)}\langle JKM\mid\theta_{Xj}\mid J'K'M'\rangle$$
$$\times\langle J'K'M'\mid\theta_{Yj}\mid JKM\rangle,\qquad(25)$$

[4] M. W. P. Strandberg, *Microwave Spectroscopy* (Methuen and Company, Ltd., London, England, 1954), p. 137.

where j is one of the molecular axes and θ_{Gj} is the direction cosine from the G space fixed axis (X or Y) to the j molecule fixed axis (x, y, or z). These F_j are tabulated in Table I.

Equation (22) becomes

$$V(\nu)=\frac{4\pi^2N\rho_{J,K}}{ckTh}\mu_j^2F_j(JK;J'K')\nu^2\frac{(\nu-\nu_0)^2-(\Delta\nu)^2}{[(\nu-\nu_0)^2+(\Delta\nu)^2]^2},\qquad(26)$$

where ν_0 is the frequency of the transition $J,K\rightarrow J',K'$. The maximum Verdet constant occurs for $\nu=\nu_0$.

$$V(\nu_0)=(4\pi^2N/ckTh)\mu_j^2F_j(JK;J'K')[\nu_0^2/(\Delta\nu)^2].\qquad(27)$$

This formula becomes

$$V(\nu_0)=1.3182\times10^{-14}\frac{\nu_0^2}{(\Delta\nu)^2}\sum_j\frac{(ABC)^{\frac{1}{2}}\mu_j^2P}{T^{\frac{3}{2}}}$$
$$\times F_j(JK;J'K'),\qquad(28)$$

where μ_j is the jth component of the molecular dipole moment in debyes, F_j is the sum defined by (25) in nuclear magnetons, A, B, and C are the rotational constants in Mc, P the pressure in mm Hg, and $(\Delta\nu)$ the half-width at half maximum at T and P. In Table I we see that the various F_j are less than $gJ/3$ where g is a typical component of the magnetic moment. Thus for a dipole moment of 1 debye, rotational constants of 10^4 Mc, resonant frequency of 20 000 Mc, linewidth of 10 Mc/mm Hg, pressure of 0.02 mm, $T=200°$K, $F_j=4g$ and $\exp(-E_n/kT)$ about 1, the maximum Verdet constant is approximately 10^{-7}g/cm gauss. The smallest magnetic moment that has been obtained from Zeeman splittings is about 0.1 nuclear magneton. This value would lead to a maximum Verdet constant of 10^{-8}/cm gauss.

MEASUREMENT OF THE MICROWAVE FARADAY EFFECT

The Faraday effect in the uv, visible, and ir regions of the spectrum uses plane polarized light. However, in the microwave region it is inconvenient to use plane polarized radiation. Ordinarily, the radiation is contained in a wave guide. The fields that can be propagated are the solutions to Maxwell's equations

TABLE I. $F_j(JK; J'K')$.

$$F_x(J, K; J+1, K+1)=\frac{1}{24}\frac{(J+K+1)(J+K+2)}{(J+1)}[(J+2)g(J+1, K+1)-Jg(J, K)]$$

$$F_z(J, K; J, K+1)=\frac{1}{24}\frac{(J+K+1)(J-K)(2J+1)}{J(J+1)}[g(J, K)+g(J, K+1)]$$

$$F_z(J, K; J+1, K)=-\frac{1}{6}\frac{(J+K+1)(J-K+1)}{(J+1)}[(J+2)g(J+1, K)-Jg(J, K)]$$

$$F_z(JK; JK)=-\frac{1}{3}\frac{K^2(2J+1)}{J(J+1)}g(J, K)$$

$$F_x(JK; J'K')=F_y(JK; J'K')$$

$$F_j(JK; J'K')=F_j(J-K; J'-K')=F_j(J'K'; JK)$$

subject to the boundary conditions imposed by the guide. The field distribution that most closely approximates plane polarized radiation is the TE_{11} mode in a circular guide. The Verdet constant for this mode will be similar to that for a plane wave.

For the Faraday effect due to the electric polarization Suhl and Walker[5] have shown that the ratio of the Verdet constant in a circular waveguide to the Verdet constant for a plane wave is given by

$$V_g^{nm}/V_p=2\lambda_g/(u_{nm}^2-n^2)\lambda_0, \qquad (29)$$

where V_g^{nm} is the Verdet constant for the TE_{nm} mode, V_p is the Verdet constant for a plane wave, λ_0 is the wavelength for the plane wave, λ_g is the guidewave length for the TE_{nm} mode, and u_{nm} is the mth zero of the derivative of the nth order Bessel function.

$$\lambda_g=\frac{\lambda_0}{[1-(\lambda_0/\lambda_c)^2]^{\frac{1}{2}}},$$

where λ_c is the cutoff wave length for the guide for the TE_{nm} mode. This formula fails near cutoff. For $\lambda_g=\lambda_0$ this expression is the largest for the TE_{11} mode, V_g^{11} being about 20% smaller than V_p. Nearer cutoff the term in λ_0/λ_c would increase V_g^{11} to V_p.

The crystal detectors commonly used in microwave spectroscopy detect the power along their antennas. Thus by using two crystal detectors with their antennas perpendicular, we can measure the value of the electric field parallel and perpendicular to the "plane of polarization" of the mode. A slight rotation θ of the mode would decrease the field from E_0 by $-E_0\theta^2/2$ and increase it from 0 to $E_0\theta$ in the parallel and perpendicular directions, respectively.

To achieve maximum sensitivity and overcome crystal noise, the magnetic field would have to be modulated. The usual Hughes-Wilson type microwave spectrometer uses an electric field modulated at a frequency of the order of 100 kc. For practical reasons, a magnetic field would have to be modulated with a frequency below 10 kc. With coherent detection, it is doubtful whether a sensitivity of better than 1 in 10^6 could be obtained in the measurement of θ^2, the ratio of the modulated crystal current to the dc crystal current for the crystal along the "plane of polarization" of the mode. Thus the smallest rotation that could be measured would be 10^{-3} rad. For a 200 gauss field and a 200-cm path length, a Verdet constant equal to 2.5×10^{-8} could be measured.

[5] H. Suhl and L. R. Walker, Phys. Rev. **86**, 122 (1952).

CONCLUSIONS

At the present time the microwave Faraday effect appears to be a method of measuring rotational magnetic moments. The predicted Verdet constant is of the same order as the predicted minimum measurable Verdet constant for reasonable assumptions concerning magnetic field, path length, and sensitivity. If an improvement in any of these factors can be gotten, the method would become practical.

A decrease in the pressure would increase the maximum Verdet constant as long as the pressure is high enough so that pressure broadening is the only significant contributor to the linewidth. At lower pressures collisions with the walls, saturation broadening, and modulation broadening are important. Thus there would be an optimum pressure at which to make the measurements.

Considering all the factors listed above, it seems reasonable that in the future the microwave Faraday effect might prove to be a useful method for measuring the rotational magnetic moments of molecules.

ACKNOWLEDGMENTS

The author wishes to acknowledge the aid of the late Professor William Moffitt who suggested this problem. The advice of Professor E. Bright Wilson, Jr., is also appreciated. Thanks are due to Dr. S. G. Reed, Jr. for the opportunity of reading a note of his on this subject.

Dipole Moment of HD. II

S. M. BLINDER*

Department of Chemistry, Harvard University, Cambridge 38, Massachusetts

(Received October 12, 1960)

The permanent electric dipole moment in the ground vibrational state of HD is computed by a variational technique (generalized perturbation method). Implicit account is thereby taken of contributions from higher molecular states of $^1\Sigma_u^+$ symmetry. The value $\langle\mu_Z\rangle_{v=0}=5.67\times10^{-4}$ Debye unit is assigned. Factors affecting the accuracy of the computation are discussed in detail. It is shown that an effective dipole moment function may be defined despite the fact that the dipole arises from a vibrational-electronic interaction.

I. INTRODUCTION

THE HD molecule is believed to have a small permanent electric dipole moment as a consequence of a perturbation arising from the asymmetry of nuclear vibration.[1,2] The complete molecular Hamiltonian contains the term

$$\mathcal{H}^{(3)}=(\hbar^2/2)[m_P^{-1}-m_D^{-1}]\times(\partial/\partial R)[(\partial/\partial Z_1)+(\partial/\partial Z_2)], \quad (1)$$

which changes sign with inversion of electronic coordinates through the molecular center. The principal terms of the Hamiltonian are invariant under inversion. Consequently, the electronic ground state, which is principally of $^1\Sigma_g^+$ symmetry, will contain a small amount of $^1\Sigma_u^+$ character. It is this admixture which destroys the rigorous inversion symmetry of the electronic wave function and hence introduces an electric dipole. In I the magnitude of the permanent moment was computed by a simplified application of perturbation theory. It was assumed that only the lowest $^1\Sigma_u^+$ state (commonly known as the B state) contributes significantly. An upper limit on the permanent moment was thereby computed. In the ground vibrational state this had the value 8.89×10^{-4} Debye unit, directed in the sense H^+D^-.

II. APPLICATION OF THE GENERALIZED PERTURBATION METHOD

In this paper we shall, by use of a variational method, extend the computation of I so as to take account of contributions to the perturbed ground state from other states of $^1\Sigma_u^+$ symmetry besides the B state. Since the most convenient basis functions do not form a mutually orthogonal set, it is most convenient to apply the formalism of the generalized perturbation method.[3] Briefly, this technique allows one to replace perturbed matrix elements of some operator $\mathcal{Q}$ as computed by second-order perturbation theory, viz.,

$$Q_{A'B'}=Q_{AB}+\sum_N{}'\{[Q_{AN}V_{NB}/(E_B-E_N)]+[V_{AN}Q_{NB}/(E_N-E_A)]\} \quad (2)$$

by

$$Q_{A'B'}=Q_{AB}-\sum_{NK}{}''\{Q_{AN}(R_B^{-1})_{NK}V_{KB}+V_{AN}(R_A^{-1})_{NK}Q_{KB}\}, \quad (3)$$

where

$$\left.\begin{aligned}\mathcal{R}_A&=\mathcal{H}_0-E_A\\ \mathcal{R}_B&=\mathcal{H}_0-E_B\end{aligned}\right\}, \quad (4)$$

and R^{-1} means the matrix inverse to R (not the matrix of the operator inverse to $\mathcal{R}$). The primed indices denote matrix elements between the perturbed states A' and B', corresponding to the unperturbed states A and B, respectively. The set of functions labeled by $A, B, N, K, \cdots$, is presumed to be complete but no presumption is made as to the mutual orthogonality of the perturbing set $N, K, \cdots$.

Accordingly, the perturbed ground state of the HD molecule is represented by a bilinear expansion in the set $\phi_n(\mathbf{R}_1\mathbf{R}_2, R)\alpha_v(R)$. We presume, as before, the validity of the adiabatic approximation (I-17) for this state. The $\alpha_v(R)$ represent the complete orthonormal set of vibrational eigenfunctions for the ground electronic state (including formally the continuum). As will be seen, it is not necessary that all these be known explicitly, as a summation procedure over the index v will be applied. For the functions ϕ_n, we choose the set

$$\left.\begin{aligned}&(2\pi)^{-1}\exp[-\delta(\lambda_1+\lambda_2)]\\ &\quad\times(\lambda_1{}^M\lambda_2{}^N\mu_1{}^J\mu_2{}^K\rho^P+\lambda_1{}^N\lambda_2{}^M\mu_1{}^K\mu_2{}^J\rho^P),\\ &\qquad\delta=0.75\\ &M, N, J, K, P=0, 1, 2, \cdots\\ &\qquad J+K=\text{odd}.\end{aligned}\right\} \quad (5)$$

It is readily verified that these possess the required symmetry characteristics. The functions (5) differ from the James and Coolidge ground-state basis functions only in the requirement that $J+K$ be odd, rather

* Present address: Department of Chemistry, Carnegie Institute of Technology, Pittsburgh 13, Pennsylvania.

[1] S. M. Blinder, J. Chem. Phys. **32**, 105 (1960), hereafter denoted by I. In referring to equations or sections in I we shall prefix the numeral "I". Thus, Eq. (I-17) means Eq. (17) of I.

[2] G. C. Wick, Atti reale accad. nazl. Lincei (Ser. 6) **21**, 708 (1935).

[3] S. M. Blinder, J. Chem. Phys. **32**, 111 (1960).

than even, corresponding to a change in sign with inversion of electronic coordinates through the molecular center ($\mu \rightarrow -\mu$). These functions were first used by Present[4] in his study of the B state of H_2. The formulas given in reference 4 and tabulated matrix elements supplied by the author[5] made application of these functions to our problem feasible.

The dipole moment operator is one of the type $\mathcal{Q}$ which does not have associated extremum properties. An approximation to its expectation value is given by Eq. (3). As discussed in reference 3, an indication of the reliability of the computed $Q_{A'B'}$ is provided by the convergence properties of the associated second-order energy expansion.

The generalized perturbation expression for $(\mu_z)_{A'B'}$ analogous to (I-38) may be written immediately in view of the correspondence between Eqs. (2) and (3),

$$(\mu_z)_{A'B'} = -(em/2)(m_P^{-1} - m_D^{-1}) \times \sum_{NK}{}'' \{Z_{AN}(R_B^{-1})_{NK} W_{KB} + W_{AN}(R_A^{-1})_{NK} Z_{KB}\}. \quad (6)$$

It is instructive, however, to derive this form independently, starting with the expression corresponding to Eq. (3);

$$(\mu_z)_{A'B'} = -\sum_{NK}{}'' \{(\mu_z)_{AN}(R_B^{-1})_{NK} H_{KB}^{(3)} + H_{AN}^{(3)}(R_A^{-1})_{NK}(\mu_z)_{KB}\}. \quad (7)$$

We make use now of the definitions (I-5), (I-19) for the operators $\mathcal{H}^{(3)}$ and μ_z and recall the convention concerning Z and D_z. By virtue of (I-31) we may write

$$(\mu_z)_{A'B'} = (e\hbar^2/2)(m_P^{-1} - m_D^{-1}) \times \sum_{NK}{}'' \sum_{M} \{Z_{AN}(R_B^{-1})_{NK}(D_Z)_{KM}(D_R)_{MB} + (D_R)_{AM}(D_Z)_{MN}(R_A^{-1})_{NK} Z_{KB}\}. \quad (8)$$

Equations (I-33) and (I-36) may be modified in view of the fact that the operators $\mathcal{R}_A$, $\mathcal{R}_B$ obey the same commutation relations as $\mathcal{H}_0$. Consequently, we have the following alternate forms for the operators D_Z and $-\partial\mathcal{H}_0/\partial R$:

$$D_Z = -(m/\hbar^2)[R_A, Z] = -(m/\hbar^2)[R_B, Z], \quad (9)$$

$$-\partial\mathcal{H}_0/\partial R = [R_A, D_R] = [R_B, D_R]. \quad (10)$$

Applying (9) and (10) to (8), and rearranging terms judiciously, we arrive at the form (6), using now the definition (I-37) for W. We have freely created and annihilated indices in summation procedures. This is permissible provided these indices (although not necessarily the A, N, K, B) represent functions belonging to complete orthonormal sets.

Next we sum over the vibrational part of the composite indices in (6). Consistent with our choice of the states A, B, we obtain

$$(\mu_z)_{A'B'} = -(em/2)(m_P^{-1} - m_D^{-1}) \times \sum_{nk}{}'' \{Z_{0n}(R_B^{-1})_{nk} W_{k0} + W_{0n}(R_A^{-1})_{nk} Z_{k0}\}_{ab}, \quad (11)$$

where n, k are the electronic quantum numbers associated with N, K. The matrix elements within the brackets in (11) remain operators in the R manifold. We note that now we need only know the vibrational eigenfunctions $\alpha_a(R)$ and $\alpha_b(R)$. If we require that the electronic wave functions have real phases (thereby making the Hermitian matrices also symmetric) and restrict our consideration to low vibrational quantum states (such that $E_A \approx E_B \approx E_0$), (11) reduces to

$$(\mu_z)_{A'B'} = -em(m_P^{-1} - m_D^{-1}) \sum_{nk}{}'' \{Z_{0n}(R^{-1})_{nk} W_{k0}\}_{ab}, \quad (12)$$

with $\mathcal{R} = \mathcal{H}_0 - E_0$.

We consider next the validity of approximating $\mathcal{H}_0$ by $\mathcal{H}^{(0)}$ [cf. Eq. (I-15)]. Matrix elements of $\mathcal{H}^{(2)}$ are certainly small compared to those of $\mathcal{H}^{(0)}$ when we are concerned only with lower vibrational levels. This is not necessarily true, however, when higher states, particularly those of the continuum, are involved. For such cases we postulate that Z_{AN}, W_{KB} are negligibly small whenever A and N or K and B represent states of widely disparate vibrational energy. This is reasonable in view of the fact that the overlap of a bound state with a continuum state is very small. Thus, only lower vibrational states will contribute to the summation (6), provided a, b are themselves small quantum numbers. The $\mathcal{H}_0$ is effectively $\mathcal{H}^{(0)}$, consequently the bracketed operator in (12) is effectively a function of R, the dependence on derivatives [in $\mathcal{H}^{(2)}$] having been removed.

TABLE I. Results.

ϕ_n	W_{0n}^2/R_{nn} Arbitrary units
$\phi_{00100} \equiv \phi_6$	125.1
$\phi_{10100} \equiv \phi_2$	163.5
$\phi_{01100} \equiv \phi_4$	146.5
ϕ_{00120}	111.3
$\phi_{11100} \equiv \phi_1$	163.8
ϕ_{20100}	111.6
ϕ_{02100}	85.5
$\phi_{00300} \equiv \phi_3$	146.8
$\phi_{10120} \equiv \phi_5$	140.9
ϕ_{01120}	104.5
ϕ_{12100}	88.9
ϕ_{21100}	106.9

[4] R. D. Present, J. Chem. Phys. **3**, 122 (1935).

[5] We are indebted to Professor Present for allowing us to use his tables.

TABLE II. Best function.

R in a_0	$\mu_z(R)$ in 10^{-4} Debye units	$-E^{(2)}$ in arbitrary units
1.1	7.49	8.98
1.2	6.89	7.06
1.3	6.25	5.59
1.4	5.68	4.51
1.5	5.23	3.74
1.6	4.93	3.20

We are now in a position to perform explicit computation. As before, we represent the ground state by the four-parameter expansion (Appendix I–B). We shall evaluate (12) for six fixed values of R, obtaining a representation for $\mu_z(R)$, then integrate graphically over the Morse vibrational eigenfunctions.

We wish to choose basis functions ϕ_n (ϕ_{MNJKP}) which impart relatively large values to the second-order energy expression [cf. Eq. (38), reference 3],

$$-E_n^{(2)}=W_{0n}^2/R_{nn}. \tag{13}$$

To circumvent excessive complication in the evaluation of matrix elements, we shall consider only functions with $P=0$. A study of the integrals involved in (13) for $P>0$ indicates, fortunately, that the ρ dependence of the ϕ_n is but of secondary importance in the present application. Table I lists the results for the dozen functions tested. Matrix elements in (13) were evaluated for $R=1.4a_0$, the equilibrium nuclear separation. All functions with sum of indices

$$M+N+J+K\leq 3,$$

and a few with sum 4 were considered. The indices were restricted, of course, by the condition $J+K=$odd. All functions of importance in the B-state computation[4] are included. The six best functions shall comprise our basis. These are labeled by a single index, denoting their order of importance. The relative significance of the ϕ_n changes somewhat for R other than $1.4a_0$. Very likely, however, six parameters may readjust with sufficient flexibility to follow these changes.

Using now the six-function basis, the required matrix elements W_{0n}, Z_{0n}, R_{nk} were evaluated. Full details on these are given in Appendix B. Inversion of the R matrices and double summation over these, as required in (12), were accomplished with the aid of an IBM 650 computer.[6]

As a check on convergence, we have duplicated all computations using a relatively unimportant function, ϕ_{01120}, in place of our best function ϕ_1.

Table II gives the $\mu_z(R)$ values for the best six-parameter perturbation function. The corresponding second-order energies are also indicated. The latter are the sums

$$\sum_{nk}{}''W_{0n}(R^{-1})_{nk}W_{k0},$$

evaluated with little additional labor. Table III duplicates these entries for the alternate six-parameter function.

A close examination of Tables II and III reveals that there is reasonably good convergence with respect to the second-order energy, especially for the larger nuclear separations. (Apparently, at $1.6a_0$, the dummy function is slightly better than the one it replaces.) The convergence of the dipole function, although not as sharp, is adequate for our purposes. It is significant to note that at 1.5 and $1.6a_0$, the two functions yield almost identical energies but somewhat less comparable values for $\mu_z(R)$. This illustrates the more stringent demands made of a wave function when properties other than the molecular energy are required.

A study of the behavior of the W, Z, and R matrix elements for smaller nuclear separations indicates that the dipole function goes through a maximum in the vicinity of $1.0a_0$. It was not deemed worthwhile to repeat the computation for smaller values of R in order to locate the maximum more precisely (see Sec. III).

The result of the generalized perturbation calculation is represented by the curve labeled V in Fig. 1. The expectation value for the permanent moment in the ground vibrational state is

$$\langle\mu_z\rangle_{v=0}=5.67\times10^{-4}\text{ Debye units},$$

somewhat lower than the value found by the method of Sec. I–IV.

III. DISCUSSION

In Fig. 1 are illustrated two representations of the dipole moment function. This is a function, independent of the vibrational state of the molecule, which yields matrix elements of the dipole moment via integrations over vibrational eigenfunctions. For an ordinary heteronuclear molecule (e.g., HCl) the validity and meaning of such a function are well established. In the case of HD, the moment arises from a vibrational perturbation. It is difficult to demonstrate, by any classical argument, that a vibration-independent dipole function is meaningful, as well, for

TABLE III. Convergence check.

1.1	7.66	8.02
1.2	7.25	6.51
1.3	6.73	5.29
1.4	6.22	4.38
1.5	5.81	3.71
1.6	5.52	3.24

[6] We are indebted to Dr. G. L. Goodman for his aid in programming this computation.

this molecule. Our quantum-mechanical treatment nevertheless suggests that such a representation is valid for the lower vibrational states of HD.

This has been demonstrated formally in Sec. I–IV and Sec. II by the procedures leading to Eqs. (I-39) and (12). We recall that these conclusions involve certain presumptions as to relative magnitude of vibrational energies and validity of summation procedures. Contingent upon these, dipole matrix elements reduce to integrals of a multiplicative operator over vibrational eigenfunctions. This is equivalent to the existence of a dipole function independent of vibrational quantum number. The characteristics dependent on vibrational state are then manifested only in weighted averages over $\mu_z(R)$. The foregoing considerations are valid only for low vibrational quantum numbers. For highly excited states, our representation of $\mu_z(R)$ is no longer adequate.

We next discuss the significance of the maximum in $\mu_z(R)$. The dipole function, as we have seen, is predominantly positive in the equilibrium region. It may reasonably be expected to vanish at both $R=0$ and $R=\infty$. Presuming the function to be continuous and smooth, the existence of a maximum is indicated. Classically, the maximum should coincide with the vibrational potential minimum. For, at R_0, where the vibrational kinetic energy assumes its maximum value, the slippage effect, hence the contribution to $\mu_z(R)$, should be maximized. Gray and Pritchard[7] have discussed the hypothetical diatomic molecule with dipole maximum near R_0. In particular, they deduce, for such a molecule, that the intensity of the $0\rightarrow2$ vibrational transition is greater than that of the fundamental ($0\rightarrow1$). Intensity measurements in the weak rotation-vibration absorption spectrum show this to be the case for HD.[8,9] The relative intensities of the transitions $0\rightarrow1$, $0\rightarrow2$, $0\rightarrow3$, $0\rightarrow4$ are roughly indicated by the ratios 1:1.9:0.24:0.08. This is, incidentally, the first known case of intensity reversal for the fundamental and first overtone. The $0\rightarrow3$ and $0\rightarrow4$ intensities are also anomalously large. Generally, the relative intensities of successive overtones fall off sharply (by successive factors approximating 100).

It is strongly indicated, then, that $\mu_z(R)$ for HD has a maximum near $R_0(1.4a_0)$. Our two theoretical studies (Secs. I–IV, II) have indicated, on the basis of extrapolation, that the maximum is situated near $0.8a_0$ (one-state perturbation assumption) or near $1.0a_0$ (generalized perturbation method). Such computations, however, involving so highly detailed an assessment of the electronic distribution, should perhaps not be expected to indicate more than the gross features of $\mu_z(R)$.

It is likely, in view of the convergence properties of the generalized perturbation computation (Sec. II), that the magnitude of $\mu_z(R)$ in the neighborhood of R_0 is reasonably reliable. Finer details of the function (slope and curvature), involving more precise knowledge of the molecular state, are, no doubt, much less dependable. Consequently, we do not attempt to compute expectation values for higher vibrational states or off-diagonal matrix elements.[10] Since these are highly sensitive to the shape of the dipole moment function, such computations would be entirely futile. It is likely, however, as discussed in reference 9, that the permanent moment decreases with increasing vibrational excitation.

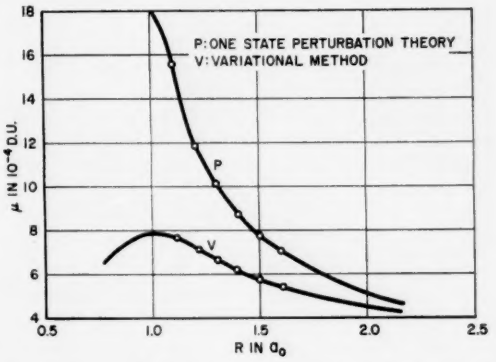

FIG. 1. Computed dipole moment function for HD; P: one-state perturbation theory; V: variational method (generalized perturbation method).

In connection with our computations of $\mu_z(R)$ for the smaller values of R, the four-parameter representation for the ground electronic state becomes less reliable as electronic correlation becomes increasingly significant. More parameters would be required to represent this effect adequately. We are less confident, then, of the corresponding $\mu_z(R)$. In support of the above, we note that the curves P and V (Fig. 1) move farther apart in this region.

It is of interest to note that, despite the existence of a nonvanishing component of $\boldsymbol{\mu}$ along the axis of rotation the molecule should not exhibit a first-order Stark effect.[11] The three components of $\boldsymbol{\mu}$ given by (I-27) and (I-28) represent permanent moments in the molecule-fixed frame of reference. These expectation values may, however, vanish in the space-fixed frame, after averaging over the rotational wave function. A rotation-averaged permanent moment, hence a first-order Stark effect, is exhibited only when there is degeneracy in the rotational level ($J>0$), among states of opposite parity. This requires $|\Lambda|>0$ for a linear molecule or $|K|>0$ for a symmetric rotor.

[7] B. F. Gray and H. O. Pritchard, J. Mol. Spectroscopy **2**, 137 (1958).

[8] R. A. Durie and G. Herzberg, Can. J. Phys. **38**, 806 (1960).

[9] This fact can also be deduced from the observed intensity ratios. See S. M. Blinder, J. Chem. Phys. **32**, 582 (1960).

[10] A calculation of relative infrared intensities for HD using an extension of Wick's theory (reference 2) is given by T.-Y. Wu, Can. J. Phys. **30**, 291 (1952).

[11] We are indebted to Professor W. A. Klemperer for bringing up this point.

The ground state of the HD molecule does not have such degeneracy since $\Lambda=0$. Admixture of $^1\Pi_u$ character into the ground state, via $\mathcal{H}_c^{(4)}$, does occur but this does not affect the multiplicity. (As a matter of fact, $\mathcal{H}_c^{(4)}$ does not even mix the Λ-doublet components $^1\Pi_u^+$ and $^1\Pi_u^-$ in symmetrical fashion.) Moreover, even the harmless M degeneracy of the rotational level is removed by the D_ϕ term of $\mathcal{H}_c^{(4)}$.

We shall demonstrate explicitly that the rotation-averaged expectation value of $\boldsymbol{\mu}$ (the permanent electric moment) vanishes identically. In the space-fixed coordinate system, the components of the operator $\boldsymbol{\mu}$ are

$$\mu_x \sin\theta\cos\phi, \quad \mu_y \sin\theta\sin\phi, \quad \mu_z\cos\theta.$$

For Σ states, there is no first-order Stark effect for the Z component of $\boldsymbol{\mu}$, as is well known. The μ_x and μ_y terms, however, are not usual and bear closer examination. A "low-frequency" matrix element of the X component is given by

$$(\langle\mu_x\sin\theta\cos\phi\rangle_{nv})_{J\Lambda M,J\Lambda''M''}=\sum_{\substack{n'v'\\J'\Lambda'M'}}[E_{nvJ}^{(0)}-E_{n'v'J'}^{(0)}]^{-1}$$
$$\times[(\mu_x\sin\theta\cos\phi)_{nvJ\Lambda M,n'v'J'\Lambda'M'}[\mathcal{H}_c^{(4)}]_{n'v'J'\Lambda'M',nvJ\Lambda''M''}$$
$$+[\mathcal{H}_c^{(4)}]_{nvJ\Lambda M,n'v'J'\Lambda'M'}(\mu_x\sin\theta\cos\phi)_{n'v'J'\Lambda'M',nvJ\Lambda''M''}]. \tag{14}$$

For the case which concerns us, $\Lambda=\Lambda''=0$. The μ_x factors involve rotational matrix elements of the form[12]

$$(\cos\chi\sin\theta\cos\phi)_{J0M;J'\Lambda'M''}$$
$$=\cos\chi_{0\Lambda}\cos\phi_{MM'}\sin\theta_{J0M,J'\Lambda'M'}.$$

For a linear molecule, the first two factors vanish identically unless $\Lambda'=\pm1$, $M'=M\pm1$. The θ-dependent functions $\Theta_{J\Lambda M}(\theta)$ are the Jacobi polynomials. Their parity (wrt the transformation $\theta\rightarrow-\theta$) is given by $(-1)^{\Lambda+M}$, independent of J. Thus, Θ_{J0M} has parity $(-1)^M$, $\Theta_{J,\pm1,M\pm1}$ has the same parity, and their product has even parity. Consequently, the matrix element of the odd function $\sin\theta$,

$$\sin\theta_{J0M;J',\pm1,M\pm1},$$

vanishes identically, as does the expectation value (14). A completely analogous procedure applies for the μ_y term.

There is, then, no first-order Stark effect from either the vibration or the rotation-induced moments. The dipole moment would manifest itself as a second-order shift in the rotation-vibration levels of the molecule. Also proportional to the square of the electric field is the molecular polarizability. The latter would have to be subtracted from the observed energy shift to give the true Stark effect. We note that since $\langle\mu_x\rangle$, $\langle\mu_y\rangle$, $\langle\mu_z\rangle$ are observed only in their squares, the x and y components become even less significant.

Finally, we shall comment on Wick's[2] treatment of matrix elements of the dipole moment operator.[13] The essence of Wick's approach is contained in the discussion following his Eq. (22). He supposes that the matrix elements $K_{m0}(K=-\partial V/\partial R)$ for $m\neq0$ are small in comparison to K_{00} (or, at least, that this is effectively so because of cancellations of positive and negative contributions). He thus considers only the $m=0$ term in the summation (22). The sums over n are then related to polarizibilities and the formulas derived earlier in his paper [Eqs. (1) and (15)] follow. Alternately, the "average perturbation energy" method could be applied. Equation (22) then becomes, in our notation,

$$\mu_z(R)\approx(em/2M)[(Z^2)_{00}K_{00}/\Delta E]. \tag{15}$$

This will provide a convenient comparison with our approach.

Regarding Wick's Eq. (22) as the common point of departure, we characterize our treatment as implicit summation over the complete orthonormal set labeled by the m and consideration of the product $ZK\equiv W$ as a single operator. This procedure leads to our Eq. (I-38). Applying the summation procedure (over n) we obtain (I-39), rewritten for purposes of comparison

$$\mu_z(R)\approx(em/2M)[(Z^2K)_{00}/\Delta E]. \tag{16}$$

The generalized perturbation treatment (Sec. II) when compared to the one-state perturbation result (Sec. I–IV) indicates that the n summation procedure is not excessively in error. Accordingly, we shall presume that comparison of (15) and (16) constitutes a test of the validity of Wick's supposition. Assuming that the ΔE's are roughly equal, we should find that

$$(Z^2K)_{00}\approx(Z^2)_{00}K_{00}.$$

On evaluating the above matrix elements at $R=1.4a_0$ (equilibrium nuclear separation using the four-parameter ground-state function (Appendix I-B), we find

$$(Z^2K)_{00}=0.529$$
$$(Z^2)_{00}K_{00}=1.64\times0.0269=0.044.$$

We conclude thereby that neglect of off-diagonal elements of K is seriously in error, affecting the computed matrix elements (not explicitly evaluated by Wick) by roughly an order of magnitude.

APPENDIX A

Some Useful Integrals

Matrix elements of the unperturbed Hamiltonian involve the integrals $X_{mnjkp}(\alpha)$ for a two-electron

[12] The eigenfunctions for a linear molecule having nonvanishing orbital angular momentum are given in G. Herzberg, *Spectra of Diatomic Molecules* (D. Van Nostrand and Company, Inc., Princeton, New Jersey, 1950), pp. 118ff.

[13] We wish to thank Professor J. H. Van Vleck for suggesting this comparison.

system[14]

$$X_{mnjkp}(\alpha)\equiv(4\pi^2)^{-1}\int\!\!\int\!\!\int\!\!\int\!\!\int\!\!\int d\lambda_1 d\lambda_2 d\mu_1 d\mu_2 d\phi_1 d\phi_2$$

$$\times(\lambda_1^2-\mu_1^2)\,\exp[-\alpha(\lambda_1+\lambda_2)]\lambda_1^m\lambda_2^n\mu_1^j\mu_2^k\rho^p. \quad \text{(A1)}$$

The indices m, n, j, k, p are restricted to values of zero or the positive integers, except that p may take the value -1. The variable ρ expresses the interelectronic separation,

$$\rho=2r_{12}/R, \quad \text{(A2)}$$

and is given explicitly in terms of the prolate spheroidal coordinates of electrons 1 and 2 by

$$\rho^2=\lambda_1^2+\lambda_2^2+\mu_1^2+\mu_2^2-2-2\lambda_1\lambda_2\mu_1\mu_2$$
$$-2\{(\lambda_1^2-1)(\lambda_2^2-1)(1-\mu_1^2)(1-\mu_2^2)\}^{\frac{1}{2}}\cos(\phi_1-\phi_2). \quad \text{(A3)}$$

We shall require the X integrals for the value 1.5 of the parameter α. Extensive tables of these integrals have been compiled by James, Coolidge, and Present in connection with their studies of the ground and excited states of H_2.

When $p=0$, the ρ dependence of the integrand is removed, and the two-electron integrals (A1) reduce to products of one-electron integrals.

$$X_{mnjk0}(\alpha)=x_{mj}(\alpha)z_{nk}(\alpha), \quad \text{(A4)}$$

having defined

$$z_{nk}(\alpha)\equiv\int_{-1}^{1}\int_{1}^{\infty}d\lambda d\mu\,\exp(-\alpha\lambda)\lambda^n\mu^k, \quad \text{(A5)}$$

$$\left.\begin{aligned}x_{mj}(\alpha)&\equiv\int_{-1}^{1}\int_{1}^{\infty}d\lambda d\mu(\lambda^2-\mu^2)\,\exp(-\alpha\lambda)\lambda^m\mu^j\\&=z_{m+2,j}(\alpha)-z_{m,j+2}(\alpha).\end{aligned}\right\} \quad \text{(A6)}$$

Both the z and x integrals vanish for odd values of the second index. They are readily evaluated in terms of the well-known functions

$$A_n(\alpha)\equiv\int_1^\infty d\lambda\,\exp(-\alpha\lambda)\lambda^n. \quad \text{(A7)}$$

Evaluation of perturbation matrix elements (Appendix B) requires also the set of integrals

$$y_{nk}(\alpha)\equiv\int_{-1}^{1}\int_{1}^{\infty}d\lambda d\mu\frac{\exp(-\alpha\lambda)\lambda^n\mu^k}{(\lambda^2-\mu^2)}. \quad \text{(A8)}$$

The μ integrals are elementary:

$$\int_{-1}^{1}[d\mu/(\lambda^2-\mu^2)]=\lambda^{-1}\log[(\lambda+1)/(\lambda-1)], \quad \text{(A9)}$$

$$\int_{-1}^{1}[d\mu\mu^2/(\lambda^2-\mu^2)]=-2+\lambda\log[(\lambda+1)/(\lambda-1)], \quad \text{(A10)}$$

$$\int_{-1}^{1}[d\mu\mu^4/(\lambda^2-\mu^2)]=-\tfrac{2}{3}-2\lambda^2+\lambda^3\log[(\lambda+1)/(\lambda-1)], \quad \text{(A11)}$$

$$\int_{-1}^{1}[d\mu\mu^6/(\lambda^2-\mu^2)]=-\tfrac{2}{5}-(2\lambda^2/3)-2\lambda^4$$
$$+\lambda^5\log[(\lambda+1)/(\lambda-1)]. \quad \text{(A12)}$$

Integration over λ involves expressions of the form

$$q_n(\alpha)\equiv\int_1^\infty d\lambda\,\exp(-\alpha\lambda)\lambda^n\log[(\lambda+1)/(\lambda-1)]. \quad \text{(A13)}$$

We were not able to evaluate these in closed form. Numerical quadrature was found to be cumbersome, in view of the large range of integration. The approach chosen involves expansion of the integrand in power series. The logarithm may be represented by

$$\log[(\lambda+1)/(\lambda-1)]=2\sum_{k=0}^{\infty}\frac{1}{(2k+1)\lambda^{2k+1}}, \quad |\lambda|>1. \quad \text{(A14)}$$

Equation (A13) then assumes the form

$$q_n(\alpha)=2\sum_{k=0}^{\infty}\frac{E_{2k-n+1}(\alpha)}{2k+1}, \quad \text{(A15)}$$

in terms of the well-known integrals

$$E_m(\alpha)\equiv\int_1^\infty d\lambda\lambda^{-m}\exp(-\alpha\lambda). \quad \text{(A16)}$$

Extensive tables of the latter are given by Placzek.[15] We note from (A7), (A16) that

$$E_{-m}(\alpha)=A_m(\alpha). \quad \text{(A17)}$$

Since the expansion (A14) is valid only for $|\lambda|>1$, whereas we consider the limit $\lambda\to1$ (the lower limit of the integrations), it is well to check the convergence of the expansion (A15). The asymptotic form of the $E_m(\alpha)$ is given by[15]

$$E_m(\alpha)\underset{m>>1}{\longrightarrow}[\exp(-\alpha)/(m+1)]. \quad \text{(A18)}$$

The ordinary ratio test applied to the infinite series (A15) then gives the ambiguous result

$$\lim_{k\to\infty}|a_k/a_{k-1}|=1. \quad \text{(A19)}$$

There exists, however, a more refined ratio test, in terms of the asymptotic form[16]

$$|a_k/a_{k-1}|\underset{k>>1}{\longrightarrow}1-(b/k)+O(1/k^2). \quad \text{(A20)}$$

The series converges whenever $b>1$. The expansion (A15), expressed in this form, gives $b=2$, and thus

[14] These were introduced by H. M. James and A. S. Coolidge, J. Chem. Phys. **1**, 825 (1933).

[15] G. Placzek, "The function $E_n(x)$," NRC Rept. No. 1547, National Research Council of Canada, Chalk River, Ontario.

[16] P. Franklin, *Treatise on Advanced Calculus* (John Wiley & Sons, Inc., New York, 1949), p. 306.

converges. Convergence is extremely slow, however: several hundred terms would be required for sufficiently accurate values. A somewhat less tedious procedure was found adequate. The first 50 terms of (A15) were summed explicitly and the remainder estimated by the integral

$$2e^{-\alpha}\int_{50}^{\infty}\frac{dk}{(2k-n)(2k+1)}$$

$$=\begin{cases}\dfrac{e^{-\alpha}}{n+1}\log\left|\dfrac{50+\frac{1}{2}}{50-(n/2)}\right|, & (n\neq -1)\\[2ex] \dfrac{e^{-\alpha}}{3(101)^3}, & (n=-1).\end{cases} \tag{A21}$$

As a check on the method, q_1 and q_2 were evaluated by numerical integration using Weddle's rule. From the q_n, the y_{nk} are evaluated recursively, applying the following relations,

$$y_{n0}(\alpha)=q_{n-1}(\alpha), \tag{A22}$$

$$y_{n,k+2}(\alpha)=y_{n+2,k}(\alpha)-z_{nk}(\alpha). \tag{A23}$$

APPENDIX B

Matrix Elements for HD

The matrix elements R_{mn} for the $^1\Sigma_u^+$ basis functions (with $P=0$) may be found by using the formulas given by James and Coolidge[14] with

$$R_{mn}=H_{mn}+\,|\,E_0\,|\,S_{mn} \tag{B1}$$

for each value of R. [The plus sign occurs in (B1) since the E_0 are inherently negative.] Several alternate forms given by Present[4] provide useful computational checks. The required formulas are listed here.

$$\left.\begin{aligned}
&H_{mnjk0,m'n'j'k'0}=h_{mnjk,m'n'j'k'}+h_{mnjk,n'm'k'j'}\\
&\qquad+h_{nmkj,m'n'j'k'}+h_{nmkj,n'm'k'j'},\\
&h_{mnjk,m'n'j'k'}=(R^4/64)\\
&\times R\{\bar{X}(02000)-\bar{X}(00020)-8\bar{X}(01000)\\
&\qquad+2\bar{X}(0200-1)-2\bar{X}(0002-1)\}\\
&+\{\tfrac{9}{4}-4n'(n'+1)+4k'(k'+1)\}\bar{X}(00000)\\
&\quad-\tfrac{9}{4}\bar{X}(02000)-6n'\bar{X}(0-1000)\\
&\quad+4n'(n'-1)\bar{X}(0-2000)\\
&\quad-4k'(k'-1)\bar{X}(000-20)\\
&\qquad+6(1+n')\bar{X}(01000),
\end{aligned}\right\} \tag{B2}$$

where

$$\bar{X}(abcde)\equiv X(1.5)_{m+m'+a,n+n'+b,j+j'+c,k+k'+d,e}.$$

$$\left.\begin{aligned}
&S_{mnjkp,m'n'j'k'p'}\\
&\equiv(1/4\pi^2)(R/2)^6\iiiiiii d\lambda_1 d\lambda_2 d\mu_1 d\mu_2 d\phi_1 d\phi_2\\
&\quad(\lambda_1^2-\mu_1^2)(\lambda_2^2-\mu_2^2)\exp[-\alpha(\lambda_1+\lambda_2)]\\
&\quad(\lambda_1^m\lambda_2^n\mu_1^j\mu_2^k\rho^p+\lambda_1^n\lambda_2^m\mu_1^k\mu_2^j\rho^p)\\
&(\lambda_1^{m'}\lambda_2^{n'}\mu_1^{j'}\mu_2^{k'}\rho^{p'}+\lambda_1^{n'}\lambda_2^{m'}\mu_1^{k'}\mu_2^{j'}\rho^{p'})=2(R/2)^6\\
&\quad\times X_{m+m',n+n'+2,j+j',k+k',p+p'}\\
&\quad-X_{m+m',n+n',j+j',k+k'+2,p+p'}\\
&\quad+X_{m+n',n+m'+2,j+k',k+j',p+p'}\\
&\quad-X_{m+n',n+m',j+k',k+j'+2,p+p'}.
\end{aligned}\right\} \tag{B3}$$

For purposes of tabulation, we express R_{mn} as follows:

$$R_{mn}=(R^4/64)\{h_{mn}{}^a-Rh_{mn}{}^b\}+(R^6/64)E_0(R)s_{mn}. \tag{B4}$$

The remainder of this appendix will be concerned with matrix elements between $^1\Sigma_g^+$ and $^1\Sigma_u^+$ basis functions. We consider first the Z_{0n}. From the definition of Z

$$Z\equiv Z_1+Z_2=(R/2)(\lambda_1\mu_1+\lambda_2\mu_2).$$

Denoting by $MNJKP$, the indices of a $^1\Sigma_g^+$ function and by $M'N'J'K'P'$, those of a $^1\Sigma_u^+$ function,

$$\begin{aligned}
Z_{MNJKP,M'N'J'K'P'}&=(R/2)^6\iiiiiii d\lambda_1 d\lambda_2 d\mu_1 d\mu_2 d\phi_1 d\phi_2\\
&\times(\lambda_1^2-\mu_1^2)(\lambda_2^2-\mu_2^2)\\
&\times\{(1/2\pi)\exp[-\delta(\lambda_1+\lambda_2)](\lambda_1^M\lambda_2^N\mu_1^J\mu_2^K\rho^P\\
&\quad+\lambda_1^N\lambda_2^M\mu_1^K\mu_2^J\rho^P)\}(R/2)(\lambda_1\mu_1+\lambda_2\mu_2)\\
&\times\{(1/2\pi)\exp[-\delta(\lambda_1+\lambda_2)](\lambda_1^{M'}\lambda_2^{N'}\mu_1^{J'}\mu_2^{K'}\rho^{P'}\\
&\quad+\lambda_1^{N'}\lambda_2^{M'}\mu_1^{K'}\mu_2^{J'}\rho^{P'})\},
\end{aligned} \tag{B5}$$

$$2\delta=\alpha=1.5.$$

In terms of the overlap integrals (B3) we may write simply,

$$\begin{aligned}
Z_{MNJKP,M'N'J'K'P'}&=\tfrac{1}{2}R\{S_{M+1,N,J+1,K,P;M'N'J'K'P'}\\
&\quad+S_{N+1,M,K+1,J,P,M'N'J'K'P'}\}.
\end{aligned} \tag{B6}$$

We consider finally the perturbation matrix elements. The electronic potential energy is given by

$$V(\mathbf{R}_1\mathbf{R}_2,R)=R^{-1}+r_{12}{}^{-1}-r_{1H}{}^{-1}-r_{1D}{}^{-1}-r_{2H}{}^{-1}-r_{2D}{}^{-1}. \tag{B7}$$

Transforming to prolate spheroidal coordinates we find

$$V=\frac{1}{r_{12}}+\frac{1}{R}\left\{1-\frac{4\lambda_1}{(\lambda_1^2-\mu_1^2)}-\frac{4\lambda_2}{(\lambda_2^2-\mu_2^2)}\right\}. \tag{B8}$$

Because of the symmetry between electrons 1 and 2 in integrals over the basis functions, the bracketed expression may be effectively replaced by

$$V_0 \equiv 1-[8\lambda_1/(\lambda_1^2-\mu_1^2)]. \tag{B9}$$

To differentiate with respect to R we must recognize the implicit dependence of λ and μ on R; thus,

$$\left.\begin{aligned}\partial\lambda/\partial R &= R^{-1}[\lambda(1-\lambda^2)/(\lambda^2-\mu^2)],\\ \partial\mu/\partial R &= R^{-1}[\mu(\mu^2-1)/(\lambda^2-\mu^2)].\end{aligned}\right\} \tag{B10}$$

Consequently,

$$-\frac{dV}{dR}=\frac{V_0}{R^2}-\frac{1}{R^2}\left\{\frac{\lambda_1(1-\lambda_1^2)}{(\lambda_1^2-\mu_1^2)}\frac{\partial V_0}{\partial\lambda_1}+\frac{\mu_1(\mu_1^2-1)}{(\lambda_1^2-\mu_1^2)}\frac{\partial V_0}{\partial\mu_1}\right\}. \tag{B11}$$

We define the matrix elements

$$K_{MNJKP,M'N'J'K'P'} = \iint d\tau_1 d\tau_2 \phi_{MNJKP}(-dV/dR)\phi_{M'N'J'K'P'}. \tag{B12}$$

In analogy with Eq. (I-D-3) and (I-D-6), we recognize the composite nature of the K

$$\begin{aligned}K_{MNJKP,M'N'J'K'P'} &= k_{M+M',N+N',J+J',K+K',P+P'}\\ &+k_{M+N',N+M',J+K',K+J',P+P'}+k_{N+M',M+N',K+J',J+K',P+P'}\\ &+k_{N+N',M+M',K+K',J+J',P+P'}.\end{aligned} \tag{B13}$$

We confine our considerations now to the case $P=P'=0$,

$$\begin{aligned}k_{mnjk0} &= (R/2)^6\iiint\!\!\iint d\lambda_1 d\lambda_2 d\mu_1 d\mu_2(\lambda_1^2-\mu_1^2)(\lambda_2^2-\mu_2^2)\\ &\quad\times\exp[-\alpha(\lambda_1+\lambda_2)]\lambda_1^m\lambda_2^n\mu_1^j\mu_2^k(-dV/dR)\\ &= (1/R^2)(R/2)^6 x_{nk}J_{mj},\end{aligned} \tag{B14}$$

having defined

$$J_{mj}\equiv R^2\iint d\lambda d\mu e^{-\alpha\lambda}\lambda^m\mu^j(\lambda^2-\mu^2)(-dV/dR). \tag{B15}$$

Substituting (B11) in (B15) and integrating by parts in the terms containing $\partial V_0/\partial\lambda$ and $\partial V_0/\lambda\mu$, we obtain, after some cancellation,

$$J_{mj}=-2F_{mj}-\alpha L_{m+1,j}+mL_{mj}+jM_{mj}. \tag{B16}$$

We have defined three new sets of integrals:

$$F_{mj}\equiv\iint d\lambda d\mu e^{-\alpha\lambda}\lambda^m\mu^j(\lambda^2-\mu^2)V_0 \tag{B17}$$

$$L_{mj}\equiv\iint d\lambda d\mu e^{-\alpha\lambda}\lambda^m\mu^j(1-\lambda^2)V_0 \tag{B18}$$

$$M_{mj}\equiv\iint d\lambda d\mu e^{-\alpha\lambda}\lambda^m\mu^j(\mu^2-1)V_0. \tag{B19}$$

By using now the definition (B9) for V_0, these may be expressed in terms of previously defined integrals,

$$F_{mj}=x_{mj}-8z_{m+1,j}, \tag{B20}$$

$$L_{mj}=z_{mj}-z_{m+2,j}+8y_{m+3,j}-8y_{m+1,j}, \tag{B21}$$

$$M_{mj}=z_{m,j+2}-z_{mj}+8y_{m+1,j}-8y_{m+1,j+2}. \tag{B22}$$

The perturbation operator W is given by

$$W=Z(-dV/dR) \tag{B23}$$

[cf. Eq. (I-37)]. We recognize that

$$Z\phi_{MNJKP}=(R/2)\{\phi_{M+1,N,J+1,K,P}+\phi_{N+1,M,K+1,J,P}\}. \tag{B24}$$

as is implicit in (B-6), when $P=P'=0$ we may write, by virtue of (B-13), (B-14), and (B-24):

$$\begin{aligned}W_{MNJK0,M'N'J'L'0} &= (R/2)(1/R^2)(R/2)^6\\ &\times\{J_{M+M'+1,J+J'+1}x_{N+N',K+K'}\\ &+J_{M+M',J+J'}x_{N+N'+1,K+K'+1}\\ &+J_{M+N'+1,J+K'+1}x_{N+M',K+J'}\\ &+J_{M+N',J+K'}x_{N+M'+1,K+J'+1}\\ &+J_{N+M',K+J'}x_{M+N'+1,J+K+1}\\ &+J_{N+M'+1,K+J'+1}x_{M+N',J+K'}\\ &+J_{N+N',K+K'}x_{M+M'+1,J+J'+1}\\ &+J_{N+N'+1,K+K'+1}x_{M+M',J+J'}\}.\end{aligned} \tag{B25}$$

An analogous procedure yields matrix elements of ZW, as required for the one-state perturbation computation (Sec. I-IV).

THE JOURNAL OF CHEMICAL PHYSICS VOLUME 35, NUMBER 3 SEPTEMBER, 1961

Photo- and Semiconduction in Crystalline Chlorophylls *a* and *b*

BARNETT ROSENBERG AND JAMES F. CAMISCOLI

Physics Department, New York University, Washington Square 3, New York

(Received November 4, 1960)

Measurements are reported on some characteristics of photoconduction and semiconduction in pure crystalline chlorophylls *a* and *b*. The semiconduction activation energy is 1.12 ev in chlorophyll *a* and 1.44 ev in chlorophyll *b* ($E/2kT$). The latter value is in excellent agreement with the triplet state energy of 1.43 ev measured by the phosphorescence method in chlorophyll *b*. The former value suggests that a possible cause of the lack of detectable phosphorescence in chlorophyll *a* is that it occurs in the infrared at about 11 000 A. The evidence indicates that the mobility of the predominant charge carriers (positive holes) is the same in both crystals. Photoconduction is easily measured in chlorophyll *b* and less easily in chlorophyll *a*, because of the much larger dark current. The photoconduction activation energy in chlorophyll *b* is 0.36 ev. This supports Rabinowitch's view that photoconduction in chlorophyll is not involved in the primary act of photosynthesis.

The oxygen adsorbed on the surface of the crystals forms an oxygen-chlorophyll complex. This leads to an increase in both the dark current and the photocurrent probably by increasing the mobility of the surface charge carriers. There is no detectable effect of oxygen upon the semiconduction activation energy, since the increase of the magnitude of the current is small (a factor of 4 to 10). The binding energy of the oxygen-chlorophyll *a* complex is about 1.4 ev; that of the oxygen-chlorophyll *b* complex 0.63 ev. There is no detectable activation energy for the formation of the complex. It is not a photo-oxidation process. Some evidence suggests that a more tightly bound oxygen complex exists which has no effect on electronic conductivity. This more stable complex is converted by light into the weakly bound complex described above (probably by photoreduction of chlorophyll in the complex). These results are similar to those of Arnold and Sherwood's work on dried chloroplasts. They favor their alternative explanation—that of an oxygen compound being responsible for thermoluminescence and a thermal spike in conductivity—rather than their first assumption, that of electron trapping and recombination in chlorophyll itself.

1. INTRODUCTION

THERE has been an increasing interest in recent years in the photoconductive and semiconductive properties of organic materials, stimulated in part by the possible implications of such electronic processes in various biological systems, where energy transfer is known to occur. This is particularly true of vision and photosynthesis. In this latter case, it provides a simple mechanism for spatial separation of oxidizing and reducing agents (positive holes and electrons), created by the absorption of photons by chlorophyll molecules.[1] In view of this very interesting possibility, the number of papers on the solid-state properties of the photosynthetic pigments has been remarkably small; a somewhat larger amount of work has been done on related compounds, such as the phthalocyanines.

The first published evidence of photoconductivity in chlorophyll *a* was obtained by Nelson,[2] who showed that the action spectrum of its photoconduction was similar to its optical absorption spectrum. This has been verified and extended by Terenin, Putzeiko, and Akimov,[3] who found similar results in studying the photovoltaic effect in crystalline chlorophyll (*a*, *b*). They also determined that the charge carriers were predominantly positive (positive holes), which is also the case for aromatic hydrocarbons and β carotene. Arnold and Maclay[4] similarly found agreement between the action spectrum of photoconduction and the optical absorption spectrum; they have also shown a transfer of holes from chlorophyll to β carotene. Vartanyan[4a] reported that the semiconduction activation energy of a chlorophyll $a+b$ mixture is 2.0 ev. However, no details were given by him concerning the material used (purity, crystallinity, etc.), and at the temperatures used (40° to 90°C) we suspect that sintering could have occurred.

Since chlorophyll occurs in *grana* in densely packed aggregates, it appeared logical to look for solid-state characteristics in dried chloroplasts. Arnold and Sherwood[5] found indeed that dried chloroplasts are semiconductive and after preirradiation exhibit thermoluminescence and a "thermal spike" in the semiconduction curve. They have also found photoconduction in these preparations.[4] These results were interpreted by them as evidence of an electron-trapping phenomenon, similar to that known to occur in inorganic semiconductors.

The experiments described below were undertaken to evaluate three particular characteristics of crystalline chlorophylls *a* and *b*. These are the semiconduction activation energy, the photoconduction activation energy and the effect of adsorbed oxygen.

2. METHODS OF PREPARATION OF CRYSTALLINE CHLOROPHYLLS *a* AND *b*

For the purposes of these measurements we needed high-purity crystalline chlorophylls *a* and *b*. The method

[1] E. Katz, in *Photosynthesis in Plants*, edited by J. Franck and W. E. Loomis (Iowa State College Press, Ames, 1949); D. F. Bradley and M. Calvin, Proc. Natl. Acad. Sci. U. S. **41**, 563 (1955).

[2] R. C. Nelson, J. Chem. Phys. **27**, 864 (1957).

[3] A. Terenin, E. Putzeiko, and I. Akimov, Discussions Faraday Soc. **27**, 1763 (1959).

[4] W. Arnold and H. K. Maclay, *The Photochemical Apparatus Its Structure and Function*, Brookhaven Symposia in Biology No. 11 (1958).

[4a] A. T. Vartanyan, Izvest. Akad. Nauk S.S.S.R. Ser. Fiz. **20**, 1541 (1956).

[5] W. Arnold and H. K. Sherwood, Proc. Natl. Acad. Sci. U. S **43**, 105 (1957).

of preparation from spinach leaves was closely similar to that of Zcheile and Comar.[6] The extract was separated into the *a* and *b* components by column chromatography on X10 confectioners sugar, and each band was rechromatographed three or more times to ensure complete separation and freedom from contamination by pheophytin and carotenoids. The extracted mid-band segments were tested by paper chromatography (developed with 70% petroleum ether, 30% diethyl ether) and rerun through the column until there was no evidence of bands other than the one of interest. The final mid-band segment was extracted with dried diethyl ether and concentrated under vacuum. The resulting small volume of solution was then evaporated to dryness over distilled water in vacuum, following the procedure of Jacobs, Vatter, and Holt,[7] to ensure crystallization. The final yield was each time about 100 mg of separated crystalline chlorophylls *a* and *b* from a starting weight of 1 kg of fresh spinach leaves. The melting points were: chlorophyll *a*, sintered at 108°C, melted at 117–121°C; chlorophyll *b*, sintered at 88°C, melted at 124–125°C. These values are in agreement with those reported in the Merck Index. No x-ray diffraction measurements were made; we used the melting point as a measure of crystallinity, since amorphous chlorophylls melt at considerably lower temperatures. The absorption spectra were taken in methyl alcohol solution with a Beckman model B spectrophotometer; they are shown in Fig. 1. The crystals were stored under vacuum in the dark until used.

3. SEMICONDUCTION ACTIVATION ENERGIES IN CRYSTALLINE CHLOROPHYLLS *a* AND *b*

The measurement of the semiconduction activation energy presupposes that the dark current varies with temperature according to the usual relation

$$j(T)=j_0 \exp(-E/2kT), \qquad (1)$$

where E is the activation energy of the process and j the current. (Because of the uncertainty in contact area we refer to current rather than conductivity.) In the field of organic semiconductors, there is no theoretical reason for choosing the exponent as $E/2kT$ rather than E'/kT. The reason for using it here is that the overwhelming experimental evidence shows that E is closely equal to the ground-state-lowest triplet-state energy separation. There is no theoretical explanation of this simple correlation. On the basis of the photoconduction properties of some organic materials, we have suggested that the intersystem crossing from the excited singlet state to the triplet state of the molecule is an essential intermediate step in the creation of mobile charge carriers.[8] The extension of this to thermal excitation from the ground state to the triplet state seems logical. This, however, does not explain the factor 2 in the exponent.

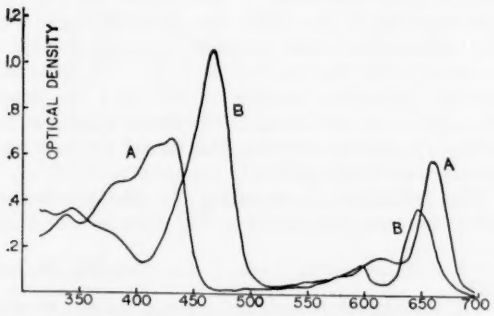

FIG. 1. Optical absorption spectra of chlorophylls *a* and *b* in methanol. Abscissa: wavelength in millimicrons.

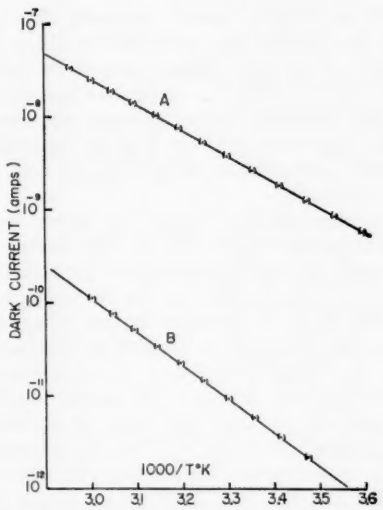

FIG. 2. Semiconduction currents in chlorophylls *a* and *b*. A. chlorophyll *a*: activation energy = 1.10 ev, B. chlorophyll *b*: activation energy = 1.43 ev.

The crystalline chlorophyll (2 to 5 mg) was compressed in a conductivity cell consisting of a front electrode of conductive glass and a back electrode of Monel metal. The two electrodes, forming a sandwich, were separated by strips of 3-mil-thick Teflon on two sides, leaving the other two sides open to the atmosphere. The whole was clamped together and placed in the conductivity chamber. In this chamber we can control the voltage applied to the two electrodes, the ambient atmosphere, the temperature of the Monel metal plate, and the admission of light through a shutter. The source of voltage was a 22.5-v battery. The current was measured with a Keithley 200B electrometer. The temperature was measured with a copper-constantan thermocouple in contact with the Monel metal plate. The cell sat on a mercury cup, set in a heavy copper bar. This

[6] F. P. Zcheile and C. L. Comar, Botan. Gaz. **102,** 463 (1941).
[7] E. E. Jacobs, A. E. Vatter, and A. S. Holt, Arch. Biochem. Biophys. **53,** 228 (1954).
[8] B. Rosenberg, J. Chem. Phys. **28,** 1108 (1958).

bar could be heated or cooled externally. The atmosphere of the chamber was controlled by filling it with tank gases of nitrogen, argon, oxygen, or hydrogen (highest purity, dried) in a continuous flow at normal atmospheric pressure. The temperature was controlled over the range from $-40°$ to $\frac{2}{3}$ of the melting-point temperature (according to the usual rule to limit sintering of the crystals).

Our experience with β carotene[9] has shown that it is essential to subject the material to a few thermal cycles in a nitrogen or argon atmosphere to get reproducible data on the cooling as well as on the heating part of the cycle. This drives off adsorbed oxygen, which has an effect on surface currents. A detailed description of this phenomenon will be given below. When this pretreatment had been accomplished, the sample was heated from about 0°C to the "two-thirds of the melting-point" temperature (below 80°C for the chlorophylls) and then cooled again. The heating and the cooling curve were identical, and independent of the rate of temperature change.

The results of two such measurements are shown in Fig. 2 for chlorophylls *a* and *b*. Similar data were obtained for four different preparations of each chlorophyll. With small variations these gave identical results. The mean values of the activation energy, and the average deviations from the mean were: chlorophyll *a*; $E=1.12\pm0.03$ ev: chlorophyll *b*; $E=1.44\pm0.03$ ev.

The currents in chlorophyll *a* are higher than in chlorophyll *b* as shown in Fig. 2 (they were measured under identical conditions); this seems to be due entirely to a lower activation energy of the former. This can be easily seen if we compare the ratio of the experimental values of the currents at a given temperature, say 300°K, with the values of the exponentials, using the above given values for E. Then we have

$$[j_A/j_B]_{T=300°K} = j_0(A)/j_0(B)[\exp(1.44-1.12)/2kT]_{T=300°K}. \quad (2)$$

This gives for the ratio $j_0(A)/j_0(B)$ a value of 0.88, which for our purposes can be considered as unity. This means that the mobility of the charge carriers is the same in crystals of chlorophyll *a* and *b*. It is only the number of charge carriers which is larger in chlorophyll *a*, due to the lower activation energy.

We should now like to discuss the relation of the semiconduction activation energies to the ground-state-lowest triplet-state energy separations. The triplet state in the chlorophylls has been investigated by two principal methods, phosphorescence emission and flash photolysis. The phosphorescence was first determined by Calvin and Dorough,[10] who reported an emission band in a mixture of chlorophyll *a* and *b* beginning at 7800–8000 A. This was later verified and extended by Kasha and Becker[11] who found the emission peak in chlorophyll *b* at 8650 A. This places the triplet state in chlorophyll *b* at 1.43 ev above the ground state. Our value of 1.44 ev for the semiconduction activation energy is in excellent agreement with this. No emission was observed from chlorophyll *a*, but from Kasha and Becker's paper it appears that they would not be able to detect phosphorescence at wavelengths longer than 9000 A.

Although the flash photolysis method can tell us nothing about the ground-state-triplet-state energy difference, it does reveal the lifetimes of the triplet states and their decay mechanisms. This method has been applied to chlorophylls *a* and *b* by Linschitz and Sarkanen,[12] and Livingston and Ryan.[13] The results show that both chlorophyll *a* and *b* can be excited to the triplet state with about equal facility, and that the lifetimes and decay mechanisms are about the same. Since the triplet state can be populated in chlorophyll *a*, the absence of a detectable phosphorescence emission can be due either to a faster radiationless $T\rightarrow S$ transition or to the emission occurring in a part of the spectrum to which the apparatus was insensitive. The former possibility is at variance with the aforementioned similarity of triplet decay mechanisms in the two chlorophylls, and we conclude that the latter must be correct. Using the value of 1.12 ev derived from the semiconduction measurements we can, with a fair degree of certainty, predict that the phosphorescence emission of chlorophyll *a* should be found around 11 000 A, and that the quantum efficiency of phosphorescence should be close to that of chlorophyll *b*.

4. PHOTOCONDUCTION ACTIVATION ENERGIES

In organic photoconductors, the photocurrent increases with temperature according to an exponential Boltzmann formula.[8,14] (The one exception so far noted is the hindered *cis* isomer of β carotene[15] which appears to have a temperature-independent photocurrent above 30°C.) We have interpreted the temperature dependence of photoconduction as due to the fact that the crossing point of the triplet-state potential curve with the excited singlet-state potential curve corresponds to a certain vibrational level of the latter. The photoconduction activation energies should then be simple multiples of the predominant vibrational quanta in the optical absorption spectrum. This turned out to be true for all cases where sufficient data are available.[8]

The technique of measuring the photoconduction activation energy is similar to that described for semi-

[9] B. Rosenberg, J. Chem. Phys. **34,** 812 (1961).
[10] M. Calvin and G. D. Dorough, Science **105,** 433 (1947).
[11] R. S. Becker and M. Kasha, J. Am. Chem. Soc. **77,** 3669 (1955).
[12] H. Linschitz and K. Sarkanen, J. Am. Chem. Soc. **80,** 4826 (1958).
[13] R. Livingston and V. A. Ryan, J. Am. Chem. Soc. **75,** 2176 (1953).
[14] J. Kommanduer, G. J. Korinek, and W. G. Schneider, Can. J. Chem. **35,** 998 (1957).
[15] B. Rosenberg, J. Opt. Soc. Am. **51,** 238 (1961).

conduction except that the cell is irradiated with constant-intensity light. The intensity should be sufficient to produce a photocurrent a few orders of magnitude higher than the dark current, over a wide enough temperature interval, to separate conveniently the two temperature dependencies.

This can be fairly readily done in chlorophyll *b* where the dark current is so low, that with our light source (a 300-w projector) we can produce a photocurrent about 100 times larger than the dark current at room temperature. In chlorophyll *a*, because of the much larger dark current, the photocurrent was never more than a few times the dark current, even at 0°C. Since our apparatus could not operate at sufficiently low temperatures, we have not made any similar measurements with chlorophyll *a*.

Figure 3 presents the results of one measurement on chlorophyll *b*. Again, the sample was repeatedly cycled in nitrogen to remove adsorbed oxygen, until the dark current was identical in the heating and the cooling parts of the cycle. Three curves are shown. The first A represents the photocurrent as the temperature is increased. The second, B, resulted from the cooling part of the cycle. Curve C is the dark current measured immediately before the photocurrent. The hysteresis effect in A and B is new. The area of the loop has been found to depend strongly on how well the oxygen had been removed from the crystals. Thermal cycling which was sufficient to remove enough surface oxygen to stabilize the dark current was insufficient to stabilize the photocurrent. There seems to be a reservoir of more tightly bound oxygen, which is only very slowly depleted at the temperatures we were permitted to use

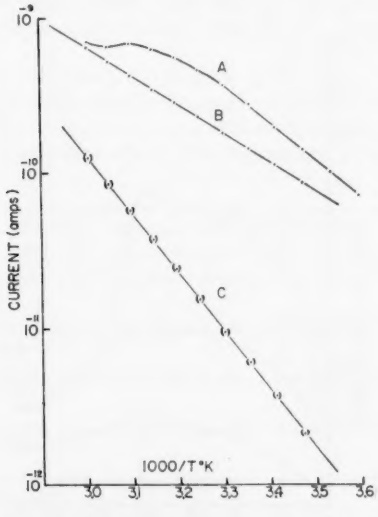

FIG. 3. Photoconduction activation energy curve in chlorophyll *b*; A. photoconduction, temperature increasing, B. photoconduction, temperature decreasing, activation energy = 0.36 ev, C. semiconduction, activation energy = 1.48 ev.

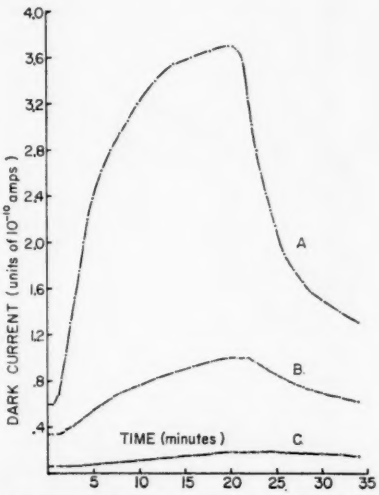

FIG. 4. The effect of oxygen adsorption on the dark current of chlorophyll *b*; A. temp. = 60°C, B. temp. = 45°C, C. temp. = 25°C, oxygen on at 0 min, off at 20 min.

(below 80°C). Its presence has a negligible effect on the dark current but light appears to convert this tightly bound oxygen into a more loosely bound form which affects the dark current, and can be driven off by heating to the temperatures used. This effect will be discussed in more detail below. The heating branch of the photocurrent curve A, has a reversed S shape typical of this effect. This interpretation suggests that repeated thermal cycling in light should diminish the hysteresis effect. This does in fact occur. We can reduce the hysteresis loop area by a factor of 10 so that the distance between the curves is only 20% or so. But so far we have not been able to completely eliminate it.

If the sample is held at the higher temperature for a while and then rapidly cooled, the resulting data should be independent of the oxygen effect, and therefore usable for the calculation of the photoconduction activation energy. This was done for curve B. Here, the data give a straight line, with the same slope for each of the five samples we have tested. These results give, for the activation energy, a value of 0.36 ± 0.01 ev. Our confidence that this value represents the true activation energy, and not an oxygen caused artifact is based in part on the previously reported photoconduction activation energy of all-*trans* β carotene,[9] which showed that the formation of an oxygen-carotene complex, while it increased the magnitude of the photocurrent, did not affect the activation energy. In that case the formation of the complex was light independent and temperature independent, whereas with chlorophyll, it is dependent on both, and makes a similar comparison of conductivities with and without oxygen very difficult.

The next step is the interpretation of 0.36 ev as a multiple of the predominant vibrational quantum, taken from the optical absorption curve. The optical

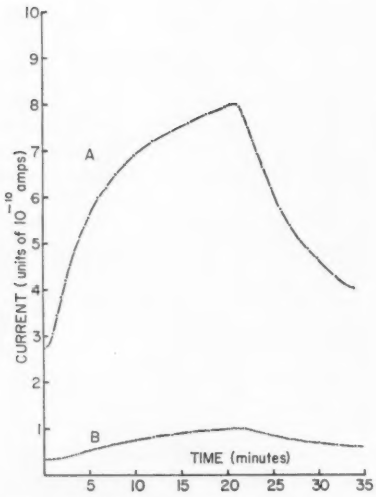

FIG. 5. The effect of oxygen adsorption on the photocurrent (A) and the dark current (B) of chlorophyll *b*; temp.=45°C, oxygen on at 0 min, off at 20 min.

absorption curve of chlorophyll *b* (Fig. 1) shows a number of smaller peaks on the short-wavelength side of the main red band. However, these peaks do not show equal energy separations, as do those that occur in the spectra of the aromatic hydrocarbons and of the carotenoids, and hence do not correspond to multiples of a single vibrational quantum. They do in fact belong to different electronic transitions.[16] We may have recourse to the fluorescence spectrum to obtain some information about the vibrational states. This spectrum has been measured in chlorophyll by Zcheile and Harris,[17] who showed that in both chlorophyll *a* and *b* the emission consisted of two peaks, forming a rough mirror image of the red absorption band. The separation of the two peaks is about 0.165 ev in chlorophyll *b*. Since we usually assume only one electronic fluorescent state in a molecule, the two peaks must be due to the emission from this state to two vibrational levels of the ground state. If mirror-image symmetry exists between absorption and emission, we can assume that the vibrational states of the excited electronic state are similar to those in the ground state. Thus we may take 0.165 ev as a rough estimate of the size of the vibrational quantum of the excited state. Comparison with our value of 0.36 ev indicates that the excitation of at least two vibrational quanta is needed for the intersystem crossing process.

Recently, Rabinowitch said[18] that the existence of a photoconduction activation energy in chlorophyll would militate against photoconduction being involved in photosynthesis, where the primary photophysical process is known to be temperature independent. The relatively large activation energy of 0.36 ev, which we have found in crystalline chlorophyll *b* would seem to strengthen this argument. However, the question is by no means resolved. It is known that chlorophyll *a* is the essential, ubiquitous pigment in photosynthesis; that all chlorophyll is present in chloroplasts as a disordered amorphous array; and finally that chlorophyll exists as a protein complex. It will be necessary to show that an amorphous chlorophyll *a*-protein complex has a photoconduction activation energy for Rabinowitch's argument to be entirely valid. We are preparing at present for such a measurement.

[16] J. R. Platt, in *Radiation Biology*, edited by A. Hollaender (McGraw-Hill Book Company, Inc., New York, 1956), Vol. III.
[17] F. P. Zcheile and D. G. Harris, J. Phys. Chem. **47**, 623 (1943).
[18] See comments by B. Rosenberg and E. Rabinowitch, Discussions Faraday Soc. **27**, 254 (1959).

5. EFFECT OF OXYGEN ADSORPTION ON SEMICONDUCTION

In a previous paper[9] it has been shown that oxygen adsorption in the dark from ambient gas on the surface of crystalline all-*trans* β carotene has a profound effect upon semiconduction. This effect was interpreted as being due to the formation of an oxygen-carotene complex with a binding energy of 0.20 ev. This decreased the semiconduction activation energy and increased the mobility of the surface charge carriers. The complex was rapidly broken and the oxygen desorbed at high temperatures (up to 120°C). This produced a reversion of the semiconduction currents back to their values in an inert-gas atmosphere. There was no energy barrier to the formation of the complex, and the process also occurred in the dark at lower temperatures (0°C). The binding energy of the complex was evaluated by the desorption rate at different temperatures, and a simple method of analyzing those data was given.

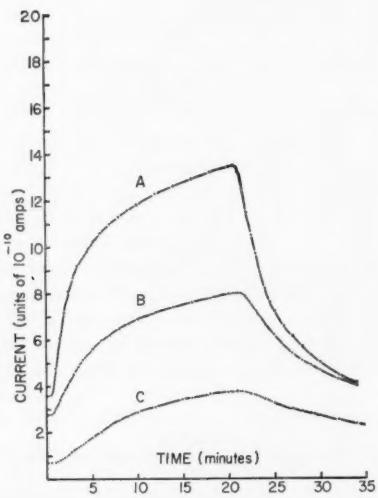

FIG. 6. The effect of oxygen adsorption on the photocurrent of chlorophyll *b*; A. temp.=60°C, B. temp.=45°C, C. temp.=25°C, oxygen on at 0 min, off at 20 min.

We then looked for similar effects in crystalline chlorophylls *a* and *b*, and found that there is an oxygen effect on the conductivity of these substances; however, it is markedly weaker and differs in a number of respects from that of carotene. Some preliminary results are described below.

The experimental procedure was to flow pure dry oxygen gas through the chamber after the chlorophyll had been well deoxygenated by heat, and to follow the progress of the dark current with time at a constant temperature. The oxygen was then flushed out of the chamber by flowing dry nitrogen through the system for a period of 20–40 min, and again the dark current was determined as a function of time. This was done at three different temperatures. The results of one such set of measurements for chlorophyll *b* are shown in Fig. 4. The narrow temperature range of 25° to 60°C was restricted at both ends. At the low-temperature end, due to the high binding energy, the time constants become too long for experimental convenience; the high-temperature limitation was required to prevent any sintering during the time of the measurements. Because of the low melting point and sintering temperature of chlorophyll this method of analysis is at the borderline of practicality, and the results are of a more limited validity than in other substances such as β carotene or anthracene.

The first significant point of the data (Fig. 4) is the amount by which the current increases after oxygen adsorption. At the highest temperature the current increased by a factor of about 4 in 20 min (a steady state was not reached within this time). This is to be compared with the case of β carotene where, under the same conditions, the dark current increased by a factor of about 10^3; thus the dark effect of oxygen adsorption by chlorophyll is much smaller than in the case of β carotene.

The second point is the decrease of the current when the oxygen atmosphere is replaced by a nitrogen atmosphere. With somewhat more extended periods, (the length of time depends on the temperature), the dark current returns completely to the original value. This has been repeated a number of times on a given sample with no resulting permanent change. Thus, as in β-carotene, the oxygen effect is completely reversible.

TABLE I. An experiment to determine an activation energy for formation of the oxygen-chlorophyll complex.

1. Dark current of deoxygenated sample at 25°C	$=0.48\times10^{-11}$ amp
2. Dark current after 20 min oxygen adsorption at 25°C	$=1.9\times10^{-11}$ amp
3. Dark current after deoxygenating sample at 25°C	$=0.45\times10^{-11}$ amp
4. Dark current after deoxygenating sample at 60°C	$=5.0\times10^{-11}$ amp
5. Dark current after 20 min oxygen adsorption at 60°C	$=26.0\times10^{-11}$ amp
6. Dark current after 20 min oxygen adsorption at 60°C and rapid cooling to 25°C	$=2.1\times10^{-11}$ amp

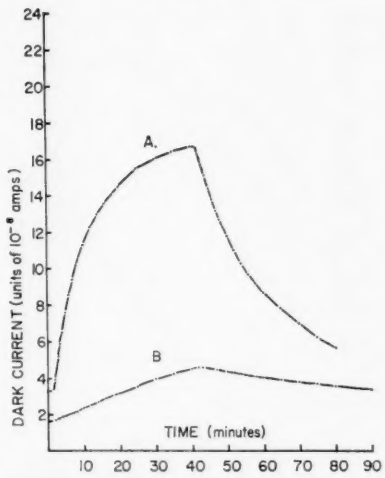

FIG. 7. The effect of oxygen adsorption on the dark current of chlorophyll *a*; A. temp.=65°C, B. temp.=55°C, oxygen on at 0 min, off at 40 min.

The third point of interest is the general shape of the curves. These broadly resemble an exponential rise and decay. However, when data were taken over a long enough period of time to ensure a close approach to the steady-state condition and plotted as if it followed an exponential law, the results showed two linear segments of differing slope (both rise and decay). This means that at least two processes with different time constants are involved. Similar situations occurred in the cases of β carotene and anthracene.[19]

A fourth point concerning the relative magnitude of the effect of oxygen as a function of temperature will be deferred momentarily to present data on the effect of oxygen on the photocurrent. The experimental procedure was again similar to that of the dark-current procedure with the exception that the sample was continuously irradiated during the measurements. Ten minutes of preirradiation in a nitrogen atmosphere were sufficient to establish a steady photocurrent before oxygen was admitted into the chamber. For comparison, Fig. 5 shows the effect of oxygen on the photocurrent and the dark current at a temperature of 45°C. In Fig. 6 the photocurrents are compared at the same three temperatures as shown in Fig. 4. The general features of these curves are the same as that for the dark currents except for the larger magnitudes of the photocurrents.

A cursory examination of Figs. 4–6 may result in two fallacious conclusions: an activation energy is involved

[19] A. G. Chynoweth, J. Chem. Phys. **22,** 1029 (1954).

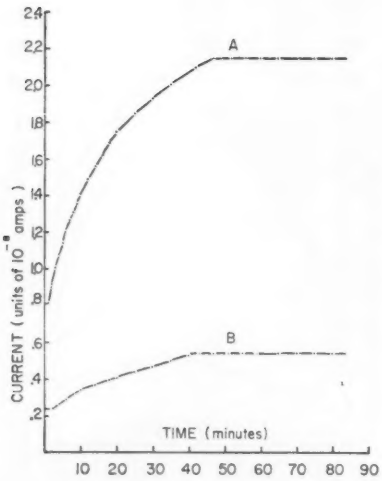

FIG. 8. The effect of oxygen adsorption on the photocurrent (A.) and the dark current (B.) of chlorophyll *a*; temp.=25°C, oxygen on at 0 min, off at 40 min.

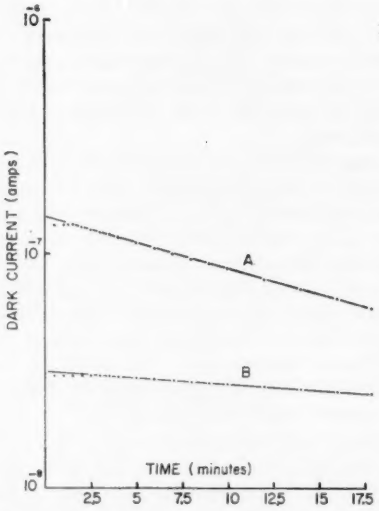

FIG. 10. The rate of dark current decrease due to oxygen desorption for chlorophyll *a*; A. temp.=65°C, B. temp.=55°C, oxygen off at 0 min.

in forming the oxygen-chlorophyll complex, and that light produces a greater rate of formation of the complex, i.e., that this is predominantly a photo-oxidation process. A detailed examination of the data shows that both conclusions are incorrect. At all temperatures, the photocurrent and the dark current are increased after 20 min oxygen adsorption by a constant factor of approximately 4. This is the average of many measurements, and any single measurement may deviate by as much as 50%. This means that the formation of the oxygen-chlorophyll complex affects the photocurrent and the dark current in the same way.

It was mentioned previously that for β carotene the formation of the oxygen-carotene complex affects both the semiconduction activation energy and the mobility of the charge carriers. In chlorophyll the dark current increase due to the formation of the complex is not large enough to detect any change in the semiconduction activation energy. It is therefore expected that only the mobility of the charge carriers changes. Indeed the

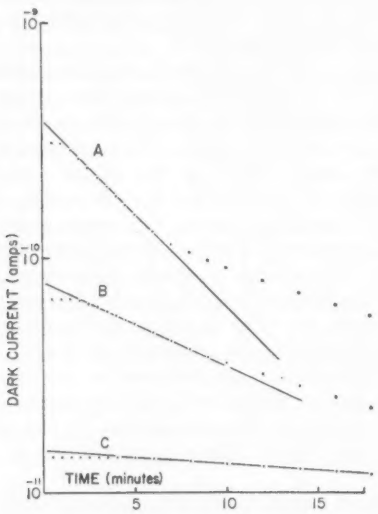

FIG. 9. The rate of dark current decrease due to oxygen desorption for chlorophyll *b*; A. temp.=60°C, B. temp.=45°C, C. temp.=25°C, oxygen off at 0 min.

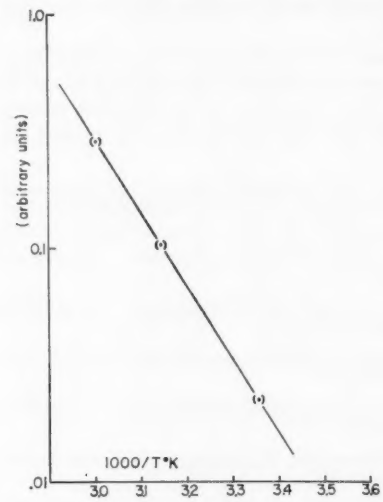

FIG. 11. The dependence of the desorption rate constant ν on temperature in chlorophyll *b*. Slope of curve equals heat of desorption, q (0.63 ev).

only factors common to the expression for the dark current and the photocurrent are the charge carrier mobility and the field strength. In the previous paper we pointed out that the field strength cannot change due to the complex formation, since the binding energy of the oxygen to the β carotene (0.20 ev) is much too small to be due to electronic charge trapped at the oxygen and thereby converting it into the negative ion as would be required for a Mott-Schottky barrier. This argument is slightly weakened in the present case since the oxygen-chlorophyll complex has a larger binding energy (see below); nevertheless we feel it still holds true. Thus only the mobility of the charge carriers remains as the factor which changes upon forming the complex. This is in agreement with the experimental fact that all curves have a common multiplier.

If there is an activation energy in forming the complex it is relatively simple to show experimentally that the energy must be small. If this activation energy exists, the complex should form more rapidly at elevated temperatures. If the sample is rapidly cooled to a lower temperature with the oxygen still present, the current at this lower temperature should be much larger than it would be if the oxygen complex had been permitted to form for the same length of time at this lower temperature. The results of such an experiment are shown in Table I. Line 6 is identical within the limits of the experiment to line 2. Therefore there is no measurable activation energy to form the complex.

We have reserved a discussion of the oxygen effect on crystalline chlorophyll *a* until this point because of the special difficulties involved in this case. In Fig. 7 the data on the dark effect are shown at two different temperatures 55° and 65°C. Note, however, that the oxygen flowed through the chamber for 40 min as compared to 20 min with chlorophyll *b*. The large difference in the two curves indicates a much longer time constant for the rise and decay curves and a stronger temperature dependence. The exact value of the binding energy will be discussed below. The indication is that the binding energy of the oxygen-chlorophyll *a* complex is much larger than that for the oxygen-chlorophyll *b* complex. The lifetime of the chlorophyll *a* complex at room temperature is many hours. In Fig. 8, the data are compared for the light and dark effects at 25°C. There is no current decay apparent in 50 min, after removal of the oxygen atmosphere. From the dark curve at 65°C, which has made a sufficiently close approach to the steady-state value to be compared to the chlorophyll *b* data, the current multiplier is again about 4.

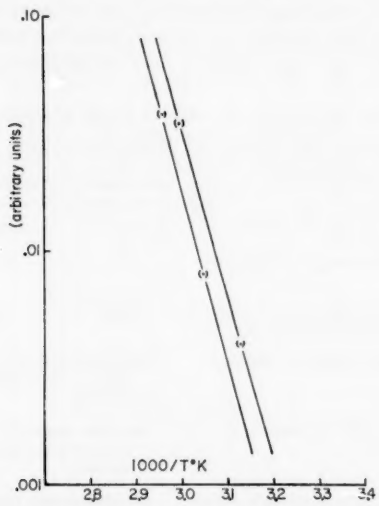

FIG. 12. The dependence of the desorption rate constant ν on temperature in chlorophyll *a* for two different samples. Slopes of curves equals heat of desorption, q (1.4 ev).

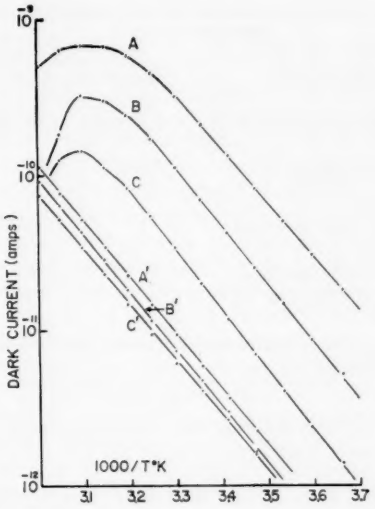

FIG. 13. Depletion of "oxygen reservoir" effect in chlorophyll *b*. See text for explanation of curves. Primes denote cooling part of cycle.

6. BINDING ENERGY OF THE OXYGEN-CHLOROPHYLL COMPLEX

In the paper on β carotene the simple kinetic theory for determining the binding energy of these complexes was given. This utilized the assumption that the current increase due to the complex formation was proportional to the fraction of the surface covered (θ) by the oxygen. The current decrease upon removal of the oxygen atmosphere is due to the evaporation of the oxygen from the surface. Therefore we have

$$\Delta I_{\text{oxygen}} = K\theta \tag{3}$$

$$I_{\text{total}} = I_{\text{nitrogen}} + \Delta I_{\text{oxygen}} = I_{\text{nitrogen}} + K\theta. \tag{4}$$

For the desorption process

$$d\theta/dt = -\nu\theta, \tag{5}$$

TABLE II. Summary of electronic conductivity in crystalline chlorophylls *a* and *b*.

Measurement	Chlorophyll *a*	Chlorophyll *b*
Semiconduction activation energy	1.12±0.03 ev	1.44±0.03 ev
Triplet-state energy (phosphorescence)	?	1.43
Photoconduction activation energy	?	0.36±0.01
Energy of vibrational level nearest crossing point for intersystem conversion	?	0.33
Ratio of mobility of charge carriers (positive holes) in chlorophyll *a* to chlorophyll *b* $\cong 1$		

where ν is the desorption rate constant when $\theta=1$. Its temperature dependence is given by

$$\nu = A \exp(-q/kT), \tag{6}$$

where q is the activation energy of desorption, which in this case is closely equal to the binding energy of the complex. The integration of Eq. (5) with the substitution for θ from Eq. (4) yields the final equation

$$(I_{\text{total}}-I_{\text{nit.}}) = (I_{\max}-I_{\text{nit.}})\exp(-\nu t). \tag{7}$$

If the $\log_e(I_{\text{total}}-I_{\text{nit.}})$ is plotted against t, straight lines should result with a slope equal to ν.

The results of such a plot are given in Figs. 9 and 10 for chlorophylls *b* and *a*, respectively. The initial portions of the decay curves are linear. However, as in β carotene, the decay process at longer times departs from linearity and is evidence for a second still unknown process. From the initial portions of the curves we can arrive at an estimate of the binding energies. The log of the slopes of the curves are plotted against the reciprocal temperature according to Eq. (6). The slope of this curve is the binding energy of the complex. These curves are shown in Figs. 11 and 12 for chlorophylls *b* and *a*, respectively. The data for chlorophyll *b* do give a 3-point fit to a straight line; and the value of the binding energy is 0.63 ev. In the case of chlorophyll *a*, since only two points are available, the entire process was repeated on a second sample. Both sets of data are given in Fig. 12. While a straight line through two points is obviously of limited interest, the fact that the two different samples give parallel lines is more significant. The resultant binding energy of the oxygen-chlorophyll a complex is tentatively given as 1.4 ev. This verifies our previous statement that the oxygen is significantly more tightly bound to chlorophyll *a* than *b*.

7. OXYGEN RESERVOIR EFFECT

In Sec. 4 the idea was introduced that the oxygen may be bound to the chlorophyll in two ways. In the first manner, the dark- and photocurrents are increased and the oxygen can be driven off by heating in nitrogen to about 60°C for a suitable length of time. When this is done, the semiconduction curves are identical for the heating and cooling cycles. However, if the sample is irradiated (still in nitrogen) at low temperatures directly after the above process, the current increases and does not diminish much when the light is removed. If, after a time in the dark sufficient for the photocurrent to decay to a steady value, the sample is now thermally cycled, there is a new hysteresis loop evident. The same effect would occur if oxygen had been permitted into the chamber and newly adsorbed on the chlorophyll. This irradiation at low temperatures, dark decay, heating, and cooling cycle can be repeated a number of times. Each time, however, the effect becomes smaller, as though a reservoir were being exhausted. The results of three such serial measurements are shown in Fig. 13. The simplest explanation of this phenomenon consistent with the above results is the following: oxygen molecules can form a complete change-transfer complex with chlorophyll, that is,

$$\text{Ch}+\text{O}_2 \rightleftharpoons [\text{Ch}^+\text{O}_2^-]. \tag{8}$$

This has a negligible effect on the electronic conductivity (it is not a simple charge-trapping phenomenon). The binding energy of this complete charge-transfer complex is higher than that of the type of complexes we have discussed above, which may be partial charge-transfer complexes. Therefore, it is not easily desorbed at the temperature of the experiment. The effect of light in a nitrogen atmosphere is to drive Eq. (8) in the reverse direction (photoreduction) and permit the oxygen to form the partial charge-transfer complex which does affect the electronic conductivity and is of a weaker binding energy (see above) so that it can be desorbed at the experimental temperature. While this explanation of the mechanism of the oxygen reservoir effect is not the only possible one, it does have the advantage of simplicity. More detailed data are obviously neces-

TABLE III. Summary of the effect of oxygen adsorption on the electronic conductivity in crystalline chlorophylls *a* and *b*.

Measurement	Chlorophyll *a*	Chlorophyll *b*
Binding energy of complex	1.4 ev (?)	0.63 ev
Activation energy to form complex	?	none
Effect of complex on semiconduction activation energy	none	none
Effect of complex on mobility	increases mobility of thermally excited charge carriers	
Effect of light in presence of oxygen	increases mobility of radiation excited charge carriers	
Effect of light in samples deoxygenated by heating	depletes deeper bound oxygen reservoir to create more loosely bound complex.	

sary, particularly on the binding energy of the postulated complete charge-transfer complex and whether light is necessary for its formation or merely enhances its formation. These results seem to have a relationship to certain properties of chlorophyll in solution such as the formation of the labile moleoxide of chlorophyll, the photo-oxidation and photoreduction of chlorophyll and the chlorophyll-sensitized photo-oxidation of other substances.[20] Further discussion of this relationship would be premature at this point.

The curves shown in Fig. 13 are similar in many aspects to the "thermal spike" found in dried chloroplasts by Arnold and Sherwood.[5] The general shape of the curve is similar, but ours is incomplete since we could not heat our samples to 140°C as was done with the chloroplasts. However the corresponding curves for β carotene (see Fig. 4 of reference 9) do show the complete curve to be in agreement with that of the chloroplasts. Of course β carotene does not require irradiation to form this "thermal spike" while chlorophyll does. The interpretation of this effect given by Arnold and Sherwood is that this represents an electron-trapping process; the traps are emptied by heat and filled by irradiation. Our results however, suggest an alternative explanation in terms of the oxygen-chlorophyll complex which is formed by the radiation (from the "reservoir") and is broken with subsequent oxygen desorption by heating. Arnold and Sherwood also suggest that this "thermal spike" is not too closely related to the thermoluminescence measured in the dried chloroplasts after irradiation. Their argument is that the thermal spike has a maximum at a lower temperature than that for thermoluminescence, and that blue light is necessary for the "thermal spike" while red light is sufficient for the thermoluminescence. However, the thermal spike reaches its maximum when the rate of current decrease due to oxygen desorption is equal to the rate of current increase with temperature. Above that temperature it desorbs even faster and the curve diminishes. The thermoluminescence is largest at the highest rate of desorption before depletion effects occur. Therefore it should be expected that the "thermal spike" should occur at a lower temperature. We have also found that red light is sufficient to cause the "thermal spike" in crystalline chlorophyll. The only explanation we have for this discrepancy is that we are working with a simpler system. It is reasonable to consider the thermoluminescence as due to the breakup of the oxygen-chlorophyll complex because of the following points of similarity: thermoluminescence in chloroplasts requires the presence of air or oxygen[21]; upon repeating the process in the same cyclic fashion as our measurements, the thermoluminescence decreased each time until after four or five repetitions it stabilized, as we have found above; the energy corresponding to the glow curve peaks shows a small peak at 0.69 ev and the predominant emission at 0.93 ev, whereas the binding energy is 0.63 ev for the oxygen-chlorophyll *b* complex and 1.4 ev (?) for the chlorophyll *a* complex (the ratio of chlorophyll *b* to chlorophyll *a* in chloroplasts is about 1:3). Arnold and Sherwood recognized the importance of an oxygen effect and suggested it as an alternative or concomitant mechanism to the electron trapping mechanism. Our present feeling is that our results strongly favor their oxygen mechanism as the only mechanism to explain the thermoluminescence and "thermal spike" effects in dried chloroplasts.

8. SUMMARY

In Table II we present a summary of the various results of the measurements of electronic conductivity in crystalline chlorophylls *a* and *b* and the relevant associated data available. In Table III we collect the data on the effect of oxygen adsorption on photoconduction and semiconduction in these crystals.

ACKNOWLEDGMENT

We should like to express our gratitude to the National Institute of Neurological Diseases and Blindness of the Public Health Service for their support of this work under Research Grant B–1936, and the Research Corporation for part support.

[20] For a general review see: R. Livingston, "Photochemistry of chlorophyll related to the primary act of photosynthesis" in *Bioenergetics, Supplement 2 of Radiation Research*, edited by L. G. Augenstine (Academic Press, Inc., New York, 1960).

[21] W. Arnold and H. Sherwood, J. Phys. Chem. **63,** 2 (1959).

Measurement of the Resistivity of Cesium at Elevated Temperatures

JULIUS HYMAN, JR.

Rocketdyne, A Division of North American Aviation, Inc., Canoga Park, California

(Received November 28, 1960)

An experiment is described in which the electrical resistivity of liquid cesium was measured from ambient temperature to 419°C, and experimental values are presented. In the low-temperature region the data agree quite well with measurements made by others. A linear approximation which best correlates the data from the melting point to 419°C to ±1% is

$$\rho_{Cs}=38.5[1+0.00308(T-50)]\ \mu\text{ ohm-cm}.$$

Here T is temperature in degrees centigrade. By use of the Widemann-Franz relation, a thermal conductivity of 0.048 to 0.050 cal/sec-deg C-cm is predicted.

INTRODUCTION

A SPECIAL liquid level transducer was designed and constructed at Rocketdyne for the measurement of cesium flow rates in an ion rocket.[1] A necessary parameter for its calibration was the electrical resistivity of liquid cesium at elevated temperatures. These data were not available in the literature; consequently a limited program to measure this parameter was initiated.

Cesium melts at 28.5°C, readily oxidizes in air, and reacts explosively with water. Furthermore, it attacks glass at high temperatures. Because of these properties it was necessary to conduct the experiment in a closed inert system. A thin wall stainless-steel tube was used, and the parallel conduction of the steel was subtracted from the experimental results.

EXPERIMENTAL PROCEDURE

Resistance of Stainless Steel Tube

Because reasonable variance is to be expected in the physical properties of commercial metals, the resistance of a sample of the tubing to be used was measured.

A 3-in. section of $\frac{1}{8}$-in. tubing (type 321 stainless steel, 0.012 wall) was fitted with two copper current electrodes. Twenty gauge wires were attached to serve as current leads. Two 30-gauge voltage-sensing electrodes were spot welded along the tube with a 1-in. separation. Between these electrodes a 30-gauge iron-constantan thermocouple was spot welded to the tube. All leads were covered with high-temperature asbestos insulation.

A transistor regulated current supply furnished a constant current of 2 amp to the test sample. This current was monitored with a Sensitive Research Instruments Corporation ammeter having a variance of $\pm\frac{1}{4}\%$ of full scale value. A Leeds & Northrup hand-balanced potentiometer of ±0.05% accuracy was used to measure the thermocouple output and the voltage drop across the 1-in. section.

The tube was suspended by the leads in an asbestos-lined copper heat sink, and the entire assembly was placed inside of a resistance furnace. The data obtained are presented in Table I.

A new tube was then prepared with current electrodes and voltage taps temporarily attached 1 in. apart. Its resistance was obtained in like manner at ambient temperature only, as it was desirable to keep this tube clean and unoxidized so that it would remain a suitable container for the cesium. The data obtained are presented in Table I. The variation of resistance of this new tube at elevated temperature was assumed to vary in the same manner as the previous sample.

Preparation of Cesium-Filled Tube

The new section of tubing was prepared for filling with cesium. The tube was first cleaned by spraying with trichloroethylene droplets carried in a high-speed nitrogen jet. One end was squeezed in a vise and fused shut with a heliarc welder using a tungsten electrode.

The empty tube was weighed on an analytical balance with electrodes attached and then filled with cesium. The filling was accomplished in an argon-filled dry box with the aid of a hypodermic syringe and needle. The tube was then squeezed shut with a vise-grip pliers and taken out of the dry box. It was weighed again to ensure that the correct amount of cesium had been used, and was then heliarc fused on the other end.

Resistance of Cesium-Filled Tube

Measurements were made with the cesium-filled tube at various temperatures over a period of several days. These data are presented in Table I in the order in which they were taken.

After measurements were completed the tube was removed from the furnace and the ends opened in an argon atmosphere. The cesium appeared to be uncontaminated, and the inside of the tube was clean. It was then sectioned for measurement of wall thickness.

[1] Julius Hyman, Jr., "A survey of methods for cesium flow measurement in an ion rocket," Research Rept. 60-3, Research Subdivision, Rocketdyne, Canoga Park, California (February 11, 1960).

TABLE I. Data from cesium resistivity measurement.

Resistance of unfilled stainless-steel tube		Resistance of new stainless-steel tube		Resistance of cesium-filled tube		Cesium resistivity	
Temp., °C	ohm/in.×10³	Temp., °C	ohm/in.×10³	Temp., °C	ohm/in.×10³	Temp., °C	μ ohm-cm
26	7.045	24	7.250	29	1.00	29	23.50
35	7.105			50	1.53	50	39.05
121	7.720			114	1.76	114	45.80
137	7.750			179	1.98	179	53.10
150	7.810			221	2.13	221	57.60
				287	2.38		
182	8.040			344	2.58	287	66.30
289	8.750			388	2.73	344	73.00
304	9.000			344	2.61	388	78.30
361	9.200			295	2.44	344	74.20
455	9.765			230	2.17	295	68.40
428	9.440			419	2.84	230	59.00
74	7.400					419	82.90
489	9.760						
72	7.350						
33	7.060						

ANALYSIS OF RESULTS

Data Reduction

The electrical resistance of cesium was determined from the data presented in Table I. The resistance data was converted to its reciprocal, conductance; and the conductance of the stainless-steel tube was subtracted from these values leaving the conductance of the column of cesium. The reciprocal of this difference is the cesium resistance.

As no attempt was made to obtain the resistance of the filled and unfilled tubes at the same temperatures, tube data is interpolated to the required temperatures.

A correction is made for thermal expansion of the stainless-steel container. A normalization of the geometry converts these resulting data to values of resistivity.

Resistivity of Cesium

The resistivity of cesium in micro-ohm-centimeters may be obtained from the resistance data

$$\rho_{Cs} = R_{Cs}(A/l) \times 10^6\ 2.54.$$

For this experiment, the distance l was 1 in. and the area A was the cross section of the inner diameter of the tube. Rather than use the nominal value, the tube was sectioned in four places, and the inside diameter was measured. The average diameter was 0.10085 in. Therefore,

$$\rho_{Cs} = 2.027 \times 10^6 R_{Cs}\ \mu \text{ ohm-cm}.$$

The product of the above factor and the resistance of the cesium column yields the final values of cesium resistivity. These values are presented in Table I. A linear approximation which correlates as resistivity observed from the melting point to 419°C within ±1% is

$$\rho_{Cs} = 38.5[1 + 0.00308(T - 50)]\ \mu \text{ ohm-cm},$$

where T is degrees centigrade.

For comparison, data obtained from the available literature[2] are presented along with the data derived from this experiment. The agreement is excellent (Fig. 1).

Error Analysis

Sources of error included the current and voltage measurements, variation in reference temperature, and geometrical error brought in by uncertainty in the size of the stainless-steel tube. The thermocouple employed had an accuracy of ±2°C at the highest temperature recorded in the experiment. The square root of the sum of the squares of all the predictable errors yields a total coefficient of error of 0.7% at 419°C.

STATISTICAL ANALYSIS

The raw data was subjected to a statistical analysis to test for experimental consistency. The two resistance curves for the filled and unfilled tubes were fit by the method of least squares to a straight line and parabola, respectively. Resistance data of the filled tube taken at

[2] M. L. Hackspill, Ann. Chem. et Phys. **28,** 8 (1913).

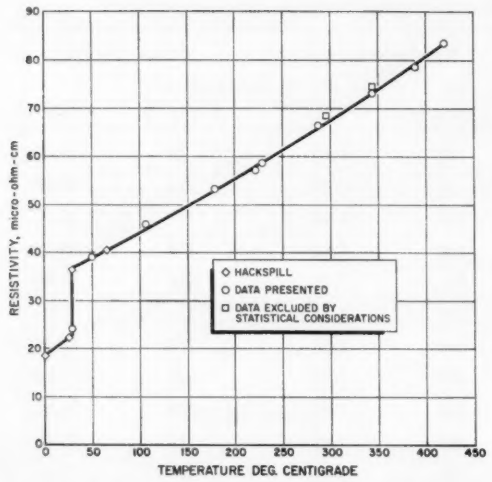

FIG. 1. Electrical resistivity of cesium as a function of resistivity.

344° and 295°C were rejected by a statistical test at the 95% confidence level. The coefficient of random error for the remaining information is 0.12%. This is considerably less than the estimate of accuracy given in the error analysis, and therefore shows that the experimental procedure was of at least as high a quality as dictated by the instruments and materials used.

THERMAL CONDUCTIVITY

By use of the Wiedemann-Franz relation, values of thermal conductivity can be computed from the values of electrical resistivity. It has been found experimentally that the product of the electrical resistivity and thermal conductivity of most pure metals divided by the absolute temperature is equal to a constant. The value given by Lorenz is defined by

$$\Lambda = (\pi^2/3)\,(k/e)^2,$$

where k is Boltzmann's constant and e is the charge on the electron. In mks units the Lorenz number has a value of

$$\Lambda = 2.43\times10^{-8}(\text{v/deg C})^2.$$

Values derived in this way are only approximate. The Lorenz numbers derived from experimental results for sodium and potassium are 2.25×10^{-8} and 2.05×10^{-8}, respectively. These agree closely with theory. However, values of 3.5×10^{-8} and 4.95×10^{-8} observed for lithium and rubidium cast some doubt on the applicability of the theoretical value.[3]

Nonetheless, these higher values are quite the exception when compared with all metals. In fact the mean of Lorenz numbers for all representative metals determined at 10°C is within 1% of the theoretical prediction.[4]

By using the theoretical value of the Lorenz number, the thermal conductivity is predicted to be almost constant, varying from 0.048 to 0.050 cal/sec-°C-cm as the temperature varies from ambient to 419°C.

---

[3] *Liquid-Metals Handbook* (U. S. Atomic Energy Commission, Department of the Navy, Washington, D. C., June 1952).

[4] D. J. Schleef, "Review of modern theory of thermal conductivity of metals," in *Thermodynamics and Transport Properties of Gases, Liquids, and Solids* (McGraw-Hill Book Company, Inc., New York, 1959).

Gaseous Detonations. XIII. Rotational and Vibrational Distributions of OH Radicals

G. B. KISTIAKOWSKY AND R. K. LYON

Gibbs Chemical Laboratory, Harvard University, Cambridge, Massachusetts

(Received December 2, 1960)

In an earlier paper in this series, some observations of the rotational temperature of OH radicals in the reaction zone of gaseous detonations were reported and interpreted as meaning that abnormal rotational excitation is produced by extremely fast chemical reactions. In the present study new experiments were made on detonations of $C_2H_2+2\frac{1}{2}O_2$ and $CO+H_2+O_2$ mixtures. An improved method of data reduction was developed and applied to both the new and the previously reported experiments. It is concluded that in all reported experiments the vibrational and rotational distributions of OH remain the same within experimental errors from the front of the wave to beyond the *C-J* plane. This is tentatively attributed to the turbulent gas flow behind the detonation front which restricts the usefulness of the present method, rather than to abnormal distributions in the reaction zone caused by fast chemical reactions.

INTRODUCTION

IN an earlier paper[1] in this series the ultraviolet absorption spectrum of OH radicals in gaseous detonations was observed as a function of location in the detonation wave with a resolution of 4 μsec. By means of the isointensity method[2] the rotational temperature of the OH radicals was calculated from the observed spectra. It was found that in detonations of $2H_2+O_2$ the rotational temperature in the reaction zone was approximately the same as that in the equilibrium gas behind the reaction zone, while in detonations of $2H_2+O_2+0.075\ C_2H_2$ the reaction-zone temperature appeared higher than the equilibrium gas temperature. However, this was a result of low confidence by the "t" test: the probability that all the experimental data are members of the same normal distribution is 0.04.

These observations appear to be inconsistent with the gas density measurements in detonation waves[3] and with theory. One expects the temperature to start at about 1600°K behind the shock front and to rise with the progress of reaction towards the equilibrium value of 2700°K. To explain this conflict Kistiakowsky and Tabbutt (KT) suggested that "the lifetime of hydroxyl radicals in partially reacted mixtures is comparable to their rotational relaxation time." This instance of rotational nonequilibrium caused by chemical reaction seemed sufficiently unusual to warrant further investigation. It also seemed worthwhile to investigate the vibrational distribution of the OH radicals during the reaction since greater departures from equilibrium were to be expected there.

METHOD OF DATA REDUCTION

Although considerable effort was spent trying to improve the experimental method of KT, no major improvement was achieved. The apparatus and experimental procedures were, therefore, essentially the same as previously[1] described. However, the method of data reduction was considerably modified and improved. The isointensity method, used by KT, suffered from the disadvantage that only a few lines could be utilized, and these were not the most reproducibly measurable lines in the spectra. The fact that it minimized systematic errors in determining the absolute temperature was of no real value to the present study, since we are mainly concerned with detecting changes in temperature accompanying changes of the location of the gas in the wave. It was, therefore, preferable to define a special set of vibrational and of rotational distribution functions V and R, which permits the use of every well-resolved reproducibly measurable line. These functions are as follows:

$$R_{AO}=\frac{(Q_2 1300+Q_1 1300)\,(Q_1 1400+P_1 1400)\,(Q_1 1500+R_2 1500)\,(Q_1 1600)}{(Q_1 100+R_2 100)\,(Q_1 200+P_1 200)\,(Q_1 400+P_2 400)\,(Q_1 500)}$$

$$R_{CO}=\frac{(Q_2 1300+Q_1 1300)\,(Q_1 1400+R_1 1400)\,(Q_1 1500+R_2 1500)\,(Q_1 1600)}{(Q_1 100+R_2 100)\,(Q_1 200+P_1 200)\,(R_2 400+P_2 400)\,(P_1 500+P_2 500)}$$

$$R_{HO}=\frac{(Q_2 1300+Q_1 1300)\,(Q_1 1400+R_1 1400)\,(Q_1 1500)\,(Q_1 1600)}{(Q_1 100)\,(Q_1 200+P_1 200)\,(P_2 400)\,(P_1 500+P_2 500)}$$

[1] G. B. Kistiakowsky and F. (1959). Also see F. Tabbutt, thesis, Harvard University, 1957.
[2] G. H. Dieke and H. M. Crosswhite, *The Ultraviolet Bands of OH* (The Johns Hopkins University, 1948), Bumblebee Ser. Rept. No. 87.
[3] G. B. Kistiakowsky and P. Kydd, J. Chem. Phys. **25**, 824 (1956).

$$V_{AO}=\frac{(Q_1411+P_2411)(\sigma_1)}{(R_2400+P_2400+Q_1400)}+\frac{(Q_1511+Q_2511)(\sigma_2)}{(R_1500+Q_1500+P_2500)}+\frac{(Q_1911)(\sigma_3)}{(Q_1900+P_1900)}$$

$$V_{HO}=V_{CO1}$$

$$V_{CO1}=\frac{(Q_1411)(\sigma_1')}{(R_2400+P_2400)}+\frac{(Q_1511+Q_2511)(\sigma_2')}{(P_1500+P_2500)}+\frac{(Q_1911)(\sigma_3')}{(Q_1900+P_1900)}$$

$$V_{CO2}=(\sigma_2'')(Q_1222/P_1200)+(\sigma_2'')(Q_11222/Q_21200).$$

In these definitions such terms as Q_1411 should be read as "the extinction coefficient of the line Q_14 of the 1→1 transition." The σ's are weighting factors to take into account the fact that the various terms in the vibrational functions could not be measured with equal accuracy. They are defined in reference 4.

The subscripts to R and V indicate the detonating mixture to which the functions were applied: AO the acetylene-oxygen (2:5 mole ratio), CO the carbon monoxide-hydrogen-oxygen (equimolar), and HO the hydrogen-oxygen (applied to both of KT's mixtures, $2H_2+O_2$ and $2H_2+O_2+0.075\ c_2H_2$). The values of the HO functions were obtained from the spectrographic records of KT, but since R_{HO} contains no lines which were used by KT for determining rotational temperatures, the use of R_{HO} gives an independent calculation of rotational temperatures from their data.

The numerical values obtained for these various functions are given in reference 4, while the results of statistical analysis of these values are given in Table I. For this analysis the experimental data were divided into two groups, Y and X. Group X consisted of all observations made within the apparatus resolution time (4 μsec) from the shock front or within the reaction-zone width, whichever was greater. Group Y contained the observations of completely equilibrated gas, and included measurements made beyond two resolution times after the shock front (or the resolution time plus the reaction-zone length, whichever was greater) to 60 μsec after the shock front. The 60-μsec limit was used because significant cooling due to the rarefaction wave may occur at times much greater than this. The two groups of the values of each of the distribution functions were then compared by the "t" test. In Table I, column D.A. gives the percentile difference of the averages, i.e., $200(\bar{X}-\bar{Y})/(\bar{X}+\bar{Y})$, where $\bar{X}$ and $\bar{Y}$ are the average values of the two groups used in the "t" test. The column headed "probability" contains the probability of occurrence of the corresponding "t" in a normal distribution. The last column will be discussed later.

ERRORS

Undoubtedly, the observed values of the distribution functions are influenced by errors of film calibration, lack of spectroscopic resolution, and other systematic errors. However, none of these errors are functions of the location of the observed gas in the detonation wave, so that if a distribution function in one region of the wave is systematically different from that in another region, a different distribution must exist.

Since the errors could be functions of temperature, the change of the distribution functions with temperature is not necessarily that calculated from theory. Indeed, it is conceivable (but unlikely) that due to an unfortunate combination of errors the distribution functions might be independent of temperature.

That this is not the case can be proven from the data. The classical theory of detonation waves shows that at the C-J plane

$$T=\tilde{M}\,D^2\gamma/R(\gamma+1)^2,$$

where $\tilde{M}$ = average molecular weight, R = gas constant, D = velocity of the detonation, and $\gamma=\tilde{C}_p/\tilde{C}_v$. From this it follows that $dT/T=2\,dD/D$ if one neglects changes in γ and $\tilde{M}$. In the acetylene-oxygen experiments the detonation wave velocity was stable to better than ½%, but in the $CO+H_2+O_2$ experiments the mean deviation of the wave velocity from one experiment to another was 1.5%. Since this observed irreproducibility of the detonation wave velocity could be the result of both the changing tilt of the wave with respect to the tube axis and of a real irreproducibility of the wave velocity, the changes in wave temperature from one experiment to another should be between zero and 3%. Hence, V_{CO1} and R_{CO} might have been measured over a small temperature range and, if so, there should be a correlation between their changes from one experiment to another.

To test this, the measurements of V_{CO1} were divided into two groups depending upon whether or not the corresponding R_{CO} was greater or less than the average value of R_{CO}. Then a "t" test was performed on the two groups. A "t" of 5.24 with 19 degrees of freedom was obtained, which corresponds to a probability of less than 10^{-4} that all the points are members of the same normal distribution. Thus, it is clear that the method is sensitive to fairly small temperature changes.

If the measured extinction coefficient is proportional to the population of a level and one assumes that the Boltzmann distribution law is obeyed, the following

[4] R. K. Lyon, thesis, Harvard University (1960).

TABLE I. *T* test analysis of experiments.

Temperature function	D. A.	Degrees of freedom	"t"	Probability	Smallest observable temperature difference in °K (50% confidence)
$C_2H_2+2.5\ O_2$					
V_{AO}	−2.8	30	0.233	0.82	72
R_{AO}	−11.1	30	1.16	0.26	39
$CO+H_2+O_2$					
R_{CO}	4.1	15	0.395	0.70	43
V_{CO1}	−2.6	15	0.437	0.67	36
V_{CO2}	−15.6	15	1.37	0.20	148
$2H_2+O_2$					
V_{HO}	24.0	11	2.10	0.06	70
$H_2+O_2+0.075\ C_2H_2$					
V_{HO}	1.1	14	0.168	0.87	40
R_{HO}	−6.1	14	0.347	0.73	73

relationships can be readily derived for the distribution functions defined above,

$$dV/V=(E_V/RT)dT/T, \quad \text{(I)}$$

$$dR/R=(E_R/RT)dT/T, \quad \text{(II)}$$

where E_V is the energy difference between the zeroth and first vibrational levels (or zeroth and second for V_{CO2}), and is equal to 10.3 kcal/mole (or 19.4 kcal/mole for V_{CO2}); E_R is the sum of the energies of the 13, 14, 15, and 16th rotational states minus the sum of the energies of the 1, 2, 4, and 5th rotational states, which is equal to 44 kcal/mole.

On eliminating T from relations I and II and integrating one obtains $\log R_{CO}=(E_R/E_V)\log V_{CO1}+$constant of integration. When a least-mean square straight line is drawn through a plot of the experimental values of $\log R_{CO}$ against $\log V_{CO1}$, a slope of 1.55, with a standard deviation of 0.42, is obtained. This is to be compared with the slope of 4.27 calculated from the values of E_V and E_R. Hence, there might exist a serious systematic error in the response of the distribution functions to temperature changes. This error can be estimated by comparing the standard deviations of R_{CO} and V_{CO1} due to temperature changes with the irreproducibility of the temperature ($\leq 3\%$) estimated above.

Taking all of the values of R_{CO} as one set and all the values of V_{CO1} as another, one can easily determine the variances of these two sets. Part of these variances is due to irreproducibility of the temperature of the gas in the observed detonation waves and part is due to random errors. The former is correlated between the two sets and the latter is, of course, not correlated.

Using the least-mean-square straight line on the log R_{CO} against log V_{CO1} plot we now define the set of numbers R_V as the values of R_{CO} on the line corresponding to each observed value of V_{CO1}. One thus has two sets of numbers (R_V and R_{CO}) whose variance due to temperature change from one experiment to another is the same. It can now be readily shown that

$$S(T)=\tfrac{1}{2}S(R_{CO}+R_V)-\tfrac{1}{2}S(R_{CO}-R_V),$$

where $S(T)$ is the correlated variance due to temperature change. From this one obtains a value of 20.2% for the standard deviation of R_{CO} due to temperature changes from one experiment to another. By back calculating one obtains 14.3% for the standard deviation of V_{CO1} due to the same cause. On the basis of the theoretical temperature sensitivities of the distribution functions (assuming as an adequate approximation a temperature of 3000°K), and the observed mean deviation of the detonation wave velocities, these standard deviations are calculated to be equal to or less than 28% and 6.5%, respectively. Hence, the random error seems to be chiefly in V_{CO1}.

As will be seen later, no significant temperature-time trends in detonation waves were found from the data. The use of the sensitivities of the distribution functions to temperature permits then an estimate of the least temperature difference which could not escape detection. For this purpose it will be assumed that the sensitivities of distribution functions R_{CO} and V_{CO1} are 66% and 200% of the theoretical values. These are the most unfavorable assumptions consistent with the findings of the preceding paragraph. On the basis of similar considerations, it can also be estimated that V_{CO2} has a sensitivity of more than 50% of the expected value. We have additionally estimated that the sensitivities

of V_{AO} and V_{HO} are the same as that of V_{CO1}, and that the sensitivities of R_{AO} and R_{HO} are the same as that of R_{CO}. With these estimates we can calculate the smallest temperature differences observable with 50% confidence, which is the last column of Table I.

DISCUSSION OF THE RESULTS

With the possible exception of V_{HO} in the $2H_2+O_2$ experiments, none of the distribution functions show a significant change from reaction zone to equilibrium gas. This could be interpreted as meaning that strongly nonequilibrium rotational and vibrational distributions exist in the reaction zone which make the partially reacted cold gas appear to be as hot as the equilibrium gas. To assume one instance of such a coincidence, which was done in the previous paper[1] in this series, is plausible, but to assume several is decidedly less so. Another explanation is more likely and is supported indirectly by the findings of Carrington[5] that the cross section for rotational relaxation of OH in hydrogen-oxygen flames is even larger than the gas-kinetic collisional cross section. It has been shown by Martin and White[6] that the flow in detonation waves with long reaction zones is highly turbulent. Hence, in the present experiments the observed temperature in the reaction zone is averaged across a mixture of gas at all stages of the reaction, including possibly even equilibrium. Schott[7] has shown that the reaction $OH+H_2 \rightleftharpoons H_2O+H$ is fast enough to remain in equilibrium throughout the reaction zone of a hydrogen-oxygen detonation. Since the formation of hydrogen atoms is exothermic, the reaction will be shifted to the left as the gas becomes hotter. Therefore, when the average temperature is determined from optical absorption measurements on the OH spectrum the contribution of the partially reacted gas is low compared with that of the equilibrated gas. This consideration suggests that it is not possible with the present method to detect the low temperatures predicted to exist directly behind the shock front.

If the high value of "t" obtained in Table I for V_{HO} in the $2H_2+O_2$ experiments is due to vibrational excitation of the OH radical by chemical reaction, one would expect the excitation to be strongest where the reaction is fastest, i.e., shortly behind the shock front. One would also expect a similar behavior in V_{HO} in the $2H_2+0_2+0.075\ C_2H_2$ experiments. But the inspection of Table I shows that in the $2H_2+O_2$ experiments V_{HO} is actually lower near the wave front and no anomaly is observed in the $2H_2+O_2+0.075\ C_2H_2$ experiments. For these reasons, it seems likely that the observed difference between the average values of V_{HO} in the reacting and equilibrium gas is merely a random fluctuation. The probability of obtaining such a high "t" in one out of eight tests that are presented in Table I is about 50%.

Acetylene oxidizes to CO and CO_2 very rapidly under the present conditions. Hence, if the high rotational temperature that KT observed in the $2H_2+O_2+0.075\ C_2H_2$ is due to the addition of acetylene, one should also expect a higher temperature in the $C_2H_2+2\frac{1}{2}\ O_2$ experiments. Also, one would expect an anomalous vibrational distribution if chemical reactions are fast enough to induce a rotational nonequilibrium. None of these expectations are fulfilled. Furthermore, the function R_{HO} is slightly lower in the reaction zone than in the equilibrium gas. Since the use of the function R_{HO} gives a more sensitive test of temperature changes than the isointensity method as used by KT, one would expect R_{HO} to be much higher in the reaction zone than in the equilibrium gas. On this basis, we conclude that the abnormally high rotational temperature previously reported in the reaction zone of the $2H_2+O_2+0.075\ C_2H_2$ detonation is not real.

ACKNOWLEDGMENTS

We wish to express our gratitude to Dr. Paul Kydd and Dr. William Klemperer for several helpful discussions. The authors wish to thank Arthur Coleman and Andrew Brown for assistance in doing numerical calculations. They are also grateful to Professor D. H. Menzel for permission to use the Harvard Observatory densitometer. One of us (RKL) wishes to thank the National Science Foundation, the Standard Oil Company of California, and the Office of Naval Research for fellowships and research assistantships. This work was supported by the funds of the Office of Naval Research.

[5] T. Carrington, J. Chem. Phys. **31**, 1418 (1959).
[6] F. J. Martin and D. R. White, *Seventh Symposium (International) on Combustion* (Butterworths Scientific Publications, Ltd., London, 1959), p. 856.
[7] G. Schott and J. L. Kinsey, J. Chem. Phys. **29**, 1177 (1958).

Light Scattering by Anisotropic Inhomogeneities in Thin Polymer Films under Strain. II*

HARI L. BHATNAGAR

National Chemical Laboratory, Poona 8, India

(Received January 27, 1961)

Scattering by anisotropic inhomogeneities embedded in thin polymer films under two- and three-dimensional strain is treated theoretically. To take into account the effect of polydispersity, the differential cross sections for scattering are obtained for an assumed Maxwellian distribution in size at constant value of p, the ratio of the minor to major axis of an inhomogeneity.

INTRODUCTION

THE orientation of polymer films brings about significant changes in their physical properties. These changes may be followed by birefringence measurements, x-ray diffraction, and infrared dichroism. Recently Stein[1] and co-workers have added the powerful method of light scattering for following the changes in the physical properties of thin polymer films under strain.

Stein[1c] has also studied the variation of birefringence arising out of three-dimensional deformation. However, to date no data on light scattering by thin polymer films under three-dimensional deformation or even two-dimensional uniform elongation are available. Such studies may be helpful in conjunction with those on simple elongation in the determination of the dimensions of the inhomogeneities.

In the present paper, scattering by anisotropic inhomogeneities embedded in thin polymer films under two-dimensional nonhomogeneous strain (three-dimensional deformation) is considered theoretically. The special case of two-dimensional homogeneous strain is separately considered for reasons which become obvious on inspection of the results for the nonhomogeneous case.

For calculating the average intensity of light scattered by a spheroid the following assumptions are made:

(1) The spheroids (inhomogeneities) have the same shape, though they may have different sizes.

(2) The particles have perfect random orientation when the film is not under strain.

(3) The particles are separated by whatever distance is necessary to produce incoherency in scattered radiation by individual spheroids. Thus, there is neither interparticle interference nor any multiple scattering. The resultant scattering is, therefore, obtained as the statistical average emitted by the dipoles induced by the incident wave in the individual spheroids which are oriented spatially in accordance with a derived distribution function. The expressions for the scattering cross sections for the various states of polarization so obtained are multiplied by the particle interference factor $p(\psi, \omega)$ obtained by Norris and Stein[1e] to take into account the interference arising due to the extension of a particle comparable with the wavelength of light in the medium. The intensities have been further averaged for an assumed Maxwellian type of distribution in the size of the particles. It should, however, be mentioned that the expressions for scattered light so obtained will be valid only for the cases, when the refractive-index ratio m of the inhomogeneities to that of the surrounding amorphous medium is close to unity (Rayleigh-Gans-Born approximation).

For medium-density polyethylene films Stein[1h] has assumed a ring-type structure for spherulites. He uses a correlation function, to take into account the internal ring-type structure of a spherulite to calculate the intensity of scattered light.

DISTRIBUTION FUNCTIONS FOR ORIENTATION OF SPHEROIDS

Let us consider a thin, elastic, cross-linked polymer film above its glass temperature. Each crosslinked domain of the film exhibits some sort of local order, due to which the density in that localized region is different from the amorphous region surrounding it. Each such region may be considered as a spheroid, which is connected to other spheroids by means of freely flexible chains which constitute the amorphous portions of the film. When the film is strained, the chain segments get partially oriented parallel to the direction of elongation. In doing so, they exert a couple on the (spheroids) cross-linked regions which suffer a translation from their positions and also change their orientation.

Let the film lie in the YZ plane of a right-handed Cartesian system, the positive X axis being the direction of incident light ($\mathbf{S}_0$). The probability that the major axis of a spheroid would lie between θ and $\theta+d\theta$ and ϕ and $\phi+d\phi$ before deformation is simply $(1/4\pi)\sin\theta d\theta d\phi$. If θ^1 and ϕ^1 specify the orientation of the spheroid after deformation then the probability that its major axis would lie between θ' and $\theta'+d\theta'$, and

* Communication No. 442 from the National Chemical Laboratory, Poona 8, India.

[1] (a) J. J. Keane, F. H. Norris, and R. S. Stein, J. Polymer Sci. **20**, 209 (1956); (b) J. J. Keane and R. S. Stein, *ibid.* **20**, 327 (1956); (c) R. S. Stein, *ibid.* **24**, 383 (1957); (d) A. Plaza, F. H. Norris, and R. S. Stein, *ibid.* **24**, 455 (1957); (e) **27**, 87 (1958); (f) R. S. Stein, *ibid.* **34**, 709 (1959); (g) A. Plaza and R. S. Stein, *ibid.* **40**, 267 (1959); (h) R. S. Stein and M. B. Rhodes, J. Appl. Phys. **31**, 1873 (1960).

ϕ' and $\phi'+d\phi'$ is given by $(1/4\pi)\sin\theta' d\theta' d\phi'$. Let X_1, Y_1, and Z_1 and X_2, Y_2, and Z_2 be the coordinates of the center of the spheroid. Then, if λ_1, λ_2, and λ_3 are the extension ratios in the three direction,

$$X_2=\lambda_1 X_1, \qquad Y_2=\lambda_2 Y_1, \quad \text{and} \quad Z_2=\lambda_3 Z_1.$$

If the film is incompressible, then

$$\lambda_1\lambda_2\lambda_3=1, \tag{1}$$

and one obtains

$$f(\theta',\phi')d\theta' d\phi' = \frac{(1-\kappa^2)^{\frac{1}{2}}(1-\kappa_1^2)^{\frac{1}{2}}\sin\theta d\theta d\phi}{4\pi[1-\{\kappa^2-(\kappa^2-\kappa_1^2)\sin^2\phi\}\sin^2\theta]^{\frac{3}{2}}}, \tag{2}$$

where $\kappa^2=1-\lambda_1^2/\lambda_3^2$ and $\kappa_1^2=1-\lambda_2^2/\lambda_3^2$. The factor $(1/4\pi)$ is obtained by the normalizing condition

$$\int_{\theta=0}^{\pi}\int_{\phi=0}^{2\pi} f(\theta',\phi')d\theta' d\phi'=1. \tag{3}$$

CALCULATION OF THE DIFFERENTIAL CROSS SECTIONS OF SCATTERING

Let $\mathbf{S}$ be the direction of observation of the scattered light specified by its direction cosines α', β', and γ' with respect to $\mathbf{S}_0$, the direction of incidence. The plane of scattering is defined as the plane containing $\mathbf{S}_0$ and $\mathbf{S}$. The amplitude $E_{||\to||}$ of the radiation scattered by a spheroidal scatterer $(a>b=c)$ per unit amplitude of the incident electric vector, with polarizabilities $\alpha_{||}$ and $\alpha_\perp$, respectively parallel and perpendicular to its major axis "a," and whose orientation is specified by θ and ϕ is given by[2]

$$E_{||\to||}=k^2[(\alpha_{||}-\alpha_\perp)(m_1\mu+n_1\nu)\{-l_1\sin\psi + (m_1\mu+n_1\nu)\cos\psi\}+\alpha_\perp\cos\psi], \tag{4}$$

where

$$l_1=\sin\theta\cos\phi, \qquad m_1=\sin\theta\sin\phi, \qquad n_1=\cos\theta,$$
$$\mu=\cos\omega, \qquad \nu=\sin\omega, \qquad k=2\pi/\lambda', \tag{5}$$

λ' being the wavelength of light in the medium.

The corresponding differential cross section, say $\sigma_{||\to||}$, is obtained by averaging the square of Eq. (4) and multiplying by the particle interference factor $p(\psi,\omega)$. Thus

$$\sigma_{||\to||}=p(\psi,\omega)\int_{\theta=0}^{\pi}\int_{\phi=0}^{2\pi} E^2_{||\to||}f(\theta',\phi')d\theta' d\phi'. \tag{6}$$

Here $\sigma_{||\to||}$ denotes the differential cross section for scattering by the inhomogeneity when the incident light is polarized with its electric vector parallel to the plane of scattering and the component of scattered light whose electric vector is polarized parallel to the plane of scattering is observed. It is unlikely that all the inhomogeneous regions will be of the same size. To take account of this possibility, Eq. (6) should be further averaged. Let $N(a)da$ be the number of particles at constant p, whose major axes lie between a and $a+da$.

[2] H. L. Bhatnagar, J. Chem. Phys. **32**, 674 (1960).

For convenience, one can assume a Maxwellian type of distribution function as introduced by Hosemann[3] and later used by Roess and Shull[4] for calculating the intensity of x-rays scattered at small angles by finely divided powders, i.e.,

$$N(a)da=\frac{2a^n\exp(-a^2/a_0^2)}{a_0^{n+1}\Gamma[(n+1)/2]}da, \tag{7}$$

where a_0 and n are adjustable parameters. It is possible to obtain a wide variety of distribution forms by varying the parameter n. Equation (7) is so normalized that

$$\int_0^\infty N(a)da=1. \tag{8}$$

Thus the average value of the differential crosssection for scattering by a spheroid at constant p is given by

$$\langle\sigma_{||\to||}\rangle=\int_0^\infty \sigma_{||\to||}N(a)da = \{\Gamma[(2n+17)/4]\}(H+1/a_0^2)^{-(2n+17)/4}D_1, \tag{10}$$

and one can obtain similar expressions for $\langle\sigma_{||\to\perp}\rangle$, $\langle\sigma_{\perp\to||}\rangle$, and $\langle\sigma_{\perp\to\perp}\rangle$ by replacing D_1 by D_2, D_3, and D_4, respectively. Here

$$H=(\pi/\lambda')^2\{p^2(1-\cos\psi)^2+(p^2\cos^2\omega+\sin^2\omega)\sin^2\psi\} \tag{11}$$

$$D_1=J'\Big[\frac{4\pi A^2\cos^2\psi}{(1-\kappa^2)^{\frac{1}{2}}(1-\kappa_1^2)^{\frac{1}{2}}} + B^2\{(L_3\cos^2\omega+L_4\sin^2\omega)\sin^2\psi + (L_2\cos^4\omega+L_1\sin^4\omega+\tfrac{3}{2}L_5\sin^2 2\omega)\cos^2\psi\} + 2AB(L_6\cos^2\omega+L_7\sin^2\omega)\cos^2\psi\Big] \tag{12}$$

$$D_2=J'B^2[L_5\cos^2 2\omega+\tfrac{1}{4}(L_1+L_2-2L_5)\sin^2 2\omega] \tag{13}$$

$$D_3=J'B^2[(L_4\cos^2\omega+L_3\sin^2\omega)\sin^2\psi + \{L_5\cos^2 2\omega+\tfrac{1}{4}(L_1+L_2-2L_5)\sin^2 2\omega\}\cos^2\psi] \tag{14}$$

$$D_4=J'\Big[\frac{4\pi A^2}{(1-\kappa^2)^{\frac{1}{2}}(1-\kappa_1^2)^{\frac{1}{2}}} + B^2\{L_1\cos^4\omega+L_2\sin^4\omega+\tfrac{3}{2}L_5\sin^2 2\omega\} + 2AB\{L_7\cos^2\omega+L^6\sin^2\omega\}\Big] \tag{15}$$

$$\begin{aligned} L_1&=I^{\frac{1}{2}}_{00J}-2I^{\frac{1}{2}}_{01J}+I^{\frac{1}{2}}_{02J},\\ L_2&=I^{\frac{1}{2}}_{22J}\\ L_3&=I^{\frac{1}{2}}_{12J}-I^{\frac{1}{2}}_{22J},\\ L_4&=I^{\frac{1}{2}}_{01J}-I^{\frac{1}{2}}_{11J}-I^{\frac{1}{2}}_{02J}+I^{\frac{1}{2}}_{12J}\\ L_5&=I^{\frac{1}{2}}_{11J}-I^{\frac{1}{2}}_{12J},\\ L_6&=I^{\frac{1}{2}}_{11J},\\ L_7&=I^{\frac{1}{2}}_{00J}-I^{\frac{1}{2}}_{01J} \end{aligned} \tag{16}$$

[3] R. Hosemann, Z. Physik **113**, 751 (1939).

[4] L. C. Roess and C. G. Shull, J. Appl. Phys. **18**, 295, 308 (1947).

and

$$J'=(p^2/\pi^3)^{\frac{1}{2}}(\kappa^4/4\pi)(1-\kappa^2)^{\frac{1}{2}}(1-\kappa_1^2)^{\frac{1}{2}}; \quad (16a)$$

A and B have been defined earlier.[2]

Integrals occurring in Eq. (16) are elliptic integrals of the type

$$I^{\frac{1}{2}}_{mnJ}=\int_0^{\pi}\int_0^{2\pi}\frac{\sin^{2m}\phi\ \sin^{2n+1}\theta d\theta d\phi}{[1-\beta^2\sin^2\theta]^{\frac{1}{2}}}\{0<\beta^2<1\}, \quad (17)$$

when $J=1$, $\kappa^2=\beta^2=1-1/\lambda^3$; $J=2$, $\beta^2=\kappa^2\cos^2\phi$, $\kappa^2=1-1/\lambda^6$ and $J=3$, $\beta^2=\kappa^2-(\kappa^2-\kappa_1^2)\sin^2\phi$.

Integrals $I^{\frac{1}{2}}_{mnJ}$ are comparatively simple to evaluate for the case of simple elongation, $J=1$ and have already been reported earlier.[2] For the other two cases, the evaluation is tedious, but straightforward.

For two-dimensional homogeneous strain $J=2$, $\kappa_1^2=0$, $\{0\leq\kappa^2<1\}$

$$I^{\frac{1}{2}}_{002}=4\pi/(1-\kappa^2)^{\frac{1}{2}} \quad (18a)$$

$$I^{\frac{1}{2}}_{012}=\frac{2\pi}{\kappa^2}\{[(1+\kappa^2)/(1-\kappa^2)^{\frac{1}{2}}]-(\sin^{-1}\kappa/\kappa)\} \quad (18b)$$

$$I^{\frac{1}{2}}_{022}=\frac{\pi}{4\kappa^4}\left[\frac{9-8\kappa^2+5\kappa^4-6\kappa^6}{(1-\kappa^2)^{\frac{1}{2}}}-4\kappa\sin^{-1}\kappa-(9/\kappa)\sin^{-1}\kappa\right] \quad (18c)$$

$$I^{\frac{1}{2}}_{112}=\frac{2\pi}{\kappa^2}[(\sin^{-1}\kappa/\kappa)-(1-\kappa^2)^{\frac{1}{2}}] \quad (18d)$$

$$I^{\frac{1}{2}}_{122}=\frac{\pi}{4\kappa^4}\left[\frac{-3+9\kappa^4-6\kappa^6}{(1-\kappa^2)^{\frac{1}{2}}}+4\kappa\sin^{-1}\kappa+(3/\kappa)\sin^{-1}\kappa\right] \quad (18e)$$

$$I^{\frac{1}{2}}_{222}=\frac{\pi}{4\kappa^4}\left[\frac{9-24\kappa^2+21\kappa^4-6\kappa^6}{(1-\kappa^2)^{\frac{1}{2}}}-(9/\kappa)\sin^{-1}\kappa+12\kappa\sin^{-1}\kappa\right]. \quad (18f)$$

For two-dimensional nonhomogeneous strain

$$J=3, \quad 0<\kappa^2<1, \quad 0<\kappa_1^2<1, \quad \kappa^2\neq\kappa_1^2$$

$$I^{\frac{1}{2}}_{003}=4\pi/(1-\kappa^2)^{\frac{1}{2}}(1-\kappa_1^2)^{\frac{1}{2}} \quad (19a)$$

$$I^{\frac{1}{2}}_{013}=\frac{2\pi}{\kappa^2}\left[\frac{\kappa}{\kappa_1}+\frac{1}{(1-\kappa_1^2)^{\frac{1}{2}}}\left\{\frac{1+\kappa^2}{(1-\kappa^2)^{\frac{1}{2}}}-\frac{\sin^{-1}\kappa}{\kappa}\right\}\right] \quad (19b)$$

$$I^{\frac{1}{2}}_{023}=\frac{\pi}{4\kappa^4}\left[\frac{4\kappa(1+\kappa^2)}{\kappa_1}+\frac{6\kappa^3}{\kappa_1^3}+\frac{3\sin^{-1}\kappa}{\kappa(1-\kappa_1^2)^{\frac{1}{2}}}-\frac{4\kappa\sin^{-1}\kappa}{(1-\kappa_1^2)^{\frac{1}{2}}}-\frac{12\sin^{-1}\kappa}{\kappa(1-\kappa_1^2)^{\frac{1}{2}}}+\frac{-2\kappa^6+\kappa^4+4\kappa^2-3+(1-\kappa_1)^{\frac{1}{2}}(-4\kappa^6+4\kappa^4-12\kappa^2+12)}{(1-\kappa_1^2)^{\frac{1}{2}}(1-\kappa^2)^{\frac{1}{2}}}\right] \quad (19c)$$

$$I^{\frac{1}{2}}_{113}=\frac{2\pi}{(\kappa^2-\kappa_1^2)}\times\left[\frac{\kappa}{\kappa_1}-\frac{(1-\kappa^2)^{\frac{1}{2}}}{(1-\kappa_1^2)^{\frac{1}{2}}}+\frac{(1-2\kappa_1^2)}{(1-\kappa_1^2)^{\frac{1}{2}}}\frac{\sin^{-1}\kappa}{\kappa}+\frac{2\kappa_1}{\kappa}\ln|J|\right] \quad (19d)$$

$$I^{\frac{1}{2}}_{123}=I^{\frac{1}{2}}_{023}-\kappa^{-1}(d/d\kappa)I^{\frac{1}{2}}_{013} \quad (19e)$$

$$I^{\frac{1}{2}}_{223}=I^{\frac{1}{2}}_{123}-\kappa^{-1}(d/d\kappa)I^{\frac{1}{2}}_{113} \quad (19f)$$

$$I^{\frac{1}{2}}_{013}=\frac{\pi}{\kappa^2}\left[\frac{-J}{\kappa_1(1-\kappa_1^2)^{\frac{1}{2}}}+\frac{(2\kappa^2-2\kappa^2\kappa_1^2-1)}{(1-\kappa_1^2)^{\frac{1}{2}}}\frac{\sin^{-1}\kappa}{\kappa}-\kappa\kappa_1\{\ln|\kappa^2-\kappa_1^2|+\ln|J_1|\}\right] \quad (19g)$$

$$I^{\frac{1}{2}}_{113}=\frac{2\pi}{(\kappa_1^2-\kappa^2)}\left[\frac{\kappa-\kappa_1}{2\kappa_1}-\frac{\kappa_1^3}{2\kappa}+\frac{(1+\kappa_1^2-\kappa^2)(1-\kappa_1^2)}{\kappa}\sin^{-1}\kappa-\frac{\sin^{-1}\kappa}{2\kappa(1-\kappa_1^2)^{\frac{1}{2}}}+\frac{(1-\kappa^2)^{\frac{1}{2}}(2-\kappa_1^2)}{2(1-\kappa_1^2)^{\frac{1}{2}}}-(\kappa_1/2\kappa)(1+\kappa_1^2-\kappa^2)\{\ln|\kappa_1^2-\kappa^2|+\ln|J_1|\}-\frac{\kappa_1^2-\kappa^2}{4\kappa\kappa_1}\left\{\ln|J_1|+\ln\left|\frac{\kappa_1+\kappa}{\kappa_1-\kappa}\right|\right\}\right] \quad (19h)$$

$$J=\kappa(1-\kappa_1^2)^{\frac{1}{2}}+\kappa_1(1-\kappa^2)^{\frac{1}{2}} \quad (19i)$$

and

$$J_1=\frac{J}{\kappa(1-\kappa_1^2)^{\frac{1}{2}}-\kappa_1(1-\kappa^2)^{\frac{1}{2}}}. \quad (19j)$$

An inspection of Eqs. (19a) to (19j) shows that the conditions under which integrations have been carried out do not permit the reduction of Eqs. (19a–j) to Eqs. (18a–f) and hence the necessity of separate treatment. One can also see that once the ratio of elongation in Y and Z direction is fixed, κ_1^2 can be treated as a constant number.

DISCUSSION

Equation (10) and similar others may be useful in the evaluation of the sizes of the inhomogeneities embedded in amorphous matrix of thin polymer films, provided proper precautions are taken to process the experimental data. Thus it is necessary that proper care should be taken of the fact that the irradiated volume of the film is different at various degrees of strain. Second, the scattering due to amorphous region in the irradiated volume should be substracted.

After these corrections,[5] dissymmetry of scattered radiation at two angles at constant ω may be used to give the relevant information about the average size of crystallites in thin films. Another important point to be remembered is the basic assumption made about the

[5] Theoretical expressions for scattering due to chain molecules under one-dimensional strain have been obtained and will be published elsewhere.

condition of incompressibility of the film and its complete elasticity. Any departure from this assumed ideal behavior will complicate the interpretation of the results further. We have restricted the present treatment to independent particles only. One may utilize the Zernick-Prins formula modified by Fournet[6] for the case of interacting anisotropic particles. However, it does not give any computational advantage and in addition more assumptions regarding the orientation of particles are to be made. For a particle with periodic internal structure, Oster and Riley[7] have made use of correlation function. Stein[1(h)] has successfully extended the use of the correlation function for calculating the intensity of scattered radiation from ring-type structures.

[6] G. Fournet, Compt. rend **228**, 1421, 1801 (1949); Acta Cryst. **4**, 293 (1951).

[7] G. Oster and D. P. Riley, Acta Cryst. **5**, 1, 272 (1952).

THE JOURNAL OF CHEMICAL PHYSICS VOLUME 35, NUMBER 3 SEPTEMBER, 1961

EPR Studies of Spin Correlation in Some Ion Radical Salts

D. B. CHESNUT AND W. D. PHILLIPS

Central Research Department, Experimental Station, E. I. du Pont de Nemours and Company, Wilmington, Delaware

(Received February 13, 1961)

Electron spin resonance studies have been carried out on a number of ion-radical salts based on the strong π-acceptor tetracyanoquinodimethane (TCNQ). These studies have established that spin correlation exists between the magnetic electrons in these salts, giving rise to a ground singlet state and a thermally accessible triplet state. Typical singlet-triplet separations (J) derived from observed temperature dependences of EPR signal intensities are 0.034 ev for the $[(C_2H_5)_2NH]^+(TCNQ)_2^-$ salt, 0.062 ev for the $(\varphi_3PCH_3)^+(TCNQ)_2^-$ and $(\varphi_3AsCH_3)^+(TCNQ)_2^-$ salts, and 0.41 ev for the (morpholinium)$^+$(TCNQ)$^-$ salt.

The triplet states of the $(\varphi_3PCH_3)^+(TCNQ)_2^-$ and $(\varphi_3AsCH)^+(TCNQ)_2^-$ salts are further manifested by an anisotropic splitting of the resonance into a doublet (zero-field splitting) and the appearance of half-field $\Delta m=\pm 2$ transitions. Detailed analysis reveals that both salts may be represented by the spin Hamiltonian

$$\mathcal{H}=\beta H\cdot g\cdot S+DS_z^2+E(S_x^2-S_y^2),$$

with $|D/hc|=0.0062$ cm^{-1}, $|E/hc|=0.00098$ cm^{-1}, and g_z, g_y, and g_x equal to 2.004_0, 2.003_1, and 2.002_7, respectively. Temperature-dependent exchange interactions observed for the $(\varphi_3PCH_3)^+(TCNQ)_2^-$ and $(\varphi_3AsCH_3)^+(TCNQ)_2^-$ salts cause the doublet zero-field components to broaden, move together, and collapse into a single, progressively sharper line as the temperature is increased. The exchange frequency follows an exponential temperature dependence and is governed by the concentration of triplet entities in the solid ($J=0.062$ ev).

The importance of paramagnetic impurities in studies of the magnetic properties of organic solids is emphasized. Examples are given which illustrate how a percent or so of doublet-state impurity species can dominate resonances near $g=2.002$ in molecular solids obeying singlet-triplet statistics.

INTRODUCTION

THERE have been a number of investigations over the past few years regarding the electrical and magnetic properties of organic solids.[1] Part of this interest has derived from observations of electron spin resonance in organic solids. In addition, the theoretical analysis of charge-transfer complexes by Mulliken in 1952[2] must be accorded substantial credit for the recent activity in this field.

Mulliken showed that intermolecular charge-transfer interactions arise largely through contributions from resonance structures involving electron transfer from a donor molecule to an acceptor molecule. For a very strong donor and a very strong acceptor, complete electron transfer could occur, and the system would be expected to exhibit paramagnetic characteristics in the ground electronic state. As opposed to solutions where charge-transfer complexes generally appear to consist of single donor and acceptor molecules, charge-transfer interactions in the solid could be more extensive than pairwise and thus provide an electron conduction mechanism. Some solids precipitated from solutions containing good electron acceptors and donors have exhibited EPR absorption indicative of unpaired electrons and have had low electrical resistivities.[3] However, there has been a general absence of structure in the EPR spectra of these solids, and obtaining single crystals has proven to be an exceedingly difficult task. Consequently, it has not been clear whether the observed paramagnetism was an intrinsic property of the solid or arose from impurities, whether or not there was a connection between the solid's paramagnetism and its

[1] For a review of this field, see C. G. B. Garrett, *Semiconductors*, edited by N. B. Hannay (Reinhold Publishing Corporation, New York, 1959), Chap. 15.

[2] R. S. Mulliken, J. Am. Chem. Soc. **74**, 811 (1952).

[3] H. Akamatsu, H. Inokuchi, and Y. Matsunaga, Nature **173**, 168 (1954); H. Kainer, D. Bijl, and A. C. Rose-Innes, Naturwissenschaften **41**, 303 (1954); H. M. Buck, J. H. Lupinski, and L. J. Oosterhoff, Mol. Phys. **1**, 196 (1958); Y. Matsunaga, J. Chem. Phys. **30**, 855 (1959).

electrical conductivity, and whether the paramagnetism arose from doublet state species or from entities exhibiting exchange interactions among unpaired electrons and residing in electronic states of higher multiplicities. A further question which has been particularly difficult to answer is whether these paramagnetic and conducting solids formed from strong acceptors and donors are charge-transfer complexes in the Mulliken sense.[2] Perhaps, at least in some instances, these organic solids are better characterized as salts and might indeed be termed charge-transfer salts.

Tetracyanoethylene has a high electron affinity and with aromatic hydrocarbons forms strong π complexes which exhibit intense charge-transfer bands in the visible.[4] Recently the new polycyanocarbon tetracyanoquinodimethane (TCNQ) has been prepared[5]

that also exhibits the characteristics of a strong π acceptor. Preliminary communications have been published on the unusual magnetic[6] and electrical[7] properties of some ion-radical salts based on TCNQ. These salts are characterized by diamagnetic cations, paramagnetic $(TCNQ)^-$ or $(TCNQ)_2^-$ anions, and by EPR characteristics which are attributable to the presence of entities residing in triplet rather than doublet electronic states. Preliminary x-ray examinations[8] have indicated that the TCNQ molecules in these salts probably are stacked in a manner favorable to overlap of the π orbitals, an arrangement which would appear to be conductive to spin correlation effects. In this paper we present results of studies on the ion-radical salts $[(C_2H_5)_3NH]^+(TCNQ)_2^-$, $(\varphi_3PCH_3)^+(TCNQ)_2^-$, $(\varphi_3AsCH_3)^+(TCNQ)_2^-$, and (morpholinium)$^+$ $(TCNQ)^-$. A detailed description is presented of the EPR studies which have established the existence of spin correlation between the magnetic electrons in these salts that gives rise to a singlet ground state and a thermally accessible triplet state. Singlet-triplet separations are calculated from observed temperature dependences of the EPR signal intensities, and crystal-field parameters are derived from the angular dependences of zero-field splitting resulting from dipolar perturbations in the triplet state.

[4] R. E. Merrifield and W. D. Phillips, J. Am. Chem. Soc. **80,** 79 (1958).

[5] D. S. Acker, R. J. Harder, W. R. Hertler, W. Mahler, L. R. Melby, R. E. Benson, and W. E. Mochel, J. Am. Chem. Soc. **82,** 6408 (1960).

[6] D. B. Chesnut, H. Foster, and W. D. Phillips, J. Chem. Phys. **34,** 684 (1961).

[7] R. G. Kepler, P. E. Bierstedt, and R. E. Merrifield, Phys. Rev. Letters **5,** 503 (1960).

[8] P. Arthur, Jr., this Laboratory (private communication).

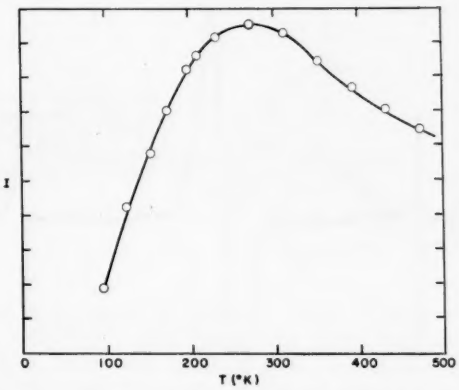

FIG. 1. Temperature dependence of the integrated EPR absorption I (in arbitrary units), of the $[(C_2H_5)_3NH]^+(TCNQ)_2^-$ salt.

EXPERIMENTAL

EPR measurements were carried out with a Varian X-band spectrometer (both 400-cps and 100-kc field modulation were used) and associated 12-in. electromagnet. Varian temperature equipment was used in which the sample is supported in a Dewar system extending through the microwave cavity. Temperature control was achieved by passing heated or cooled nitrogen about the sample. Single crystals were aligned on a goniometer visually or with x-ray techniques and transferred to a holder made of "Teflon" tetrafluoroethylene resin by a double-goniometer technique; the holder was then mounted on a cavity Dewar in such a manner as to allow free rotation of the crystal in the cavity about an axis perpendicular to the direction of the magnetic field.

Magnetic field measurements were made by determining the proton magnetic resonance frequency with a Nuclear Magnetics Corporation precision gaussmeter; the klystron frequency was measured by standard wavemeter techniques. The derivative of the absorption was observed and the intensity of a resonance line was taken as the product of the square of the separation of the points of maximum slope of the absorption and the maximum amplitude of the derivative curve. Preparation and chemical characterization of the solids used in this study have been described previously.[5]

RESULTS AND DISCUSSION

1. Temperature Dependences of Resonance Intensities

The presence of unpaired electrons has been manifested in many charge-transfer complexes in the solid by the appearance of electron paramagnetic resonance (EPR) absorption.[3,9] In most cases, only a single, rela-

[9] D. Bijl, H. Kainer, and A. C. Rose-Innes, J. Chem. Phys. **30,** 765 (1959).

FIG. 2. Room-temperature spectrum of an arbitrarily oriented crystal of the 1:1 (morpholinium)$^+$(TCNQ)$^-$ salt. The separation of the outermost lines is approximately 88 gauss.

tively narrow resonance located near $g=2.002$ was observed. The existence of structure to the resonance that was observed occasionally usually could be attributed to the presence of an anisotropic g value. In some instances, resonance intensity comparisons were made with some standard free radical such as α,α'-diphenyl-β-picryl hydrazyl (DPPH) and generally it was found that the EPR intensity exhibited by the complex was substantially less (often one or two orders of magnitude less) than that of an equivalent amount of the standard. The validity of such a comparison at one temperature, of course, depends on standard and complex exhibiting the same ground electronic state multiplicity.

Bijl, Kainer, and Rose-Innes[9] first considered the temperature dependences of the EPR signal intensities I of solid charge-transfer complexes. If the ground state is a doublet,

$$I \propto 1/T. \tag{1}$$

If there is pairwise spin correlation with a ground singlet state and an associated excited triplet state separated by the exchange interaction J,

$$I \propto 1/T[\exp(+J/kT)+3]. \tag{2}$$

On the other hand, if two-electron coupling predominates but with a negative exchange interaction so that the triplet state is lowest,

$$I \propto 1/T[\exp(-J/kT)+3]. \tag{3}$$

It should be pointed out that Eqs. (2) and (3) are not necessarily restricted to pairwise correlation but also would be valid approximations for situations involving multispin correlation in which only the lowest singlet and triplet states are significantly populated.

Bijl, Kainer, and Rose-Innes[9] examined in the solid the temperature dependences of the EPR absorption intensities of a series of charge-transfer complexes based on quinones and p-phenylenediamines. In all cases, strict conformity to a Curie law dependence [Eq. (1)] was exhibited. Subsequent to this study, Singer and Kommandeur[10] reported that the perylene-iodine complex displayed an exponential EPR intensity temperature dependence which would be given by Eq. (2) for a value of J large with respect to kT. Recently, Huggins and LeBlanc[11] have reported that the β-carotene/I_3^- complex exhibits a weak EPR signal intensity following a $1/T$ dependence.

The ion-radical salt $[(C_2H_5)_3NH]^+(TCNQ)_2^-$ exhibits a single EPR peak in both crystalline and single-crystal forms with a g factor near the free electron value. The temperature dependence of the integrated EPR signal intensity for the salt is shown in Fig. 1. It can be fitted to Eq. (2) (ground singlet and upper triplet states) to give a value of J, the singlet-triplet separation, of 0.034 ev. A value of $J=0.041$ ev is obtained for this salt from direct susceptibility measurements.[7] The discrepancy between the EPR and susceptibility determinations of J is considered to be within the combined limits of accuracy of the two methods of measurement. It is estimated that values of J derived from our EPR intensity measurements are accurate to about $\pm 10\%$.

Expected zero-field splittings for the $[(C_2H_5)_3NH^+](TCNQ)_2^-$ entities in the triplet state (see Sec. 2) are not observed over the accessible temperature range. As will be shown later, zero-field splittings for this salt are washed out down to liquid-nitrogen temperatures by exchange narrowing effects arising from the high concentration of triplet-state entities (see Sec. 4). The salts, $(\varphi_3PCH_3)^+(TCNQ)_2^-$ and $(\varphi_3AsCH_3)^+(TCNQ)_2^-$, probably closely related structurally to $[(C_2H_5)_3NH]^+(TCNQ)_2^-$, exhibit zero-field splittings expected for triplet states below about -100°C. Below -100°C the temperature dependences of the integrated intensities of the zero-field components of the phosphonium and arsonium salts may be fitted to Eq. (2) with $J=0.062$ ev.[12]

The room-temperature EPR spectrum of an arbitrarily oriented single crystal of the 1:1 (morpholinium)$^+$(TCNQ)$^-$ salt is shown in Fig. 2. The spectrum of this salt is composed of an outer doublet whose spacing is orientation dependent and a broad center line whose location is essentially isotropic; the spectrum is centered about $g=2$. The origin of the outer doublet for

[10] L. S. Singer and J. Kommandeur, Bull. Am. Phys. Soc. **4**, 421 (1959).

[11] C. M. Huggins and O. H. LeBlanc, Jr., Nature **186**, 552 (1960).

[12] Over the range 103°–173°K in which dipolar splittings are observed, measured values of D, E, and J for the

$(\varphi_3PCH_3)^+(TCNQ)_2^-$ and $(\varphi_3AsCH_3)^+(TCNQ)_2^-$

salts are identical. However, a discontinuity is observed in the magnetic susceptibility (by R. G. Kepler of this Laboratory) and in the integrated resonance intensity at about 315°K for the phosphonium salt. A possible explanation of this anomaly is the reduction of J as a result of a discontinuous lattice expansion.

this salt unquestionably is the same as that for the $(\varphi_3PCH_3)^+(TCNQ)_2^-$ and $(\varphi_3AsCH_3)^+(TCNQ)_2^-$ salts, namely, a zero-field splitting of a thermally accessible triplet state. Although only a preliminary examination has been made of the (morpholinium)$^+$(TCNQ)$^-$ salt, it is introduced at this point to emphasize the rather general and demonstrable occurrence of triplet rather than doublet electronic states for the class of solid ion-radical salts based on TCNQ. As for the previously discussed TCNQ salts, the temperature dependence of the integrated intensity of the outer doublet follows a singlet-triplet model [Eq. (2)] with $J=0.41$ ev. Surprisingly, the central peak of the (morpholinium)$^+$(TCNQ)$^-$ salt also obeys Eq. (2) with $J=0.28$ ev rather than Eq. (1) expected for a doublet-state impurity.

It is not at present known what species is responsible for the center line of the (morpholinium)$^+$(TCNQ)$^-$ salt. Employing the above two values of J, a ratio of about 15 is obtained for the concentration of the species responsible for the outer doublet to that of the species giving rise to the center peak. Until the (morpholinium)$^+$(TCNQ)$^-$ salt can be studied in more detail, it is only to be considered another example of the general pairwise electron correlation existing in TCNQ ion-radical salts. Nevertheless, it is felt that this salt strikingly illustrates the pitfalls to be encountered in the study of the magnetic properties of paramagnetic organic solids in the absence of adequate chemical purification and without single crystals.

2. Zero-Field Splittings

The existence of a triplet state is best shown by the presence of an anisotropic splitting of the resonance line into a doublet (zero-field splitting) as well as observation of the usually forbidden $\Delta m=\pm 2$ transition which in the strong field approximation will occur at exactly half the magnetic field (at constant frequency) required to observe the usual $\Delta m=\pm 1$ transitions. As mentioned in Sec. 1, zero-field splittings for the $[(C_2H_5)_3NH]^+(TCNQ)_2^-$ salt are not observed over the accessible temperature range due to exchange effects. However, zero-field splittings have been exhibited by the [methyltriphenylphosphonium (and arsonium)]$^+(TCNQ)_2^-$ and (morpholinium)$^+$(TCNQ)$^-$ salts. While only preliminary observations have been made on the (morpholinium)$^+$(TCNQ)$^-$ salt, complete studies of the $(\varphi_3PCH_3)^+(TCNQ)_2^-$ and $(\varphi_3AsCH_3)^+(TCNQ)_2^-$ salts have been made and are presented below.

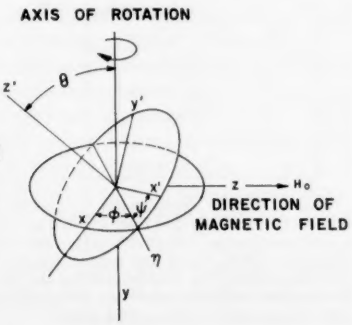

FIG. 3. System of coordinates.

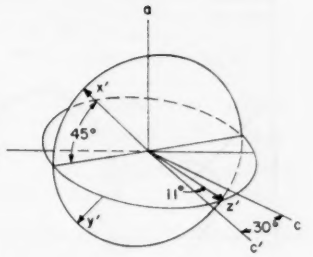

FIG. 4. Principal axes of the g and Λ tensors and the crystal axes for the $(\varphi_3PCH_3)^+$ and $(\varphi_3AsCH_3)^+(TCNQ)_2^-$ salts.

The spacings between the two resonances of both the phosphonium (see Fig. 7) and arsonium salts are field independent (measured in fields of 3500 and 8500 gauss) so that in both salts the two resonances cannot arise from g-factor differences between doublet-state species. Since the arsonium and phosphonium salts show the same splitting[12] (for a given orientation) interactions involving the P^{31} and As^{75} nuclei also are ruled out. The observed doublets apparently represent true zero-field splittings arising from the dipolar interaction of two electrons in a triplet state. Observations of the zero-field splittings and the $\Delta m=\pm 2$ transitions are limited to low temperatures because of the presence of exchange effects which cause the doublet to collapse and the $\Delta m=\pm 2$ transition to disappear at higher temperatures. In the following sections, unless otherwise noted, we limit ourselves to the EPR characteristics measured at $-150°C$; the temperature dependent exchange effects are discussed in Sec. 4.

The spin Hamiltonian for two electrons in a triplet state far removed[13] from the associated singlet ground state may be written[14]

$$\mathcal{H}=\beta H\cdot g\cdot S+S\cdot\Lambda\cdot S. \tag{4}$$

For rhombic symmetry, the tensors g and Λ are defined by writing out Eq. (4),

$$\mathcal{H}=\beta(H_xg_xS_x+H_yg_yS_y+H_zg_zS_z)+DS_z^2+E(S_x^2-S_y^2). \tag{5}$$

This equation is valid in the crystal coordinate system in which the tensors g and Λ are diagonal. For an arbitrary orientation the laboratory coordinate system will not coincide with the principal axes of these tensors. Since our situation here is one in which the

[13] In these systems the triplet state is some 0.062 ev above the singlet ground state. Thus, all interactions which mix singlet and triplet states are neglected in first order.

[14] See W. Moffitt and M. Gouterman, J. Chem. Phys. **30**, 1107 (1959) for a derivation of the spin Hamiltonian resulting from the dipolar interaction of two electrons in a triplet state.

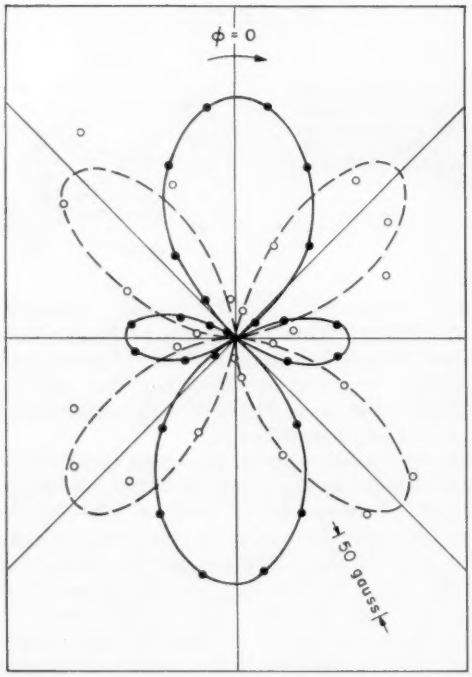

FIG. 5. Angular dependences of the zero-field doublet spacing and $\Delta m=\pm 2$ absorption intensity (in arbitrary units) about the a axis for the $(\varphi_2PCH_3)^+(TCNQ)_2^-$ and $(\varphi_2AsCH_3)^+(TCNQ)_2^-$ salts at -150°C. Solid and open circles are experimental values for, respectively, the doublet spacing and the $\Delta m=\pm 2$ intensity. The dashed intensity curve was calculated for values of $D/g\beta=+66.0$ gauss and $E/g\beta=-10.5$ gauss.

dipolar interaction is small relative to the Zeeman splitting ($\sim$100 gauss versus 3500 gauss), it is convenient to quantize along the magnetic field (chosen as the z axis of the laboratory system) and solve the quantum-mechanical problem of Eq. (5) after having performed a unitary transformation of the associated g and Λ matrices.

Consider the situation as shown in Fig. 3 where the coordinate system $x'y'z'$ associated with the principal axes of the Λ tensor is defined in terms of the laboratory coordinate system xyz through the Eulerian angles θ, ϕ, and ψ.[15] We desire to know the variation of the zero-field splitting and the g factor with the angles θ, ϕ, and ψ.

The basis functions are:

$$|+1\rangle=\alpha\alpha$$
$$|0\rangle=(1/\sqrt{2})(\alpha\beta+\beta\alpha)$$
$$|-1\rangle=\beta\beta. \qquad (6)$$

[15] The Eulerian angles ϕ, θ, and ψ as shown in Fig. 3 are defined in terms of successive counterclockwise rotations about the axes $-y$, η, and z', respectively. See H. Goldstein, *Classical Mechanics* (Addison-Wesley Publishing Company, Inc., Reading, Massachusetts, 1957), pp. 107–109.

If the dipolar term is treated by first-order perturbation theory, it is found that only terms in S_z^2, S_x^2, and S_y^2 contribute to the first-order energy. Thus, if the transformed spin Hamiltonian has the form

$$\mathcal{H}=g\beta HS_z+\Lambda_{xx}'S_x^2+\Lambda_{yy}'S_y^2+\Lambda_{zz}'S_z^2+\cdots, \qquad (7)$$

one finds to first order

$$E_1=\langle+1|\mathcal{H}|+1\rangle=g\beta H+\Lambda_{zz}'+\tfrac{1}{2}(\Lambda_{xx}'+\Lambda_{yy}')$$
$$E_0=\langle 0|\mathcal{H}|0\rangle=\Lambda_{xx}'+\Lambda_{yy}'$$
$$E_{-1}=\langle-1|\mathcal{H}|-1\rangle=-g\beta H+\Lambda_{zz}'+\tfrac{1}{2}(\Lambda_{xx}'+\Lambda_{yy}'). \qquad (8)$$

The doublet separation d between the transitions

$$|+1\rangle\rightleftarrows|0\rangle, \qquad |0\rangle\rightleftarrows|-1\rangle,$$

is then

$$d=(E_1-E_0)-(E_0-E_{-1})$$
$$=2\Lambda_{zz}'-\Lambda_{xx}'-\Lambda_{yy}'. \qquad (9)$$

In terms of D, E, and the angular variables, d may be written as

$$d=C_1\cos^2\phi+C_2+C_3\cos\phi\sin\phi, \qquad (10)$$

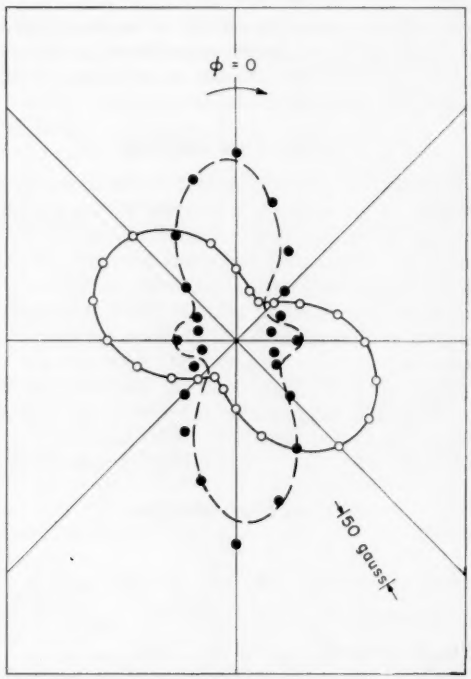

FIG. 6. Angular dependences of the zero-field doublet spacing and $\Delta m=\pm 2$ absorption intensity (in arbitrary units) about the c' axis for the $(\varphi_2PCH_3)^+(TCNQ)_2^-$ and $(\varphi_2AsCH_3)^+(TCNQ)_2^-$ salts at -150°C. Open and solid circles are experimental values for, respectively, the doublet spacing and the $\Delta m=\pm 2$ intensity. The dashed intensity curve was calculated for values of $D/g\beta=+66.0$ gauss and $E/g\beta=-10.5$ gauss.

where

$$C_1 = 3D\sin^2\theta - 3E\cos 2\psi(1+\cos^2\theta)$$
$$C_2 = -D + 3E\cos 2\psi$$
$$C_3 = 6E\sin 2\psi\cos\theta. \qquad (11)$$

The angle ϕ corresponds to the angle of rotation of the crystal about an axis perpendicular to the magnetic field; for a given rotation axis, all other parameters are constant. A similar functional relation is found for the g factor (of the $\Delta m = \pm 1$ transitions). Assuming a small g-factor anisotropy,

$$g = K_1\cos^2\phi + K_2 + K_3\cos\phi\sin\phi, \qquad (12)$$

where

$$K_1 = (g_y - g_x)(\cos^2\theta\cos^2\psi - \sin^2\psi) + (g_z - g_x)\sin^2\theta$$
$$K_2 = g_x + (g_y - g_x)\sin^2\psi$$
$$K_3 = (g_x - g_y)\sin 2\psi\cos\theta. \qquad (13)$$

Here g is defined in terms of the mean resonant field of the doublet.

Preliminary work[8] on the crystal structure of the $(\varphi_3XCH_3)^+(TCNQ)_2^-$ complexes (where X is P or As) has shown the unit cell to be triclinic; however, since the a axis makes angles of very nearly 90° to the two other unit cell axes, one can, for our purposes, describe the crystal axes as pseudo-monoclinic. The axes are shown in Fig. 4. Measurements were made about the three unit cell directions (a, b, c) and about c', an axis normal to the a and b axes.

Figure 4 also shows the orientation of the principal axes of the g and A tensors which best fit the observed data. Figures 5 and 6 show the doublet splitting observed about several axes. The values of the crystal-field parameters found for the phosphonium and arsonium salts are

$$|D/g\beta| = 66.0 \text{ gauss}; \qquad (|D/hc| = 6.17\times10^{-3}\text{ cm}^{-1})$$
$$|E/g\beta| = 10.5 \text{ gauss}; \qquad (|E/hc| = 9.82\times10^{-4}\text{ cm}^{-1})$$
$$|g_x| = 2.004_0 \pm 0.0005$$
$$|g_y| = 2.003_1 \pm 0.0005$$
$$|g_z| = 2.002_7 \pm 0.0005.$$

The values of D and E are estimated to be good to about 5%. Although the absolute signs of D and E are indeterminate from the present observations, the relative signs can be obtained from a knowledge of the orientation of the crystal axes and the sense of rotation of the crystal with respect to the laboratory coordinate system. The principal axes as shown in Fig. 4 lead to a solution in which D and E have opposite signs; interchanging the x' and y' directions would result in D and E having the same sign. However, we have found that "experimental" relative signs (not absolute values) of D and E for these two salts are very sensitive to small variations in crystal alignment relative to the external field. Therefore, we feel that for the present not too much significance should be attached to the above relative sign determination, although it does represent the best fit to the experimental data we have yet been able to achieve. Clearly, a physical interpretation of the relative signs of D and E must await an accurate knowledge of the crystal structure.

TABLE I. Crystal-field parameters for some triplet states.

	$\lvert D/hc\rvert$ (cm^{-1})	$\lvert E/hc\rvert$ (cm^{-1})
$(\varphi_3XCH_3)^+(TCNQ)_2^-$ [a]	0.0062	0.00098
Naphthalene[b]	0.1006	0.0138
Ethylene[c]	0.20 (calc)	0.23 (calc)

[a] X=P or As.
[b] Values measured by C. A. Hutchison, Jr., and B. W. Mangum, J. Chem. Phys. **29**, 952 (1958).
[c] Values estimated by W. Moffitt and M. Gouterman, J. Chem. Phys. **30**, 1107 (1959).

The values of D, E, and g have been derived independent of any assumptions regarding the crystal structure of the phosphonium and arsonium salts. Since it is in principle possible to theoretically calculate these parameters from a knowledge of the solid's structure, it is worthwhile to compare what is known from the the preliminary structure analysis with the results obtained in the present investigation. The tentative trial structure[8] is one in which the molecular planes of the TCNQ molecules lie approximately equally spaced in ab planes (the normal to the molecular planes thus being approximately in the c' direction), the molecules forming a face-to-face stack in the general c or c' direction. Packing considerations indicate the "quinoid" axis of the TCNQ molecules to be rotated somewhat from a parallel alignment with the a axis. The methyltriphenylphosphonium (or arsonium) cations form insulating layers parallel to bc planes, separating adjacent two-dimensional layers of the stacked TCNQ's. The threefold axis of the methyltriphenylphosphonium (or arsonium) cation is approximately parallel to the a axis. Formally, there are two "molecules" per unit cell, i.e., two methyltriphenylphosphonium ions, two $TCNQ^-$ ions and two TCNQ molecules.

It seems reasonable to expect that for triplet states involving π systems of rhombic symmetry, the greater the two-dimensional extent of the molecular plane the larger $|D|$ will be with respect to $|E|$.[16] From Table I, the ratio between D and E varies from 0.9 in ethylene to 7.3 in naphthalene; in the salts under discussion the ratio is $|D/E| = 6.3$. That the dipolar parameters of the TCNQ salts are small relative to those of naphthalene and that $|D| > |E|$ appears consistent with a model in which the triplet electrons exist in an extended π system which allows the effective distance of separation of the electrons to be larger than for naphtha-

[16] The parameter D in this discussion is always associated with the principal axis normal to the molecular plane.

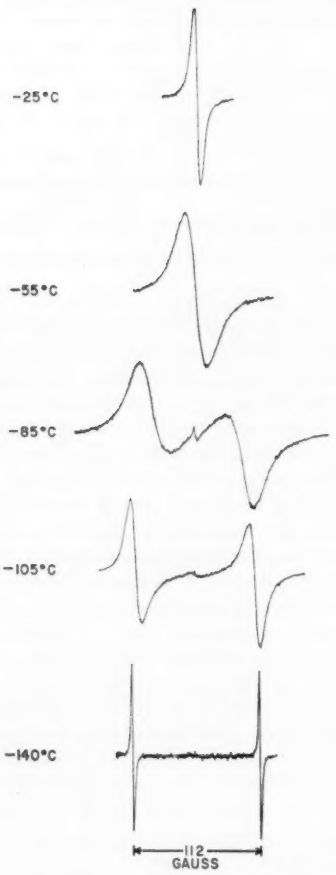

FIG. 7. Temperature dependence of the EPR absorption of a crystal of the $(\varphi_3PCH_3)^+(TCNQ)_2^-$ or $(\varphi_3AsCH_3)^+(TCNQ)_2^-$ salts for an arbitrary orientation. The spectra were obtained with different spectrometer gain settings at the different temperatures.

lene. This conclusion and the fact that the direction of the z' axis of the Λ and g tensors lies close to the c and c' axes of the unit cell tend to substantiate the trial crystal structure and indicate that the triplet-state entity is confined to the vicinity of the TCNQ molecules with the methyltriphenylphosphonium (or arsonium) cations functioning mainly as a crystal-field source. The relatively small values of D and E (again in comparison to the naphthalene case) would seem to argue against the possibility of the triplet electrons residing on a single TCNQ molecule. It seems likely that the triplet entity is composed of at least two of the TCNQ units; the electron pair giving rise to the triplet state may be distributed over all four TCNQ molecules in the unit cell. The resolution of this very important question is essential for a complete understanding of the unusual magnetic and electrical properties of these and other TCNQ ion-radical salts.

3. $\Delta m = \pm 2$ Transition

Just as the dipolar perturbation causes a splitting of the resonance absorption into a doublet, so will the dipolar interaction cause a mixing of the originally pure basis functions (eigenfunctions of S^2 and S_z in zeroth order). In the absence of this mixing, only the usual $\Delta m = \pm 1$ transitions are allowed; with the mixing, however, the forbiddenness of the $\Delta m = \pm 2$ transition is partially removed. Such a transition has been observed by van der Waals and de Groot[17] in the phosphorescent state of naphthalene. Because the mixing of states is quite anisotropic, the intensity of the $\Delta m = \pm 2$ transition must also show a marked dependence on crystal orientation.

Again by use of first-order perturbation theory, the transition probability of the $\Delta m = \pm 2$ transition was calculated for an arbitrary orientation in terms of the dipolar parameters. The transition occurs (at constant frequency) at exactly half the mean resonant field of the zero-field doublet and varies with angle according to

$$I_{\Delta m=\pm 2} \propto (a^2-b^2)\cos^4\phi + 2ab\cos^3\phi + (b^2+2ac+e^2-d^2)\cos^2\phi + (2bc+2de)\cos\phi\sin\phi + (c^2+d^2), \quad (14)$$

where

$$a = -2E\sin 2\psi\cos\theta$$
$$b = -E\cos 2\psi(1+\cos^2\theta) + D\sin^2\theta$$
$$c = E\sin 2\psi\cos\theta$$
$$d = -E\sin 2\psi\sin\theta$$
$$e = \tfrac{1}{2}\sin 2\theta(E\cos 2\psi + D).$$

Within the accuracy of the location of the principal axes and the evaluation of D and E the experimental results are in agreement with the proposed model.[18] Figures 5 and 6 contain the observed and calculated intensity variations of the $\Delta m = \pm 2$ transitions about several axes. The agreement is particularly striking about the c' axis where an asymmetrical variation is predicted and observed. It is interesting to note that along with the anisotropy of the intensity there is also an anisotropy of the linewidth of the $\Delta m = \pm 2$ resonance; a similar but smaller anisotropy is found for the components of the $g=2$ doublet.

The resonance field of the $\Delta m = \pm 2$ transition was measured about one axis and was found to be exactly one-half as large as the mean resonance field of the $\Delta m = \pm 1$ transitions at each angle. The linewidth of the half-field transition is essentially that of the components of the zero-field doublet, about 1–2 gauss (at -150°C).

[17] J. H. van der Waals and M. S. de Groot, Mol. Phys. **2**, 333 (1959).

[18] It is felt that the sensitivity of the intensity to the measured linewidth and the consequent uncertainty in the intensity determination is responsible for the greater part of the discrepancy between the observed and calculated results.

4. Temperature-Dependent Exchange Effects

Striking temperature effects are observed in the EPR spectra of the $(\varphi_3PCH_3)^+(TCNQ)_2^-$ and $(\varphi_3AsCH_3)^+(TCNQ)_2^-$ salts (Fig. 7). At low temperatures (approx $-160°C$) and for an arbitrary orientation the doublet components are sharp (about 1–2 gauss in width, Lorentzian in shape) and well-resolved. As the temperature is increased the components broaden and move together, eventually collapsing into a single line which becomes progressively sharper, approaching a limit of about 1 gauss at room temperature. This behavior is characteristic of an exchange interaction, a process which first removes fine structure (exchange broadening) and then sharpens up the single remaining resonance line (exchange narrowing). Anderson[19] has shown that if a system capable of absorption at two characteristic absorption frequencies ν_1 and ν_2 is making transitions of the Markovian type from one resonance frequency to the other with an average frequency ν, the separation $\Delta\nu_{12}$ of the two resonant absorptions is given by

$$(\Delta\nu_{12})^2=(\nu_1-\nu_2)^2-8\nu^2 \quad \text{for} \quad (\nu_1-\nu_2)^2>8\nu^2$$
$$(\Delta\nu_{12})^2=0 \quad \text{for} \quad (\nu_1-\nu_2)^2<8\nu^2, \qquad (15)$$

and the linewidth Δw by

$$\Delta w\sim\nu \quad \text{for} \quad (\nu_1-\nu_2)^2>8\nu^2$$
$$\Delta w\sim 2(\nu_1-\nu_2)^2/\nu \quad \text{for} \quad (\nu_1-\nu_2)^2<8\nu^2. \qquad (16)$$

Such a model of exchange narrowing adequately describes phenomena such as the physical exchange of protons between alcohol and water observed in NMR studies or the loss of hyperfine structure in the EPR spectra of radicals in solution due to the spin exchange of the unpaired electrons. In the present system the effect is believed due to the mutual spin-exchange of triplet entities.

Knowledge of the doublet spacing in the absence of exchange (here, at low temperatures) permits calculation of an exchange frequency ν at any given temperature where the doublet splitting is still nonzero. Assuming the exchange to be thermally activated, one may write

$$\nu=\nu_0\exp(-\Delta E_a/kT). \qquad (17)$$

Data analyzed in this way for the $(\varphi_3XCH_3)^+(TCNQ)_2^-$ salts (where X is P or As) are shown in Fig. 8. One finds $\nu_0=4.0\pm1.0\times10^9$ cps and $\Delta E_a=0.062\pm0.005$ ev. It is interesting to note that the activation energy for exchange is the same as the energy of the singlet-triplet separation in these two systems. The probability for exchange to occur and, thus, the exchange frequency, will depend upon the effective concentration of magnetic species. For example, one must use dilute solid solutions of DPPH in the corresponding hydrazine to observe the hyperfine structure of the

[19] P. W. Anderson, J. Phys. Soc. Japan **9**, 316 (1954).

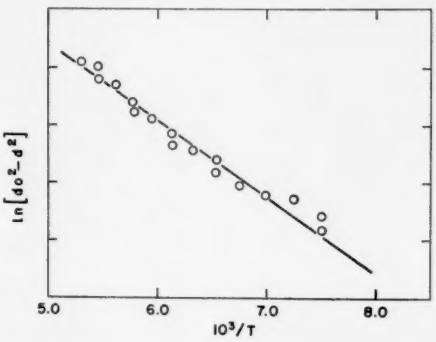

FIG. 8. Dependence of exchange frequency on temperature for an arbitrary orientation of the $(\varphi_3PCH_3)^+(TCNQ)_2^-$ salt. d_0 and d are equal to, respectively, $(\nu_1-\nu_2)$ and $(\Delta\nu_{12})$ of Eqs. (15) and (16).

DPPH radical in the solid since the pure material yields only a single exchange-narrowed resonance.[20] For the ion-radical salts, magnetic dilution comes about by depopulating the triplet state. In the temperature range in which the exchange effects are measurable, the concentration of triplet entities is varying as

$$N_T\cong N_0 3\exp(-J/kT). \qquad (18)$$

It would then be expected that the temperature dependence of the apparent exchange frequency in these systems is the same as that observed for the triplet-state population. Consequently ΔE_a, the activation energy for exchange, should be the same energy quantity as J, the singlet-triplet separation. The pre-exponential factor should depend upon the distribution and geometry of the molecules in the crystal that participate in the exchange process. Exchange mechanisms other than that discussed above may of course exist that would be capable of producing the observed temperature effects on the $(\varphi_3PCH_3)^+(TCNQ)_2^-$ and $(\varphi_3AsCH_3)^+(TCNQ)_2^-$ spectra. If such a mechanism had a characteristic frequency greater than that for the concentration dependent spin exchange between triplet entities, it would of course dominate and the equality between J and ΔE^a observed above would not be expected to hold.

The $[(C_2H_5)_3NH]^+(TCNQ)_2^-$ salt for which J is 0.034 ev exhibits only a single, sharp resonance down to $-160°C$ at which temperature some slight broadening is discernible. That part of the (morpholinium)$^+$(TCNQ)$^-$ spectrum associated with triplet-state electrons 0.41 ev above the ground state (the outer doublet) shows no change in the shape and spacing of the zero-field split resonances (for a fixed orientation) up to the salt's decomposition temperature of about 125°C. These results and the measurements on the $(\varphi_3PCH_3)^+(TCNQ)_2^-$ and $(\varphi_3AsCH_3)^+(TCNQ)_2^-$ salts appear

[20] See, for example, R. W. Holmberg, R. Livingston, and W. T. Smith, Jr., J. Chem. Phys. **33**, 541 (1960).

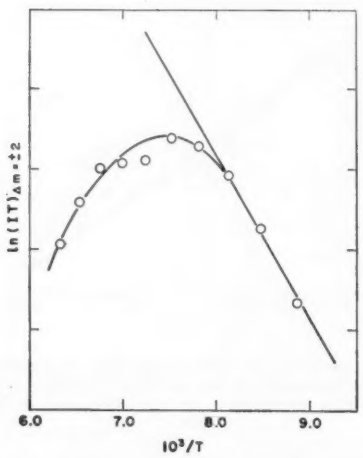

FIG. 9. Intensity (in arbitrary units) dependence of the $\Delta m = \pm 2$ resonance on temperature for the $(\varphi_3PCH_3)^+(TCNQ)_2^-$ salt. The straight line is a plot of Eq. (19) for J equal to 0.062 ev.

consistent with the model in which the temperature dependence of the exchange frequency is governed mainly by the concentration of magnetic species, determined in the present examples by the thermal population of a triplet state.

Our experiments on the $(\varphi_3PCH_3)^+$ and $(\varphi_3AsCH_3)^+(TCNQ)_2^-$ salts at -150°C indicate that although the exchange rate is no longer fast enough to affect the zero-field splitting, it is still fast enough to remove any hyperfine structure which might be present. The isotropic hyperfine splitting of the $TCNQ^-$ radical has been observed in solution, with nitrogen and proton coupling constants of 0.98 and 1.39 gauss, respectively.[21] It is difficult to estimate the isotropic hyperfine splitting in the solid since the spin density is probably distributed over several TCNQ units. There will also be anisotropic contributions to the hyperfine splitting in the solid. From our previous determination of the temperature dependence of the exchange frequency, it is calculated that to resolve splittings of the order of 1 gauss would require temperatures below 100°K; such experiments are currently underway.

If a temperature-dependent exchange effect is present which removes the dipolar-induced zero-field splitting, it would be expected that such an exchange effect would also remove the dipolar-induced mixing of states resulting in the vanishing of the $\Delta m = \pm 2$ transition. At low temperatures (slow exchange), the intensity of the half-field resonance will be governed by the limiting form of Eq. (2) for small T,

$$I_{\Delta m=\pm 2} \propto (1/T) \exp(-J/kT). \qquad (19)$$

As the presence of the exchange effect is felt by the system, the intensity should go through a maximum and rapidly decrease. Such is indeed the case as can be seen in Fig. 9 which shows the temperature dependence of the $\Delta m = \pm 2$ transition for the $(\varphi_3PCH_3)^+(TCNQ)_2^-$ salt.[22] The intensity drops off as exchange sets in, while the limiting slope of the function $\ln(IT)$ at small T is just that determined by the singlet-triplet separation ($J = 0.062$ ev) for this salt. As the intensity passes through its maximum and decreases, an associated increase of the linewidth occurs that eventually makes further accurate intensity determinations impossible.

The exchange effects observed thus far are felt to arise from randomly fluctuating interactions of nearby triplet entities. To a first approximation, such interactions do not affect the over-all geometry or distribution of the stationary-state wave functions associated with each triplet entity. Similar exchange effects could also result from a rapid tumbling of the triplet entity in the solid. In light of the large and asymmetrical molecules involved, this seems an extremely unlikely possibility. Furthermore, such a rapid molecular tumbling should lead to removal or at least marked reduction of any g-factor anisotropy. Measurements made on $(\varphi_3PCH_3)^+(TCNQ)_2^-$ crystals at -150°C (where the exchange effect is very small) and at $+23$°C (where the exchange frequency is very large) show the same degree of anisotropy of the g factor (the value of the g factor is essentially unchanged also), thus eliminating the possibility of molecular tumbling.

5. Concluding Remarks

Results of the studies on the TCNQ ion-radical salts suggest that extreme caution must be exercised in drawing conclusions regarding the magnetic properties of organic solids from temperature dependences of magnetic susceptibilities and EPR signal intensities alone. Positive conclusions regarding spin correlation in paramagnetic organic solids may be drawn from observations on single crystals of zero-field splittings and $\Delta m = \pm 2$ transitions. For this reason, the TCNQ

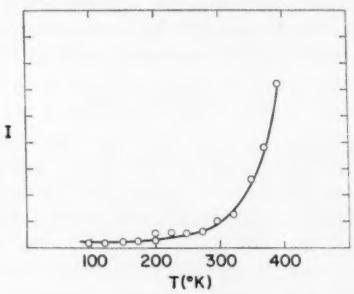

FIG. 10. Temperature dependence of the integrated EPR absorption I (in arbitrary units) of the chloranil-diaminodurene complex.

[21] W. D. Phillips, J. C. Rowell, H. Foster, and D. B. Chesnut (to be published).

[22] Figure 9 represents data from one crystal orientation. Preliminary experiments indicate a small but definite dependence of the temperature of maximum $(IT)_{\Delta m=\pm 2}$ on crystal orientation.

ion-radical salts are of particular interest because single crystals can be prepared and zero-field splittings and $\Delta m = \pm 2$ transitions are observed.

However, even with the observation of zero-field splittings, ambiguity may remain with respect to detailed interpretation. A case in point is the (morpholinium)$^+$(TCNQ)$^-$ salt to which brief mention was made earlier. The EPR spectrum of this salt consists of an outer zero-field doublet and a central singlet (Fig. 2), both sets of lines exhibiting temperature dependences compatible with a singlet-triplet model. On this model, the ratio of species giving rise to the outer doublet to those giving rise to the central resonance is about 15. The species giving rise to the central peak thus constitute 6% of the solid and are assigned tentatively to impurities. Although it may appear difficult to account for such a high percentage of impurity, it should be recognized that the chemistry and electronic structure of these and other charge-transfer salts are, at best, complex. For example, crystals of the 2:3 (morpholinium)$_2^{2+}$(TCNQ)$_3^{2-}$ salt have been isolated which give rise to two separate sets of zero-field doublets as well as a single central peak. The 1:1 (morpholinium)$^+$ (TCNQ)$^-$ salt is red and has an electrical resistivity of 10^6 ohm cm, whereas the 2:3 salt is black and has a resitivity of 10^3 ohm cm, both at room temperature.[23] Even the (φ_3PCH$_3$)$^+$(TCNQ)$_2^-$ and (φ_3AsCH$_3$)$^+$(TCNQ)$_2^-$ salts, the purest so far obtained,[5] exhibit up to nine resonances (below -125°C, at very high gain) in addition to the strong outer doublet. The nine resonances account for about 2–3% of the total resonance absorption intensities of these salts at low temperatures and exhibit angular dependences of displacement from the center similar to that of the dominant doublets. Possible origins of these "extra" lines could be hyperfine or zero-field splittings of impurity or dislocation species in the solid. It is conceivable, however, that spin correlation in these systems is more extensive than pairwise. In this event, other triplet states as well as states of higher multiplicity might be present which would give rise to resonances each of whose intensities would depend on the thermal accessibility of the state involved. It is not possible at this time to decide between the various alternative explanations for the origin of the "extra" lines in the ion-radical salts. However, it is felt that impurities and crystal defects must be eliminated as being responsible for the "extra" lines before extensive electron correlation can be considered more seriously.

The situation with respect to interpretation is, however, far more serious for organic solids that exhibit a single resonance around $g=2.002$. The chances for the presence of impurities, particularly in ion-radical salts, are great, and most radical impurities would be expected to possess doublet ground states and exhibit resonances around $g=2.002$. Such an impurity species could mask in EPR the presence of a majority species that possessed, say, a ground singlet state with a fairly high triplet state ($J>0.1$ ev).

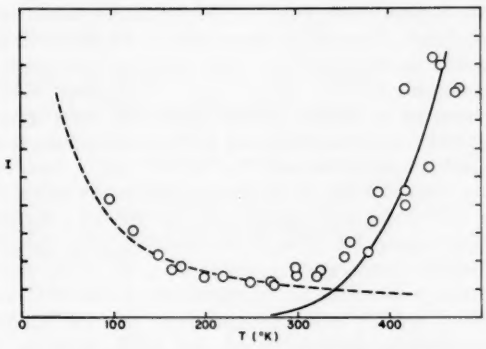

FIG. 11. Temperature dependence of the integrated absorption intensity I (in arbitrary units), for Na$^+$TCNE$^-$. Circles represent measured intensities. The solid curve is that calculated for a singlet-triplet model with $J=0.26$ ev. The dashed curve is calculated for 0.03% of a doublet-state impurity following a $1/T$ temperature dependence.

An example of this behavior is provided by the 1:1 complex formed between chloranil and diaminodurene.[24] These complexes are deep black in color and exhibit[23] a room-temperature electrical resistivity of 2.8×10^3 ohm cm. The electrical resisitivity decreases exponentially with increasing temperature yielding an activation energy for conductivity of 0.25 ev. The room-temperature EPR spectrum of the chloranil-diaminodurene complex consists of a single peak with a width of 2.9 gauss and located at $g=2.003$. The 23° signal intensity corresponds to about 2×10^{-3} unpaired electrons per complex unit. The temperature dependence of the integrated signal intensity for this complex (Fig. 10) increases continuously over the accessible temperature range of -180° to $+120$°C. Between -25° and 120°C, the intensities can be fitted to Eq. (2) for a singlet-triplet model with $J=0.15$ ev. Below -25°C, however, the intensity does not fall off sufficiently rapidly for this model. The temperature dependence of the EPR intensity of the chloranil-diaminodurene complex can be accounted for reasonably well over the entire temperature range if it is assumed that the solid is contaminated with as little as 0.04% of doublet-state impurity exhibiting a simple $1/T$ temperature dependence in addition to the 99.96% of singlet-triplet material with $J=0.16$ ev. In the light of this result, it is possible that previous failures to detect deviations from Curie-law behavior in complexes involving quinones and *p*-phenylenediamines[9] was due in part to the presence of dominating doublet-state impurity species.

An even more striking example of the effects of impurities on the EPR characteristics of an ion-radical

[23] Measured by R. G. Kepler of this Laboratory.

[24] Prepared by L. R. Melby of this Laboratory.

salt is provided by Na^+TCNE^- (TCNE = tetracyanoethylene). The EPR characteristics of the $TCNE^-$ radical in solution have been described previously.[25] In solution $TCNE^-$ behaves as a conventional radical possessing a doublet ground state. The temperature dependence of the integrated EPR intensity for a powdered sample of the solid Na^+TCNE^- salt is, however, that shown in Fig. 11. It is seen that in the range 25° to 175°C the EPR signal intensity follows a singlet-triplet model for $J=0.26$ ev. However, after passing through a minimum at about 0°C, the EPR signal intensity increases for temperatures below 0°C and follows a $1/T$ Curie-law dependence to −180°C. The temperature dependence of the EPR intensity of Na^+TCNE^- can be accounted for quite accurately over the range −180° to 175°C if the solid is considered to consist of 99.97% of species possessing a singlet-triplet electronic system with $J=0.26$ ev and 0.03% of a doublet-state impurity. Qualitatively similar behavior is exhibited by the Na^+TCNQ^- salt.

The temperature dependences of the resonance intensities for the conventional charge-transfer complex chloranil-diaminodurene and the simple ion-radical salts Na^+TCNE^- and Na^+TCNQ^- indicate that some measure of spin correlation does exist in these systems. While in the absence of single-crystal studies the assignment of triplet character to the paramagnetic states involved must be regarded as only tentative, it is suggested that the nature of the interaction in these systems is not unlike that found, for example, in the $(\varphi_3PCH_3)^+(TCNQ)_2^-$ salt where there is clear evidence for a pairwise spin correlation.

[25] W. D. Phillips, J. C. Rowell, and S. I. Weissman, J. Chem. Phys. **33**, 626 (1960).

ACKNOWLEDGMENTS

We would like to express our appreciation to Dr. H. S. Jarrett for helpful discussions and to Dr. H. Foster, Dr. R. K. Waring, Mr. G. Watunya, and Mr. F. Ferrari for experimental assistance. We are indebted to Dr. Paul Arthur, Jr., and Dr. R. G. Kepler for permitting us to quote some of their results prior to publication. Finally the successes of Dr. R. J. Harder, Dr. W. R. Hertler, and Dr. L. R. Melby in purifying and preparing single crystals of the TCNQ salts have made possible the more significant studies reported in this paper.

THE JOURNAL OF CHEMICAL PHYSICS VOLUME 35, NUMBER 3 SEPTEMBER, 1961

Irreversible Thermodynamics of Systems Containing Radiation. Application to Photochemical Reactions

ROBERT G. MORTIMER* AND ROBERT M. MAZO

Gates and Crellin Laboratories of Chemistry,† California Institute of Technology, Pasadena, California

(Received January 23, 1961)

The general theory of the irreversible thermodynamics of chemically reacting systems interacting with radiation is developed. From this, a limit to the efficiency of photochemical processes is derived, and this is compared with approximate experimental efficiencies of published researches. The computed efficiencies are appreciably lower than the theoretical limit; reasons for this are discussed.

I. INTRODUCTION

THE behavior of a radiation field in the presence of absorbing matter has been extensively investigated, largely from the point of view of astrophysical applications.[1] The chemical study of the interaction of radiation and matter has been largely concerned with such topics as quantum yields and the mechanism of photochemical reactions. Of particular interest are those photochemical reactions which proceed with a positive free-energy increment (i.e., which will not go "in the dark"). Typical important examples are photosynthesis and ozonization of oxygen in the upper atmosphere. In this paper we give a general treatment of the irreversible thermodynamics of systems containing radiation and apply our results to the determination of the efficiency of photochemical reactions which will not go "in the dark." Although most of the complication inherent in the general treatment will be unnecessary for the particular application which we make, we nevertheless present it here, for it is not without intrinsic interest and possible applicability.

II. GENERAL THEORY

Strictly speaking, one can only assign a temperature to radiation which is in thermal equilibrium with matter. However, Planck[2] has shown that it is very often convenient to ascribe a temperature T_r to nonequilibrium radiation. If the intensity at a point, at frequency ν, in a direction characterized by the unit vector $\mathbf{n}$, be denoted by $I_\nu(\mathbf{n})$, then T_r is defined by

$$T_r=\frac{h\nu}{k\ln[(2h\nu^3/c^2I_\nu)+1]}. \tag{1}$$

Although T_r depends on position in space, frequency, and direction, it is still a useful concept when the radiation can be considered to be in *local* thermodynamic equilibrium. We shall assume local equilibrium in the following development.

We shall use the convention that a time derivative taken at a fixed point is written as a partial derivative, while the Stokes operator is written as an ordinary derivative. A general development of the sort which follows unfortunately requires the introduction of a multiplicity of symbols. We here use the notation of the paper by Kirkwood and Crawford[3] to which the reader is referred for a discussion of the macroscopic equations of transport in the absence of radiation. In addition a glossary of symbols is provided.

Our system is governed by the following equations: (a) the energy-balance equation, which we shall develop in detail (b) the equation of motion of matter,

$$\rho(d\mathbf{v}/dt)=\rho\mathbf{X}+\nabla\cdot\mathfrak{d}, \tag{2}$$

where $\mathfrak{d}$ is the total stress tensor (c) the equations of continuity of the chemical species present and their sum, the total equation of continuity of matter[3]; and (d) the equation of transfer of radiation.[1]

We obtain an energy-balance equation by equating the sum of the rate of increase of energy in a region of the system,

$$\int_V(\partial/\partial t)\,(\rho E_k+\tfrac{1}{2}\rho v^2+\tilde{E}_r)\,dV, \tag{3}$$

and the rate of energy flow through the surface of the region,

$$\int_A[\mathbf{j}_E+(\rho E_k+\tfrac{1}{2}\rho v^2)\mathbf{v}+\mathbf{F}]\cdot d\mathbf{A}, \tag{4}$$

to the rate at which work is done on the matter in the region,

$$\int_V\sum_{i=1}^{s}\mathbf{j}_i\cdot\mathbf{X}_i dV+\int_V\rho\mathbf{v}\cdot\mathbf{X}dV+\int_A\mathbf{v}\cdot\mathfrak{d}\cdot d\mathbf{A}. \tag{5}$$

We neglect forces due to reflection of radiation at discontinuities such as the boundary of the system.

Applying Gauss' divergence theorem to the surface integrals, we may equate integrands, since our region is

* National Science Foundation Predoctoral Fellow.
† Contribution No. 2672.

[1] S. Chandrasekhar, *Radiative Transfer* (Dover Publications, New York, 1960).

[2] M. Planck, *The Theory of Heat Radiation*, translated by M. Masius (Dover Publications, New York, 1959).

[3] J. Kirkwood and B. Crawford, Jr., J. Phys. Chem. **56**, 1048 (1952).

arbitrary, to obtain

$$\sum_{i=1}^{s}\mathbf{j}_i\cdot\mathbf{X}_i+\nabla\cdot\mathbf{v}\cdot\mathfrak{d}+\rho\mathbf{v}\cdot\mathbf{X}=(\partial/\partial t)[\rho(E_h+\tfrac{1}{2}v^2)+\tilde{E}_r]$$
$$+\nabla\cdot[\mathbf{j}_E+\rho(E_h+\tfrac{1}{2}v^2)\mathbf{v}+\mathbf{F}]. \quad (6)$$

From Eq. (6), Eq. (2), and the equation of continuity,[3] we obtain an energy-balance equation, which we separate into two equations with a separation constant $\rho\epsilon$ which has the significance of energy absorbed per unit volume per unit time by the matter from the radiation.

$$\rho(dE_h/dt)=\mathfrak{d}:\nabla\mathbf{v}+\sum_{i=1}^{s}\mathbf{j}_i\cdot\mathbf{X}_i-\nabla\cdot\mathbf{j}_E+\rho\epsilon. \quad (7)$$

$$\partial\tilde{E}_r/\partial t=-\nabla\cdot\mathbf{F}-\rho\epsilon. \quad (8)$$

Equation (7) is not yet in the most useful form. We substitute

$$\mathbf{j}_E=\mathbf{q}'+\sum_{i=1}^{s}\mathbf{j}_i\bar{E}_i=\mathbf{q}+\sum_{i=1}^{s}\mathbf{j}_i(T_h\bar{S}_i+\mu_i), \quad (9)$$

and introduce $\mathbf{j}_{Sh}$ the nonradiative entropy flux, and $\nabla_T\mu_i'$. After some manipulation, we obtain

$$\rho(dE_h/dt)=\mathfrak{d}:\nabla\mathbf{v}-T_h\nabla\cdot\mathbf{j}_{Sh}-\mathbf{q}\cdot\nabla\ln T_h$$
$$-\sum_{i=1}^{s}\mathbf{j}_i\cdot\nabla_T\mu_i'-\sum_{i=1}^{s}\mu_i\nabla\cdot\mathbf{j}_i+\rho\epsilon. \quad (10)$$

In order to put Eq. (8) in its most useful form, we express $\nabla\cdot\mathbf{F}$ in terms of the entropy flux. From the definitions of $\mathbf{F}$ and $\mathbf{S}$, we find

$$\nabla\cdot\mathbf{F}=(\partial/\partial x)\iint I_\nu l\,dv\,d\Omega+(\partial/\partial y)\iint I_\nu m\,dv\,d\Omega$$
$$+(\partial/\partial z)\iint I_\nu n\,dv\,d\Omega \quad (11)$$

$$\nabla\cdot\mathbf{S}=(\partial/\partial x)\iint L_\nu l\,dv\,d\Omega+(\partial/\partial y)\iint L_\nu m\,dv\,d\Omega$$
$$+(\partial/\partial z)\iint L_\nu n\,dv\,d\Omega. \quad (12)$$

We know[1,2] that

$$\partial L_\nu/\partial I_\nu=T_r^{-1}. \quad (13)$$

Thus, if conditions for interchanging the order of differentiation and integration are met,

$$T_r\nabla\cdot\mathbf{S}=\nabla\cdot\mathbf{F}. \quad (14)$$

One special case for which this is satisfied is that of a monochromatic plane wave. Although a plane wave cannot have a finite intensity,[2] many photochemical experiments are performed using nearly monochromatic, nearly unidirectional radiation, so we shall consider this case from this point on. One could treat the general case as a superposition of plane waves, or perhaps by defining a mean temperature.

In order to obtain an entropy equation, we differentiate the Gibbs equation[3] with respect to time and solve for dS_h/dt;

$$\rho(dS_h/dt)=(\rho/T_h)(dE_h/dt)-(p/\rho T_h)(d\rho/dt)$$
$$-(\rho/T_h)\sum_{i=1}^{s}\mu_i(dx_i/dt). \quad (15)$$

We know also[2]

$$\partial\tilde{S}_r/\partial t=(1/T_r)(\partial\tilde{E}_r/\partial t). \quad (16)$$

We substitute Eqs. (8) and (10) into Eqs. (16) and (15), and obtain two entropy-balance equations, which we combine;

$$\rho(dS_h/dt)+(\partial\tilde{S}_r/\partial t)=\Phi-\nabla\cdot\mathbf{j}_{Sh}-\nabla\cdot\mathbf{S}. \quad (17)$$

The entropy source Φ is a sum of

$$\phi_1=T_h^{-1}(\mathfrak{d}+p\mathbf{1}):\nabla\mathbf{v}$$
$$\phi_2=-(\rho/T_h)\sum_{k=1}^{l}\Delta F_k(d\lambda_k/dt)$$
$$\phi_3=-T_h^{-1}\sum_{i=1}^{s}\mathbf{j}_i\cdot\nabla_T\mu_i'$$
$$\phi_4=-T_h^{-1}\mathbf{q}\cdot\nabla\ln T_h$$
$$\phi_5=\rho\epsilon(T_h^{-1}-T_r^{-1}). \quad (18)$$

Each of these terms can be separated into a product of a "generalized force" with a "flux." We choose $\rho\epsilon$ as a flux and $T_h^{-1}-T_r^{-1}$ as a force, and split the other terms in the conventional manner.

According to the theorem of Onsager, if certain hypotheses are met,[4] the entropy production is a sum of products of forces and fluxes, and the matrix of phenomenological coefficients expressing the linear dependence of the forces on the fluxes is symmetric. In an isotropic medium if the fluxes depend on the forces linearly, then scalar fluxes can only depend on scalar and tensor forces, but not on vector forces. This situation arises because, to make a scalar depend linearly on a vector, the coupling coefficient must be a vector. In an isotropic medium, there are no available vectors (in the absence of external fields) which do not depend on the vector forces. But if the coupling constant depends on the vector forces, the hypothesis of linearity is violated. There are, however, isotropic tensors, so that scalars may be isotropically coupled to tensors. This result is known in the literature as a Curie's theorem, and the usual reference is our reference 5. (However, the referee of the first version of this paper has quite rightly pointed out that reference 5 does not contain the above statement.)

We restrict our attention to isotropic media and assume that the relation between chemical reaction

[4] B. D. Coleman and C. Truesdell, J. Chem. Phys. **33,** 28 (1960).

[5] P. Curie, *Oeuvres* (Gauthier-Villars, Paris, 1908), p. 127.

rates and the stress tensor, temperature gradient, and concentration gradients are linear. We do not assume that the reaction rates are linear functions of the various ΔF's or of the radiation flux. Such an assumption would restrict our considerations to physically uninteresting situations and is, in any case, unnecessary. It follows that the rates of chemical reactions will be affected only by the radiation and by the forces described by the stress tensor; the latter effect has never been experimentally demonstrated, and would be expected to be very small, if found.

III. PHOTOCHEMICAL EFFICIENCY

Since we are dealing with reactions that will not proceed in the dark, the Gibbs free energy of the system will increase as these reactions proceed photochemically. This increase of free energy of products over reactants is in principle completely available to do work through electrochemical or other processes using the reverse reactions. We define the efficiency as follows,

$$\eta \equiv \epsilon^{-1} \sum_{k=1}^{h} \Delta F_k (d\lambda_k/dt). \tag{19}$$

Those reactions (call them reactions $h+1, h+2, \cdots, t$) which do not happen to be coupled through phenomenological coefficients with a photochemical reaction of positive ΔF are excluded from the sum for reasons we will discuss.

We require that the entropy production be nonnegative, according to the second law of thermodynamics. Since the forces giving rise to ϕ_3 and ϕ_4 cannot influence those giving rise to ϕ_1, ϕ_2, and ϕ_5, by Curie's theorem, and since the effect of the force connected with ϕ_1 on the chemical reactions is assumed negligible, we require the sum of ϕ_2 and ϕ_5 to be nonnegative;

$$-(\rho/T_h) \sum_{k=1}^{t} \Delta F_k (d\lambda_k/dt) + \rho\epsilon (T_h^{-1} - T_r^{-1}). \tag{20}$$

However, if some, say $t-h$, of the reactions are not photochemical and are not coupled to photochemical reactions, they obey a separate inequality, and Eq. (20) still holds if these reactions $h+1, \cdots, t$ are excluded from the sum.

The free-energy increments of the photochemical reactions we are considering are positive, so if their $d\lambda_k/dt$ are to be positive, either $\rho\epsilon$ must be positive or some of the coupled reactions must have a negative product $\Delta F_l (d\lambda_l/dt)$, in which case our nominally photochemical reactions are being driven by coupled reactions instead of photochemically, and we can say nothing about photochemical efficiency. It may even turn out that η is negative.

Now from Eq. (20) we conclude

$$\eta = \epsilon^{-1} \sum_{k=1}^{h} \Delta F_k (d\lambda_k/dt) \leq 1 - (T_h/T_r). \tag{21}$$

TABLE I. Comparison of efficiencies.

Reaction	$I_2 = 2I$		$3O_2 = 2O_3$		$2NH_3 = N_2 + 3H_2$	
Reference	7		8		11	
Wavelength (A)	5050	5180	1295	1470	1295	1470
Approx. T_r (°K)	3450	3400	4750	5225	5400	5900
Max. eff.	0.91	0.91	0.94	0.94	0.94	0.95
Exptl. eff.	0.45		0.31		0.43	

This limit is the same functional form as the Carnot efficiency of a reversible heat engine operating between sinks of temperature T_r and T_h.

Clearly the maximum efficiency can only be approached if the (negative) free-energy production, due to reactions which go spontaneously ("in the dark"), can be minimized. For reactions which are photochemically catalyzed, rather than driven, η will, in general, be negative. Equation (21) still holds but tells us nothing of interest.

In a study of the production of light from thermal energy, Weinstein[6] stated in a footnote that arguments similar to his could be used to show that Eq. (21) is the limiting efficiency for the conversion of radiant energy into work.

IV. CALCULATIONS

Let us now compare our theoretical limit with experimental average efficiencies, which may be calculated approximately from data reported in the literature. The results of three such approximate comparisons are given in Table I.

Rabinowitch and Wood[7] studied the dissociation of iodine gas into normal iodine atoms by visible light from a carbon arc. In order to make an approximate calculation, it was necessary to compute first the approximate radiation temperature at their reaction vessel, and then to calculate the approximate experimental efficiency of their reaction.

Since the comparison is approximate, only two wavelengths of the continuous spectrum of Rabinowitch and Wood were chosen at which to calculate the radiation temperature, the wavelength of maximum emission of the arc and the wavelength of maximum absorption. The radiation temperatures were estimated as follows: The reported number of photons absorbed per unit volume per unit time was multiplied by the energy per photon at the wavelength of maximum absorption as an approximation to the total rate of energy absorption per unit volume. From this, the total incident intensity was calculated, using the reported mean absorption coefficient α_L of 18.0 cm^{-1} atm^{-1}, the given cell length of 2 cm, and the reported I_2 pressure of 0.15 mm.

[6] M. A. Weinstein, J. Opt. Soc. Am. **50**, 597 (1960).
[7] E. Rabinowitch and W. C. Wood, J. Chem. Phys. **4**, 496 (1936).

These figures yield a transmitted intensity of 0.984 I_0, so the incident intensity was set equal to the rate of energy absorption divided by 0.016.

From this, it was possible to get the scale on the ordinate of a curve of the spectral distribution Rabinowitch and Wood gave for their arc by graphical integration under the curve, allowing one to read the intensity per unit wavelength interval at any wavelength directly from the given curve. This was converted to intensity per unit frequency interval.

The intensity was now converted to intensity per unit solid angle by assuming that the arc subtended an area of 1 cm^2 and that the incident intensity came equally from all parts of this area, which was located 16 cm from the reaction vessel. The radiation temperature was calculated at 5180 and 5050 A by substituting the intensity per unit frequency interval per unit solid angle into Eq. (1), giving 3400° and 3450°K for T_r.

In order to estimate the experimental efficiency, it was assumed that it would be possible to dissociate enough iodine molecules to make the iodine atom concentration equal to the iodine molecule concentration, and it was assumed that these conditions could have been approximated by an experiment of the type done by Rabinowitch and Wood. A standard free-energy change for the dissociation reaction of 28.9 kcal/mole was taken, and the standard formula used

$$\Delta F = \Delta F^0 + RT \ln Q. \tag{22}$$

A quantum yield of unity was assumed, and using 55.4 kcal/einstein, as the average photon energy, the average efficiency was calculated with Eq. (19). The theoretical limit was calculated by Eq. (21), assuming that the radiation temperature did not vary over the reaction vessel.

Groth[8] studied the formation of ozone from oxygen, using light in the vacuum ultraviolet from a xenon lamp with a partial pressure of Xe of 0.1 mm and a partial pressure of Ne of 20 mm. Oxygen was passed through an illuminated vessel at varying rates and the ozone production was studied as a function of this rate. The ozone formation was assumed entirely due to the two emission lines at 1295 and 1470 A. In order to get the intensity per unit frequency interval, it is necessary to know both the width and the shape of these lines. The literature seems to contain no information on the width of these lines in the emission spectrum, but McLennar and Turnbull[9] reported that the extreme width of the absorption line at 1470 A was about 5 A at a pressure of 20 mm, including the wings of the line. Not knowing the shape of the line, we make the very rough approximation that each line may be approximated by a block of radiation 1 A wide. This is a reasonable width, according to the work of Margenau and Watson.[10] A more reasonable shape would be Gaussian, but this would lead to a different radiation temperature for each frequency over the line, and we would have to take some sort of average temperature. Using a square line shape gives us effectively some sort of average temperature, and simplifies the calculations.

The assumption was made that each line was of equal intensity in photons per unit time. This is only very roughly correct, since Groth reported that 73% of the absorbed energy came from the 1470-A line. The approximate incident radiation temperature was calculated as before from Eq. (1), making reasonable assumptions about the area subtended by the source and the distance from the source to the reaction vessel.

However, in this case, there is another complication, since the absorption coefficient of oxygen at the wavelengths in question is very large. The transmitted intensity was accordingly very small after the light passed through only a few millimeters of the cell. We make the very rough approximation that the mean radiation temperature was about equal to the arithmetic mean of the incident radiation temperature and room temperature.

The experimental efficiency was estimated from the reported quantum yield of about 2.0. Since no data on actual concentrations were given, the standard free-energy change of the ozonization reaction, was taken as an upper limit to the actual free energy change, and Eq. (19) was used, assuming equal numbers of photons absorbed from each of the two spectral lines.

The data of Wijnen and Taylor[11] were even harder to work with, since they used a reaction vessel surrounding their light source, which was a xenon lamp similar to that of Groth, except that it operated at a xenon pressure of 1.5 mm, with no other gas present. This would give sharper emission lines than would Groth's lamp, so the radiation temperature was approximated by repeating the calculations on Groth's lamp assuming a block of radiation 0.3 A wide for each line.

In order to estimate the experimental efficiency, it was assumed that the only products of the ammonia decomposition studied were nitrogen and hydrogen, and that the free-energy change could be approximated by the standard free-energy change of 8.0 kcal per mole of NH_3. Quantum yields of from 2 to 11 were reported, so the efficiency was calculated on the basis of a quantum yield of 11, and it was again assumed that the two spectral lines had equal intensities in photons per unit time. Thus the efficiency was approximated by 11 times the standard free-energy change divided by the average energy per einstein of photons at 1295 and 1470 A.

[8] W. Groth, Z. physik. Chem. **37B,** 308 (1937).
[9] J. C. McLennar and R. Turnbull, Proc. Roy. Soc. (London) **A139,** 683 (1933).
[10] H. Margenau and W. W. Watson, Revs. Modern Phys. **8,** 22 (1936).
[11] M. H. J. Wijnen and H. A. Taylor, J. Chem. Phys. **21,** 233 (1953).

V. DISCUSSION

The conclusion that radiant energy cannot be fully utilized in a photochemical process should not be surprising when one realizes that it has long been known[2] that plane waves and parallel beams of monochromatic photons, which we might think of as sources of pure available energy, cannot have finite intensities.

The result obtained might be anticipated if one thought of radiation as a means of transferring energy between blackbodies which could be used as heat sinks with ordinary heat engines.

However, the calculations of the previous section comparing experimental efficiencies with the theoretical limit are unsatisfactory as illustrations of a limiting efficiency for several reasons. The experiments cited were designed to investigate quantum yields or reaction kinetics, not necessarily to attain high photochemical efficiencies. For example, the investigators cited used conveniently available wavelengths, instead of trying to maximize the efficiency by using the longest wavelength which would cause the reaction to proceed. If two wavelengths of light will initiate photochemical reactions of the type considered with equal quantum yields, the shorter wavelength will give a lower efficiency, since each photon is associated with more energy, but causes no more molecules to react than a less energetic photon.

Again, relatively high intensities were used, resulting in high radiation temperatures, and making the efficiency limit close enough to unity so as to be experimentally indistinguishable from unity.

Also, in order to minimize thermal or photochemical backreactions, products were kept at low concentrations, which by Eq. (23) lowers the free-energy change of the reactions, lowering the efficiency.

Finally, the numbers obtained are very rough approximations, since the data necessary for calculation of radiation temperatures and experimental efficiencies were incomplete, and many numbers had to be estimated.

With properly designed experiments to study efficiency as a function of radiation temperature, and with careful control of experimental conditions, it might be possible to approach the limiting efficiency fairly closely and to show the functional form of the limit experimentally.

ACKNOWLEDGMENT

We are indebted to Dr. Oliver R. Wulf for valuable discussions during the entire course of the research.

GLOSSARY OF SYMBOLS

$d\mathbf{A}$ Element of area times the normal unit vector

c Speed of light

E_k Internal energy per unit mass

$\bar{E}_i$ Partial specific internal energy

$\tilde{E}_r$ Space density of radiant energy

$$\mathbf{F}=\mathbf{e}_x\iint I_\nu l\,d\nu d\Omega+\mathbf{e}_y\iint I_\nu m\,d\nu d\Omega+\mathbf{e}_z\iint I_\nu n\,d\nu d\Omega$$

(l, m, n are direction cosines, $\mathbf{e}_x$, $\mathbf{e}_y$, $\mathbf{e}_z$ are unit vectors)

Radiation energy flux

ΔF_k Free-energy change per unit mass of the kth reaction

h Planck's constant

$\bar{H}$ Partial specific enthalpy

I_ν Intensity of radiation per unit area per unit time per unit solid angle per unit frequency integral

$$\mathbf{j}_E=\mathbf{q}'+\sum_{i=1}^{s}\mathbf{j}_i\bar{E}_i=\mathbf{q}+\sum_{i=1}^{s}\mathbf{j}_i(T_k\bar{S}_i+\mu_i)$$

Energy flux

$\mathbf{j}_i$ Diffusion flux of component i

$$\mathbf{j}_{Sk}=(\mathbf{q}/T_k)+\sum_{i=1}^{s}\mathbf{j}_i\bar{S}_i$$ Nonradiative entropy flux

k Boltzmann's constant

L_ν Radiant entropy intensity similar to I_ν

m_i Mass of component i

$$m=\sum_{i=1}^{s}m_i$$

p Total pressure

$\mathbf{q}$ Second-law heat flux

$\mathbf{q}'$ First-law heat flux

$Q=a_C^c a_D^d\cdots/a_A^a a_B^b\cdots$ Activity quotient for reaction

R Gas constant

S_k Entropy per unit mass

$\bar{S}$ Partial specific entropy

$\tilde{S}_r$ Space density of radiant entropy

$$\mathbf{S}=\mathbf{e}_x\iint L_\nu l\,d\nu d\Omega+\mathbf{e}_y\iint L_\nu m\,d\nu d\Omega+\mathbf{e}_z\iint L_\nu n\,d\nu d\Omega$$

Radiation entropy flux

t Time

T_k Thermodynamic temperature

T_r Radiation temperature

$\mathbf{v}$ Macroscopic local velocity

dV Element of volume

x_i Mass fraction of component i

$\mathbf{X}_i$ Force on component i due to vector fields and radiation absorption

$$\mathbf{X}=\sum_{i=1}^{s}\mathbf{X}_i$$

$\mathbf{1}$ Unit tensor

ϵ Rate of energy absorption per unit mass

η Efficiency

λ_k Progress variable of the kth reaction
μ_i Chemical potential per unit mass
$\nabla_T\mu_i' = \nabla\mu_i - \mathbf{X}_i + \bar{S}_i\nabla T_k$ Gradient of chemical potential in an equivalent field-free isothermal system
ν Frequency of radiation
ρ Density of matter
δ Total stress tensor
Φ Entropy source strength
$d\Omega$ Element of solid angle

THE JOURNAL OF CHEMICAL PHYSICS VOLUME 35, NUMBER 3 SEPTEMBER, 1961

Cohesive Energies of Europium, Gadolinium, Holmium, and Erbium*

O. CONRAD TRULSON,† DONALD E. HUDSON, AND FRANK H. SPEDDING

Institute for Atomic Research and Department of Physics, Iowa State University, Ames, Iowa

(Received September 12, 1960)

A mass spectrometric method has been employed to study the solid-gas phase change in four rare-earth metals. The enthalpies of sublimation in kcal/M reducted to 298°K are: Eu, 43.11±0.25; Gd, 81.22±0.32; Ho, 75.04±0.44; and Er, 75.39±0.34. The corresponding cohesive energies in kcal/M as determined from presently available thermodynamic data are: Eu, 43.4; Gd, 81.9; Ho, 75.5; and Er, 75.7.

A summary of the cohesion in the rare-earth series is included. A qualitative explanation of the unexpected variations is given in terms of the energetics of the metallic and gaseous states.

I. INTRODUCTION

THIS is the third in a series of papers on the cohesive energies of rare-earth metals obtained by a mass spectrometric method. The purpose of this series has been to obtain precise experimental information on the rare-earth series to form a basis for a systematic theoretical interpretation. The first paper by R. G. Johnson *et al.*,[1] dealing with praseodymium and neodymium, will hereafter be referred to as A. The second, by W. R. Savage *et al.*,[2] reported on dysprosium, samarium, thulium, and ytterbium and will be referred to as B.

From the results of the earlier two publications it was apparent that the cohesive energies varied considerably from one rare earth to another, contrary to a prediction of Wigner and Seitz.[3] There appeared to be two regions of anomaly in the series where the cohesive energies were about half the value predicted (i.e., at europium and ytterbium). The immediate purpose of the present study was to determine heats of sublimation of those metals between europium and ytterbium to see if further deviations in cohesion occurred. This paper describes measurements on four critical rare earths, three of which have very low volatility and require much higher sensitivity than was previously available.

In this work the Clapeyron equation was employed to determine the enthalpy of sublimation from measured relative vapor pressures and temperatures of solid samples. A mass spectrometer was used to select the atomic species effusing from a Knudsen cell. The collector current was proportional to the rate of effusion from the cell: at low pressures effusion rate is proportional to the vapor pressure. The term cohesive energy as used here refers to the enthalpy of sublimation at absolute zero, in agreement with current usage in solid-state physics.

A critique of the method and a description of the apparatus and procedure are found in references A and B. These works will be considered to be a preamble to the present material, and only significant differences in instrumentation or procedure will be treated in detail here. A detailed account of the present experiments is also available.[4]

II. EXPERIMENTAL APPARATUS

The experimental apparatus was essentially the same as described in B. The Knudsen cell and heater unit are shown in Fig. 1 of B, and are described in detail in Sec. II of B. Figure 2 of B shows schematically the details of the ion source including the cell assembly, the ionization filament, and the slit system used to extract the ion beam from the source.

* Contribution No. 929. Work was performed in the Ames Laboratory of the U. S. Atomic Energy Commission.

† Present address: Union Carbide Corporation, Parma Research Laboratory, Cleveland 1, Ohio.

[1] R. J. Johnson, D. E. Hudson, W. C. Caldwell, F. H. Spedding, and W. R. Savage, J. Chem. Phys. **25**, 917 (1956).

[2] W. R. Savage, D. E. Hudson, and F. H. Spedding, J. Chem. Phys. **30**, 221 (1959).

[3] E. P. Wigner and F. Seitz, *Solid-State Physics* (Academic Press, Inc., New York, 1955), Vol. 1, pp. 97–126. (Table II of this reference is taken from Natl. Bur. Standards Circular 500 prepared by Rossini *et al.* The cohesive energies of the rare earths given in that circular are based upon calculations using certain estimated data. The assertion on p. 122 that the values are "nearly equal" must be interpreted in this context merely as qualitative comment.)

[4] O. C. Trulson, (unpublished Ph.D. thesis, Iowa State University, Ames, Iowa, 1959).

In the study of europium metal a Pt-Pt 13% Rh thermocouple was used to measure the cell (and sample) temperature. The thermocouple was recalibrated against a standard thermocouple whose accuracy, certified by the National Bureau of Standards, was better than 0±0.5°C. A further check on temperature gradients in the Knudsen cell, along with the new calibration, resulted in an estimated over-all standard error in cell temperature of 1.6°C. This figure arises primarily from residual uncertainties regarding tiny temperature gradients in the cell and from the error in the NBS standard. The combined *precision* of calibration and measurement was the order of 0.3°; however, the important distinction between empirical precision and meaningful absolute accuracy even in careful temperature measurements must be regarded with care when standard errors in the neighborhood of 1° are quoted at high temperatures.

An optical pyrometer was used to measure the cell temperature for gadolinium, holmium, and erbium. The pyrometer (with observer) was recalibrated for the present work against the standard thermocouple from 800° to 1250°C. The NBS standard thermocouple was then double-checked in an NBS certified standard copper melt (mp 1083.4±0.1°C) and gave 1082.9°C; however, the original NBS thermocouple calibration was employed. In the pyrometer calibration, the sighting blackbody orifice geometry was made identical to the Knudsen cell geometry in order to remove orifice correction errors. The instrumental precision of calibration was estimated to be close to 2.0°. Window corrections were redetermined and applied to all data with an uncertainty of 0.5°. The net estimated instrumental standard error for the pyrometer was conservatively taken to be 2.1°C. (The final pyrometer uncertainty in a special case in addition involves a random reading error which contributes to the overall statistical fluctuations in the data.)

Two detectors were used on the mass spectrometer. For europium, the collector-detector system described in A was used. However, for gadolinium, holmium, and erbium the apparatus was modified so that the ion beam could be amplified by an electron multiplier. In this case the beam impinged directly upon a converter dynode from which electron secondaries were emitted and multiplied. The custom-built multiplier unit was designed with box-like dynodes after the DuMont 6292 photomultiplier. Twelve dynode stages were employed in addition to the converter. The use of Ag-Mg surfaces and a relatively low voltage per stage resulted in a stable net gain of about 10^4 and a low noise level the order of 10^{-19} amp. This exceptional stability and low noise appear to be a result of local processing procedure. A report on the multiplier instrumentation is being prepared for publication in *The Review of Scientific Instruments*; some details are found in a thesis by one of us.[5]

[5] O. C. Trulson, (unpublished M.S. thesis, Iowa State University, Ames, Iowa, 1956).

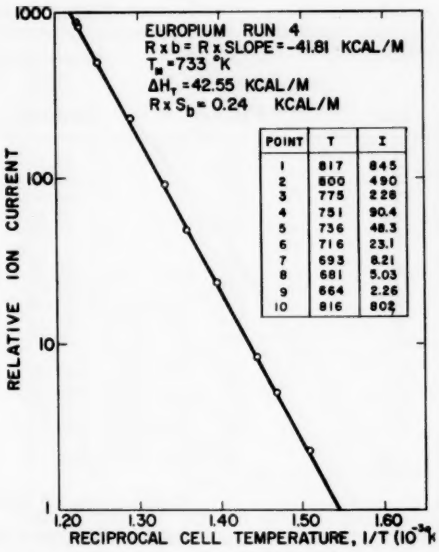

FIG. 1. Typical plot of enthalpy sublimation data for europium.

III. PROCEDURE

A. Experimental Details

Approximately 10 observations of relative vapor pressure and cell temperature were taken at equilibrium for each sublimation run as described in B. The checkpoint procedure showed that drift was entirely negligible in the present experiment. Operating conditions were nearly the same for all the metal samples. The residual background pressure was 5×10^{-6} to 1×10^{-5} mm Hg at the highest cell temperatures. No effects on the heats of sublimation were observed in repeated measurements at various residual pressures.

To minimize the effects of contamination, the heater, empty cell, and filament units were outgassed in an auxiliary vacuum system prior to installation in the mass spectrometer. The outgassing temperature (1250°C) was considerably higher than occurred during the sublimation runs. The tungsten filament was outgassed and aged at about 2100°C for several hours before each series of runs. In every case the original crystalline sample was prepared with a very clean (filed) surface. This clean, shiny appearance was unchanged upon microscopic inspection after each series of runs. It may be assumed, at least under Knudsen conditions, that contamination was not a variable in this work.

B. Analysis of Data

Experimental observations of ion currents and cell temperatures were analyzed by means of the Clapeyron equation as described in Sec. III of B

$$\Delta H_T = -Rd\ \ln I/d(1/T) + RT/2 = -Rb + RT/2, \quad (1)$$

TABLE I. Summary of results for europium.

Run	Midrange temperature T_m (°K)	Experimental slope $-bR$ (kcal/mole)	Temperature term $RT_m/2$ (kcal/mole)	Latent heat ΔH_T (kcal/mole)	Weight $1/S_b^2$
1	737	41.42	0.73	42.15	131
2	731	41.44	0.72	42.17	49
3	741	41.37	0.73	42.11	19
4	733	41.81	0.72	42.54	69
5	730	41.38	0.72	42.11	56
6	735	41.67	0.73	42.40	32
7	728	40.25	0.72	40.97	13
8	714	40.40	0.70	41.11	71
9	714	41.13	0.70	41.83	10
10	740	40.41	0.73	41.15	31
11	745	42.78	0.74	43.52	14
12	751	42.50	0.74	43.24	13
13	694	41.52	0.68	42.21	8
14	693	42.04	0.68	42.73	19
Mean	727			42.06	

Expected standard deviation of mean, S_e 0.09 kcal/mole

Standard deviation of mean, S_b 0.16 kcal/mole

Instrumental error ($2\times1.6\times42.1/727$) 0.19 kcal/mole

Net experimental error 0.25 kcal/mole

Orifice correction -0.02 kcal/mole

Enthalpy of sublimation, ΔH_{727} 42.04 ± 0.25 kcal/mole

where ΔH_T is the heat of sublimation; R is the universal gas constant; I is the ion current; T is the absolute temperature; and b is the slope of a plot of $\ln I$ vs $1/T$. Such a plot is substantially straight over a moderate range of $1/T$. The $RT/2$ term was taken at the "midrange" temperature (T_m) corresponding to the central value of $1/T$ rather than at the central value of T. The value $R=1.9869$ cal mole^{-1} deg^{-1} was used.

The accuracy of such an analysis depends on the fulfillment of certain stringent experimental requirements. The constant of proportionality between vapor pressure and beam current must be truly independent of cell temperature. Geometrical factors must remain constant during each run and the ionization efficiency of the filament must not change with incident atom flux or with time. Constant geometry was readily attained. Surface conditions of the ribbon ionization filaments can affect the ionization efficiency. Preliminary experiments to insure the constancy of the ionization efficiency were made as described in Sec. III C of A. The study has been extended in more detail as part of a separate project on surface ionization by H. G. Fox of this laboratory,[6] and the results will be described in a future publication. For the present study only filament temperatures above which ionization efficiency was independent of incident atom flux were used.

Details concerning the treatment of the experimental data are found in Sec. III C of B. A "data plot" of $\ln I$ vs $1/T$ was employed for each run and analyzed by a standard least-squares method for the best value of the slope b. The corresponding standard error in b from the statistics alone is S_b. For an individual run, $\Delta H_T=-Rb+RT_m/2$, and the statistical error in ΔH_T is almost exactly RS_b. For convenience the term "experimental slope" will be employed for the positive term $-Rb$ in this equation. A small systematic correction arising from thermal expansion of the effusion orifice was added to the final ΔH values.

C. Treatment of Errors

The experimental error assigned to the ΔH values is the compounded error due to random effects and to instrumental uncertainties in the ion current and temperature (Sec. III D of B). The net random error manifests itself directly in the statistical fluctuations of the several runs taken with each sample so that component random effects need not be considered separately. The instrumental error arising from the ion current measurement was negligible compared to that arising from the temperature measurement. The fractional instrumental error in ΔH due to temperature uncertainties is twice the fractional error in temperature when the *absolute* error in T is (conservatively) assumed to be independent of T. The instrumental temperature error was combined by root mean square methods with the net random error to obtain the final experimental uncertainty.

[6] H. G. Fox, (unpublished M.S. thesis, Iowa State University, Ames, Iowa, 1959).

The net random error in the weighted mean of a series of runs was taken simply to be the observed standard deviation S_0 of the mean as normally computed[7a] and represents primarily the run-to-run fluctuations. A check on the validity of the statistical procedures may be had by comparing the "external" or observed consistency of the data (measured by S_0) with its "internal" or expected consistency (measured by S_e) as described by Topping.[7b] The quantity S_e is simply the value of S_0 that would be predicted from the predetermined random errors in the individual runs of a series without heeding run-to-run fluctuations. A ratio S_0/S_e much greater than unity indicates either additional random effects operating from run to run or else unsuspected (varying) systematic errors in the individual runs. A ratio much less than unity usually indicates some anomaly in connection with the individual points within a single run so that incorrect weights are assigned. The comparison also helps to check for gross mistakes. When no further improvement in experimental control is feasible, the larger of S_0 or S_e is used. (In the present work, S_0 was comparable to or greater than S_e; this situation suggested that the ordinary statistical weighting procedure should be used rather than the "lumped data" procedure. In any case, the tiny effects arising from obscure differences in statistical procedure have no physical significance.)

The accuracy of these measurements depends on the insensitivity of the net instrumental gain to variations in cell temperature. The extreme precautions to avoid such effects have been described.[1,2,4] In addition, the present method yields results in excellent agreement with accurate independent determinations where circumstances permit a comparison. It is believed that such systematic effects are sufficiently small to justify the omission of a special error term.

IV. DATA AND RESULTS

The experimental heats of sublimation at T°K are tabulated in this section. These results were reduced to 298°K and 0°K (cohesive energies) by means of the Kirchhoff equations. Running conditions and handling techniques for each element depended upon the relative volatility and chemical activity of the sample.

A. Europium

The europium metal was produced in the Ames Laboratory by a method described by F. H. Spedding, *et al.*[8] A spectroscopic analysis of the europium samples indicated a purity of better than 99.5%, the major impurities being Sm and Ca. Mass spectrometric analysis indicated that the samarium impurity appeared to predominate, and that the other rare earths were negligible. The samples were solid polycrystals over the temperature range covered. Europium metal reacts rapidly with water vapor or moist air, and special handling techniques were required to prevent surface reactions. For this purpose, a dry box was constructed over the source region of the mass spectrometer. Final cleaning (filing) and transportation of the metal to the ion source was accomplished in the dry box. Dry helium was used to flush the box and the spectrometer during all handling of the sample (by means of clean forceps). After the sublimation runs the spectrometer was again vented to dry helium and the sample was removed to the dry box. No visible reaction was apparent on the sample surface after the runs. Measurements were made with the ionization filament above 2100°K to ensure a constant ionization efficiency. With the system hot and operating, the pressure was always less than 5×10^{-6} mm Hg. Sublimation results for europium metal were taken at an average midrange temperature of 727°K. Two samples were loaded separately and seven runs were made on each while in the spectrometer during a 3.5-hr period. Both samples were cut from the same piece and the results for each were statistically indistinguishable. (The Eu^{153} beam was used.)

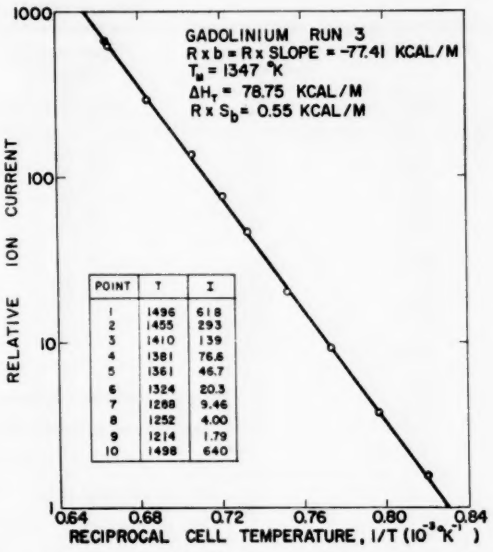

FIG. 2. Typical plot of enthalpy sublimation data for gadolinium.

Figure 1 is a typical plot of the data which were obtained for a single europium sublimation run. The experimental data for this plot are shown as an inset on the figure; the ordinate multiplier is 10^{-14} amp. Results for the 14 sublimation runs are shown in Table I. The mean enthalpy of sublimation was found to be 42.04± 0.25 kcal/mole at 727°K. The enthalpies of sublimation at 298°K and 0°K were obtained by means of the

[7] (a) J. Topping, *Errors of Observation and Their Treatment* (The Institute of Physics, London, 1955), Sec. 42, pp. 88–89. Our S_0 is $\sigma/(\Sigma\omega_i)^{\frac{1}{2}}$ on p. 89, top. (b) Sec. 43, pp. 91–93. Our S_e is the α of Eq. 13, p. 92, as applied to ΔH.

[8] F. H. Spedding, J. J. Hanak, and A. H. Daane, Trans. AIME **212**, 378 (1958).

TABLE II. Summary of results for gadolinium.

Run	Midrange temperature T_m (°K)	Experimental slope $-bR$ (kcal/mole)	Temperature term $RT_m/2$ (kcal/mole)	Latent heat ΔH_T (kcal/mole)	Weight $1/S_0^2$
1	1371	76.94	1.36	78.30	3.6
2	1346	76.16	1.33	77.50	11.4
3	1347	77.41	1.33	78.75	13.0
4	1358	76.40	1.34	77.75	31.9
5	1360	77.85	1.35	79.20	8.8
6	1359	76.73	1.35	78.08	5.0
7	1393	77.32	1.38	78.71	6.5
8	1398	77.13	1.38	78.52	5.0
9	1397	77.97	1.38	79.36	5.2
Mean	1370			78.25	

Expected standard deviation of mean, S_e 0.21 kcal/mole

Standard deviation of mean, S_0 0.22 kcal/mole

Instrumental error ($2\times2.1\times78.3/1370$) 0.24 kcal/mole

Net experimental error 0.32 kcal/mole

Orifice correction -0.05 kcal/mole

Enthalpy of sublimation, ΔH_{1370} 78.20 ± 0.32 kcal/mole

Kirchhoff equation using high-temperature heat content data taken at this Laboratory[9] and using the assumption of a monatomic vapor in its electronic ground state. The result was $\Delta H_{298}=43.11\pm0.25$ kcal/mole. No low-temperature heat-capacity data are available. However, a classical estimate was employed to give $\Delta H_0=43.4\pm0.4$ kcal/mole. It is known that the europium atomic ground-state is a complex multiplet with splittings in the order of a few hundred wave numbers.[10] This situation results in a slightly higher vapor specific heat than used above and results in a small but appreciable systematic correction to the cohesive energy. Uncertainties in the interpretation of rare-earth spectra have caused this correction generally to be omitted in the literature. However, it appears that the correction may be possible for europium and work on this direction is under way.

F. H. Spedding *et al.*[8] have measured the heat of sublimation of europium by the weight-loss method. They found the heat of sublimation to be 41.101 kcal/mole with a standard error of 0.112 kcal/mole at a midrange temperature of 798°K. The difference between the two results is 0.85 kcal/mole when reduced to the common reference temperature 727°K, or about twice the sum of the standard errors. The error in the weight-loss method does not include instrumental uncertainties.[11] The agreement is considered to be highly satisfactory for a measurement in which the achievement of high precision is difficult.

[9] F. H. Spedding, J. Berg, and A. H. Daane (private communication).

[10] H. N. Russell and A. S. King, Astrophys. J. **90**, 155 (1939).

[11] J. J. Hanak (private communication, 1958).

B. Gadolinium

The gadolinium metal as produced in the Ames Laboratory contained only trace impurities consisting mostly of calcium with lesser amounts of other rare earths. No special handling techniques were necessary since the sample remained clean and bright after the sublimation runs. The smallest ion current was approximately 10^{-17} amp. Measurements were made with the

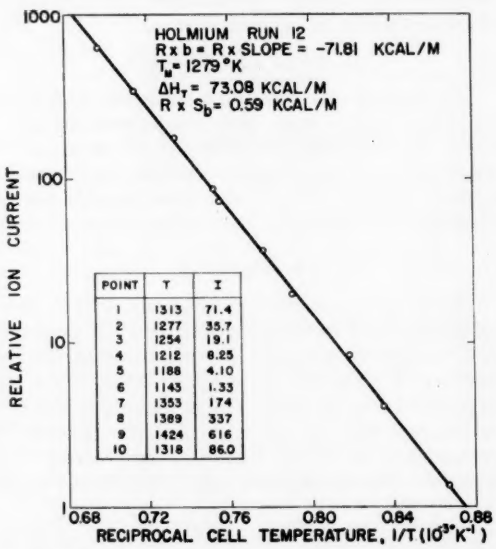

FIG. 3. Typical plot of enthalpy sublimation data for holmium.

TABLE III. Summary of results for holmium.

Run	Midrange temperature T_m (°K)	Experimental slope $-bR$ (kcal/mole)	Temperature term $RT_m/2$ (kcal/mole)	Latent heat ΔH_T (kcal/mole)	Weight $1/S_b^2$
1	1260	69.33	1.25	70.58	4.0
2	1226	71.47	1.21	72.69	2.0
3	1250	67.02	1.24	68.26	1.7
4	1233	73.43	1.22	74.66	5.0
5	1236	77.00	1.22	78.23	1.8
6	1290	71.14	1.28	72.42	6.0
7	1294	76.28	1.28	77.56	1.0
8	1289	73.24	1.28	74.52	3.3
9	1291	72.51	1.28	73.80	6.8
10	1291	72.36	1.28	73.64	2.5
11	1285	72.07	1.27	73.34	2.8
12	1279	71.81	1 27	73.08	11.4
13	1274	75.77	1.26	77.04	2.9
14	1283	69.75	1.27	71.03	5.4
15	1289	69.99	1.28	71.27	2.7
16	1191	72.17	1.18	73.35	9.1
17	1189	73.76	1.18	74.80	9.6
18	1191	70.61	1.18	71.92	2.6
19	1184	71.36	1.17	72.53	9.3
20	1194	70.16	1.18	71.34	13.3
21	1194	71.21	1.18	72.40	11.9
Mean	1248			72.96	

Expected standard deviations of mean, S_e 0.19 kcal/mole

Observed standard deviation of mean, S_0 0.37 kcal/mole

Instrumental error ($2\times2.1\times72.96/1248$) 0.24 kcal/mole

Net experimental error 0.44 kcal/mole

Orifice correction -0.04 kcal/mole

Enthalpy of sublimiation, ΔH_{1248} 72.93 ± 0.44 kcal/mole

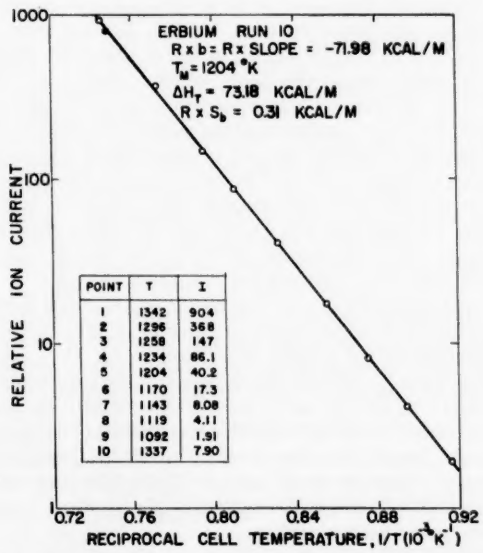

FIG. 4. Typical plot of enthalpy sublimation data for erbium.

ionization filament above 2350°K, and there were no systematic differences in the heats of sublimation taken with the filament at 2350° and 2550°K. Data were taken at cell temperatures near 1370°K. The final result was obtained from nine sublimation runs taken with a single sample. (The Gd^{158} beam was used.)

A typical gadolinium sublimation run is shown in Fig. 2, and a summary of all results is given in Table II. The enthalpy of sublimation was found to be 78.20 ± 0.32 kcal/mole at 1370°K. The heat of sublimation was reduced to 298° and 0°K from the high-temperature heat capacity estimated by Stull and Sinke[12] on the basis of low-temperature data reported by M. Griffel *et al.*[13] The vapor was assumed to be ideal, monatomic, and in its ground state. The results were $\Delta H_{298}=81.22\pm0.32$ kcal/mole and $\Delta H_0=81.91\pm0.32$ kcal/mole. No previous experimental results are available for gadolinium.

[12] D. R. Stull and G. C. Sinke, "The thermodynamic properties of the elements in their standard states," (The Dow Chemical Company, Midland, Michigan, 1955).

[13] M. Griffel, R. E. Skochdopole, and F. H. Spedding, Phys. Rev. **93**, 657 (1954).

TABLE IV. Summary of results for erbium.

Run	Midrange temperature T_m (°K)	Experimental slope $-bR$ (kcal/mole)	Temperature term $RT_m/2$ (kcal/mole)	Latent heat ΔH_T (kcal/mole)	Weight $1/S_b^2$
1	1215	69.73	1.20	70.94	1.0
2	1198	72.81	1.19	74.00	4.4
3	1208	71.74	1.20	72.93	6.9
4	1207	72.46	1.19	73.66	4.8
5	1210	73.46	1.20	74.66	12.0
6	1214	71.18	1.20	72.38	5.4
7	1202	72.81	1.19	74.01	16.5
8	1204	72.50	1.19	73.70	4.9
9	1195	73.27	1.18	74.45	5.9
10	1204	71.98	1.19	73.17	40.7
11	1209	70.67	1.20	71.87	7.1
12	1212	69.92	1.20	71.12	9.8
13	1207	71.64	1.19	72.84	21.1
14	1223	72.12	1.21	73.34	18.9
Mean	1208			73.22	

Expected standard deviation of mean, S_e	0.16 kcal/mole
Observed standard deviation of mean, S_0	0.24 kcal/mole
Instrumental error (2×2.1×73.2/1208)	0.25 kcal/mole
Net experimental error	0.34 kcal/mole
Orifice correction	−0.04 kcal/mole
Enthalpy of sublimation, ΔH_{1208}	73.18±0.34 kcal/mole

C. Holmium

The holmium metal as produced in the Ames Laboratory showed trace amounts of Ca, Fe, Ta, and Yt, and the over-all purity was much better than 99%. The samples were chemically stable at room temperature so that special handling techniques were not required. The smallest ion current was about 10^{-16} amp. For all runs the ionization filament was run above 2300°K where the ionization efficiency was independent of the incident atom flux. Sublimation results for solid holmium were obtained from data taken near 1248°K. The weighted mean latent heat was determined from a set of 21 runs taken with two samples which were from the same piece and which showed no statistical differences.

A typical plot of the data is shown in Fig. 3, and Table III summarizes all of the results. The enthalpy of sublimation for holmium was found to be 72.93±0.44 kcal/mole at 1248°K. Heat capacity results for holmium metal have been obtained by B. C. Gerstein *et al.*[14] from 15° to 300°K. The low-temperature results were extrapolated to high temperatures by the present authors to give an estimate of the heat content of the condensed phase for data reductions to 298° and 0°K. The enthalpies of sublimation at these temperatures were $\Delta H_{298}=75.04\pm0.44$ kcal/mole and $\Delta H_0=75.47\pm0.44$ kcal/mole. No previous experimental heat of sublimation results for holmium metal are known to the authors

D. Erbium

The latent heat of sublimation of erbium metal was determined from a set of 14 sublimation runs taken at an average temperature of 1207°K. Results were obtained with a single sample of better than 99% purity, the major impurities being calcium and other rare earths as detected spectroscopically and by the mass spectrometer. Careful handling sufficed to prevent contamination and the samples remained clean and bright after the runs. (The Er^{166} beam was used.) The smallest ion current was approximately 10^{-17} amp. The ionization filament was run above 2200°K, which was well above the temperature (1900°K) at which surface adsorption first affected the ionization efficiency.

A typical plot of one sublimation run is shown in Fig. 4, and all of the results are in Table IV. The enthalpy of sublimation for erbium was found to be 73.18±0.34 kcal/mole at 1208°K. High-temperature heat content results for erbium metal have been estimated by Stull and Sinke[12] from heat capacity measurements[15] obtained in the Ames Laboratory from 15° to 320°K. Thermodynamic reduction gave $\Delta H_{298}=75.39\pm0.34$ kcal/mole and $\Delta H_0=75.67\pm0.35$ kcal/mole. No previous values are known for comparison.

[14] B. C. Gerstein, M. Griffel, L. D. Jennings, R. E. Miller, R. E. Skochdopole, and F. H. Spedding, J. Chem. Phys. **27**, 394 (1957).

[15] R. E. Skochdopole, M. Griffel, and F. H. Spedding, J. Chem. Phys. **23**, 2258 (1955).

TABLE V. Cohesion of the rare-earth metals.

Metal	Atomic No.	No. of electrons in solid state[17]		No. of electrons in neutral gas[18]			ΔH_{298} kcal/mole
		4*f*	Outer electrons	4*f*	5*d*	6*s*	
Pr	59	2	3	2*	1	2	85.1
Nd	60	3	3	3*	1	2	75.0
Sm	62	5	3	6	0	2	49.9
Eu	63	7	2	7	0	2	43.1
Gd	64	7	3	7	1	2	81.2
Tb	65	8	3	8	1	2	91.9[a]
Dy	66	9	3	9*	1	2	71.4
Ho	67	10	3	10*	1	2	75.0
Er	68	11	3	11*	1	2	75.4
Tm	69	12	3	13	0	2	57.5
Yb	70	14	2	14	0	2	40.0
Lu	71	14	3	14	1	2	102.8[a]

[a] D. M. Jackson, O. C. Trulson, D. E. Hudson, and F. H. Spedding, preliminary results from this Laboratory.

V. SUMMARY OF RARE-EARTH COHESIVE ENERGIES

The sublimation enthalpies of all of the stable rare earths have been measured accurately by the mass-spectrometric method in this Laboratory.[1,2] The cohesive energy is the enthalpy of sublimation at 0°K, ΔH_0; the values are generally less than 1 kcal/mole more than ΔH_{298}. The values of ΔH_{298} for the rare earths are tabulated in Table V. (An accurate tabulation of ΔH_0 is omitted for the present because low-temperature specific heats are not available for some of the elements. The tabulation adequately illustrates the cohesion of the series.) For consistency, only the mass spectrometric values are included. In those cases where other precise measurements have been made in the Ames Laboratory, the agreement has been excellent.[8,16]

A critical feature of Table V is the configuration assignments. The solid assignments are supported by the magnetic measurements of Legvold, Spedding, and coworkers.[17] The gaseous assignments are those given by Herzberg,[18] but some are still open to question.

Contrary to earlier estimates, the cohesive energies of the rare-earth metals are quite dissimilar. Some of the indicated differences may be associated with the number of valence electrons per atom available for binding. Spectroscopic information indicates that the outer incomplete electronic shells of the neutral rare-earth atoms are of 4*f*, 5*d*, and 6*s* character. In the solid the two 6*s* electrons are assumed to be relatively free and thus promote cohesion. Conversely, the 4*f* electrons are assumed to be fixed to the ion cores and to be responsible for the magnetic behavior of the solids. Electrons of 5*d* character play a part in determining the relative cohesive energies of the solids. For those rare earths which exhibit large cohesive energies, the 5*d* electrons are assumed to be relatively free to aid in cohesion. However, in those with very low cohesive energies the 5*d* electrons are probably absent (Eu, Yb).

The observed variations in cohesion are quantitatively rather more than are reasonable from consideration only of the number of electrons available for solid binding. An attractive explanation is suggested by the electron configurations of Table V. Consider the sequence Er, Tm, Yb, Lu. Erbium sublimes from a "trivalent" metal into a trivalent gas and has a normal cohesion (75.4 kcal/mole). (The term "valency" in connection with the metallic state is used only for convenience of description.) Thulium appears to sublime from a trivalent metal into a divalent gas. The net energy of the two trivalent metals, aside from the over-all lanthanide contraction, should be comparable in magnitude. However, it is reasonable to suppose that the divalent gas atom is intrinsically more tightly bound than the adjacent trivalent gas atom. Hence, Tm has a smaller energy difference (57.5 kcal/mole between the solid and gaseous states than does Er. Ytterbium, on the other hand, should be more loosely bound in the divalent metal than is Tm in the trivalent metal. Furthermore, divalent Yb in the gas should have binding comparable to its trivalent neighbor Tm, again ignoring the over-all contraction. Hence, Yb (40

[16] Complete references are listed in references (1) and (2) of this paper.

[17] (a) B. L. Rhodes, S. Legvold, and F. H. Spedding, Phys. Rev. **109**, 1547 (1958); (b) C. J. Kevane, S. Legvold, and F. H. Spedding, *ibid.* **88**, 1092 (1953); (c) S. Legvold and F. H. Spedding (private communications, 1958–60).

[18] G. Herzberg, *Atomic Spectra* (Dover Publications, New York, 1944), pp. 140–141. The * indicates assignments which are still in some question, and for which the 4*f* shell is shown with one more electron in some references.

kcal/mole) is somewhat more loosely bound than Tm because the metal has more energy, and much more lightly bound than Er both because its metal has more energy and because its gas has less energy. The next element, Lu, exhibits a trivalent metal subliming into a trivalent gas and shows a large cohesive energy. A similar argument applies in detail to the Nd, Sm, Eu, Gd sequence.

The argument given cannot account for small departures of a few kcal/mole from the qualitative regularities expected. The over-all contraction is well exhibited between Gd and Tb and between Dy and Ho; however, it is poorly exhibited between Ho and Er and shows a cohesion anomaly between Pr and Nd. It is clear that the numerical details of the cohesion await a thorough theoretical treatment of a very complex problem. It does appear that some of the unexpected variations in cohesion are due to the energetics of the gaseous state and are not related intrinsically to the physical conditions within the solid.

In conclusion, we feel that the qualitative features of the large variations in rare-earth cohesion may be understood on the basis of rather gross considerations of solid and gaseous energetics. The necessary reasonable presumptions are: (1) that a trivalent metal has lower energy than a divalent metal; (2) that a divalent gas has lower energy than a trivalent gas; and (3) that a trivalent metal may sublime into a divalent gas. This third point is suggested from the magnetic measurements on the solids and by spectroscopic data on the gases; it now is supported by the data on cohesion. Finally, the information obtained from cohesive energy measurements on the rare earths presents an interesting problem in regard to metallic cohesion and thus provides an important subject for theoretical study.

ACKNOWLEDGMENTS

The authors wish to thank Dr. A. H. Daane for furnishing the pure rare-earth samples. Constructive and stimulating discussions with Professor R. E. Rundle are gratefully appreciated. Mr. H. G. Fox provided necessary surface ionization data and assisted in data-taking. Mr. D. M. Jackson carried out numerical analyses on an IBM 650 digital computer and helped to maintain the experimental apparatus.

THE JOURNAL OF CHEMICAL PHYSICS VOLUME 35, NUMBER 3 SEPTEMBER, 1961

Nature of the Metal-Ligand Bond in Some Complex Cyanides from a Study of Raman Intensities*

GEORGE W. CHANTRY AND ROBERT A. PLANE

Department of Chemistry, Cornell University, Ithaca, New York

(Received February 8, 1961)

A study of the Raman spectra of solutions of $Zn(CN)_4^{=}$, $Cd(CN)_4^{=}$, $Hg(CN)_4^{=}$, $Co(CN)_6^{-3}$, $Cu(CN)_4^{-3}$, $Ag(CN)_4^{-3}$, and $Fe(CN)_6^{-4}$ shows that these complex ions fall into two distinct sets. For the first set, consisting of the first four species, the A_1CN frequencies are 2143, 2145, 2148, and 2152 cm^{-1} and the $\bar{\alpha}_{CN}'$ lie intermediate between those determined for free CN^- and CH_3CN. For the latter three species, the corresponding frequencies are 2094, 2097, and 2094 cm^{-1}. Furthermore, members of the latter set have abnormally large Raman intensities, i.e., large $\bar{\alpha}_{CN}'$, and an additional ultraviolet absorption band at 2600 A. For the first group, the assumption of partial sigma bonding of metal to C, consistent with the principle of essential electroneutrality, explains both the observed force constants and the values of $\bar{\alpha}_{CN}'$. The low intensity found for the ν_2 mode is explained in terms of the effect on this quantity of the large amount of s character in the carbon sigma orbital. The second group cannot be simply treated and appears to present an example of the breakdown of bond localized polarizabilities.

THE force constants of a ligand molecule usually change when the ligand coordinates to a metal atom, and a study of such changes can provide valuable information about the nature of the metal-to-ligand bonding. Thus, Woodward and Hall,[1] by comparing the CO force constants in $Ni(CO)_4$, BH_3CO, and CO, have shown recently that the NiC bonds in $Ni(CO)_4$ have appreciable double bond character. A knowledge of the NiC force constant alone could not provide this information since standard values for NiC single and double bonds are not available for comparison. A weakness of the method lies in the approximations which must be made in deriving the force constants. This means that their values are subject to possible errors of the same magnitude as the difference between the force constants of the free and bound ligand. Additional information bearing on metal-ligand bonding can be gained from measurement of the intensities in the Raman effect. Raman intensities are determined by the derivatives of molecular polarizability with respect to elongations of various bond lengths. With the approximation that the polarizability changes are localized in the distorted bonds, the derivatives bear a formal analogy to force constants. Again the individual derivatives with respect to the metal-ligand bond give little information since standard values for single and double bonds are lacking. However, a study of the various derivatives associated with the ligand itself should give some indication of the amount and character of electron donation from the ligand to the metal. For this reason, absolute Raman intensities have been measured for a set of complex cyanides, two of which, $Cu(CN)_4^{-3}$ and $Zn(CN)_4^{-2}$ are isoelectronic with $Ni(CO)_4$. The other complex ions included in the present study are $Fe(CN)_6^{-4}$, $Co(CN)_6^{-3}$, $Ag(CN)_4^{-3}$, $Cd(CN)_4^{-2}$, and $Hg(CN)_4^{-2}$. Intensities have also been recorded for CH_3CN and CN^-, with a view to using their bond derived polarizabilities as standards for the elucidation of the metal-ligand bond order.

EXPERIMENTAL

Raman spectra of the various complexes were measured on solutions of the sodium or potassium salts. The preparation of most of these and the identification of their spectra have previously been described.[2] $K_2Fe(CN)_6$ was purified by recrystallization of the A.R. salt; this resulted in a marked weakening of the yellow color. $Na_3Co(CN)_6$ was prepared by a standard method,[3] and on recrystallization gave an almost white product. A.R. grade NaCN was used without further purification. The spectrum of acetonitrile was recorded from a solution in CCl_4 which served as internal standard. Likewise, the spectra of the inorganic ions were recorded from aqueous solutions containing either ClO_4^- or NO_3^- as internal standard. Spectra were measured using the Cary model 81 Raman spectrophotometer. Both Hg 4358 A and Hg 4047 A served as exciting lines, except in the case of $Fe(CN)_6^{-4}$ which decomposes rapidly when irradiated by 4047 A. The determination of the absolute intensities for CCl_4, NO_3^-, and ClO_4^-, and the determination of the wavelength sensitivity of the instrument have been previously described.[4]

RESULTS

The frequencies and intensities of all A_1 lines detected are given in Tables I and II. The intensities in both

* This work was supported by the United States Air Force through the Air Force Office of Scientific Research and Development Command.

[1] L. A. Woodward and J. R. Hall, Spectrochimica Acta **16**, 654 (1960).

[2] G. W. Chantry and R. A. Plane, J. Chem. Phys. **33**, 736 (1960).

[3] *Inorganic Syntheses*, edited by W. C. Fernelius (McGraw-Hill Book Company, Inc., New York, 1946), Vol. II, p. 226.

[4] G. W. Chantry and R. A. Plane, J. Chem. Phys. **32**, 319 (1960).

TABLE I. Raman intensity data.

Species	A_1 frequencies (cm^{-1})	Relative intensity/CN[a]
CCl_4	459	1.00
CN^-	2079	1.00
$Zn(CN)_4^{=}$	2143	1.55
$Cd(CN)_4^{=}$	2145	1.60
$Hg(CN)_4^{=}$	2148 340	1.60 0.013
$Co(CN)_6^{-3}$	2152 404	1.68 0.015
$Cu(CN)_4^{-3}$	2094	2.78
$Ag(CN)_4^{-3}$	2097	3.15
$Fe(CN)_6^{-4}$	2094	3.48

[a] The intensities are those of the isotropic part of the scattering, and have been corrected for all frequency dependent factors.

tables have been corrected for all wavelength dependences and also for the anisotropy factor $[6/(6-7\rho)]$. It should be noted that the intensities in Table I are the quantities found, divided by the number of cyanides in the complex in order to facilitate comparison between molecules having different numbers of cyanide groups. The intensities given for $Zn(CN)_4^{=}$, $Cd(CN)_4^{=}$, $Hg(CN)_4^{=}$, and $Co(CN)_6^{-3}$ are the mean values of several investigations using both exciting lines, and are precise to a few percent. Those for the remainder are not so accurate due to the difficulty of resolving the A_1 line from that of free cyanide ion less than 20 cm^{-1} away. However, when allowance is made for this increased uncertainty, no difference is found between the intensities excited by Hg 4358 A and Hg 4047 A, so that there is no indication of resonance effects in any of the ions studied. The intensities and degrees of depolarization of CH_3CN have been determined previously by Evans and Bernstein,[5] whose results are also quoted in Table II.

The Raman intensities of CH_3CN present many interesting facets, and it seems worth while to carry out a normal coordinate treatment for this molecule. The Crawford and Brinkley[6] force field is employed, with the CC force constant as given. The G matrix elements have been given by Pillai and Cleveland[7] for the general case where no assumptions are made about the magnitude of the HCH angles, and these authors have also listed a set of potential constants. We have assumed tetrahedral angles for the methyl group since it does not seem worth while to make the required slight corrections to G when there are such gross approximations in F.

The A_1 parts of the transformation $\mathfrak{L}$ and of its inverse $\mathfrak{L}^{-1}$ are found to be

$\mathfrak{L}$	Q_1	Q_2	Q_3	Q_4
S_1	1.009280	−0.022714	0.022582	0.011939
S_2	0.008014	0.390014	0.007975	0.049125
S_3	−0.143850	−0.016401	1.548449	−0.097673
S_4	−0.059689	−0.251004	0.134038	0.286300

$\mathfrak{L}^{-1}$	S_1	S_2	S_3	S_4
Q_1	0.986230	0.025310	−0.010251	−0.049235
Q_2	−0.038134	2.313130	0.022206	−0.387729
Q_3	0.099149	0.150696	0.627647	0.184126
Q_4	0.124947	1.963201	−0.276509	3.056434

with the chemical atomic weights used for the masses of the atoms. (Entries in these matrices are established to but two figures; six are retained for mathematical consistency. cf. reference 7.) The symmetry coordinates used in deriving these matrices are

$$S_1=1/\sqrt{3}(\Delta r_1+\Delta r_2+\Delta r_3)$$
$$S_2=\Delta R$$
$$S_3=1/6^{\frac{1}{2}}(\Delta\alpha_1+\Delta\alpha_2+\Delta\alpha_3-\Delta\beta_1-\Delta\beta_2-\Delta\beta_3)$$
$$S_4=\Delta L,$$

where r denotes a CH distance, R the CN distance, α an HCH angle, β an HCC angle, and L the CC distance. In calculating the bond derived polarizabilities, it is convenient to proceed via the derivatives with respect to the symmetry coordinates and to assemble these into a row vector $[\bar{\alpha}'_s]$. Likewise, the derivatives with respect to normal coordinates are assembled into a row vector $[\bar{\alpha}'_Q]$ and then these two vectors are related by[8]

$$[\bar{\alpha}_Q']=[\bar{\alpha}_s']\mathfrak{L}.$$

TABLE II. Raman intensity data.

Species	A_1 frequencies (cm^{-1})	Relative intensity: Present work	Relative intensity: Evans and Bernstein[5]
CCl_4	459	1.000	1.000
CH_3CN	2941	5.01 (ρ=0.09)	4.42 (ρ=0.09)
	2248	1.85 (ρ=0.10)	1.38 (ρ=0.20)
	1371	0.054 (ρ=0.60)	0.079 (ρ=0.52)
	919	0.107 (ρ=0.20)	0.112 (ρ=0.17)

[5] J. C. Evans and H. J. Bernstein, Can. J. Chem. **33**, 1746 (1955).

[6] B. L. Crawford and S. R. Brinkley, J. Chem. Phys. **9**, 69 (1941).

[7] M. G. K. Pillai and F. F. Cleveland, J. Mol. Spectroscopy **5**, 212 (1960).

[8] This equation, which is merely a form of the rule for partial differentiation, is a convenient starting point for proving the two intensity sum rules [B. L. Crawford, J. Chem. Phys. **20**, 977 (1952)], for by transposition: $[\bar{\alpha}'_Q]'=\mathfrak{L}[\bar{\alpha}'_s]'$; multiplying the two together: $[\bar{\alpha}'_Q]\times[\bar{\alpha}'_Q]'=[\bar{\alpha}'_s]\mathfrak{L}\mathfrak{L}[\bar{\alpha}'_s]'=[\bar{\alpha}'_s]G[\bar{\alpha}'_s]'$. The L.H.S. is the sum of the corrected intensities and the R.H.S. is an isotopic invariant when the known corrections to G are applied. In a similar manner, Crawford's F sum rule can be demonstrated.

For acetonitrile the four derivatives with respect to the normal coordinates and to the symmetry coordinates are

$$\bar{\alpha}_{Q1}'=1.503\ \text{A}^2\ g^{-\frac{1}{2}} \qquad \bar{\alpha}_{s_1}'=1.49\ \text{A}^2$$

$$\bar{\alpha}_{Q2}'=0.915\ \text{A}^2\ g^{-\frac{1}{2}} \qquad \bar{\alpha}_{s_2}'=2.61\ \text{A}^2$$

$$\bar{\alpha}_{Q3}'=0.156\ \text{A}^2\ g^{-\frac{1}{2}} \qquad \bar{\alpha}_{s_3}'=0.042\ \text{A}^2$$

$$\bar{\alpha}_{Q4}'=0.220\ \text{A}^2\ g^{-\frac{1}{2}} \qquad \bar{\alpha}_{s_4}'=0.272\ \text{A}^2.$$

The low value of $\bar{\alpha}_{s_3}'$ is to be noted since the theory of Raman intensities proposed by Wolkenstein[9] predicts that it should be zero and in fact the corresponding quantity for the methyl groups in the tetramethyls of group IV elements has been shown to be zero.[10] It is not obvious whether the finite value for CH_3CN arises from a failure of the Wolkenstein theory or from inadequacies of the force field. The low value does not rule out the latter possibility. The final derivatives with respect to the three bond lengths are found to be

$$\bar{\alpha}_r'=0.86\ \text{A}^2$$

$$\bar{\alpha}_R'=2.61\ \text{A}^2$$

$$\bar{\alpha}_L'=0.272\ \text{A}^2.$$

The first of these (for a CH bond) is somewhat lower than the value for ethane determined by Yoshino and Bernstein (1.04 A^2),[11] and when it is borne in mind that these authors found the quantity to be constant for a wide range of compounds and that Chantry and Woodward[12] found it to have the same value for the tetramethyls of group IV elements, it seems that the low value found here cannot be attributed to any change of electronic configuration. More likely the diminution is due to residual refractive index effects and to the effect of the internal field. If this is the case, all three derivatives will be decreased by about the same factor. Nevertheless, that for the CC bond ($\bar{\alpha}_L'$) is but half the value for the corresponding bond in ethane. This result is a confirmation of the earlier suggestion that as the amount of *s* character in the carbon hybrids increases, the value of $\bar{\alpha}_{CC}'$ diminishes[4]; in CH_3CN the presumed sp^3-sp bonding should drop the value below that in ethane. The extreme example of this effect occurs in diacetylene where the intensity of that mode which is primarily the stretching of the central CC bond is so small that it has only recently been detected.[13] The same effect shows itself in the complex cyanides. Of those studied, only two have ν_2 of observable intensity, and these are quite weak (see Table I).

[9] M. Wolkenstein, Compt. rend. acad. sci. U.R.S.S. **32**, 185 (1941).

[10] D. N. Waters and L. A. Woodward, Proc. Roy. Soc. (London) **A246**, 119 (1958).

[11] T. Yoshino and H. J. Bernstein, *Molecular Spectroscopy (Proceedings of the Institute of Petroleum and the Hydrocarbon Research Group Conference, London)* (Pergamon Press, New York, 1959).

[12] G. W. Chantry and L. A. Woodward (unpublished work).

[13] A. Vallance Jones, Proc. Roy. Soc. (London) **A211**, 285 (1952).

TABLE III. Derived bond polarizabilities.

Species	$\bar{\alpha}_{CN}'$, A^2
CN^-	1.71
$Zn(CN)_4^{-2}$	2.12
$Cd(CN)_4^{-2}$	2.16
$Hg(CN)_4^{-2}$	2.16
$Co(CN)_6^{-3}$	2.21
CH_3CN	2.61
$Cu(CN)_4^{-3}$	2.84
$Ag(CN)_4^{-3}$	3.03
$Fe(CN)_6^{-4}$	3.18

Calculation of the bond derived polarizabilities for the complex cyanides is hindered by the nonobservability of the ν_2 vibration for most of them. In essence, three force constants must be determined from one frequency. Any force field derived under these conditions would be so approximate that the calculations would not be justified; so this has been performed only for $Hg(CN)_4^{-2}$ and $Co(CN)_6^{-3}$, where the ν_2 frequency is observable. For the rest, the bond derived polarizabilities were calculated using the approximation

$$l_{11}^2=G_{11}=\mu_C+\mu_N,$$

where l_{11} is the first row and first column entry in $\mathfrak{L}$, and μ denotes the reciprocal mass. This approximation is not expected to cause appreciable error since the diagonal entries in $\mathfrak{L}^{A_1}$ will not be sensitive functions of the potential constants chosen, due to the wide separation of the two frequencies. The $\mathfrak{L}^{A_1}$ matrices, in the same units as previously, for $Hg(CN)_4^{-2}$ and $Co(CN)_6^{-3}$ are

$Co(CN)_6^{-3}$		Q_1	Q_2
	S_1	0.392814	0.019786
	S_2	−0.221297	0.185181

$Hg(CN)_4^{-2}$		Q_1	Q_2
	S_1	0.393086	0.011577
	S_2	−0.217409	0.189729

where

$$S_1=1/N^{\frac{1}{2}}(\Delta R_1+\Delta R_2+\Delta R_N)$$

$$S_2=1/N^{\frac{1}{2}}(\Delta r_1+\Delta r_2+\Delta r_N)$$

with R being the CN length and r, the MC length. The final derived bond polarizabilities are listed in Table III.

DISCUSSION

Before considering the Raman intensities, it will be instructive to see what information can be gained from the force constants of the complexes. Since those of $Hg(CN)_4^{-2}$ are the most complete, they will be dis-

cussed first. Pauling[14] has argued that the magnitude of the charge on the central atom in complexes such as these cannot exceed unity. Clearly this can come about in two ways; either by partial σ bonding to the metal by the lone pair of electrons of the carbon atom, or else by full σ bonding followed by an outflow of negative charge from the metal by partial π bonding. If the first mechanism is followed, then HgC bond order will be higher in $Hg(CN)_2$ than in $Hg(CN)_4^{-2}$, if, as seems likely, the formal charge on Hg is about the same in both. Woodward and Owen[15] have carried out simple valence force field calculations for these species. They find that the HgC force constant is indeed much higher in $Hg(CN)_2$ than in $Hg(CN)_4^{=}$, and that the CN constants of both are higher than in CN^-, with $Hg(CN)_2$ showing the greater augmentation. This latter result is expected because the lone pair of electrons on the C atom weakens the bonding and its partial withdrawal leads to tighter bonding and a larger CN force constant. Thus, the evidence from force constants supports the "σ alone" picture of the bonding in these complexes since any appreciable HgC π bonding should lower the CN force constant relative to CN^-.

The previous results, however, have been obtained by assuming that the force constant coupling the CN bond length to the HgC bond length is zero. This is probably a very rough approximation, and Woodward and Owen are careful to point out that the apparent increase in the CN force constant may be illusory because of it. If this coupling constant is denoted by F_{12} and the two remaining A_1 constants (F_{11} and F_{22}) are solved in terms of it, the graph of each plotted against F_{12} takes the form of an ellipse. The ellipse calculated for $Hg(CN)_4^{=}$ shows a flat minimum near the origin [as is also true for the very similar ellipse for $Hg(CN)_2$]. Judging from molecules for which complete force fields have been determined, F_{12} in all probability lies between -1.0×10^5 d/cm and $+2.0\times10^5$ d/cm. Because of the flat minimum in this region, the value of F_{22} is specified with some accuracy (between 2.09×10^5 d/cm and 1.88×10^5 d/cm). This quantity is equal to the HgC stretching force constant plus the HgC, HgC interaction constant for $Hg(CN)_2$, or plus three times this value for $Hg(CN)_4^{=}$. Since this interaction constant is positive and since the value of F_{22} is greater for $Hg(CN)_2$ than for $Hg(CN)_4^{=}$, there can now be no doubt that the HgC stretching force constant is greater for $Hg(CN)_2$. Thus, the conclusion reached above is confirmed. Unfortunately, this analysis also shows that no conclusion can be drawn as to the nature of the HgC bond from the CN force constant. The limits of F_{11} (15.89×10^5 d/cm to 19.23×10^5 d/cm) include both the value of CN^- (16.55×10^5 d/cm) and of CH_3CN (17.73×10^5 d/cm). Similarly, little can be learned this way about $Co(CN)_6^{-3}$, even though both frequencies are known, and still less about $Zn(CN)_4^{=}$ and $Cd(CN)_4^{=}$. However, since the ν_1 frequencies of these three species are nearly coincident with that of $Hg(CN)_4^{=}$, it is possible to take this fact as indication that the bonding in them is similar.

The cyanide complexes of Cu, Ag, and Fe have their ν_1 frequencies some 50 cm^{-1} lower than that of $Hg(CN)_4^{=}$. Presumably their CN force constants are also lower. Chiorbolli and Testa[16] have claimed to have observed the ν_2 vibration of $Cu(CN)_4^{-3}$ at 502 cm^{-1}, but Jones[17] thinks this assignment unlikely and on the basis of another of their quoted low frequencies (288 cm^{-1}), for which additional evidence suggests the assignment as ν_2, has calculated a set of potential constants. We have searched this region with our spectrophotometer and although we find some lines there, none appears polarized. Although our measurements were made at the limit of our sensitivity and it is possible that there is a coincident depolarized line, it seems that further discussion of force constants for $Cu(CN)_4^{-3}$ should await confirmation of the earlier work. Even if the value of the CN force constant were known, an unambiguous decision between the two models for CuCN bonding could not be made because both predict this quantity to be less than in the isoelectronic $Zn(CN)_4^{-2}$.

A comparison of the Raman intensities of the complex cyanides shows that they again divide into the same two groups. The ν_1 intensities of the first group, $Zn(CN)_4^{=}$, $Cd(CN)_4^{=}$, $Hg(CN)_4^{=}$, $Co(CN)_6^{-3}$, are nearly identical and are about half the values found for the second group, $Cu(CN)_4^{-3}$, $Ag(CN)_4^{-3}$, $Fe(CN)_6^{-4}$. Table III shows that the values for the bond derived polarizabilities for the first group lie midway between the values for CN^- and CH_3CN. Thus, these data in conjunction with the feeble ν_2 intensities conform to a model for these four complexes of partial MC σ bonds (without π bonding) occurring to an extent consistent with essential electrical neutrality. For the second group, the $\bar{\alpha}_{CN}'$ values exceed that for CH_3CN. This might be taken to imply an MC bond order greater than unity; but such an inference does not seem justified. The essential reason for the larger $\bar{\alpha}_{CN}'$ in CH_3CN than in CN^- is the same as that for the increased force constant, namely the effect of electron correlation. When, however, the MC bond order exceeds unity, bonding electrons are removed from the CN region and hence $\bar{\alpha}_{CN}'$ should not increase, but would probably decrease. Thus it would seem that the intensity data for the latter group conform to expectations based on neither bonding picture. The inconsistency is shown clearly by a consideration of the ν_2 vibrations for the isoelectronic pair $Fe(CN)_6^{-4}$ and $Co(CN)_6^{-3}$. Since this line is observed for the latter but not the former, it would seem that the MC bond order is higher in $Co(CN)_6^{-3}$, as the "σ alone"

[14] L. Pauling, J. Chem. Soc. **1948**, 1461.
[15] L. A. Woodward and H. F. Owen, J. Chem. Soc. **1959**, 1055.
[16] P. Chiorbolli and C. Testa, Ann. chim. (Rome) **47**, 639 (1957).
[17] L. H. Jones, J. Chem. Phys. **29**, 463 (1958).

picture would predict. In fact, Samuel and Kahn[18] came to this conclusion even before Placzek's[19] development of the theory of Raman intensities, and yet the intensity of ν_1 for $Fe(CN)_6^{-4}$ is twice that for $Co(CN)_6^{-3}$. In passing it should be remarked that the failure of $Co(CN)_6^{-3}$ to show a resonance Raman effect despite its absorbing at both 4358 A and 4047 A is readily explained. The absorption is due to the longer wavelength ligand field band, which is essentially an atomic transition.

At the present stage of development of this subject there seems little alternative, for the second group of complexes, to abandoning the first postulate of bond polarizability theory. Thus, for these species, it seems that polarizability changes cannot be localized in bonds. Apparently there is extensive delocalization of electrons so that even the bonding electrons near the metal atom are affected by changes in the CN distance. Although this explanation lacks, at present, theoretical foundation, such electronic effects should be manifest in absorption spectra. The CN^- ion in aqueous solution shows a single intense absorption band which starts at about 2400 A and continues to rise below 2000 A. The spectra of $Hg(CN)_4^=$, $Cd(CN)_4^=$, $Zn(CN)_4^=$ are identical with that of CN^-. This absorption can be attributed to a charge transfer process within the CN^-. The spectrum of $Co(CN)_6^{-3}$ has an identical short wavelength absorption, but has, in addition, two ligand field bands at 2600 and 3080 A. As these are atrributable to transitions of the nonbonding *3d* electrons of Co, there is again an identical spectrum of the CN electrons.

The three complexes which exhibit anomalous Raman intensities are found to have anomalous ultraviolet spectra; for all three there is an additional intense absorption band at 2600 A. For $Fe(CN)_6^{-4}$, this band coincides nearly with the higher frequency ligand field band; but unlike the latter, its intensity is altered when the ion associates with cations.[20] This alteration indicates that the molecular orbitals of either the ground state or the upper state involve atomic orbitals on the nitrogen atoms; otherwise it is difficult to see why the transition should be sensitive to the peripheral environment of the complex. A very tentative explanation for the relation between the anomalous ultraviolet absorption absorptions and Raman intensities can be given if an excited electronic state of $Ag(CN)_4^{-3}$, for example, is pictured by ignoring σ bonds as being made up of the four states

$$M^{++}CN^{=}CN^{-}CN^{-}CN^{-}, \qquad M^{++}CN^{-}CN^{=}CN^{-}CN^{-},$$

etc. These divide into a triply degenerate F_2 and an A_1 state. The new ultraviolet band represents the transition from the ground state to the F_2 component. If the A_1 lies somewhere nearby, there should be some partial admixture of it into the ground state. The admixture should decrease the CN force constant and alter the Raman intensity. Since the $CN^=$ bond length would presumably be longer than that of CN^-, stretching the CN bond should increase the extent of admixture of $CN^=$ in the ground state. In all probability $CN^=$ has a higher polarizability than CN^-. Thus, the molecular polarizability should increase much more rapidly with CN extension for the second group of ions than for the first group, where electron donation from the metal is more difficult.

[18] R. Samuel and M. J. Kahn, Z. Physik **84,** 87 (1933).
[19] G. Placzek, Handbuch Radiol. **6**(2), 205 (1934).
[20] S. R. Cohen and R. A. Plane, J. Phys. Chem. **61,** 1096 (1957).

Charge Distribution and Electric Field Gradients in Ionic Crystals*

GENEVA G. BELFORD, ROBERT A. BERNHEIM,† AND H. S. GUTOWSKY

Noyes Chemical Laboratory, University of Illinois, Urbana, Illinois

(Received February 16, 1961)

A method is presented by means of which one can investigate the validity of the point-charge model often used for the calculation of electric field gradients in ionic crystals. The asymmetry parameter of the electric field gradient at a nucleus and the Eulerian angles describing the orientation of the field gradient's principal axes with respect to the crystallographic axes are linear functions of the point charges assigned to each set of atoms in the lattice. If the unit cell is of low symmetry and if there are more than one set of nuclei for which quadrupole interaction data can be observed, the number of observables and equations may equal or exceed the number of unknown charges, thereby enabling the charge distribution to be determined and its internal consistency checked. Such is the case for spodumene, for which the charge distribution thus calculated is neither internally consistent nor very reasonable. An analysis is made of the sensitivity of the apparent charge distribution to experimental errors in the quadrupole interactions, and the errors are found to be much too small to account for the anomalies. However, further investigations, including a refinement of the crystallographic parameters of spodumene, are necessary before the anomalies could be attributed to deficiencies in the point-charge model. With allowance for the uncertainties in the charge distribution, the analysis lends some support to a value of ≈ 0.04 b for Q_7, the nuclear quadrupole moment of Li^7. Further charge distribution anomalies result from a similar, but less detailed treatment of another silicate, beryl, which gives a very approximate value of $Q_9 \approx 0.1$ b for Be^9.

1. INTRODUCTION

THE evaluation of field gradients in ionic solids has been of recent interest from two main points of view.[1-3] These two approaches are a natural consequence of the fact that the experimentally accessible quantity, the quadrupole coupling constant e^2qQ/h is the product of the nuclear quadrupole moment Q and the electric field gradient q at the nuclear site. Neither Q nor q may be observed directly. Therefore, in some instances Q is obtained by observing the quadrupole coupling in a particularly simple solid for which the field gradient at the nucleus can be calculated in a reliable manner. On the other hand, if there is a reliable value for Q from independent experiments, it can be used to obtain the field gradient q at a nucleus in a crystal for which the quadrupole coupling constant has been observed. This "experimental" value for q can then be compared with values calculated on the basis of various models for the charge distribution in the lattice. In this manner, questions can be investigated such as the volume dependence of field gradients in crystals,[3] or the validity of the point-charge model for the distribution of electric charge in an ionic solid.[2,3]

Because of the complexities associated with more sophisticated and probably more realistic models, most field gradient calculations in ionic solids have been based upon the point-charge model.[1-3] However, even such a simple model leaves one facing serious difficulties. First, there is the question of the charge, $e_j = z_j e$, to be allocated to each type of lattice site j. Then there is the uncertainty arising from the antishielding factor γ_∞ for the ion in which the nucleus of interest is embedded.[1,4] This factor modifies the quadrupole coupling constant as shown by the following equation for an axially symmetric field,

$$e^2qQ/h = (eQ/h)(1-\gamma_\infty)\phi_{zz}. \quad (1)$$

Here, ϕ_{zz} is the direct contribution to the field gradient along the axis of symmetry, the z axis, from all charges external to the atom or ion. This quantity can be obtained quite readily, but only in terms of the e_j, by calculating the lattice sums[2,3]

$$\phi_{zz} = \sum_j e_j \sum_i [(3\cos^2\theta_{iz} - 1)/r_i^3], \quad (2)$$

where the origin is the nuclear site in question. Thus, even if an experimental determination of the crystal structure provides θ_{iz} and r_i of sufficient accuracy to calculate ϕ_{zz} by means of Eq. (2), the number of parameters, besides Q, which remains includes the various e_j as well as γ_∞. Even for the simplest ionic solid MX, there would be three unknowns ($e_M = z_M e$, $e_X = z_X e$, and γ_∞) and only two equations [Eq. (1) and the condition $z_M = -z_X$ for charge neutrality].

Originally, the approach to this problem was to use theoretical values of γ_∞ calculated for the free ion.[4] However, this neglects polarization and overlap effects of the neighboring ions, which can be important in the solid. Therefore, when an experimental coupling constant disagrees with the value calculated using the free ion value for γ_∞, and Eqs. (1) and (2), the disagreement could arise from γ_∞ being wrong, or from the approximations of the point charge model and charge distribution assumed in Eq. (2), or even from uncer-

* This work was supported in part by the Office of Naval Research and by the U. S. Atomic Energy Commission. Taken in main from the Ph.D. thesis of R. A. Bernheim, University of Illinois (1959).

† DuPont Teaching Fellow in Chemistry. Now at Department of Chemistry, Columbia University, New York.

[1] T. P. Das and E. L. Hahn in *Solid State Physics*, edited by F. Seitz and D. Turnbull (Academic Press, Inc., New York, 1958), Suppl. 1.

[2] R. Bersohn, J. Chem. Phys. **29**, 326 (1958).

[3] R. A. Bernheim and H. S. Gutowsky, J. Chem. Phys. **32**, 1072 (1960).

[4] G. Burns, J. Chem. Phys. **31**, 1253 (1959) and earlier work cited there, particularly that of R. M. Sternheimer.

tainties in the value for Q. This paper is concerned primarily with means of improving and checking the reliability of the field gradient ϕ_{zz} calculated on the basis of the point-charge model. Of course, the most direct method for doing this is to use the same model to calculate other internal electrical properties which may be compared with other observed quantities. One such approach, used previously,[3] is to calculate ϕ_{zz} for different nuclear sites in the same crystal; for example, at both the M and X nuclei in MX. Unfortunately, this ordinarily is of limited value because at least one new unknown, the γ_∞ for the second nuclear species, is introduced as well as one known quantity, the observed coupling constant of this species. However, there may be some net gain if each nuclear species has a range of acceptable values for each of the unknown parameters. The acceptable ranges for these parameters may overlap only partially for the different nuclear species, giving reasonably narrow final sets of values.

A more direct procedure is presented below. It is shown that the charge distribution may be determined and its internal consistency checked by using observable quadrupole interaction parameters which are independent of the values for γ_∞ and Q. These are the orientation of the principal field gradient axis system with respect to the crystal axes and the asymmetry parameter, which is defined as

$$\eta=(\phi_{xx}-\phi_{yy})/\phi_{zz}. \tag{3}$$

This approach is limited, however, to crystals of rather low symmetry. Otherwise η may be zero and the axis systems may coincide, independent of the charges assigned to each type of lattice site. Two examples, spodumene and beryl, are considered. There are numerous experimental data available for spodumene, which enable us to make a detailed investigation of the charge distribution in the crystal. The situation is less favorable in beryl, for which there are fewer data available. In both cases, the field gradients ϕ in the crystal are calculated in terms of the point charges z_j from the available crystallographic data. In turn, the z_j are obtained insofar as possible from an analysis of the quadrupole resonance observations. The numerical values thus obtained for ϕ_{zz} permit some consideration to be given to the values for the nuclear quadrupole moments of Li^7 and Be^9 and for γ_∞ of the Li^+ and Be^{++} ions in a crystal. Finally, it is pointed out again,[3] that accurate redeterminations of the crystal structure are needed for many substances. Small errors in the atomic positions lead to much larger fractional errors in the calculated field gradients because of the $1/r_i^3$ dependence in the latter.

2. COMPUTATIONAL PROCEDURES

The general techniques of the calculations were the same as those mentioned previously.[2,3] The digital computer program used to perform the numerical calculations has some notworthy features. An important consideration in writing the program was versatility to provide for the possibility of using the program, perhaps with fairly easy modifications, for computations other than those immediately at hand. With this in mind, the heart of the program was made a routine which computes vectors $\mathbf{r}_i$ giving the positions of every crystal ion, relative to the central ion, within an arbitrary spherical shell of radius R about the central ion.

The positions of ions within a unit cell are given by vectors $\mathbf{x}_i$ relative to the central ion. The location of a unit cell is specified by the vectors $l_1\mathbf{a}$, $l_2\mathbf{b}$, and $l_3\mathbf{c}$, where l_1, l_2, and l_3 are arbitrary integers and the vectors $\mathbf{a}$, $\mathbf{b}$, and $\mathbf{c}$ are in some convenient basis system. Then, the key program computes

$$\mathbf{r}_i=l_1\mathbf{a}+l_2\mathbf{b}+l_3\mathbf{c}+\mathbf{x}_i, \tag{4}$$

for all i corresponding to a given type of ion within the unit cell at $l_1=l_2=l_3=0$ and for the neighboring unit cells obtained by systematically selecting values of l_1, l_2, and l_3, subject to the limitation that $r_i<R$, where r_i is the length of the vector $\mathbf{r}_i$.

After each $\mathbf{r}_i$ is computed, an auxiliary routine is entered which computes

$$[3(\mathbf{r}_i\cdot\mathbf{t}/r_i)^2-1]/r_i^3, \tag{5}$$

where $\mathbf{t}$ is a unit vector of arbitrary direction, and adds this term to the proper sum. Obviously, other useful functions for a crystal may be computed by writing a new auxiliary routine. Several such routines have been written. Among these are routines for calculating the second moment for the magnetic resonance absorption of nuclei in single crystals and in crystal powders.

The numerical calculations themselves were performed with the University of Illinois electronic digital computer, the Illiac.[5] In the course of the calculations some of the field gradients listed by Bersohn[2] were

TABLE I. Atomic contributions to the lattice sums for the field gradient in spodumene at lithium, computed[a] for a summation sphere of radius 60 A. O^I- and O^{II}-type atoms are bonded to only one Si atom[b] while O^{III}-type atoms are linkage oxygens. All sums are in units of $e\times10^{24}$ cm^{-3}.

Atom	Charge	ϕ_{zz}	ϕ_{yy}	ϕ_{xx}	ϕ_{ii}
O^I	z_1	−0.14993	+0.16106	−0.01119	−0.05799
O^{II}	z_1	+0.28089	−0.16289	−0.11799	−0.02065
O^{III}	z_2	−0.02057	+0.08691	−0.06636	−0.05010
Si	z_3	+0.05382	−0.03515	−0.01870	+0.05821
Al	z_4	−0.02134	+0.04142	−0.02008	−0.05750
Li	z_5	+0.00223	+0.00368	−0.00591	−0.00827

[a] The crystallographic data used are from the work cited in reference 6.

[b] It is assumed that the charges on these two oxygen atoms are the same even though they are in somewhat different crystallographic environments. This assumption seems reasonable in view of the chemical similarity of O^I and O^{II}, which should be by far the major factor determining the net charge on the atoms.

[5] We are indebted to the Digital Computer Laboratory and its staff for their assistance.

TABLE II. Atomic contributions to the lattice sums for the field gradient in spodumene at aluminum, computed[a] for a summation sphere of radius 60 A. O^{I}- and O^{II}-type atoms are bonded to only one Si atom[b] while O^{III}-type atoms are linkage oxygens. All sums are in units of $e\times10^{24}$ cm^{-3}.

Atom	Charge	ϕ_{zz}	ϕ_{yy}	ϕ_{xx}	ϕ_{ii}
O^{I}	z_1	−0.15303	−0.16561	+0.31864	−0.15809
O^{II}	z_1	+0.12090	+0.14153	−0.26244	+0.02389
O^{III}	z_2	+0.01760	+0.01930	−0.03691	+0.07310
Si	z_3	−0.03235	+0.03733	−0.00501	+0.11130
Al	z_4	−0.02617	−0.01734	+0.04351	−0.06599
Li	z_5	+0.04138	−0.03210	−0.00928	−0.05748

[a] The crystallographic data used are from the work cited in reference 6.
[b] It is assumed that the charges on these two oxygen atoms are the same even though they are in somewhat different crystallographic environments. This assumption seems reasonable in view of the chemical similarity of O^{I} and O^{II}, which should be by far the major factor determining the net charge on the atoms.

checked to assure ourselves that our program was operating correctly. For the field gradient at Cu in Cu_2O we found, using the same crystal parameters as did Bersohn, that

$$\phi_{zz}=-1.033\times e\times10^{24}\ \text{cm}^{-3}. \tag{6}$$

for a summation radius of 30 A. For the field gradient at Li in $LiNO_3$ we found

$$\phi_{zz}=(0.01871-0.04054z_N)\times e\times10^{24}\ \text{cm}^{-3}, \tag{7}$$

where z_N is the charge on the nitrogen atom and the summation radius was 50 A. Both of these results agree with the values reported earlier.[2]

3. SPODUMENE

Crystal Structure and Quadrupole Coupling Data

Spodumene, $LiAl(SiO_3)_2$, is monoclinic and has the pyroxene structure in which $SiO_3^{=}$ groups are joined together in chains of indefinite length.[6] One oxygen of each $SiO_3^{=}$ group is a linkage atom between two Si atoms in the chain. The remaining two oxygen atoms stick out from the chain and are the nearest neighbors of the Li^+ and Al^{3+} ions. The linkage and the side group types of oxygen atoms, of course, differ greatly and therefore need to be treated separately in the analysis of the charge distribution.

The quadrupole interactions of both Li^7 and Al^{27} have been observed and analyzed in detail for spodumene.[7,8] For Li^7 the relevant data are as follows:

$$e^2Q_7q_{zz}/h=75.7\pm0.5\ \text{kc/sec} \tag{8}$$

$$\eta(\text{Li})=0.79\pm0.01. \tag{9}$$

The principal axis system for the Li^7 coupling tensor is oriented with respect to the unit cell such that the y principal axis is parallel to the b crystal axis, and the z principal axis lies between the a and the c axis at an angle of $\beta(\text{Li})=46.5\pm1°$ with the c axis. For Al^{27} the results are:

$$e^2Q_{27}q_{zz}/h=2.950\pm0.02\ \text{Mc/sec} \tag{10}$$

$$\eta(\text{Al})=0.94\pm0.01. \tag{11}$$

The principal axis system for the Al^{27} coupling tensor is oriented with respect to the crystal such that the x principal axis is parallel to the b crystal axis and the z principal axis lies in the ac plane at an angle of $\beta(\text{Al})=34\pm1°$ with the c axis, the relative order of the axes being zac.

For both the Li and Al atoms, the coincidence in direction of one of the principal axes with a crystalline axis is a result of symmetry. Therefore, for each atomic species, the only angular parameter which is a function of the charge distribution is the angle about the parallel axis by which the field gradient axis system is rotated with respect to the crystal system. The other expressions which are functions only of the charge distribution are the two asymmetry parameters Eqs. (9) and (11), and the charge neutrality condition. This makes a total of five independent relations and, in principle, there are five types of atoms for which the charges are to be determined, Li, Al, Si, and the two sets of O.

Calculation of Lattice Sums

The lattice sums ϕ, defined in Eq. (2), were calculated for both the Li and Al positions along each of the three principal axes. Actually, one of the sums at each position is redundant because it can be obtained from the other two by Laplace's equation. However, an independent calculation of the third by means of Eq. (2) provides a check on the internal consistency of the calculations. Thus for spodumene the internal agreement of the calculations is a few parts per thousand while for beryl it is only a few parts per hundred.

In addition to the principal components, the lattice sums ϕ_{ii} were calculated for an arbitrary direction at the Li and Al positions in the spodumene crystal. This arbitrary direction was taken to be perpendicular to the c axis, in the ac plane. It is the angle between the principal axes and this arbitrary axis in the ac plane which is a function of the charge distribution. The various lattice sums, calculated from the reported crystallographic data, are summarized in Tables I and II.

Determination of the Charge Distribution

We have four experimentally-determined parameters: $\eta(\text{Al})$, $\beta(\text{Al})$, $\eta(\text{Li})$, $\beta(\text{Li})$. We wish to obtain information about the charge distribution from these parameters and the calculated field gradient atomic sums. Let z_1 be the charge on each one of the two types of nonlinkage oxygens (assuming the charges on these to be equal), z_2 the charge on the linkage oxygen, and z_3, z_4, and z_5 the charges on Si, Al, and Li, respectively.

[6] B. E. Warren and J. Biscoe, Z. Krist. **80,** 391 (1931).
[7] G. M. Volkoff, Can. J. Phys. **31,** 820 (1953).
[8] H. E. Petch, N. G. Granna, and G. M. Volkoff, Can. J. Phys. **31,** 837 (1953); see also L. B. Robinson, *ibid.* **36,** 1295 (1958).

TABLE III. Summary of the charge distribution analysis for spodumeme, made by means of Eqs. (12A–E) which incorporate the atomic sums given in Tables I and II.[a]

	Charge distribution				Residues			
Solution	$z_1(O^{I,II})$	$z_2(O^{III})$	z_3(Si)	z_4(Al)	δ(B)	δ(C)	δ(D)	δ(E)
B	−1.24	+0.19	+0.42	+2.75	+0.38	...	...	...
C	+0.09	+0.32	−0.51	−0.98	...	−0.17	...	...
D	−0.43	−0.76	+0.81	+0.61	...	...	+0.041	...
E	−0.22	−0.87	+0.39	+0.84	...	...	...	−0.088
LS[b]	−0.37	−0.72	+0.56	+0.77	+0.021	−0.0058	+0.020	−0.037

[a] The charge distribution is calculated by assuming that the charge on Li, z_5, is +1.
[b] This is a least-squares solution as described in the text.

First of all, these charges are connected by the condition of charge neutrality,

$$4z_1+2z_2+2z_3+z_4+z_5=0. \quad (12A)$$

Secondly, the parameter η, as defined by Eq. (3), leads to an equation of the form,

$$\sum_{j=1}^{5}\{-(\phi_{xx})_j+(\phi_{yy})_j+\eta(\phi_{zz})_j\}z_j=0, \quad (13)$$

where $(\phi_{xx})_j$ is the total calculated atomic sum for all atoms of charge z_j, and similarly for $(\phi_{yy})_j$ and $(\phi_{zz})_j$. For lithium, this equation becomes

$$-0.23484z_1+0.05506z_2-0.10374z_3+0.04690z_4+0.00322z_5=0, \quad (12B)$$

and for aluminum,

$$0.06088z_1-0.03300z_2+0.06497z_3+0.04973z_4-0.08220z_5=0. \quad (12C)$$

Finally, we make use of the field gradient component ϕ_{ii} calculated for the coordinate system b, c, i, where b and c are crystal axes and i is an axis in the ac plane and perpendicular to c. It can be readily derived[7] that in case the b axis coincides with one of the principal axes (say z), and if x, y, z is a principal axis system, then

$$\phi_{ii}=\phi_{xx}\cos^2\alpha+\phi_{yy}\sin^2\alpha, \quad (14)$$

where α is the angle between the x axis and the i axis, measured towards the y axis. At the lithium atom, we note that the b and y axes coincide, and that $\alpha=133.5°$. Thus we get the relationship

$$\sum_{j=1}^{5}\{(\phi_{ii})_j-(\phi_{xx})_j(0.4739)-(\phi_{zz})_j(0.5262)\}z_j=0. \quad (15)$$

Substitution of the calculated atomic sums listed in Table I yields the result,

$$-0.07273z_1-0.00543z_2+0.04255z_3-0.03682z_4-0.00622z_5=0. \quad (12D)$$

At this aluminum atom the b and x axes coincide, and $\alpha=146°$. From this information one obtains, finally,

$$-0.13522z_1+0.07138z_2+0.08721z_3-0.06768z_4-0.03252z_5=0. \quad (12E)$$

Equations (12A–E) form a set of five linear, homogeneous equations in five unknowns. Since the determinant of the coefficients does not vanish, this system is incompatible; i.e., there does not exist a set of charges z_j which satisfy all five equations simultaneously. We can therefore set ourselves two goals: first, to try to find some charge distribution reasonably consistent with all five equations, and, second, to attempt to pin down the cause of the incompatibility.

With the first goal in mind, we calculated solutions to the various sets of four equations selected from the system. These solutions were calculated with the assumption that the charge on the lithium z_5 was +1. Of course, the numerical results obtained are good for any assumed z_5 if one considers the charge values as being not absolute charges z_1, etc. but as charge ratios z_1/z_5, z_2/z_5, etc. Results of these calculations are given in Table III. The capital letter labeling the solution corresponds to that of the equation which was *omitted* from the original set of five equations to obtain the four which were solved. The last four columns of the table give the residues resulting from back-substitution of the charge distributions into the original equations. Thus, for example, if z_{1b}, z_{2b}, z_{3b}, z_{4b}, z_{5b} is a given charge distribution, corresponding to solution B,

$$\delta(B)=\sum_{j=1}^{5}b_jz_{jb}, \quad (16)$$

where the b_j are the coefficients of Eq. (12B). Table III gives only the residues for the omitted equations, since the calculated charge distributions are approximately exact solutions to the remaining equations, the residues being negligibly small. Also, solution A has been omitted from the table, since the charge neutrality condition should be satisfied exactly and the large residue obtained indicated that this solution has little meaning.

A fifth solution was then calculated in an attempt to find some charge distribution which would be a "best" fit to all of the five equations. A least-squares calculation was chosen; in detail it amounted to the following. Let the kth equation be given by

$$\sum_{j=1}^{5} k_j z_j = 0. \tag{17}$$

Also let

$$N_k = \sum_{j=1}^{4} k_j^2 \tag{18}$$

and

$$r_k = \sum_{j=1}^{5} \frac{k_j z_j}{(N_k)^{\frac{1}{2}}}, \tag{19}$$

where $k = a, b, c, d, e$ denotes Eq. (12A), $\cdots$, Eq. (12E), respectively. Then the least-squares (LS) solution was obtained by setting $z_5 = 1$ and minimizing the function,

$$F = \sum_{k=b}^{e} r_k^2, \tag{20}$$

under the linear constraint implicit in Eq. (12A), with respect to the variables z_1, z_2, z_3, z_4. This was carried out by the straightforward Lagrange multiplier process. The equations obtained are linear and readily solved. The results, including residues, are displayed in Table III.

It is worthwhile to mention the two intuitive interpretations of this least-squares process. In the first place, the process minimizes the sums of the squares of what can be described as "normalized" residues, since $r_k = \delta(k)/N_k$. The inclusion of the factor N_k avoids weighting the equations according to the magnitudes of their coefficients, which is an invalid procedure because multiplication of coefficients by an arbitrary constant has no effect on the solution to a homogeneous equation. The second interpretation is a geometrical one. The five linear equations (with z_5 set equal to 1) correspond to hyperplanes in four-dimensional Euclidean space. A charge distribution corresponds to a point in that space. The quantity r_k is, for a given charge distribution, just the distance from the point to the plane defined by the kth equation. Thus the least-squares process simply yields the point lying on plane A which is nearest (in the least-squares sense) to all of the other four planes. Obviously, the procedure is quite analogous to the usual method of fitting a straight line to a number of data points lying in a plane.

The geometrical analogy provides us with a clue as to the explanation for the large discrepancies among the charge distributions obtained and listed in Table III. Consider the case where there are a number of coplanar data points through which we wish to draw a straight line. It is easy to visualize a situation in which a very good straight-line fit could be made to the data, while straight lines drawn through various pairs of points slope in several different directions. Although our four-dimensional situation is not readily visualized, it seems reasonable not to place too much importance on the disagreement among solutions B, C, D, and E, but to concentrate on trying to explain the magnitude of the residues for the LS solution. Moreover, at least one feature of the LS charge distribution seems chemically unreasonable. The charge on the aluminum is found to be somewhat *less* than that on the lithium even though their formal charges are 3+ and 1+, respectively.

Analysis of Errors in the Apparent Charge Distribution

There are five obvious sources of error involved in setting up Eqs. (12B–E): (1) The numerical calculation of the atomic sums; (2) the experimental determination of β(Li) and β(Al); (3) the experimental determination of η(Li) and η(Al); (4) the experimental determination of the crystallographic lattice parameters used to calculate the atomic sums; and (5) the point-charge model.

We are reasonably confident that the first source of error may be neglected. Both the success of convergence tests and the internal consistency of the results as expressed by the Laplacean relationship, $(\phi_{zz})_j + (\phi_{yy})_j + (\phi_{zz})_j = 0$, indicate that the field gradient components are calculated to a sufficient degree of accuracy for our purposes.

The second and third sources of error were investigated as described in the Appendix. The results show that in order to make each of the solutions B through E equal to the LS solution, the errors in β(Li), β(Al), η(Li), and η(Al) would have to be 23°, 10°, 0.09, and 0.41, respectively. The smallest of these errors still differs by almost an order of magnitude from the given experimental error. It is necessary to conclude that the basic incompatibility of Eqs. (12A–E) does not result from the stated experimental error in the determination of η and β. Furthermore, it seems very unlikely that gross, systematic errors could have been made in the careful study of the magnetic resonance spectra of spodumene.[7,8] Therefore, the only possible sources of incompatibility which remain suspect are the experimental determination of the crystal parameters[6] and the point-charge model.

Moreover, the x-ray data were taken at an early time, spodumene in 1931 and beryl in 1926, when the experimental tools available were not good enough to allow structural determinations of the precision desirable for our calculations. Accordingly, precise redeterminations of the structures are required before the approach presented here can yield any conclusions about the applicability of the point charge model to spodumene and beryl.

Quadrupole Coupling Constants

Thus far we have not considered the quadrupole coupling constants ν_7 and ν_{27} as defined in Eq. (1) and observed[8] for Li^7 and Al^{27}, respectively. In the case of aluminum, the quadrupole moment is known from independent experiments[9] to be $Q_{27}=+0.149$ b. Moreover, the antishielding parameter γ_∞ has been calculated for the free ion[10] and found to be -2.59. The LS charge distribution from Table III, when combined with the atomic sums in Table II, leads to a value for ϕ_{zz} at the aluminum atom of $+0.0279\times e\times 10^{24}$ cm^{-3}. Substitution of these numerical values in Eq. (1) gives us a predicted value for ν_{27} of 0.52 Mc/sec which is to be compared with the observed value of 2.95 Mc/sec.

This large discrepancy could result from the same factors responsible for the other anomalies discussed in the preceding section, but it could also reflect a difference in γ_∞ for the free aluminum ion and that in the crystal.[10] Inspection of the atomic sums in Table II which contribute to ϕ_{zz}(Al) reveals that the Li and Si atoms make virtually no contribution for any semi-reasonable charge distribution. Furthermore, for the LS charge distribution, the contributions from the various oxygen atoms cancel. Therefore, ϕ_{zz}(Al) is determined by z_{Al} and the aluminum atomic sum. If, instead of using the LS value of $+0.77$ for z_{Al} we use $+3$, the value calculated for ν_{27} becomes approximately 2.3 Mc/sec. The much better agreement of this value with experiment supports the view that the LS charge distribution rather than the value of γ_∞ is mainly responsible for the low calculated value of 0.52 Mc/sec for ν_{27}.

In the case of Li^7, there is some uncertainty in the value of the nuclear quadrupole moment. The best result available appears to be the value $Q_7=-0.042$ reported by Harris and Melkanoff.[11] The antishielding parameter calculated[10] for the free ion is $+0.256$. The use of these values, along with the atomic sums and LS charge distribution from Tables I, II, and III gives a predicted value of -70.0 kc/sec for ν_7, which compares very favorably with the observed coupling[8] of 75.7 kc/sec. However, this agreement is fortuitous in view of the uncertainties in the charge distribution. ϕ_{zz}(Li) is dominated by the contributions from the oxygen atoms; the contribution from Li itself is negligible but not that from Al and Si. For example, if we were to assume that $z_{Al}=+3$ instead of the LS value $+0.77$, the predicted value of ν_7 would be -140 kc/sec instead of -70 kc/sec. Nonetheless, our results add some support for a value of $|Q_7|$ within a factor of 2 from 0.04.

TABLE IV. Atomic contributions to the lattice sums for the field gradients in beryl, computed[a] for a summation sphere of radius 60 A. O^{I}- and O^{II}-type atoms are bonded to only one Si atom,[b] while O^{III}-type atoms are linkage oxygens. All sums are in units of $e\times 10^{24}$ cm^{-3}.

Atom	Charge	ϕ_{zz}(Be)	ϕ_{yy}(Be)	ϕ_{zz}(Be)	ϕ_{zz}(Al)
$O^{I,II}$	z_1	-0.11600	$+0.46346$	-0.34746	-0.18480
O^{III}	z_2	$+0.04735$	-0.13344	$+0.08609$	-0.01139
Si	z_3	$+0.11734$	-0.08692	-0.02441	$+0.06741$
Al	$+3$	-0.08620	$+0.21495$	-0.12876	$+0.02297$
Be	$+2$	$+0.00598$	$+0.02941$	-0.03539	-0.12744

[a] The crystallographic data used are from the work cited in reference 13.
[b] It is assumed that the charges on these two oxygen atoms are the same even though they are in somewhat different crystallographic environments; see Table I.

4. BERYL

Our study of beryl was prompted largely by its chemical similarity to spodumene, both being silicates, and by the availability of experimental data on the quadrupole interactions in the crystal.[12] Unfortunately, the latter are insufficient for as detailed a study of the charge distribution as was made for spodumene. Moreover, the internal inconsistencies found in the analysis for spodumene discourage the transferring to beryl of the charge distribution found for the silicate group in spodumene. Nonetheless, several assumptions of questionable validity are required in order to obtain results of any sort from an alternate treatment.

Beryl, which is $Be_3Al_2(SiO_3)_6$, differs from spodumene in that the silicate groups are arranged in rings of six instead of in long chains.[13] They are similar in that both have two types of oxygen atoms that have to be treated separately; one links the silicate groups together, while the other is bonded to only one silicon but also is a nearest neighbor to the cations. The crystal symmetry is such that it determines the orientation of the field gradient tensors at the Be and Al nuclei; moreover, it requires an axially symmetric field gradient at the Al. Therefore, instead of two β's and two η's as in spodumene, we have only η(Be). In addition, there are, of course, the coupling constants for the two quadrupolar nuclei, Be^9 and Al^{27}. The observed quadrupole interaction data for beryl are given below.[12] For Be^9:

$$e^2Q_9q_{zz}/h=0.504\pm0.004 \text{ Mc/sec}, \tag{21}$$

$$\eta(\text{Be})=0.090\pm0.005; \tag{22}$$

and for Al^{27}

$$e^2Q_{27}q_{zz}/h=3.093\pm0.015 \text{ Mc/sec}. \tag{23}$$

[9] H. Lew and G. Wessel, Phys. Rev. **90**, 1 (1953).
[10] T. P. Das and R. Bersohn, Phys. Rev. **102**, 733 (1956). Our use of the γ_∞ value which was calculated for Al^{3+} in this reference is inconsistent with the LS $+0.77$ charge on the aluminum. One would expect $Al^{+0.77}$ to be more readily polarizable than Al^{3+}, but it seems unlikely that the resultant change in γ_∞ could remove the discrepancy between the predicted and observed values for ν_{27}.
[11] E. G. Harris and M. A. Melkanoff, Phys. Rev. **90**, 585 (1953). However, see also J. W. Richardson, Revs. Modern Phys. **32**, 461 (1960) and I. Mannari and T. Arai, J. Chem. Phys. **28**, 28 (1958).
[12] L. C. Brown and D. Williams, J. Chem. Phys. **24**, 751 (1956).
[13] W. L. Bragg and J. West, Proc. Roy. Soc. (London) **A111**, 691 (1926).

The atomic sums pertinent to these data were calculated for the five types of atoms in beryl, using the available crystallographic data.[13] The results are listed in Table IV. In performing these calculations, the contributions of all atoms within a sphere of radius 60 A were summed. The convergence of some of the atomic sums was examined and was found to be good within 2% for summation spheres larger than 35 A in radius.

Of the observed quadrupole interactions, only η(Be) can be expressed directly as a function of the atomic sums and the charge distribution. This relation and the charge neutrality condition are, of course, insufficient to determine the five unknown charges. Equations (21) and (23) could be used provided we knew γ_∞ for the Be and Al ions in the crystal, or if we assumed the values in the crystal to be the same as those calculated[10] for the free ions. However, even the latter would leave us short one relation so some assumption concerning the charge distribution is inevitable.

Because of current interest[14,15] in the value for the Be^9 quadrupole moment, we have elected to assume that $z_{Be}=+2$ and $z_{Al}=+3$, and that γ_∞(Al) and γ_∞(Be) are those for the free ions,[10] -2.59 and $+0.186$. This enables us to obtain the rest of the charge distribution from experimental data and then to obtain a value for Q_9 from Eq. (21). The charges z_1, z_2, and z_3, on $O^{I,II}$, O^{III}, and Si, were obtained from the equation for charge neutrality,

$$2z_1+z_2+z_3=-2, \tag{24}$$

and from the two additional linear equations in z_1, z_2, and z_3 which result when Eq. (22) for η(Be) and Eq. (23) for ν_{27} are expressed in terms of the atomic sums in Table III. In this fashion, we obtain $z_1=-1.35$, $z_2=-0.74$, and $z_3=+1.44$. The value of Q_9 resulting from the use in Eq. (21) of this charge distribution is 0.20 barn, which is an order of magnitude larger than that previously found from an atomic beam measurement[14] ($Q_9=0.03$ b) and from an analysis of the quadrupole interactions in beryllium metal[15] ($Q_9=0.032$ b).

This discrepancy can result from the same factors which led to the internal inconsistencies in the treatment of spodumene. For example, one would expect the charge distribution on the silicate group to be similar in beryl and spodumene. However, the results obtained for z_1, z_2, and z_3 in beryl are -1.35, -0.74, and $+1.44$, while in spodumene the LS values are -0.37, -0.72, and $+0.56$. It is of some interest that if the latter are used to calculate Q_9 from the beryl data, a value of $Q_9\approx 0.045$ is found, which is in much better agreement with the other findings.[14,15] However, refinement of the crystallographic parameters for beryl is essential before any conclusions can be reached about the cause(s) of the difficulties.

[14] A. Lurio and A. G. Blackman, Bull. Am. Phys. Soc. **5**, 344 (1960).
[15] M. Pomerantz and T. P. Das, Phys. Rev. **119**, 70 (1960).

ACKNOWLEDGMENT

We wish to thank Professor Richard Bersohn for helpful discussions of the calculations presented here.

APPENDIX

To determine whether or not the experimental errors in β and η can explain the LS residues, we have developed an approximate method for calculating the magnitude of errors required to produce these residues. As an example of the method, the calculation for δ(D), which depends mainly upon error in β(Li), will be outlined here. The other calculations proceed in a similar fashion except that the estimates for δ(B) and δ(C) must take into account experimental errors in both η and β, and, therefore, the analysis is slightly more complicated.

Suppose the field gradient components calculated were not those for the true principal axis system x, y, z, but for an axis system x', y', z' differing from x, y, z by a rotation of angle ϵ about the y axis ($y=y'$). In the nonprincipal system the equation for ϕ_{ii} is readily derived to be

$$\phi_{ii}=\phi_{zz}'\cos^2\alpha+\phi_{xz}'\sin^2\alpha+2\phi_{xz}'\cos\alpha\sin\alpha, \tag{A1}$$

where primes denote field gradient tensor components in the x', y', z' system and α and ϕ_{ii} are as previously defined. It should be remembered that although α is an angle which we select, its numerical value is determined actually by the experimental results for β and the unit cell geometry.

Now the equation we solved for δ(D) included Eq. (A1) with the last term equal to zero. Hence the residue δ(D) obtained should be just equal to this last term, evaluated for the Li nucleus. In order to estimate this term, we note that, transforming into the principal axis system,

$$\phi_{zz}'=(\phi_{xx}-\phi_{zz})\sin\epsilon\cos\epsilon=\left(\frac{\phi_{xx}}{\phi_{yy}}-\frac{\phi_{zz}}{\phi_{yy}}\right)\phi_{yy}\sin\epsilon\cos\epsilon. \tag{A2}$$

Finally, by using the experimentally determined η(Li) value from which we note that $\phi_{xx}/\phi_{yy}\approx 1/9$ and $\phi_{zz}/\phi_{yy}\approx -10/9$, and by introducing the charge distribution, we obtain

$$\delta(\mathrm{D})\approx(11/18)\,|\sin2\epsilon|\,|\sin2\alpha|\,\Big|\sum_{j=1}^{5}(\phi_{yy})_j z_j\Big|. \tag{A3}$$

An ϵ equal in magnitude to 23° would be required for this approximation to hold for the LS solution. In view of the fact that the approximation in Eq. (A3) for δ(D) is not sensitive to small errors in α, ϕ_{xx}/ϕ_{yy}, ϕ_{zz}/ϕ_{yy}, or the lattice sums, it is evident that δ(B) cannot be accounted for simply on the basis of the error, $|\epsilon|\leqslant 1°$, cited[8] in the determination of β(Li).

Rotational Isomerism in 2,3 Dihalopropenes

EARL B. WHIPPLE

Union Carbide Research Institute, P.O. Box 324, Tuxedo, New York

(Received January 18, 1961)

Previously reported variations in different solvents of the long-range (1,3) NMR coupling constants in 2,3 dihalopropenes have suggested the existence of rotational isomers in rapid equilibrium. This view is supported by infrared spectra. By assuming an angular dependence of the form $J=J_0\cos^2\phi$ between the observed coupling constants and the dihedral angle of the methylene C—H bonds as suggested in calculations by Karplus, the identities of the isomers are deduced, the equilibrium constants calculated, and the energy differences expressed as a function of solvent dielectric constant using an Onsager cavity model. The results for 2,3 dichloropropene are compared with published dipole moment measurements in solution and in the vapor at elevated temperatures.

1. INTRODUCTION

IT was reported earlier[1] that the long-range coupling constants in the NMR spectra of a series of 2,3 dihalopropenes, $H_2C{=}CY{-}CH_2Z$, vary both with substituent and environment, and the latter fact led to the suggestion that these compounds exist as rotational isomers in rapid equilibrium. It was further proposed that a balance of steric and electrostatic effects similar in nature but opposite in direction from that earlier postulated by Nakagawa *et al.*[2] for haloacetyl halides might be involved, although no direct experimental evidence bearing on the presence, identities, or amounts of distinct dihalopropene conformers was given.

Evidence for the existence of discreet rotational isomers is present, however, in the infrared and Raman spectra of dihalopropenes in solution.[3] Furthermore, Karplus has recently described an approximate theory of the π-electron contribution to the long-range coupling constants in propylene which predicts, to the extent that other contributions are negligible, a simple dependence of the form $J=J_0\cos^2\phi$ on the dihedral angle between a methyl C—H bond and the π axis of the ethylenic system.[4] By combining these results and making a few simplifying approximations it becomes possible to identify two rotational isomers which are physically reasonable in the light of existing knowledge about propenyl systems, and which give a simple explanation of the solvent effects consistent with available measurements of the dipole moments.

2. EXPERIMENTAL RESULTS

Infrared Spectra

The infrared spectra[5] from 2–16 μ of 2-bromo, 3-chloro-propene-1 in various solvents are shown in Fig. 1. Similar spectra were also recorded, but are not shown, for 2,3 dichloropropene. The assignments of group frequencies for the latter have been discussed by Gerding and Haring.[6] The bands at about 1600 cm^{-1}, 1100 cm^{-1}, and 1380 cm^{-1}, which are assigned to the C=C and C—C stretching and the $=CH_2$ symmetrical bending fundamentals, respectively, all show doublet splittings on the order of 20 cm^{-1} in both compounds. The spectra of a number of related compounds, e.g., 2-bromopropene, allyl chloride, methallyl chloride, and *trans* 1,2,3 tribromopropene all fail to show such doublings. Moreover, the relative intensities of the doublet components are strongly affected by solvent, while frequency shifts are slight, and in both dihalopropenes the trends in the variation of intensity with solvent are the same. This behavior suggests the presence of discreet rotational isomers which, on the basis of the solvent shifts, are designated as polar and nonpolar forms with the frequency assignments indicated in Table I.[3] The polar form is that whose relative proportion increases in solvents of high dielectric constant.

NMR Spectra

The 60 Mc proton magnetic resonance spectra of 2-bromo,3-chloropropene in the same solutions for which the infrared spectra in Fig. 1 were recorded are shown in Fig. 2. These can be treated with satisfactory accuracy as AMX_2 systems in which the splittings follow

[1] E. B. Whipple, J. H. Goldstein, and G. R. McClure, J. Am. Chem. Soc. **82,** 3811 (1960).

[2] I. Nakagawa, I. Ichishima, K. Kuratani, T. Miyazawa, T. Shimanouchi, and S. Mizushima, J. Chem. Phys. **20,** 1720 (1952).

[3] The presence of doubled C=C vibrations in the Raman spectra of various halogenated propylenes and the possibility of rotational isomerism has been discussed by A. Kirrman, Bull. soc. chim. France **1948,** 170–3, and preceding papers. Other possible explanations for the doubling are indicated in reference 6.

[4] M. Karplus, J. Am. Chem. Soc. **82,** 4431 (1960).

[5] The spectra in Fig. 1 were recorded on a Beckman IR-4 double beam spectrometer using rock salt prisms and a scanning rate of 1 μ/min. 0.1-mm path length cells were used for 10% vol. solutions in carbon tetrachloride and acetonitrile, while the neat liquid was measured in a 0.024 mm cell. Slower scans of 200 mμ/min and separate solvent compensation curves were used in order to obtain the data in Table I.

[6] H. Gerding and H. G. Haring, Rec. trav. chim. **74,** 957 (1955).

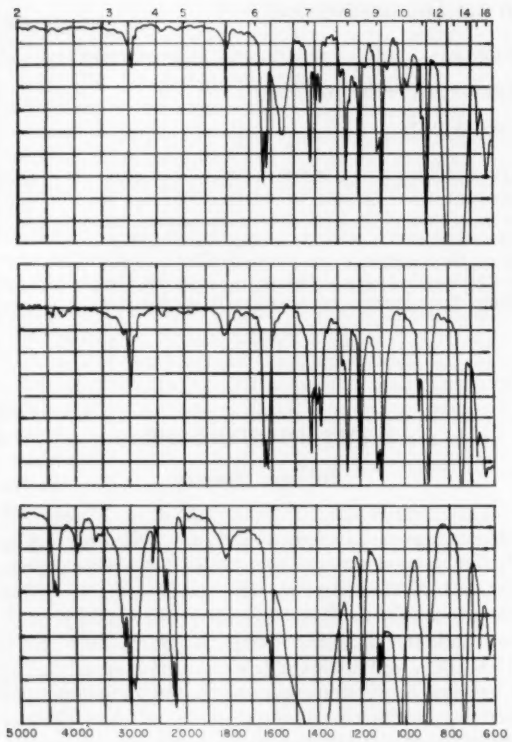

FIG. 1. Infrared spectrum of 2-bromo, 3-chloropropene. (Top) 10% solution in carbon tetrachloride; (middle) liquid; and (bottom) 10% solution in acetonitrile.

from simple rules.[7] It is apparent from the figure that the coupling constant J_{MX} has disappeared in the more polar solvent, while analysis of the multiplet splittings shows that J_{AX} has decreased from 1.42–0.90 sec^{-1}. On the basis of earlier assignments,[1] proton A is *cis* to the methylene group.

A similar series of measurements was performed on 2% solutions of 2,3 dichloropropene in various solvents, and the values of $J(cis)$ are recorded in Table II. A similar trend occurs in $J(trans)$, which is smaller by about 0.5 sec^{-1} than J (*cis*).

3. THEORETICAL

Karplus[4] has recently expressed the contribution from the π-electron system to the long-range nuclear spin coupling constants in alkenes and alkynes as the product of individual second-order interactions between the nuclei and unpaired electrons in excited triplet states according to

$$J=2.1\times10^{-15}\sum_T \frac{a_H a_{H'}}{(\Delta W)_T}. \qquad (1)$$

Here the a_H terms correspond to the hyperfine splitting constants in cps in the electron resonance spectra of the π-electron radical fragments constituting a given triplet state of the system, and $(\Delta W)_T$ is the singlet-triplet excitation energy in electron volts. Inserting available data for the lowest-lying triplet state of propylene in (1) has yielded a calculated 1,3 coupling constant in very close agreement with that observed for J (*cis*), indicating that this term alone is largely responsible for the total value.[4,8]

Since one of the a_H terms included in the above calculation contains as a factor the square of the cosine of the dihedral angle ϕ between the π axis of the central carbon and the plane of the methyl C—H bond, the observed *cis* 1,3 coupling constant should show an angular dependence approximated by $J=J_0\cos^2\phi$. If more than one methylene proton is involved and internal motions occur, the coupling must be suitably averaged over the bonds and the motion.[9] In allylic systems with two methylene protons, for example, the classical expression for the observed coupling constant would be

$$\bar{J}_2=\frac{1}{2}J_0\frac{\int_0^{2\pi}\exp[-V(\varphi)/kT](\tfrac{1}{2}+\sin^2\varphi)d\varphi}{\int_0^{2\pi}\exp[-V(\varphi)/kT]d\varphi}, \qquad (2)$$

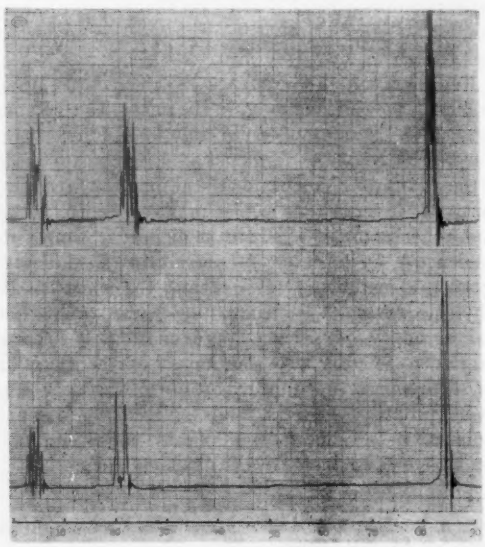

FIG. 2. Proton magnetic resonance spectrum of 2-bromo, 3-chloropropene at 60 Mc in carbon tetrachloride (top) and acetonitrile (bottom) solutions.

[7] See F. S. Mortimer, J. Mol. Spectroscopy **3**, 335 (1959), for a detailed analysis of the 2,3 dichloropropene spectrum.

[8] The theory would predict, however, that $J_{1,3}(cis)$ and $J_{1,3}$ (*trans*) have equal values. Since the latter are generally smaller by about 0.5 sec^{-1}, contributions other than from the maximum term in (1) are indicated in the *trans* coupling constant.

[9] J. C. Schug, P. E. McMahon, and H. S. Gutowsky, J. Chem. Phys. **33**, 843 (1960).

TABLE I. Frequencies, approximate relative intensities,[a] and tentative assignments[b] of doubled bands in the infrared spectrum of 2-bromo, 3-chloropropene.

	"Polar form"			"Nonpolar form"		
Solvent[c]	C—C str[d] 1123 cm^{-1}	$=CH_2$ scissor 1376 cm^{-1}	C=C str 1619 cm^{-1}	C—C str[d] 1108 cm^{-1}	$=CH_2$ scissor 1396 cm^{-1}	C—C str 1634 cm^{-1}
CCl_4	0.39	0.51	0.48	0.61	0.49	0.52
Liquid	0.48	0.65	0.52	0.52	0.35	0.48
CH_3CN	0.69	...	0.69	0.31	...	0.31

[a] Each doublet separately normalized to 1.0.
[b] See reference 6.
[c] 10% by vol. concentrations of solute.
[d] Note discussion in text.

where φ is measured from the allylic substituent and $V(\varphi)$ is the potential function for internal rotation.

Two simplifying assumptions were made in order to apply Eq. (2) to the NMR spectra of dihalopropenes. The first is that the constant J_0 derived from (1) is unaffected by allylic substitution in propenes. This finds some empirical justification in the fact that the observed coupling constants in propargyl halides differ only slightly (2.6–2.8 vs 2.8) from that in methylacetylene,[10] in each instance rotation being free. No angular dependence can be apparent from the coupling constants involving symmetrical methyl groups with barrier heights insufficient to prevent rotational averaging, since the expression corresponding to (2) in this case reduces to

$$\bar{J}_3=\tfrac{1}{3}J_0\{\cos^2\varphi+\cos^2[\varphi+(2\pi/3)+\cos^2(\varphi-(2\pi/3)]\}$$
$$=\tfrac{1}{2}J_0. \qquad (3)$$

The first assumption hence allows the substitution of an empirical value[11] for $\frac{1}{2}J_0$ in Eq. (2). The second assumption is that the potential function $V(\varphi)$ can be replaced without serious error by a delta-type function which is infinite everywhere except at the angles φ_N and φ_P corresponding to the two potential minima indicated by the infrared spectra of dihalopropenes. With this approximation Eq. (2) takes the very simple form

$$\bar{J}_2=X_PJ_P+X_NJ_N=J_P+X_N(J_N-J_P) \qquad (4a)$$

$$J_P=\bar{J}_3(\tfrac{1}{2}+\sin^2\varphi_P) \qquad J_N=\bar{J}_3(\tfrac{1}{2}+\sin^2\varphi_N), \qquad (4b)$$

where X represents the mole fractions and the subscripts refer to the polar and nonpolar designations employed in Table I.

For 2-bromo, 3-chloropropene small apparent increases in X_N produce appreciable increases in $\bar{J}_2$ (see Figs. 1 and 2) indicating that J_N is considerably greater than J_P, while the value $\bar{J}_3=1.4$ sec^{-1} from 2-bromopropene[12] places an upper limit on their difference according to Eq. (4b). In very polar solvents, where X_N is small, the observed couplings should most closely approach J_P. The observed value, $J_2=0.9$ sec^{-1}, in acetonitrile solution would restrict J_P to the range $\frac{1}{2}J_3=0.7\leq J_P<0.9$, and since X_N is clearly nonvanishing as evidenced in Fig. 1, it is concluded that $J_P=\frac{1}{2}\bar{J}_3=0.7$ sec^{-1}. To infer the value of J_N, one can assume that in nonpolar solvents the extinction coefficients of the polar and nonpolar forms are approximately equal for the C=C stretching vibration and obtain values $X_N=0.52$, $X_P=0.48$ from their relative intensities. Inserting these along with $J_P=0.7$ and $\bar{J}_2=1.42$ into Eq. (4a) yields $J_N=2.1$ sec^{-1} which is the maximum value allowed by Eq. (4b).

Similar conclusions would be reached by the same reasoning using data for 2,3 dichloropropene and/or the relative intensities of the $=CH_2$ deformation doublet in 10% CCl_4 solution. Values well outside the allowed range result, however, if either the C—C vibration or any of the ir intensities in polar solvents are used. If the present reaoning is correct, it follows that the extinction coefficient for the C—C stretch are not equal for the two isomers and that the solvent variation of extinction coefficients is different in general for the two forms.

On solving for the dihedral angles according to Eq. (4b) the indicated conformations are I and either II or III in Fig. 3. Since III is obviously more polar than II, it can be eliminated on the basis of the direction of the solvent effect to leave I and II. The latter is consistent with the structure of propylene obtained through microwave and thermodynamic measurements,[13,14] and also corresponds to the low-energy form of haloacetyl halides.[2] The polar form I is twisted by 30° from the structure IV that would be predicted along with II by analogy with propylene. However, electrostatic repulsion between the halogens might be

[10] E. B. Whipple, J. H. Goldstein, and W. E. Stewart, J. Am. Chem. Soc. **81**, 4761 (1959).
[11] Since the available data show that the coupling constants in propylene are affected by vinyl substitution, the value of J_0 in (2) should be determined from a propene with corresponding vinyl substitution.
[12] E. B. Whipple, J. H. Goldstein, and Leon Mandell, J. Am. Chem. Soc. **82**, 3010 (1960).
[13] D. R. Herschbach and L. C. Krisher, J. Chem. Phys. **28**, 728 (1958).
[14] W. G. Dauben and K. S. Pitzer, *Steric Effects in Organic Chemistry*, edited by M. S. Newman (John Wiley & Sons, Inc., New York, 1956).

TABLE II. Solvent effects on rotational isomers in 2,3 dichloropropene.[a]

Solvent	ϵ[b]	$\bar{J}_2$	K	log K	$\frac{2(\epsilon-1)}{2\epsilon+1}$
N-pentane	1.844	1.27[c]	1.38[e]	0.140	0.360
Cyclohexane	2.015	1.22[c]	1.60	0.204	0.405
CCl_4	2.228	1.18[c]	1.82	0.260	0.452
CS_2	2.641	1.03[d]	3.06	0.486	0.522
Chloroform	4.806	1.04[d]	2.94	0.468	0.717
1,2 dichloroethane	10.36	0.94[d]	4.52	0.655	0.862
Acetone	20.7	0.83[c]	8.86	0.948	0.929
Acetonitrile	37.5	0.84[c]	8.20	0.914	0.961

[a] 2% vol. solutions.
[b] Taken from *Handbook of Chemistry and Physics* (Chemical Rubber Publishing Company, Cleveland, Ohio, 1959), 41st ed. Data are not corrected for solute.
[c] From 1st order methylene splittings.
[d] From 1st order vinyl splittings.
[e] J_2=1.38 sec^{-1} from 2-chloropropene.

expected to alter IV somewhat in the direction of I. It is noteworthy here that in haloacetyl halides, where electrostatic repulsions would presumably operate in an opposite sense, the second form is reported to be twisted some 30° in an opposite direction than I relative to IV.

It is of interest to reconsider the frequencies and relative intensities of the doubled bands in the infrared spectra on the basis of structures I and II. The arguments identifying these structures assume that the high-frequency components of bands principally involving C=C stretching and/or $=CH_2$ deformational motions are due to the less polar form II, and that the extinction coefficients for these vibrations are approximately equal for the two isomers in nonpolar environments. Since II has the same conformation as the haloacetyl halide isomer with the higher frequency,[2] a precedent exists for the assignment of the double bond stretching mode. In the case of a vinylidene group, moreover, molecular models clearly indicate a considerable steric interaction with the allylic halogen in II, and the effect of an added coupling between vibrations involving these groups should be to raise their frequencies. Hence there exists some justification for the assignment of the high-frequency $=CH_2$ deformation to II. While the assumption of equal extinction coefficients in nonpolar solvents cannot be further justified, it does appear reasonable inasmuch as there is no *a priori* reason to expect the transition moments to differ appreciably for these vibrations. If equality in the vapor is assumed, however, Buckingham's theory[15] would predict a difference ΔA_s in the absolute intensities of I and II in solution approximated by

$$\alpha(\Delta A_s/A_v)=\gamma\Delta\mu[(\epsilon-1)/(2\epsilon+1)]+\beta, \qquad (5)$$

where α and β are solvent parameters approaching one and zero, respectively, as the refractive index approaches unity, A_v is the absolute intensity of the corresponding band in the vapor; γ is a solute parameter on the order of 10^{18} in cgs units, $\Delta\mu$ is the difference in equilibrium dipole moments between I and II, and ϵ is the dielectric constant of the solvent. Since $\Delta\mu$ is approximately 1.5*D* in dichloropropene, it stands to reason that the extinction coefficients would remain comparable only in solvents with low dielectric constant as is implied by the data.

The anomalous behavior of the doublet intensities assigned to the C—C stretching mode cannot be simply explained. The possibilities of appreciable interaction with C—H deformational frequencies[6] makes it less proper to describe this band in terms of simple models based on localized vibrations. To the extent that such consideration is justified, one might expect the *trans* coplanar arrangement of the halogens in II to lead to a lower extinction coefficient for a C—C stretching vibration than the unsymmetrical arrangement in *I* somewhat analogously to the behavior in *trans* and *cis* dihaloethylenes. This would require a reversal of the frequency assignments and solvent effects on the extinction coefficients more than sufficient to offset the changes in concentration, which is not outside the realm of possibility. While it is not considered unreasonable to expect that the extinction coefficients of a mode so intimately involving the principal dipole moment of the molecule might differ significantly in the two forms, the nature of the difference remains osbcure and the frequency assignments of the bands are uncertain.

It is also possible to rationalize in terms of the structures I and II the qualitative trends of substituent

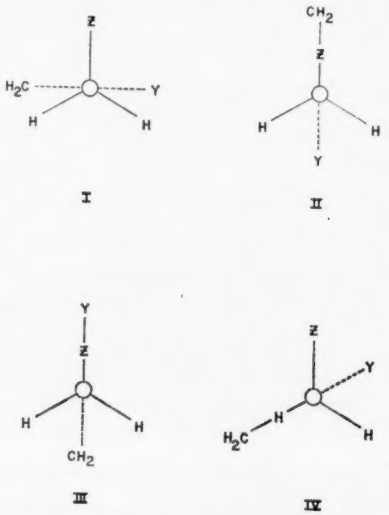

FIG. 3. Various conformations of dihalopropenes, $H_2C{=}CY{-}CH_2Z$.

[15] A. D. Buckingham, Proc. Roy. Soc. (London) **A255**, 32 (1960).

effects described earlier for 2,3 disubstituted propenes.[1] For negatively polarized 2-substituents one might expect both the increasing electronegativity and decreasing size across a series $Z=$I, Br, Cl in the 3-substituent to favor II over I, accounting for the observed order $\bar{J}_2(Z=\text{Cl})>\bar{J}_2(Z=\text{Br})>\bar{J}_2(Z=\text{I})$ for $Y=$Cl, Br. If the Z substituent is fixed and negatively polarized, then increasing electronegativity of the Y substituent should favor II while decreasing size might favor I. Since the indicated polarizations as indicated by bond dipoles are nearly equal for $Y=$Cl and $Y=$Br, then the latter effect should predominate, leading again to the observed order $\bar{J}_2(Y=\text{Br})>\bar{J}_2(Y=\text{Cl})$. If the Y substituent is positively polarized, as in the case of methyl groups, both steric and electrostatic effects should favor I, and values of $\bar{J}_2$ close to the predicted minima have been observed in both polar and nonpolar solvents.[1]

3. SOLVENT EFFECTS AND DIPOLE MOMENTS FOR 2,3 DICHLOROPROPENE

The simplest approximate model for the effect of solvent is that of a point dipole μ in the Onsager reaction field inside a spherical cavity within the medium of dielectric constant ϵ. The potential energy due to the environment, which is an added term in the total energy of the molecular system, is then given by

$$E_s=-[2(\epsilon-1)/(2\epsilon+1)](\mu^2/a^3), \qquad (6)$$

If ΔE_0 is the energy difference between isolated molecules of I and II, then the energy difference in a solvent

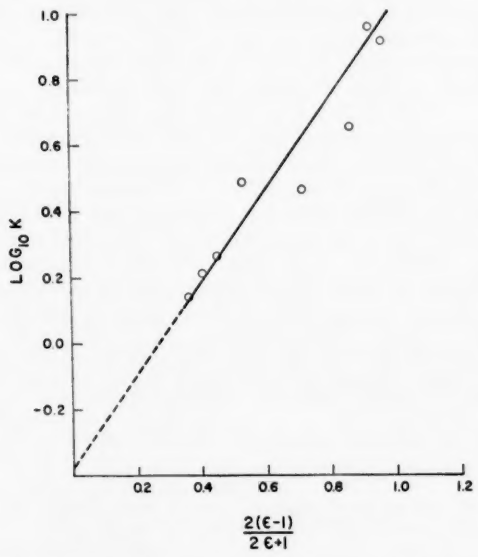

FIG. 4. Variation of rotational isomer ratio in 2,3 dichloropropene with solvent dielectric constant.

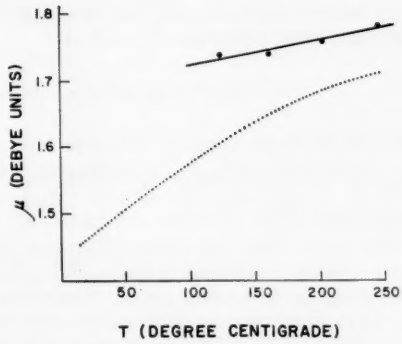

FIG. 5. Estimated and observed[18] dipole moment of 2,3 dichloropropene vapor at various temperatures.

will be given approximately by

$$\Delta E=\Delta E_0-(8\pi Nd/3M)[(\epsilon-1)/(2\epsilon+1)](\mu_I^2-\mu_{II}^2); \qquad (7)$$

the cavity radius having been estimated on the rather arbitrary assumption of voidless packing of spheres from the density and molecular weight of the liquid solute. The dipole moments corresponding to conformations I and II of 2, 3 dichloropropene can be approximated by vector addition of bond moments taken from vinyl chloride (1.44D), propylene (0.35D), and n-propyl chloride (2.10D).[16] The resultant dipole moments for conformers I and II are, respectively, 2.37D and 0.83D.

If I and II are considered to be in simple equilibrium, their relative proportions should be governed by

$$\kappa=X_I/X_{II}=2(Z_I/Z_{II})\exp[-\Delta E/RT], \qquad (8)$$

in which Z_I and Z_II are the partition functions of the two isomers and a statistical weight of 2 is included for I to allow for its equivalent conformation obtained on 180° rotation. Combining with (7) and inserting numerical values one obtains at $T=25$°C

$$\log\kappa=\log Z(Z_\text{I}/Z_\text{II})-\frac{\Delta E_0}{2.303RT}+1.42\left[\frac{2(\epsilon-1)}{2\epsilon+1}\right]. \qquad (9)$$

In Table II are listed value of the equilibrium constant calculated from the *cis* 1,3 coupling constants of 2,3 dichloropropene in various solvents, and the experimental points are compared with the slope predicted by Eq. (9) in Fig. 4. The agreement is essentially perfect, although there is an appreciable scatter of experimental points due to inaccuracies on the order of 0.05 sec^{-1} in the measurement of the coupling constants.

One obtains from Fig. 4 an equilibrium constant of

[16] J. W. Smith, *Electric Dipole Moments* (Butterworths Scientific Publications, Ltd., London, 1955). As a check on the bond moment approximation, calculated dipole moments of 2-chloropropene (1.65D) and allyl chloride (1.98D) agree closely with the observed values, 1.68D and 1.98D, respectively. All the dipole moment data are for the vapor phase.

1.905 in benzene solution, and using this together with the resultant bond moments of I and II,

$$\bar{\mu}=(X_I\mu_I^2+X_{II}\mu_{II}^2)^{\frac{1}{2}}, \qquad (10)$$

the calculated dipole moment of $1.98D$ is in almost perfect agreement with the experimental value of $1.99D$.[17] On extrapolating the line in Fig. 4 to $\epsilon=1$ and assuming equal partition functions for I and II in the liquid state, the energy difference between the two isomers is estimated to be 914 cal mole^{-1} with II being the more stable form. This corresponds to the lower energy isomer of the haloacetyl halides.[2] If the indicated energy difference were presumed to persist in the vapor and the assumption of equal partition coefficients similarly extended, the vapor dipole moment as a function of temperature could be estimated on the basis of Eqs. (9) and (10), and the results are compared with experimental values obtained by Oriani and Smythe[18] in Fig. 5. Here the agreement is only fair, but comparable to that obtained by the previous authors with an adjustable two-parameter function of the Gwinn and Pitzer type.[18,19] The very small observed effect of temperature on the dipole moment would seem to indicate that the energy difference in the vapor is less than that obtained for the liquid, but the model is obviously too crude to permit immediate conclusions based on small discrepancies. That a moderate correspondence with experiment is obtained without the benefits of adjustment or hindsight does, on the other hand, appear to support the essential correctness of the model.

ACKNOWLEDGMENTS

The author is indebted to Dr. Charles Angell for a number of discussions concerning the infrared spectra and to Dr. Verner Schomaker for several helpful corrections and suggestions in the preliminary manuscript.

[17] W. H. King and H. S. Smith, J. Am. Chem. Soc. **72,** 3459 (1950).

[18] R. A. Oriani and C. P. Smythe, J. Chem. Phys. **17,** 1174 (1949).

[19] W. D. Gwinn and K. S. Pitzer, J. Chem. Phys. **16,** 303 (1948).

Infrared Spectrum of CF_3SF_5*

D. F. EGGERS, JR., AND H. E. WRIGHT

Department of Chemistry, University of Washington, Seattle 5, Washington

AND

D. W. ROBINSON

Department of Chemistry, Johns Hopkins University, Baltimore 18, Maryland

(Received February 13, 1961)

The infrared spectrum of CF_3SF_5 has been measured and analyzed between 30 and 4000 cm^{-1}. A band found at 218.5 cm^{-1} is believed responsible for satellite lines observed previously in the microwave spectrum; the barrier to internal rotation might then be much lower than obtained previously by assuming these satellites were due to torsional oscillation. Twelve of the seventeen fundamentals were assigned in the infrared spectrum and estimates are given for the others. A plausible assignment is given for the overtone and combination bands also observed; this gives no evidence for any of the inactive fundamentals.

INTRODUCTION

THE substance CF_3SF_5, trifluoromethylsulfur pentafluoride, was prepared and characterized by Silvey and Cady.[1] A partial infrared spectrum was reported, without interpretation, by Clifford, El-Shamy, Emeleus, and Haszeldine.[2] The microwave spectrum was investigated by Kisliuk and Silvey,[3] who reported that the spectrum was that of a symmetric top and that the assumption that it is trifluoromethylsulfur pentafluoride gives a very reasonable CS distance of 1.86 A, assuming reasonable values for the other structural parameters. On the basis of relative intensities for several satellite lines observed with the sample at −78°C, they also estimated that two of the "vibrational" frequencies should lie at about 95 cm^{-1} and at 230 cm^{-1}. Upon assuming that the first of these is due to hindered torsional oscillation, they derived a potential barrier of about 220 cm^{-1}, which has twelve maxima and minima.

Such a large potential barrier seems difficult to understand, especially when we compare it with the sixfold barrier for nitromethane, which is 2.11 cm^{-1}.[4] Townes and Schawlow[5] have commented on the surprisingly large value of the potential barrier found in CF_3SF_5. An alternate interpretation is that the satellites observed by Kisliuk and Silvey were not due to excited torsional states, but rather to excited states of a conventional vibrational mode. The most likely possibilities are degenerate bending modes, which might be roughly described as having the CF_3 and SF_5 groups bending as more or less rigid units. Since these may occur in phase and out of phase, there should be two separate frequencies, each of which is doubly degenerate, assuming either free internal rotation or else that any hindering barrier does not greatly split the vibrational degeneracy of the free case. Unlike the internal rotation, each of these frequencies should be observable in the vibrational spectrum. Kisliuk and Silvey derived their vibrational frequency estimates on the basis of assuming the excited states were nondegenerate. If now we assume each of their excited states was doubly degenerate, the estimated vibration frequencies are raised to 187 cm^{-1} and 320 cm^{-1}. We have, therefore, investigated the infrared spectrum of CSF_5 in the gas phase.

EXPERIMENTAL

Several samples were used in the investigation, all of which were prepared by Silvey and Cady. The sample used in the investigation of prism spectra was further purified by gas chromatography over a silica-gel column at 100°C, and the infrared spectrum showed no evidence of even the strongest bands of SF_6 or SF_4. The compound $CF_2(SF_5)_2$ might have been present, but only in trace amounts; in any event, most of its strong absorption bands are covered by those of CF_3SF_5. The sample studied with the grating instrument was purified by passing through Ascarite to remove lower fluorides of sulfur; a small trace of SF_6 was found to be present, but SF_4 was absent.

The instrument used in the prism investigation has been described by Kaplan and Eggers[6]; prisms of cesium bromide, potassium bromide, sodium chloride, and calcium fluoride were used in appropriate spectral regions. All spectra were studied in conventional 10-cm gas cells, with pressures ranging from 10 to about 0.005 cm Hg. The range of frequencies covered extends from about 340 cm^{-1} to 4000 cm^{-1}. The geometrical slit-width, expressed as the width at the half-intensity point,

* Supported in part by the National Science Foundation and by the U. S. Air Force through the Air Force Office of Scientific Research of the Air Research and Development Command, under a contract at Washington, and under a contract at Johns Hopkins.

[1] G. A. Silvey and G. H. Cady, J. Am. Chem. Soc. **72**, 3624 (1950).

[2] A. F. Clifford, H. K. El-Shamy, H. J. Emeleus, and R. N. Haszeldine, J. Chem. Soc. **1953**, 2372.

[3] P. Kisliuk and G. A. Silvey, J. Chem. Phys. **20**, 517 (1952).

[4] E. Tannenbaum, R. J. Myers, and W. D. Gwinn, J. Chem. Phys. **25**, 42 (1956).

[5] C. H. Townes and A. L. Schawlow, *Microwave Spectroscopy* (McGraw-Hill Book Company, Inc., New York, 1955), p. 335.

[6] L. D. Kaplan and D. F. Eggers, Jr., J. Chem. Phys. **25**, 876 (1956).

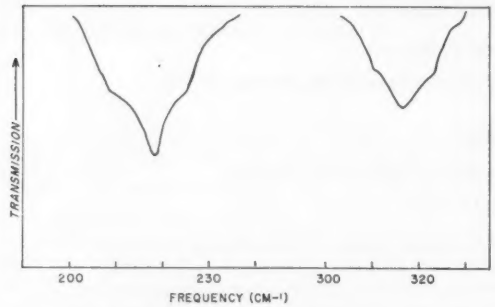

FIG. 1. Infrared spectrum of CSF_8 in the far-infrared region. Pressure x-path length was 3.6 cm atm for the lower frequency; 2.5 cm atm for the higher frequency.

was about 2 cm^{-1} in all the prism work. In many bands, the width observed is considerably larger than this, which results in somewhat less precise location of the true vibration frequency.

The instrument used in the grating investigation is described by Robinson.[7] It uses a GE H4AB 100-w filament with ThO_2 coating as the source, and a Golay cell with a diamond window as the detector. Two gratings were used in investigating this region, but the only absorption bands found were in the region using the grating with spacing 135 cm^{-1}. Stray radiation was reduced by using an aluminum plate, ground with 320 mesh emery, plus one restrahlen plate, either of sodium fluoride for the region around 320 cm^{-1} or of sodium chloride for the region around 220 cm^{-1}. The entire region from 30–380 cm^{-1} was searched for absorption bands, using a cell of 30-cm length with polyethylene windows and sample pressures up to 10 cm Hg. Spectral slitwidth was about 4 cm^{-1}.

The spectra experimentally observed in the various regions are shown in Figs. 1–4; the regions showing no absorption were omitted from these figures. The bands obtained, along with rough intensity estimates, are listed in Table I. There is very good agreement between our spectrum and that reported by Clifford *et al.*,[2] in the range covered by the latter workers. We have, however, found seven bands which they did not report, at 797,

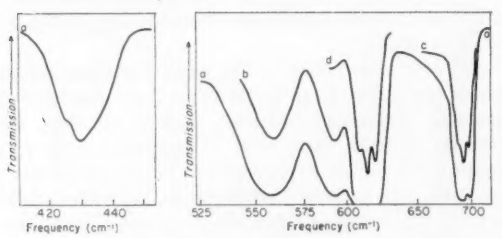

FIG. 2. Infrared spectrum of CSF_8 in the CsBr (left) and KBr (right) prism regions. Pressure x-path length was 1.32 cm atm (a); 0.40 cm atm (b); 0.066 cm atm (c); and 0.00066 cm atm (d).

[7] D. W. Robinson, J. Opt. Soc. Am. **49**, 966 (1959).

TABLE I. Infrared spectrum and assignments of CSF_8.

Frequency (cm^{-1})	Intensity[a]	Assignment
218.5	w	ν_{17}
316	w	ν_{16}
429	w	ν_{15}
559	m	ν_{14}
593	m	ν_{13}
608	vs	P branch
614	vs	ν_5
618	vs	R branch
692	s	ν_4
697	s	R branch
751	vs	P branch
756	vs	ν_3
761	vs	R branch
797	vvw	$\nu_{13}+\nu_{17}=811.5$
833	vw	$\nu_5+\nu_{17}=832.5$
851	w	$2\nu_{15}=858$
885	vvs	ν_2
890	vvs	
904	vvs	ν_{12}
1011	vw	$\nu_{13}+\nu_{15}=1022$; $\nu_4+\nu_{16}=1008$
1075	vw	$\nu_3+\nu_{16}=1072$
1115	vvw	$2\nu_{14}=1118$; $\nu_4+\nu_{15}=1121$
1150	vw	$\nu_{13}+\nu_{14}=1152$
1170	vs	ν_1
1222	m	$2\nu_5=1228$; $\nu_{12}+\nu_{16}=1220$
1257	vvs	ν_{11}
1302	m	$\nu_4+\nu_5=1306$
1348	w	$\nu_2+\nu_{13}=1349$
1386	w	$\nu_1+\nu_{17}=1388.5$; $2\nu_4=1384$
1433	vvw	$\nu_2+\nu_{14}=1449$; $\nu_3+\nu_4=1448$
1476	vw	$\nu_2+\nu_{13}=1483$; $\nu_{11}+\nu_{17}=1475.5$
1517	w	$\nu_5+\nu_{12}=1518$; $2\nu_3=1512$
1590	w	$\nu_4+\nu_{12}=1596$; $\nu_3+\nu_4=1582$
1634	vw	$\nu_2+\nu_5=1646$
1765	vw	$\nu_1+\nu_{13}=1763$
1786	vvw	$\nu_2+\nu_{12}=1794$; $\nu_1+\nu_5=1784$
1855	vvw	$\nu_1+\nu_4=1862$; $\nu_{11}+\nu_{13}=1850$
2005	vw	$\nu_3+\nu_{11}=2013$
2050	vw	$\nu_1+\nu_2=2060$
2143	vw	$\nu_2+\nu_{11}=2147$
2331	vw	$2\nu_1=2340$
2361	vvw	ternary combination; trace of CO_2?
2422	w	$\nu_1+\nu_{11}=2427$
2500	vw	$2\nu_{11}=2514$

[a] w=weak, m=medium, s=strong, v=very.

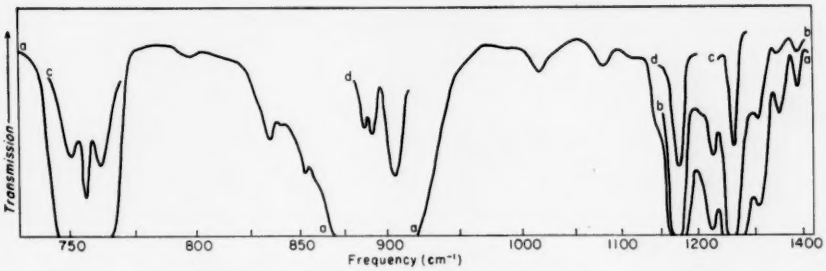

FIG. 3. Infrared spectrum of CSF_5 in the NaCl prism region. Pressure x-path length same as for Fig. 2.

833, 851, 1433, 1786, 2331, and 2361 cm^{-1}, all quite weak; since Clifford *et al.* did not report their pressure or path-length, we feel these bands may have been below the limit of detection in their sample. In contrast to this view, however, they also report a very weak doublet at 2980 and 2860 cm^{-1}, which we did not find. This would require at least a ternary combination, so we have tentatively omitted it.

BARRIER TO INTERNAL ROTATION

A satellite line was observed in the microwave spectrum of CSF_5 at $-78°C$, with roughly one-half the intensity of the ground-state line. Upon assuming the excited state was nondegenerate, this gave a value of 93.5 ± 25 cm^{-1} for the energy level. The value of 219 cm^{-1} for the barrier was then obtained by approximating the cosine potential with a parabola in the vicinity of a minimum and choosing the barrier height to give a torsional oscillation frequency of 93.5 cm^{-1}.[3]

An alternative assignment is that this microwave satellite is due to a doubly-degenerate vibration, which gives, on the same basis, a value of 187 ± 25 cm^{-1} as the energy level. We have observed an infrared band at 218 cm^{-1}; the fact that this value is a bit outside the limit of error is not regarded as significant. Another microwave satellite, with an intensity 2/11, that of the ground-state line, gave a frequency of about 230 cm^{-1}, assuming it is nondegenerate. An alternative assignment is that this is also a degenerate vibrational state, which raises its estimate to about 320 cm^{-1}; no limits of error were given. In agreement with this alternate prediction, we find an infrared band at 316 cm^{-1}, which is surely within the limits of error. For both this infrared band and that at 218 cm^{-1}, one would almost surely expect them to be doubly degenerate.

One would, of course, like to have a more positive identification of the microwave lines with these particular infrared vibrations. Since the molecule is relatively heavy, an infrared determination of the α value is out of the question, so that further microwave work seems indicated. Kisliuk and Silvey indicated that they observed further satellites, presumed to be due to the higher excited states of the torsional (or rather bending) vibration; intensity measurements on these lines would be most interesting. Intensity ratios between the first satellite and the ground-state line, measured at several different low temperatures, would also be very informative.

Accepting this alternate assignment of the microwave satellite line opens again the question of the height of the barrier to internal rotation. The infrared evidence is negative in character but suggests that the barrier might be quite low. All of the observed infrared bands can be assigned, either as fundamentals or as combinations of the fundamentals observed in the infrared; this leaves no bands which must be assigned as a combination of the torsional oscillation and a type E fundamental, which is allowed by selection rules.

VIBRATIONAL ANALYSIS: SYMMMETRY CONSIDERATIONS

Before proceeding to a vibrational analysis, one must make certain choices or assumptions regarding the molecular configuration. We assume, first, that the molecule may be thought of as an SF_5 group and a CF_3 group, linked through a CS bond. The former is assumed

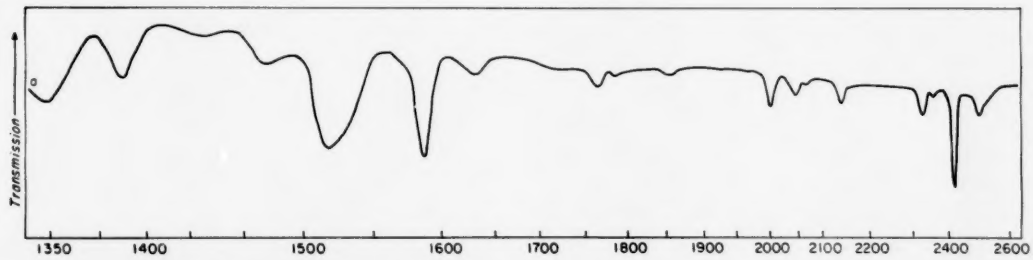

FIG. 4. Infrared spectrum of CSF_5 in the CaF_2 prism region. Pressure x-path length was 1.32 cm atm.

TABLE II. Comparison of several possible symmetries for CSF_5.

Property	High barrier	Low barrier
Effective symmetry	C_s	C_{4v}
No. of fundamentals	24	17
No. of infrared-active fundamentals	24	13
No. of Raman-active fundamentals	24	16
No. of polarized Raman fundamentals	15	6

to have C_{4v} symmetry, the latter C_{3v} symmetry. Two limiting cases may be distinguished further, on the basis of possible internal torsional motion. In the first, the barrier to internal rotation is very high, so that the molecular symmetry is C_s; in the second, the barrier is lower or even zero, and the effective molecular symmetry may be higher than C_s. Unfortunately, it is very difficult to relate the barrier height to the type of selection rules obeyed by the molecule. Crawford and Wilson[8] have shown that the G matrix for a molecule such as this can always be factored into a symmetry group higher than C_s by an appropriate choice of coordinates in one of the constituent groups. The F matrix, then, alone determines whether the molecule will obey selection rules of higher or lower symmetry, i.e., the extent to which the various nontorsional force constants vary with torsional angle. It is even possible that one might have a barrier considerably higher than the value of Kisliuk and Silvey, and the selection rules would still be those of a point group with higher symmetry than that of C_s.

In any event, the conventional group-theoretical analysis,[9] assuming only C_s symmetry, shows that there should be 24 fundamentals, 15 of species A', and 9 of species A''. All fundamentals are allowed in both the infrared and Raman, with those of species A' polarized in the Raman. For the low-barrier case, using the methods of Crawford and Wilson, one chooses the SF_5 group as the "framework," and the CF_3 group as the attached top, and finds that the secular equation may be factored on the basis of C_{4v} symmetry. This gives six vibrations of species A_1, two of species B_1, one of species B_2, and seven of species E. The torsional motion is found in species A_2. Only vibrations of species A_1 and E are permitted in the infrared, though all but the torsion are permitted in the Raman. These conclusions are summarized in Table II.

The experimental data are in much better agreement with the low-barrier selection rules than those of the high barrier. Comparison with similar molecules shows that all fundamentals should lie below about 1300 cm^{-1}. Even if one stretches the data by counting separately what are probably resolved P, Q, and R branches, he can only find seventeen medium and strong bands. If one recognizes the PQR structures as belonging to single bands, the total comes to only eleven.

[8] B. L. Crawford and E. B. Wilson, Jr., J. Chem. Phys. **9,** 323 (1941).

[9] E. B. Wilson, J. C. Decius, and P. C. Cross, *Molecular Vibrations* (McGraw-Hill Book Company, Inc., New York, 1958).

ASSIGNMENT OF FUNDAMENTALS

We shall carry out the vibrational assignment on the basis of a low torsion barrier, and mention later the evidence which the analysis adds to this assumption. The fundamentals will be numbered one through six in the A_1 species, seven in the A_2 species, eight and nine in the B_1 species, ten in the B_2 species, and eleven through seventeen in the E species. Since there seem to be no Raman data, some ambiguity remains in choosing the A_1 fundamentals. It is, in principle, possible to distinguish these two symmetry species on the basis of their band contours.[10]

This is rather difficult in practice for two reasons. First, the CSF_5 molecule is not very different from a spherical top; second, the effects of Coriolis coupling may cause a perpendicular band to look much like a parallel band. The calculated separation of P and R branches for a parallel band is 10 cm^{-1}. If one ignores the Coriolis coupling; i.e., assumes that ζ is zero or very small, the separation of P and R branches in a perpendicular band is only about 15% greater, estimating as shown by the curves in the paper by Gerhard and Dennison. While it was not possible for them to show curves for the parallel bands, one infers that the perpendicular bands might have much less pronounced valleys between the P and Q and the Q and R branches. If now we recognize the possibility of Coriolis coupling, perpendicular bands may be changed in several ways.[11]

For large negative values of ζ, the centers of the subbands will be spread out further, and the band will show only a smooth contour, with no valleys whatever. For large positive values of ζ, the centers of the subbands will be drawn closer together giving the band an appearance much like a parallel band. This has been observed in the ν_6 perpendicular band of fluoroform, as shown by Edgell and May.[12]

Another method has, therefore, been used to help distinguish between A_1 and E fundamentals: one compares the frequencies with those of similar compounds for which Raman data are available. The CF_3 group has been extensively studied; for present purposes the work of Edgell and May,[13] Taylor,[14] and McGee, Cleveland, *et al.*[15] will suffice.

Fortunately, a molecule containing the SF_5 group has also been studied; Cross, Roberts, Goggin, and Woodward[16] have studied the Raman and infrared spectrum

[10] S. L. Gerhard and D. M. Dennison, Phys. Rev. **43,** 197 (1933).

[11] G. Herzberg, *Infrared and Raman Spectra* (D. Van Nostrand Company, Inc., Princeton, New Jersey, 1945), p. 428ff.

[12] W. F. Edgell and C. May, J. Chem. Phys. **21,** 1901 (1953).

[13] W. F. Edgell and C. May, J. Chem. Phys. **22,** 1808 (1954).

[14] R. C. Taylor, J. Chem. Phys. **22,** 714 (1954).

[15] P. R. McGee, F. F. Cleveland, A. G. Meister, C. E. Decker, and S. I. Miller, J. Chem. Phys. **21,** 242 (1953).

[16] L. H. Cross, H. L. Roberts, P. Goggin, and L. A. Woodward, Trans. Faraday Soc. **56,** 945 (1960).

of SF_5Cl, though the infrared was limited to the region above 500 cm^{-1}.

The comparison with these other molecules is most readily made on the basis of the symmetry species of coordinates wholly within one or the other group as a starting point. Six such coordinates are found in the CF_3 group, and are the three CF stretches and three FCF angle changes; each of these gives rise to an A_1 vibration and an E vibration. In the CF_3X series, one finds CF stretching vibration in the range 1050–1220 cm^{-1} with the E vibration appearing at the higher frequency. The bands observed in CSF_8 at 1170 and 1257 cm^{-1} are therefore assigned as ν_1 and ν_{11}, a_1 and e, respectively. We were unable to resolve rotational contours in either of these bands. In CH_3CF_3, there are reasons for assigning the higher of the two corresponding bands as a_1,[17] so it may later be necessary to interchange our assignment. The FCF angle-change vibrations are more clear-cut; the a_1 vibration appears in the range 740–780 cm^{-1} and is strong in the infrared. The e vibration, on the other hand, appears in the range 540–560 cm^{-1} and is only of medium strength. The CSF_8 bands at 756 and 559 cm^{-1} are then assigned as ν_3 and ν_{14}, a_1 and e, respectively. There can be little doubt about the former, as the 756 band shows well-developed P, Q, R structure and is so strong. One might also choose a value 593 for ν_{14}; however, we shall prefer to have this later for one of the vibrations of the SF_5 group. Neither the 559 nor the 593 cm^{-1} bands shows any sign of rotational branches.

We turn now to the internal vibrations of the SF_5 group. SF stretching gives rise to four vibrations; and in SF_5Cl they are found at 908 (e), 854, 706 (a_1), and 624 cm^{-1} (b_1). The vibrations in CSF_8 at 904, 885–890, and 692 cm^{-1} are then assigned as $\nu_{12}(e)$, $\nu_2(a_1)$, and $\nu_4(a_1)$, respectively. We should estimate, in view of the high order of agreement in the other vibrations, that a value of about 620 should be approximately correct for $\nu_8(b_1)$; however, it is forbidden in the infrared. The FSF bending motions are found in SF_5Cl at values of 602 (a_1), 578 (e), 504 (b_2), 442 (e), and 396 (b_1) cm^{-1}. The CSF_8 bands at 614, 593, and 429 cm^{-1} are then assigned as $\nu_5(a_1)$, $\nu_{13}(e)$ and $\nu_{15}(e)$, respectively. In the absence of Raman data, values around 500 and 400 cm^{-1} would seem about right for the fundamentals $\nu_{10}(b_2)$ and $\nu_9(b_1)$.

There are, finally, vibrations which cannot be regarded as localized in either of the groups; for these, of course, comparison with other molecules may be of little value. These might be described as the torsion, stretching of the CS bond and the two bending vibrations of the two groups as a whole with respect to the CS bond. These are numbered $\nu_7(a_2)$, $\nu_6(a_1)$, $\nu_{16}(e)$, and $\nu_{17}(e)$, respectively.

The bands observed in the far infrared at 316 and 218.5 cm^{-1} are assigned as ν_{16} and ν_{17}, both species e, in view of the rather high order of agreement with the modified microwave results. The CC stretching vibration appears at 349 cm^{-1} in C_2F_6,[18] while in S_2F_{10} the SS stretching vibration has been assigned a value of 246 cm^{-1}.[19] One should estimate, then, that the CS stretching vibration in CSF_8 should be somewhere in between, very roughly 300 cm^{-1}. This vibration might be detected better in the Raman spectrum. Although the interthe rotation (or torsional oscillation) is not active in nal infrared, combinations with E vibrations are allowed. We have not found any evidence for the torsional frequency in this way; perhaps this suggests that the frequency is low, as would be associated with a low potential barrier to torsion.

If the departure from C_{4v} symmetry toward C_s symmetry were quite small, it might cause only slight changes in the spectrum and hence be overlooked in a first approximation. Correlation tables show that the species A_1, A_2, B_1, and B_2 become either A' or A'', and that the species E becomes $A'+A''$. Since both A' and A'' are allowed in the infrared, all of the fundamentals are allowed; further, the E vibrations are permitted to split into two components.

All of the fundamentals assigned as type e appear as single bands, with a suggestion of structure for some; this might also be due to molecular rotation. Some structure is observed in four of the five fundamentals assigned as a_1 vibrations, but this is to be expected from rotation. However, the double peak at 885 and 890 cm^{-1} does not have the usual appearance of a parallel band, though it was assigned in that way. It is possible that Coriolis coupling has altered the intensity of one of the rotational branches; or possibly, these peaks might be assigned as the e vibration, just starting to split, and the 904 peak as the a_1 vibration. Higher resolution and Raman-polarization data would aid here.

The b_1 and b_2 fundamentals would also become allowed for deviation from C_{4v} symmetry. Without Raman data, it is difficult to know where one should look for them. Possibly the best test would be ν_{10}, estimated to fall around 500 cm^{-1}; our spectra showed nothing in this region.

OVERTONES AND COMBINATIONS

Further bands observed in the infrared are also listed in Table I. The general order of agreement in the overtone and combination assignment is very high. We have used eleven of the twelve active fundamentals in assigning binary combination and overtone bands with no alternative choices; seven of these were used two or more times. All twelve fundamentals were used, though sometimes as alternative choices, in assigning other binary combinations. We have assigned a total of 25 binary overtone and combination bands, out of a total possible

[17] J. R. Nielsen, H. H. Claasen, and D. C. Smith, J. Chem. Phys. **18**, 1471 (1950).

[18] D. H. Rank and E. L. Pace, J. Chem. Phys. **15**, 39 (1947).

[19] J. K. Wilmshurst and H. J. Bernstein, Can. J. Chem. **35**, 191 (1957).

number of 78 which can be formed from twelve fundamentals. We also tried to assign a number of the weaker bands as binary difference bands, assuming the transitions would originate either from ν_{16} or ν_{17}. This was notably unsuccessful, either because there was no observed fundamental at the position for the other level, or else the corresponding sum band was not observed. Conversely, we examined the spectra for difference bands corresponding to binary combination bands which were assigned using either ν_{16} or ν_{17}. In about half the cases, the difference band is covered by strong absorption of another fundamental; in the others, there is an alternate assignment, or the sum band is exceedingly weak, or else in a region (cesium bromide prism below 400 cm^{-1}) where our signal-to-noise was rather poor.

SUMMARY AND CONCLUSIONS

The substance CSF_6 has a vibrational spectrum consistent with a low torsional barrier of the two groups with respect to each other. Twelve of the seventeen fundamentals have been assigned, and rough values proposed for the remaining five. In view of this, no thermodynamic properties are reported at the present time. Further work is in progress, aimed at determination of the Raman spectrum including polarization measurements and the low-temperature infrared spectrum.

THE JOURNAL OF CHEMICAL PHYSICS VOLUME 35, NUMBER 3 SEPTEMBER, 1961

Normal Vibrations of the Polymer Molecules of Helical Configuration. II. A Simple Method of Factoring of the Secular Equation

HIROYUKI TADOKORO

Department of Polymer Science, Faculty of Science, Osaka University, Nakanoshima, Kitaku, Osaka, Japan

(Received February 28, 1961)

A simple method of the factoring of the secular equation useful for helical polymer molecules under the factor group $D(2m\pi/n)$ was derived. This method is also applicable to the molecules under the point groups D_n, C_{nv} and the groups which contain the subgroup D_n or C_{nv}. As an example the secular equation of the skeletal vibrations of the polyoxymethylene molecule was factored by this method.

INTRODUCTION

IN a previous paper[1] we have reported the method of calculation of the normal vibrations of helical polymer molecules, with the examples for the skeletal vibrations of polyoxymethylene and polyethylene molecules. In that paper the factoring of the **G** and **F** matrices for the degenerate species into real matrices [Eqs. (11) and (21) of the work cited in reference 1] was carried out after the example of the symmetry coordinates of the benzene molecule.[2] In the present paper we have derived a simple method of the factoring of the secular equation especially useful for the cases of the helical polymer molecules under the factor group $D(2m\pi/n)$.[3] This method can be also applicable to the cases of the point groups D_n, C_{nv} and the groups which contain the subgroup D_n or C_{nv}.

[1] H. Tadokoro, J. Chem. Phys. **33,** 1558 (1960).
[2] B. L. Crawford, Jr., and F. A. Miller, J. Chem. Phys. **17,** 249 (1949).
[3] As to the notation $D(2m\pi/n)$, see the work cited in reference 1 or Liang and Krimm's paper [C. Y. Liang and S. Krimm, J. Chem. Phys. **25,** 563 (1956)]. The n and m are the numbers of chemical units and turns in a unit cell of the one-dimensional space group, respectively. For example, in the case of polyoxymethylene molecule, $n=9$ and $m=5$. [H. Tadokoro, T. Yasumoto, S. Murahashi, and I. Nitta, J. Polymer Sci. **44,** 266 (1960)].

SYMMETRY IN THE CHEMICAL UNIT

For the convenience of the following discussion the relationships among the basis coordinates, the **G** (or **F**) matrices and the transformation matrices used in this paper are summarized in Table I. As the first step we construct the intermediate symmetry coordinates associated with the symmetry in each chemical unit. In the helical molecules under the factor group $D(2m\pi/n)$ there are two types of twofold axes which are perpendicular to and intersect the helix axis. For instance the polyoxymethylene molecule has two kinds of twofold axes, passing through the carbon and the oxygen atoms, respectively. Polytetrafluoroethylene molecule also has two kinds of twofold axes, passing through the carbon atoms and the center of the C—C bonds, respectively. In the case of C_{nv}, for instance, the trioxane molecule (C_{3v}), we may use the symmetry elements of mirror planes instead of the twofold axes. When we consider the factor group of the molecule, the first and the second types of twofold axes have the following relations. When n=odd, the first type of twofold axis of the jth chemical unit coincides with the second type of twofold axis of the $\{(n+1)/2+j-1\}$th chemical unit. When n=even, the first and the second types of twofold axes form classes separately.

The intermediate symmetry coordinates associated with the symmetry in the chemical unit may be written as follows:

$$\mathbf{s}=\begin{Vmatrix}\mathbf{s}(1)\\ \mathbf{s}(2)\\ \vdots\\ \mathbf{s}(j)\\ \vdots\\ \mathbf{s}(n)\end{Vmatrix}, \quad \text{and} \quad \mathbf{s}(j)=\begin{Vmatrix}\mathbf{s}(j)_{Is}\\ \mathbf{s}(j)_{IIs}\\ \\ \mathbf{s}(j)_{Ia}\\ \\ \mathbf{s}(j)_{IIa}\end{Vmatrix}=\begin{Vmatrix}s(j)_1\\ s(j)_2\\ \vdots\\ s(j)_l\\ \vdots\\ s(j)_r\end{Vmatrix}, \tag{1}$$

where $\mathbf{s}$ denotes a column vector consisting of the symmetry coordinates associated with a unit cell, and $\mathbf{s}(j)_l$ is the lth symmetry coordinate of the jth chemical unit; $\mathbf{s}(j)_{Is}$ and $\mathbf{s}(j)_{IIs}$ are the symmetry coordinates symmetrical to the first and the second type of twofold axes perpendicular to the helix axis, respectively; $\mathbf{s}(j)_{Ia}$ and $\mathbf{s}(j)_{IIa}$ are those antisymmetrical to the first and the second type of twofold axes, respectively. For instance in the case of the methylene group, the CH_2 symmetric stretching, bending, and twisting modes are symmetrical to the twofold axis (the bisector of the angle HCH), and the CH_2 antisymmetric stretching, rocking and wagging modes are antisymmetrical to the twofold axis. The coordinates $s(j)_l$'s should be arranged in the order, those belonging to $\mathbf{s}(j)_{Is}$, $\mathbf{s}(j)_{IIs}$, $\mathbf{s}(j)_{Ia}$, and $\mathbf{s}(j)_{IIa}$. The redundant coordinates associated only with each chemical unit, if they appear, may also be eliminated in this stage by suitable transformation.

After these transformations $\mathbf{G}$ or $\mathbf{F}$ matrices of Eqs. (6) of the work cited in reference 1 may be written as follows:

$$\mathbf{A}=\boldsymbol{\alpha}_0+\boldsymbol{\beta}_0+\boldsymbol{\beta}_0'+\boldsymbol{\gamma}_0+\boldsymbol{\gamma}_0'+\boldsymbol{\delta}_0+\boldsymbol{\delta}_0',$$

$$\mathbf{B}=\boldsymbol{\alpha}_0-(\boldsymbol{\beta}_0+\boldsymbol{\beta}_0')+(\boldsymbol{\gamma}_0+\boldsymbol{\gamma}_0')-(\boldsymbol{\delta}_0+\boldsymbol{\delta}_0'),$$

$$\mathbf{E}_{\pm k}{}^c=\boldsymbol{\alpha}_0+\boldsymbol{\beta}_0\epsilon^{\pm k}+\boldsymbol{\beta}_0{}'\epsilon^{\mp k}+\boldsymbol{\gamma}_0\epsilon^{\pm 2k}+\boldsymbol{\gamma}_0'\epsilon^{\mp 2k}+\boldsymbol{\delta}_0\epsilon^{\pm 3k}+\boldsymbol{\delta}_0'\epsilon^{\mp 3k}, \quad k=1, 2, \cdots; \tag{2}$$

$\boldsymbol{\alpha}_0$ denotes the $\mathbf{G}$ (or $\mathbf{F}$) matrix for one chemical unit in terms of the coordinates $\mathbf{s}$, and $\boldsymbol{\beta}_0$, $\boldsymbol{\gamma}_0$, and $\boldsymbol{\delta}_0$ are the cross terms of the types $\mathbf{s}(j)\mathbf{s}(j+1)$, $\mathbf{s}(j)\mathbf{s}(j+2)$, and $\mathbf{s}(j)\mathbf{s}(j+3)$, respectively. The $\epsilon=\exp(i\omega)$ and $\omega=2m\pi/n$. Prime denotes the transpose and superscript c was used to indicate the complex matrix.

The matrices $\mathbf{E}_k{}^c$ will have the Hermitian form as follows:

$$\mathbf{E}_k{}^c=\begin{Vmatrix}
 & \mathbf{S}'(E_k{}^c)_{Is} & \mathbf{S}'(E_k{}^c)_{IIs} & \mathbf{S}'(E_k{}^c)_{Ia} & \mathbf{S}'(E_k{}^c)_{IIa}\\
\mathbf{S}(E_k{}^c)_{Is} & \boldsymbol{\alpha}_1, & \boldsymbol{\beta}_1'(1+\epsilon^k)+\boldsymbol{\beta}_2'(\epsilon^{-k}+\epsilon^{2k}), & \boldsymbol{\gamma}_1'(\epsilon^{-k}-\epsilon^k)+\boldsymbol{\gamma}_2'(\epsilon^{-2k}-\epsilon^{2k}), & \boldsymbol{\delta}_1'(1-\epsilon^k)+\boldsymbol{\delta}_2'(\epsilon^{-k}-\epsilon^{2k})\\
\mathbf{S}(E_k{}^c)_{IIs} & \boldsymbol{\beta}_1(1+\epsilon^{-k})+\boldsymbol{\beta}_2(\epsilon^k+\epsilon^{-2k}), & \boldsymbol{\alpha}_2, & \boldsymbol{\beta}_3'(1-\epsilon^{-k})+\boldsymbol{\beta}_4'(\epsilon^k-\epsilon^{-2k}), & \boldsymbol{\gamma}_3'(\epsilon^{-k}-\epsilon^k)+\boldsymbol{\gamma}_4'(\epsilon^{-2k}-\epsilon^{2k})\\
\mathbf{S}(E_k{}^c)_{Ia} & \boldsymbol{\gamma}_1(\epsilon^k-\epsilon^{-k})+\boldsymbol{\gamma}_2(\epsilon^{2k}-\epsilon^{-2k}), & \boldsymbol{\beta}_3(1-\epsilon^k)+\boldsymbol{\beta}_4(\epsilon^{-k}-\epsilon^{2k}), & \boldsymbol{\alpha}_3, & \boldsymbol{\beta}_5'(1+\epsilon^k)+\boldsymbol{\beta}_6'(\epsilon^{-k}+\epsilon^{2k})\\
\mathbf{S}(E_k{}^c)_{IIa} & \boldsymbol{\delta}_1(1-\epsilon^{-k})+\boldsymbol{\delta}_2(\epsilon^k-\epsilon^{-2k}), & \boldsymbol{\gamma}_3(\epsilon^k-\epsilon^{-k})+\boldsymbol{\gamma}_4(\epsilon^{2k}-\epsilon^{-2k}), & \boldsymbol{\beta}_5(1+\epsilon^{-k})+\boldsymbol{\beta}_6(\epsilon^k+\epsilon^{-2k}), & \boldsymbol{\alpha}_4
\end{Vmatrix}, \tag{3}$$

where Greek letters $\boldsymbol{\alpha}_1$, $\boldsymbol{\beta}_2$, $\boldsymbol{\gamma}_3$, etc., represent real submatrices. Equation (3) is written for the case: $\boldsymbol{\delta}_0=\mathbf{0}$ (for simplicity). When $\boldsymbol{\delta}_0\neq\mathbf{0}$, further terms will be added.

In the cases of $k=0$ ($\epsilon^{\pm k}=1$) and $k=n/2$ ($\epsilon^{\pm k}=-1$),[4] which correspond to the A and B species, respectively, the matrices can be further factored into the following two real submatrices:

$$\mathbf{E}_{k=0}{}^c=\mathbf{A}=\begin{Vmatrix}\boldsymbol{\alpha}_1, & 2(\boldsymbol{\beta}_1'+\boldsymbol{\beta}_2'), & \mathbf{0}, & \mathbf{0}\\ 2(\boldsymbol{\beta}_1+\boldsymbol{\beta}_2), & \boldsymbol{\alpha}_2, & \mathbf{0}, & \mathbf{0}\\ \mathbf{0}, & \mathbf{0}, & \boldsymbol{\alpha}_3, & 2(\boldsymbol{\beta}_5'+\boldsymbol{\beta}_6')\\ \mathbf{0}, & \mathbf{0}, & 2(\boldsymbol{\beta}_5+\boldsymbol{\beta}_6), & \boldsymbol{\alpha}_4\end{Vmatrix}=\begin{Vmatrix}\mathbf{A}_1, & \mathbf{0}\\ \mathbf{0}, & \mathbf{A}_2\end{Vmatrix}, \tag{4}$$

[4] The $k\omega=m\pi$, because $m=$ odd number, when $n=$ even.

$$\mathbf{E}_{k=n/2}{}^{c}=\mathbf{B}$$

$$=\begin{Vmatrix} \alpha_1, & 2(\delta_1'+\delta_2'), & \mathbf{0}, & \mathbf{0} \\ 2(\delta_1+\delta_2), & \alpha_4, & \mathbf{0}, & \mathbf{0} \\ \mathbf{0}, & \mathbf{0}, & \alpha_2, & 2(\beta_3'+\beta_4') \\ \mathbf{0}, & \mathbf{0}, & 2(\beta_3+\beta_4), & \alpha_3 \end{Vmatrix} = \begin{Vmatrix} \mathbf{B}_1, & \mathbf{0} \\ \mathbf{0}, & \mathbf{B}_2 \end{Vmatrix}, \quad (5)$$

In Eq. (5) the order of the coordinates was changed to the order $\mathbf{S}(B)_{Is}$, $\mathbf{S}(B)_{IIa}$, $\mathbf{S}(B)_{IIs}$ and $\mathbf{S}(B)_{Ia}$.

In the unitary transformation $\mathbf{U}\mathbf{G}_0\mathbf{U}^{\dagger}$, the basis coordinates transform from the coordinates $\mathbf{s}$ into the complex symmetry coordinates $\mathbf{S}$ associated with the unit cell symmetry $C(2m\pi/n)$:

$$\mathbf{S}(A)=(1/n)^{\frac{1}{2}}\sum_{j=1}^{n}\mathbf{s}(j),$$

$$\mathbf{S}(B)=(1/n)^{\frac{1}{2}}\sum_{j=1}^{n}(-1)^{j-1}\mathbf{s}(j),$$

$$\mathbf{S}(E_{\pm k}{}^{c})=(1/n)^{\frac{1}{2}}\sum_{j=1}^{n}\epsilon^{\pm k(j-1)}\mathbf{s}(j), \qquad k=1, 2, \cdots. \quad (6)$$

TRANSFORMATION TO REAL MATRICES

The complex matrices $\mathbf{E}_{\pm k}{}^{c}$ can be easily transformed to real matrices by the following unitary transformation,

$$\mathbf{u}_k \begin{Vmatrix} \mathbf{E}_k{}^{c}, & \mathbf{0} \\ \mathbf{0}, & \mathbf{E}_{-k}{}^{c} \end{Vmatrix} \mathbf{u}_k{}^{\dagger} = \begin{Vmatrix} \mathbf{E}_k, & \mathbf{0} \\ \mathbf{0}, & \mathbf{E}_k \end{Vmatrix}, \quad (7)$$

where

$$\mathbf{u}_k=(\tfrac{1}{2})^{\frac{1}{2}}\begin{Vmatrix} 1 & 0 & 0 & 0 & 1 & 0 & 0 & 0 \\ 0 & \epsilon^{k/2} & 0 & 0 & 0 & \epsilon^{-k/2} & 0 & 0 \\ 0 & 0 & i & 0 & 0 & 0 & -i & 0 \\ 0 & 0 & 0 & -i\epsilon^{k/2} & 0 & 0 & 0 & i\epsilon^{-k/2} \\ -i & 0 & 0 & 0 & i & 0 & 0 & 0 \\ 0 & -i\epsilon^{k/2} & 0 & 0 & 0 & i\epsilon^{-k/2} & 0 & 0 \\ 0 & 0 & 1 & 0 & 0 & 0 & 1 & 0 \\ 0 & 0 & 0 & -\epsilon^{k/2} & 0 & 0 & 0 & -\epsilon^{-k/2} \end{Vmatrix}, \quad (8)$$

$$\mathbf{E}_k=\begin{Vmatrix} \alpha_1, & 2\left(\beta_1'\cos\frac{k\omega}{2}+\beta_2'\cos\frac{3k\omega}{2}\right), & -2(\gamma_1'\sin k\omega+\gamma_2'\sin 3k\omega), & 2\left(\delta_1'\sin\frac{k\omega}{2}+\delta_2'\sin\frac{3k\omega}{2}\right) \\ 2\left(\beta_1\cos\frac{k\omega}{2}+\beta_2\cos\frac{3k\omega}{2}\right), & \alpha_2, & 2\left(\beta_3'\sin\frac{k\omega}{2}+\beta_4'\sin\frac{3k\omega}{2}\right), & 2(\gamma_3'\sin k\omega+\gamma_4'\sin 3k\omega) \\ -2(\gamma_1\sin k\omega+\gamma_2\sin 3k\omega), & 2\left(\beta_3\sin\frac{k\omega}{2}+\beta_4\sin\frac{3k\omega}{2}\right), & \alpha_3, & -2\left(\beta_5'\cos\frac{k\omega}{2}+\beta_6'\cos\frac{3k\omega}{2}\right) \\ 2\left(\delta_1\sin\frac{k\omega}{2}+\delta_2\sin\frac{3k\omega}{2}\right), & 2(\gamma_3\sin k\omega+\gamma_4\sin 3k\omega), & -2\left(\beta_5\cos\frac{k\omega}{2}+\beta_6\cos\frac{3k\omega}{2}\right), & \alpha_4 \end{Vmatrix}. \quad (9)$$

TABLE I. Relationship among the coordinates, the **G** (or **F**) matrices and the transformation matrices for the case of the group $D(2m\pi/n)$.

Basis coordinates	**G** (or **F**) matrices	Transformations (matrices)
Internal coordinates	Eq. (1) or (2) of work cited in reference 1	Orthogonal transformation in each chemical unit. The redundant coordinates associated only with each chemical unit may be eliminated.
s Eq. (1) Intermediate symmetry coordinates associated with the symmetry in each chemical unit C_2	$\mathbf{G}_0$ (or $\mathbf{F}_0$), Eq. (2) of work cited in reference 1 consisted of $\boldsymbol{\alpha}_0$, $\boldsymbol{\beta}_0$, ⋯ instead of $\boldsymbol{\alpha}$, $\boldsymbol{\beta}$, ⋯.	
S Eq. (6) Intermediate complex symmetry coordinates associated with the symmetry of the unit cell $C(2m\pi/n)$ by regarding a chemical unit as a rigid unit.	$\mathbf{A}_1$, $\mathbf{A}_2$, $\mathbf{B}_1$, $\mathbf{B}_2$ and $\mathbf{E}_{\pm k}{}^e$, Eqs. (2)–(5) Hermitian matrices	**U** Eq. (3) of work cited in reference 1. Unitary transformation
Q Eq. (10) Complete real symmetry coordinates for $D(2m\pi/n)$	$\mathbf{E}_k$ Eq. (9) Real symmetry matrices	$\mathbf{u}_k$ Eqs. (7) and (8) Unitary transformation

In the matrix (8), $\epsilon^{k/2}=\exp(ik\omega/2)$ is introduced by taking account of the difference of the angle between the two types of twofold axes.

The final symmetry coordinates $\mathbf{Q}(E_k)$ are linear combinations of the original coordinates with the coefficients of real trigonometric functions:

$$\mathbf{Q}(E_k)_{Is}=(2/n)^{\frac{1}{2}}\sum_{j=1}^{n}\mathbf{s}(j)_{Is}\begin{matrix}\cos\\ \sin\end{matrix}[k(j-1)\omega],$$

$$\mathbf{Q}(E_k)_{IIs}=(2/n)^{\frac{1}{2}}\sum_{j=1}^{n}\mathbf{s}(j)_{IIs}\begin{matrix}\cos\\ \sin\end{matrix}[k(j-\tfrac{1}{2})\omega],$$

$$\mathbf{Q}(E_k)_{Ia}=(2/n)^{\frac{1}{2}}\sum_{j=1}^{n}\mathbf{s}(j)_{Ia}\begin{matrix}-\sin\\ \cos\end{matrix}[k(j-1)\omega],$$

$$\mathbf{Q}(E_k)_{IIa}=(2/n)^{\frac{1}{2}}\sum_{j=1}^{n}\mathbf{s}(j)_{IIa}\begin{matrix}\sin\\ -\cos\end{matrix}[k(j-\tfrac{1}{2})\omega], \qquad (10)$$

where the upper or lower term is to be used for each one of the pairs of the degenerate coordinates.

The calculation of the normal vibrations of the polyoxymethylene molecule is going on by use of this method and will be reported in the near future.

EXAMPLE: SKELETAL VIBRATIONS OF POLYOXYMETHYLENE MOLECULE

The factoring of the secular equation of the skeletal vibrations of the polyoxymethylene molecule, carried out in the previous paper,[1] will be performed here systematically by the present method, especially for the degenerate species.

We will start from the elements of the **G** or **F** matrix shown in Eq. (16) of the work cited in reference 1. The intermediate symmetry coordinates **s** may be taken as follows:

$$\mathbf{s}(j)_{Is}=\Delta\Theta_j,$$

$$\mathbf{s}(j)_{IIs}=\left\|\begin{matrix}(\tfrac{1}{2})^{\frac{1}{2}}\Delta(R_j+R_j')\\ \Delta\Theta_j'\end{matrix}\right\|,$$

$$\mathbf{s}(j)_{IIa}=(\tfrac{1}{2})^{\frac{1}{2}}\Delta(R_j-R_j'). \qquad (11)$$

Then the matrices $\boldsymbol{\alpha}_0$ and $\boldsymbol{\beta}_0$ will have the following forms:

$$\boldsymbol{\alpha}_0=\left\|\begin{matrix}c, & \sqrt{2}^{-1}(e+e_0), & g, & \sqrt{2}^{-1}(e-e_0)\\ \sqrt{2}^{-1}(e+e_0), & a+b, & \sqrt{2}f, & 0\\ g, & \sqrt{2}f, & d, & 0\\ \sqrt{2}^{-1}(e-e_0), & 0, & 0, & a-b\end{matrix}\right\|,$$

$$\boldsymbol{\beta}_0=\left\|\begin{matrix}c_0, & \sqrt{2}^{-1}(e+e_0), & g, & \sqrt{2}^{-1}(e_0-e)\\ 0, & \tfrac{1}{2}b_0, & \sqrt{2}^{-1}f_0, & -\tfrac{1}{2}b_0\\ 0, & \sqrt{2}^{-1}f_0, & d_0, & -\sqrt{2}^{-1}f_0\\ 0, & \tfrac{1}{2}b_0, & \sqrt{2}^{-1}f_0, & -\tfrac{1}{2}b_0\end{matrix}\right\|, \qquad (12)$$

where the notations a, b, c, etc., represent the same meaning as those in the work cited in reference 1.

After the unitary transformation $\mathbf{U}\mathbf{G}_0\mathbf{U}^\dagger$, we have the real matrices

$$\mathbf{A}_1=\left\|\begin{matrix}c+2c_0, & \sqrt{2}(e+e_0), & 2g\\ \sqrt{2}(e+e_0), & a+b+b_0, & \sqrt{2}(f+f_0)\\ 2g, & \sqrt{2}(f+f_0), & d+2d_0\end{matrix}\right\|, \qquad (13)$$

$$\mathbf{A}_2=a-b-b_0, \qquad (14)$$

and the complex matrices

$$\mathbf{E}_k{}^c=\begin{Vmatrix} c+2c_0\cos k\omega, & \sqrt{2}^{-1}(e+e_0)(1+\epsilon^k), & g(1+\epsilon^k), & \sqrt{2}^{-1}(e-e_0)(1-\epsilon^k) \\ \sqrt{2}^{-1}(e+e_0)(1+\epsilon^{-k}), & a+b+b_0\cos k\omega, & \sqrt{2}(f+f_0\cos k\omega), & \tfrac{1}{2}b_0(\epsilon^{-k}-\epsilon^k) \\ g(1+\epsilon^{-k}), & \sqrt{2}(f+f_0\cos k\omega), & d+2d_0\cos k\omega, & \sqrt{2}^{-1}f_0(\epsilon^{-k}-\epsilon^k) \\ \sqrt{2}^{-1}(e-e_0)(1-\epsilon^{-k}), & \tfrac{1}{2}b_0(\epsilon^k-\epsilon^{-k}), & \sqrt{2}^{-1}f_0(\epsilon^k-\epsilon^{-k}), & a-b-b_0\cos k\omega \end{Vmatrix} \tag{15}$$

$k=\pm1, \pm2, \pm3$ and ±4.

Furthermore by the unitary transformation (7) we have the real matrices $\mathbf{E}_k$'s. For example,

$$\mathbf{E}_1=\begin{Vmatrix} c+2c_0\cos\omega, & \sqrt{2}(e+e_0)\cos\tfrac{1}{2}\omega, & 2g\cos\tfrac{1}{2}\omega & \sqrt{2}(e-e_0)\sin\tfrac{1}{2}\omega \\ \sqrt{2}(e+e_0)\cos\tfrac{1}{2}\omega, & a+b+b_0\cos\omega, & \sqrt{2}(f+f_0\cos\omega), & b_0\sin\omega \\ 2g\cos\tfrac{1}{2}\omega, & \sqrt{2}(f+f_0\cos\omega), & d+2d_0\cos\omega, & \sqrt{2}f_0\sin\omega \\ \sqrt{2}(e-e_0)\sin\tfrac{1}{2}\omega & b_0\sin\omega, & \sqrt{2}f_0\sin\omega, & a-b-b_0\cos\omega \end{Vmatrix}. \tag{16}$$

The matrices $\mathbf{G}_{E_1}$ and $\mathbf{F}_{E_1}$ in Eqs. (21) in the work cited in reference 1 may be transformed into the form shown in Eq. (16) by the orthogonal transformation using the following matrix:

$$\mathbf{u}=\begin{Vmatrix} \sqrt{2}^{-1}, & \sqrt{2}^{-1}, & 0, & 0 \\ \cos(\omega/4), & -\sin(\omega/4), & 0, & 0 \\ 0, & 0, & \sqrt{2}^{-1}, & -\sqrt{2}^{-1} \\ 0, & 0, & \sin(\omega/4), & \cos(\omega/4) \end{Vmatrix}. \tag{17}$$

ACKNOWLEDGMENTS

The author expresses his sincere thanks to Professor S. Murahashi and Professor S. Seki for their continuous encouragement through this investigation and to Professor S. Shimanouchi of the University of Tokyo for his helpful advice and criticism. The author is also indebted to Dr. S. Naya of Kansei Gakuin University and Dr. N. Yajima of this Faculty for their helpful discussions. *Note added in proof*: A short communication by the authors on the normal vibrations and Raman spectrum of polyoxymethylene has been recently published in J. Chem. Phys. **35,** 369 (1961).

Thermodynamic Properties of Nonstoichiometric Urania-Zirconia Solid Solutions

S. ARONSON* AND J. C. CLAYTON

Bettis Atomic Power Laboratory, Pittsburgh 30, Pennsylvania

(Received February 6, 1961)

Thermodynamic information has been obtained, at temperatures in the neighborhood of 1000°C, on nonstoichiometric urania-zirconia solid solutions, $U_yZr_{1-y}O_{2+x}$, with y values of 0.90, 0.80, and 0.70 and x values between 0.04 and 0.17. A solid-state electrochemical technique was used. Partial molar free energies, entropies, and enthalpies of solution of oxygen in the solid were calculated. The results are compared with results previously obtained on nonstoichiometric urania and urania-thoria solid solutions.

INTRODUCTION

STUDIES of phase equilibria in the urania-zirconia system[1–6] indicate that uranium dioxide and zirconium dioxide form limited regions of solid solution at low temperatures. The limit of solubility of ZrO_2 in UO_2 at room temperature determined by Lambertson and Mueller,[1] about 40 mole percent ZrO_2, is probably too high. The limit of about 13 mole percent established by Voronov and co-workers[3] and corroborated by the work of Evans[4] and Schaner[5] is probably more nearly correct. The latter workers[3–5] have found, however, that when solid solution samples containing more than 13 mole percent zirconia are quenched from high temperatures (>1700°C), they retain their single-phase structure. The rates of precipitation of the zirconia-rich phase upon cooling are, apparently, very slow. As noted by Voronov *et al.*, these slow rates of phase change probably are the reason for the high solubility limit found by Lambertson and Mueller.

Roberts and co-workers[6] have reported work on the oxidation of urania-zirconia samples. The cubic solid solution containing 25 mole percent zirconia oxidized to a composition $U_{0.75}Zr_{0.25}O_{2.23}$ before other phases appeared. The lattice parameter decreased from 5.395 to 5.339 A upon oxidation to $U_{0.75}Zr_{0.25}O_{2.23}$.

In the present study, thermodynamic properties of urania-zirconia solid solutions $U_yZr_{1-y}O_{2+x}$ with y values of 0.90, 0.80, and 0.70 and values of x between 0.04 and 0.17 have been measured using a solid-state electrochemical technique previously applied to nonstoichiometric uranium dioxide and urania-thoria solid solutions.[7,8] The thermodynamic parameters in the UO_2–ZrO_2 system are compared to those found in the urania and the urania-thoria systems by means of the equations developed in a previous paper.[8]

EXPERIMENTAL

The experimental procedures have been discussed in some detail in previous papers.[7,8] The electrochemical cells used were of the type Fe, FeO | (ZrO_2+CaO) | $U_yZr_{1-y}O_{2+x}$, Pt. The solid electrolyte was a solid solution of 15 mole percent CaO in ZrO_2. The apparatus used for the electrochemical measurements was identical with that described in the work on urania-thoria solid solutions.[8]

The solid solutions of compositions $U_yZr_{1-y}O_2$ were prepared from ball-milled mixtures of UO_2 and ZrO_2 powders. The ball-milled powders were heated in hydrogen at 1725–1750°C for 20 hr to form the solid solutions and were then removed from the furnace. Controlled amounts of oxygen were added to the samples by controlled oxidation in oxygen at 200–400°C. The oxidized samples were annealed for 24 hr at 800°C in vacuum to homogenize the oxygen.

X-ray spectrometer patterns of the unoxidized and oxidized samples showed the presence of only the fluorite structure in all cases. For the determination of the lattice parameters, each powder was mixed with ThO_2 powder, which has a fluorite structure of known lattice parameter, and the angular distances between corresponding spectrometer peaks were measured. The measured lattice parameters of the $U_yZr_{1-y}O_{2+x}$ compositions, with an estimated accuracy of ±0.003 A, are shown in Fig. 1. The values of the lattice parameters of the unoxidized samples are between 0.010 and 0.015 A higher than the parameters measured by Evans[4] on samples of corresponding compositions which had been rapidly cooled from the melts. Evans found, however, that the lattice parameter of the sample containing 10 mole percent ZrO_2 increased from 5.4317 to 5.4411 A when the sample was heated for 250 hr at 1350°C. It is, therefore, possible that the differences in heat treatment of the samples in the two studies are responsible for the

* Present Address: Brookhaven National Laboratory, Upton, Long Island, New York.

[1] W. A. Lambertson and M. H. Mueller, J. Am. Ceram. Soc. **36,** 365 (1953).

[2] G. M. Wolten, J. Am. Chem. Soc. **80,** 4772 (1958).

[3] N. M. Voronov, E. A. Voitekhova, and A. S. Danilin, *Proceedings of the Second United Nations International Conference on the Peaceful Uses of Atomic Energy, Geneva, 1958* (United Nations, Geneva, 1958), Vol. 6, p. 221.

[4] P. E. Evans, J. Am. Ceram. Soc. **43,** 443 (1960).

[5] B. E. Schaner (deceased), private communication based on microstructural examination of UO_2–ZrO_2 mixtures (to be published).

[6] L. E. J. Roberts, L. E. Russell, A. G. Adwick, A. J. Walter, and M. H. Rand, *Proceedings of the Second United Nations International Conference on the Peaceful Uses of Atomic Energy, Geneva, 1958* (United Nations, Geneva, 1958), Vol. 28, p. 215.

[7] S. Aronson and J. Belle, J. Chem. Phys. **29,** 151 (1958).

[8] S. Aronson and J. C. Clayton, J. Chem. Phys. **32,** 749 (1960).

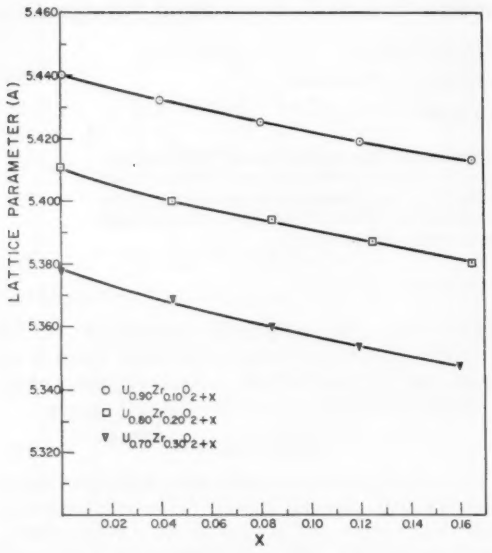

FIG. 1. Lattice parameters of $U_yZr_{1-y}O_{2+x}$ compositions.

differences in the values of the lattice parameters. The value of the lattice constant reported by Roberts *et al.*,[6] for $U_{0.75}Zr_{0.25}O_2$, 5.395 A, is in agreement with the data in Fig. 1. The value of the lattice constant reported by Roberts *et al.*, for $U_{0.75}Zr_{0.25}O_{2.23}$, 5.339 A, appears to be somewhat lower than would be expected from examining the data in Fig. 1. The reason for this discrepancy is not known.

To determine whether small amounts of a second phase were present in the samples containing 0.20 and 0.30 mole percent ZrO_2, microscopic observations were made on high density $U_yZr_{1-y}O_2$ plates. The plates were fabricated from the $U_yZr_{1-y}O_2$ powders which were ball-milled again, were pressed into plates, and were sintered for an additional 20 hours at 1725–1750°C. Microscopic observations were made on polished and etched sections of the plates. No second phase was observed. The phase studies of the urania-zirconia system discussed in the foregoing[3–5] indicate that the solid solutions containing

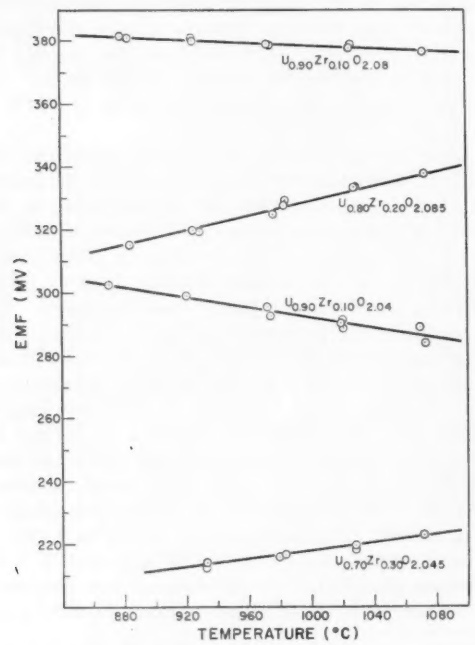

FIG. 2. Electromotive force of cells

Fe, FeO | (ZrO_2+CaO) | $U_yZr_{1-y}O_{2+x}$, Pt.

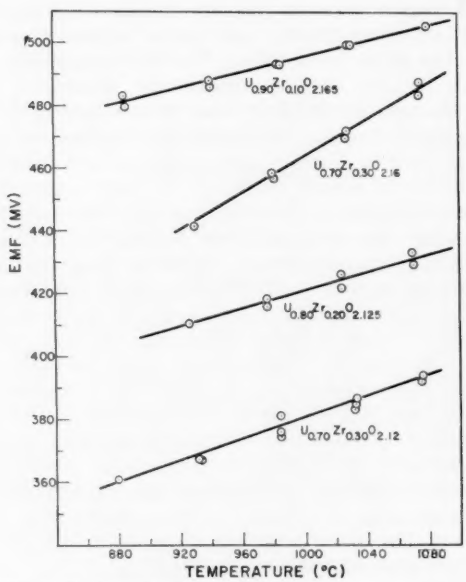

FIG. 3. Electromotive force of cells

Fe, FeO | (ZrO_2+CaO) | $U_yZr_{1-y}O_{2+x}$, Pt.

20 and 30 mole percent ZrO_2 are in metastable rather than thermodynamic equilibrium. The long-time stability of these solid solutions was checked by annealing $U_{0.8}Zr_{0.2}O_2$ and $U_{0.7}Zr_{0.3}O_2$ samples in vacuum at 1050°C for 20 hr. No changes in lattice parameter were observed indicating that the solid solutions are stable at least up to a temperature of 1050°C.

The oxygen contents of the $U_yZr_{1-y}O_{2+x}$ samples were determined by weight changes on reduction in hydrogen to $U_yZr_{1-y}O_2$ at 800°C. A spring balance made of Nispan C alloy was employed for the determinations. The estimated accuracy of the oxygen determinations is ± 0.01 in the value of x.

RESULTS

Figures 2 and 3 show plots of emf as a function of temperature for some selected compositions of

$U_yZr_{1-y}O_{2+x}$. The variation of emf with temperature was approximately linear in all cases. Some instability of the emf cell was observed with several of the samples at temperatures below about 930°C. The instability consisted of a slow increase in voltage at constant temperature. The effect became stronger as the temperature was lowered and was approximately 10 mv/hr at 880°C. The cause of this instability was not determined. Since this instability occurred in some samples of a given composition, but not in others of the same composition, it was not ascertained whether the urania-zirconia samples were solely responsible for the effect. When the effect was present, the temperature was not lowered below about 930°C. This limit is observed in some of the data in Figs. 2 and 3.

Thermodynamic information was obtained from the EMF data in the manner previously described.[7,8] The electrochemical reactions which occur in the cell Fe, FeO | (ZrO_2+CaO) | $U_yZr_{1-y}O_{2+x}$ are the formation of iron oxide on the left and the removal of oxygen from the solid solution on the right. The partial molar free energy of solution of oxygen in $U_yZr_{1-y}O_{2+x}$, $\bar{F}_{O_2}$, can be obtained from the relationship

$$\bar{F}_{O_2}=2\Delta F^\circ_{Fe_{0.95}O}-\Delta F_{cell},$$

where ΔF_{cell} is the free energy change for the electrochemical cell and $\Delta F^\circ_{Fe_{0.95}O}$ is the standard free energy of formation of iron oxide in equilibrium with iron. The ΔF_{cell} is related to the measured emf by the standard expression

$$\Delta F_{cell}=-4F(\text{emf});$$

F is Faraday's number.

The partial molar entropy $\bar{S}_{O_2}$ and enthalpy $\bar{H}_{O_2}$ of solution of oxygen in the solid solution are calculated from the standard relationships

$$\bar{S}_{O_2}=-\partial\bar{F}_{O_2}/\partial T$$

$$\bar{H}_{O_2}=\bar{F}_{O_2}+T\bar{S}_{O_2}.$$

TABLE I. Partial molar free energies, entropies, and enthalpies of solution of oxygen in $U_yZr_{1-y}O_{2+x}$.

y	$2+x$ (±0.01)	$-\bar{F}_{O_2}$ (kcal/mole) 1250°K	$-\bar{S}_{O_2}$ (eu/mole)	$-\bar{H}_{O_2}$ (kcal/mole)	$-Q$ (eu/mole)
0.90	2.04	58.3	23	87	54
0.90	2.04	58.6	22	86	53
0.90	2.04	59.7	25	91	56
0.90	2.08	51.8	28	87	50
0.90	2.08	52.1	32	92	54
0.90	2.08	53.6	31	92	53
0.90	2.12	47.5	37	94	53
0.90	2.12	56.6	37	93	53
0.90	2.12	47.6	37	93	53
0.90	2.165	41.0	44	96	55
0.90	2.165	41.3	41	93	52
0.80	2.045	66.0	28	101	57
0.80	2.045	65.7	32	106	61
0.80	2.085	56.6	37	103	57
0.80	2.085	56.1	36	101	56
0.80	2.085	56.6	40	108	60
0.80	2.125	48.2	43	102	57
0.80	2.125	49.9	46	106	60
0.80	2.125	50.4	48	110	62
0.80	2.165	40.4	48	101	57
0.80	2.165	42.0	54	110	63
0.70	2.045	66.8	35	111	62
0.70	2.045	64.2	36	109	63
0.70	2.045	66.1	38	114	65
0.70	2.085	55.3	38	103	56
0.70	2.085	57.9	45	114	63
0.70	2.12	50.9	48	111	61
0.70	2.12	52.0	46	109	59
0.70	2.16	42.9	57	114	65
0.70	2.16	44.6	55	113	63

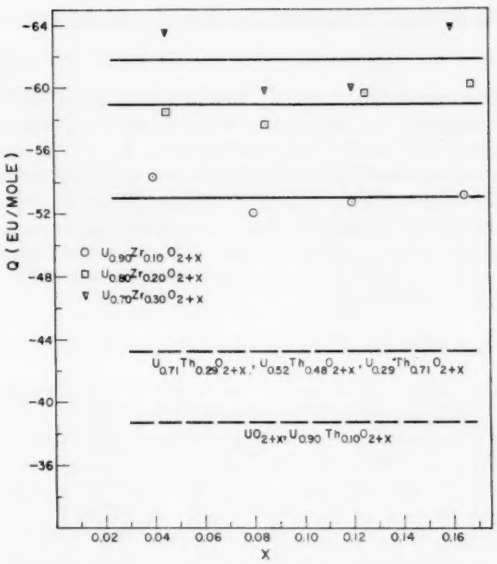

FIG. 4. Plot of Q values for $U_yZr_{1-y}O_{2+x}$ compositions.

The thermodynamic data for the $U_yZr_{1-y}O_{2+x}$ compositions are shown in Table I. The values of the parameter Q in the last column of Table I are discussed and utilized in the discussion which follows.

It is seen in Table I that the partial molar entropies increase negatively with increasing oxygen content or increasing zirconium content. This result is similar to that obtained for urania and urania-thoria solid solutions. The partial molar enthalpies of solution for the $U_yZr_{1-y}O_{2+x}$ compositions increase negatively with increasing zirconium content. They are higher negatively than those obtained for urania and urania-thoria compositions. The partial molar free energies for the $U_yZr_{1-y}O_{2+x}$ compositions are also higher negatively than the values for the corresponding $U_yTh_{1-y}O_{2+x}$ compositions. A partial explanation of the results is presented in the following discussion.

DISCUSSION

The oxidation of urania-zirconia solid solutions is discussed on the basis of the same reaction scheme used for

the oxidation of urania-thoria solid solutions[8];

$$O_2(gas)+4U^{+4}+2\ \text{i.s.}=2O^{i}+4U^{+5}. \quad (1)$$

The symbols, i.s. and O^{i}, have the meanings, vacant interstitial sites and interstitial oxygen ions, respectively. The mechanism represented in Eq. (1) is supported by electrical measurements on nonstoichiometric UO_2.[9] An equation was developed for the partial molar entropy of solution $\bar{S}_{O_2}$ on the assumption that changes in the configurational entropies of the uranium cations and the interstitial oxygen ions are of primary importance.[8] The equation is

$$\bar{S}_{O_2}=-2R\ln[x/(1-x)]-4R\ln[2x/(y-2x)]+Q. \quad (2)$$

The values of x and y are those in the formula $U_yM_{1-y}O_{2+x}$ where M is the substitutional metal cation, in this case zirconium. An examination of the derivation of Eq. (2)[8] shows that the metastability of the urania-zirconia solid solutions containing 20 and 30 mole percent zirconia does not, necessarily, invalidate Eq. (2) for use in the urania-zirconia system. The zirconium ions are probably frozen into permanent, approximately random, positions in the cationic lattice when the solid is rapidly cooled from above 1700°C. The U^{+4} and U^{+5} ions exchange positions primarily by electronic transfer of charge rather than by ionic movement. The latter conclusion is deduced from electrical data on nonstoichiometric uranium dioxide.[9] The factor Q in Eq. (2) includes a term for the decrease in entropy which occurs upon removing one mole of oxygen from the gas phase and a term for the contribution to the vibrational entropy of the solid of the added interstitial oxygen ions.

It would appear reasonable for the factor Q to remain approximately constant with changes in oxygen or uranium content as was found to be the case in urania and urania-thoria solid solutions. Plots of Q versus oxygen content for the three zirconium compositions are shown in Fig. 4. The values of Q in Fig. 4 are averages of the Q values found in Table I. The values of Q in Table I were calculated from Eq. (2) using the experimental entropy values given in Table I.

It is observed in Fig. 4 and Table I that Q is reasonably constant with respect to variations in oxygen content. The Q values are, however, much higher negatively for the urania-zirconia solid solutions than for urania and urania-thoria compositions.[8] The reason for the large effect of zirconium addition on the factor Q is not known. Calculations of the vibrational frequencies of the interstitial oxygen ions were made, using the Einstein relationship between vibrational entropy and vibrational frequency, in a manner similar to the calculation made for urania-thoria solid solutions.[8] Using values for Q in the range of -50 to -60 eu/mole, vibrational frequencies in the neighborhood of 10^{14} cps were calculated. A vibrational frequency of 10^{13} cps was calculated for urania and urania-thoria solid solutions using a Q value of -40 eu/mole. It is not clear why the incorporation of zirconium should have such a large effect on the vibrational entropies of the interstitial oxygen ions and their neighboring ions. It is, therefore, evident that Eq. (2), which is able to account for much of the experimental data in this and the previous studies, is inadequate for a detailed description of the urania-base solid solutions.

It is possible that the high negative values of Q compared to that obtained in the case of urania-thoria may be, at least partially, related to the high negative values observed for the partial molar enthalpy $\bar{H}_{O_2}$ in the urania-zirconia solid solutions. The values of $-\bar{H}_{O_2}$ are seen in Table I to be in the range of 85–115 kcal/mole compared to values of about 65–85 kcal/mole for urania and urania-thoria. If the differences in the values of Q among the systems represent differences in vibrational entropy as discussed above, then the lower vibrational entropies in urania-zirconia would be accompanied by lower vibrational energies in urania-zirconia as compared to urania-thoria. This would lead to higher negative values for $\bar{H}_{O_2}$. The partial molar enthalpy is a complex function, as is discussed elsewhere,[10] and it is difficult, at this time, to explain the differences in enthalpy values which occur upon varying the oxygen or uranium content in the nonstoichiometric oxides.

A comparison of the thermodynamic properties of the urania, the urania-thoria, and the urania-zirconia systems indicates that thorium cations are more similar to uranium cations than are zirconium cations. Their substitution for uranium cations in the lattice has less effect on the thermodynamic parameters than the substitution of zirconium ions. This finding is reasonable on the basis of the closer similarity of uranium and thorium, compared to uranium and zirconium, in ion size, valence structure and the crystallographic structure of the oxides.[11,12] Urania and thoria form a continuous range of solid solutions in contrast to urania-zirconia where limited solid solution ranges are present.[1–5,13]

ACKNOWLEDGMENTS

The authors are grateful to the Atomic Energy Commission and the Westinghouse Electric Corporation for permission to publish this work. The authors wish to acknowledge the able assistance of J. E. Rulli in carrying out the experimental measurements. They also wish to thank Dr. J. Belle for his helpful discussion of this work.

[9] S. Aronson, J. E. Rulli, and B. E. Schaner, "Electrical conductivity and thermoelectric power measurements on UO_{2+x}" (to be published).

[10] S. Aronson, Bettis Tech. Rev. (to be published).

[11] L. Pauling, *The Nature of the Chemical Bond* (Cornell University Press, Ithaca, New York), Chap. 7.

[12] G. T. Seaborg and J. J. Katz, *The Actinide Elements* (McGraw-Hill Book Company, Inc., New York, 1954), Chap. 17 by G. T. Seaborg and Chap. 18 by W. H. Zachariasen.

[13] W. Trzebiatowsky and P. W. Selwood, J. Am. Chem. Soc. **72**, 4504 (1950).

THE JOURNAL OF CHEMICAL PHYSICS VOLUME 35, NUMBER 3 SEPTEMBER, 1961

Vibronic Coupling. I. Mathematical Treatment for Two Electronic States

ROBERT L. FULTON* AND MARTIN GOUTERMAN

Conant Chemical Laboratory, Harvard University, Cambridge 38, Massachusetts

(Received February 6, 1961)

A general mathematical treatment of vibronic coupling of two electronic states in molecules and dimers is presented. The 2×2 matrix Hamiltonian which is derived is shown to reduce to two one-dimensional Hamiltonians provided a certain minimum amount of symmetry is present. Some general selection rules governing electronic transitions to these states from the ground state are obtained, showing that the spectral distribution in hot bands may differ considerably from that in normal bands when vibronic coupling occurs. A special model which considers the coupling to arise from a single mode of vibration is presented. Two limiting cases which can be treated approximately by perturbation theory are considered in detail. These are shown to give rise to a "pseudo Jahn-Teller effect" and to vibrational borrowing in the two different limits.

I. INTRODUCTION

OVER the past five years there has been a growing interest in problems of vibronic coupling, that is, the interaction of nuclear vibration and electronic motion in molecules. Unusual effects caused by such couplings have been traced to either linear or quadratic terms in the nuclear displacements.[1] It is with the former that this paper is primarily concerned.

In molecules, linear vibronic coupling terms have been extensively investigated in two physical situations. The one is the case of vibrational borrowing, an effect that appears most clearly with forbidden electronic transitions made allowed through the simultaneous excitation of certain asymmetric vibrations. Such borrowing by the lowest singlet excited state of benzene has been recently discussed by Liehr[2] and by Murrell and Pople.[3] The other physical situation is the one originally investigated by Jahn and Teller.[4] They pointed out that the nuclei of molecules in degenerate electronic states would, in general, be unstable with respect to linear displacements along certain asymmetric normal coordinates. Interest in this effect was revived with the papers by Moffitt and Liehr[5] and by Öpik and Pryce.[6] Subsequent work by these and other authors traced the consequences of such linear displacements in a variety of physical situations.[7–10]

In addition to their occurence in molecules, linear vibronic coupling plays an important role in another rather different physical case, the coupling between excited states in condensed systems. This paper limits itself to the simplest such system, the dimer. Stimulating qualitative discussions of this problem have been given by Simpson and Peterson[11] and by McClure.[12] Cases where the "exciton" coupling between the electronic states is respectively weak or strong have been distinguished, and the effects on the spectra in the two cases described. Recently, the beginning of a formal treatment of this problem was given by Moffitt and Witkowski.[13]

In this paper we present a general mathematical treatment of vibronic coupling between two electronic states. We begin by showing that vibronic coupling in molecules and exciton coupling in dimers can both be reduced to the same 2×2 matrix Hamiltonian in the nuclear coordinates. We then show that if a certain minimum amount of symmetry is present, the matrix Hamiltonian can be reduced to two one-dimensional Hamiltonians, which display the vibronic problem through the explicit appearance of a symmetry operator. Using more special assumptions, we then further reduce the problem to dependence on a nuclear displacement parameter λ and an electronic energy parameter ϵ. The case $\lambda \gg \epsilon$ approaches the Jahn-Teller limit in molecules and characterizes weak exciton coupling in dimers. The case $\lambda \ll \epsilon$ characterizes vibrational borrowing in molecules and strong exciton coupling in dimers. We conclude by presenting the solutions to the vibronic problem in these two limiting cases.

II. MOLECULAR CASE

The molecular Hamiltonian may be written as

$$H = T_n + T_e + V(q, Q), \tag{2.1}$$

where T_n and T_e are the nuclear and electronic kinetic energies and $V(q, Q)$ is the potential energy of the system depending on the electronic and nuclear co-

* National Science Foundation Predoctoral Fellow, 1958–61.

[1] H. C. Longuet-Higgins, *Advances in Spectroscopy* (Interscience Publishers, Inc., New York, in press), Vol. II.

[2] A. D. Liehr, Z. Naturforsch. **13a**, 311 (1958).

[3] J. N. Murrell and J. A. Pople, Proc. Phys. Soc. (London) **69**, 245 (1956).

[4] H. A. Jahn and E. Teller, Proc. Roy. Soc. (London) **A161**, 22 (1937).

[5] W. Moffitt and A. D. Liehr, Phys. Rev. **106**, 1195 (1957).

[6] U. Öpik and M. H. L. Pryce, Proc. Roy. Soc. (London) **A238**, 425 (1957).

[7] W. Moffitt and W. Thorson, Phys. Rev. **108**, 1251 (1957).

[8] H. C. Longuet-Higgins, U. Öpik, M. H. L. Pryce, and R. A. Sack, Proc. Roy. Soc. (London) **A244**, 1 (1958).

[9] W. D. Hobey and A. D. McLachlan, J. Chem. Phys. **33**, 1695 (1960).

[10] H. M. McConnell and A. D. McLachlan, J. Chem. Phys. **34**, 1 (1961).

[11] W. T. Simpson and D. L. Peterson, J. Chem. Phys. **26**, 588 (1957).

[12] D. S. McClure, Can. J. Chem. **36**, 59 (1958).

[13] A. Witkowski and W. Moffitt, J. Chem. Phys. **33**, 872 (1960).

ordinates symbolized by q and Q, respectively. We assume in writing (2.1) that the uniform motion of the center of mass and the rotation of the molecule have been removed and that any dependence on spin may be neglected. The eigenvalues and eigenfunctions of H are usually approached through the adiabatic approximation.[14] This proceeds by first determining the solutions of

$$[T_e+V(q,Q)]\psi_m(q,Q)=W_m(Q)\psi_m(q,Q), \quad (2.2)$$

where the nuclear coordinates are treated as parameters. The wave functions $\psi_m(q,Q)$ depend not only on the electronic coordinates, but also parametrically on the nuclear coordinates. Eigenfunctions of (2.1) are then written in the form

$$\Psi(q,Q)=\sum_m \phi_m(Q)\psi_m(q,Q), \quad (2.3)$$

where the functions $\phi_m(Q)$ are found[14] by requiring that Ψ satisfy the eigenvalue equation

$$H\Psi(q,Q)=E\Psi(q,Q). \quad (2.4)$$

Although the adiabatic approach outlined above probably gives the most accurate prescription for finding the eigenfunctions of (2.1), its very generality leads to difficulties in dealing with the resulting equations. We shall, therefore, follow the simpler harmonic approximation[1,14] which allows us to make judicious use of the symmetry of the molecule, if present. The resulting equations still retain considerable novelty and can be expected to give valuable insight into the nature of vibronic coupling.

Proceeding by the harmonic approximation, we take as the basis functions for the electronic coordinates the orthonormal solutions[15] of the equation

$$[T_e+V(q,Q_0)]\psi_k(q)=W_k\psi_k(q). \quad (2.5)$$

This equation differs from (2.2) in that the nuclear coordinates in the Hamiltonian have been fixed at the positions denoted by Q_0. Therefore, the functions $\psi_k(q)$ depend only on electronic coordinates, a convention we shall maintain throughout this paper; however, their exact form depends on the choice of Q_0. Eigenfunctions of (2.4) are assumed to have the form

$$\Psi(q,Q)=\sum_k \phi_k(Q)\psi_k(q), \quad (2.6)$$

where normalization of $\Psi(q,Q)$ requires

$$\sum_k \int \phi_k^*(Q)\phi_k(Q)\,dQ=1. \quad (2.7)$$

Upon substituting (2.6) into (2.4), multiplying by $\psi_j^*(q)$, and integrating over the electronic coordinates, we obtain

$$T_n\phi_j(Q)+\sum_k V_{jk}(Q)\phi_k(Q)=E\phi_j(Q), \quad (2.8)$$

where

$$V_{jk}\equiv\int dq\psi_j^*(q)[T_e+V(q,Q)]\psi_k(q). \quad (2.9)$$

The functions $\phi_k(Q)$ are therefore determined by the set of coupled equations (2.8). The potential functions $V_{jk}(Q)$ are usually represented as power series expansions in the normal coordinates Q_μ. We follow the customary procedure and assume that Q_0 has been so chosen that $V_{00}(Q_0)$ is a minimum, i.e., there are no linear terms in Q_μ in the ground state.

It is shown in Appendix I that the condition under which coupling between two electronic states may be ignored is

$$|V_{jk}(Q)|\ll|V_{jj}(Q)-V_{kk}(Q)|\simeq|W_j-W_k|, \quad (2.10)$$

where Q is in the range of nuclear vibrations. In this paper we shall restrict consideration to three electronic states: ψ_0, a totally symmetric ground state; and ψ_1, and ψ_2, two excited states which differ in symmetry. We shall assume that only for the latter two is (2.10) violated. We shall also assume that the Hamiltonian (2.1) transforms as the totally symmetric representation of the group used to classify the electronic states ψ_k. It is to be noted that this is a conscious restriction on the symmetry of the molecule as it allows the total states to be classified according to a particular symmetry group.

The vibrational functions $\phi_0(Q)$ of the ground state are determined by

$$[T_n+V_{00}(Q)]\phi_0(Q)=E\phi_0(Q), \quad (2.11)$$

since we have assumed that the terms $V_{0k}(Q)$ may be neglected. The linear terms in the normal coordinates have been removed from $V_{00}(Q)$ by our choice of Q_0. Therefore, after a suitable choice of coordinates Q_μ, $V_{00}(Q)$ becomes

$$V_{00}(Q)=W_0+\sum_\mu(\partial^2V_{00}/\partial Q_\mu^2)\,|_{Q_0}Q_\mu^2. \quad (2.12)$$

Thus, to the neglect of anharmonic terms, $\phi_0(Q)$ is simply a product of harmonic oscillator functions, each depending on a Q_μ.

The vibronic problem arises in the case of the states ψ_1 and ψ_2. The equations determining ϕ_1 and ϕ_2 may be written as a matrix equation

$$\mathbf{H}'\boldsymbol{\phi}'=E\boldsymbol{\phi}', \quad (2.13)$$

[14] Max Born and Kun Huang, *Dynamical Theory of Crystal Lattices* (Oxford University Press, New York, 1954), pp. 170, 406–407.

[15] The distinction made by Liehr (reference 2, p. 312) between exact and approximate solutions of (24) causes no difficulty in the harmonic approximation. The equations of this paper hold for approximate solutions as long as we satisfy the less stringent condition

$$\int dq\psi_j^*(q)H(Q_0)\psi_k(q)=W_k\delta_{jk}.$$

where

$$\mathbf{H}'=\{T_n+\tfrac{1}{2}[V_{11}(Q)+V_{22}(Q)]\}\mathbf{1}$$
$$+\tfrac{1}{2}[V_{11}(Q)-V_{22}(Q)]\mathfrak{d}_3+V_{12}\mathfrak{d}_1 \quad (2.14)$$

$$\boldsymbol{\phi}'=\begin{pmatrix}\phi_1(Q)\\ \phi_2(Q)\end{pmatrix} \quad (2.15)$$

$$\mathbf{1}=\begin{pmatrix}1&0\\0&1\end{pmatrix},\qquad \mathfrak{d}_1=\begin{pmatrix}0&1\\1&0\end{pmatrix},\qquad \mathfrak{d}_3=\begin{pmatrix}1&0\\0&-1\end{pmatrix}. \quad (2.16)$$

The $\mathfrak{d}_j$ are the familiar Pauli spin matrices. The identity of (2.13) with (2.8) is readily seen by writing the matrix equation in terms of its components. In writing (2.13) and (2.14) we have assumed that the electronic wave functions have been chosen real, as is always possible in the absence of a magnetic field. Although $\mathbf{H}'$ is the matrix derived directly from (2.8), it proves convenient in our later discussion to work not with it, but with a Hamiltonian obtained by the following unitary transformation:

$$\mathbf{H}=\mathbf{S}^{\dagger}\mathbf{H}'\mathbf{S} \quad (2.17)$$

$$\mathbf{S}=2^{-\frac{1}{2}}(\mathfrak{d}_1+\mathfrak{d}_3), \quad (2.18)$$

which yields the following eigenvalue equation

$$\mathbf{H}\boldsymbol{\phi}=E\boldsymbol{\phi}, \quad (2.19)$$

where

$$\mathbf{H}=[T_n+\tfrac{1}{2}(V_{11}+V_{22})]\mathbf{1}+\tfrac{1}{2}[V_{11}-V_{22}]\mathfrak{d}_1+V_{12}\mathfrak{d}_3 \quad (2.20)$$

$$\boldsymbol{\phi}=2^{-\frac{1}{2}}\begin{pmatrix}\phi_1+\phi_2\\ \phi_1-\phi_2\end{pmatrix}. \quad (2.21)$$

The assumption that the states $\psi_1(q)$ and $\psi_2(q)$ are of different symmetry is shown in Appendix II to guarantee, for most groups, the existence of a Hermitian symmetry operator G having the properties

$$[G,\ T_n]_-=[G_1V_{11}]_-=[G,\ V_{22}]_-=[G,\ V_{12}]_+=0 \quad (2.22)$$

$$G^2=1, \quad (2.23)$$

where

$$[A,\ B]_{\pm}=AB\pm BA. \quad (2.24)$$

The properties of G given by (2.22) and (2.23) together with those of the $\mathfrak{d}_j$ matrices may be shown to imply that

$$[G\mathfrak{d}_1,\ \mathbf{H}]_-=0 \quad (2.25)$$

$$(G\mathfrak{d}_1)^2=\mathbf{1}. \quad (2.26)$$

From (2.25) we may conclude that all eigenstates of $\mathbf{H}$ may be chosen to be eigenstates of $G\mathfrak{d}_1$. From (2.26) it follows that the eigenvalues of $G\mathfrak{d}_1$ are ±1. As we shall show later, these properties allow the reduction of the matrix eigenvalue equation to one-dimensional form.

III. DIMERIC CASE

We shall consider the case of a dimer formed from two identical molecules A and B, in such a way that there exists a symmetry operation under which the molecules are exchanged. The dimer has a Hamiltonian identical with (2.1). However, because the coupling between the two molecules is assumed to be weak, it is convenient to separate the Hamiltonian as follows:

$$H=H^A+H^B+V^{AB}(q,Q)+T_n{}^{AB}, \quad (3.1)$$

where

$$H^A=T_n{}^A+T_e{}^A+V(q^A,Q^A). \quad (3.2)$$

H^A and H^B represent the Hamiltonians of the single isolated molecules; $V^{AB}(q,Q)$ represents the interactions between the two molecules; and $T_n{}^{AB}$ represents the kinetic energy associated with their relative motion. Again we shall follow the harmonic rather than the adiabatic approximation.

The wave functions for the Hamiltonian are obtained, as in the molecular case, by first solving the electronic equation with fixed nuclei. These positions are fixed, as before, by requiring that the ground state energy of the dimer be a minimum with respect to nuclear displacement. We obtain an equation completely analogous to (2.5):

$$[T_e{}^A+V(q^A,Q_0{}^A)+T_e{}^B+V(q^B,Q_0{}^B)$$
$$+V^{AB}(q,Q_0)]\psi_k(q)=W_k\psi_k(q). \quad (3.3)$$

At this point the dimeric problem takes on its special aspect. We shall assume that $V^{AB}(q,Q_0)$ is sufficiently small that it is best included with the subsequent treatment of nuclear kinetic energies. In place of (3.3) we obtain an equation which is fully separable into the equations for each molecule:

$$[T_e{}^A+V(q^A,Q_0{}^A)]\psi_R{}^A(q)=W_R\psi_R{}^A(q). \quad (3.4)$$

We shall follow Moffitt and Witkowski in neglecting electron exchange and, thereby, charge transfer states. We then obtain as solutions of (3.3) with $V^{AB}(q,Q_0)$ omitted:

$$\psi_k(q)=\psi_R{}^A(q^A)\psi_S{}^B(q^B). \quad (3.5)$$

We shall consider that the states $\psi_R{}^A(q^A)$ and $\psi_S{}^B(q^B)$ are individually normalized. Hence, with the neglect of electron exchange, $\psi_k(q)$ is also normalized.

As in the molecular case, the next problem is to determine when the dimeric states $\psi_k(q)$ will vibronically couple. We must, however, first examine the question within each molecule. If we define

$$V_{RS}{}^A(Q^A)=\int dq^A\psi_R{}^A(q^A)[T_e{}^A+V(q^A,Q^A)]\psi_S{}^A(q^A), \quad (3.6)$$

we shall assume that within each monomeric unit

$$|V_{RS}{}^A(Q^A)|\ll|V_{RR}{}^A(Q^A)-V_{SS}{}^A(Q^A)|, \quad (3.7)$$

that is, the energy separation between the electronic states within each molecule is large compared to their vibronic coupling. This situation is quite different for

the dimer as a whole, as can be seen from an evaluation of the terms in the dimeric analog of (2.9):

$$V_{jk}(Q)=\iint dq^A dq^B \psi_N{}^A(q^A)\psi_M{}^B(q^B)$$
$$\times[T_e{}^A+V(q^A,Q^A)+T_e{}^B+V(q^B,Q^B)$$
$$+V^{AB}(q,Q)]\psi_S{}^A(q^A)\psi_R{}^B(q^B)$$
$$=\delta_{MR}V_{NS}{}^A(Q^A)+\delta_{NS}V_{MR}{}^B(Q^B)$$
$$+\iint dq^A dq^B \psi_N{}^A\psi_M{}^B V^{AB}(q,Q)\psi_S{}^A\psi_R{}^B, \quad (3.8)$$

which become for diagonal terms

$$V_{kk}(Q)=V_{NN}{}^A(Q^A)+V_{MM}{}^B(Q^B)$$
$$+\iint dq^A dq^B \psi_N{}^A\psi_M{}^B V^{AB}(q,Q)\psi_N{}^A\psi_M{}^B. \quad (3.9)$$

Consider a pair of states $\psi_N{}^A\psi_M{}^B$ and $\psi_N{}^A\psi_R{}^B$, N, M, R, all different. It may be seen from Eqs. (3.6)–(3.9) that in zeroth order ($V^{AB}=0$) the vibronic coupling is negligible in the dimer as a whole since it is negligible in each monomeric unit. We assume that V^{AB} is not large enough to introduce significant coupling between states that differ in zeroth-order energy. We shall now confine consideration to two states in each molecule: $\psi_N{}^A$, a ground state, and $\psi_M{}^A$, an excited state. From these we can construct three dimeric states:

$$\psi_0=\psi_N{}^A\psi_N{}^B; \qquad \psi_a=\psi_M{}^A\psi_N{}^B; \qquad \psi_b=\psi_N{}^A\psi_M{}^B.$$

The latter two are to zeroth order degenerate. It then follows from the last four equations that they will be intimately coupled by a term of the order of V^{AB}.

We now proceed to solve the dimeric problem by the procedure used in the molecular case. We obtain for the ground state an equation identical with (2.11), with T_n and $V_{00}(Q)$ given by

$$V_{00}(Q)=V_{NN}{}^A(Q^A)+V_{NN}{}^B(Q^B)$$
$$+\iint dq^A dq^B \psi_N{}^A\psi_N{}^B V^{AB}(q,Q)\psi_N{}^A\psi_N{}^B \quad (3.10)$$

$$T_n=T_n{}^A+T_n{}^B+T_n{}^{AB}. \quad (3.11)$$

As in the molecular case, $\phi_0(Q)$ is simply a product of harmonic oscillator functions if anharmonic terms in $V_{00}(Q)$ are ignored. However, if the last term of $V_{00}(Q)$ in Eq. (3.10) depends only on Q^{AB}, the relative positions of the two dimers, the solutions are simply the product of oscillator functions within each molecule times additional functions for the relative vibrational motion. One notes then a systematic degeneracy for vibrational excitations within each molecule.[13]

The vibronic coupling equations arising for states ψ_a and ψ_b may be obtained by the same procedure used in the molecular case. The total states, assumed normalized, will be of the form

$$\Psi(q,Q)=\phi_a(Q)\psi_a(q)+\phi_b(Q)\psi_b(q). \quad (3.12)$$

The dimeric analog of (2.8) yields:

$$\mathbf{H}\boldsymbol{\phi}=E\boldsymbol{\phi} \quad (3.13)$$

$$\mathbf{H}=[T_n+\tfrac{1}{2}(V_{aa}+V_{bb})]\mathbf{1}+\tfrac{1}{2}(V_{aa}-V_{bb})\boldsymbol{\sigma}_3+V_{ab}\boldsymbol{\sigma}_1 \quad (3.14)$$

$$\boldsymbol{\phi}=\begin{pmatrix}\phi_a\\ \phi_b\end{pmatrix}, \quad (3.15)$$

where V_{bb} is given by Eq. (3.9), V_{aa} is given by the same equation with M and N exchanged, and

$$V_{ab}=\int dq \psi_M{}^A\psi_N{}^B V^{AB}(q,Q)\psi_N{}^A\psi_M{}^B. \quad (3.16)$$

Equation (3.14) is essentially identical to Eq. (33) derived by Moffitt and Witkowski.[13]

It is shown in Appendix II that our assumption that the dimer has a symmetry operation that exchanges A and B guarantees the existence of an operator G with the properties that:

$$[G, T_n]_-=[G, V_{ab}]_-=0, \quad (3.17)$$
$$GV_{bb}=V_{aa}G, \quad (3.18)$$
$$GV_{aa}=V_{bb}G, \quad (3.19)$$
$$G^2=1. \quad (3.20)$$

The properties of G given in Eqs. (3.17)–(3.20) imply that $(G\boldsymbol{\sigma}_1)^2=1$ and that $G\boldsymbol{\sigma}_1$ commutes with the dimeric Hamiltonian, (3.14). Thus, equations identical with (2.25) and (2.26) hold for the dimer.

IV. REDUCTION OF THE MOFFITT-WITKOWSKI EQUATION TO ONE-DIMENSIONAL FORM

It is useful to summarize the matrix eigenvalue equations for molecules [appearing among Eqs. (2.19)–(2.23)] and for dimers [Eqs. (3.13)–(3.20)] by a single set of equations. These may be given as follows:

$$\mathbf{H}=[T_n+U_0]\mathbf{1}+U_a\boldsymbol{\sigma}_3+U_s\boldsymbol{\sigma}_1 \quad (4.1)$$

$$[G, T_n]_-=[G, U_0]_-=[G, U_s]_-=[G, U_a]_+=0 \quad (4.2)$$

$$G^2=1. \quad (4.3)$$

In the molecular case, we identify

$$U_0=\tfrac{1}{2}(V_{11}+V_{22}) \quad (4.4i)$$
$$U_s=\tfrac{1}{2}(V_{11}-V_{22}) \quad (4.4ii)$$
$$U_a=V_{12}, \quad (4.4iii)$$

while in the dimeric case

$$U_0=\tfrac{1}{2}(V_{aa}+V_{bb}) \tag{4.5i}$$

$$U_s=V_{ab} \tag{4.5ii}$$

$$U_a=\tfrac{1}{2}(V_{aa}-V_{bb}). \tag{4.5iii}$$

For both systems we need to solve

$$\mathbf{H}\boldsymbol{\phi}=E\boldsymbol{\phi} \tag{4.6}$$

with the conditions that

$$[G\mathfrak{s}_1,\mathbf{H}]_-=0, \tag{4.7}$$

$$(G\mathfrak{s}_1)^2=\mathbf{1}. \tag{4.8}$$

The reduction of the matrix eigenvalue equation to two one-dimensional equations can be carried out with the aid of projection operators $\mathbf{P}^+$ and $\mathbf{P}^-$ defined as

$$\mathbf{P}^\pm\equiv\tfrac{1}{2}(\mathbf{1}\pm G\mathfrak{s}_1). \tag{4.9}$$

It may be easily verified that such operators acting on an arbitrary vector $\boldsymbol{\chi}$ project out eigenstates of $G\mathfrak{s}_1$, that is,

$$G\mathfrak{s}_1\boldsymbol{\phi}^\pm=\pm\boldsymbol{\phi}^\pm$$

$$\boldsymbol{\phi}^\pm\equiv\mathbf{P}^\pm\boldsymbol{\chi}. \tag{4.10}$$

Since $G\mathfrak{s}_1$ commutes with $\mathbf{H}$, all solutions of (4.6) can be obtained as either $\boldsymbol{\phi}^+$ or $\boldsymbol{\phi}^-$. However, the following simple identity shows that these latter contain only one independent component each:

$$\mathbf{P}^+\boldsymbol{\chi}=\tfrac{1}{2}\begin{pmatrix}1 & G\\ G & 1\end{pmatrix}\begin{pmatrix}\chi'\\ \chi''\end{pmatrix}=\tfrac{1}{2}\begin{pmatrix}\chi'+G\chi''\\ G\chi'+\chi''\end{pmatrix}=\tfrac{1}{2}\begin{pmatrix}\chi'+G\chi''\\ G(\chi'+G\chi'')\end{pmatrix}.$$

Hence one component of $\boldsymbol{\phi}^+$ may be generated from the other by means of the symmetry operator G. A similar argument holds for $\boldsymbol{\phi}^-$ and $-G$. We may, therefore, represent any solution of (4.6) in either one of two forms:

$$\boldsymbol{\phi}^+=\begin{pmatrix}\phi^+\\ G\phi^+\end{pmatrix} \quad \text{or} \quad \boldsymbol{\phi}^-=\begin{pmatrix}\phi^-\\ -G\phi^-\end{pmatrix}. \tag{4.11}$$

Using these forms with Eqs. (4.1) and (4.6), we obtain the following equations for the independent components ϕ^+ and ϕ^-:

$$H^+\phi^+=[T_n+U_0+U_sG+U_a]\phi^+=E^+\phi^+ \tag{4.12}$$

$$H^-\phi^-=[T_n+U_0-U_sG+U_a]\phi^-=E^-\phi^-. \tag{4.13}$$

Here we have written E^+ and E^- since, in general, the spectra of H^+ and H^- do not coincide.

We shall choose ϕ^+ and ϕ^- to be normalized to unity. It then follows from Eqs. (2.21) that in the molecular case the solutions will be either

$$\begin{pmatrix}\phi_1\\ \phi_2\end{pmatrix}=\tfrac{1}{2}\begin{pmatrix}\phi^++G\phi^+\\ \phi^+-G\phi^+\end{pmatrix}$$

or

$$\begin{pmatrix}\phi_1\\ \phi_2\end{pmatrix}=\tfrac{1}{2}\begin{pmatrix}\phi^--G\phi^-\\ \phi^-+G\phi^-\end{pmatrix}, \tag{4.14}$$

while in the dimeric case, from (3.15),

$$\begin{pmatrix}\phi_a\\ \phi_b\end{pmatrix}=2^{-\frac{1}{2}}\begin{pmatrix}\phi^+\\ G\phi^+\end{pmatrix} \quad \text{or} \quad \begin{pmatrix}\phi_a\\ \phi_b\end{pmatrix}=2^{-\frac{1}{2}}\begin{pmatrix}\phi^-\\ -G\phi^-\end{pmatrix}. \tag{4.15}$$

It is now useful to consider these solutions in two extreme cases, which may be solved by ordinary techniques.

Case (a): $U_s=0$

Under the condition that U_s vanishes, H^+ is equal to H^- and the energy levels are at least doubly degenerate. For each solution ϕ^+ there is another solution with $\phi^-=\phi^+$. It may be seen from (4.14) that the degenerate states in the molecular case are

$$\Psi=\tfrac{1}{2}(\phi^++G\phi^+)\psi_1+\tfrac{1}{2}(\phi^+-G\phi^+)\psi_2$$

$$\Psi=\tfrac{1}{2}(\phi^+-G\phi^+)\psi_1+\tfrac{1}{2}(\phi^++G\phi^+)\psi_2, \tag{4.16}$$

while in the dimeric case, from (4.15), these are

$$\Psi=2^{-\frac{1}{2}}[\phi^+\psi_a\pm G\phi^+\psi_b]. \tag{4.17}$$

The functions ϕ^+ may be found by customary procedures, that is, expansion of U_0 and U_a in terms of normal coordinates, since the operator G is absent.

Case (b): $U_a=0$

In the case that U_a vanishes, it follows from (4.2) that G commutes with both Hamiltonians $H^\pm$. Therefore, the solutions ϕ^+ and ϕ^- may be chosen to be eigenfunctions of G with eigenvalues ±1. It may be seen from Eqs. (4.12)–(4.14) that for solutions such that

$$G\phi^+=+\phi^+, \qquad G\phi^-=-\phi^- \tag{4.18}$$

we have

$$\phi_2=0$$

and

$$(T_n+U_0+U_s)\phi_1=E\phi_1.$$

The molecular solutions are

$$\Psi=\phi_1\psi_1, \tag{4.19}$$

while the dimeric solutions are

$$\Psi=2^{-\frac{1}{2}}\phi_1(\psi_a+\psi_b). \tag{4.20}$$

Similarly, it may be shown that for solutions such that

$$G\phi^+=-\phi^+, \qquad G\phi^-=+\phi^-, \tag{4.21}$$

we have

$$\phi_1=0$$

and

$$(T_n+U_0-U_s)\phi_2=E\phi_2.$$

The molecular solutions are

$$\Psi=\phi_2\psi_2, \tag{4.22}$$

while in the dimeric case

$$\Psi=2^{-\frac{1}{2}}\phi_2(\psi_a-\psi_b). \tag{4.23}$$

In this case also the operator G has been removed from the Hamiltonians so that solutions ϕ_1 and ϕ_2 may be obtained by the usual techniques.

V. INTENSITIES

In this section we shall be concerned with the calculation of the intensities of the vibronic structure of transitions from the ground state to the two coupled excited states. We consider first the molecular and then the dimeric case.

In the molecular case, if we assume that only the transition to the state ψ_1 is allowed, the transition dipole $\mathbf{R}$ becomes equal to the quantity

$$\mathbf{R}=\int dq\psi_1{}^*\mathbf{M}\psi_0\int dQ\phi_1{}^*\phi_0$$

$$=\mathbf{M}_1(\phi_1,\phi_0). \tag{5.1}$$

Here $\mathbf{M}$ is the usual dipole operator and we have indicated convenient abbreviations for the two integrals. In the preceding section, we have seen that the vibrational levels in general will be split into two systems. Their transition dipole may be obtained from Eqs. (4.14) and (5.1):

$$\mathbf{R}^+=\tfrac{1}{2}\mathbf{M}_1(\phi^++G\phi^+,\phi_0)$$

$$\mathbf{R}^-=\tfrac{1}{2}\mathbf{M}_1(\phi^--G\phi^-,\phi_0), \tag{5.2}$$

which show that the intensities also differ between the two systems.

Selection rules may be found upon recognizing that G is a unitary operator (see Appendix I). A typical argument proceeds from identities satisfied by the overlap integral, thus:

$$(\phi^++G\phi^+,\phi_0)=(\phi^++G\phi^+,G^\dagger G\phi_0)=(\phi^++G\phi^+,G\phi_0), \tag{5.3}$$

which makes use of the property of an operator A and its adjoint $A^\dagger$, namely:

$$(\phi',A^\dagger\phi)=(A\phi',\phi). \tag{5.4}$$

A similar argument shows that

$$(\phi^--G\phi^-,\phi_0)=-(\phi^--G\phi^-,G\phi_0). \tag{5.5}$$

Since G commutes with the Hamiltonian of the ground state (2.11) and has eigenvalues ±1, we may choose ϕ_0 such that

$$G\phi_0=\pm\phi_0. \tag{5.6}$$

On combining (5.3), (5.5), and (5.6), it follows that if the plus sign holds in (5.6), transitions are allowed to the plus system and are forbidden to the minus system; while if the minus sign holds in (5.6), transitions occur only to the minus system. Now the plus sign holds for the lowest vibrational level of the ground state, while the minus sign may hold for certain excited vibrational levels. From the fact, previously noted, that in general the energy spectra of the plus and minus systems will not be the same, we conclude that the spectral distribution in hot bands may differ considerably from that in normal bands. This fact may be used to indicate the presence of vibronic coupling.

The more general situation is encountered in the case in which transitions from the ground state to both states ψ_1 and ψ_2 are allowed. In such a case the transition dipole becomes

$$\mathbf{R}=\mathbf{M}_1(\phi_1,\phi_0)+\mathbf{M}_2(\phi_2,\phi_0)$$

$$\mathbf{R}^\pm=\tfrac{1}{2}\mathbf{M}_1(\phi^\pm\pm G\phi^\pm,\phi_0)+\tfrac{1}{2}\mathbf{M}_2(\phi^\pm\mp G\phi^\pm,\phi_0). \tag{5.7}$$

Selection rules derived above, for the case of $\mathbf{M}_2$ vanishing, may be extended from the fact that

$$(\phi^+-G\phi^+,\phi_0)=-(\phi^+-G\phi^+,G\phi_0)$$

$$(\phi^-+G\phi^-,\phi_0)=(\phi^-+G\phi^-,G\phi_0). \tag{5.8}$$

From this latter and Eqs. (5.3) and (5.5), it follows that transitions from a particular ground state level can occur to either plus or minus systems. However, either the plus states will be associated with $\mathbf{M}_1$ and the minus states with $\mathbf{M}_2$, or vice versa. The two polarizations will not occur together.

In the dimeric case, the transition dipole is given by

$$\mathbf{R}=\mathbf{M}_a(\phi_a,\phi_0)+\mathbf{M}_b(\phi_b,\phi_0). \tag{5.9}$$

We may define two other dipoles $\mathbf{M}^+$ and $\mathbf{M}^-$ by

$$\mathbf{M}^\pm=2^{-\frac{1}{2}}(\mathbf{M}_a\pm\mathbf{M}_b). \tag{5.10}$$

On substituting (4.15) and (5.10) into (5.9), we obtain

$$\mathbf{R}^\pm=\tfrac{1}{2}\mathbf{M}^+(\phi^\pm\pm G\phi^\pm,\phi_0)+\tfrac{1}{2}\mathbf{M}^-(\phi^\pm\pm G\phi^\pm,\phi_0). \tag{5.11}$$

Equation (5.11) can be seen to be identical to the molecular case with $\mathbf{M}^+$ replacing $\mathbf{M}_1$ and $\mathbf{M}^-$ replacing $\mathbf{M}_2$, thus giving the same selection rules.

More specific details of the spectral characteristics of the transitions depend, of course, on the problem being treated. If symmetry is present, the problem may simplify and more details can be given than in the preceding general analysis.

VI. SPECIAL MODEL. MOLECULAR CASE

Thus far the treatment has been restricted only by the assumptions of the harmonic approximation and

the limitation of the coupling to two electronic states of different symmetry. It is instructive to consider in more detail a special model which would suggest itself when considering a physical problem and which demonstrates the main features of the coupling problem. A similar model which is available in the dimeric case is presented in Appendix III.

The Hamiltonians (4.12) and (4.13) may be written as

$$H^{\pm}=T_n+\tfrac{1}{2}(V_{11}+V_{22})\pm\tfrac{1}{2}(V_{11}-V_{22})G+V_{12}, \qquad (6.1)$$

using the definitions given in (4.4). We may expand the terms V_{jk} in terms of the symmetry coordinates appropriate to the problem:

$$V_{jk}=W_k\delta_{jk}+\sum_{\mu} l_{\mu}{}^{jk}Q_{\mu}+\tfrac{1}{2}\sum_{\mu\nu} k_{\mu\nu}{}^{jk}Q_{\mu}Q_{\nu}. \qquad (6.2)$$

In these equations, terms $l_{\mu}{}^{11}$ and $l_{\mu}{}^{22}$ are nonvanishing for totally symmetric coordinates only; similarly terms $k_{\mu\nu}{}^{11}$ and $k_{\mu\nu}{}^{22}$ are nonvanishing for $Q_{\mu}Q_{\nu}$ which transform as the totally symmetric representation. The terms $l_{\mu}{}^{12}$ are nonvanishing for coordinates having the symmetry of $\psi_1\psi_2$. The leading terms for $j=k$ in (6.2) are simply the electronic energies W_1 and W_2 of the states ψ_1 and ψ_2. To make the problem tractable, we shall make two physical assumptions; the first is:

$$\text{(a)} \quad \Big|\sum_{\mu}(l_{\mu}{}^{11}-l_{\mu}{}^{22})Q_{\mu}+\tfrac{1}{2}\sum_{\mu\nu}(k_{\mu\nu}{}^{11}-k_{\mu\nu}{}^{22})Q_{\mu}Q_{\nu}\Big| \ll |W_1-W_2|$$

where the Q_{μ} extends over the range of nuclear vibrations; the second is:

$$\text{(b)} \quad \Big|\sum_{\mu\nu} k_{\mu\nu}{}^{12}Q_{\mu}Q_{\nu}\Big| \ll \Big|\sum_{\mu} l_{\mu}{}^{12}Q_{\mu}\Big|.$$

Assumption (a) is satisfied if the two states ψ_1 and ψ_2 are so similar that any differences in their individual equilibrium configurations and force constants may be neglected. This assumption may be expected to hold in many problems of interest. The second assumption requires that the linear coupling terms dominate over the quadratic ones. If this assumption fails, the problem becomes considerably more difficult. We shall proceed assuming it is true and leave the question of its validity to experimental investigation. For illustrative purposes, we shall make one further assumption, which can, however, be relaxed without difficulty:

$$\text{(c)} \quad l_{\mu}{}^{12}=0, \qquad k_{\mu\rho}{}^{ii}=0 \qquad \mu\neq\rho,$$

that is, the vibronic problem occurs in only one of the normal coordinates. With these assumptions, the Hamiltonians become

$$H^{\pm}=T_n+\tfrac{1}{2}(W_1+W_2)+\sum_{\mu} l_{\mu}Q_{\mu}+\tfrac{1}{2}\sum_{\mu\nu} k_{\mu\nu}Q_{\mu}Q_{\nu} \pm\tfrac{1}{2}(W_1-W_2)G+l_{\rho}{}^{12}Q_{\rho}, \qquad (6.3)$$

where

$$l_{\mu}=\tfrac{1}{2}(l_{\mu}{}^{11}+l_{\mu}{}^{22})$$
$$k_{\mu\nu}=\tfrac{1}{2}(k_{\mu\nu}{}^{11}+k_{\mu\nu}{}^{22}). \qquad (6.4)$$

The commutation relations given in (4.2) are satisfied in the case of the Hamiltonians (6.3) by

$$GQ_{\rho}=-Q_{\rho}G$$
$$GQ_{\nu}=Q_{\nu}G, \qquad \nu\neq\rho, \qquad (6.5)$$

which demonstrates that G reflects Q_{ρ} but leaves the other coordinates unchanged. Since Q_{ρ} is not a totally symmetric coordinate, after a suitable normal coordinate transformation (which allows displacement along coordinates with $l_{\mu}\neq 0$) the Hamiltonians (6.3) may be written as the sum of two commuting operators H_0 and $H_{\rho}{}^{\pm}$.

$$H_0=\sum_{\nu}{}'[(P_{\nu}{}^2/2M_{\nu})+\tfrac{1}{2}k_{\nu}Q_{\nu}{}^2]+\tfrac{1}{2}(W_1+W_2)$$

$$H_{\rho}{}^{\pm}=(P_{\rho}{}^2/2M_{\rho})+\tfrac{1}{2}k_{\rho}Q_{\rho}{}^2\pm\tfrac{1}{2}(W_1-W_2)G+l_{\rho}{}^{12}Q_{\rho}, \qquad (6.6)$$

where the prime on the summation indicates that the sum does not extend over $\nu=\rho$, and the masses M_{ν} are chosen so that the length of each normal coordinate equals the square root of the sum of the squares of its constituent Cartesian displacements.[16] H_0 is simply a sum of harmonic oscillator Hamiltonians and gives the usual solutions, products of eigenfunctions in each mode Q_{ν}. The vibronic problem, therefore, manifests itself only in $H_{\rho}{}^{\pm}$, where the noncommutivity of G and Q_{ρ} prevents any simple treatment of the eigenvalues.

Before we discuss $H_{\rho}{}^{\pm}$ in detail, it is convenient to transform it to dimensionless quantities. We let $\omega^2\equiv k_{\rho}/M_{\rho}$. Then,

$$p\equiv(M_{\rho}\hbar\omega)^{-\frac{1}{2}}P_{\rho}$$
$$q\equiv(M_{\rho}\omega/\hbar)^{\frac{1}{2}}Q_{\rho}$$
$$\lambda\equiv(M_{\rho}\hbar\omega^3)^{-\frac{1}{2}}l_{\rho}{}^{12}$$
$$\epsilon=\tfrac{1}{2}(\hbar\omega)^{-1}(W_1-W_2). \qquad (6.7)$$

In terms of these quantities, $H_{\rho}{}^{\pm}$ may be written as

$$(\hbar\omega)^{-1}H_{\rho}{}^{\pm}\equiv h^{\pm}=\tfrac{1}{2}(p^2+q^2)+\lambda q\pm\epsilon G. \qquad (6.8)$$

The new variables are seen to satisfy the commutation relations

$$[q, p]_-=i$$
$$[q, G]_+=0. \qquad (6.9)$$

From the first of these, q and p may be considered to be canonical variables in a system of units in which $\hbar=1$.

[16] It may be noted that if all the nuclei are of mass M, then $M_{\mu}=M$ for all μ and the matrices describing the normal coordinate transformation are orthogonal.

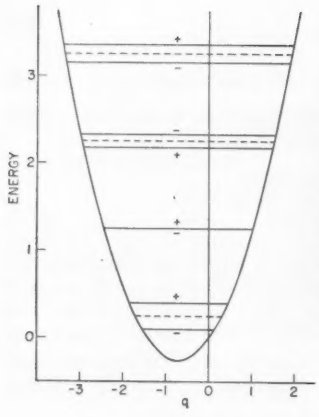

FIG. 1. Plot of displaced oscillator potential for $\lambda=0.71$. The energy levels (in units of $\hbar\omega$) for $\epsilon=0$ are shown by dotted lines; those for $\epsilon=0.25$ are shown by solid lines. The levels for $\epsilon=0$ are doubly degenerate. The plus and minus character of the levels for $\epsilon=0.25$ is indicated.

VII. LIMITING CASES

The Hamiltonians $h^{\pm}$ given in (6.8) represent the vibronic problem in a form that cannot be further reduced. General solutions to the eigenvalue equations have not been found. In this section we present perturbation solutions to some interesting cases.

In case (a) we take $\epsilon \ll \lambda$. In molecules this case arises when the energy separation between states ψ_1 and ψ_2 is small. It represents, in some sense, a *pseudo Jahn-Teller effect*, the latter occurring when ϵ vanishes for symmetry reasons. In the dimeric case, $\epsilon \ll \lambda$ means that the energy associated with the shape changes in the excited state of each monomer is large compared to the energy of interaction. It has been called *weak exciton coupling*.

In case (b) we take $\epsilon \gg \lambda$. In the molecular case, this situation occurs if the energy separation between ψ_1 and ψ_2 is large compared to the coupling introduced by nuclear displacements. We shall show that this corresponds to the familiar case of *vibrational borrowing*. In the dimeric case, $\epsilon \gg \lambda$ arises when the electronic coupling between the excited states dominates over energy terms introduced by nuclear displacements in the excited monomeric units. It has been called strong exciton coupling.

Finally, in case (c) we consider the situation where $\epsilon \sim \lambda \ll 1$, a case not distinguished experimentally. We show results for it can be obtained from the other two limits.

Case (a), $\epsilon \ll \lambda$: Displacement Limit

In this case we write the Hamiltonian $h^{\pm}$ as

$$h^{\pm}=h_0 \pm \epsilon G \tag{7.1}$$

where

$$h_0=\tfrac{1}{2}(p^2+q^2)+\lambda q.$$

We treat h_0 as the unperturbed Hamiltonian and $\pm\epsilon G$ as the perturbing term. The unperturbed Hamiltonian is just that for a displaced harmonic oscillator and may be brought into normal form by introducing a new coordinate

$$q_\lambda=q+\lambda \tag{7.2}$$

which is conjugate to p. In terms of q_λ, h_0 may be written

$$h_0=\tfrac{1}{2}(p^2+q_\lambda^2)-\tfrac{1}{2}\lambda^2. \tag{7.3}$$

The eigenstates of h_0 will be denoted by $|n, \lambda\rangle$

$$h_0|n, \lambda\rangle=(n+\tfrac{1}{2}-\tfrac{1}{2}\lambda^2)|n, \lambda\rangle, \tag{7.4}$$

the eigenvalues being characteristic of the harmonic oscillator. The first order corrections to the energy are given by the quantities $\pm\epsilon\langle n, \lambda|G|n, \lambda\rangle$. Upon using the results given in Appendix IV, we find that the eigenvalues of $h^{\pm}$ correct to first order are

$$\epsilon_n^{\pm}=n+\tfrac{1}{2}-\tfrac{1}{2}\lambda^2 \pm (-1)^n \epsilon \exp(-\lambda^2) L_n^0(2\lambda^2), \tag{7.5}$$

where $L_n^{\alpha}(x)$ is the Laguerre polynomial defined in the appendix.

In Fig. 1 we plot the displaced oscillator potential and indicate the energy levels for $\epsilon=0$ and 0.25, $\lambda=0.71$. It is of interest to note that for λ of such size, the Laguerre polynomials cannot be approximated, the eigenvalues do not fall into any simple pattern. This phenomenon is shown in Fig. 2 where the eigenvalues are plotted as a function of ϵ for $\lambda=1$. Preliminary machine calculations indicate that this haphazard character of the energy levels in the displacement limit (weak exciton coupling) becomes even more pronounced in intermediate cases ($\epsilon \sim \lambda$).

The intensities for $0-n$ transitions can be obtained rather simply for the case of $\epsilon=0$. If only transitions to the state ψ_1 are allowed, the intensities depend on[17]

$$|\mathbf{M}_1|^2 |\langle 0, 0|n, \lambda\rangle|^2=|\mathbf{M}_1|^2(1/2^n n!)\lambda^{2n}\exp(-\lambda^2/2), \tag{7.6}$$

which are the Franck-Condon integrals relating a displaced oscillator to an undisplaced one. The result is the appearance of an apparently symmetric progression in an asymmetric mode, a spectroscopic criterion for shape changes in the excited state. If the eigenstates for $\epsilon \neq 0$ are corrected to first order, the intensities can be shown to depend on sums over Laguerre polynomials.

Case (b), $\epsilon \gg \lambda$: Harmonic Limit

In this case, we write the Hamiltonian as

$$h^{\pm}=h_0^{\pm}+\lambda q, \tag{7.7}$$

where

$$h_0^{\pm}=\tfrac{1}{2}(p^2+q^2)\pm\epsilon G.$$

[17] We assume that the normal coordinate Q_ρ and the corresponding force constant k_ρ are the same in the excited states as in the ground states. There is a distinct possibility that the various modes of Q_ρ symmetry in the ground state may have different force constants and may even be mixed together in the excited state. If so, these results will be altered.

We treat $h_0^{\pm}$ as the unperturbed Hamiltonian and λq as the perturbation. The eigenstates for the undisplaced harmonic oscillator, denoted here by $|n,0\rangle$, have the well-known properties

$$\tfrac{1}{2}(p^2+q^2)\,|n,0\rangle=(n+\tfrac{1}{2})\,|n,0\rangle, \tag{7.8i}$$

$$G\,|n,0\rangle=(-1)^n\,|n,0\rangle, \tag{7.8ii}$$

$$2^{-\frac{1}{2}}(q-ip)\,|n,0\rangle=(n+1)^{\frac{1}{2}}\,|n+1,0\rangle, \tag{7.8iii}$$

$$2^{-\frac{1}{2}}(q+ip)\,|n,0\rangle=n^{\frac{1}{2}}\,|n-1,0\rangle. \tag{7.8iv}$$

The phases of the last two relations have been chosen so as to agree with the usual definitions of the harmonic oscillator eigenfunctions in the coordinate representation. From these properties, it follows that

$$h_0^{\pm}\,|n,0\rangle=[n+\tfrac{1}{2}\pm(-1)^n\epsilon]\,|n,0\rangle, \tag{7.9}$$

explicitly demonstrating that the $|n,0\rangle$ are also eigenstates of $h_0^{\pm}$.

It may be seen from (7.8iii) and (7.8iv) that the perturbation λq introduces no first-order corrections to the eigenvalues. Application of second-order perturbation theory is found to give rise to the following eigenvalues:

$$\epsilon_n^{\pm}=n+\tfrac{1}{2}\pm(-1)^n\epsilon\mp\frac{(-1)^n\lambda^2(2n+1)\epsilon}{1-4\epsilon^2}-\frac{\lambda^2}{2(1-4\epsilon^2)}. \tag{7.10}$$

Some insight into the nature of these eigenvalues may be gained if we forego the classification of states into plus and minus systems, as in the corresponding extreme case discussed earlier. The eigenvalues (7.10) may then be written as

$$\epsilon_n^{(1)}=n\left(1-\frac{2\lambda^2\epsilon}{1-4\epsilon^2}\right)+\tfrac{1}{2}+\epsilon-\frac{\lambda^2}{2(1-2\epsilon)}$$

$$\epsilon_n^{(2)}=n\left(1+\frac{2\lambda^2\epsilon}{1-4\epsilon^2}\right)+\tfrac{1}{2}-\epsilon-\frac{\lambda^2}{2(1+2\epsilon)}. \tag{7.11}$$

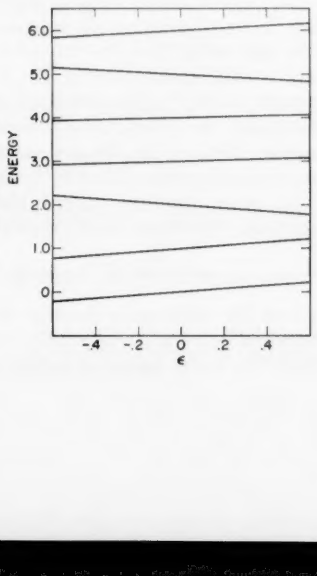

FIG. 2. Plot of the energy levels (in units of $\hbar\omega$) of the plus system as a function of ϵ for $\lambda=1$. The energy levels of the minus system are found by the substitution $\epsilon\rightarrow-\epsilon$.

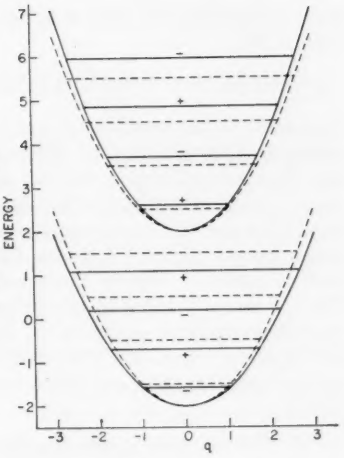

FIG. 3. Plot of the potential energy curves and energy levels for $\epsilon=2$. The dotted lines are for $\lambda=0$; the solid lines for $\lambda=0.71$. The plus and minus character of the levels is indicated.

Since the energy in macroscopic units is given by $\hbar\omega\epsilon_n^{(0)}$, the eigenvalues (7.11) may be thought of as arising from harmonic oscillators of slightly different frequencies. The $\epsilon_n^{(1)}$ levels are in the region of the electronic energy of ψ_1, while the $\epsilon_n^{(2)}$ levels are in the region of ψ_2. In the extreme case of $\lambda=0$, the states corresponding to these energy levels, ψ_1 and ψ_2 in the molecular case, $2^{-\frac{1}{2}}(\psi_a+\psi_b)$ and $2^{-\frac{1}{2}}(\psi_a-\psi_b)$ in the dimeric case, are completely uncoupled. The effect of a small λ term couples the states slightly with a concomitant increase in the frequency of the higher energy state and a decrease in that of the lower energy. This result is illustrated in Fig. 3. We may expect similar changes in apparent force constants in the more general case in which more than one coordinate is involved in the coupling of electronic states, as long as ϵ dominates over the various λ values.

The relative intensities of the vibrational transitions may be found by calculating the first-order corrections to the states. If the transition to ψ_1 is allowed, we find that the $0-0$ transition associated with this level is essentially unchanged in intensity by small values of λ. The $0-1$ transition which is in the region of ψ_2, becomes allowed with an intensity proportional to [17]

$$[\lambda^2/2(1-2\epsilon)^2]\,|\mathbf{M}_1|^2,$$

higher transitions not being allowed to this order of approximation. This illustrates the familiar phenomenon of vibrational borrowing by "forbidden" electronic states.

A comparison of the results obtained in the two limiting cases indicates that extrapolations between these cases are quite treacherous.

Case (c), $\epsilon\sim\lambda\ll1$

This case is seen to be but a subcase of either of the two previous cases. The energy levels, correct to first

order in ϵ and second order in λ, are most easily found from (7.10):

$$\epsilon_n^{\pm}=n+\tfrac{1}{2}\pm(-1)^n\epsilon\mp(-1)^n\lambda^2(2n+1)\epsilon-\tfrac{1}{2}\lambda^2. \quad (7.12)$$

Expansion of the exponential and the Laguerre polynomial in (7.5) also lead to (7.12) in this approximation. The energy levels in this case may be classified as in case (b) if we forego the classification into plus and minus systems with the result that we have a series of states having slightly increased force constants and another series of slightly decreased force constants. The $\epsilon_n^{(1)}$ and $\epsilon_n^{(2)}$ levels in this instance, however, are not widely separated as in case (b) but rather lie in the same spectral region. The intensities, to the same order of approximation, may also found from either case (a) or (b).

VIII. CONCLUSIONS

We began by showing that vibronic coupling between two electronic states, both in molecules and in dimers, can be represented by the same coupled oscillator equation, the equation derived by Moffitt and Witkowski. This result, though not surprising, has probably not been generally appreciated since molecular and exciton problems arise in a rather different way. We then reduced the coupled equations to a more convenient one-dimensional form. The basis for the reduction is the presence of certain elements of symmetry. In the molecular case, the symmetry is provided by the assumption that the electronic wave functions ψ_1 and ψ_2 transform as different irreducible representations. In the dimeric case, we assumed the existence of a symmetry operation that exchanges the monomeric units. In both cases the symmetry assumption provides a constant of motion $G\vartheta_1$. This constant allowed the reduction to the more easily appreciated one-dimensional equations. The price for this simplification was the explicit appearance in the reduced Hamiltonian of the symmetry operator G.

To make the problem more concrete, we then made a number of simplifying physical assumptions as to the nature of the coupling elements and reduced consideration to one normal mode. The problem could then be discussed in terms of the two dimensionless parameters: λ, which represents nuclear displacement, and ϵ, which represents the energy separation between states. It is hoped that the treatment of this paper, which gives equal importance to both elements, will clarify aspects of both molecular and dimeric cases.

Workers on molecular problems, either on the Jahn-Teller effect or on vibrational borrowing, have concentrated their attention on nuclear displacements as the cause of perturbation. On the other hand, workers on exciton problems have concentrated on the electronic interaction energy as the case of perturbation. This difference in emphasis has obscured the basic identity of the problems. The results of this paper suggest that a fruitful experimental problem may be the search for molecular and dimeric systems with similar vibronic coupling effects.

ACKNOWLEDGMENTS

One of us (M.G.) would like to thank Dr. Glenn H. Spencer, now with the Chemistry Department of Stanford University, for many helpful discussions during the early, formative stage of the work reported in this paper.

APPENDIX I

The conditions (2.10) under which the electronic wave functions do not mix appreciably are most readily determined by introducing matrix operators which act on column vectors. We define the kmth element of the matrix operator $\mathbf{A}$ by

$$A_{km}\equiv\int dq\psi_k^*(q)\,A(p, q, P, Q)\psi_m(q), \quad (A1.1)$$

where p, q, P, and Q symbolize the electronic and nuclear momenta and coordinates. The column vector is defined as

$$\boldsymbol{\phi}=\text{col}(\phi_1, \phi_2, \cdots). \quad (A1.2)$$

The matrix element of $\mathbf{A}$ between states $\boldsymbol{\phi}'$ and $\boldsymbol{\phi}$ is given by

$$(\boldsymbol{\phi}', \mathbf{A}\boldsymbol{\phi})=\sum_{kl}(\phi_k', A_{kl}\phi_l), \quad (A1.3)$$

where

$$(\phi_k', A_{kl}\phi_l)=\int dQ\phi_k'^*(Q)\,A_{kl}(P, Q)\phi_l(Q).$$

In terms of these definitions, (2.8) may be written in the compact form

$$[\mathbf{T}+\mathbf{V}]\boldsymbol{\phi}=E\boldsymbol{\phi}, \quad (A1.4)$$

where $\mathbf{T}$ and $\mathbf{V}$ are defined by using T_n and $V(q, Q)$ in (A1.1). The normalization condition (2.7) is expressed as

$$(\boldsymbol{\phi}, \boldsymbol{\phi})=1. \quad (A1.5)$$

We now write $\mathbf{V}$ as the sum of a diagonal matrix $\mathbf{V}_D$ and a nondiagonal matrix, $\mathbf{V}_N$. If $\mathbf{V}_N$ vanished, there would clearly be no mixing of electronic states. We formulate the criterion of nonmixing as the smallness of mixing induced by the nonvanishing of $\mathbf{V}_N$. This is most readily accomplished by treating $\mathbf{V}_N$ as a perturbation. Since the unperturbed Hamiltonian $\mathbf{T}+\mathbf{V}_D$ is diagonal, the unperturbed states may be taken as

$$\boldsymbol{\phi}_{k\nu}{}^0=\text{col}(0, \cdots, 0, \phi_{k\nu}{}^{(0)}, 0, \cdots), \quad (A1.6)$$

where the subscript ν denotes one of the vibrational levels of ϕ_k. The corresponding energy is denoted by $E_{k\nu}{}^0$. The states corrected to first order are then deter-

mined by usual perturbation theory to be

$$\phi_{k\nu}^{1}=\phi_{k\nu}^{0}+\sum_{l\neq k}\phi_{l\mu}^{0}\frac{(\phi_{l\mu}^{0},\ \mathbf{V}_N\phi_{k\nu}^{0})}{E_{k\nu}^{0}-E_{l\mu}^{0}}. \qquad \text{(A1.7)}$$

From this expression we conclude that electronic states k and l are not mixed appreciably when the inequality

$$\left|\int dQ\phi_{l\mu}^{(0)*}V_{lk}\phi_{k\nu}^{(0)}\right|\ll\left|E_{k\nu}^{0}-E_{l\mu}^{0}\right| \qquad \text{(A1.8)}$$

holds. If the vibrational states are low lying so that

$$E_{k\nu}^{0}\approx W_k, \qquad E_{l\mu}^{0}\approx W_l,$$

the inequality takes the form

$$\left|\int dQ\phi_{l\mu}^{(0)*}V_{lk}\phi_{k\nu}^{(0)}\right|\ll\left|W_k-W_l\right|, \qquad \text{(A1.9)}$$

which is the most useful criterion of nonmixing. Indeed, if (A1.9) holds for low lying vibrational states, we may expect that (A1.8) holds when $E_{l\mu}^{0}$ is comparable with $E_{k\nu}^{0}$, k and l being fixed. This may be seen in the case of $W_k\gg W_l$, for example. In this case, choosing $E_{k\nu}^{0}\approx W_k$, $\phi_{l\mu}$ corresponds to a high vibrational level and, therefore, oscillates rapidly as a function of Q. Since $V_{lk}\phi_{k\nu}^{(0)}$ is a slowly varying function of Q, neighboring volumes of the integrand in (A1.8) will tend to cancel. The integral will, therefore, be small and in all likelihood (A1.8) will be fulfilled. The condition expressed in (2.10) is seen to be a qualitative statement of (A1.9).

APPENDIX II

In order to show the existence of the operator G having the properties

$$[G,\ T_n]_-=[G,\ V_{11}]_-=[G,\ V_{22}]_-=[G,\ V_{12}]_+=0 \qquad \text{(A2.1)}$$

in the molecular case, we examine the symmetries of V_{11}, V_{22}, V_{12}. We consider only V_{12} in detail, the analysis in the other cases being similar. We define symmetry operators G_q^{α} and G_Q^{α} which act on the coordinates q and Q, respectively. Since $V(q, Q)$ is assumed to transform as the totally symmetric representation of the group, we have

$$G_q^{\alpha}G_Q^{\alpha}V(q, Q)=V(q, Q)G_q^{\alpha}G_Q^{\alpha}. \qquad \text{(A2.2)}$$

Operating on $V_{12}(Q)$ by G_Q^{α}, we obtain

$$G_Q^{\alpha}V_{12}(Q)=\int dq\psi_1^{*}(q)G_Q^{\alpha}V(q, Q)\psi_2(q). \qquad \text{(A2.3)}$$

Since the symmetry operators are unitary operators,[18] we may write (A2.3) as

$$\int dq\psi_1^{*}(q)G_q^{\alpha\dagger}G_q^{\alpha}G_Q^{\alpha}V(q, Q)\psi_2(q)$$

$$=\int dq(G_q^{\alpha}\psi_1(q))^{*}V(q, Q)G_q^{\alpha}\psi_2(q)G_Q^{\alpha}, \qquad \text{(A2.4)}$$

where we have used (A2.2) and the adjoint property of operators. We have assumed that ψ_1 and ψ_2 are one-dimensional representations of the group, allowing us to write

$$G_q^{\alpha}\psi_1(q)=\chi_1(\alpha)\psi_1(q)$$
$$G_q^{\alpha}\psi_2(q)=\chi_2(\alpha)\psi_2(q) \qquad \text{(A2.5)}$$

where $\chi_l(\alpha)$ is the character associated with the αth symmetry operation and the lth representation. On inserting (A2.5) into (A2.4), we arrive finally at the result

$$G_Q^{\alpha}V_{12}(Q)=\chi_1(\alpha)\chi_2(\alpha)V_{12}(Q)G_Q^{\alpha}, \qquad \text{(A2.6)}$$

bearing in mind that the characters of one-dimensional representations are real. A perusal of the group tables[19] indicates that with the exceptions of the groups C_4, C_{4h}, S_4 and S_8, we may choose G_Q^{α} such that

$$(G_Q^{\alpha})^2=1 \qquad \text{(A2.7)}$$

and

$$\chi_1(\alpha)\chi_2(\alpha)=-1 \qquad \text{(A2.8)}$$

for a particular α. Proceeding in a similar fashion with V_{11} and V_{22}, we find that these transform as the totally symmetric representation of the group. The kinetic energy operator T_n is assumed from the outset to commute with all group operators. Identifying this operator with G, we have the properties (A2.1).

To show that G is Hermitian, we note that (A2.7) combined with the unitary property of the group operators

$$G^{\dagger}G=1$$

implies that

$$G^{\dagger}=G. \qquad \text{(A2.9)}$$

In order to show the existence of the operator G having the properties

$$GV_{aa}=V_{bb}G$$
$$GV_{bb}=V_{aa}G$$
$$GV_{ab}=V_{ab}G, \qquad \text{(A2.10)}$$

we first note that the assumption that there exists a symmetry operator which exchanges the monomeric units implies that we can set the nuclei of one molecule in one-to-one correspondence with those of the second molecule in such fashion that under the symmetry

[18] L. D. Landau and E. M. Lifshitz, *Quantum Mechanics—Non-Relativistic Theory* (Addison-Wesley Publishing Company, Inc., Reading, Massachusetts, 1958), p. 330.

[19] E. Bright Wilson, Jr., J. C. Decius, and Paul C. Cross, *Molecular Vibrations* (McGraw-Hill Book Company, Inc., New York, 1955), pp. 323–330.

operation the corresponding nuclei are exchanged. It is then apparent from (3.9) and (3.16) that if we define G as the operator which performs this exchange of nuclei, the properties (A2.10) are fulfilled. [It is to be remembered that in the integrals in (3.9) and (3.16) the electron coordinates are integrated over and, therefore, play the role of dummy variables.] Since two successive exchanges restore the nuclei to their original position, we have

$$G^2=1. \tag{A2.11}$$

The Hermitian property of G follows from (A2.11) and the fact that the symmetry operators are unitary.

APPENDIX III. SPECIAL MODEL, DIMERIC CASE[20]

In the dimeric case, the various terms U_0, U_a, and U_e may be expanded as in the molecular case giving rise to an identical model when the corresponding assumptions are made. It is of interest, however, to relate the various terms of the expansion to properties of the individual monomers. To do this we insert (4.5) into (4.12) and (4.13), obtaining

$$H^{\pm}=T_n+V_{aa}\pm V_{ab}G, \tag{A3.1}$$

where we recall that V_{aa} and V_{ab} are defined by

$$V_{aa}=V_{MM}(Q^A)+V_{NN}(Q^B)+\int dq\psi_M{}^A\psi_N{}^B V^{AB}\psi_M{}^A\psi_N{}^B$$

$$V_{ab}=\int dq\psi_M{}^A\psi_N{}^B V^{AB}\psi_N{}^A\psi_M{}^B. \tag{A3.2}$$

The first two terms of V_{aa} depend only on the internal coordinates Q^A and Q^B of the monomers A and B, respectively. If we expand about that point where the linear terms vanish in the ground state, we obtain

$$V_{NN}(Q^B)=W_N+\tfrac{1}{2}\sum_{\mu\nu}k_{\mu\nu}{}^N Q_\mu{}^B Q_\nu{}^B$$

$$V_{MM}(Q^A)=W_M+\sum_\mu l_\mu{}^M Q_\mu{}^A+\tfrac{1}{2}\sum_{\mu\nu}k_{\mu\nu}{}^M Q_\mu{}^A Q_\nu{}^A. \tag{A3.3}$$

From the fact that V^{AB} depends only on two body interactions between the two fragments, and from our use of the harmonic approximation, it follows that V_{ab} depends only on the coordinates $Q_\rho{}^{AB}$ describing the relative orientation of the two fragments. Although the last term in V_{aa} may, in general, depend on coordinates Q^A and Q^B as well as $Q_\rho{}^{AB}$, we shall simplify the problem by assuming that only the latter is important. We may, therefore, write

$$V_{ab}=W_S+\sum_\rho l_\rho{}^S Q_\rho{}^{AB}+\tfrac{1}{2}\sum_{\rho\sigma}k_{\rho\sigma}{}^S Q_\rho{}^{AB}Q_\sigma{}^{AB}$$

$$\int dq\psi_M{}^A\psi_N{}^B V^{AB}\psi_M{}^A\psi_N{}^B=W^{AB}+\sum_\rho l_\rho{}^{AB}Q_\rho{}^{AB}+\tfrac{1}{2}\sum_{\rho\sigma}k_{\rho\sigma}{}^{AB}Q_\rho{}^{AB}Q_\sigma{}^{AB}. \tag{A3.4}$$

In certain special cases it may be convenient to work with the expansions (A3.3) as given. However, for comparison with the molecular case, it is convenient to transform to a set of normal coordinates defined as

$$Q_\mu{}^{\pm}=2^{-\frac{1}{2}}(Q_\mu{}^A\pm Q_\mu{}^B), \tag{A3.5}$$

which are so chosen that

$$GQ_\mu{}^{\pm}=\pm Q_\mu{}^{\pm}G. \tag{A3.6}$$

On substituting (A3.2)–(A3.6) into (A3.1) and noting that $k_{\mu\nu}{}^N=k_{\nu\mu}{}^N$ and $k_{\mu\nu}{}^M=k_{\nu\mu}{}^M$, we obtain

$$H^{\pm}=T_n+W_N+W_M+W^{AB}+2^{-\frac{1}{2}}\sum_\mu l_\mu{}^M(Q_\mu{}^+ + Q_\mu{}^-)+\sum_\rho l_\rho{}^{AB}Q_\rho{}^{AB}+\tfrac{1}{4}\sum_{\mu\nu}(k_{\mu\nu}{}^M+k_{\mu\nu}{}^N)(Q_\mu{}^+Q_\nu{}^+ + Q_\mu{}^-Q_\nu{}^-)+\tfrac{1}{2}\sum_{\mu\nu}(k_{\mu\nu}{}^M-k_{\mu\nu}{}^N)Q_\mu{}^+Q_\nu{}^-+\tfrac{1}{2}\sum_{\rho\sigma}k_{\rho\sigma}{}^{AB}Q_\rho{}^{AB}Q_\sigma{}^{AB}\pm[W_S+\sum_\rho l_\rho{}^S Q_\rho{}^{AB}+\tfrac{1}{2}\sum_{\rho\sigma}k_{\rho\sigma}{}^S Q_\rho{}^{AB}Q_\sigma{}^{AB}]G. \tag{A3.7}$$

The Hamiltonians (A3.7) are the dimeric equivalent to the equations for the molecular case obtained on substituting (6.2) into (6.1). In complete analogy with the molecular case, two physical assumptions are necessary to make the problem tractable. The first is

$$\text{(a')} \quad |\sum_\rho l_\rho{}^S Q_\rho+\tfrac{1}{2}\sum_{\rho\sigma}k_{\rho\sigma}{}^S Q_\rho{}^{AB}Q_\sigma{}^{AB}| \ll W_S.$$

Assumption (a') states that only the constant exciton coupling term need be considered. A second physical assumption is required to assure that the vibronic coupling depends on the linear terms in the nuclear displacements rather than the quadratic ones. We shall assume this to be true for the coordinates of relative motion $Q_\rho{}^{AB}$. However, for the internal modes it is necessary to assume

$$\text{(b')} \qquad k_{\mu\nu}{}^N=k_{\mu\nu}{}^M,$$

i.e., that the force constants are the same in the ground and excited states of the monomeric units.

After assumptions (a') and (b') are made, it is clear that the only terms in $H^{\pm}$ that do not commute with G are the terms $l_\mu{}^M Q_\mu{}^-$ and those terms $l_\rho{}^{AB}Q_\rho{}^{AB}$ for which $GQ_\rho{}^{AB}=-Q_\rho{}^{AB}G$. In general, linear vibronic coupling in the modes of relative motion $Q_\rho{}^{AB}$ has been neglected.

[20] The remaining unpublished work by Moffitt and Witkowsky inspired the derivation given here. However, the present treatment differs from theirs in proceeding from the one-dimensional Hamiltonians. Moreover, they restricted themselves to one stretching mode in each monomer and one mode of relative motion.

In dealing with the problem in Q_μ^- we make an assumption for illustrative purposes similar to (c) in the molecular case, namely,

(c′) only one monomeric normal mode changes its equilibrium position in the excited state,

i.e., has $l_\mu^M \neq 0$.

It can be seen from (A3.7) that a nonzero l_μ^M affects both Q_μ^+ and Q_μ^-. With the former it acts in the customary manner of a change of equilibrium position. However, with the latter it introduces vibronic coupling. The "weak" or "strong" exciton coupling cases are determined by the competition between the exciton coupling energy given by W_s and the shape change in the monomer excited state reflected in l_μ^M.

APPENDIX IV

The overlap integrals are[21]

$$\begin{aligned}\langle m, \lambda \,|\, n, 0\rangle &= \exp[-\tfrac{1}{4}\lambda^2](-2^{-\frac{1}{2}}\lambda)^{n-m}(m!/n!)^{\frac{1}{2}} \\ &\quad \times L_m^{n-m}(\lambda^2/2) \\ &= \exp[-\tfrac{1}{4}\lambda^2](2^{-\frac{1}{2}}\lambda)^{m-n}(n!/m!)^{\frac{1}{2}} \\ &\quad \times L_n^{m-n}(\lambda^2/2), \quad \text{(A4.1)}\end{aligned}$$

where the associated Laguerre polynomials are defined by

$$L_n^\alpha(x) \equiv (x^{-\alpha}/n!)e^x(d^n/dx^n)(x^{n+\alpha}e^{-x}) \quad \text{(A4.2)}$$

and $|n, \lambda\rangle$ is the eigenstate satisfying

$$[\tfrac{1}{2}(p^2+q^2)+\lambda q]\,|n, \lambda\rangle = (n+\tfrac{1}{2}-\tfrac{1}{2}\lambda^2)\,|n, \lambda\rangle. \quad \text{(A4.3)}$$

To evaluate the matrix elements of the reflection operator G, we note that

$$\langle q' \,|\, G = \langle -q' \,| \quad \text{(A4.4)}$$

and

$$\langle q' \,|\, n, \lambda\rangle = \langle q'+\lambda \,|\, n, 0\rangle, \quad \text{(A4.5)}$$

where $\langle q' |$ is the left eigenstate of the position operator q. (A4.5) is merely the eigenfunction of the displaced harmonic oscillator expressed in terms of the original coordinates. The matrix elements of G, therefore, become

$$\begin{aligned}\langle m, \lambda \,|\, G \,|\, n, \lambda\rangle &= \int dq' \,\langle m, 0 \,|\, q'+\lambda\rangle\langle -q'+\lambda \,|\, n, 0\rangle \\ &= (-1)^n \int dq' \,\langle m, 0 \,|\, q'+2\lambda\rangle\langle q' \,|\, n, 0\rangle \\ &= (-1)^n \langle m, 2\lambda \,|\, n, 0\rangle. \quad \text{(A4.6)}\end{aligned}$$

Upon inserting the identities (A4.1), we find

$$\begin{aligned}\langle m, \lambda \,|\, G \,|\, n, \lambda\rangle &= (-1)^m \exp[-\lambda^2](2^{\frac{1}{2}}\lambda)^{n-m}(m!/n!)^{\frac{1}{2}} \\ &\quad \times L_m^{n-m}(2\lambda^2) \\ &= (-1)^n \exp[-\lambda^2](2^{\frac{1}{2}}\lambda)^{m-n}(n!/m!)^{\frac{1}{2}} \\ &\quad \times L_n^{m-n}(2\lambda^2). \quad \text{(A4.7)}\end{aligned}$$

In both (A4.1) and (A4.7), the first expression is convenient when $n \geqslant m$, while the second is convenient when $n \leqslant m$. It should be noted that the Laguerre polynomials defined by (A4.2) are equal to those given by Morse and Feshbach[22] divided by $\Gamma(n+\alpha+1)$.

[21] S. Koide, Z. Naturforsch. **15a,** 123–128 (1960), Eqs. (14) and (15). To obtain (A4.1) from this paper, set $\lambda = \sqrt{2}\alpha$ where α is defined by Koide. We note that there is an error in sign in (15) which has been corrected when writing (A4.1).

[22] Philip M. Morse and Herman Feshbach, *Methods of Theoretical Physics, Part I* (McGraw-Hill Book Company, Inc., New York, 1953), pp. 784, 785.

On the Evaluation of Integrals Occurring in the Theory of the Correlated Electronic Wave Functions*

LEVENTE SZÁSZ†

Strawbridge Observatory, Haverford College, Haverford, Pennsylvania

(Received February 27, 1961)

It can be shown that the simplest generalization of the Hylleraas method for atoms with arbitrary number of electrons leads to integrals of six and nine dimensions, respectively, where the interelectronic distances occur in the integrands. The purpose of the present paper is to show that the nine-dimensional integrals can be treated by a similar procedure to that which was suggested for the evaluation of the six-dimensional integrals by Hylleraas and Breit.

I. FORMULATION OF THE PROBLEM

IT is generally recognized that the computation of atomic wave functions more accurate than the wave functions yielded by the Hartree-Fock method would be desirable. There are essentially only two methods which have been applied with success for this purpose: the method of superposition of configurations, and the Hylleraas method. In recent years, considerable work has been done computing wave functions with the method of superposition of configurations.[1] The advantage of this method is that the computation of the matrix components of the Hamiltonian is relatively simple; on the other hand, the convergence toward the true energy is often very slow. The Hylleraas method has given much better results than the superposition of configurations in the case of the helium atom, and it has been successful also in the computation of the wave function of the lithium atom.[2] But until recently, it was generally believed that the method was too complicated for the computation of wave functions of atoms with more than three electrons.

In a recent paper,[3] the present author has suggested a simple generalization of the Hylleraas procedure for atoms with an arbitrary number of electrons. The wave function, suggested in the work mentioned above, was

$$\Psi=[1/(N!)^{\frac{1}{2}}]\tilde{A}\{\varphi_1(1)\varphi_2(2)\cdots\varphi_N(N)\times[1+\sum_{i=1}^{N}\sum_{j=i+1}^{N}w_{ij}(ij)]\}, \quad (1)$$

where $\varphi_1, \varphi_2, \cdots\varphi_N$ are one-electron spin-orbitals, $\tilde{A}$ is the antisymmetrizer operator, N is the number of electrons, and the correlation functions w_{ij} have the following form:

$$w_{ij}(1,2)=\sum_{m,n,l}c_{ij}{}^{mnl}(r_1-r_2)^{2m}(r_1+r_2)^{n}r_{12}{}^{l}, \quad (2)$$

where the $c_{ij}{}^{mnl}$ are variational parameters. (The i and j indices of the w functions refer to the spin-orbitals φ_i and φ_j that means we define one w function for every pair of spin-orbitals.) The matrix components of the Hamiltonian with respect to the function (1) have been evaluated in terms of the spin-orbitals φ_i and the correlation functions w_{ij}, and it has been shown that these matrix components are relatively simple expressions even with a larger number of electrons.

If one derives formulas for the matrix components of the Hamiltonian with respect to the wave function (1), it turns out that the occurring integrals are essentially of the following two types:

$$I_1=\int f_1(\mathbf{r}_1)f_2(\mathbf{r}_2)r_{12}{}^{s}dv_1dv_2, \quad (3)$$

and

$$I_2=\int f_1(\mathbf{r}_1)f_2(\mathbf{r}_2)f_3(\mathbf{r}_3)(r_{12}{}^{s}r_{23}{}^{t}/r_{13})dv_1dv_2dv_3, \quad (4)$$

where the f_i functions have the form

$$f_i(\mathbf{r})=g_i(r)Y_{l_im_i}(\vartheta\phi), \quad (5)$$

$Y_{l_im_i}$ being the normalized spherical harmonics, and the exponents of the r_{13} and r_{23}, s, and t are positive integers or zero. It is of course possible to evaluate both integrals carrying out the integration over the polar coordinates of the vectors $\mathbf{r}_1$, $\mathbf{r}_2$, and $\mathbf{r}_3$. A much simpler method has been suggested by Breit[4] for the evaluation of integrals of type (3). Instead of integrating over the polar coordinates $r_1\vartheta_1\phi_1$, $r_2\vartheta_2\phi_2$, Breit introduced the variables

* This research was supported in part by a contract from the Office of Naval Research. This contract was administered by the University of Pennsylvania.

† Present address: Solid-State and Molecular Theory Group, Massachusetts Institute of Technology, Cambridge, Massachusetts.

[1] L. C. Green, C. D. Chandler, and P. P. Rush, Phys. Rev. **104,** 1593 (1956); R. K. Nesbet and R. E. Watson, *ibid.* **110,** 1073 (1958); H. Shull and P. O. Löwdin, J. Chem. Phys. **30,** 617 (1959); S. F. Boys, Proc. Roy. Soc. (London) **A201,** 125 (1950); **206,** 489 (1951); **207,** 181, 197 (1951); **217,** 136, 251 (1953); Phil. Trans. Roy. Soc. (London) **A245,** 95, 139 (1952); A. P. Jucys, J. Exptl. Theoret. Phys. (USSR) **23,** 129 (1952); A. P. Jucys, V. V. Kibartas and I. I. Glembotskii, *ibid.* **27,** 425 (1954); A. P. Jucys, I. I. Glembotskii, and V. V. Kibartas, *ibid.* **29,** 617 (1955); A. P. Jucys, V. V. Kibartas, and V. I. Kavetskis, *ibid.* **29,** 623 (1955); R. E. Watson, Phys. Rev. **119,** 170 (1960).

[2] H. M. James and A. S. Coolidge, Phys. Rev. **49,** 688 (1936).

[3] L. Szász, Z. Naturforsch. **15a,** 909 (1960).

[4] G. Breit, Phys. Rev. **35,** 569 (1930). The case where the functions f_1 and f_2 do not depend on the angles was considered by E. Hylleraas, Z. Physik **48,** 469 (1928); **54,** 347 (1929). The problem of integrals of type (3) has been recently investigated by J. L. Calais and P. O. Löwdin, Preprint No. 50, Quantum Chemistry Group, University of Uppsala, Sweden, 1960 (unpublished).

$r_1r_2\theta$, $\vartheta_1\phi_1\phi_{21}$, where θ is the angle between the vectors $\mathbf{r}_1$ and $\mathbf{r}_2$ and $\vartheta_1\phi_1\phi_{21}$ are the Euler angles. The purpose of the present paper is to show that a similar procedure is possible with the integral (4).

II. CHOICE OF VARIABLES AND EXPANSION OF THE INTEGRAL

Our goal is to show how the integral (4) can be reduced to a triple integral over the coordinates r_1, r_2, and r_3. Let $r_1\vartheta_1\phi_1$, $r_2\vartheta_2\phi_2$, and $r_3\vartheta_3\phi_3$ be the polar coordinates of the vectors $\mathbf{r}_1$, $\mathbf{r}_2$, and $\mathbf{r}_3$, and let us define the $(X'Y'Z')$ coordinate system by rotating the (XYZ) coordinate system first about the Z axis through the angle φ_3 and then rotating it about the Y' axis through the angle ϑ_3 (see Fig. 1). Let us denote the polar coordinates of $\mathbf{r}_1$ and $\mathbf{r}_2$ with respect to the coordinate system $(X'Y'Z')$ by $r_1\theta_{13}\phi_{13}$ and $r_2\theta_{23}\phi_{23}$. In terms of these new coordinates, we have for the interelectronic distances

$$\left.\begin{aligned} r_{13}&=\{r_1^2+r_3^2-2r_1r_3\cos\theta_{13}\}^{\frac{1}{2}}\\ \text{and}\qquad r_{23}&=\{r_2^2+r_3^2-2r_2r_3\cos\theta_{23}\}^{\frac{1}{2}}\end{aligned}\right\}. \tag{6}$$

Now let us realize that because of the presence of the r_{13}^s, r_{23}^t terms in the integral (4) it is desirable to introduce r_{13} and r_{23} as integrational variables if we want a formula for arbitrary s and t. It is not possible, however, to introduce r_{13}, r_{23}, and r_{12} as integrational variables simultaneously because r_{12} will depend on the other two, but this is also not necessary since we can expand $1/r_{12}$ in terms of functions of $r_1\theta_{13}\phi_{13}$ and $r_2\theta_{23}\phi_{23}$.

Let us therefore introduce as the new set of independent variables

$$(r_1\theta_{13}\phi_{13}),\qquad (r_2\theta_{23}\phi_{23}),\qquad (r_3\vartheta_3\phi_3).$$

Suppose that f_1 and f_2 have the form

$$\left.\begin{aligned} f_1(r_1\vartheta_1\phi_1)&=g_1(r_1)\,Y_{l_1m_1}(\vartheta_1\phi_1)\\ f_2(r_2\vartheta_2\phi_2)&=g_2(r_2)\,Y_{l_2m_2}{}^*(\vartheta_2\phi_2)\end{aligned}\right\}. \tag{7}$$

Let us denote the normalized spherical harmonics with respect to the coordinate system $(X'Y'Z')$ by $Y_{l_1m_1}(\theta_{13}\phi_{13})$ and $Y_{l_2m_2}(\theta_{23}\phi_{23})$. One can easily derive the relationships

$$\left.\begin{aligned} Y_{l_1m_1}(\vartheta_1\phi_1)&=\sum_{m'=-l_1}^{+l_1}M_{m_1m',l_1}(\vartheta_3\phi_3)\,Y_{l_1m'}(\theta_{13}\phi_{13})\\ \text{and}\qquad Y_{l_2m_2}{}^*(\vartheta_2\phi_2)&=\sum_{m'=-l_2}^{+l_2}M_{m_2m',l_2}{}^*(\vartheta_3\phi_3)\,Y_{l_2m'}{}^*(\theta_{23}\phi_{23})\end{aligned}\right\}. \tag{8}$$

The rotation matrices $M_{mm',l}$ can be easily derived with the methods described by Rose.[5]

Next let us expand $1/r_{12}$ in terms of $Y_{lm}(\theta_{13}\phi_{13})$ and $Y_{lm}(\theta_{23}\phi_{23})$. We have

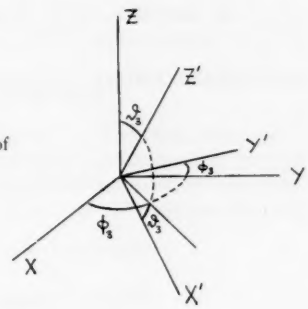

FIG. 1. The rotation of the coordinate system.

$$\frac{1}{r_{12}}=\sum_{l=0}^{\infty}K_l(r_1r_2)\,P_l(\cos\theta_{12})$$

$$=\sum_{l=0}^{\infty}K_l(r_1r_2)\,\frac{4\pi}{2l+1}\sum_{m=-l}^{+l}Y_{lm}{}^*(\theta_{13}\phi_{13})\,Y_{lm}(\theta_{23}\phi_{23}). \tag{9}$$

[$K_l(r_1r_2)$ is $r_1{}^l/r_2{}^{l+1}$ if $r_1<r_2$, and it is $r_2{}^l/r_1{}^{l+1}$ if $r_2<r_1$.]

By putting (8) and (9) into (4), we get

$$\begin{aligned} I_2=\int g_1(r_1)\,g_2(r_2)\,g_3(r_3)\,r_{13}{}^s r_{23}{}^t\sum_{l=0}^{\infty}\sum_{m=-l}^{+l}K_l(r_1r_2)\\ \times[4\pi/(2l+1)]\,Y_{lm}{}^*(\theta_{13}\phi_{13})\,Y_{lm}(\theta_{23}\phi_{23})\\ \times\sum_{m'=-l_1}^{+l_1}M_{m_1m',l_1}(\vartheta_3\phi_3)\,Y_{l_1m'}(\theta_{13}\phi_{13})\\ \times\sum_{m''=-l_2}^{+l_2}M_{m_2m'',l_2}{}^*(\vartheta_3\phi_3)\,Y_{l_2m''}{}^*(\theta_{23}\phi_{23})\\ \times Y_{l_3m_3}(\vartheta_3\phi_3)\,r_1{}^2dr_1r_2{}^2dr_2r_3{}^2dr_3\\ \times\sin\theta_{13}d\theta_{13}\sin\theta_{23}d\theta_{23}\sin\vartheta_3d\vartheta_3d\phi_{13}d\phi_{23}d\phi_3. \end{aligned} \tag{10}$$

In the last expression we have converted dv_1 and dv_2 into expressions containing the new variables, and it is easy to see that

$$\left.\begin{aligned} \sin\vartheta_1d\vartheta_1d\phi_1&\rightarrow\sin\theta_{13}d\theta_{13}d\phi_{13},\\ \text{and}\qquad \sin\vartheta_2d\vartheta_2d\phi_2&\rightarrow\sin\theta_{23}d\theta_{23}d\phi_{23}.\end{aligned}\right\} \tag{11}$$

The integral (10) can be further simplified if we realize that r_{13} and r_{23} do not depend on ϕ_{13} and ϕ_{23}; therefore, the integration with respect to these variables can be carried out immediately. Taking into account that the spherical harmonics have the form

$$Y_{LM}(\theta\phi)=P_{LM}(\theta)[1/(2\pi)^{\frac{1}{2}}]\exp(iM\phi),$$

we get integrating over ϕ_{13} and ϕ_{23}:

$$\begin{aligned} I_2=\sum_{l=0}^{\infty}\sum_{m}\frac{4\pi}{2l+1}\int g_1(r_1)\,g_2(r_2)\,g_3(r_3)\,r_{13}{}^s r_{23}{}^t K_l(r_1r_2)\\ \times P_{lm}(\theta_{13})\,P_{lm}(\theta_{23})\,M_{m_1m}{}^{l_1}(\vartheta_3\phi_3)\,P_{l_1m}(\theta_{13})\\ \times M_{m_2m}{}^{l_2}{}^*(\vartheta_3\phi_3)\,P_{l_2m}(\theta_{23})\,Y_{l_3m_3}(\vartheta_3\phi_3)\,r_1{}^2dr_1r_2{}^2dr_2r_3{}^2dr_3\\ \times\sin\theta_{13}d\theta_{13}\sin\theta_{23}d\theta_{23}\sin\vartheta_3d\vartheta_3d\phi_3, \end{aligned} \tag{12}$$

[5] M. E. Rose, *Elementary Theory of Angular Momentum* (John Wiley & Sons, Inc., New York, 1957), p. 62.

where the summation over m runs from $-L$ to $+L$, where L is the smallest of the three indices l_1, l_2, and l.

III. INTERELECTRONIC DISTANCES AS INTEGRATION VARIABLES

We now introduce as integrational variables the interelectronic distance r_{13} instead of θ_{13}, and the interelectronic distance r_{23} instead of θ_{23}. With the aid of the relationships (6), we obtain

$$\left.\begin{aligned}\sin\theta_{13}d\theta_{13}&\rightarrow(r_{13}dr_{13}/r_1r_2)\\ \sin\theta_{23}d\theta_{23}&\rightarrow(r_{23}dr_{23}/r_2r_3)\end{aligned}\right\}. \tag{13}$$

On putting (13) into (12), we have

$$\begin{aligned}I_2=\sum_{l=0}^{\infty}\sum_m\frac{4\pi}{2l+1}\int g_1(r_1)\,g_2(r_2)\,g_3(r_3)\,r_{13}{}^s r_{23}{}^t K_l(r_1r_2)\\ \times P_{lm}(\theta_{13})\,P_{lm}(\theta_{23})\,M_{m_1m}{}^{l_1}(\vartheta_3\phi_3)\,P_{l_1m}(\theta_{13})\\ \times M_{m_2m}{}^{l_2*}(\vartheta_3\phi_3)\,P_{l_2m}(\theta_{23})\,Y_{l_3m_3}(\vartheta_3\phi_3)\\ \times r_1dr_1r_2dr_2dr_3r_{13}dr_{13}r_{23}dr_{23}\sin\vartheta_3d\vartheta_3d\phi_3.\end{aligned} \tag{14}$$

We have now introduced r_{13} and r_{23} as integrational variables, but we still have functions of θ_{13} and θ_{23} in the integrand. Let us remember, however, that the associated Legendre polynomials can be expressed in the following form:

$$\begin{aligned}&P_{lm}(\theta)\\ &=\text{const}(\sin\theta)^m\left[(\cos\theta)^{l-m}-\text{const}(\cos\theta)^{l-m-2}+\cdots\right].\end{aligned} \tag{15}$$

In the expression (14) we have two Legendre functions depending on θ_{13} and two depending on θ_{23}. Let us note furthermore, that the second indices of the two Legendre polynomials which depend on θ_{13} are equal because of the integration over ϕ_{13}, and the same is true of course for the two polynomials depending on θ_{23}. Therefore we shall have the following expression:

$$\begin{aligned}&P_{lm}(\theta_{13})\,P_{l_1m}(\theta_{13})\\ &\quad=\text{const}(\sin\theta_{13})^{2m}\{\text{terms depending on }\cos\theta_{13}\},\end{aligned} \tag{16}$$

and a similar expression for $P_{lm}(\theta_{23})\,P_{l_2m}(\theta_{23})$. In other words, the functions depending on θ_{13} will contain terms of the form $(\cos\theta_{13})^K$ and terms like $(\sin\theta_{13})^{2m}$; that means the exponent of $(\sin\theta_{13})$ is always an even number. But then we can substitute

$$\cos\theta_{13}=(r_1{}^2+r_3{}^2-r_{13}{}^2)/2r_1r_3$$

and

$$(\sin\theta_{13})^{2m}=\left[1-\left(\frac{r_1{}^2+r_3{}^2-r_{13}{}^2}{2r_1r_3}\right)^2\right]^m \tag{17}$$

and similar expressions for the functions of θ_{23} in terms of $r_2r_3r_{23}$. That means, the Legendre polynomials depending on θ_{13} and θ_{23} can always be expressed as rational functions of $r_1r_3r_{13}$ and $r_2r_3r_{23}$, respectively.

Now let us take a look at the integral (14). After carrying out the integration over ϑ_3 and ϕ_3 and converting the Legendre polynomials into expressions depending on r_{13} and r_{23}, we end up with an integral over r_1, r_2, r_3, r_{13}, and r_{23}. The integration over r_{13} and r_{23} can be carried out immediately with the formulas

$$\left.\begin{aligned}\int_{|r_1-r_3|}^{r_1+r_3}r_{13}{}^l dr_{13}&=\omega_l(r_1r_3)\\ \text{and}\\ \int_{|r_2-r_3|}^{r_2+r_3}r_{23}{}^l dr_{23}&=\omega_l(r_2r_3)\end{aligned}\right\}, \tag{18}$$

where

$$\omega_l(r_1r_2)=(l+1)^{-1}\left\{\begin{aligned}&-(r_1-r_2)^{l+1}\quad\text{if } r_1>r_2\\ (r_1+r_2)^{l+1}\\ &-(r_2-r_1)^{l+1}\quad\text{if } r_2>r_1\end{aligned}\right\}.$$

After integrating over r_{13} and r_{23}, the remaining integral will be a triple integral over r_1, r_2, and r_3 which usually can be evaluated only numerically because the functions g_1, g_2, g_3 in the most cases are given only in form of a table and not in analytical form.

IV. EXAMPLES

For practical purposes, we give here the rotation matrix for $l=1$

$$M_{mm'}{}^l=f_{mm'}{}^l(\vartheta_3)\,\exp(im\phi_3), \tag{19}$$

$$\begin{array}{lll}f_{11}{}^1=\tfrac{1}{2}(1+\cos\vartheta_3) & f_{01}{}^1=-\sqrt{2}^{-1}\sin\vartheta_3 & f_{-1,1}{}^1=\tfrac{1}{2}(1-\cos\vartheta_3)\\ f_{10}{}^1=\sqrt{2}^{-1}\sin\vartheta_3 & f_{00}{}^1=\cos\vartheta_3 & f_{-1,0}{}^1=-\sqrt{2}^{-1}\sin\vartheta_3\\ f_{1-1}{}^1=\tfrac{1}{2}(1-\cos\vartheta_3) & f_{0-1}{}^1=\sqrt{2}^{-1}\sin\vartheta_3 & f_{-1,-1}{}^1=\tfrac{1}{2}(1+\cos\vartheta_3).\end{array}$$

We would like to show by two examples how the present method works. Let us consider first the integral (14) with $l_1=l_2=l_3=0$. In this simple case we have

$$Y_{l_3m_3}=Y_{00}=1/(4\pi)^{\frac{1}{2}},\qquad\text{and}\qquad P_{l0}(\theta_{13})=P_{l0}(\cos\theta_{13}),$$

$$P_{l0}(\theta_{23})=P_{l0}(\cos\theta_{23}),\qquad P_{l_10}(\theta_{13})=P_{l_20}(\theta_{23})=P_{00}=1/\sqrt{2}.$$

For the rotation matrices, we have in this case $M_{00}{}^0=1$. We obtain, therefore,

$$I_2=\sum_{l=0}^{\infty} I_2{}^l, \tag{20}$$

with

$$I_2{}^0=[(4\pi)^{\frac{1}{2}}/4]\int g_1(r_1)\,g_2(r_2)\,g_3(r_3)\,K_0(r_1r_2)\,\omega_{s+1}(r_1r_3)\,\omega_{t+1}(r_2r_3)\,r_1r_2dr_1dr_2dr_3, \tag{21}$$

$$I_2{}^1=[(4\pi)^{\frac{1}{2}}/16]\int g_1(r_1)\,g_2(r_2)\,g_3(r_3)\,K_1(r_1r_2)\,(1/r_3{}^2)\,\{(r_1{}^2r_2{}^2+r_1{}^2r_3{}^2$$

$$+r_2{}^2r_3{}^2+r_3{}^2r_3{}^2)\,\omega_{s+1}(r_1r_3)\,\omega_{t+1}(r_2r_3)-(r_1{}^2+r_3{}^2)\,\omega_{s+1}(r_1r_3)\,\omega_{t+3}(r_2r_3)$$

$$-(r_2{}^2+r_3{}^2)\,\omega_{s+3}(r_1r_3)\,\omega_{t+1}(r_2r_3)+\omega_{s+3}(r_1r_3)\,\omega_{t+3}(r_2r_3)\}\,dr_1dr_2dr_3, \tag{22}$$

and the integrals for $l=2, 3, \cdots$ can be computed easily taking into account formula (17) for the $P_{l0}(\cos\theta)$.

Let us consider now a case where the functions depend on the angles. Let us consider first the integration over ϕ_3 in the integral (14). Because of the form of the rotation matrix given above, the integral vanishes unless

$$m_1-m_2=m_3. \tag{23}$$

Let $m_1=m_2=1$, $m_3=0$ with $l_1=l_2=1$, $l_3=0$. Then we shall have

$$I_2=\sum_{l=0}^{\infty}\sum_{m}\frac{4\pi}{2l+1}\int g_1(r_1)\,g_2(r_2)\,g_3(r_3)\,r_{13}{}^s r_{23}{}^t K_l(r_1r_2)\,P_{lm}(\theta_{13})\,P_{lm}(\theta_{23})\,f_{1m}{}^1(\vartheta_3)\,P_{1m}(\theta_{13})\,f_{1m}{}^1(\vartheta_3)\,P_{1m}(\theta_{23})$$

$$\times\tfrac{1}{2}(4\pi)^{\frac{1}{2}}\cdot r_1dr_1r_2dr_2dr_3r_{13}dr_{13}r_{23}dr_{23}\sin\vartheta_3d\vartheta_3, \tag{24}$$

where the summation over m is limited to $m=0$ if $l=0$, and runs from -1 to $+1$ if $l\geq 1$. We give the expression for $l=0$

$$I_2{}^0=[(4\pi)^{\frac{1}{2}}/2]\int g_1(r_1)\,g_2(r_2)\,g_3(r_3)\,r_{13}{}^s r_{23}{}^t K_1(r_1r_2)\,P_{00}(\theta_{13})\,P_{00}(\theta_{23})\,f_{10}{}^1(\vartheta_3)\,f_{10}{}^1(\vartheta_3)\,P_{10}(\theta_{13})\,P_{10}(\theta_{23})$$

$$\times\sin\vartheta_3d\vartheta_3r_1dr_1\cdot r_2dr_2dr_3r_{13}dr_{13}r_{23}dr_{23}. \tag{25}$$

We integrate over ϑ_3 and obtain

$$\int_0^{\pi}[f_{10}{}^1(\vartheta_3)]^2\sin\vartheta_3d\vartheta_3=\tfrac{2}{3}$$

and substitute for the Legendre polynomials

$$\left.\begin{aligned} P_{00}(\theta_{13})&=P_{00}(\theta_{23})=1/\sqrt{2}\\ P_{10}(\theta_{13})&=\left(\frac{3}{2}\right)^{\frac{1}{2}}\cos\theta_{13}=\left(\frac{3}{2}\right)^{\frac{1}{2}}\frac{r_1{}^2+r_3{}^2-r_{13}{}^2}{2r_1r_3}\\ P_{10}(\theta_{23})&=\left(\frac{3}{2}\right)^{\frac{1}{2}}\cos\theta_{23}=\left(\frac{3}{2}\right)^{\frac{1}{2}}\frac{r_2{}^2+r_3{}^2-r_{23}{}^2}{2r_2r_3}\end{aligned}\right\}. \tag{26}$$

On putting (26) into (25), we get finally

$$I_2{}^0=[(4\pi)^{\frac{1}{2}}/16]\int g_1(r_1)\,g_2(r_2)\,g_3(r_3)\,K_0(r_1r_2)\,(1/r_3{}^2)\,\{(r_1{}^2r_2{}^2+r_1{}^2r_3{}^2+r_2{}^2r_3{}^2+r_3{}^2r_3{}^2)\,\omega_{s+1}(r_1r_3)\,\omega_{t+1}(r_2r_3)$$

$$-(r_1{}^2+r_3{}^2)\,\omega_{s+1}(r_1r_3)\,\omega_{t+3}(r_2r_3)-(r_2{}^2+r_3{}^2)\,\omega_{s+3}(r_1r_3)\,\omega_{t+1}(r_2r_3)+\omega_{s+3}(r_1r_3)\,\omega_{t+3}(r_2r_3)\}\,dr_1dr_2dr_3. \tag{27}$$

The expressions for $l>0$ can be computed similarily.

V. REMARKS

Finally, we would like to say a few words about the computation of triple integrals like the expressions (21), (22), and (27). As was mentioned above, the actual computation of these integrals can be carried out numerically, and does not represent a great problem if a fast computer is available. There is one point, however, which we would like to emphasize. As we see from formula (14), integrals of type (4) will always represent a sum of integrals (the summation over l) and the integrals with increasing l will be expressions of increasing complexity. Fock *et al.*[6] have computed the integral (21) and (22) for $s=t=1$ in the case of the Be atom, and have shown, that the integral with $l=1$ is negligible with respect to the integral with $l=0$. This indicates that probably in all practical cases it will be sufficient to compute the first one or two terms in the series of the formula (14).

ACKNOWLEDGMENT

I am very much indebted to Professor L. C. Green for several discussions and for reading the manuscript.

[6] V. Fock, M. Vesselow, and M. Petrashen, J. Exptl. Theoret. Phys. (USSR) **10**, 723 (1940); M. Vesselow, M. Petrashen, and A. Kritchagina, *ibid.* **10**, 857 (1940).

THE JOURNAL OF CHEMICAL PHYSICS VOLUME 35, NUMBER 3 SEPTEMBER, 1961

Effect of an Attractive Potential on the Classical Theory of Vibrational Energy Exchange

R. E. TURNER*

Clarendon Laboratory, Oxford, England

AND

DONALD RAPP

Lockheed Aircraft Corporation, Missiles and Space Division, Sunnyvale, California

(Received February 26, 1961)

The usual theory of vibrational energy transfer between molecules uses a purely repulsive exponential potential with an energy zero at the bottom of the van der Waals attractive potential well. One therefore uses a velocity distribution modified by a factor $\exp(\epsilon/kT)$ to take the attractive forces into account. This method is an artifice to avoid dealing with the detailed dynamics of motion in the attractive potential well. In the present paper, the complete dynamical problem for a "Morse"-type potential, consisting of an atrractive term in addition to the exponential repulsion, has been solved. A more rigorous correction for the attractive forces is therefore proposed.

RECENTLY, Rapp[1] has shown that the transition probability for energy exchange in a head-on collision between a molecule A and an atom B or a harmonic oscillator BC is, in the "adiabatic" approximation, identical with the quantum-mechanical result in the classical limit obtained by Herzfeld. He also points out that the assumption necessary in going to the classical limit is probably more valid than the other assumptions of the theory. Consequently, any improvement on present calculations could be done classically with possibly a better insight into the assumptions involved.

The model chosen for these calculations is one-dimensional with the two atoms BC coupled by a harmonic force. A molecule A then collides with one of the molecules with an energy exchange in the classical case or a certain probability of energy exchange in the quantum case. In both quantum and classical cases the energy of interaction between the molecule A and the atom B is assumed to be an exponential repulsive one. The attractive part of the interaction, which is present in the true interaction, is taken account of by multiplying the distribution of initial energies of molecule A, over which the result has to be averaged, by a factor $\exp(\epsilon/kT)$, where ϵ is the depth of the potential well.

Rapp's calculations can be extended to a general interaction potential between A and BC. In the "adiabatic" approximation one has for the equation of motion of the distance X between the center of masses of A and BC

$$\tilde{m}(d^2X/dt^2)+[\partial V(X)/\partial X]=0,$$

where $\tilde{m}$ is given in reference 1, and $V(X)$ is the interaction between A and one of the atoms BC.

If this equation is solved for X as a function of time, then the force acting on the oscillator due to A is

$$F(t)=-[m_C/(m_B+m_C)](\partial V/\partial X)\,|_{X=X(t)},$$

assuming A collides with B.

* Pressed-Steel Research Fellow.

[1] D. Rapp, J. Chem. Phys. **32**, 735 (1960).

The energy transmitted to the oscillator during the collision is calculated from Eq. (12) of reference 1.

To investigate the effect of an attractive potential the simplest interaction potential to use is a Morse potential,

$$V(X)=\epsilon\{\exp[-(X-X_0)/L]-2\exp[-(X-X_0)/2L]\},$$

where ϵ is the depth of the potential well, X_0 the position of the potential minimum, and L a parameter which can be chosen so that the potential agrees as closely as possible with the true potential at the point of strongest interaction. With this potential the equation of motion for X can be solved exactly and the energy exchange is found to be

$$E=(\tfrac{1}{2}\mu)\left(\frac{m_C}{m_B+m_C}\right)^2(4\pi\tilde{m}L)^2\times\{\omega\cosh[(\pi L\omega/v_0)(1+2\phi/\pi)]-(v_0/2L)\tan\phi\sinh[(\pi L\omega/v_0)(1+2\phi/\pi)]\}^2\times\operatorname{cosech}^2(2\pi\omega L/v_0),$$

where the notation is as in reference 1 and

$$\phi=\tan^{-1}(\epsilon/E_0)^{\frac{1}{2}}.$$

When $\pi\omega L/v_0\gg 1$ then,

$$E=\frac{8\pi^2\tilde{m}^{*2}}{\mu}[m_C/(m_B+m_C)]^2\omega^2L^2\exp(-2\pi\omega L/v_0^*).$$

Thus the result is identical with that for a purely exponentially repulsive potential except for the replacement of $\tilde{m}$ by an effective mass

$$\tilde{m}^*=\tilde{m}\{1-[(\epsilon/2\tilde{m})L^2\omega^2]^{\frac{1}{3}}\}$$

and the initial velocity of A, v_0, by an effective velocity $v_0^*=v_0[1-(2/\pi)\tan^{-1}(\epsilon/E_0)^{\frac{1}{2}}]^{-1}$. Thus, the speeding up of the molecule in the attractive part of the potential can be taken care of by assuming that the molecule has an effective mass $<\tilde{m}$ and an effective velocity $>v_0$. It is interesting to note that at high collision energies, $E_0\gg\epsilon$, $v_0^*\to v_0$ but $\tilde{m}^*$ does not go to $\tilde{m}$.

This problem has been considered by Cottrell and Ream[2] using a semi-classical time-dependent perturbation procedure. Their result differs from ours in that $\tilde{m}^*$ is replaced by $\tilde{m}$; we believe that this is due to an error in their calculation of the Fourier transform of $F(t)$.

TABLE I.

Temperature (°K)	$P_{1\to0}$ (exptl)[4]	$P_{1\to0}$ (Robben)[3]	$P_{1\to0}$ (calc)
500	1×10^{-3}	8×10^{-4}	7×10^{-3}
1000	2×10^{-3}	1×10^{-3}	1.4×10^{-2}

The remainder of the calculation of the transition probability is the same as in Rapp's paper except that the factor $\exp(\epsilon/kT)$ is to be omitted since we have calculated the effect of the attractive potential.

The modifications to Rapp's result are:

(i) The factor $\exp(\epsilon/kT)$ is to be replaced by unity.

(ii) The transition probability is to be multiplied by a factor $(\tilde{m}^*/\tilde{m})^2=\{1-[(\epsilon/2\tilde{m})L^2\omega^2]^{\frac{1}{3}}\}^2$.

(iii) The θ' is to be multiplied by

$$[1-(2/\pi)\tan^{-1}(\epsilon/E_0)^{\frac{1}{2}}]^2,$$

where E_0 is to be taken as the most probable collision energy for vibrational energy exchange.

The "anomalous" short vibrational relaxation time[3,4] of nitric oxide compared to N_2 and O_2 has been attributed[4] to strong attractive forces between NO molecules. Using very approximate potential parameters obtained from the $(NO)_2$ dimer, Robben[4] used the usual $\exp(\epsilon/kT)$ correction to calculate vibrational energy-transfer probabilities in fair agreement with experiment. The use of the ordinary transport property potential predicts transition probabilities too low by 10^5. We have calculated transition probabilities with Robben's potential parameters and our correction instead of $\exp(\epsilon/kT)$. The results are shown in Table I. In view of the uncertainty in the potential parameters and the wide scatter in the experimental data, the rough agreement is all we can expect.

[2] T. L. Cottrell and N. Ream, Trans. Faraday Soc. **51**, 159 (1955).

[3] F. Robben, P. R. Monson, and J. J. Allport, J. Chem. Phys. **33**, 630 (1960).

[4] F. Robben, J. Chem. Phys. **31**, 420 (1959).

Vibrational Spectra of Inorganic Molecules. II. Infrared Reflection Spectra of Liquid Lithium, Sodium, Potassium, and Silver Nitrates

J. K. WILMSHURST AND S. SENDEROFF

Parma Research Laboratory, Union Carbide Corporation, Parma 30, Ohio

(Received February 24, 1961)

The optical constants of liquid lithium, sodium, potassium, and silver nitrates have been obtained by a one-angle-reflection method using the analysis of Robinson and Price. The derived absorption spectra are consistent with the Raman spectra observed by Bues and suggest that in all melts, the point group symmetry of the cations about the nitrate ion does not contain D_{3h} as a subgroup. Further, in both lithium and silver nitrate the highest symmetry subgroup common to the nitrate ion and the surrounding cations is at most C_{2v} and in these melts the nitrate ion is not rotating freely about its threefold axis. In all the melts there is a low-frequency band which must be ascribed to a cation-anion vibration of a lattice-like type. The intensity of the a_2'' band has been discussed and the bond dipole moment derived has been interpreted in terms of the polarizing field of the cations.

THE vibrational spectra of molten ionic salts are of considerable interest to the spectroscopist since these systems present an example of a highly associated liquid state involving intense intermolecular forces. From this point of view, they are also of interest to the theoretical chemist and it might be expected that the study of these spectra would assist him in choosing suitable models for theoretical liquid-state calculations. However, until recently, the experimental difficulties associated with obtaining the spectra of ionic liquids, necessarily at quite elevated temperatures, have left this field relatively untouched. Thus, to date, only a few Raman spectra have been obtained, notably by Bues,[1,2] and until 1960 no infrared data had been reported.

The study of the infrared spectra of ionic liquids is made difficult by the lack of window materials that can withstand the higher temperatures and the corrosive nature of the ionic melts, and yet remain transparent over a sufficiently wide range of frequencies, especially the lower frequencies. Thus, the common high-temperature window materials, such as sapphire,[3] periclase,[4] Irtran AB-1,[5] and barium fluoride, all cut off at fairly high frequencies (1500, 1000, 1000, and 800 cm^{-1}, respectively) and, hence, have only very limited applicability in this field. Type II diamond which transmits below 250 cm^{-1} would of course be an excellent window material, but is rather costly. Therefore, to make any progress, it becomes necessary to devise a system of sampling such that the use of windows can be avoided. Three methods are available. First, a drop of the liquid may be held in a wire loop[6] in the field of a reflecting microscope and its absorption spectrum studied; second, a mirror may be placed below the surface of the melt and the absorption spectrum obtained by reflection from this mirror, the light having passed through the liquid film twice and, third, the reflection spectrum from the surface of the melt may be observed. The first two methods have the disadvantage that the thickness of the film cannot be adjusted easily and, in general, for molecules with reasonable absorption coefficients, only intense broad bands would be observed. The second method has the additional disadvantage that the reflection spectrum from the liquid surface is included in the observed absorption spectrum and complicates any interpretation. The third method avoids these difficulties. One objection to this method may arise from the fact that it appears to depend on a surface property of the material rather than upon a bulk property. However, considering the relatively long wavelengths of the light used and the low absorption coefficients of the materials, we feel confident that the results obtained do correspond to a sufficiently thick surface layer (of the order of thickness, $\sim 10\mu$, that would indeed be used in the equivalent absorption experiment) such as to enable us to consider them as being bulk properties.

Recently Greenberg and Hallgren[7,8] have made a clever adaptation of the first method, using a fine platinum mesh screen to supply a number of "loops" and, hence, dispensing with the need of a microscope; their data for alkali nitrates show that, for at least one band, the sample thickness obtained is too great. They have also used the second method,[7] but a perusal of their published spectra indicates that little, if any, light was reflected from their mirror, the spectrum corresponding essentially to that obtained by reflection from the liquid surface.

In the present investigation, the infrared reflection spectra of lithium, sodium, potassium, and silver nitrates in the liquid state was obtained. By a suitable optical arrangement, accurate intensity measurements were made and the data were analyzed by the method

[1] W. Bues, Z. physik. Chem. **10,** 1 (1957).
[2] W. Bues, Z. anorg. u. allgem. Chem. **279,** 104 (1955).
[3] Alpha-alumina, obtainable from Linde Company, Division U.C.C., Tonawanda, New York.
[4] Beta-magnesia, obtainable from Norton Company, Worcester, Massachusetts.
[5] Trade name of Kodak Labs, Rochester, New York.
[6] J. P. Young and J. C. White, Anal. Chem. **31,** 1892 (1959).
[7] J. Greenberg and L. J. Hallgren, Rev. Sci. Instr. **31,** 444 (1960).
[8] J. Greenberg and L. J. Hallgren, J. Chem. Phys. **33,** 900 (1960).

of Robinson and Price[9] using a Royal McBee LGP-30 computer. The spectra agree in most aspects with the Raman spectra obtained by Bues[1] and suggest some short-range order in all the melts, with the nitrate ion incapable of free rotation about its threefold axis in the silver and lithium nitrate melts. The refractive indices of these liquids were also obtained as a function of frequency and the extrapolated values agree well with those reported by other workers[10,11].

EXPERIMENTAL

The optical arrangement used to obtain the reflection spectrum of a liquid surface is shown in Fig. 1. Since the liquid surface must necessarily be horizontal the optical arrangement has been built around it. Thus, the light source S and chopper are placed beneath the optical bench OB, the beam of light being focused on the sample at an incident angle of $\sim 23°$ to the normal by the spherical mirror F_1, placed above the optical bench. The reflected light from the sample is then reflected off the mirror M_1 and focused on the monochromator slit J by means of the spherical mirror F_2. By rotating the mirror M_1 through 180° to M_1' the incident light from F_1 is then focused onto a standard mirror M_2 and thence by means of F_2 onto the monochromator slit. Thus, by moving only M_1 the reflectivity of the sample can be compared directly with that of the standard mirror, the effects of all other mirrors in the optical train being identical in both arrangements. The sample sits in a furnace on top of a vertically adjustable mount and is adjusted to give maximum reflection intensity. The alignment of the optical train was checked frequently using a standard mirror in place of the sample. The reflectivities obtained using this arrangement are reproducible to $\sim 2\%$ and the greater part of this irreproducibility is believed to be in the electronics of the spectrometer.

The reflection spectra were obtained with a Perkin-Elmer model 12C spectrometer equipped with NaCl, KBr, and CsI optics using electronic recording. The reflectivity of the standard mirror was assumed to be 98% over the entire infrared region and the observed reflectivity was reduced 1% to allow for the difference in preferential polarization by the liquid surface compared to that by the standard mirror due to the finite angle of incidence. This small correction for polarization is of course unwarranted, considering the uncertainty in the reflectivity of the standard mirror, and is equivalent to assuming the standard mirror to have a reflectivity of 97%. In this way then, the reflectivity of the surface of liquid lithium, sodium, potassium, and silver nitrates was obtained as a function of frequency and the plots of reflection coefficient against frequency are shown in Figs. 2(A)–5(A), respectively.

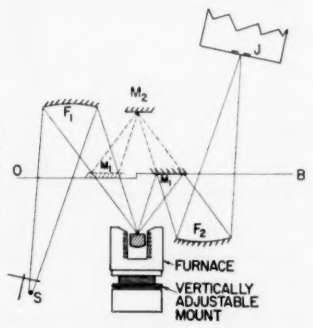

FIG. 1. Schematic diagram of the optical arrangement used to obtain the reflection spectra of molten materials.

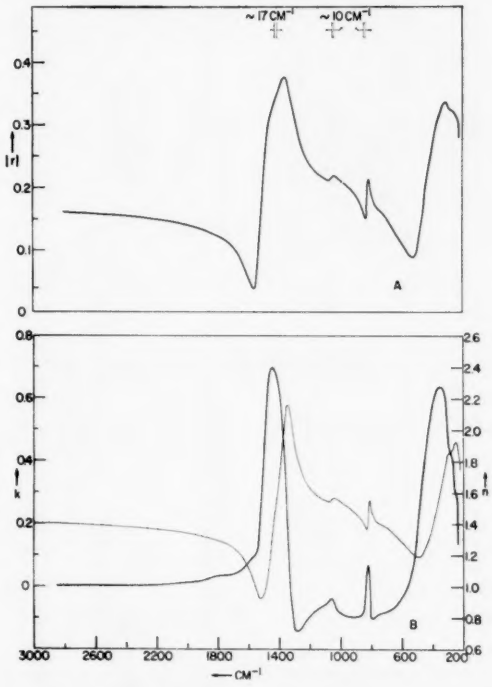

FIG. 2. (A) The infrared reflection spectrum of molten lithium nitrate at 313°C) (B) — the derived absorption spectrum, — the derived refractive-index dispersion curve.

ANALYSIS OF THE REFLECTION DATA

The coefficient of reflectivity $\mathbf{r}$ is a complex quantity and is related to the complex coefficient of refraction $\mathbf{n}$ as

$$\mathbf{r}=(\mathbf{n}-1)/(\mathbf{n}+1),$$

where $\mathbf{n}=n-ik$ and $\mathbf{r}=r\exp(i\theta)$. Equating real and imaginary parts in this expression the refractive index

[9] T. S. Robinson and W. C. Price, *Molecular Spectroscopy*, edited by G. Sell (The Institute of Petroleum, London, 1955), p. 211.
[10] H. Bloom and D. C. Rhodes, J. Phys. Chem. **60**, 791 (1956).
[11] O. H. Wagner, Z. physik. Chem. **131**, 409 (1928).

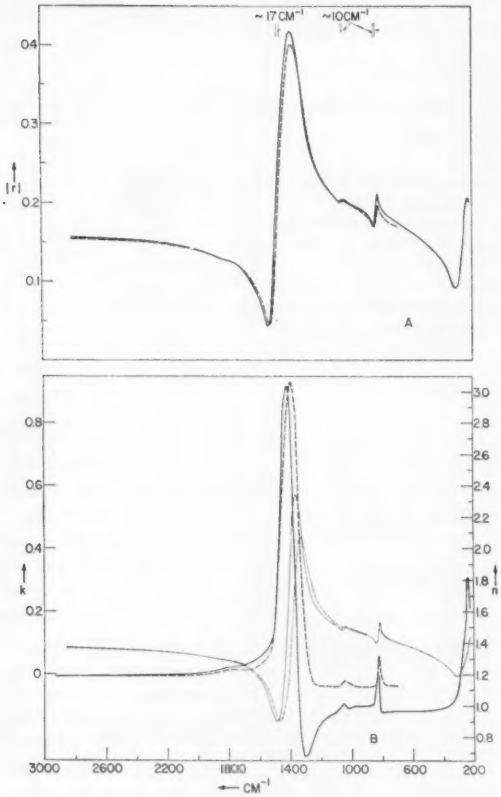

FIG. 3. (A) The infrared reflection spectrum of molten sodium nitrate: — at 347°C; M at 480°C; (B) — the derived absorption spectrum at 347°C; — the derived refractive index dispersion curve at 347°C; --- the derived absorption spectrum at 480°C; --- the derived refractive index dispersion curve at 480°C.

and absorption coefficient can be expressed as

$$n=\frac{1-r^2}{1-2r\cos\theta+r^2}. \tag{1a}$$

$$k=\frac{-2r\sin\theta}{1-2r\cos\theta+r^2}. \tag{1b}$$

Since we have measured r^2 as a function of the frequency ν we require only a knowledge of the phase factor θ as a function of frequency to determine n and k and it can be shown[9] that at any frequency $\bar{\nu}$, $\theta(\bar{\nu})$ can be obtained from the complete set of r values by evaluating the integral[12]

$$\theta(\bar{\nu})=(2\bar{\nu}/\pi)\int_0^\infty \frac{\ln r_{\bar{\nu}}-\ln r_\nu}{\bar{\nu}^2-\nu^2}d\nu. \tag{2}$$

Thus, with the experimental data, and a program set up for the LGP-30 computer[13] to integrate Eq. (2) and solve Eqs. (1a) and (1b), values of n and k as a function of frequency have been obtained for liquid lithium sodium, potassium, and silver nitrates and these are shown in Figs. (2B)–(5B), respectively.

It is of interest to note that at the lower frequencies the absorption coefficients tend to have a "negative bias." This is associated with a positive phase for r, whereas theoretically, the phase of r should always be negative, i.e., $-\pi\leqslant\theta\leqslant 0$. The reason for this is simply the unavailability of a complete set of values for r, both to $\nu=0$ and $\nu=\infty$ giving rise to "cutoff" errors in the evaluation of the integral in Eq. (2). This lack of a complete set of r values also manifests itself in the retention of some dispersion in the k—ν curve on the low-frequency side of the absorption bands and in addition results in slight shifts of the absorption frequency and in alterations of the absolute magnitude of the absorption coefficients.[14]

ASSIGNMENT OF THE FREQUENCIES

The vibrational frequencies observed in the present investigation for liquid lithium, sodium, potassium, and

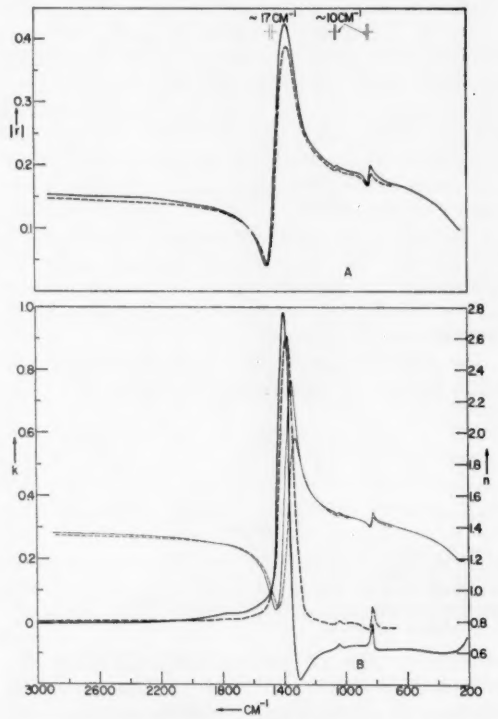

FIG. 4. (A) The infrared reflection spectrum of molten potassium nitrate: — at 347°C; M at 468°C; (B) — the derived absorption spectrum at 347°C, — the derived refractive index dispersion curve at 347°C, --- the derived absorption spectrum at 468°C, — the derived refractive index dispersion curve at 468°C.

[12] This integral was reported incorrectly by Robinson and Price (reference 9).

[13] We are indebted to Dr. H. J. Bowlden of this Laboratory for writing the computer program.

[14] H. J. Bowlden and J. K. Wilmshurst (to be published).

silver nitrates are given in Table I together with the Raman data of Bues[1] and the infrared results of Greenberg and Hallgren[8] for the liquids and the data where available for the solids.

If the nitrate ion is assumed to be planar with point group symmetry D_{3h}, then the six fundamental vibrations divide up into symmetry species as $a_1'(R, p)+a_2''(I)+2e'(R, dp; I)$ where R, I, p, and dp denote Raman active, infrared active, polarized, and depolarized, respectively. On this basis the vibrational assignment can be made as follows: The very strong Raman band at $\sim$1050 cm^{-1} is assigned to the a_1' stretching mode ν_1 of the nitrate ion, while the strong infrared band around 1390 cm^{-1}, corresponding to a medium Raman band, is assigned to the e' nitrate-ion stretching mode ν_3. The medium-strength infrared band at $\sim$830 cm^{-1}, having no Raman counterpart, is taken as the a_2'' nitrate-ion bending mode ν_2. The remaining e' bending mode of the nitrate ion ν_4 is assigned to the Raman band at $\sim$720 cm^{-1}. This band was too weak to be observed by us in the reflection spectra but was observed by Greenberg and Hallgren[8] in absorption. This now completes the gross assignment of the nitrate-ion frequencies and this assignment is in complete agreement with that accepted for the frequencies of the nitrate ion in the solid and in aqueous solution.[15] The overtone

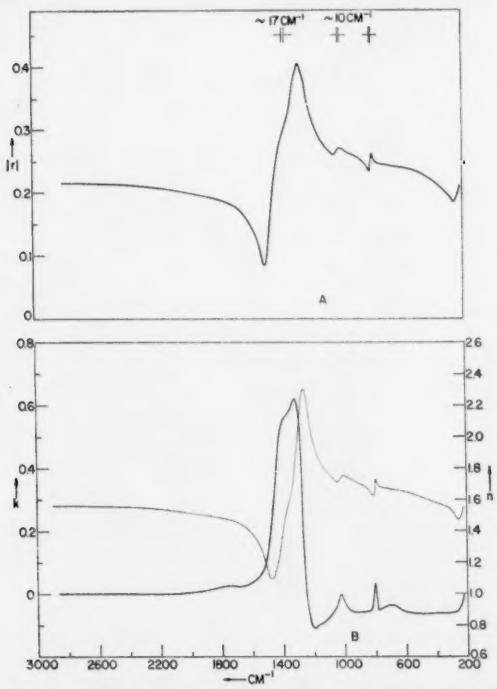

FIG. 5. (A) The infrared reflection spectrum of molten silver nitrate at 305°C; (B) — the derived absorption spectrum, — the derived refractive index dispersion curve.

[15] J. P. Mathieu and McK. Lounsbury, Discussions Faraday Soc. **9**, 196 (1950).

TABLE I. Vibrational assignment for lithium, sodium, potassium, and silver nitrates.

$LiNO_3$			$NaNO_3$				KNO_3				$AgNO_3$				
Infrared, liquid cm^{-1}		Raman[c] liq. cm^{-1}	Solid[d] cm^{-1}	Infrared, liquid cm^{-1}		Raman[c] liq. cm^{-1}	Solid[d] cm^{-1}	Infrared, liquid cm^{-1}		Raman[c] liq. cm^{-1}	Solid[d] cm^{-1}	Infrared, liquid cm^{-1}	Raman[c] liq. cm^{-1}	Solid[d] cm^{-1}	Assignment D_{3h} symmetry
P. I.[a]	$G+H^b$			P.I.[a]	$G+H^b$			P.I.[a]	$G+H^b$			P.I.[a]			
	2817				2777				2740						$2\nu_3$
	2439				2381				2353						$\nu_1+\nu_3$
	2083				2062				2062						$2\nu_1$
~1780	1770			~1785	1770			~1750	1754			~1755			$\nu_1+\nu_4$
	...	1639				1661	1661			1660			1604		$2\nu_2$
~1565															$\nu_2+\nu_4$[e]
~1460	broad band	1476	1390	1412	broad band	1387	1387	1391	broad band	1382	1361	~1395	1425	1372	ν_3, e' stretching
~1375		1366									1343	~1310	1277		
1059	1053	1061	1086	1053	1047	1053	1069	1046	1042	1048	1050	1029	1035	1045	ν_1, a_1' stretching
821	816			827	816			829	826			800	803		ν_2, a_2'' bending
...	741	724	728	...	714	722	728	714	714	715	714	~695	724		ν_4, e' bending
343				238				<220				<220			lattice vibration

[a] Present investigation.
[b] Greenberg and Hallgren, reference 8.
[c] Bues, reference 1.
[d] Quoted in reference 1.
[e] Active in the infrared only in C_{3v} symmetry or less.

TABLE II. Maximum barriers restricting rotation calculated assuming Coulombic interactions only.

Molecule	Barrier (kcal mole^{-1})
$LiNO_3$	36.87
$NaNO_3$	5.93
KNO_3	0.88
$AgNO_3$	1.55

bands observed by both Bues[1] and Greenberg and Hallgren[8] are easily explained in terms of these fundamentals.

While the gross features of the spectra have now been explained and the nitrate ion in the melt is presumably identical in internal structure with that in the solid and in aqueous solution as would be expected from chemical considerations, a few fine points in the spectra remain to be explained. The first of these points concerns the observed splitting of $\nu_3(e')$ in both liquid lithium and silver nitrate. The two bands into which $\nu_3(e')$ is split were, unfortunately, not completely resolved in either case, although the discontinuity in the reflection spectrum and the broadening and drop in peak intensity of $\nu_3(e')$ in the absorption spectrum leave little doubt of the reality of the splitting which has, in fact, been resolved in the Raman effect. Such a splitting could arise only if the threefold axis of symmetry of the nitrate ion were destroyed and this may be brought about in either one of two ways, namely, by associated species M–O–NO_2 in the melt, or by the action of the cation field about the nitrate ion. If the former effect were responsible for this splitting, then the number of associated species in both lithium and silver nitrates would have to exceed, by a considerable amount, the number of unassociated species, or three bands should be observed around 1390 cm^{-1}, two from the associated species and one from the unassociated species. Considering the high conductivity of these melts, their usual ionic behavior in respect to other physical properties, and the continuity of these physical properties from lithium to sodium to potassium, where in the latter melts assocated molecules do not apparently exist, at least to any great extent [since $\nu_3(e')$ is not split], we conclude that the splitting of $\nu_3(e')$ cannot be due to the associated species. A further point against the postulation of such an associated species is the failure to observe any additional band around 1000 cm^{-1} in the Raman spectrum due to the MO–NO_2 stretching mode which must certainly be present considering the concentration of this associated species that would be necessary to mask the third band that should occur around 1400 cm^{-1} due to the unassociated species. Thus, the splitting of $\nu_3(e')$ must arise from the effect of the cation field about the nitrate ion removing the threefold axis of symmetry and producing at most a common symmetry between nitrate and cation field of C_{2v}. However, this alone is not sufficient to produce the observed splitting, for if the nitrate ion were freely rotating about its threefold axis, the vibrational frequency would simply be averaged over every available configuration and only one broad band would be observed regardless of the cation field. Thus, the nitrate ion cannot be freely rotating about its threefold axis in either lithium or silver nitrate liquids and must be restricted. The splitting of a vibrational frequency by a potential barrier hindering rotation is a very complicated function of the barrier height and no estimate of the barrier height can be made here except that it must be greater than 1200 cal mole^{-1} (i.e., $>RT$) in both lithium and silver nitrates. Since $\nu_3(e')$ is not split in either the sodium or potassium nitrate melts, the potential barrier hindering rotation is presumably much lower and the nitrate ions may be freely rotating in these melts. This splitting of $\nu_3(e')$ has also been observed in solid KNO_3 and may arise from the same cause as described above, although other explanations are possible in the case of crystals.

The second point of interest arises from the appearance of $\nu_1(a_1')$ in the infrared spectrum where it should be inactive. It has already been shown above that the greatest common symmetry between the cation field and the nitrate ion in lithium and silver nitrates is at most C_{2v} and in this case ν_1 should become active, as is observed. In both sodium and potassium nitrates, however, there is no real reason to believe that the greatest common symmetry between the nitrate ion and cation field is only C_{2v} and the appearance of ν_1 in these spectra implies only that the cation symmetry cannot contain D_{3h} as a subgroup.

The remaining point of great interest concerns the intense low-frequency infrared band observed in the nitrate melts at 343 cm^{-1} for $LiNO_3$, 238 cm^{-1} for $NaNO_3$, and <220 cm^{-1} in KNO_3 and $AgNO_3$. This band is certainly not due to any internal vibration of the nitrate group and, since the nitrate group is nonpolar (D_{3h} symmetry), it cannot be assigned to the torsional motion of the nitrate group in the cation field. Further the mass sensitivity of the frequency suggests that the vibration responsible includes the motion of the cation. Therefore, we assign it here to the vibration of a quasi-lattice-like structure in the liquid.

RESTRICTED ROTATION

In both liquid lithium and silver nitrates the nitrate ion is not rotating freely about its three-fold axis. If it is assumed that the average coordination about the nitrate ion is octahedral, there will be a twelve fold barrier restricting this rotation and it is interesting to attempt to estimate the maximum value of this barrier. This can be done simply by considering the difference between only the Coulombic forces

$$\sum_{i=1}^{3}\sum_{j=1}^{4}\tfrac{2}{3}(e^2/r_{ij}),$$

where e electronic charge, r_{ij} is the cation-oxygen dis-

tance and the charge on the oxygen atom is taken as $\frac{2}{3}$ e, at the positions corresponding to the maximum and minimum of the potential barrier. Thus, in this way the maximum barriers hindering rotation can be determined and these are given in Table II. These barriers will be reduced considerably, of course, if the repulsive potential term is included and it is interesting to note that only in the case of lithium nitrate is the maximum barrier probably sufficiently above RT (1.2–1.4 kcal) to be capable of preventing free rotation. While this explains the lithium, sodium, and potassium nitrate data, the results for silver nitrate are in complete opposition.

In silver nitrate, the barrier height could be increased by the addition of covalent forces in the melt and at first sight the decrease in frequency of both the stretching modes ν_1 and ν_3 are in agreement with this. However, ν_2, the bending mode, has also decreased, whereas if radial covalent forces are assumed to explain the restricted rotation ν_2 should increase. Alternatively, of course, bonding between the d orbitals of the silver atoms on either side of the plane of the nitrate ion with the π orbitals of the nitrate ion would cause a lowering of ν_1, ν_3, and ν_2 and this in conjunction with the radial forces may explain the observed results satisfactorily. The only other simple explanation consistent with a decrease in ν_1, ν_3, and ν_2, as well as permitting restricted rotation, is that the local cation symmetry, is different in silver nitrate than in the alkali nitrates.

REFRACTIVE INDICES AND DIELECTRIC CONSTANT

If the immediate dispersion region at the resonance frequencies is omitted, the refractive index n can be shown to depend on the frequency ν as

$$n(\nu)=n_\infty+\sum_i[A_i/(\nu_i^2-\nu^2)],$$

where the summation extends over all the i resonances and A_i is the oscillator strength of the ith resonance. The refractive index data obtained here for each of the nitrate melts could, of course, be fitted to this equation but the results were not considered likely to be of sufficient interest to warrant the work involved. Therefore only the high-frequency tail of the band at $\sim$1400 cm^{-1} was fitted by least squares to the simplified two-parameter expression

$$n(\nu)=n_\infty+[A_{1400}/(\nu_{1400}^2-\nu^2)],$$

and then extrapolated to determine the refractive indices at the frequency of the sodium D line. These extrapolated refractive indices agree quite well with those obtained from the usual refractive index measurements (Table III), the deviations being in the expected direction, since strictly n_∞ is not a constant but corresponds to the tail of the uv dispersion region.

TABLE III. The refractive index data at the frequency of the sodium D line.

Molecule	Present investigation	Literature
$LiNO_3$	1.422 (at 313°C)	1.441 (at 313°C)[a]
$NaNO_3$	$1.418-0.4\times10^{-4}t$[b]	$1.495-2.0\times10^{-4}t$[c]
KNO_3	$1.447-1.8\times10^{-4}t$[b]	$1.473-1.7\times10^{-4}t$[c]
$AgNO_3$	1.587 (at 305°C)	1.659 (at 305°C)[c]

[a] Reference 11.
[b] The refractive index values determined in the present work are only reproducible to 1% and since a working range of only ≈100°C is available with the nitrates, the temperature coefficients reported here are not reliable.
[c] Reference 10.

TABLE IV. Integrated intensity and the molecular dipole derivative for the ν_2 band.

Molecule	Integrated intensity (Γ)	$(\partial\mu/\partial Q)$	μ
$LiNO_3$	3.894 cm^{-1}	0.459 cm^{-1} sec^{-1}	0.012 debye
$NaNO_3$	2.198	0.375	0.010
KNO_3	1.694	0.362	0.010
$AgNO_3$	1.567	0.314	0.008

At the low-frequency end of the spectrum there is insufficient data to extrapolate the refractive index to zero frequency. However, if it is assumed that no further dipolar absorption occurs at any frequency below the limit of observation, then in the case of lithium nitrate, the refractive index at zero frequency n_0 must be less than the value observed at the lowest frequency of measurement and greater than the value obtained by extrapolation of the low-frequency wing of the second to last dispersion region at $\sim$830 cm^{-1}, and we therefore obtain

$$1.40<n_0<1.77.$$

Now the dielectric constant ϵ is related to the refractive index at zero frequency as

$$\epsilon=n_0^2$$

and, therefore, the dielectric constant of liquid lithium nitrate must lie in the range

$$1.96<\epsilon<3.13.$$

Unfortunately, the dielectric constant of solid lithium nitrate is not known. However, in the solid alkali halides,[16] the dielectric constant of the lithium derivative is usually $\sim$1.8 times that of the corresponding sodium derivative and, hence, taking the dielectric constant of solid sodium nitrate[16] as 6.85, the dielectric constant of solid lithium nitrate is found to be $\sim$12. Thus, the dielectric constant of the liquid in this case is $\sim\frac{1}{4}$ to $\frac{1}{6}$ that of the solid.

BAND INTENSITIES

The retention of some dispersion in the k/ν curves together with the necessity of considering a point group

[16] *American Institute of Physics Handbook* (McGraw-Hill Book Company, Inc., New York, 1957), Sec. 5, p. 115.

TABLE V. Integrated intensity and molecular dipole derivative for the ν_2 band.

Molecule	Integrated intensity (cm^{-1})	$(\partial\mu/\partial Q)$ (cm^{-1} sec^{-1}) Liquid	Solid
$NaNO_3$	135	2.94	217
KNO_3	121	3.06	...

symmetry less than D_{3h} for the nitrate ion, makes both the experimental determination and theoretical discussion of the band intensities very difficult. However, for the one band at $\sim$820 cm^{-1}, the $k-\nu$ curve does not, in general appear to behave too badly, while regardless of the symmetry of the cation arrangement,[17] there are no other vibrations within this symmetry species. Thus we will consider this band in detail.

The integrated intensity Γ of the band at $\sim$820 cm^{-1} in each of the nitrate melts is given in Table IV together with the molecular dipole derivative calculated from the expression

$$\Gamma=\int k d\nu=(n\pi/3c^2)(\partial\mu/\partial Q)^2,$$

where n is the number of molecules per cubic centimeter and c is the velocity of light. Now the molecular dipole derivative can be simply related to the N—O bond dipole moment μ as

$$\partial\mu/\partial Q=3\mu\{(3m^{-1}+M^{-1})(r^2)^{-1}\}^{\frac{1}{2}}$$

where M, m=mass of the oxygen and nitrogen atoms, respectively, in atomic weight units and r=N—O bond length and, hence, we can calculate the N—O bond moment in each of the different melts and these results are given in Table IV.

The magnitude of the N—O and N=O bond moments are usually taken as 0.3 and 2.0 debye, respectively,[18] and accordingly, the values derived here, appear surprisingly small at first glance. However, the bond moment observed here μ will probably be reduced from the value μ_0 expected in a free field, due to polarization of the bond by the cations and we can write it as

$$\mu=\mu_0-\mu^{\text{induced}}, \tag{3}$$

where the induced moment can be written in terms of the cation field E at the bond and the bond polarizability α as

$$\mu^{\text{induced}}=\alpha\cdot E.$$

If the N—O bond is assumed to lie in a cavity of radius R, with the nitrogen atom at the center of the cavity and the center of electric charge in the bond at a distance "a" from the nitrogen atom, the cation field E due to a resultant positive charge spread over the whole cavity wall, can be calculated to be

$$E=(e/\epsilon)(aR)^{-1}\ln[(R+a)/(R-a)],$$

where ϵ is the dielectric constant of the medium. Thus Eq. (3) becomes

$$\mu_{\text{obs}}=\mu_0-(\alpha e/\epsilon)(aR)^{-1}\ln[(R+a)/(R-a)].$$

With the assumption that a=0.95 A, $\alpha=25\times10^{-25}$, and ϵ=2.5 in lithium nitrate, μ_0 is calculated to be 0.815D. This moment must, of course, be the same in the other nitrate melts and hence, we can calculate that the dielectric constant of the sodium, potassium, and silver nitrate melt relative to that of lithium nitrate is 0.76, 0.58, and 0.61, respectively.

It should be noted that a small change in ϵ going from the liquid to the solid, or to aqueous solution, can alter μ and hence, the band intensity, by a large amount. In a similar manner, it may be expected that the change in dielectric constant between liquid and solid would also alter the intensity of the stretching band at $\sim$1400 cm^{-1} and for this reason the intensity of this band was determined for both sodium and potassium nitrate liquids (Table V). The molecular dipole derivative calculated from the band intensity for liquid sodium nitrate, is only $\sim$0.01 times that calculated for the solid[19] and this is easily explained qualitatively, purely on the basis of a higher dielectric constant in the solid, than in the liquid.

[17] Except in the most unlikely case that the highest symmetry subgroup common to both the nitrate ion and the cation field is C_{2v}.

[18] C. P. Smyth, *Dielectric Behaviour and Structure* (McGraw-Hill Book Company, Inc., New York, 1955), p. 244.

[19] C. Haas and D. F. Hornig, J. Chem. Phys. **26**, 707 (1957).

Nuclear Quadrupole Resonance in $TiCl_4$, $ThCl_4$, $NbCl_5$, and $TaCl_5$†

ALLAN H. REDDOCH*

Lawrence Radiation Laboratory and Department of Chemistry, University of California, Berkeley, California

(Received February 14, 1961)

The chlorine resonance in titanium tetrachloride has been re-examined, confirming the existence of four resonances. A chlorine-35 resonance at about 6 Mc has been discovered in thorium tetrachloride. The frequency suggests highly ionic bonding, which contradicts earlier conclusions from x-ray studies. Some double-bond character may be present in the Th–Cl bond.

Niobium and chlorine resonances have been discovered in niobium pentachloride. The niobium resonances are described by a single set of parameters, the coupling constant eqQ being approximately 78 Mc, and the asymmetry parameter, $\eta=0.32$. Because of the large asymmetry parameter, it was possible to observe two $\Delta M=2$ and one $\Delta M=3$ transitions. Only a single Cl^{35} resonance was found at about 13 Mc, although two more chlorine resonances would be expected on the basis of crystal structure. The frequency of the chlorine resonance suggests appreciable covalency in the niobium-chlorine bond in niobium pentachloride.

A single resonance has been found in tantalum pentachloride at about 13 Mc. It is believed to be a chlorine-35 resonance. A fairly simple method is outlined for determining the asymmetry parameter of the electric-field gradient from the observed transition frequencies without directly solving the secular equations.

I. INTRODUCTION

THE theory of nuclear quadrupole resonance has shown that the resonance frequencies can give information concerning the chemical bonds in the sample as well as information relating to the structure of the lattice.[1]

Thorium chloride was investigated in order to study the nature of the bonds in the compounds. The spectrum of $TiCl_4$ was reinvestigated to test the equipment and to serve as a model of fairly ionic compounds. Other Group IV and V chlorine compounds were studied to get a better picture of such ionic compounds.

II. EXPERIMENTAL PROCEDURE

Most of the measurements below 13 Mc/sec were made using a circuit similar to that of Pound and Watkins.[2] At higher frequencies a self-quenched super-regenerative circuit based on Dean's design was used.[1] A phase-sensitive detector similar to Watkin's circuit was employed.

Zeeman modulation was used, the magnetic field consisting of square pulses of alternating polarity with a frequency of about 100 cps and an amplitude of about 15 gauss.

Resonant frequencies were measured with a General Radio Company military-type heterodyne frequency meter (model LR). Frequency comparisons were made as the resonance was recorded. The average of values obtained with the frequency increasing and decreasing was used to avoid errors arising from the time constant of the filter circuit. Checks for internal consistency, estimates of possible systematic errors, and comparison with reported frequencies suggest that the present measurements should be accurate to within 0.3 kc/sec.

When the super-regenerative spectrometer was used, frequency measurements were made at different quench frequencies in order to distinguish the central line from the sidebands. However it was found that with the self-quenched circuit, this procedure was not infallible, because the quench-frequency adjustment sometimes changed the central radio frequency sufficiently to yield an ambiguous result.

Room temperatures were measured with a mercury thermometer and should be accurate to 0.1°C. The low temperatures were measured with a thermocouple and should be accurate to 0.5°C. However, the relative accuracy of individual temperatures at either dry-ice or liquid-nitrogen temperatures should be about 0.1°C.

The samples usually consisted of 5 to 10 g of polycrystalline material in a sealed tube. The coils of the oscillator tank circuit were wound directly on the sample tube. Further details are given elsewhere.[3]

III. RESULTS AND DISCUSSION

A. Titanium Tetrachloride

The chlorine resonance in titanium tetrachloride has been reported previously by Dehmelt[4] and by Hamlen and Koski.[5] The latter workers could see only three of the four lines reported by Dehmelt, possibly because the sidebands of their super-regenerative spectrometer obscured the details of the spectrum. The present results, obtained with a marginal oscillator, show four lines very clearly. The frequencies of these lines are given in Table I. The lines are about 2.5 kc/sec wide

* Present address: National Research Council, Ottawa 2, Ontario, Canada.

† This work was done under the auspices of the U. S. Atomic Energy Commission and is based on a thesis submitted in partial fulfillment of the requirements for a Ph.D. degree at the University of California, Berkeley.

[1] T. P. Das and E. L. Hahn, *Nuclear Quadrupole Resonance Spectroscopy*, Solid State Physics series, Supplement I (Academic Press, Inc., New York, 1958).

[2] G. D. Watkins, thesis, Harvard University, 1952.

[3] A. H. Reddoch, thesis, Lawrence Radiation Laboratory Report UCRL 8972, November 1959.

[4] H. G. Dehmelt, J. Chem. Phys. **21**, 380 (1953).

[5] R. P. Hamlen and W. S. Koski, J. Chem. Phys. **25**, 360 (1956).

TABLE I. Observed chlorine-35 frequencies in $TiCl_4$.

Temperature (°C)	Frequencies[a] (Mc/sec)			
−74.0	5.9354	5.9799	6.0138	6.0495
−196.0	5.9802	6.0380	6.0807	6.1118

[a] Estimated error: ±0.0003 Mc/sec.

and appear to be of equal intensity. The temperature dependence is normal.

A number of other tetrahalides, including $SiCl_4$, $GeCl_4$, $SnCl_4$, and $SnBr_4$, have spectra consisting of four lines.[6,7] The spectra of these compounds show three lines close together with a fourth line at a somewhat lower frequency. It has been suggested that the similarity of the spectra indicates a common crystal structure.[6,8] The detailed structure of these compounds is not known although Shimomura has concluded that the quadrupole spectrum of $SnBr_4$ is the result of a tetrahedral molecule in a monoclinic lattice.[8]

Although the spectrum of $TiCl_4$ does not show any significant splitting into a singlet and triplet, it seems quite possible that $TiCl_4$ has the same crystal structure as the other tetrahalides having four-line spectra. The lower frequency of the resonance and the presumably greater ionicity of $TiCl_4$ may tend to change the structure of the spectrum. The physical properties of these tetrahalides, the ionic radii, and the common crystal structure (SnI_4) of the heavier tetrahalides of Ti and other Group IV elements are all consistent with a common crystal structure for the corresponding lighter tetrahalides.

B. Thorium Tetrachloride

A sample of $ThCl_4$ was prepared by the direct reaction of chlorine with high-purity thorium metal at 400°C, followed by sublimation of the product. The sample was protected from oxygen and water vapor at all times.

The chlorine spectrum consists of a single line for each isotope, as would be expected from the crystal structure. The frequencies at several temperatures are given in Table II. The signal-to-noise ratio increased with decreasing temperature, and only at low temperatures was it possible to measure accurately the frequency of the weaker Cl^{37} line. The ratio of the frequencies of the two isotopes (1.2688) agrees well with similar ratios reported elsewhere (1.2685 to 1.2690)[9] and supports the assignment of the resonances and the accuracy of the measurements.

The theory of Townes and Dailey yields an estimate of 87% for the ionicity of the Th—Cl bond, if 15% *s*-hybridization of the chlorine orbitals is assumed. The generally accepted value of 1.4 for the electronegativity of thorium[10] gives a point that lies very close to the curve of Townes and Dailey[1] relating ionicity and electronegativity. The value of 1.6 for the thorium electronegativity recently proposed by Fineman and Daignault[11] moves the point to the left, so that is is now above the curve. The bond could then be assigned the ionicity predicted by the curve (74%) and the deviation from the curve could be ascribed to 22% π character.

In any case, the Th—Cl bond seems to be quite ionic. This conclusion does not support the statement by Zachariasen,[12] based on crystal structure, that the bond is predominantly covalent. The flattened tetrahedron found in the crystal is not a simple coordination structure and undoubtedly reflects some covalency. However, it appears that a small amount of covalent character may have an appreciable effect on the bond angles in the crystal.

The physical properties of $TiCl_4$ and $ThCl_4$ are quite different in spite of the similarity of their resonant frequencies and ionicities. The differences may arise from different molecular structures in the crystals. If $TiCl_4$ remains a regular tetrahedron in the solid, it may be described as "shielded".[13] In other words the symmetric arrangement of large chlorine ions around the titanium ion tends to neutralize the charge of the latter as far as other external ions are concerned. External charges are also kept some distance from the titanium ion. Thus while there may be strong intramolecular ionic forces, the intermolecular forces are weak. The compound is similar to covalent compounds in having a low melting point. While low temperatures can disrupt the intermolecular bonds, it cannot break the strong intramolecular bonds, and thus the compound has no electrical conductivity at the melting point.

In $ThCl_4$ the flattened tetrahedra permit fairly strong intermolecular ionic forces. The compound has a fairly

TABLE II. Observed chlorine frequencies in $ThCl_4$.

Isotope	Frequency[a] (Mc)	Temperature (°C)
Cl^{35}	5.9193	25.3
Cl^{35}	5.9199	0.0
Cl^{35}	5.9202	−74.0
Cl^{35}	5.9181	−195.9
Cl^{37}	4.6645	−195.9

[a] Estimated error: ±0.0003 Mc/sec.

[6] A. L. Schawlow, J. Chem. Phys. **22,** 1211 (1954).
[7] R. Livingston, J. Phys. Chem. **57,** 496 (1953).
[8] K. Shimomura, J. Sci. Hiroshima Univ. **17A,** 383 (1954).
[9] T. C. Wang, Phys. Rev. **99,** 566 (1955).
[10] W. Gordy and W. J. Orville Thomas, J. Chem. Phys. **24,** 439 (1956).
[11] M. A. Fineman and R. Daignault, J. Inorg. Nuclear Chem. **10,** 205 (1959).
[12] W. H. Zacharaisen, in *The Actinide Elements*, edited by G. T. Seaborg and J. J. Katz, National Nuclear Energy Series, Vol. 14A (McGraw-Hill Book Company, Inc., New York, 1954).
[13] A. E. Van Arkel, *Molecules and Crystals*, translated by J. C. Swallow (Butterworths Scientific Publishing Company, Ltd., London, 1949).

high melting point. The melting temperature is high enough to break some of the intramolecular bonds and the compound has a moderate electrical conductivity at the melting point.

The most striking feature of the resonance in $ThCl_4$ is the temperature dependence. Most compounds have a temperature coefficient of about -10^{-4}/°C. For $ThCl_4$, the frequency has a maximum in the region of -50°C, and the maximum coefficient in the range studied is about 4×10^{-6}/°C. This behavior is similar to that reported for $TiBr_4$.[14] For WCl_6 the temperature coefficient is positive, having a value of 2×10^{-4}/°C.[5]

In a plot of ionicity against electronegativity the point for WCl_6 lies appreciably above the curve of Townes and Dailey as does the point for $TiBr_4$. If the value of 1.6 is used for the thorium electronegativity, $ThCl_4$ also lies above the curve.

Such deviations may be ascribed to partial π bonding in these compounds. Such π bonding would permit an explanation of the temperature coefficients of these compounds. As the bonds lengthen with increasing temperature, the π character should decrease. Such a decrease would cause the resonant frequency to rise. At the same time, the factors that tend to decrease the frequency, such as torsional oscillations, would be operating. The net temperature coefficient would be the difference between these effects and would depend on the relative magnitude of the effects. A rough calculation based on the relation between bond order and bond lengths gives the right order of magnitude. The effect

TABLE III. Frequencies, in Mc/sec of resonances in $NbCl_5$[a].

	24.5°C		−195.7°C	
Transition	Obs	Calc	Obs	Calc
Nb^{93} 1/2–3/2[b]	5.4228_7	5.4228_6	5.7154_3	5.7154_2
Nb^{93} 3/2–5/2[b]	6.0621_1	6.0618_5	6.0516_4	6.0513_3
Nb^{93} 5/2–7/2[b]	9.5612_5	9.5612_7	9.5466_3	9.5466_3
Nb^{93} 7/2–9/2[b]	12.9032_0	12.9033_0	12.9132_3	12.9133_9
Nb^{93} 1/2–5/2[c]	11.486±0.002	11.4847		
Nb^{93} 1/2–7/2[c]	21.046±0.001	21.0460		
Cl^{35} 1/2–3/2	13.0581_4[d]		13.280[e]	
Cl^{37} 1/2–3/2	10.2909[f]		10.476[e]	

[a] Parameters used in calculation of Nb frequencies are:

Parameter	24.5°C	−195.7°C
eqQ	78.080_9±0.002 Mc	78.260_4±0.002 Mc
η	0.32249±0.00002	0.34974±0.00002

[b] Estimated accuracy of frequencies is ±0.0003 Mc/sec.
[c] Measured at 23.5°C with super-regenerative circuit.
[d] Measured at 23.5°C.
[e] Measured at −196°C.
[f] Measured at 25.0°C.

[14] R. G. Barnes and R. D. Engardt, J. Chem. Phys. **29,** 248 (1958).

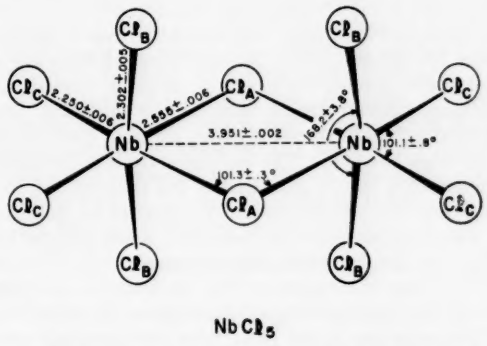

FIG. 1. Structure of $NbCl_5$. Atomic radii are not to scale.

is similar to that proposed by Oka[15,16] and co-workers to explain the increased halogen coupling constants in the higher vibrational states of ICN and BrCN.

The recent observation of quadrupole resonance in paramagnetic compounds by Barnes and Segel[17] suggests that it may be possible to find a chlorine resonance in UCl_4 analogous to that found in $ThCl_4$, since the compounds are isomorphous and have similar properties.

C. Niobium Pentachloride

In $NbCl_5$, resonances may be expected from Nb^{93} as well as from the two chlorine isotopes. Since Nb^{93} has a spin of $\frac{9}{2}$, at least four lines may be expected from this nucleus. The observed resonances are listed in Table III together with their assignments and the calculated values of the niobium frequencies. The calculated values were obtained from the secular equation for $I=\frac{9}{2}$. The two parameters were obtained by a least-squares fitting to the four principal frequencies. The agreement between the observed and calculated frequencies is quite good and supports the assignment of the transitions.

If a small correction is applied for the difference in temperature between the two room-temperature measurements of the chlorine frequencies, the frequency ratio is found to be 1.2688. This value supports the assignment of these lines to the chlorine isotopes.

No quantitative measurements were made of the niobium intensities but qualitatively the intensities follow the pattern expected from the assignment of the resonances. The chlorine lines are about 2 kc/sec wide while the four main niobium lines are about 7 kc/sec wide. The other three niobium lines appear to be 10 to 20 kc/sec wide.

Zalkin and Sands have shown that $NbCl_5$ in the solid forms dimeric Nb_2Cl_{10} units (Fig. 1).[18] The niobium

[15] T. Oka, H. Hirakawa, and A. Miyahara, J. Phys. Soc. Japan **12,** 39 (1957).
[16] T. Oka and H. Hirakawa, J. Phys. Soc. Japan **12,** 820 (1957).
[17] R. G. Barnes and S. L. Segel, Phys. Rev. Letters **3,** 462 (1959).
[18] A. Zalkin and D. E. Sands, Acta Cryst. **11,** 615 (1958).

atoms are at the centers of two adjacent distorted octahedra of chlorine atoms. The octahedra share a common edge. The dimer contains two equivalent niobium atoms and three nonequivalent sets of chlorine atoms: two bridging chlorine atoms between the niobiums, four more chlorines in the same plane, and four more above and below the plane. The authors state that the molecules occupy lattice sites having two different symmetries, but that all the molecules appear to be identical.

From this structure, one resonance would be expected from the niobium while three resonances would be expected from the chlorines, the one from the bridging chlorines probably being separated from the other two. If the molecules at the two lattice sites were not completely equivalent, some doubling of these resonances might occur.

The absence of any doubling is consistent with all the molecules being equivalent. The 2 kc/sec width of the chlorine line at 13 Mc/sec precludes any splitting in frequency of more than one in 10^4. Presumably the dimensions of the molecules would not differ by much more than this order of magnitude.

The failure to find more than one chlorine resonance is quite puzzling. Searches were made from 2.5 to 40 Mc/sec. The observation of the weak niobium line at 21 Mc/sec indicates that considerable sensitivity was available.

The observed chlorine resonance may arise from the two bridging chlorines, because the remaining chlorines ought to give a pair of resonances which are fairly close together in frequency and similar in intensity.

The tentative assignment of the observed chlorine resonances and the absence of the others make it difficult to give a chemical interpretation of the results.

The frequency of the chlorine resonance suggests appreciable ionicity as well as covalency. However a purely ionic model in which the ions have point charges of $+5$ and -1 gives values of eqQ and η for the niobium resonance which are two or three times too small. The calculation was quite crude, because only the six nearest chlorines and one nearest niobium were considered.

Murakawa found a coupling constant of 0.15 Mc/sec for the ground state of the Nb^{93} atom ($4d^4\,5s$) and 0.09 Mc/sec for the excited state ($4d^3\,5s^2$).[19] His values are much lower than the value found here for $NbCl_5$ and are probably the result of the nonpenetrating character of the d orbitals. In the compound, the bonding orbitals are probably s-p-d hybrids. Such orbitals can have large coupling constants because of the more penetrating nature of the p components, which give contributions to the field gradient q of the form $\langle p \mid q \mid p \rangle$, and because of cross terms of the form $\langle s \mid q \mid d \rangle$, which can also be large.

The nonzero asymmetry parameter indicates a lack of axial symmetry at the niobium. Hence the nuclear eigenstates are mixtures of the spin states and under the selection rule $\Delta M = 0, \pm 1$ transitions are possible between any pair of states.

As in the work of Cohen,[20] the relative intensities of the transitions were calculated. The $\pm\frac{9}{2}$ states do not mix appreciably, and so the transitions to the $\frac{5}{2}$, $\frac{3}{2}$, and $\frac{1}{2}$ states were too weak to observe here. All the other transitions were seen with the super-regenerative spectrometer and qualitatively have the expected intensities. With the Pound-Watkins circuit, only the four main transitions and the $\frac{1}{2}\rightarrow\frac{5}{2}$ transition could be seen.

Molybdenum chloride, $MoCl_5$ has the same crystal structure as $NbCl_5$,[21] however, it is paramagnetic. It might be possible to examine the chlorine resonances in this compound.

D. Tantalum Pentachloride

Tantalum pentachloride is throught to have the same crystal structure as niobium pentachloride.[18] The chemical and physical properties of the two compounds are similar. A single weak resonance was found at 13.391 Mc/sec at 24.3°C. No other lines were found up to 25 Mc/sec.

Tantalum has a very large quadrupole moment. If the field gradients due to the chlorines were similar in $TaCl_5$ and $NbCl_5$, the tantalum resonances would have frequencies of 100 to 200 Mc/sec. The present equipment did not operate in this range.

The observed resonance must be a chlorine line and probably arises from Cl^{35}. A weaker line from Cl^{37} should occur at 10.5 Mc/sec. It was not seen, probably because it was too weak. If the observed line came from Cl^{37}, a fairly strong line would be expected at 16.8 Mc/sec, and its absence would be difficult to understand.

The observed line seems to correspond to the chlorine resonance at 13.058 Mc/sec in $NbCl_5$ and illustrates the chemical similarity of the Ta and Nb compounds. The failure to observe other chlorine lines in $TaCl_5$ corresponds to the situation in $NbCl_5$.

E. Miscellaneous

Niobium oxychloride ($NbOCl_3$)[22] has some structural features in common with $NbCl_5$. For this reason an attempt was made to find resonances in the compound. No resonances were found between 5.3 and 38.3 Mc/sec. However the sample was not very large (2 g), and the failure may not be too significant.

A 13-g sample of zirconium tetrachloride was examined in order to compare its resonances with those of $TiCl_4$ and $ThCl_4$. No resonances were found between 3.4 and 25.2 Mc/sec.

ACKNOWLEDGMENTS

Thanks are due Professor B. B. Cunningham, in whose laboratory and under whose supervision the work

[19] K. Murakawa, J. Phys. Soc. Japan **13**, 101 (1958).

[20] M. H. Cohen, Phys. Rev. **96**, 1278 (1954).

[21] D. E. Sands and A. Zalkin, Acta Cryst. **12**, 723 (1959).

[22] D. E. Sands, A. Zalkin, and R. E. Elson, Acta Cryst. **12**, 21 (1959).

was done, for suggesting this study. The author thanks Dr. G. O. Brink and Dr. J. D. Axe for valuable assistance and Dr. R. E. Elson of the Lawrence Radiation Laboratory and Dr. R. M. Horning of the Stauffer Chemical Company for providing samples of niobium, tantalum, and zirconium compounds.

The following financial assistance during the course of the work is gratefully acknowledged: an R. S. McLaughlin Traveling Fellowship from Queen's University, Kingston, Ontario; a special Scholarship for Study Abroad from the National Research Council, Canada; a General Electric Fellowship from the University of California.

APPENDIX. DETERMINATION OF η

Any algebraic equation of the form

$$\sum_{i=0}^{n} a_i E^i = 0,$$

where $a_n = 1$, such as the secular equation for $I = \frac{9}{2}$,

$$E^5 - 11(3+\eta^2)E^3 - 44(1-\eta^2)E^2 + \tfrac{44}{3}(3+\eta^2)^2 E + 48(3+\eta^2)(1-\eta^2) = 0,$$

may be written in terms of its roots E_j in the form

$$\prod_{j=1}^{n} (E - E_j) = 0.$$

By expanding the latter form and equating the coefficients of like powers of E in the two forms, the following equations, among others, are obtained;

$$a_{n-1} = -\sum E_j$$

$$a_1 = (-1)^{n-1}\left(\prod E_j\right)\sum (1/E_j)$$

$$a_0 = (-1)^n \left(\prod E_j\right).$$

The observed frequencies are proportional to differences between roots of the secular equation. Thus if the lowest root is called E_0, the other roots may be written as $E_0 + k\nu_1$, $E_0 + k(\nu_1 + \nu_2)$, etc., where k is a factor containing eQq. For $I = \frac{9}{2}$, we have $k = h/6A = 24h/eQq$.

Since a_{n-1} equals zero for half-integral spins, the sum of the roots is zero and thus E_0 may be eliminated. Each root E_j may then be expressed as a product of k and an experimental numerical factor. These expressions may be substituted in the equations for a_1 and a_0 above.

Thus for $I = \frac{9}{2}$ these two equations yield

$$a_1 = \tfrac{44}{3}(3+\eta^2)^2 = Nk^4$$

and

$$a_0 = 48(3+\eta^2)(1-\eta^2) = Mk^5,$$

where M and N are numerical factors derived from the observed frequencies.

Elimination of k from these equations yields a numerical value P for the expression $(3+\eta^2)^3/(1-\eta^2)^2 = P$. This equation is fairly easy to solve for η by approximation methods. It is then easy to find k and thus eQq.

The procedure is fairly rapid and quite accurate. For $NbCl_5$ it gave $eqQ = 78.0812$ Mc/sec and $\eta = 0.32256$, while the least-squares procedure based on accurate solutions of the secular equations gave $eqQ = 78.0809$ Mc/sec, $\eta = 0.32249$.

Other coefficients of the secular equation might have been used, but they would require more manipulation. Since the observed frequencies give only approximations to the exact roots, excessive manipulation will probably increase the errors of the resulting estimates of η and eqQ.

Any useful pair of coefficients in any of the secular equations for $I = \frac{5}{2}, \frac{7}{2}$, and $\frac{9}{2}$ will yield an equation of the form $(3+\eta^2)^3 = P(1-\eta^2)^2$.

In the course of this work the secular equation for $I = \frac{9}{2}$ was solved to eight significant figures for 100 equally spaced values of η^2 by using a digital computer. These solutions are given elsewhere.[3]

Hyperfine Structure and g-Tensor Anisotropy of the Paramagnetic Resonances of Manganese in TiO_2

HARRO G. ANDRESEN

U. S. Army Signal Research and Development Laboratory, Fort Monmouth, New Jersey

(Received Feburary 8, 1961)

Several characteristic resonances of the paramagnetic spectrum of a manganese-doped TiO_2 single crystal in its rutile structure were measured with high precision in order to improve the accuracy of the spin Hamiltonian parameters. The measurements were performed at room temperature and at X-band frequencies. Especially, the anisotropy of the g tensor and that of the A tensor were evaluated using the resonance data measured at orientations of the magnetic field parallel to the three magnetic axes of the rutile crystal. The hyperfine structure patterns of the manganese resonances are discussed qualitatively for various crystal orientations; two properly selected $|\Delta m_I|=1$ transitions were used to estimate the upper limit of the quadrupole-term parameters of the spin Hamiltonian.

The paramagnetic resonances of manganese in rutile were also investigated at liquid nitrogen temperature and at X-band frequencies. Aside from a spectrum that is very similar to the spectrum already observed at room temperature and assigned to tetravalent manganese atoms, having a spin value of $S=\frac{3}{2}$, additional manganese resonances of strong intensity were observed. Though it is very likely that these resonances can be attributed to manganese atoms of a different valence state, the paramagnetic data at X-band frequencies are insufficient to determine the origin of these resonances unambiguously.

INTRODUCTION

THE paramagnetic resonances of a manganese-doped single crystal of TiO_2 in its rutile structure, measured at X-band frequencies and at room temperature, have already been described in a previous paper.[1] By using the data of the angular dependence of the magnetic resonance fields (Fig. 1), it was possible to show that the manganese atoms replace the Ti^{4+} ions in the rutile lattice and exist as tetravalent ions having a spin value of $S=\frac{3}{2}$. Because of the orthorhombic symmetry of the crystal field at the location of the manganese atoms, the paramagnetic resonance spectrum was analyzed using a spin Hamiltonian[2] of the following form:

$$\mathcal{H}=g\beta\mathbf{S}\cdot\mathbf{H}+D[S_z^2-\tfrac{1}{3}S(S+1)]+E(S_x^2-S_y^2)+A\mathbf{S}\cdot\mathbf{I}. \quad (1)$$

The centers of all observed hyperfine structure complexes can be described with an accuracy of better than 1% by the energy levels predicted by Eq. (1) and the parameters $g=1.99$, $|D|=12.1$ kMc, $|E|=3.88$ kMc, and $|A|=215$ Mc.

For several crystal orientations, however, and especially for an orientation of the magnetic field parallel to the magnetic X axis of the rutile crystal, the discrepancies between predicted and experimentally observed resonances are well above the limit of the experimental error. These discrepancies may be explained by two different arguments. In the evaluation of the parameters of the spin Hamiltonian (1), the influence of the hyperfine structure terms has been considered only in the first approximation so that the deviations can possibly be explained by second-order shifts of the hyperfine structure patterns. The alternative argument is that the paramagnetic spectrum must be interpreted with a more general form of the spin Hamiltonian. The discrepancies between theory and experiment were eliminated in this paper by assuming that both the g and the A tensors are anisotropic and by fitting the parameters of the spin Hamiltonian more accurately to the observed spectrum. Furthermore, a more careful evaluation of the g and A tensors seemed to be interesting, since both quantities are influenced essentially by the character of the chemical bond of the manganese atoms in the rutile crystal, as described below. The tetravalent manganese atoms are isoelectronic with the Cr^{3+} ions. By comparing the paramagnetic data of the manganese and chromium ions when they replace the Ti^{4+} ions in the rutile lattice,[3] one can observe that the g factor of manganese ($g=1.99$) is considerably larger than the g factor of Cr^{3+} ($g=1.97$). In addition, the hyperfine structure splitting of manganese in rutile, measured as $|A|=215$ Mc, is surprisingly small since one can show that Mn^{4+} should have a hyperfine structure parameter A which is larger than 365 Mc. One arrives at this larger value if the bonds of Mn^{4+} and Cr^{3+} in the rutile crystal are assumed to be exactly equivalent, and if one takes into consideration the hyperfine structure splitting of $(Cr^{53})^{3+}$ in rutile,[3] the different spins and magnetic moments of the Mn^{55} and Cr^{53} nuclei, and the contraction of the electron orbits due to the higher effective charge of Mn^{4+}. The comparatively large g factor as well as the small A parameter indicate, that in contrast to the predominantly ionic bonds of Cr^{3+} in rutile, the manganese atoms have strong admixtures of co-

[1] H. G. Andresen, Phys. Rev. **120**, 1606 (1960).

[2] B. Bleaney and K. W. H. Stevens, Repts. Progr. in Phys. **16**, 107 (1953).

[3] H. J. Gerritsen, S. H. Harrison, H. R. Lewis, and J. P. Wittke, Phys. Rev. Letters **2**, 153 (1959).

valent bonds[4–8] so that the notation Mn^{IV} $(3d^3)$ instead of Mn^{4+} describes more appropriately the bonding situation.[7]

THEORY

The unit cell of the tetragonal rutile crystal consists of two nonequivalent Ti^{4+} ions (Fig. 2). Each of the Ti^{4+} ions is surrounded by a slightly deformed oxygen octahedron, so that the local symmetry of a Ti^{4+} site is only orthorhombic.

Instead of the spin Hamiltonian (1), the more general form (2) has been used to evaluate more accurately the paramagnetic resonance spectrum of Mn^{IV} in rutile.

$$\mathcal{H}=\beta(g_xH_xS_x+g_yH_yS_y+g_zH_zS_z)+D[S_z^2-\tfrac{1}{3}S(S+1)]$$
$$+E(S_x^2-S_y^2)+A_xS_xI_x+A_yS_yI_y+A_zS_zI_z$$
$$+Q'[I_z^2-\tfrac{1}{3}I(I+1)]+Q''(I_x^2-I_y^2)-\gamma\beta_N\mathbf{H}\cdot\mathbf{I}. \quad (2)$$

The coordinate system of the spin Hamiltonian (2) is defined by the three magnetic axes of the rutile crystal (Fig. 2); the axis of quantization Z was chosen parallel to the c axis of the crystal. Since the surroundings of the two nonequivalent lattice sites differ from one another only by a rotation of 90° around the c axis of the crystal, the observed paramagnetic spectrum is the same for $H||X$ and $H||Y$. The paramagnetic spectrum is, therefore, independent of the sign of the parameter E, since changing the sign of E is merely equivalent to an exchange of the X and Y axis. In the evaluation of the spectrum, the sign of E has been chosen arbitrarily in such a manner that the resonances, occurring at a magnetic field of 1260 gauss and an angle of $\Theta=90°$, must be attributed to an orientation of the magnetic field parallel to the Y axis, whereas the two hyperfine structure patterns, occurring at $\Theta=90°$ and magnetic fields of 3288 and 3475 gauss, respectively, have to be associated with $H||X$ (Fig. 1).

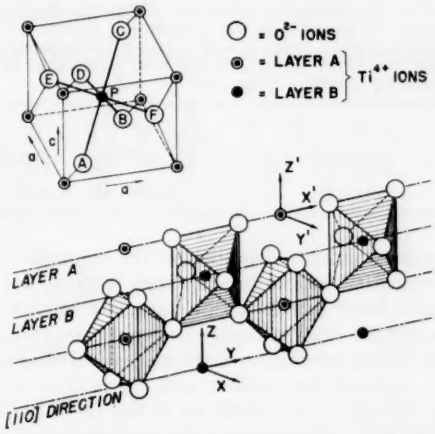

FIG. 2. Crystal structure of TiO_2 (rutile) and magnetic axes.
$\angle APE=\angle BPE=90°$; $\angle DPC=\angle APB=78°$
$EP=1.99$ A, $AP=BP=1.89$ A.

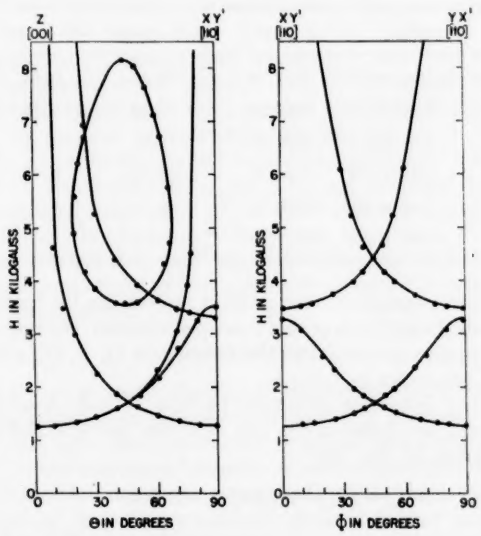

FIG. 1. The solid lines represent theoretical resonance fields, calculated for the center of Mn^{IV} hyperfine structure complexes with the parameters stated in the text. The points shown in the figure are resonance fields, which were observed at room temperature and a frequency of 9.505 kMc. Θ is the angle between the Z axis and the magnetic field H; Φ is the angle between the X axis and the projection of the magnetic field in the XY plane.

Since the D and E parameters of the spin Hamiltonian of manganese in rutile are rather large, the simplifying assumption of the "strong field case" is not valid for the magnetic fields that have been used in this experiment. The hyperfine structure terms of the spin Hamiltonian, however, can be treated as a small perturbation, so that the center of each hyperfine structure complex can be described in the first approximation solely by the g, D, and E terms of the spin Hamiltonian (2). After calculating the g, D, and E parameters in this first approximation, one can use these values to determine the eigenfunctions that diagonalize the fine structure terms of the spin Hamiltonian. Knowing the electronic eigenfunctions numerically, one can then calculate the contributions of the hyperfine structure terms up to the second-order approximation. Finally, the resulting displacements of the center of each hyperfine structure complex due to the second-order contributions of the hyperfine structure terms can be used to evaluate the g, D, and E parameters with higher precision.

[4] W. Low, *Paramagnetic Resonance in Solids. Solid-State Physics* (Academic Press, New York, 1960), Suppl. 2.
[5] J. S. Van Wieringen, Discussions Faraday Soc. **19**, 118 (1955).
[6] O. Matumura, J. Phys. Soc. Japan **14**, 108 (1959).
[7] K. A. Mueller, Phys. Rev. Letters **2**, 341 (1959).
[8] The author is indebted to Professor W. Low for pointing out that the covalent bonding is only one of the reasons why the g factor of manganese is larger than that of Cr^{3+}. The other reason is that for Mn^{4+} the separation of the Γ_5 and Γ_2 state is probably twice as large as that of Cr^{3+}.

TABLE I. Transformation properties of the spin Hamiltonian parameter. (If one chooses the quantization axes of the spin Hamiltonian parallel to the X and Y axes of the magnetic complex, the parameters of the first row must be replaced by the corresponding quantities of the other two rows).

Z	D	E	Q'	Q''
X	$\frac{1}{2}(3E-D)$	$-\frac{1}{2}(D+E)$	$\frac{1}{2}(3Q''-Q')$	$-\frac{1}{2}(Q'+Q'')$
Y	$-\frac{1}{2}(3E+D)$	$\frac{1}{2}(D-E)$	$-\frac{1}{2}(3Q''+Q')$	$\frac{1}{2}(Q'-Q'')$

For an arbitrary orientation of the magnetic field, this evaluation scheme becomes very lengthy, but for magnetic fields parallel to the magnetic axes of the rutile crystal, the evaluation becomes comparatively simple. For an orientation of the magnetic field parallel to the c axis of the rutile crystal, the position of the energy level W_{k,m_I} is determined by Eq. (3). (The first index of W_{k,m_I} characterizes the fine structure level, the second index the hyperfine structure level.)

$$W_{k,m_I}=W_{k,0}+B_k m_I+C_k m_I^2$$

with

$$W_{k,0}=W_k+\left[\sum_{\nu,\nu\neq k}\frac{A_y^2|S_y^{k\nu}|^2+A_x^2|S_x^{k\nu}|^2}{2(W_k-W_\nu)}-\frac{1}{3}Q'\right]I(I+1)$$

$$B_k=A_z S_z^{kk}-\sum_{\nu,\nu\neq k}\frac{A_x A_y[\,|S_+^{k\nu}|^2-|S_-^{k\nu}|^2]}{4(W_k-W_\nu)}-\gamma\beta_N H_z$$

$$C_k=\sum_{\nu,\nu\neq k}\frac{2A_z^2|S_z^{k\nu}|^2-A_y^2|S_y^{k\nu}|^2-A_x^2|S_x^{k\nu}|^2}{2(W_k-W_\nu)}+Q'. \quad (3)$$

The symbols are:

W_k = energy level k of the fine structure terms. The numerical values of these indices refer to the order of ascending energy, assuming that the sign of the parameter D is positive.

$S_y^{k\nu}$ = matrix element of S_y; the indices k and ν indicate that this matrix element is attributed to the electronic wavefunctions of the energy levels k and ν. The definition of the symbols $S_x^{k\nu}$, $S_z^{k\nu}$, $S_+^{k\nu}$, and $S_-^{k\nu}$ is equivalent to those given for $S_y^{k\nu}$.

m_I = magnetic quantum number of the nuclear angular momentum I.

TABLE II. Magnetic resonance fields of the hyperfine structure components of the 4→3 transition for the crystal orientation $\Theta=0°$. The resonances were measured at room temperature and at a frequency of $\nu=9.5046$ kMc.

Transition	H [gauss]	Δ^1H [gauss]	Δ^2H [gauss]
$\Delta m_I=0$, $\|m_I\|=5/2$	1051.04	77.50	0.39
$\|m_I\|=3/2$	1128.54	77.89	0.41
$\|m_I\|=1/2$	1206.43	78.30	0.45
$\|m_I\|=1/2$	1284.73	78.75	0.34
$\|m_I\|=3/2$	1363.48	79.09	
$\|m_I\|=5/2$	1442.57		

All other symbols are the same as those used in the spin Hamiltonian (2).

Equation (3) is based on the simplifying assumption, that the parameter Q'' of the quadrupole terms of the spin Hamiltonian (2) is small compared with the term $A_z S_z^{kk}$.[9] In this case, every energy level of the hyperfine structure can be described solely by a single nuclear eigenfunction $|I, m_I\rangle$. Equation (3) includes the influence of the magnetic terms $A_x S_x I_x+A_y S_y I_y+A_z S_z I_z$ up to the second-order approximation; all other hyperfine structure terms have been evaluated only in the first-order approximation. It may also be used when the magnetic field is parallel to the X or Y axis of the magnetic complex, provided one chooses the quantization axis of the spin Hamiltonian parallel to these directions and takes into consideration the transformation properties of the spin Hamiltonian parameters while changing the orientation of the quantization axis Z to another axis of the magnetic complex.[10]

TABLE III. Magnetic resonance fields of the hyperfine structure components of the 2→1 transition for the crystal orientation $\Theta=90°$, $\Phi=90°$. The resonances were measured at room temperature and at a frequency of $\nu=9.5046$ kMc.

Transition	H [gauss]	Δ^1H [gauss]	Δ^2H [gauss]
$\Delta m_I=0$, $\|m_I\|=5/2$	1072.93	74.73	0.47
$\|m_I\|=3/2$	1147.66	75.20	0.47
$\|m_I\|=1/2$	1222.86	75.67	0.55
$\|m_I\|=1/2$	1298.53	76.22	0.51
$\|m_I\|=3/2$	1374.75	76.73	
$\|m_I\|=5/2$	1451.48		

The components of the g and A tensors can be transformed solely by a proper index permutation; the transformation properties of the parameters D, E, Q', and Q'' are shown in Table I.

The hyperfine structure pattern of the $\Delta m_I=0$ transitions between the fine structure levels k and l is given by Eq. (4);

$$W_{k,m_I}-W_{l,m_I}=W_{k,0}-W_{l,0}+[B_k-B_l]m_I+[C_k-C_l]m_I^2. \quad (4)$$

Since the experiment was performed with fixed frequency and a variable magnetic field, Eq. (4) has to be transformed to a magnetic field scale in order to be used for the comparison of experiment and theory. By considering only the first approximation of the hyperfine structure terms for the evaluation of the spin Hamiltonian, one may neglect the magnetic field dependence of the electronic eigenfunctions. The field dependence

[9] The matrix elements S_x^{kk} and S_y^{kk} are identically zero for a parallel orientation of the magnetic field with regard to the magnetic axes of the crystal.

[10] K. D. Bowers and J. Owen, Repts. Progr. in Phys. **18**, 304 (1955).

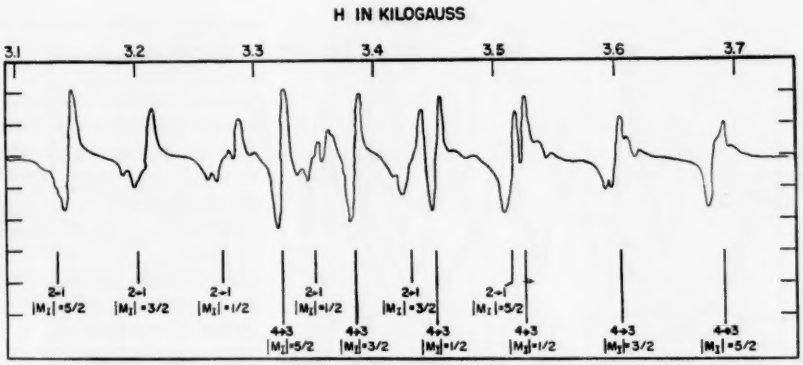

FIG. 3. Hyperfine structure pattern of the 2→1 and 4→3 transition for the crystal orientation $\Theta=90°$ and $\Phi=0°$; the fine structure energy levels are labeled in the order of ascending energy. The figure shows also the magnetic resonance fields which have been assigned to the $\Delta m_I=0$ transitions.

of the fine structure energy levels is then solely determined by the term $g_z\beta(S_z^{kk})H_z$, and the hyperfine structure of the transition $k\rightarrow l$, expressed in a magnetic field scale, becomes

$$H(m_I)=H_0+\left(\frac{A_z}{g_z\beta}+\cdots\right)m_I+(\text{second-order terms})\,m_I^2. \tag{5}$$

Equation (5) proves, that for magnetic field orientations parallel to the magnetic axes of the crystal, the over-all splitting of the hyperfine structure patterns is in the first approximation independent of D, E, the magnetic field H, and the specific transition, and is given by the terms $2A_xI/g_x\beta$, $2A_yI/g_y\beta$, and $2A_zI/g_z\beta$, depending upon which of the three axes is being considered. On comparing theory and experiment in a higher than first-order approximation, the magnetic field dependence of the electronic eigenfunctions has to be considered.

EXPERIMENTS

Unless otherwise mentioned, the measurements were performed at room temperature and at a frequency of 9.5047 kMc; the experimental setup has been described in a previous paper.[1] In order to reduce the errors due to uncertainties of the crystal orientation, the evaluation of the spin Hamiltonian parameters was based entirely on transitions occurring in the angle-independent regions of the curves shown in Fig. 1.

The magnetic resonance fields of the hyperfine structure complexes for $H\|Z$, $H\|Y$, and $H\|X$ were used to determine the g and A tensors of the spin Hamiltonian (2). It was possible to determine these specific orientations with an accuracy of better than $\pm0.2°$ by slightly tilting the crystal inside the cavity until the magnetic resonance fields in the region of 1250 gauss (Fig. 1) showed a minimum with regard to any further variation of the crystal orientation.

The hyperfine structure for $H\|Z$ and $H\|Y$ consists of six $\Delta m_I=0$ transitions between hyperfine structure levels, resulting from the spin $I=\frac{5}{2}$ of the Mn^{55} nucleus. The values of these magnetic resonance fields as well as the first and second differences between successive field values are tabulated in Tables II and III. The absolute accuracy of the magnetic field values in Tables II and III is better than ±0.3 gauss, whereas the differences between successive resonance fields could be determined with an accuracy of better than 0.06 gauss.

For $H\|X$, the hyperfine structure patterns of the transitions between the fine structure energy levels 4, 3 and 2, 1, respectively, are depicted in Fig. 3. Some resonances are clearly split into several lines; two of these lines may be attributed to $|\Delta m_I|=2$ transitions and one line to a $\Delta m_I=0$ transition. The $|\Delta m_I|=2$ transitions are to be expected since, for $H\|X$ and magnetic fields in the region of 3000 gauss, the fine structure levels 2 and 3 are both nearly independent of the magnetic field. Therefore, the simplifying assumption $|A_xS_x^{kk}|\gg|\frac{1}{2}(Q'+Q'')|$ cannot be used for this special case, so that every hyperfine structure level must be described by a mixture of various nuclear eigenfunctions $|I, m_I\rangle$.

The magnetic fields $H_1=3288$ gauss and $H_2=3475$ gauss at $\Theta=90°$ and $\Phi=0°$, can be attributed to the centers of the hyperfine structure patterns of the 2→1 and 4→3 transition, respectively. The difference of these fields can be used to determine the E/D ratio. If the E/D ratio differs only slightly from the value $\frac{1}{3}$, the difference between H_2 and H_1 will be small and the E/D ratio can be calculated with high precision.[1]

At X-band frequencies, transitions between energy levels 3 and 2, which are comparatively sensitive to a variation of the parameter D, can be observed only for magnetic field orientations of $\Phi=90°$ and Θ values between 60° and 30°; the corresponding magnetic resonance fields are depicted by the curve of Fig. 1, which has a maximum as well as a minimum at $\Theta=45°$ and $\Phi=90°$. At field orientations between $\Theta=38°$ and $\Theta=50°$, the hyperfine structure pattern of the 3→2 transition consists of eleven nearly equally spaced resonances (Fig. 4). Nine of these resonances, which have nearly the same intensity, may be interpreted by

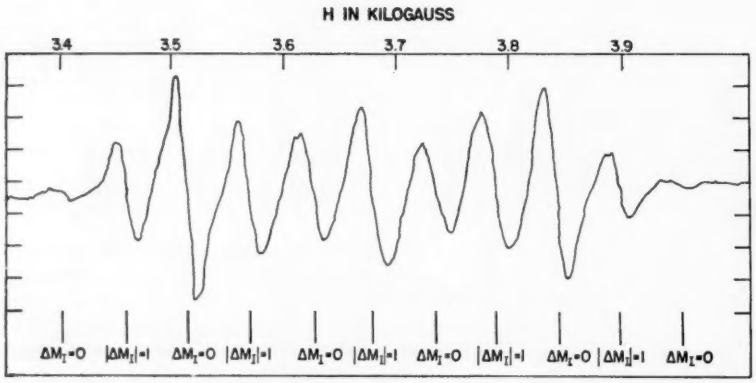

FIG. 4. Hyperfine structure of the 3→2 transition for the crystal orientation $\Theta=38°$ and $\Phi=90°$; the fine structure energy levels are labeled in the order of ascending energy.

five $|\Delta m_I|=1$ transitions and four $\Delta m_I=0$ transitions. Peculiar to the hyperfine structure pattern at these orientations is the nearly vanishing intensity of the two $\Delta m_I=0$ transitions occurring at the low- and high-field side of the hyperfine structure complex. This intensity behavior is depicted in Fig. 4, showing the hyperfine structure pattern of the 3→2 transition at $\Theta=38°$ and magnetic fields in the region of 3600 gauss; the intensity ratio of the weak to the strong resonances is roughly 1:20. This specific hyperfine structure pattern has been used to determine the parameter D.

On using the magnetic resonance fields of the transitions described above and neglecting the second-order corrections due to the hyperfine structure terms, one obtains the following results for the parameters of the spin Hamiltonian (2):

$$g_x=2.008,$$
$$g_y=1.9943,$$
$$g_z=1.9927,$$
$$|D|=12.23\pm0.03 \text{ kMc},$$
$$|E/D|=0.32065\pm0.0003,$$
$$|E|=3.918\pm0.01 \text{ kMc},$$
$$|A_x|=217\pm3 \text{ Mc},$$
$$|A_y|=211.0\pm0.7 \text{ Mc},$$
$$|A_z|=218.1\pm0.7 \text{ Mc}.$$

The g values of atoms with less than a half-filled $3d$ shell should always be smaller than the g value of the free electron; the surprisingly large value of g_x indicates, therefore, that the second-order corrections will be essential, at least for $H||X$.

On considering the second-order corrections according to Eq. (3), one obtains the following values for the components of the g tensor:

$$g_x=1.995\pm0.005, \quad g_y=1.9909\pm0.0005,$$
$$g_z=1.9898\pm0.0005.$$

The comparatively large error limits of the g_x value is due to the fact that for $H||X$ the assumptions of Eq. (3) are not valid for two of the energy levels.

At X-band frequencies, one can observe only one hyperfine structure complex for $H||Y$ and $H||Z$, and the over-all splittings of the two hyperfine structure patterns being observed for $H||X$ are equal within the error limits of the experiment. Therefore, it is impossible to determine in this frequency range the signs of the A-tensor components with regard to the sign of the D parameter, so that the second-order corrections for the calculation of the A-tensor components due to Eqs. (3) and (4) can merely be used to determine the error limits of the first-order values.

In order to make use of the high accuracy of the magnetic resonance fields for $H||Z$ and $H||Y$, the comparison between experiment and theory has been extended to the second-order term of Eq. (5). The coefficient of the term quadratic in m_I, which is independent of the signs of the A-tensor components, allows to check the accuracy of the electronic eigenfunctions being used in the second-order approximation. According to Tables II and III, the second differences Δ^2H between successive resonance fields are nearly constant. For $H||Z$ and $H||Y$ the average second differences are $\Delta^2H_{(z)}=0.40\pm0.03$ gauss and $\Delta^2H_{(y)}=0.50\pm0.03$ gauss, respectively. The second differences were calculated using the magnetic field dependence of the fine structure energy levels for the transformation of the hyperfine structure splitting, given by Eqs. (3) and (4) to a splitting being measured on a magnetic field scale. On neglecting the magnetic field dependence of the electronic eigenfunctions, one obtains the results $\Delta^2H_{(z)}=0.57$ gauss and $\Delta^2H_{(y)}=0.66$ gauss; if one includes the correction due to the magnetic field dependence of the electronic eigenfunctions, these quantities are changed to the values $\Delta^2H_{(z)}=0.43$ gauss and $\Delta^2H_{(y)}=0.496$ gauss, which agree satisfactorily with the experimental values.

The behavior of the hyperfine structure pattern for magnetic field orientations not parallel to the magnetic axes can be observed most conveniently for the 2→1

transition while varying the magnetic field orientation in the XY plane. At $\Phi=90°$ ($H||Y$) the hyperfine structure pattern consists of pure $\Delta m_I=0$ transitions; for $\Phi=75°$, five additional resonances can be observed, occurring about halfway between the six main $\Delta m_I=0$ lines. These resonances may be attributed to "forbidden" transitions $|\Delta M|=1$, $|\Delta m_I|=1$, with M being the quantum number of the Z component of the electron angular momentum. The analysis of these additional resonances, as described below, yields an upper limit for the quadrupole-term parameters Q' and Q'' that is small compared to the parameter of the magnetic hyperfine structure interaction. Therefore, the intensities of the $|\Delta m_I|=1$ transitions at $\Theta=90°$, $\Phi=60°$ cannot be explained by a mixing of various $|I, m_I\rangle$ eigenfunctions due to a quadrupole interaction, since this effect should yield intensities proportional to $(Q', Q''/A S_z{}^{21})^2$. The comparatively strong intensities of the observed $|\Delta m_I|=1$ transitions indicate, rather, that the mixing of $|I, m_I\rangle$ eigenfunctions must be explained by the combined effect of the large D and E parameter, together with the magnetic part of the hyperfine structure interaction. Figure 5 shows the low- and high-field part of the hyperfine structure pattern at $\Theta=90°$, $\Phi=60°$. The $|\Delta m_I|=1$ transitions, occurring at the high-field side of the hyperfine structure complex, are clearly split into two lines.[11] After considerably reducing the amplitude of the magnetic field modulation, the splittings of both $|\Delta m_I|=1$ transitions, shown in Fig. 5, were determined to be $3{,}3\pm0.2$ gauss and $5{,}4\pm0.2$ gauss, respectively. For estimating the order

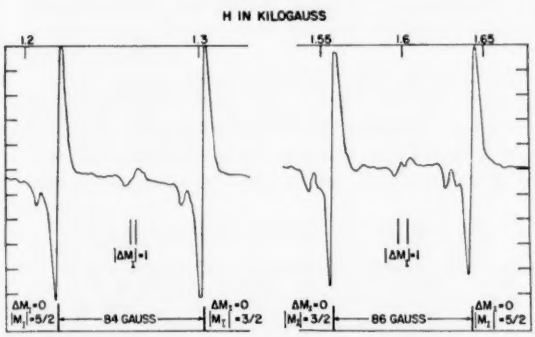

FIG. 5. Low- and high-field part of the hyperfine structure pattern of the 2→1 transition for a crystal orientation $\Theta=90°$ and $\Phi=60°$; the fine structure energy levels are labeled in the order of ascending energy. The splittings of the $|\Delta m_I=1|$ transitions are especially marked.

[11] The satellite lines of the $\Delta m_I=0$ transitions must be attributed to imperfections of the single crystal, since it can be proved experimentally that the relative position of these lines depends upon the sign of the slope of the curves in Fig. 1; e.g., measuring the hyperfine structure pattern at $\Phi=60°$ and $\Phi=120°$, the satellite lines change their position relative to the strong $\Delta m_I=0$ resonances from the low-field side to the high-field side. This method is very convenient for discriminating resonances due to imperfections of the single crystal against real hyperfine structure splittings.

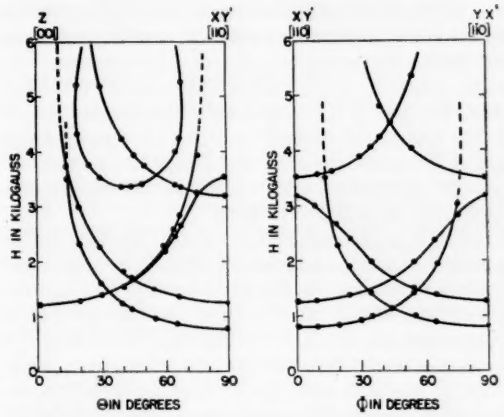

FIG. 6. Angular dependence of the paramagnetic resonances of manganese in rutile. The measurements were performed at liquid nitrogen temperatures and at a frequency of 9.410 kMc.

of magnitude of the quadrupole terms of spin Hamiltonian (2), the difference of these splittings has been analyzed using the relations of Eqs. (3) and (4). Since the intensity of the $|\Delta m_I|=1$ transitions is weak compared with the intensity of the $\Delta m_I=0$ transitions, only a comparatively small error will be introduced by using Eq. (3). According to Eq. (4), the difference ΔH between the splittings of the two $|\Delta m_I|=1$ transitions shown in Fig. 5 is given by Eq. (6).

$$8[C_2+C_1]=\Delta H(d/dH)(W_2-W_1). \qquad (6)$$

By introducing the quantities C_2 and C_1, as defined in Eq. (3), the upper limit of the parameter $-\frac{1}{2}(3Q''+Q')$ can be estimated to be $|\frac{1}{2}(3Q''+Q')|<2$ Mc. By decreasing the angle Φ, the intensity of the $|\Delta m_I|=1$ transitions increases until it becomes comparable with the intensity of the $\Delta m_I=0$ transitions at $\Phi=30°$. The hyperfine structure splitting at magnetic field orientations in the angular range $0°\leqslant\Phi<45°$, is rather complicated and consists of $\Delta m_I=0$, $|\Delta m_I|=1$ as well as of $|\Delta m_I|=2$ transitions. The intensities of these "forbidden" transitions may be assigned to a quadrupole interaction, since for magnetic field orientations close to $\Theta=90°$, $\Phi=0°$ the matrix element $S_z{}^{21}$ turns out to be quite small.

The paramagnetic resonance spectrum of manganese in rutile has also been measured at liquid nitrogen temperature. The measurements were performed at a frequency of 9.410 kMc. Figure 6 shows the magnetic resonance fields as a function of the crystal orientation. Aside from a spectrum that is very similar to the room temperature spectrum of Mn^{IV}, additional manganese resonances of strong intensity can be observed; the 90° period of the paramagnetic spectrum in the XY plane (Fig. 6) indicates that these resonances must also be attributed to manganese atoms substituting the Ti^{4+} ions in the rutile crystal. At liquid nitrogen tempera-

ture, the values of the parameters D and E/D, describing the Mn^{IV} spectrum, are slightly smaller than those that have been determined at room temperatures. The values are: $|D| = 11.76 \pm 0.1$ kMc $|E/D| = 0.308 \pm 0.001$. For the $H \parallel Y$ and a magnetic resonance field of 790 gauss, the over-all splitting of the hyperfine field of 790 gauss, the over-all splitting of the hyperfine structure pattern of the additional resonances was determined to be 284 ± 0.5 gauss.

The splitting is considerably smaller than the over-all hyperfine structure splitting of the Mn^{IV} resonances which is approximately 380 gauss for $H \| Y$. Since the over-all splitting of the hyperfine structure pattern is independent of D, E, the magnetic field, and the specific electronic transition for field orientations parallel to the magnetic axes, the additional resonances can be possibly explained by manganese atoms of a different valence state. If one assumes that the additional resonances are due to Mn^{2+} ions, which is partly confirmed by the small hyperfine structure parameter $|A_y| = 158$ Mc the hyperfine structure complex occurring at a magnetic field of 790 gauss and $H \| Y$ can be attributed to a $m = +\frac{5}{2} \rightarrow m = -\frac{5}{2}$ transition. It is strange, however, that this highly forbidden transition could be observed with such high intensity, and that at X-band frequencies no other transitions were observed showing the same small over-all hyperfine structure splitting.[12] Due to these uncertainties, it would be desirable to investigate at liquid nitrogen temperature the paramagnetic spectrum of manganese in rutile also at other frequencies in order to explain more conclusively the resonances that are not due to Mn^{IV} atoms.[13]

ACKNOWLEDGMENT

The author is obliged to M. Katzman for proofreading the manuscript as well as for his encouragement and constructive interest in this work.

[12] Assuming that the resonances can be really attributed to Mn^{2+} ions, these arguments indicate that both the D parameter and the U/D ratio must be rather large.

[13] In a private communication, Professor W. Low pointed out that the manganese resonances occurring at 790 gauss may be possibly explained by Mn^{3+} ions.

THE JOURNAL OF CHEMICAL PHYSICS VOLUME 35, NUMBER 3 SEPTEMBER, 1961

Motions of Molecules in Condensed Systems. X. The Infrared Spectrum and Structure of a Single Crystal of Cyclopropane

CHARLES BRECHER, ESTHER KRIKORIAN,* JOSEPH BLANC,† AND RALPH S. HALFORD

Department of Chemistry, Columbia University, New York 27, New York

(Received January 13, 1961)

The absorption of polarized infrared radiation by thin sections of single crystals of cyclopropane, grown in a specially designed apparatus, has been recorded in the frequency range between 700 and 5000 cm^{-1}, and compared with spectra, similarly recorded, of liquid and vapor. The assignment of molecular modes is completed: The ν_5 fundamental, not previously measured, is located in the crystal at 1078 cm^{-1}, while ν_4 and ν_{13} appear at 1133 and 1194 cm^{-1}, respectively, confirming previously uncertain assignments. The frequencies of the primary lattice modes of the molecule in the crystal are inferred from combinations. Site group and factor group splittings are seen to be of the same magnitude ($\approx$10 cm^{-1}). The cyclopropane crystal is found to be orthorhombic (C_{2v} or D_{2h}), with the molecules located at sites of C_s symmetry. An arrangement of the molecules, described by space group P_{nm} (C_{2v}^7), which gives the most efficient packing, is proposed as the actual crystal structure.

INTRODUCTION

INFRARED spectroscopy can be a useful tool for the investigation of molecular crystals, and the general theory has been treated by many investigators.[1] Such studies promise to be most fruitful when conducted with crystals compared of relatively small and highly symmetrical molecules, in which the changes caused by the crystal field on the selection rules governing the absorption of infrared radiation by the molecule are most readily observable.[2,3] It is desirable, of course, that the free molecule be well understood; specifically, that its symmetry have been reasonably well established, and that a relatively complete assignment of the normal modes of vibration have been made. Some independent knowledge of the crystal structure is always helpful, and indeed, as in the investigations of benzene, can become essential for complete interpretation of spectra.

Cyclopropane provides a highly interesting problem for this kind of investigation, made even more challenging by the incompleteness of the available information. The D_{3h} symmetry of the molecule, and the molecular dimensions, have been reasonably well established, by both spectroscopic[4] and electron diffraction[5] investigations. However, the assignment of the fourteen normal modes of vibration is incomplete, with one mode missing entirely (except by inference from combination bands) and one or two others still somewhat uncertain. Thermodynamic studies[6] have given the assurance that there is no phase transition in the solid state, but, except for what has been obtained by an optical study[7] (which we shall mention later), prior work affords no detailed information on the crystal structure.

We report here the results of an investigation of the absorption of polarized infrared radiation by single crystals of cyclopropane, including comparisons with spectra for liquid and vapor phases. Our findings contribute to a greater knowledge of the molecule itself (particularly as regards the assignment of normal modes), point to the actual crystal structure, and furnish an unusual amount of information concerning molecular motions in the crystal.

EXPERIMENTAL

All experiments in this investigation were conducted using Matheson[8] research-grade cyclopropane having an initial minimum purity of 99.5%, which was subsequently cycled through at least five fractional distillations. The infrared spectrum of this material was observed with the vapor contained in a cell having a path length of 10 cm, at a pressure of 180 mm Hg. This pressure was chosen so as to provide an absorbing path

* Present address: Hunter College, 695 Park Ave., New York 21, New York.

† Present address: RCA Laboratories, Princeton, New Jersey.

[1] (a) R. S. Halford, J. Chem. Phys. **14,** 8 (1946); (b) D. F. Hornig, *ibid.* **16,** 1063 (1948); (c) H. Winston and R. S. Halford, *ibid.* **17,** 607 (1949); (d) T. H. Walnut, *ibid.* **20,** 58 (1952).

[2] Benzene has already been intensively investigated: (a) R. S. Halford and O. A. Schaeffer, J. Chem. Phys. **14,** 141 (1946); (b) R. D. Mair and D. F. Hornig, *ibid.* **17,** 1236 (1949); (c) S. Zwerdling and R. S. Halford, *ibid.* **23,** 2221 (1955); (d) C. A. Swenson, W. B. Person, D. A. Dows, and R. M. Hexter, *ibid.* **31,** 1324 (1959), and later papers by Person *et al.*

[3] The results of the following crystal investigations, already completed in this laboratory, will be published in this journal shortly: (a) acetylene: E. Krikorian, Ph.D. dissertation, Columbia University (1956); (b) 1,2-dichloroethane: M. Gershenzon, Ph.D. dissertation, Columbia University (1956); (c) ethylene: C. Brecher, Ph.D. dissertation, Columbia University (1959); (d) allene: J. Blanc, Ph.D. dissertation, Columbia University (1959); (e) dimethyl acetylene: R. Kopelman, Ph.D. dissertation, Columbia University (1960); (f) methyl acetylene: R. Kopelman and R. S. Halford (to be published).

[4] (a) A. W. Baker and R. C. Lord, J. Chem. Phys. **23,** 1636 (1955); (b) Hs. H. Gunthard, R. C. Lord, and T. K. McCubbin, Jr., *ibid.* **25,** 768 (1956); (c) P. M. Mathai, G. G. Shepherd, and H. L. Welsh, Can. J. Phys. **34,** 1448 (1956); (d) earlier work summarized by G. Herzberg, *Infrared and Raman Spectra* (D. Van Nostrand Company, Inc., New York, 1945), p. 352.

[5] (a) L. Pauling and L. O. Brockway, J. Am. Chem. Soc. **59,** 1223 (1937); (b) O. Bastiansen and O. Hassel, Tidskr. Kjemi, Bergvesen Met. **6,** 71 (1946); (c) Some other cyclopropane data are published by J. D. Dunitz and V. Schomaker, J. Chem. Phys. **20,** 1703 (1952), in a paper on cyclobutane.

[6] R. A. Ruehrwein and T. M. Powell, J. Am. Chem. Soc. **68,** 1063 (1946).

[7] W. Wahl, Proc. Roy. Soc. (London) **A89,** 327 (1913).

[8] The Matheson Company, Inc., East Rutherford, New Jersey.

of material roughly equivalent to that presented by the crystal and liquid specimens (which will be discussed later). The spectrum of the vapor is in agreement with those obtained by previous investigators, and shows no absorptions attributable to the presence of any impurity.

The apparatus used to produce the single crystal specimens was, except for a newly designed crystallization chamber or cell, the same as that originally used by Zwerdling and Halford,[9] and we shall not repeat its description here. The cell, while completely different in its mechanical construction (to accommodate the much lower temperatures attained with the use of liquid nitrogen as a refrigerant), still follows the same basic design principles as regards the crystallization process. A detailed description of its construction will appear elsewhere.[10] It is sufficient here to note that the cell is composed of two KBr disks, roughly 20 mm in diam and about 0.05 mm apart, encased in a cylinder of silver-impregnated Teflon, with access to the interior of the cell provided by stainless-steel capillary tubing. Thermal contact is made between the cell and the liquid nitrogen reservoir, and controlled input of current to heaters located at the top and the bottom of the cell makes it possible to attain a wide range of temperature conditions.

Two single crystal specimens were produced. The first was grown by controlled feed of the vapor into the cell (first at a rather low rate to insure good nucleation, then at increasingly higher rates to maintain optimum growth conditions), following usual procedures.[9] The face which this sample presented to the infrared radiation is denoted henceforth, for reasons which will become clear later, as the 001 face. The second specimen was initiated in the same manner, but a mishap which occurred during its growth caused the temperatures within the cell to rise to the melting point, destroying the visible crystal segment. However, a seed presumably remained at the top of the cell, for a subsequent lowering of the temperature at the top caused quite rapid crystallization there, fed by distillation from the liquid (which had sunk to the bottom of the cell), producing a specimen of excellent quality. The face which this specimen presented to the infrared beam is denoted henceforth as the 0*kl* face. The crystal specimens were semicircular cross sections occupying the upper half of the cell, thus having an area of about 150 mm^2 and a thickness of about 0.05 mm. Both specimens were clear and transparent, and extinguished sharply and uniformly between crossed polaroids, giving no indication of containing any crystal segments with different orientation. In addition, specimens of liquid, and of a polycrystalline mass formed by rapid freezing of the liquid, were obtained in the same cell.

[9] S. Zwerdling and R. S. Halford, J. Chem. Phys. **23,** 2215 (1955).

[10] E. Krikorian and R. S. Halford (to be published). See also references 3(a) and 3(b).

The spectra were recorded using a Perkin-Elmer model 12B instrument equipped with Nernst glower and Golay detector, modified for double beam operation so as to permit direct recording of relative transmission (the original Savitzky-Halford instrument[11]), with the empty half of the cell used as reference. Slit schedules were used which maintained a noise-to-signal ratio of about 2%. A NaCl prism was used in the spectral region between 700 and 1400 cm^{-1}, a CaF_2 prism between 1400 and 5000 cm^{-1}, and the scanning speeds were adjusted stepwise in an attempt to compensate partially for the nonlinear dispersion of the prisms. Polarized radiation was produced with a polarizer[12] consisting of eight sheets of AgCl inclined at the Brewster angle and installed within a rotatable aluminum cylinder. The directions of the two perpendicular extinction axes of each specimen were determined in visible light, and spectra were recorded with the electric vector of the infrared radiation polarized, in turn, along each of the two extinction axes of the specimen, and also with the light unpolarized. The crystallographic significance of these extinction axes will be deduced presently. The spectrum of each single crystal specimen was recorded at two different temperatures, −160° and −190°C, in order to detect any temperature-dependent phenomena. Finally, unpolarized spectra of the polycrystalline mass at −190°C and of the liquid at −125°C were also recorded, as was the spectrum of the vapor, mentioned earlier. All spectroscopic observations were repeated to increase the reliability of the data, and the requisite spectroscopic blanks were recorded.

SPECTRA

The infrared spectra of cyclopropane vapor at 25°C, liquid at −125°C, and the 0*kl* single crystal at −190°C, recorded with equivalent absorbing paths, are shown in Fig. 1. Of these, it is sufficient at this point to note merely that their general features are what would be expected: (a) More bands are detected in the liquid than in the vapor, and still more in the crystal, while bands already present in the vapor are generally intensified in liquid and crystal; (b) vapor bands show a PQR structure and the liquid bands are rather broad, while the crystal bands are quite sharp (so sharp, in fact, that the spectrometer could not resolve their true shapes); and (c) bands shift in frequency very little (less than 1%) from phase to phase.

In Fig. 2 are shown the spectra of the 001 crystal at −190°C, taken with the light first unpolarized, then polarized with its electric vector along the direction of each of the two perpendicular crystal extinction axes, in turn. The data, including the absorption frequencies, their polarization behavior, and their assignments, are summarized in Table I.

Figure 3 shows the only frequency ranges in which

[11] A. Savitzky and R. S. Halford, Rev. Sci. Instr. **21,** 203 (1950).

[12] E. Charney, Ph.D. dissertation, Columbia University (1956).

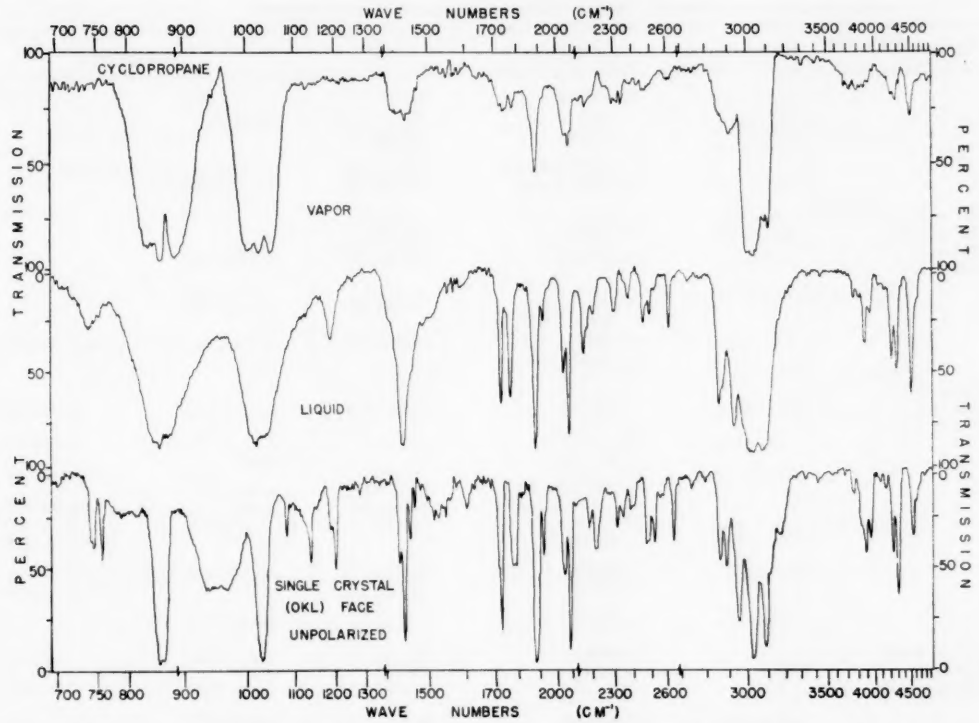

FIG. 1. Infrared spectra of cyclopropane vapor (at 25°C), liquid (at −125°C), and crystal (at −190°C), recorded with equivalent absorbing paths. The crystal cross section contains one crystallographic axis (tentatively identified as the *b* axis) and undetermined projections of the other two. (In this and subsequent figures, the Miller indices used are descriptive only, and do not rigorously identify the crystallographic planes.)

any important difference was observed between the spectra of the same crystal specimen at the two different temperatures of investigation, −160° and −190°C (i.e., other than the expected sharpening of the bands at the lower temperature). The significance of this temperature effect will be discussed later.

The spectra of the polycrystalline sample and the polarized spectra of the 0*kl* single crystal are not reproduced here, but much information was obtained from them. All bands observed in the polycrystalline sample are present in the 0*kl* single crystal spectra and in the converse; hence, no modes of the 0*kl* crystal were accidently oriented so as to make their interaction with the infrared radiation geometrically impossible. On the other hand, certain bands of the 0*kl* crystal (e.g., 756 and 1459 cm^{-1}) are absent, or nearly so, from the spectra of the 001 crystal, indicating that their moments were located almost exactly parallel to the light path and perpendicular to the cross-section plane of the 001 crystal, which direction we call axis III.

It is observed also that certain bands (e.g., 742, 1133, 1200, and 1434 cm^{-1}) which appear in the axis I polarization of the 001 crystal are absent from the perpendicular axis II polarization, while certain other bands appearing on axis II (e.g., 747, 1189, 1424, and 1449 cm^{-1}) are absent from axis I. One of the two perpendicular polarizations of the 0*kl* crystal yielded a spectrum almost identical to the axis I spectrum of the 001 crystal. The other 0*kl* polarization yielded a composite containing not only all bands present on axis II of the 001 crystal (albeit with decreased intensity), but also a number of absorptions almost coinciding in frequency with axis I bands absent from axis II (e.g., 1200 and 1434 cm^{-1}), as well as all 0*kl* absorptions not found in the 001 crystal. Thus the relationship between the two single crystal specimens, and the reason for their names, now becomes clear. Both specimens contained axis I in their cross-sectional planes, but axis III bands are almost totally absent from the spectra of the 001 crystal, indicating its cross-sectional plane to be very nearly a major crystal face. The 0*kl* crystal, on the other hand, was rotated around axis I relative to the other specimen, revealing some linear combination of axes II and III in its cross-section. By comparing this polarization with that of axis II alone, it was possible to determine with reasonable confidence the appearance or absence of bands on axis III, and to estimate the relative intensities of bands on axis III as compared to the other two axes.

TABLE I. The infrared absorption bands of cyclopropane.[a]

Vapor (cm^{-1})	Liquid (cm^{-1})	Crystal (cm^{-1})	Polar.	Assignment
		742 m	I	
	741 m, bd	747 m	II	$\nu_{14}(E'')$
		756 m	III≫II>I	
		776[b] vvw, bd	I≳II≈III	$\nu_{11}-\nu_{(R_x,R_y)}(A_1''+A_2''+E'')$
		798[b] w, bd	I≈II≈III	$\nu_{11}-\nu_{R_z}(E')$
841 vs P				
852 pd Q'	865 vs, bd	855 vs	III≳II	$\nu_7(A_2'')$
866 vs Q		865 vs	I≈II≈III	$\nu_{11}(E')$
895 vs R				
		937[b] s, bd	I≈II≈III	$\nu_{11}+\nu_{R_z}(E')$
		941[c] s, bd		
		960[b] s, bd	I≳II≈III	$\nu_{11}+\nu_{(R_x,R_y)}(A_1''+A_2''+E'')$
		965[c] s, bd		
1009 vs P				
1028 vs Q	1026 vs, bd	1027 vs	I≈II≈III	$\nu_{10}(E')$
1051 vs R				
		1078 m	I	$\nu_5(A_2')$
		≈1096[d] vw, bd	I≈II≈III	$\nu_{10}+\nu_{R_z}(E')$
		≈1124[d] vw, bd	I≈II≈III	$\nu_{10}+\nu_{(R_x,R_y)}(A_1''+A_2''+E'')$
	≈1129 vw, sh	1133 m	I	$\nu_4(A_1'')$
	1191 m, bd	1189 m	II	$\nu_{13}(E'')$ and $\nu_3(A_1')$
		1200 m	I>III	
		≈1270–75 vvw, pd		$\nu_3+\nu_{T_z}$
1422 m, sat P		1424 m	II	
1442 m, Q	1432 s	1434 s	III>I	$\nu_9(E')$
1455 m, sat R				
	1453 w, sh	1449 m	II	$\nu_2(A_1')$
		1459 w	III	
	1504 m, sh, bd	1496 vw, sat	I≈II≈III	$2\nu_{14}(E')$
		≈1509[b] vvw pd	I≈II≈III	$\nu_2+\nu_{(T_x,T_y)}(E')$
		≈1513[c] vvw pd		
		1518 m	II>III	$2\nu_{14}(A_1')$
		1532[b] w, sat	II≈III	$\nu_2+\nu_{T_z}(A_2'')$
		1538[c] w		
		1600 w	I>II≈III	$\nu_7+\nu_{14}(E')$
		1714 m, sh	II>III	$2\nu_7(A_1')$
1740 w	1725 s	1724 s	I≈II≳III	$2\nu_{11}(A_1'+E')$
1776 w	1764 m	1774 w	II≈III≫I	$\nu_{10}+\nu_{14}(A_1''+A_2''+E'')$
		1786 m		
		1812 vw, sat	II≈III>I	$\nu_5+\nu_{14}(E'')$
1881 m	1882 s	1883 s	I≈II≈III	$\nu_{10}+\nu_{11}(A_1'+A_2'+E')$
		1894 s, sh	I	
	1918 w	1923 m	I>II≳III	$\nu_5+\nu_{11}(E')$
	2040 m	2035 m, sh	I≈II≈III	$\nu_7+\nu_{13}(E')$
		2049 m	II>III>I	$\nu_{11}+\nu_{13}(A_1''+A_2''+E'')$
2058 m, sh P		2083 s	II≈III	
2083 m Q	2082 s	2091 m, sh	I	$\nu_5+\nu_{10}(E')$
2102 m, sh R				
		2126 vw	II>III	$2\nu_5(A_1')$
2183 w	2169 m	2172 w	II≳III	$\nu_9+\nu_{14}(A_1''+A_2''+E'')$
	2209 w, sat	2196 m	II>III	$\nu_2+\nu_{10}(E')$
		2206 m	I	
		2217 w, sh	II≳III	$\nu_{10}+\nu_{13}(A_1''+A_2''+E'')$

TABLE I (*continued*)

Vapor (cm^{-1})	Liquid (cm^{-1})	Crystal (cm^{-1})	Polar.	Assignment
2314 w	2304 w	2294 w	I≈II≈III	$\nu_9+\nu_{11}(A_1'+A_2'+E')$
		2311 w 2319 w	II≈III I	$\nu_2+\nu_{11}(E')$ *or* $\nu_4+\nu_{13}(E')$
	2372 vw	2370 vw	I≈II≈III	$2\nu_{13}(A_1'+E')$
2456 vw	2450 w	2444 m 2456 m	I>II>III I>II>III	$\nu_9+\nu_{10}(A_1'+A_2'+E')$ $\nu_2+\nu_{10}(E')$
	2486 m	2487 m	II>I≈III	$\nu_5+\nu_9(E')$
	2518 w	2523 w 2540	I≈III II	$\nu_{10}+2\nu_{14}(A_1'+A_2'+2E')$
2612 w	2610 m	2608 m	I≈II≈III	$\nu_3+\nu_9(E')$
		2726 vw	I≈II≈III	$\nu_{10}+2\nu_{11}(A_1'+A_2'+2E')$
2862 w, sh	2859 s	2855 m	II>I≈III	$2\nu_9(A_1'+E')$
2875 w, sh	2870 s	2877 m	II>I≈III	$\nu_2+\nu_9(E')$
2921 m, sat	2928 s	2934 s	I≈II≈III	$\nu_9+2\nu_{14}(A_1'+A_2'+2E')$
3003 vs, pd *P* 3025 vs *Q* 3048 vs, pd *R*	3013 vs	3004 vs	I≈II≈III	$\nu_8(E')$ *and* $\nu_1(A_1')$
3101 s, sat *Q* 3120 s, sat *R*	3081 vs	3073 vs	II≈III>I	$\nu_6(A_2'')$ *and* $\nu_{12}(E'')$
	3178 vw, sh	3168 m, sat	I≈III>II	$\nu_3+2\nu_{11}(A_1'+E')$
3805 vs	3814 w, sat	3824 m, sat	I≈II≈III	$\nu_6+\nu_{14}(E')$ *or* $\nu_{12}+\nu_{14}(A_1'+A_2'+E')$
3892 vw	3874 m	3863 m	I>II≈III	$\nu_1+\nu_{11}(E')$ *or* $\nu_3+\nu_{11}(A_1'+A_2'+E')$
	3929 w, sat	3918 m	I>II≈III	$\nu_7+\nu_{12}(E')$
4206 w, sat	4201 m	4194 m	II≈III>I	$\nu_3+\nu_8(E')$ *and* $\nu_3+\nu_{13}(A_1''+A_2''+E'')$
4281 w	4276 m	4264 s	I≈II≈III	$\nu_6+\nu_{13}(E')$ *or* $\nu_{12}+\nu_{13}(A_1'+A_2'+E')$
4522 w	4517 s	4510 m	II≈III≫I	$\nu_9+\nu_{12}(A_1''+A_2''+E'')$
		4560 m, sh	II≈III	$\nu_2+\nu_6(A_2'')$ *and* $\nu_{12}+2\nu_{14}(A_1''+A_2''+2E'')$
	4621 vw	4614 w, sh	II≈III	$\nu_6+2\nu_{14}(A_1''+A_2''+2E'')$

[a] Translatory and rotatory lattice modes are denoted ν_T and ν_R, respectively. The molecular directions with which the motions are associated are included in the subscript. Symbols: vs=very strong; s=strong; m=medium; w=weak; vw=very weak; vvw=very, very weak; bd=broad; pd=poorly defined.

[b] Appears only in the spectrum taken at −160°C.

[c] Appears only in the spectrum taken at −190°C.

[d] Appears at both temperatures, but is too poorly defined for precise measurement.

Parenthetically, we note that comparison between the unpolarized spectra of the 0*kl* crystal and of the polycrystal indicates no significant difference in the relative intensities of the axis II and axis III bands between the two specimens. As the polycrystal is assumed to be a random arrangement of crystallites, this indicates that the cross-sectional plane of the 0*kl* crystal was probably very nearly the 011 face. However, this has no bearing on the results of this investigation, and we will not press the point.

ASSIGNMENT OF BANDS

Previous investigations of the molecular vibrations of cyclopropane[4] have demonstrated satisfactorily that the symmetry of the isolated molecule is described by point group D_{3h}. The assignments have been made with ease and consistency, and no contradictory evidence has been found. The results of the present investigation are in complete accord with this, and hence the interpretation of the data has been carried out under the assumption of D_{3h} symmetry for the isolated cyclopropane molecule.

The molecule has 21 normal modes of vibration, of which seven are degenerate, leaving only fourteen distinct frequencies. The modes are distributed among the irreducible representations of D_{3h} as follows: $3\ A_1'+1\ A_1''+1\ A_2'+2\ A_2''+4\ E'+3\ E''$. Only the A_2'' and E' modes are allowed in the infrared. The E' modes are allowed also in the Raman effect, as are the A_1' and E'' modes. The A_1'' and A_2' modes are not active in

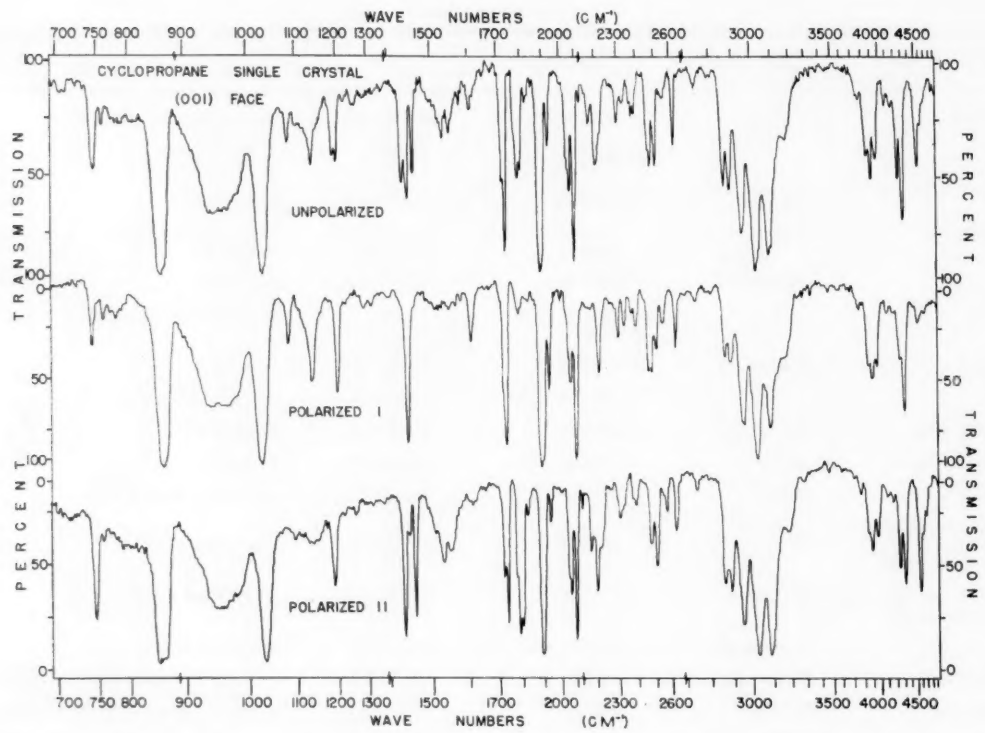

FIG. 2. Infrared spectra of a major crystallographic plane of cyclopropane single crystal (at −190°C). This cross section is tentatively identified as the *bc* plane, with polarization I corresponding to the *b* axis.

TABLE II. The fundamental vibrations of cyclopropane.[a]

Mode	Species	Motion	Vapor (cm^{-1}) Raman	Vapor (cm^{-1}) IR	Liquid (cm^{-1}) Raman	Liquid (cm^{-1}) IR	Crystal (cm^{-1}) IR
ν_1	A_1'	C—H stretch	3038	*f*	3027		
ν_2	A_1'	CH_2 deformation	1454	*f*	1453	1453	1454
ν_3	A_1'	Ring breathing	1188	*f*	1188	1191	1194
ν_4	A_1''	CH_2 twist	*f* (1133)	*f*	1131	1129	1133
ν_5	A_2'	CH_2 wag	*f*	*f*			1078
ν_6	A_2''	C—H stretch	*f*	3101		3081	3073
ν_7	A_2''	CH_2 rock	*f*	852			855
ν_8	E'	C—H stretch	3020	3025	3009	3013	3004
ν_9	E'	CH_2 deformation	1442	1442	1434	1432	1434
ν_{10}	E'	Ring deformation		1028	1023	1026	1027
ν_{11}	E'	CH_2 wag	866	866	866	865	865
ν_{12}	E''	C—H stretch	3082	*f*	3075		3073
ν_{13}	E''	CH_2 twist	1188	*f*	1178	1191	1200
ν_{14}	E''	CH_2 wag	739	*f*	741	741	749

[a] Note: Raman and parenthesized data are from references 4(a) and 4(c); infrared data are from this work. Bands forbidden in the vapor are denoted by the letter *f*.

either infrared or Raman effect. The modes are listed and described in Table II, and will now be discussed in detail, beginning with the infrared-allowed modes.

E' Modes

The four degenerate modes ν_8, ν_9, ν_{10}, and ν_{11} appear in the infrared spectrum of the vapor. The present work locates their Q branches at 3025, 1442, 1028, and 866 cm^{-1}, in agreement with results reported by Baker and Lord[4a] and by Herzberg.[4d] In the liquid the bands appear, broader and more intense, at 3013, 1432, 1026, and 865 cm^{-1}. In the crystal the bands are much sharper and splitting is observed in at least one band, ν_9. The ν_8, ν_{10}, and ν_{11} bands are found in the crystal at 3004, 1027, and 865 cm^{-1} and appear on all three axes, while the ν_9 mode appears as a doublet at 1434 and 1424 cm^{-1}, the former component on axes I and III, the latter on axis II.

A_2'' Modes

The two parallel modes ν_6 and ν_7 appear in the infrared spectrum of the vapor. Their Q branches are found by this work at 3101 and 852 cm^{-1} (the latter a sharp subsidiary Q branch in the midst of the ν_{11} band), in agreement with results reported by Lord. In the liquid ν_6 appears, intensified, at 3081 cm^{-1}, but ν_7 is completely hidden by the strong and broad ν_{11} band. In the crystal ν_6 is found at 3073 cm^{-1} and ν_7 at 855 cm^{-1}. Both bands are severely overlapped by others (ν_6 by ν_{12} and ν_7 by ν_{11}), but the shape of the lower band indicates that ν_7 appears on axes II and III but only weakly, if at all, on axis I. Its polarization tends to confirm the correctness of the assignment of this mode by Baker and Lord. The 3073 cm^{-1} band is significantly less intense on axis I than on axes II and III, but the coincidence of the ν_{12} band prevents complete polarization.

E'' Modes

The degenerate modes ν_{12}, ν_{13}, and ν_{14} are not allowed in the infrared under D_{3h} selection rules. They have been located in the Raman effect in the vapor by Mathai, Shepherd, and Welsh[4c] at 3082, 1188, and 739 cm^{-1}, and two of them in the liquid as well (ν_{12} at 3075 cm^{-1}, ν_{14} at 741 cm^{-1}) by both Welsh and Lord. We see no evidence of these bands in the infrared spectrum of the vapor, but ν_{13} and ν_{14} are definitely observed in the liquid, at 1191 and 741 cm^{-1}. In the crystal, ν_{14} appears as a triad at 742, 747, and 756 cm^{-1}, the first component on axis I, the second on axis II, and the third on axis III. The ν_{13} mode appears as a doublet at 1189 and 1200 cm^{-1}, the former on axis II and the latter on axes I and III, although the coincident ν_3 mode may add some contribution to this band in both liquid and crystal. However, the appearance of this mode on three orthogonal axes offers confirmation of the correctness of its assignment by Welsh, since, as will be seen, the coincident ν_3 mode, being nondegenerate, could not so appear. The ν_{12} region, in the crystal as in the liquid, is almost coincident with the infrared-active ν_6 mode, but the apparent failure of the latter to polarize completely in the crystal may be attributed to the activation of the superimposed ν_{12} mode.

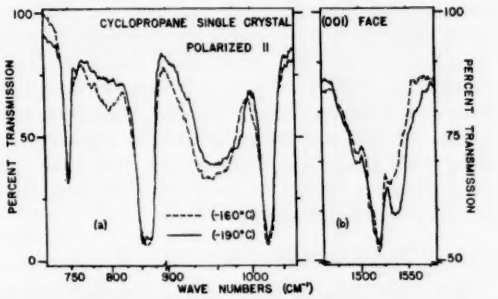

FIG. 3. Temperature effects in the infrared spectrum of cyclopropane single crystal. Note that parts (a) and (b) have different intensity scales.

A_1' Modes

The totally symmetric modes ν_1, ν_2, and ν_3 are not allowed in the infrared, but appear in the Raman effect. They have been located in the vapor by Welsh at 3038, 1454, and 1188 cm^{-1}, with ν_2 having been displaced from its expected 1475 cm^{-1} location by Fermi resonance with the nearby overtone 2 ν_{14}. In the liquid the bands are reported at 3027, 1453, and 1188 cm^{-1}. We do not detect these bands in the infrared spectrum of the vapor, but in the liquid the shoulder at 1453 cm^{-1} on the strong ν_9 band is probably due to activation of ν_2. In the crystal we observe a doublet at 1449 and 1459 cm^{-1}, the former on axis II and the latter on axis III, which must be the factor group components of ν_2. The ν_1 and ν_3 modes are both almost coincident with other bands (ν_1 with ν_8, ν_3 with ν_{13}), and their presence cannot be definitely confirmed in the infrared spectrum of either liquid or crystal.

A_1'' Mode

The ν_4 mode, not allowed in either Raman or infrared by D_{3h} selection rules, has been estimated by Lord at about 1125 cm^{-1}. Welsh reports an extremely weak band in the Raman effect at 1133 cm^{-1} in the vapor and 1131 cm^{-1} in the liquid which he ascribes to this mode (weakly activated in the vapor perhaps through Coriolis interactions). In the infrared spectrum of the liquid we detect for this mode a very weak shoulder at 1129 cm^{-1}. In the crystal we observe for ν_4 a sharp band of moderate intensity located at 1133 cm^{-1}, appearing on axis I only. The polarization of this band indicates the correctness of Lord's assignment for this mode.

A_2' Mode

The ν_5 mode is inactive in both Raman and infrared under D_{3h} selection rules, and heretofore had never

been located directly. Lord estimates its position at about 975 cm^{-1}, based largely on questionable assignments of two or three combination bands. In this investigation, a weak sharp band is found in the infrared spectrum of the crystal at 1078 cm^{-1}, appearing on axis I only, which would be very difficult to explain as anything other than the ν_5 fundamental. This band is not detected in the liquid because of the great breadth and intensity of the neighboring ν_{10} band.

Combinations of Molecular Modes

More than twice as many combination and overtone bands are observed in the infrared spectrum of the crystal as in the vapor. All bands detected in this investigation below 3500 cm^{-1}, and the most prominent ones above that point, are listed in Table I, along with their polarization behavior and our assignments for them. As the choice of possible assignments for most bands was not completely unambiguous, we have selected, wherever possible, those whose resultant species are infrared-active under D_{3h} selection rules and are qualitatively consistent with the observed polarization behavior. Where two assignments for a band are deemed equally satisfactory, both are given.

Two features of these assignments deserve further mention. One is the reassignment of those combination bands on which Baker and Lord based their estimate of the location of the ν_5 fundamental, in the light of our direct observation of this mode. For example, one of these bands, which had been assigned as $\nu_4+\nu_5$ (A_2''), we observe in the crystal as a doublet at 2082 and 2092 cm^{-1}, and we must reassign it as $\nu_5+\nu_{10}$ (E'). The others are also readily reassigned. Another interesting feature is the assignment of two distinct bands, at 1496 and 1518 cm^{-1}, as the overtone $2\,\nu_{14}$ ($A_1'+E'$). The A_1' component has been shifted to higher frequency and intensified by Fermi resonance with ν_2, but the frequency of the unaffected E' component indicates that the true location of $2\,\nu_{14}$ is at least 20 cm^{-1} above that of ν_2. This implies that the mixing of states between the two A_1' modes is far from complete, justifying our assignment of the bands at 1449 and 1459 cm^{-1} as being caused mainly by the fundamental ν_2. As for the other assignments, no serious inconsistencies arise; hence, we shall not discuss them further.

Combinations with Lattice Modes

The six external degrees of freedom of the cyclopropane molecule belong to the following irreducible representations of D_{3h}: $1\ A_2'+1\ A_2''+1\ E'+1\ E''$. These degrees of freedom of the isolated molecule become translatory and rotatory lattice modes when the molecule is placed in the crystal. Although the frequencies of these lattice modes themselves are well below the range of direct observation in this investigation, we do observe a number of bands arising from combinations of lattice modes with molecular fundamentals. These bands are markedly broader than the rest, and, furthermore, are the only ones to show significant frequency and intensity changes with temperature. At −160°C, the most prominent of these bands are located at about 937 and 960 cm^{-1}, while two others, much weaker, appear at about 797 and 776 cm^{-1}. These four bands are symmetrically arrayed in pairs on either side of ν_{11}, and are identified as sums and differences of that fundamental with lattice modes of approximately 70 and 92 cm^{-1}. The lower two (ν_{11}—70 and ν_{11}—92) show the diminished intensity relative to that of their corresponding sum bands that would be expected from the relative population of lattice modes in thermally excited states, as given by the Boltzmann factor. Furthermore, as seen in Fig. 3(a), the two difference bands show the expected marked decrease in intensity at the lower temperature (−190°C), almost to the point of vanishing. In addition, the sum bands shift to slightly higher frequencies (941 and 965 cm^{-1}, corresponding to lattice modes of about 74 and 97 cm^{-1}), indicating not surprisingly, that greater restraining forces act on the molecule at the lower temperature. Two other bands, located at about 1096 and 1124 cm^{-1}, largely obscured by the sharper but more intense ν_5 and ν_4 molecular modes (hence measurable only in polarized spectra not containing axis I), are identified as sums of the same lattice modes with ν_{10}. The corresponding differences would underlie the ν_{11} sum bands, and could account for their small decrease in intensity at the lower temperature.

We feel that these two lattice modes are rotatory in origin, as their appearance in the infrared in combination with E' fundamentals would not violate D_{3h} selection rules (while the appearance of one translatory mode in such combinations would). If this were the case, and if roughly the same force constant were involved in the two librations, then their frequencies would be inversely proportional to the square roots of the moments of inertia. The ratio of the frequencies of the two lattice modes is 1.31, while the ratio of the square roots of the two moments of inertia of cyclopropane is 1.26. Thus the lower of the two lattice modes (70 cm^{-1} at −160°C, 74 cm^{-1} at −190°C) is assigned tentatively to the A_2' libration, around the axis with the larger moment of inertia (the threefold axis), and the higher mode (92 cm^{-1} at −160°C, 97 cm^{-1} at −190°C) to the degenerate E'' libration.

The other bands which showed a marked temperature effect fall in the region just above 1500 cm^{-1}, but are much less well defined. One weak band appears at 1532 cm^{-1} at −160°C, and becomes more intense and shifts to 1538 cm^{-1} at −190°C [Fig. 3(b)]. This band, unlike the ones previously mentioned, polarizes sharply, appearing on axis II and perhaps axis III but hardly at all on axis I, and also is much farther (roughly 110 cm^{-1}) from the nearest E' band (ν_9). We therefore assign this band as the sum of ν_2 (A_1') with a lattice mode having a frequency of approximately 78 cm^{-1}

at −160°C and 84 cm^{-1} at −190°C. This lattice mode we believe to be of translatory origin, as the appearance of such modes in the infrared in combination with A_1' fundamentals would be allowed according to D_{3h} selection rules (which would not be the case for rotatory lattice modes), and its polarization indicates that it probably corresponds to the A_2'' translational degree of freedom of the molecule (perpendicular to the σ_h plane). Some additional evidence for this mode is provided by an extremely weak and poorly defined band, appearing in the 1270–1275 cm^{-1} region, which could be the sum of the same lattice mode with ν_3.

The one remaining temperature-dependent band, very weak and poorly defined, appears at about 1509 cm^{-1} at −160°C and at about 1513 cm^{-1} at −190°C on all three axes, and is identified as the sum of another lattice mode with ν_2. This mode, also translatory in origin, probably corresponds to the E' translational degrees of freedom of the molecule and is located at about 55 and 59 cm^{-1} at −160° and −190°C, respectively. No evidence for this mode is found elsewhere, and the poor quality of the one band in which it is found leaves its frequency somewhat uncertain. Nevertheless, this uncertainty notwithstanding, we have succeeded to an unusual degree in identifying systematically a complete set of the primary lattice modes of the cyclopropane crystal (Table III).

TABLE III. Primary lattice modes of the cyclopropane crystal.

Mode	Species	Type	Frequency (cm^{-1}) −160°C	−190°C
ν_{R_z}	A_2'	Rotatory	70	74
ν_{T_z}	A_2''	Translatory	78	84
$\nu_{(T_x,T_y)}$	E'	Translatory	55	59
$\nu_{(R_x,R_y)}$	E''	Rotatory	92	97

DETERMINATION OF THE CRYSTAL STRUCTURE

The molecule in the crystal is under the influence of a field determined by the geometrical arrangement of its neighbors. The symmetry of this field, described by the site group (which is a subgroup of both the molecular point group and the factor group of the crystal space group), is not in general the same as that of the isolated molecule. Thus bands which are not allowed in the infrared in the free molecule may become active in the crystal, depending on the mapping of their species into those of the site group and on the selection rules of the site group. The mapping of the site group species into the factor group (which describes the symmetry of the complete unit cell) can then show the distribution of the molecular modes on the crystal axes. When, as now, the crystal structure is unknown, subgroups of the molecular point group can be tested systematically for selection rules in accord with observations, and those that survive elimination can be further tested systematically within appropriate factor groups against the directional properties of individual absorptions, to identify space groups and details of structure that are required by the spectroscopic information. We shall limit our considerations to the behavior of molecular fundamentals only.

Identification of the Crystal System

Mention has already been made of the polarization behavior of the various components of molecular fundamentals in the crystal. Three of these appear along axis I only, four along axis II only, and two along axis III only. Furthermore, it is seen that these axes are independent of frequency, their directions having been determined initially in visible light. The existence of a set of crystal absorption bands, identified as factor group components of molecular fundamentals (notably the triad at 742, 747, and 756 cm^{-1}), such that each member of the set appears exclusively along a different one of three mutually perpendicular and frequency-independent axes, may be taken as presumptive evidence that the three directions coincide with the three major crystal axes, which are thus orthogonal and nonequivalent. Thus the cyclopropane crystal is shown to belong to the *orthorhombic* system. The factor group must therefore by isomorphous with an orthorhombic space group, and hence must be either C_{2v}, D_2, or D_{2h}, and no other. Furthermore, the observation of factor group splitting in at least one nondegenerate fundamental (ν_2) indicates that there are at least two molecules per unit cell.

Identification of the Site Group

We consider first the molecular modes which are not allowed activity in the infrared by D_{3h} selection rules:

1. At least one A_1' mode (ν_2) definitely appears in the infrared spectrum of the crystal. The subgroups of D_{3h} which allow activation of A_1' are C_{3v}, C_{2v} ($\sigma_h \rightarrow \sigma_v$), C_3, C_2, C_s (σ_h), and C_s (σ_v). Of these, C_{3v} and C_3 are not subgroups of the orthorhombic factor groups C_{2v}, D_2, and D_{2h}, and so cannot be site groups of the molecule in the crystal, and are discarded.

2. The one A_1'' fundamental (ν_4) also definitely appears. Of the subgroups which allow activation of A_1' in an orthorhombic crystal, only C_2, C_s (σ_h) and C_s (σ_v) also allow activation of A_1''.

3. The one A_2' fundamental (ν_5) also definitely appears, but this gives no additional information at this point.

4. At least two E'' modes (ν_{13} and ν_{14}) definitely appear, with components along each of the three orthogonal crystal axes. This eliminates C_s (σ_h) from consideration. Thus, based on the appearance of forbidden bands, the choice of possible site groups is restricted to only two, C_2 and C_s (σ_v).

The forbidden bands are observed also in the liquid, a fact which can be explained formally by a site of

TABLE IV. Correlation mapping.

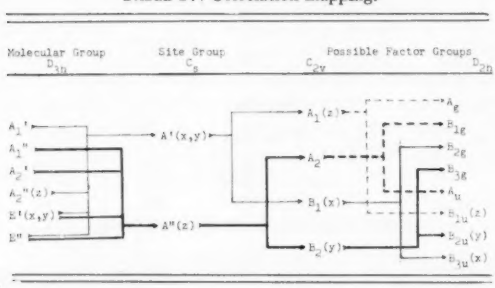

trivial symmetry C_1. This cannot be the site in the crystal, however, because of the polarization behavior of the bands, which we now consider:

1. The A_1' and A_2'' modes definitely appear along axes II and III, but not along axis I.
2. The A_1'' and A_2' modes definitely appear along axis I, but not along axes II and III.
3. The E' and E'' modes definitely appear along all three axes. The only site group whose mapping into an orthorhombic factor group (Table IV) would allow the A_1' and A_2'' modes to polarize together and oppositely from the A_1'' and A_2' modes, and allow the E' and E'' modes to appear on all three axes, is C_s (σ_v). Furthermore, with the site group uniquely determined as C_s (σ_v), we can eliminate D_2, which contains no reflection planes, as a possible factor group, leaving only C_{2v} and D_{2h}.

Mapping into the Factor Group; Splittings

The mapping of the molecular point group D_{3h}, through the site group C_s, into the factor group C_{2v} (Table IV), reveals that the A_1'' and A_2' modes, allowed infrared activity by the site group, are split by the correlation field (factor group splitting) into two components, one spectroscopically inactive and the other along the crystallographic axis perpendicular to the reflection plane of the site. This axis must correspond to axis I, the only experimental axis along which these modes are observed. Similarly, the A_1' and A_2'' modes may appear in the infrared in the crystal, but only along the other two axes (hence axes II and III), with the two components split by the correlation field. Finally, each degenerate E' or E'' mode, which has been split by the static field (site group splitting) into two components, is further split by the correlation field, with one site group component split into an inactive and an axis I component, the other into an axis II and an axis III component. With factor group D_{2h} the total number of factor group components is doubled (eight instead of four), but four of these belong to gerade representations of the factor group and are inactive in the infrared. The discussion regarding the species of factor group C_{2v} holds equally well for the four ungerade representations of D_{2h}.

Experimentally, we observe only four fundamentals for which correlation field splitting has been detected (Table I). Among these we find only one mode, ν_{14} (E''), for which all three infrared-active factor group components are resolved separately and distinctly. One of the others is the nondegenerate mode ν_2 (A_1'), for which separate axis II and axis III components are observed but which does not appear at all on axis I. For the remaining two modes, ν_9 (E') and ν_{13} (E''), the axis I and axis III factor group components coincide within the instrumental limits of detection (conservatively, about 2 cm^{-1}), an interesting situation because the axis I and axis III bands arise from different site group components, which had presumably been split by the static field at the site.

It is also noticed that all four modes show the same correlation field splitting (between axes II and III) of roughly 10 cm^{-1} ($\pm<1$ cm^{-1}), with the axis III component invariably the higher. Although we cannot observe the factor group splitting between the axis I and the inactive component, it is reasonable to believe that this splitting would be about the same as the other. The behavior of the degenerate bands indicates that the inactive component is the higher of the two in frequency, for then the disparity between ν_9 and ν_{13} on one hand the ν_{14} on the other (the frequency of the axis I component being higher than that of axis II in the former case and lower in the latter) can be explained by site group splittings whose values are roughly the same fraction of the frequencies of the fundamentals involved; i.e., about 10 cm^{-1} for ν_9 and ν_{13} and about 5 or 6 cm^{-1}, but opposite in sign, for ν_{14}. Were the inactive factor group component to be lower in frequency than the axis I component, it would be necessary for the site group splitting for ν_9 and ν_{13} to be essentially negligible while that for ν_{14} would be at least 15 cm^{-1}, a not impossible but certainly less attractive explanation. At any rate, we see here for cyclopropane, as has already been found for benzene[2d] (and contrary to earlier assumptions[2c]), that the splitting due to the correlation field is of the same magnitude as that due to the static field at the site.

Identification of the Space Group

The order of the factor group is equal to the product of the number of nonequivalent molecules per unit cell with the order of the site group. There are two symmetry elements in C_s, while C_{2v} and D_{2h} have four and eight, respectively. Thus, with a site group of C_s, there must be two translationally nonequivalent molecules in the primitive C_{2v} unit cell, and four in the primitive D_{2h} unit cell. For the respective nonprimitive structures, these numbers are multiplied by the number of equivalent positions (two for end-centered and body-centered arrangements, four for face-centered arrangements).

There are 22 space groups isomorphous with factor group C_{2v}, of which the first ten (in the Schoenflies

notation) are primitive. An inspection of crystallographic tables[13] reveals that numbers 3, 5, 6, 8, 9, 10, 13, 17, 19, and 21 do not contain reflection planes as sites, and can thus be discarded. Similarly, of the 28 space groups isomorphous with factor group D_{2h} (the first 16 being primitive), numbers 2, 4, 6, 8, 10, 14, 15, 22, 24, and 27 do not contain reflection planes as sites, and can be likewise discarded. We can carry the analysis no further on spectroscopic grounds alone, and are left with a rather large assortment of 30 possible space groups for the structure of the cyclopropane crystal.

We can make a reasonable and unique choice among these possibilities now if we assume that the molecules of cyclopropane are packed in the crystal as closely as their geometry allows, i.e., with the least possible unoccupied space consistent with the van der Waals radii of the hydrogens and methylene groups. Such packing would be expected for molecules having no permanent dipole or significant charge separation, the interactions between which might possibly require a looser packing. With other hydrocarbons close packing is the rule, and hence is hardly a daring assumption here, particularly in view of the fact that cyclopropane does not even have any π-bond electron clouds, whose interactions would otherwise also have to be considered. Furthermore, we also know that the density of the cyclopropane crystal is greater than the known density of the liquid, having observed that pieces of crystal sink to the bottom of the liquid during the melting process. Thus we propose that, of the 30 possible space groups, the best choice for the crystal structure of cyclopropane will be that one which yields the structure having the highest density and no choice can be accepted unless its density exceeds the known one for the liquid.

Against this criterion we have tested the 30 possible space groups. While we see no justification for discussing here the detailed examination of each individual space group, we do find that most of them require molecular arrangements which, for the known dimensions of the molecule ($r_{CC}=1.524$ A, $r_{CH}=1.08$ A, and $\angle HCH=120°$), and for reasonable values for the van der Waals radius of the hydrogens (say 1.1 to 1.3 A), would have densities significantly lower than that of liquid cyclopropane at the melting point (about 0.8 g/cc [14]). Such structures can be discarded without qualms. Furthermore, among the structures which do not yield densities significantly lower than that of the liquid (including, for example, C_{2v}^4, C_{2v}^7, D_{2h}^3, D_{2h}^{11}, and D_{2h}^{12}), we calculate the density of the arrangement given by space group C_{2v}^7 (P_{nm}) to be more than 5% higher than that given by any of the other space groups. This preferable structure, which is depicted in Fig. 4, we shall now briefly describe.

[13] R. W. G. Wyckoff, *The Analytical Expression of the Results of the Theory of Space Groups* (Carnegie Institute of Washington, Washington, D. C., 1930).

[14] G. Egloff, *Physical Constants of Hydrocarbons* (Reinhold Publishing Corporation, New York, 1940), Vol. II, p. 42.

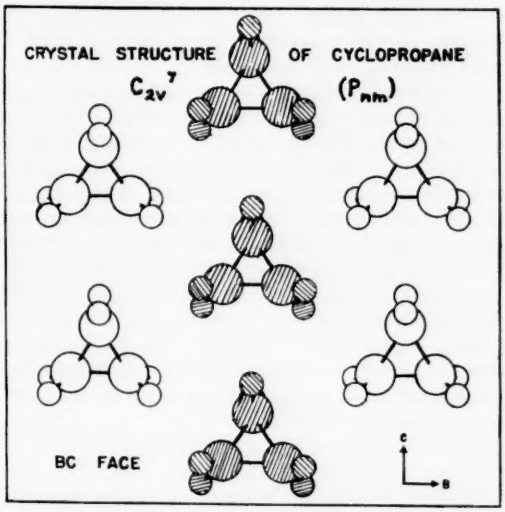

FIG. 4. Proposed crystal structure of cyclopropane, belonging to space group $C_{2v}^7(P_{nm})$. The shaded molecules are not in the same plane as the unshaded ones, and are inclined oppositely. This tilt is probably in the neighborhood of 10° to 15°. Note that the structure depicted could produce crystal cleavage planes which would appear optically to be nearly trigonal.

The structure required by space group C_{2v}^7 has two molecules in an orthorhombic unit cell, one at the corner and the other at the body center, and is primitive. The two molecules are situated at sites of C_s (the reflection plane coinciding with a σ_v plane of the molecule and lying in the *ac* crystallographic plane), but are tilted in opposite directions around the axis perpendicular to the reflection plane. This axis, which for best packing should be about 75% longer than the other two, is denoted axis *b* according to convention ($b>a$), while axis *c*, which is parallel to the twofold screw axis, is probably shorter than axis *a*. The angle between the plane of the cyclopropane ring and the *ac* plane which gives the closest packing is small but nonzero, and we place it between 10° and 15°.

The correspondence between this structure and the observed spectra is clear. Axis I, which is unique in some manner, being common to the cross-sectional plane of both single crystal specimens and the only one along which the A_1'' and A_2' modes appear, corresponds to the *b* axis, which is the longest of the three and perpendicular to the reflection plane. Also, inasmuch as the plane of the molecular ring is so close to the *bc* plane, and because of the similarity of the molecular motions involved, the correlation field splitting between the factor group components along the *a* and *c* axes can be expected to be in the same direction, and of roughly the same magnitude, as that between the inactive and the *b* axis components. This is consistent with observation, indicating the correspondence of axis II to the *c* axis, and of axis III to *a*, (and therefore of the so-called 001 face to the *bc* plane). Furthermore,

and for similar reasons, we would not expect to observe splitting of the degenerate lattice modes, which is again consistent with experiment.

An optical investigation of the cyclopropane crystal (among others) was carried out by Wahl.[7] He found that the crystal displays two distinct cleavage systems, one apparently rhombohedral, the other orthorhombic. As can be seen from Fig. 4, the crystal structure which we propose can readily give rise to both types of cleavage systems. Furthermore, it is evident that Wahl's description of the crystal as orthorhombic but pseudotrigonal is quite apt here, with axis a being the pseudotrigonal axis and the ratio of the lengths of axes b and c being rather nearly $\sqrt{3}$. Thus, the C_{2v}^7 structure herein proposed is consistent with the only independent information we have been able to locate on the structure of the cyclopropane crystal.

CONCLUSION

We have been especially fortunate in the amount of new and significant information furnished by this investigation. The assignment of the normal modes of the cyclopropane molecule has been completed, and certain recent assignments made by Lord and by Welsh have been verified. All bands observed in the infrared spectrum of the crystal (and of the liquid as well) have been assigned. We have been able to characterize, with varying degrees of confidence, a complete set of the lattice modes of the molecule in the crystal. Also, both the static field and correlation field splittings were detected for four different molecular modes, both types of splittings appearing consistently alike in their magnitudes.

An analysis of the occurrences and polarizations of induced absorptions establishes uniquely both the crystal system as orthorhombic and the symmetry of the molecular sites as C_s (the plane coincident with σ_v of the molecule). Further, we have been encouraged by the number, variety, and consistency of these findings to attempt a tentative determination of the complete crystal structure, belonging to space group C_{2v}^7. Pending a conclusive determination through x-ray diffraction, we feel this to be the most reasonable structure for the cyclopropane crystal.

The spectroscopic behavior of this substance appears completely in accord with the general theory of vibration spectra in molecular crystals.

ACKNOWLEDGMENTS

This research was supported in part by a grant from The Petroleum Research Fund administered by the American Chemical Society. Grateful acknowledgment is hereby made to the donors of said fund. The partial support of this investigation by funds provided by the Signal Corps, Department of the Army is also gratefully acknowledged. Finally, we wish to express our appreciation to the Socony-Mobil Oil Company and to the United States Rubber Company, for providing one-year research fellowships to two of us (C.B. and J.B.) during the course of this research project.

Motions of Molecules in Condensed Systems. XI. Infrared Spectrum and Structure of a Single Crystal of Ethylene

CHARLES BRECHER AND RALPH S. HALFORD

Department of Chemistry, Columbia University, New York 27, New York

(Received January 13, 1961)

The infrared absorption spectra of thin sections of single crystals of ethylene have been recorded in the frequency range between 650 and 3600 cm^{-1}, using polarized infrared radiation. Comparisons are made with similarly recorded spectra of the liquid and vapor phases. A complete assignment of the absorption bands is given. The frequencies of some primary lattice modes of the molecule in the crystal, and of some inactive molecular modes, are inferred from combinations. The ethylene crystal is found spectroscopically to be monoclinic (C_{2h}) or orthorhombic (D_{2h}), with the molecules located at sites of C_i symmetry. Using the known lattice of the carbon atoms, a molecular arrangement, described by space group $P\ 2_1/n$ (C_{2h}^5), is derived as the true crystal structure.

INTRODUCTION

SPECTROSCOPIC investigations have been quite successful at increasing our knowledge of structure, motion, and molecular interactions in the solid state.[1] Ethylene is admirably suited for such an investigation. The D_{2h} symmetry of the molecule, and the molecular dimensions, have been reasonably well established by both spectroscopic[2] and electron diffraction[3] investigations. A complete assignment of the normal modes of vibration of the molecule exists, and there is a reasonable expectation that the stringent selection rules of this highly symmetrical molecule might be at least partially relaxed in the crystal, resulting in induced absorption by modes forbidden in the vapor. Prior thermodynamic studies[4] have demonstrated the absence of a phase transition in the solid state, and considerable, but by no means complete, information is available on the crystal structure.[5,6]

We report here the results of an investigation of the absorption of polarized infrared radiation by crystalline ethylene. Our findings add to knowledge of the crystal structure as well as to various aspects of general knowledge concerning the solid state.

EXPERIMENTAL

All experiments in this investigation were conducted using Phillips research-grade ethylene,[7] having a nominal purity of better than 99.9%, which had been subjected, during the course of the experimentation, to five additional fractional distillations. Vapor spectra of this material, contained at a pressure of 250 mm Hg in a cell having a path length of 10 cm, revealed no evidence of absorptions that could be attributed to the presence of any impurity.

The crystal specimens were semicircular cross sections, having an area of about 150 mm^2 and a thickness of about 0.05 mm, and were grown in an apparatus designed especially for the production and growth of single crystals in the liquid nitrogen temperature region.[8] Three crystal specimens were grown and investigated spectroscopically. Two of these were developed from seeds which had been produced through the controlled flow of vapor into the cold cell. Technical difficulties made it necessary to complete the growth of the full-size specimens from these seeds by feeding material from the liquid state. The third specimen was produced through the spontaneous recrystallization of a polycrystalline mass held within three degrees of the melting point for 24 hr. The specimens were clear and transparent, and extinguished very sharply between crossed polaroids in white light. A polycrystalline sample, produced through the rapid feed of vapor into the cold cell, and a liquid sample, produced and contained in the same cell used for the crystals, were also investigated.

The spectra were recorded using a Perkin-Elmer model 12B instrument, equipped with Nernst glower and Golay detector, modified for double-beam operation so as to permit direct recording of relative transmission.[9] A NaCl prism was used in the spectral range between 650 and 1350 cm^{-1}, and a CaF_2 prism between

[1] For example, cyclopropane: C. Brecher, E. Krikorian, J. Blanc, and R. S. Halford, J. Chem. Phys. **35,** 1097 (1961), preceding paper. References to other works are given therein.

[2] (a) Early work summarized by G. Herzberg, *Infrared and Raman Spectra* (D. Van Nostrand Company, Inc., Princeton, New Jersey, 1945), p. 325ff; (b) D. H. Rank, E. R. Shull, and D. W. Axford, J. Chem. Phys. **18,** 116 (1950); (c) R. L. Arnett and B. L. Crawford, Jr., *ibid.* **18,** 118 (1950); (d) B. L. Crawford, Jr., J. E. Lancaster, and R. G. Inskeep, *ibid.* **21,** 678 (1953); (e) T. Feldman, J. Romanko, and H. L. Welsh, Can. J. Phys. **34,** 737 (1956); (f) R. C. Golike, I. M. Mills, W. B. Person, and B. L. Crawford, Jr., J. Chem. Phys. **25,** 1266 (1956); (g) J. Romanko, T. Feldman, E. J. Stansbury, and A. McKellar, Can. J. Phys. **32,** 735 (1954); (h) H. C. Allen and E. K. Plyler, J. Am. Chem. Soc. **80,** 2673 (1958); (i) J. M. Dowling and B. P. Stoicheff, Can. J. Phys. **37,** 703 (1959).

[3] (a) L. Pauling and L. O. Brockway, J. Am. Chem. Soc. **59,** 1223 (1937); (b) L. S. Bartell and R. A. Bonham, J. Chem. Phys. **27,** 1414 (1957); **31,** 400 (1959).

[4] C. J. Egan and J. D. Kemp, J. Am. Chem. Soc. **59,** 1264 (1937).

[5] W. Wahl, Proc. Roy. Soc. (London) **A89,** 327 (1913).

[6] (a) W. H. Keesom and K. W. Taconis, Physica **2,** 463 (1935); (b) C. W. Bunn, Trans. Faraday Soc. **40,** 23 (1944).

[7] Phillips Petroleum Company, Inc., Bartlesville, Oklahoma.

[8] E. Krikorian and R. S. Halford (to be published). See also E. Krikorian, Ph.D. dissertation, Columbia University (1956); M. Gershenzon, Ph.D. dissertation, Columbia University (1956).

[9] A. Savitzky and R. S. Halford, Rev. Sci. Instr. **21,** 203 (1950).

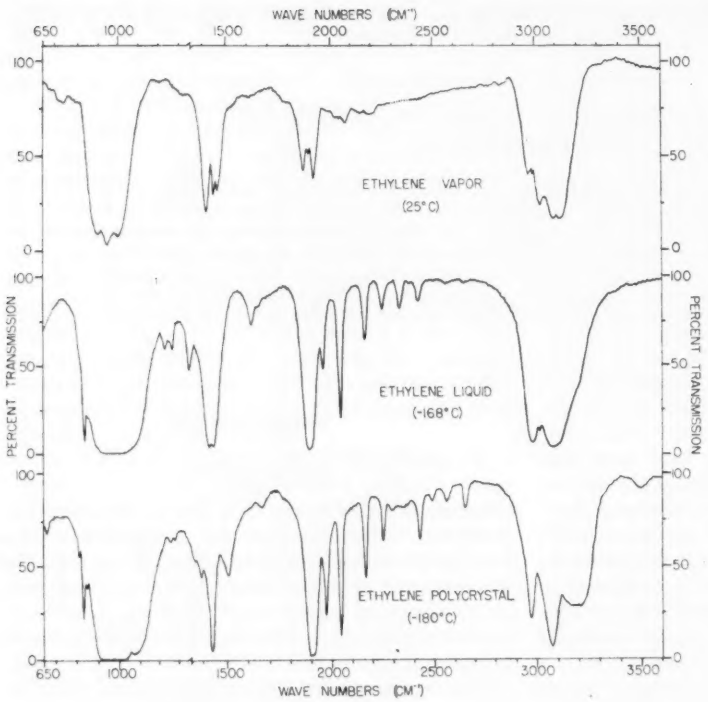

FIG. 1. Infrared spectra of ethylene vapor (at 25°C), liquid (at −168°C), and polycrystal (at −180°C), recorded with equivalent absorbing paths.

1350 and 3600 cm^{-1}. The spectrometer was further modified by the addition of a linear frequency drive,[10] consisting of a simple analog computer circuit which causes a servo motor to drive the monochromator at the controlled varying rate of speed necessary to compensate for the nonlinear dispersion of the prism used, so as to present a spectrum linear in frequency to within 5 cm^{-1}. A simple calibration chart can be consulted when it is desired to read off frequencies with the usual precision.

The polarizer used was a stack of eight sheets of AgCl inclined at the Brewster angle and fixed within an adjustable cylinder.[11] It was aligned in each case so that the plane of the electric vector of the radiation would be parallel to one of the two extinction axes of the crystal that had been determined visually.

Spectra of the three single crystals, at −180°C, were recorded in unpolarized light, and with the light polarized along each of the two crystal extinction axes, in turn. Slit schedules were adjusted to produce a noise-to-signal ratio of about 2%. All spectroscopic observations were repeated, and the requisite spectrometric blanks recorded. Unpolarized spectra of the polycrystal (at −180°C), liquid (at −168°C), and vapor (at 25°C and equivalent absorbing path), were similarly recorded.

[10] C. Brecher and R. S. Halford (to be published).
[11] E. Charney, Ph.D. dissertation, Columbia University (1956).

SPECTRA

The infrared spectra, for equivalent absorbing paths, of ethylene vapor at 25°C, ethylene liquid at −168°C, and polycrystalline ethylene at −180°C, are shown in Fig. 1. Eight absorption bands are observed in the spectrum of the vapor, 20 in the liquid, and 29 in the crystal. As expected, bands present in the vapor are intensified in the liquid and crystal and are much sharper in the latter, but the bands shift very little in frequency (in the order of 1%) among the three phases.

Figure 2 shows three spectra for a single crystal specimen at −180°C, one taken with the light unpolarized, and the others with the electric vector of the light polarized along the direction of first one, then the other, of the two perpendicular extinction axes of the crystal. A compilation of all infrared absorption bands of ethylene measured in this investigation, and our assignments for them, is provided in Table I.

Inasmuch as the spectra of only one of the three single crystal specimens is reproduced here, a few words are in order regarding the information obtained from the others. Highly important is the fact that the spectra for one of the two polarizer settings, denoted axis 1, are essentially identical in the three distinct specimens. Absorption frequencies and band shapes are the same from specimen to specimen, and intensities agree to better than 2%, which is within the instrumental noise level. This agreement is all the more

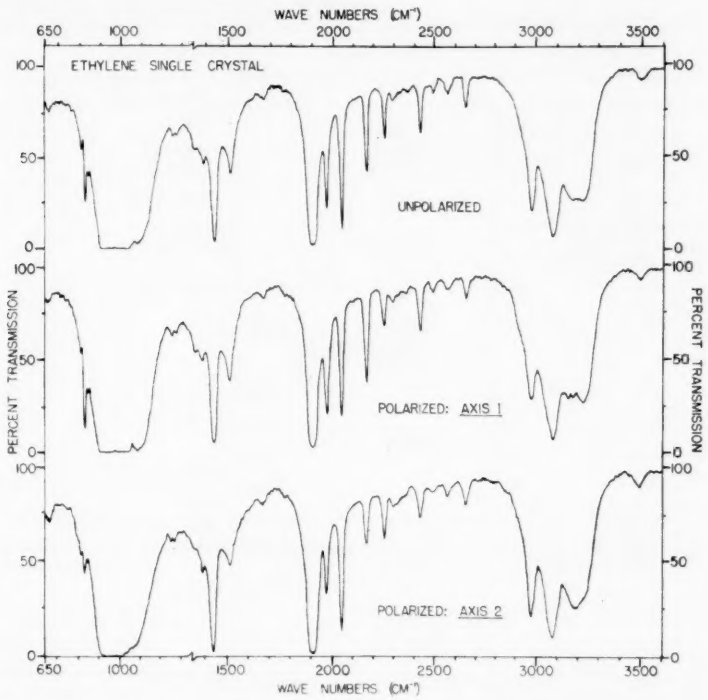

FIG. 2. Infrared spectra of a specimen of ethylene single crystal (at −180°C). This cross section contains the crystallographic *b*-axis, to which the axis 1 polarization corresponds.

noteworthy in view of the significant variations, from specimen to specimen, in the intensities and band shapes observed in the opposite (axis 2) polarizations.

All bands observed in the spectrum of the polycrystal appear in all spectra of all the single crystal specimens, which shows that no modes of the single crystal were in any case accidentally oriented so as to make their interaction with the infrared radiation geometrically impossible. Polarization effects are generally small and all bands show substantial absorption in each polarization, indicating that no transition moment is perpendicular to a crystal extinction axis. The behavior of the few bands displaying significant dichroism was investigated over a range of polarizer settings, and it was ascertained that the alignments of the polarizer which yielded the maximum dichroic effect coincided with the directions of the crystal extinction axes as determined in visible light. These directions are thus shown to be independent of frequency and hence crystallographically significant. Further discussion, however, will be deferred until after a detailed examination of the spectra, which now follows.

ASSIGNMENT OF BANDS

As already amply demonstrated by previous investigators,[2] and in accord with the results of the present work, the isolated ethylene molecule is planar, with a symmetry described by point group D_{2h}. The molecule has 12 normal modes of vibration, which are associated with the irreducible representations of D_{2h} in the following manner: $3A_g+1A_u+2B_{1g}+1B_{1u}+1B_{2g}+2B_{2u}+2B_{3u}$. The six gerade modes are allowed only in the Raman effect, and the A_u mode is spectroscopically inactive, while the five modes belonging to species B_{1u}, B_{2u}, and B_{3u} are allowed only in the infrared. (In the point group D_{2h}, as in all groups containing an inversion center, Raman and infrared activity are mutually exclusive.) No first overtones may appear in the infrared, and the only allowed combinations are those belonging to the three afore-mentioned B_{nu} species. The modes are listed and described in Table II, and will now be discussed in detail, starting with the infrared-active modes.

Ungerade Modes

The six ungerade fundamentals consist of $\nu_4(A_u)$, $\nu_7(B_{1u})$, ν_9 and $\nu_{10}(B_{2u})$, and ν_{11} and $\nu_{12}(B_{3u})$. All but ν_4 are active in the infrared in the vapor and have been measured by many investigators. In agreement with these earlier results, the present work locates the Q branches of ν_7, ν_{11}, and ν_{12} at 949, 2989, and 1444 cm^{-1}, respectively, and locates the band center (between the P and R branches) of ν_9, which has no absorption maximum for its Q branch, at 3105 cm^{-1}. Unfortu-

TABLE I. The infrared absorption bands of ethylene.[a]

Vapor[b] (cm^{-1})	Liquid[b] (cm^{-1})	Crystal[b] (cm^{-1})	Polar.	Assignment
		666 vvw, pd		?
		810 vw		$\nu_{10}-\nu_{Rx}$ (B_{1u})
	828 vs	826 m 828 s	2 1	ν_{10} (B_{2u})
		844 vw		$\nu_{10}+\nu_{Rx}$ (B_{1u})
896 vs, sat P 949 vs, Q 1005 vs, sat R	961 vs, bd	970 vs, bd		ν_7 (B_{1u})
		1083 vs, sat	1>2	$\nu_4+\nu_{Rz}$ (B_{1u}) or $\nu_4+\nu_{Ry}$ (B_{2u}) ?
	1221 vw 1239 band center 1257 vw			ν_6 (B_{1g})
		1260 vvw		$\nu_6+\nu_{Tx}$ (B_{2u}) ?
		1280 vvw		$\nu_3-\nu_{Tz}$ (B_{1u})
	1339 m			ν_3 (A_g)
		1364 vw	1>2	$\nu_{12}-\nu_{Rz}$ (B_{2u})
		1392 w		$\nu_3+\nu_{Tz}$ (B_{1u})
1417 s P 1444 s Q 1466 s, sat R	1428 vs 1437 band center 1446 vs	1436 vs 1440 vs	2 1	ν_{12} (B_{3u})
		1512 m	1>2	$\nu_{12}+\nu_{Rz}$ (B_{2u})
	1620 w			ν_2 (A_g)
	1658 vvw			$2\nu_{10}$ (A_g)
		1672 vvw		$\nu_2+\nu_{Tz}$ (B_{1u})
1867 m P 1889 m Q 1915 m R	1895 vs	1902 vs		$\nu_7+\nu_8$ (B_{2u})
	1962 m, sat	1969 s	1>2	$\nu_4+\nu_8$ (B_{2u})
2020 vvw P 2047 vvw Q 2074 vvw R	2043 s	2043 s		$\nu_6+\nu_{10}$ (B_{3u})
2140 vvw P 2167 band center 2194 vvw R	2167 w	2166 m	1>2	$\nu_2+\nu_{10}$ (B_{2u})
	2253 vw	2255 w	2>1	$\nu_4+\nu_6$ (B_{1u})
		2300 vvw		$\nu_3+\nu_7$ (B_{1u})
	2340 vw, pd			$\nu_3+\nu_4$ (A_u) ?
		2380 vvw, pd		$\nu_8+\nu_{12}$ (B_{1u})
	2434 vw	2434 w	1>2	$\nu_2+\nu_{10}$ (B_{2u})
		2498 vvw	1>2	$3\nu_{10}$ (B_{2u})
	2569 vvw	2568 vvw		$\nu_2+\nu_7$ (B_{1u})
	2659 vvw	2658 vvw		$\nu_6+\nu_{12}$ (B_{2u})
2967 m, sat P 2989 m, sat Q 3018 m, sat R	2983 vs	2973 s		ν_{11} (B_{3u})
	3016 vw, sat, pd			ν_1 (A_g)
3089 vs P 3105 band center 3121 vs R	3085 vs, bd	3075 vs, bd		ν_9 (B_{2u})
		3155 s, pd	1>2	$\nu_6+\nu_7+\nu_8$ (B_{2u})
		3180 s, pd	2>1	$\nu_4+\nu_6+\nu_8$ (B_{3u})
	3220 vw, sh	3221 s, pd	1>2	$\nu_3+\nu_7+\nu_8$ (B_{3u})
		3500 vvw, pd		$\nu_2+\nu_7+\nu_8$ (B_{3u})

[a] Translatory and rotatory lattice modes are denoted ν_T and ν_R, respectively. The molecular directions with which the motions are associated are included in the subscript.

[b] Symbols: vs=very strong; s=strong; m=medium; w=weak; vw=very weak; vvw=very very weak; bd=broad; pd=poorly defined.

TABLE II. The fundamental vibrations of ethylene.[a]

Mode	Species	Motion	Vapor (cm^{-1}) Raman	Vapor (cm^{-1}) IR	Liquid (cm^{-1}) Raman	Liquid (cm^{-1}) IR	Crystal (cm^{-1}) IR
ν_1	A_g	C—H stretch	3026	*f*	3019	3016	
ν_2	A_g	C—C stretch	1623	*f*	1621	1620	[1616]
ν_3	A_g	CH_2 deformation	1342	*f*	1340	1339	[1336]
ν_4	A_u	CH_2 twist	*f* (1027)	*f*			[≈1010?]
ν_5	B_{1g}	C—H stretch	3103	*f*	3075		
ν_6	B_{1g}	CH_2 rock		*f*	1236	1239	
ν_7	B_{1u}	CH_2 wag	*f*	949		961	970
ν_8	B_{2g}	CH_2 wag	950	*f*	943		
ν_9	B_{2u}	C—H stretch	*f*	3105		3085	3075
ν_{10}	B_{2u}	CH_2 rock	*f*	(810)		828	827
ν_{11}	B_{3u}	C—H stretch	*f*	2989		2983	2973
ν_{12}	B_{3u}	CH_2 deformation	*f*	1444		1437	1438

[a] Infrared data are from this work, with bracketed numbers inferred from combinations with lattice modes; Raman and parenthesized data are from the works of other investigators (see text). Bands forbidden in the vapor are denoted by *f*.

nately, due to the overlap of the intense ν_7 band nearby, we could not locate the band center of ν_{10} (which not only has no *Q* branch absorption maximum but also is the weakest of the infrared-active fundamentals), but it has been placed by others at 810 cm^{-1}.

In the liquid these bands are greatly intensified, the ν_7 band so much that it is essentially totally absorbing through a range of over 100 cm^{-1}. We measure the center of the ν_7 band at 961 cm^{-1}. The ν_{10} band, which can now be measured, appears at 828 cm^{-1}, while ν_9, ν_{11}, and ν_{12} are found at 3085, 2983, and 1437 cm^{-1}, respectively.

In the crystal, the ν_7 band is again extremely intense and broad, with its band center located at about 970 cm^{-1}. The ν_9 and ν_{11} modes appear at 3075 and 2973 cm^{-1}, respectively. Factor group splitting is detected for the remaining two modes, with ν_{10} appearing at 828 cm^{-1} along axis 1 and 826 cm^{-1} perpendicular to it, and ν_{12} appearing at 1440 cm^{-1} along axis 1 and at 1436 cm^{-1} perpendicular to it. The ν_{10} band is the only fundamental which displays any important dichroism, appearing always more intensely along axis 1 than perpendicular to it, although the latter intensities differed widely among the three crystal specimens.

The inactive mode ν_4 is not observed in the infrared spectrum of the vapor, but has been located by Arnett and Crawford[2e] at 1027 cm^{-1}. This mode cannot be measured in either liquid or crystal because of the overlap of the extremely intense ν_7 band, but has been tentatively located in the crystal at around 1010 cm^{-1} by inference from a questionable identification of a lattice mode combination.

Gerade Modes

The six gerade fundamentals ν_1, ν_2, and $\nu_3(A_g)$, ν_5 and $\nu_6(B_{1g})$, and $\nu_8(B_{2g})$ are not active in the infrared in the vapor. They have been located in the Raman effect (most recently by Feldman, Romanko, and Welsh[2e]) at 3026, 1623, 1342, 3103, 1236, and 950 cm^{-1}, respectively, all in the vapor except for ν_6 (which is too weak to be measured in the vapor and for which the frequency in the liquid is given). It should be noted that the frequencies of ν_5 and ν_8 almost coincide with those of the infrared-active modes ν_9 (3105 cm^{-1}) and ν_7 (949 cm^{-1}), making it impossible for us to draw any definite conclusions about their appearance or absence in the infrared spectra of the condensed phases. The situation of the ν_1 mode, sandwiched between two intense infrared-active modes only about 100 cm^{-1} apart, is not very promising either. However, the three remaining modes ν_2, ν_3, and ν_6 fall in regions in which infrared bands do not appear, hence the presence or absence of these gerade modes in the condensed phase spectra can be ascertained with confidence.

We definitely observe the three gerade modes ν_2, ν_3, and ν_6 in the infrared spectrum of the liquid, at 1620, 1339, and 1239 cm^{-1}. The bands are medium to weak in intensity, and fall in all cases within 3 cm^{-1} of the known Raman frequencies. The gerade overtone $2\nu_{10}$, in Fermi resonance with ν_2 is also detected, at 1658 cm^{-1}. Finally, and in spite of the overlapping of the intense ν_9 and ν_{11} bands on either side, we do detect a poorly defined band at about 3016 cm^{-1}, which must be the ν_1 fundamental. We therefore conclude that the liquid state definitely induces infrared activity of the gerade modes.

On the other hand, the gerade modes are definitely absent from the infrared spectra of the crystal. In no case can any trace of absorptions be found within 25 cm^{-1} of the frequencies at which these modes appear in the liquid, a range within which these modes must certainly fall in the crystal, particularly in view of their extremely small frequency shifts from vapor to liquid. Indeed, we have been able to locate two of these modes in the crystal, ν_2 at 1616 cm^{-1} and ν_3 at 1336 cm^{-1}, by inference from the identification of combinations with lattice modes. We must conclude that the crystalline state definitely does not induce infrared activity of the gerade modes, a highly important point which will be developed later in connection with the crystal structure.

Combinations of Molecular Modes

Only three binary combinations can be detected in the infrared spectrum of the vapor: $\nu_7+\nu_8(B_{3u})$ at 1889 cm^{-1}, $\nu_6+\nu_{10}(B_{3u})$ at 2047 cm^{-1}, and $\nu_3+\nu_{10}(B_{2u})$ at 2167 cm^{-1}. In the liquid, the number of combinations observed increases to 10 (including one assigned as a ternary sum), and in the crystal to 15 [including four ternary sums and the second overtone $3\nu_{10}(B_{2u})$]. All combinations are readily identifiable, and all belong to those D_{2h} species for which activity is allowed in the infrared. The few combinations that show any important dichroism in any of the specimens all belong to molecular species B_{2u} (to which also belongs ν_{10}, the only fundamental which polarizes strongly), but in no case does the polarization ever approach completeness. All bands detected in this investigation, along with our assignments for them, are listed in Table I.

Combinations with Lattice Modes

The external degrees of freedom of the ethylene molecule belong to the irreducible representations of point group D_{2h} in the following manner: The three translations to B_{1u}, B_{2u}, and B_{3u}, and the three rotations to B_{1g}, B_{2g}, and B_{3g}, respectively. Lattice modes, which are the counterparts in the crystal of these degrees of freedom of the isolated molecule, are expected at frequencies much too low for direct measurement in this investigation. However, combinations between these lattice modes and molecular fundamentals should fall within our range of measurement, and we do detect some bands attributable to such combinations. Two such bands, weak but quite sharp, are found at 810 and 844 cm^{-1}, symmetrically placed on either side of the ν_{10} band at 827 cm^{-1}, and are assigned as the difference and sum of a lattice mode of 17 cm^{-1} with the fundamental ν_{10}. Unfortunately, the sum band is greatly obscured by overlapping of the intense ν_7 band, preventing a meaningful comparison between its intensity and that of the difference band, but because of the low frequency of this vibration these two intensities should not be greatly different even at $-180°C$. This lattice mode must be rotatory in origin, probably the libration around the molecular figure axis (the B_{3g} libration), as the combination of such a gerade motion with the ungerade mode ν_{10} would be allowed activity in the infrared even according to the strict D_{2h} selection rules.

Another pair of lattice mode combinations are observed at 1364 and 1512 cm^{-1}, symmetrically arrayed about the ν_{12} band at 1438 cm^{-1}, and are identified as the difference and sum of that fundamental with a lattice mode of 74 cm^{-1}. The two agree in dichroic behavior (more intense along axis 1 than perpendicular to it), and the relative intensities of the two bands are consistent with the relative population of lattice modes in thermally excited states as given by the Boltzmann factor. As before, this lattice mode is also of rotatory origin, but in this case the libration is probably around the molecular axis of largest moment of inertia (the B_{1g} libration). Such combination with the B_{3u} mode ν_{14} would belong to the infrared-active B_{2u} species of group D_{2h}, and we observe polarization behavior consistent with other bands of this species.

Still another pair of lattice mode combinations are found at 1280 and 1392 cm^{-1}. In this case, however, there is situated between them, not an ungerade mode, but the gerade fundamental ν_3, which is forbidden and unseen. The bands are assigned as the difference and sum of this Raman-active fundamental with a lattice mode of 56 cm^{-1}, thus, by inference, locating ν_3 in the crystal at 1336 cm^{-1}, only 3 cm^{-1} below its location in the liquid. Here too, the relative intensities of the pair of bands are consistent with the Boltzmann factor. This lattice mode, unlike the previous two, must be of translatory origin (ungerade, probably B_{1u}), in order for its combination with the gerade mode ν_3 to be active in the infrared. A very weak absorption at 1672 cm^{-1} is identified as the sum of the same 56 cm^{-1} lattice mode with ν_2 (which has the same species, A_g as ν_3), thus locating ν_2 in the crystal, by inference, at 1616 cm^{-1}. The difference band is too weak to be observed.

Finally, there are two more bands which are identified as lattice mode combinations, but their assignments are much more uncertain. One band, at 1083 cm^{-1}, must be the sum of $\nu_4(A_u)$ with a rotatory (gerade) lattice mode. Unfortunately, both the difference band and the fundamental itself are completely hidden by the extremely intense ν_7 band centered at 970 cm^{-1}, and neither can be measured. If the same 74 cm^{-1} rotatory lattice mode that has been found previously is also involved here, we can infer the frequency of ν_4 in the crystal to be in the neighborhood of 1010 cm^{-1}. However, the B_{2g} libration, not previously found, is also a possibility here, as the resultant species of the combination, B_{2u}, would be consistent with the observed polarization behavior. The remaining possible lattice mode combination appears at 1260 cm^{-1}, and is probably the sum of ν_6 with a translatory (ungerade)

lattice mode of about 24 cm^{-1}. However, as the difference band is too weak to be observed and the fundamental is not active in the infrared, we have used the frequency of the fundamental in the Raman effect in the liquid, so the true value of this lattice mode is quite uncertain.

An unusual feature is observed in the infrared spectrum of the liquid. Two bands show a peculiar doubling effect, the ν_{14} band with components at 1428 and 1446 cm^{-1}, 9 cm^{-1} on either side of the band center, and the ν_6 band with components at 1221 and 1257 cm^{-1}, 18 cm^{-1} on either side of the band center. This structure, which is not observed in the spectrum of the liquid at a higher temperature, may be associated with the persistence of quasi-lattice modes in the liquid just above the melting point.

DETERMINATION OF THE CRYSTAL STRUCTURE

The spectroscopic selection rules which an isolated molecule obeys are determined by the symmetry of the molecule itself. Similarly, the selection rules which govern the individual molecule in the crystal are determined by the static symmetry of the field caused by its surroundings, described by the site group. The refined rules, involving the dynamic interactions of the molecule with its neighbors, are determined by the symmetry of the complete unit cell, described by the factor group. The spectra of the crystal thus contain considerable information about its structure.

Identification of the Crystal System

We have already made note of the sharpness of the crystal extinctions as determined in visible (white) light, and of the important fact that the directions of the crystal extinction axes so determined were, for all absorption bands showing significant dichroism, the directions yielding the maximum dichroic effect, which was true for all three single-crystal specimens. We thus see that these directions are independent of frequency and crystallographically significant. Such a situation, of course, would not occur for any arbitrary cross section of any arbitrary crystal. The directions of the perpendicular extinction axes would be independent of frequency only if they coincided with crystallographically significant directions. This, in turn, could be true only if at least one crystal axis were perpendicular to the plane of the other two (i.e., monoclinic or higher symmetry), and then only if this axis were contained in the cross-sectional plane of the crystal specimen.

In line with this, we have previously noted that the spectra of the so-called axis 1 polarizations were the same for all three specimens, in spite of the significant differences in the polarizations perpendicular to that axis. Thus axis 1 is seen to coincide with a crystal axis contained in the cross-section plane of all three specimens. This is supported by the observation of factor group correlation splittings, 4 cm^{-1} in $\nu_{12}(B_{3u})$ and 2 cm^{-1} in $\nu_{10}(B_{2u})$, between the two polarizations. The specimens, then, differ only in their orientation around that crystal axis, presenting to view different proportions of the other two axes. Furthermore, the fact that the so-called axis 2 polarizations differed from specimen to specimen demonstrates that there are two nonequivalent crystallographic directions perpendicular to axis 1, and hence the crystal is not uniaxial. Therefore, the ethylene crystal belongs to either the orthorhombic or the monoclinic system.

Identification of the Site Group

The site group is a subgroup both of the molecular point group and of the factor group of the crystal space group. To determine the site group for ethylene, we first recall that not the slightest trace of any Raman-active gerade molecular fundamentals can be observed in the infrared spectra of the crystal. This is highly significant, in view of the definite presence of absorptions corresponding to these modes in the infrared spectrum of the liquid (in which the site has, of course, only the trivial symmetry C_1). Thus the site of the molecule in the crystal must have inversion symmetry, as only in such a case would the appearance of these modes in the infrared be forbidden. The only subgroups of the molecular point group D_{2h} which contain a center of inversion are C_{2h} and C_i, and these are the only ones which we shall consider further. This, in turn, limits the choice of possible factor groups to only two, C_{2h} (monoclinic) and D_{2h} (orthorhombic), as these are the only monoclinic or orthorhombic factor groups containing sites having a center of inversion.

The site group is fixed uniquely by other observations. Firstly, as determined from the polycrystal, no crystal bands are absent from the spectra of any of the single crystal specimens. Secondly, no bands polarize completely; that is to say, all crystal absorptions show significant contributions both along, and perpendicular to, axis 1 (which coincides with a crystallographic axis). As seen from the mapping of the molecular point group D_{2h}, through the site group C_{2h}, into the factor groups C_{2h} and D_{2h} (Table III), one of the infrared-active molecular species is allowed to appear only along one crystal axis, along which the other two are forbidden, and conversely. The appearance together of all three species of infrared-active molecular modes both along, and perpendicular to, any crystal axis, is forbidden. As this situation is decidedly at variance with our observations, we must reject C_{2h} as a possible site group. The mappings through site group C_i, on the other hand, show that the appearance of all infrared-active molecular modes is allowed on all three crystal axes. We therefore conclude that in the crystal of ethylene, the molecules are located at sites having C_1 symmetry, and C_i alone.

TABLE III. Correlation mappings.

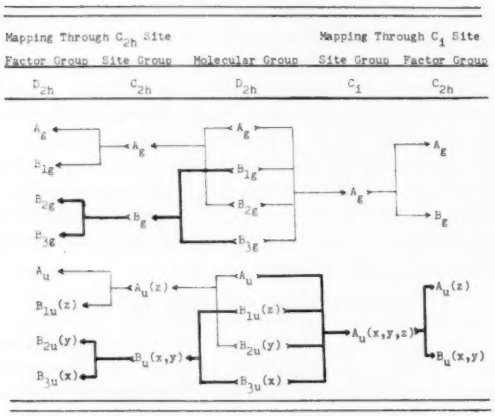

Identification of the Space Group

The order of the factor group is equal to the product of the number of molecules per primitive unit cell with the order of the site group. There are two symmetry elements in C_i, while the possible factor groups C_{2h} and D_{2h} have four and eight, respectively. Thus, with a site group of C_i, there must be two molecules in a primitive C_{2h} (monoclinic) unit cell, and four in a primitive D_{2h} (orthorhombic) unit cell. Either is consistent with observation of factor group splittings, previously mentioned, which indicates that the unit cell contains at least two molecules. The two possibilities cannot be distinguished further on purely spectroscopic grounds.

Fortunately, much useful information on the ethylene crystal is available from other sources. Bunn,[6b] through information obtained from x-ray diffraction,[6a] has given a description of the crystal structure of ethylene as defined by the lattice of the carbon atoms alone. This lattice is rectangular, with the unit cell dimensions at -175°C being: $a=4.87$ A, $b=6.46$ A, and $c=4.14$ A. There are two molecules per unit cell, one at the corner and the other at the body center. The molecular figure axis (carbon-carbon) is parallel to the ab plane for both molecules of the unit cell, making an angle of roughly 36° with the a axis. The two molecules tilt in opposite directions around the c axis, so the structure is primitive. Only the carbons were located experimentally, and the structure with respect to them alone is orthorhombic, P_{nnm} (D_{2h}^{12}). It was assumed, pending evidence to the contrary, that the hydrogens were arranged so that this symmetry of the carbon lattice would be maintained in the complete crystal structure. This structure is shown in Fig. 3.

Depending on the locations of the hydrogens, there are, however, three and (assuming no increase in the size of the unit cell) only three crystal structures that are all equally consistent with this known lattice of the carbons: P_{nnm} (D_{2h}^{12}), P_{nn} (C_{2v}^{10}), and $P2_1/n$ (C_{2h}^5). Our spectroscopic determination of the site symmetry C_i enables us to identify now the true crystal structure of ethylene. Both P_{nnm} (D_{2h}^{12}) and P_{nn} (C_{2v}^{10}), the two possible orthorhombic space groups, require the molecule to be located at sites other than C_i (the former requires a C_{2h} site, the latter a C_2 site), and hence must be rejected. Only in the structure $P2_1/n$ can the molecules be located at sites of inversion symmetry only. This structure can be obtained from the P_{nnm} structure simply by rotating the two molecules of the unit cell around their figure axes, in opposite directions. A reasonable estimate of this angle of rotation can be obtained by assuming that the intermolecular distances between one hydrogen and its two closest neighbors should be equal. Such an arrangement is certainly more acceptable physically, and yields more efficient packing, than that required by P_{nnm} (where the interhydrogen distance between neighboring molecules along the c axis is some 30% shorter than the next closest distance, between molecules along a body diagonal). The angle of tilt around the figure axis from the P_{nnm} position required to make the two closest interhydrogen distances equal is about 27°, and is equivalent to orienting the two molecules of the unit cell so that the plane of each molecule would be perpendicular to a body diagonal of the cell. This structure (Fig. 3), the rectangular lattice notwithstanding, is monoclinic. The b axis is the unique monoclinic axis, to which the experimental direction called axis 1 must obviously correspond.

It is worthy of note, at this point, that an earlier optical investigation of the crystal, carried out by Wahl,[5] indicated that the ethylene crystal does indeed belong to the monoclinic system, in agreement with our conclusions. We therefore may describe the true crystal structure of ethylene as "pseudo-orthorhombic," with a rectangular lattice (β, the monoclinic angle, being "accidentally" 90°), but not possessing higher than monoclinic symmetry in the complete unit cell, and belonging to space group $P2_1/n$ (C_{2h}^5).

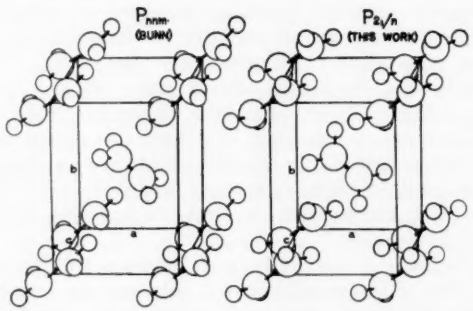

FIG. 3. Crystal structure of ethylene. Both structures depicted are consistent with available x-ray information, but only the structure on the right, belonging to space group $P2_1/n(C_{2h}^5)$, is consistent also with the results of this spectroscopic investigation.

CONCLUSION

This investigation increases our understanding of molecular crystals in general and of ethylene in particular. The infrared spectra of the ethylene crystal have been recorded in polarized radiation and compared with spectra for liquid and vapor. All bands observed have been measured and assigned. We have tentatively assigned frequencies for four of the lattice modes of the molecule in the crystal, and have also inferred the frequencies of three molecular fundamentals which do not appear in the infrared spectrum of the crystal.

Through an analysis of the spectra we have determined uniquely the symmetry of the molecular sites in the crystal as C_i. With the aid of material otherwise available on the crystal structure, we have identified uniquely the space group of the ethylene crystal as $P2_1/n$ (C_{2h}^5). A complete structure is suggested.

The general theory of vibration spectra in molecular crystals appears to be quite well obeyed by this example.

ACKNOWLEDGMENTS

This research was supported in part by a grant from the Petroleum Research Fund administered by the American Chemical Society. Grateful acknowledgment is hereby made to the donors of said fund. The partial support of this investigation by funds provided by the Signal Corps, Department of the Army is also gratefully acknowledged. Finally, we wish to thank the Socony-Mobil Oil Company for providing a one-year research fellowship to one of us (C.B.) during the course of this research project.

Electronic Spectra and Hydrogen Bonding. I. Phenol and Naphthols

HIROAKI BABA AND SATOSHI SUZUKI

Research Institute of Applied Electricity, Hokkaido University, Sapporo, Japan

(Received February 7, 1961)

The effect of hydrogen bonding on the electronic absorption spectra of phenol, α naphthol, and β naphthol has been investigated with particular attention to the relation between the nature of electronic transitions and their behavior in hydrogen bond formation. The spectra were obtained down to 2000 A in isooctane solution in the presence of varying concentrations of dioxane. From the analysis of the observed spectra, the equilibrium constants for the hydrogen bonds and the spectra of the hydrogen-bonded species were determined. The hydrogen bond energies are given for the ground and excited states of the solute molecules. The experimental results clearly indicate that effects of hydrogen bonding on electronic spectra differ markedly with transitions. Both the frequency shifts and the intensity changes differ in magnitude and even in sign according to the properties of the transitions concerned. It is shown that the transition at 47 000 cm^{-1} of α naphthol is displaced to higher frequencies upon formation of the hydrogen bond. No appreciable changes are produced by hydrogen bonding in the spectral patterns of the individual transitions, aside from broadening or smoothing of the vibrational structure. The behavior of the transitions in hydrogen bond formation is interpreted on the basis of the electronic structure of the solute molecules. Two factors are shown to be important for accounting for the mechanism of the hydrogen bonding effect: (a) a change in the electron density at the oxygen atom of the O—H group accompanying an electronic transition; (b) a decrease in the electronegativity of the same oxygen atom resulting from hydrogen bond formation.

I. INTRODUCTION

SINCE the effect of hydrogen bonding on the electronic spectra of organic compounds was unambiguously and quantitatively detected,[1] ultraviolet and visible spectroscopy have been applied by a number of authors[2] to the study of the hydrogen bond. As a result of these investigations, it has been recognized that the phenomenon of the hydrogen bonding effect on the electronic spectra is useful in several aspects. First, thermodynamic quantities for some hydrogen bonding equilibria can be determined through this phenomenon. Second, the anomaly in solvent effect on electronic spectra, which occurs frequently when a polar substance is used as solvent, may be interpreted in terms of the hydrogen bonding effect. Further, as was suggested by one of the authors,[3] valuable information concerning the electronic structure of organic molecules may be derived from their spectral behavior in the formation of hydrogen bonds.

The primary purpose of this series of papers is to reveal the relation between the nature of electronic transitions in a resonating molecule and their behavior in hydrogen bond formation. It is expected that such a study will serve to clarify the electronic properties of the excited states as well as of the ground state of the molecule.

With this purpose in mind, the effect of hydrogen bonding on the ultraviolet absorption spectra of phenol, α naphthol, and β naphthol has been re-examined in the present paper. In order to eliminate the interference of the ordinary effect of the solvent, three-component systems which consist of an inert solvent, a solute of a resonating molecule, and a substance that forms a hydrogen bond with the solute molecule were employed in the usual manner.[1,2] Measurements of the absorption spectra were carried out over the whole ultraviolet region down to 2000 A. Similar measurements have been made for both phenol[1,4–7] and the naphthols,[7–9] but they are limited to only the lower frequency part of the spectra.

II. EXPERIMENTAL

Materials

Isooctane (2, 2, 4 trimethylpentane; Enjay Company, Inc., U. S.) was carefully purified by distillation and by being passed through a freshly activated silica-gel column.

Phenol was distilled under reduced pressure; bp 81°C (17 mm Hg), mp 40.5–41.0°C. The α naphthol was recrystallized from ligroin, and β naphthol from water and ligroin. Both were further purified by vacuum sublimation; mp 93.0–93.5°C and 119.0–119.5°C, respectively. Each of the three samples was subjected to vacuum sublimation whenever it was used for a measurement. It was confirmed that Beer's law

[1] H. Baba and S. Nagakura, J. Chem. Soc. Japan, Pure Chem. Sect. **72,** 3 (1951); J. Am. Chem. Soc. **74,** 5693 (1952).

[2] For references on this subject, see (a) G. C. Pimentel and A. L. McClellan, *The Hydrogen Bond* (W. H. Freeman and Company, San Francisco, 1960), Chap. 4; (b) H. Baba, Bull. Research Inst. Appl. Elec., Hokkaido University **9,** 84 (1957). (c) E. Lippert, *Hydrogen Bonding*, edited by D. Hadži (Pergamon Press, New York, 1959), pp. 217–257.

[3] H. Baba, Bull. Chem. Soc. Japan **31,** 169 (1958).

[4] H. Tsubomura, J. Chem. Soc. Japan, Pure Chem. Sect. **73,** 920 (1952).

[5] S. Nagakura, J. Chem. Soc. Japan, Pure Chem. Sect. **74,**153 (1953); J. Am. Chem. Soc. **76,** 3070 (1954).

[6] S. Mizushima, M. Tsuboi, T. Shimanouchi, and Y. Tsuda, Spectrochim. Acta **7,** 100 (1955).

[7] S. Nagakura and M. Gouterman, J. Chem. Phys. **26,** 881 (1957).

[8] S. Nagakura, J. Chem. Soc. Japan, Pure Chem. Sect. **75,** 734 (1954).

[9] N. Mataga, Y. Kaifu, and M. Koizumi, Bull. Chem. Soc. Japan **29,** 115 (1956).

holds for all these substances in isooctane over the range of concentrations used in the present experiments.

Dioxane was boiled under reflux for 10 hr with hydrochloric acid, dried over potassium hydroxide, and distilled over sodium. It was then repeatedly fractionally crystallized.

Apparatus

Measurements of absorption spectra were made with a Hitachi photoelectric spectrophotometer of type EPU-2A at controlled temperatures. The slit width was chosen in such a way that the effective bandwidth of the exit beam might be sufficiently narrow as compared with the width of absorption bands. Silica cells of 2.5 or 10 mm length were used, each of which was fitted with a ground-glass stopper. A careful operation of the spectrophotometer permits the measurement of spectra down to 1985 A, provided the isooctane purified in the above-mentioned way is used as solvent.

Procedure and Results

A set of spectra were measured for a three-component system: isooctane, a hydroxylic compound, and dioxane, in which the concentration of dioxane was varied from 0 to 0.5 mole/liter. In absorbance measurements the mixture of isooctane and dioxane, where the concentration of dioxane was identical with that in the sample solution, was adopted as the reference liquid. For solutions containing dioxane in relatively high concentrations, the spectra in the vicinity of 2000 A could not be obtained owing to the absorption of dioxane.

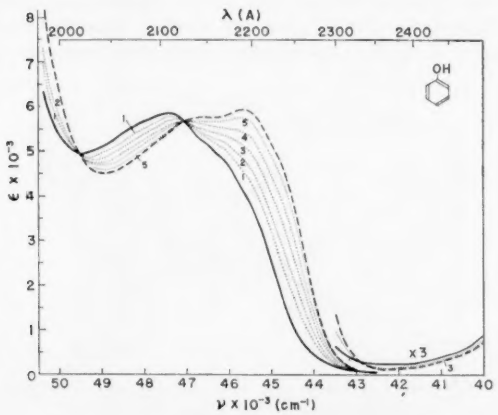

FIG. 1. Effect of hydrogen bonding on electronic absorption spectrum of phenol in isooctane at 20°C (higher frequency region). Solid curve, free molecule; broken curve, hydrogen bonded molecule; dotted curves, spectra in the presence of dioxane, numbered from 1 to 5 in order of increasing concentration of dioxane. Dioxane concentrations: 1, 0.0205; 2, 0.0410; 3, 0.0819; 4, 0.165; 5, 0.494 mole/liter. Phenol concentration: 3.953×10^{-4} mole/liter. Experimental conditions for curves at the lower right-hand corner are identical with those for Fig. 2.

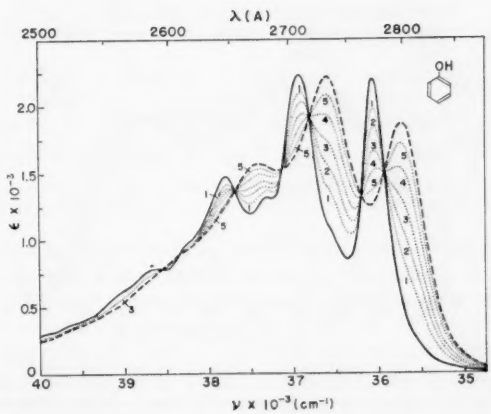

FIG. 2. Effect of hydrogen bonding on electronic absorption spectrum of phenol in isooctane at 20°C (lower frequency region). Solid curve, free molecule; broken curve, hydrogen-bonded molecule; dotted curves, spectra in the presence of dioxane, numbered from 1 to 5 in order of increasing concentration of dioxane. Dioxane concentrations: 1, 0.0199; 2, 0.0398; 3, 0.0796; 4, 0.165; 5, 0.496 mole/liter. Phenol concentration: 3.084×10^{-4} mole/liter.

The results of the spectral measurements are shown in Figs. 1–6. Analysis and interpretation of the spectra will be presented in the succeeding sections.

III. EQUILIBRIUM CONSTANTS AND SPECTRA OF HYDROGEN-BONDED MOLECULES

As is seen in Figs. 1–6, remarkable changes are produced in spectra by changing the solvent from pure isooctane to the isooctane-dioxane mixture. It may safely be assumed that these spectral changes are due solely to the formation of a hydrogen bond between the hydroxylic solute and dioxane. In case the solute is phenol, for instance, the hydrogen bond is represented by the following equilibrium reaction:

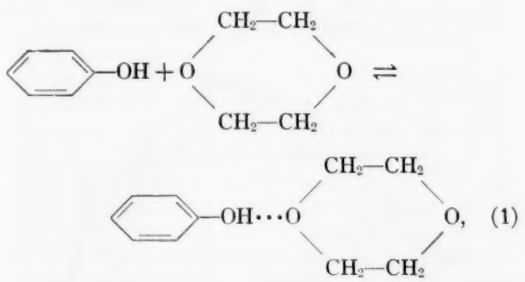

(1)

where phenol acts as a proton donor and dioxane as a proton acceptor. No consideration is here given to the hydrogen-bonded form in which two solute molecules are associated with one dioxane molecule,[1] since in the present experiment the concentration of the solute is far smaller than that of dioxane.

The equilibrium constants K of the hydrogen bonding

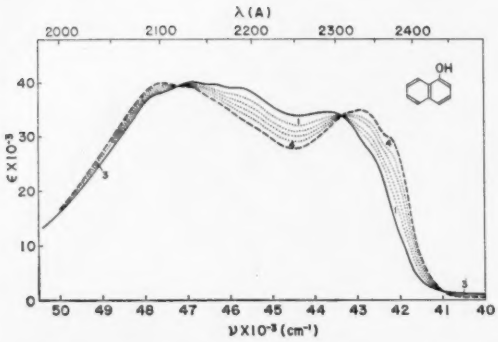

FIG. 3. Effect of hydrogen bonding on electronic absorption spectrum of α naphthol in isooctane at 20°C (higher frequency region). Solid curve, free molecule; broken curve, hydrogen bonded molecule; dotted curves, spectra in the presence of dioxane, numbered from 1 to 4 in order of increasing concentration of dioxane. Dioxane concentrations: 1, 0.020; 2, 0.040; 3, 0.081; 4, 0.168 mole/liter. α-naphthol concentration: 6.80×10^{-5} mole/liter.

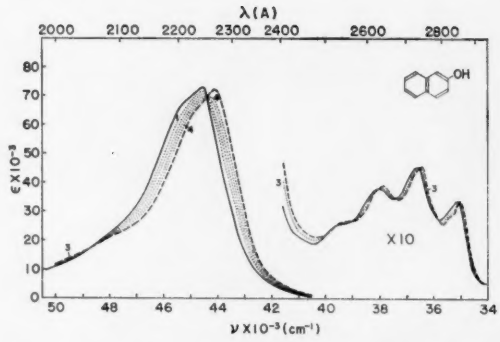

FIG. 5. Effect of hydrogen bonding on electronic absorption spectrum of β naphthol in isooctane at 20°C (higher frequency region). Solid curve, free molecule; broken curve, hydrogen bonded molecule; dotted curves, spectra in the presence of dioxane, numbered from 1 to 4 in order of increasing concentration of dioxane. Dioxane concentrations for left-hand curves: 1, 0.020; 2, 0.040; 3, 0.079; 4, 0.166 mole/liter. β-naphthol concentration for left-hand curves: 2.89×10^{-5} mole/liter. Experimental conditions for right-hand curves are identical with those for Fig. 6.

reactions were obtained by the use of the equation

$$1/(\epsilon-\epsilon_f)=[1/K(\epsilon_b-\epsilon_f)](1/C)+[1/(\epsilon_b-\epsilon_f)], \quad (2)$$

where ϵ_f is the molar extinction coefficient of the non-hydrogen-bonded or free solute molecule and ϵ_b is that of the hydrogen-bonded molecule; ϵ is the molar extinction coefficient as observed for a solution in which the initial concentration of dioxane is C. All these extinction coefficients refer to a given frequency. Equation (2) can easily be derived on the assumption that the initial concentration of the solute is negligibly small compared to that of dioxane; such is actually the case in the present study. From Eq. (2) a plot of $1/(\epsilon-\epsilon_f)$ vs $1/C$ is expected to give a straight line. Further, if this line is extrapolated to the point at which $1/(\epsilon-\epsilon_f)=0$, the equilibrium constant will be obtained as

$$K=-1/C^*$$

with $1/C^*$ equal to the value of $1/C$ at that point.

When both the concentration of the solute and the cell length are kept constant throughout a set of spectra, ϵ's in Eq. (2) may be replaced by the corresponding absorbances A's. Thus $1/(A-A_f)$ was plotted against $1/C$ for various frequencies. These plots gave good straight lines, and the extrapolation of the lines for each of the solutes led to K values which were equal to one another within experimental error. This fact indicates that the spectral changes which occur in different transitions of each solute molecule on

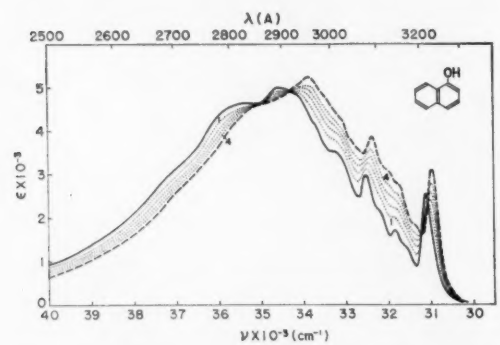

FIG. 4. Effect of hydrogen bonding on electronic absorption spectrum of α naphthol in isooctane at 20°C (lower frequency region). Solid curve, free molecule; broken curve, hydrogen bonded molecule; dotted curves, spectra in the presence of dioxane, numbered from 1 to 4 in order of increasing concentration of dioxane. Dioxane concentrations: 1, 0.020; 2, 0.040; 3, 0.080; 4, 0.167 mole/liter. α-naphthol concentration: 1.49×10^{-4} mole/liter.

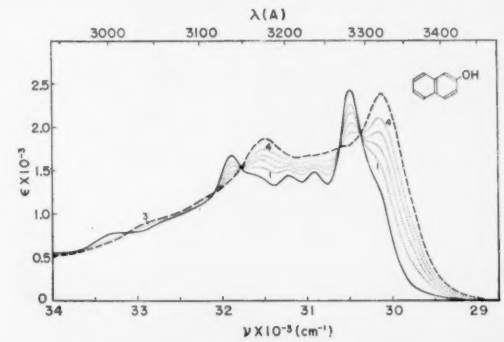

FIG. 6. Effect of hydrogen bonding on electronic absorption spectrum of β naphthol in isooctane at 20°C (lower frequency region). Solid curve, free molecule; broken curve, hydrogen bonded molecule; dotted curves, spectra in the presence of dioxane, numbered from 1 to 4 in order of increasing concentration of dioxane. Dioxane concentrations: 1, 0.020; 2, 0.040; 3, 0.080; 4, 0.166 mole/liter. β-naphthol concentration: 1.96×10^{-4} mole/liter.

changing the solvent are due to one and the same cause, that is, the formation of a hydrogen bond. Some examples of the plots are shown in Fig. 7.

The K values determined in this way at 20°C are listed in Table I. The free energy changes ΔF as computed by the equation $\Delta F=-RT\ln K$ are also given in the table.

According to Eq. (2) the molar extinction coefficient ϵ_b of the hydrogen-bonded species can be obtained from the value of $1/(\epsilon-\epsilon_f)$ at the point where $1/C=0$. In this study, however, the determination of ϵ_b was made on the basis of[10]

$$\epsilon_b=\epsilon+(1/KC)(\epsilon-\epsilon_f), \tag{3}$$

which is equivalent to Eq. (2). Using the observed spectral data in Figs. 1–6 and the K values in Table I, the values of ϵ_b were determined for various frequencies ν. It was found that for a given frequency the values of ϵ_b obtained from ϵ values corresponding to different dioxane concentrations agree with one another very well. Plots of ϵ_b against ν yielded the spectra for the hydrogen-bonded molecules, which are shown in Figs. 1–6 as broken-line curves.

The foregoing results of the determination of K and ϵ_b are consistent with the view that the spectral changes accompanying the solvent change from isooctane to the isooctane-dioxane mixture are caused solely by hydrogen bonding. This view is further substantiated by the existence of several isosbestic points in each set of spectra. On the other hand, the solvent change may give rise to a change in the refractive index of the medium. It is then possible, from the viewpoint of the usual solvent effect, that this may be another cause of the spectral changes in question. However, the change of the refractive index is considered to be so small that the latter possibility is completely excluded. Indeed, according to the measurements of the present authors, the refractive index values (n_D^{20}) for pure isooctane and for the isooctane-dioxane mixture containing dioxane of concentration 0.5 mole/liter are, respectively, 1.3909 and 1.3917, the difference being extremely small.

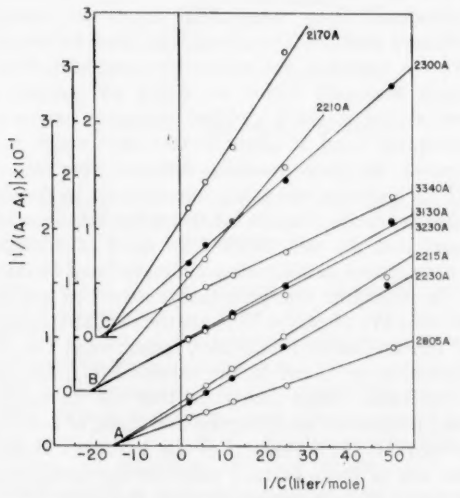

FIG. 7. Plots of $1/(A-A_f)$ vs $1/C$ (20°C). A, phenol; B, α naphthol; C, β naphthol. For experimental conditions, see Figs. 1–6.

TABLE I. Thermodynamic quantities of hydrogen bonds.

Compound	K (20°C)	ΔF (20°C) (kcal/mole)	ΔH (kcal/mole)
Phenol	16.4±0.4	−1.63±0.015	−5.5±0.1
α naphthol	20.9±0.7	−1.77±0.02	−5.4±0.2
β naphthol	18.3±0.8	−1.69±0.03	−5.9±0.3

IV. FREQUENCY SHIFTS

Frequency shifts due to hydrogen bonding were determined from the spectra of the free and hydrogen-bonded species. The results are summarized in Table II, where ν_f and ν_b denote the frequencies of the absorption maxima for free and bonded molecules, respectively, and $\delta\nu$ represents the frequency shift

$$\delta\nu=\nu_b-\nu_f. \tag{4}$$

The electronic transitions in each compound are referred to as I, II, ···, in order of increasing frequency. The assignment of these transitions follows the one proposed in previous papers.[11,12] For the states of α and β naphthol the symmetry types of the corresponding states of the parent compound, naphthalene, are given in parentheses. In case an electronic transition shows vibrational structure, $\delta\nu$ is given for each of the vibrational components.

From Table II it may be seen that in an electronic transition $\delta\nu$ is virtually constant for all the vibrational components, and that the frequency shifts differ considerably among different electronic transitions.

In connection with the hydrogen bonding frequency shift it is of interest, as suggested by Nagakura and Gouterman,[7] to examine the frequency shift that occurs in passing from a parent molecule (e.g., benzene) to the corresponding substituted molecule (e.g., phenol). The latter frequency shift is written as

$$\Delta\nu=\nu_{max}(\text{substituted molecule})-\nu_{max}(\text{parent molecule}). \tag{5}$$

[7] [10] H. Baba, Monograph Research Inst. Appl. Elec., Hokkaido University No. 4 (1954), p. 61.

[11] H. Baba, Bull. Chem. Soc. Japan **34**, 76 (1961).

[12] H. Baba and S. Suzuki, Bull. Chem. Soc. Japan **34**, 82 (1961).

TABLE II. Frequency shifts due to hydrogen bond formation.

Compound	Transition	Assignment	Frequency[a] (cm^{-1}) ν_f	ν_b	$\delta\nu$ (cm^{-1})		Δq_0[b]
	I	$^1A_1 \rightarrow {}^1B_2^-$	36 070	35 730	−340		
			36 920	36 600	−320		−0.103
			37 790	37 420	−370	mean	
			38 610	(38 300)	(−310)	−340	
Phenol							
			(45 400)	(44 800)	(−600)		
	II	$^1A_1 \rightarrow {}^1A_1^+$	46 300	45 650	−650	mean	−0.087
			47 400	46 700	−700	−650	
			31 100	30 960	−140		
	I	$(^1A_g) \rightarrow (^1B_{3u}^-)$	31 520	(31 360)	(−160)		−0.038
			31 830	(31 700)	(−130)	mean	
			32 510	32 360	−150	−150	
α naphthol	II	$(^1A_g) \rightarrow (^1B_{2u})$	34 570	33 840	−730	mean	
			(35 710)	(35 090)	(−620)	−730	−0.049
	III	$(^1A_g) \rightarrow (^1B_{3u}^+)$	43 570	42 880	−690		−0.010
	IV		46 820	47 280	+460		
	I	$(^1A_g) \rightarrow (^1B_{3u}^-)$	30 470	30 100	−370	mean	−0.056
			31 890	31 490	−400	−390	
			35 140	35 030	−110		
β naphthol	II	$(^1A_g) \rightarrow (^1B_{2u})$	36 600	36 470	−130	mean	−0.043
			38 040	37 880	−160	−130	
	III	$(^1A_g) \rightarrow (^1B_{3u}^+)$	44 580	44 090	−490		−0.049

[a] Values of doubtful accuracy are given in parentheses.
[b] See Sec. VIII.

The relation between $\delta\nu$ and $\Delta\nu$ is illustrated in Table III for phenol and in Fig. 8 for the naphthols.

V. INTENSITY CHANGES

Oscillator strengths for the transitions of both the free and the bonded species were determined by the familiar equation

$$f = 4.32 \times 10^{-9} \int \epsilon d\nu.$$

When an electronic band is not fully separated from other bands, a question arises inevitably as to the limit of the integration. In the present study the following procedures were adopted: If there is a clear minimum between two adjacent bands, the center of this minimum is chosen as the limit of the integration; if there is not any such minimum, the overlapping bands are decomposed into constituent bands in somewhat arbitrary manner. The absorption curve for transition IV of α naphthol was reasonably extrapolated to the higher frequency region for which no spectral data were available. The β naphthol appears to have a weak absorption band at about 48 000 cm^{-1} which is presumably due to a transition different from transition III.[13] This point was taken into account in the determination of the f value for transition III. It is to be noted that the said 48 000-cm^{-1} band of β naphthol becomes more distinct upon hydrogen bond formation.

Ths oscillator strengths thus determined are given in Table IV, where f_f and f_b are the oscillator strengths for free and bonded molecules, respectively. For ready comparison of f_f and f_b, the values of f_b/f_f are added to the table. These data show that the intensities of some transitions are increased and those of others are reduced by the formation of the hydrogen bond. In each row of Table IV the f value for the corresponding transition of the parent molecule is also given.

TABLE III. Relation between $\delta\nu$ and $\Delta\nu$ for phenol.

Transition	ν_{max}[a] (cm^{-1}) Benzene	Phenol	$\Delta\nu$ (cm^{-1})	$\delta\nu$ (cm^{-1})
I	39 400	36 700	−2700	−340
II	49 500	47 000	−2500	−650

[a] H. B. Klevens and J. R. Platt, Tech. Rept., Laboratory of Molecular Structure and Spectra, University of Chicago, Pt. 1, p. 145 (1953–1954).

[13] A more distinct electronic band appears at 47 000 cm^{-1} in the spectrum of β naphthylamine, which is considered to correspond to the weak absorption of β naphthol in question (see reference 12).

VI. CONSTANCY OF SPECTRAL PATTERNS

It has been shown in the foregoing sections that hydrogen bonding brings about noticeable changes both in frequency and in intensity of a transition. Nevertheless, as may be seen from Figs. 1–6, no essential change takes place in the shape of an electronic band upon hydrogen bond formation. The situation will be best understood by reference to Figs. 9(a) and 9(b), where the spectra for phenol and α naphthol are partly reproduced, as typical examples.

In Fig. 9(a) the spectrum for transition I of the hydrogen-bonded phenol molecule is moved along the frequency axis toward higher frequencies by $|\delta\nu|$ of this transition (340 cm^{-1}). Although a broadening or a

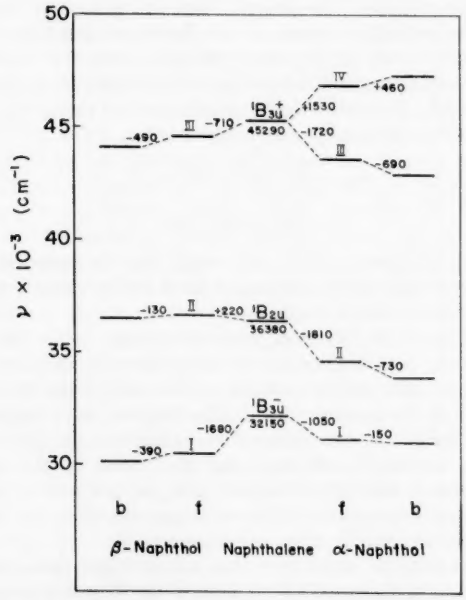

FIG. 8. Relation between $\delta\nu$ and $\Delta\nu$ for α and β naphthol. f and b refer to free and hydrogen bonded molecules, respectively. Data on naphthalene are taken from reference 12.

blurring occurs in the vibrational structure upon hydrogen bond formation, there exists a similarity between the spectra of the free and bonded molecules. The sharp vibrational components a, b, c, and d of the free molecule remain in the spectrum of the bonded molecule without undergoing great changes, giving the components a′, b′, c′, and d′. Other relatively diffuse components at 36 560, 37 310, and 38 300 cm^{-1} are smoothed out. It is natural to consider that the component at 37 310 cm^{-1} merges near the minimum between b′ and c′ when the hydrogen bond is formed; this accounts for the broadening which is seen to occur in the said minimum.

Figure 9(b) shows the spectra of α naphthol in the region of transitions I and II. In this case the spectrum of the bonded molecule is moved to higher frequencies by 150 cm^{-1}, that is, by $|\delta\nu|$ of transition I. There is a considerable degree of correspondence between the vibrational components a, b, ···, f and a′, b′, ···, f′, whereas discrepancies occur between the components p, q and p′, q′. This in turn suggests that the vibrational components p and q should be associated with an electronic transition entirely different from transition I to which the components a, b, ···, f belong.

It has been shown previously that the hydrogen bonding frequency shifts vary in magnitude and sometimes in sign among different kinds of electronic transitions. Thus, overlapping of two adjacent transi-

TABLE IV. Intensity changes due to hydrogen bond formation.

Compound	Transition	f_f	f_b	f_b/f_f	f for parent compound
Phenol	I	0.0213	0.0247	1.16	0.0014[a]
	II	0.103	0.111	1.08	0.10[a]
α naphthol	I	0.015$_7$	0.016$_8$	1.05	0.002[b]
	II	0.102	0.105	1.04	0.11[c]
	III	0.328	0.385	1.17	1.70[b]
	IV	0.892	0.836	0.94	
β naphthol	I	0.0211	0.0256	1.21	0.002
	II	0.0811	0.0805	0.99	0.11
	III	1.06	1.02	0.97	1.70

[a] H. B. Klevens and J. R. Platt, Tech. Rept., Laboratory of Molecular Structure and Spectra, University of Chicago, Pt. 1, p. 145 (1953–1954).
[b] H. B. Klevens and J. R. Platt, J. Chem. Phys. **17**, 470 (1949).
[c] Obtained from Am. Petrol. Inst. Research Project 44, "Ultraviolet spectral Data," Serial No. 654.

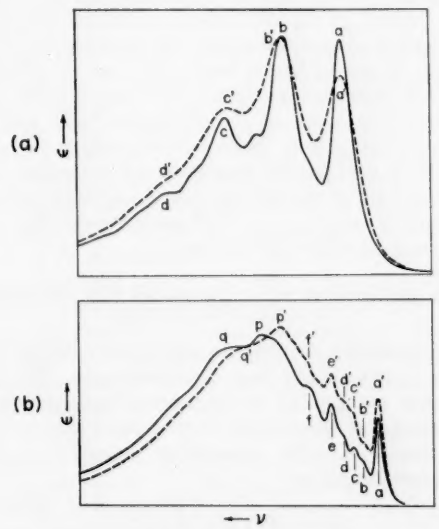

FIG. 9. Comparison of spectral patterns of free and hydrogen bonded molecules; (a) phenol, (b) α naphthol.

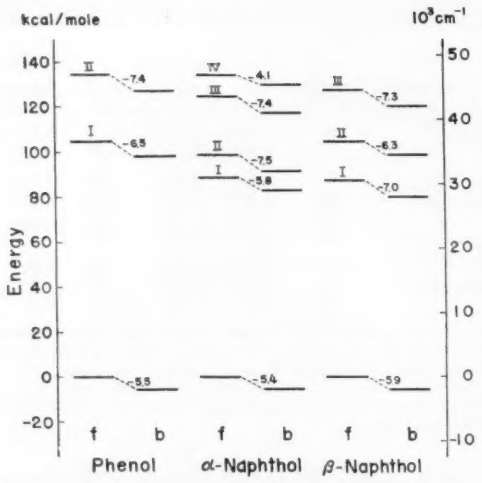

FIG. 10. Changes of energy levels for hydroxylic compound-dioxane systems due to hydrogen bond formation; f and b refer to free and hydrogen bonded forms, respectively.

tions will be either increased or decreased by hydrogen bond formation, according to the relative values of the frequency shifts produced in the two transitions. For instance, the overlapping of transitions I and II of α naphthol is increased, whereas the overlap between transitions III and IV of the same compound is appreciably reduced by the formation of the hydrogen bond (see Fig. 3).

In Fig. 1 it is seen that a considerable change is caused by hydrogen bonding in the spectral pattern of transition II of phenol. An explanation for this change is as follows. In the free molecule of phenol, transition II overlaps another transition lying in higher frequency region. If the hydrogen bond gives rise to different shifts in these two transitions, it is then possible that the apparent shape of the absorption band may be altered in going from the free to the hydrogen bonded species. It is of interest to note in this connection that the spectrum of the bonded species resembles the corresponding benzene spectrum[14] more closely than does the spectrum of the free species.

VII. HYDROGEN BOND ENERGIES FOR GROUND AND EXCITED STATES

The procedure for determining the equilibrium constants K has already been described in Sec. III. The enthalpy changes ΔH accompanying hydrogen bond formation can be obtained from a knowledge of the variation of K with temperature, according to the well-known equation

$$\Delta H = -R[d \ln K/d(1/T)].$$

In the present experiment the values of K were determined for each substance at five temperatures between 0° and 40°C. The $\ln K$ values plotted against $1/T$ were found to fall on a straight line. From the slope of this straight line, which was actually determined by the method of least squares, the value of ΔH was derived. The result is given in the last column of Table I. It may be noted that the values of K, ΔF, and ΔH for phenol, given in Table I, are considered to be of the highest accuracy as obtained by the present method of spectroscopy.

The enthalpy change derived in this way is of course to be associated with the ground state of a given molecule, so that it will hereafter be denoted by ΔH_g. Now, suppose an electronic transition takes place in the molecule from the ground state to an excited state. The enthalpy change of the hydrogen bond in the excited state is in general different from that in the ground state, and the former will therefore be denoted by ΔH_e. It may be easily understood that the hydrogen bonding frequency shift is given by

$$\delta\nu = \Delta H_e - \Delta H_g, \tag{6}$$

that is,

$$\Delta H_e = \Delta H_g + \delta\nu. \tag{7}$$

It is noted that $-\Delta H_g$ and $-\Delta H_e$ may be regarded as the energies of the hydrogen bond in the ground and excited states, respectively.

Figure 10 illustrates how the energy levels for a system consisting of one of the hydroxylic compounds and dioxane will be changed in isooctane by the formation of the hydrogen bond. The diagram was obtained by combining the observed excitation energies for the free hydroxylic molecule and the values of the appropriate enthalpy changes (ΔH_g or ΔH_e). The enthalpy changes for different states are given in the diagram, in units of kilocalories per mole.

It is to be noted here that an electronic transition should be discussed on the basis of the Franck-Condon principle. Thus, as was clearly indicated by Pimentel,[15] the excited state related to ΔH_e of Eq. (7) corresponds actually to a Franck-Condon excited state which is defined in terms of the potential curves for the hydrogen bond concerned. In other words, the hydrogen bond energy for the excited state as given by $-\Delta H_e$ may be unequal to that for the equilibrium excited state. It was suggested by Mataga, Kaifu, and Koizumi,[9] however, that no such consideration is required regarding the first excited state of α and β naphthol.

VIII. DISCUSSION

General Consideration

There are two different views concerning the nature of hydrogen bonding; one is based on the electrostatic

[14] J. R. Platt and H. B. Klevens, Chem. Revs. **41**, 301 (1947)

[15] G. C. Pimentel, J. Am. Chem. Soc. **79**, 3323 (1957).

theory and the other on the covalent theory.[16] In the following discussion the electrostatic view will be adopted for convenience. It is to be noted that so far as the subject treated here is concerned the covalent theory leads to practically the same results, as pointed out by one of the authors.[2b]

Several theoretical considerations have been presented on the effect of hydrogen bonding on electronic spectra.[1,15,17,18] In the present study, this problem will be discussed in terms of the following two factors.[1,10]

(a) The charge distribution in a resonating molecule varies according as the molecule is in the ground state or in an excited state. In the particular case of the hydroxylic compounds being investigated, a π-electronic transition will be accompanied by a change in the electron density at the oxygen atom, which would exert an influence on the ionic character of the O—H bond; the proton-donating power of the O—H group may thus be altered by the electronic transition.

(b) When a resonating molecule forms a hydrogen bond, it will be influenced by the perturbation of the partner in the hydrogen bond, and consequently the electronic structure of the molecule will be altered. Such a perturbation effect varies according as the resonating molecule is in the ground state or in an excited state. In the particular case of the hydrogen bond between one of the hydroxylic compounds and dioxane, the σ electrons associated with the O—H bond of the compound will be somewhat displaced toward the oxygen atom under the influence of the effectively negative charge of the oxygen atom of dioxane, and therefore the electronegativity of the hydroxyl oxygen atom will be smaller in the hydrogen-bonded form than in the free form. Thus, the interaction of the nonbonding pair of electrons at the hydroxyl oxygen with the ring π electrons is expected to be increased by hydrogen bond formation. These considerations may apply to the excited states as well as to the ground state of the hydroxylic compound.

With the above two factors (a) and (b) in mind, the observed spectral changes due to hydrogen bonding will be examined with reference to the results of molecular orbital calculations recently made by the present authors[11,12] concerning the electronic spectra of phenol[19] and the naphthols. In these calculations it was shown that the influence of substitution on the spectrum of an aromatic hydrocarbon is brought about not only by the so-called electron migration phenomenon, but also by the fact that the degree of the mixing of excited configurations is altered upon substitution.

Frequency Shifts

As is seen in Eq. (6), the hydrogen bonding frequency shift is resultant from the difference between the energy of the hydrogen bond in the excited state ($-\Delta H_e$) and that in the ground state ($-\Delta H_g$). From the viewpoint of factor (a), this difference should be correlated with the change of π-electron density at the hydroxyl oxygen Δq_O which accompanies an electronic transition. If $\Delta q_O<0$, an increase in the formal positive charge of the oxygen, and hence an increase in the proton-donating power of the O—H group, will result from the electronic transition concerned. Theoretical values of Δq_O as obtained by the molecular orbital calculations[11,12] are given in the last column of Table II. For all the transitions cited in Table II the Δq_O values are seen to be negative. It is therefore expected that with all the transitions $-\Delta H_e>-\Delta H_g$, i.e., $\delta\nu<0$. Thus, setting aside for the moment transitions III and IV of α naphthol, it can be said that the theoretical prediction is in accord with the experimental results listed in Table II. Further, according to the molecular orbital calculations,[20] the energies required for the electronic transitions under consideration decrease as the electronegativity of the hydroxyl oxygen is reduced. Thus the relation $-\Delta H_e>-\Delta H_g$ is expected also from the mechanism of factor (b).

The situation is somewhat complicated in the case of transitions III and IV of α naphthol. Undoubtedly these originate in two different electronic transitions, because they shift in opposite directions upon formation of the hydrogen bond. On the contrary, the parent compound, naphthalene, shows in the region of transitions III and IV of α naphthol only one strong absorption due to a ${}^1A_g\rightarrow{}^1B_{3u}{}^+$ transition. Theoretically, naphthalene has a ${}^1B_{1g}{}^+$ state near the ${}^1B_{3u}{}^+$ state.[21] The ${}^1A_g\rightarrow{}^1B_{1g}{}^+$ transition is a forbidden one, so that it is not found in the spectrum of naphthalene itself. In the case of α naphthol, owing to the influence of the substituent, interaction may occur between the ${}^1B_{3u}{}^+$ and ${}^1B_{1g}{}^+$ states to give two mixed states. Transitions III and IV of α naphthol can then be assigned to the transitions from the ground state to the mixed states. Taking into account the intensities of these transitions, the present authors reached a tentative conclusion that transition IV corresponds mainly to the ${}^1A_g\rightarrow{}^1B_{3u}{}^+$ transition and III to the ${}^1A_g\rightarrow{}^1B_{1g}{}^+$ transition of the parent compound.[12] If this is the case, the fact that Δq_O is negative for the $({}^1A_g)\rightarrow({}^1B_{3u}{}^+)$ transition of α naphthol is incompatible with the actual observation that transition IV is shifted to the blue by hydrogen bonding. It should be noticed, however, that the ab-

[16] See, for example, reference 2a, Chap. 8.

[17] H. Tsubomura, J. Chem. Soc. Japan, Pure Chem. Sect. **73**, 841 (1952); R. Miyasaka, Busseiron Kenkyu No. **62**, 94 (1953); N. S. Bayliss and E. G. McRae, J. Phys. Chem. **58**, 1002 (1954).

[18] G. J. Brealey and M. Kasha, J. Am. Chem. Soc. **77**, 4462 (1955).

[19] For other theoretical studies on the electronic spectra of substituted benzenes see (a) A. L. Sklar, J. Chem. Phys. **7**, 984 (1939); (b) K. F. Herzfeld, Chem. Revs. **41**, 233 (1947); (c) F. A. Matsen, J. Am. Chem. Soc. **72**, 5243 (1950); (d) L. Goodman and H. Shull, J. Chem. Phys. **27**, 1388 (1957).

[20] See Fig. 3 of reference 11 and Fig. 5 of reference 12.

[21] R. Pariser, J. Chem. Phys. **24**, 250 (1956).

solute magnitude of the above Δq_0 value is relatively small.

There is a parallelism between the values of $\delta\nu$ and $\Delta\nu$ (see Table III and Fig. 8). The latter frequency shift is caused by the interaction of the nonbonding pair of electrons in the substituent group with the ring π electrons.[19] As is seen from factor (b), this interaction will be reinforced by hydrogen bond formation. It is therefore not surprising to find a parallelism between the $\delta\nu$ and $\Delta\nu$ values.

In substituted aromatic hydrocarbons, the vibrational structure of an electronic band is due primarily to the vibrations of the aromatic ring. The frequencies of these ring vibrations will not be changed appreciably by hydrogen bonding, although a great change may occur in the frequency of the substituent group. The above consideration well accounts for the experimental fact that the vibrational components belonging to each of the transitions are uniformly shifted by hydrogen bond formation.

All the transitions treated in the present study are of $\pi\rightarrow\pi^*$ type. It should be noticed that among them transition IV of α naphthol shows a blue shift when the hydrogen bond is formed. Other transitions are shifted to the red in agreement with what is commonly believed with respect to $\pi\rightarrow\pi^*$ transitions.[2]

Intensity Changes

When a substituent group is introduced into an aromatic hydrocarbon, a change occurs in the intensity of the electronic transition of that hydrocarbon.[19] This intensity change is caused by the interaction of nonbonding electrons of the substituent with π electrons contained in the aromatic ring. Such interaction leads to the configurational mixing as well as to the electron migration, and consequently both increase and decrease of the intensity may result from the substitution.[11,12,19d]

Now, if the hydroxylic compound forms the hydrogen bond, the interaction between the nonbonding electrons and the ring π electrons will be enhanced on account of factor (b), and therefore the intensity of an electronic transition in the hydroxylic compound will be changed. From the preceding argument it is expected that, upon formation of the hydrogen bond, the intensity of the transition will either increase or decrease according as the corresponding transition increases or decreases in intensity in passing from the parent compound to the hydroxyl derivative. This expectation is found to be nearly fulfilled on inspection of the data presented in Table IV.

In connection with the above problem, it is of interest to compare the f value for a transition in a hydroxyl derivative, $f(\mathrm{OH})$, with that for the corresponding transition in the corresponding amino derivative, $f(\mathrm{NH_2})$. The amino group is known to be of more electron-donating nature than the hydroxyl group, and the interaction between the nonbonding electrons and the ring π electrons is therefore expected to be stronger in the amino derivative. Thus, for instance, the values of $f(\mathrm{NH_2})/f(\mathrm{OH})$ are 1.22, 1.56, and 0.81, respectively, for transition I of phenol, transitions I and III of β naphthol,[11,12] the corresponding values of f_b/f_t being 1.16, 1.21, and 0.97 (see Table IV).

Spectral Patterns

It may be understood from the foregoing discussion that when the hydrogen bond is formed no significant change takes place in the spectral pattern associated with each of the transitions, aside from broadening or smoothing of the vibrational structure. The problem of the broadening of the vibrational components can be treated, after the manner of Pimentel,[15] in terms of the potential curves for the hydrogen bond O—H···O, where the potential energies of the donor-acceptor system in its ground and excited states are plotted against the O···O distance.

The potential curves will be uniquely determined if a definite orientation of the acceptor relative to the donor molecule be given. In practice such an orientation cannot be expected on account of the thermal motion. The curves would therefore more or less vary from one donor-acceptor pair to another, giving rise to a distribution of frequency shifts for each of the vibrational components. This is considered to be one cause for the broadening of the vibrational peaks. Further, according to the Franck-Condon principle a transition vertically upward from the minimum of the lower potential curve takes place with the largest probability, but nonvertical transitions may also occur to some extent. This might be another cause of the broadening under consideration.

As has already been shown, the hydrogen bonding frequency shifts of different transitions differ in magnitude and sometimes in sign. It is obvious that this in turn provides a clue for distinguishing the individual electronic bands when they are not well separated. A good example is found in the case of transitions III and IV of α naphthol. In the pure isooctane solution, α naphthol shows in the region 40 000–50 000 $\mathrm{cm^{-1}}$ only a diffuse absorption minimum, so that it is not possible to decide whether there are two electronic transitions or only one transition in this region. When the hydrogen bond is formed, the said minimum becomes fairly clear. This proves conclusively that two different transitions do exist in that region.

IX. SUMMARY AND CONCLUSION

The effect of hydrogen bonding on the electronic absorption spectrum of the hydroxylic compounds investigated in the present study can be summarized as follows:

(1) Noticeable changes in the spectrum are produced by hydrogen bond formation over the whole spectral

region. The value of the equilibrium constant for the hydrogen bond is uniquely determined with respect to various frequencies within the spectral region.

(2) Frequency shifts accompanying the formation of the hydrogen bond differ in their magnitude or sign among different electronic transitions. For a given transition, all the vibrational components show a uniform shift.

(3) There is a parallelism between the frequency shifts due to hydrogen bonding and the shifts produced in going from the parent molecule to the substituted molecule.

(4) Intensity changes accompanying the formation of the hydrogen bond differ among different electronic transitions. Both increase and decrease of the intensity may be caused by hydrogen bonding.

(5) There is a parallelism between the intensity changes due to hydrogen bonding and the changes produced in going from the parent molecule to the substituted molecule.

(6) No appreciable change is brought about in the shape of the absorption curve for each electronic transition, but broadening or smoothing of the vibrational components may take place.

Each of the statements of the above paragraphs may be equally applicable to the electronic spectra of other similar compounds.

In conclusion it should be emphasized that electronic absorption bands exhibit different behaviors in hydrogen bond formation, depending upon the properties of the transitions associated with the bands. It is then expected that valuable information can be obtained as to the origin of a given electronic band from its behavior in hydrogen bonding. Studies made along these lines will be reported in succeeding papers.

ACKNOWLEDGMENT

The authors wish to express their sincere thanks to Professor K. Higasi for his interest and encouragement.

Letters to the Editor

THE Letters to the Editor section is subdivided into three parts entitled Communications, Comments and Errata, and Notes. These three sections are all subject to the same limitations on length. The textual material of each Letter is limited to a number of words equal to 950 minus the following: (a) 200 words for each average-sized figure; (b) 50 words for each displayed equation; (c) 7 words for each line of table including headings and horizontal rulings. No proof will be sent to the authors of "Communications" and "Comments and Errata." Proof will be sent to the authors of "Notes." The publication charge for Letters is $30 per page, with a minimum of $30 per Letter. If honored, the Institution will be entitled to 100 reprints without covers. See issues of May–September, 1957, for descriptions of categories.

Communications

On the Mechanism of Nuclear Relaxation in Gaseous and Liquid CHF_3*

C. S. JOHNSON, JR.,† AND J. S. WAUGH‡
Department of Chemistry, Research Laboratory of Electronics, and Laboratory of Chemical and Solid State Physics, Massachusetts Institute of Technology
AND
J. N. PINKERTON
Lyman Laboratory of Physics, Harvard University, Cambridge, Massachusetts
(Received June 22, 1961)

GUTOWSKY *et al.*[1] have reported that the ratio of proton and F^{19} relaxation times T_{1H}/T_{1F} becomes as large as two at high temperatures in liquid fluoroform. We wish to remark that this ratio in the gas phase is greater than 100, and to offer approximate but detailed arguments to support their assertion[1] that spin-rotational interactions are important for the F^{19}.

Both relaxation times in the gas, as measured at 40.0 Mc/sec by standard pulse methods, are proportional to density (at 296°K, $T_{1H}=450\pm40$ msec amagat^{-1} and $T_{1F}=3.7\pm0.4$ msec amagat^{-1}), as expected for collisionally interrupted intramolecular interactions in the limit of extreme narrowing.[2] Such behavior is described quantitatively for H_2 (though with some assumptions of uncertain generality) by the Bloembergen-Schwinger formula.[3] No counterpart of this formula yet exists for symmetric top molecules, but for purposes of estimation it is reasonable to describe the relaxation of nuclear species k by

$$T_{1k}^{-1}\simeq 4\pi^2\tau_c[c_k^2\langle J^2\rangle+d_k^2]. \quad (1)$$

τ_c is interpreted as the mean life of an m_J state, and c_k and d_k are suitably averaged dipolar and spin-rotational interaction constants. Both terms should actually contain functions of J and K, but by analogy with H_2 the above simplification should be adequate in the limit of high temperatures. Contributions from chemical shift anisotropy are negligible for H^1 and overwhelmed by spin-rotational interactions for F^{19} (see below), and have therefore been omitted.

Within this context, the observed difference in the H^1 and F^{19} relaxation times cannot be ascribed to different dipolar interactions. One can estimate from structural parameters[4] that $d_H\simeq 3\mu_H\mu_F r_{HF}^{-3}h^{-1}=10.4$ kc, and similarly $d_F\simeq 8.6$ kc. Thus it must be the spin-rotational interactions which have very different strengths.

The latter have not been measured, but can be estimated from chemical shifts, using the method of Pinkerton and Anderson.[5] Taking $\sigma_F(CHF_3)-\sigma_F(F_2)$, 509 ppm[6,7] and inserting appropriate moments of inertia we obtain $\beta_F\equiv 1.09(c_{xx})_F+(c_{zz})_F=-16.7$ kc, in a coordinate system whose z axis lies along the C—H bond. To make a similar estimate for the proton we have measured $\sigma_H(CH_4)-\sigma_H(CHF_3)$ in the gas, using a Varian spectrometer at 60 Mc, and found it to be 6.07 ppm. Together with the absolute shielding in CH_4,[8,9] this gives $\sigma_H(CHF_3)=24.7$ ppm and $\beta_H=0.527$ kc, an unusually small value.

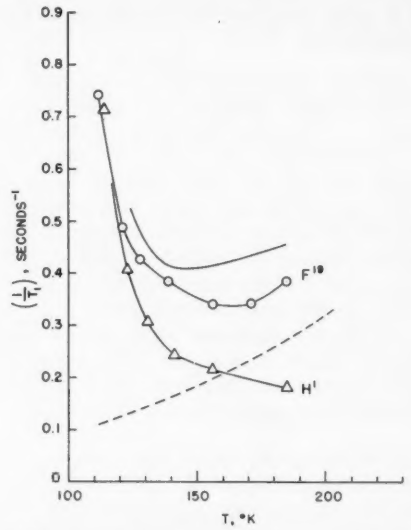

FIG. 1. Temperature dependence of proton and F^{19} relaxation times in liquid CHF_3. The dashed curve is obtained by extrapolating the observed temperature and density dependence of T_{1F} in the gas, using the equation of state measurements of Hou [Y.-C. Hou, thesis, University of Michigan, 1956; Chem. Abstr. **50**, 1395d (1957)]. The highest curve is the sum of the dashed curve and the experimental results for T_{1H}. Experimental points are from reference 1.

Assuming $\beta_k\simeq c_k$, using the dipolar interactions mentioned above, and setting $J^2\simeq 400$, we predict from Eq. (1) that $T_{1H}/T_{1F}\simeq 500$. Thus we conclude that the fluorine relaxation, but not the proton relaxa-

tion, in the gas is heavily dominated by the spin-rotational interaction.

Equation (1) can be solved for τ_c, which should in principle be the same whether proton or F^{19} data are used. The actual values found are $\rho\tau_c \approx 3\times10^{-10}$ and 0.6×10^{-10} sec, respectively. Measurements of rotational relaxation times by means of dielectric dispersion[10] give $\rho\tau_c \approx 1.1\times10^{-10}$ sec, in satisfactory agreement with the above, particularly considering that the meaning of τ_c is not exactly the same in both experiments.

Further support of the idea that c_F dominates the F^{19} relaxation can be obtained from the temperature dependence of $T_{1F/\rho}$, which should be approximately proportional to $T^{-0.5}$ when dipolar interations dominate but to $T^{-1.5}$ when spin-rotational interactions are most important.[11] Experimentally, we find $T_{1F}/\rho \propto T^{-1.55}$ between 273° and 373°K, a result which is also consistent with the temperature dependence of nonresonant microwave absorption.[10]

Gutowsky *et al.*[1] argue that F^{19} spin-rotational interactions are probably important in liquid CHF_3 as well. There it is likely that a major contribution to T_1^{-1} arises from the Brownian BPP mechanism,[3] and one may assume this to be about the same for H^1 and F^{19}. Any additional contribution from a c_F term may be estimated from Eq. (1) by extrapolating our experimental results on the gas to densities and temperatures appropriate to the liquid. While this may seem to amount to misuse of a simple collision model, it is known to lead to sensible results in other cases.[12] The results of this calculation are shown in Fig. 1. The agreement with the measured T_{1F} and its temperature dependence support the contention that spin-rotational interactions are important, and that something like free molecular rotation in the liquid state occurs for periods of the order of τ_c or longer.

* This work was supported in part by the U. S. Army Signal Corps, the Air Force Office of Scientific Research, and the Office of Naval Research, and in part by the National Science Foundation.

† National Science Foundation Predoctoral Fellow.

‡ Alfred P. Sloan Research Fellow.

[1] H. S. Gutowsky, I. J. Lawrenson, and K. Shimomura, Phys. Rev. Letters **6,** 349 (1961).

[2] A. Abragam, *The Principles of Nuclear Magnetism* (Oxford University Press, London, 1961), pp. 279, 320–321.

[3] N. Bloembergen, E. M. Purcell, and R. V. Pound, Phys. Rev. **73,** 679 (1948).

[4] S. N. Ghosh, R. Trambarulo, and W. Gordy, J. Chem. Phys. **20,** 605 (1952).

[5] J. N. Pinkerton and C. H. Anderson, Bull. Am. Phys. Soc. **6,** 281 (1961).

[6] H. S. Gutowsky and C. J. Hoffman, J. Chem. Phys. **19,** 1259 (1951).

[7] L. H. Meyer and H. S. Gutowsky, J. Phys. Chem. **57,** 481 (1953).

[8] W. G. Schneider, H. J. Bernstein, and J. A. Pople, J. Chem. Phys. **28,** 601 (1958).

[9] G. F. Newell, Phys. Rev. **80,** 476 (1950).

[10] A. A. Maryott, A. Estin, and G. Birnbaum, J. Chem. Phys. **32,** 1501 (1960).

[11] C. S. Johnson, Jr. and J. S. Waugh, J. Chem. Phys. (to be published).

[12] W. P. A. Hass, G. Seidel, and N. J. Poulis, Physica **26,** 834 (1960).

Infrared Spectrum and Structure of the NF_2 Radical*

MARLIN D. HARMONY† AND ROLLIE J. MYERS

Department of Chemistry, University of California, Berkeley, California

AND

L. J. SCHOEN, DAVID R. LIDE, JR., AND D. E. MANN

National Bureau of Standards, Washington 25, D. C.

(Received May 26, 1961)

A RECENT investigation of the dissociation of gaseous tetrafluorohydrazine[1] appears to have established the existence of the equilibrium $N_2F_4 \rightleftharpoons 2NF_2$. The reported equilibrium constants suggest that there is sufficient dissociation at slightly elevated temperatures to permit spectroscopic studies on the NF_2 radical. Investigations of the infrared spectrum were begun independently at the University of California and the National Bureau of Standards. Since the results are in substantial agreement, a joint report is presented here.

The spectrum was obtained in both laboratories on a Beckman IR-7 spectrometer[2]; accurately known ammonia lines were used for the wavelength calibration. The sample was contained in 9-cm Pyrex cells with windows (NaCl or AgCl) attached by means of O-rings. Samples of N_2F_4 with stated purity varying from 92 to 99% were used without further purification.[3] Initial N_2F_4 pressures of 1 to 10 mm Hg were used, and the temperature was varied from 25° to about 175°C. At temperatures above 175°C some decomposition or reaction with the cell materials was found to occur.

As the sample cell was heated above room temperature, bands of the parent N_2F_4 molecule decreased sharply in intensity and two new absorption bands appeared. Since these changes were completely re-

TABLE I. Wavenumbers of Q branches in 1074 cm^{-1} band.

K	$P_{Q(K)}$ obs[a]	$P_{Q(K)}$ calc[b]	$R_{Q(K)}$ obs[a]	$R_{Q(K)}$ calc[b]
3		1064.4	1088.2	1088.2
4	1060.6	1060.4	1092.0	1092.1
5	1056.7	1056.5	1096.1	1096.1
6	1052.5	1052.5	1100.1	1100.0
7	1048.4	1048.6	1104.1	1104.0
8	1044.4	1044.6	1107.9	1108.0
9	1040.4	1040.6	1111.9	1111.9
10			1116.0	1115.9
11			1119.9	1119.8

[a] Estimated accuracy of measurement is about 0.1 cm^{-1}.

[b] Calculated for a symmetric rotor with constants given in text.

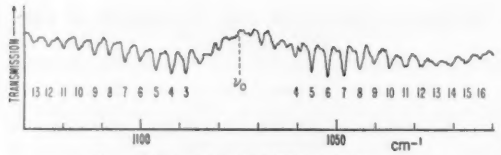

FIG. 1. The ν_1 band of NF_2 at 1074 cm^{-1}.

versible, the new bands can be reasonably ascribed to the NF_2 radical. One of the bands, with center at 1074 cm^{-1}, shows well-resolved rotational fine structure which allows it to be unambiguously assigned as the symmetric stretching mode $\nu_1(a_1)$ of NF_2. The other absortpion appears in the 930–940 cm^{-1} region but is badly overlapped by residual N_2F_4 absorption. While little information can be obtained on its contour, it is reasonable to assign this band as $\nu_3(b_1)$. This assignment for the stretching fundamentals shows a close correspondence with F_2O, where[4] $\nu_1=929$ cm^{-1} and $\nu_3=826$ cm^{-1}. It has not yet been possible to detect the bending fundamental of NF_2; at pressures which are low enough to give a significant concentration of NF_2, this band is expected to be very weak.

The resolved ν_1 band (Fig. 1) has the typical appearance of a perpendicular band of a near-prolate symmetric rotor. Calculations based on an estimated $K=-0.95$ predict sharp Q branches for the subbands with $K>3$ but an irregular structure near the band center; the observed spectrum is in qualitative agreement. From consideration of the calculated effects of molecular asymmetry on the Q branches involving $K=1$ and $K=2$, the numbering given in Fig. 1 seems the most probable. However, it could be off by one unit in K. The wavenumbers of the well-defined Q branches are listed in Table I. When these data are analyzed by the usual symmetric-top formula, one obtains $\nu_0=1074.3\pm0.1$ cm^{-1} and

$$A''-\tfrac{1}{2}(B''+C'')=A'-\tfrac{1}{2}(B'+C')=1.98_1\pm0.01\ cm^{-1}$$

The observed value of $A''-\frac{1}{2}(B''+C'')$ permits a fairly good determination of the FNF angle. With an assumed N–F distance of 1.37 A, as in NF_3, and an inertial defect of 0.15 amu A^2 one calculates $\angle FNF=104.2°$. An increase of 0.01 A in the assumed N–F distance increases the angle by about 0.5°. This result points out a further similarity with F_2O, where $\angle FOF=104.2°$.

Low-temperature matrix isolation studies on NF_2 have also been carried out at the University of California.[5] With an N_2 matrix at 20°K ($M/R=1000$) the NF_2 absorptions are very sharp and are clearly resolved from those of N_2F_4. The matrix values for ν_1 and ν_3 are 1069.6 and 930.7 cm^{-1}, respectively. It has been observed for similar molecules that stretching frequencies in the N_2 matrix are about 5 cm^{-1} below the gas phase values. This shift is in agreement with the K numbering given in Table I and establishes the gas phase value for ν_3 as close to 935 cm^{-1}. A more complete report on the matrix results will be published after this work has been extended to the bending region.

* The research at the University of California was supported by a grant from the Petroleum Research Fund administered by the American Chemical Society. Grateful acknowledgment is hereby made to the donors of this fund.

† IBM Fellow, 1960–61.

[1] F. A. Johnson and C. B. Colburn, J. Chem. Phys. **33,** 1869 (1960).

[2] We wish to thank Dr. S. C. Wait and Mr. J. Comeford for assistance in the spectroscopic measurements at the National Bureau of Standards.

[3] The NBS sample was kindly provided by Dr. Clyde McKinley, Research and Development Department, Air Products, Inc., Allentown, Pennsylvania.

[4] H. J. Bernstein and J. Powling, J. Chem. Phys. **18,** 685 (1950).

[5] We should like to thank Professor G. C. Pimentel and Dr. G. E. Leroi for invaluable assistance in this matrix work.

Antiferromagnetic to Ferromagnetic Transitions in Organic Free Radicals*

A. S. EDELSTEIN AND M. MANDEL

Department of Physics, Stanford University, Stanford, California

(Received June 19, 1961)

ORGANIC free radicals have been under investigation at this laboratory for several years. They serve as fairly convenient media for studying exchange and cooperative effects.

Previous work showed anomalies in the temperature dependence of the susceptibilities of picryl amino carbazyl (PAC)[1] and Wurster's blue perchlorate ion (WB).[1] A more detailed study of the high- and low-temperature portions of the susceptibility curves was undertaken to investigate cooperative effects. Since the magnetic-resonance absorption curve for these sub-

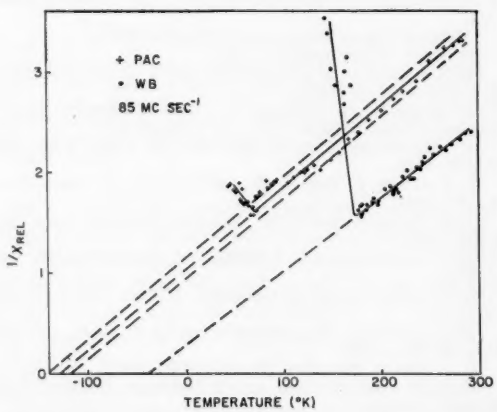

FIG. 1. Relative magnetic susceptibilities of PAC and WB in the high-temperature region. (Measured by ESR at 85 Mc sec^{-1}.)

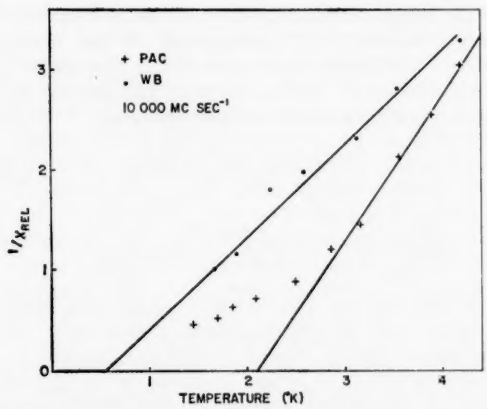

FIG. 2. Relative magnetic susceptibilities of PAC and WB in the liquid-helium temperature region. (Measured by ESR at 10 000 Mc sec^{-1}.)

stances is approximately Lorentzian, the product of the height times the peak-to-peak linewidth squared of the derivative is proportional to the susceptibility. This product will be called the relative magnetic susceptibility χ_{rel}. Relative magnetic-susceptibility measurements at temperatures from 1.5–293°K on WB and PAC show two distinct regions obeying a Curie-Weiss law $\chi_{\text{rel}}=c/(T-\theta)$. The high- and low-temperature

TABLE I. Values obtained for θ.

	θ at high temperature	θ at low temperature
WB	$-39°\pm15°$K	$0.55°\pm0.1°$K
PAC	$-130°\pm10°$K	$2.1°\pm0.1°$K

measurements were made at 85 and 10 000 Mc sec^{-1}, respectively. For both substances the high-temperature region has a large negative θ while the low-temperature region has a small positive θ as shown in Figs. 1 and 2. Fitting a curve of the form $\chi_{\text{rel}}=c/(T-\theta)$ to the data gives the value of θ in Table I.

The manner in which $1/\chi_{\text{rel}}$ departs from a linear dependence upon T is in keeping with representative antiferromagnetic behavior at high temperatures and representative ferromagnetic behavior at low temperatures; i.e., in antiferromagnetism there is an abrupt departure and a cusp at the Néel temperature while in ferromagnetism the departure from linearity is gradual as the temperature approaches the Curie point from above.

Static susceptibility measurements on WB in the high-temperature region by Duffy[2] give $\theta=36°\pm5°$K while those by Hausser[3] give a somewhat lower value. The low-temperature θ for PAC is in agreement with specific-heat measurements since C_v starts departing from a $1/T^2$ dependence at about 3°K.[4]

Yvon *et al.*[5] have observed different high- and low-temperature θ's with the same sign in other organic free radicals.

Our results may be due to a lattice phase change such as occurs in dysprosium[6] and erbium.[7] These elements also exhibit antiferromagnetic behavior at high temperatures and ferromagnetic behavior at low temperatures. Another possibility is that antiferromagnetic coupling at low temperatures induces the molecules to form clusters. The spins of these clusters then interact via a weak ferromagnetic coupling.

We wish to express our appreciation to Professor George Pake, Professor James Burgess, and Robert S. Rhodes for many helpful discussions.

* Supported by Air Force Office of Scientific Research.

[1] R. S. Rhodes, J. H. Burgess, and A. S. Edelstein, Phys. Rev. Letters **6,** 462 (1961).
[2] W. T. Duffy (private communication).
[3] K. H. Hausser, Z. Naturforsch. **11a,** 20 (1956).
[4] J. P. Goldsborough, M. Mandel, and G. E. Pake, Proc. of VII Internat. Conf. on Low Temperature Physics, 1960.
[5] J. Yvon, J. Horowitz, and A. Abragam, Revs. Modern Phys. **25,** 165 (1953).
[6] J. F. Elliott, S. Leyvold, and F. H. Spedding, Phys. Rev. **94,** 1143 (1954).
[7] J. F. Elliott, S. Leyvold, and F. H. Spedding, Phys. Rev. **100,** 1595 (1955).

Theory of the Variation of the Nuclear Quadrupole Interaction in Covalent Bonds with Applied Electric Field

N. BLOEMBERGEN
Harvard University, Cambridge, Massachusetts
(Received July 7, 1961)

THE linear variation of the nuclear quadrupole interaction with applied electric field has recently been observed and discussed in ionic crystals.[1] A similar effect of comparable magnitude is predicted in this communication for nuclei covalently bonded in molecular crystals. Denote by W_i the energy of state $|i)$ of a molecule in a fixed orientation in space. Consider the nuclear quadrupole interaction operator[2] $\mathcal{H}_Q$ and the electric field operator $\mathcal{H}_E=-\sum e_k E_{z,k} z_k$ as small perturbations. The effect which is bilinear in Q and E can quite generally be written as

$$\Delta W_m=\sum_i \frac{(0, m \mid \mathcal{H}_Q \mid i, m)\,(i \mid \mathcal{H}_E \mid 0)}{W_0-W_i} + \text{complex conj.} \quad (1)$$

Here ΔW_m is the change in energy of the nuclear spin state m on application of the field E. The sum is over all excited states of the molecule. A nonvanishing result is obtained only if the wave functions Ψ_0 and Ψ_i do not have even or odd parity around the nucleus in question,

since $\mathcal{H}_Q$ is an even and $\mathcal{H}_E$ an odd operator. The nucleus must not be at a center of symmetry. Equation (1) is not well suited for explicit calculations because the wave functions and eigenvalues of the excited states are not known.

We shall now consider the specific case of the C—Cl bond in paradichlorobenzene. Take the positive z direction pointing from chlorine to carbon atom. Only the z component of the electric field will produce a linear effect.

It is now possible to estimate the effect in terms of the ground-state molecular-orbital wave function[3]

$$\Psi = p\Psi_{3p}{}^{\mathrm{Cl}} + s\Psi_{3s}{}^{\mathrm{Cl}} + \lambda\Psi_{\mathrm{C}}, \tag{2}$$

where $s^2 = 1 - p^2$ is the degree of sp hybridization on the Cl atom; Ψ_{C} is the appropriately directed orbital on the carbon, and $I = (1-\lambda^2)/(1+\lambda^2)$ gives the ionic character of the bond. The values of p, s, and λ can be found by the Ritz variational procedure,[3] both without and with electric field $E_z{}^{\mathrm{loc}}$. It should be kept in mind that the field acting at the position of the bond is not the same as the externally applied electric field E_0. Since no simple procedure is available to calculate the internal field at a point of low symmetry in a lattice, we shall use the Lorentz expression valid at a site of cubic symmetry.

$$E_z{}^{\mathrm{loc}} = \tfrac{1}{3}(\epsilon+2)\,E_z{}^{\mathrm{app}}. \tag{3}$$

The largest uncertainty of the calculations presented here probably resides in this proportionality factor, which is taken as 1.6, since $\epsilon = 2.8$.

The $3s$ lone-pair wave function on the Cl atom should be orthogonal to the hybridized atomic-bond orbital and have the form $p\Psi_{3s} - s\Psi_{3p}$. The energy of the pair is raised by the hybridization. The p_x and p_y lone-pair orbitals are assumed not to taken part in the bonding. The variational procedure could of course readily be extended to include π bonding, d hybridization, etc. Detailed calculations will be presented at a later date. They should also include the variation in internuclear distance R.

An approximate expression for the electric field gradient at the Cl nucleus, sufficiently accurate for the present purpose, is in the notation of Das and Hahn,[2]

$$q_{zz}{}^{\mathrm{Cl}} = (1-s^2-I)\,q_{\mathrm{at}} + 2eI(1-\gamma_\infty)\,R^{-3}. \tag{4}$$

The variation in this quantity on application of an electric field is caused by variation in s, I, and the internuclear distance R. The change in the PQR frequency is

$$\Delta\nu_E = \tfrac{1}{2}e^2Qh^{-1}\{-2sq_{\mathrm{at}}(ds/dE) - [q_{\mathrm{at}} - 2e(1-\gamma_\infty)\,R^{-3}](dI/dE) - 6eI(1-\gamma_\infty)\,R^{-4}(dR/dE)\} \times \tfrac{1}{3}(\epsilon+2)\,E_z{}^{\mathrm{app}}. \tag{5}$$

The largest contributions come from the variation in ionic character and hybridization of the bonding orbital. Admittedly crude approximate expressions for these variations, obtainable from the general Ritz procedure at constant R outlined above are

$$\left(\frac{\partial s}{\partial E}\right)_R = \frac{-e\langle z_{sp}\rangle(1-s^2)^{\frac{1}{2}}}{W_{3p}-W_{3s}}, \tag{6}$$

$$\left(\frac{\partial I}{\partial E}\right)_R = \frac{-4\lambda e I_0 SR}{(1+\lambda^2)\,(1+\lambda^2+2\lambda S)^2(W_c - W_{m0})}. \tag{7}$$

In Eqs. (6) and (7), as well as in Eq. (4), certain integrals over the charge-overlap region have been omitted. In Eq. (6), $W_{3p}-W_{3s}\sim 10.5$ ev is the difference in binding energy of $3p$ and $3s$ orbital on the Cl atom, $e\langle z_{sp}\rangle$ is the matrix element of the electric dipole moment connecting these orbitals. Slater-type wave functions give $\langle z_{sp}\rangle = a_0$, the Bohr radius. With $s^2 = 0.15$, corresponding to 15% hybridization,[2] and $\frac{1}{2}e^2Qq_{\mathrm{at}}h^{-1} = 55$ Mc/sec,[2] the first term gives a contribution to $\Delta\nu_E$ equal to 670 cps for $E_z{}^{\mathrm{app}} = 10^4$ v/cm.

The second term adds to the first one. If the electric field is pointing from the Cl to the C atom, both the hybridization and the ionic character are increased, the quadrupole splitting is decreased. The overlap integral S between the hybridized carbon and chlorine orbitals has a value of about 0.4. The difference in binding energy between the carbon orbital and the molecular orbital is taken as 2 ev. With the internuclear distance $R = 1.76\times10^{-8}$ cm and the ionic character $I = 20\%$, the second term in Eq. (6) then gives a shift of 200 cps. The total predicted shift is therefore 870 cps for $E_z{}^{\mathrm{app}} = 10^4$ v/cm. This will be compared with the experimental value in the following paper.[4]

[1] J. Armstrong, N. Bloembergen, and D. Gill, Phys. Rev. Letters **7**, 11 (1961).
[2] T. P. Das and E. L. Hahn, *Nuclear Quadrupole Resonance Spectroscopy, Suppl. I, Solid-State Physics* (Academic Press Inc., New York, 1958).
[3] C. A. Coulson, *Valence* (Oxford University Press, New York, 1952).
[4] J. Armstrong, N. Bloembergen and D. Gill, J. Chem. Phys. **35**, 1132 (1961), this issue.

Linear Effect of Electric Field on the Cl^{35} Quadrupole Interaction in Paradichlorobenzene*

J. Armstrong, N. Bloembergen, and D. Gill
Harvard University, Cambridge, Massachusetts

(Received July 7, 1961)

THE nuclear quadrupole interaction may vary as a linear function of an applied electric field, if the nucleus is not at a center of symmetry.[1] The effect has recently been observed[2,3] in $NaClO_3$, $KClO_3$, and $NaBrO_3$. It was anticipated theoretically[4] that effects

of the same order of magnitude should occur in covalently bonded substances. Experimental results are reported here on the Cl^{35} zero-field quadrupole resonance in *p*-dichlorobenzene.[5] They are in substantial agreement with the theoretical expectations.

The α phase of *p*-dichlorobenzene has C_{2h} point symmetry.[5] The crystal is not piezoelectric. The center of each molecule is a center of symmetry of the crystal. The symmetry at the position of the four Cl atoms in the unit cell is C_1. If the influence of neighboring molecules is neglected and a single molecule in a fixed orientation in space is considered, there are two symmetry planes through the Cl—C bond. Take the positive z direction at each Cl nucleus pointing to the nearest carbon. Only the electric-field component E_z^{loc} will give rise to a linear effect. The resonance of the two Cl nuclei in the same molecule are shifted by equal, but opposite amounts.

If π bonding is neglected and the asymmetry parameter is taken as zero, the second moment of the zero-field quadrupole resonance in a polycrystalline specimen should increase with the external electric field E_0 according to[2]

$$\langle \Delta\nu^2 \rangle_E = \tfrac{9}{20} R_{zzz}{}^2 E_0{}^2 (\tfrac{1}{2} eQh^{-1})^2. \qquad (1)$$

The factor $\frac{1}{3}$ in Eq. (5) of reference 2 should have been $\frac{9}{20}$ as in the present case, since the electric field E_0 is always at right angles to the rf magnetic field in our experimental configuration.[2] The spatial average

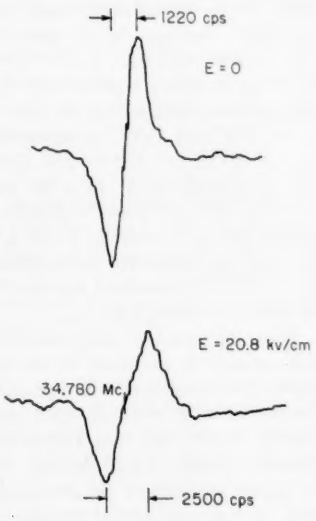

FIG. 1. The absorption derivative of the zero field quadrupole resonance in polycrystalline paradichlorobenzene at 77°K, with and without applied electric field. Second moments in Table I were derived from more accurate curves, taken with a much slower rate of frequency sweep.

$\langle \cos^2\theta_E \sin^2\theta_H \rangle / \langle \sin^2\theta_H \rangle = \frac{9}{20}$ rather than $\langle \cos^2\theta_E \rangle = \frac{1}{3}$ should be taken, where θ_E and θ_H are the angles between the z axis and the directions of the electric field and magnetic rf field, respectively.

TABLE I. The observed width between points of maximum slope $\delta\nu$ and the second moment $\langle \Delta\nu^2 \rangle$ of the Cl^{35} zero-field quadrupole resonance in paradichlorobenzene as a function of applied electric field E_0.

E_0 kv/cm	δ_ν cps	$\langle \Delta\nu^2 \rangle$ in cps^2
0	1240	0.57×10^6
14.9	1800	0.85
17.9	2200	1.0
23.8	2900	1.45

Liquid paradichlorobenzene was poured between a sandwich of condenser plates. The leads to the condenser were supplied with rf chokes. Electric fields up to 25 000 v/cm were applied. A few turns of copper ribbon around the condenser assembly formed the tank coil of a modified Pound spectrometer.[2] The Cl^{35} resonance was observed at 34.780 Mc/sec at 77°K. Recordings of the absorption derivative with and without electric field are shown in Fig. 1. The linear relationship between the second moment and $E_0{}^2$ was confirmed experimentally, as shown in Table I. The observed value for $|R_{zzz}|$ is 6.2×10^9 cm^{-1}. This corresponds to a shift of the resonant frequency of 590 ± 60 cps for an applied field of 10^4 v/cm along the Cl—C bond direction. This is almost three times as large as the corresponding effect in $NaClO_3$. Electrostrictive effects which would give contributions to the second moment proportional to $E_0{}^4$ are completely negligible.

The experimental value is consistent with the theoretical estimate[4] of 870 cps. If the factor 1.6 which was assumed to exist between the externally applied field and the local field at the C—Cl bond is accepted, the experimental result indicates that the amount of hybridization is somewhat smaller than 15% which was assumed in the theory. The hybridization lies probably between 5 and 10%. No agreement could be obtained with our experimental results without some hybridization.

It may be concluded that the electric field effect gives valuable information about the nature of the bond. More detailed studies on single crystals would reveal the effects of π bonding and hybridization with neighboring molecules. A systematic study of a large number of substances by solid-state "Stark-type" spectroscopy appears worthwhile and will give more information about the structure than the zero-field quadrupole splitting alone.

* Research supported by the U. S. Joint Services.

[1] N. Bloembergen, Science **133**, 1363 (1961).
[2] J. Armstrong, N. Bloembergen, and D. Gill, Phys. Rev. Letters **7**, 11 (1961).
[3] T. Kushida and K. Saiki, Phys. Rev. Letters **7**, 9 (1961).
[4] N. Bloembergen, J. Chem. Phys. **35**, 1131 (1961), this issue.
[5] T. P. Das and E. L. Hahn, *Nuclear Quadrupole Resonance Spectroscopy, Suppl. I, Solid-State Physics* (Academic Press Inc., New York, 1958), pp. 113.

Comments and Errata

On the Calculation of Second Moments of Nuclear Magnetic Resonance Lines for Large Molecules. Adamantane Molecule

GEORGE W. SMITH
Research Laboratories, General Motors Corporation, Warren, Michigan
(Received June 19, 1961)

THE NMR second moment S of adamantane ($C_{10}H_{16}$) has been studied by McCall and Douglass.[1] Their experimental rigid lattice second moment is 39 gauss^2. Their theoretical value is the sum of an intramolecular contribution S_1 of 31.5 gauss^2 (based on $r_{CC}=1.54$ A, $r_{CH}=1.07$ A, and tetrahedral angles) and an intermolecular contribution S_2 of 7 gauss^2. A revised calculation[2] of S_1 gives 34.8 gauss^2. Both values of S_1 seem too high to be accounted for by the predominant CH_2 interaction. One would expect a value for S_1 on the order of the 17 gauss^2 of cyclohexane.[3] Therefore, the writer has undertaken an independent calculation of S for adamantane.

We calculated S_1 from the Van Vleck second-moment formula[4] using r_{ij} determined trigonometrically. This value was checked against S_1 as found using r_{ij} measured from a carefully scaled model of adamantane (Fig. 1). The x-ray value[5] of $r_{C-H}=1.09$ A was used. We have

$$S_1=358.1\sum_i\left(\frac{n_i}{N_0}\right)\sum_{(j\neq i)}^{j} r_{ij}^{-6} \quad (r_{ij}\text{ in A}), \qquad (1)$$

where n_i is the number of equivalent protons of type i and N_0 is the total number of protons in the molecule. In adamantane there are four tertiary protons (CH) and 12 secondary protons (CH_2).

From trigonometric computation we find $S_1=15.77$ gauss^2. Measurements from the model yield (with much less work) 16.12 gauss^2. An error in the computation of McCall and Douglass has been found[6] which reduces their value for S_1 to 20.16 gauss^2. Use of the x-ray value of r_{C-H} reduces this further.

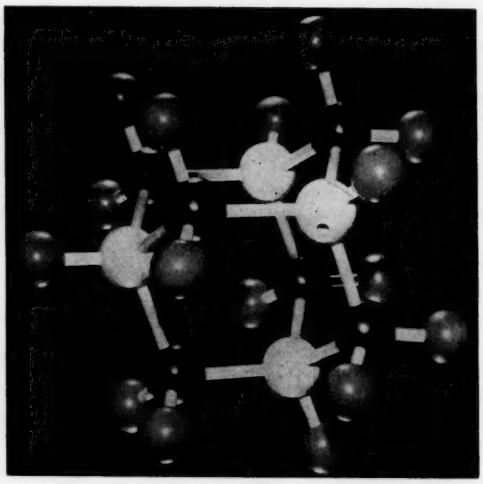

FIG. 1. The adamantane ($C_{10}H_{16}$) molecule. Models of this type were used to determine r_{ij} for S_1 and S_2 by measuring the distance between various proton pairs and applying proper scale factor. Two colors are used to label the carbon atoms for easier cognizance of various symmetries. The atoms are labeled as follows: black=secondary carbon; white=tertiary carbon; grey=hydrogen.

TABLE I. Intermolecular second moment.

$\mathfrak{N}$	M A	S_2' gauss^2	S_2^{term} gauss^2	S_2 gauss^2
0	2.44	0	7.80	7.80[a]
12×3	3.40	3.48	2.90	6.38[a]
12×13	3.97	4.91	1.81	6.72[a]
12×36+6×4	5.25	5.83	0.79	6.62
11 520	14.17	6.60[b]	0.04	6.64

[a] These numbers are inaccurate since some values of r_{ij} for S_1 are greater than M. Accuracy is further reduced by ambiguity in choice of M when M is small.

[b] Includes all first and second neighbors, plus a contribution of 0.11 gauss^2 due to 3rd and 4th nearest neighbor protons with $r_{ij}\leq M$, plus estimate (~0.03 gauss^2) for those on 5th, 6th, 7th, and 8th neighbors with $r_{ij}\leq M$. ($\mathfrak{N}=12\times256+6\times256+24\times218+12\times140$.)

S_2 was calculated from an equation similar to (1). Here the r_{ij} were found solely from models positioned at first- through fourth-nearest-neighbor distances. The crystal structure is f_{CC}[7] (the degeneracies of the first four neighbor positions are 12, 6, 24, 12). S_2 is the sum of two contributions: S_2' the Van Vleck expression for $r_{ij}\leq M$ and S_2^{term} an approximation for the terms $r_{ij}>M$ given by[8] $S_2^{\text{term}}=358.1\times4\pi n_k(3M^3V_0)^{-1}$. V_0 is the cell volume in A^3, n_k is the number of protons per cell, and M is the cutoff radius in A. Results for S_2 for various M are shown in Table I. $\mathfrak{N}$ is the number of interactions considered in determining S_2'. The number of r_{ij} actually measured was far fewer than $\mathfrak{N}$ because of various symmetries.

It can be seen that good consistency for S_2 (6.62 and 6.64 gauss^2) is obtained in the last two rows of the table. The consistency is especially good in that the derivation of S_2' depends upon the use of models while that of S_2^{term} does not. For adamantane, M may be chosen as small as 5.25 A. Only 20 different radii had to be measured from the models in this case. We feel that the use of molecular models can be applied profitably to second moment calculations of other substances.

We can now choose $S_2=6.63$ gauss^2 with a good deal of confidence. This compares favorably with the computed value of 7 gauss^2 of McCall and Douglass[1] who use a different method. Our value for the total rigid-

lattice second moment is therefore 15.77+6.63=22.40 gauss^2. An experimental error in their work has since been found[2] by McCall and Douglass. Recent rough measurements by them yield a value in fair agreement with our calculated value.

Rapid enough random rotational motion of the adamantane molecule should average the intramolecular moment to zero and reduce the intermolecular value. A rough estimate of the second moment can in this case be obtained by replacing all the intermolecular r_{ij} by the center-center intermolecular distances[3] (i.e., by concentrating all nuclear moments at their molecular centers). One then obtains as a rough estimate 0.93 gauss^2. The calculated value of McCall and Douglass is 0.95 gauss^2. Their experimental result is 0.9 gauss^2.

[1] D. W. McCall and D. C. Douglass, J. Chem. Phys. **33,** 777 (1960).
[2] D. W. McCall (private communication, 1961).
[3] E. R. Andrew and R. G. Eades, Proc. Roy. Soc. (London) **A216,** 398 (1953).
[4] J. H. Van Vleck, Phys. Rev. **74,** 1168 (1948).
[5] W. Nowacki and K. W. Hedberg, J. Am. Chem. Soc. **70,** 1497 (1948).
[6] G. W. Smith (private communication to D. W. McCall, 1961).
[7] W. Nowacki, Hevl. Chim. Acta **28,** 1233 (1945).
[8] J. A. Ibers and D. P. Stevenson, J. Chem. Phys. **28,** 929 (1958).

Erratum: Development of the Liquid Equation and the Partial Structure of Water

[J. Chem. Phys. **34,** 2174 (1961)]

ROBERT GINELL
Department of Chemistry, University of Utah, Salt Lake City, Utah

(Received July 17, 1961)

IN calculating the values for Tables I and II, the value used for J should have been $J=0.3150v_0$ ml according to the work of Gibson and Loeffler from whom the value is derived, where v_0 is the specific volume at 1 atm and the temperature. Consequently for this value of J, Eq. (21) becomes

$$\phi_T=\phi_0\exp\left\{\int_{T_0}^{T}\beta dT-\int_{T_0}^{T}\left(\frac{\partial \ln J/L}{\partial T}\right)_p dT\right\}, \qquad (21')$$

and the table values are changed accordingly. The correct values are given in Tables I and II.

TABLE I. Water: variation with temperature at 1-atm pressure, $J=0.3150v_0$ ml.

°C Temp	ϕ_t/ϕ_{25}	Z_nA_{25}	$\Sigma C_i/A_{25}$	$[(v-b)/A_{25}]10^{-5}$	L[a] atm
25	1	0.04169	1.3276	0.3257	2956.8
35	1.02344	0.04141	1.3325	0.3389	3015.0
45	1.03708	0.04106	1.3388	0.3530	3040.7
55	1.04191	0.04064	1.3464	0.3678	3037.7
65	1.03897	0.04020	1.3540	0.3831	3012.1
75	1.02878	0.03974	1.3617	0.3990	2965.7

[a] Data from Gibson and Loeffler.

TABLE II. Water: variation with pressure at 20°C, $J=0.31563$ ml, $L=2911.4$ atm.[a]

p atm	v	Z_nA_{25}	$\Sigma C_i/A_{25}$	$[(v-b)/A_{25}]10^{-5}$
1	1.0020	0.04309	1.2857	0.3099
25	1.0009	0.001731	32.030	0.3085
50	0.9998	0.0008697	63.838	0.3071
100	0.9976	0.0004388	128.68	0.3043
200	0.9934	0.0002233	250.23	0.2990

[a] $A_{20}=0.968458\ A_{25}$.

Comparison of $CH_3\cdot$ and $CF_3\cdot$ Hydrogen Abstraction Reactions*

G. O. PRITCHARD AND G. H. MILLER
Chemistry Department, University of California, Santa Barbara, Goleta, California

(Received April 27, 1961)

DENOTING the activation energies for the hydrogen abstraction reactions of $CH_3\cdot$ and $CF_3\cdot$ radicals as E_m and E_f, respectively, and assuming that radical recombination reactions have zero activation energy, Dodd[1] has found for nonparaffins

$$E_m-E_f=6.4-0.64E_f. \qquad (1)$$

Based on an Evans-Polanyi-type relationship $E=\alpha D(R-H)-\beta$ Dodd shows that the paraffins should obey

$$E_m-E_f=4.0-0.13E_f, \qquad (2)$$

which in fact the experimental values approximately do.

A re-evaluation of Dodd's and more recent data indicate that (1) is erroneous, as the values of E_m or E_f which dictate the slope of this line are the ones to which the greatest uncertainty is attached. From Table I it is seen that E_m-E_f is about 3 kcal/mole for all RH. A consideration of the errors in the E_m-E_f values for the paraffins makes it difficult to assess whether (2) is strictly obeyed as the limits of error are large. As such, it is not an effective test of the Evans-Polanyi relationship.

TABLE I.

	E_m[a] kcal/mole[b]	E_f kcal/mole[c]	$E_m - E_f$
methane	12.8; 14.3; 14.7[d]	10.3±0.5[e]; 10.4[f]; 9.5±2[g]	>3
ethane	10.4±0.4; 11.2±0.3[h]; 11.5±0.2[i]	7.5±0.5[e]; 7.3±0.9[i]	~3–4
propane	(9.5)[k]	6.5±0.5[l]; 6.0±0.9[i]	...
n-butane	8.3±0.2	5.1±0.3[l]; 5.5±1[g]	3.2±0.5
isobutane	7.6±0.2	4.7±0.3[l]; 4.5[f]; ~2.8[i]?	2.9±0.5
2,3-dimethyl-butane	6.9±0.2; 7.8±0.4	1.5±1.4[i]?	....[m]
neopentane	10.0±0.3	7.4±0.6[i]	2.6±0.9
cyclopentane	8.3±0.2; 9.3[n]	4.5±0.6[i]	>3
cyclohexane	8.3±0.2	5.0±0.2[n]	3.3±0.4
benzene	9.2±0.4	6.3±0.2[o]; ~7.5[i]	2.9±0.6
toluene	8.3±0.3	5.4±0.3[o]; 5.8±1.4[i]	2.9±0.6
o-xylene	(8.6)[k]	5.6±0.5[o]	...
acetone	9.7±0.1	6.9±0.1[p]; 7.8±0.9[i]	2.8±0.2
trifluoroacetone	8.9[q]	6.6[q]	~2.3
trifluoroaceto-phenone	(10.2)[k]	7.2±0.5[r]	...
acetaldehyde	7.5±0.3; 6.8[s]	4.0[f]	~3
trifluoroacetal-dehyde	(11.2)[k]?	8.2±0.5[f]	...
hydrogen	11.1[t,u]	8.6±0.5[i]; 9.5±0.7[v]	~2.5
deuterium	11.8[t]; 11.9[w]; 11.7±0.1[x] 12.7±0.5[y,z] 12.1±0.6[aa]	9.5±0.4[h]; 10.2±0.7[v]	~2.5
HD→CX_3H	10.0–10.7[t]	10.5±1.5[v]	....[m]
DH→CX_3D	10.7–11.3[t]	10.5±1.5[v]	....[m]

[a] A. F. Trotman-Dickenson, *Gas Kinetics* (Butterworths Scientific Publications, Ltd., London, 1955).

[b] Unless indicated, E_m values are determined using acetone or acetone-d_6, so that any errors will probably be systematic. No effect is attributed to isotopic substitution in the methyl radical. Acetone-d_6 values may be low by 1 kcal/mole, see reference a.

[c] Reference 2 values recalculated using E_f=5.1±0.3 kcal/mole for *n*-butane as a standard. Isobutane and 2,3 dimethylbutane are considered spurious due to the large difference in reactivities compared with deuterium.

[d] F. S. Dainton, K. J. Ivin, and F. Wilkinson, Trans. Faraday Soc. **55,** 929 (1959).

[e] P. B. Ayscough, J. C. Polanyi, and E. W. R. Steacie, Can. J. Chem. **33,** 743 (1955).

[f] R. E. Dodd and J. W. Smith, J. Chem. Soc. **1957,** 1465.

[g] G. O. Pritchard, H. O. Pritchard, and A. F. Trotman-Dickenson, Chem. & Ind. **1955,** 564.

[h] M. H. J. Wijnen, J. Chem. Phys. **23,** 1357 (1955).

[i] Reference 2.

[j] J. R. McNesby and A. S. Gordon, J. Am. Chem. Soc. **77,** 4719 (1955).

[k] Estimated, using $E_m - E_f$=3 kcal/mole.

[l] P. B. Ayscough and E. W. R. Steacie, Can. J. Chem. **34,** 103 (1956).

[m] No worthwhile estimate possible.

[n] J. R. McNesby and A. S. Gordon, J. Am. Chem. Soc. **79,** 825 (1957).

[o] S. W. Charles and E. Whittle, Trans. Faraday Soc. **56,** 794 (1960).

[p] Reference 5.

[q] R. A. Sieger and J. G. Calvert, J. Am. Chem. Soc. **76,** 5197 (1954).

[r] R. M. Smith and J. G. Calvert, J. Am. Chem. Soc. **78,** 2345 (1956).

[s] P. Ausloos and E. W. R. Steacie, Can. J. Chem. **33,** 31 (1955).

[t] E. Whittle and E. W. R. Steacie, J. Chem. Phys. **21,** 993 (1953).

[u] Value based on discussion in reference 2; cf. also J. F. Henderson and E. W. R. Steacie, Can. J. Chem. **38,** 2161 (1960).

[v] P. B. Ayscough and J. C. Polanyi, Trans. Faraday Soc. **52,** 960 (1956).

[w] J. R. McNesby, A. S. Gordon, and S. R. Smith, J. Am. Chem. Soc. **78,** 1287 (1956).

[x] T. G. Majury and E. W. R. Steacie, Discussions Faraday Soc. **14,** 45 (1953).

[y] R. E. Rebbert and E. W. R. Steacie, Can. J. Chem. **32,** 113 (1954).

[z] $HgMe_2$ source.

[aa] J. Chanmugam and M. Burton, J. Am. Chem. Soc. **78,** 509 (1956).

As $D(CH_3-H) = D(CF_3-H)$[2,3] $E_m - E_f$ must be considered mainly in terms of the attacking radical for a particular *RH*.[4] That the major contributing factor is the enhanced electronegativity of the $CF_3\cdot$ over the $CH_3\cdot$ radical has already been proposed.[2] (Evidence that the activation energy for the recombination of $CF_3\cdot$ may differ from that of $CH_3\cdot$ by as much as 2 kcal/mole[5] will reduce $E_m - E_f$ to about 2 kcal/mole throughout.)

* This work was supported by a grant from the National Science Foundation.

[1] R. E. Dodd, J. Chem. Phys. **26,** 1353 (1957).

[2] G. O. Pritchard, H. O. Pritchard, H. I. Schiff, and A. F. Trotman-Dickenson, Trans. Faraday Soc. **52,** 849 (1956).

[3] J. B. Farmer, I. H. S. Henderson, F. P. Lossing, and D. G. H. Marsden, J. Chem. Phys. **24,** 348 (1956).

[4] J. M. Tedder, Quart. Revs. (London), **24,** 336 (1960).

[5] G. O. Pritchard and J. R. Dacey, Can. J. Chem. **38,** 182 (1960).

On a Reported New Form of Ice

J. SCHIFFER AND D. F. HORNIG

Frick Chemical Laboratory, Princeton University, Princeton, New Jersey

(Received May 31, 1961)

IT has been reported that when H_2O vapor is condensed slowly on a NaCl plate and warmed to −20°C a new form of "ice" is obtained.[1] Its infrared spectrum is characterized by considerably sharper lines, higher stretching frequencies, and lower librational frequencies than those of either cubic or hexagonal ice.[2] It was noticed that, although other regions are somewhat different, the librational frequency reported is surprisingly close to that of water molecules trapped in alkali halide pellets.[3] Moreover, the "transition" temperature was surprisingly close to the freezing point of saturated salt solutions, −21.2°C. We have therefore repeated and extended the observations of Lüttke and Mecke and it seems clear that the spectrum reported was actually that of sodium chloride hydrate, $NaCl\cdot 2H_2O$.

According to the phase diagram of the NaCl—H_2O system,[4] the eutectic temperature for the coexistence of ice and $NaCl\cdot 2H_2O$ is −21.2°C so that in the presence of excess NaCl all of the ice deposited is expected to transform to the hydrate if the temperature is raised above that of the eutectic. It was indeed found that the spectrum of ice deposited at lower temperatures transformed to that reported when it was warmed to −20°C. Moreover, when the "ice" was pumped off without further warming it was found that the surface of the NaCl plate had been etched, showing that the H_2O had interacted with the NaCl. This could be seen clearly on microscopic examination. Subsequent polishing left the NaCl plate clear and transparent to infrared radiation.

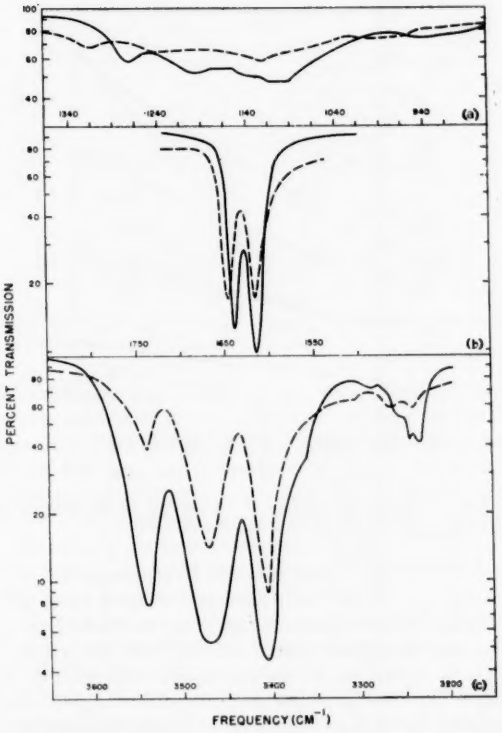

FIG. 1. Infrared spectra of $NaCl \cdot 2H_2O$ (- - - -), and $NaBr \cdot 2H_2O$ (————) at −190°C. (a) Libration overtone region, (b) bending region, (c) stretching region.

A similar process was carried out at −16°C on single crystal plates of NaBr to produce the well-known hydrate $NaBr \cdot 2H_2O$.[5] The infrared spectra of the two hydrates are compared in Fig. 1. It is clear that except for some frequency shifts and slight changes in relative intensities the spectra are essentially the same in all three regions. Consequently, it seems certain that the "ice" of Lüttke and Mecke is actually $NaCl \cdot 2H_2O$ and that the structure of this hydrate is very similar to that of $NaBr \cdot 2H_2O$.

As part of a study of salt hydrates we have also studied these crystals when they contained small admixtures of HDO in place of H_2O or D_2O. The uncoupled OH and OD peaks in the bromide and chloride are also very similar and give evidence of both OH—X^- and OH···O bonding. The details of these studies will be reported in a forthcoming publication.

[1] R. Mutter, R. Mecke, and W. Lüttke, Z. physik. Chem. **19,** 83 (1959).
[2] D. F. Hornig, H. F. White, and F. P. Reding, Spectrochim. Acta **12,** 338 (1958); C. Hass and D. F. Hornig, J. Chem. Phys. **32,** 1763 (1960).
[3] J. T. Mullhaupt, thesis, Brown University, 1958.
[4] *Natrium,* Vol. 21 of *Gmelins Handbuch der Anorganischen Chemie* (Verlag Chemie, Berlin, 1928), 8th ed. p. 332.
[5] W. A. Wooster, Nature **130,** 698 (1932).

Erratum: Effect of Electron Energy on Some Electron-Impact Processes

[J. Chem. Phys. **34,** 2046 (1961)]

SEYMOUR MEYERSON
Research and Development Department, American Oil Company, Whiting, Indiana

(Received July 14, 1961)

ALL the ring-deuterated species, properly identified as $o-d$ and $m-d$, appeared in print, inadvertently, as $x-d$. In Tables I, II, IV, and V, $x-d$ should be changed to read $o-d$; in Tables III and VI, it should be changed to read $m-d$. In the Experimental section, "$x-d$" species are referred to on lines 3, 4, 5, and 17. Proper notations for the ring-deuterated compounds, wherever they appear, are: *p*-xylene-$o-d$, toluene-$o-d$, and benzyl chloride-$m-d$.

Erratum: Binding Energies of Alkali Halide Molecules

[J. Chem. Phys. **34,** 2069 (1961)]

G. M. ROTHBERG
Department of Physics, Rutgers University, New Brunswick, New Jersey

(Received July 17, 1961)

EQUATIONS (6)–(8) describe the electric field F_1 and not the field F_2. To obtain F_2 merely interchange x and y and α_1 and α_2.

Addendum: Kinetic Model for Solid-State Reactions

[J. Chem. Phys. **34,** 2010 (1961)]

R. E. CARTER
General Electric Research Laboratory, Schenectady, New York

(Received June 19, 1961)

THE writer's attention has been drawn[1] to the analysis of Ginstling and Brounshtein[2] who have also treated the diffusion-controlled reaction of spherical particles.

In their analysis these investigators assumed a constant diffusion coefficient and did not allow for a change of volume as spheres of component A react to form AB. Any analysis which demands a constant diffusion coefficient is severely handicapped since experimental evidence has shown that diffusion coefficients are concentration dependent through nonstoichiometric product layers.

A more realistic approach is to consider only the total flux of material through the reaction layer as was done in this paper. This flux is always the product of the cross-sectional area, the diffusion coefficient, and the activity gradient. While in most chemical reactions these terms are difficult to determine individually, the total flux can usually be measured by observing the over-all reaction rate, while any local variation in the flux will cause obvious concentration changes in the product layer.

Ginstling and Brounshtein begin their derivation from Fick's second law for a constant diffusion coefficient, but they fix the concentration gradient to give a constant flux through each annular section of the reaction layer. Their analysis is therefore not restricted to a constant diffusion coefficient although they do not discuss the fact. The two analyses are therefore identical except for the inclusion of the volume change allowed for in the analysis presented in this paper. If this derivation is repeated for the case of no volume change, an equation is obtained which is identical with that of Ginstling and Brounshtein.

Ginstling and Brounshtein describe the rate of reaction of spheres by the equation

$$\tfrac{2}{3}x+(1-x)^{\frac{2}{3}}=1-(K/r_0^2)t, \qquad (1)$$

where x = the fraction of each sphere which has reacted and r_0 is the initial radius of each sphere. The rate of oxidation of uniformly sized spheres discussed in this paper is shown in Fig. 1 and plotted according to

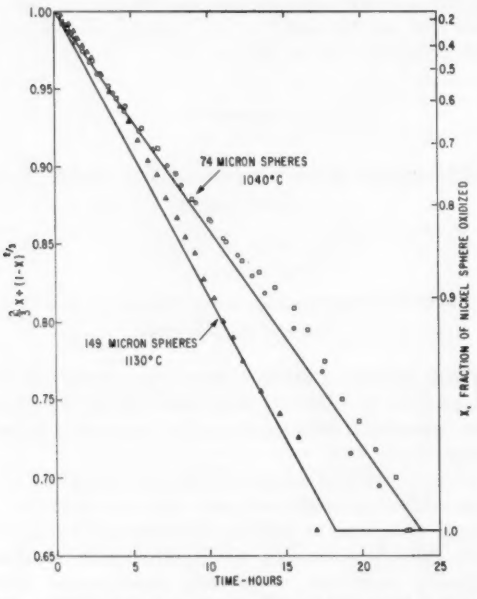

FIG. 1. Plot of $\frac{2}{3}x+(1-x)^{\frac{2}{3}}$ vs time for the oxidation of nickel spheres in oxygen: □, ○, 74 μ spheres, 1040°C; △, 149 μ spheres, 1130°C; x = the fraction of the sphere reacted.

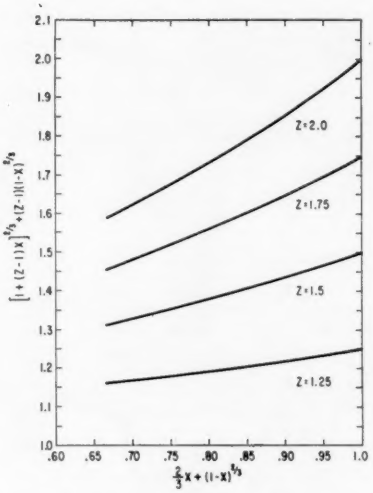

FIG. 2. Plot of the function of x according to the analysis of this paper vs that of Ginstling and Brounshtein.

Eq. (1). As shown, the data can be represented as well by Eq. (1) as by the equation developed here. The influence of the volume change z, for NiO=1.52, must therefore be almost constant throughout the reaction. This is shown to be approximately true in Fig. 2, where the two functions of x are plotted against one another for various values of z. If the influence of z on the rate were constant, straight lines would be obtained. In fact the departure from a straight line is just observable for values of z up to 1.5 and becomes significant only for z greater than 2.

We must conclude, therefore, that although the analysis given in this paper more nearly represents an actual chemical system, the analysis of Ginstling and Brounshtein is probably as accurate as any kinetic data being analyzed.

[1] J. R. Hutchins, III, Corning Glass Works, Corning, New York (private communication).
[2] A. M. Ginstling and B. I. Brounshtein, J. Appl. Chem. (U.S.S.R.) **23**, 1249 (1950) [English translation, p. 1327].

Notes

Rate of the Reaction NO+N*

JOHN T. HERRON
Mass Spectrometry Section,
National Bureau of Standards, Washington, D. C.
(Received April 5, 1961)

CLYNE and Thrush[1] have reported the rate of the reaction NO+N→N_2+O over the temperature range 476° to 755°K to be $k=3.0\pm0.6\times10^{13}\exp(-200\pm700/RT)$ cc mole^{-1} sec^{-1}. In an earlier study

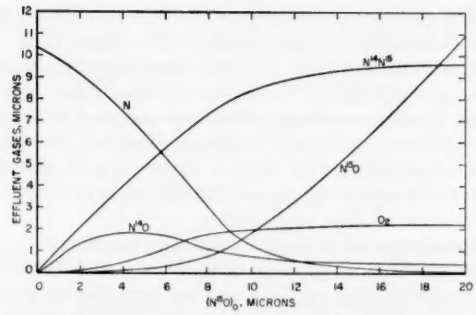

FIG. 1. Steady state partial pressures of effluent gases as a function of initial $N^{15}O$ partial pressure.

Kistiakowsky and Volpi[2] gave a lower limit to this reaction of $k=5\times10^{13}$ cc mole^{-1} sec^{-1} at room temperature. The later workers used a mass spectrometer to follow the reaction, although they were unable to simultaneously observe both NO and N during the course of the reaction.

By using a mass spectrometer of greater sensitivity, and working at lower reactant partial pressures, it is possible to measure the rate of the reaction.

The reactor used in this work was a modified version of that first described by Eltenton[3] and described in detail elsewhere.[2,4–6]

Nitrogen gas was partially dissociated in a 2450-Mc electrodeless discharge. The products flowed through a 0.7-cm diameter tube, across the 1-mil sampling leak of the mass spectrometer, and then to the pump. Reactant gas was added through a concentric tube 1.1 to 2.7 cm upstream of the leak. For total pressures of 0.33 to 0.87 mm and nitrogen flows of 16 to 65 cc/min, the distance between the point at which reactant was admitted and the leak corresponded to reaction times of 0.5×10^{-3} to 1.7×10^{-3} sec. The reaction was studied at room temperature.

Changes in the partial pressures of stable materials were observed by means of conventional mass spectrometric techniques, using 70-v ionizing electrons. Relative nitrogen atom partial pressures were observed using 14.5-v ionizing electrons. The latter were related to absolute partial pressures by means of the assumed stoichiometry of the reaction.[7]

Early in the course of this investigation it was found that NO was being reformed by secondary reactions of nitrogen and oxygen atoms. To overcome this difficulty 96% $N^{15}O$ was used as a reactant.

A typical set of data is shown in Fig. 1. The products of the reaction are $N^{14}N^{15}$, $N^{14}O$, and O_2. Other than confirming its presence, no attempt was made to analyse for atomic oxygen. Over the range of initial $N^{15}O$ partial pressures used, the partial pressure of $N^{14}N^{15}$ produced was equal to the amount of $N^{15}O$ consumed, as would be expected from the stoichiometry of the reaction. This was not exactly true for nitrogen atoms, although the uncertainty in this measurement was considerably greater.

The best value for the rate of the reaction, calculated from the usual second order rate expression was $k=1.0\pm0.5\times10^{13}$ cc mole^{-1} sec^{-1}. The deviation given is three times the standard deviation of the average. This value agrees, within the limits of experimental error, with that calculated from the data of Clyne and Thrush for the reaction at room temperature (300°K), $k=2.2\pm0.6\times10^{13.0\pm0.5}$ cc mole^{-1} sec^{-1}.

The $N^{14}O$ and O_2 observed as products of the reaction are probably the results of heterogeneous reactions occurring within the ion source of the mass spectrometer. This is discussed in more detail elsewhere.[8]

* This work was supported in part by the Advanced Research Projects Agency.

[1] M. A. A. Clyne and B. A. Thrush, Nature **189,** 56 (1961).
[2] G. B. Kistiakowsky and G. G. Volpi, J. Chem. Phys. **28,** 665 (1958).
[3] G. C. Eltenton, J. Chem. Phys. **15,** 455 (1947).
[4] D. S. Jackson and H. I. Schiff, J. Chem. Phys. **23,** 2333 (1955).
[5] J. T. Herron, thesis, McGill University, April 1957.
[6] J. T. Herron and H. I. Schiff, Can. J. Chem. **36,** 1159 (1958).
[7] G. B. Kistiakowsky and G. G. Volpi, J. Chem. Phys. **27,** 1141 (1957).
[8] J. T. Herron, J. Research Natl. Bur. Standards **65A,** Sept.–Oct. 1961.

Photochromism of *N*-3-Pyridylsydnone

T. MILL,* A. VAN ROGGEN,† AND C. F. WAHLIG

Organic Chemicals Department, E. I. du Pont de Nemours and Company, Experimental Station, Wilmington, Delaware

(Received April 14, 1961)

IN a study of the photochromism and electron spin resonance (ESR) absorption of *N*-3-pyridylsydnone, Gutowsky, Rutledge, and Hunsberger[1] have reported inability to detect ESR absorption immediately after blue color was produced by ultraviolet irradiation. The powder subsequently developed a detectable ESR, varying with time in warm air or vacuum, which was accompanied by further color changes. This letter reports additional experiments which indicate that (1) two optical absorption bands in the visible range are involved: the shorter wavelength band (I) is associated with ESR absorption; the longer one (II) is responsible for the blue color; (2) irradiation with ultraviolet light at low temperatures produces a colorless species which is converted to the blue product on subsequent warming; and (3) the ESR absorption spectrum differs significantly from that of free radicals induced by electron irradiation. Photoconductive and microscopic examinations indicate that the photochromism results from color centers analogous to those of the alkali halides.

All of the following experiments were done in air unless otherwise specified.

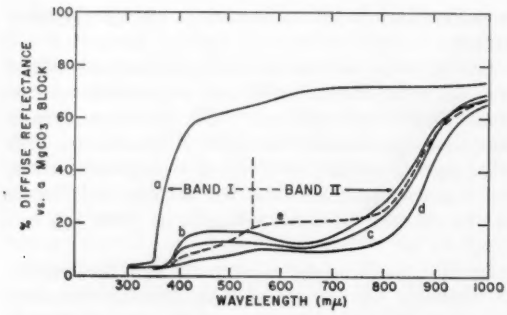

FIG. 1. The diffuse spectral reflectance of *N*-3-pyridylsydnone as a function of exposure to a GE type RS sun lamp at a distance of 10 in.: (a) the unexposed sample, (b) after 1 min, (c) after 3 min, (d) after 20 min, and (e) the sample which was exposed 3 min, subsequently bleached by momentary heating in air at 80°C.

Irradiation of *N*-3-pyridylsydnone powder reduced the reflectance throughout the visible range (Fig. 1). Part of the reflectance in band II was regained on warming, whereas the reflectance in band I was reduced further. The result was a brown color which obscured further photochromism.

The intensity of the ESR absorption of irradiated samples was approximately proportional to the time of irradiation, and it was further increased by subsequent thermal bleaching. Correlation of the ESR with band I was suspected and confirmed by exposing the related compound, *N*-phenylsydnone, to uv radiation. This produced both a strong ESR signal similar in skewed shape to that of uv-irradiated *N*-3-pyridylsydnone and a decrease of reflectance at wavelengths corresponding only to band I which could not be even partially reversed by heating.

In agreement with Gutowsky, these observations indicate that two species can be derived from *N*-3-pyridylsydnone, one blue, another paramagnetic. However, the problem of how energy is stored in the photochemically activated form is rendered more complex by the observation of still another species. When irradiated at −78°C in air or in vacuum the sydnone showed no visible color change, and in vacuum developed no ESR absorption. Studies in the range of −30° to −78°C nevertheless indicated a purely thermal activation energy for subsequent color development of 11–13 kcal. Thus, the photoproduct is colorless and without ESR absorption.

The thermal shift[2] of band II absorbance to band I and the association of ESR[3] with band I are characteristic of *F*- and *F'*-center bands in the alkali halides. In addition, an extensive search for photochromism in *N*-3-pyridylsydnone solutions indicated that it was indeed limited to the solid state. Additional behavior of color centers was therefore sought, in particular the motion of electrons in forming an *F'*-type center (band II).

The presence of charge carriers was established by the observation of photoconductivity (light/dark dc current ratio about *2* to *3*) in well-formed crystals irradiated strongly enough to produce the blue color. Moreover, a momentary surge of current occurred when the crystals were thermally bleached. However, the blue coloration, observable with a microscope as streaks parallel to crystalline planes, did not move in a field of 1000 v/cm at room temperature.

Irradiation of *N*-3-pyridylsydnone powder with 2-Mev electrons resulted in a blue color and an ESR spectrum showing partially resolved hyperfine structure not observed in uv-irradiated samples. This high-energy irradiation, therefore, not only causes the color formation associated with crystalline imperfections, but also breaks bonds in the molecules of the parent compound. The free radicals so formed are trapped in the rigid matrix of the sydnone, and contribute to the composite ESR spectrum. As the *g* values of the imperfections and the free radicals differ only slightly, their spectra overlap, and the observed spectrum cannot easily be related to a definite free radical structure. Comparison of the spectra after uv- and electron-irradiation strongly suggests that uv irradiation produces color centers rather than free radicals.

It is suggested that the time dependences of the spin signal in air and in vacuum, observed by Gutowsky, Rutledge, and Hunsberger, are compatible with the known influence of an ambient vapor of the lattice-anion component of ionic crystals that exhibit color centers.[4] In the case of meso-ionic *N*-3-pyridylsydnone, a component of air, oxygen, happens to serve as the lattice anion.

* Present Address: Stanford Research Institute, Menlo Park, California.

† Polychemicals Department.

[1] H. S. Gutowsky, R. L. Rutledge, and I. M. Hunsberger, J. Chem. Phys. **29**, 1183 (1958).

[2] N. F. Mott and R. W. Gurney, *Electronic Processes in Ionic Crystals* (Oxford University Press, London, 1948), 2nd ed., p. 130.

[3] C. A. Hutchison, Jr., and G. A. Noble, Phys. Rev. **87**, 1125 (1952).

[4] F. Seitz, Revs. Modern Phys. **23**, 328 (1951).

Proton Magnetic Resonance Study of Ferroelectric $NaH_3(SeO_3)_2$ and $LiH_3(SeO_3)_2$

R. BLINC* AND M. PINTAR

Nuclear Institute "J. Stefan", Ljubljana, Yugoslavia

(Received May 5, 1961)

IN order to obtain additional information on the dynamics and distribution of hydrogen atoms in ferroelectrics of the KH_2PO_4 type, proton magnetic resonance measurements have been made on polycrystalline $NaH_3(SeO_3)_2$ and $LiH_3(SeO_3)_2$, in which ferroelectric behavior was recently discovered. Complemen-

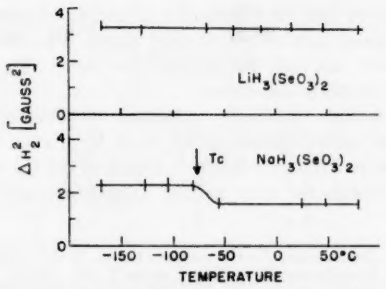

FIG. 1. Second moments of the proton magnetic resonance absorption plotted against temperature.

tary studies of the hydrogen vibration spectra in the nonferroelectric and ferroelectric phases have been made as well.

The temperature dependences of the second moments of the proton magnetic-resonance absorption lines of $NaH_3(SeO_3)_2$ and $LiH_3(SeO_3)_2$ are given in Fig. 1. $LiH_3(SeO_3)_2$, which is ferroelectric up to the melting point at 110°C, exhibits no linewidth transition in the temperature range −175° to 80°C. On the other hand, a small, but significant linewidth transition was found in $NaH_3(SeO_3)_2$ in the vicinity of the Curie point at −79°C.

The hydrogen vibration spectra of both $NaH_3(SeO_3)_2$ and $LiH_3(SeO_3)_2$ show, as in the case of KH_2PO_4, two broad OH stretching bands, centered around 2750 cm^{-1} and 2200–2400 cm^{-1}. This demonstrates the presence of strong hydrogen bonds connecting the SeO_3 ions and thus confirms the proposed x-ray structures.[1,2] The 2200–2400 cm^{-1} band seems in both crystals to be split into two components, the splitting being increased on going to the ferroelectric phase. On deuteration, this splitting disappears in the lithium salt, and two OD stretching bands appear at 2100 and 1720 cm^{-1}, again at nearly the same frequencies as in KD_2PO_4. This is true also for the OH deformation bands at 1580 and 1000–1230 cm^{-1} in both $NaH_3(SeO_3)_2$ and $LiH_3(SeO_3)_2$ as well as for the γ_{OD} band of the deuterated lithium salt at 915 cm^{-1}.

The occurrence of a proton magnetic-resonance linewidth transition in the vicinity of the Curie point in $NaH_3(SeO_3)_2$ indicates that the ferroelectric transition is connected with a rearrangement of the proton sites. The second moments above and below the Curie point are consistent, respectively, with a dynamically disordered and a dynamically ordered distribution of protons between two equilibrium sites in the O–H—O bonds, similar to that found in KH_2PO_4.[3] The absence of a linewidth transition in $LiH_3(SeO_3)_2$, which exists only in an ordered, ferroelectric phase, is consistent with this interpretation.

The assumption of a dynamic order-disorder phase transition of basically the same nature as in KH_2PO_4 is further supported by the hydrogen vibration spectra. These exhibit no drastic frequency shifts on going through the Curie point as expected in displacement-type transitions.[4] The apparent doubling of the OH stretching bands likewise suggests the existence of two equilibrium positions for the protons in the O–H—O bonds.

Although the rearrangement of the proton sites seems to trigger the transition, there should be—according to some preliminary calculations—significant contributions to the internal field, arising from polarizabilities and displacements of the SeO_3 and Li^+ (or Na^+) ions. This could perhaps explain the changes occurring in the SeO_3 absorption bands in the 600–900 cm^{-1} region on cooling to 77°K.

The authors wish to thank Dr. A. Unterleitner for a communication on the structure of $NaH_3(SeO_3)_2$ prior to publication and to Dr. S. Detoni for taking some of the vibrational spectra. One of the authors (R. B.) would like to acknowledge discussions with Prof. J. S. Waugh of the Massachusetts Institute of Technology in the final stage of this work.

* Present address: Alfred P. Sloan Post-Doctoral Fellow at the School for Advanced Study, Massachusetts Institute of Technology, Cambridge 39, Massachusetts.

[1] A. Unterleitner (private communication).
[2] K. Vedam, Y. Okaya, and R. Pepinsky, Phys. Rev. **119,** 1252 (1960).
[3] G. E. Bacon and R. L. Pease, Proc. Roy. Soc. (London) **A230,** 359 (1955).
[4] W. Cochran, Phys. Rev. Letters **3,** 412 (1959).

On the Quasi-Crystalline Model of Water

S. K. JOSHI

Physics Department, The University of Allahabad, Allahabad 2, U. P., India

(Received December 28, 1960)

ATOMIC motions in liquids pose a complicated problem and a satisfactory theory for them is lacking. Very recently scattering of cold neutrons has been used to study the atomic motions in liquid water.[1–5] Hughes *et al.*,[3,4] from their experiments infer that these atomic motions in water are similar to those of a solid rather than a gas. Singwi and Sjölander[5] from the analysis of the available neutron-scattering experiments find that the general trend of both the quasi-elastic and inelastic scattering of cold neutrons and the magnitude of the diffusive broadening seem to support a quasi-crystalline model of water.[6–8] From these studies one understands that as far as thermal vibrations and the other rapid changes and interactions of the order of 10^{-13}-sec period are concerned, the behavior of the liquid is quite similar to that of a solid. Singwi and Sjölander[5] assuming the Debye frequency spectrum for water have calculated the differential scattering cross section for very slow neutrons and they find that the

calculated cross section with an assumed value of 135°K for the Debye temperature gives a very reasonable fit with the experimental results of Hughes *et al.*[3,4] In this note an attempt is made to estimate the parameter Debye Θ for water, by a method often used in evaluating Θ for solids. In view of the above mentioned statements we are justified in following this procedure.

In the Debye model the appropriate expression for Θ to be used here is given by[9]

$$\Theta=(h/k)\nu_m,$$

where

$$\nu_m^{-3}=(4\pi V/9N)[(2/c_t^3)+(1/c_l^3)],$$

h is Planck's constant, k is Boltzmann's constant, and N is the number of vibrating units in the volume V of the specimen. The velocities of c_t and c_l of the transverse and the longitudinal waves, respectively, can be expressed in terms of the elastic moduli of the isotropic solid. In terms of adiabatic compressibility β, Poisson's ratio σ, and the density ρ we can write

$$2/c_t^3+1/c_l^3=\rho^{\frac{3}{2}}\beta_a^{\frac{1}{2}}\{2[2(1+\sigma)/3(1-2\sigma)]^{\frac{3}{2}}+[(1+\sigma)/3(1-\sigma)]^{\frac{3}{2}}\}.$$

For water at 25°C, $\rho=0.997$ g/cm³ and $V=m_{H_2O}/\rho=3.00\times10^{-23}$ cm³, where m_{H_2O} is the mass of the water molecule. We assume that the value of σ for ice measured by Northwood[10] is also valid for 'solid' water. Some sort of estimate of the compressibility β_∞ of water at very high frequencies has to be made. The compressibility contains a contribution from the structural relaxation. At very high frequencies this effect must drop out, producing a dispersion in the velocity of sound. The dispersion frequency of water presumably lies in the range 10^{11}–10^{12} cps, and the neutron-scattering process is therefore completed in a time which is short compared with the structural relaxation time. Thus neglecting structural compressibility, the high-frequency compressibility of water will be very nearly equal to the instantaneous compressibility β_∞. Hall[11] has given a value of 18×10^{-12} cm²/d for the instantaneous isothermal compressibility $\beta_{T\infty}$. The instantaneous adiabatic compressibility $\beta_{a\infty}$ will be given by the conversion formula

$$\beta_{a\infty}=\beta_{T\infty}-(T\alpha^2V/C_p).$$

Here α is the coefficient of linear expansion and C_p is the specific heat at constant pressure, and again for 'solid' water we have used the values of α and C_p for ice measured by Powell,[12] and Giauque and Stout,[13] respectively. This gives $\beta_{a\infty}=17.95\times10^{-12}$ cm²/d.

The calculated value of Θ comes out to be 155°K, which is in fair agreement with the Θ value used by Singwi and Sjölander.[5] Actually the agreement is better than expected in view of the uncertainties in (a) Hall's theory from which β_∞ is taken, (b) the assumption that solid water can be treated by a formalism[5] appropriate, if at all, to isotropic monatomic solids and (c) the assumption that the values of σ, α, and C_p measured for ice are good ones to use in solid water. Therefore, the agreement can not be claimed to prove the quasi-crystalline model for water.

The author is deeply indebted to Professor K. Banerjee for his interest, to Dr. G. S. Verma for discussion, and to Professor Henry S. Frank of the University of Pittsburgh for very helpful suggestions and comments.

[1] B. N. Brockhouse, Nuovo cimento Suppl. **9,** 45 (1958).
[2] B. N. Brockhouse, Phys. Rev. Letters **2,** 287 (1959).
[3] D. J. Hughes, H. Palevsky, W. Kley, and E. Tunkelo, Phys. Rev. Letters **3,** 91 (1959).
[4] D. J. Hughes, H. Palevsky, W. Kley, and E. Tunkelo, Phys. Rev. **119,** 872 (1960).
[5] K. S. Singwi and Alf Sjölander, Phys. Rev. **119,** 863 (1960).
[6] J. D. Bernal and R. H. Fowler, J. Chem. Phys. **1,** 515 (1933).
[7] J. A. Pople, Proc. Roy. Soc. (London) **A205,** 163 (1951).
[8] J. Frenkel, *Kinetic Theory of Liquids* (Clarendon Press, Oxford, England, 1946).
[9] M. Blackman, *Encyclopedia of Physics* (Springer-Verlag, Berlin, Germany, 1955), Vol. 7, Pt. I, p. 328.
[10] T. D. Northwood, Can. J. Research **25A,** 88 (1947).
[11] L. Hall, Phys. Rev. **73,** 775 (1948).
[12] R. W. Powell, Advances in Phys. **7,** 276 (1958).
[13] W. F. Giauque and J. W. Stout, J. Am. Chem. Soc. **58,** 1144 (1936).

Electron Spin Resonance Spectrum and Structure of $CH_3\dot{C}H(CO_2H)$

J. R. Morton and A. Horsfield

Basic Physics Division, National Physical Laboratory, Teddington, Middlesex, England

(Received April 13, 1961)

THE electron spin resonance spectrum of the radical $CH_3\dot{C}H(CO_2H)$ was first detected in a single crystal of x-irradiated *l*-alanine by van Roggen, van Roggen, and Gordy,[1] and this work was later refined by Miyagawa and Gordy.[2] We have had occasion to re-examine the spectrum of γ-irradiated *l*-alanine using a superheterodyne spectrometer operating at 9000 Mc/sec. Our analysis of the spectra differs in some details from that of the aforementioned authors, and we also obtained information about the structure of the radical from the anisotropy of the methyl-hydrogen coupling.

Single crystals of *l*-alanine were grown from aqueous solutions and γ-irradiated with an estimated dose of 5 megarad per crystal. The crystals were orthorhombic, and electron spin resonance spectra were obtained every 15° by rotating the crystal about each of its orthorhombic axes in turn. The axis of rotation was in each case held perpendicular to the magnetic field, so that the four radical sites per unit cell became equivalent in pairs. A further simplification, when all four radical sites became indistinguishable, occurred when one of the axes was parallel to the magnetic field. The analysis

TABLE I. Coupling tensors (Mc/sec) of radical $CH_3\dot{C}H(CO_2H)$.

Nucleus	Tensor in a, b, c axis-system			Principal values	Direction cosines in a, b, c axis system		
α proton	42.0	17.9	20.7	(−)25.0	(0.835,	−0.468,	−0.289)
	17.9	51.5	9.3	(−)49.8	(0.231,	0.776,	−0.587)
	20.7	9.3	70.4	(−)89.4	(0.499,	0.423,	0.756)
Methyl protons	67.0	0.0	0.0	(+)67.0	(1.000,	0.000,	0.000)
	0.0	71.0	4.4	(+)67.5	(0.000,	0.782,	−0.624)
	0.0	4.4	73.0	(+)76.5	(0.000,	0.624,	0.782)

of the spectrum was simplified by the fact that the three methyl protons always coupled equally, presumably due to the rotation of the methyl group about the $\dot{C}—CH_3$ bond, and gave rise to four lines of intensity ratio 1:3:3:1. The numerical value of the methyl proton coupling, however, was slightly (approximately 10%) anisotropic. The α proton, i.e., that attached directly to the free-radical carbon atom, gave rise to a further splitting which had a large anisotropic component.

The coupling due to the α proton may be represented by a tensor, in which the diagonal elements α_{aa}, α_{bb}, α_{cc} are the couplings when the applied field is along the (100), (010), and (001) crystal directions, respectively, and the off-diagonal elements are represented by α_{ab}, α_{bc}, and α_{ca}. Table I shows the α-proton coupling tensor, together with its principal values, and the direction cosines of the latter in the a,b,c axis system. The tensor elements are in Mc/sec, with an estimated error of ± 2Mc/sec. The principal values of the α-proton tensor are similar to those observed in other radicals, for example, in irradiated glycine,[3] malonic acid,[4,5] succinic acid,[6,7] glutaric acid,[8] and adipic acid,[9] and have accordingly been given a negative sign although this is not determinable from the spectra. The principal values of the α-proton coupling tensor of l-alanine quoted by Miyagawa and Gordy[2] are 19.6, 75.6, and 75.6 Mc/sec. As these authors suggest, the tensor is probably not axially symmetric and we would suggest that our analysis is the more complete.

As has already been stated, the coupling for each of the three equivalent methyl protons is slightly anisotropic, and may be expressed in a tensor form analogous to the α-proton coupling. The coupling tensor of the methyl protons is also listed in Table I.

It will be noted that the diagonalized tensor for the methyl proton coupling is essentially axially symmetrical, and the unique axis is presumably parallel to the $\dot{C}—CH_3$ bond. This may be confirmed by comparing the direction cosines of the unique axis of the methyl tensor with those of the intermediate axis of the α-proton tensor. It is expected that the least, intermediate and largest principal values of an α-proton tensor will occur for directions parallel to the $\dot{C}—H$ bond, perpendicular to the radical plane, and in the radical plane but perpendicular to the $\dot{C}—H$ bond, respectively. From Table I the angle between the unique axis of the methyl tensor and the intermediate axis of the α-proton tensor may be calculated as $88.5° \pm 3°$. It may therefore be concluded that the unique axis of the methyl tensor lies in the radical plane, and is, in fact, the $\dot{C}—CH_3$ bond. The angle between this bond and the $\dot{C}—H$ bond may also be calculated from Table I, and is $121.2° \pm 3°$.

The electron-resonance spectra of irradiated l-alanine thus support a planar skeleton for the radical $CH_3\dot{C}H(CO_2H)$, with sp^2 hybridization of the free radical carbon atom.

The authors gratefully acknowledge helpful discussions with Dr. D. H. Whiffen.

The research forms part of the program of the Basic Physics Division of the National Physical Laboratory, and is published by permission of the Director.

[1] A. van Roggen, L. van Roggen, and W. Gordy, Bull. Am. Phys. Soc. **1**, 266 (1956).
[2] I. Miygawa and W. Gordy, J. Chem. Phys. **32**, 255 (1960).
[3] D. K. Ghosh and D. H. Whiffen, Mol. Phys. **2**, 285 (1959).
[4] H. M. McConnell, C. Heller, T. Cole, and R. W. Fessenden, J. Am. Chem. Soc. **82**, 766 (1960).
[5] A. Horsfield, J. R. Morton, and D. H. Whiffen, Nature **189**, 481 (1961).
[6] C. Heller and H. M. McConnell, J. Chem. Phys. **32**, 1535 (1960).
[7] D. Pooley and D. H. Whiffen, Mol. Phys. **4**, 81 (1961).
[8] A. Horsfield, J. R. Morton, and D. H. Whiffen, Mol. Phys. (to be published).
[9] A. Horsfield and J. R. Morton (to be published).

Isotopic Fractionation of Lithium in Sputtering

J. M. FLUIT, L. FRIEDMAN,* A. J. H. BOERBOOM, AND J. KISTEMAKER

Laboratorium voor Massaspectrografie, Kruislaan 407, Amsterdam/0, The Netherlands

(Received April 19, 1961)

THE phenomenon of cathode sputtering has been discussed in terms of two mechanisms, which are only vaguely distinguishable.

The evaporation mechanism was proposed by Hippel,[1] Blechschmidt,[2] and more recently by Townes.[3] Massey and Burhop[4] assert that it is the most widely accepted theory of cathode sputtering. Wehner[5] in a review of

TABLE I.

Experiment	Ion energy in kev	Measured beam intensity on 2, 1 cm² in μA	Time in min	Isotopic abundance of Li^6 in %
1	20	100	3	7.76
2	5	100	3	7.78
3	20	20	15	7.78
4	5	20	15	7.73
5	analysis of the isotopic composition of target			7.63
6	...	...	...	7.66
7	...	...	...	7.62

the literature favors the momentum interchange model as being more consistent with the available experimental results. It is clear that the momentum transfer must take place between the incident ions and atoms in the sputtered target and eventually sufficient energy must be transferred to the sputtered atom to permit its escape from the solid.

Sputtering which takes place more or less directly as a result of the impact of incident ion or one of its early collision partners on the sputtered atom takes place via a "momentum transfer" mechanism. If on the other hand the sputtering takes place by evaporation of the sputtered atom from a small "hot zone" produced by ion impact then the evaporation model is considered operative.

The models become distinguishable with difficulty when the "hot zone" is limited to only a few atoms or if the momentum transfer process involves many atoms.

If one accepts the evaporation model and assumes that as little as a tenth of the total ion energy is deposited in the "hot zone" then, with 5–20-kev ions, a large number of atoms may be contained in this zone. With low-sputtering rates one should then be able to observe isotopic fractionation in the process.

With momentum transfer sputtering the chances of observing any preferential isotope effect would be very small. These considerations led to an investigation of the sputtering of lithium metal by argon ions in an attempt to determine the role of evaporation in the sputtering process.

Lithium metal was selected for this study because of the relatively large possible separation factor for low-evaporation rates and the relative ease of isotopic analyses of submicrogram quantities collected in the sputtering experiments. A separation factor of 1.08 was estimated by Trauger *et al.*[6] as an upper limit for the molecular distillation of lithium and separation factors of 1.052 and 1.064 were observed by these workers.

Samples of lithium metal were cut in an argon atmosphere and inserted in the target chamber of the Amsterdam isotope separator. The surface of the metal was oriented at approximately 45° with respect to the plane of the incident ion beam. A conical quartz cup was mounted to collect the sputtered lithium. Sputtering experiments were carried out with 5 and 20 kev Ar^{40} ion beams. The intensities of the ion beams were controlled to permit roughly 0.1 μg of lithium to be sputtered. The sputtered lithium was transferred from the quartz cups to sample filaments of a multiple-filament surface-ionization mass spectrometer source for isotopic analysis. The product was dissolved in a few microlitres of distilled water and transfer was made with a quartz micropipette. Blank runs were made and from integrated intensity measurements less than 1% of the total sample concentrations were detected in the blanks.

The results of the sputtering experiments at different beam intensities and with different beam energies are presented in the table along with isotopic analysis of the target lithium. Measurements with 100 and 20 μA beams with constant integrated beam intensity were made to test for a possible effect of diffusion and mixing of material near the surface on the isotopic composition of the sputtered product. No effect of this type or of the energy of the incident ion was detected. A small enrichment in Li^6 over that in the target material was detected but this was less than $\frac{1}{5}$ of the effect measured in evaporation experiments noted above. This indicates that evaporation of the type observed in ordinary distillation experiments plays only a minor role in the sputtering process. This conclusion is based on the above observations, namely that with about 10^{16} atoms sputtered and molten zones which are assumed to contain an aggregate of the order of at least 10^{19} atoms one should see isotopic fractionation in lithium with enrichment factors of 1.05–1.08 with evaporation mechanism.

The precision of isotopic analysis is indicated by fluctuations in the analyses of the target material. All analyses represent the means of at least 20 mass spectrometric isotopic rations.

We thank Dr. P. K. Rol for stimulating discussions at the beginning of these experiments. We wish to thank Mr. S. Doorn and Mr. J. van Roon for their assistance in carrying out these experiments. This work is part of the research program of the Stichting voor Fundamenteel Onderzoek der Materie and was made possible by financial support of the Stichting Zuiver Wetenschappelijk Onderzoek and the U.S. Atomic Energy Commission to L.F.

* Permanent address: Brookhaven National Laboratory, Upton, New York. Guest scientist at FOM-Laboratorium voor Massaspectrografie, Amsterdam, The Netherlands.

[1] A. von Hippel, Ann. Physik **81,** 1043 (1926).
[2] E. Blechschmidt, Ann. Physik **81,** 999 (1926).
[3] C. H. Townes, Phys. Rev. **65,** 319 (1944).
[4] H. S. W. Massey and E. H. S. Burhop, Electronic and Ionic Impact Phenomena (Oxford University Press, New York, 1952), p. 590.
[5] G. K. Wehner, *Advances in Electronics and Electron Physics* (Academic Press, Inc., New York, 1955), p. 239.
[6] D. B. Trauger, J. J. Keyes, Jr., G. A. Kuipers, and D. M. Lang, *Proceedings of the Symposium on Isotope Separation, Amsterdam,* 1957 (North Holland Publishing Company, Amsterdam, 1958), p. 350.

On the Polyelectrolyte-Simple Electrolyte Interaction Parameter

NORIO ISE
School of Chemistry, Rutgers, The State University, New Brunswick, New Jersey
(Received Apil 12, 1961)

RECENTLY, Strauss and Ander, and Eisenberg and Casassa,[1] have studied the interaction between polyelectrolytes and simple electrolytes. If we know the degree of ionization of the macro-ions, these studies allow us to estimate the polyelectrolyte-simple electrolyte interaction parameter β_{23}. In spite of the importance of this quantity, which appears in the second virial coefficient together with the polyelectrolyte-polyelectrolyte interaction parameter β_{22} the theoretical derivation has not been published. In this note, a formulation of β_{23} will be given from an interionic interaction theory, which was used for the interpretation of various solution properties in previous papers,[2] and tested by calculating the molecular dimension from experimental values of β_{23}.

For simplicity, the following assumptions are made: (1) the degree of ionization, the sizes of counter- and by-ions, and the dielectric constant of the solvent are independent of the concentration of simple electrolytes; (2) the intrinsic viscosity $[\eta]$ is given by Einstein's viscosity relation; and (3) $[\eta]C_s^m$ (C_s=salt concentration in mole/liter, m=a constant) is independent of C_s.[3] Then Eqs. (17) and (18) in reference 2(a) give us the following equation for β_{23} at zero polymer concentration:

$$\beta_{23}=(\alpha+1)\frac{\partial \log\gamma_{\pm}}{\partial c_s}=-\frac{N\alpha^2 e_0^2\kappa}{6\times10^3 n_s m_s \epsilon kT}$$
$$\times\left\{\left[1-2n_s v_s\right]\left[\frac{\sigma(\kappa\delta_1)}{\alpha}+\sigma(\kappa R)-\frac{\sigma(\kappa\delta_2)}{2m_s}\right]\right.$$
$$\left.+\sigma(\kappa\delta_2)+n_s\frac{\partial\sigma(\kappa\delta_2)}{\partial n_s}\right\}+\left\{\frac{3\times10m\alpha^2 e_0^2 C_{s0}^m[\eta_0]M}{5\pi\epsilon kTNR^4C_s^{1+m}}\right\}, \quad (1)$$

where N is Avogadro's number, M the molecular weight of polyelectrolyte, and $[\eta_0]$ the intrinsic viscosity in a solution of simple electrolyte of concentration C_{s0} ($[\eta_0]=[\eta](C_s/C_{s0})^m$). Reference 2(a) is to be referred to for other definitions.

A quantitative test of Eq. (1) can be made. One may calculate R, the radius of the macro-ion (assumed to be spherical), using Eq. (1) and the experimental results of Strauss and Ander for the sodium polyphosphate-NaBr system. $[\eta_0]C_{s0}^m=0.179$, with $m=1$, was estimated from the data of Strauss and Wineman.[4] A degree of ionization i of 0.25 was used, based on the result of Wall *et al.*[5] and other observations[6]; δ_1 and δ_2 were assumed 5 A; and $\epsilon=80$ and $T=298°$K were used. The R values obtained are shown in Table I.

TABLE I.

C_s	β_{23}[a]	R	R_E
0.02039	-16.4×10^3	260A	...
0.07896	-4.10×10^3	176	...
0.2549	-0.968×10^3	130	165A[b]
0.4107	-0.592×10^3	112	122[c]

[a] Calculated from Strauss and Ander's result, using $M=332\,000$, and literature values of β_{22} and $i=0.25$.
[b] $C_s=0.25$.
[c] $C_s=0.40$.

The R value may be compared with the radius of an equivalent sphere R_E. R_E can be estimated using $[\eta]$ from Einstein's viscosity relation, judging from the nature of our model. One obtains $R_E=176$ and 238 A at $C_s=0.40$ and $C_s=0.25$, respectively, using Strauss and Wineman's result.[4] Therefore, assuming $R_E\propto M^{\frac{1}{3}}$, R_E for our case ($M=332\,000$) can be estimated and is shown in the fourth column of Table I. In the light of the crude approximations involved in the calculation, one could assert that the agreement between R and R_E is fairly satisfactory and it could be concluded that Eq. (1) is not far from reality.

Needless to say, the basic feature leading to Eq. (1) is that all the interionic interactions, including macro-ion and the intramacro-ion interactions, are taken into consideration. It is very interesting that in a differential quantity such as β_{23}, the electrostatic effect of macro-ions does not vanish at zero polymer concentration.

The dependences of β_{23} on the degree of polymerization, and on the size of counterion will be discussed later.

The writer's appreciation goes to Professor U. P. Strauss for his useful comments. The writer is indebted to the Colgate Postdoctoral Fellowship, during the tenure of which this paper was prepared.

[1] U. P. Strauss and P. Ander, J. Am. Chem. Soc. **80,** 6494 (1958); H. Eisenberg and E. F. Casassa, J. Polymer Sci. **47,** 29 (1960).
[2] (a) N. Ise and M. Hosono, J. Polymer Sci. **39,** 389 (1959); (b) N. Ise *ibid.* **39,** 412 (1959); (c) I. Sakurada and N. Ise, Makromol. Chem. **15,** 126 (1960).
[3] R. A. Cox, J. Polymer Sci. **47,** 441 (1960).
[4] U. P. Strauss and P. L. Wineman, J. Am. Chem. Soc. **80,** 2366 (1958). The data of NaPP-7 (weight average molecular weight = 690000) was used to estimate $[\eta_0]$ C_0^m, using their finding at $C_s=0.415$ that $[\eta]$ is proportional to the square root of the molecular weight. The m value (1) thus obtained is larger than that reported by Cox,[3] who found $m=0.6$ for high molecular-weight fractions. The reason for the discrepancy is not clear but this difference does not have an appreciable effect on R. It is interesting that the experimental data of Na RNA in Cox's work fits $m=1$ much better than $m=0.6$ over the range 10^{-2}–10^{-3} mole/liter of simple electrolyte concentrations.
[5] J. R. Huizenga, P. H. Grieger, and F. T. Wall, J. Am. Chem. Soc. **72,** 2636 (1950); F. T. Wall, H. Terayama, and S. Techakumpuch, J. Polymer Sci. **20,** 477 (1956).
[6] S. Bluestone, Ph.D. thesis, Rutgers, The State University, New Brunswick, New Jersey (1960).

Electron Spin Resonance Absorption of Tris-*p*-Nitrophenylmethyl*

M. THOMAS JONES
Department of Chemistry, Washington University
St. Louis 30, Missouri
(Received April 26, 1961)

THE isotropic hyperfine structure of the electron spin resonance spectra of the nitrogen 14 and nitrogen 15 substituted tris-*p*-nitrophenylmethyl radical[1,2] has been resolved. Ninety-nine and 81 lines of the possible 343 and 196 lines of the nitrogen 14 and nitrogen 15 radical, respectively, have been resolved. The spectra (Fig. 1) have been analyzed in terms of the ortho and meta coupling constants and the nitrogen coupling constant for the nitro group in the para position.

In Fig. 1, the derivatives of the resonance absorption of approximately 5×10^{-4} molar solutions of the radical in 1,2-dimethoxyethane at 22°C are shown. The resolution was not improved by lowering the temperature. The major contaminant in the nitrogen 15 spectrum is the compound in which two of the nitrogens are nuclei of mass 15; the other is of mass 14. This compound should be present to the extent of 12%. The ratio of the most intense line in the compound containing nitrogen 15 in three para positions to that containing nitrogen 15 in two and nitrogen 14 in one is 24:1. Therefore, little trouble should be expected from this contaminant. The spectra were recorded on a spectrometer designed and constructed by Professor J. Townsend of the Department of Physics of Washington University. The field was modulated at 100 kc with an amplitude of 2×10^{-2} gauss. The steady field was supplied by a 12-in. Varian magnet. The linewidths are about 0.07 and 0.12 gauss measured from points of extreme slope for the nitrogen 14 and 15 compounds, respectively.

Following the suggestion that the coupling constants for the ortho and meta protons in the radical are close to those in the triphenylmethyl radical, the absolute values of the various constants are assigned as follows:

	Gauss
N^{15} (in *p*-nitro group)	$=0.94(\pm0.02)$
N^{14} (in *p*-nitro group)	$=0.66(\pm0.01)$
H (meta)	$=1.14(\pm0.02)$
H (ortho)	$=2.50(\pm0.02)$.

The uncertainties given are measures of precision. From these spectra one cannot unambiguously assign the coupling constants for the ortho and meta protons.

The ortho and meta proton coupling constants in the triphenylmethyl radical as determined by Chesnut and Sloan[3] are, respectively, 2.53 and 1.11 gauss. The fact that the spin densities at the carbon atoms adjacent to the ortho and meta protons in the tris-*p*-nitrophenylmethyl radical appear to be unchanged suggests that the spin density at the para carbon atom may be unchanged by the substitution of a nitro group for a proton. Unfortunately, this study cannot yield more information about this point.

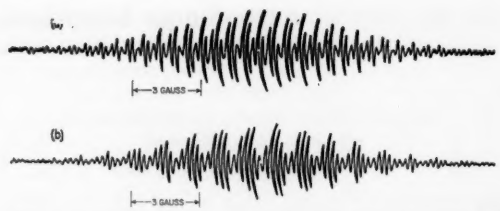

FIG. 1. dX''/dH vs H for the tris-*p*-nitrophenylmethyl radical in DME at a concentration of approximately 5×10^{-4} molar. The temperature was 22°C. (a) Nitrogen 14 labeled radical; (b) nitrogen 15 labeled radical.

The author wishes to express his appreciation for Professor S. I. Weissman's helpful discussions, criticisms, and support.

* This work was supported by the U. S. Air Force through the Air Force Office of Scientific Research of the Air Research and Development Command. Reproduction in whole or in part is permitted for any purpose of the U. S. Government.
[1] T. L. Chu, G. E. Pake, D. E. Paul, J. Townsend, and S. I. Weissman, J. Phys. Chem. **57,** 504 (1953).
[2] J. P. Lloyd and G. E. Pake, Phys. Rev. **92,** 1576 (1953).
[3] D. B. Chesnut and G. J. Sloan, J. Chem. Phys. **33,** 637 (1960).

Note on the Statistical Theory of Mass Spectra

JOHN C. SCHUG AND NORMAN D. COGGESHALL
Gulf Research & Development Company, Pittsburgh, Pennsylvania
(Received March 30, 1961)

THE statistical theory of mass spectra[1] permits one to make reasonable predictions if appropriate values are chosen for its parameters.[1–4] But interpretation of these parameters in terms of transition complexes[1] has proven difficult. Since the theoretical expressions cannot be analytically integrated, it has been necessary to use trial and error calculations to determine the parameters. In this note, we present a simplification, through which the parameters can be studied without trial and error methods.

The theory expresses dissociation rate constants in terms of state density functions.[1] When the molecule is treated as a collection of oscillators, the expressions become

$$k_i=\nu_i(1-\epsilon_i/E)^s, \qquad (1)$$

where ν_i is a frequency factor, ϵ_i is the activation energy for dissociation, E is the excess internal energy of the decaying ion, and s is the number of vibrational degrees of freedom in the activated complex. If secondary dis-

TABLE I. Parameters necessary to interpret abundances of indicated ions (j) relative to that of $C_6H_{13}^+(i)$ in low-voltage pattern of n-octane.[2b]

s	Ion (j)	Minimum E_1	Maximum ν_i/ν_j
$3n-7=71$	$C_3H_7^+$	22.1 ev	1×10^{-14}
	$C_4H_9^+$	12.5	1×10^{-5}
	$C_5H_{11}^+$	6.55	5×10^{-2}
$71/3=23.7$	$C_3H_7^+$	7.20	1×10^{-4}
	$C_4H_9^+$	4.35	8×10^{-2}
	$C_5H_{11}^+$	2.45	8×10^{-1}
$71/5=14.2$	$C_3H_7^+$	4.55	1×10^{-2}
	$C_4H_9^+$	2.72	5×10^{-1}
	$C_5H_{11}^+$	1.54	1

sociations are neglected, the fractional abundance of the ith fragment is

$$F_i=\int_{\epsilon_i}^{E_m}(dF_i/dE)dE=\int_{\epsilon_i}^{\epsilon_j}(dF_i/dE)dE + \int_{\epsilon_j}^{E_m}R_{ij}(E)(dF_j/dE)dE, \quad (2)$$

where E_m is the maximum excess parent-ion energy, and

$$R_{ij}(E)=dF_i/dF_j=(\nu_i/\nu_j)[(E-\epsilon_i)/(E-\epsilon_j)]^s.$$

The mean value theorem for integrals[5] permits the removal of $R_{ij}(E)$ from beneath the integral sign, provided that it be evaluated at a particular energy inside the integration range. Thus

$$F_i \geqslant R_{ij}(E_1)F_j; \qquad \epsilon_j \leqslant E_1 \leqslant E_m. \quad (3)$$

This equation can be rearranged to

$$E_1 \geqslant [(F_i\nu_j/F_j\nu_i)^{1/s}\epsilon_j-\epsilon_i]/[(F_i\nu_j/F_j\nu_i)^{1/s}-1], \quad (4)$$

which is applicable when $(F_i\nu_j/F_j\nu_i)>1$. Alternatively, if it is possible to specify an energy, E_2, such that $E_2 \geqslant E_m \geqslant E_1$, then it follows that

$$\nu_i/\nu_j \leqslant (F_i/F_j)[(E_2-\epsilon_j)/(E_2-\epsilon_i)]^s. \quad (5)$$

Relative abundances of $C_nH_{2n+1}^+$ ions in low-voltage patterns of n-paraffins[2b] have been examined in the light of these relations. First, Eq. (4) was applied by assuming that activation energies correspond exactly with appearance potentials, and that (ν_i/ν_j) is unity for pairs of simple C—C bond dissociations; s was taken as $(3n\text{-}7)$, the total number of vibrational degrees of freedom in the transition complex. For the various pairs of ions, Eq. (4) showed that $E_1 \geqslant 6$ to 31 ev. These results contradict the theory, for the spectra were obtained with ionizing voltages 1.5 to 2.0 v above parent-ion appearance potentials.[2b]

Equation (5), applied to the same data by setting $E_2=2.0$ ev, showed that the ratios of the several pairs of frequency factors had to be smaller than 10^{-2} to 10^{-17}. Most values in this range are unrealistic. For example, a number of frequency factors were estimated from skeletal frequencies based on a zig-zag chain model[6] and allowing for small differences in force constants between radicals and ions. Ratios of these estimated frequency factors were always in the neighborhood of unity.

Some typical results are given in Table I, which also indicates how the data can be made more acceptable by reducing the number of active vibrational degrees of freedom.[7] In many of the cases examined, it was necessary to reduce s to $\frac{1}{10}$th its original value in order for Eqs. (4) and (5) to produce reasonable results.

Such inconsistencies are not limited to lower n-paraffins. Calculations based on the spectrum of n-pentadecane, obtained at this laboratory, encounter the same difficulties.

Although it appears that low-voltage mass spectra are not amenable to interpretation by the simplified statistical theory, there remains the possibility that some fragment-ions may result from two-step processes.[8] Also, we should point out that identical treatments of high-energy spectra give much more reasonable results.

[1] H. M. Rosenstock, M. B. Wallenstein, A. L. Wahrhaftig, and H. Eyring, Proc. Natl. Acad. Sci. U. S. **38,** 667 (1952).
[2] L. Friedman, F. A. Long, and M. Wolfsberg, (a) J. Chem. Phys. **27,** 613 (1957); (b) *ibid.* **30,** 1605 (1959); (c) *ibid.* **31,** 755 (1959).
[3] A. Kropf, E. M. Eyring, A. L. Wahrhaftig, and H. Eyring, J. Chem. Phys. **32,** 149 (1960).
[4] E. M. Eyring and A. L. Wahrhaftig, J. Chem. Phys. **34,** 23 (1961).
[5] I. S. Sokolnikoff, *Advanced Calculus* (McGraw-Hill Book Co., Inc., New York, 1939), p. 113.
[6] K. S. Pitzer, J. Chem. Phys. **8,** 711 (1940).
[7] W. A. Chupka, J. Chem. Phys. **30,** 191 (1959).
[8] J. H. Beynon, R. A. Saunders, A. Topham, and A. E. Williams, J. Phys. Chem. **65,** 114 (1961).

Use of Distorted Atomic Orbitals in Molecular Wave Functions*

R. L. MILLER† AND PETER G. LYKOS‡
Department of Chemistry, Illinois Institute of Technology, Chicago 16, Illinois

(Received May 16, 1961)

A CRITICAL examination into the meaning of the integrals over atomic orbitals used in semiempirical molecular calculations has recently been set forth.[1] In an attempt to gain insight into their meaning, we have undertaken a preliminary study of two similar types of three-parameter, distorted atomic orbitals for the $^2\Sigma_g^+$ and $^2\Pi_u$ states of H_2^+.

We have followed the formalism and extended the results given by Mulliken *et al.*[2] For the $^2\Sigma_g^+$ state we have used distorted atomic wave functions of the form

$$\sigma_1(\zeta)=N[C_1 1s(\zeta)+C_2 2p\sigma(\zeta)+C_3 3d\sigma(\zeta)] \quad (1)$$

and

$$\sigma_2(\zeta)=N'e^{-\zeta r}[C_1'+C_2'z+C_3'z^2]. \quad (2)$$

TABLE I. Energy of the lowest $^2\Sigma_g^+$ and $^3\Pi_u$ states of H_2^+.

Fxn.	$-E_B$[a](a.u.)	$-E'$ (a.u.)	$-E''$ (a.u.)	R (a.u.)	ζ	C_1	C_2	C_3
$\sigma_1(\zeta)$	0.60262	0.60183	0.59980	2.0	1.244	0.531	0.104	0.0345
$\sigma_2(\zeta)$	0.60262	0.60143	0.59980	2.0	1.309	0.502	0.103	0.0568
$\pi_1(\zeta)$	0.13451	0.13404	0.13305	8.0	0.5697	0.553	0.150	0.0585
$\pi_2(\zeta)$	0.13451	0.13324	0.13305	8.0	0.5732	0.568	0.146	0.0126

[a] See text for explanation of the various headings.

These are formed as appropriate linear combinations of Slater-type orbitals (STO's) with a common orbital exponent ζ, which is determined variationally together with the linear coefficients so as to minimize the total energy of the system. A symmetric combination of a $\sigma_1(\xi)$ atomic orbital at each nucleus is then taken to build up the molecular orbital (MO) approximation to the $^2\Sigma_g^+$ state. A similar MO is formed from $\sigma_2(\xi)$ functions.

In an analogous fashion, for the $^2\Pi_u$ state, we have considered functions of the form

$$\pi_1(\zeta) = N[C_1 2p\pi(\zeta) + C_2 3d\pi(\zeta) + C_3 4f\pi(\zeta)] \quad (3)$$

and

$$\pi_2(\zeta) = xe^{-\zeta r}[C_1' + C_2' z + C_3' z^2].$$

In molecule formation the phrase "deformed orbital" has been used to describe the relaxation of the orbital scale parameter only.[3] Here we are allowing the symmetry of the orbital as well as its scale to adjust variationally in the two similar ways suggested by the form of the potential.

Collected in Table I are results for the functions described above, together with the corresponding values for the accurate theoretical energy E_B, due to Bates *et al.*[4] For comparison, we have included E'' the energy obtained when C_3 or C_3' is set equal to zero. (For the $^2\Sigma_g^+$ state this is the Dickinson[5] function.) The C_i in the table constitute the orbital eigenvectors, and ζ the orbital exponent corresponding to E', the energy obtained for the three parameter functions. For the purpose of these comparisons we have chosen R, the internuclear separation, to be around the equilibrium distances.

If we use the total energy as a measure of "goodness" of these approximate wave functions, we find that the distorted atomic orbitals used here are superior to all three parameter atomic orbitals which have been used in a similar way by other workers.[6,7] Since we are using STO's as our ultimate basis functions, the distorted orbital functions of type 2, i.e., $\sigma_2(\zeta)$, $\pi_2(\zeta)$, are more complicated and lead to results which are not quite as good as those of type 1, i.e., $\sigma_1(\zeta)$, $\pi_2(\zeta)$.

Further work is in progress in which we are (1) treating a wide range of internuclear separation, (2) obtaining corresponding antibonding functions, and (3) considering a series of model systems whose orbital characteristics will be of interest as applied to other molecular systems.[8]

We should like to thank Dr. H. N. Schmeising of this laboratory for his considerable help in the computer programming, and the Illinois Institute of Technology for a grant of Univac 1105 machine time.

* Based on part of a thesis to be submitted by R.L.M. in partial fulfillment of the requirements for the Ph.D. degree, at the Illinois Institute of Technology.

† National Science Foundation, Science Faculty Fellow, on leave of absence from the University of Illinois, Navy Pier, Chicago (1960–1961).

‡ This work was supported in part by a grant from the National Institutes of Health.

[1] P. G. Lykos, J. Chem. Phys. (to be published).
[2] R. S. Mulliken, C. A. Reike, D. Orloff, and H. Orloff, J. Chem. Phys. **17,** 1248 (1949).
[3] T. Arai, Revs. Modern Phys. **32,** 370 (1960).
[4] D. R. Bates, K. Ledsham, and A. L. Stewart, Trans. Roy. Soc. (London) **A246,** 215 (1953).
[5] B. N. Dickenson, J. Chem. Phys. **1,** 317 (1933).
[6] M. Geller, A. A. Frost, and P. G. Lykos, paper presented at September 1958 National A.C.S. meeting in Chicago.
[7] O. J. Sovers and W. Kauzmann (to be published).
[8] See, for example, E. Clementi, J. Chem. Phys. **34,** 1468 (1961).

Tables for the Internal Rotation Problem*

MICHIRO HAYASHI AND LOUIS PIERCE

Department of Chemistry, University of Notre Dame, Notre Dame, Indiana

(Received June 7, 1961)

THIS work respresents an extension of the tabulation by Herschbach[1] of matrix elements and perturbation sums associated with certain of the periodic solutions[2,3] of Mathieu's equation. The original tables (Herschbach's) were designed for application to problems involving hindered internal rotation in molecules, particularly the analysis of microwave spectra of molecules with a single internal top having threefold symmetry attached to an asymmetric frame, e.g., ethyl fluoride (CH_3CH_2F).[4,5] However, the tables are also a useful starting point for the application of perturbation theory to the problem of hindered internal rotation in molecules having two symmetric internal tops, e.g.,

dimethyl silane $(CH_3)_2SiH_2$[6] or ethyl silane $(CH_3CH_2SiH_3)$. Extension of the original tables was undertaken by us mainly because of our interest in the two-top problem. In general the two-top problem requires matrix elements at intervals of the reduced barrier parameter (the parameter s of Mathieu's equation) which are smaller than those in the original tables.

The original tables[1] give matrix elements of the operators $p=-i\partial/\partial\alpha$, p^2, p^3, and $\cos 6\alpha$ for the lowest eight (E levels) or lowest nine (A levels) torsional states ($v=0$ to 8 or 9) associated with a threefold barrier.[7] These elements depend only on a reduced barrier parameter $s=4V_3/9F$ and are given for 20 values of s in the range 2–100. The present extension tabulates the same quantities for eight values of s in the range 24–96. The present tables also give matrix elements of $\sin 3\alpha$ and $(1-\cos 3\alpha)$ for the lowest eight torsional states at 22 values of s in the range 16 to 100. Matrix elements of $\sin 3\alpha$ are not required for the one-top problem, but are necessary for perturbation treatment of molecules with two or more internal tops. In addition we have also extended Herschbach's Tables[5] of w_l and $W_{vv'}^{(n)}$. The w_l quantities are Fourier coefficients of Mathieu eigenvalues, and the $W_{vv'}^{(n)}$ are perturbation sums required in the application of the so-called "principal axis" method[4,5] to the analysis of microwave spectra of molecules having threefold symmetric internal tops.

The tables were compiled with the aid of an IBM 1620 digital computer. General statements concerning accuracy made in the introduction to Herschbach's tables apply also to the present tables. Mimeographed copies of the tables are available from Professor Louis Pierce. Microfilm copies can be obtained from the American Documentation Institute.[8]

Tables of perturbation sums directly applicable to the problem of coupling of internal torsion and overall rotation in two-top molecules have also been compiled by us. The two-top tables will be described elsewhere.[9]

* The compilation of these tables was made possible by a grant from the National Science Foundation.

[1] D. R. Herschbach, *Tables for the Internal Rotation Problem* (Department of Chemistry, Harvard University, 1957). Mimeographed copies available on request to Professor E. B. Wilson, Jr. See also, D. R. Herschbach, J. Chem. Phys. **27,** 975 (1957).

[2] *Tables Relating to Mathieu Functions* (Columbia University Press, New York 1951).

[3] R. W. Kilb, *Tables of Degenerate Mathieu Functions* (Department of Chemistry, Harvard University, 1956). Mimeographed copies available on request to Professor E. B. Wilson, Jr.

[4] R. W. Kilb, C. C. Lin, and E. B. Wilson, Jr., J. Chem. Phys. **26,** 1695 (1957).

[5] D. R. Herschbach, J. Chem. Phys. **31,** 91 (1959).

[6] L. Pierce, J. Chem. Phys. **34,** 498 (1961).

[7] For notation, see references 4 and 5.

[8] These tables have been deposited as Document number 6825 with the ADI Auxiliary Publications Project, Photoduplication Service, Library of Congress, Washington 25, D. C. A copy may be secured by remitting $7.50 for photoprints, or $2.75 for 35-mm microfilm. Advance payment is required. Make checks or money orders payable to Chief, Photoduplication Service, Library of Congress.

[9] L. Pierce and M. Hayashi (to be published).

Low Temperature Specific Heat of Molybdenum*

C. A. Bryant† and P. H. Keesom

Department of Physics, Purdue University, Lafayette, Indiana

(Received May 24, 1961)

In connection with an investigation of superconducting Mo-Rh alloys, we measured two pure molybdenum specimens and report the results here. Mo A(1) was a pellet prepared by melting Mo powder of 99.8% purity in a helium arc furnace and quenching on a water-cooled copper hearth.[1] The other specimen was a rod, sintered and ground by the Johnson-Matthey Company, which had a nominal 99.99% purity and more nearly the density of a perfect crystal (10.29 g/cm³). The values of γ and θ_0 given in Table I characterize the least-mean-squared deviation fit of the expression

$$C/T=\gamma+(12\pi^4/5)R\theta_0^{-3}T^2$$

to the specific heat data $C(T)$. Errors are three times the standard statistical variance, while systematic devi-

Table I. Results of heat capacity measurements on molybdenum.

Measurement	Temperature range °K	Purity %	Density g/cm³	θ_0 °K	γ, millijoule/mole deg²
Mo A(1)[a]	1.0–4.2	99.8	9.985	427±26	1.93±0.03
Mo rod[a]	1.1–4.5	99.99	10.14	458±15	1.91±0.02
Horowitz and Daunt[4]	1.3–10.5	99.9		445	2.14±0.2
Rayne[5]	0.1–1	99.9			2.20±0.1
Clusius and Franzosini[6]	10–273	99.99	10.231	454	2.1±0.2

[a] Present work.

ations are estimated to be not more than an additional percent (we used the 1958 helium vapor pressure temperature scale). Data were taken only between 1 and 4.5°K, helium exchange gas being used to cool the specimens[2] with the exception of one run of the Mo rod. In that measurement, a mechanical heat switch was used instead of exchange gas,[3] with the same result.

The variation in θ_0 is not surprising in view of the different methods of preparation. The best value is taken to be 458 ± 15°K, for the denser specimen. Values for the coefficient of the electronic term γ, while agreeing for our two specimens, are lower than all those previously reported,[4–6] although only the difference from Rayne's measurements is greater than combined errors. We are not able to judge whether the disagreement is a consequence of differences in the samples or in the method of measurement.

* Supported by a Signal Corps contract.

† Present address: IBM Research Center, Yorktown, New York.

[1] We are indebted to Dr. B. T. Matthias and Mr. E. Corenzwit of the Bell Telephone Laboratories for preparing the molybdenum pellet.

[2] A description of the cryostat is given by N. Pearlman and P. H. Keesom, Phys. Rev. **88,** 398 (1952). In our Mo measurements, a carbon resistance thermometer replaced their phosphor bronze wire and was calibrated against the 1958 temperature scale.

[3] G. M. Seidel and P. H. Keesom, Rev. Sci. Instr. **29,** 606 (1958).

[4] M. Horowitz and J. G. Daunt, Phys. Rev. **91,** 1099 (1953).

[5] J. Rayne, Phys. Rev. **95,** 1428 (1954).

[6] K. Clusius and P. Franzosini, Z. Naturforsch. **14A,** 99 (1959).